

PROCEEDINGS OF 48TH INTERNATIONAL WIRE AND CABLE SYMPOSIUM

Sponsored by
International Wire and Cable Symposium, Inc. (IWCS)
Eatontown, New Jersey
Website: <http://www.iwcs.org/iwcs/>
Email: iwcs@monmouth.com

With Participation by
US Army Communications-Electronics Command (CECOM)
Fort Monmouth, New Jersey

Supporting Associate
Europacable, Brussels, Belgium

**TRUMP TAJ MAHAL CASINO-RESORT
ATLANTIC CITY, NEW JERSEY
NOVEMBER 15, 16, 17 AND 18, 1999**

APPROVED FOR PUBLIC RELEASE: DISTRIBUTION UNLIMITED

DTIC QUALITY INSPECTED 1

20000210 057

MISSION

The International Wire and Cable Symposium provides a forum for the exchange of technical information amongst suppliers, manufacturers, and users on technological advancements in materials, processes, and products used for voice, data and video signal transmission systems.

TECHNICAL PAPERS

Tuesday, November 16, 1999

9:00 am	PLENARY SESSION	Development and Growth of a Modern North American Communications Network Designed to Meet the Needs of the New Millennium
		Track 1-- Fiber
10:30 am	SESSION 1	Fiber Optic Cable Design I
10:30 am	SESSION 2	Fiber Properties
		Track 2 -- Materials
10:30 am	SESSION 3	Fiber Ribbons
		Track 3 -- Copper
10:30 am	SESSION 4	Metallic Cables in Telecommunications Networks
		Track 1 -- Fiber
1:30 pm	SESSION 5	Fiber Optic Cable Design II
1:30 pm	SESSION 6	Fiber Optic Cable Installation
		Track 2 -- Materials
1:30 pm	SESSION 7	Cable Materials
		Track 3 -- Copper
1:30 pm	SESSION 8	LAN/Data Cables

Wednesday, November 17, 1999

		Track 1 -- Fiber
8:00 am	SESSION 9	Fiber Optic Submarine Cables
8:00 am	SESSION 10	Fiber Optic Connector & Components
8:00 am	SESSION 11	Fiber & Cable Processing
		Track 2 -- Materials
8:00 am	SESSION 12	Flame Retardant Materials
		Panel Discussions
2:15 pm	SESSION 13	Wireless in the Home and Office
2:15 pm	SESSION 14	Twisted-Pair LAN Cabling – An Interactive Technical Update
4:00 pm	SESSION 15	Poster Papers

Thursday, November 18, 1999

		Track 1 -- Fiber
8:30 am	SESSION 16	Fiber Optic Aerial Cables
8:30 am	SESSION 17	Splicing / Testing & Field Evaluation I
		Track 2 -- Materials
8:30 am	SESSION 18	Optical Fiber Coatings
		Panel Discussion
8:30 am	SESSION 19	Manufacturing & Processes/Productivity Improvements
		Track 1 -- Fiber
1:00 pm	SESSION 20	Fiber Optic Aerial / Premises Cables
1:00 pm	SESSION 21	Testing & Field Evaluation II
		Track 2 -- Materials
1:00 pm	SESSION 22	Jacketing
		Track 3 -- Copper
1:00 pm	SESSION 23	Coax/HF Cables

PAPERS

The papers in this volume were printed directly from unedited reproducible copies prepared by the authors. Responsibility for contents rests upon the authors and not the symposium committee or its members. All rights reserved by the International Wire and Cable Symposium, Inc., 174 Main Street, Eatontown, New Jersey 07724.

PROCEEDINGS/PUBLICATIONS INTERNATIONAL WIRE AND CABLE SYMPOSIUM (IWCS)

Proceedings - Bound - Available from IWCS

39th IWCS Proceedings - 1990 - \$15.00	46th IWCS Proceedings - 1997 - \$30.00
40th IWCS Proceedings - 1991 - \$25.00	47th IWCS Proceedings - 1998 - \$30.00
44th IWCS Proceedings - 1995 - \$40.00	48th IWCS Proceedings - 1999 - \$50.00

Copies of original proceedings not listed above can be reproduced for \$75.00 per copy plus shipping.

CD's 46th, 47th & 48th IWCS CD - \$10.00

Publications - Bound - Available from IWCS

Index of IWCS Papers (1983-1990); PUB #1001RP-1991	-	\$15.00
PIC Insulation Testing Field Experience; PUB #1003RP-1992	-	\$25.00

Extra Copies of the 1998 Proceedings can be obtained for: 1 - \$50; 2 - \$100; 3 - \$150; 4 - \$190; 5 - \$230; 6 - \$270; 7 - \$310; 8 - \$350; 9 - \$390; 10 - \$430; 11 and above - \$430 plus \$30 for each additional copy.

Shipping/Handling:

Proceedings

\$ 8.00 per copy USA only
\$20.00 per copy Surface Mail (overseas - 4 to 6 weeks)
\$35.00 per copy Airmail (Europe)
\$40.00 per copy Airmail (Asia)

Publications

\$ 4.00 per copy USA Only
\$10.00 per copy Surface Mail (overseas - 4 to 6 weeks)
\$15.00 per copy Airmail (Europe and Asia)

CDs

\$ 3.00 per copy USA Only
\$ 7.00 per copy Canada
\$10.00 per copy Air/Surface Mail

Payment: Make a check or bank draft payable in U.S. Dollars drawn on a U.S. Bank, to the INTERNATIONAL WIRE & CABLE SYMPOSIUM, INC. or use your VISA/MC/AMEX by providing number and expiration date and forward request to: International Wire and Cable Symposium, Inc., 174 Main Street, Eatontown, NJ 07724. Telephone inquiries may be directed to Ms. Pat Hudak (732) 389-0990. Prices are subject to change.

Photocopies are available for complete sets of papers for 1964 through 1998. Information on prices and shipping charges should be requested from the: US Department of Commerce, National Technical Information Service (NTIS), Springfield, Virginia 22161, Telephone: (703) 487-4650

Include Title, Year and "AD" Number

13th Annual Wire Cable Symposium (1964)	- AD 787164
15th Annual Wire Cable Symposium (1966)	- AD A006601
16th International Wire Cable Symposium (1967)	- AD 787165
17th International Wire Cable Symposium (1968)	- AD 787166
18th International Wire Cable Symposium (1969)	- AD 787167
19th International Wire Cable Symposium Proceedings 1970	- AD 714985
20th International Wire Cable Symposium Proceedings 1971	- AD 733399
21st International Wire Cable Symposium Proceedings 1972	- AD 752908
22nd International Wire Cable Symposium Proceedings 1973	- AD 772914
23rd International Wire Cable Symposium Proceedings 1974	- AD A003251
24th International Wire Cable Symposium Proceedings 1975	- AD A017787
25th International Wire Cable Symposium Proceedings 1976	- AD A032801
26th International Wire Cable Symposium Proceedings 1977	- AD A047609
27th International Wire Cable Symposium Proceedings 1978	- AD A062322
28th International Wire Cable Symposium Proceedings 1979	- AD A081428
29th International Wire Cable Symposium Proceedings 1980	- AD A096308
30th International Wire Cable Symposium Proceedings 1981	- AD A110859
31st International Wire Cable Symposium Proceedings 1982	- AD A125662
32nd International Wire Cable Symposium Proceedings 1983	- AD A136749
33rd International Wire Cable Symposium Proceedings 1984	- AD A152119
34th International Wire Cable Symposium Proceedings 1985	- AD A164384
35th International Wire Cable Symposium Proceedings 1986	- AD A180828
36th International Wire Cable Symposium Proceedings 1987	- AD A189610
37th International Wire Cable Symposium Proceedings 1988	- AD A200903
38th International Wire Cable Symposium Proceedings 1989	- AD A216023
39th International Wire Cable Symposium Proceedings 1990	- AD A233634
40th International Wire Cable Symposium Proceedings 1991	- AD A244038
41st International Wire Cable Symposium Proceedings 1992	- AD A259235
42nd International Wire Cable Symposium Proceedings 1993	- AD A279242
43rd International Wire Cable Symposium Proceedings 1994	- AD A293473
44th International Wire Cable Symposium Proceedings 1995	- AD A303506
45th International Wire Cable Symposium Proceedings 1996	- AD A324572
46th International Wire Cable Symposium Proceedings 1997	- AD A338941
47th International Wire Cable Symposium Proceedings 1998	- AD A358377
Kwic Index of Technical Papers, International Wire Cable Symposium (1952-1982)	- AD A027588



MESSAGE FROM THE PRESIDENT/DIRECTOR

Preparation for this year's symposium was as always exciting and interesting. It is admitted that much of the work required is redundant, but what is magical each year, is the assemblage of information that represents the latest in new developments and usage of wire/cable technology. The papers included in these proceedings represents changing trends in an emerging evolution of ideas, that are essential for advancing the designs required for new networks and modernization of the telecommunication industry. An IWCS attendee once wrote or stated that the symposium is an ideal forum for discussing new ideas and products and to spot the industry's trend for new technologies. What is extremely exciting about the IWCS, is the large international participation that are represented not only by the large number of attendees but also by the large number of technical papers presented. This offers the IWCS attendees the opportunity to review the changes that are taking place world-wide.

The technical program includes three special panels in addition to the three distinct tracks devoted to copper, fiber cables and materials. The invited panels features experts in each field to discuss a) Wireless in the Home and Office; b) Twisted-Pair LAN Cabling - An Interactive Technical Update; and c) MFG & Processes/Productivity Improvements. The opening or plenary session speakers MG Robert L. Nabors, Commanding General, United States Army, Fort Monmouth, NJ and Stephen R. Baker, Worldwide Fiber Inc., Vancouver, British Columbia, Canada should provide the interest and enthusiasm for the beginning of a great symposium. Wednesday Luncheon speaker Dr. Lowell Catlett, who was truly a great success at last year's luncheon is back again to give us some insights on a Guide to the 21st Century. The ever popular poster session and the suppliers forum will provide attendees the opportunity to discuss one-on-one with the poster presenter and suppliers topic of special interest.

Committee members Hirotoshi Hondo, The Furukawa Electric Company Limited, Japan; Fred Narayan, Phelps Dodge International Corporation and Michel Rousseau, Alcatel, France are retiring from the committee this year. The committee and I extend to Hondo, Fred and Michel our sincere thanks and appreciation for their dedication and support of the symposium's program and objections.

The IWCS Committee, CECOM, Fort Monmouth and Europacable, Brussels extend to each and every attendee and supporter of the symposium, a hearty welcome and thanks for your continued support. With your support the committee will continue to provide you with the latest information on new developments and advancement in wire/cable technology.

I anticipate this will again be a great symposium, especially with the return to Atlantic City. Many of us will remember the days when we had only one track and copper along with materials were the main topics of interest. The only other attraction in Atlantic City at that time, was the Boardwalk with its small shops and restaurants; no casinos and bright lights as you will find during this year's symposium.

Elmer F. Godwin
President/Director

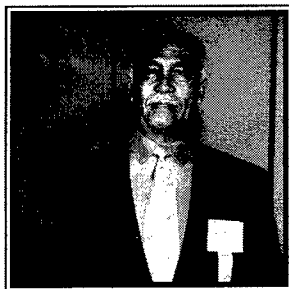
HIGHLIGHTS OF THE 47TH IWCS

International Wire and Cable Symposium

November 16, 17, 18 and 19, 1998

Philadelphia Marriott Hotel, Philadelphia, Pennsylvania

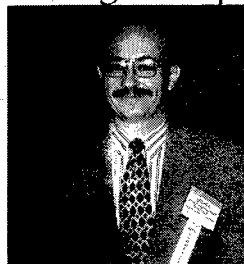
Announcements/Greetings



Elmer F. Godwin
President/Director, IWCS
Eatontown, NJ



Guest Speakers Plenary Session



DR. MAREK KAPUSCINSKI
Chairman, Plenary Session, NORDX/CDT
Quebec, Canada



DR. ARNO PENZIAS
Retired Lucent Technologies
Norcross, GA



John R. Sicotte
IWCS Chairman
Corning Incorporated
Corning, NY

Luncheon Speaker



DR. LOWELL CATLETT
Las Cruces, New Mexico

Scholarship Recipients



Xavier Mann Of IWCS
(on left) presenting Scholarship check to
John D. Taliaferro of Virginia Tech



Jothan Bowen
Attending
Texas A&M University



Outstanding Technical
John Sicotte of IWCS (on left) making Presentation to (from left to right) **Debra A. Simoff**, **Dr. Mark A. Paczkowski**, & **Valerie J. Kuck**, Lucent Technologies, Murray Hill, NJ (who are also accepting for) **Dr. Daryl Inniss**, **Dr. Thomas A. Strasser**, **J. Renee Pedrazzani**, **Dr. Rolando P. Espindola**, **Dr. Robert M. Atkins**, **Katherine T. Nelson**, **John M. Borick** and **Jennifer Aspell**, Lucent Technologies, Murray Hill, NJ; and **Regina Ragan**, California Institute of Technology, Pasadena, CA

Award Winners

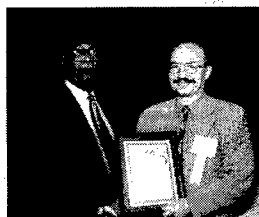


Outstanding Poster Paper
John Sicotte of IWCS (on left) making presentation to **Marko Makinen** who is accepting for **Katja Lyytikainen**, Nextrom Oy, Vantaa, Finland



Best Presentation
John Sicotte of IWCS (on left) making presentation to **Dr. Neil R. Haigh**, BICC Cables Ltd., Helsby, United Kingdom

IWCS Retirees



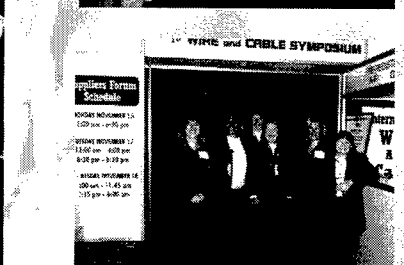
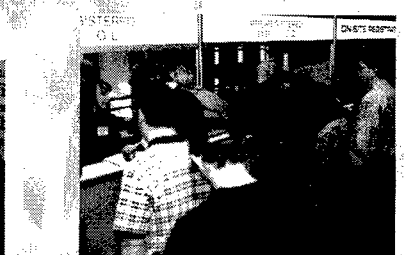
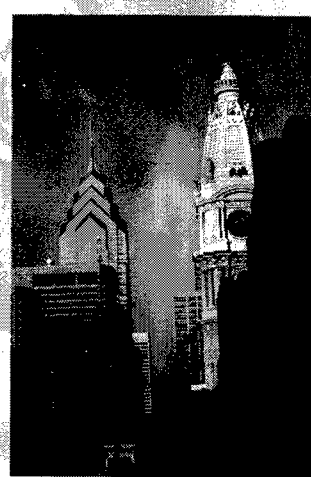
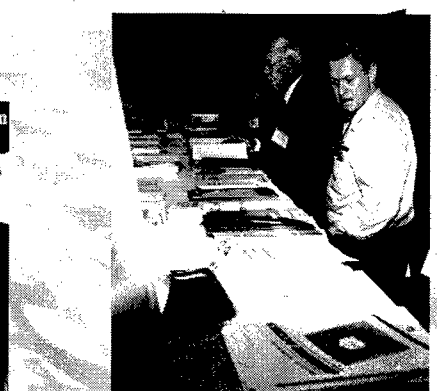
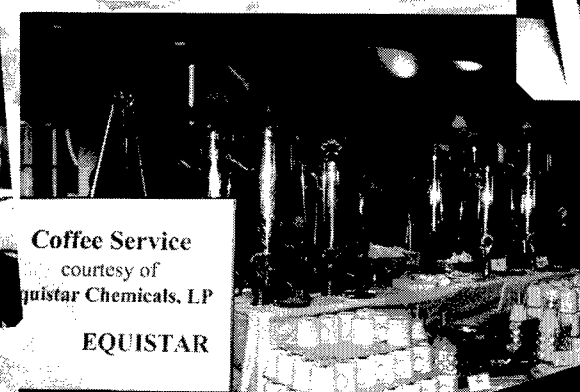
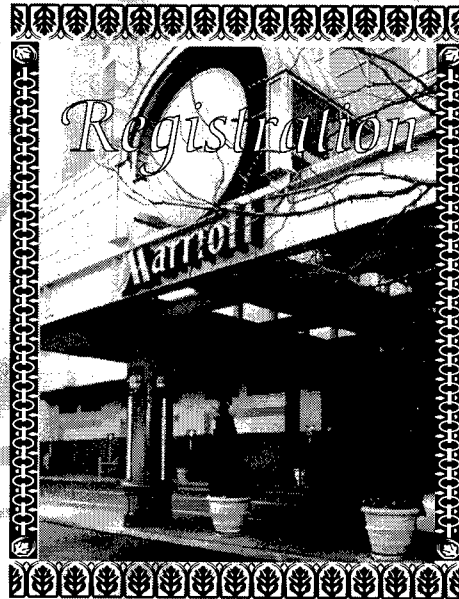
Elmer F. Godwin of IWCS (on left) presenting a Retirement Certificate to **Mr. Marek Kapuscinski**, NORDX/CDT, Quebec, Canada

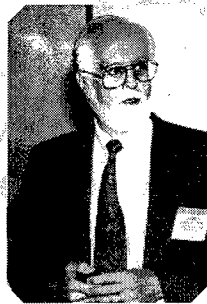
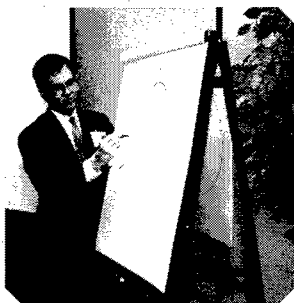
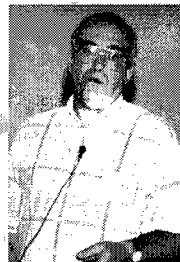


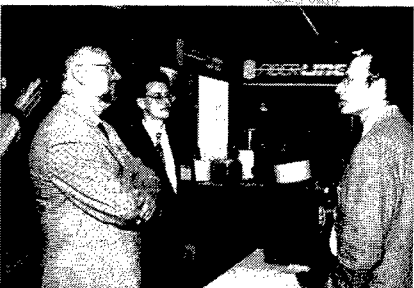
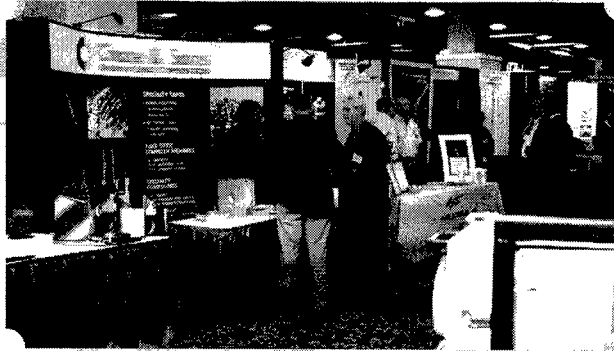
Elmer F. Godwin of IWCS (on left) presenting a Retirement Certificate to **James A. Caballero**, Synergistics Industries (NJ) Inc., Farmingdale, NJ

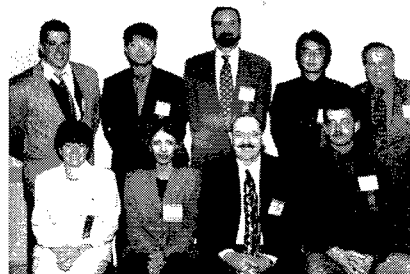
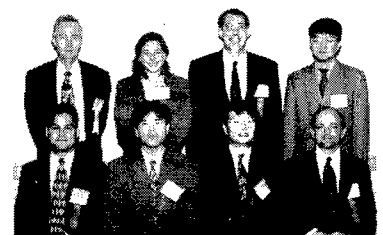
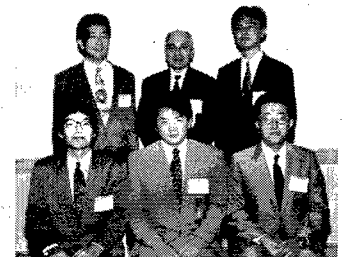
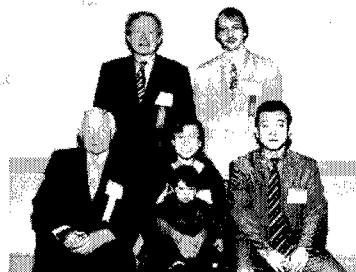
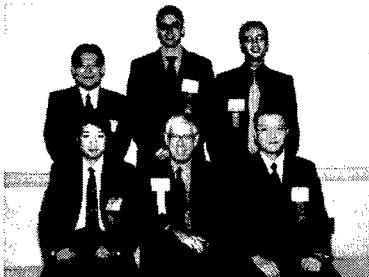
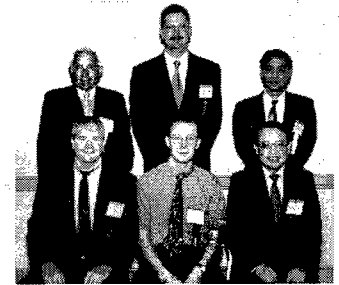
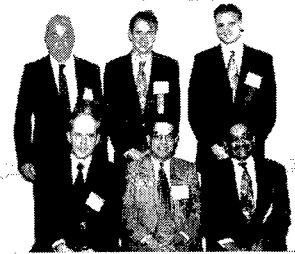
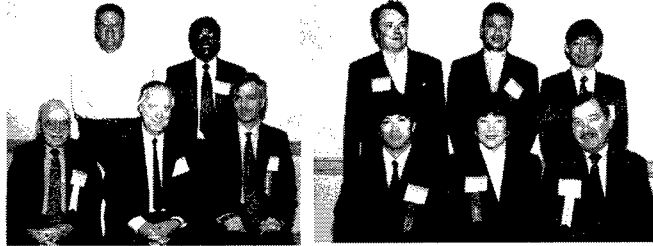


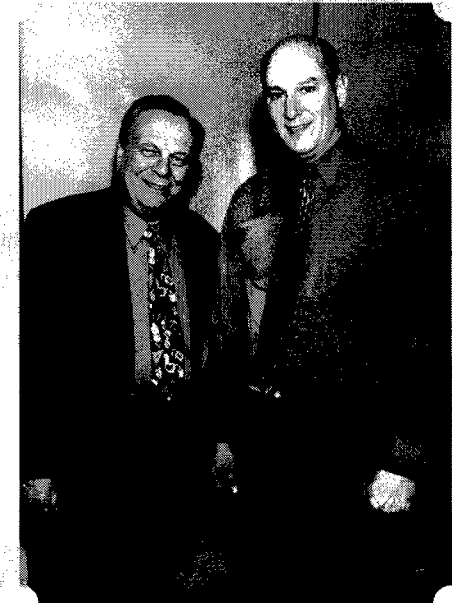
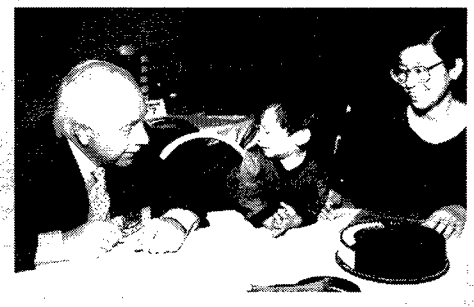
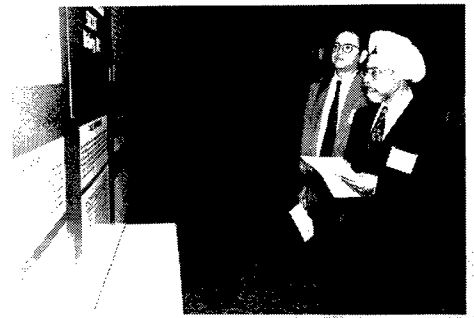
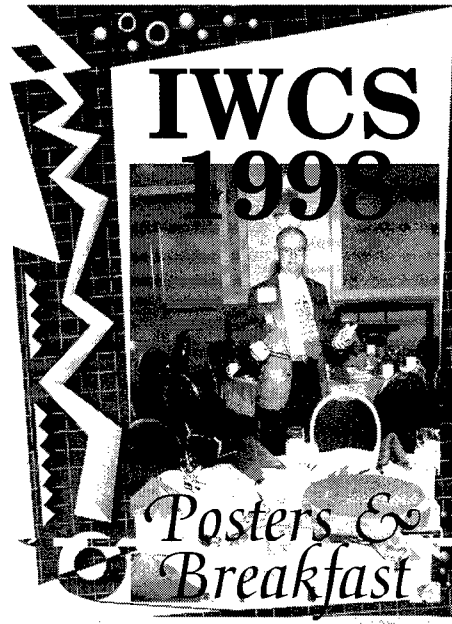
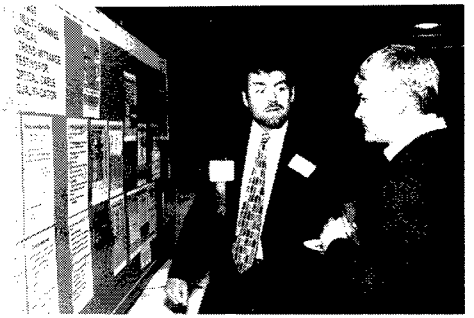
Elmer F. Godwin of IWCS (on left) presenting a Retirement Platter to **Leo Chatter**, DCM Industries, Inc., Union City, CA

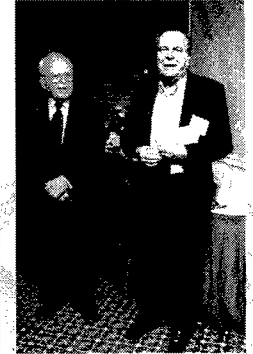
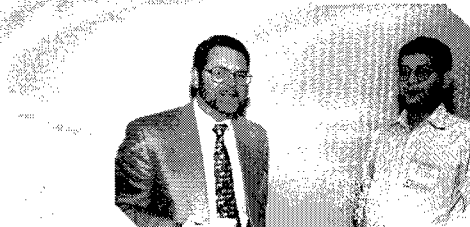
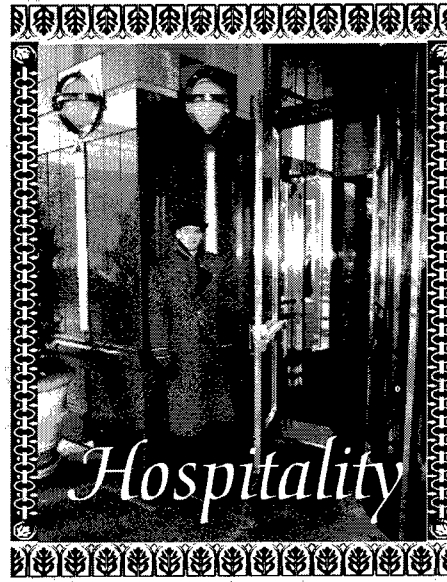


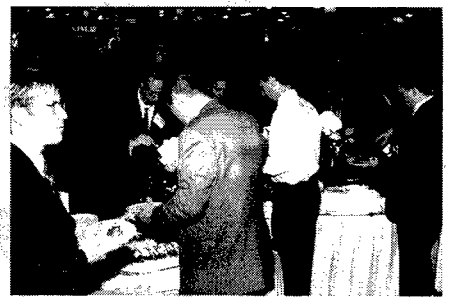
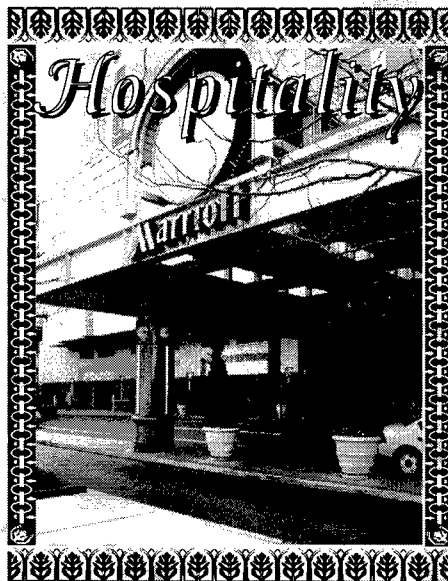
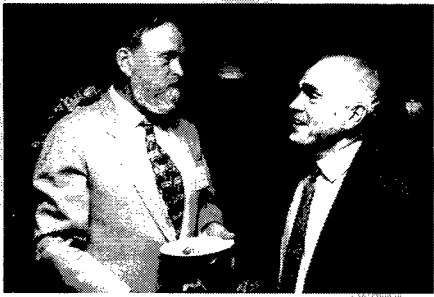












ELMER F. "ACE" GODWIN SCHOLARSHIP

1994

Sara Ransom, Massachusetts Institute of Technology,
Freshman — Materials Science Engineering Major

Jurron Bradley, Vanderbilt University, Senior —
Chemical Engineering Major

1995

Jason Chang, Princeton University, Freshman —
Chemistry Major

Fionna Murray, Virginia Tech, Junior — Mechanical
Engineering Major

1996

Anthony Tindall, Cornell University, Freshman —
Mechanical Engineering Major

John Belle, North Carolina State University,
Sophomore — Electrical Engineering Major

1997

Michael Rich, Georgia Institute of Technology, Fresh-
man — Electrical Engineering Major

Janet Armstrong, Rutgers University, Ph.D. Candidate,
Ceramic Engineering Major

Billy Oates, Georgia Institute of Technology, Senior,
Mechanical Engineering and Math Major

1998

Jothan Bowen, Texas A&M University, Freshman —
Digital Communications and Computers

John D. Taliaferro, Virginia Tech, Junior — Chemical
Engineering

AWARDS

Outstanding Technical Paper

- H. Lubars and J. A. Olszewski, General Cable Corp. — "Analysis of Structural Return Loss in CATV Coaxial Cable"
- J. P. McCann, R. Sabia and B. Wargotz, Bell Laboratories — "Characterization of Filler and Insulation in Waterproof Cable"
- D. E. Setzer and A. S. Windeler, Bell Laboratories — "A Low Capacitance Cable for the T2 Digital Transmission Line"
- R. Lyenger, R. McClean and T. McManus, Bell Northern Research — "An Advanced Multi-Unit Coaxial Cable for Toll PCM Systems"
- J. B. Howard, Bell Laboratories — "Stabilization Problems with Low Density Polyethylene Insulations"
- Dr. H. Martin, Kabelmetal — "High Power Radio Frequency Coaxial Cables, Their Design and Rating"
- D. Doty, AMP Inc. — "Mass Wire Insulation Displacing Termination of Flat Cable"
- T. S. Choo, Dow Chemical U.S.A. — "Corrosion Studies on Shielding Materials for Underground Telephone Cables"
- N. J. Cogelia, Bell Telephone Laboratories and G. K. Lavoie and J. F. Glahn, US Department of Interior — "Rodent Biting Pressure and Chemical Action and Their Effects on Wire and Cable Sheath"
- T. K. McManus, Northern Telecom Canada Ltd. and R. Beveridge, Saskatchewan Telecommunications, Canada — "A New Generation of Filled Core Cable"
- F. Suzuki, S. Sato, A. Mori and Y. Suzuki, Sumitomo Electric Industries, Ltd., Japan — "Microcoaxial Cables Insulated with Highly Expanded Polyethylene By Chemical Blowing Method"
- S. Masaki, Y. Yamazaki and T. Ideguchi, Nippon Telegraph and Telephone Public Corporation, Japan — "New Aluminum Sheath Cable Used for Electromagnetic Shielding"
- P. Kish and Y. BeBorgne, Northern Telecom Canada Limited, Montreal, Canada — "General Crosstalk Model for Paired Communication Cables"
- C. J. Arroyo, N. J. Cogelia, Bell Laboratories, and B. J. Darsey, Western Electric — "Thermal Behavior of Experimental Plenum Cable Sheaths Determined in a Radiant Heat Chamber"
- R. H. Whiteley, Raychem Ltd. — "A Comprehensive Small Scale Smoke Test"
- V. A. Fentress, Raychem Corp. and D. V. Nelson, Stanford University — "Fracture Mechanics Evaluation of the Static Fatigue Life of Optical Fibers in Bending"
- M. Fujise and Y. Iwamoto, KDD Research & Development Laboratories, Tokyo, Japan — "Self-Core-Alignment Arc-Fusion Splicer Based on a Simple Local Monitoring Method"
- James A. Krabec and John W. Kincaid, Jr., Belden Technical Research Center — "Advances in the Optimization of Multi-Layer Shield Design"
- Simon D. Dadakarides and Bruce B. Lusignam, Stanford University — "Magnetically Loaded Cables"

Best Presentation

- 1968 N. Dean, B.I.C.C.—"The Development of Fully Filled Cables for Distribution Network"
- 1969 J. D. Kirk, Alberta Government Telephones—"Progress and Pitfalls of Rural Buried Cable"
- 1970 Dr. O. Leuchs, Kable and Metalwerke—"A New Self Extinguishing Hydrogen Chloride Binding PVC Jacketing Compound for Cables"
- 1971 S. Nordblad, Telefonaktiebolaget L. M. Ericsson—"Multi-Paired Cable of Nonlayer Design for Low Capacitance Unbalance Telecommunications Network"
- N. Kojima, Nippon Telegraph and Telephone—"New Type Paired Cable for High Speed PCM Transmission"
- 1972 S. Kaufman, Bell Laboratories—"Reclamation of Water-Logged Buried PIC Telephone Cable"
- 1973 R. J. Oakley, Northern Electric Co., Ltd.—"A Study Into Paired Cable Crosstalk"
- 1974 G. H. Webster, Bell Laboratories—"Material Savings by Design in Exchange and Trunk Telephone Cable"
- 1975 J. E. Wimsey, United States Air Force—"The Bare Base Electrical Systems"
- 1976 Michael DeLucia, Naval Ship Research and Development—"Highly Fire-Retardant Navy Shipboard Cable"
- 1977 William L. Schmacher, AMP Inc.—"Design Considerations for Single Fiber Connector"
- 1978 Richard C. Mondello, Bell Labs—"Design and Manufacture of an Experimental Lightguide Cable for Undersea Transmission Systems"
- 1979 I. Wadehra, IBM Corporation—"Performance of Polyvinyl Chloride Communication Cables in Modified Steiner Tunnel Test"
- 1980 J. J. Refi, Bell Laboratories—"Mean Power Sum Far-End Crosstalk of PIC Cables as a Function of Average Twist Helix Angle"
- 1981 G. S. Anderson, Belden Corporation—"Installation of Fiber Optic Cable on 457 Meter Tower"
- 1982 A. Yoshizawa, The Furukawa Electric Co., Ltd.—"Structure and Characteristics of Cables for Robots"
- 1983 J. R. Bury, Standard Telecommunication Laboratories, Ltd., Hailow, England—"Development of Flame Retardant, Low Aggressivity Cables"
- 1984 William E. Dennis, Dow Corning Corporation, Midland, Michigan—"Hydrogen Evolving Tendencies of Cable Fillers and Optical Fiber Coatings"
- 1985 Stephen Hornung, British Telecom Research Laboratories—"Manufacture and Performance of Fibre Units for Installation by The Viscous Drag of Air"
- 1986 Dave Fischer, Superior Cable Corp.—"Progress Towards the Development of Lighting Test for Telecommunication Cables"
- John C. Chamberlain, Siecor Corp.—"Zero Halogen Fire Retardant Fiber Optic Shipboard Cable"

Outstanding Technical Paper

1987

Stephen B. Pierce — Conel Laboratories — "Digital Transmission on Customer Premises Wiring"

1988

Martin C. Light Jr., James A. Moses, Mark A. Sigmon and Christopher A. Story — Siecor Corp. — "Design and Performance of Telecommunication Cable Optimized for Low Fiber Count"

1989

Michel Plasse, Lise Desroches and Paul-Andre Guilbert — Northern Telecom Canada Limited — "High Performance Twisted-Pair Cable for LAN Systems"

1990

Trevor N. Bowmer, Russell J. Miner, Irene M. Plitz, Joseph N. D'Amico and Lal M. Hore — Bellcore — "Thermal Stability Tests for Polyolefin Insulations"

1991

Shigeru Tomita, Michito Matsumoto, Tetsuro Yabuta and Takuya Uenoya — NTT — "Preliminary Research into Ultra High Density and High Count Optical Fiber Cables"

1992

Nathan E. Hardwick III and Kris Kathiresan — AT&T Bell Laboratories and J. G. Hartley — Georgia Institute of Technology — "Analysis of Fiber Optic Cable Design Conditions in Vicinity of Steam Lines — Ruptured and Pristine"

1993

Dr. Yoshinori Namiyama and Toshio Kawazawa — KDD R&D Laboratories; and Naoki Norimatsu — KDD Company, Limited — "PMD Reduction of Optical Fiber Cables for Transoceanic Optical Amplifier Submarine Cable Systems"

1994

Toshio Kurashima, Kazuo Hogari, Satoshi Matsushashi, Dr. Tsuneo Horiguchi, Dr. Yahei Koyamada and Yutaka Wakui — NTT Access Network Systems Laboratories; and Hiroshi Hirano — NTT Technical Assistance & Support Center — "Measurement of Distributed Strain in Frozen Cables and Its Potential for Use in Predicting Cable Failure"

1995

Jean Luc Lang and Jean-Francois Libert — Alcatel Submarine Network; David I. Curtis and Peter Worthington — STC Submarine Systems Ltd. — "Optical Performance of Submarine Cables in Optically Amplified High Bit Rate Systems"

Outstanding Poster Paper

William Wood — Bell Communication Research — "Performance Analysis of Optical Fiber Cleavers"

Dr. R. Raman — Conel Laboratories — "Loss at Dissimilar Fiber Splices"

Werner Bernard and Susan C. Grant — Siecor Corporation — "Fiber Optic Drop Cables in the Subscriber Loop"

Steve Lischynsky, Helmut Lukas, Robin McIntyre and Grant Pacey — Bell-Northern Research Ltd. — "New Technology for a Single Mode Mechanical Splice"

G. Scott Glaesemann — Corning Inc. — "The Effect of Proof Testing on the Minimum Strength of Optical Fiber"

Svend Hopland and Albert Klykken — Norwegian Telecom — "Installation of Submarine Fiberoptic Cables in Rugged Coastal Terrain"

Willem Griffioen — PTT Research — "Mechanical Lifetime of Optical Fibers"

Dr. Sverker Forsberg — Swedish University of Agricultural Sciences; and Jan Björkman — Telia AB — "Release of Lead from Lead-Sheathed Telecom Cables in Soil"

Richard S. Wagman, Gregory A. Lochkovic and Kevin T. White — Siecor Corporation — "Component Optimization for Slotted Core Cables Using 8-Fiber Ribbons"

Best Presentation

Richard Rossi — General Cable Company — "Cable Sheathing Design and Performance Criteria"

Janice B. Haber — AT&T Laboratories — "Single-Mode Media and Apparatus for Fiber to the Home"

Michel de Vecchis — Les Cables de Lyon — "Results on a Large Scale Installation of a Fibre Optic Distribution Network"

Harold W. Friesen — AT&T Bell Laboratories — "An Improved Characteristic Impedance Measurement Technique"

Sue V. Wolfe — STC Submarine Systems — "Structure and High Voltage DC Behaviour of Submarine Cable Mouldings"

Peter Latoszynski — Telecom Australia — "Development of Co-Extruded Polyethylene/Polyamide 12 Insect Resistant Telecommunications Cable"

Timothy S. Dougherty — AT&T Network Cable Systems — "The Temperature of Aerial Plant and Its Effect Upon Foam-Skin Insulation Life" and Wolfgang Wenski — Kabelmetal Electro GmbH — "First Large Scale FITL Installation: Experience From Opal '93"

Barry J. Keon — Telstra — "The Effects of Optical Fiber Coating and Ink Materials on the Corrosion of the Glass Surface"

Dr. Dan L. Philen — AT&T Bell Laboratories — "Optical Fiber for Amplified Undersea Systems"

*Outstanding Technical Paper
(continued)*

1996

Mitsuru Kamikatanano and Matsuhiro Miyamoto — Fujikura Limited; and Osamu Ogawa — Tokyo Electric Power Company — "A Time-Varying Optical Fiber Strain Measurement by Using Brillouin Ring Amplifying System"

1997

Debra A. Simoff, Dr. Mark A. Paczkowski, Dr. Daryl Inniss, Dr. Thomas A. Strasser, J. Renee Pedrazzani, Dr. Rolando P. Espindola, Dr. Robert M. Atkins, Katherine T. Nelson, Valerie J. Kuck, John M. Borick and Jennifer Aspell — Lucent Technologies; and Regina Ragan — California Institute of Technology — "Coatings Having Enhanced UV Transparency for the Fabrication of Optical Fiber Gratings"

1998

Dr. Bernt-Åke Sultan — Borealis AB; Dr. Thomas Hjertberg and Karin Ericsson — Chalmers University of Technology; and Matti Hirvensalo and Marjo Hänninen — Borealis Polymers Oy — "Novel Halogenfree Flame Retardant Polyolefins Intended for Internal Wiring — Properties and Flame Retardant Mechanism"

Outstanding Poster Paper (continued)

Jan Björkman — Telia Network Services; and Dr. Torbjörn Svensson — Telia Research AB — "Ageing of Fibres and Ribbon in Water and Filling Compound"

Katja Lyytikäinen — Nokia-Maillefer Oy — "Numerical Simulation of Optical Fiber Coating Process"

Dr. Osman S. Gebizlioglu, Joel D. Mann and C. R. Kurkjian — Bellcore — "The Effect of Preparation Conditions on the Strength of Fusion Splices I: Use of AFM Imaging"

Best Presentation (continued)

Dr. Priya L. Tabaddor — Lucent Technologies Incorporated, Bell Laboratories — "An Evaluation of Protective Polymer Coatings for Optical Fiber Applications"

Dr. Neil R. Haigh — BICC Cables Limited — "Applicability of All-Dielectric Self Supporting Cable Systems to Very High Voltage Overhead Power Lines"

Dr. Priya L. Tabaddor — Lucent Technologies Incorporated — "Mechanics of Delamination Resistance Testing"

48th GOLD SUSTAINING CONTRIBUTORS

Alcatel

30, rue Pierre Bérégovoy
92111 Clichy Cedex
France

AlphaGary Corporation

170 Pioneer Drive
Leominster, MA 01453

Chase & Sons

19 Highland Avenue
Randolph, MA 02368

CommScope, Inc.

1375 Lenoir Rhyne Blvd.
Hickory, NC 28603

Corning Incorporated

1 Riverfront Plaza
Corning, NY 14831

Dow Chemical Company

200 Larkin Center
Midland, MI 48674

DSM Desotech

1122 St. Charles St.
Elgin, IL 60120

Equistar Chemicals, LP

One Houston Center, Suite 1600
1221 McKinney Street
Houston, TX 77252-2583

Ericsson Cables AB

Telecom Cables Division
Kabelvagen
S-824 34, Hudiksvall
Sweden

Facile Holdings, Inc.

185 Sixth Avenue
Paterson, NJ 07509

FiberCore Jena GmbH

Göschwitzer Straße 20
D-07745 Jena
Germany

The Furukawa Electric Co., Ltd.

6, Yawata-Kaigandori
Ichihara, Chiba 290-8555
Japan

Fusion UV Systems, Inc.

910 Clopper Road
Gaithersburg, MD 20878

Information Gatekeepers Inc.

214 Harvard Avenue
Boston, MA 02134

Lucent Technologies

2000 N.E. Expressway
Norcross, GA 30071

NEPTCO, Inc.

30 Hamlet Street
Pawtucket, RI 02861

Nova-Borealis Compounds

176 Thomas Road
Port Murray, NJ 07865

Penreco

138 Petrolia Street
Karns City, PA 16041

Siecor

PO Box 489
Hickory, NC 28603

SpecTran Communication Fiber Technologies, Inc.

50 Hall Road
Sturbridge, MA 01566

The Stewart Group Inc.

2311 F. Distribution Center Drive
Charlotte, NC 28269-4269

Sumitomo Electric U.S.A., Inc.

21221 S. Western Ave., Ste 200
Torrance, CA 90501

Teknor Apex Company

505 Central Avenue
Pawtucket, RI 02861

Telcordia Technologies

445 South Street - Room 1J142G
Morristown, NJ 07960-6438

Twaron Products Inc.

801-F Blacklawn Road
Conyers, GA 30012

UBE America Inc.

55 East 59th Street, 18th Floor
New York, NY 10022

Union Carbide Corporation

39 Old Ridgebury Rd, Section N-1
Danbury, CT 06817-0001

Weber & Scher Mfg. Co., Inc.

PO Box 366
1231 US Highway 22 East
Lebanon Borough, NJ 08833

JOIN IN OUR CELEBRATION
of
50 Years of Leadership, Vision
and
Service to The Wire and Cable Industry

The 50th Anniversary Symposium will take place in November, 2001 at Walt Disney World's Coronado Springs Resort in Orlando, Florida. We are adding some unique aspects to the program that year to mark this very special occasion. We hope to provide a festive theme that will appeal to our attendees as well as their families. Plan now to join in the celebration!

There are several ways in which you can participate. Certainly plan to attend the symposium and bring your family. Special family registration fees will be provided.

We are attempting to develop two special exhibits, one displaying IWCS memorabilia and another presenting artifacts representing 50 years of technological development in the wire and cable industry. If you have any such items, please indicate your willingness to let us use them by contacting the IWCS office.

Finally, we need financial sponsors to help offset the cost of this very special celebration. We have already solicited your company and would appreciate your help in gaining their support! The following table lists our current sponsors and the amount of their contribution or pledge. Decide now to be a sponsor by contacting **Ray Jaeger at (508) 347-7477!**

CURRENT SPONSORS

DIAMOND BENEFACTOR

AlphaGary Corp.	\$50,000
-----------------	----------

RUBY BENEFACTOR

DSM Desotech Inc.	\$35,000
Union Carbide Corp.	\$35,000

EMERALD BENEFACTOR

Corning Inc.	\$15,000
Lucent Technologies, Inc.	\$15,000
Siecor	\$10,000
CommScope	\$10,000

SAPPHIRE BENEFACTOR

Siemens AG	\$5,000
Furukawa Industrial S.A. Produtos Elétricos	\$5,000

BENEFACTOR

Nippon Telegraph & Telephone Corp.	\$4,000
Furukawa Electric Co., Ltd.	\$3,000
Sumitomo Electric Industries, Ltd.	\$3,000
Fujikura Ltd.	\$3,000
Plasma Optical Fibre B.V.	\$2,000

48TH INTERNATIONAL WIRE AND CABLE SYMPOSIUM (IWCS) SYMPOSIUM COMMITTEE

IWCS STAFF

ELMER F. GODWIN
(President/Director)
GEF Associates
3A Buttonwood Drive
Shrewsbury, NJ 07702
Tel: (732) 389-0990 (Office)
Fax: (732) 389-0991 (Office)
E-mail: iwcs@monmouth.com

IRVING KOLODNY
(Director's Assistant)
31 Maple Run Drive
Jericho, NY 11753
Tel & Fax: (516) 932-0699
E-mail: ikolodny@msn.com

MICHAEL A. DELUCIA
(Director's Assistant)
1775 Crofton Parkway
Crofton, MD 21114
Tel & Fax: (410) 721-5588
E-mail: mdelucia@clark.net

PATRICIA HUDAK
(Administrative Assistant)
174 Main Street
Eatontown, NJ 07724
Tel: (732) 389-0990
Fax: (732) 389-0991
E-mail: iwcs@monmouth.com

1999 OFFICERS

MICHEL ROUSSEAU
(Chairman)
Alcatel
54, RUE La Boétie
75008 Paris, France
Tel: +33-1-4076-2909
Fax: +33-1-4076-1423
E-mail: michel.rousseau@accyd.alcatel.fr

DR. HOWARD WICHANSKY
(Vice-Chairman)
Cdr, US Army CECOM
ATTN: AMSEL-RD-ST-WL-AW
Fort Monmouth, NJ 07703-5203
Tel: (732) 427-4713
Fax: (732) 427-2150
E-Mail: wichansk@mail1.monmouth.army.mil

XAVIER MANN
(Secretary)
Fitel Lucent Technologies
One Lucent Drive
Carrollton, GA 30117
Tel: (770) 838-5278
Fax: (770) 836-8820
E-mail: xmann@fitel.com

JAMES R. LEECH
(Treasurer)
Union Carbide Corp.
Weston Canal Center
PO Box 450
Somerset, NJ 08875-0450
Tel: (732) 271-7935
Fax: (732) 271-7949
E-mail: leechjr@ucarb.com

1999 COMMITTEE MEMBERS

NILS ARTLÖVE
Telia AB
123 86 Farsta
Sweden
Tel: +46-8-713-1212
Fax: +46-8-713-2926
E-mail: Nils.A.Artlove@telia.se

INGE B. KOVACS
Consultant for Polychex Ltd
180 Durham Court
Hackettstown, NJ 07840
Tel: (908) 852-1610
Fax: (908) 852-1518
E-mail: ibkovacs@goes.com

JAMES REESE
DSM Desotech Inc.
1122 St. Charles Street
Elgin, IL 60120-8498
Tel: (847) 468-7720
Fax: (847) 468-7785
Email: jreese@dsmdesotech.com

JOHN R. SICOTTE
Corning Incorporated
35 W. Market Street
Corning, NY 14831
Tel: (607) 974-4447
Fax: (607) 974-7041
E-mail: sicottejr@corning.com

HÉLIO J. DURIGAN
Furukawa Industrial S.A. Produtos
Elétricos
Rua Hasdrubal Bellegard, 820
81450-140
Curitiba - PR
Brazil
Tel: +55-41-341-4085
Fax: +55-41-341-4046
Email: hdurigan@furukawa.com.br

FRED NARAYAN
Phelps Dodge International Corp.
2121 Ponce de Leon Blvd.
Coral Gables, FL 33134
Tel: (305) 447-4322
Fax: (305) 447-4321
Email: fnarayan@phelpsd.com

JOHN R. SACH
Pirelli Cables & Systems NA
710 Industrial Drive
Lexington, SC 29072
Tel: (803) 951-4020
Fax: (803) 951-4044
E-mail: John.Sach@us.pirelli.com

JOHN P. VARACHI, JR.
Telcordia Technologies, Inc.
445 South St; Rm MCC 1J142G
Morristown, NJ 07960-6438
Tel: (973) 829-4920
Fax: (973) 829-5965
E-mail: jvarachi@telcordia.com

YASUHIRO KAMIKURA
The Furukawa Electric Co., Ltd
Telecommunication Group
6-1, Marunouchi, 2-chome
Chiyoda-ku, Tokyo, 100-8322
Japan
Tel: +81-3-3286-3192
Fax: +81-3-3286-3708
Email: kamikura@ho.furukawa.co.jp

GARY WOODDELL
Equistar Chemicals, LP
One Houston Center, Suite 1600
1221 McKinney Street
PO Box 2583
Houston, TX 77252-2583
Tel: (713) 309-4957
Fax: (713) 652-4687
Email: gary.wooddell@equistarchem.com

ADVISORY

DR. PETER R. BARK
Siecor
P.O. Box 489
489 Siecor Park
Hickory, NC 28603
Tel: (828) 323-6205
Fax: (828) 323-6264
E-mail: peter.bark@siecor.com

DIETER S. NORDMANN
(European Representative)
Alcatel Contracting
P.O. Box 160; Kabelkamp 20
D30179 Hannover, Germany
Tel: +49-511-676-2020
Fax: +49-511-676-3042
E-mail: Norddieter@aol.com

DR. REINER J. GERDES
TransTel Group Inc.
5555 Oakbrook Pkwy, Ste 110
Norcross, GA 30093
Tel: (770) 368-8343
Fax: (770) 368-8382
E-mail: rgerdes@transtelgroup.com

CONSULTANTS

HANS A. MAYER
Engineering Consultant
8 Hilton Street
Beaumaris, VIC 3193
Melbourne, Australia
Tel: +61-3-9589-5120
Fax: +61-3-9589-5115

DAVE FALLOWFIELD
TELUS Communications Inc.
6B, 10020 100 Street NW
Edmonton, Alberta
Canada T5J 0N5
Tel: (403) 493-4928
Fax: (403) 493-3115
E-mail: david.fallowfield@telus.com

MANUEL R. SANTANA
Lucent Technologies
Bell Laboratories, Rm 1D32
2000 NE Expressway
Norcross, GA 30071
Tel: (770) 798-2754
Fax: (770) 798-4654
E-mail: msantana@lucent.com

DR. RAYMOND E. JAEGER
SpecTran Corporation
50 Hall Road
Sturbridge, MA 01566
Tel: (508) 347-2261
Fax: (508) 347-8626
E-mail: cmaruk@spectran.com

**EUROPACABLE
REPRESENTATIVE
DR. WALTER PFANDL**
Siemens AG
Abt. ICPCEE
Aust. 101
D96465 Neustadt b. Coburg
Germany
Tel: +49-9568-932700
Fax: +49-9568-932008
Email: Walter.Pfandl@nec.siemens.de

TABLE OF CONTENTS

TUESDAY MORNING—8:00 AM—10:00 AM

Xanadu Theatre

Announcements/Greetings

Elmer F. Godwin, President/Director, IWCS, Inc., Eatontown, NJ

Michel Rousseau, Chairman, IWCS, Alcatel, Paris, France
John R. Sach, Chairman, Plenary Session, Pirelli Cables & Systems North America, Lexington, SC

PLENARY SESSION: Development and Growth of a Modern North American Communications Network Designed to Meet the Needs of the New Millennium

Speakers: MG Robert L. Nabors, Commanding General, United States Army, Communications-Electronics Command and Fort Monmouth, NJ

Stephen R. Baker, Vice President & Chief Technology Officer, Worldwide Fiber Inc., Vancouver, British Columbia, Canada

TUESDAY MORNING—10:30 AM—12:35 PM

Tiara Ballroom A

TRACK 1—FIBER

SESSION 1: FIBER OPTIC CABLE DESIGN I

Chairperson: Manuel R. Santana, Lucent Technologies, Bell Labs., Norcross, GA

Development of Slotted Core Cable Using Nonzero-Dispersion Shifted Fiber—*M. Nakano, M. Miura, H. Mizuguchi*, Lucent Technologies Yazaki Ltd., Gotemba-city, Japan..... 5

The Status and Future of High Fiber Count Cable Designs—*E. R. Logan, H. M. Nassar, R. S. Wagman*, Siecor, Hickory, NC 12

Novel Optical Fiber Cable for Distribution Use in Access Network—*H. Iwata, S. Tomita, K. Hogari, K. Sato, A. Hirooka*, NTT Access Network Service Systems Laboratories, Ibaraki, Japan 20

Development of High-Density Mid-Span Access Cable—*H. Yatabe, H. Kambe, R. Matsuoka, Y. Kamata, M. Mikami*, Furukawa Electric Co., Ltd., Chiba, Japan..... 25

Study on Weight Reduction of High-Fiber-Count Slotted Rod Cable—*R. Takaoka, I. Kobayashi, E. Konda, H. Hiramatsu, Y. Kamikura*, Furukawa Electric Co., Ltd., Chiba, Japan 31

TUESDAY MORNING—10:30 AM—12:35 PM

Tiara Ballroom B

TRACK 2—FIBER

SESSION 2: FIBER PROPERTIES

Chairperson: John R. Sicotte, Corning Inc., Corning, NY

System PMD Requirements for Multi-Channel Analog and Digital Operation on Dispersion Unshifted Optical Fiber—*R. J. Whitman*, Corning Inc., Corning, NY 37

CMT-Cable Design for SI-PMMA-POF Applications Under Highly Environment-Stress —*O. Ziemann*, Deutsche Telekom, Berlin, Germany; *H. Steinberg*, Alcatel autoelectric, Floss, Germany; *P. E. Zamzow*, Alcatel Kabel, Hannover, Germany 44

Study on Mechanical and Optical Characteristics of Reverse Dispersion Fiber Cables—*M. Morimoto, I. Kobayashi, H. Hiramatsu, K. Mukasa, R. Sugizaki, Y. Suzuki, Y. Kamikura*, Furukawa Electric Co., Ltd., Chiba, Japan..... 51

The Influence of Proof-test Dwelltime on Fiber Reliability—*F. P. Kapron*, Telcordia Technologies, Morristown, NJ 55

TUESDAY MORNING—10:30 AM—12:35 PM

Diamond Ballroom A/B

TRACK 2—MATERIALS

SESSION 3: FIBER RIBBONS

Chairperson: Dr. Walter Pfandl, Siemens AG, Neustadt b. Coburg, Germany

A Study of the Fiber Strains in Central Tube Ribbon Cables—*Z. Gao, W. Pfandl, R. Engel, A. Stingl*, Siemens AG, Neustadt, Germany 61

Optimization of Fiber Ribbon Sub-Unit Robustness by Means of a Lateral Fiber-To-Matrix Adhesion Gradient—*K. Konstadinidis, K. W. Jackson, N. W. Sollenberger, S. Siddiqui, C. R. Taylor, V. Chandrasekhar, R. P. DeFabritis, H. Ly, J. R. Szewc*, Bell Laboratories, Lucent Technologies, Inc., Norcross, GA 66

Craft-Friendly 24-Fiber Ribbon Design—*N. A. Punch, Jr., S.K. Moorjani, S. T. Bissell, K. E. Williams*, Siecor, Hickory, NC 72

TUESDAY MORNING—10:30 AM—12:35 PM

Diamond Ballroom C/D

TRACK 3—COPPER

SESSION 4: METALLIC CABLES IN TELECOMMUNICATIONS NETWORKS

Chairperson: Hans A. Mayer, Engineering Consultant, Melbourne, Australia

Fiberglass Reinforced Aerial Service Wire Mechanical Behavior and Installation Guidelines—*L. M. Slavin, K. Hsing, E. E. Scerbo, L. Hore*, Telcordia Technologies, Morristown, NJ 79

Cost Driven Innovative Solutions for the Local Loop Part II: Realisation—*P. Matthijsse*, KPN - Fixed Network Operator, The Netherlands 87

Bridge Taps Analysis in Copper Networks used for ISDN-Narrow Band and xDSL Systems—*R. Lazareni*, CPqD Foundation, Campinas, SP, Brazil 93

Investigation of the Multipurpose Loss Calculation Algorithm for Integrated Services Digital Network (ISDN) Management System—*S. Kanbayashi, H. Oishi, N. Kuwaki*, Nippon Telegraph and Telephone Corp., Chiba, Japan; *K. Watanabe, K. Takahashi*, Nippon Telegraph and Telephone Corp., Saitama, Japan 101

TUESDAY AFTERNOON—1:30 PM—4:55 PM

Tiara Ballroom A

TRACK 1—FIBER

SESSION 5: FIBER OPTIC CABLE DESIGN II

Chairperson: Gary Wooddell, Equistar Chemicals, LP, Houston, TX

A New Type of High Fiber Count, Low Dimension Optical Cable with Simplified Installation Characteristics—*S. Pastuszka, K. Nothofer, A. Weiss*, Alcatel Kabel AG & Co., Mönchengladbach, Germany; *J. P. Bonicel*, Alcatel Cable, Clichy, France; *M. G. S. Emeterio*, Alcatel Cable Ibérica, Maliano, Spain; *P. Gaillard*, Alcatel OFCCC, Claremont, NC 106

Study on Bending Strain of SZ Slotted Core Cable with Fiber Ribbons—*N. Okada, M. Yamanaka, K. Watanabe, M. Miyamoto*, Fujikura Ltd., Chiba, Japan 112

Optimal Design Strategies for Central Tube Ribbon Cables Comprising 864 Fibers and Beyond—*K. W. Jackson, N. E. Hardwick, M. D. Kinard, M. R. Santana, R. Travieso*, Lucent Technologies Inc., Norcross, GA 118

Study of New Slotted Core Cables for Underground Access Networks—*Y. Sato, N. Okada, M. Yamanaka, K. Watanabe, M. Miyamoto*, Fujikura Ltd., Chiba, Japan 127

Development of a Riser Rated Outdoor/Indoor Central Tube Ribbon Cable—*R. H. Norris, R. D. Small, Jr. and P. A. Weimann*, Lucent Technologies, Norcross, GA 134

Semi-Tight Bound Type Fiber Optic Cable—*E.-D. Park, M. Son, B.-G. Lee, Y.-S. Kim*, LG Cable Ltd., Kyungbuk, Korea 141

Ultra Flexible & High Fiber Count Optical Cable for Metropolitan Duct Using Slotted Rod with Segmented-Rib—*Y. Kurosawa, K. Omura, O. Arai, T. Sato, I. Abe, H. Nakai*, Hitachi Cable, Ltd., Ibaraki-ken, Japan 148

TUESDAY AFTERNOON—1:30 PM—4:55 PM

Tiara Ballroom B

TRACK 1—FIBER

SESSION 6: FIBER OPTIC CABLE INSTALLATION

Chairperson: Dieter Nordmann, Alcatel Contracting, Hannover, Germany

Versatile Outside Plant Solution for Optical Access Networks—*W. Griffioen, A. van Wingerden, C. van't Hul*, NKF Kabel, Delft, The Netherlands 152

Deployment of a Long Distance Optical Cable Network in the Canals and Rivers Right of Way—*D. J. Benzel, J.-P. Hulin*, Alcatel Cable and Components, Calais, France; *D. Rivard, A. Veyrat*, LD Cable, Paris, France; *V. Stappers, B. Joly*, Alcatel Cable Interface, Bezons, France; *F. Richaume*, MKI France 157

A Theoretical Study on Cable Design for Blowing Installation in Consideration of Pushing Force at Duct Inlet—*I. Sakabe, Y. Kitamura, W. Kat-surashima, G. Morikawa*, Sumitomo Electric Industries, Ltd., Yokohama, Japan 165

Optical Fiber Cable Links Within Gas Pipelines as an Alternative Telecommunications Route Technology—*P. E. Gregor, L. Kuhn, A. Weiss*, Alcatel Kabel AG & Co., Mönchengladbach, Germany 170

Experiences from Construction and Operation of Fiber Optic Cable Plants in Sewer Systems—*H. G. Haag, W. Liese, K. Nothofer, W. Teschner, A. Weiss*, Alcatel, Mönchengladbach, Germany; *W. Stapel*, HSE Hamburger Stadtentwässerung, Hamburg, Germany 176

Installation Solutions for an Optical Transport Network Based on Aerial Cables and Railway Infrastructure—*P. Bonanni, S. Ghirardini*, Infostrada, Milano, Italy; *G. Clerico*, Pirelli Cavi e Sistemi, Milano, Italy; *E. Cottino, F. Mancarella, U. Morganti, Sirti, S.p.A.* - Cassina de' Pecchi, Italy 184

TUESDAY AFTERNOON—1:30 PM—4:55 PM

Diamond Ballroom A/B

TRACK 2—MATERIALS

SESSION 7: CABLE MATERIALS

Chairperson: James R. Leech, Union Carbide Corp., Somerset, NJ

Small-Scale Rheological Tests to Describe Wire and Cable Extrusion—*S. H. Wasserman*, Union Carbide Corp., Somerset, NJ 190

Materials Advances in Next Generation Loose Tube Cables—*B. G. Risch, G. Dallas, M. Barber*, Alcatel, Claremont, NC 199

Improved Polyethylene and Extrusion Process for High Quality Slotted Core Profiles—*R. C. Dammert, L. Rogstedt, H.-B. Martinsson*, Borealis AB, Stenungsund, Sweden; *E.-L. Heino*, Borealis Polymers Oy, Porvoo, Finland; *T. Vainio, J. Hillberg*, Nextrom Oy, Vantaa, Finland 205

Fiberglass Reinforced Aerial Service Wire: Materials Investigation and Failure Analysis—*O. S. Gebizlioglu, K. W. Moyers, T. N. Bowmer*, Telcordia Technologies, Morristown, NJ 213

Test Methods for Aramid Yarn: Their Impact on Fiber Optic Cable Design—*A. S. Koralek, A. L. Finnimore, D. L. Atkinson*, E. I. DuPont de Nemours & Co., Inc., Richmond, VA; *D. C. Breen*, DuPont International, S.A., Geneva, Switzerland; *H. A. McGuinness, A. G. O'Donnell*, DuPont (UK), Ltd. 221

TUESDAY AFTERNOON—1:30 PM—4:55 PM

Diamond Ballroom C/D

TRACK 3—COPPER

SESSION 8: LAN/DATA CABLES

Chairperson: Fred Narayan, Phelps Dodge International Corp., Coral Gables, FL

Analysis of UTP Patch Cable Performance for High Bit Rate Applications—*J. Kincaid, P. Vanderlaan, C. Dole*, Belden Electronics Division, Richmond, IN 233

Telecommunications Connecting Hardware: Solving the Performance Validation Puzzle— <i>V. Rybinski, S. Vaden</i> , The Siemon Co., Watertown, CT and Superior Modular Products, Swannanoa, NC	240
Optical Fiber and Balanced Cabling Links—The Perfect Basis for Future Proofed Gigabit LANs— <i>S. Mohr, J. H. Kosilek</i> , Siemens AG, Munich, Germany	248
Cabling Concept for Multimedia-Applications or Cabling for Multimedia—Does Copper Solve it All?— <i>K. Lesten, J. Bör</i> , Kerpenwerk GmbH & Co., Stolberg, Germany.....	255
Coupling Attenuation—A New Measuring Technique to Qualify the EMC Behavior of Various Data Cables— <i>D. Wilhelm, A. Obst</i> , GHMT, Bexbach/Saar, Germany	260
Correlations Between Crosstalk and Symmetry of Data Cables— <i>Jörg Bör</i> , Kerpenwerk GmbH & Co., Stolberg, Germany	268
A Digital Common-Mode Noise Canceller for Twisted-Pair Cable— <i>D. K. Fenton, T. H. Yeap</i> , University of Ottawa, Ontario, Canada	275

TUESDAY EVENING
Grand Ballroom

HOSPITALITY HOUR	SUPPLIERS FORUM
(6:30 PM-8:00 PM)	(6:30 PM-8:30 PM)
Admission by badges issued to all registrants	

WEDNESDAY MORNING—8:00 AM-11:25 AM

Tiara Ballroom A

TRACK 1—FIBER

SESSION 9: FIBER OPTIC SUBMARINE CABLES <i>Chairperson:</i> Nils Artlöve, Telia AB, Farsta, Sweden Laser Welded Metallic Tubes in Fibre Optical Cables— <i>J. S. Andreassen, I. Vintermyr</i> , Alcatel Kabel Norge AS, Oslo, Norway	285
Evaluation of Bending Stiffness of Fiberoptic Submarine Cable in Both Elastic and Plastic Regions— <i>T. C. Chu</i> , Tyco Submarine Systems Ltd., Eatontown, NJ.....	292
Fibre Optics for the Off Shore Industry— <i>M. Isacson, K. Sjölin, J. Jørgensen</i> , Ericsson Cables AB Kabelvägen, Hudiksvall, Sweden	297
192-Fibre Count Submarine Cable for Repeaterless Systems— <i>I. Vintermyr, R. Vogt, J. S. Andreassen</i> , Alcatel Kabel Norge AS, Oslo, Norway.....	305
Development of Submarine Optical Cable Unit Using a Large Effective Area Fiber— <i>K. Mitsuhashi, T. Hayano, T. Shimomichi, T. Abiru, K. Oohashi, M. Miyamoto</i> , Fujikura Ltd., Chiba, Japan	312
Development of New Tight-Fit-Type Submarine Cable with Large Core Fibers for WDM System— <i>O. Nagatomi, K. Yamamoto, H. Wakamatsu, R. Kanda, R. Morikawa</i> , Ocean Cable Co., Ltd., Fukuoka, Japan	317

WEDNESDAY MORNING—8:00 AM-11:25 AM

Tiara Ballroom B

TRACK 1—FIBER

SESSION 10: FIBER OPTIC CONNECTORS & COMPONENTS <i>Chairperson:</i> Yasuhiro Kamikura, Furukawa Electric Co., Ltd., Chiba, Japan MT-RJ Optical Connector— <i>K. Takizawa, N. Imazu, T. Arikawa, Y. Tamaki</i> , Fujikura Ltd., Chiba, Japan...	324
Design and Performance of Modular Jack Type Mini-MT Connectors— <i>M. Takaya, S. Nagasawa, Y. Murakami</i> , NTT Access Network Service Systems, Ibaraki, Japan; <i>S. Hatano</i> , NTT Advanced Technology Corp., Tokyo, Japan	332
A Novel Polishing Method for Physical Contact (PC) Connection of Multifiber Connector— <i>X. Jie, T. Yamazaki, N. Shimoji, K. Iwashita, K. Suzuki</i> , Furukawa Electric Co., Ltd., Chiba, Japan	340
New Push-On Type MT-Connector for Optical Fiber— <i>K. Fujiwara, Y. Hayashi, H. Furukawa, Y. Nomura</i> , Fujikura Limited, Chiba, Japan	346
The Development of Wide Range of Wavelength WDM Fused Optical Fiber Coupler— <i>T. Takahashi, K. Terui, S. Katsuki, M. Tabata, H. Maeyasiki</i> , Showa Electric Wire & Cable Co., Ltd., Kanagawa, Japan	352
Ultra-High Density 4X1600 Optical Switch— <i>Y. Ito, S. Naraoka, M. Okuda, S. Omizu</i> , Furukawa Electric Co., Ltd., Chiba, Japan	359
Automated Optical Fiber Cabling System for Intelligent Buildings— <i>K. Sasakura, J. Yamaguchi, T. Yoshizawa, K. Kobayashi, K. Kaneko</i> , NTT Telecommunications Energy Laboratories, Tokyo, Japan	364

WEDNESDAY MORNING—8:00 AM-11:25 AM

Diamond Ballroom A/B

TRACK 1—FIBER

SESSION 11: FIBER & CABLE PROCESSING <i>Chairperson:</i> Dieter Nordmann, Alcatel Contracting, Hannover, Germany Numerical Simulation of Optical Fiber Preform Neck-Down for Draw Process Optimization— <i>M. Nicolardot, G. Orcei</i> , Alcatel, Conflans Ste Honorine, France.....	369
Statistical Process Control Techniques for On-Line Measurement of Autocorrelated Process Variables— <i>T. G. Goddard</i> , Lucent Technologies, Norcross, GA	377
Novel Non-Metallic Multilayer Fiber Optic Cables Based on Cone Extrusion Process— <i>M. T. Heino, J. T. Ravela, M. T. Suvanto</i> , NK Cables Ltd., Helsinki, Finland; <i>R. P.-G. Phillips</i> , Nextrom Ltd., Ecublens, Switzerland; <i>T. P. Vainio</i> , Nextrom Ltd., Vantaa, Finland	385
Development of a Newly Designed Ultra High Fiber Count Ribbon Cable with Folder Units— <i>O.-J. Kwon, Y.-H. Jeon, S.-H. Kim, K.-J. Lew</i> , Daewoo Telecom, Incheon-city, Korea	393

WEDNESDAY MORNING—8:00 AM—11:25 AM**Diamond Ballroom C/D****TRACK 2—MATERIALS****SESSION 12: FLAME RETARDANT MATERIALS**

Chairperson: Inge B. Kovacs, Consultant for Polycheck Ltd., Hackettstown, NJ

HFFR^a Cable Materials: Trends in Silane Coupling Agent Technology—*H. Mack*, Degussa-Hüls AG, Rheinfelden, Germany 401

Continued Development of the Plenum-Outdoor Totally Dry Optical Fiber Cable Designs—*D. A. Keller, J. Rosko, R. Yoder, B. Charuk, D. Rouse*, Alcatel-Berk-Tek, Fuquay-Varina, NC; *B. Risch, B. Overton, G. Camilo, S. Munday*, Alcatel Cable, Claremont, NC 409

Flame Retardant Cables with Enhanced Performance—*K. Nothofer, A. Weiss*, Alcatel Kabel AG & Co., Mönchengladbach, Germany; *J. P. Bonicel*, Alcatel Cable, Clichy, France; *J. Hosner*, Alcatel Cables Switzerland, Cortaillod; *D. Benzel*, Alcatel Cable, Calais, France 416

The Development and Performance of a Calibration Cable for the NFPA 262/UL 910 Plenum Cable Fire Test—*J. T. Chapin*, Lucent Technologies, Norcross, GA; *L. L. Bleich*, Lucent Technologies, Omaha, NE; *P. Gandhi, T. Ebert*, Underwriters Laboratories, Northbrook, IL 421

WEDNESDAY AFTERNOON—11:30 AM—2:00 PM**Xanadu Theatre****AWARDS LUNCHEON**

Speaker: Dr. Lowell Catlett, Professor, New Mexico State University, Las Cruces, NM

WEDNESDAY AFTERNOON—2:15 PM—5:15 PM**Tiara Ballroom A****PANEL DISCUSSION****SESSION 13: WIRELESS IN THE HOME AND OFFICE**

Chairperson: Dr. Reiner J. Gerdes, TransTel Group Inc., Norcross, GA

CELLULAR DIGITAL PACKET DATA TECHNOLOGY

Wireless: Good Enough to Back Up or Replace Landlines?—*R. J. Gerdes*, TransTel Group, Inc., Norcross, GA 427

Cellular Digital Packet Data Technology—*D. Gambrell*, GTE Wireless, Alpharetta, GA 428

Wireless Alternative to Cables Television—*L. Akinson*, BellSouth, Roswell, GA (Abstract not received at time of printing) 429

Broadband and Midband Wireless Access—*R. Merrett*, British Telecom, Ipswich, UK 429

WEDNESDAY AFTERNOON—2:15 PM—5:15 PM**Tiara Ballroom B****PANEL DISCUSSION****SESSION 14: TWISTED-PAIR LAN CABLING—AN INTERACTIVE TECHNICAL UPDATE**

Chairperson: Fred Narayan, Phelps Dodge International Corp., Coral Gables, FL

Moderator: Masood Shariff, Bell Labs. of Lucent Technologies, Middletown, NJ

LAN Twisted Pair Cabling—Overview of Current TIA Standards Activities—*M. Shariff*, Bell Labs. of Lucent Technologies, Holmdel, NJ 430

Development of a PSNEXT, PSELFEXT and Return Loss Model for Category 5e Channels—*P. Kish*, NORDX/CDT, Inc., Point-Claire, Quebec, Canada.... 431

New Developments in Twisted Pair Cable Standards—*R. Wessels*, CommScope Inc. of North Carolina, Hickory, NC 434

Installation Effects Upon Cabling Performance—*P. Vanderlaan*, Belden Electronics Division, Richmond, IN 435

New Developments in Connecting Hardware Specifications—*V. Rybinski*, The Siemon Co., Watertown, CT 436

New Developments in Connecting Hardware Measurement Procedures—*S. Vaden*, Superior Modular Products, Swannanoa, NC 437

WEDNESDAY AFTERNOON—4:00 PM—6:30 PM**Grand Ballroom A****SESSION 15: POSTER PAPERS**

Chairpersons: Dr. Reiner J. Gerdes, TransTel Group Inc., Norcross, GA

Dieter S. Nordmann, Alcatel Contracting, Hannover, Germany

Universal Fiber Optic Cable with Pultruded Core—*R. Uteschill, R. Klug*, IPT—Innovative Pultrusions Technologie, Kapfenberg, Austria 438

All-Dielectric Self-Supporting Cables (ADSS) with Ballistic Protection for Use in the Countryside—*S. S. Natume, A. M. Simião, J. M. I. Furtado, L. Silvério*, Furukawa Industrial S.A. Produtos Elétricos, Curitiba, Paraná, Brazil 446

Evaluation of Damping Effectiveness of Impact Dampers on ADSS Cable—*D. S. Sunkle, D. F. McKenna, J. J. Olenik*, Preformed Line Products, Cleveland, OH 452

Verification by Means of Temperature Characteristic Test and Cable Laying Test on Optimum Design in Fiber Excess Length of Slotted Type Optical Cable—*N. Kimura, Y. Sudo, T. Ohsako, H. Keruma, K. Nemoto*, Ocean Cable Co., Ltd., Tochigi, Japan ... 459

Study to Determine the Drag Coefficient for Submarine Cables—*P. Dupire, Y. Charles, J. Libert*, Alcatel Submarine Networks, Calais, France 464

OPMA—A High Mechanical and Heat Performance Alternative Optical Cable for Aerial Application—*M. A. Scocco, E. C. Mendes, M. V. Giacaglia*, Pirelli Cabos S.A., Sorocaba, Brazil; *D. A. Fulop*, Telefonica, Telecomunicações de São Paulo, São Paulo, Brazil; *M. Naur, J. R. da Mota*, Telemar-MG, Telecomunicações de Minas Gerais, Belo Horizonte, Brazil 471

Effect of Thermal Aging on High Frequency Transmission Characteristics of Coaxial Drop Cables— <i>S.-H. Chou, J.-C. Lin, H.-F. Lin, Y.-H. Hwang, C.-H. Hsieh, H.-P. Hsu, Y.-c. Lin, Y.-K. Tu, Chunghwa Telecom, Taiwan, R.O.C.</i>	476
Cabling of Dispersion Compensating Fibres— <i>L. Grüner-Nielsen, S. N. Knudsen, Lucent Technologies Denmark, Brøndby, Denmark</i>	483
Intermittent Waterblocking for Submarine Cable Applications— <i>T. A. Bookwalter, R. K. Jones, J. B. Wojno, Alcatel Submarine Networks, Inc., Portland, OR</i>	488
Novel Compact Loose Tube Cable Incorporating Evolved Dry Waterblocking Method— <i>A. G. Bringuier, Siecor, Hickory, NC; J. R. Priest, Owens Corning, Granville, OH</i>	492
Selecting Proper Superabsorbent Tape for Slotted Core Optical Cables Capable of Blocking Manhole Water— <i>C.-M. Hsiao, H.-J. Chen, J.-C. Lii, T.-C. Chang, H.-P. Hsu, Y.-c. Lin, Y.-K. Tu, Chunghwa Telecom, Taiwan, R.O.C.</i>	501
A Positive Dispersion Shifted Single Mode Fibre Made by PCVD Process— <i>Y. Huang, R. Matai, W. Yu, S. Wang, Yangtze Optical Fibre and Cable Co. Ltd., Wuhan, Hubei, China</i>	506
The Principle of Design and Manufacturing for a Large Effective Area Dispersion Shifted Single Mode Fibre Made by PCVD Process— <i>W. Wei, R. Matai, Z. Mu, J. Cain, Yangtze Optical Fibre & Cable Co. Ltd., Wuhan, P.R. China</i>	511
Bending Performance Study of Large Effective Area G.655 Fibre— <i>M. Cheng, G. Niu, M. Zhang, Yangtze Optical Fibre and Cable Co., Ltd., Wuhan, P.R. China</i>	516
Dynamic Menisci on Moving Fibers— <i>A. Abraham, C. Polymeropoulos, Rutgers, The State University of New Jersey, Piscataway, NJ</i>	520
Effect of Temperature, Strain and Installation on PMD in High Fiber Count Ribbon Cables— <i>S. S. Sodhi, A. C. Gregory, G. E. Grogan, Siecor, Hickory, NC</i>	525
Ribbon Cross-Section Measurement Methods Comparison— <i>G. A. Mills, R. J. Speights, Siecor Operations LLC, Hickory, NC</i>	529
Computational Fluid Dynamics (CFD) Analysis of Ribbon Processing— <i>S. X. Shen, Alcatel Telecommunications Cable, OFCCC, Claremont, NC</i>	533
Application of Monte Carlo Simulation Techniques to Optical Fiber Communication Link Models— <i>J. D. Schell, 3M Telecom Systems Division, Austin, TX</i>	543
The OTDR Technique as a Promising Approach for Distributed Measurements in Optical Fibres— <i>F. Ravet, B. Heens, O. Lair, Y. Defosse, J.-C. Froidure, M. Blondel, Multitel Telecom, Mons, Belgium</i>	550
Cost Reduction of Miniature Optical Connector with Glass-Ceramic Ferrule— <i>J. Hirose, J. Takeshita, F. Shimizu, Y. Nakamura, Nishi Nippon Electric Wire & Cable Co., Ltd., Kasugaura, Oita, Japan; H. Takeuchi, Nippon Electric Glass Co., Ltd., Noto-gawa, Shiga, Japan</i>	555
Fiber Performance in Ferrule-Less Interconnects— <i>T. P. Berger, 3M, Telecom Systems Division, Austin, TX; J. W. Laumer, C. B. Walker, Jr., J. C. Novack, 3M, Fiber Optics & Electronics Materials Technology Center, St. Paul, MN</i>	560

Performance of Plug and Jack— <i>H.-F. Lin, C.-H. Hsieh, S.-H. Chou, Y.-H. Hwang, J.-C. Lin, H.-P. Hsu, Y.-c. Lin, Y.-K. Tu, Chunghwa Telecom, Taiwan, R.O.C.</i>	565
---	-----

THURSDAY MORNING—8:30 AM—11:55 AM

Tiara Ballroom A

TRACK 1—FIBER

SESSION 16: FIBER OPTIC AERIAL CABLES <i>Chairperson: Xavier Mann, Fitel Lucent Technologies, Carrollton, GA</i>	
Development of an Ultra High Fiber Count Ribbon ADSS Cable Design— <i>J. W. Thornton, N. S. Hatch, R. G. Gravely, III, Fitel Lucent Technologies, Carrollton, GA</i>	571
Development of New Aerial Self-Supporting Cable with Excess Fiber Ribbon Length in SZ-Slot— <i>D. Iwakura, I. Kobayashi, R. Takaoka, H. Hiramatsu, Y. Kamikura, Furukawa Electric Co., Ltd., Chiba, Japan</i>	578
All-Dielectric, Self-Supporting, Tracking Resistant Cable for Use on Long Span, High Voltage Overhead Power Lines— <i>A. M. Simião, J. A. M. Neto, C. Kuniyoshi, J. M. I. Furtado, L. Silvério, Furukawa Industrial S.A. Produtos Elétricos, Paraná, Brazil</i>	585
The Development of All Dielectrical Self-Supporting Fiber Optical Cable (ADSS) for Use on Power Lines in China— <i>F. Binlan, Electric Power Research Institute of China, Beijing, P. R. China</i>	593
ADSS Cable Design for No Voltage Limits— <i>K.-T. Park, J.-H. Kim, Samsung Electronics Co., Ltd., Kumi-City, Republic of Korea</i>	598
Stress-Strain, Creep, and Temperature Dependency of ADSS (All Dielectric Self Supporting) Cable's Sag & Tension Calculation— <i>C. Militaru, Alcoa Fujikura Ltd., Spartanburg, SC</i>	605
ADSS Cables Electrical Corrosion Tests— <i>C. Militaru, Alcoa Fujikura Ltd., Spartanburg, SC</i>	614

THURSDAY MORNING—8:30 AM—11:55 AM

Tiara Ballroom B

TRACK 1—FIBER

SESSION 17: SPLICING/TESTING & FIELD EVALUATION I <i>Chairperson: Michel Rousseau, Alcatel, Paris, France</i>	
Numerical Simulation of High Quality Fiber Optic Splices for High Precision Loss Evaluation— <i>B. Zamzow, G. Ruegenberg, Siemens AG, Munich, Germany; M. Anderson, Siecor Corp., Hickory, NC; W. Knop, RXS Kabelgarnituren GmbH, Hagen, Germany</i>	621
Fibre Optic Splice Loss Assessment by Means of Unidirectional OTDR Measurement— <i>D. Suino, CSELT, Torino, Italy; F. Montalti, Telecom Italia, Roma, Italy</i>	629
Cleavability of Titania-Clad Optical Fibers— <i>J. C. Meyer, Corning Inc., Wilmington, NC</i>	636
Development of New Optical Fiber Fusion Splicer for Factory Use— <i>K. Ohzawa, S. Yaguchi, J.-i. Suzuki, N. Kawanishi, S. Saito, Fujikura Ltd., Chiba, Japan</i>	644

Recovery Analysis of Damaged OPGW Cables Due to Lightning Strikes— <i>B. J. G. de Aragão, C. Pito-mbo, P. J. P. Curado, A. Bagarolli, S. Millo</i> , Fundação CPqD, Campinas, Brazil; <i>A. M. D. Luz, F. R. B. Benayon, L. M. Lauria</i> , Embratel, Rio de Janeiro, Brazil	650
BOTDR Analysis of Cable Tensile Testing— <i>R. Wag-man, J. Englebert, A. Gregory, K. Lail</i> , Siecor, Hick-ory, NC	658
A New Monitoring Technique for Passive Optical Networks— <i>M. Bottanelli, E. Cottino, M. Maglio</i> , Sirti S.p.A., Cassina de' Pecchi (MI), Italy	666

THURSDAY MORNING—8:30 AM–11:55 AM

Diamond Ballroom A/B

TRACK 2—MATERIALS

SESSION 18: OPTICAL FIBER COATINGS

Chairperson: James Reese, DSM Desotech Inc., Elgin, IL

Low Speed Carbon Deposition Process for Hermetic Optical Fibers— <i>E. A. Lindholm, J. Li, A. S. Hokans-son, J. Abramczyk</i> , Spectran Specialty Optics Co., Avon, CT; <i>S. A. Arthur, D. R. Tallant</i> , Sandia Nation-al Laboratories, Albuquerque, NM	672
Cure Behavior of Optical Fiber Primary Coating on Drawing Tower— <i>J. Yoshizawa, Y. Naito, H. Takase, Z. Komiya, T. Ukachi</i> , JSR Corporation, Ibaraki, Japan	680
Advances in Design and Development of Optical Fibers for Harsh Environments— <i>J. Li, E. Lindholm, J. Horska, J. Abramczyk</i> , SpecTran Specialty Optics, Avon, CT	687
Colored Matrix— <i>S. Coons, N. Moore, T. Norlin, A. Toussaint</i> , DSM Desotech Inc., Elgin, IL	695
Simulation of Flow in Die and Applicator for Optical Fiber Manufacture— <i>K. Rattan, Y. Jaluria</i> , Rutgers, New Brunswick, NJ	700
Metal-Free Heat-Resistant Optical Fiber for Fiber Optics Sensing Systems in Oil Wells— <i>M. Shimizu, Y. Kubo, T. Hattori, K. Tsuneishi</i> , Sumitomo Electric Industries, Ltd., Yokohama, Japan; <i>R. Rubino, D. Norton</i> , CiDRA Corp., Wallingford, CT	708
A Study on UV-Transparent UV-Curable Resin for Fiber Bragg Gratings Written Through a Fiber Coat-ing— <i>T. Iio, K. Hosotani, H. Kuzushita, T. Genji, K. Imamura</i> , Mitsubishi Cable Industries, Ltd., Hyogo, Japan	714

THURSDAY MORNING—8:30 AM–11:55 AM

Diamond Ballroom C/D

TRACK 3—COPPER

PANEL DISCUSSION

SESSION 19: MFG & PROCESSES/PRODUCTIVITY IMPROVEMENTS

Chairperson: Fred Narayan, Phelps Dodge International Corp., Coral Gables, FL

Improvements in Maintainability and Process Con-trol in Data/Telecom Drawing Machinery— <i>S. Kil-gallen</i> , Henrich, Inc., Huntersville, NC	720
--	-----

Development on Increasing Productivity for LAN Copper Pair— <i>P. P. Letout</i> , Pourtier Pere & Fils, France	721
A Broad and Flexible Approach of Cable Manufac-turing: Tight Buffer, Loose Tube and Ribbon Cables— <i>F. Legros</i> , Swisscab, Switzerland; <i>P. Letout</i> , Pourtier Pere et Fils, France	722
ACSR Cable Process with Double Twist Stranding Machines— <i>J. Reigt, C. M. Caballé, S.A.</i> , Barcelona, Spain	723
Layout/Methodology for the Production of Category 7 Cables— <i>B. W. Hamner, W. Thompson</i> , Nextrom Ltd., Concord, Ontario, Canada	727
Intelligent Robot Reel Handling, Storage and Man-agement for Fiber Optic Cable Producers— <i>O. Volgger</i> , ROBOTECH, Logistic Systems GmbH, Dornbirn, Austria; <i>F. J. Hardy</i> , Cable Consultants Corp., Larchmont, NY	728

THURSDAY AFTERNOON—1:00 PM–3:05 PM

Tiara Ballroom A

TRACK 1—FIBER

SESSION 20: FIBER OPTIC AERIAL/PREMISES CABLES

Chairperson: Dave Fallowfield, TELUS, Communications Inc., Alberta, Canada

Ballistic Resistant Armored Fiber Optical Cable for Aerial Applications— <i>K. E. Bow, M. D. Luker</i> , Dow Chemical Co., Midland, MI; <i>M. A. Adams</i> , Jet Propulsion Laboratory, Pasadena, CA	730
Development of the Branch Type of Premises Opti-cal Cable to Reduce Construction Cost— <i>O. Koyasu, K. Kobayashi, M. Miyamoto</i> , Fujikura Ltd., Chiba, Japan; <i>Y. Hamada</i> , Nishi Nippon Electric Wire & Cable Co., Ltd., Ooita, Japan	737
Managing Temperature-Induced Loss of 50/125µm Duplex Optical Cables— <i>T. P. Berger</i> , 3M Telecom Systems Division, Austin, TX	744
Duplex Cable Design for Enhanced Indoor and Security System— <i>H.-S. Lee, J.-J. Hwang, J.-H. Kim</i> , Samsung Electronics Co., Ltd., Gumi-City, Republic of Korea	749
Development and Application of a Composite Fiber/Copper Cable with Remote Powering Capabili-ties— <i>J. Heery, M. Gimblet, J. Register</i> , Siecor, Hick-ory, NC	755

THURSDAY AFTERNOON—1:00 PM–3:05 PM

Tiara Ballroom B

TRACK 1—FIBER

SESSION 21: TESTING & FIELD EVALUATION II

Chairperson: Dr. Reiner J. Gerdes, TransTel Group Inc., Norcross, GA

Ribbon Slotted Core Cable with Non-zero Disper-sion Shifted Optical Fiber for WDM Metropolitan Network— <i>M. Katayama, M. Kaino, Y. Kubo, M. Saeki</i> , Sumitomo Electric Industries, Ltd., Yoko-hama, Japan	764
--	-----

Optical Talk Set Based on Fiber Ring Interferometer— <i>Y. Nakamura, S. Niimi, K. Arai, Y. Unami, Fujikura Ltd., Chiba, Japan</i>	769
Strain Distribution Measurement in Bent Optical Cables Using a Fiber Ribbon with Multi-Pointed Fiber Bragg Gratings— <i>T. Genji, K. Imamura, T. Nakai, Y. Imada, Mitsubishi Cable Industries, Ltd., Hyogo, Japan</i>	775
Investigation of 1625 NM Loss Performance of Fibreoptic Cables Intended for Use at 1550 NM— <i>S. Hopland, Telenor Nett AS, Oslo, Norway</i>	780
Loss Behaviour of Optical Fibre Cable Network for Future WDM Systems— <i>E. Jauhainen, R. Pulliainen, Sonera Ltd., Helsinki, Finland</i>	789

THURSDAY AFTERNOON—1:00 PM–3:05 PM

Diamond Ballroom A/B

TRACK 2—MATERIALS

SESSION 22: JACKETING

Chairperson: James R. Leech, Union Carbide Corp., Somerset, NJ

Materials Reliability of Flooded and Dry-Core ADSS Cable— <i>S. Neogi, B. G. Risch, M. Soltis, OFCCC, Alcatel, Claremont, NC</i>	795
Design of Polyethylene Cable Jacket Compounds of Superior Jacketing Performance— <i>T. Chen, J. R. Leech, Union Carbide Corp., Somerset, NJ</i>	807
The Impact of Carbon Black Morphology and Dispersion on the Weatherability of Polyethylene— <i>C. V. Bellinghen, Cabot Corp., Pepinster, Belgium; J. V. Accorsi, Cabot Corp., Billerica, MA</i>	815
Development of a New Uni-Modal Fibre Optic MDPE Jacketing Compound— <i>E. Brunner, L. Westling, Nova-Borealis Compounds LLC, Port Murray, NJ</i>	824
Thermoplastic Polyurethane Materials for Cable Jacketing — <i>J. L. DeGross, BASF Corp., Wyandotte, MI</i>	831

THURSDAY AFTERNOON—1:00 PM–3:05 PM

Diamond Ballroom C/D

TRACK 3—COPPER

SESSION 23: COAX/HF CABLES

Chairperson: Hélio J. Durigan, Furukawa Industrial S.A. Produtos Elétricos, Curitiba, Brazil

STP-Cable for Tyre Pressure Control System Operating at 433/315 MHZ— <i>D. S. Parmar, G. Behlau, H. Wichmann, Kroschu Kabelwerke, Kromberg & Schubert GmbH u. Co., Rhede, Germany</i>	846
Outdoor Coverage by Radiating Cables— <i>E. Mahlandt, Radio Frequency Systems GmbH, Hannover, Germany</i>	852
Modelling the Transfer Impedance of Shielded Cables— <i>T. Nälsén, S. Andersson, Habia Cable AB, Söderfors, Sweden</i>	859
Development of the Braidless Coaxial Drop Cable— <i>D. J. Yamasaki, Siecor, Hickory, NC</i>	864
Bending Fatigue Failure Analysis & Testing of a Radar Frequency Co-Axial Cable— <i>S. Kery, Northrop Grumman Corp., Baltimore, MD</i>	872

OPENING SPEAKERS



MICHEL ROUSSEAU
Chairman, IWCS
Alcatel
Paris, France

Michel Rousseau is the Technical Director for Alcatel's Cables and Components Sector.

He received a Dipl. Ing. degree from the Ecole Nationale Supérieure des Télécommunications and a Dr. Ing. degree on quantum electronics from the University of Paris-Sud (France). He graduated from the Centre des Hautes Etudes de l'Armenent (Ministry of Defense, France).

He joined Alcatel in 1972 as a Research Engineer in the Laboratories of Marcoussis. Subsequently, he has held different positions related to Business and Technology Management in the cable domain.

He is the author of over 25 technical papers and co-author of the book "Optique & Télécommunications".



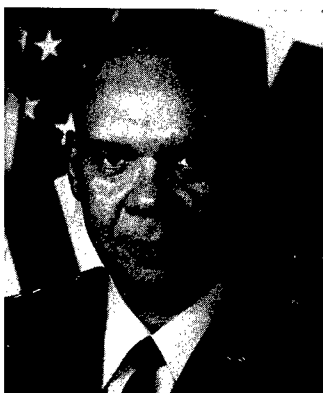
JOHN R. SACH
Chairman, Plenary Session
Pirelli Cables & Systems North America
Lexington, SC

John R. Sach is currently the Chief Engineer for Pirelli Cable and Systems NA Communications Division. His responsibilities include research, development and design of optical fiber cables.

Sach joined Pirelli in 1975 as a Development Engineer working in high frequency coaxial cables. Subsequently he has worked in England, Italy and North American for Pirelli holding several position in the area of Research and Development.

Sach holds a Bachelors degree in Engineering Metallurgy from Imperial College London University. He is a member of the Optical Society of America.

PLENARY SESSION



MAJOR GENERAL ROBERT L. NABORS

COMMANDING GENERAL

United States Army

**Communications-Electronics Command
and Fort Monmouth, New Jersey**

Major General Robert L. Nabors has been the Commander of the Communications-Electronics Command and Fort Monmouth since September 1, 1998.

MG Nabors was born in Boston, Massachusetts, and grew up in Lackawanna, New York. He holds a Bachelor of Science degree in Systems Engineering from the University of Arizona; a Master of Science degree in Systems Management from the University of Southern California; and served as a Senior Fellow in the National Security Affairs Program at Harvard University. He is also a graduate of the Senior Officials in National Security Program at Harvard University. His military schooling includes the Signal Officer Candidate School, the Signal Officer Basic and Advanced Courses and the Armed Forces Staff College.

MG Nabors' initial duty assignment was with the 67th Signal Battalion at Fort Riley, Kansas. After a tour in Vietnam, MG Nabors served at Fort Dix, New Jersey; Aberdeen Proving Ground, Maryland; and Worms, Germany. In November 1979, MG Nabors was selected as Aide-de-Camp for the Commanding General, VII Corps. MG Nabors was attached to the J-6 Staff of the Combined Forces Command/United States Forces, Korea and subsequently served as the S-2/3 of the 41st Signal Battalion. In December 1983, he was assigned to the Office of the Director of Plans, Programs, and Policy at the United States Readiness Command, and was then selected to command the 509th Signal Battalion in Italy.

MG Nabors served as Special Assistant to the U.S. Army's Director of Information Systems for Command, Control, Communications, and Computers (DISC4). He was also Chief, Integration Division, Architecture Directorate. Prior to assuming command of the 2nd Signal Brigade in December 1990, MG Nabors served as Deputy Commander, White House Communications Agency.

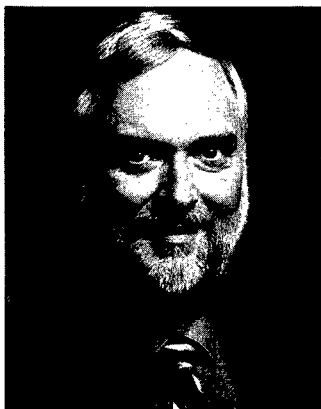
MG Nabors served as the Executive Officer for the DISC4 before his assignment as Director, Single Agency Manager for Pentagon Information Technology Services. MG Nabors assumed command of the 5th Signal Command on November 22, 1995.

MG Nabors' awards and decorations include the Defense Superior Service Medal; Legion of Merit with four Oak Leaf Clusters; the Bronze Star Medal; Meritorious Service Medal with four Oak Leaf Clusters; the Joint Service Commendation Medal; the Army Commendation Medal with four Oak Leaf Clusters; the Department of the Army Staff Identification Badge; the Joint Meritorious Unit Award; and the Presidential Support Badge. MG Nabors is a member of the American Mensa Society.

MG Nabors and his wife, Valerie, have three adult children: Robert, Richard and Jonathan.

PLENARY SESSION

"DEVELOPMENT AND GROWTH OF A MODERN NORTH AMERICAN COMMUNICATIONS NETWORK DESIGNED TO MEET THE NEEDS OF THE NEW MILLENNIUM"



STEPHEN R. BAKER

**Vice President and Chief Technology Officer
Worldwide Fiber Inc.
Vancouver, British Columbia, Canada**

Mr. Baker is the Chief Technology Officer for Worldwide Fiber Inc. and was instrumental in developing the business plan for the wholesale services division. He is currently responsible for the design, planning and implementation of the WFI technical infrastructures including the DWDM and ATM technologies that are the basis for a new service paradigm for wholesale services.

Previous to joining WFI Mr. Baker held several senior positions with Sprint Canada (CallNet Enterprises) including Vice President Strategic Technology Planning. In his position at Sprint Canada and Integrated Network Services (acquired by CallNet), Mr. Baker was responsible for the design and implementation of all of the data services offered by Sprint Canada.

The topic for the speech will be the growth and development of Worldwide Fiber Inc. from a cable construction company to a world class Telecommunications service provider. Using

their expertise as a Canadian cable construction company, and with a great deal of insight WFI was able to step up to the role of North American cable developer. As part of their strategy for their development business WFI is able to retain their own fibers from the installed cable routes. With this as the basis for their network WFI was able to leverage this asset into the development of the services that will catapult WFI into the future as a major telecomm player.

Without the encumbrances of a traditional network WFI has designed a network that will offer the fastest network connections at speeds up to 10 gigabits per second for transparent optical connections between any cities in North America and Europe, and ATM speeds up to 2.5 Gigabits per second. Using this advanced design WFI will be able to offer these new services as well as a full range of traditional services at a very low cost allowing WFI to build its revenue base quickly and profitably.

LUNCHEON SPEAKER

"A GUIDE TO THE 21ST CENTURY"



DR. LOWELL CATLETT

**Professor, New Mexico State University
Las Cruces, New Mexico**

Dr. Lowell Catlett, a full-time professor at New Mexico State University is an exciting futurist whose knowledge of technologies and their implications on the way we will live and work is addressed in his varied and upbeat presentations. His vast knowledge astounds corporate and association audiences both nationally and internationally. His presentations are thought-provoking and highly-entertaining.

Dr. Catlett received his doctorate in Economics from Iowa State University, and has twice received the Don C. Roush Award for Excellence in Teaching. He is also a recipient of the prestigious Burlington Foundation Faculty

Achievement Award for Outstanding University Teaching. In 1994 he was one of two Western Regional recipients of the NASULGC's Excellence in College and University Teaching in the Food and Agricultural Sciences Award.

Lowell recently received the College of Agriculture and Home Economics Advisor of the Year as well as Teacher of the Year at New Mexico State University.

He is a consultant to the U.S. Departments of Agriculture, the Interior, Defense and Labor. He has also been a consultant to many Fortune 500 companies.

DEVELOPMENT OF SLOTTED CORE CABLE USING NONZERO-DISPERSION SHIFTED FIBER

Masakazu Nakano, Makiko Miura, Hideaki Mizuguchi

Lucent Technologies Yazaki LTD.

1157-106 Hotozawa, Gotemba-city, Shizuoka-Pref., 412-0046, JAPAN

ABSTRACT

We report on the development of single slotted core cable utilizing G.655 nonzero-dispersion fiber (NZDF). This cable can accommodate up to 300 fibers arranged in five layer stacks of 4-fiber ribbon. The type of fiber has a small amount of positive dispersion from 1530nm to 1620nm, and a dispersion slope of less than 0.05ps/nm²/km. The mechanical and optical performance of the experimental cable was evaluated in both the C and L band. This type of cable may offer considerable advantages for the economical construction of long haul networks for high bit rate transmission.

INTRODUCTION

10 Gb/s DWDM is currently the leading technology for high bit rate commercial telecommunications transmission, and it is generally assumed that 40Gb/s transmission systems will be commercially available in the near future. However, high bit rate long haul networks based on conventional single mode (G.652) fiber must incorporate significant amounts of dispersion management, and considerable attention may need to be paid to careful dispersion mapping. This has the effect of either reducing the repeater-less span length, increasing costs, or both. Consequently, the majority of new long haul transmission networks currently being installed use NZDF. This type of fiber was originally developed by Lucent Technologies Bell Laboratories to overcome

some of these limitations. NZDF has enough dispersion to provide adequate suppression of non-linear effects such as four-wave mixing, while at the same time allowing significantly longer uncompensated transmission spans, especially at high bit rates.

In Japan, the overwhelming majority of fiber optic cable is based on the slotted core structure, primarily because it affords easy access to the fiber, even in a high density cable. Unfortunately however, a significant fraction of the Japanese fiber optic cable infrastructure uses G.653 dispersion shifter fiber (DSF). Because DSF has too little dispersion in the C-band to adequately suppress 4-wave mixing in DWDM systems, there is considerable interest in Japan in the use of the higher dispersion L-band for high bit rate DWDM transmission.

CABLE STRUCTURE

Our experimental cable structure is shown in Figure 1. This cable consists of a single, 15-slot slotted rod, with each slot containing a five layer stack of 4-fiber ribbons. The NZDF we chose has positive dispersion of 2.6 - 6.0 ps/nm/km from 1530 to 1565nm (C-band) and 4.0 - 8.6 ps/nm/km from 1565 to 1620nm (L-band), a dispersion slope of less than 0.05 ps/nm²/km and a mode field diameter of 8.4+/-0.6 micron. Our reasons for choosing this fiber were that it was readily available and it is by far the most commonly selected type.

The cable has a diameter of approximately 20mm and is completely non-inductive, with a

dielectric core and an Aramid FRP central strength member. Water-blocking (WB) tape is wrapped around the slotted rod for water resistance. The outer jacket material is extruded polyethylene.

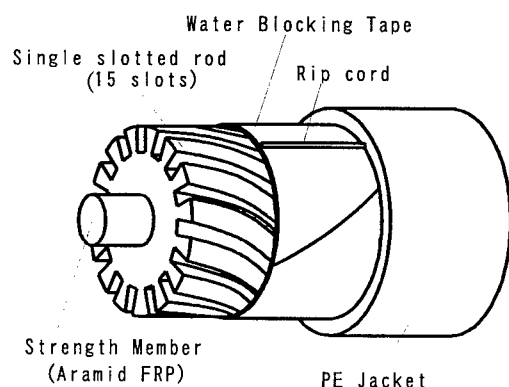


Figure 1. Cable structure

Table 1. Physical dimensions of experiment cable

Component	Dimension (mm)
Ribbon thickness	0.4
Ribbon width	1.1
Strength member diameter	4.5
Slot rod diameter	16.5
WB tape thickness	0.25
Jacket thickness	1.5
Cable outer diameter	20

EXPERIMENTAL RESULTS

4-fiber ribbon characteristics

a. Macro-bending performance.

Macrobending performance of the fiber easily satisfies the requirement of less than 0.5dB at 1550nm specified by ITU-T G.655. Even at 1625nm the macro-bending performance was more than sufficient to provide good cabling performance.

b. Micro-bend performance.

The Micro-bend test is performed by applying pressure to a 100 mm section of the fiber ribbon using two pieces of sandpaper attached to metal plates. The pressure is applied via an electronically controlled load cell in order to ensure good reproducibility.^[1] The Micro-bend characteristics are shown in Table 2, along with the results for G.652 fiber, shown for comparison.

As can be seen, the micro-bend performance of the NZDF ribbon was better than that of comparable G.652 ribbon at 1550nm. Consequently, we deem the micro-bend performance of NZDF ribbon to be more than adequate for use in slotted core cable.

Table 2. Micro-bend performance of NZDF

Items	NZDF	G.652
Additional loss at 784N	0.14dB	0.34dB
0.01dB loss pressure	192N	104N

Optical performance

a. Attenuation.

Figures 2. and 3. show the optical attenuation following each manufacturing process. The 1550nm performance was measured using bi-directional OTDR, but the 1625nm performance was measured using the cutback method. As can be seen, the various manufacturing processes introduced no significant additional attenuation in either the C or L band. Figure 4. shows the attenuation distribution at 1625nm. The optical attenuation of this cable was relatively low and showed little variation, with a maximum measured value of less than 0.25dB/km.

These results are not surprising in view of the robustness of NZDF against micro and macro-bending loss, and demonstrate that the slotted core cable structure is capable of providing good optical performance with NZDF in either the C or L bands.

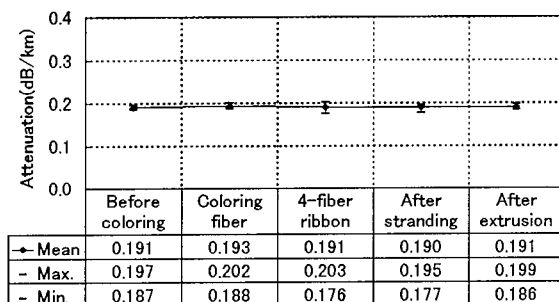


Figure 2. Attenuation performance at 1550nm

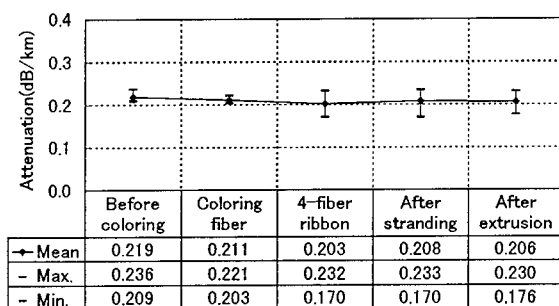


Figure 3. Attenuation performance at 1625nm

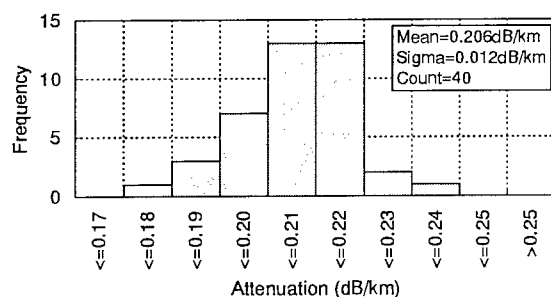


Figure 4. Distribution of attenuation at 1625nm

b. Cable cut-off wavelength.

Table 3. shows the cable cut-off wavelength characteristics of a 22 meter cable. The measurement method followed IEC 793-1. Again, the result satisfies the ITU-T G.655 latest recommendation of less than 1260nm.^[2]

Table 3. 22 meter cable cut-off wavelength (nm)

Item	Mean	Sigma	Max.	Min.
λ_{cc}	1110.1	28.1	1193	1064

c. Temperature cycle performance.

Figure 5. shows the temperature cycle performance over a temperature range from -30 to +70 Celsius using a cycling profile as shown in Figure 6. Attenuation was measured using bi-directional OTDR on each individual fiber. The maximum loss change at 1550 nm was less than 0.02dB/km at 70 Celsius.

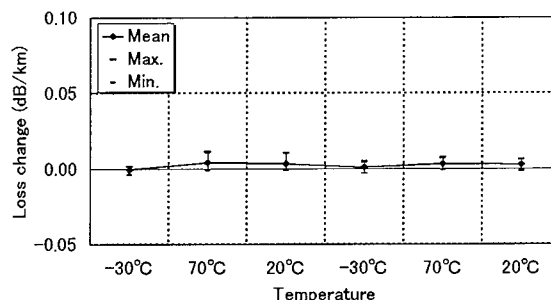


Figure 5. Temperature cycling performance

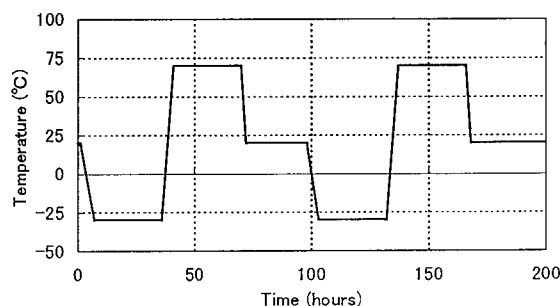


Figure 6. Temperature cycling test profile

Dispersion characteristics

The dispersion characteristics of the utmost importance when constructing a network for high bit rate transmission. Again, the cable should have low enough chromatic dispersion to minimize the need for dispersion compensation without sacrificing reasonable robustness against signal degrading non-linearities. Furthermore, as transmission rate increases, it is important to minimize the Polarization mode dispersion of the cable.

a. Chromatic dispersion.

The chromatic dispersion characteristics depend on both the refractive index profile of the fiber and the material dispersion of the glass. In view of the critical importance of both the dispersion slope and chromatic dispersion to successful high bit rate transmission, we measured both over a temperature range of -30 to +70 Celsius. The results as shown in Tables 4-1. and 4-2. demonstrate that the chromatic dispersion remains stable over this range.

Table 4-1. Dispersion slope (ps/nm²/km)

Temp.	Mean	Sigma	Max.	Min.
20°C	0.0407	0.0014	0.044	0.039
-30°C	0.0409	0.0012	0.044	0.040
70°C	0.0409	0.0013	0.044	0.040

Table 4-2. Dispersion at particular wavelength (ps/nm/km)

λ	Temp.	Mean	Sigma	Max.	Min.
1530nm	20°C	3.571	0.386	4.02	2.81
	-30°C	3.616	0.377	4.04	2.87
	70°C	3.534	0.381	3.97	2.79
1565nm	20°C	4.996	0.350	5.41	4.27
	-30°C	5.046	0.347	5.45	4.34
	70°C	4.965	0.349	5.38	4.25
1620nm	20°C	7.235	0.301	7.59	6.57
	-30°C	7.294	0.306	7.66	6.63
	70°C	7.214	0.306	7.58	6.55

b. Polarization mode dispersion.

Polarization mode dispersion is an increasingly important concern for long haul DWDM networks. While there is still ongoing discussion regarding the matter, the conventional view is that a reasonable target for the PMD link design value is 0.1ps/rt-km. Although it is not uncommon for fiber manufacturers to specify fiber PMD, the authors are unaware of any demonstrated relationship between fiber PMD and cable PMD. Indeed, the PMD must be expected to vary depending on the cable structure because of the effect cable structure has on the polarization mode coupling. Therefore, since in our view no claim can be made for the value of cable PMD

based on the fiber PMD value, we deemed it essential to evaluate the PMD performance of the cable over a range of temperatures. The PMD Coefficient (PMD Coef.) results are shown in Table 5.

Figure 7. shows the PMD Coef. versus temperature from -30 to +70 Celsius for 2 cycles (as previously shown in Figure 6). The PMD was evaluated using the spectral scanning method while the cable was wound loosely on a drum. As can be seen, the PMD Coef. shows no significant variation with temperature.

Table 5. PMD Coef. result (ps/rt-km)

Items	Mean	Sigma	Max.	Min.
PMD Coef.	0.0482	0.0134	0.094	0.033

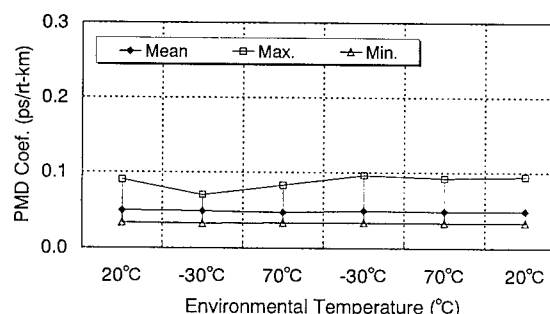


Figure 7. PMD versus Temperature

It is generally found that the PMD of slotted core cable is slightly higher than that of loose tube cable. Although the reason is not yet certain, one proposed way to account for the difference between these cables is the effect of residual strain from the cable structure. Accordingly, we looked for a relation between PMD performance and residual strain.

Results are shown in Table 6. Typical slotted core cable has a maximum residual strain value of 0.05%. We refer to this condition as "Case A". Our experimental cable incorporated high residual strain (> 0.1%) ribbons in one slot for evaluation purposes. We refer to this condition as "Case B". Results show no significant relation between PMD and residual strain.

Table 6. Relationship between PMD
and Residual strain (ps/rt-km)

Items	Mean	Sigma	Max.	Min.
Case A	0.0466	0.0084	0.060	0.033
Case B	0.0493	0.0160	0.086	0.037

Cable installation performance

a. Mass fusion splicing.

Mass fusion splicing performance must meet established criteria in order to reduce installation costs. Table 7. shows the results of mass fusion splicing of 4 fiber ribbons following optimization of the splicing parameters. We evaluated 2 types of splices: NZDF/NZDF (standard splice) and NZDF/G.652 (transition splice). In both cases the splice loss satisfies the criteria set forth in Japanese network construction specifications. The higher loss of the transition splice is expected based on theoretical considerations, but since such a splice is very infrequent, it poses no significant problem for network deployment.

Table 7. Result of Mass fusion splice loss (dB)

Items	Mean	Sigma	Max.	Min.
Standard	0.044	0.014	0.08	0.02
Transition	0.070	0.033	0.17	0.02

b. Other installation related issues.

Table 8. shows other parameters relevant to cable installation. These characteristics do not differ from standard single mode fiber cable and are shown only for completeness.

Table 8. Other installation performance
parameters

Parameter	Value
Cable Tensile Strength (Even Break)	>10kN
2 Meter Jacket Rip Failure Probability	<5%
Ribbon Strip Force (Using Hot Stripper)	8.73±1.18N

Mechanical performance

a. Residual strain.

Table 9. shows the residual strain characteristics after cabling. The strain was measured in a 500 meter straight section of cable using Brillouin Optical Time Domain Reflectometry (B-OTDR) in a controlled temperature environment. As described previously, typical slotted core cable has a residual strain of <0.05% under installation conditions. In our test cable, the fiber to fiber variation of residual strain was consistently low. Table 10. shows in some detail the effect on residual strain of the various manufacturing steps. It is important to note that the maximum changes observed during the different processes typically occurred in different fibers.

Table 9. Residual strain result
under the straight condition (%)

Items	Mean	Sigma	Max.	Min.
Straight	0.019	0.009	0.03	0.00

Table 10. Strain change following
each process (%)

Items	RMS	Sigma	Max.	Min.
Ribbon	0.010	0.006	-0.03	0.00
Stranding	0.008	0.007	0.03	-0.01
Extrusion	0.007	0.006	-0.02	0.02

b. Other mechanical performance.

Table 11. shows representative cable mechanical characteristics. In each test, optical loss was measured in both C and L-band. The basic mechanical test method was in conformance with IEC-794-1. Cable performance satisfies all test requirements.

Table 11. Mechanical test results

Items	Test Condition	Results	
Tensile strength	1.96kN, 1minute hold	No loss increase @1550nm No residual loss @1625nm	
Tensile strain	1.96kN, 1minute hold	<0.15% at cable and fiber strain <0.02% residual strain	
Compression	1.96kN/100mm 10minute hold	No loss increase @1550nm No residual loss @1625nm	<2.5% crushable rate after test
Impact	39.2N, 150mm, 25times	No residual loss @1550nm No residual loss @1625nm	<5.0% crushable rate after test
Torsion	+/-360degree, 2m 3cycles	No loss increase @1550nm No residual loss @1625nm	
Flexing	600mm, 360degree 9m, 5cycles	No loss increase @1550nm No residual loss @1625nm	
Repeatable bend	400mm, +/-180degree 5cycles	No loss increase @1550nm No residual loss @1625nm	
Bend	400mm, 360degree 1turns	No loss increase @1550nm No residual loss @1625nm	
Vibration	+/-5mm, 15Hz, 10 ⁶ cycles	No loss increase @1550nm No residual loss @1625nm	

c. Water penetration performance.

This type of cable has a WB tape for water resistance. One of the standard Japanese testing conditions specifies a one-meter static head, 20m cable length, 24 hours, no water leak through the open end using artificial seawater. As expected from Japanese manufacturers' experience with standard single mode fiber, our results demonstrate specification conformance of the cable using NZDF. (The maximum penetration of water through in the cable was less than 10m, similar to standard fiber.)

CONCLUSION

We have developed a slotted core cable using NZDF that is suitable for long distance high bit-rate transmission networks. The basic 4-fiber ribbon performance was the same as, or better than similar cable using G.652 fiber. The polarization mode dispersion was quite low and shows robustness against variations in environmental conditions such as temperature and strain. Mean Mass fusion splicing loss was about 0.05dB using standard splicing conditions and although transition splice losses were somewhat higher, they nonetheless fall within the

permissible range generally specified in Japan for actual network construction. Based on the results presented here, Japanese network operators can safely realize the superior transmission characteristics of NZDF cable without fear of compromising general cable performance specifications. It is hoped that this type of terrestrial cable will be used to construct future long haul high bite rate networks.

ACKNOWLEDGEMENTS

The authors gratefully acknowledge James Refi, William Baron, Jinkee Kim and Wayne Lewis for numerous technical discussions.

REFERENCE

- [1] M.A. Saifi etc. "Reliability Issues With Fiber Ribbons", SPIE Volume 2074, 1993
- [2] ITU TELECOMMUNICATION STANDARDIZATION SECTOR, COM 15-152-E, April 1999, PROPOSED REVISIONS OF RECOMMENDATIONS G.652 and G.655.

SPEAKER



Masakazu Nakano
Lucent Technologies Yazaki Ltd.
1157-106, Hotozawa, Gotemba-city, Shizuoka-
Pref. 412-0046 JAPAN

M.Nakano received his B.E. degree from Nihon University in 1991. He has been engaging in Business & Technology Development Department and his main work is development of evaluation technology with optical fiber, ribbon and cable.

THE STATUS AND FUTURE OF HIGH FIBER COUNT CABLE DESIGNS

Eric R. Logan, Hani M. Nassar, Richard S. Wagman

Siecor
Hickory, North Carolina

ABSTRACT

During the evolution of high fiber count cables, single tube, loose tube and slotted core cables have emerged as the primary designs. The feasibility of expanding the fiber count of these three designs was analyzed. Further, the design characteristics were compared to determine factors important for future development.

Eleven cables from the three design categories were selected and compared by cable specifications, cable performance, and installation characteristics. The eleven cables range in fiber count from 400 to 3200 and range in status from production to early concept designs.

Single tube designs (864 to 1296 fibers) and slotted core designs (2000 to 3200 fibers) were identified as next generation cables. The totally dry nature of the slotted core design and the high fiber packing density of the single tube designs were identified as important design characteristics.

INTRODUCTION

The need for high fiber count (HFC) cables is expanding with the emergence of higher bandwidth applications and the desire to move fiber closer to the end user. HFC cables are being installed in long distance applications, metropolitan ring networks, and as the first branches in the feeder loop.

Within the last 20 years, HFC cables have been presented at conferences and symposiums. While the number of fibers defining HFC has increased through time, 400 is the threshold for this paper. Figure 1 shows the frequency of presentations with time. In 1981, three papers were presented with maximum fiber counts of 2000, 3000 and 4000.^{1,2,3} This initial interest in HFC cables was driven by comparisons to the copper cable infrastructure. After this initial discussion, HFC cables were not presented until

1989. Issues such as installation methods and hydrogen generation dominated the discussions through the 1980's.

In 1991, a 4000 fiber cable and its application in Japan's fiber to the home (FTTH) network strategy was presented by NTT.⁴ This paper initiated several more HFC papers in the early 1990's for the Japanese market. In 1995 and 1996, the first HFC cables for the U.S. market^{5,6} were presented.

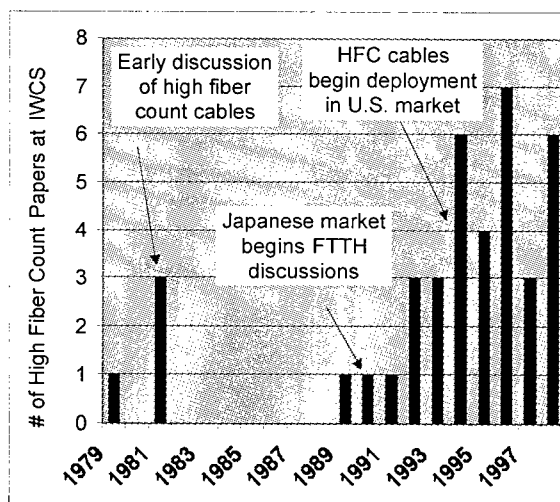


Figure 1 – Trend of High Fiber Count Cable Presentations

Although a variety of cable designs have been presented for HFC cables, three primary designs have emerged over time: single tube, loose tube and slotted core.⁷ The upper range for HFC cables in large scale production is now 800 to 1000 fibers.

The first objective of this study is to determine the feasibility of increasing the fiber count of the three HFC designs. The second objective is to compare the designs and determine characteristics that will impact future development.

This study identifies issues for future expansion of HFC cable designs. The three cable types are described, and examples of each type ranging in status from commercialized to conceptual cables are compared in the following areas:

- Cable specifications – Size, weight, and stiffness
- Cable performance – Environmental and mechanical testing
- Installation characteristics – Inner duct size, maximum cable length, minimum bend radius and cable splicing

The feasibility of expanding the fiber count of the three major designs above the current production level is summarized. Design advantages are highlighted in specific areas, and the effects of these advantages on future development are summarized.

HFC CABLE DESIGNS

The three cable types provide different methods of packaging and protecting the optical fibers from external forces. Each design has several cable construction options. The general cable designs and options are discussed, and the eleven specific designs selected for analysis are described.

General Cable Types and Options

Single Tube. These cables use 24-Fiber or 36-Fiber ribbons that may be split into 12-Fiber units for mass fusion splicing. The buffer tube contains a filling compound that prevents water migration and reduces stress on the optical fibers. The sheath can be designed with parallel strength elements in the outer jacket as shown in Figure 2 or with smaller stranded strength elements. The strength elements can be metallic or dielectric, and a steel armor can be applied for underground applications.

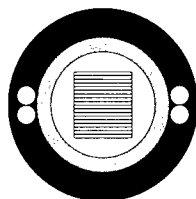


Figure 2 - Typical Single Tube HFC Cable

Loose Tube. These cables offer a variety of fiber organizations because of the identification provided by the buffer tubes. Three fiber organizations are considered in this paper: 12-Fiber loose bundles, 12-Fiber ribbons, and 24-Fiber ribbons. The buffer tubes contain filling compound; however, the cable core interstices are typically dry. The tubes are S-Z stranded for improved mid-span access. The strength elements can be metallic or dielectric, and a steel armor can be applied for underground applications. A loose tube cross-section is shown in Figure 3.

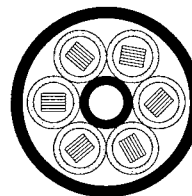


Figure 3 - Typical Loose Tube HFC Cable

Slotted core. These cables contain 8-Fiber or 16-Fiber ribbons that may be split into 4-Fiber or 8-Fiber units for mass fusion splicing. Current commercialized cables contain a single slotted rod as shown in Figure 4, while higher fiber counts have been obtained using an outer layer of U-Grooves.⁸ S-Z stranding is preferred for mid-span access⁹; however, unidirectional stranding simplifies manufacturing. Water blocking is achieved with water swellable tapes providing a totally dry cable design. The central strength element can be metallic or dielectric.

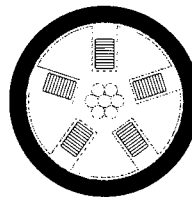


Figure 4 - Typical Slotted Core HFC Cable

Selected Cable Designs for Analysis

Future development of HFC cables was evaluated by analyzing specific cables within the three design families. Eleven cables were selected from a broad status of development.

The eleven designs are shown in Figure 5. The cross-sections are categorized and plotted versus fiber count. The cable designation, fiber count and fiber organization are shown for each design. The cable designation is described below:

- ST = single tube
- LT = loose tube
- SC = slotted core
- Number = approximate fiber count divided by 100
- "F" = bundled fibers
- i.e.: SC32 = slotted core 3200 fiber

ST4, LT4, LT8 and SC10 are in large scale production, and the seven other designs are development and concept cables. The single tube and loose tube designs are all dielectric while the slotted core designs are non-armored with a stranded steel central member. The single tube and loose tube designs have a tensile rating between 2700 and 4000 N, while the slotted core designs range between 4000 and 8000 N. A more accurate design comparison could be performed if the type of strength element was constant; however, a more practical approach was to compare the designs as they exist today.

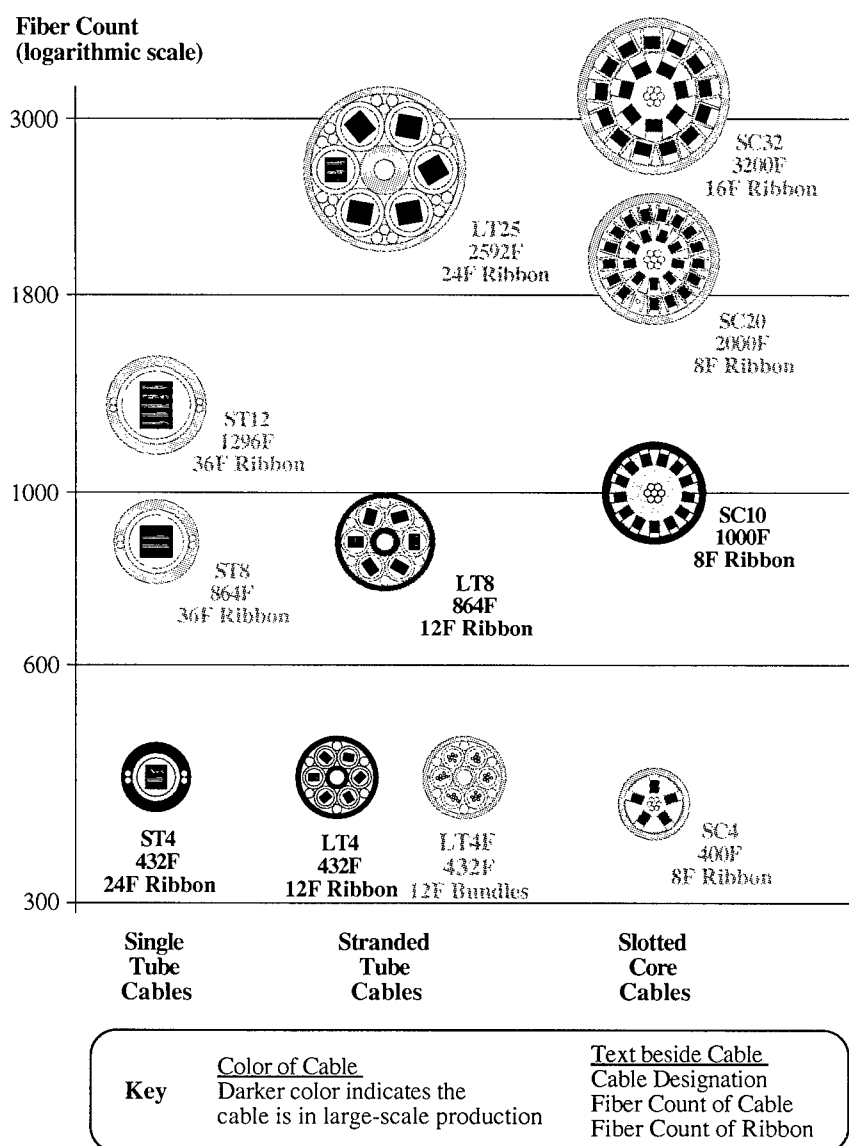


Figure 5 - Cables Selected for Comparison

DESIGN ANALYSIS

HFC cable designs are a class of fiber optic cable designs. Other classes included self supporting, drop, and submarine cables. Each class has key requirements that define superior performance. For example, cable and fiber strain are important for self supporting cables while cost is a dominant factor for drop cables.

The parameters used to compare the eleven different cable designs were divided into three categories: cable specifications, cable performance, and installation characteristics. These data represent key factors that will influence the future development of HFC cables.

Cable Specifications

HFC designs are normally larger, heavier and stiffer than lower fiber count fiber optic cables. For this reason, cable size, weight, and stiffness are key specifications.

Cable Size. Fiber packing density is a measure of cable size. It is the ratio of fiber count and cable cross-sectional area. The trends in fiber packing density are best seen when plotted versus fiber count on a logarithmic scale¹⁰. Figure 6 shows that single tube designs are clearly the most efficient; however, the SC32 cable has the highest packing density. The fiber count of the ribbon affects packing density. For example, square ribbon stacks obviously provide the most efficient packing density for the single tube and loose tube designs.

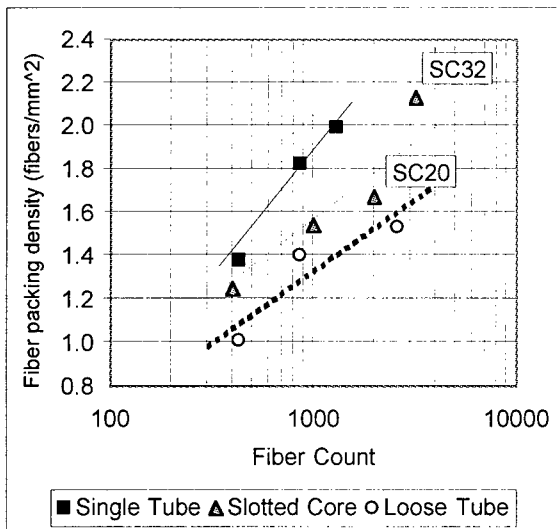


Figure 6 – Fiber Packing Density

The slotted core designs are not as simple; however it is clear that changing from 8-Fiber ribbons to 16-Fiber ribbons caused a major change in packing density between the SC20 and SC32 designs.

Cable Weight. All of the designs were comparable below 2000 fibers as shown by Figure 7. This was a surprising conclusion given the variations in cable compositions. Above 2000 fibers, design differences begin to impact cable weight. The difference in weight between the SC32 and LT25 cables is primarily due to packing density and water blocking method (dry vs. filled).

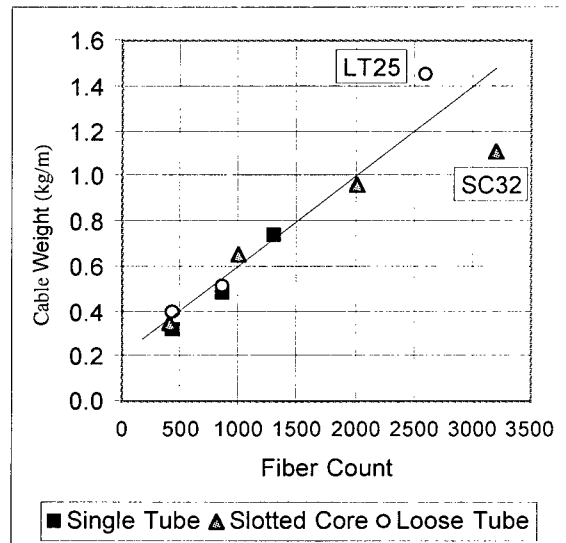


Figure 7 – Cable Weight

Cable Stiffness. Cable stiffness (B) is a new test metric adopted by IEC and can be calculated using different methods¹¹. It is a function of the moment of inertia (I) and the modulus of elasticity (E) for each cable component. Thus $B = EI$. For a hollow cylinder,

$$I = \frac{\pi(D_o^4 - D_i^4)}{64} \quad \text{Equation (1)}$$

If an actual cantilever test is conducted, then

$$B = \frac{L^3 F}{3y} \quad \text{Equation (2)}$$

Where:

L = Length of sample under bending stress,
F = Force applied to the sample, and
y = Deflection of the sample at the point
where force is applied.

Figure 8 shows the relationship between cable stiffness and fiber count. As expected, the correlation is exponential given that moment of inertia is proportional to the fourth power of diameter. Slotted core designs are clearly the most flexible in this study which is a result of the high concentration of rigid components in the center of the cable. On the other hand, single tube designs are the least flexible due to the concentration of rigid components towards the outer edge of the cable.

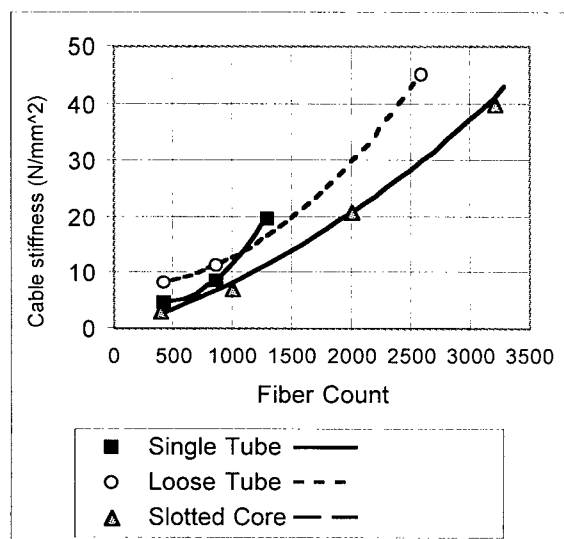


Figure 8 – Cable Stiffness

Cable Performance

Environmental and mechanical performance measures were developed to compare the eleven designs. Each cable was ranked on a scale from 1 to 4 as shown in Figure 9. While all of the cables have adequate performance, the ranking indicates the relative ease of attaining superior performance with 4 being the best and 1 being the lowest. For example, the SCR cables are more mechanically robust than the other designs and receive a rating of "4". On the other hand, their environmental rating is "1" because they have higher attenuation than cables containing filling compound.

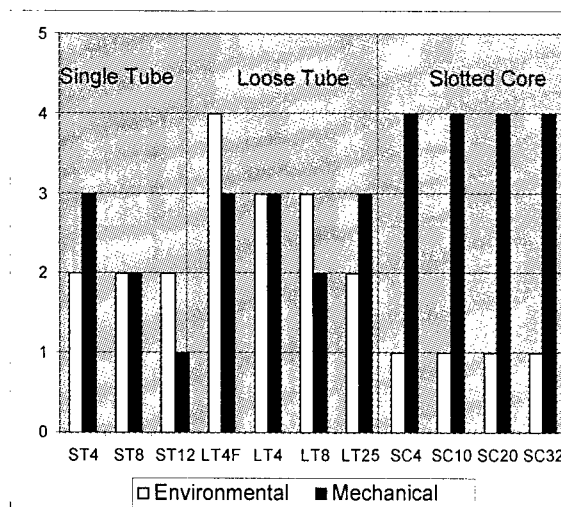


Fig 9: Performance Comparison

Environmental Performance. The attenuation of an optical fiber in the deployed stage should be relatively constant. Influences such as temperature changes and tensile loading on the cable can cause the attenuation to vary. Loose fibers have the best environmental performance as compared to ribbons since the ribbon structure constrains the movement of the fibers. For that reason, the only design not using ribbons, LT4F, was rated highest in environmental performance. The loose tube and single tube designs were rated higher than slotted core designs because the filling compound and buffer tube size allow greater movement of the ribbons which reduces stress in the ribbon stack.

Mechanical Performance. Fiber optic cables are designed to withstand damage from mechanical forces during cable placement and after installation. Crush, impact, twist, and low temperature bending are examples of the forces encountered in the field. For many of the mechanical forces, a bigger cable is better since a larger cable has more surface area to distribute impact and crush forces as well as higher torsional rigidity against twisting forces. The rankings in Figure 9 show that slotted core cables have better performance than single tube cables. There are two main reasons for this ranking.

The first reason concerns the compressive resistance of stranded buffer tubes versus slotted rods. Figure 10 shows buffer tube deformation under compressive forces. The advantage of a slotted core cable over a stranded tube design is that the leg of a slotted

rod acts like two buffer tubes welded together. This is an advantage because thickness has an exponential effect on mechanical strength.

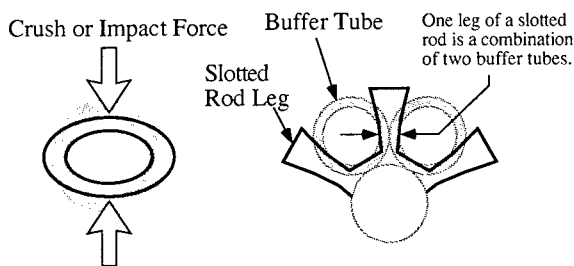


Figure 10 - Mechanics of Tube and Slotted Rods

The second reason for the mechanical performance rankings is that the single tube cable does not follow the "bigger is better" tendency. As diameter increases, wall thickness must be increased to maintain the same robustness (resistance to compressive forces). However, increasing wall thickness increases stiffness. Calculated values of robustness and stiffness are plotted versus buffer tube diameter in Figure 11. Two curves are shown for each parameter to illustrate the effect of relative thicknesses ($T=1$ and $T=2$). The wall thickness of the single tube designs in this study was designed to maintain a small cable diameter and low cable stiffness. This resulted in lower mechanical performance for the single tube cables.

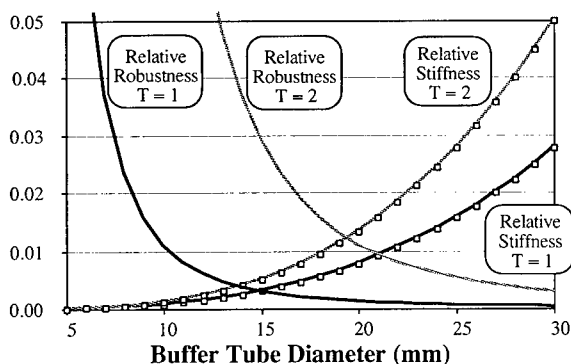


Figure 11 - Buffer Tube Properties Versus Diameter

Installation Characteristics

Cable placement and cable splicing were selected as key considerations for HFC cables. The ease of cable placement is important due to limited duct space in metropolitan areas. Cable splicing was selected because it is a key technical challenge for HFC cables.

Cable Placement. Three placement criteria were selected for analysis: duct size, cable length, and cable bend radius.

The minimum duct size required for each design is shown in Figure 12. Two levels of fill ratio (cable area divided by duct area) were selected to represent various installation methods. In several cases, the same duct size is required for different fiber counts. For example, ST8 and ST12 both require a 31.7 mm (1.25 inch) duct using a fill ratio of 80%. This is due to the increments of commercially available duct sizes. This shows that cable diameter is more important when the size is near the step changes in duct size using a given fill ratio.

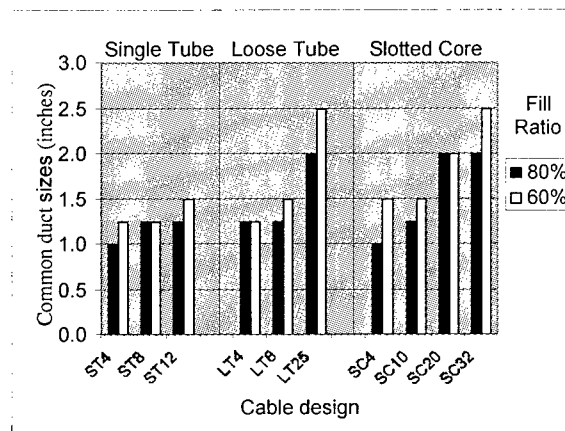


Figure 12 - Inner Duct Sizes

The maximum length of HFC cables is typically limited by reel size. For the calculations in Figure 13, a 96" reel was used because it is one of the largest sizes used today. The maximum required length of HFC cables is difficult to determine because of the variables such as network architecture and geography. Based on today's use of HFC cables, the lengths of the LT25, SC20 and SC32 are too short for some applications.

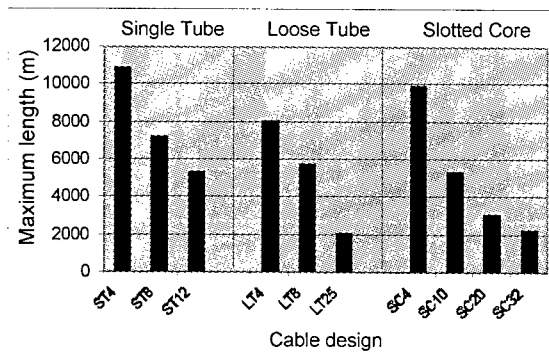


Fig. 13 - Maximum Cable Length

Minimum cable bend radius is shown in Figure 14. The rules of thumb for calculating bend radius range from 10 to 20 times cable diameter. Although these rules of thumb are simplifications of complex three dimensional calculations, they provide a quick insight into the bending requirements of HFC designs. For example, the LT25, SC20 and SC32 designs might require sheaves larger than 1.5 meters during installation. This size is significantly larger than the standard equipment used today.

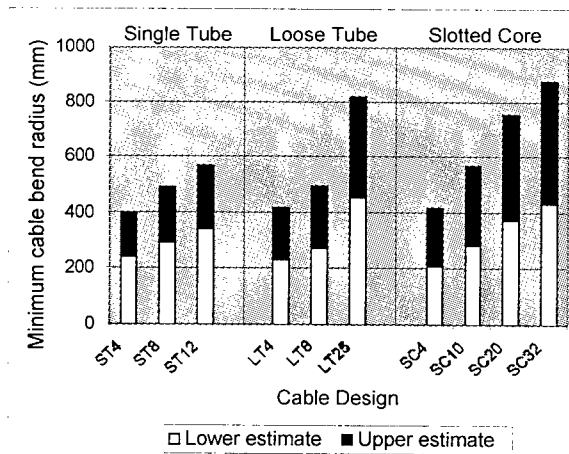


Figure 14 - Minimum Cable Bend Radius

Cable Splicing. Accessing and splicing the ribbons is a major concern since this represents a large portion of the time to install HFC cables. The advantages and disadvantages of the three HFC designs are described below.

Single tube designs offer simplicity by having all ribbons within one buffer tube. The easy sheath removal and the unique ribbon identification are other advantages. The primary disadvantage is

the requirement to split the ribbons into 12 fiber increments before splicing.

Loose tube designs feature the ability to route unopened buffer tubes within a splice closure during mid-span access. This provides extra protection and eliminates the cleaning of fibers not being accessed. Tube color coding and unique ribbon print allow easy location of the ribbons. The primary disadvantage of this design is the time required to remove six individual buffer tubes during end access. A disadvantage of the LT4F design is the identification, splicing and routing of 432 individual fibers within a splice closure.

Slotted core designs are totally dry with no use of filling or flooding compounds. This eliminates the time required to clean the fibers and allows for faster splicing preparation. SZ stranding offers excellent mid-span access as compared to unidirectional stranding. SZ stranding is even more important for dual layer designs because accessing the inner core is very difficult with unidirectional stranding. One current disadvantage is the lack of unique identification for the ribbons. This increases the time to select the correct ribbon number because the installer has to trace the ribbon back to the slotted rod.

SUMMARY

The first objective of this study was to determine the feasibility of increasing the fiber count of the three HFC designs. The slotted core design can be expanded above 1000 fibers with S-Z stranding. This has been a key technical challenge for the slotted core designs. S-Z stranding is essential for the dual layer 2000 and 3200 fiber designs. The single tube design can be expanded above 432 fibers with 36-Fiber ribbons. This change in ribbon width optimizes packing density between 864 and 1296 fibers. The size of the loose tube design is a limitation above 864 fibers. The 864 fiber design is optimized using 12-Fiber ribbons because of the relatively square ribbon stack. The 2592 fiber loose tube design using 24-Fiber ribbons was not competitive in most of the design comparisons.

The second objective was to compare the designs and determine characteristics that will impact future development. One difference among the three designs was the use of filling compound versus a totally dry cable. The dry

slotted core design provides major advantages in cable splicing. Another difference of the designs was fiber packing density. The high packing density of the single tube design allows 1296 fibers to be installed in a 31.7 mm (1.25 inch) inner duct. This is important in the U.S. market because 1.25 inch is a common duct size.

CONCLUSION

Single tube, loose tube, and slotted core cable designs were studied for HFC cable applications. Eleven specific designs were described and compared using cable specifications, cable performance, and installation characteristics. The feasibility of expanding the fiber count was discussed. Single tube designs from 864 to 1296 fibers and slotted core designs from 2000 to 3200 fibers are the most feasible next generation HFC designs. The totally dry nature of the slotted core design and the high fiber packing density of the single tube design are the most significant characteristics which will shape future development.

ACKNOWLEDGEMENTS

The authors would like to thank Brad Blazer for his assistance in calculating cable stiffness for this paper.

REFERENCES

1. Y. Koyamada et al., "A Study on High Density Optical Cables With a Great Many Fibers," *30th IWCS Proceedings* (1981): 244-254.
2. P. Bark et al., "High Fiber Count Cables of the Mini-Bundle Design," *30th IWCS Proceedings* (1981): 255-258.
3. H. Haag et al., "High-Density Optical Fiber Cables for the Local Network," *30th IWCS Proceedings* (1981): 259-269.
4. S. Tomita et al., "Preliminary Research into Ultra High Density and High Count Optical Fiber Cables," *40th IWCS Proceedings* (1991): 8-15.
5. W. McCallum, M. Light, R. Wagman, "Design and Development of a Compact High Fiber Count Ribbon Cable," *44th IWCS Proceedings* (1995): 8-15.
6. K. Jackson et al., "Design and Performance of a High-Capacity, Compact, Modular Ribbon Cable Comprising 24 Fiber Ribbon," *45th IWCS Proceedings* (1996): 623-630.
7. S. McCreary et al., "Analysis of a Modular 24-Fiber Ribbon for the Distribution Network," *47th IWCS Proceedings* (1998): 432-439.
8. H. Iwata et al., "Development of 3000-Fiber Cable Using 16-Fiber Ribbons," *45th IWCS Proceedings* (1996): 638-644.
9. H. Iwata et al., "Development of 2000-Fiber Cable with SZ-Stranded U-Grooves and Slotted Rod," *47th IWCS Proceedings* (1998): 34-40.
10. F. Sears et al., "Design and Performance of a 3200-F hybrid SCR/U-groove cable using 16-F ribbons," *45th IWCS Proceedings* (1996): 645-656.
11. International Electrotechnical Commission 794, Optical Fibre Cables, Part 1, Generic specification, Section 2, Basic optical cable test procedures, Cable Stiffness, Method E17.

PRESENTING AUTHOR



Eric R. Logan, P.E. is the Supervisor of High Fiber Count Cable Development at Siecor RD&E in Hickory, NC. His responsibilities include development of single tube and loose tube high fiber count ribbon cables. He received a B.S.M.E. in 1991 from North Carolina State University. He is a licensed professional engineer in North Carolina. Since he joined Siecor in 1991, he has worked in various aspects of process and product development within RD&E. He has authored 2 publications.

Novel Optical Fiber Cable for Distribution Use in Access Network

**Hideyuki IWATA, Shigeru TOMITA, Kazuo HOGARI,
Kiminori SATO and Akira HIROOKA**

NTT Access Network Service Systems Laboratories

Hanabatake, Tsukuba, Ibaraki, 305-0805 JAPAN

Phone +81(298)52-2522

Fax +81(298)60-6130

E-mail address: iwata@ansl.ntt.co.jp

ABSTRACT

The cost of optical fiber cables must be reduced to make it possible to construct optical access networks economically for fiber to the home (FTTH).

In this paper, we describe the requirements and performance of a new type of optical fiber distribution cable for use with a relatively small fiber count.

This cable can be used for aerial applications. This development will lead to a reduction in cable diameter and weight. This in turn will make installation easier and simplify the manufacturing process thus reducing the cable cost.

1. INTRODUCTION

Optical access networks must be constructed economically and immediately to enable us to realize FTTH. We have already reported SZ slotted rod cable for aerial applications. ⁽¹⁾

This cable is suitable for easy branching with the mid-span access technique.

We currently use slotted rod cable with fiber ribbons for the distribution area. This cable is advantageous in terms of its diameter and weight when the fiber count is high, but its cost effectiveness decreases when the fiber count is low. We have developed a new cable without a slotted rod to overcome this demerit.

In this paper, we describe the requirements and performance of this new type of optical fiber cable.

2. REQUIREMENTS FOR AERIAL DISTRIBUTION CABLE

A) Fiber ribbon count

The cable should employ 4-fiber ribbons. This is because they reduce the joining time and provide good handling. It must also be possible to divide this fiber ribbon into mono-coated fibers to make it easy to join it to drop cable without using the fan-out technique and so reduce joining costs.

B) Cable weight and diameter

A reduction in the cable diameter increases cable flexibility. A reduction in the cable weight increases the installation length, lowers the required cable installation force and reduces the number of cable installation machines required for long distance installation. For aerial applications our new cable is lightweight and has a small diameter, and long lengths can be easily installed by hand without the need for an installation machine. This naturally reduces the installation cost.

C) Workability

Cable branching through the use of mid span access technologies enables access networks to be economically constructed when the service demand is unpredictable. The simple cable structure reduces branching time.

D) Reliability

Such cables are also expected to offer long term stability when exposed to mechanical forces and harsh environments. They must provide stable optical transmission for changes in temperature, vibration and mechanical forces. Optical fiber strain is increased by fiber elongation. This is caused by the force applied during installation and by such factors as temperature change, bending or windy conditions after installation. Additional strain is caused by optical network units (ONUs) and bundles of drop cables suspended beneath the cable.

E) Cost reduction

We must reduce the cable cost by simplifying the cable structure and manufacturing process. Moreover, we must reduce the total cost which includes the cost of joining and installation.

3. AERIAL CABLE DESIGN

Figure 1 shows the configuration of aerial cable, which is suspended between poles. This cable is exposed to high and low temperatures and very windy conditions.

In some cases, ONUs are suspended beneath the cable and bundles of drop cable are attached to it with spirally wound wire. The cable must also be capable of supporting the weight of an installation worker.

A) Messenger Wire

We calculated the maximum allowable tension to determine the messenger wire diameter based on the conditions shown in Table 1. The span length was 60 m or 45 m with initial dips of 0.87 m or 0.49 m, respectively. These values are based on the need to maintain a cable height of 5 m from the ground at 35 °C.

ONUs were not suspended from the cable in wind class A areas. A Drop cable was not bundled with this cable for span lengths larger than 45 m.

The dip d is expressed by the following equation(2),

$$d^3 + \left[\frac{3S^2}{8} \left(\frac{T_0}{EA} - \alpha(t-t_0) \right) - d_0^2 \right] d = \frac{3WS^4}{64EA} \quad (1)$$

where W is the effective cable weight, EA is the cable stiffness, α is the equivalent linear expansion coefficient of the cable, t is the temperature and T_0 is the initial tension on the cable. The tensile force T , T_0 is expressed by the following equation,

$$T = \frac{S^2 W}{8d}, \quad T_0 = \frac{S^2 W_0}{8d_0} \quad (2)$$

where W is the cable effective weight, S is the span length and d_0 is the initial dip.

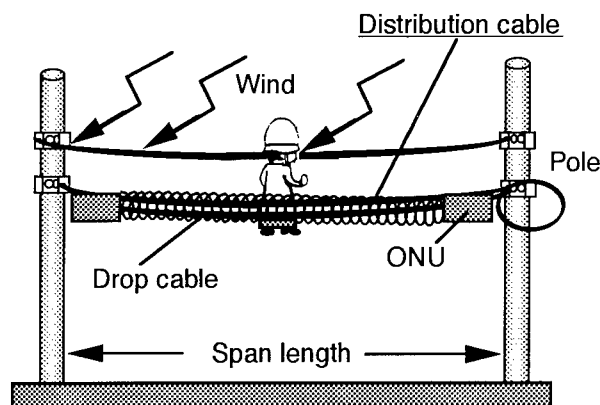


Figure 1 Configuration of aerial cable

Table 1 Applicable conditions for messenger wire

Factor	Weight		Notes	
Windy condition (kN/m ²)	Class A 0.98	Class B 0.49	Class A 40m/min	Class B 28m/min
Temperature change	1.0 kN		-30~+35°C 1.111 × 10 ⁻⁵ /deg.	
Bundle with drop cable	2.16 kN		< 45 m span Drop cable	
Installation on cable	2.94 kN		One person Tools	
Suspended ONU	0.20 kN		2 sets	

The cable effective weight W is expressed by

$$W = \sqrt{W_c^2 + (WP \times H)^2} \quad (3)$$

where WP is the wind force, H is the cable height and W_c is the cable weight.

We calculated the relationship between W_c and H for the messenger wire area, when the wind condition was A or B and the span length 45 m or 60 m. Figure 2 shows the calculated results for messenger wire areas of 10 mm².

We calculated the failure rate of a fiber using n is 22 and ϵ_p is 1 %. Figure 4 shows the relationship between excess cable length for the messenger wire and the failure rate when strain is induced during manufacture.

Based on the results, when the excess cable length is from 0.12 to 0.18, both manufacture strain values satisfied the required failure rate.

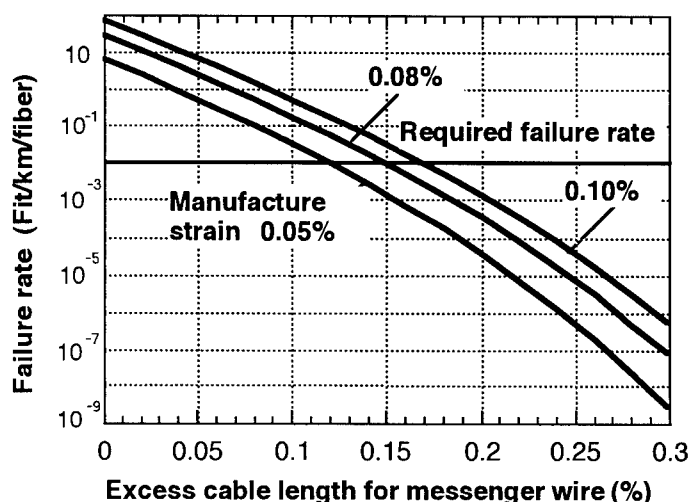


Figure 4 Excess cable length vs failure rate

4. 24-FIBER AERIAL CABLE

We designed the cable structure to meet these requirements.

A) Structure

Cross-sectional views of the current and new 24-fiber cables are shown in Figure 5. The cable consists of 4-fiber ribbons, a cable sheath and a tensile strength member without a slotted rod. The stacked ribbons are stranded in the cable sheath.

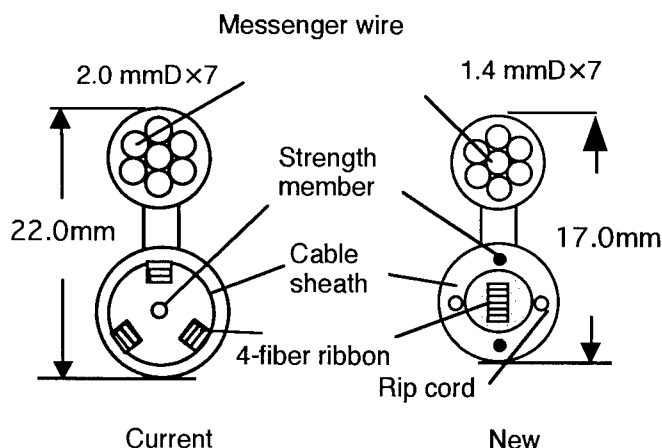


Figure 5 Structure of 24-fiber cable

The cable is 17 mm high and weighs 0.15 kg/m. Rip cords are used to allow the cable sheath to be removed easily.

B) Performance

Table 4 shows the attenuation, mechanical and temperature characteristics of the cable.

The attenuation performance was similar to that of currently used optical cable. The optical loss changes were measured for temperatures between -30 and +60 °C with the cable on the pole. The mechanical performance at a wavelength of 1550 nm in terms of bending, lateral pressure, tensile and squeezing tests was found to be similar to that of current cable.

Table 4 Prototype cable performance

Test item	Result
Attenuation at 1550 nm	< 0.25 dB/km
Temperature cycle at 1550 nm: -30 ~ +70 °C	< 0.06 dB/km
Bending: 160 mmR	No loss increase
Lateral pressure: 1960 N/100 mm	No loss increase
Tension: 0.25%	No loss increase
Squeeze: R=250 mm	No loss increase
Impact: 1 m/9.8 N	No loss increase
Fiber ribbon pull out force: > 9.8 N/10 m	> 9.8 N/10 m

C) Mid span access performance

We measured the optical loss change at a wavelength of 1550 nm while working on mid-span access. Figure 6 shows the handling characteristics. The procedure is divided into five stages, cutting the combined part, exposing both rip cords, dividing the cable sheath by pulling the rip cords, removing buffer material, extracting the fiber ribbons.

The maximum optical loss change for dividing the cable sheath was about 1 dB, but there were no loss changes with the other procedures.

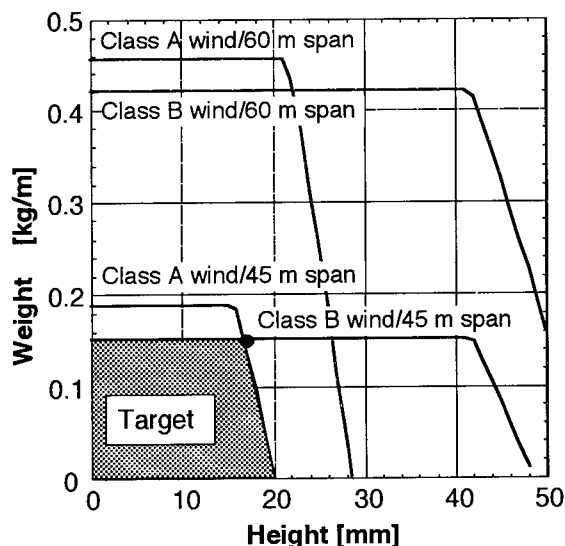


Figure 2 Cable height vs weight

Based on the results, the target weight should be less than 0.15 kg/m and its height should be less than 17 mm to enable small count cable to withstand harsh conditions. Below we describe our successful achievement of these weight and height requirements.

B) Self supporting cable structure

A self supporting cable structure can reduce working time and improve installation safety. The optical fiber strain in a cable is increased by cable elongation which depends on environmental and installation conditions. Our cable is provided with excess length to enhance the reliability of the optical fiber. Figure 3 shows the relationship between temperature and elongation under harsh conditions. Our calculations were based on these conditions, namely class A area wind and a 45 m span.

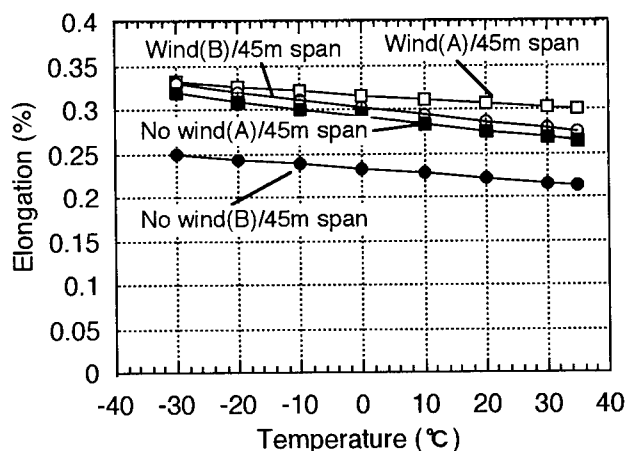


Figure 3 Temperature vs elongation

- 1) Wind A/ 45 m span : Bundle
- 2) No wind A/45 m span : Bundle, installation
- 3) Wind B/ 45 m span : Bundle, ONU
- 4) No wind/ 45 m span : Bundle, ONU installation

Table 2 shows the messenger wire elongation for harsh environmental and installation conditions. First, we calculated the failure rate of a fiber using eqs.(4), (5), (6) . (3)

$$\bar{\epsilon} = \left[\frac{1}{L_0} \int_0^{L_0} \left\{ \frac{1}{t_s} \int_0^{t_s} \epsilon^n dt \right\} dl \right]^{\frac{1}{\beta^n}} \quad \text{-----(4)}$$

$$\lambda = \alpha N_p \frac{B_p/E^2}{(B/E^2)^\beta} \frac{(\epsilon^n t_s)^\beta}{\epsilon_p^{n_p} t_p} \quad \text{-----(5)}$$

$$F = \lambda / (2.7 \times 10^{-13} t_s) \quad \text{-----(6)}$$

where $\bar{\epsilon}$ is equivalent strain, α is the failure rate, F is the failure rate of a fiber, L_0 is fiber length, N_p is the failure number during a proof test, ϵ is fiber strain, ϵ_p is the applied fiber strain during the proof test, t_s is the time in use, t_p is the proof test time, n is the fatigue coefficient, α is the constant, β is the constant.

Table 2 Calculation parameters for reliability of optical fiber

Factor	Fiber Strain $\epsilon(\%)$	Additional Length L/L_0	Additional Times t/t_s
Manufacture	0.05~0.1	1	1
During installation	0~0.10	1	1.7E-5
Bending	0.05	1/50	1
Suspended ONU	0~0.01	1	1
Installation on cable	0~0.15	1	1
Temperature change	0.04~0.08	1	1/2
Windy condition	0.05~0.26	1	1/10

* $L_0=1$ km, $t_s=20$ years

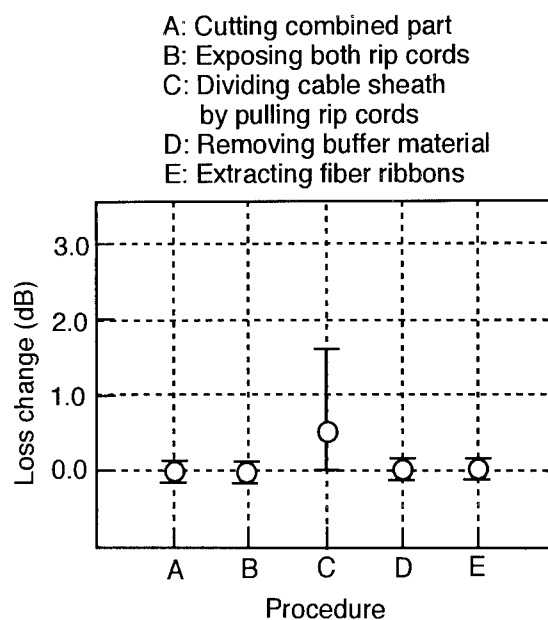


Figure 6 Handling characteristics

5. CONCLUSION

We described the design and performance of a new type of optical fiber distribution cable without a slotted rod for use with a small fiber count. This cable will lead to a reduction in cable diameter and weight. This in turn will make installation easier and simplify the manufacturing process thus reducing the cable cost.

Our cable provides good levels of performance and is promising with regard to upgrading the access network for FTTH.

ACKNOWLEDGMENTS

The authors wish to thank H. Shirakawa and T. Aihara for continuous encouragement.

REFERENCES

- [1] H. Iwata et al., "Design of aerial optical fiber cable system suitable for easy branching" 46th IWCS, pp. 4-11 (1997).
- [2] S. Hatano et al., "Design consideration and characteristics of self supporting optical fiber cable" IEICE Trans. Com. vol. E18-B, pp. 9-16 (1982).
- [3] Y. Mitsunaga et al., "Strength assurance of optical fiber based on screening test" IEICE Trans. Com. vol. E66-B, no. 7, pp. 829-836 (1983).



Hideyuki Iwata

NTT

Access Network Service

Systems Laboratories

Tsukuba, Ibaraki,

305-0805, JAPAN

Hideyuki Iwata is a research engineer. He was born in 1965 and received B.E. and M.E. degrees in electronic engineering from Yamagata University in 1989 and 1991, respectively. He joined NTT in 1991. Since 1993 he has been engaged in research on high-density underground and aerial optical fiber cable. Mr. Iwata is a member of IEICE of Japan.

DEVELOPMENT OF HIGH-DENSITY MID-SPAN ACCESS CABLE

Hiroshi Yatabe Hideaki Kambe Ryuichi Matsuoka
Yoshiyuki Kamata Masatoshi Mikami

The Furukawa Electric Co.,Ltd. Ichihara, Chiba, Japan

ABSTRACT

We have developed a new structure of cable to improve the customer satisfaction, and also to realize the high-density and mid-span access at the same time, by designing double layer cable with spiral slotted rod for the internal layer and SZ slotted rod for the external layer. Separating the different use of the ribbon by the layer, the ribbons admitted in the internal layer using for the trunk line and external layer for the subscriber network, we made it possible to meet the demands. We obtained an excellent results of transmission and mechanical, and temperature characteristics from the trial cable, and also suitable for practical use.

1. Introduction

Recently in Japan, as the subscriber network constructed by optical fiber become increasingly popular, an optical fiber cable consist of SZ slotted rod, which possesses outstanding mid-span access characteristics is in greater demand. But we were in difficult situation to realize reduction of the diameter and higher density at the same time, because the compression ratio of fiber is very low. Other hand, we often use the spiral slotted type for the trunk line, which has very poor mid-span accessibility, since the compression ratio of fiber is higher than SZ slotted type. So until now, we decided the cable

structure from the service. Therefore, there was a possibility of installing two different kinds of cables even though there are same route or not. But only single communication cable is available to install at the aerial area, and also we had serious problem about the lack of duct under the present condition. As you can see, there was no existence of optical fiber cable, which has good performance of higher density and mid-span access in Japan. To satisfy these demands, development of a new optical fiber cable was needed.

2. Cable design

We designed the cable structure by analyzing the problems, as we said before, also from the point of improving the customer satisfaction.

2.1 Requirements for cable structure

Requirements for the new cable structure are follows.

1) Higher density

In order to construct an economical subscriber network, reducing the cost of cable and installation is necessary. Also, only single communication cable is available to install at the aerial area, and moreover we had serious problem about the lack of duct under the present condition. Therefore, higher count cable is in greater demand.

2) Mid-span accessibility

To construct the subscriber network, mid-span access plays an important part. So, new cable structure must be possible to access to the fiber ribbons easily at any place along the cable in order to drop to the customer.

2.2 Improving the customer satisfaction

We had to consider many matters to improve the customer satisfaction, which are indispensable for realizing the new cable structure.

1) Reduction of cost

Until now, we decided the cable structure from the service, so there was a possibility of installing two different kinds of cables, even though there are same route or not. Therefore, matters we said before increase the costs of cable and installation. It was necessary to reduce these extra costs.

2) Safety of fiber

We had a doubt about the safety of fiber during mid-span access, since the fibers using for the trunk and subscriber network are sometimes gathered in single cable. Under the present condition, there was a possibility of influence to the fibers using for the trunk line during the mid-span access. Furthermore, it was very difficult to care the different use of ribbons. Therefore, it was necessary to solve these problems.

3) Ribbons

Ribbons using for the trunk line must be composed of 4-fiber ribbons, considering the joining performance of fibers. And also, ribbons using for the subscriber network must be composed of 2-fiber ribbons, which are most suitable, considering about the transmission system.

2.3 Conventional cable

Slotted type of optical fiber cables, which are popular in Japan, classify by two types. One is spiral type cable which are often used to construct the trunk line, and other is SZ slotted type cable which are used to construct the subscriber network. The advantages and disadvantages of the conventional cables are shown in Table 1. Also, structures of the cables are shown in Fig.1 and 2.

Table1 Comparison of the conventional type

	Conventional cable	
	Spiral slotted rod	SZ slotted rod
Practical use	Trunk line	Subscriber network
Core	Spiral	SZ reverse
High density	Good	Poor
Mid-span access	Poor	Good
Ribbon	4-fiber ribbon	2-fiber ribbon

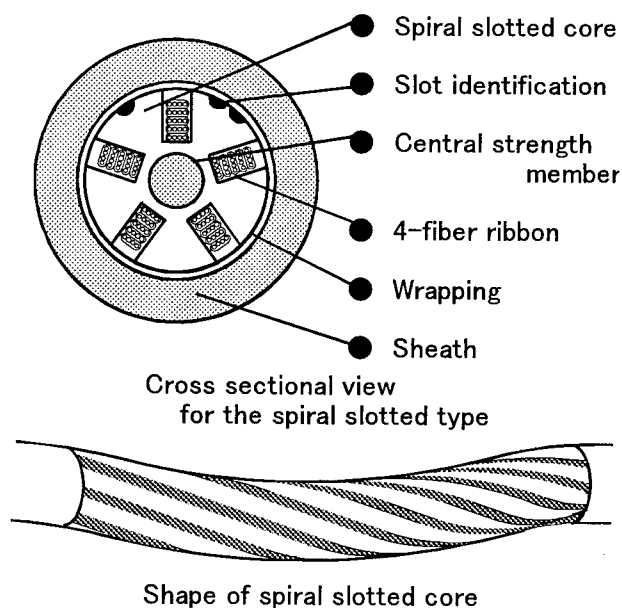


Fig.1 Structure of spiral slotted type

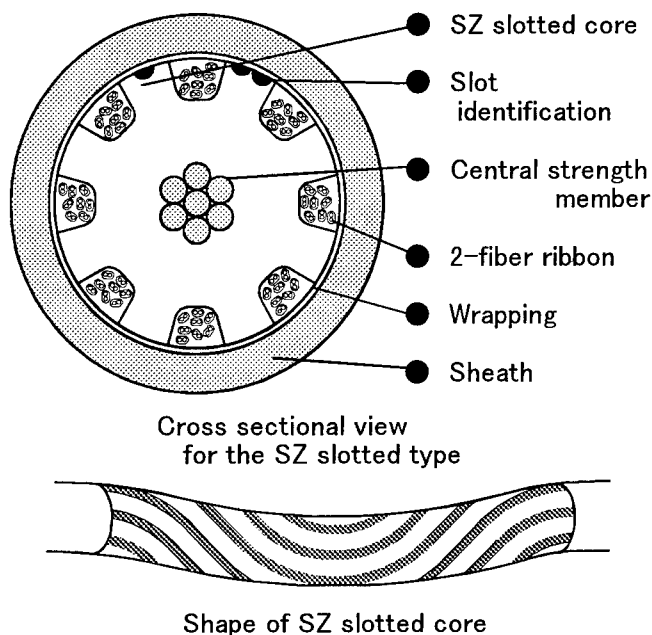


Fig.2 Structure of SZ slotted type

Fig.1 shows the spiral slotted cable including 100-fibers, and Fig.2 shows the SZ slotted cable admitting 128-fibers. In spite of the numbers of fiber are almost same between those structures, which admitted inside of the slotted rod, but the diameter of a cable is different. Saying in other words, fiber density is different. The diameter of spiral slotted rod is about 9mm, and fiber density is about 1.6fiber/mm². Other hand, the diameter of SZ slotted core is about 15mm, and fiber density is about 0.7fiber/mm². As you can see from above, spiral slotted cable is superior in high density to SZ slotted cable.

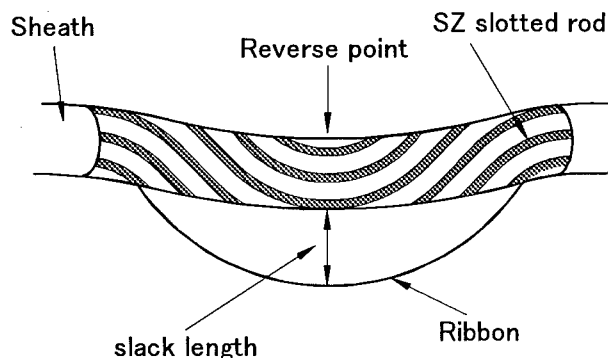


Fig.3 Fiber slack of SZ slotted rod

By the way, thinking about the mid-span access, SZ slotted type is superior. SZ slotted rod, which is shown in Fig.3, changes the slot direction periodically and it has the hill-like locus near the reverse point. Therefore, if the sheath near the reverse point is removed, the ribbons can be easily taken out from the slotted rod.

2.4 Design of cable structure

The cable structure was designed like Fig.4, by considering about the improvement of customer satisfaction, high-density, and mid-span access.

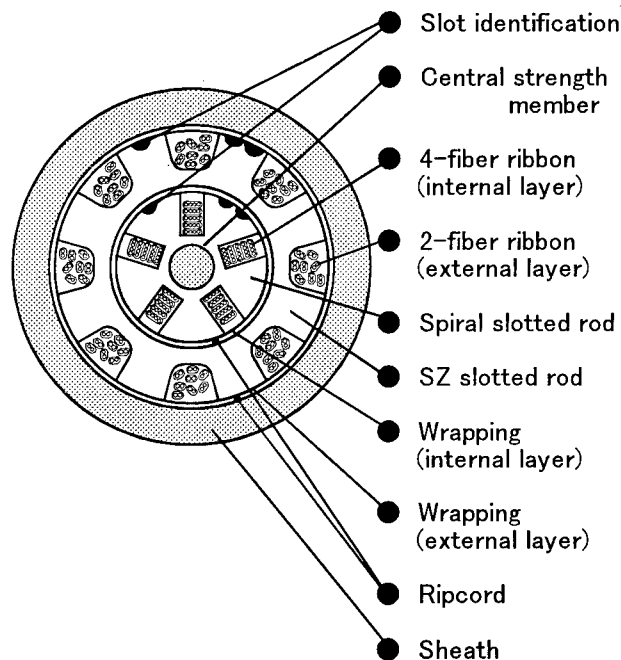


Fig.4 Cross section of new double layer cable

This cable structure is consist of double layer with spiral slotted rod for the internal layer and extruding SZ slotted rod above it. The advantages of this cable which are shown in Table 2, is that high-density and mid-span access was realized at the same time, by separating the different use of the ribbons, internal layer which

admits the ribbons using for the trunk line and external layer for the subscriber network. And also, putting together the different use of two cables into one, is another advantage of this cable. Furthermore, there is no need to worry about the safety of ribbons during the mid-span access, which are used for the trunk line, since we separated the different use for the ribbons by the layer. That means, this double layer structure made it possible to care the ribbons easily during the installation.

In order to improve the cable handling during the installation, we applied the ripcord longitudinally over the internal layer to rip the external layer easily.

Table2 Ability of new double layer cable

	New double layer cable
Practical use	Trunk line Subscriber network
Core	Spiral for internal layer SZ reverse for external layer
High density	Good
Mid-span access	Good
Others	Gathered different cable into one Safety during mid-span access Easy to care

2.5 Manufacturing method

First of all, we investigated the manufacturing method of double layer cable, especially the extruding process of SZ slotted rod. In this process, extruding SZ slotted rod above the internal layer, we designed and developed an equipment in order to prevent the effects to the ribbons which are admitted in internal layer.

3. Cable characteristics

We manufactured the trial cable in order to evaluate the cable characteristics.

3.1 Attenuation characteristic

An attenuation characteristic of the trial cable was investigated in each manufacturing process. The results are shown in Fig.5 and 6. The change of the attenuation, 4-fiber ribbons admitted in the internal layer and 2-fiber ribbons admitted in the external layer, during each process were less than 0.04 dB/km. From these factors, the manufacturing processes were confirmed that they were excellent.

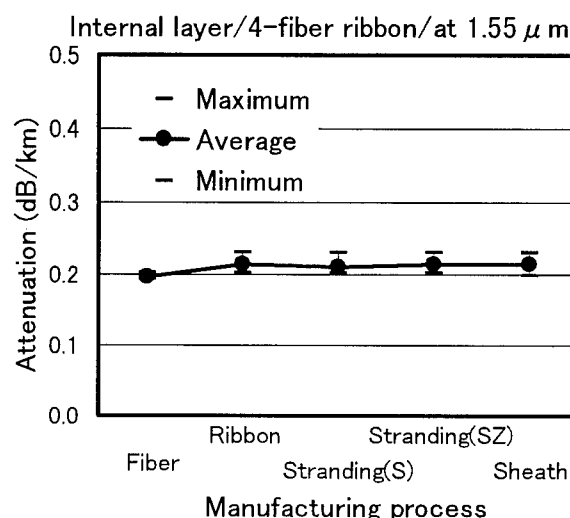


Fig.5 Changes of attenuation (internal layer)

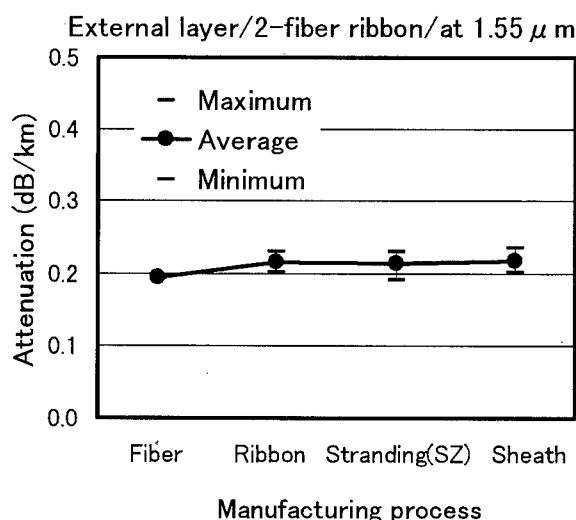


Fig.6 Changes of attenuation (external layer)

3.2 Temperature characteristics

Changes of attenuation were investigated at temperature range from -30 through $+70$, and the results are given in Fig.7. Increases of the attenuation during the investigation were less than 0.03 dB/km, showing a good temperature performance.

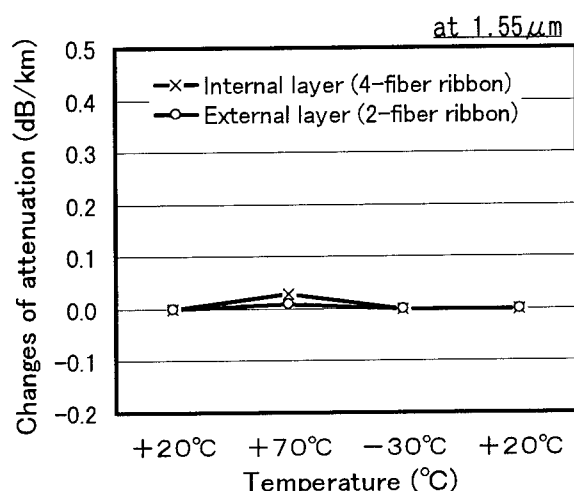


Fig.7 Changes of attenuation during the temperature cycling

3.3 Mechanical test

The trial cable was evaluated for tensile test, squeezing test, lateral pressure test, impact test, and twist test. The results are shown in Table 3.

Table3 Results of mechanical test

Test Item	Test methods	Result
Tensil	0.2% of elongation	Less than 0.01dB
Bending	Bending daimeter : 6D Bending angle : $\pm 90^\circ$	Less than 0.01dB
Squeezing	Wheel : R250 0.2% of elongation	Less than 0.01dB
Lateral pressure	Length : 100mm Load : 1960N	Less than 0.01dB
Impact	Weight : 1kg Height : 1m	Less than 0.01dB
Twist	Angle : $\pm 90^\circ$ /m	Less than 0.01dB

measuring at $1.55\mu\text{m}$

From each test, the changes of the loss were not observed, showing a good mechanical characteristic.

3.4 Mid-span access

We measured the slack length of the fiber ribbon when fiber picked out from the slotted rod, after removing sheath in a length of 500mm. From the result, the slack length of fiber was more than 15mm, having sufficient length for jointing fibers.

3.5 Ripping characteristics

We also investigated the ripping characteristics of external layer, whether it functions very well or not. From the result, external layer was ripped easily. Therefore, the operation of installation and fiber jointing will be not so troublesome compare to former type.

4. Conclusion

We have developed a new structure of cable to improve the customer satisfaction, and also to realize the high-density and mid-span access at the same time, by designing double layer cable. To improve the customer satisfaction, we notice about the problems at the aerial area, since only single communication cable is available to install, and about the lack of duct under the present condition.

This high-density mid-span access cable holds three major characteristics. First, characteristic of trunk cable which has very high compression ratio. Next, characteristic of subscriber network cable, which are suitable for the mid-span access. Last, the characteristic of this cable, is that there is no need to worry about the safety of ribbons during the mid-span access, which are used for the trunk line, since we separated the different use for the ribbons by the layer. And also, easy to care about the different

use of ribbons.

The double layer cable admitting the 100-fiber spiral slotted rod using 4-fiber ribbon inside of the former 128-fiber SZ slotted cable using 2-fiber ribbon, total of 228-fiber which we manufactured for the practical cable. From the above, diameter of the cable is about 20mm and the compression ratio is about 80% higher than former 128-fiber SZ slotted cable.

SPEAKER



Hiroshi Yatabe

The Furukawa Electric Co., Ltd.
6, Yawata Kaigandori Ichihara, Chiba
290-8555, Japan

Hiroshi Yatabe received his B.E. degree in electrical engineering from Waseda University in 1995. He joined The Furukawa Electric Co., Ltd. and has been engaged in development and design of optical fiber cable. He is now process engineer in Production Engineering Section of Transmission System Division.

STUDY ON WEIGHT REDUCTION OF HIGH-FIBER-COUNT SLOTTED ROD CABLE

Ryuji Takaoka

Ichiro Kobayashi

Eiji Konda

Hideyo Hiramatsu

Yasuhiro Kamikura

The Furukawa Electric Co., Ltd.

6, YAWATAKAIGANDORI, ICHIHARA, CHIBA, 290-8555, JAPAN

ABSTRACT

The weight reduction and flexibility improvement of slotted rod cable has been investigated. This time high-fiber-count and large size slotted rod cable using 8-fiber ribbons was chosen for the subject of our study because whose weight reduction is most desirable. Strength member material, slotted rod polyethylene material and reduction of slotted rod size were considered for weight reduction. We simulated the effect of each factor by calculating the cable weight and the result showed a possibility of about 40 % weight reduction. On the base of the result of these calculation we manufactured a trial cable of the lightest weight structure. The trial cable was excellent in optical and mechanical characteristics, and the expected weight reduction was realized.

INTRODUCTION

As the use of optical fiber cables is expanding in access networks, optical fiber cables which facilitate installation and jointing work are demanded. In order to install longer cable length into conduit, light weight cable is demanded to reduce the friction force between the cable and the conduit. Cable

flexibility to allow easy ribbon extraction from the slots for mid-span branching are demanded. Furthermore, for multiple cable installation, downsized small cable are also demanded.⁽¹⁾ In order to satisfy these requirements, we developed a new optical fiber cable which is small in size and light in weight with good flexibility.

RIBBON SLOTTED ROD CABLE

We examined 1000-fiber slotted rod cable using 8-fiber ribbons. This cable is the largest and heaviest cable, and much weight reduction is expected. This cable is composed of a tensile strength member, polyethylene slotted rod, fiber ribbons, wrapping tape and polyethylene sheath. (shown in Fig.1 and table 1)

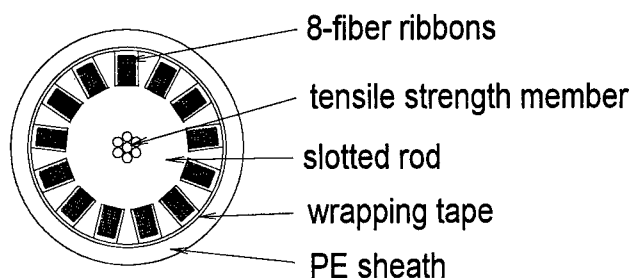


Fig. 1 Cross section of 1000 fiber cable

Table 1 1000 fiber cable structure

Fiber count	1000
Fiber ribbon	8-fiber ribbon×125
Tensile strength member	7×2.0mm steel strand
Slotted rod and sheath material	Polyethylene
Cable diameter (mm)	30

Weight of each constituent of the cable was calculated and the results are shown in Fig. 2

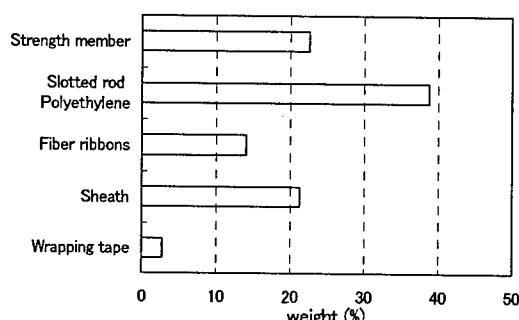


Fig.2 Breakdown of 1000 fiber cable weight

Weight of tensile strength member and slotted rod polyethylene constitutes the majority of the cable weight. Whereas, fiber ribbons and wrapping tape occupy a small portion.

Next, we calculated the flexural rigidity (EI) of each constituent of the cable. The results are shown in Fig.3.

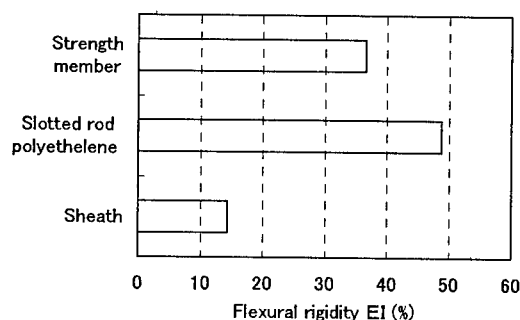


Fig.3 Comparison of Flexural rigidity

Tensile strength member and slotted rod polyethylene constitute more than 80% of flexural rigidity of the cable.

WEIGHT REDUCTION OF SLOTTED ROD

Tensile strength member and slotted rod polyethylene are the majority of the slotted rod weight. So, the reduction of the slotted rod weight is effective in reduction of the total cable weight. Therefore we examined the weight reduction as follows.

Change of strength member

At present 7×2.0mm steel strand is used as strength member. Taking into account the cable weight reduction, other tensile strength members such as shown in table 2 were considered.

Table2 Comparison of strength member weight

	weight (kg/km)
7×2.0mm steel strand	173
7×1.2mm steel strand	62
5.2mm nonmetallic FRP	28

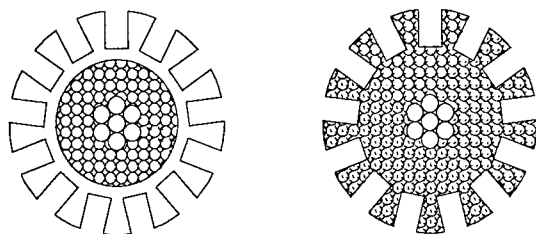
If 5.2mm nonmetallic FRP is used, the strength member weight can be reduced by about 140kg/km. Even with 7×1.2mm steel strand, the reduction is more than 100kg/km.

Slotted rod polyethylene

By foaming the slotted rod polyethylene, the cable weight can be reduced. We studied two kinds of foamed slotted rod. One type has a foamed inner layer and solid outer layer. The other type is entirely made of foamed polyethylene. We defined cell content as the volume percentage of the foam in the foamed

polyethylene. When a slotted rod is composed of foamed polyethylene with $\alpha\%$ cell content, a specific gravity : ρ of the foamed polyethylene is expressed as follows.

$$\rho_{\text{Foamed PE}} = \left(1 - \frac{\alpha}{100}\right) \cdot \rho_{\text{Solid PE}}$$



inner layer foamed all layer foamed

Fig. 4 Cross section of formed slotted rod

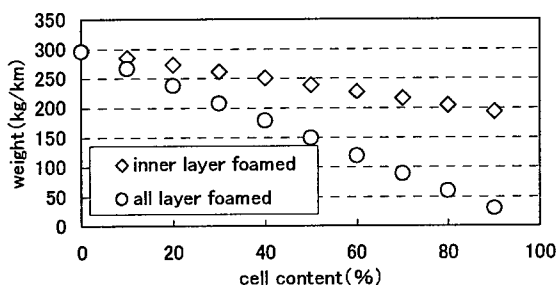


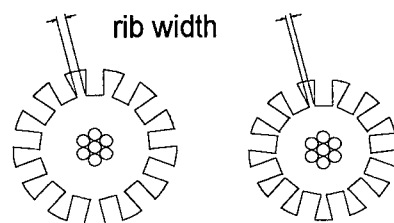
Fig. 5 Comparison of slotted rod weight

Figure.4 shows the cross section of the examined foamed slotted rods. Figure.5 shows how the cable weight is reduced as cell content increases. We have confirmed that the foamed polyethylene slotted rod of up to 40% cell content have sufficient mechanical characteristics.⁽²⁾ Therefore, from Figure.5, when cell content is 40%, the cable weight is reduced by about 50kg/km in case of inner layer foamed polyethylene and over 100kg/km in case of all layer foamed polyethylene.

Downsized slotted rod

The present 8-fiber ribbon slotted rod has

sufficient mechanical characteristics. The rib width is an important parameter to determine the mechanical strength of the slotted rod. If the rib width can be reduced, the slotted rod can be downsized as in Fig.6. Figure 6 shows a comparison of the present and the downsized slotted rods. Figure 7 shows the relationship between rib width and slotted rod weight.



diameter 24.6mm
rib width 1.3mm

diameter 22.3mm
rib width 0.7mm

Fig. 6 Comparison slotted rod size

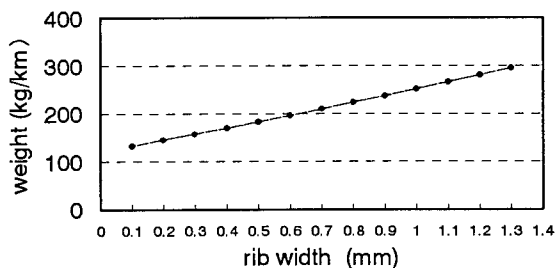


Fig. 7 Comparison of slotted rod weight

By improving the manufacturing technique, it is now possible to decrease the rib width to 0.7mm. From Fig.7, this means the reduction of the slotted rod weight by about 90kg/km. As the slotted rod becomes smaller, the weight of wrapping tape and polyethylene sheath is also reduced.

IMPROVEMENT OF FLEXIBILITY

Flexural rigidity of slotted rod plays the majority roll in cable flexural rigidity. So, the

reduction of the slotted rod flexural rigidity is effective in the improvement of cable flexibility. The various weight reduction method in the previous section are also effective in reducing the cable flexural rigidity. In other words, the weight reduction results in the flexibility improvement at the same time.

CALCULATION OF CABLE WEIGHT

Each method of weight reduction is independent from each other, therefore the best result is obtained by combining those methods. However, the combination of all layer foamed slotted rod and the downsized slotted rod was eliminated because of the lack in mechanical strength. The best combinations to reduce the weight and improve the flexibility without jeopardizing the mechanical strength are shown in Table 3.

Table 3 Slotted rod design

Design	1	2
Strength member	5.2mm nonmetallic FRP	
Foamed layer	Inner layer	All layer
Rib Width	0.7mm	1.3mm

Weight calculation

We calculated the weight of the cables with the slotted rods of Table 3. The results are shown in Fig. 8.

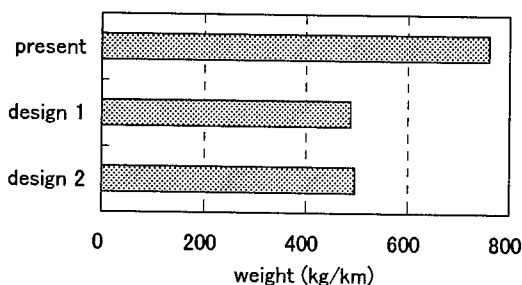


Fig. 8 Comparison of cable weight

Design 1 is slightly lighter than Design 2, but the difference is small. Design 1 proved to be much more effective than expected.

Flexural rigidity

We calculated the flexural rigidity of the cables of Table 3. The results are shown in Fig. 9.

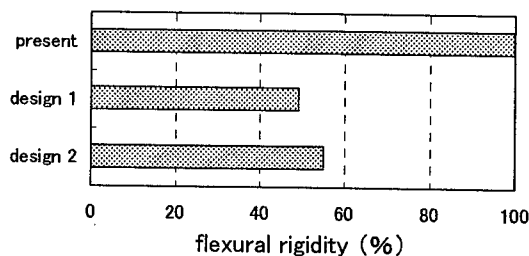


Fig. 9 Comparison of cable flexural rigidity (relative value)

Flexural rigidity of Design 1 is smaller than Design 2. The results indicate that the downsize is quite effective in improving the flexural rigidity.

Optimal cable design

The above considerations led to the optimal cable design which is light and flexible. As shown in Fig. 10 and, Table 4, this design uses nonmetallic tensile strength member and downsized slotted rod with foamed inner layer.

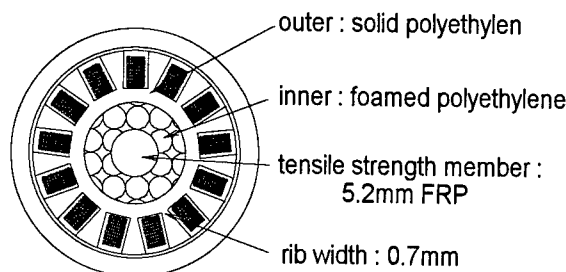


Fig. 10 Cross section of the optimal cable design

Table 4 the optimal cable design size

Fiber count	1000-fiber
Slotted rod diameter	22.3mm
Foamed layer	Inner layer only
Cable diameter	27.1mm
Cable weight	490kg/km

TRIAL CABLE

Based on the above investigations, we made a trial 1000 fiber count cable shown in Fig. 10.

Transmission characteristics

Figure 11 shows the change in transmission loss in cabling process. No increase of transmission loss was observed at any stage of the process.

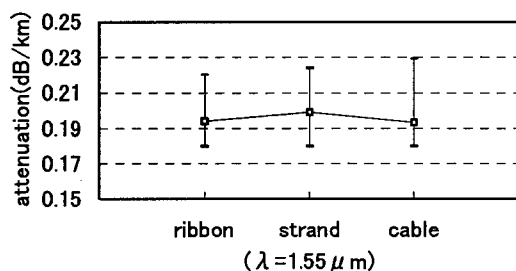


Fig. 11 Change in transmission loss

Mechanical and Temperature characteristics

Table 5 shows the results of various tests. The tensile, bending, torsion, crush, impact squeezing and temperature characteristics were satisfactory.

Table 5 Result of tests (at $\lambda = 1.55 \mu\text{m}$)

Item	Result
Tensile (3920N)	<0.01dB No residual loss
Bending (R=240mm)	
Torsion ($\pm 90^\circ$ /1m)	
Crush (1960N/100mm)	
Impact (1kg · 1m)	
Squeezing (R=600mm)	<0.1dB No residual loss
Temperature -30~+70°C	

Weight and flexibility

The cable weight was measured to be 0.49kg/m. The result coincided with calculation. The flexibility test shown in Fig.12 showed the improvement of the cable flexibility.

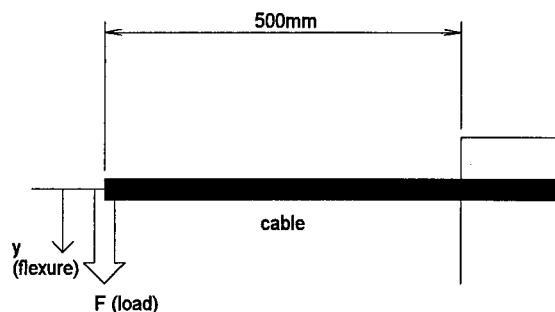


Fig. 12 Flexibility test condition

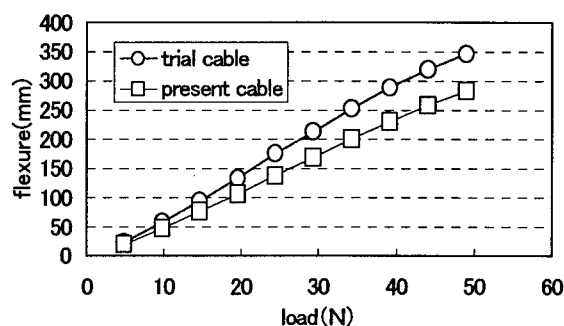


Fig. 13 Result of flexibility test

CONCLUSION

We investigated the weight reduction and the improvement of flexibility of high-fiber-count slotted rod cable. The calculation results showed the possibility of cable weight reduction by about 40% and improved flexibility. The trial cable was excellent in optical and mechanical characteristics, and the cable weight reduction and flexibility improvement coincided with the calculated expectation.

REFERENCES

- (1) H.Iwata et al. "Development of 2000-fiber Cable with SZ-stranded U-grooves and Slotted Rod" 47th IWCS,pp.34-39(1998).
- (2) I.kobayashi et al. "Development of New Slotted Rod Cable Composed of Foamed Polyethylene Slotted Rod" 47th IWCS,pp.49-56(1998).
- (3) H.Iwata et al. "Study on advanced function of optical fiber cable for access" IEICE SSE97-177,OSC97-106
- (4) F.Hosoi et al. "Development of downsized slotted rod optical fiber cables" 45th IWCS,pp.506-510(1995).



Ryuji Takaoka

Ryuji Takaoka received his M.E.degree in Mechanical Engineering from keio University in 1996. He joined The Furukawa Electric co.,ltd. in 1996 and has been engaged in research and development of optical fiber cables. He is now a research engineer of Opto-Technology Laboratory.

SYSTEM PMD REQUIREMENTS FOR MULTI-CHANNEL ANALOG AND DIGITAL OPERATION ON DISPERSION UNSHIFTED OPTICAL FIBER

Robert J. Whitman

Corning Incorporated, Corning New York

Abstract

The statistical nature of PMD and its variance with time, environment, deployment and wavelength has led to many theoretical assumptions and debates. This paper presents an engineering approach to PMD requirements for digital and analog systems to provide guidance for end-users, system vendors and optical fiber manufacturers regarding actual system needs. A comprehensive review of system requirements for both analog and digital systems is presented along with appropriate assumptions for typical system deployments. These assumptions then are applied to existing analog and digital system PMD models to determine the impact on system performance.

Brief introduction to PMD

PMD has been a topic of concern for many years. Unfortunately, there still is significant misconception in the marketplace with regard to PMD and the functional requirements for system operation. In this paper, an engineering approach is taken to examine the functional requirements for system operation and explain the new approaches for specifying PMD. Specific system configurations of interest are medium to long distance (200-400 km) digital systems at OC-192 rates and 80-channel analog systems.

For single-mode operation the fundamental mode contains two orthogonal polarization states. A non-symmetric fiber index of refraction creates a relative delay and phase offset between the polarization states. When the orthogonal modes recombine at a detector, the relative delay appears as a pulse spread. This relative delay is known as the differential group delay (DGD). The DGD varies with time, wavelength, deployment and environmental

conditions. Discrete, or measured, values of DGD also are referred to as the instantaneous PMD. The variation of the DGD can be described by a Maxwell probability density function with a single scaling parameter, the PMD value. The PMD value is the average of the DGD values across the wavelength band, normalized by the square root of the length. The PMD value has been the parameter used in specifications by optical fiber manufacturers and standards organizations.

Standards organizations, end-users and optical fiber suppliers, due to the variability in the attribute itself, have challenged traditional specifications for PMD. Previous studies have shown that, due to PMD variability, the theoretical limit for measurement reproducibility is approximately $\pm 15\%$ ¹. Formulating specifications around a parameter that varies with this magnitude requires non-traditional approaches. The approach that has gained widespread acceptance in the industry uses the statistical averaging that takes place when concatenating lengths of optical fiber. The PMD of the concatenated fibers, or link, can be specified as opposed to individual PMD maximum values. This provides a more accurate and functional representation of the true PMD encountered in the system. Figure 1 demonstrates the distribution tightening, or averaging, that takes place when comparing distributions of individual fibers (Cables), a concatenated link distribution (Link) and the assumed worst case individual fiber maximum. Notice that the link distribution has a much tighter range than that of the cables, while also demonstrating a more realistic representation of the system PMD.

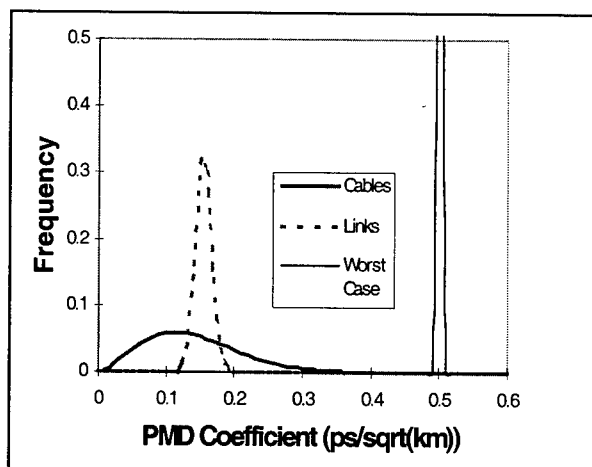


Figure 1. PMD Distribution Comparison

When determining system availability, system designers must take into account the random behavior of the DGD values. A certain amount of DGD can be accounted for by the system designer by allocating a receiver sensitivity power penalty. This penalty traditionally has been 1 dB. Assuming that, as long as the DGD at a given wavelength is in excess of the value used to calculate the allocated penalty, the system will be unavailable. For wavelength division multiplexed systems, there have been demands for unavailability as low as 0.04 min/year/circuit. This corresponds to a probability of 1.3×10^{-7} that the end-to-end DGD value will exceed acceptable (design) levels. The number of measurements required to meet such a low probability is not feasible. Therefore a means of characterizing the PMD process distribution must be used to statistically provide a specification that meets such rigorous requirements. Two methods for statistically quantifying PMD have been introduced by the International Electrotechnical Commission (IEC) standards body, IEC SC 86AWG1, to meet this need.²

Statistical specifications

Method 1 defines the statistical PMD performance of a distribution of fibers in a link by providing a statistical upper bound (PMD link coefficient). This upper bound provides a more realistic indication of maximum PMD likely to be encountered in a concatenated link. Any PMD distribution can be analyzed statistically and compared to the upper bound to evaluate

conformance. The purpose of Method 1 is to define a PMD specification that can easily be used to evaluate conformance to a stated limit. Optical fiber manufacturers, cable manufacturers, system vendors and end-users currently are using this method to define the requirements for PMD performance in systems. For system design purposes, a probability of exceeding an instantaneous PMD (or total system delay) is required due to PMD variability with time, wavelength and deployment. Method 2 was developed to meet the system design requirement.

In the Method 2 approach, a portion of the total dispersion budget is allotted for fiber PMD and it is assumed that exceeding the PMD budget results in system downtime. Method 2 is used to assist in system design by providing a probability of exceeding a specified instantaneous delay that can be converted to system downtime. But the shortcoming of Method 2 is that in and of itself it does not allow evaluation of conformance to a specification. Since the methods are complimentary, conformance with the Method 2 approach can be verified by demonstrating equivalence to Method 1. The focus will be placed on the Method 1 approach as it is more applicable, widely recognized and easily understood.

Both methods use the concatenated link approach in determining fiber/cable PMD. The concatenation of individual cable sections is described in Equation 1. The outcome of Equation 1 is the PMD coefficient of the link. The following discussion is based on the Method 1 approach.

$$X_M = \sqrt{\frac{\sum_{i=1}^M x_i^2}{M}} \quad \text{(Equation 1)}$$

where:

- M Number of equal length cables comprising the link (Conservative for unequal lengths with an average length ≤ 10 km)
- x_i The PMD coefficient of fiber in an individual cable (ps/ $\sqrt{\text{km}}$)
- X_M The PMD coefficient of a concatenated link of M cables (ps/ $\sqrt{\text{km}}$) (Also known as the Link Quadrature Average)

Equation 1 shows that the link PMD coefficient, X_M , can be determined from the PMD coefficients of the individual fiber sections, x_i . The probability distribution of the link PMD coefficient depends on the distribution of the individual PMD values and the number of cables in the link. By taking advantage of the reduced variation of a concatenated link, the fiber or cable manufacturer can specify a PMD statistical upper limit (PMD link value). The manufacturer will supply the PMD link value, which consists of a link PMD limit (X_M), a given number of individual fibers/cables, and an associated probability of exceeding the limit (normally 99.99 percentile). This upper limit can be used as a more realistic and functional specification of PMD for end users. The methods for calculating the PMD link value typically are agreed upon between the buyer and the manufacturer. Currently three methods are available for determining the PMD link value and associated probability, one is a numeric method and the other two are analytical. For more details refer to the IEC contribution.

This statistical approach offers flexibility for defining specifications in both fiber and cable, while providing more functional PMD performance information for system design. When using the statistical approach in defining a fiber or cable specification, the statistics are performed on the measured PMD distributions. Additionally, if the fiber to cable correlation is known, a cable factor can be applied to the fiber distribution to generate a cable distribution. For additional details on PMD link value calculations and statistical specifications refer to reference [2].

Determining digital system requirements

With the advent of EDFAs, transmission distances are no longer limited by optical fiber attenuation. Now, dispersion compensation errors, non-linearities and PMD are the factors that limit system performance. For digital systems, PMD generally is not a concern at bit rates of 2.5 Gb/s and below. As system bit rates continue to rise to 10Gb/s and beyond, PMD will have a greater impact on system performance. If PMD is properly controlled, as is true with current distributions of most major fiber and component manufactures, the effect can be minimized enough to allow error-free transmission for long distances (400 km and more).

In the past the industry has generally accepted a maximum of one-tenth of the bit period as the maximum allowable PMD without experiencing performance impairments^{3,4}. This is a simplified approach but is satisfactory for approximating requirements. Figure 2 shows the theoretical PMD limited distances for one-tenth bit period delays and various bit rates⁵. This graph is a good starting point for reviewing overall system PMD and the impact on system performance.

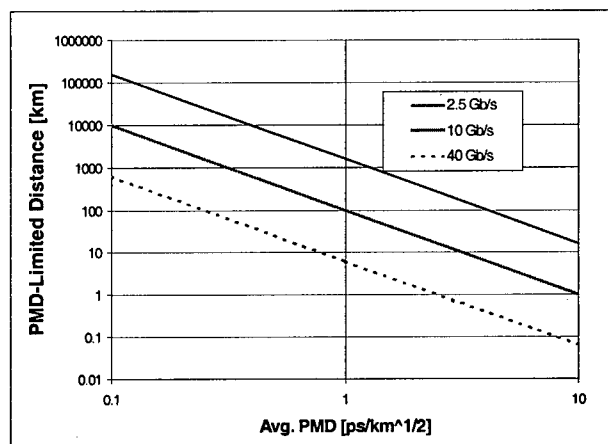


Figure 2. Theoretical PMD-limited transmission distance vs. PMD coefficient

For systems operating at 10 Gb/s (OC-192) one-tenth of the bit period is 10 ps. This generally accepted allowable end-to-end PMD limit is known here as τ_{sys} . Also included in this limit is the assumption that one-third of the bit period is allotted for dispersion and a Maxwellian factor of three to account for variability. When evaluating the PMD performance of a system, the other factors that must be taken into account are PMD of components, total system length and the number of fiber-optic spans.

A simplified approach to approximate PMD requirements on optical/fiber/cable is provided below. System designers may choose to use the statistical methodologies being advanced in standards bodies (Method 2) for more accurate requirements determination.

When determining the functional requirements for system operation, the necessary fiber/cable PMD performance for a given bit rate can be calculated by using Equation 2.

$$QA = \left[\frac{\tau_{sys}^2 - n_2^2 PMD_{EDFA}^2 - n_3^2 PMD_{DCM}^2}{L_s} \right]^{1/2} \quad (\text{Equation 2})$$

QA	Fiber/Cable Link Quadrature Average
τ_{sys}	Allowable end to end PMD
n_2	Number of EDFAs
n_3	Number of DCMs
L_s	Total system length
PMD_{EDFA}	PMD of each Amplifier
PMD_{DCM}	PMD of each Dispersion Compensation Module

Given a reasonable set assumptions, the requirements for acceptable system performance can easily be calculated. The following example is representative of current OC-192 requirements.

Bit rate	10 Gb/s
Corresponding τ_{sys}	10 ps
Total Distance	400 km
Number of spans/DCMs/EDFAs	5 each
EDFA PMD	0.5 ps
DCM PMD	1.5 ps
All components add in quadrature.	

For the above assumptions the required Fiber/Cable QA is $\leq 0.47 \text{ ps}/\sqrt{\text{km}}$.

Based on the given assumptions, the statistical specification methodology can be applied to determine the appropriate PMD link value to meet this requirement on the fiber/cable.

PMD specifications should be set to meet the needs of the system design. Continued tightening of specifications without technical justification unnecessarily adds cost and complexity. Currently, some fiber-optic cable manufacturers are specifying an individual maximum of $0.5 \text{ ps}/\sqrt{\text{km}}$. Cablers, who have a $0.5 \text{ ps}/\sqrt{\text{km}}$ individual maximum, meet or exceed this requirement for 10 Gb/s operation. Leading-edge cablers will start to supplement this upper end specification with a PMD link value, which better describes the underlying distribution. As presented here, $0.5 \text{ ps}/\sqrt{\text{km}}$ quadrature average meets the functional PMD requirements for 10 Gb/s operation and is less restrictive than the individual maximum specification. It is recommended that optical fiber and cable manufacturers move to the more functional and

descriptive statistical specifications, i.e. the PMD link value. Due to the sensitivity of deployment, PMD measurement variability and commercial needs for an upper limit, leading optical fiber manufacturers typically specify individual uncabled fiber PMD at lower levels to enable desired cable PMD performance.

Second order PMD- digital system impact

Generally PMD is described by the DGD, fluctuating with wavelength, time and environment. As long as the signal spectrum is sufficiently narrow the first order effect of PMD is simply the delay between orthogonal modes. When using directly modulated chirped lasers or other broad-spectrum sources, the PMD may change within the signal spectrum and result in additional signal distortions. These distortions are the result of what is known as higher order PMD, particularly second order PMD.⁴

Second order PMD is defined in two parts as the variation of the polarization dispersion vector over the signal spectral width and the rotation of the principal states of polarization with frequency. Second order PMD is a linear effect and scales with the length of the system. Consequently, it has the same effect and dimensions as chromatic dispersion.

Second order PMD can either add or subtract to chromatic dispersion, contributing either positively or negatively to system performance. Because of this relationship, unlike first order PMD, second order PMD heavily relies on chromatic dispersion and laser spectral width. First order PMD is a function of birefringence and mode coupling; second order PMD is a function of wavelength, time and presence of chromatic dispersion. For properly compensated, unchirped digital transmission, second order PMD has a negligible effect. Second order PMD only becomes an issue for uncompensated, highly chirped systems. For highly mode coupled fibers, an approximation has been developed, based on theoretical and empirical data, to determine the second order PMD coefficient from the first order PMD coefficient⁶.

$$PMD_{2nd \text{ order}} \approx \frac{(PMD_{1st \text{ order}})^2}{\sqrt{3}} \quad (\text{Equation 3})$$

Previously, it was stated that for narrow signal widths, second order PMD was of little concern. Recently a study was performed to determine the impact of transmitter bandwidth on 10 Gb/s transmission. Figure 3 shows the system outage probability for three mean PMD values of 10, 20 and 30 ps assuming the system is properly compensated for chromatic dispersion and system outage is defined as BER > 10⁻¹². For the generally accepted limits for 10 Gb/s transmission, the second order PMD effect on system outage probability is negligible up to transmitter chirp of 30 GHz⁴.

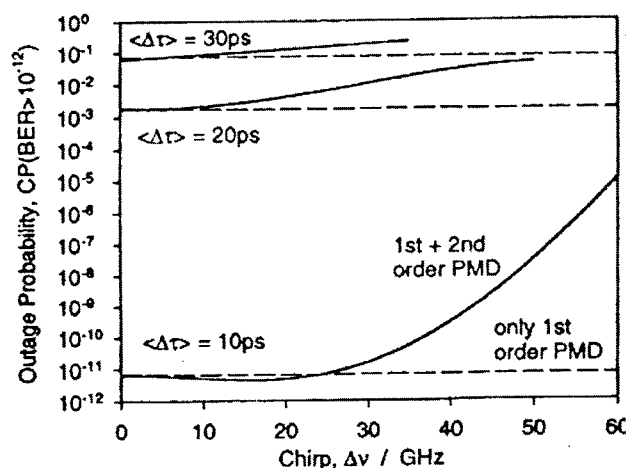


Figure 3. System outage probability vs transmitter chirp

Analog system requirements

In analog systems, second order PMD is the primary contributor to PMD induced system impairments. Analog systems use the entire signal during transmission and are much more susceptible to signal distortions than the ones and zeros of digital systems. As such, analog systems require a very high signal to noise ratio, known as carrier to noise ratio (CNR). The chief contributor to CNR is composite second-order distortion (CSO). CSO has three primary contributors, namely chromatic dispersion, PMD and polarization dependent loss. The generally accepted threshold CSO level is -55 dB to -60 dB to avoid system impairments. Due to variations in CSO a guardband value of -70 dB has been proposed.

In determining the PMD requirements for typical 80-channel analog systems of distances

between 30 and 40 km, the following model can be used⁷.

$$CSO = N\gamma^2 m_0^2 \left\{ \phi''^2 \omega_d^2 + \frac{\pi^2 \omega_d^2 \langle \Delta \tau \rangle^4}{256} + \frac{\pi \Delta T^2 \langle \Delta \tau \rangle^2}{48} \right\}$$

where :

N is the number of mixing products

γ is the chirp parameter

m_0 is the modulation index

ϕ'' is equal to $-\lambda^2 DL / 2\pi c$ where D is the chromatic dispersion in ps/nm * km

ω_d is $2\pi f$ where f is the channel frequency

$\Delta \tau$ is the average PMD

ΔT is the PDL

The model is applicable to directly modulated systems, particularly at 1300 nm where the level of chirp is important. For externally modulated systems, chirp is negligible and CSO impairments are not expected. Typical assumptions for today's systems include the following:

System Length:	30-40 km
Chirp levels:	2-5 GHz
Number of channels:	80
Tolerable CSO level:	65-70 dB
PDL:	-0.02

For current specifications PMD is not a limiting factor for 80-channel systems at these lengths, which are typical of today's systems. The limitations come from laser chirp, attenuation and chromatic dispersion, limiting distances to 30-40 km. Additionally, externally modulated signals operating at 1550 nm have no limitations by PMD but are limited by the high chromatic dispersion in this region.

As previously mentioned, PMD in analog systems primarily is a second order effect. The resulting effect is an additional contribution to chromatic dispersion. To ensure adequate PMD limits are imposed, an analytical approach should be taken.

Determine the second order PMD requirement

- The ITU-T chromatic dispersion limit is 3.5 ps/nm•km at 1310 nm.
 - Budget 0.5 ps/nm•km of this limit for PMD
 - Including a variability factor for the statistical nature of PMD
 - Yields a second order PMD requirement of 0.2 ps/nm•km.

Using Equation 3 to approximate the first order PMD requirement

$$\text{PMD}_{2\text{nd order}} \approx \frac{(\text{PMD}_{1\text{st order}})^2}{\sqrt{3}}$$

Using the second order limit determined above (0.2 ps/nm•km) the first order PMD limit can be approximated.

$$\text{PMD}_{1\text{st order}} \approx 0.5 \text{ ps}/\sqrt{\text{km}}$$

The result is a first order requirement of 0.5 ps/ $\sqrt{\text{km}}$, which is consistent with the standards requirements for digital 10 Gb/s system operation⁶.

Implications of WDM

Up until now PMD has been treated as a single channel effect. Previous studies have discussed the wavelength dependence of PMD and the concept that the PMD variability can have a measurable bandwidth. This bandwidth could indicate that channel independence cannot be taken for granted⁸. Additionally, Matera determined that the PMD bandwidth is inversely proportional to the DGD⁹; Bruyère also came to the same conclusion in 1996¹⁰. As such, for a lower DGD there is a greater probability of correlation of one channel to its neighbor than for a higher DGD. These concepts must be incorporated in system downtime calculations.

To determine channel independence a correlation bandwidth ($\Delta\lambda_c$) must be defined. In Figure 4a the correlation bandwidth is shown graphically as the bandwidth of PMD at a given

wavelength channel. If the correlation bandwidth is short relative to the channel spacing, all channels are independent as shown in Figure 4b. If the correlation bandwidth is long compared to the channel spacing, the channels are no longer independent relative to PMD, as shown in Figure 4c.

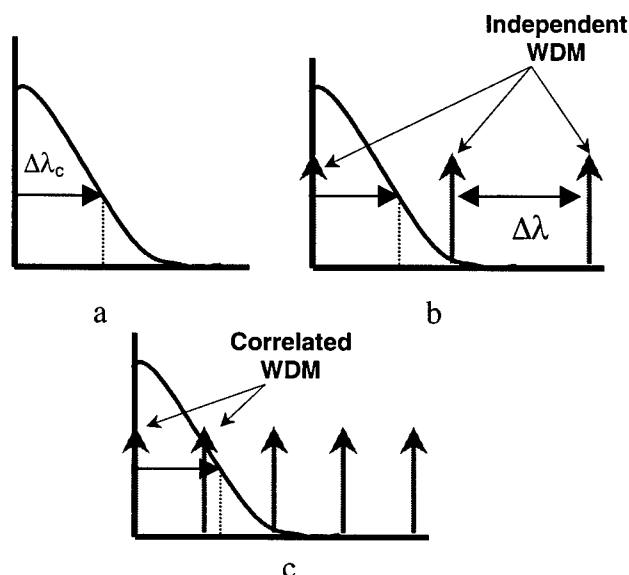


Figure 4. Channel Independence Determination

(The x-axis is frequency (Ghz), the y-axis is the DGD variation at a given channel)

If the probability of a single channel outage is given by p , and the number of WDM channels is N , and if all channels are independent, then the outage probability (OP) equals $N \cdot p$. If the channels are not independent the ratio of the correlation bandwidth ($\Delta\lambda_c$) and the channel spacing ($\Delta\lambda$) must be multiplied by the previous product to determine the outage probability. Equation 4 demonstrates the relationship when the correlation bandwidth is greater than the channel spacing, indicating that the channels are not independent.

$$\text{OP} = N \cdot p \left[\frac{\Delta\lambda}{\text{Max} [\Delta\lambda_c, \Delta\lambda]} \right] \quad (\text{Equation 4})$$

Conclusion

It has been shown that for current manufacturing PMD distributions, typical 80-channel analog

systems are not limited by PMD but by laser chirp and chromatic dispersion. Also, this analysis indicates that current distributions and specifications for unshifted optical fiber performance in installed outside plant are adequate for medium to long length digital DWDM systems at OC-192 rates. In fact, an individual section maximum of 0.5 ps/√km is more restrictive than necessary for today's performance requirements. For bit rates greater than OC-192, logical solutions include the use of non-zero dispersion-shifted fibers, due to the reduced PMD penalty incurred from less dispersion compensation requirements.

Statistical specifications are gaining wide acceptance in the industry. Statistical specifications aid the fiber manufacturers, cable manufacturers, system vendors and end-users in defining more accurate and functional PMD specification requirements for current and future systems.

The discussion on second order PMD revealed that it has the same effect and dimensions of chromatic dispersion. Second order PMD is a contributing factor in analog system degradation but is significant only in the presence of high chromatic dispersion, directly modulated, high chirp systems. Second order PMD is not a factor in properly compensated 10 Gb/s digital systems and can either add or subtract from the total chromatic dispersion.

Acknowledgments

The author would like to acknowledge the contributions of several individuals including but not limited to Tom Hanson, Dan Gallagher, Leslie Antos, Dipak Chowdhury and Mike McDonald.

References

- ¹ N. Gisin, B. Gisin, J.P Von der Weid, R. Passy, "How accurately can one measure a statistical quantity like polarization-mode dispersion?," IEEE Photonics Technology Letters, Vol. 8, No. 12, Dec. 1996, pp 1671-1673
- ² U.S. Contribution to IEC SC 86A/WG1, September 1997
- ³ F. Kapron, A. Dori, J. Peters, H. Knehr, "Polarization-Mode Dispersion: Should you be concerned?," NFOEC'96, pp. 757-768, September 1996

⁴ H. Bulow, "System Outage Probability Due to First and Second Order PMD," IEEE Photonics Technology Letters, Vol. 10, No. 5, May 1998

⁵ J. Peters, A. Dori, F. Kapron, "Bellcore's Fiber Measurement Audit of Existing Cable Plant for use with High Bandwidth Systems," NFOC'97, pp. 19-30, September 1997

⁶ P. Ciprut, B. Gisin, N. Gisin, R. Passy, J. Von der Weid, F. Prieto, C. Zimmer "Second Order Polarization Mode Dispersion: Impact on Analog and Digital Transmissions," Journal of Lightwave Technology, Vol. 16, No. 5 May 1998

⁷ A. Zainul, "Contributions to composite second order distortion for 80 channel analog systems from chromatic dispersion, PMD and PDL," SPIE Vol. 3491, September 1998

⁸ C. Poole, J. Winters, J. Nagel, "Dynamical equation for Polarization Dispersion," Optics Letters, Vol 16, No. 6, March 15, 1991.

⁹ F. Matera and C. G. Someda, "Random Birefringence and Polarization Dispersion in Long Single-Mode Optical Fibers," Anisotropic and Nonlinear Optical Waveguide, C.G. Someda, and G. Stegeman eds. (Elsevier, Amsterdam, 1992).

¹⁰ F. Bruyère, "Impact of First and Second Order PMD in Optical Digital Transmission Systems," Optical Fiber Technology, Vol.2, pp. 269-280, January 1996

Author



Bob Whitman received his B.S. degree in Industrial Engineering from Hofstra University in 1989. He spent eight years as a US Naval Officer in the Nuclear Engineering program. Bob joined Corning Incorporated Telecommunications Product Division as a Senior Applications Engineer in 1997. His current responsibilities include technical support for optical fiber to Corning's cable manufacturer and end-user customers.

CMT-CABLE DESIGN FOR SI-PMMA-POF APPLICATIONS UNDER HIGHLY ENVIRONMENT-STRESS

Olaf Ziemann¹⁾, Helmut Steinberg²⁾, Peter E. Zamzow³⁾

¹⁾ Deutsche Telekom, T-Nova, D-10589 Berlin, Germany, Goslarer Ufer 35

²⁾ ALCATEL autoelectric, D-92685 Floss, Germany, Vohenstraußer Str. 20

³⁾ ALCATEL Kabel, D-30179 Hannover, Germany, Kabelkamp 20

ABSTRACT

The industrial use of step Index-Polymer Optical Fibers (SI-POF) of PMMA-material, as well as the use in automotive applications and private networks, must be prepared for extreme surrounding circumstances. Quite often there are arising the following stress-parameter in the POF-praxis:

- small curve radius with mechanical radical strength
- selective high temperature load
- chemical aggressive and abrasive environment

These influences lead to a catastrophic increase in the attenuation. Possible mechanical destruction of the POF-fibers shortens drastically the life expectancy of the POF-transmission line.

The use of POF-cables for a structured cabling or in the automotive area often requires a reliable and economic protection sheath. The known PA-coating may not be enough in some cases for the protection of a long-lifetime and stable POF-transmission line.

The suggested solution to protect a SI-POF-core with a CMT-jacket (Corrugated Metal Tube = CMT) guides to remarkable results.

In this case the CMT-coated fibers are checked with different temperatures between +60°C and +120°C under mechanical critical loads ($R > 10 D$).

It was shown how the attenuation at the different wavelengths of 520 nm (green), 580 nm (yellow), 650 nm (red) are changing under mechanical stress and temperature-effects.

The POF-CMT-design shows universal usability for a safe structured wiring and for the automotive area in the engine section.

Introduction

Electronic components along with the necessary transmission media are exposed to an extremely

harsh surrounding in automotive applications. For this reason the ability to operate, considering EMI-aspects, comes first. Apart from thermal stress (up to 125 °C and even more nearby the engine) on-board networks for the use in automotive must have an extremely high mechanical and chemical resistance against aggressive media like diesel oil, brake fluid etc. In contrast to this in the future reliable data highways will be necessary. Miniaturization and a progressive development in electronics increasingly influence the standards of transmission systems for automotive.

Examples are:

- integrated monitoring
- auto-diagnosis
- intelligent information systems
- opto-electric displays
- reliability and safety

Conventional cable technologies on copper basis can be combined with advanced POF-systems and their components („piggyback-method“) in order to perform higher communication standards.

The transmission capacity of POF at wavelengths of 520 nm (green), 590 nm (yellow) and 650 nm (red) is characterized by attenuation and bandwidth. The typical PMMA SI-POF attenuation is 15 dB/100 m (at 650 nm) and the data rate is 150 Mbit/s for 50 m fiber length.

In building Networks a reach value of 100 m is required. The use of green or yellow LED or red VCSEL improve the parameters of POF systems to this demand. With new multi step index or Multi Core POF bit rates up to 500 Mbit/s (IEEE1394) are possible.

POF solutions with a metallic CMT protective cover

The simple processing of a POF is defined by its mechanical reaction when bent until its structural limits. For the application it must be guaranteed that the POF-bending-radius $R > 10 \times \text{core}$

diameter is not fallen below. This simple definition of the limits ensures an optimal POF-connection in the optical network. The temperature range for unprotected POF-cores is between - 40° C to + 85° C (upper limit exposure time short in comparison to total life time). Conventional POF solutions are usable in the inside compartment of vehicles. The use in sections with higher temperatures and/or aggressive environments (e.g. engine section) needs more resistant POF cables. Nevertheless, handling has to be as easy as for existing copper solutions [1]. A considerable mechanical and thermal protection can be achieved by special micro-tubes, fig. 1.

These laser-welded and corrugated metallic micro-tubes (CMT) protect the POF primarily and can be manufactured for a variety of possible applications with different materials:

- copper
- aluminum
- brass
- bronze
- steel
- high-grade steel alloys

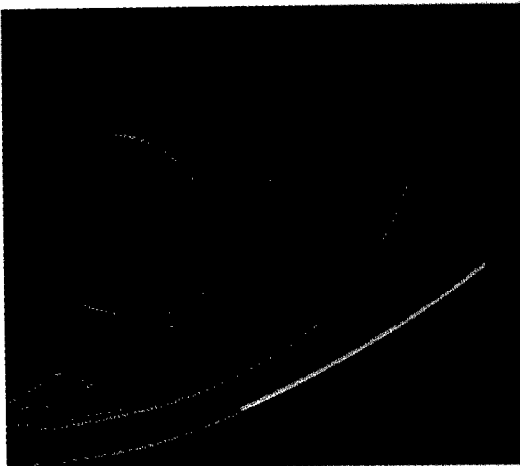


Fig. 1: POF cables with CMT sheath

Performance features of CMT POF design are:

- highest transverse pressure stability
- temperature protection
- chemical resistance
- vibration stability
- high elastic tensile strength

Requirements for POF systems

Building networks:

The fig. 2 shows the typical length distribution for building networks (based on statistical data from Berlin 1987). Most of the links are shorter than 100 m, corresponding with the reach requirements of classical standards as IN11801.

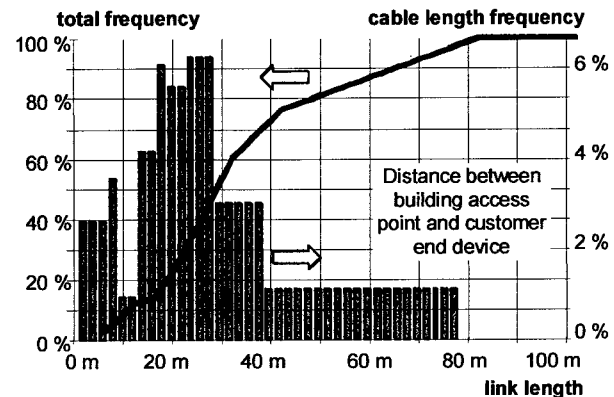


Fig. 2: Cable length statistics for Berlin area

Important points for the cable requirements are:

- typical temperature range from -20°C up to +70°C
- long life time (15 to 20 years)
- simple installation and handling

The use of CMT cables can improve the parameters of the installation system.

Automotive application

The rough environment in automotive expands the requirements for POF use to:

- local high temperatures
- vibrations
- mechanical stress during installation
- chemical aggressive agencies
- 5..20 m reach for automotive
- 50..100 m reach for aircraft's

The figures 3 and 4 show typical application scenarios in in-house and automotive networks. The building in fig. 3 is connected via a broadband access line to a network operator (e.g. TDSL, [2]). The digital data will be distributed inside of the building with a low cost POF communication network.

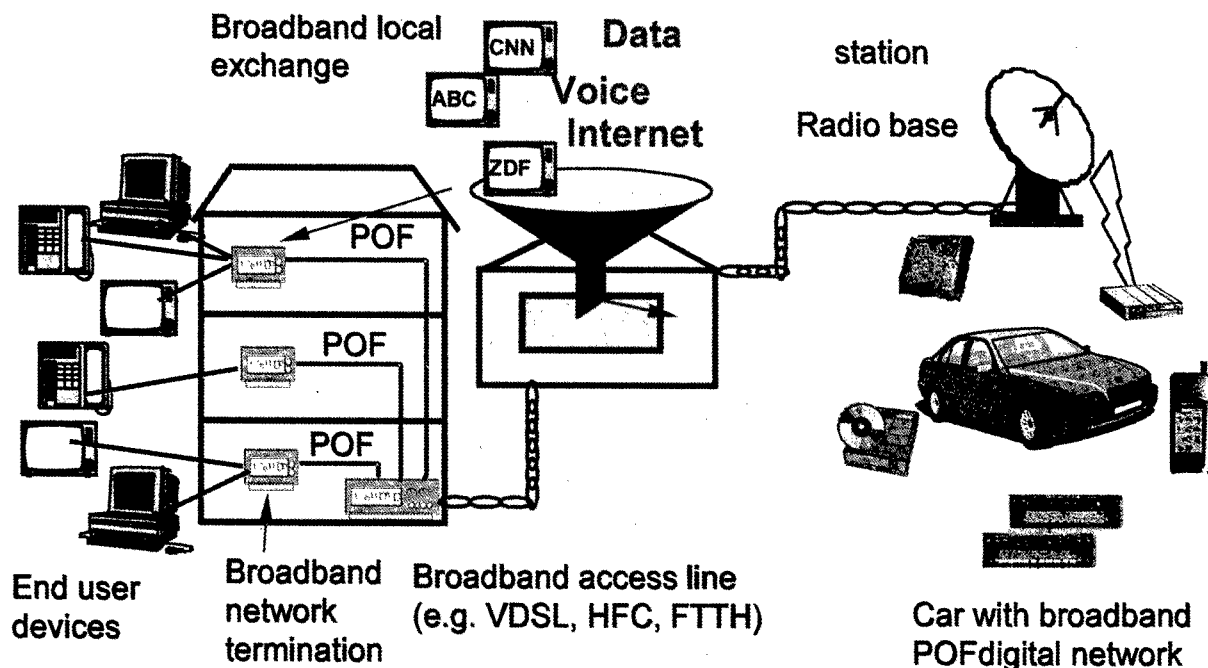


Fig. 3: Application of POF networks in building wiring and automotive networks

Cars can be connected to the access network via broadband radio systems. Inside of the car, all electronic devices are connected with a POF bus (e.g. MOST, [3]).

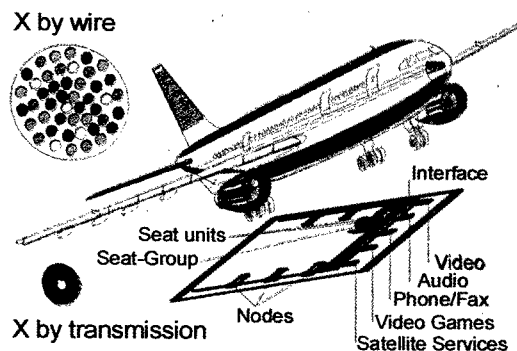


fig. 4: Aircraft application

In this paper we like to present first results for the usability of CMT POF design, taking into account the mentioned demands. The following sections will describe the mechanical, thermal and chemical properties as well as the additional benefit of hybrid solution (data transmission and power supply).

Thermo mechanical properties of POF-CMT

For the mechanical protection preferably high-grade steel alloys are used. The transverse pressure stability of these CMT-elements is extremely high. In comparison to even microtubes the use of CMT-elements increases the transverse pressure stability by 5 to 10 times. The usual thickness of high-grade steel walls is 150 μm to 200 μm .

The parameters of CMT (material, thickness and corrugation depth) will be defined by the application dependent requirements. In the actual design, between the CMT and the optical core a foam buffer is used. All mechanical forces act on the metal sheath, whereas the POF core remains unstressed [4, 5].

In order to investigate the temperature behavior of the CMT-POF cable, we made some tests. The fig. 5 shows the general test procedure. The used device [6] enables the simultaneous automatic test of up to 20 fibers at the wavelengths 520 nm, 590 nm and 650 nm (see fig. 6), corresponding to the attenuation windows of PMMA POF.

In a first test, 4 fibers were placed into the climatic chamber:

- 10 m fiber without CMT
- 10 m fiber with CMT, complete inside the chamber
- 10 m fiber with CMT, 20 cm of each meter inside the chamber
- 10 m fiber with CMT, complete inside the chamber with 5 sheath defects/m

The results can be seen in fig. 7

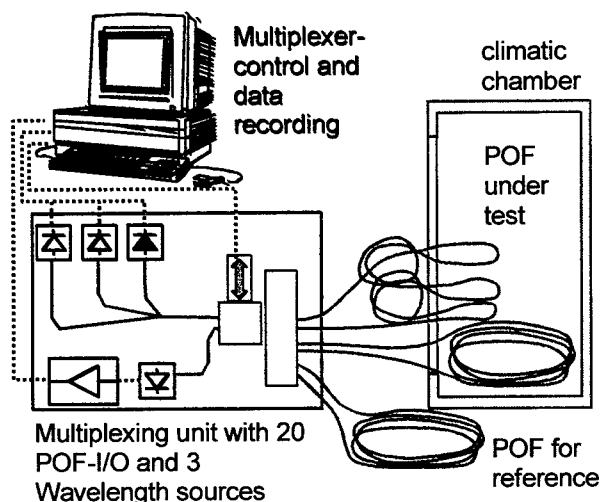


Fig 5: Equipment for climatic tests

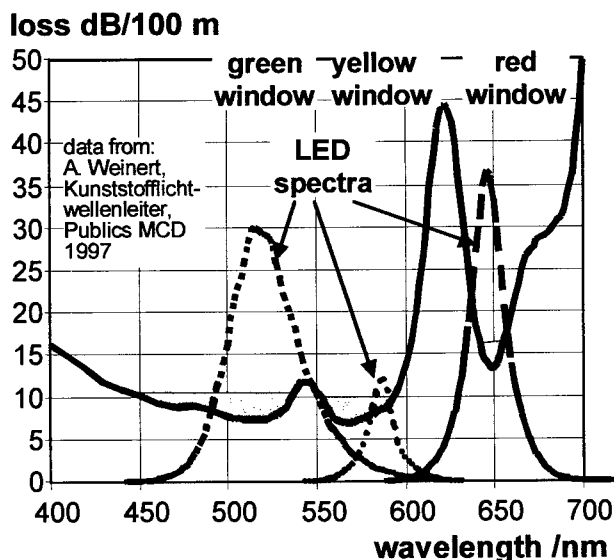


Fig 6: POF attenuation minima and spectra of the used LED

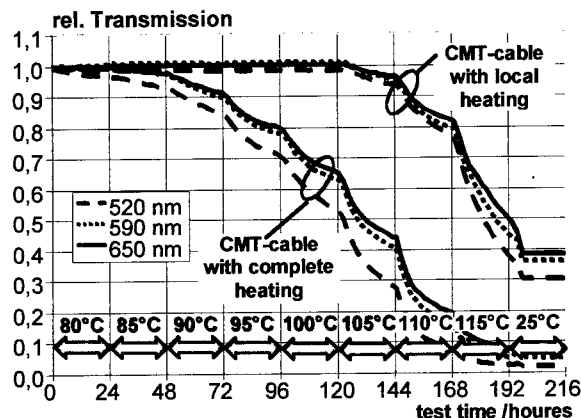


Fig 7: Results of temperature step test

The temperature was set to +85°C at the test begin. Every day, the value was increased by 5 K, climbing up to a maximum of 115°C. The last day was made with room temperature, in order to find reversible effects. The relative humidity was set to 95% below 100°C (than with constant absolute humidity).

It can be seen very clear, that the aging of the complete heated cable starts at about 85°C, as expected for PMMA fibers. The local heated fiber is able to resist about 20 K more. This is very attractive for automotive applications with small size heat sources.

The second test was made with 100°C/95 %RH for 6 days. Fig. 8 shows the results, measured at 650 nm.

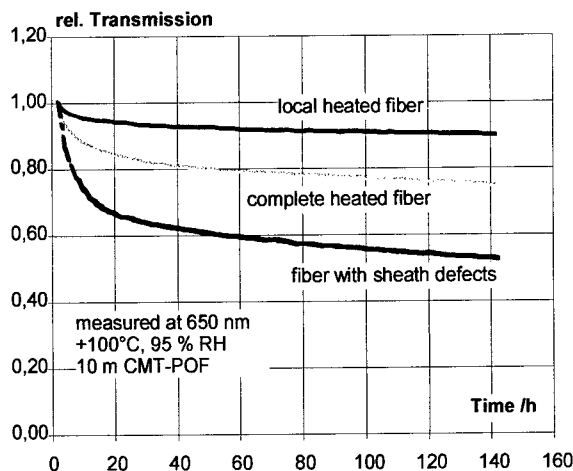


Fig. 8: Long term climatic test results

It can be seen, that the local heated fiber has nearly no transmission loss over the test duration. The complete heated fiber shows

higher attenuation increment. The highest additional loss shows the fiber with sheath defects (5 defects/meter). This shows the good influence of the CMT. In the present design, there might be a gap between POF and metal. Further improvements will avoid this gap, giving cable less susceptible for sheath defects.

Electrical properties of CMT

The main advantage of this hybrid-elements is immediately recognizable as the electrical and optical systems paths can be put together. In this way a weight and volume reduction of wire harnesses is achieved and the primary protection of the POF-core is guaranteed. Thus an adjusted wiring-concept along with a high degree of automation can be realized. For the electric dimensions adjustment of the CMT-conductor, implementing the hybrid-POF-solution, the following requirements must be met:

- copper-conduction-value $57 \text{ m}/\Omega \text{ mm}^2$
- 2 kV-Voltage resistance (insulated conductor opposite to ground)

CMT-technology enables solutions with a variety of metal-alloys:

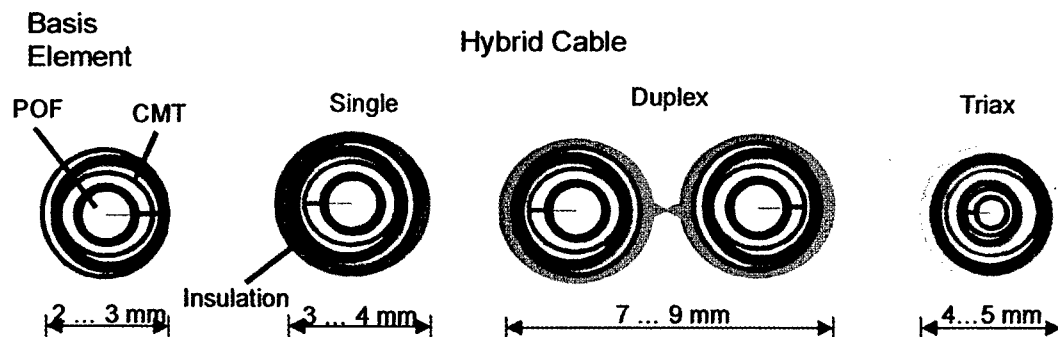
- copper
- aluminum
- brass

In the utility vehicle sector solutions leading to an additional reduction of weight are preferred [7, 8]. An aluminum alloy for hybrid-POF-CMT-cable elements, for example, performs:

- reduction of weight
- high mechanical transverse stability
- good electric contact
- primary POF-protection
- economic solution for hybrid-networks
- high safety level
- substitute for large core cross-sections

In the case of copper as CMT material a comparison between the tube and a round cable is mentioned in the CMT-equivalent of the cross-section area in Fig. 10.

About 95% of all copper cables inside cars have cross sections below $2,5 \text{ mm}^2$. A standard 2,2 mm diameter POF with a $400 \mu\text{m}$ thick metal sheath gives a metal cross section of $3,3 \text{ mm}^2$. That means, the sheath can be used as conductor for most of the applications (excluding power cables from the battery to the generator and the engine starter). In future automobile generations the use of two voltages 14/42V will reduce the portion of the "power-cables" drastically. Therefore a change of a new harness topology with new transmission media is necessary. Another reason for a new on board electronic architecture is the increasing use of mechatronic-components in automotive. This applications based on a power supply and a data communication port with different lines. In fig. 10, the relation between POF outer diameter (D_o) and sheath thickness on the one hand and the metal cross section on the other hand is shown.



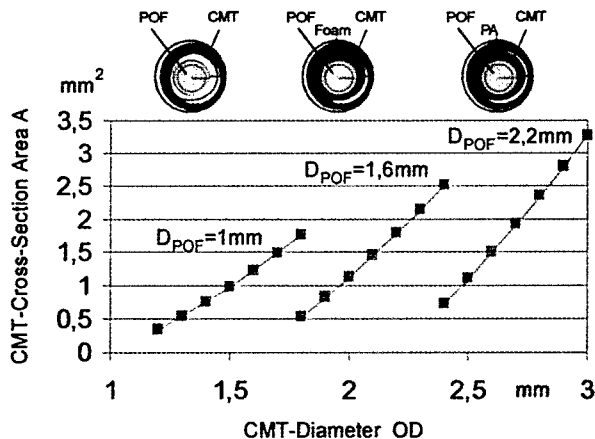


Fig. 10: Electrical CMT-Equivalent

The special importance of these hybrid solution is given by the increasing total cable length in comfortable cars (typical 4 to 5 km).

Outlook

The use of electronic components in automotive has increased immensely in the last few years. By the introduction of multimedia services the on-board network will obtain new structures. In the future reliability and quality of a vehicle will be increasingly determined by the design of the integrated harness. Growing individualization of several variants leads to new solutions. Hybrid-systems-solutions will combine complex on-board networks and optimize the harness' branching. The necessary standardization of component parts must take place so that rising comfort does not influence reliability and that economic production lines can be used [10]. An advanced cable-solution is the hybrid-POF-CMT-line as it performs quality and safety along with an efficient production process.

The paper has shown once more, that SI POF can cover a wide range of present applications ([9] and [11]).

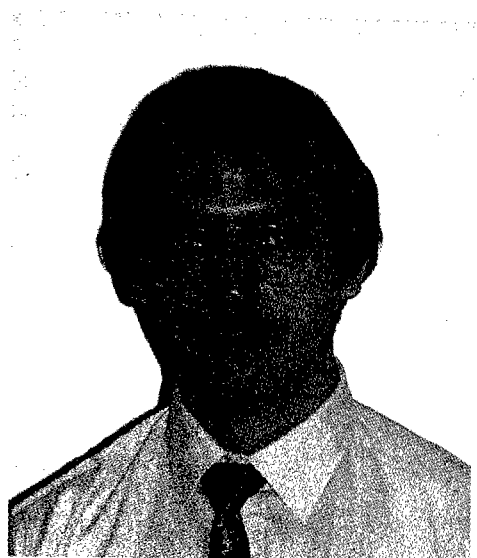
Acknowledgement

The climatic test was performed at the Federal Institute of Materials Research and Testing. The authors like to thank Mr. Mäder and Mr. Kadoke for there kind cooperation.

References

- [1] Jürgen Krauser, Olaf Ziemann, Polymer Optical Fiber Cables for In-house Cabling, ANCIT Workshop. Access Network construction and installation techniques, Volume 1, Proceedings, Torino March 1998
- [2] <http://adsl.telekom.de>
- [3] <http://www.oasis.de>
- [4] Haag, Hög, Staschewski, Peter Zamzow, Application of micro-spiral-corrugated welded tubes with optical fibres. Wire Association International 68th Annual Convention, Ohio, Cleveland, USA 1998
- [5] Dr. Gerhard Wanser, Kabelmetal Hannover 1967, Cables with welded and corrugated metal sheaths.
- [6] W.-F. Frank, A. Bräuer, W. Daum, H. J. Tessmann, A. Weinert, O. Ziemann: "Polymer optical fibres in Germany: Reliability test for use in premise wiring", 7. International Plastic Optical Fibres Conference 1998, Berlin, S. 287-289
- [7] Scheideler, W.; Steinberg H.; Zamzow, P. New POF-Cable Generation with Corrugated Micro Tubes (CMT) in Bus Systems for Automobiles. IWCS Symposium 1998, Philadelphia
- [8] N.N. Mechatronische Lösungen auf der Überholspur, Markt & Technik Nr. 47/20.11.98, S. 36
- [9] O. Ziemann, J. Krauser, W. Daum, Application windows for step index and graded index POF, 8. international POF conference, July 1999, Tokyo, pp. 44-47
- [10] G. Widawski, Outlook of Plastic Optical Fibers for high speed transmission links, , 8. international POF conference, July 1999, Tokyo, pp. 114-171
- [11] P. E. Zamzow, H. Steinberg, P. Roef, SI-POF-Hybrid-Cable-Systems in application for aircraft and earth moving applications, 8. international POF conference, July 1999, Tokyo, pp. 120-123

Authors



Dr. Olaf Ziemann was born in 1965. He has studied Physics at the university of Leipzig. Between 1990 and 1995 he was a member of the Institute for Communication and Measurement at the Technical University of Ilmenau. He graduated in 1995 at the topic „Coherent optical transmission systems“. In the same year, he joined the Technology center Darmstadt of the Deutsche Telekom in Berlin. His special interests are in the field of optical access network technologies and home wiring systems. In 1996 O. Ziemann was involved in the foundation of the new sub committee „Polymer Optical Fibers“ in the Information Technology Society (ITG-FG 5.4.1) and is still leading this group. Presently O. Ziemann is engaged in research projects for the use of POF transmission systems in future broadband access systems, as investigated in the Full Service Network Initiative for example.

STUDY ON MECHANICAL AND OPTICAL CHARACTERISTICS OF REVERSE DISPERSION FIBER CABLES

Masahito Morimoto Ichiro Kobayashi Hideyo Hiramatsu Kazunori Mukasa
Ryuichi Sugizaki Yoshihisa Suzuki Yasuhiro Kamikura

THE FURUKAWA ELECTRIC CO., LTD.
6, Yawata-kaigandori, Ichihara-shi, Chiba, 290-8555, JAPAN

ABSTRACT

We developed novel dispersion compensation cables of ribbon slotted rod type and loose-tube type using Reverse Dispersion Fiber (RDF) which can compensate not only the chromatic dispersion but also the dispersion slope. Both developed cables had good optical and mechanical properties and the feasibility of these cables for practical use was confirmed.

INTRODUCTION

As the telecommunication demand increases, the deployment of DWDM system to transmit large volume of information economically has been progressing worldwide. For examples, transmission experiment for 3Tbit/s ($160\text{G} \times 19\text{ch}$)¹ have been reported.

As the transmission speed of each wave length increases from 2.5G to 10G, 40G and 80G, Reverse Dispersion Fiber will play an important roll in high-speed transmission systems.^{2,3}

For the long distance telecommunication, a transmission line composed of fibers of small dispersion and non-linear effects is demanded to suppress the signal distortion.

In order to satisfy these demands, we developed a new type of dispersion compensation cable using RDF⁴ which compensates not only the chromatic dispersion but also the dispersion slope in the 1550 nm region and possesses small non-linear effects.

FEATURES OF RDF

RDF and the transmission system using RDF have the following features.

(1) Dispersion Compensation Module or Dispersion Compensating Fiber (DCF) is not needed

The conventional long distance transmission line is composed of DSF (Dispersion Shifted Fiber), but when this line is used for DWDM, transmission distance is limited by the pulse distortion caused by FWM and the residual dispersion.

Hence, the long-haul transmission system which is composed of DSF often uses Dispersion Compensation Module to compensate dispersion.

In the meantime, in the system composed of SMF, DCF is used to compensate signal distortion.

But both Dispersion Compensation Module and DCF have the shortcomings of high insertion loss, and imperfect dispersion compensation.

The RDF, however, is not a component such as Dispersion Compensation Module or DCF but a transmission fiber itself with a dispersion characteristic which is reverse of SM fiber in value and slope.

So the system using RDF can reduce extra components such as Dispersion Compensation Module or DCF, and realize low residual dispersion.

Moreover, it improves the system performance since RDF has lower loss than Dispersion Compensation Module or DCF.

(2) High power EDFA can be used

RDF has a negative chromatic dispersion in contrast to the positive dispersion of SMF in 1550 nm region. Therefore the dispersion can be easily compensated by concatenating RDF and SMF. When the output of EDFA is launched into SMF (Fig.1), the pulse distortion becomes smaller compared with DSF system because of the larger effective area and smaller non-linear effects of SMF than DSF.

Therefore high power EDFA can be used in the RDF system.

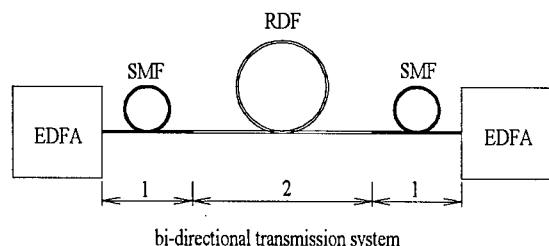
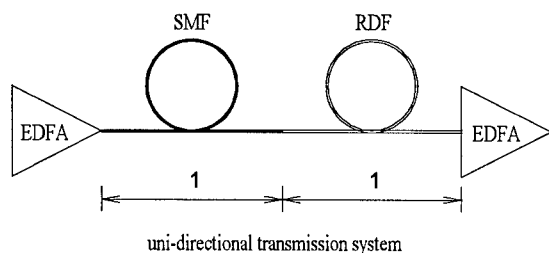


Fig.1 Examples of RDF System

(3) Wide-band transmission is possible

The dispersion slope of RDF is negative which is reverse of that of SMF. Therefore, by combining adequate lengths of RDF and SMF, a flat dispersion slope can be realized in the wide wavelength range between 1530 and 1570 nm (Fig.2)

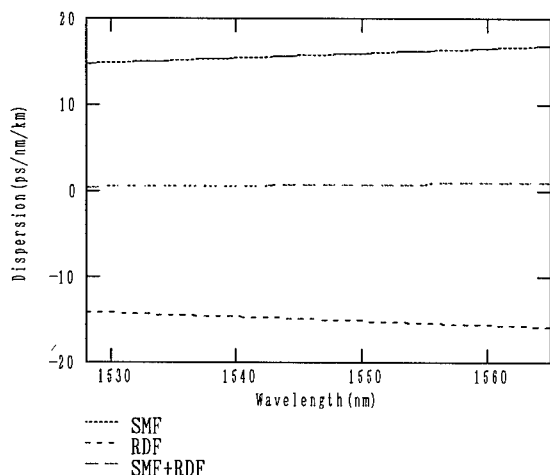


Fig.2 Dispersion Characteristics of RDF and SMF

CABLE CHARACTERISTICS

We manufactured two type trial cables using RDF and confirmed that the optical and mechanical characteristics are suitable for the practical application to DWDM.

Cable structure

We manufactured ribbon slotted-rod type and

loose tube type cables using RDF. Fig.3 and Fig.4 show the cross section of these cables.

The slotted rod has five slots with each slot capable of accommodating 5 layers of 4-fiber ribbon.

The dimension of 4-fiber ribbon is 1.1mm × 0.3mm.

As for the loose tube type, each tube has 6 fibers inside and is SZ stranded around the central strength member.

RDF in the tubes are ultraviolet (UV) resin coated fibers with outer diameter of 250μm.

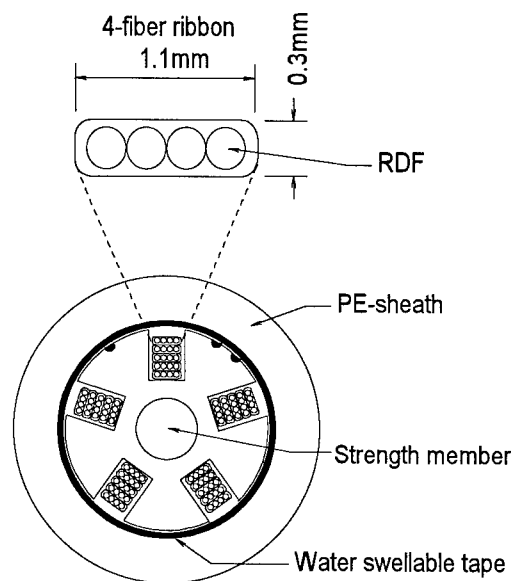


Fig.3. Cable Cross section (ribbon slotted-rod type)

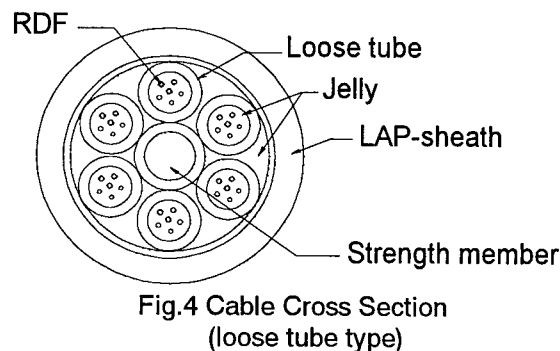


Fig.4 Cable Cross Section (loose tube type)

TRANSMISSION CHARACTERISTICS

(1) Spectral Attenuation

The spectral attenuation characteristic of the trial cable is shown in Fig.4. The measurement was done under the following conditions.

Temperature : approx. 20°C
 Cable length : 3000m
 Cable state : wound around a drum of 900mm OD with tension of several kilogram force

Good results were obtained for both types of the cable in the range of 1530 to 1570 nm.

In the range of 1570 to 1600 nm, ribbon slotted-rod type showed a slightly larger attenuation than loose tube type.

This loss increase is supposed to be caused by lateral pressure from the slot wall and can be improved by controlling the excess ribbon length in the slot.

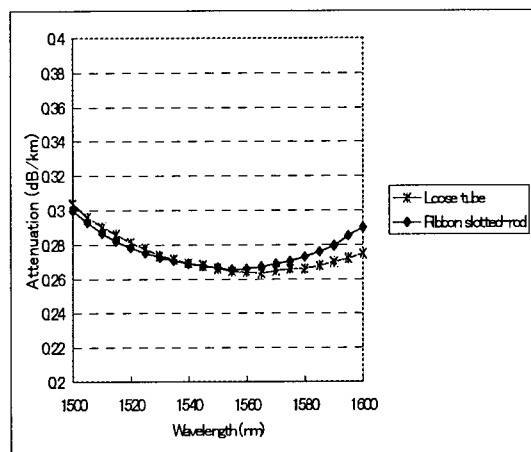


Fig.4 Spectral Attenuation of trial cables

(2) Temperature dependence of attenuation

The temperature characteristics of the attenuation of these cables are shown in Fig.5 and Fig.6. The loss change in -30 to 70°C was less than 0.02 dB/km.

The measurement wavelength is 1550nm.

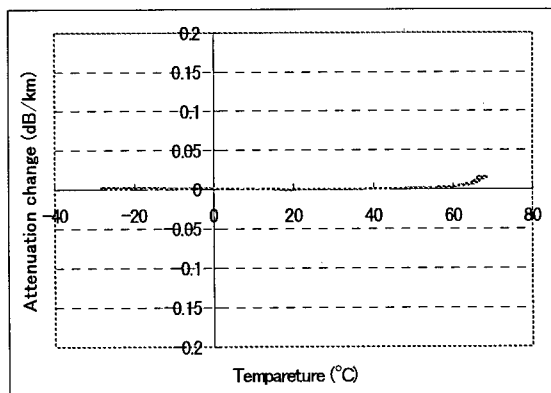


Fig5. The temperature characteristics of Attenuation (ribbon slotted-rod type)

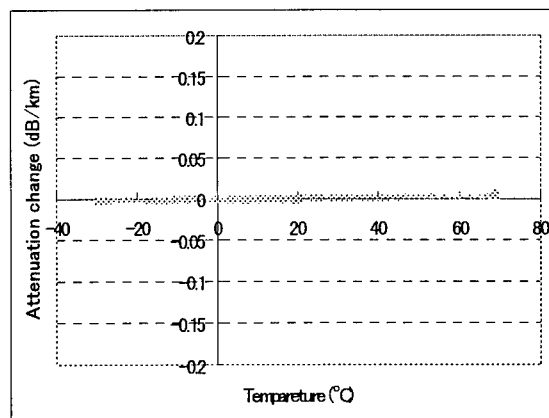


Fig6. The temperature characteristics of Attenuation (loose tube type)

(3) PMD characteristic

The change of Polarization Mode Dispersion (PMD) during the cabling process and its temperature dependency from -30 to +70°C were measured.

Measurement conditions are as follows.

Fiber length : 3000m

Fiber state : wound around a bobbin of 280mm OD with tension of 30 gram force.

Cable length : 3000m

Cable state : wound around a drum of 900mm OD with tension of several kilogram force.

Measurement was done by Jones Matrix methods.

The results are shown in Fig.7 and a good average PMD of 0.1ps/√km was obtained for both types of cable.

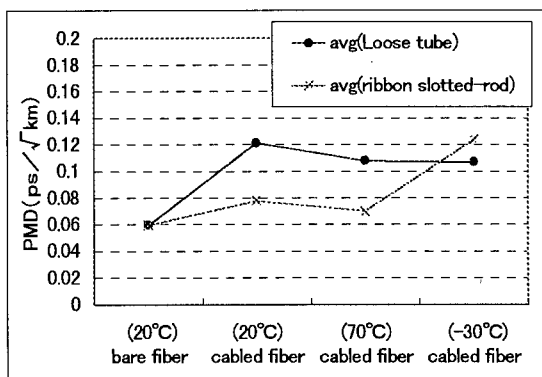


Fig7. PMD of fiber and trial cables

(4) Temperature dependence of dispersion

The temperature characteristic of chromatic dispersion of these cables between 1530 and 1570 nm were measured when temperature

was changed from -30 to $+70^{\circ}\text{C}$. As shown in Fig.8, RDF has a positive temperature coefficient of dispersion, which means that the chromatic dispersion increases as the temperature goes higher. SMF, on the other hand, has a negative coefficient thus the dispersion compensation is possible for a wide range of temperature in this wavelength band.

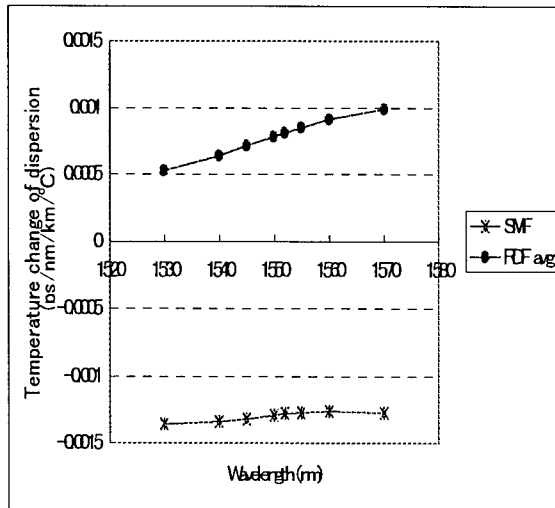


Fig.8 Temperature characteristics of dispersion

(5) Mechanical characteristics

Various mechanical tests were conducted and good results were obtained for both types of cable as listed in Table 1.

CONCLUSION

We developed two types of dispersion compensation cables using RDF that compensates not only the chromatic dispersion but also the dispersion slope. These trial cables showed good optical and mechanical characteristics and the feasibility of these cables for practical usage was confirmed. We believe that this new cables will contribute to accelerate the growing transmission capacity of DWDM system.

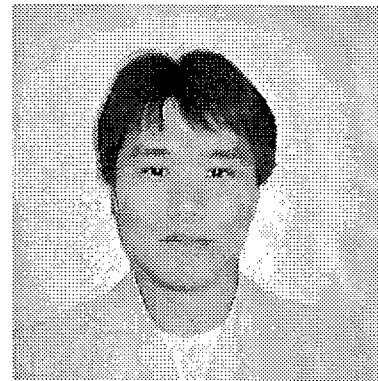
Table 1 Mechanical Characteristics

Test Item	Condition	Results (1550nm)
Bending	10 D D: cable diameter	<0.05 dB/km
Tensile	1km cable weight	
Lateral force	2000N/100mm	
Torsion	$\pm 360^{\circ}$ /1m	
Impact	10N \times 1m impact surface diameter: ϕ 10mm	

REFERENCE

- [1] S.Kawanishi et al., OFC'99 PD1 (1999)
- [2] M.Murakami, H.Maeda and T.Imai
Proceedings of ECOC'98 TuB21 (1998)
- [3] K.Yonenaga and Y.Miyamoto
Technical Digest OFC'99 FD4 (1999)
- [4] K.Mukasa et.al., ECOC'97 vol.1, pp127-130(1997)

Authors



Masahito Morimoto

The Furukawa Electric co.,ltd.
6,Yawata Kaigandori, Ichihara,
Chiba, 2908555, Japan

Masahito Morimoto received his M.E. degree in Electrical Engineering from Ritsumeikan University in 1993. He joined The Furukawa Electric co.,ltd. in 1993 and has been engaged in research and development of optical fiber cables. He is now a research engineer of Opto-technology laboratory. He is a member of The Physical Society of Japan.

THE INFLUENCE OF PROOFTTEST DWELLTIME ON FIBER RELIABILITY

Felix P. Kapron

Telcordia Technologies (formerly Bellcore)
Morristown, New Jersey 07960-6438

973-829-5225, fkapron@telcordia.com

ABSTRACT

The topic of prooftesting is briefly reviewed, and we then show that the dwelltime portion of this process has a substantial effect on fiber lifetime and failure rate. Some portions of the proof test standards may need to be re-examined to take this into account.

INTRODUCTION

Proof testing full lengths of optical fiber is performed on virtually all fiber that is commercially sold. There are three portions to the proof testing process: loading or tension ramp-up, steady tension (dwell), and unloading or tension ramp-down. The details of these portions have commercial implications on fiber breakage and yield.

This work was motivated by studying proof testing documents from the working groups (WGs) of two optical fiber reliability standards bodies. One document [1] is from WG FO-6.6.8 in the Telecommunications Industry Association (TIA), and the other [2] is from WG 1 in Subcommittee 86A of the International Electrotechnical Commission (IEC).

The older standardized proof testing test procedures were specified by the dwelltime at the proof stress level, normalized to one second. The dwelltime of a practical proof tester is usually below this value because of the fiber speeds and tension lengths involved. The standards at that time called for the proof stress to be increased according to a specific formula. This was intended to "equalize" for variations in proof testing tension-lengths and speeds among different machines.

The current proof testing procedures [1, 2] remove this normalization procedure and do not require any restriction on the ratio of dwelltime to proof stress. Instead the emphasis is on the unloading process, which has a considerable effect on the projected mechanical reliability. However, the duration of dwelltime is not negligible, and this paper investigates for the first time the relation between dwelltime and the prediction of fiber reliability.

THE PROOFTESTING PROCESS

Proof testing requires that a specified tension or proof stress be applied sequentially along the full length of fiber. It is done during fiber manufacturing, on-line just following the fiber drawing and coating process, or off-line as part of the testing process.

Figure 1 is a simplified schematic illustration of a common process. The fiber passes at a linear speed s between rotating capstans 1 and 3. The load-wheel 2, by application of a weight or a braking action, helps maintain a constant proof stress σ_p from the time the fiber leaves capstan 1 until it arrives at capstan 3 over the fiber tension-length L_0 . This time between capstans is the dwelltime t_d .

The associated stress vs. time for proof stressing is shown schematically in Figure 2 for a particular point of the fiber moving along through the three proof testing steps. The bending stress at all wheels is not to exceed 10% of the proof stress.

- As the point on the fiber moves onto the left capstan 1, the stress loading increases from near-zero to the proof stress level σ_p during a loadtime t_l . The stress rate is taken to be constant, and during this first step any crack in

the fiber weakens in a process of dynamic fatigue.

- As the fiber moves off the capstan toward the load-wheel 2, passing around the wheel and then onto the right capstan 3, the proofstress is constant. The duration of this dwell is related to the fiber speed and the tension-length as given by the dwelltime $t_d = L_0 / S$. In this step the fiber weakens in a process of static fatigue.
- Finally, the point on the fiber moves off the right capstan 3, and the stress unloading decreases from the proofstress back down to near-zero, during an unloadtime t_u . As with loading, this step is dynamic fatigue.

PROOFTESTING EFFECTS

Fiber Weakening

The theory of crack weakening has been developed over several decades. To estimate fiber reliability, quantified by either the lifetime or the failure rate, the so-called power law has been widely used. A good summary of this theory is given in a draft IEC document [3], and we will use equations from it in the discussions below.

The document does not account for any possible 2nd region of crack behavior [4]. Here n and B have two sets of values depending upon the magnitude of the stress rate. It is under study for possible incorporation into the document.

Any crack in the fiber weakens during each of the three steps of applied stress. If the strength of a particular crack decreases to the level of the applied stress at a particular instant, the fiber breaks. Imagine that for a particular fiber type the proofstress machine is adjusted to increase the proofstress and/or any of the stress times. Intuitively you would expect that a crack would weaken more with the adjusted machine, and that more cracks would fracture in this case. Equations support this scenario.

For example, if a crack of initial strength S before prooftesting survives the prooftesting, it is reduced to a strength S_p after prooftesting as given by [3]

$$S_p^{n-2} = S^{n-2} - \frac{\sigma_p^n t_p}{B} \quad (1)$$

Here B is the crack strength preservation parameter or B-value; fibers with a higher value of this parameter will experience relatively less weakening. In the above equation the effective prooftime is given by

$$t_p = t_d + \frac{t_l + t_u}{n+1} \quad (2)$$

where n is the stress corrosion susceptibility parameter or n-value. Note in Eq. (2) that dwelltime is the biggest contributor to the prooftime. By Eq. (1) the weakening of a crack clearly increases with the dwelltime.

Unloading

The unloading process is of special interest. If a crack survives the loading and dwell steps, its strength just before unloading must be at least equal to the proofstress at that time. At the beginning of the unloading step, if there happens to be a crack with a strength equal to the proofstress level, the crack will fracture and the fiber will break. Some cracks just slightly stronger (by an amount that can be calculated) will fracture also. Cracks that are still stronger will survive the unloading process but will weaken to a strength below the proofstress level. Still stronger cracks will weaken to above that level.

Because of the unloading process, prooftesting cannot absolutely guarantee that every crack in the surviving fiber will have a strength at least equal to the proofstress. The strength of the weakest crack after prooftesting determines the worst-case reliability of the fiber - the minimum lifetime and the largest fit-rate. This weakening increases with the unload time, so the current test procedures [1, 2] have limitations on how large that time should be.

Fortunately, there is a statistical distribution of crack strengths in a fiber, usually modeled by a Weibull distribution, and the probability of such weak cracks is very small (but calculable).

Several years ago, Bellcore (now Telcordia Technologies) analyzed some fibers that had broken in the field due to exposure to sudden high stress levels. Fractographic analysis showed that the strength of some of these cracks just before the sudden stress was below the specified proofstress level for the fiber. The reason may be related to the above weakening during unloading, or perhaps due to longer-term weakening in the field prior to the sudden stress.

RELIABILITY FORMULAE

In making reliability estimates, the condition usually assumed in the field is that of a cabled fiber subjected to a low level of applied service stress σ_a along its entire length L . This is a simplified version of the actual situation. In practice a proofstested fiber experiences a stress history in cabling and in installation that can be taken into account. In the field, instruments can measure the variation of stress with length [5] for the deployed fiber, and calculations could incorporate those variations for a particular installation.

Reliability in service is characterized by a lifetime or by a failure rate. We make the assumption that the B-value and proofstesting unload time are both small, and they will not explicitly appear [3] in the equations.

For a survival probability P , the fiber lifetime to failure is [3]

$$t_f = \left\{ \left[\frac{\beta^{m_s}}{L} \ln \frac{1}{P} + (\sigma_p^n t_p)^{m_s} \right]^{\frac{1}{m_s}} - \sigma_p^n t_p \right\} \sigma_a^{-n} \quad (3)$$

Note that as the applied stress increases, the lifetime will decrease quite rapidly. The failure rate is normalized to fiber length and is expressed as failures per 10^9 km. This defines the instantaneous FIT rate [3]

$$\lambda_i = 3.6 \times 10^{12} m_s \left(\frac{\sigma_a}{\beta} \right)^{m_s} \left[t_f + t_p \left(\frac{\sigma_p}{\sigma_a} \right)^n \right]^{m_s-1} \quad (4)$$

In both of these equations, m_s is the Weibull m-value (related to the slope of a failure probability plot) under static fatigue, and can be related to the dynamic fatigue values. Parameter β is a Weibull beta-value (related to the plot "intercept").

It should be emphasized that Weibull parameters from the lower-strength region (near proofstress) of the distribution are used, since the applied stress in the field is a fraction of the proofstress. Measurements in this region [6] require longer gage lengths and many samples, and therefore very long lengths of fiber are required.

Note that the prooftime t_p appears in Eqs. (3) & (4), and there is a dependence on dwelltime

through Eq. (2). The resulting effect is the concern of the calculations.

NUMERICAL RESULTS

First establish some parameters for the proofstesting. The proofstress is taken to be 0.69 GPa (100 kpsi), with the applied service stress 15% of that value. The loadtime and unloadtime are both taken to be 15 ms, while the dwelltime is allowed to vary.

The fiber parameters are [3] 20 for the n-value, 2.359 for the dynamic Weibull m-value, and $\ln \beta = 25.499$ for a particular effective prooftime.

For lifetime calculations the fiber length is taken to be 1000 km, and the dwelltime is initially varied to be 0.1 s, 0.5 s, 1 s, and 2 s. Results for lifetime as a function of the failure probability $F = 1 - P$ are shown in Figure 3. As the risk of failure decreases, so does the lifetime, as expected.

Note also that for any fixed failure probability, the lifetime increases as the dwelltime increases. This is shown if one chooses the most stringent failure probability $F = 10^{-6}$.

Results for failure rate are independent of fiber length because the FIT-rate is normalized to length. Also, for the assumed parameters, the second term within the rectangular brackets of Eq. (4) is much larger than a time of even 100 yr, so the failure rate is essentially constant with time. Hence the results for FIT-rate are given instead as a continuous function of dwelltime in Figure 5. Note how the failure rate decreases as the dwelltime increases.

DISCUSSION AND CONCLUSIONS

It is widely known, and can be proven from the above equations, that for a fixed applied stress below the proofstress the effect of increasing the proofstress level is to increase fiber reliability. This is manifested in increased lifetime and reduced failure rates. We have shown here that increasing dwelltime has a similar effect.

Therefore, this parameter should not be neglected in current proofstest procedures [1, 2]. As was the case in earlier versions of the procedures, the prooftime or dwelltime may need to be specified, and the tradeoff of

proofstress with these times may need to be reinstated.

REFERENCES

- [1] *Proof Testing Optical Fibers by Tension*, FOTP-31, TIA/EIA-455-31C, T.A. Hanson ed., Feb. 1995.
- [2] *Fibre proof test*, IEC 60793-1-30 Ed. 1.0, T.A. Hanson ed., in ballot.
- [3] *Power law theory of optical fibre reliability*, IEC 62048 TR Ed. 1.0, F.P. Kapron ed., in ballot.
- [4] *Incorporating Multi-Region Crack Growth into Mechanical Reliability Predictions for Optical Fiber*, T.A. Hanson and G.S. Glaesemann, J. of Materials Science, Vol. 32, 1997, pp. 5305-5311.
- [5] *Fiber-Strain Measurement Using Brillouin Optical-Fiber Time-Domain Analysis*, C.J. Sandwith et al., 1996 IWCS, pp. 415-427.
- [6] *Optical Fiber Failure Probability Predictions From Long-Length Strength Distributions*, G.S. Glaesemann, 1991 IWCS, pp. 819-825.

BIOGRAPHY

Felix Kapron has been active in fiber optics for 30 years, after a Ph.D. from the University of Waterloo in Canada. At Corning Glass Works he was on the team announcing the first low-loss fibers. He joined Bell-Northern Research to help start the fiber optics R&D program, and was at ITT, concerned with international technology transfers.

Since 1987 Dr. Kapron has been at Bellcore (now Telcordia Technologies), responsible for groups dealing with fiber, components, measurements, and subsystems. He has a dozen U.S. patents and a hundred publications, and has been on the boards of several journals and conferences (such as IWCS and NFOEC). Felix has given courses and tutorials, and has leadership positions in fiber optic standards bodies. He is a Fellow of the IEEE.

(photo not available)

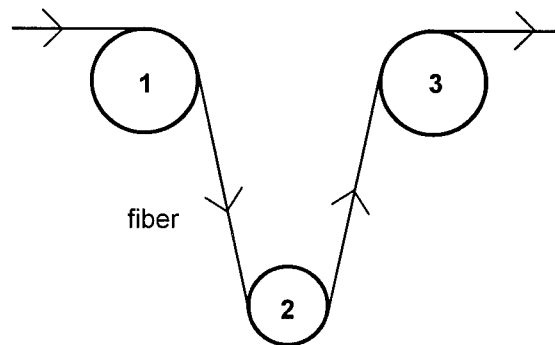


Figure 1 - Simplified Representation of Prooftesting

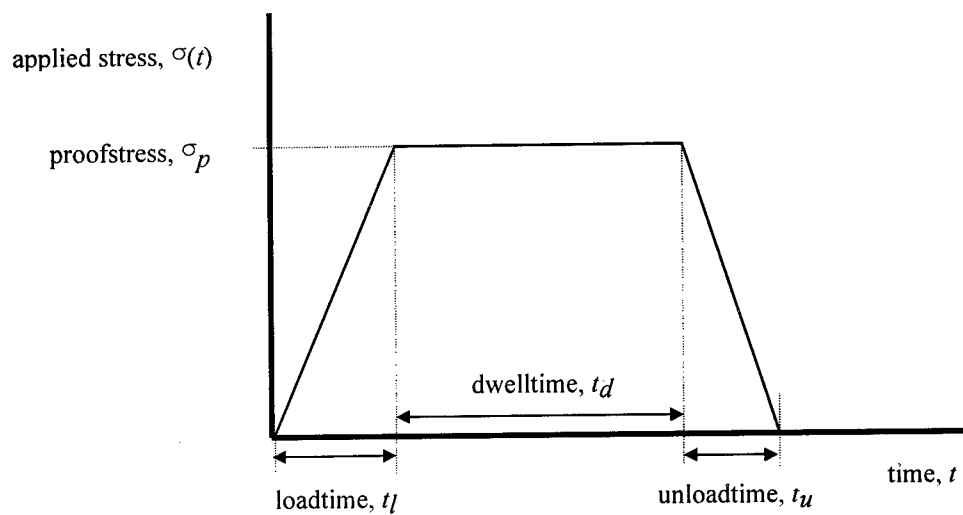


Figure 2 - Applied Stress vs. Time During Prooftesting

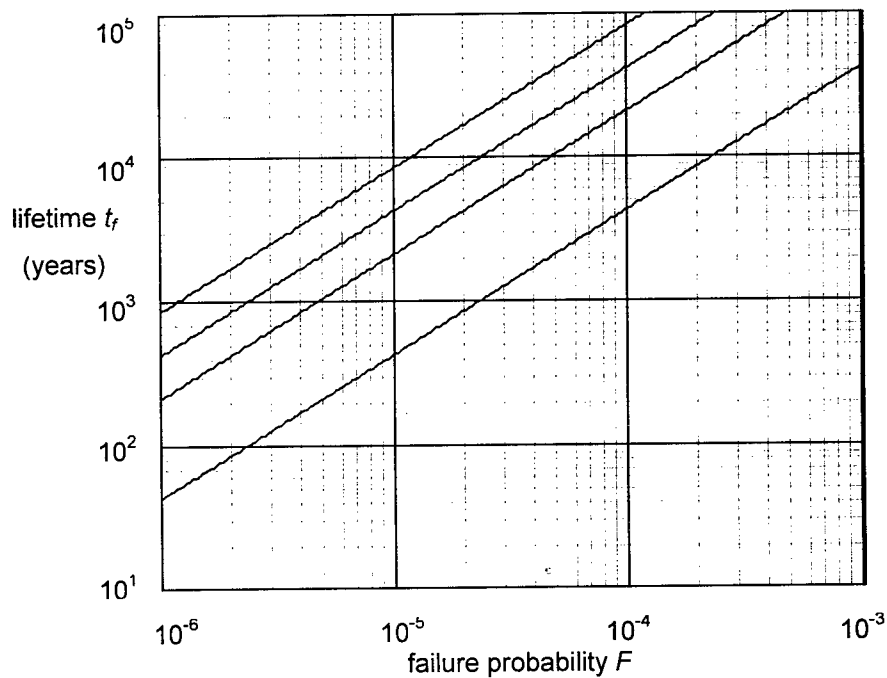


Figure 3 - 1000-km Lifetime vs. Failure Probability for Dwelltimes (lines bottom to top) of 0.1, 0.5, 1, and 2 s.

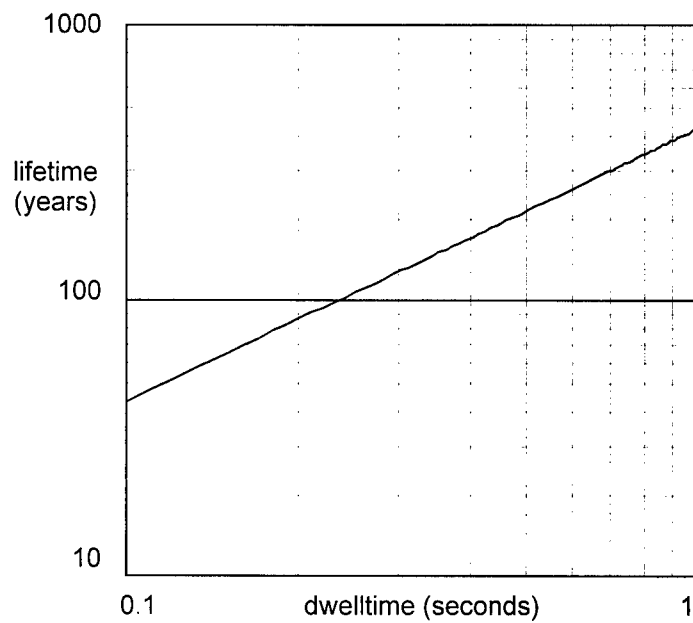


Figure 4 - 1000-km Lifetime (at 10^{-6} Failure Probability) Increasing With the Dwelltime

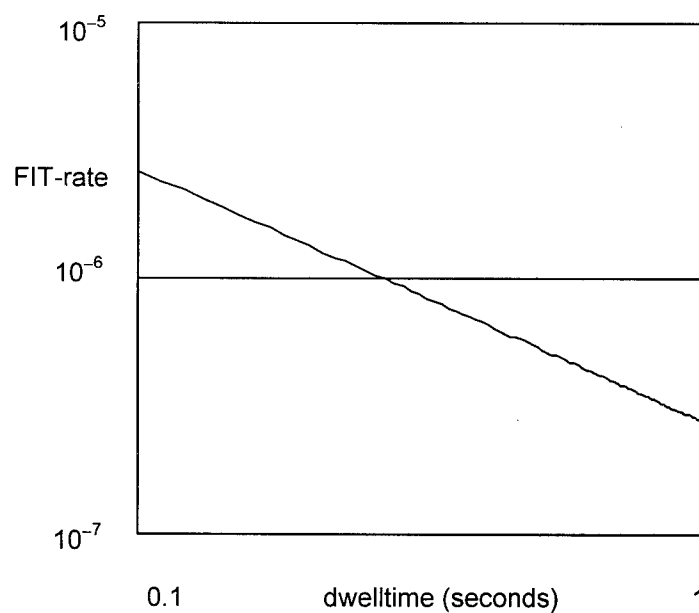


Figure 5 - FIT-Rate Decreasing With Dwelltime Increasing

A STUDY OF THE FIBER STRAINS IN CENTRAL TUBE RIBBON CABLES

Zhan Gao, Walter Pfandl, Reinhard Engel and Andreas Stingl

Siemens AG, Neustadt, Germany

ABSTRACT

Fiber strains can be induced in central tube ribbon cables during cable production and cable installation. This paper has focused on the calculation of the fiber strains caused by the ribbonizing, ribbon stranding and cable bending.

12F-ribbons including Bragg grating fibers have been produced in order to measure the fiber strains in ribbons caused by the ribbonizing and ribbon stranding. By using these ribbons, a 18x12F central tube ribbon cable was manufactured and the fiber strains caused by the cable bending have been determined. A good agreement between the calculation and measurement has been found.

INTRODUCTION

The fiber strain is one of the major parameters which strongly influence the mechanical and optical behaviors of the fiber. Also for the lifetime prediction and determination of the actual transfer speed of light in the fiber, the fiber strain must be controlled.

Since last years the use of high fiber count cables has dramatically increased because of the rapid development of the demand on information transfer in the business. In most of these cables, fiber ribbons have replaced the single fibers, because they are a mean for compact cables and effective mass splicing. In the ribbon, fibers are bonded together by the ribbon coating and have more influence on each other than separate single fibers. Therefore, the analysis of the fiber strain is more important for the ribbon cables. During the development of the slotted core ribbon cable, investigations¹ have been done for calculation and measurement of the fiber strains. However, for the design of central tube ribbon cables the fiber strain analysis has not been strongly used. This paper deals with the analysis of the fiber strains in central tube ribbon cables caused by the

ribbonizing, ribbon stranding and bending of the cable.

RIBBONIZING

During the production of ribbons, for example a 12F-ribbon, the external fibers 1 and 12 have different boundary conditions than the internal fibers 2 to 11 when the fibers are drawn through the ribbon tool. The internal fibers have only top and bottom friction in the ribbon tool, however the external fibers have an additional side friction. This results in different shear stresses on the surfaces of the internal and external fibers. In general, the shear stress of the external fibers is higher than that of the internal fibers. Therefore, the external fibers are elongated more than the internal fibers in the ribbon tool.

The shear stress which acts on the fiber in the ribbon tool is caused by the viscosity of the resin material. For the most real materials, the viscosity depends on the shear rate which can be calculated from the velocity profile. In the Cartesian coordinate (Fig.1), the velocity profile of the resin is described by the following equation:

$$\frac{\partial p}{\partial x} = \frac{\partial}{\partial y} \left(\eta \frac{\partial u_x}{\partial y} \right) + \frac{\partial}{\partial z} \left(\eta \frac{\partial u_x}{\partial z} \right) \quad (1)$$

where p is the pressure, η the viscosity and u_x the velocity in x-direction.

To solve the equation (1), a model has been generated which uses the following assumptions and boundary conditions.

- 1) The flow is steady.
- 2) There is no slide between the resin and the fiber surfaces and between the resin and the surfaces of the ribbon tool.
- 3) The temperature in the ribbon tool is homogeneous and constant.

- 4) All fibers have the same diameter and are arranged in a line.
- 5) No gap between the fibers.

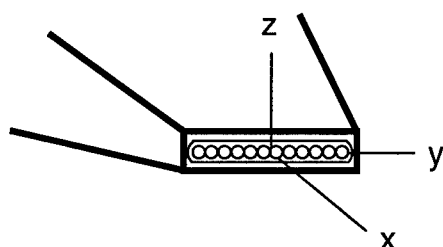


Fig.1: Cartesian coordinate in the model.

For a 12F-ribbon, the fiber tensions in the ribbon tool have been calculated for different line speeds. It has been found that the fiber tension increase with the line speed and the tension of the external fibers is always higher than that of the internal fibers. In Fig.2 the difference in the fiber tensions between the external and internal fibers is given for various line speeds. It is shown that the difference of the fiber tension increases with line speed.

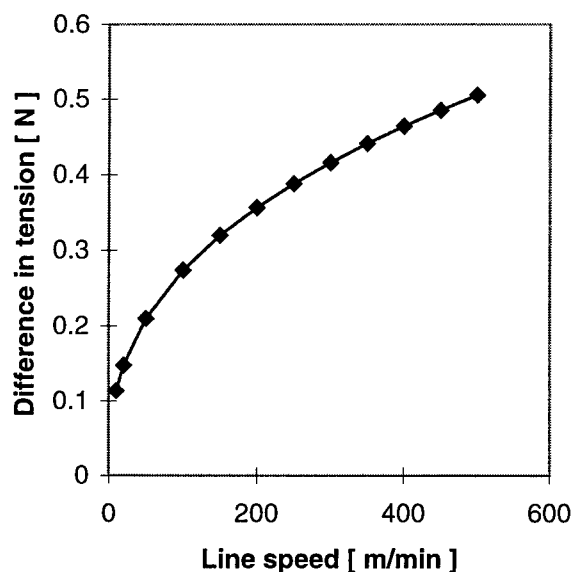


Fig.2: Difference of the fiber tensions between the external and internal fibers in the ribbon tool.

Immediately after shearing in the ribbon tool, the ribbon matrix is cured and the fibers are fixed in the ribbon matrix. If the ribbon after the production is free from the line tension, the external fibers will try to go to back more than

the internal fibers, however they will be prevented by the internal fibers, because all fibers are bonded together by the ribbon matrix. Therefore, the external fibers are elongated and the internal fibers are compressed in the ribbon. It has been shown in the calculation that these fiber strains depend on the line speed (Fig. 3).

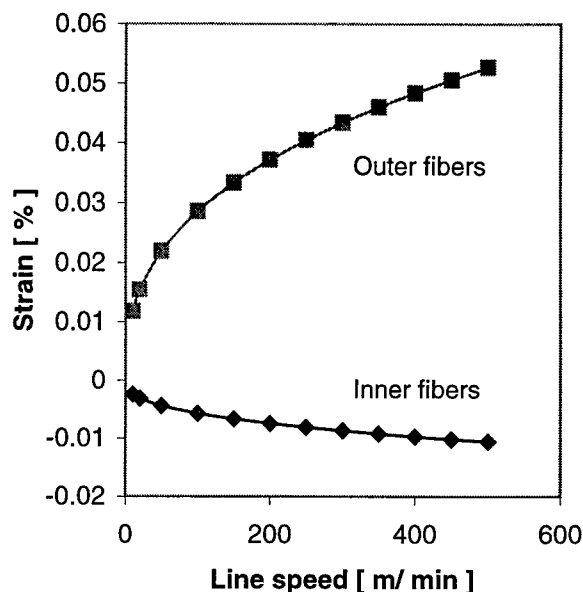


Fig.3: Strains of the internal and external fibers in 12F-ribbons produced at different line speeds.

For the measurement of the fiber strains in the ribbon, Bragg-gratings have been used in our experiment because of their high measurement resolution. The characteristic wavelength of the Bragg-gratings used in our experiment is around 1530 nm which increases or decrease if the Bragg-grating fiber is elongated or compressed (Fig.4).

It has been found in the bending test of the Bragg grating fibers that they are insensitive to the bending.

In order to validate the calculation, a 12F-ribbon has been produced by using 7 Bragg grating fibers and 5 standard SM-fibers. All fibers have the same diameter. Immediately after the production, the ribbon was loosely wound on a drum and the strains of the Bragg grating fibers were measured. The results are shown in the Fig.5 in comparison to the calculated data. The external fibers are elongated and the internal fibers are compressed. There is a good agreement between the measurement and calculation.

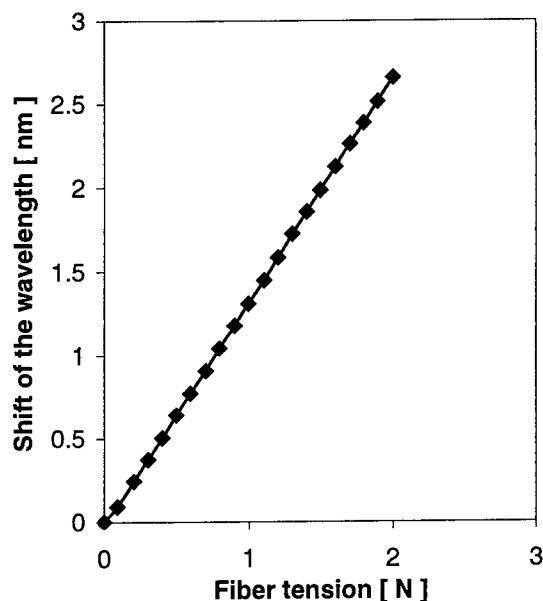


Fig.4: Wavelength shift of a Bragg-grating fiber under tension.

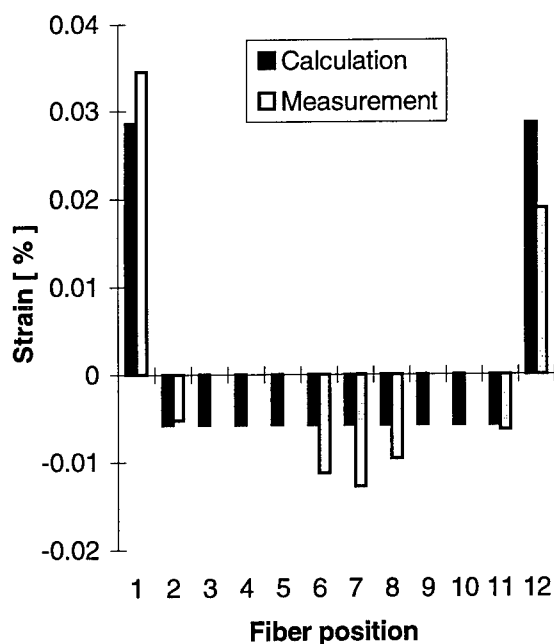


Fig.5: Fiber strains in a 12F-ribbon.

After 1h storage at the ambient temperature, the strains of the Bragg grating fibers were measured again. The strains decreased only a little bit, caused by some stress relaxation of the ribbon matrix. The measurement was done once again after 24h storage in ambient

condition and no changes were found in comparison to the previous measurement.

RIBBON STRANDING

In the central tube ribbon cable, the ribbons have to be stranded for a good bending performance of the cable. Due to the stranding, each fiber in the ribbon has different length. The external fibers are further elongated and the middle fibers further compressed. These additional fiber strains can be calculated by using following equation

$$\sum F_i = 0 \quad (2)$$

where F_i is the tension or compression of the fiber i in the ribbon.

The equation (2) means that in a straight cable the total tension of the ribbon is zero in the longitudinal direction of the ribbon. It has been assumed that the ribbon is free from longitudinal forces. The equation (2) can be solved according to the ribbon geometry and the stranding pitch of the ribbon.

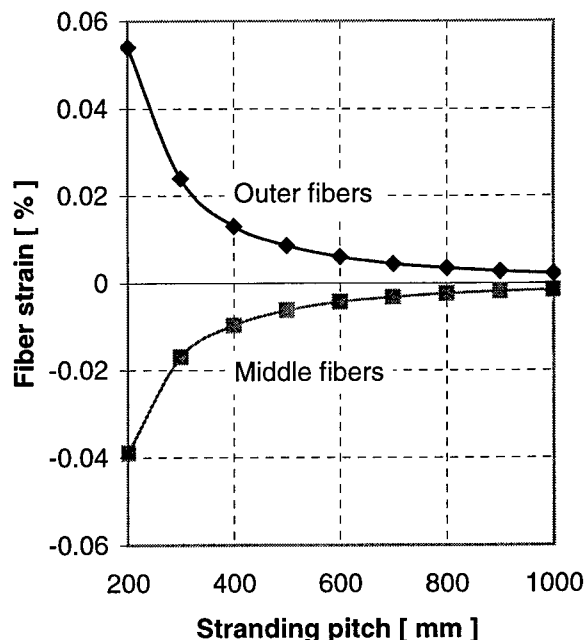


Fig.6: Fiber strains in a 12F-ribbon caused by the stranding with different pitches.

For a 12F-ribbon, the fiber strains caused by different stranding pitches have been calculated (Fig.6). It is shown that for this type of ribbon the fiber strain considerably increases, if the stranding pitch of the ribbon is below 400mm.

In order to check the calculation, a 12F-ribbon made of the Bragg grating fibers was stranded with different pitches and the strains in the Bragg grating fibers were measured. The measurement has also shown that the external fibers are elongated by the stranding and the middle fibers compressed. In the Fig.7 the results are given for the stranding pitch of 500mm in comparison to the calculation data.

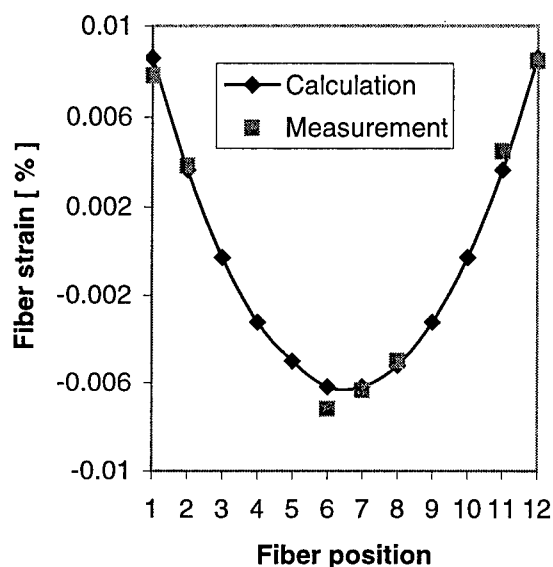


Fig.7: Fiber strains in a 12F-ribbon caused by the stranding with a pitch of 500 mm.

CABLE BENDING

Because of its flat shape, a ribbon has different bend inertia in its long edge and short edge. In the cable, ribbon is stranded, therefore the bend inertia of the ribbon changes along the cable (Fig.8). For the calculation we divide the stranded ribbon into two parts according to their bend inertia, the easy bend parts and the heavy bend parts (Fig.8).

In the easy bend parts, the long edge of the ribbon is parallel to the bend axis and the bend inertia of these parts is low. In the heavy bend parts, the long edge of the ribbon is perpendicular to the bend axis and the bend inertia of the heavy bend parts is high.

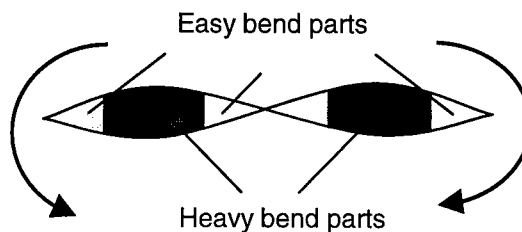


Fig.8: Bend inertia changing along a stranded ribbon.

During the bending of cable, the heavy bend parts will first try to keep straight in the cable. At a small bend radius, the heavy bend parts will be bent and this results in high fiber strains in the ribbon. Therefore, ribbons will rotate in the tube to reduce the fiber stress. By using the minimum energy principle, the fiber strains induced by the cable bending have been calculated for a 18x12F-ribbon cable with a stranding pitch of 400mm and the max. strains in the corner fibers are shown in Fig.9 for different bend radii.

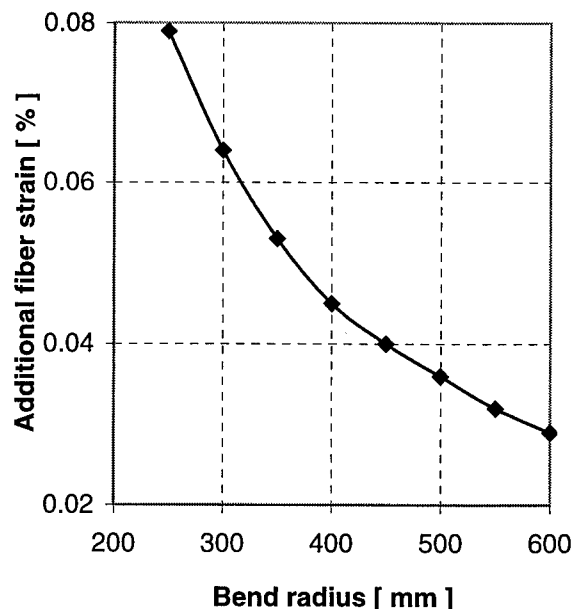


Fig.9: Max. strains in the corner fibers of a 18x12F-ribbon cable caused by cable bending.

Furthermore, a cable including 18 x12F-ribbons with a stranding pitch of 400 mm has been produced. In this cable, ribbons made of Bragg grating fibers have been used to measure the fiber strains caused by the cable bending. The max. fiber strain measured in the corner fibers is about 0.07% for a bend radius of 250 mm. This value is very close to the calculated data.

By using the model of Glaesemann², the fiber lifetime of the 18x12F central tube ribbon cable has been estimated according to the fiber strains achieved above. For a good designed cable the lifetime of the fiber is over 25 years even at small bend radii.

CONCLUSION

Calculation and measurement have shown that the fiber strains can be caused by the ribbonizing, ribbon stranding and cable bending. The value of the fiber strain depends on the material properties of the ribbon matrix, production parameters, cable parameters and installation parameters. For the 18x12F central tube ribbon cable with optimum cable parameters, the total fiber strain is lower than 0.2% even at small bend radii. This means that the fiber lifetime in this cable is over 25 years.

ACKNOWLEDGEMENTS

The authors would like to thank Mr. Siegfried Unterberger for the careful production of the ribbons including the Bragg grating fibers and Mr. Thomas Miholic spending his time for the measurement of the Bragg grating fibers.

REFERENCES

- [1] H. Ishikawa et al, "A Study on Behavior of Fiber Ribbons in SZ-Grooved Spacer and its Application to Aerial Cable", IWCS Proceeding 1997.
- [2] K. G. Hodge et al, "Predicting the Lifetime of the Optical Fibre Cables Using Applied Stress Histories and Reliability Model", IWCS Proceeding 1992.



Zhan Gao received his B.S. and M.S. degrees in Material Science and Engineering at the University Tongji, Shanghai, China in 1985 and 1988, respectively. In 1994, he received his Ph.D. from the University Erlangen-Nuremberg in Germany. In 1991, he joined Siemens AG in Neustadt, Germany. After working on material and cable testing, he is now responsible for the cable modeling.

Mailing address:

Siemens AG, ICP CCE KT
Austrasse 101, 96465 Neustadt, Germany

OPTIMIZATION OF FIBER RIBBON SUB-UNIT ROBUSTNESS BY MEANS OF A LATERAL FIBER-TO-MATRIX ADHESION GRADIENT

Kariofilis Konstadinidis, Kenneth W. Jackson, Neil W. Sollenberger, Shahab Siddiqui, Carl R. Taylor, Vidyananda Chandraiah, Raymond P. DeFabritis, Heng Ly, John R. Szwec

Bell Laboratories, Lucent Technologies, Inc., 2000 NE Expressway, Norcross, GA

ABSTRACT

Precision procedures are available that have been used successfully to separate ribbons into robust sub-units. Some customers want to separate the ribbons by hand. In this paper we describe a concept that has been used to design optical fiber ribbon structures that can be hand-separated into highly robust sub-units without sacrificing easy fiber access or increasing ribbon thickness. The method consists of a differentially enhanced adhesion between contiguous fibers on either side of the separation and the matrix.

INTRODUCTION

The ability to divide a ribbon into mechanically robust sub-units is an important end-use feature for ribbon cable customers. Equally important is the ability to remove quickly and easily the bonding matrix from the fibers when accessing individual fibers from the midspan of a ribbon. To accomplish quick and easy midspan access requires a ribbon having low adhesion of the matrix to the colored fibers. This low ink-to-matrix adhesion contravenes the equally important need to sub-divide the ribbon into robust sub-units for highly productive mass fusion splicing.

We have studied the effect of selectively increasing the matrix-to-fiber adhesion of two consecutive fibers on the mechanical robustness of the sub-units created by dividing the ribbon between the two high adhesion fibers by hand. The adhesion of the matrix to the colored fibers was varied using four UV curable ink formulations with different surface properties and three different matrix materials. The

adhesion was measured using a 90° peel test of the colored fiber from the ribbon. The robustness of the sub-units was measured both visually and mechanically. Using optical microscopy, we evaluated the robustness of the split and measured the area of colored fiber exposure. We also used commercially available ribbon stripping tools to strip the sub-units at different tool temperatures. The results showed that increased matrix-to-ink adhesion of the edge fibers improved the robustness of hand-divided ribbons, reduced the area of exposed fiber and increased the strippability of the sub-units. At the same time, the fibers remained accessible at midspan both with the gel method used for live fiber access¹ and glue/tape techniques.

DESIGN OBJECTIVES

Easy access ribbon designs with a low adhesion, high modulus matrix have been popular in recent years.^{2,3} Easy access ribbons can be divided into two broad categories depending on whether the matrix can be peeled off the ribbon in a controlled or continuous fashion. In the former, the tape in the glue/tape method controls the matrix peel and the matrix breaks where the tape ends. In the later, once the glue initiates the matrix break, the peel can be continued by hand beyond the tape section. In such designs the adhesion between the ribbon matrix and the colored fibers can be extremely low. Such designs are often suboptimal for hand-division into sub-units because multiple fibers are exposed and become loose during handling (Fig. 1 bottom). When that happens, re-ribbonization of the

become loose during handling (Fig. 1 bottom). When that happens, re-ribbonization of the fibers to the desired sub-unit fiber count for mass fusion splicing is required.

An alternative design for 24 fiber ribbons uses two 12-fiber ribbons held together with a second layer of matrix.⁴ The disadvantages of such a design are increased ribbon thickness (which reduces fiber packing density in the cable), and more difficult midspan access of live fibers. In addition, the constituent 12-fiber ribbons are exposed to an extra processing step through a narrow die, which increases the probability of ribbon or fiber damage.

An optimized controlled-matrix-peel design that balances fiber/matrix adhesion and matrix mechanical properties allows for division into sub-units and preserves a robust integral sub-unit structure.⁵ Hand division into sub-units, however, is operator-dependent and can result in 180° exposed fibers for any easy access ribbon (Fig. 1, middle). Subsequent aggressive handling of the ribbon can separate an exposed fiber from the sub-unit.

A novel approach to addressing this issue that preserves easy access and the inherent high packing density of thin ribbons is described in this paper. It consists of increasing the ink/matrix adhesion of the fibers at the separation (aqua and blue in the case of a 12-12 division of a 24-fiber ribbon). As will be demonstrated below, the effect on sub-unit robustness and ribbon stripping can be significant without any detrimental effect on ease of fiber access.

MATERIALS

Four UV curable ink formulations and three matrix materials were used to make the ribbons for this study. M1 and M2 are continuous peel matrix materials and were used to make 12-fiber ribbons with the lowest adhesion ink formulation A. M3 is a controlled peel matrix and was used to make 12-fiber ribbons with ink formulation A, and 24-fiber ribbons with all four ink formulations. The 24-fiber ribbons were fabricated using ink A in fiber positions 2-11 and 14-23 and fibers with test inks in fiber positions 1, 12, 13, and 24.

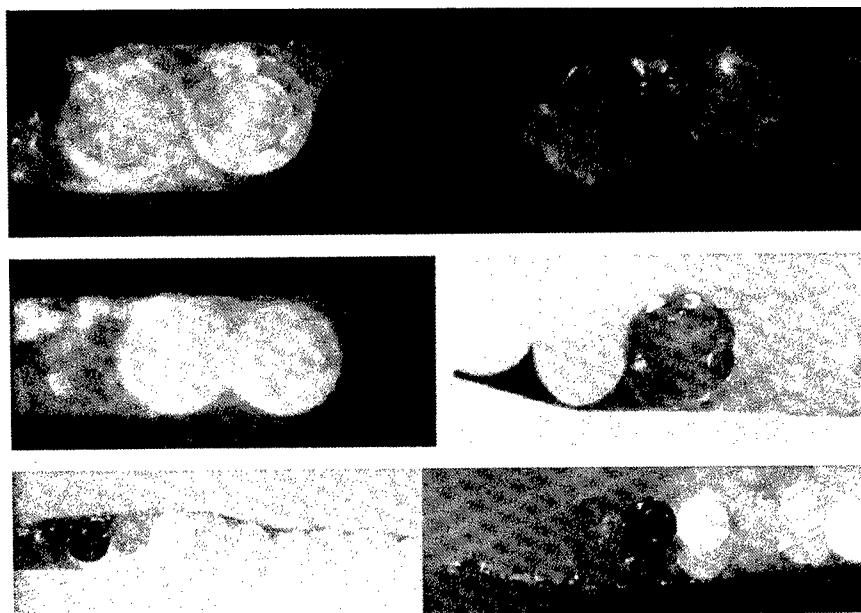


Figure 1. Top: An optimal 12-12 division of a 24-fiber ribbon with the blue and aqua fibers having 270° matrix coverage (matrix M3). Middle: A suboptimal 12-12 division with the aqua fiber having 180° matrix coverage (matrix M3). Bottom: A 6-6 division of a 12-fiber ribbon with matrix M2 (continuous peel matrix) with several fibers exposed and/or loose.

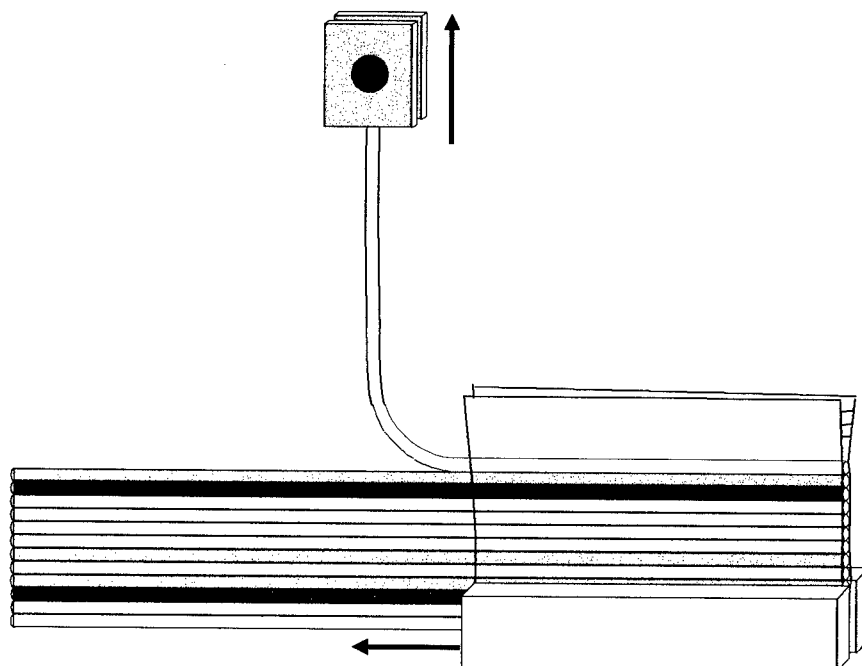


Fig. 2. Schematic of the fiber peel test for measuring fiber adhesion to the matrix in a ribbon.

FIBER-MATRIX ADHESION MEASUREMENTS

The adhesion of the colored fibers to the matrix in a ribbon was measured using a custom-built 90° fiber peel fixture on a Model 4501 Instron® Tensile Testing Machine. In the test set-up the bottom fixture consists of a vise holding the ribbon in a horizontal position sitting on its narrow side. The number of fibers in the vise (and thus unavailable for measurement) depends on the ribbon fiber count: 5 for 12-fiber and 10 for 24-fiber ribbon. The length of the sample was 17 cm, of which 9 cm had the matrix removed to expose all fibers. Starting from the top fiber (blue or aqua), a single fiber at a time was secured to the top fixture and pulled at a constant rate of 7.5 cm/min. The force required to cleanly pull the colored fiber out of the ribbon was recorded and averaged over the 8 cm length. The edge fiber measurements (blue or aqua) were discarded since to a great extent they measure the tear strength of the matrix. For the remaining fibers the measurement represents the force required to peel the fiber out of the matrix socket and is a measure of fiber-matrix adhesion in the ribbon. For each ribbon the measurements were performed in both directions (blue to aqua and

aqua to blue) and the results were averaged. A schematic of the test set-up is shown in Fig. 2.

The results of the measurements are shown in Table I. The first two entries (M1/A and M2/A) are from 12-fiber ribbons with continuous peel matrix M1 or M2 and with all the fibers colored with ink A. The other four entries are from 24-fiber ribbons with controlled peel matrix M3. In those samples the ink used for the blue and aqua fiber was varied while ink A was used for the other ten colors. The value for ink A is the average of all 12 colors from all measurements with matrix M3. The results for inks B, C, and D are averages for the blue and aqua fibers in positions 12 and 13 for each ink formulation.

Table I. Fiber-matrix adhesion in a ribbon as measured by the 90° peel test.

Matrix	Ink	Adhesion (normalized)
M1	A	0.3
M2	A	0.4
M3	A	1
M3	B	1.4
M3	C	2.1
M3	D	2.2

Table II. Exposed fibers after hand division of fiber ribbons into sub-units

Table II. Exposed fibers after triad division of fiber ribbons into sub-units											
Ink	Ink/Matrix Adhesion		Matrix	% of samples with given number of 180° exposed fibers							Average # of 180°-exposed fibers
				0	1	2	3	4	>4		
6-6 division of 12-fiber ribbons											
All 12 colors		All 12 colors									
A	0.3		M1	0	0	0	0	19	81	6.5	
A	0.4		M2	0	13	13	6	19	49	4.3	
A	1		M3	44	25	31	0	0	0	0.9	
12-12 division of 24-fiber ribbons											
blue & aqua	other 10 colors	blue & aqua	other 10 colors								
A	A	1	1	M3	27	57	14	2	0	0	0.9
B	A	1.4	1	M3	25	46	29	0	0	0	1.0
C	A	2.1	1	M3	83	9	8	0	0	0	0.2
D	A	2.2	1	M3	80	20	0	0	0	0	0.2

RIBBON SUB-UNIT PERFORMANCE

Eight one-meter long pieces of each fiber ribbon sample were divided into two 6-fiber or 12-fiber units by hand. Cross-sections of each sample were made using a stripping tool and the number of exposed fibers was counted and recorded. For a perfect split the number of exposed fibers is two (the edge fibers, aqua and blue for 24-fiber, or white and red for 12-fiber ribbons) with a minimum exposed area per fiber (approximately 90°). If, for example, the matrix peels off as shown in Figure 1 (middle), then the number of exposed fibers is three, with one fiber having 180° exposure. Table II above shows the results for the different ink/matrix combinations.

6-6 division test results

Fiber ribbons with continuous peel matrix materials M1 and M2 performed the worst. It was practically impossible to divide those ribbons into sub-units without exposing many fibers. Similar performance is expected in 24-fiber ribbons having a continuous peel matrix. Ribbons with controlled peel matrix M3 perform much better having an average of less than one 180°-exposed fiber. Their performance is the same as that of 24-fiber ribbons with the same inks and matrix as shown in Table II.

12 – 12 division test results

Ribbons with the same low adhesion inks in fiber positions 12 and 13 as in all other positions resulted in sub-units having one or more 180°-exposed fibers in more than 70 percent of the samples. When higher adhesion inks were used to color fibers in positions 12 & 13 the result was sub-units having no 180°-exposed fibers in more than 80 percent of the samples, the average being 0.2. Due to the higher adhesion to the matrix, the edge fibers are less likely to separate from the matrix even when they are 180°-exposed.

Ribbon strip test results

The ribbon strip test provides a method for evaluating the strippability of fiber optic ribbon structures. The ribbon structure lends itself to fusion or mechanical multi-fiber (mass) splicing or termination. As part of the mass splicing process, the coating and matrix material of the ribbon is removed in one process. Before stripping for mass fusion splicing, a 24-fiber ribbon has to be divided into two 12-fiber sub-units. The structural integrity and robustness of each 12-fiber sub-unit is important for the successful removal of the protective coatings from the fibers in one piece. This test was performed using two different ribbon stripping

tools, which are used by splicing technicians for mass fusion splicing. One feature of the ribbon stripping tools is a surface element for heating the part of the coating/matrix material composite to be removed. The temperature of each heated surface is initially set by the tool manufacturers and can vary from 70°C to 165°C. Table III identifies the ribbon stripping tools and the temperatures used for this test.

Table III. Tools and conditions used for ribbon stripping test.

Ribbon Stripping Tool	Factory-Set Temperature (°C)	Test Temperature Settings (°C)
Tool A	90 - 100	75, 105, 135
Tool B	145 - 165	120, 140, 160

The stripping tools were set to the desired temperature and measured. Five attempts were made to strip 30 ± 3 mm of the matrix material and the fibers' protective coating(s) from each ribbon at each tool, temperature setting, and for each unaged/aged condition of the ribbon. Each strip was then rated using the guidelines presented in Table IV.

Table IV. Ribbon Strip Rating Guidelines

Rating Scale	Description
1	Coating/Matrix composite removed in one piece, fibers cleaned with one alcohol wipe.
2	Coating/Matrix composite disintegrates, fibers cleaned with one alcohol wipe.
3	Coating not removed from all fibers after one wipe or fiber breaks.

Table V. Twenty four-fiber ribbon sub-unit stripping results after 12-12 division using Tool A.

Ink/Matrix Adhesion		Strip Rating	
blue & aqua	other 10 colors	Unaged	30 days @85°C in filling compound
1	1	1.0	1.1
2.1	1	1.1	1.2
2.2	1	1.0	1.1

Table VI. Twenty four-fiber ribbon sub-unit stripping results after 12-12 division using Tool B.

Ink/Matrix Adhesion		Strip Rating	
blue & aqua	other 10 colors	Unaged	30 days @85°C in filling compound
1	1	1.0	2.0
2.1	1	1.0	1.4
2.2	1	1.0	1.3

The average of all the individual ratings is recorded as the result. A summary of the results for the ribbon stripping tests for Tool A is presented in Table V. The results show that there is no difference in the performance at the different adhesion levels as all unaged and aged samples performed

A summary of the results for the ribbon stripping tests for Tool B is presented in Table VI. Previous work has demonstrated that other factors such as the condition of the ribbon stripping tool can also influence ribbon stripping performance.⁶ Tool B was selected in this study because it had been used considerably (worn blades) which made it more sensitive to changes in the ribbon structure. The results for the unaged samples among the 3 different inks do not differ. After aging, however, the higher the adhesion of aqua and blue fibers to the matrix the better the sub-unit stripping performance. The improved quality of the sub-units in combination with the high adhesion of the edge fibers to the matrix (which itself is the sole contributor to the improved quality) provide a sub-unit structure that is robust and readily strippable.

FIBER ACCESS

For the particular case of a 24-fiber ribbons with the aqua and blue fibers having twice as high adhesion to the matrix than the other 20 fibers (using ink C, for example), it was found that the ability of the matrix to be peeled off the fibers using the glue and tape method was not affected. Peelability of a ribbon matrix material depends both on its adhesion to the colored fibers and on its mechanical properties. In this particular case the matrix material is strong enough to withstand the locally higher adhesion force during peel. Accessibility of the fibers using the gel method was also not affected. As with all ribbon attributes, sub-unit separation and

robustness strongly depends on a balance between ink-matrix adhesion and matrix mechanical properties.

CONCLUSIONS

Increasing adhesion of the blue and aqua fibers to the matrix in a 24-fiber edge-bonded ribbon resulted in substantially increased robustness of the 12-fiber sub-units even after hand division. Doubling the matrix adhesion of the blue and aqua fibers compared to the other 10 colors increased the reliability of the hand-splitting procedure and increased the strippability of the 12-fiber sub-units to match that of an edge-bonded 12-fiber ribbon. The effect of having high adhesion fibers on both sides of a division line is two-fold. First, if hand division is used, a minimum surface area of the edge fibers is exposed. And second, since the exposed fibers have high adhesion to the matrix, they do not become separated from the sub-unit even during field handling. The concept of selective adhesion enhancement can also be extended to other modular sub-unit configurations.

ACKNOWLEDGEMENTS

The authors would like to acknowledge the contributions of Soo-Gun Oh, John Turnipseed, and David Au.

REFERENCES

1. G. E. Bodeep, V. B. Chandraiah, K. W. Jackson, S. C. Mettler, and N. W. Sollenberger, *NFOEC Proceedings*, Vol.2, 1997, pp. 291-302.
2. G. A. Lochovic, S. K. Moorjani, N. I. Patel, R. J. Speights, B. L. Stephens, *Proceedings of the 46th International Wire and Cable Symposium*, 1997, pp. 260-273.
3. W. E. Beasley, P. Neveux, Y. Yamane, *NFOEC Proceedings*, Vol. 2, 1994, pp. 401-409.
4. S. A. McCreary, W. E. Beasley, S. R. Stokes, R. G. Lindsay, Jr, *Proceedings of the 47th International Wire and Cable Symposium*, 1998, pp. 432-439.

5. K. Konstadinidis, N. W. Sollenberger, S. Siddiqui, K. W. Jackson, J. M. Turnipseed, T. W. Au, R. P. DeFabritis, C. R. Taylor, *Proceedings of the 46th International Wire and Cable Symposium*, 1997, pp. 274-280.
6. P. K. Kim, N. W. Sollenberger, K. W. Jackson, *Proceedings of the 44th International Wire and Cable Symposium*, 1995, pp.635-639.

BIOGRAPHY



Kariofilis Konstadinidis

2000 NE Expressway, Norcross, GA 30071

Kariofilis Konstadinidis is a Member of Technical Staff in the Materials Technology and Quality Engineering group at Bell Laboratories of Lucent Technologies Inc., Norcross, GA. He is involved in the development, qualification, and implementation of UV curable materials for optical fiber applications. He received his Diploma in Chemical Engineering from the Aristotle University of Thessaloniki, Greece, in 1987 and his Ph.D. in Chemical Engineering from the University of Minnesota in 1992. He joined Lucent in 1992.

CRAFT-FRIENDLY 24-FIBER RIBBON DESIGN

N. Andrew Punch, Jr., Shail K. Moorjani,
Steven T. Bissell, and Karen E. Williams

Siecor, Hickory, North Carolina

ABSTRACT

To satisfy the need for a mechanically and optically robust 24-fiber ribbon, development was undertaken to determine the optimum mechanical design and material selection to attain the following goals:

- processing and handling robustness
- the ability to separate the 24-fiber ribbon into two robust 12-fiber ribbons
- low cabled ribbon attenuation

To guarantee good separability of the modular 24-fiber ribbon into two 12-fiber ribbons, standard 12-fiber ribbons were chosen as sub-units since they provide good cabled attenuation performance. The goal of the 24-fiber ribbon design was to join these two sub-units into a robust, yet separable, ribbon without affecting the performance of the 12-fiber ribbons.

A ribbon has been developed that fulfills the objectives previously stated, through the selection of an encapsulating material which is characterized by a low modulus and an appropriate adhesion to the inner sub-unit material.

BACKGROUND

High fiber count optical cables continue to receive increasing attention due to the explosive need for bandwidth predicted during the first decade of the twenty-first century.¹ The demand for even greater bandwidth, combined with limited availability of duct space in the infrastructure, resulted in the development of high fiber count 12-fiber ribbon cables.

However, as this demand for additional fibers increased, it was no longer practical to

continue to increase the fiber count of single tube 12-fiber ribbon cables beyond the current maximum of 216 fibers due to inherent cable design issues. Increasing the cable ribbon stack height to accommodate additional ribbons leads to a disproportionate height to width ratio of the ribbon stack. This disproportion can lead to manufacturing issues due to the possible instability of the ribbon stack during processing. Additionally, as the height of the ribbon stack increases, the cable diameter must increase to allow continued robust cable performance, possibly causing problems with duct spacing. The combination of these two considerations makes it unrealistic to pursue higher fiber count single tube 12-fiber ribbon cables beyond what is commercially available today.

As a result of the inherent difficulties in increasing the fiber counts of 12-fiber ribbon cables, 24-fiber ribbon based single tube cables have been developed. The 24-fiber ribbons provide a high fiber packing density for a given cable cross-sectional area, leading to greater duct space efficiency than is found in 12-fiber ribbon cables. In addition, the added width of the 24-fiber ribbon provides a more stable and proportional base for the ribbon stack inside the buffer tube as fiber counts increase. Cabled fiber counts up to 432 fibers can be obtained in single tube cables using 24-fiber ribbons while maintaining craft friendliness, ease of manufacture, and inner duct friendly sizing.

INTRODUCTION

In the push to increase the fiber density of optical cables, cable designs must not add difficulty in handling during field installations. Commonly available field installation items, such as enclosures and

mass fusion splicing equipment, are designed to support 12-fiber ribbon cables, among which few if any are also optimized for 24-fiber ribbon designs. In order to save costs and utilize existing field installation items, the 24-fiber ribbon must be separable into robust 12-fiber ribbon sub-units.

The separated 12-fiber ribbons must maintain their integrity for both mass fusion splicing and routing through enclosures and distribution panels.² Hence, reliable separation of the 24-fiber ribbon into two robust 12-fiber ribbons is paramount for quick and efficient installation of 24-fiber ribbon cables.

Mechanical robustness of the 24-fiber ribbon structure is required both during cable manufacturing and in the field. In the manufacturing environment, the ribbon is subjected to various tensile and torsional forces as it is spooled from its manufacturing reel during the cabling process. During cable installation, the 24-fiber ribbons must maintain the 24-fiber ribbon structure until they are intentionally separated into 12-fiber ribbons, spliced, and loaded into trays and enclosures.

DESIGN APPROACH

During the 24-fiber ribbon development, experimentation was undertaken to determine the optimum mechanical design and material selection to attain the following goals:

- processing and handling robustness of the 24-fiber ribbon structure
- the ability to separate the 24-fiber ribbon into two robust 12-fiber ribbons
- low cabled ribbon attenuation

The cabled attenuation performance of the current single tube 12-fiber ribbon design was designated as the benchmark for 24-fiber ribbon cable optical performance.

Mechanical Structure

The first phase of the development process was to determine the optimum 24-fiber ribbon structure. Various options were investigated but with the primary focus on the following:

- 24 fibers encapsulated by a single layer of matrix material (Figure 1)
- A modular design with two 12-fiber ribbons fully encapsulated by an outer layer of matrix material. (Figure 2)

In initial trials, single layer 24-fiber ribbons were found to be difficult to separate accurately into 12-fiber sub-units. Additionally, once this design is separated into 12-fiber ribbon sub-units, minimal matrix material remains to protect interior fibers 12 and 13, which are the newly exposed edge fibers of the sub-units.² This condition lowers the 12-fiber ribbon sub-unit robustness, resulting in stray fibers protruding from the sub-unit matrix shell.

The shortcomings of the single layer design led us to a modular design. Siecor's previous experience with modular ribbons, coupled with initial 24-fiber feasibility experimentation, indicated the superiority of this design.³ Existing 12-fiber ribbons were chosen as sub-units for the modular 24-fiber structure since the robustness and cabled attenuation performance were already proven in manufacturing and field installation environments.⁴

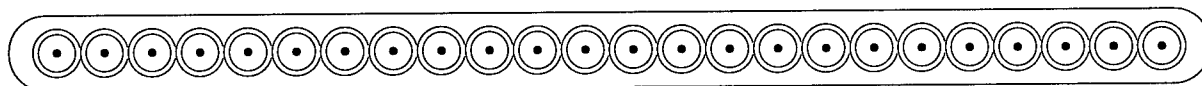


Figure 1: Single Layer 24-fiber Ribbon Design

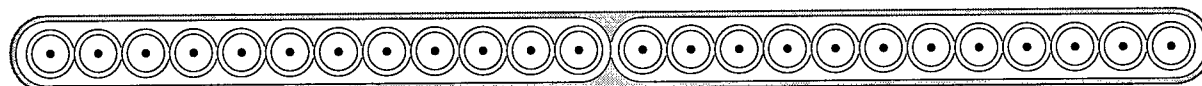


Figure 2: Modular 24-fiber Ribbon Design

Table 1: Matrix Material Properties

Material	Encapsulating Layer Modulus (with respect to sub-unit matrix modulus)	Adhesion to 12-Fiber Ribbon Sub-units
A	Medium	High
B	Medium	Medium
C	High	Low
D	Low	Medium

In addition, previous work with determining the optimum thickness layer for proper hand separation and robustness for the encapsulating layer was applied to the development of the 24-fiber ribbon.³ The encapsulating layer of the 24-fiber ribbon structure was then tasked with providing separability, as well as robustness before and after separation, while maintaining the cabled attenuation performance.

Matrix Material Selection Criteria

Determining the ideal ribbon matrix material for the encapsulating layer necessitates a close examination of the performance requirements. A robust, yet separable, ribbon requires a material that does not tear easily due to normal stresses and strains experienced in cable manufacturing and handling, but which will yield to separation once a sufficient force is applied. Due to previous experience with modular ribbon designs, it was already known that the modulus of the encapsulating material had to be less than the modulus of the sub-unit matrix material to ensure proper hand separation.³ If the modulus of the encapsulating layer is higher than the sub-unit material modulus, there is an increased probability of fracturing the sub-unit material during sub-unit separation, yielding stray fibers. As a result, the development efforts for the 24-fiber encapsulating layer focused on determining the ideal matrix material possessing a modulus less than the sub-unit matrix material in conjunction with the proper adhesion level.

Adhesion of the 24-fiber ribbon matrix material to the 12-fiber ribbon sub-units plays a very significant part in the balance between robustness and separability. Low adhesion between layers of matrix material could result

in a premature release from the 12-fiber ribbon sub-units, leading to 24-fiber ribbon separation either during processing, or in the field during installation. Conversely, high adhesion between the two ribbon matrices may cause a cohesive failure of the 12-fiber ribbon structure during a separation attempt, yielding stray fibers. Hence, an optimum amount of adhesion between the 24-fiber and the 12-fiber matrix materials is required.

Matrix materials with different levels of modulus and adhesion were selected as potential candidates for the 24-fiber ribbon encapsulating material. The evaluated materials, with their respective characteristics, can be found in Table 1. The modulus level of the encapsulating matrix was varied, with the high value material approaching the modulus of the sub-unit material. Three different levels of adhesion were investigated.

Ribbons were manufactured with the encapsulating matrix materials listed in Table 1 and were tested to determine the optimum combination of modulus and adhesion.

PHYSICAL RIBBON TESTING

Hand Separation Test Method

A ribbon separability test was developed to quantify ribbon separation-by-hand performance. In preliminary testing, it became apparent that different methods of separation by hand produced varied results with the same ribbon. As a result, three methods of hand separation were defined, listed in Table 2. The test methods differ by how much support is given to the individual 12-fiber ribbon sub-units during the separation process.

Table 2: Ribbon Hand Separation Scale and Test Methods

Separation Rating	Hand Separation Method
1	2-fiber
2	6-fiber
3	12-fiber
4	Not hand separable **

** Tool required for separation of 24-fiber ribbon into two 12-fiber ribbons

The 2-fiber method provides the least support to the 12-fiber ribbons' structures, pushing on the outer 2 fibers of each ribbon sub-unit (fibers 1 and 2, 23 and 24). The 6-fiber method supports half of each 12-fiber ribbon, with force applied to the outer 6 fibers of each sub-unit ribbon. The 12-fiber method, which most closely resembles the separation procedure used in the field, supports all 12 fibers of each sub-unit ribbon during separation.

To perform the 2-fiber and 6-fiber methods, the tester holds the ribbon 1.5" (38 mm) from its end between the thumb and the middle finger of one hand, separating the ribbon using the index fingers of both hands by pushing about 0.25" (7 mm) of the ribbon in opposite directions. Tips of the index fingers are used, one pushing towards the tester, the other away from the tester, for a separation length of 1.5" (38 mm). The separation of the sub-units is accomplished by moving the sub-units perpendicular to the ribbon's plane.

For the 12-fiber method, the end of the ribbon is held between the thumb and the index finger of each hand, with each thumb and finger set covering one of the 12-fiber sub-unit ribbons. Separation is achieved by simultaneously pulling one 12-fiber ribbon sub-unit towards, and the other 12-fiber ribbon sub-unit away from the tester, pulling perpendicular to the ribbon's plane.

A successful separation is one that produces two 12-fiber ribbons from the 24-fiber ribbon without causing any stray fibers. Ten successful separations with a given test method determine the rating.

Testing begins with the 2-fiber method. If the 2-fiber method fails, the 6-fiber method is tried. If the 6-fiber method fails, the 12-fiber

method is tried. Ribbons that cannot be successfully separated with the 12-fiber method receive a rating of 4, indicating that they are not reliably separable without a tool.

Handleability and Robustness Test Method

Resistance to twist tests a standard part of ribbon qualification. Given that the majority of current ribbon designs pass the standard resistance to twist test found in Bellcore GR-20, Issue 1, ribbons were subjected to a more strenuous twist-to-failure test in order to better evaluate ribbon robustness for handleability.⁵

The twist-to-failure test setup consists of applying force to a ribbon by hanging a 1 kg mass from one end, and attaching the other end to a turning apparatus. The ribbon passes through a slot, 300 mm from the turning apparatus, that confines the twist to a distance of 300 mm. This slot allows additional ribbon length to move into the 300 mm long twisting area. The ribbon is twisted in one direction until it fails, with the tester counting the number of turns.

Failure is defined as either a twisting of fibers about each other due to a shattering of the 12- and 24-fiber ribbon matrix materials, a separation of the 24-fiber ribbon into two 12-fiber ribbons, or a combination of these effects. A cutoff failure level of 4 turns was established as a baseline, based on preliminary testing of prototype ribbons in cabling trials. Ribbons that fall below the 4 turn threshold run the risk of compromising the mechanical integrity of the ribbon structure during the cabling processes, or during handling and routing during termination.

Table 3: Ribbon Separation and Twist-to-Failure Test Results

Hand Separation Results			
Material	n	Average (rating)	Maximum (rating)
A	10	3.5	4
B	10	1.3	2
C	10	1.0	1
D	10	1.5	2

Twist-to-Failure Results			
Material	n	Average (turns)	Maximum (turns)
A	10	5.7	5.75
B	10	5.1	5.75
C	10	2.7	4.00
D	10	5.1	5.25

Test Results

The results of both the hand separation, and the handleability and robustness tests are shown in Table 3.

provide moderate adhesion to the 12-fiber ribbon sub-units, shown in the results for materials B and D. The twist-to-failure test results indicate that robustness was not compromised to improve ribbon separability.

FINAL MATERIAL SELECTION

Hand Separation, Handleability, and Robustness

Results of testing in Table 3 show that 24-fiber ribbons made with encapsulating layers of different modulus and adhesion levels provide varying degrees of performance with respect to hand separability and robustness. Material A is extremely robust due to the high adhesion to the sub-units; however, its hand separability is poor due to its medium modulus and high adhesion combination which results in stray fibers during hand separation testing. This occurs when the encapsulating layer tears away the matrix material of the sub-units at the separation point. Material C, a low adhesion encapsulating material, provides excellent separation capability, but lowers the ribbon robustness below acceptable values due to separation of the layers of matrix material when placed under stress.

An optimized balance between separability and processing robustness was found by using medium and low modulus materials that

Surface Coefficient of Friction

To make the final choice between the two leading candidates B and D, it became necessary to consider other physical properties of the matrix material, most importantly surface friction. A ribbon matrix material must have an optimum surface friction value to allow ribbon to ribbon strain relief through sliding during cable bending. In the course of cable manufacturing, ribbon-to-ribbon movement can only be facilitated if the surface friction is low enough to allow each ribbon to slide freely and act independently of adjacent ribbons. This independent motion becomes even more imperative in non-filled dry cable designs where the movement of ribbons is dependent solely on ribbon surface friction.

Examining the surface friction properties of the two remaining candidates revealed a stark contrast. Material D possesses a surface friction less than half that of material B. As a result, material D was selected as the encapsulating layer matrix material to be taken to cable testing.

Table 4: Testing Results for Commercially Available Ribbon Designs

Ribbon Design	n	Twist to Failure		Hand Separation	
		Average	Max	Average	Max
1	10	3.9	4.3	4.0	4.0
2	10	5.3	5.8	4.0	4.0
Siecor	10	5.1	5.3	1.4	2.0

Cable Testing

The low modulus, medium adhesion, encapsulating matrix, chosen based on handleability and friction characteristics, was required to meet the cabled attenuation performance level of the 12-fiber ribbon design. Individual and cabled ribbons were subjected to and passed industry standard tests for ribbons and cables as detailed in Bellcore GR-20, Issue 1.⁵ Design aspects of a 432 fiber cable, including 24-fiber ribbons, were presented at the National Fiber Optic Engineering Conference in 1998.⁶

During hand separation testing, Ribbon 1 consistently failed to separate at the fiber 12 and 13 interface, separating instead at other positions among the 12-fiber subgroups. The dual layer construction of Ribbon 2, possessing appreciable adhesion between the ribbon matrix layers, ensures a high twist-to-failure rating, but does not provide good hand separation capability. Both ribbons also exhibited stray fibers after hand separation testing. In summary, a separation tool is absolutely necessary to reliably separate the alternatively designed ribbons into 12-fiber sub-units.

ANALYSIS OF ALTERNATE DESIGNS

There are other 24-fiber ribbon designs commercially available that are markedly different from the Siecor final design. Comparison testing of the Siecor ribbon and two other ribbon designs commonly available in the marketplace, referred to as "1" and "2," are shown in Table 4.

Ribbon 1 has a single layer encapsulated structure for the 24-fiber ribbon. Ribbon 2 has a dual layer mechanical structure similar in design to the Siecor 24-fiber ribbon; however, the 24-fiber encapsulant layer has a modulus greater than the inner 12-fiber sub-unit matrix material.

As evident in Table 4, the single layer construction of Ribbon 1 does not provide a good combination of handleability characteristics in terms of the twist-to-failure and the hand separation of the sub-units.

CONCLUSION

Customers desiring high fiber count ribbon cables containing 24-fiber ribbons require excellent cable attenuation performance, and easy separation of the 24-fiber ribbons into two robust 12-fiber ribbon sub-units. Manufacturing requires a ribbon that is robust such that it does not mechanically degrade during the cabling process.

A ribbon has been designed to meet all of these requirements. The modulus of the encapsulating 24-fiber matrix, coupled with its adhesion to the matrix of the 12-fiber ribbon sub-units, were determined to be the major factors in achieving these goals. It has been shown that a combination of low modulus and medium adhesion provides the optimum material for fulfilling the objectives of the 24-fiber ribbon.

REFERENCES

1. S. Carlson and M. Roetter, "Justifying the Need for Fiber Networks," *America's Network* 103, no. 3 (1999): 20-26.
2. S.A. McCreary et al., "Analysis of a modular 24-Fiber Ribbon for the Distribution Network," *44th International Wire and Cable Symposium Proceedings* (1998): 432-439.
3. R.S. Wagman, G.A. Lochkovic, and K.T. White, "Component Optimization for Slotted Core Cables Using 8-Fiber Ribbons," *44th International Wire and Cable Symposium Proceedings* (1995): 472-478.
4. G.A. Lochkovic et al., "An Overview of Key Ribbon Handleability Attributes," *46th International Wire and Cable Symposium Proceedings* (1997): 260-273.
5. Bellcore GR-20-CORE, Generic Requirements for Optical Fiber and Fiber Optic Cable, Issue 1, September 1994.
6. E.R. Logan et al., "Evaluating High Fiber Count Cable Designs for Field Performance," *National Fiber Optic Engineering Conference Proceedings 1* (1998): 385-395.



Shail K. Moorjani

Siecor
Research, Development and Engineering
PO Box 489 (RD)
Hickory, NC 29603-0489

Shail K. Moorjani is a Materials Engineer at Siecor RD&E in Hickory, North Carolina. He received a B.Tech. in Chemical Engineering from Osmania University, India in 1993. He joined Siecor in 1996 after receiving his M.S. degree in Chemical Engineering from Michigan State University. In his current position, he works on material selection and design for use in fiber optic ribbons and cables.

FIBERGLASS REINFORCED AERIAL SERVICE WIRE MECHANICAL BEHAVIOR AND INSTALLATION GUIDELINES

Lawrence M. Slavin, Kai Hsing, Ernie E. Scerbo, Lal Hore

**Telcordia Technologies
Morristown, New Jersey**

ABSTRACT

A detailed investigation was conducted to characterize the mechanical properties of the fiber reinforced aerial service wire (FRASW) system, with the objective of specifying and recommending augmented product requirements and installation practices. The investigation included tensile load tests performed on relatively long samples of FRASW products, in which the elongation characteristics of the wire and clamp hardware were independently measured and characterized. In order to confirm the behavior of the FRASW system in actual application, as well as to verify the predictive technique necessary to provide installation guidelines, a series of full-scale simulations was performed, including application of an equivalent heavy storm load to the suspended drop. A comparison of the measured mechanical response of the FRASW drops with predicted values indicates excellent agreement. The results of the study are reflected in Telcordia generic requirements document GR-1069-CORE, December 1998.

INTRODUCTION

Due to its advantages in electrical transmission, handling and installation, fiberglass reinforced aerial service wire (FRASW) has become the dominant product for such applications, replacing the previous metallic (steel) based F-type drop wires. However, during a late winter storm in April 1996, unusually large amounts of ice and wet snow were deposited on aerial service wires across isolated sections of the northeast. As a result, heavy loads of extended duration were imposed on the wires which

caused thousands of aerial drops to sag excessively, interfering with traffic and snow plows. Most of the affected service lines were of the fiberglass reinforced type. Approximately 25,000 drops were "damaged".

A combination of the large stretch/creep of the FRASW and inappropriate installation practices was determined to be responsible for the excessive sagging conditions and associated problems that had been experienced in the field. Such experiences indicate that the FRASW characteristics should be better understood and that previous generic requirements (TR-NWT-001069¹) and installation practices should be augmented to address heavy loadings such as those associated with potential storm conditions, or the role of FRASW clamp hardware.

The present paper focuses on the results of the "long gauge-length" strength and elongation product testing, full-scale simulations at Telcordia's outdoor facility at Chester NJ, and a resulting refined analytical model and its ability to reasonably predict FRASW sag and tension. Due to the intimate relationship between the wire and its support clamps, the clamp behavior was also investigated and characterized. A companion paper discusses materials issues and potential failure modes of the FRASW type product, as identified during the investigation.²

LONG GAUGE-LENGTH TESTING

Figure 1 illustrates the test configuration used to confirm and/or measure the strength and elongation of the FRASW product, including both the wire and clamp deflection. A similar long gauge-length -- approximately 100 inches (250 cm) -- test setup has been incorporated into the recently issued generic requirements document

GR-1069-CORE³ for the elongation test requirement as a replacement for the previous TR-1069 test performed on a relatively short sample in a tensile testing machine. The basic reason for replacing the previous elongation test configuration is to allow independent measurement of the wire elongation and clamp deflection, as well as to obtain a wire elongation measurement relatively unaffected by the local wire deformation in the proximity of the clamps. It is noted that the clamp deflection has been reported to be a significant contributor to the resulting wire sag.⁴ In addition, a repeated loading cycle has been introduced in order to simulate the effect of several storm events during the life of the product.

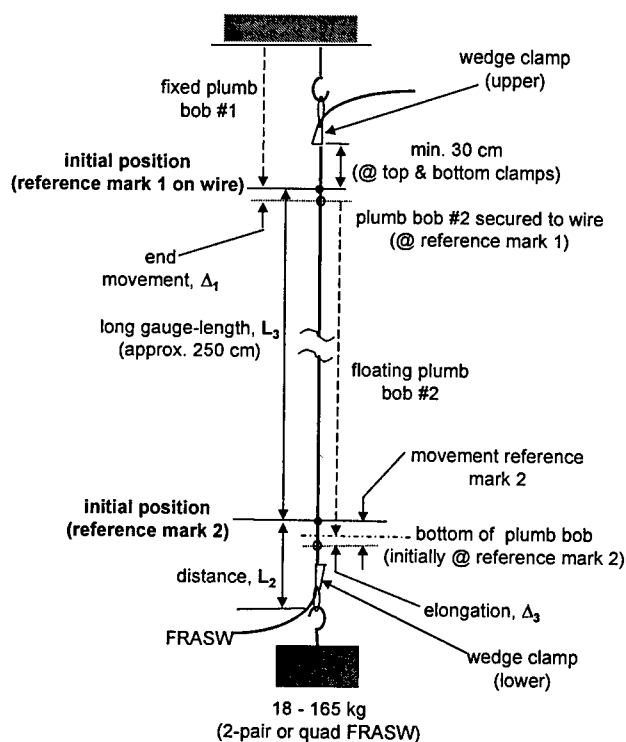


Figure 1 Long Gauge-Length Strength & Elongation Testing

During the combined strength and elongation testing of the present characterization study, an increasing sequence of weights, beginning at 40 lbs (18 kg) and accumulating to a maximum of 365 lbs. (165 kg), was supported by the 2-pair or quad product, using standard wedge-type clamps. For the 6-pair product, 500 lbs. (225 kg)

maximum load was applied. During several intermediate, unloaded intervals, dielectric strength/voltage breakdown tests were performed.

A wide variety of tests were performed on available FRASW products, in combination with several types of wedge-clamps. Most of the wire samples were of the 2-pair twisted variety, consistent with its present dominant use in the field, but quad and 6-pair twisted were included. Several minor variations in the test procedure were included, such as use of an "aged" sample, as well as repeated use of a prior tested wire.

Total Elongation

A typical set of elongation results is indicated in Figure 2. The results represent the increase in strain relative to the initial strain at 40 lbs. (18 kg), and is interpreted as the sum of an "elastic" (recoverable) contribution and a "residual" (permanent/non-recoverable) component. The latter is particularly significant since it determines the increase in wire length following a storm loading -- and is therefore an important contributor to the increase in final sag.

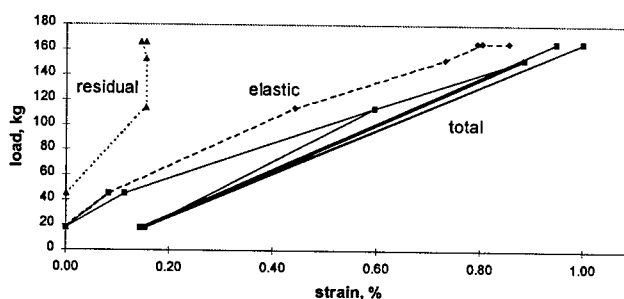


Figure 2 Typical FRASW Elongation Characteristics, Repeated Loading Cycle

Figure 3 illustrates the "total" (elastic plus residual) elongation results at 335 lbs (150kg) for 2-pair FRASW, or 470 lbs. (210 kg) for 6-pair product. The results are shown in comparison to the present 1.0% Requirement (R) of TR-1069, as well as the 0.90% Requirement (R) and 0.75% Objective (O) of GR-1069.

In general, the GR-1069 specifications are somewhat stricter than the previous TR-1069 requirements, but are feasible, based upon the

performance of this representative cross-section of available products.

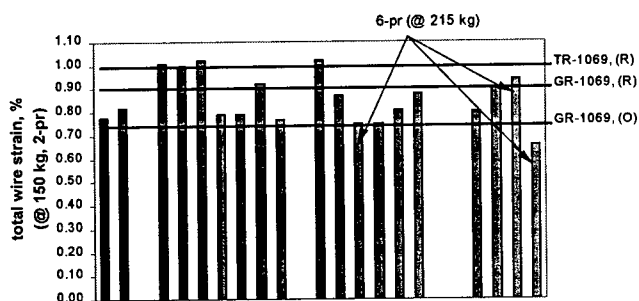


Figure 3 Long Gauge-Length Test Samples (Total Strain)

Residual Elongation

Considering the residual wire elongation, the results shown in Figure 4 indicate that most FRASW products meet the previous 0.3% elongation requirement of TR-1069, including the effects of repeated loading. Figure 4 also illustrates the residual elongation results in comparison to the 0.25% Requirement (R) and 0.20% Objective (O) of GR-1069.

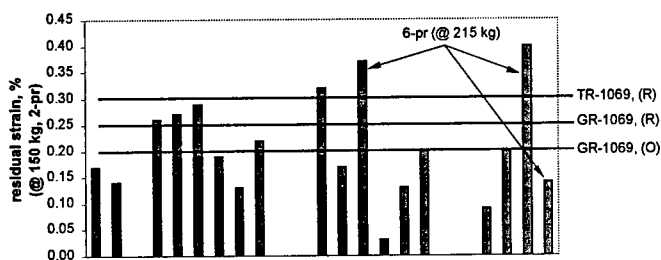


Figure 4 Long Gauge-Length Test Samples (Residual Strain)

The behavior of the sample illustrated in Figure 2 indicates an apparent upper limit of the residual strain, achieved between 100 and 250 lbs. (45 and 115 kg) -- considerably below the maximum applied load. A possible interpretation is that the relatively loose stranding of the individual fibers of the fiberglass reinforcement becomes taut as this limit is reached,

corresponding to a permanent elongation effect, in addition to the elastic strain component. Beyond this point, essentially only elastic (recoverable) strain occurs.

In an attempt to better display the relationship between residual strain and load, for all samples tested, the strain has been normalized with respect to that achieved at 250 lbs. (115 kg) -- or 300 lbs. (135 kg) for 6-pair FRASW. The results in Figure 5 indicate that, although there is significant scatter as may be expected for such tests and measurements, there is a degree of cluster about the strain achieved at this load level. Obvious exceptions correspond to the case in which the wire sample of a previous test was re-used and for which the subsequent residual strain was negligible, consistent with the tautening effect discussed above, tending to generate erratic data points. An exponential fit is included for a typical sample, in which 90% of the observed residual strain is assumed to be achieved at the indicated load. The exponential fit is reasonable and useful with respect to subsequent prediction and development of installation guidelines.

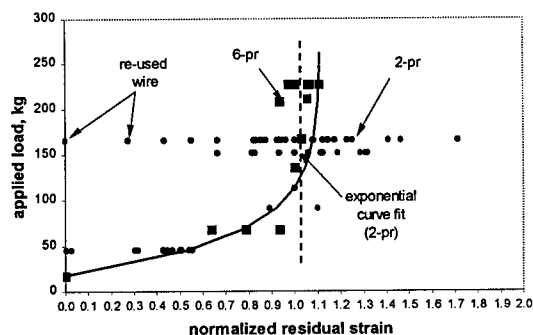


Figure 5 Long Gauge-Length Test Samples (Normalized Residual Strain)

Elastic Elongation

The corresponding calculated elastic stiffnesses of the 2-pair wires were in the range of 40,000 to 50,000 lbs./in./in. (180,000 to 220,000 N/cm/cm), with the 6-pair samples indicating 80,000 to 90,000 lbs./in./in. (160,000 to 180,000 N/cm/cm). Although the elastic characteristics represent a temporary elongation, essentially vanishing after the storm loading has passed, this behavior

directly affects the relatively large temporary sag occurring while the storm loading is present. Furthermore, the corresponding temporary sag is directly related to the peak wire tension serving to support the wind and ice loads, and determines the maximum recommended span length. The greater the sag, the lower the required tension. Thus, a stiffer wire (as well as a wire and/or clamp with reduced residual elongation characteristics) will lead to a greater storm tension, for a given span length, and a possible greater FRASW tensile strength requirement. Thus, the decreased residual elongation corresponding to "re-use" or "re-sagging" of a previously stretched wire, does represent a potential problem.

Clamp Deflection

As seen in Figure 6, the clamp deflection is primarily a permanent or residual phenomenon, corresponding to a ratcheting effect for the typical wedge-type clamps. This deflection results in a significant contribution to the final (after-storm, unloaded) sag, which reflects the magnitude of the permanent wire elongation and clamp deflection. The issue of the clamp deflection is not addressed in the previous TR-1069 but is reflected in the GR-1069 upgrade.

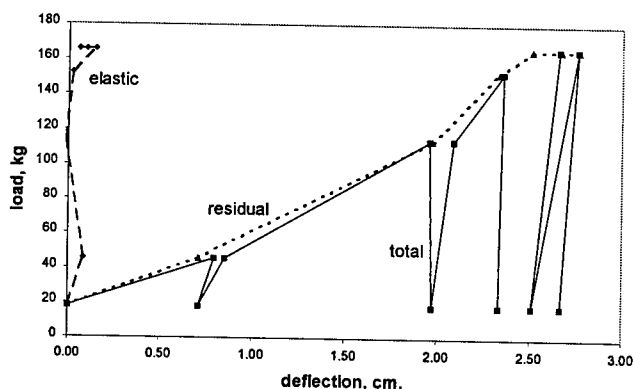


Figure 6 Typical Clamp Deflection Characteristics

Figure 7 illustrates the effective clamp deflection due to the wedge clamps, as determined at the upper and lower clamps of Figure 1. The indicated clamp deflection levels of GR-1069 have been selected to be generally consistent with this observed data, with a lower value as

the desired objective. The magnitude of the clamp deflections is consistent with that of previous reported studies.⁴

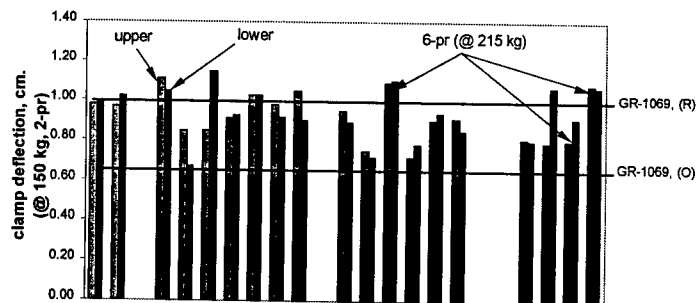


Figure 7 Long Gauge-Length Test Samples (Clamp Deflection)

FRASW SYSTEM FAILURES

The test results indicate a somewhat increased rate of failures due to the repeated loading effect. The difference does not appear to be major, but the trend verifies the advisability of incorporating and maintaining such a test condition in GR-1069. The apparent weakening of the FRASW due to the unloading/loading cycles is consistent with previous Telcordia experiences in which samples of FRASW returned from the field, following previous usage and exposure to heavy storm loadings, had considerably greater difficulty passing the TR-1069 qualification test than new product for which the tests had originally been intended.

Several clamp-related failures -- and consideration of the overall importance of the clamp in the FRASW system -- emphasize the need for appropriate generic requirements controlling this important hardware item as well as clarification of mechanical testing details in GR-1069 and appropriate field installation information.

The present test program revealed a potentially serious issue related to the wire response following removal of a previous high load, such as following a severe storm, and/or temporary removal of the drop from the support hook(s). The appearance of small kinks or bulges in the

wire, at approximately 1 ft. (30 cm) intervals, often followed removal of the load to the 40 lbs. (18 kg) pre-load level. This effect became significantly aggravated upon total load removal to perform the dielectric strength test.

Figure 8 shows a cross-sectional view of insulated copper wires attempting to penetrate the jacket of a FRASW sample previously subjected to a severe (breaking) tensile load. This phenomenon raises serious concern about the use and re-use of existing drops that may have been subjected to high loads. For example, the effect of wire vibrations may lead to subsequent penetration of the jacket after bulges have been initiated during a storm condition. Extensive field testing, including simulations are recommended to support a reliable installation practice that addresses this issue.

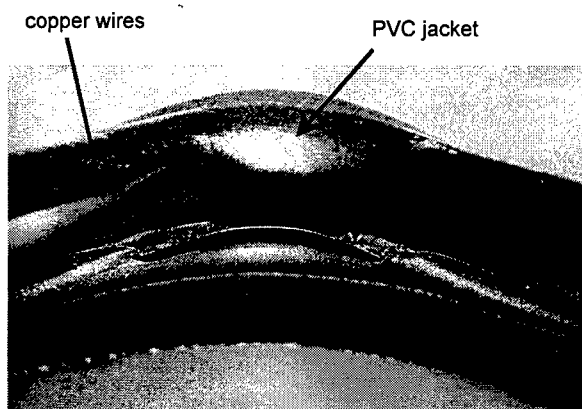


**Figure 8 Copper Wires Penetrating Jacket
(After Severe Tensile Load)**

A companion paper discusses in detail materials issues and potential failure modes of the FRASW type product and mounting system, as identified during the investigation.²

FULL-SCALE SIMULATIONS

Full-scale simulations of the response of FRASW to storm loading were an important element of the investigation. Similar tests conducted in 1996 vividly illustrated the excessive sagging -- both temporary (during storm loading) and permanent/residual (following

storm loading) -- and illustrated the deficiency in the general understanding by the industry of the FRASW system and its mechanical behavior and long-term performance.⁵ This lack of understanding has direct bearing upon the ability to provide useful installation guidelines and operational limits. Thus, full-scale simulations have been conducted at Telcordia's outdoor test facility at Chester, New Jersey to verify that the recent investigation has, in fact, resulted in a better understanding and ability to accurately predict field behavior.

Briefly, the procedure included initial installation of a selected FRASW product at a nominal initial tension condition -- e.g., 40 lbs. (18 kg) for the 2-pair product. A taut, light-weight string suspended between end hooks served as a reference for measuring the sag. An equivalent National Electrical Safety Code (NESC)⁶ Heavy Storm loading, corresponding to ½-in. (1.25 cm) radial ice buildup plus 4 lbs./ft.² (190 Pa) lateral wind pressure -- i.e., 40 mph (65 kph) wind -- applied to wire plus ice, was then accomplished by lashing a steel chain to the FRASW. The weight of the chain was specifically selected to equal the resultant force due to the vector sum of the vertical ice weight and horizontal wind force -- approximately 0.75 lbs./ft. (1.1 kg/m). The span lengths ranged from approximately 100 to 130 ft. (30 to 40 m).

After a brief period (approximately 2 hours), the storm load was removed. After another short interval, the storm load was re-applied and allowed to remain for a typical period of 1 to 3 days, followed by a final unloaded period of 1 hour. The sag and tensions were noted during the various phases, including the peak sag and tension during the storm application, and following the storm. Electrical parameters related to transmission, consistent with the requirements of GR-1069, were measured prior to, and after completion of, each complete simulation. As in the long gauge-length strength and elongation testing program, most tests were conducted on the widely used 2-pair configuration.

In general, relatively small differences were detected during the time intervals of the unloaded or loaded cycle, although some trend for increasing sag (and decreased tension) was apparent due to the application of the second storm loading, as well as slightly decreasing sag

(and increased tension) due to a small recovery following the storms. These experiences are generally consistent with trends noted during the long gauge-length elongation tests. The results of the electrical measurements indicate no degradation in electrical parameters as a result of the simulation tests. This is comforting, since the effect of bulges or kinks in the FRASW were often apparent following the simulation and removal of loading.

THEORETICAL MODELING & PREDICTIONS

In addition to providing a realistic experiment to help determine and reveal unanticipated issues related to the FRASW application, the full-scale simulations served the important function of helping verify the theoretical mathematical model and predictive method. Thus, a mathematical model was applied to predict the mechanical behavior (i.e., sag and tension) of the wire before, during, and following the simulated storm loading. The same model may be used to provide recommended installation guidelines.

The effects incorporated in the theoretical model include mechanics of the wire sag and tension, kinematics of wire and clamp elongation vs. sag, wire elongation (temporary/elastic and permanent/residual) vs. tension characteristics, clamp deflection vs. tension characteristics, and thermal expansion/contraction.

For typical applications in which the sag is small compared to the span length, the model reduces to a non-linear, cubic equation in terms of (peak) sag or tension. It is recognized that such an equation does yield a closed form solution for the case of "constant coefficients", corresponding to a constant modulus of elasticity and coefficient of thermal expansion, and uniform wire loads. However, in the most general case, there will be load-dependent coefficients, complicating the analytical solution of the problem. An iterative technique was therefore utilized to determine a solution for each specified set of conditions and load characteristics.

The wire behavior is approximated by a linear elastic and exponential residual strain model, such as discussed above. The residual clamp deflection is represented by a linear response with load, and negligible elastic deflection,

consistent with the observations, also discussed above.

Figure 9 illustrates the measured and predicted peak sag, indicating excellent agreement, including that corresponding to the initial, during, and after storm(s) sag. The difference between the measured and predicted values is typically less than 10%, and sometimes much lower -- with the predicted sag generally more conservative; i.e., slightly greater than the actual measured value. The excellent agreement is due to incorporation of the improved characterization of the strains and deflections, including the exponential residual strain model.

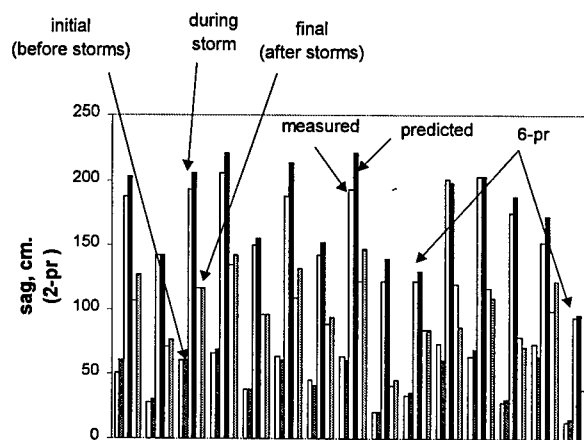


Figure 9 Full-Scale Simulations (Peak Sag)

Regarding the corresponding tension, The agreement between measured and predicted values is within 5%, again representing outstanding agreement. The predicted peak tension values are typically slightly greater than the measured quantities, providing a degree of margin when using the present predictive technique.

SPAN LENGTH LIMITATIONS

Previous installation information providing initial sag and tension guidelines and maximum span lengths have not had the benefit of the present extensive FRASW investigation discussed in this, and the companion, paper.² In general, it is desired to specify initial sag conditions and the corresponding final, unloaded (following storm)

sag as a function of span length, as well as engineering limitations for the maximum span length. Recommended limitations may be based upon combined ice and wind loads as specified in the NESC. For example, the Heavy Storm region of the United States corresponds to the ½-in. (1.25 cm) radial ice thickness plus 40 mph (65 kph) winds modeled in the full-scale simulations discussed above. It should be noted that since the NESC specified storm load is considerably less severe than a "50 year storm" design condition -- i.e., the worst storm expected to occur in a 50 year interval -- it is reasonable to anticipate that the specified storm may occur several times in the lifetime of a given service wire. This is consistent with the present strength and elongation tests, and GR-1069 requirements, that subject the FRASW product to repeated loading conditions.

Recommended span limitations for product meeting the previous TR-1069 requirements are partially based upon the assumed greater vulnerability of the FRASW to repeated loading, but especially due to observed local kinks following the effective storm loading -- as apparent in the long gauge-length tests as well as the full-scale simulations. This effect was apparent, to varying degrees, in several products in spans on the order of 100 ft. (30 m) or greater, corresponding to induced wire tensions exceeding 200 lbs. (900 N). Thus, **product meeting only the previous TR-1069 requirements is considered vulnerable in span lengths above approximately 100 to 150 ft. (30 to 45 m).** In contrast, improved product meeting GR-1069 increases the recommended maximum span lengths to approximately 175 to 250 ft. (55 to 75 m). In addition, the final unloaded sags are slightly reduced for the GR-1069 compatible product, which is also considered capable of withstanding several winter storms.

It is noted that although initial sags may be similar to those provided in previous FRASW guidelines, the final sags based upon the present study and model are significantly greater -- by approximately 1 - 2 ft. (½ m) -- than that given previously. This is due to the more realistic understanding of the FRASW system behavior, including the significant contribution of the clamps' deformation to the final unloaded sag.

The recommended span lengths for the GR-1069 compatible product are comparable to that provided for the older C or F Drop Wire. However, a significantly lower installed sag for the FRASW, in comparison to that of the previous type drop wires, is necessary to compensate for the greater increase in sag that will result from a storm loading imposed upon this product. Thus, craft installation procedures that merely match the sag of existing drops (C or F Drop, or existing FRASW that may have been exposed to a previous winter storm load) are not consistent with the present recommendations.

The present guidelines do not consider the re-sagging of existing drops following a severe storm, which is beyond the scope of the present study. The limited residual strain phenomenon discussed above implies that the procedure of "re-sagging" an existing drop that has been "stretched out" would result in a stiffer wire when exposed to the next storm loading. This would have the benefit of subsequent reduced temporary and permanent sag, but should also directly result in increased tension. In combination with a possibly degraded wire due to its previous load history and environmental aging, this effect may lead to early mechanical or electrical failure during the next severe storm loading, particularly for product meeting only the previous TR-1069. Furthermore, the tendency for bulges or kinks that may have developed following a severe storm (for TR-1069 compatible product) to eventually penetrate the jacket remains an issue.

CONCLUSION

A detailed fiberglass reinforced aerial service wire (FRASW) characterization study has been performed to better understand the behavior of this widely used product, including when subject to winter storm conditions. Thus, extensive mechanical testing and analysis of wire samples from a variety of suppliers was conducted. The test program included long gauge-length testing in which relatively long lengths -- approximately 125 in. (310 cm) between clamps -- of FRASW were subject to static tensile loads applied by weights suspended from the wire. The test procedure allowed verification of the strength of the wire, as well as independent measurement of the elongation properties of the wire and

clamp system, including the effect of repeated loading.

Samples of the FRASW and clamps were analyzed to help understand the associated behavior and vulnerability. These results indicate potential vulnerabilities of the clamp and clamp/wire interface, including an important effect in which kinks or bulges result following a temporary application of a significant tensile load, as discussed in a companion paper.

To confirm the behavior of the FRASW system in actual application, as well as to verify the developed predictive technique necessary to provide reliable installation guidelines, a series of full-scale simulations were performed at Telcordia's outdoor test facility at Chester, New Jersey. The resulting sag and tension were monitored before, during, and after a "heavy storm" condition. A comparison of the measured mechanical response of the FRASW drops with the predicted values shows excellent agreement. Recommended span lengths are considerably lower for product meeting only the previous TR-1069 requirements, and are limited to 150 ft. (45 m) or less. For GR-1069 compatible product, span lengths as much as 250 ft. (75 m) are possible.

ACKNOWLEDGEMENT

The authors would like to thank Orlando Chavez and Chris March of Telcordia Technologies for their valuable assistance in helping organize and implement the long gauge-length FRASW tests and full-scale simulations, including performing the associated electrical measurements.

REFERENCES

¹ TR-NWT-001069, *Generic Requirements for Non-Metallic Reinforced Aerial Service Wire*, Issue 1, June 1992.

² T. N. Bowmer, O. Gebizlioglu, K. Moyers, *Fiberglass Reinforced Aerial Service Wire Aerial Service Wire: Materials Investigation and Failure Analysis*, International Wire and Cable Symposium, 1999.

³ GR-1069-CORE, *Generic Requirements for Non-Metallic Reinforced Aerial Service Wire*, Issue 1, December 1998.

⁴ J.-H. Walling, et al, *The Sag Behavior of Aerial Service Wires Using Different Wedge Clamps*, International Wire & Cable Symposium, 1995.

⁵ J.-H. Walling, *About the Influence of Residual Elongation and Thermal Expansion on the Sagging Performance of Glass Fiber Reinforced Aerial Service Wires*, International Wire & Cable Symposium, 1997.

⁶ *National Electrical Safety Code, C2-1997*, 1997 Edition, Institute of Electrical and Electronics Engineers, Inc.

BIOGRAPHY



Lawrence M. Slavin
Telcordia Technologies
445 South Street
Morristown, New Jersey 07960

Lawrence (Larry) M. Slavin is Director of the Network Facilities, Components, and Power group of Telcordia Technologies, responsible for reliability of the outside plant telecommunications network, including metallic media and installation practices. He is presently the telecommunications representative to the National Electrical Safety Code (NESC) committee, helping establish strength and loading criteria for overhead lines. Larry joined Telcordia in 1989, following a career of more than 28 years at Lucent Bell Laboratories. Larry received a B.S. in Mechanical Engineering from the Cooper Union for the Advancement of Science and Art in 1961, and an M.S. in Applied Mechanics and a Ph.D. in Mechanical Engineering from New York University in 1963 and 1969, respectively.

COST DRIVEN INNOVATIVE SOLUTIONS FOR THE LOCAL LOOP

Part II: Realisation

Pieter Matthijsse

KPN - Fixed Network Operator, The Netherlands

ABSTRACT

In co-development with two selected industrial partners, NKF and TKF, KPN tested a new innovative concept for the local loop, FLASHNET. Main goals are in reducing the initial investment costs per line for new constructions and in creating the possibility for later upgrading to fibre without digging new trenches. Basic elements are the complete change over to un-armoured cables in ducts, introduction of multi-customer joints and a turn-key supplier relation. The whole network is underground. In various pilots the two differently engineered concepts, which were developed in a competitive mode, have been tested. Apart from technical and operational aspects also costs were evaluated thoroughly. Although several learning points have been gained, results are very positive up to now. Next steps are the selection of the best concept and making a start with the large-scale deployment of FLASHNET.

INTRODUCTION

Faced with the need for both cost reduction and future-proofness in the most cost-intensive part of the cable network, the local loop, KPN started in 1997 a major innovation project "FLASHNET". Chosen target architecture was copper with an option for future migration to fibre. Basic elements in the project are the specification of the network in terms of maximum cost per copper line and general functionalities, exploiting the competitive forces and applying total network concepts and turn-key deliveries.

The industrial partners NKF and TKF have been selected from an international tender and were prepared to go into a "development race" where the "best partner" gets the contract for the turn-key delivery of local loop networks (Fig 1). Offers resulting from the tendering phase reasonably

fulfilled the cost and futureproofness requirements and have been presented at the 47th IWCS in 1998 (see ref 1).

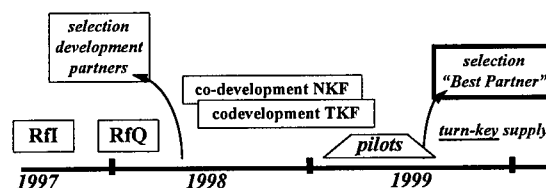


Fig.1 Time schedule for the FLASHNET project

In this paper the results of the industrial development phase and the pilots which are going on at this moment, have been described. Main topics are i) technical network solutions, ii) installation technologies, iii) migration to fibre, iv) process development, v) pilots and vi) cost evaluation.

As the process of selecting a "best partner" has not yet been finished by now, throughout the paper the issues will be described in general. Details from the specific solutions will be given, often by indicating the two different options, but without indicating the specific partner.

TECHNICAL NETWORK SOLUTIONS

Architecture

The offered general architecture for the FLASHNET network is indicated in Fig 2. It is a star-tree, very much like the traditional network structure determined by the laws of shortest total trench length to minimize costs. In parallel with the copper cables, to a greater part installed in HDPE ducts, a second duct system is installed for later up-grading with fibre. For cost reasons the introduction of the multi-customer joints (MCJ) with much more customers than the current 2 to 4 is very essential. Branching out to the customers premises is done either by a bundle of separate 16 mm tubes or by means of a "tube-in-tube" construction (modified JetNet[®]; see ref 2). The

whole network is underground. Only in special regions with high churn rates and in multiple of office buildings, aboveground cable distribution cabinets will be applied.

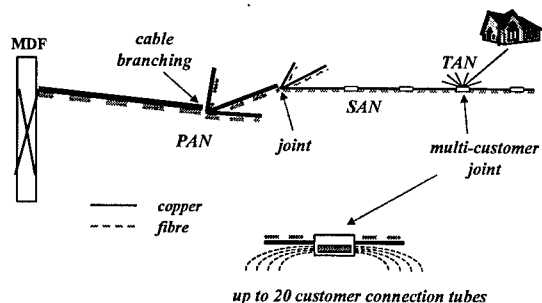


Fig 2: General architecture of FLASHNET

Copper capacity at the customer side is 200 %, i.e. two wire pairs enter every house. In the primary and secondary cables the capacity is reduced to 125 %. Spare capacity is available in each MCJ, i.e. along the whole length of the SAN.

Components

A complete range of new cables had to be developed. Due to additional requirement that also the repair and maintenance of the extensive installed base has to be done with the new cables the resulting cable range resembles the major current cable counts i.e. 300, 100, 50 and 2 pairs. For business customers intermediate pair counts are proposed also. Compared with the current situation a significant reduction in total number of cable types has been achieved.

All cables are un-armoured and have the layered quad construction. Foam-skin PE is applied as wire insulation resulting in smaller cable diameter than the current ones with a solid polyethylene insulation. As for the transmission characteristics much attention has been given to an optimal behaviour at high frequencies in view of the ongoing introduction of ADSL systems.

One partner offered a complete 0.4 mm wire diameter cable range giving significant investment cost reduction, especially for the shorter distances. Currently the great majority of the KPN cables has 0.5 mm diameter wires. Another option offered was a 900 pair armoured cable for direct burying in addition to the above mentioned duct cables. This offers cost advantages for new installations and for repair compared with the 3x300 pair duct cables alternative.

The major innovation with respect to cable jointing is the introduction of the MCJ which consists of i) the copper connection closure, ii) the fibre splicing closure and iii) a handhole as overall

housing for the copper and fibre closures and for fixing the ducts.

As rather low fibre penetration rates are expected in the coming years, in both FLASHNET solutions a modular approach has been applied. For first installations the copper closure and the handhole will be installed only. To enable the later mounting of the fibre closure the handhole is made expandable by adding a higher case on the existing bottom plate. In one concept additional space is reserved from the very beginning for later storage of a fibre cable loop at the bottom of the handhole (see Fig 3). This results in a broader handhole. Different types of copper and fibre closures were offered.

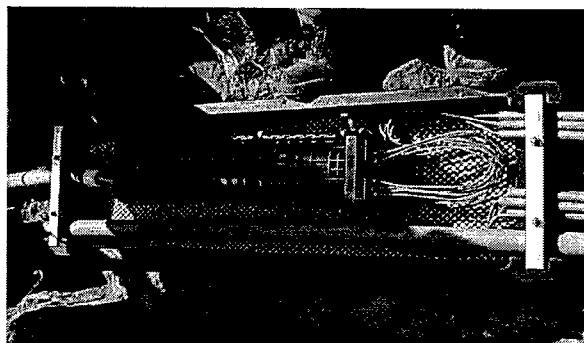


Fig 3: One proposed FLASHNET MCJ

For the jointing or branching points in the network in one solution thermoshrinkable jointing sleeves are applied for fixation of the ducts with in the interior a similar but smaller jointing sleeve. In the other solution a mechanical joint and a handhole of the same type as in the MCJ is used. The offered wire splicing method for standard use in new installations are the labour saving mini-splicing modules and conventional twist jointing with plastic mini-sleeves respectively.

Water ingress protection

Of special concern for the total design is the "water management". Transmission part has to be perfectly watertight. The ducting and the duct fixing part of the underground housing however has to be "mud-tight" only but allows water ingress. A point of concern herein is the transition region in which water with small floating particles deposits a sediment after some years. This can have a sticking effect on the inside tubing or influence the afterwards manipulation.

To provide "mud-tight" connection, a complete range of inserts, couplings and repair sets had to be developed. Very often however, use could be made of standard solutions from other technologies. For the MCJ the ingress of water through

the base plate is essential to prevent it from floating on places with a high ground water level. At the customer side any duct water should be prevented from dripping or being "blown" into the house.

An aluminum sheath is applied as lateral moisture blocking. Longitudinal watertightness is achieved by waterblocks every 4 m. In one solution swelling tape is used for the drop cable. Petroleum jelly is not applied in any of the cables.

For the splice closures the application of shrinking sleeves has proven to be a reliable method for achieving waterblocking. The mechanical closure construction allows for perfect watertightness, the installation process however, appears to be more man-dependent than allowed according to our quality standards. Although we realise that our engineers are still in an early stage on the learning curve, we yet required for the availability of a simple check, e.g. air pressure, to enable the engineers to check the installation just after finishing. Careful processing of the resulting quality data also allows KPN to enter into a quality improvement process on this issue. Compared with the conventional network we expect less errors originating from water-ingress due to i) the expected positive influence of the duct on protection against light mechanical violence and ii) the considerable lower number of closures.

INSTALLATION METHODS

Cables

The blown-in method is generally applied. Peculiar is the installation of the biggest 300 pair duct cable for the primary routes. In one solution this 35 mm, 2000 kg/km cable was proposed in a 50 mm duct, in the other a 63 mm duct. This latter proved to be more reliable with the currently applied blowing / pushing technology. Single jet installation lengths of more than 1 km including several 90° bends have been obtained repeatedly now, both in experiments and in practice.

Pulling cables as was proposed in one solution caused severe damage of the HDPE ducts in an environment with many bends and had to be cancelled for field installations. Only for the short TAN tubes a specially designed pulling string proved to be very practical in the solution with 16 mm tubes.

In the proposed tube-in-tube concept bundles of 7 guiding tubes have to be installed on several places (TAN; fibre SAN) in the field into 40 mm ducts. Although throughout the development phase and in the pilots several learning points

were gained, the method appears to be reliable and suited for field use (see also ref 3).

For all proposed cable-duct combinations also pre-ducting in the factory can reduce cost. Installation methods may very well deviate from the field methods but are not described here.

Splice and branching closures

Compared with the current TAN closures the MCJ is much bigger (see figs 3 and 4).

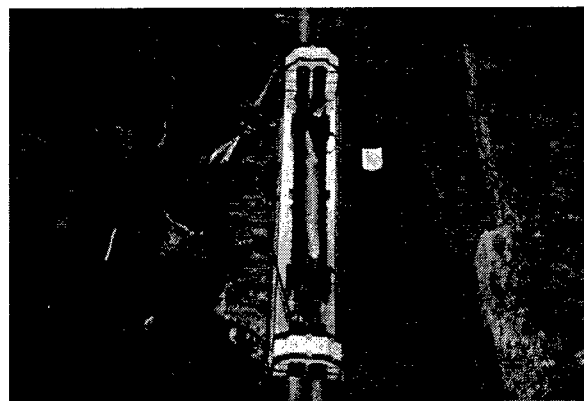


Fig 4: Installation of an MCJ applying a tube-in-tube concept

All installation work has to be done in a self dug pit in the ground, very often with water at the bottom. This environment requires special precautions and careful working with respect to watertight assembling of the different units. Also the blowing in of the tiny drop cables in this harsh environment will ask special attention. Apart from optimization of the components and installation methods itself, focus is also on the related training and engineers certification processes.

In-house installations

On several aspects separate solutions had to be designed for high rise buildings and for space limited situations in and around Telecom offices. In the latter case it turned out to be rather difficult to guide the 50 mm and 63 mm ducts to the usual indoor cable splicing point. The application of corrugated flexible tubes improved this considerably. For fittings in the basements of high rise buildings special precautions had to be made for security reasons. One of these is the outdoor underground positioning of the MCJ instead of in the basement.

Trench management

A point of special concern is the increase of required space in the ground for digging of trenches. Reasons are the bigger diameters, the

stiffer construction, the spare tubes for fibre migration and the MCJ volume. Together with the sharply increased installation activities of new operators strong limitations on space may be expected on several routes, especially in the older City Centres. Although this is not an exclusive FLASHNET attention point it will ask for special attention in the next phase. Options for a range of mini-components will be elaborated after the selection phase.

MIGRATION TO FIBRE

Due to the unclearness of future fibre penetration, the fibre migration scenarios must be flexible. Both point-to-point and point-to-multipoint, applying splitters, must be possible in parallel. Single fibre working, as is assumed in one of the solutions, gives some relief here. In both concepts up-grading to a 100% connection density is possible.

For the PAN network, a fibre cable has to be installed as soon as the first customer has to be connected to fibre. In one solution a 144 fibre cable in a 40 mm duct is applied. In the other a 63 mm duct with three sub-ducts is applied resulting in the additional advantages: i) no need for fibre splicing in the PAN branching point and ii) fibre cable installation can be limited to one SAN branch only.



Fig 5: Y-branch as applied in connecting the MCJ with the customer premise

In the SAN network both solutions differ considerable. In one solution a 40 mm parallel duct passes every MCJ (see fig 3). Connecting the first customer means blowing in the required cable throughout the whole SAN and storing several loops of cable in every MCJ for later use. At the specific customer MCJ only, an additional 2 fibre cable is pulled into the 16 mm TAN tube and spliced with the SAN cable applying the window-cut method. For the other solution, a separate 40 mm tube is installed along the copper SAN without any MCJ connections. For the first customer, a bundle of mini-ducts has to be installed into this

duct. After that the specific customer MCJ is connected with the SAN duct applying a special Y-connector. A blown-in 8 fibre mini-cable connects the PAN/SAN branching point with the specific MCJ. This feeds the 2 fibre TAN cable, which is blown into the JetNet® ducting system, passing a second Y-connector (see Fig 5).

PROCESS DEVELOPMENT

Strong emphasis has been on the *process renewal* related with the change over to turn-key deliveries by an external partner. Having in mind the IWCS focus on technology some selected process aspects will be highlighted only.

In Fig 6 a summarized flow chart is given of the developed operational process for initiating a FLASHNET construction project. Every demand is checked with a continuously up-dated operational plan for a certain region. The demand itself can be initiated from several sources, one of which may be the turn-key partner having knowledge of future construction plans. Ordering will be initiated in terms of a high abstraction level set of "order items", each with a fixed price. Currently this order item for the KPN internal construction department is on the level of "connecting a house somewhere in the Netherlands".

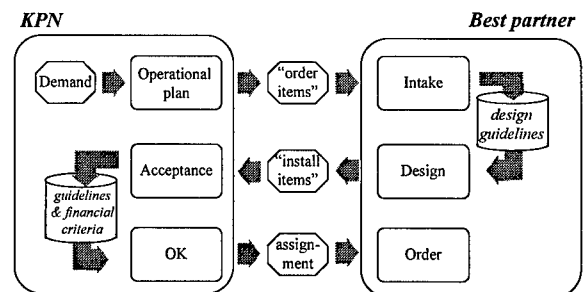


Fig 6: Proces flow chart for initiating a turn key FLASHNET project.

At this stage, both partners developed a set of priced "install items". Instead of the current single order item for residential areas, both sets consist of 6 to 10 major items and some more detailed ones. In future, based on gained experience, this set should evolve into the required higher abstraction level. Based on this high level ordering a completely engineered design is made which is offered for acceptance.

In a similar way many other processes, e.g. forecasting, servicing, logistics, had to be re-designed.

Some specific issues are registration and purchasing. In both network concepts a single duct can contain a mixture of tubes and/or cables and in addition, splitters may be applied. For the short term this has been solved with work-arounds in the registration systems. For the long term new advanced registration systems will be required. Local loop components and installation labour are acquired separately up to now. In the new approach the complete network is purchased from the best partner. This change in supply chain will have large impact on the component suppliers and subcontractors businesses.

PILOTS

A number of separate pilots have been built. All related ordering, delivery and acceptance processes were simulated as if a complete turn-key delivery took place. These pilots involved:

- 1- In three residential areas, a total of about 350 houses have been or will be connected shortly by means of one of the two FLASHNET concepts.
- 2- Primary route 300 or 900 pair cable has been installed applying installations of pre-ducted cables as well as installation with the new high power blowing technology.
- 3- In a test and training centre the two partners have fed their new ducted primary cable into a telecom office, coupled it with the new indoor cable and finished it on the MDF.
- 4- An apartment block has been connected already and another high rise building block will follow shortly.
- 5- Testing of repair, extension and mutation processes has been done in two purposely built SAN/TAN networks. Both consisted of a FLASHNET network with 10 simulated house connections and a similar conventional network (see Fig 7).

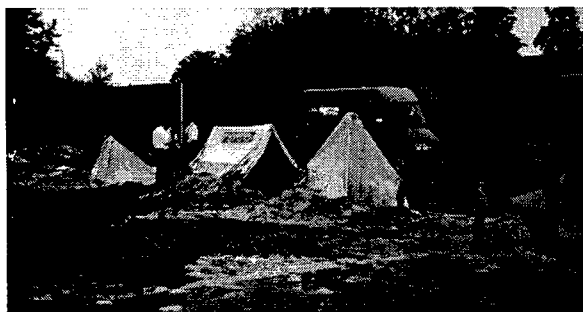


Fig 7: Overview of the site in one of the test networks in the operational pilot

In these networks the usual telecom operators underground work was carried out to: i) learn from the engineers experience which were specially trained by the partners, ii) measure the required times in the new FLASHNET networks as well as in the conventional networks. Of special interest here was the repair of the conventional cables with the ducted new ones.

6- Engineering realistic cases. Five different areas were selected where new building of residential houses and business offices was planned. Both partners made a complete engineering including the list of order items and the total price. The results showed several learning effects, but also provided perfect bench-marking results. In addition, we did the same for a 720 houses "monitoring" network which was the same (theoretical) reference network as was used in the original RfQ.

The findings and learnings from these pilots have been inserted in the other sections of this paper or are still in the evaluation phase. General finding is that in this case "just doing it" added considerable value to the test results from the preceding development phase.

COST EVALUATION

Main goal of the FLASHNET project is the achievement of cost reduction, both for investment and operational costs.

Investment cost

In Fig 8 a comparison of the currently offered cost level is given. It indicates the averaged cost levels from the two partners for each of the engineered cases (see section on pilots) and the reference configuration (RC) from the RfQ.

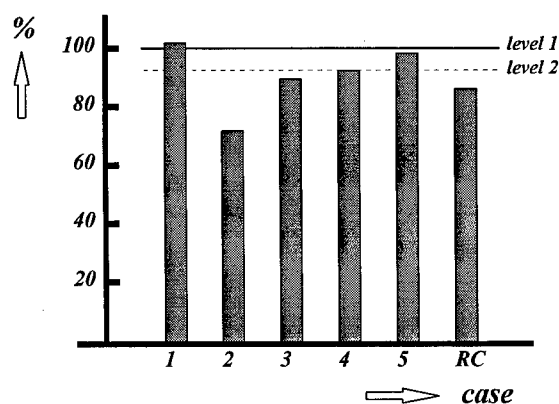


Fig 8: Investment cost comparison for some fully engineered areas.

The costs refer to the SAN/TAN networks only. Level 1 is the originally set cost target, whereas level 2 is the revised target due to the achieved price drop in the conventional network.

The figure shows that cost reduction is still on target. The cost level may be influenced negatively however, taking into account that the average construction project size is much smaller than in the engineered case areas.

Operational cost

The major cost contributor here is the corrective maintenance (see ref 1). In the FLASHNET network a decrease in network disturbances may be expected as the number of splicing or branching points has been reduced significantly. From the engineered project cases a ratio of 1: 4 or even 1: 8 has been derived.

Repairing the old network with new components gives a tendency to cost increases. A first evaluation of the results of the operational pilot however, shows that for this item the difference is in the order of 10 to 30% only, which certainly will improve further once practical experience grows. For several other items operational costs were lower.

First indications point therefore to an operational cost level which meets the expectation. Taking into account the potential for further improvements, as is the case in every major network change, even a much lower operational cost level may be within reach.

CONCLUSIONS

Two years after the start of the FLASHNET project the first pilot customers have been connected. To a great part this is based on the commitment and the performance of both industrial partners and their sub-contractors. Original goals of the project are still on target and it may be expected that the offered innovative solutions will lead to the required short term cost reduction without violating the long term objective, i.e. migration to fibre without new trenches.

As a next major step the "best partners concept" will be selected after which the large scale roll-out phase can start. Latest state will be presented at the conference.

Taking into account the enormous changes in applied technologies and processes within our company however, we are also aware of the necessity of further improvements. Relevant issues are e.g. the long term impact of "clear" water ingress, fibre migration scenarios and its relation with the currently deployed overlay optical access

networks, the potential application of intelligent position registration devices in the MCJs, FLASHNET in typical business environments, etc...

Together with the gradual but complete phasing out of the conventional mix of lead-shielded paper and plastic isolated directly buried armoured cables the introduction of FLASHNET will be a major topic in the next years to come.

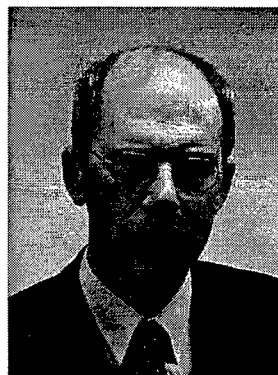
ACKNOWLEDGEMENTS

The author wishes to acknowledge his colleagues in the FLASHNET project team for the continuous support and the valuable contributions to this paper and his industrial partners NKF and TKF for their enormous dedication and achievements

REFERENCES

- [1] P.Matthijsse; "Cost driven innovative solutions for the local loop"; Proc. 47th IWCS (1998), pp. 170-175
- [2] W.Griffioen et al; "A new, extremely versatile access network cabling concept for migration to optical fibre". Proc. 45th IWCS (1996), pp 485-489
- [3] G.Plumettaz; "A new universal tool for the placement of microcables in the local and business access network"; Proc. EuroCable Conf. 1999, pp 76-80

BIOGRAPHY:



Pieter Matthijsse was graduated at the Eindhoven Technical University in 1971. After his PhD study in Fourier Optics at the Leuven University in Belgium he joined KPN Research in 1976 and worked on optical network technology. From 1985 on his main task

was on PCVD fibre production process development at Philips Optical Fibre in Eindhoven. In 1991 he returned to KPN where, in several responsibilities, he worked on access network development. Full address: KPN - Fixed Network Operator; PO Box 30150, 2500 The Hague, The Netherlands; email: p.matthijsse@kpn.com

Bridge Taps Analysis in Copper Networks used for ISDN-Narrow Band and xDSL Systems

Reginaldo Lazarini

CPqD Foundation - Telecommunications Research and Development Center
Campinas - SP - Brazil

ABSTRACT

The majority of access networks used for telecommunication systems existent at the moment is still structured on copper networks. These copper networks were originally projected for transmission of voice signals of the traditional telephone systems (POTS) and they are characterized by a narrowband transmission line, losses and interference, which all limits the maximum range without using a regenerator to few kilometers. There are some factors of these copper networks that need to be precisely compensated in the transmission of digital signals at higher velocities, even if they do not affect the voice band. Besides the proper distance between the subscriber and the central office, the presence of bridge taps and gauge (or diameter) changes affect the transmission characteristics of the cable.

INTRODUCTION

Bridge taps generally do not interfere significantly in the signals of the voice frequency; however, they can degrade the performance of the transmission of digital signals. The effect of the losses due to bridge taps in the transmission of digital signals increase with the frequency.

The presence of a bridge tap in the subscriber line will add losses to the signal transmitted. The attenuation basically occurs because of the reflected power in direction of the generator since there is no matching of transmission line at the points of the bridge taps.

Bridge taps provoke reflections due to transmission discontinuity which is caused by

its open termination. The reflected signals will be added to the transmitted signal of the subscriber line.

Bridge tap is an open terminated transmission line ($Z_L = \infty$), so it will appear an impedance at the point of bridge tap different from the characteristic impedance (Z_0) of the transmission line, increasing the total loss.

To analyse bridge taps it's necessary verify some transmission line parameters like: the impedance (Z_0), the physical parameters of the wire and the cable, the resulting impedance at the point of bridge tap, the bridge tap and the line transmission length, the bridge tap position in the transmission line, the transmission line mismatching in a certain frequency, the signal frequency travelling in the transmission line, the propagation velocity (V_p) of the signal, etc.

IMPEDANCE AT THE POINT OF BRIDGE TAP

Figure 1 shows a transmission line (for instance, a copper pair) with a bridge tap, and the impedances and lengths involved.

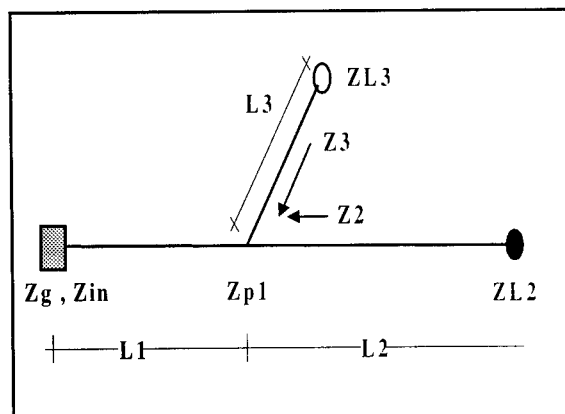


Figure 1 : Transmission Line with Bridge Tap.

The impedance at the point of bridge tap (Z_{p1}) is the result of reflected impedance (Z_2) by the load impedance (Z_{L2}) in L_2 part, with the reflected impedance by the open line (Z_3) in L_3 .

The impedance Z_{p1} will be given by:

$$\frac{Z_2 Z_3}{Z_2 + Z_3} \quad (1)$$

The impedance Z_{L3} tends to infinite (∞) because the bridge tap, in general, is an open transmission line.

IMPEDANCES IN A TRANSMISSION LINE WITH BRIDGE TAPS

In a transmission line with " n " bridge taps there are, as shown below in Figure 2, the impedances of each bridge tap, the reflected and resulting impedances at the point of bridge tap, the load and the generator impedances and the reflected impedance to the generator.

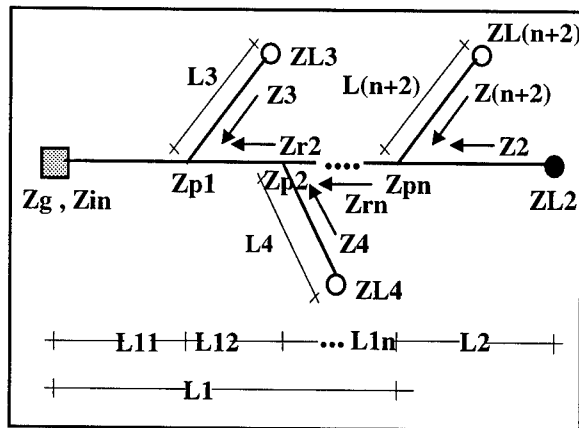


Figure 2 : Transmission Line with " n " Bridge Taps.

The impedances involved in a transmission line with " n " bridge taps are:

- Z_g is the serial impedance of the generator.
- Z_{L2} is the load impedance of the transmission line. It must be matched with the characteristic impedance (Z_0) of the transmission line, to avoid reflection losses.
- Z_0 is the characteristic impedance of the transmission line.

d) $Z_{L3}, Z_{L4}, \dots, Z_{L(n+2)}$ are the termination impedances of the bridge taps $L_3, L_4 \dots L(n+2)$, respectively (in general tending to ∞).

e) $Z_{p1}, Z_{p2}, \dots, Z_{pn}$ are the resulting impedances at the point of bridge taps. They represent the association of two (2) impedances: the one reflected by the impedance of transmission line part ahead of the bridge tap and the other reflected by the bridge tap termination.

f) $Z_3, Z_4, \dots, Z(n+2)$ are the reflected impedances by the bridge taps (open transmission lines) at the points of bridge taps.

g) Z_2 is the impedance reflected by Z_{L2} .

h) $Z_{r2}, Z_{r4}, \dots, Z_{rn}$ are the reflected impedances by the impedance of the transmission line part ahead of bridge taps, at the points of bridge taps.

i) Z_{in} is the reflected impedance by the transmission line with the bridge taps, at the generator side.

BRIDGE TAPS LENGTH

Figure 3 shows bridge taps length for 26 AWG gauge (0.40 mm diameter) with polyethylene insulation (ANSI Standard) as a function of the frequency, where it's possible to get all theoretical frequencies corresponding to associated odd numbers multiple of $\lambda/4$ (a quarter part of the wavelength), for a determined physical bridge tap length. For these frequencies, the corresponding length represents a reflected impedance at the point of bridge tap tending to zero (0). Exemplifying, for 300 kHz, the approximate lengths of 156, 469 and 782 meters are related to $\lambda/4$, $3\lambda/4$ and $5\lambda/4$, respectively.

The resulting impedance tending to 0 (zero) represents a signal attenuation, due to the bridge tap. The reflected impedance of the bridge tap is a short circuit ($Z(n+2)=0$) at the point of bridge tap. The velocity of transmission (v_p) considered for simulations is the specific velocity for each frequency, proportional to the velocity of light in free space (3×10^8 m/s). For those bridge taps lengths, shown in Figure 3,

with 2 (two) or more critical frequencies indicated, it becomes implicit that the bridge tap has a big length so it's possible to have various wavelengths.

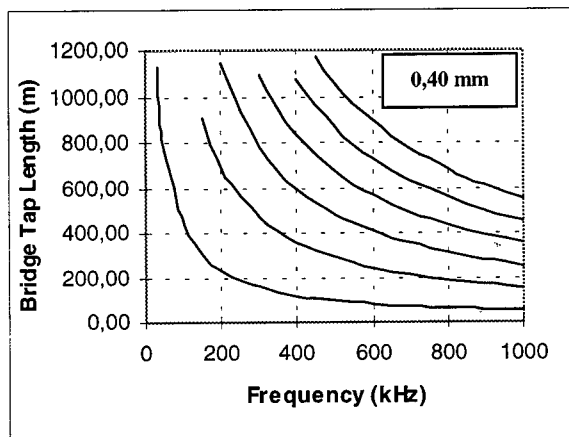


Figure 3 : Bridge Tap Length Associated to Odd Multiples Numbers of $\lambda/4$ ($d = 0.40$ mm).

The simulation was made for a transmission line with $L1=1000$ meters and $L2=1000$ meters, with the transmission of a CW signal (sine wave) between 2,5 kHz and 1 MHz.

For real cases, the velocity of propagation is different from the velocity of light and $v_p < c$.

Figure 4, equivalent to Figure 3, shows the curves for 24 AWG gauge (0.50 mm).

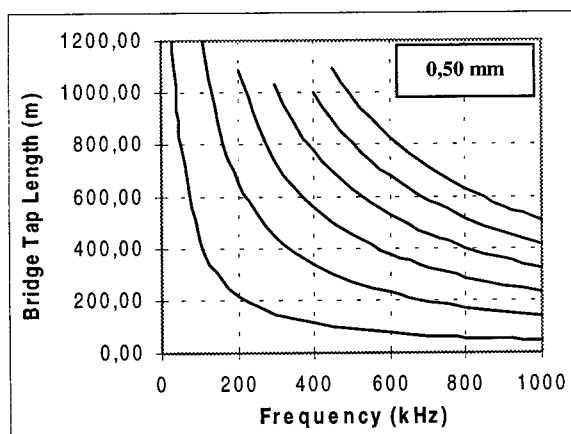


Figure 4 : Bridge Tap Length Associated with Odd Multiple Numbers of $\lambda/4$ ($d = 0.50$ mm).

It must be observed that changing the velocity of propagation in the transmission line, automatically, changes the frequency for which

the bridge tap lengths represent a short circuit with high losses.

When varying the conductors gauge there are different velocities of propagation (R , L , C and G vary with the frequency), and this represents different critical frequencies to the bridge taps.

TRANSMISSION LINE MISMATCHED

Transmission lines (copper pair, for instance) are mismatched when the load impedance is different from its characteristic impedance, so there is no total power transference to the load ($ZL2 \neq Z_0$).

The influence of $ZL2$ in bridge tap will depend on how mismatched the transmission line is ($ZL2$ value), the bridge tap length ahead bridge tap ($L2$) and on the physical and transmission characteristics of copper pair which constitute the transmission line.

The frequencies to which the impedance in the bridge tap tends to 0 (zero) will be, the frequencies caused by the bridge tap overlapped to those frequencies in which the mismatched implies in a critical reflected impedance, at the point of bridge tap.

When $ZL2 = \infty$ and $L2=L3$, for instance, the frequencies are the same.

The resulting impedance at the points of bridge taps when there are 2 bridge taps is a function of the reflected impedances by bridge taps terminations ($ZL3$ and $ZL4 = \infty$) and of the reflected impedances due to the mismatched of the transmission line ($ZL2 \neq Z_0$) (See Figure 3).

The values of the resulting impedances at the points of bridge taps will therefore depend on the position of bridge taps in the transmission line, on the $ZL2$ value and on the physical and transmission characteristics of transmission line, which result in its attenuation and velocities values.

The attenuation, due to bridge taps, will be much bigger the nearest of 0 (zero) the resulting impedances values at the point of bridge tap are ($Zp1$ and $Zp2$).

For very large bridge taps (bigger than 5λ), having the same characteristics of the transmission line wires, there is a plane attenuation of 3.52 dB (2/3 of the signal power).

BRIDGE TAPS THEORY

To analyse a bridge tap in a transmission line (twisted copper pair, for instance) we must have some transmission line parameters : wire gauge (d), spacing (S) between conductors, DC resistance (R_{cc}), relative magnetic permeability (μ_r), relative dielectric constant (ϵ_r) and material resistivity (ρ) or conductivity (σ). With this parameters it's possible to get the values of primary parameters (R , L , C and G) of the transmission line.

With some of this parameters below, it's possible to calculate the AC resistance (R_{ac}) due to the skin effect.

The proximity effect and the induction effect in adjacent circuits is too complex to calculate and, in case of induction, it depends on many factors, as the number of adjacent pairs, pair position in the cable, dielectric characteristics, etc. What can be done is simulate a resistance model which represents the resistance as a function of frequency.

Another hypothesis to data entrance, is the existence of tables with the standard values of the primary parameters (R , L , C and G) of the transmission line. The values must be put in the table according to the frequency.

Table 1 shows the values of the primary parameters for a wire with 26 AWG (0.40 mm) gauge, according to ANSI Standards.

F (kHz)	R (PE) (ohm/km)	L (PE) (mH/km)	C (PE) (nF/km)	G (PIC) (μ mho/ km)
10	280,01	0,59	50,00	0,53
20	280,11	0,59	50,00	0,97
30	281,00	0,59	50,00	1,38
40	281,75	0,58	50,00	1,76
50	282,72	0,58	50,00	2,15
100	290,43	0,58	50,00	3,93
150	302,07	0,57	50,00	5,59
200	316,39	0,56	50,00	7,18
300	349,17	0,55	50,00	10,21
500	417,43	0,53	50,00	15,93
700	481,18	0,51	50,00	21,35
1000	566,52	0,49	50,00	29,12

Table 1 : Primary Parameters of 0.40 mm (26 AWG) - Values ANSI.

With R , L , C and G values, it's possible to calculate the velocity of propagation V_p and the characteristic impedance of the transmission line.

Propagation constant (γ) has two parts : the real part is, by definition, the attenuation constant and the imaginary part is the phase constant of propagation constant, which is related to velocity of propagation of the signal travelling on the transmission line.

The loss (by attenuation), in dB, in the transmission line, can be given by following expression :

$$P(dB) = 20 \log \left(\left| e^{-\text{Re}(\gamma l)} \right| \right) \quad (2)$$

where " l " is the length of transmission line. The real part of γ is the attenuation constant of the transmission line.

The impedance at the generator side (Z_{in}) due to the transmission line will be :

$$Z_{in} = Z_0 \frac{1 + \rho e^{-2\gamma l}}{1 - \rho e^{-2\gamma l}} \quad (3)$$

where ρ is the reflection coefficient of the transmission line.

Now we can use the transmission line data to calculate the desired parameters. According to Figure 1, they are :

- $Z/2$: load impedance of the transmission line.
- $Z/3$: bridge tap impedance (∞).
- Z_g : generator impedance (135 ohms, for instance).
- V_g : voltage of generator.
- l_1 : transmission line length up to point of bridge tap.
- l_2 : transmission line length from point of bridge tap until load.
- l_3 : bridge tap length.

The impedance at the point of bridge tap (Z_{p1}) will be :

$$Z_{p1} = \frac{Z_2 Z_3}{Z_2 + Z_3} \quad (4)$$

where Z_2 and Z_3 are the impedances reflected by load and by bridge tap, respectively.

The input voltage (V_{in}) will be given by :

$$V_{in} = V_g \frac{Z_{in}}{Z_{in} + Z_g} \quad (5)$$

where Z_{in} is the input impedance, reflected by transmission line with bridge tap.

Therefore, to $L1$ part, we have the voltage V_0 of the signal propagating in the direction + of the transmission line given by :

$$V_0 = V^+ = \frac{V_{in}}{1 + \rho e^{-\gamma 2l_1}} \quad (6)$$

Therefore, the calculated voltage in any part of the transmission line between the generator and the point of bridge tap (V_x) will be, then, given by the expression :

$$V_x = V^+ (e^{-\gamma x} + \rho e^{-\gamma(2l_1 - x)}) \quad (7)$$

The voltage in the direction + ahead point of bridge tap (V^{++}), that is part $L2$ will be :

$$V^{++} = \frac{V(l_1)}{1 + \rho e^{-\gamma 2l_2}} \quad (8)$$

Therefore, the calculated voltage between the point of bridge tap and the load (V_y) will be, observing the equation (7) :

$$V_y = V^{++} (e^{-\gamma y} + \rho e^{-\gamma(2l_2 - y)}) \quad (9)$$

Then the expression (9) can be used to calculate the final load voltage, changing the frequency and others transmission line parameters, for instance, the lengths $L1$ and $L2$. As the parameters are optional to the user, then the bridge tap length ($L3$) can be equal to zero (0) and, evaluate the load voltage without bridge taps. Now, inserting any bridge tap, we can calculate the new load voltage with the

presence of a bridge tap in the transmission line. The resulting difference is the loss due to the bridge tap.

To obtain the resulting load voltage, in dB, we have :

$$V_y (dB) = 20 \log(|V_y|) \quad (10)$$

We will obtain the voltage as a function of frequency and others parameters of the transmission line.

To analyse a transmission line with 2 or more bridge taps, the proceeding follows the same steps presented to the analyses of a bridge tap.

LOSSES DUE TO BRIDGE TAPS

The electromagnetic losses in a transmission line are due to, essentially, the attenuation presented by the signal transmitted due to the loop resistance and the presence of bridge taps in the line, therefore, function of transmission line and bridge taps lengths. Second order losses, such as discontinuities through the transmission line, gauge changes, splices, connections, impedance mismatching, represent, in general, small values.

Figure 5 shows the loss in a transmission line due to a signal which is propagating with the typical velocity of propagation of twisted pairs. The velocity of propagation considered to the simulation changes with the frequency of the signal in the transmission line. The length of the simulated transmission line is 2000 meters and the loss values shown, are exclusively due to the presence of bridge tap. The length of the bridge tap is 150 meters and the Figure shows the losses, as a function of frequency, to 0.40 mm (280,0 ohms/km) and 0.50 mm (179,0 ohms/km) diameters of a copper pair with polyethylene insulation (PE) ANSI Standard. The bridge tap is located 1000 meters from the generator.

The transmission line is terminated with a resistive impedance which value is the same to the value of characteristic impedance of the line, to high frequencies.

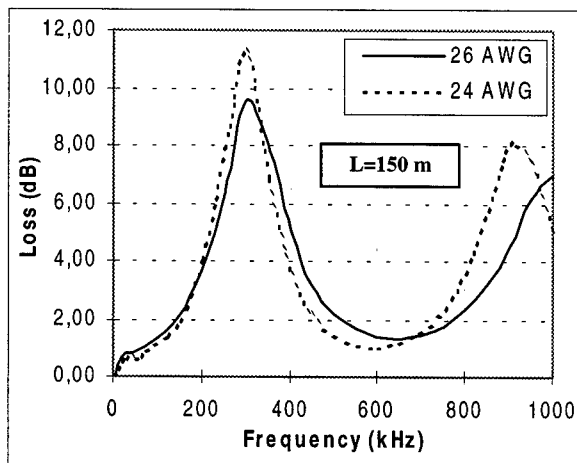


Figure 5 : Loss Due to Bridge Tap in a Transmission Line.

Figure 6 shows the loss in the transmission line defined in Figure 5 above, but now the bridge tap length is 200 meters. The Figure 6 shows the losses as a function of frequency for 26 AWG (0.40 mm) and 24 AWG (0.50 mm) gauges.

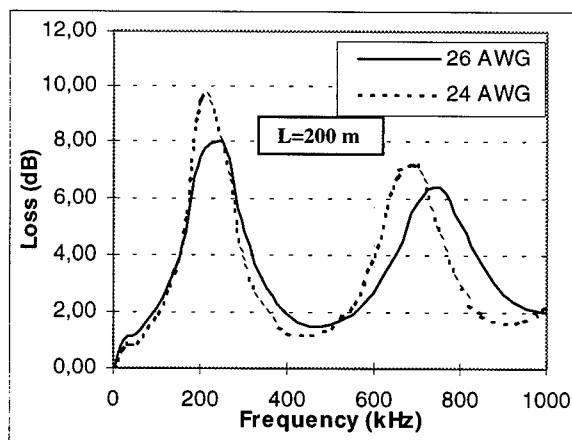


Figure 6 : Loss Due to Bridge Tap in a Transmission Line.

The loss in a transmission line exclusively due to the presence of 2 (two) bridge taps is, in practice, the sum of the loss of each of the bridge taps.

BRIDGE TAPS IN ISDN BASIC ACCESS, HDSL AND ADSL SYSTEMS

The frequencies of 40, 150 and 300 kHz are associated with the spectrum and the test frequency of the ISDN Basic Access, High-Bit-Rate Digital Subscriber Lines (HDSL) and Asymmetric Digital Subscriber Lines (ADSL) systems.

Figure 7 shows the loss in a transmission line with wires that have a diameter of 0.40 mm (26 AWG) and 0.50 mm (24 AWG), or the loop resistance of 140.2 and 89.5 ohms/km, respectively, in low frequency with polyethylene (PE) insulation from ANSI Standard and 26 AWG with plastic (PIC) insulation (135.1 ohms/km) and paper insulation (135.2 ohms/km). The simulated transmission line has a termination of 135 ohms resistive, a length of 2000 meters and the values of the losses are exclusively due to the presence of the bridge tap. The transmitted signal frequency is 40 kHz and the Figure 7 shows the losses according to the bridge tap length for a propagation velocity V_p whose value is a function of the signal frequency and cable characteristics of the transmission line.

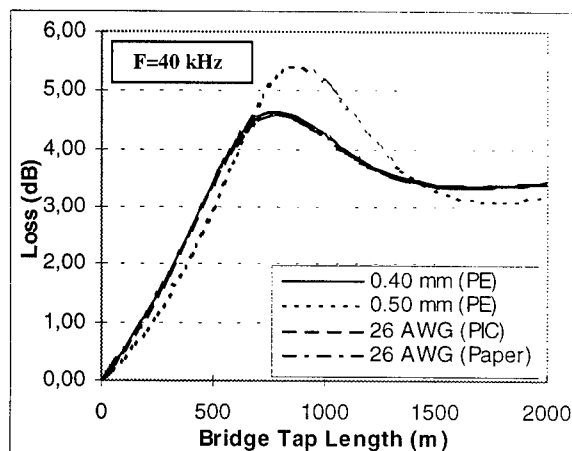


Figure 7 : Loss Due to Bridge Tap in a Transmission Line (40 kHz).

Figure 8 shows the loss in a transmission line with wires that have a diameter of 0.40 mm (26 AWG) and 0.50 mm (24 AWG), or the loop resistance of 140.2 and 89.5 ohms/km, respectively, in low frequency with polyethylene (PE) insulation from ANSI Standard and 26 AWG with plastic (PIC) insulation (135.1 ohms/km) and paper insulation (135.2 ohms/km). The simulated transmission line has a termination of 135 ohms resistive, a length of 2000 meters and the values of the losses are exclusively due to the presence of the bridge tap. The transmitted signal frequency is 150 kHz and the Figure 8 shows the losses according to the bridge tap length for a propagation velocity V_p whose value is a function of the signal frequency and cable characteristics of the transmission line.

CONCLUSION

This paper showed the theoretical curves with the losses due to bridge taps in a transmission line and helped in the analysis of copper pairs networks used in ISDN Basic Access and xDSL systems.

This paper established the analysis procedures and the choice of copper pairs of the metallic networks configured with bridge taps, taking into consideration the transmission of digital signals of the Basic Access of ISDN-Narrowband and xDSL systems.

The paper presented a study about bridge taps in copper pairs and its contribution to the total loss of the transmission line when ISDN-NB Basic Access or xDSL systems are used.

It also established conditions to take advantage of the telephonic networks of copper pairs, which are now existent, without necessarily the exclusion or removal of eventual bridge taps.

It also showed that, for very large bridge taps (bigger than 5 times the length of the wave λ), having the same characteristics of the wires that make the main transmission line, there is a plane attenuation of 3.52 dB (2/3 of the signal power).

REFERENCES

- 1 "ISDN Basic Access Digital Subscriber Lines" - Technical Reference - TR-TSY-000393 - Bellcore
- 2 "Transmission and Multiplexing (TM), High-Bit-Rate Digital Subscriber Line (HDSL) Transmission System on Metallic Local Lines; HDSL Core Specification and Applications for 2048 kbit/s Based Access Digital Sections Including HDSL Dual-Duplex Carrierless Amplitude Phase Modulation (CAP) Based System" - Technical Report - 1995 - ETSI
- 3 "Network and Customer Installations Interfaces - Asymmetric Digital Subscriber Lines (ADSL) Metallic Interface" - T1.413-1995 - ANSI
- 4 Lazarini, R., Zaina, Cláudio M., "Transmission Parameters in Copper Networks", CPqD - Telebrás, PD.12.AT.GER.0002A/RT-05-AB. 63p., 1994.

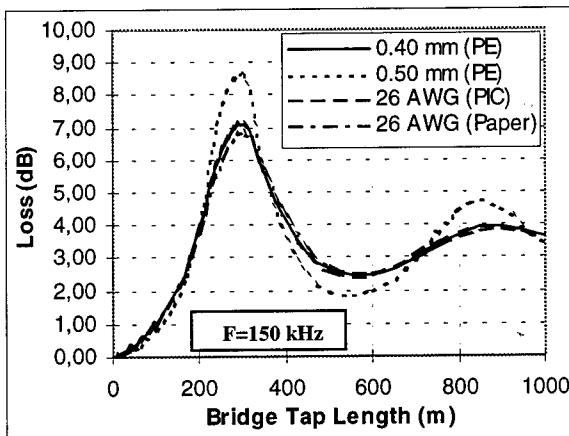


Figure 8 : Loss Due to Bridge Tap in a Transmission Line (150 kHz).

Figure 9 shows the loss in a transmission line with wires that have a diameter of 0.40 mm (26 AWG) and 0.50 mm (24 AWG), or the loop resistance of 140.2 and 89.5 ohms/km, respectively, in low frequency with polyethylene (PE) insulation from ANSI Standard and 26 AWG with plastic (PIC) insulation (135.1 ohms/km) and paper insulation (135.2 ohms/km). The simulated transmission line has a termination of 100 ohms resistive, a length of 2000 meters and the values of the losses are exclusively due to the presence of the bridge tap. The transmitted signal frequency is 300 kHz and the Figure 9 shows the losses according to the bridge tap length for a propagation velocity V_p whose value is a function of the signal frequency and cable characteristics of the transmission line.

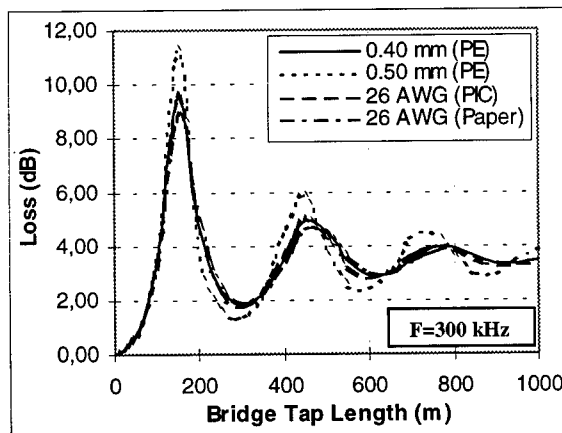


Figure 9 : Loss Due to Bridge Tap in a Transmission Line (300 kHz).



Reginaldo Lazarini
Foundation CPqD
Telco R&D Center
Campinas /SP Brazil
Email :
jeregis@cpqd.com.br
Tel. +55 19 705-6283
Fax +55 19 705-6699

Reginaldo Lazarini is a Telecommunications Engineer and a Researcher at CPqD Foundation - Telecommunications Research and Development Center, Brazil. He was born in 1955. He received his engineer degree (BS) in Telecommunications Engineering from Universidade Estadual de Campinas (UNICAMP) and received the MS degree from Instituto de Pesquisas Espaciais (INPE). He has worked in CPqD since 1985 and he has engaged with EMI/EMC and new technologies for copper networks. He worked in a technical cooperation project with IBM-Brazil to characterize and evaluate the IBM semi-anechoic chamber. Now he is the coordinator of Copper Networks for ISDN and xDSL Project. He is working with ADSL systems for INTERNET services in São Paulo Telco Company. He is a Brazilian delegate in ITU-T SG-6 (Outside Plant) for question 4 - Copper Networks for New Services (ISDN, ADSL/HDSL, etc) and he presented various contributions in this area.

Investigation of the multipurpose loss calculation algorithm for Integrated Services Digital Network (ISDN) management system

**Satoru Kanbayashi^{*1}, Haruo Oishi^{*1}, Nobuo Kuwaki^{*1}, Kazunari Watanabe^{*2}
and Kazuhisa Takahashi^{*2}**

**^{*1}Access Network Service Systems Laboratories
Nippon Telegraph and Telephone Corporation
Chiba-shi, Chiba 261-0023, Japan**

**^{*2}Saitama Branch
Nippon Telegraph and Telephone Corporation
Urawa-shi, Saitama 336-0015, Japan**

ABSTRACT

An algorithm has been developed for calculating the loss in a subscriber line in order to determine whether ISDN can be provided over the line. The line loss is the main factor determining whether ISDN can be provided. This algorithm can calculate the loss in a complicated subscriber line with several bridged taps. It is based on 1) the theoretical calculation of the loss in a four-pole network, 2) programming with recursive calls, and 3) the definition of the attributes of the subscriber-line facilities as a matrix. This algorithm has been used successfully in the ISDN management system at NTT's Saitama branch since December 1998.

INTRODUCTION

As the demand for ISDN continues to grow in Japan, NTT will have to evaluate the capability of more and more lines to handle ISDN. Three factors must be evaluated: the loss, the direct current resistance, and the distance between the NTT building and the subscriber. If the loss is too high, and the line has at least one

bridged tap, disconnecting one or more of them will decrease the loss. However it can be very difficult to calculate the loss accurately, because a subscriber line can have many bridged taps to provide flexibility in accommodating connection. The more accurate the calculation, the more efficiently the disconnections can be made.

We have thus developed an ISDN management system with a multipurpose loss-calculation algorithm. This algorithm use the theoretical loss in a four-pole network and a more complex calculation to calculate the loss more accurately than do current methods.

In this paper we first describe the principle of our multipurpose loss-calculation algorithm. Next, we show the primary line constants and the secondary constants used in the algorithm. We then evaluate how well our algorithm calculates the loss. Finally, we describe the management system that uses this new algorithm.

ALGORITHM PRINCIPLE

Our algorithm calculates the loss accurately by using a simple program comprising about 500 lines. It is based on: 1)

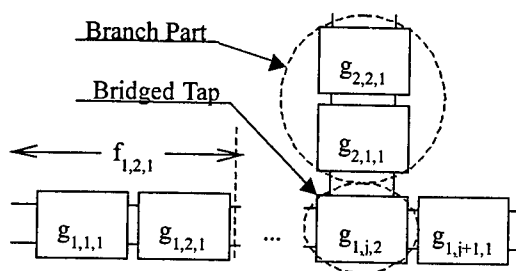


Fig. 1. Subscriber-Line Model

the theoretical calculation of the loss in a four-pole network, 2) programming with recursive calls, and 3) the definition of the attributes of the subscriber-line facilities as a matrix.

A subscriber-line model with bridged taps is shown in Fig. 1. It contains a set of some four-pole networks. The networks are grouped according to cable type in order to calculate the constants needed for the calculation. In the figure, $g_{1,j,2}$ is a bridged tap and a four-pole matrix. The calculated four-pole constants give the loss value of the subscriber line.

Figure 2 shows the four-pole network model. The Four terminal constants of the network are A, B, C, and D:

$$\begin{aligned} A &= D = \text{Cosh}(\gamma l), \\ B &= Z_c \text{Sinh}(\gamma l), \\ C &= Z_c^{-1} \text{Sinh}(\gamma l), \end{aligned} \quad (1)$$

and

$$\gamma = \alpha + j\beta, \quad (2)$$

where Z_c , α and β are secondary constants and α , β , and Z_c are the image attenuation constant, the image phase constant, and the image characteristic impedance, respectively. A matrix of all the facility attributes is shown as a multiplication of matrices. Equation (1) shows that the four-terminal constants can be derived from the secondary constants. The recursive calls used in the algorithm are a set of simple equations based on the subscriber line model in Fig. 1. The basic function for a recursive call is

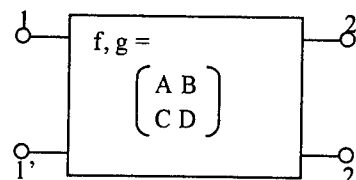


Fig. 2. Four-Pole Network Model

shown as $g_{i,j,k}$, where j means the matrix for the j th network from the beginning of the subscriber line or the bridged tap, and i means the i th branch. When coefficient k is 0, the four-pole network is a termination network. When k is 1, the network is neither a bridged tap nor a termination. When k is greater than 1, the network is the k -1th bridged tap. The synthesized matrix from the first four-pole network to the j th one is

$$f_{i,j} = f_{i,j-1} g_{i,j,k}. \quad (3)$$

The matrix for the entire subscriber line is

$$f_{i,j_{\max}} = f_{i,j_{\max}-1} g_{i,j_{\max},k}, \quad (4)$$

where j_{\max} means that the unit is a termination. The synthesized matrix of a branch is transformed into a matrix before the unit branches. The function for this transformation is

$$g_{i,j,k} = h(f_{k,j_{\max}}). \quad (5)$$

The function f is

$$\begin{aligned} f_{i,j} &= f_{i,j-1} h(f_{i,j_{\max}}) & (k > 2) \\ f_{i,j} &= f_{i,j-1} g_{i,j,k} & (k = 1) \\ f_{i,j} &= f_{i,j-1} \times 1 & (k = 0) \end{aligned} \quad (6)$$

where the function at $k > 2$ represents a recursive call. This programming with recursive calls gives an accurate loss value for a complicated subscriber line.

A subscriber-line matrix is defined to simplify the programming. Each unit of the subscriber line, as shown in Fig. 1, has a matrix of attributes: the cable type, diameter, and

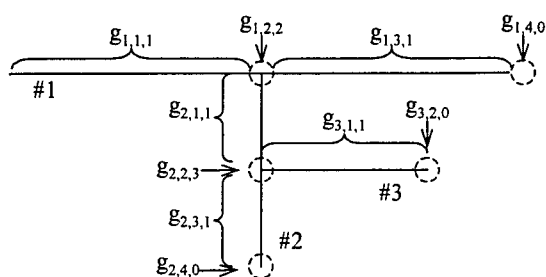


Fig. 3. Subscriber-Line Matrix Model

Table 1 Example of Subscriber Line Matrix

$g_{i,j,k}$	Length	Type	Diameter
$g_{1,1,1}$	l_1	Type ₁	ϕ_1
$g_{1,2,2}$	l_0	Type ₀	ϕ_0
$g_{1,3,1}$	l_2	Type ₂	ϕ_2
$g_{1,4,0}$	l_0	Type ₀	ϕ_0
$g_{2,1,1}$	l_3	Type ₃	ϕ_3
$g_{2,2,3}$	l_0	Type ₀	ϕ_0
$g_{2,3,1}$	l_4	Type ₄	ϕ_4
$g_{2,4,0}$	l_0	Type ₀	ϕ_0
$g_{3,1,1}$	l_5	Type ₅	ϕ_5
$g_{3,2,0}$	l_0	Type ₀	ϕ_0

length. It also includes coefficient k , indicating the position of the network.

A simple example of a subscriber-matrix is shown in Fig. 3 and Table 1. The table shows the matrix for each $g_{i,j,k}$ in Fig. 3. In the terminations and bridged taps, the cable length, type, and diameter are meaningless.

PRIMARY LINE CONSTANTS AND SECONDARY CONSTATS

The four terminal constants require secondary constant, but secondary constants of the cables installed in Japan are unknown. The only attributes we can get are the length diameter, and type. We thus use typical values for the secondary constants to calculate the four terminal constants for NTT's existing cables.

To calculate the secondary constants,

the primary line constants are required^[1]. The primary line constants are calculated using the equations in Draft ITU-T Recommendation G.996.1^[2]. The primary line constants are R , L , G , and C , which are shown in Ω/km , $\mu\text{H}/\text{km}$, $\mu\text{S}/\text{km}$, and nF/km , respectively, all at a temperature of 20°C .

$$R = (\text{roc}^4 + \text{ac} \times f^2)^{1/4},$$

$$L = \text{xa} + \text{xb} \times f^{1/2} + \text{xc} \times f^{1/3},$$

$$G = \omega \text{Ctan} \delta, \quad (7)$$

$$C = 45 \times 10^{-12}.$$

The f is shown in kHz. Typical coefficient values for two types of calls are shown in Table 2.

EVALUATION

We evaluated the performance of our algorithm by comparing the estimated loss with the experimentally measured loss for the model shown in Fig. 3. The conditions shown in Table 1 were $l_1=800$ m, $l_2=800$ m, $l_4=l_5=0$ m, and $\phi_1=\phi_2=\phi_3=0.4$ mm. Type₁, Type₂, and Type₃ were formed polyethylene insulated cable. The length of the branch #2 cable was 0, 100, 400, or 500 m. The temperature was 20°C . Table 3 shows the typical coefficients for the primary line constants of formed polyethylene insulated cable.

As shown in Fig. 4, the estimated loss was close to the measured loss in all four cases. The differences were due to use the typical secondary constants values. These results show that this algorithm is accurate enough to manage line facilities.

MANAGEMENT SYSTEM

For an ISDN management system to be practical, a receptionist or an operator must be able to operate it without any special

Table 2 Coefficient for Primary Line Constants in ITU-T Draft G.996.1

Cable Type		roc	ac	xa	xb	xc	tanδ
Paper	0.4 mm	2.688×10^{-1}	2.267×10^{-13}	6.834×10^{-7}	-2.094×10^{-10}	7.205×10^{-10}	2.500×10^{-2}
	0.5 mm	1.724×10^{-1}	9.374×10^{-14}	7.351×10^{-7}	1.930×10^{-11}	-2.330×10^{-9}	2.500×10^{-2}
	0.65 mm	1.041×10^{-1}	2.787×10^{-14}	8.006×10^{-7}	2.696×10^{-10}	-5.340×10^{-9}	2.500×10^{-2}
	0.9 mm	5.589×10^{-2}	7.180×10^{-15}	8.304×10^{-7}	5.111×10^{-10}	-8.161×10^{-9}	2.500×10^{-2}
Polyethylene	0.32 mm	4.175×10^{-1}	6.998×10^{-13}	6.003×10^{-7}	-3.919×10^{-10}	3.081×10^{-9}	4.000×10^{-4}
	0.4 mm	2.714×10^{-1}	1.705×10^{-13}	7.257×10^{-7}	-2.059×10^{-10}	9.678×10^{-10}	5.000×10^{-4}
	0.5 mm	1.742×10^{-1}	7.346×10^{-13}	7.618×10^{-7}	-1.547×10^{-11}	-1.656×10^{-9}	5.000×10^{-4}
	0.65 mm	1.048×10^{-1}	2.436×10^{-14}	8.139×10^{-7}	2.354×10^{-10}	-4.801×10^{-9}	5.000×10^{-4}
	0.9 mm	5.630×10^{-2}	6.486×10^{-15}	8.407×10^{-7}	4.816×10^{-10}	-7.721×10^{-9}	5.000×10^{-4}

Table 3 Coefficient for Primary Line Constants in Experiments

Cable Type		roc	ac	xa	xb	xc	tanδ
Formed Polyethylene	0.4 mm	2.717×10^{-1}	1.607×10^{-13}	7.283×10^{-7}	-2.428×10^{-10}	1.446×10^{-9}	4.501×10^{-4}

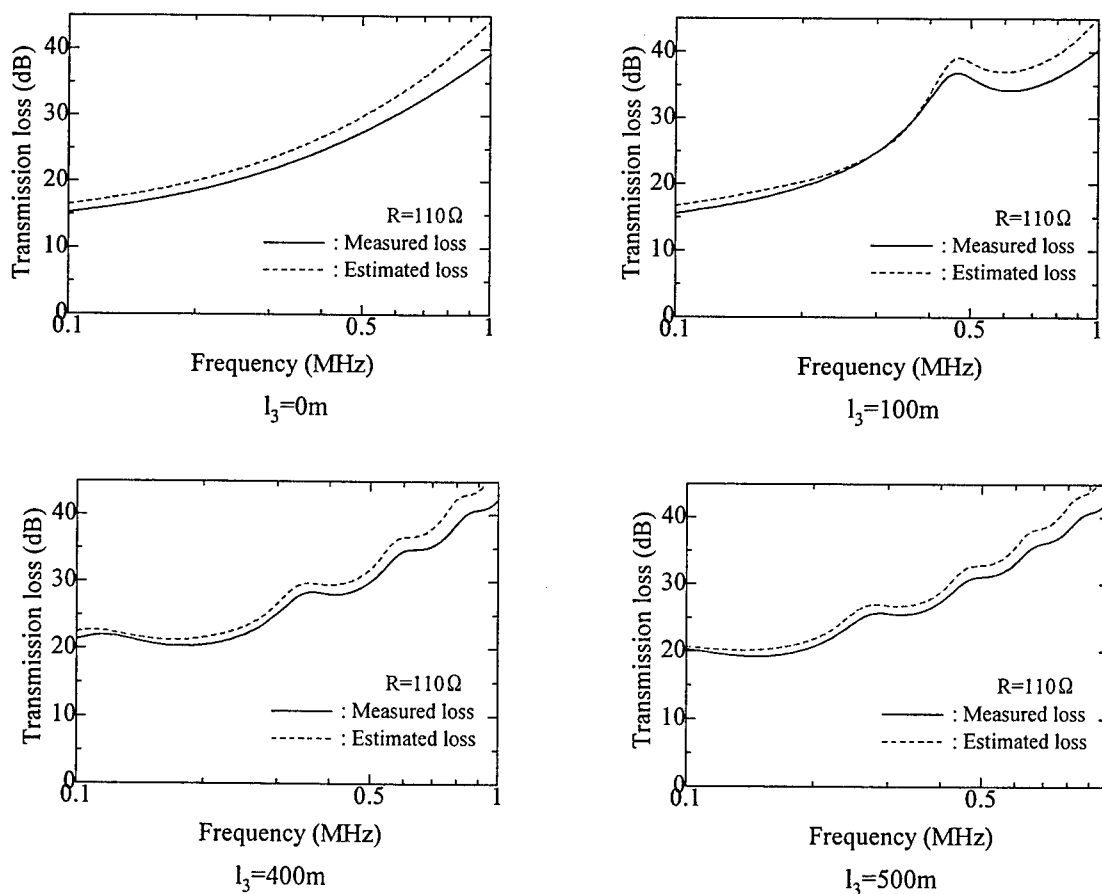


Fig. 4 Comparison with Experience

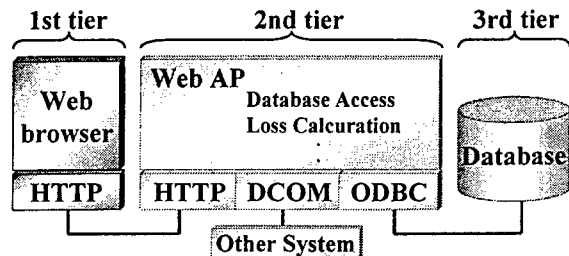


Fig. 5 Block Diagram of Management System

knowledge or skills. The system must therefore have a simple interface, be easy to maintain and provide a quick response. We have implemented such a management system.

Figure 5 shows a block diagram of our ISDN management system. It is composed of three tiers. The first tier is a web browser client. The second tier is an application server. The third tier is a database of the facilities. The first tier is connected with the second tier by the hyper text transfer protocol (HTTP.) The second tier is connected with the third tier by the open database connectivity (ODBC) interface. The application server has a distributed component object model (DCOM) interface. Other systems can use the loss-calculation an algorithm as distributed object model.

The system has several management functions. The main ones are providing the operator with a web browser interface, locating data in the database automatically, and automatically indicating which bridged taps should be disconnected. It selects which taps to disconnect based on the loss required and the distance of the taps from the maintenance office. These functions are simple to operate.

CONCLUSION

This algorithm has been used in the ISDN management system at NTT's Saitama branch since December 1998. The results show that it is very effective in the practical management of an ISDN.

We are now testing the use asymmetric digital subscriber line system.

ACKNOWLEDGEMENTS

We are grateful Mr. Fukuo Kobayashi and Mr. Shigemi Asakura for their helpful discussions.

REFERENCE

- [1] The institute of Electronics, Information and Communication Engineers, "Transmission theory of communication line," 1979 (in Japanese).
- [2] ITU, "TEST PROCEDURES FOR DIGITAL SUBSCRIBER LINE (DSL) TRANSCEIVERS," Draft ITU-T Recommendation G.996.1.

BIOGRAPHIE



Satoru Kanbayashi is a 1997 graduate of Hokkaido University where he received his B.S. and M.S. in Civil Engineering. He has worked in NTT Access Network Service Systems Laboratories since 1997.

A NEW TYPE OF HIGH FIBER COUNT, LOW DIMENSION OPTICAL CABLE WITH SIMPLIFIED INSTALLATION CHARACTERISTICS

Stefan Pastuszka¹, JeanPierre Bonicel², Marta Garcia S. Emeterio³,
Pierre Gaillard⁴, Klaus Nothofer¹, and Alexander Weiss¹

¹ALCATEL Kabel AG & Co, Mönchengladbach, Germany

²ALCATEL Cable, Clichy, France

³ALCATEL Cable Ibérica, Maliano, Spain

⁴ALCATEL OFCCC, Claremont NC, USA

ABSTRACT

Cables with very small semi-tight buffered tubes containing up to 12 optical fibers per unit have been developed. These tubes are made of soft thermoplastic material with significantly improved strippability compared to traditional loose-tube buffers. The diameter of the tubes could be reduced to nearly 50% of a comparable loose-tube. Due to their flexibility, they significantly simplify the handling of the cable, e.g., for routing in splice boxes or for mid-span access. However, when using this kind of tubes, a completely different cable construction comes into consideration. The new cable type is presented and compared to the standard loose-tube cables. It fulfills almost the same requirements as the well-established cable constructions and is especially suited for use as access cable, riser cable, etc., where low dimensions are essential. However, the fibers in loose tubes being totally free, the loose-tube cable constructions are still considered the most appropriate solution for long distance application in terms of long-term reliability.

INTRODUCTION

Due to the deregulation of the telecom market in Europe, a large number of new network operators is emerging. These new operators have to build their own networks or to rent dark fibers from other providers. A key factor for the new operators to be successful in this business is the possibility to install their networks quickly and at low cost. Since, especially in cities, the traditional installation methods are contrary to this objective, alternatives enabling fast implementation of fiber optic networks have to be applied.¹ This includes the usage of small existing ducts, sewer sys-

tems², etc. However, the development of such new rights of way implies the trend to optical cables with a drastically increasing fiber density showing accordingly a small diameter.³

In the course of this evolution, cables with reduced diameter and simplified installation behaviour have been developed. Their low dimensions allow to implement high fiber capacity in tight spaces while the installation time (for, e.g., cable access and splicing) and therefore the cost is significantly reduced. These cables are based on very small and flexible semi-tight buffered tubes containing up to 12 optical fibers. These FlexTubes™ are protected by a jacket construction which works without a central strength member. In this paper, the design of the cable is described and compared to common loose tube cables. We focus on the main performance parameters as well as on the easier installation of the new cable type.

CABLE DESIGN

Presently, the standard for fiber optic cables used in long-distance or access networks is set by the well known and proven loose tube design. In this type of cable, the optical fibers are loosely contained in tubes which are stranded around a central strength element. This allows for a certain amount of longitudinal elongation and compression of the cable, since the fibers inside the tubes may move radially inwards or outwards from their equilibrium position as soon as the cable is subject to longitudinal forces. Thus, inside a certain range of forces, no fiber strain will occur. However, this basic principle imposes a lower limit on the size of a loose tube cable.

When attempting to further reduce the diameter of fiber optic cables or to increase the fiber count

at a given cable size, new designs like, e.g., ribbon or central tube cables could be employed. Nevertheless, to achieve miniaturization and simultaneously keep the advantages of the loose tube cables regarding easy identification and handling of the different subunits as well as usage of standard splicing equipment, we developed a new cable design based on very small semi-tight buffered tubes. Moreover, this new design overcomes the disadvantages of the standard loose tube cables which are the poor stripability and stiffness of the tubes as well as their "long-term memory" due to the stranding pitch.

Semi-tight buffered tube design

Figure 1 shows cross sections of a typical loose tube and one of the newly developed semi-tight buffered tubes, each containing 12 optical fibers.

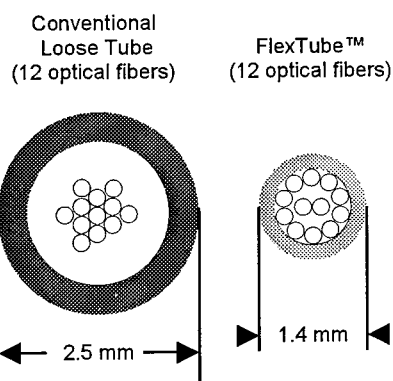


Fig. 1: Comparison of a conventional loose tube to a semi-tight buffered tube, each containing 12 optical fibers

In both cases the tubes are filled with a gel to ensure longitudinal watertightness of the tube. The semi-tight buffered tube has an outer diameter of only 1.4 mm and a wall thickness of 0.2 mm. In comparison to conventional loose tubes, the total cross section of the tube is reduced by approximately 70%. In other words, this way the fiber density is increased by a factor of 3.2 to approximately 8 fibers/mm². While the materials routinely used for the production of loose tubes are relatively rigid, very soft thermoplastic material with a low elongation at break has been chosen for the semi-tight buffered tube.⁴ Consequently, the tube is highly flexible and can be easily stripped even by fingernails. The softness of the tube material also reduces the risk of attenuation increase due to microbending losses

Cable construction

When using semi-tight buffered tubes made from soft material, a completely different cable layout as compared to the common loose tube cables

comes into consideration. Since the tubes are comparatively sensitive to perpendicular forces, the combination of a central strength element to which the tubes are fixed by binders does not apply. Thus, the cable core was chosen to be loose and to be confined by a jacket which contains compression resistive elements. To keep the cable completely dielectric, fiber reinforced plastic (FRP) rods were selected. However, in cases where a completely dielectric structure is not mandatory, also metallic elements may be used. Figure 2 shows the cross section of such a cable containing 144 optical fibers. The tubes

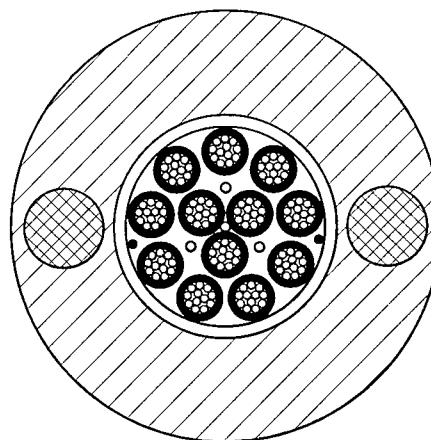


Fig. 2: Cross section of a 144 fiber cable containing 12 semi-tight buffered tubes with 12 fibers each.

inside the cable core may be either stranded SZ or helically with a long pitch. The cables according to this design are preferably dry-core cables in which the longitudinal watertightness is achieved by the application of water swellable elements. The two radial strength members which are embedded in the cable jacket serve for both the compression resistance and the tensile strength of the cable. If higher tensile strengths are required, additional strain bearing elements (e.g. aramide yarns) may be applied over the cable core. Depending on the application of the cable, a proper balance can be selected to provide a certain tensile strength and keep the diameter of the cable small at the same time. Figure 3 shows the dimensions of the basic cable type without additional strain bearing elements like displayed schematically in Fig. 2. In these cables, the size of the radial strength members was selected in a way to make them suitable both for blowing and pulling installation techniques (compare also the physical properties given in Table 1). With these parameters, the relative advantage concerning size and weight compared to loose-tube cables is more significant in the region of high fiber count (approx. 100 and

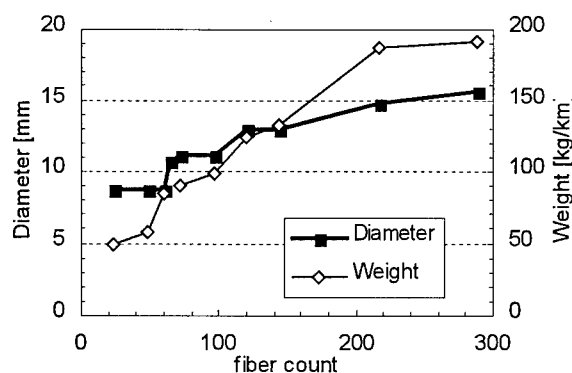


Fig. 3: Diameter and weight of the cable design without aramide yarns, the tensile strenght being achieved via the radial strength members – suitable for blowing and pulling installation.

higher) while the dimensions are of the same order for low fiber count. For cables specially adapted to the low forces occurring during blowing processes, the overall cable diameter could be reduced by up to 2 mm.

Generally, the design of the newly developed cables combines the advantages of the loose-tube cables (fibers protected in tubes which are easily identified) and the central tube cables (the absence of a central strength member simplifying, e.g., mid-span access).

MAIN PERFORMANCE PARAMETERS

Careful testing of several cables of the type described above shows that they have a comparable performance like the common loose tube designs. In this section we focus on the most relevant tests for the new cable design like temperature and tensile performance. The specified main performance parameters are listed in table 1 according to the european normative standard EN 187000.

Table 1: Main performance parameters

Parameter	Value
Attenuation 1310 nm	≤ 0.35 dB/km
1550 nm	≤ 0.25 dB/km
Bending radius static	10 × cable O.D.
dynamic	20 × cable O.D.
Tensile performance (short term)	1.5 × kilometric weight
Temp. range installation	-10 ... 50 °C
operation	-30 ... 70 °C
Crush resistance	25 daN

Standard single mode fibers (ALCATEL Color-Lock™) being used in the manufactured cables, the specified values of attenuation could be easily kept. The attenuation was measured after each step of the manufacturing process. The average attenuation was found to be not increased compared to the original fiber values. At a wavelength of 1550 nm the attenuation of the cabled fibers was measured to be lower than 0.22 dB/km.

The most critical issue for the new cable design using semi-tight buffered tubes as described above is the performance at low temperatures. Since the fibers do not have space inside the tubes to compensate longitudinal contraction of the cable like in conventional loose tube designs, the temperature performance must be achieved by different measures. Firstly, the dimension of the compression resistive elements in the cable jacket must be properly selected to keep the jacket contraction at a minimum. Secondly, the gap between the cable core and the inner surface of the jacket has to be carefully adjusted in order to limit fiber bending/microbending losses due to core movement caused by temperature changes. Moreover, the greatest challenge in producing this type of cable is to adjust the process parameters of the jacketing operation to ensure the core being relaxed after the initial shrinkage of the jacket. The core tension and the tension of the radial strength members have thus to be carefully chosen during the process. Without the core being relaxed, the cable would show a limited tensile performance.

Temperature cycling tests according to the Bellcore GR-20 standard reveal that the cable performance is good even at low temperatures for a carefully balanced cable layout. The results of attenuation measurements carried out on a 144 fiber cable in a climatic chamber are displayed in Figure 4. The change of attenuation is related to the initial values taken at +20 °C. The filled symbols represent the average over the ensemble of measured fibers (the error bars correspond to the standard deviation) and the open symbols indicate the maximum values measured on individual fibers (accuracy ± 0.004 dB/km). Two temperature cycles were performed subsequently. It can be seen that the change of attenuation is comparatively high at -40 °C and negligible for all other temperatures. However, also the change of attenuation at -40 °C is well compliant with the Bellcore specification (average change lower than 0.05 dB/km, change on individual fibers lower than 0.15 dB/km). Consequently, a working temperature range of -30 °C to +70 °C can be readily

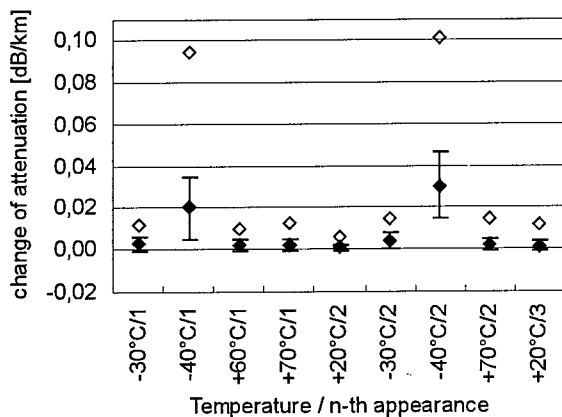


Fig. 4: Temperature cycling of a 144 fiber cable according to the new design. The relative change of attenuation related to the attenuation at 20 °C (average and maximum values) are displayed as a function of temperature and cycle number.

granted. Results obtained on other cables show the same overall behaviour.

To be sure about the temperature stability of the cables, a long-term heat aging test was carried out according to the Bellcore GR-20 specification. This test allows a maximum permanent attenuation increase of 0.05 dB/km for the average and 0.15 dB/km for individual fibers at 1550 nm after 168 hours at 85 °C. With a permanent attenuation increase lower than 0.01 dB/km (maximum values), the tested cables fulfill this requirement very well.

Another temperature cycle was performed directly after the heat aging test following the same temperature profile as described above. The results at -40 °C were better compared to the values measured prior to the heat aging. The reason for this behaviour is most probably a further relaxation of the core.

Apart from low-temperature induced contraction of the cable, its tensile performance is of great interest. Since there is theoretically no tube excess length in the cable core, the range of zero fiber elongation when pulling on the cable is limited. However, by carefully selecting the size of the FRP rods which act as strain bearing elements, the specified tensile performance can be easily kept. As an example, we discuss the tensile test carried out on the 144 fiber cable for which the temperature cycling results were already displayed in Figure 4. The tensile strength was tested according to EN 187000/501. According to the cable weight of approx. 130 kg/km a force of $T_{\max} = 2000$ N was applied. The testing standard requiring no residual attenuation after the test and a fiber elongation lower than 5 ‰ at T_{\max} , the cable is very well compliant with a fiber

elongation of 2.0 ‰. With the 2000 N applied, the elongation of the cable amounted to 3.4 ‰, the change of attenuation in this situation being less than 0.01 dB/100m. A residual attenuation after relaxation of the cable could not be observed.

INNOVATIVE ACCESS METHOD

As already mentioned in the introduction, a key advantage of the new cable design with semi-tight buffered tubes is its quick and easy installation behaviour. This is because of the easy cable access on the one hand, and due to the flexibility and excellent handleability of the semi-tight buffered tubes on the other hand.

Our experiments show that there are several ways of fast cable access on the new design. One of these is the following: First, the cable is cut or shaved along the FRP rods like shown in Figure 5. Afterwards, a ring cut is placed around

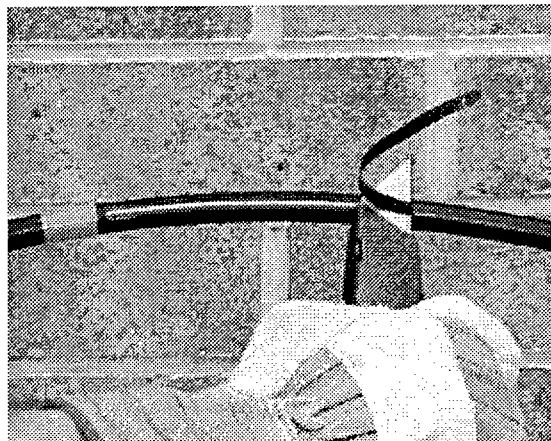


Fig. 5: Removal of the jacket material over the FRP rods.

the cable at a given position. Since the jacket material is thin on the inner side of the FRP rods, it is now easy to grip the jacket with a plier and to remove the two shells of jacket above and below the plane defined by the FRP rods. This easy way to remove the jacket is displayed in Figure 6. The procedure is also applicable for midspan access where two ring cuts have to be placed and the jacket material over the FRP rods is cut on the distance in between these ring cuts. After cutting the FRP rods to length and removing the swella-ble materials, the cable is ready for installation in, e.g., splice boxes. Figure 7 shows a cable prepared for midspan access.

Because of the flexibility of the semi-tight buffered tubes, they can be easily routed inside splice

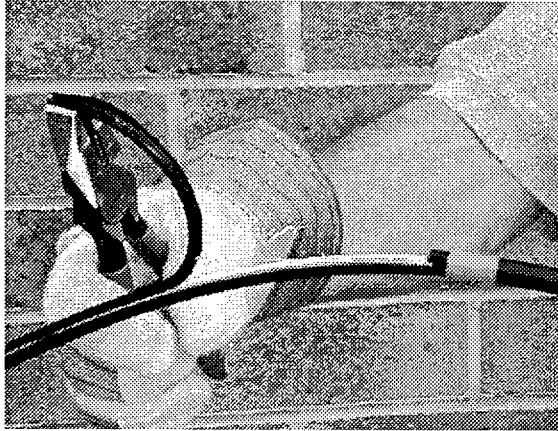


Fig. 6: Removal of the jacket (two shells).

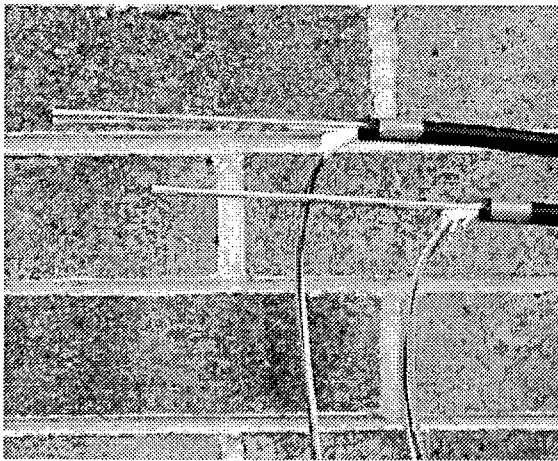


Fig. 7: After the FRP rods have been cut to the required length and the water swellable materials have been removed, the midspan access is complete.

boxes or optical distribution frames. Moreover, the thin tube material with a low elongation at break parameter drastically improves the access to the fibers. The tube may be stripped even by fingernails without any specialized tooling.

Comparative measurements of the access times have been carried out on cables according to the new design and on comparable loose tube constructions. They show that the cable access with the new design is significantly faster than for the corresponding loose tube cable. The results for cables of both types containing 48 and 144 optical fibers (12 fibers per tube) are displayed in Figure 8. The access procedure is resolved to the different access steps starting with the removal of the cable jacket and ending with the cleaning of the optical fibers. It can be seen in the diagram that two additional steps are needed in case of the loose-tube cables: the removal of the binders

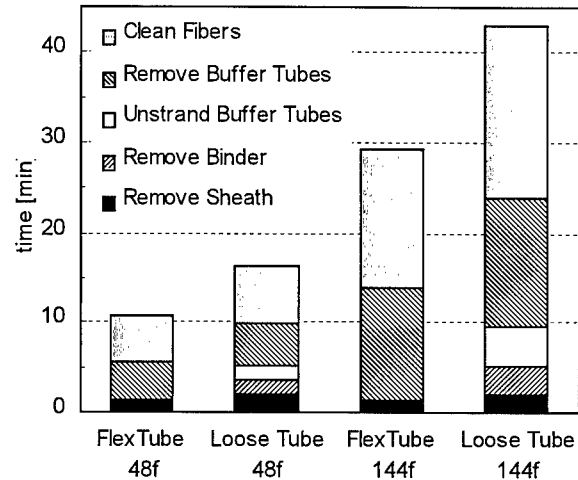


Fig. 8: Comparison of access times (single end access) for FlexTube™ and standard loose-tube cables with the same modularity.

fixing the SZ strand and the unstranding of the tubes (including cutting the central strength member). These steps already account for 15-20 % of the total cable access time and can be saved when using the new cable type. For the access steps which are common to both cable designs, a close examination shows that in average the removal of the cable jacket proceeds 30 % faster for the new cable while the time-saving for stripping of the tubes and cleaning of the fibers amounts to approximately 15 % and 20 %, respectively. The overall time-saving for the access to a cable according to the new design is approximately 33 % as compared to the common loose-tube cable, i.e., the access time is reduced by 1/3.

CONCLUSIONS AND OUTLOOK

The new cable design described in this paper significantly reduces installation time and therefore cost as compared to standard loose tube cables. At the same time, these cables allow higher fiber densities and show comparable performance as the well-established loose tube cables. This type of cable is suitable for all duct applications where high fiber count is needed but space is restricted. Especially for access networks the new design is of great advantage. Flame retardant versions of the cables come into consideration for riser cables or in-house cabling in general while armored variants are currently being developed for direct buried applications.

ACKNOWLEDGEMENTS

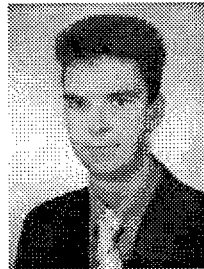
The authors would like to thank Stefan Richter and Serge Pouilly for their work on the process development and industrialization of the new cable. Furthermore, we thank Geoff Witt for his work on the cable access method.

REFERENCES

- 1 J.P. Bonicel *et al.*, "A Very Innovative Technology for Right Of Way Application", Proc. 47th International Wire and Cable Symposium, 1998, p. 815-824
- 2 W. Liese *et al.*, "Experiences from Construction and Operation of Fiber Optic Cable Plants in Sewer Systems", Proc. 48th International Wire and Cable Symposium 1999, in print
- 3 P. Gaillard *et al.*, "Optimization of Loose Tube Cable Designs: The Next Step", same proceedings as Ref. 1, p. 913-920
- 4 B.G. Risch *et al.*, "Materials Advances in Next Generation Loose Tube Cables", same proceedings as Ref. 2.

Stefan Pastuszka

ALCATEL Kabel AG&Co
Bonnenbroicher Str. 2-14
D-41048 Mönchengladbach
GERMANY



Stefan Pastuszka (30) studied physics at the University of Heidelberg. In 1997 he received his PhD for his work on semiconductor surface physics carried out at the Max-Planck Institute for Nuclear Physics. After one year as a post-doctoral research fellow at the Max-Planck Institute he joined ALCATEL in April 1998. His first position being in the optical fiber cable engineering group, he is now active in the technical marketing section of ALCATELs Telecom Cable Networks Product Line Europe since July 1999.

Study on bending strain of SZ slotted core cable with fiber ribbons

Naoki Okada, Masayoshi Yamanaka, Koichiro Watanabe, Matsuhiro Miyamoto

Fujikura Ltd.
Research and development department
Telecommunication cable division
1440, Mutsuzaki, Sakura-shi, Chiba, Japan

ABSTRACT

In this paper we present the analysis of the fiber strain of the ribbon in the SZ-slotted core cables. Especially, we have tried to analyze the strain of the fiber ribbon in bent cable. As a result, the estimating method of the fiber strain in bent cable have been established, and the structural parameter dependence of the fiber strain have been analyzed. This designing method will be useful to develop new SZ-stranded structure.

INTRODUCTION

In recent years, the optical access networks are under construction to achieve the FTTH networks in the future. The SZ-slotted core cables with 4-fiber ribbons have been used for the optical access networks because of its good mid span capability in Japan [1,2]. And the trials adapting this SZ-stranded structure to higher count cables and underground cables are under consideration [3,4].

Until now, the fiber strain of the SZ stranded ribbon in straight cable had been reported, however the analysis on bent cable has not been studied. Especially, in case of the designing SZ-stranded structure, it is necessary to expect the fiber strain not only on straight cable but also on bent cable. The development of SZ-stranded ribbon cables were based on empirical approach, therefore, we have tried to analyze the fiber strain of the SZ slotted core cable wound on a drum theoretically and experimentally.

CABLE STRUCTURE

The structure of the SZ-slotted core cable with the fiber ribbons are shown in Fig.1, and the structural parameters of an SZ-slotted core are shown in Fig.2. These parameters should be designed taking both the cable characteristics and the mid span access performance into consideration. The good cable characteristics can be obtained keeping enough fiber bending radius and lower fiber strain in the cable, on the other hand, the large slack of the fiber at any mid span access point makes the operation of branching fiber easier. Moreover, it is desired that the cable diameter should be designed smaller from the view point of easy installation and economical cable structure. In order to achieve these demands, it is desirable to design the SZ-slotted core structure smaller with shorter SZ lay length.

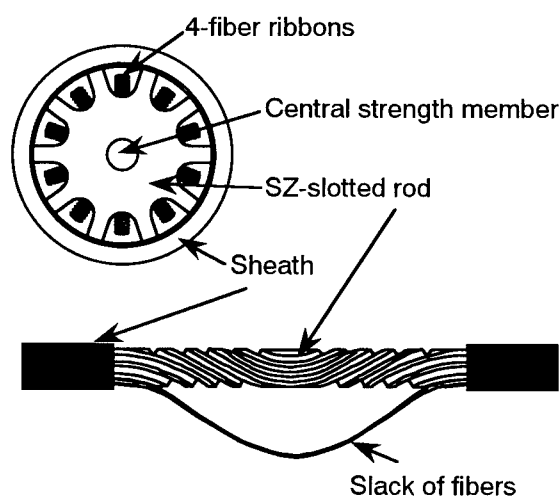


Fig.1 Structure of the SZ-slotted type optical cable with 4-fiber ribbons

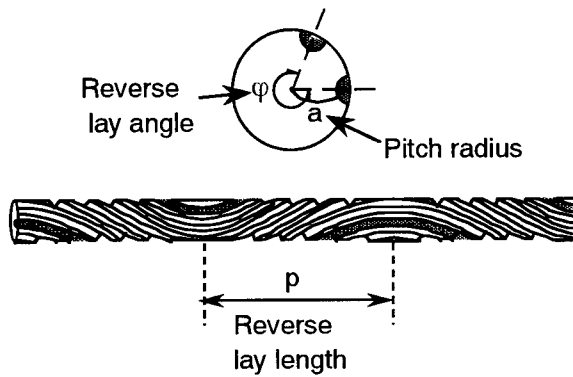


Fig.2 Structural parameters of a SZ-slotted rod

In case of inserting the fiber ribbons into an SZ-slotted rod, it had been confirmed that these ribbons should be stacked and back twisted in order to get good transmission characteristics as shown in Fig.3. This stranding method is different with that of the ordinary helical slotted core cables.

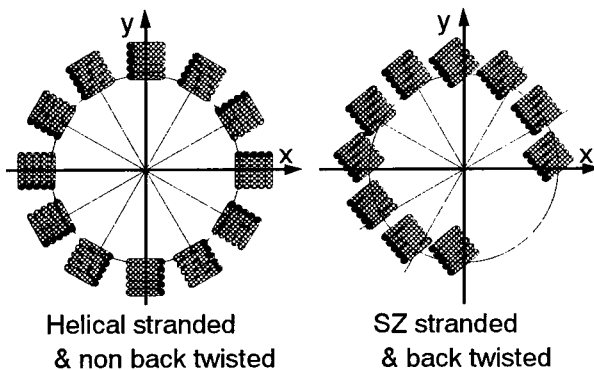


Fig.3 The stranding models of ordinary helical slotted core and SZ slotted core

ANALYSIS PROCEDURE

The analysis has been performed by the estimated fiber strain (EFS) defined as follows.

At first, we have established the fiber locus equations which show the center of a ribbon and the both side fibers of a ribbon are established. Moreover, the equations can be got not only for straight cable but also for bent cable.

Secondly, in order to analyze the fiber strain, the locus length of the fiber in cable is calculated by curvilinear integral. The length of the center of ribbon is as same as original ribbon length. In cable, the locus length of each fiber in a ribbon is different from the original ribbon

length. Therefore, the fiber strain can be estimated by the length difference between the center of the ribbon in straight cable and the side fiber of the ribbon.

Establishment of fiber locus equation in straight cable

The structural parameters of the SZ-stranded ribbon have already defined as shown in Fig.1. And Fig.4 shows that a ribbon is SZ-stranded with back twisting. In this figure, θ , ν and τ are stranded angle of the ribbon, stranded direction of the ribbon, and back twisted angle. The fiber locus equation can be expressed by Eq.1 and Eq.2 which give the coordinates of the center and the both side fibers of a ribbon respectively.

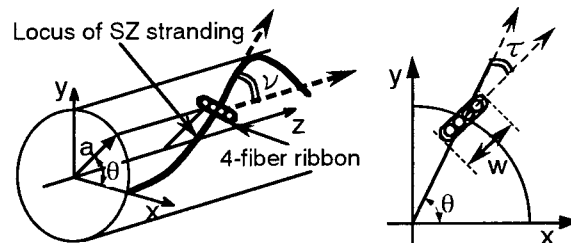


Fig.4 Coordinates and structural parameters of SZ-stranded ribbon

$$\left. \begin{aligned} x &= a \cos \theta \\ y &= a \sin \theta \\ z &= \frac{p}{2} - \frac{p \sin^{-1} \left(1 - \frac{2\theta}{\varphi} \right)}{\pi} \end{aligned} \right\} \quad (1)$$

$$\left. \begin{aligned} x_{1,2} &= a \cos \theta \pm A \cos(\theta - \tau) \\ y_{1,2} &= a \sin \theta \pm A \sin(\theta - \tau) \\ z_{1,2} &= \frac{p}{2} - \frac{p \sin^{-1} \left(1 - \frac{2\theta}{\varphi} \right)}{\pi} + \frac{1}{2} w \sin \nu \sin \sigma \end{aligned} \right\} \quad (2)$$

Establishment of fiber locus equation in bent cable

Fig.5 shows that a ribbon is SZ-stranded with back twisting in bent cable. In this figure, r , α and ξ are bent radius of a cable, bent direction of a cable with x-axis and bent angle of a cable. The fiber locus equation can be expressed by Eq.3 and Eq.4 which give the coordinates of the center and the both side fibers of a ribbon in bent cable respectively.

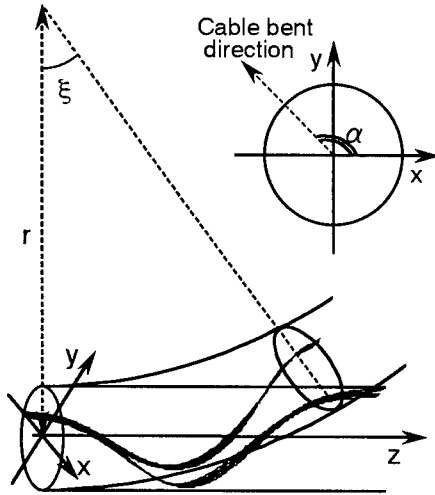


Fig.5 Bent cable with SZ-stranded ribbon.

$$\left. \begin{aligned} x_b &= B \cos \alpha + a \sin \alpha \sin(\alpha - \theta) \\ y_b &= B \sin \alpha - a \cos \alpha \sin(\alpha - \theta) \\ z_b &= \{r - a \cos(\alpha - \theta)\} \sin \xi \end{aligned} \right\} \quad (3)$$

$$\left. \begin{aligned} x_{b1,2} &= C_{1,2} \cos \alpha - D_{1,2} \sin \alpha \\ y_{b1,2} &= C_{1,2} \sin \alpha + D_{1,2} \cos \alpha \\ z_{b1,2} &= \{r - a \cos(\alpha - \theta) \mp a \cos(\alpha - \theta + \tau)\} \sin \xi \\ &\quad \pm \frac{1}{2} w \cos \xi \sin v \sin \alpha \end{aligned} \right\} \quad (4)$$

Then,

$$\sigma = \tan^{-1}(\sec v \tan \tau)$$

$$\tau = \frac{\pi}{2} + \theta - \frac{\varphi}{2}$$

$$\frac{p}{r} = \frac{p \sin^{-1}\left(1 - \frac{2\theta}{\varphi}\right)}{\pi}$$

$$v = \tan^{-1}\left(a\pi \sqrt{1 - \left(1 - \frac{2\theta}{\varphi}\right)^2} \varphi / 2p\right)$$

$$A = \frac{1}{2} w \sqrt{\cos^2(\sigma + \pi) + \cos^2 v \sin^2(\sigma + \pi)}$$

$$B = r - \{r - a \cos(\alpha - \theta)\} \cos \xi$$

$$C_{1,2} = r - \{r - a \cos(\alpha - \theta) \mp a \cos(\alpha - \theta + \tau)\} \cos \xi$$

$$D_{1,2} = -a \sin(\alpha - \theta) \mp a \sin(\alpha - \theta + \tau)$$

Definition of the estimated fiber strain (EFS)

The locus length of the fiber in cable is calculated by curvilinear integral expressed by Eq.5. We assume that the maximum fiber strain in a cable is occurred at both side fiber in a ribbon. Therefore, the estimated fiber strain (EFS) was defined by the length difference between the center of a ribbon in straight cable

and the side fibers of a ribbon as Eq.6.

$$\left. \begin{aligned} L &= \int_0^p \sqrt{\left(\frac{dx}{d\theta}\right)^2 + \left(\frac{dy}{d\theta}\right)^2 + \left(\frac{dz}{d\theta}\right)^2} d\theta \\ L_{b1,2} &= \int_0^p \sqrt{\left(\frac{dx_{b1,2}}{d\theta}\right)^2 + \left(\frac{dy_{b1,2}}{d\theta}\right)^2 + \left(\frac{dz_{b1,2}}{d\theta}\right)^2} d\theta \end{aligned} \right\} \quad (5)$$

$$\varepsilon(\%) = \frac{L_{b1,2} - L}{L} \times 100 \quad (6)$$

ANALYSIS RESULTS

The fiber strain in a cable can be estimated by the method mentioned above. At first, in order to inspect this method, we have compared the results of calculated EFS with experimental results. And then, the structural parameters dependence of the EFS have been analyzed.

Comparison of the EFS with experimental results

At first, the fiber strain of the 100 fiber SZ-slotted core cable with 4-fiber ribbons have been estimated. The two types of SZ-stranded structures have been investigated, one is the non back twisted structure and the other is the back twisted structure. At the same time, the strain of the helical slotted core cable have been estimated also. The structural parameters of each cables are listed in Table 1.

Table 1 Structural parameters

Structural parameters	SZ-slotted core cable	Helical slotted core cable
Pitch radius	a 3 mm	3 mm
Reverse lay length (Pitch)	p 150 mm	500 mm
Reverse lay angle	φ 275 deg.	—
Fiber ribbon	4-fiber ribbon	4-fiber ribbon

The results of the EFS analysis in each straight cable are shown in Fig.6. The stranding pitch dependence was investigated. In case of SZ-stranded fiber ribbon, it is confirmed that the fiber strain can be reduced by the back twisted structure. This result means that the back twisted structure is suitable for SZ-slotted ribbon core cable as previously reported.

And the strain of the SZ-stranded fiber ribbon is slightly larger than the ordinary helical stranded fiber ribbon. Here, the actual stranding pitch of SZ-stranded core cable and helical stranded core cable are 150mm and 500mm.

The fiber strain of each cable were measured by BOTDR on the installed condition, however the measured value was least as same as estimated value.

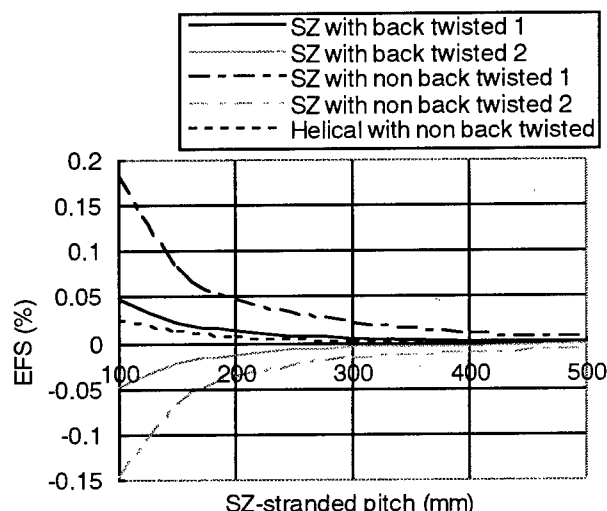


Fig.6 Estimated fiber strain of SZ-stranded and herical stranded fiber ribbon in straight cable

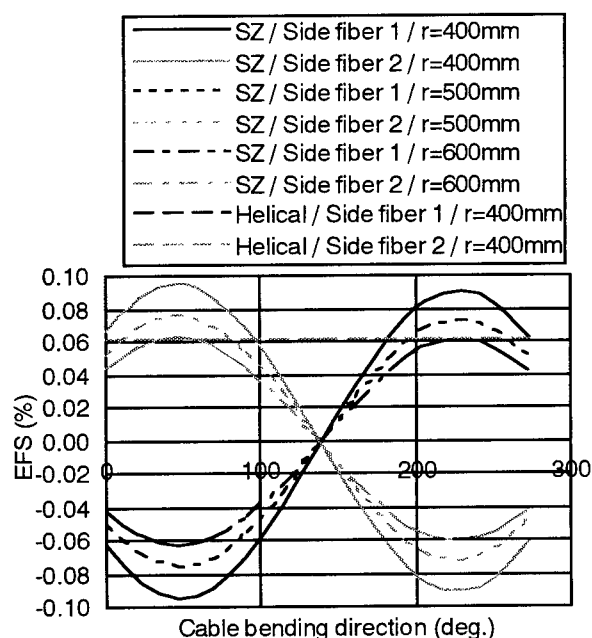


Fig.7 Estimated fiber strain of SZ-stranded and herical stranded fiber ribbon in bent cable

Fig.7 shows the calculated results of EFS in bent cable. The fiber strain is calculated on several cable bending direction, because the fiber strain is influenced by that direction on SZ-stranded structure. As results, it is verified that the fiber strain is effected by bent diameter of

cable and the fiber strain is larger than that of the ordinary helical stranded structure. We have tried to measure these fiber strain by BOTDR in order to confirm the theoretical results. The results of measured strain are also plotted in Fig.7. The measured strain is smaller than calculated strain, however the similar tendency against the cable bent direction are remarkable.

As a result, the EFS as calculated above procedure can predict the fiber strain in bent SZ-slotted core ribbon cable. This designing method will be useful to design new SZ-stranded structure in the future.

Structural parameter dependence of EFS in bent SZ-slotted core ribbon cables

We evaluated the structural parameter dependence of the fiber strain in bent SZ-slotted core ribbon cables by EFS. The EFS was calculated on each bent direction, and that results were analyzed. In recent years, the trial of the high density and high count SZ-slotted core cable have been investigated, these analysis are useful for these SZ-slotted core cables design.

Reverse lay length dependence. The reverse lay length dependence of EFS have been calculated as shown in Fig.8. As a result, it seems that fiber strain in bent cable is not influenced by the reverse lay length. However, the stranding fiber radius becomes smaller as the reverse lay length is shorter, therefore the

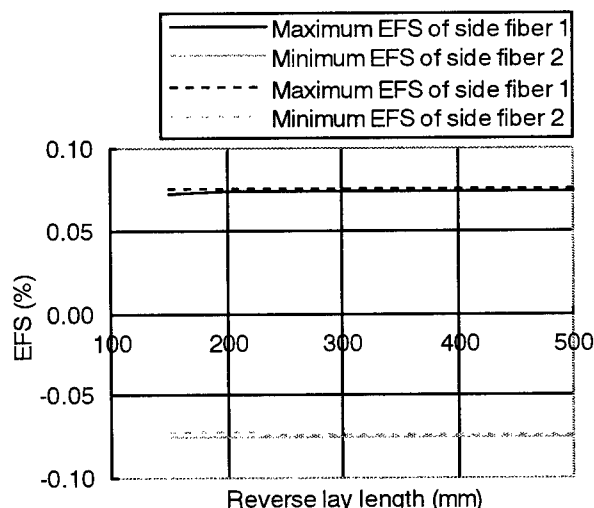


Fig.8 Reverse lay length dependence of EFS

bent radius of the fiber in a cable should be considered rather than the fiber strain.

Pitch radius dependence. The pitch radius dependence of EFS have been calculated as shown in Fig.9. The pitch radius dependence of EFS is also small. This means that the higher count of SZ-slotted core cables can be designed.

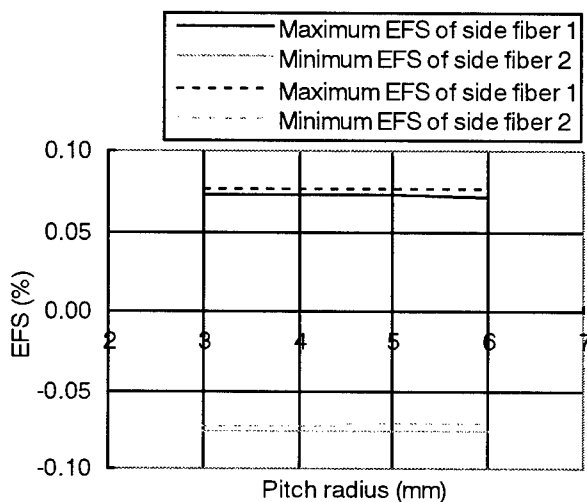


Fig.9 Pitch radius dependence of ESF

Cable bent radius dependence. The cable bent radius dependence of EFS have been calculated as shown in Fig.10. The cable bent radius dependence of EFS is large. It is hard to keep the good cable performance on small radius drum wound conditions.

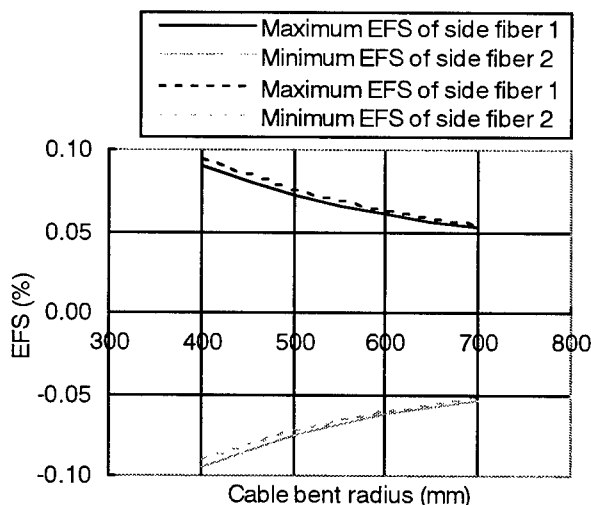


Fig.10 Cable bent radius dependence of ESF

Ribbon width dependence. The ribbon width dependence of EFS have been calculated as

shown in Fig.11. The ribbon width dependence is also large. As a result, the smaller ribbon width is desired. It seems harder to obtain the good performance for the SZ-slotted core structure with high fiber count ribbons.

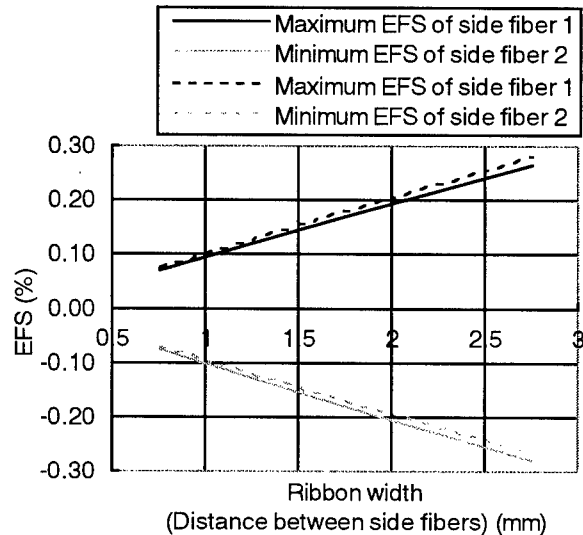


Fig.11 Ribbon width dependence of ESF

CONCLUSION

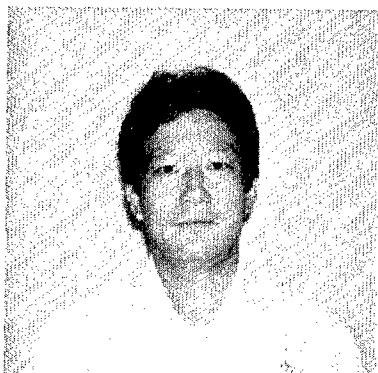
In this paper we present the analysis of the fiber strain of the ribbon in the SZ-slotted core cables. The estimating method of the fiber strain in bent cable have been established, and the structural parameter dependence of the fiber strain have been analyzed. As a result of the analysis about the straight cable, the back twisted ribbon structure makes fiber strain lower. On the other hand, in case of bent cable, it is confirmed that the fiber strain becomes larger than that of the helical slotted core cable. The fiber strain in bent SZ-slotted core ribbon cable is influenced by cable bent direction, cable bent radius, and ribbon width strongly. These calculated results shows similar tendency with the empirical results. This estimating method of the fiber strain in bent cable will be useful to design new SZ-stranded structure.

REFERENCES

- [1] H. Iwata, et al., "Design of aerial optical fiber cable system suitable for easy branching", Proc. of 46th IWCS 1997

- [2] N. Okada, et al., "Study of the SZ-slotted rod type optical cable with the 4-fiber ribbons for aerial applications", Proc. of 46th IWCS 1997
- [3] H. Iwata, et al., "Development of 2000-fiber cable with SZ-stranded U-grooves and slotted rod", Proc. of 47th IWCS 1998
- [4] N. Okada, et al., "Study of the SZ-stranded 2000-fiber cable with 8-fiber ribbons for underground access networks", Proc. of 47th IWCS 1998

AUTHORS



Naoki Okada

Research and development department
Telecommunication cable division
Fujikura Ltd.
1440, Mutsuzaki, Sakura-shi, Chiba, 285, Japan

Naoki Okada was born in 1964. He joined Fujikura Ltd. after his graduation from Chiba University with a B.E. degree in 1986 and has been engaged in research and development of optical fiber cables. He is now an engineer in the Telecommunication Cable Department and a member of the IEICE of Japan.

OPTIMAL DESIGN STRATEGIES FOR CENTRAL TUBE RIBBON CABLES COMPRISING 864 FIBERS AND BEYOND

K.W. Jackson, N.E. Hardwick, M.D. Kinard, M.R. Santana, R. Travieso
Lucent Technologies Inc., Bell Laboratories
2000 NE Expressway, Norcross, GA. 30071

ABSTRACT

In this paper we present optimal design strategies for extending the fiber counts of central tube ribbon cables to 864 fibers and beyond. We analyze both the geometric and mechanical constraints in terms of the core configuration, the sheath design, and the cable packaging. The influence of fiber counts ranging from 12 to 36 fibers per ribbon is examined with respect to packing density, bending performance, handling, robustness, and low-temperature added loss. New design charts are presented which illustrate the sensitivity of the design optimum to critical decision variables. The optimal design problem is formulated in the continuum domain and is also demonstrated to be amenable to the more general discrete optimization techniques of nonlinear integer programming (NLP).

Lastly, we present the design and performance characteristics of a new metallic 864-fiber central tube ribbon cable for use in high capacity networks. The 864 fibers are packaged within a compact 1-inch sheath that incorporates a steel armor layer to assure robust mechanical and environmental performance in the aerial, buried, and underground environments. The design of an even smaller 864-fiber dielectric cable for use in non-rodent prone environments is also presented.

INTRODUCTION

Since the initial introduction of UV ribbon technology in central tube cable cores in 1989, the fiber counts in these cables have tended to increase geometrically. The growth curve for these cables, as shown in Figure 1, has been driven by a burgeoning demand for bandwidth from both traditional and non-traditional service providers.

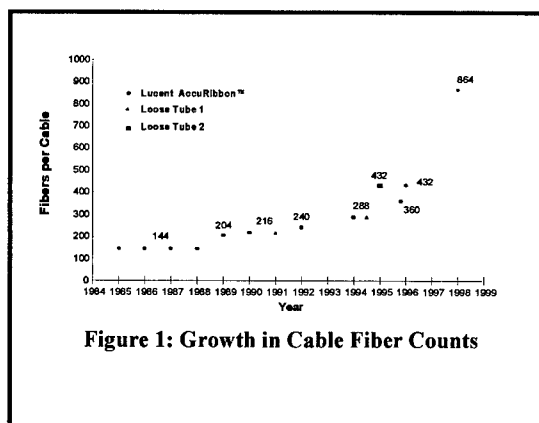


Figure 1: Growth in Cable Fiber Counts

Notwithstanding the advent of the EDFA and DWDM, the limited access to physical route space and a limited temporal window of opportunity has caused demand for higher fiber count cables to continue to prevail. Technology advances that have sustained the growth of ribbon cable fiber counts and packing density include an increase in the fiber count per ribbon,

increasingly precise fiber geometry, and the introduction of sophisticated and high performance mass fusion splicing machines. More precise fibers and sophisticated splicing machines have, in turn, further reduced mass fusion splice loss and increased cable joining productivity. The growth in fiber counts per ribbon/cable has been achieved through the design of an industry standard 24-fiber modular ribbon that easily separates into user-defined subunits for flexible fiber management.

OPTIMIZATION STRATEGIES FOR MAXIMIZING FIBER COUNTS IN CENTRAL TUBE RIBBON CABLES

In high fiber count cables there are several constraints that impose limitations on the core configuration, sheath design, and cable packaging. The foremost among these is probably the requirement that the cable be easily installed in the standard 1 1/4 inch diameter inner duct. This means that the cable sheath must generally be less than one-inch in diameter, even when benign installation methods such as blowing are used. As the cable fiber count increases, the duct constraint severely reduces the design space available to the cable designer. Moreover, a minimum sheath thickness is required to provide acceptable tensile and compressive strength, handling robustness, and to accommodate bending stresses. Ultimately, this chain of constraints restricts the inner diameter of the core tube. Thus, achieving the most efficient fiber packing density within a restricted core diameter becomes a paramount optimization objective.

The optimization procedure involves defining a fiber count objective function that is to be maximized with respect to the decision variable of fiber count per ribbon. A feasible solution is subject to a minimum required free volume within the core tube to allow substantially stress-free movement of the ribbons within the core as the cable is installed. The optimization problem can be

formulated in closed form if one assumes fiber counts in a continuum domain. Earlier work by Jackson, et.al. describes some of the basic concepts involved (1,2). Alternatively, a general and more accurate formulation and solution can be conducted in the discrete domain using iterative nonlinear integer programming (NLP) methods (3). The NLP formulation can handle multiple nonlinear constraints and can easily be solved on a desktop PC. We outline both approaches and present graphical results for the continuum formulation because parametric insights are more intuitive for this case. We then describe the NLP analysis and compare the two. The methods provide a general theoretical framework for maximizing the fiber count within core tubes and can be extended to apply to more general cable configurations.

RIBBON SIZE-CORE OPTIMIZATION

The Ribbon Size-Core Optimization approach is unique in that the number of fibers in a ribbon (and not just the stack height) is factored-in to attain the highest feasible fiber packing density. Specifically, for very high fiber counts, the number of fibers per ribbon must grow to achieve the highest fiber count for a given ratio of stack to core tube characteristic dimensions. For given mechanical properties of the ribbon matrix, a critical ratio of stack diagonal to core tube inner diameter, d/D , as illustrated in Figure 2, can be used to limit stresses that increase fiber loss when the cable is bent.

Although the specific value of d/D depends on the ribbon design, stack lay length, fiber excess length, and proprietary processing parameters, its upper bound will always be limited by the number of fibers that can be reliably packaged in a given core.

CONTINUUM FORMULATION

In the continuum formulation, the number of fibers, N , for a given core

tube ID, D_c , is to be maximized subject to the constraint that the d/D performance ratio remains constant along with the fiber count per ribbon. For economy of notation define the constant,

$$k_1 = d/D_c.$$

The cross-sectional area of the ribbon stack, A_s , is represented as

$$A_s = N A_f \cdot \theta \quad (1)$$

In Equation (1), A_f is the cross-sectional area of one coated fiber and θ is a geometric constant that accounts for the cross-sectional area of matrix material. For the ideal ribbon, θ describes a square "box" which exactly encloses the coated fiber OD, so $\theta = 4/\pi$. For thicker ribbons, or ribbons with greater fiber spacing, θ will be larger. Since both of the area terms are constant:

$$A_f \cdot \theta = k_2$$

Therefore,

$$N = \frac{A_s}{A_f \theta} = \frac{A_s}{k_2} = \frac{b \cdot h}{k_2} \quad (2)$$

In Equation (2), b and h are the width and height of the ribbon stack cross-section. For a given tube size, the stack diagonal is

$$d^2 = b^2 + h^2 = (k_1 D_c)^2 = k_1^*$$

where k_1^* is a convenient representation of the d/D_c , which is held constant.

From this expression,

$$h = (k_1^* - b^2)^{1/2}$$

Substitution of the foregoing expression into Equation (2) gives

$$N = \frac{b(k_1^* - b^2)^{1/2}}{k_2} \quad (3)$$

To optimize the fiber count, N , for a particular ribbon width, b , Equation (3) is

differentiated with respect to b and set equal to zero giving the intuitively expected result that $b = h$, or a square stack is optimal for fixed fiber count ribbons.

More subtle insights can be obtained from a graphical representation of the packing density equations and relaxing some of the foregoing constraints. Figure 2 shows a graph of the characteristic ratio, d/D , as a function of fiber count with the inner diameter of the core tube and the ribbon fiber count plotted as fixed parameters. The curves are normalized about an arbitrary, reasonable value of d/D .

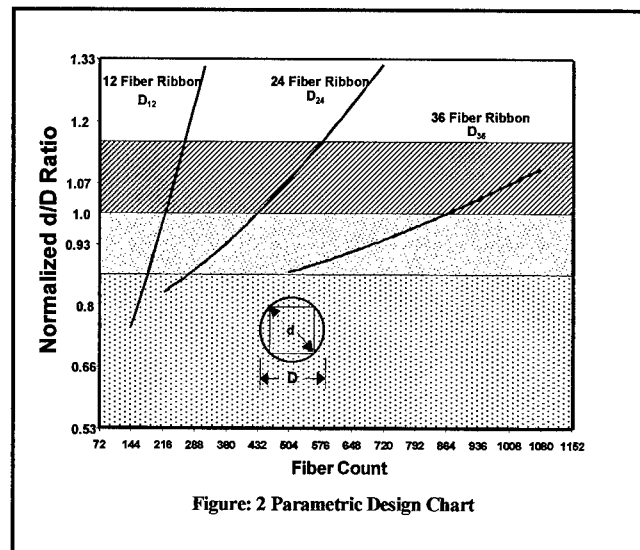


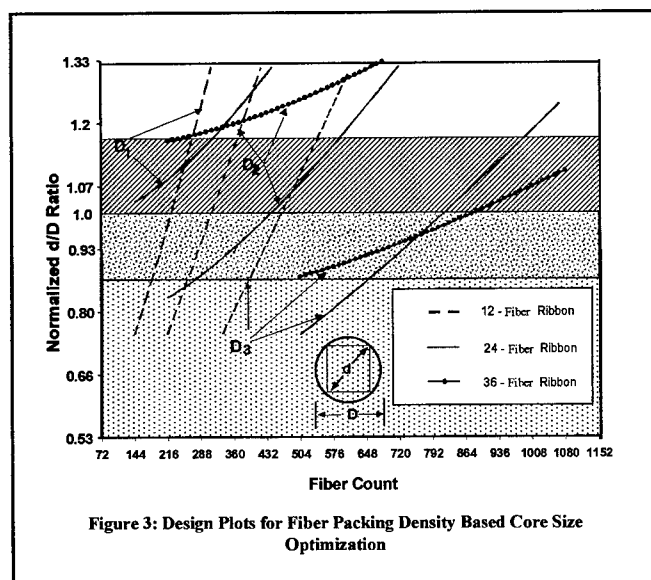
Figure: 2 Parametric Design Chart

Thus, D_{12} , D_{24} , and D_{36} represent the core tube ID for a cable comprising 12, 24, or 36-fiber ribbons. Superimposed on the graph are four d/D "zones" that indicate performance regimes (discussed later). The zone boundaries are as not as sharply delineated as illustrated and depend on a number of factors such as fiber coating design, ribbon matrix properties, surface finish, filling compound yield stress, and the range of operating temperature for the cable. In Figure 2, the reduced slope for the 36-fiber ribbon curve indicates a relative improvement in packing efficiency. Evolving toward the larger core ID's that are required for higher

fiber count cables, the decreasing slopes illustrate the positive influence of larger size ribbons relative to the d/D zonal constraints.

Digressing to explain the d/D zones, the lowest zone represents the highest cable performance and where manufacturing processes and installation conditions are most benign to the fibers. The second zone represents a more challenging zone with respect to manufacturing and installation process control and the third zone represents leading-edge process and installation technology. For d/D ratios comprising the top zone, one begins to encounter installation constraints with small radii cable bends.

Figure 3 illustrates more comprehensive permutations of ribbon size and core tube ID variations with additional curves. Curves are shown for each core tube and ribbon size to facilitate a better understanding of the design tradeoffs. D_1 , D_2 , and D_3 are some standard set of core tube dimensions chosen by the cable designer.



Although stack stability and inefficient packing could preclude use of the curves in some regions, the curves illustrate additional optimization insights. Note that the slopes are essentially the

same for each ribbon size regardless of D and the curves shift to higher fiber counts for larger core tube ID's. The similar slopes indicate that the increase in cable fiber count is the same for a particular ribbon size as the stack height (and diagonal, d) increases. This rate of increase is the same for any core size although maximum the total ribbon count can increase with D . Because of the slope decrease with increase in ribbon size (e.g. fiber count per ribbon), the greater numerical fiber count improvement relative to the d/D increase is the essence of the Ribbon Size-Core Optimization concept.

In this analysis, moving to the larger fiber count ribbon is always a better approach for achieving the maximum cable fiber count; however, given a particular cable fiber count and fixed D , a smaller size ribbon may have better manufacturing robustness as defined by a smaller d/D ratio. The insight here, which may be a bit counter-intuitive, is that for a fixed core tube ID it is not optimal to always use the larger size ribbon. This type behavior is confirmed because the curves plotted for the same core diameters intersect. Since the slope always decreases for larger size ribbons, the maximum fiber counts are always achieved with the larger ribbons provided that the allowable d/D ratio lies above the d/D ratio at the intersection. (Recall that the higher zones involve more risk to the fibers.) For fiber counts less than those at the intersection, (or cases where d/D ratios that exceed the intersection d/D ratio are not tolerable) smaller size ribbons would be preferred. This result is consistent with the Taguchi parameter design philosophy where dimensions are selected to render a product robust with respect to uncontrolled variations in components and the environment (4). The intersection of the 24 and 36-fiber ribbon curves for $D=D_3$ illustrates the foregoing principle.

Another important criterion for optimizing the maximum fiber count requires one to establish the d/D value where curves of different ribbon sizes

intersect. Then, if this d/D ratio at the intersection is acceptable, the larger size ribbon is more efficient. On the other hand, if the leading edge d/D ratio is less than the crossover ratio, smaller size ribbons provide the most efficient cable fiber count. Similarly, if the designer has a specific design requirement for a fiber count below the crossover fiber count, choosing the smaller size ribbon would increase the manufacturing robustness. The same manufacturing and reliability advantages favor the larger size ribbons when the required fiber count exceeds the corresponding value at the crossover point for ribbons of the same thickness.

A closed form expression to calculate the crossover point for two ribbon widths has been derived. The significance of the crossover point is that a higher fiber count ribbon can provide a more robust design if either a higher fiber count or a larger core diameter is preferred (relative to the crossover value). In contrast, a lower fiber-count ribbon can provide a more robust design if either a lower fiber count or smaller core diameter is preferred.

DISCRETE FORMULATION

In the discrete optimization we relax the constraint of a fixed fiber count per ribbon and require that the feasible fiber counts always be integers. Nonlinear equations of constraint that specify a minimum clearance between any fiber and the core tube wall are also incorporated into the governing equations. The general equations that describe the formulation are as follow:

$$\text{Maximize } N = \sum_{i=1}^m n_i X_i \quad (4)$$

subject to

$$X_i \text{ is an integer ; } i=1,2,\dots,m \quad (5)$$

$$f_j(X_i, R_0, w_i, t_i) \leq C \quad (6)$$

$$j=1,2,\dots;i; i=1,2,\dots,m$$

In Equation (4),

n_i is fiber count for ribbon of type i

X_i is number of ribbons of count, n_i , and

$f_j(X_i, R_0, w_i, t_i)$ represents a set of constraint equations for the minimum distance, C , from any fiber in ribbon of type i to the core tube wall. This latter functional expression includes the core tube radius, R_0 with w_i and t_i being the dimensions of ribbons of type i . (So, w_i would correspond to b of the continuum analysis.)

A simple example along with Figure 4 serves to clarify the general equations. Suppose one considers the use of three different fiber count ribbons in a cable, for example, 36, 24, and 12 fiber ribbons in a given core tube of size R_0 . It is desired to find the optimum number of ribbons of each fiber count and the maximum number of fibers that can be packaged with this arrangement, given a minimum clearance between any fiber and the core tube wall. Mathematically, we are given n_i and C and wish to solve for the optimal number of 36, 24 and 12 fiber ribbons and the resulting total fiber count.

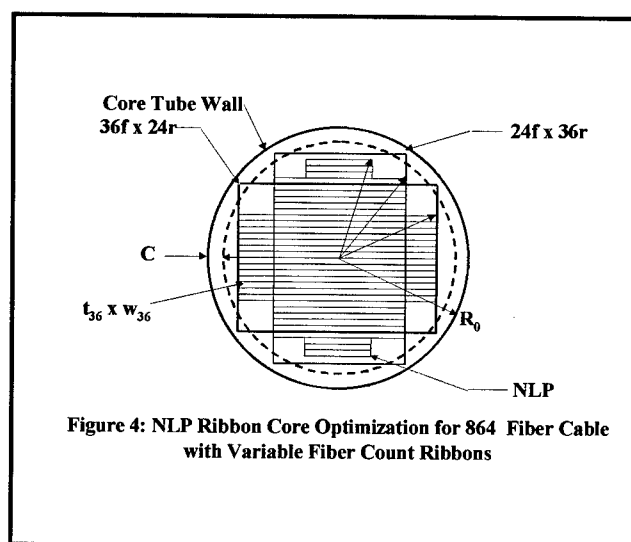


Figure 4: NLP Ribbon Core Optimization for 864 Fiber Cable with Variable Fiber Count Ribbons

As illustrated in Figure 4, an optimal solution is to employ fourteen 36-fiber ribbons, twelve 24-fiber ribbons and six

12-fiber ribbons, thereby forming a symmetrically disposed stack of 864 fibers in the given core tube. In contrast, had ribbons of a fixed fiber count been used it would be necessary to increase the core tube ID by about 20% for the same fiber count of 864. (Note that A_s is equal for either 24- or 36-fiber ideal ribbon stacks.) Because the available space increases as the square of the core tube diameter, the use of variable fiber count ribbons becomes even more effective as the diameter increases. This could have application for cable cores that are composites of different fiber types.

It is interesting that an extension of the foregoing ideas demonstrate that ribbon structures can provide the ultimate fiber packing density within a cable. In the limit as the granularity of fiber counts between different ribbon sizes is reduced, a virtual ultimate optimum of a cylindrically shaped "stack" is asymptotically approached (while maintaining the highly-desirable flexibility of a single fiber in the direction of the most flexible bending of the ribbon).

PRACTICAL AND MATHEMATICAL OPTIMALITY

Having derived expressions for mathematically optimal configurations for ribbon placement in tubes, it is useful to distinguish between mathematical and practical optimal core configurations. One the most important considerations involves outside plant fiber administration and management. Manufacturing and financial issues are also important factors that can further constrain the practical optimal design. Specifically, it is not feasible to design an optimal cable core for every fiber count because users prefer to deploy a minimum number of cable sizes. So, a given cable must typically accommodate a range of fiber counts and must be compatible with a pre-existing set of industry standard cable and ribbon sizes. These initial/boundary conditions can significantly influence how a family

of cable designs is extended to higher fiber counts.

As an example, consider an existing family of fiber optic cable designs whose largest cable can accommodate fiber counts from 288-576 using 24-fiber ribbons and whose d/D was established for the midpoint of 432 fibers. The next range of fiber counts to be accommodated would be 576-864 with a midpoint of 720. Figure 3 illustrates that both a 24 and a 36-fiber ribbon are equally feasible choices. While a 36-fiber ribbon option has smaller overall variation in the d/D from its nominal value at 720 fibers, the 24 fiber ribbon has a lower d/D for a larger percentage of the range of fiber counts that the cable is designed to accommodate. Moreover, the 24-fiber ribbon does not introduce another ribbon size into the product mix. Although a stack comprising twenty-four, 36-fiber ribbons may be more geometrically stable during manufacture than thirty-six 24-fiber ribbons, a twenty-four fiber ribbon itself will have a greater mechanical robustness for a given ribbon thickness. Increasing the thickness of a 36-fiber ribbon to achieve parity in mechanical robustness with that of a 24-fiber ribbon in turn would decrease the packing density and shift the crossover in favor of the 24-fiber ribbon.

DESIGN AND PERFORMANCE OF AN 864 FIBER CABLE COMPRISING 24 FIBER RIBBONS

Based on the foregoing considerations we have designed, manufactured, tested, and installed 864-fiber ribbon cables comprising 24-fiber ribbons. Figures 5 and 6 show the cross-section of the cable for the metallic and dielectric sheath designs, respectively. Figure 7 shows a longitudinal view of the metallic (armored) version of the 864 fiber cable. The 864 fibers are packaged within a compact, one-inch diameter sheath, which can readily be placed in 1 1/4 inch inner ducts.

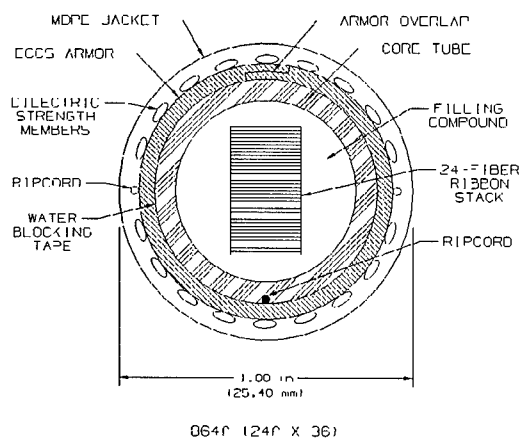


Figure 5: 864-Fiber Metallic Cable

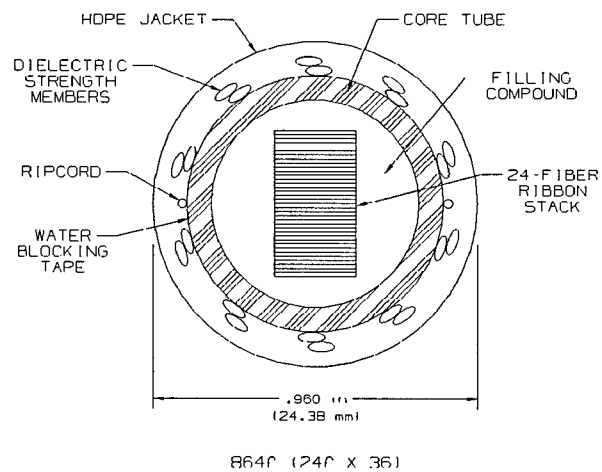


Figure 6: 864-Fiber Dielectric Cable

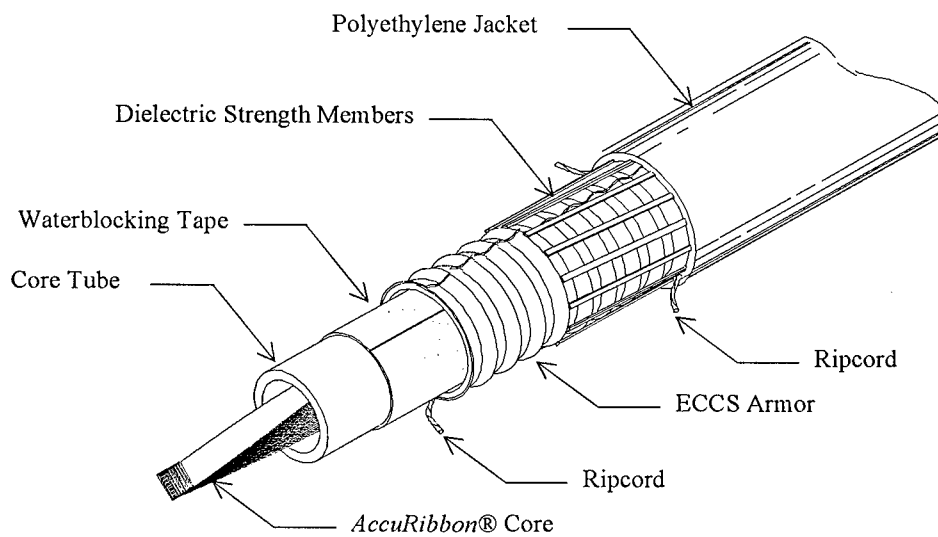


Figure 7: 864 Metallic Sheath AccuRibbon® Cable

The metallic design also incorporates an armor layer of electrolytically, chrome-coated steel to provide an extra measure of mechanical robustness to the sheath. Installation testing verifies the design to withstand aggressive handling in the aerial, buried, and underground environments. The corrosion-resistant armor, which is coated and bonded to the outer jacket, also provides long term protection of the core from rodent destruction and environmental degradation.

Three ripcords, one under the armor and two in the jacket, combined with a medium density polyethylene jacket, provide easy sheath removal and rapid access to any fiber in the core. Using a newly developed differentially-enhanced edge fiber adhesion technology, the twenty-four fiber ribbons can be easily hand-divided into rugged, 12-fiber subunits for mass fusion splicing. Moreover, routing and organization of fibers within closures is simplified with the use of Industry standard twenty-four fiber ribbons which also optimize slack fiber storage. As shown in Figure 5, a somewhat smaller traditional dielectric sheath design for the 864 cable can be used where rodent protection is not required. Both cables pass or exceed Industry requirements for Outside Plant Cables.

CONCLUSIONS

Both a continuous and discrete algorithm for maximizing the packing density of ribbons in a core tube have been described. The most general formulation involves nonlinear integer programming. This analysis demonstrates that variable fiber count ribbons can increase the fiber packing density with ribbons in a tube by more than 30% relative to that of constant fiber count ribbons in a square stack. Design charts were also presented which quantitatively illustrate the various practical tradeoffs involved when optimizing packing density in a cable that must accommodate a broad range of fiber counts.

Designs for new metallic and dielectric 864-fiber count central tube ribbon cables that use Industry standard 24-fiber ribbons are described. The metallic design maximizes duct space utilization and provides excellent mechanical, environmental, and rodent protection combined with an easy entry sheath and omnidirectional bending flexibility. The companion dielectric design of the 864-fiber cable is ideal for less harsh environments.

ACKNOWLEDGEMENTS

The authors acknowledge the work of R. D. Bailey, R. J. Brown, J. Kim, A. J. Konop, C. J. Lever, M. L. Reams, P. M. Thomas, D. E. West, and many others to develop and manufacture the 864-fiber cables.

REFERENCES

1. Jackson, K.W., R.J. Brown, M.D. Kinard, K.M. Kroupa, M.R. Santana, P.M. Thomas, 1996. "Design and Performance of a High-Capacity, Compact Modular Ribbon Cable Comprising 24 Fiber Ribbons", 45th IWCS Proceedings, pp 623-630.
2. Jackson, K.W., T.D. Mathis, P.D. Patel, M.R. Santana and P.M. Thomas, 1997. *Optical Fiber Telecommunications IIIA, Chapter 5, Advances in Cable Design*, Academic Press.
3. Montgomery, D.C., 1997. *Introduction to Statistical Quality Control*, 3rd Edition, Wiley, pp 590-600.
4. Winston, W.L., 1995. *Introduction to Mathematical Programming, Application and Algorithms*, Duxbury.



Kenneth W. Jackson

Kenneth W. Jackson is a Distinguished Member of Technical Staff in the Fiber Optic Material & Packaging Technology Development Department at Lucent Technologies, Inc., Bell Laboratories, Norcross, GA. He joined AT&T Bell Laboratories in 1981 having received an M.S.M.E. and Ph.D. in Mechanical Engineering from the Georgia Institute of Technology. Since 1981 he has worked in R&D in areas of Optical Fiber Fabrication, Fiber Optic Connector Design and Fabrication, Materials' Design and Fiber Optic Cable Design and Development. He has been awarded 12 patents and has 20 publications. He is a registered Professional Engineer in the state of Georgia, a member of ASME and the American Statistical Association.

Study of new slotted core cables for underground access networks

Yoshiyasu Sato, Naoki Okada, Masayoshi Yamanaka,
Koichiro Watanabe, Matsuhiro Miyamoto

Telecommunication cable division Research and Development
department Fujikura Ltd. 1440, Mutsuzaki, Sakura-shi, Chiba, Japan

ABSTRACT

In recent years, we had developed very small optical slotted rod cables, considering economical cable. In this paper, we have developed new cables from the viewpoint of easy installation. First method is the reduction of cable weight by adopting lighter materials of strength members and a slotted rod. Second method is a cable with special arranged low friction polyethylene sheath. The efficient installation can be achieved by new cables. We've designed 1000-fiber cables with eight fiber ribbons by these methods and made these cables on an experimental basis. Here, we've studied and reported transmissions, temperature characteristics, mechanical characteristics and frame retardant characteristics of the trial manufactures.

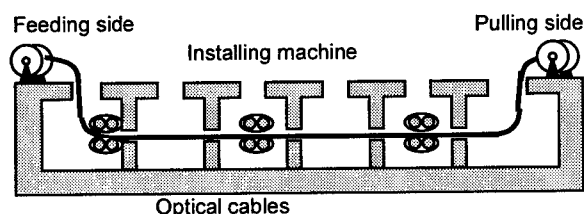


Fig.1 Installing cables into underground ducts

INTRODUCTION

In recent years, the optical networks are under construction to achieve the FTTH in future. For economical construction of the optical networks, the following points are important for designing optical cables.

(1). Small and lightweight cable

In the case of installing cables into underground ducts (as shown in Fig.1), smaller and lightweight cable is easier and faster to install.

(2). Low friction sheath cable

The tensile force while installing can be decreased due to low friction. In other words, maximum installation length will grow. These two points contribute to economical installation work.

Estimation of installable length of cables 1), 2), 3)

The pulling force to install cables can be expressed as follows, supposing friction constant during installing cables in straight ducts.

$$F = \mu \times W \times L$$

F : tensile force of installing cables

μ : friction coefficient

W : cable weight

L : length of installing cables

Assuming that tensile force is fixed, Fig.2 shows the relation between weight and length of installable cable. Fig.3 shows the relation between friction coefficient of cables and the length of installing cables. Therefore application of these two methods makes easier installation work, and will greatly contribute to the economy of cable network construction including installation.

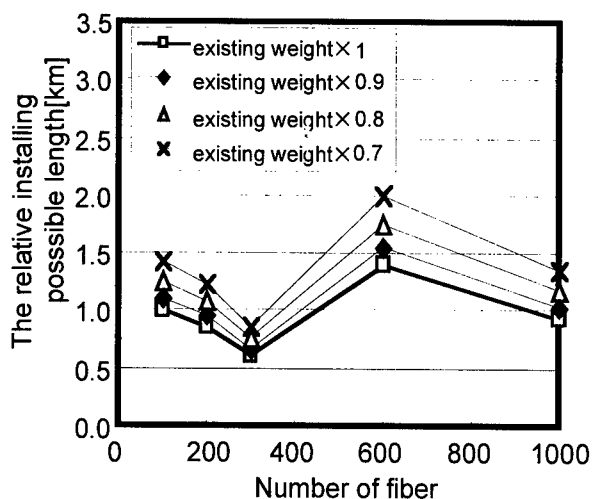


Fig.2 The relation between the friction coefficient of cables and installable length

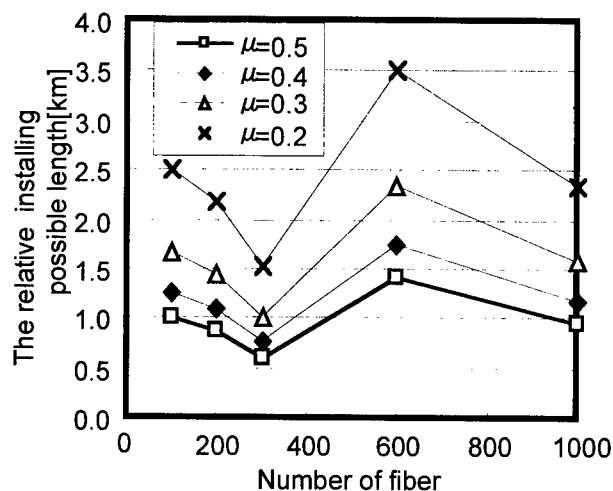


Fig.3 The relation between cable weight and installable length

CABLE DESIGN

1. Material of strength member in slotted rod

Fig.4 indicates cross sectional view of the cables designed in this study. The conventional cables have steel wires for a central strength member. In this paper, 1000-fiber cables with several kinds of the non-metallic strength member, such as Glass-FRP, aramid-FRP, carbon-FRP, and PBO (p-phenylene-2,6-benzobisoxazole)-FRP, have been investigated. The weight of cables with these FRP is compared with conventional one in Fig.5. Table.1 shows physical properties of strength member. In case of the glass FRP, the cable weight is obviously larger than those of the other cases.

The Young's modulus of the glass- FRP is

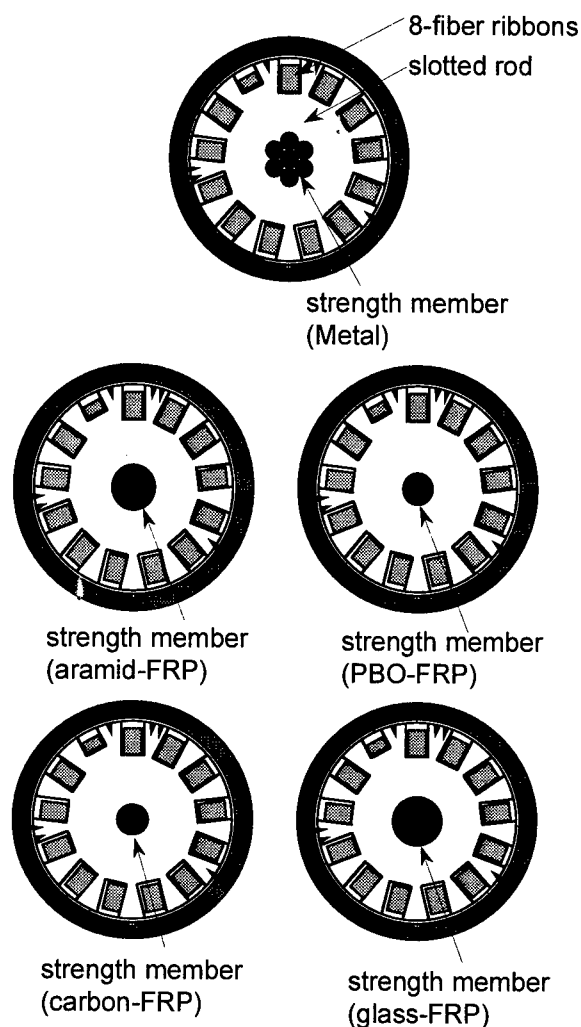


Fig.4 Cross sectional view of the cables

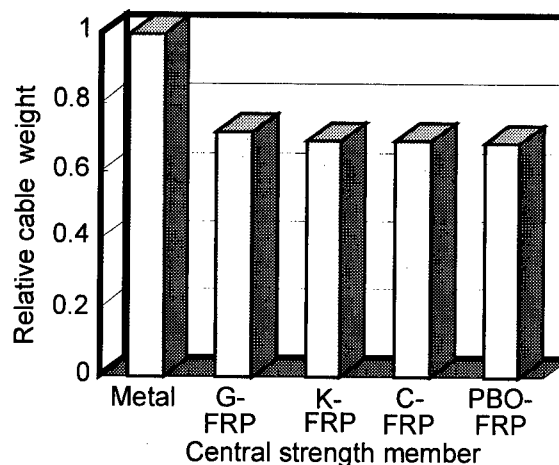


Fig.5 The comparison of cable weight with various strength member

smaller than the other FRP as shown in Table.1, moreover the specific gravity of glass-FRP is larger than that of the other FRP. Therefore, the diameter of glass-FRP must be designed larger.

Table.1 Physical properties of strength

	G-FRP	K-FRP	C-FRP	PBO-FRP
elastic modulus	5000	6400	13000	13400
specific gravity	1.98	1.32	1.48	1.43
economy	Excellent	Good	Fair	Fair
induction	Good	Good	NG	Good

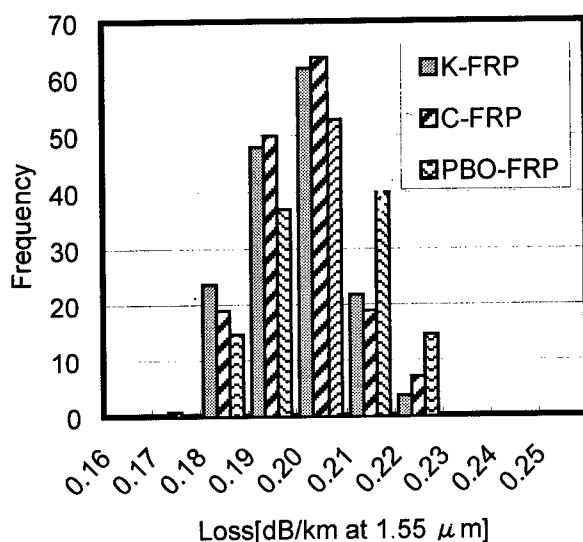


Fig.6 Transmission characteristics of the trial cables

Then, aramid FRP, carbon FRP, and PBO FRP will be desirable to design the lightweight cable. And the required strength member can be reduced because of decreasing tensile force while installing. For example, the cable weight of the 1000-fiber cable can be reduced about 30% compared with the ordinary cable as shown in Fig.5.

The prototype cables with aramid-FRP, carbon-FRP and PBO-FRP were manufactured and evaluated. As results, all cables showed good transmission characteristics and good cable performances as shown in Fig.6 and 7 and Table.2. Among three FRP cables, aramid-FRP or PBO-FRP seems feasible because carbon-FRP is more rigid and conductive.

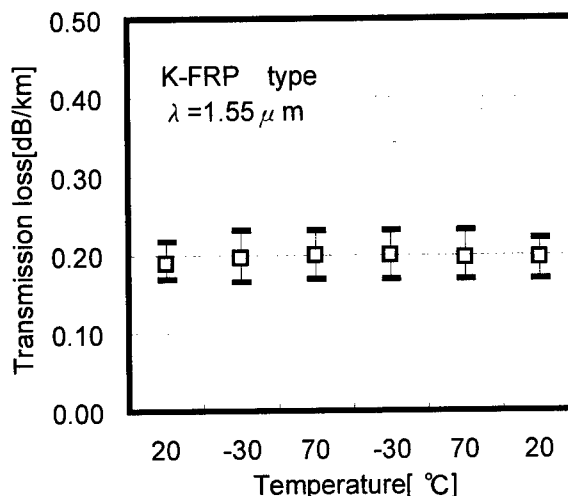


Fig.7-1 Temperature characteristics of the trial cable with K-FRP

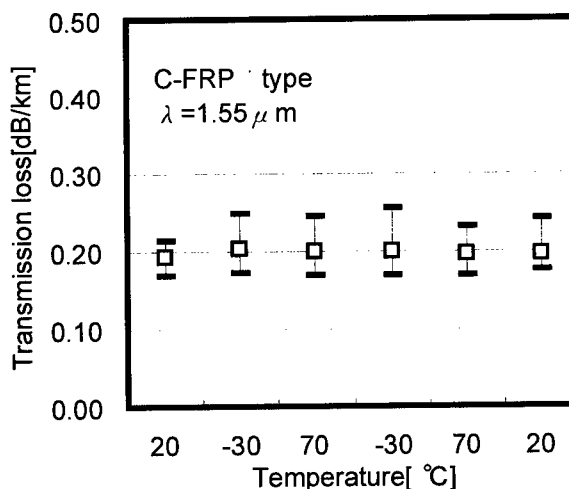


Fig.7-2 Temperature characteristics of the trial cable with C-FRP

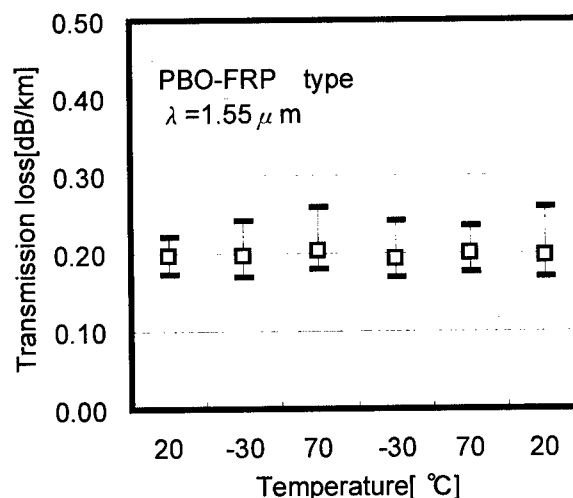


Fig.7-3 Temperature characteristics of the trial cable with PBO-FRP

Table.2 Mechanical characteristics of the trial 1000-fiber cables

Test items	Test conditions	Results		
		K-FRP	C-FRP	PBO-FRP
Bending	480mm ϕ *90deg	No loss change	No loss change	No loss change
Lateral pressure	2kN/ 100mm	No loss change	No loss change	No loss change
Torsion	+ - 90deg/m	No loss change	No loss change	No loss change
Impact	20mm *1kg*1m	No loss change	No loss change	No loss change
Squeezing	4kN/600m mR-roller	Less than 0.02dB /100m	Less than 0.02dB /100m	Less than 0.02dB /100m
Tensile	4kN	Less than 0.02dB /100m	Less than 0.02dB /100m	Less than 0.02dB /100m

Measurement wavelength at 1.55. m

2. the special slotted rod with foamed polyethylene

We have designed the special slotted rod as shown in Fig.8. Only inner part is made of formed polyethylene, and outer ribs are made of ordinary solid polyethylene. It is necessary that the surface of the slots should be smooth in order to get good transmission characteristics. Therefore, the solid surface is selected for outer ribs. Fig.9 shows the relative cable weight of the light weight cables with formed polyethylene slotted rod and with various strength members. The foamed slotted rod are realized by applying foamed polyethylene to only inner part. According to this method, for example, the weight of 1000-fiber cable is reduced to be about 10% lighter than that of solid slotted-rod cable. As shown in fig.10 and 11, all cables have good transmission and temperature characteristics. However, the slotted rod with foamed polyethylene seems to be degraded as to frame retardant characteristics as shown in Table.3.

Table. 3 Frame retardant characteristics

strengthen member	slotted rod	damage length[m]
K-FRP	solid	<0.9
K-FRP	formed	<1.3

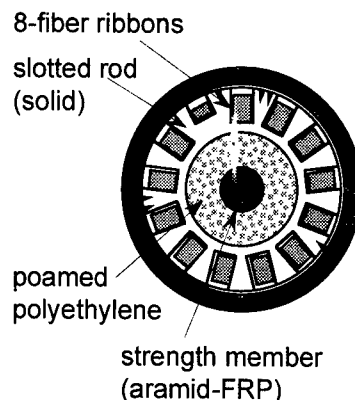


Fig.8 Cross sectional view of lightweight cable composed of FRP strength member and slotted rod of which only inner part is made of formed polyethylene.

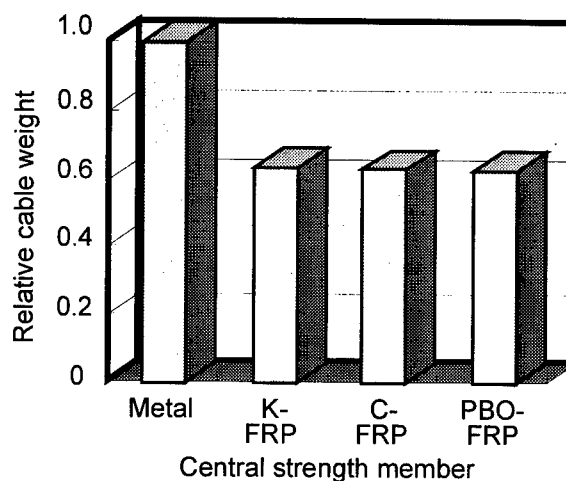


Fig.9 The relative weight of FRP cables with special slotted-rod where only inner part is made of formed polyethylene.

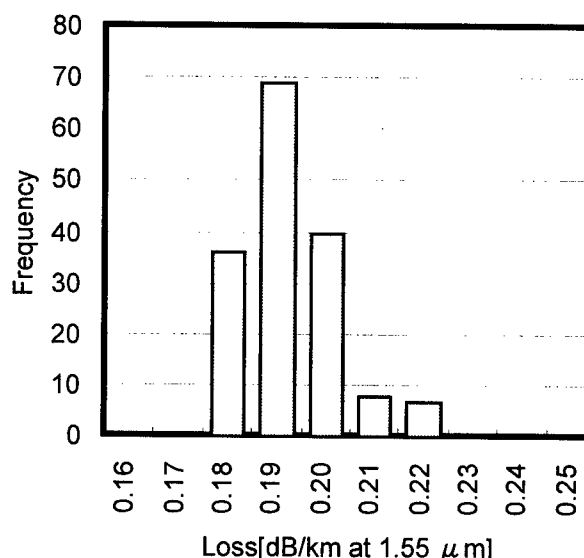


Fig.10 Transmission characteristics of the trial cables

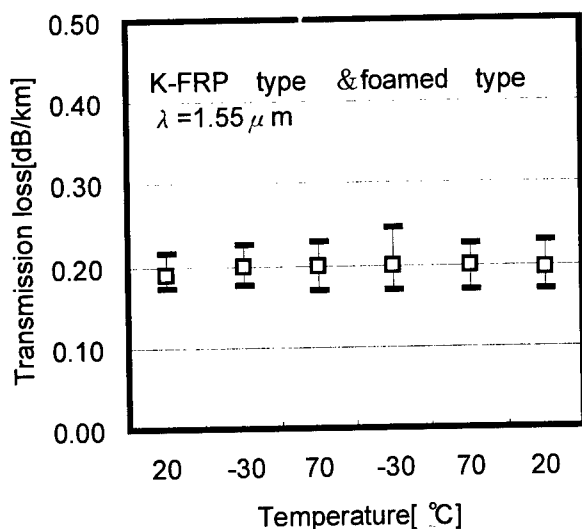


Fig.11 Temperature characteristics of the trial cables

Table.4 The reliability of newly developed LLDPE including additive in polyethylene

Method	Including additive	Polymer blend	Peculiar surface
Details	additive dispersed in polymer	chemical composition of silicon located on chain molecule	decreasing surface area
slip efficiency	Excellent	Good	Fair
reliability	Good	Excellent	Good
past practice	Good	Fair	Fair
economy	Excellent	Fair	Excellent
total	Excellent	Good	Fair

3. Low friction sheath

In order to install cables into the underground ducts easily, the lower friction of sheath is desirable as shown in Fig.2 and 3. Table.4 indicates various methods of decreasing friction coefficient.

Therefore, we have investigated the friction coefficient of materials such as LDPE, LLDPE, HDPE and newly developed LLDPE including additive in polyethylene. Fig.12 shows the measurement set-up of friction coefficient. The test sample of sheet is prepared by heating press. As shown in fig.13, friction coefficient between the same materials decreases in following order.

LDPE > LLDPE > HDPE > LLDPE (additive)

As results, new LLDPE sheath including additive in polyethylene shows the lowest friction coefficient. It is confirmed that the friction coefficient of the LLDPE (additive) sheath can be decreased about 70% compared with that of LDPE as shown in Fig.13. Introduction of additive into polyethylene seems excellent. We have studied reliability of newly developed LLDPE including additive in polyethylene as shown in Table.5. We confirmed that the material had good performance of sheathing characteristics and reliability as good as LLDPE

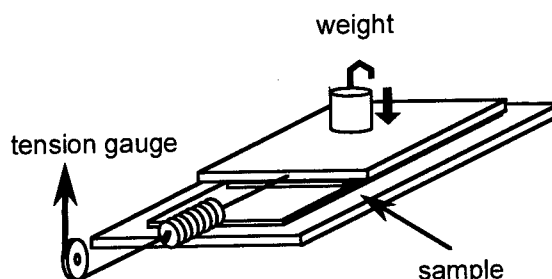


Fig.12 Method of measurement of friction coefficient

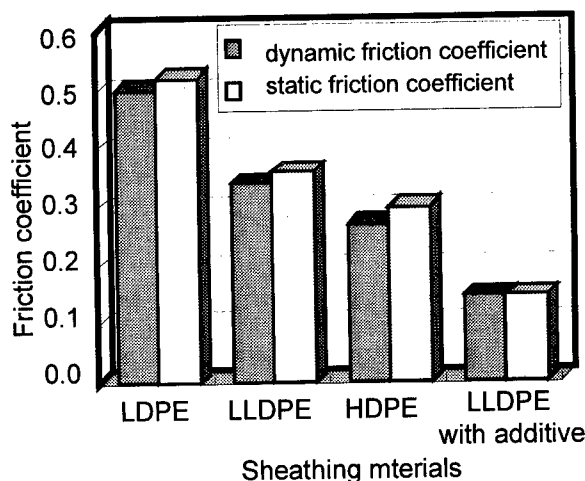


Fig.13 The relation between the additive including in LLDPE and the friction coefficient for the same materials

as shown in Table.6. The additive concentration was determined by the relation between the additive and friction coefficient as shown in Fig.14. In relation to the friction coefficient between the same materials, there is saturation of the friction coefficient for the increase of additive more than 1000ppm. Therefore, it is determined that the ratio of additive is 1000ppm. In addition, Fig.14 also shows that it is possible to control the friction coefficient from 0.15 to 0.35 by changing the concentration of additive in LLDPE. As mentioned above, we have successfully developed the new lightweight cables with low friction sheath. This cable structure is suitable for the underground ducts to make the installation easier and more efficiently.

CONCLUSION

As results, we have developed new lightweight cables having FRP strength member composed of aramid yarn and with polyethylene sheath including additive for low friction. This newly developed lightweight cables were fabricated and tested. It was verified that these newly studied cables have good cable characteristics. This cable structure is suitable for underground ducts.

REFERENCES

- 1) Technical report of IEICE SSE97-177, OCS97-106(1998-02)
- 2) IEICE '81/10 Vol.J64-B No.10
- 3) H.Iwata, S.Tomita and Y.Dei "Advanced Technologies of High Density Optical Fiber Cable" Communication Cables and Related Technologies (EC'98) '98 P24

Table.5 Reliability of newly developed LLDPE

test items	test conditions	terms	LLDPE	LDPE
ESC	50deg 10%	48 hours	Good	Good
heat deterioration	100deg	50 days	Good	Good
chemical resistance	50deg 10% sulfuric acid	50 days	Good	Good
	50deg 10% phydrochloric acid	50 days	Good	Good
	50deg 3% NaOH	50 days	Good	Good
	50deg 10% Oil	50 days	Good	Good
retention of low friction	70deg	30 days	Good	Good
	50deg water	30 days	Good	Good
	50deg alkaline water	30 days	Good	Good

Table.6 Initial sheathing characteristics

Test item	LDPE	LLDPE	LLDPE with additive
beaking load[MPa]	16.2	20.8	20
breaking elongation[%]	683	826	810
embrittlement test[-60deg]	0/10	0/10	0/10

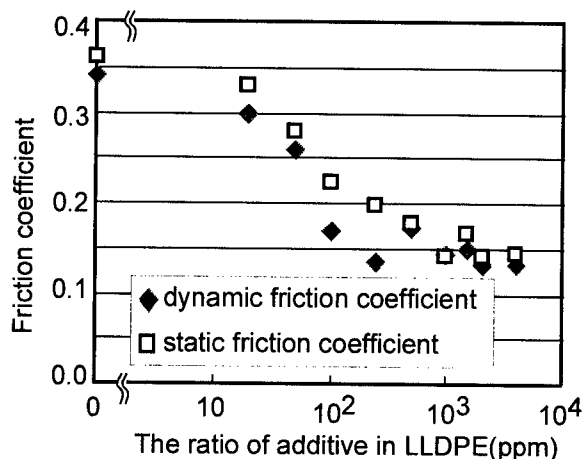
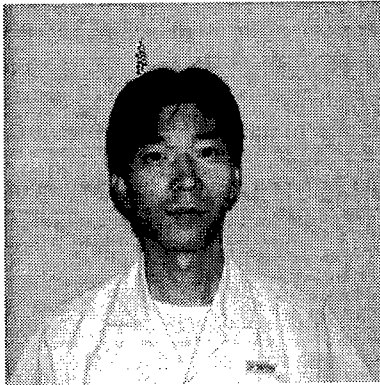


Fig.14 Friction coefficient as a function of additive concentration

AUTHOR



Yoshiyasu Sato

Research and development department
Telecommunication cable division
Fujikura Ltd.
1440, Mutsuzaki, Sakura-shi, Chiba, 285-8550,
Japan

Yoshiyasu Sato was born in 1969. He joined Fujikura Ltd. after his graduation from Tokyo Institute of Technology with a M.E. degree in 1995 and has been engaged in research and development of optical fiber cables. He is now an engineer in the Telecommunication Cable Department and a member of the IEICE of Japan.

DEVELOPMENT OF A RISER RATED OUTDOOR/INDOOR CENTRAL TUBE RIBBON CABLE

Richard H. Norris, Richard D. Small, Jr. and Peter A. Weimann
Lucent Technologies
Norcross, Georgia 30071

Abstract

This paper summarizes the development of a riser rated, outdoor/indoor cable with a central core ribbon structure, suitable for service in both outside plant and indoor environments. In order to pass UL riser cable fire tests, this product utilizes a low-smoke, zero halogen (LSZH) flame retardant polyolefin jacket to compensate for combustible components of the design. This product line also features a new two-rod, dielectric strength member design that provides easier handling and enhanced mechanical properties. The *Filled Outdoor/Indoor Cable* currently accommodates 12 to 216 fibers, but efforts are underway to expand fiber counts to 432 fibers.

Introduction

With ever-increasing demands for higher fiber counts, lower splice losses and decreased installation costs, telecommunications service providers are seeking a universal ribbon cable product which can extend the traditional outside plant cable into the indoor environment. Such a cable would furnish service providers with significant installation benefits by eliminating splicing at the central office vault, as well as minimizing storage slack within the vault. This cable would also eliminate the optical loss associated with a traditional central office vault splice. The challenge in designing such a cable is to provide the robustness and environmental resistance of the traditional outside plant cable, while imparting the fire resistance and low smoke characteristics required of indoor cables.

A high fiber count ribbon cable has been developed which meets the aforementioned requirements. The *Filled Outdoor/Indoor Cable* design is a central core tube cable that utilizes a grease-filled core for resistance to water penetration along with a highly filled, low-smoke zero halogen (hereafter abbreviated LSZH) polyolefin jacket for flame retardancy. This design is UL riser rated, and meets all the mechanical and environmental criteria of Bellcore GR-20-CORE, GR-409-CORE and applicable NEC codes. The cable also incorporates a new dielectric sheath design

that employs only two rods as linear strength members.

In this design, as in most outside plant cable designs, the filling compound is the most highly combustible constituent. To offset the flammability of this component, a design using LSZH polyolefins for both the jacket and core tube was considered as one original option. This design passed the International Electrotechnical Commission (IEC) 332-3^[1] and IEC 61034-2^[2] testing. However, incompatibility between the LSZH core tube material and filling compound eliminated this design option. Consequently, mass balance calculations were performed to shift the mass of flame retarding material contained in the original core tube to the jacket. These calculations were confirmed by thorough analyses of the cable construction, including the calculation of the ratio of fuel to flame retardant in the cable, and measurement of the heat of combustion of each cable component. Subsequently, this modified design has passed UL riser testing. Figure 1 displays a cross-sectional schematic of the resulting *Filled Outdoor/Indoor* cable.

Cable Design

Development of this new product line was driven by customer requests for high fiber count ribbon cables that can be used in multiple-building networks without requiring central office vault splices. The design challenge was to provide an economical cable that is robust, environmentally sound and craft-friendly. In order to meet these requirements, a dielectric design was chosen, utilizing the current technology of central core design and making use of linear strength members.^[3]

However, the most important requirement for this new design was to meet the indoor flame requirements outlined by the National Electric Code^[4]. For indoor cable applications, any cable is required to receive a minimum rating of Optical Fiber Non-conductive Riser (OFNR). To obtain this rating, the cable must pass the rigorous requirements of Underwriters Laboratory (UL) 1666 flame test.^[5]

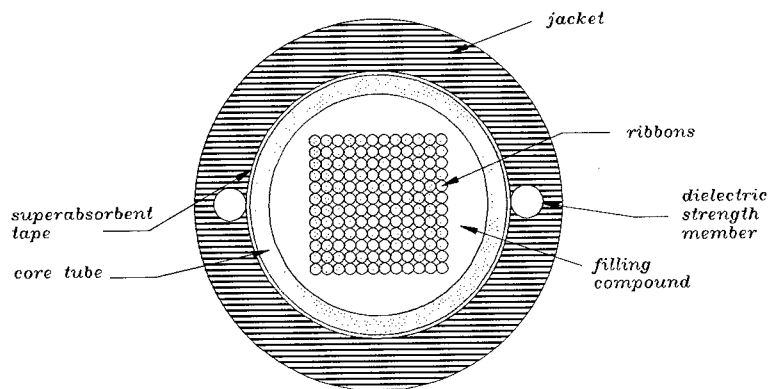


Figure 1 - Schematic of the Filled Outdoor/Indoor Cable Design

Another very important consideration in cable flammability is the smoke production of the materials of construction. In a fire, smoke is the greatest hazard to individuals and equipment. [6,7]

The polyethylenes that are currently used as jacketing materials in outside plant applications do not exhibit flame retardancy. Initially, flame retardancy was achieved in polyolefin cable jackets through addition of antimony oxide, a halogen additive that produces irritating smoke. Today, commercially available flame-retardant polyolefins used for jacketing contain less toxic, non-halogen metal hydrates for fire retardancy [8].

Core Design

The cable core design consists of a grease-filled, polymer core tube to provide enhanced mechanical protection and support for up to 18 twelve-fiber ribbons housed inside. The ribbons are bounded in a singular filling compound inside the core tube. This filling compound prevents migration of water and other liquids along the core of the cable. Filling compound also provides a hydrostatic component of resistance to the core structure during compressive loadings. However, most filling compounds are highly combustible, petroleum-based materials. Therefore, they can be unsuitable for use in outdoor/indoor cables, which may encounter environments where contact with fire or intense heat might occur.

Two candidate polymers were chosen and tested as core tube materials for this application: a polypropylene that is currently used for core tubes in traditional OSP cable designs, and a LSZH flame retardant polyolefin. A comparison of the mechanical properties of each, shown in Table 1, reveals that the polypropylene has superior

mechanical properties. In contrast, the LSZH polyolefin has a density approximately twice that of the polypropylene, due to the presence of a high loading of flame-retardant fillers. These fillers increase the weight of the final product, but also aid in reducing thermal shrinkage. In addition, the heat of combustion of the LSZH polyolefin is two-thirds that of the polypropylene, making the LSZH material a potentially attractive candidate for use as the core tube of an outdoor/indoor cable. However, as discussed below, the LSZH polyolefin also has poor resistance to adsorption of petroleum derivatives from the filling compound.

Lastly, the core tube is encompassed with a non-woven tape which is impregnated with a water-swallowable polymer to prevent water passage between the core tube and jacket. The polymer in the tape also provides mildly inherent flame retardancy.

Sheath Design

The primary function of the cable jacket is to protect the optical fibers from damage resulting from processing, installation and adverse environmental conditions. In addition, the sheath must exhibit sufficient stiffness to resist excessive tensile and compressive strains resulting from the aforementioned procedures. In this design, stiffness was achieved with the use of dielectric strength members and sufficient polymer coverage.

The *Filled Outdoor/Indoor* cable contains two diametrically opposite longitudinal dielectric strength members, which are mechanically coupled to the outer polymer jacket to provide a robust composite structure. The placement of these two members offers several cable design advantages. These strength members are unique in that they have sufficient compressive and tensile stiffness to

Material	Density (g/cm ³)	Tensile Strength at break (ksi/MPa)	Elongation (%)	Low Temperature Brittleness (°C)	Heat of Combustion (BTU/lb)
polypropylene	0.897	3.6 (24.8)	490	<-25	19943
LSZH polyolefin	1.50	2.0 (13.8)	170	-25.5	6687

Table 1: Core tube material comparison

compensate for both thermal shrinkage and excessive tensile/compressive overload. With diametrically opposite positioning, the members always force the neutral axis (the line of zero strain in pure bending) to pass through their centers and the core center.^[3] This orientation imparts a preferential bend in the cable, but also imparts minimum strain and provides both flexibility and stability. The two rod strength member design has been thoroughly tested such that regardless of the direction of the bend in the cable, under any combinations of tensile/torsional loading, the cable will twist locally to maintain the neutral axis through the strength members, thus minimizing fiber strain.^[3] The strength members also possess a special surface treatment to minimize rod protrusion at free ends.

In this cable design, the jacketing material must provide the protection from harsh environments that is necessary in the outside plant environment, as well as the flame retardancy essential for indoor riser applications. To meet these demanding requirements, a LSZH polyolefin jacketing compound has been chosen for the *Filled Outdoor/Indoor* cable. With a heat of combustion of 6864 BTU/lb., this material provides excellent flame retardancy. In order to provide resistance to degradation resulting from exposure to ultraviolet light, the LSZH polyolefin is compounded with 2.6 parts carbon black per 100 parts base polymer. This material also has sufficient mechanical robustness such that cables sheathed with it pass all mechanical and environmental requirements of Bellcore GR-20-CORE testing.

Cable Testing

Fire and Materials Testing

Two nearly identical prototype cables with standard dimensions were fabricated and tested in accordance with IEC 332-2 and 61034-2. The construction of these cables was slightly different from that of the final design. Each cable had 144 fibers in ribbon

form, and each employed a dielectric crossply design with filling compound and a LSZH polyolefin jacket. The only difference between these two cables was that one cable had a polypropylene core tube, while the other utilized a LSZH polyolefin for the core tube. Upon initial testing, both cables complied with IEC 61034-2, exhibiting low smoke density under the defined burning conditions. In initial IEC 332-2 testing, the LSZH-core cable met the test requirements, while the polypropylene-core cable failed. The defined criteria in clause 2.8 states "the maximum extent of the charred portion measured on the test sample should not have reached a height exceeding 2.5 m above the bottom edge of the burner, neither at the front or at the rear"^[1]. The polypropylene-core cable was damaged over the whole test length on the front (burner) side, and damaged 2.5m on the back side. In contrast, 1.0 m of the passing LSZH-core cable was damaged on the front side only.

While the above fire tests were in progress, the aging performance of the LSZH polyolefin core tube of the passing cable was also examined. LSZH core tubes containing 144 fibers and filling compound were aged for seven days at 85°C/0% relative humidity. The filling compound and ribbons were then removed from both the aged core tube and a reference "as-received" LSZH core tube. Small film samples were cut from each tube, and the temperature-dependent mechanical properties of each film were subsequently examined using dynamic mechanical analysis (DMA). Both samples were examined over the range from -40° to 70°C, corresponding to the required service temperature range for outside plant cables.

Modulus vs. temperature results for as-received and aged LSZH core tube samples are shown in Figure 2. For comparison, the result of an identical test performed on an as-received polypropylene core tube is also included in Figure 2. At temperatures higher than -20°C, the mechanical properties of the as-received LSZH core tube are worse than that of the polypropylene. Accelerated aging of the LSZH core tubes containing filling compound results in

significant degradation of the tube's mechanical properties, due to swelling of the polymer by petroleum derivatives in the filling compound.

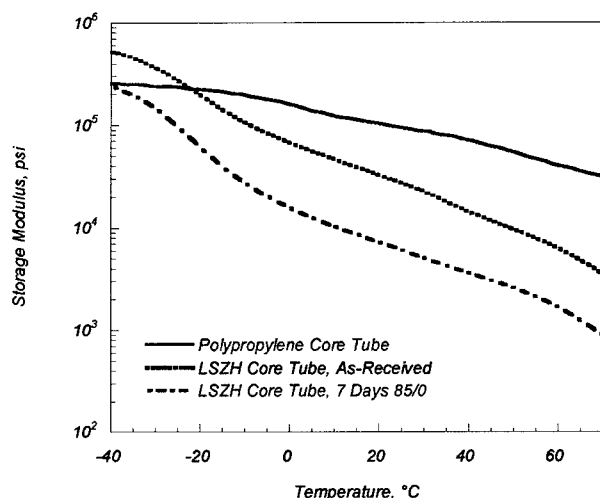


Figure 2 – Storage modulus vs. temperature results for an as-received polypropylene core tube, an as-received LSZH polyolefin core tube, and an LSZH polyolefin core tube aged 7 days at 85°C/0% relative humidity.

At 40°C, the modulus of the aged LSZH core tube is almost a full order of magnitude less than that of the as-received LSZH core tube, and is almost two orders of magnitude less than that of the polypropylene.

As a result of the fire tests discussed above, it was concluded that the polypropylene-core cable did not contain enough flame retardant material in the jacket to adequately protect the cable core. Once the jacket was breached, flame rapidly consumed the grease-filled polypropylene core tube, resulting in failure. In contrast, the LSZH-core cable had sufficient flame retardant to shield the combustible filling compound from the intense heat and flame. However, the aging tests performed on the LSZH core tube found that this material was incompatible with the filling compound, due to high adsorption of petroleum derivatives.

Taking into account the above conclusions, the current materials design for the *Filled Outdoor/Indoor* cable was developed. The intent of the new design was to utilize a robust polypropylene

core tube, while increasing the flame retardancy of the jacket to insure compliance with riser fire tests. The strategy employed was to add an amount of flame-retardant material equivalent to that found in the core tube of the passing LZSH-core cable to the outer jacket of the polypropylene-core cable. Analytically, the approach determined the cross-sectional area of both the core tube and jacket:

$$A = \pi \left(\left[\frac{OD}{2} \right]^2 - \left[\frac{ID}{2} \right]^2 \right)$$

Next the mass of each component (core tube and jacket) was determined by multiplying the cross-sectional areas by their respective densities.

$$M = A \times \rho$$

Then the mass of new design jacket, M_{NJ} , was determined by adding the original core tube mass to the original jacket mass.

$$M_{NJ} = M_J + M_C$$

The new jacket area, A_{NJ} , is then determined by dividing the new jacket mass by the material's density.

$$A_{NJ} = \frac{M_{NJ}}{\rho}$$

With this new area, the new cable outer diameter could be calculated.

A cable with the construction shown in Figure 1 was fabricated and submitted to Underwriters Laboratories in Northbrook, Illinois for testing in accordance with UL 1666. The results shown in Table 2 reveal the cables tested pass the requirements for the UL 1666 riser rating.

Sample	Max flame height (ft-in(m))	Maximum Damage Height (ft-in(m))			Maximum Temperature (°F(°C))
		Melt	Char	Ash	
A	6-0(1.83)	6-3(1.91)	6-0(1.83)	5-9(1.75)	444(229)
A-1	7-9(2.36)	11-6(3.50)	12-0(3.66)	9-6(2.90)	655(346)
A-2	3-6(1.07)	5-0(1.52)	5-3(1.60)	5-0(1.52)	406(208)

Table 2 – Filled Outdoor/Indoor UL 1666 test results.

Test	Specification	Test Description
Impact Test	FOTP 25	4 kg from 150mm – 25 cycles
Tensile Load and Bend	FOTP 33A	2700N-mandrel diameter: 30x cable diameter
Hot and Cold Bend Test	FOTP 37A	4 wraps on mandrel diameter: 20X cable OD; -30°C and 65°C
Compression Test	FOTP 41	220N/cm
Twist Test	FOTP 85	± 180° twist – 10 cycles
Cyclic Flex	FOTP 104	Sheave diameter: 20x cable OD 30 cycles/min for 25 cycles
External Freezing	FOTP 98	1 hour minimum freeze at -2°C

Table 3: Required mechanical testing for cable qualification.

Qualification Testing

This two-rod dielectric design was then subjected to a series of mechanical tests to assure the reliability of the cable. The testing was in accordance with the requirements outlined in the Bell Communications Research (Bellcore) procedure^[9] and the Fiber Optical Test Procedures of Electronic Industries Association (EIA)^[10] 455 test specification. The tested cable met or exceeded all the test requirements, as shown in the summary given in Table 3.

The optical performance of the design was also evaluated. The cable has low average added loss requirements of 0.35 and 0.25 dB/km at 1310 and 1550nm, respectively. Figure 3 displays the typical optical loss distribution for this design. In addition to as-cabled loss evaluations, the cable was subjected to standard Bellcore GR-20 environmental testing. Results are tabulated in Figure 4 for temperature cycling results over the range of -40°C to 85°C.

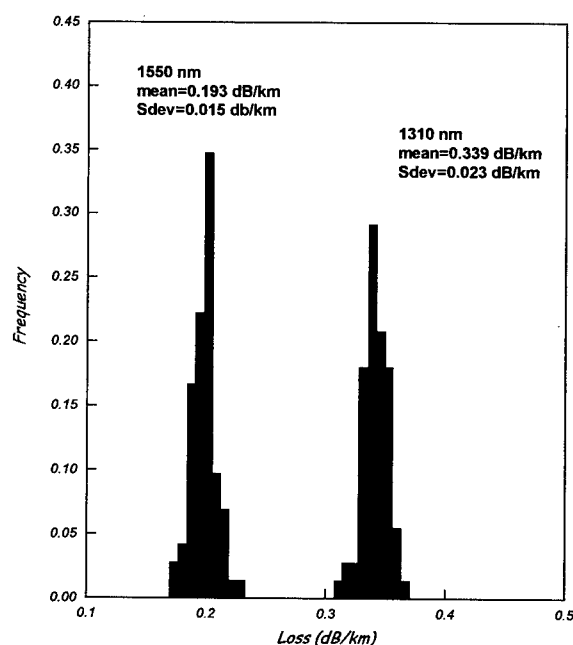


Figure 3: Optical Performance

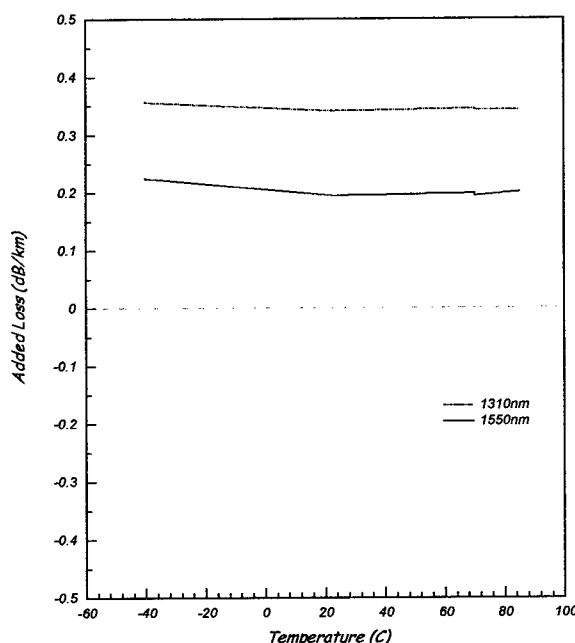


Figure 4: Environmental Performance

Field Installation Testing

The *Filled Outdoor/Indoor* cable was subjected to a rigorous battery of simulated field installation tests, performed at the Lucent Technologies OSP Fiber-Optic Cable Installation & Test Laboratory, located in Chester, New Jersey. The tests are designed to simulate both typical and extreme conditions the

cable might experience during a field installation. Table 4 includes a listing of the field tests performed on the two-rod dielectric design, and a brief description of each test. ^[3]

The cable was found to behave acceptably in all simulated installation testing with no permanent attenuation or detectable damage to the sheath. This design is intended for relatively short lengths, usually from the 1st manhole to the inner building termination point. However, these results indicate that aerial or burial installation would be acceptable means of installation.

Conclusions

The *Filled Outdoor/Indoor* cable has been presented and described. The cable design is UL 1666 riser rated and meets all requirements for Bellcore GR-20, Bellcore GR-409 and EIA/TIA 455 specification. This rugged dielectric cable derives its tensile and compressive strength by employing a new, two-rod strength member design. The composite sheath construction easily allows the standard 600 lb. (2700N) load rating, thus making it compatible with all common installation procedures.

Acknowledgements

The authors gratefully acknowledge the assistance and support of many individuals who were instrumental in the development and testing of the *Filled Outdoor/Indoor* cable at Lucent Technologies.

Test Category	Description
Initial attenuation measurement	Pre-test baseline
Pulling grip	Determine performance of pulling grips
Cable jettling	Determine cable jettability
Underground placing	Determine cable behavior during underground placing
Tension/Bending	Pull cable around quadrant block and various sheave sizes
Capstan Assist	Determine performance on intermediate capstan assist winch
Aerial Coiling	Performance as coiled
Direct Buried Plowing	Performance during plowing operation
Abusive Tests	Truck run-over and cable kinking
Final attenuation measurement	Comparison to baseline
Ultimate strength tests	Determine post-testing ultimate strength losses
Sheath Dissection	Evaluate internal components for test-related damage
Ribbon Inspection	Evaluate ribbons for test-related damage

Table 4: Field Installation Simulation Tests

References

1. IEC 332-3 Standard "Tests on Electrical Cables Under Fire Conditions" for Category C, Second Edition, International Electrotechnical Commission, 1992.
2. IEC 61034-2 Standard "Measure of Smoke Density of Cables Burning Under Defined Conditions", Second Edition, International Electrotechnical Commission, 1997.
3. P.D. Patel, M.R. Reynolds, M.D. Kinard, A.J. Panuska, "LXE-A Fiber-Optic Cable Sheath Family with Enhanced Fiber Access," 37th International Wire and Cable Symposium Proceedings, 1988, pp. 72.
4. NFPA 70, National Electrical Code 1999 Edition, Article 700-50b, National Fire Protection Association, 1998.
5. UL 1666 "Test for Flame Propagation Height of Electrical and Optical-Fiber Cables in Installed Vertically in Shafts", Second Edition, Underwriters Laboratories, Inc., January 1991.
6. National Fire Protection Association, Board of Directors Report, December 1982.
7. S.M. Chastain and J.W. Thornton, "Development of a Riser Rated Indoor/Outdoor Loose Tube Fiber Optic Cable", 45th International Wire and Cable Symposium Proceedings, 1996, pp. 369.
8. M.J. Keogh, in "Past, Present and Future Developments in Flame Retarded Polyolefins", Proceeding of the Second Conference on Recent Advances in Flame Retardancy, May 1991, pp. 161.
9. Bellcore GR-20-CORE, "Generic Requirements for Optical Fiber and Fiber Optic Cable", Issue 1, September 1994.
10. EIA Standard 455 and Addenda, Standard Test Procedures for Fiber Optic Fibers, Cables Transducers, Connecting and Terminating Devices, Electronics Industries Association.



Richard H. Norris
Lucent Technologies
Norcross, GA 30071

Richard H. Norris is a Member of the Technical Staff at Lucent Technologies in Norcross, Georgia. Dr. Norris joined Lucent Technologies in 1997 in the capacity of Development Engineer. He received his B.S. degree in Materials Engineering from North Carolina State University and M.S. and Ph.D. degrees in Metallurgical Engineering from the Georgia Institute of Technology. He is currently working in the area of Outside Plant Cable design and development. His technical affiliations include the Society of Plastics Engineers, ASM International, TMS and he is also a registered Professional Engineer.

SEMI-TIGHT BOUND TYPE FIBER OPTIC CABLE

Euy-Don Park, Min Son, Byung-Gon Lee, Yeon-Soo Kim

LG Cable Ltd., 643 Jinpyung-dong, Kumi, Kyungbuk, Korea

ABSTRACT

As the optical fiber networks have been deployed widely toward subscriber area today, the cable handleability, cable size and cost-effectiveness becomes to be considered more important factors than before. And the compatibility to existing facilities and technology for the cable manufacturing, cable installation and splicing works are also important for the reduction of total cost to build access optical network.

We have exploited the buffering area of conventional loose tube cable and designed a new type of downsized optical fiber cable of which outer diameter is smaller than conventional loose tube cable by about 30 percentages. The unit of this new cable has semi-tight coating configuration as the optical fibers in the shape of bundle are tightly bound by the secondary coating layer.

This new cable has been evaluated according to the Bellcore GR-20-CORE and all the optical, mechanical and environmental performances are confirmed to meet all test items of the standard.

INTRODUCTION

Two different concepts of tightly bound fiber structure and loosely buffered fiber structure are available for the design of optical fiber cable structure. In the tight-bound cable structure concept, the optical fibers are fixed to the other cable elements like central strength member and outer sheath layer without the consideration of free movable space for the optical fibers. In the loose buffer structure concept, the optical fibers are not bound tightly to the adjacent cabling members and have freely movable

space within limited range. The loose tube of this type cable is designed to have buffer area which is for, so called, tensile window. The tensile window is to provide freely movable space to the optical fibers in the cable that is to be placed under the condition of tensile load or thermal expansion and contraction. Such designs have been used for years, and corresponding machinery, tooling and process are well known. And their reliability is based on a strong background regarding designing, manufacturing and field experience so far.

This buffer area which is a design parameter to provide good mechanical and environmental performance for loose tube cable is generally three or four times larger than that of total cross-sectional area of fiber bundle. And practically very conservative loose tube cable design which has large buffer area have been used to anticipate the potential for the manufacturing process condition deviation, installation and operating conditions over lifetime of cable. The buffering area of this type cable lead to large size, less fiber density in cable and less cost-effectiveness of the cable.

As the optical cable is extending to access network, more chance to face insufficient spaces to lay the cable, the smaller size and higher density cable becoming more attractive, because the reduction of cable installation cost can be achieved by using optical cable having reduced diameter, higher fiber density and handleability. By the optimization with existing loose tube cable and tight bound cable design concepts for these requirements, we have newly designed a semi-tight bound cable. The packing density of the unit of this cable is about three times higher than that of the conventional loose tube unit.

The unit of this cable is designed to have the

optical fiber bundle which is tightly bound by secondary coating layer. All interstices of tightly bound bundle are coated with filling compound as thin layer. The optical fibers in the semi-tight coating are movable longitudinally even though they are bound axially and they have nearly zero value of excess fiber length.

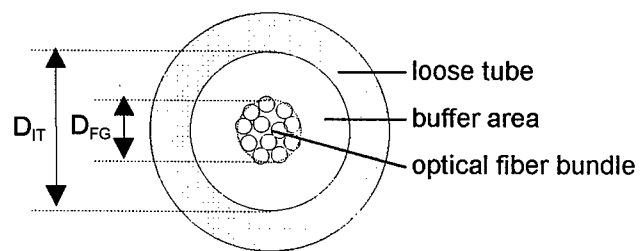


Figure 1. Configuration of loose buffer tube

BUFFER AREA ANALYSIS AND NEW CABLE DESIGN

The buffer area, A_B , of the unit of loose tube cable shown in figure 1 can be calculated by equation 1.

$$A_B = A_{IT} - A_{FIT} = \frac{\pi}{4} \{ D_{IT}^2 - n(D_F)^2 \} \quad (1)$$

where

A_{IT} is the inside cross sectional area of loose tube,

A_{FIT} is the total cross sectional area of fibers in the tube,

D_{IT} is the inner diameter of tube,

D_F is the outer diameter of coated fiber,

n is the number of fiber in the tube.

And the diameter of fiber group, D_{FG} , can be calculated by equation 2.

$$D_{FG} = 2 \cdot D_F \cdot \sqrt{\frac{n}{\pi}} \quad (2)$$

The normalized buffer area, A_{NB} , is defined as the buffer area allocated to single fiber, which is given by equation 3.

$$A_{NB} = \frac{A_B}{n} \quad (3)$$

The packing density of the loose tube is expressed given from the total cross sectional area of fiber, A_{FIT} , and the inside cross sectional area of loose tube, A_{IT} . For the conventional dimension of loose tube cable, where the inner tube diameter, D_{IT} , is 2mm and the number of fiber in a tube, n , is 12, the A_{NB} is around 0.2mm²/fiber, A_{FIT} is 0.05mm²/fiber, and the packing density is about 20 percentages as shown in figure 2. The figure 2 shows the maximum packing density is around 80 percentages as long as the optical fibers in the tube are maintained as bundle status. To have perfect bound condition as fiber bundle shape, the inner diameter of tube, D_{IT} , is 1.0mm theoretically. To increase the packing density, we designed the inner diameter of tube, D_{IT} , to be 1.2mm that is around 1.0mm of calculated value with the consideration of manufacturing process variation.

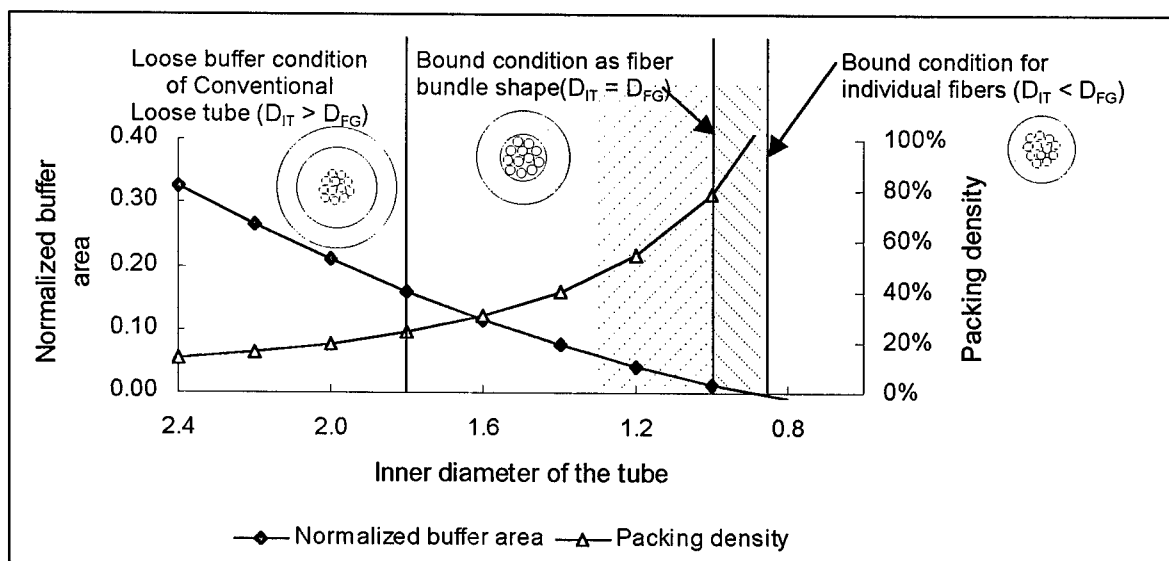


Figure 2. Inner diameter of tube vs. normalized buffer area and packing density

If the inner diameter of tube, D_{IT} , is smaller than the fiber group diameter, D_{FG} , some individual fibers of the fiber bundle are under the condition of increased fiber strain risk. The whole fibers are perfectly bound by the coating material filled into the interstices of the fiber bundle when the normalized buffer area, A_{NB} , is zero.

EFL Analysis

The excess fiber length in the loose tube is designed to minimize the fiber strain induced during the cabling process, installation process and operating condition over the lifetime of the cable. The excess fiber length is formed by the fiber curvature modeled as the figure 3. The bending radius of fiber curvature should be maintained about the limited value to get lifetime reliability of the mechanical strength of the optical fiber and to avoid microbending loss.

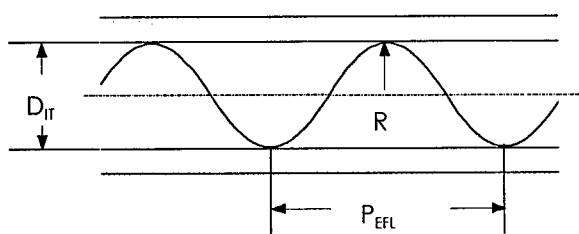


Figure 3. Schematic diagram of fiber curvature in loose tube

The total composite fiber bending radius, FBR_{total} , after cabling and drum packaging can be calculated by the equation (4).

$$\frac{1}{FBR_{total}} = \frac{1}{FBR_{EFL}} + \frac{1}{FBR_{ST}} + \frac{1}{FBR_{CA}} \quad (4)$$

where

FBR_{EFL} is fiber bending radius induced by the excess fiber length,

FBR_{ST} is fiber bending radius induced by fiber stranding,

FBR_{CA} is fiber bending radius induced by cable packaging on drum.

To meet the criteria of minimum 32mm, the fiber bending radius induced by the excess fiber length, FBR_{EFL} , should be more than 100mm when the minimum value of fiber stranding bending radius and cable packaging bending radius is given as 60mm and 200mm, respectively. The fiber bending radius, excess fiber length and the inner diameter of tube are

correlated as following equation 5 through 7.

$$EFL = \frac{L_F - P_{EFL}}{P_{EFL}} = \frac{\sqrt{(P_{EFL})^2 + (\pi(D_{IT} - D_{FG}))^2} - P_{EFL}}{P_{EFL}} = \sqrt{1 + \left(\frac{\pi(D_{IT} - D_{FG})}{P_{EFL}}\right)^2} - 1 \quad (5)$$

$$P_{EFL} = \frac{\pi(D_{IT} - D_{FG})}{\sqrt{(EFL + 1)^2 - 1}} \quad (6)$$

$$FBR_{EFL} = \left(\frac{D_{IT} - D_{FG}}{2}\right) \cdot \left(1 + \left(\frac{P_{EFL}}{\pi(D_{IT} - D_{FG})}\right)^2\right) = \left(\frac{D_{IT} - D_{FG}}{2}\right) \cdot \left(1 + \frac{1}{(EFL + 1)^2 - 1}\right) \quad (7)$$

where

L_F is length of fiber in a pitch of EFL

P_{EFL} is the pitch of EFL,

D_{FG} is diameter of fiber group.

R is fiber bending radius

The calculation results shown in figure 4 indicates that the maximum allowable excess fiber length is 0.25 percentage for the conventional cable of which inner tube diameter, D_{IT} , is 2.0mm. As we design the inner tube diameter of 1.2mm, this allowable maximum value is reduced to 0.05 percentage. And by the considering the variation of process condition to control the excess fiber length, the nominal design value of zero was selected for the semi tight bound cable.

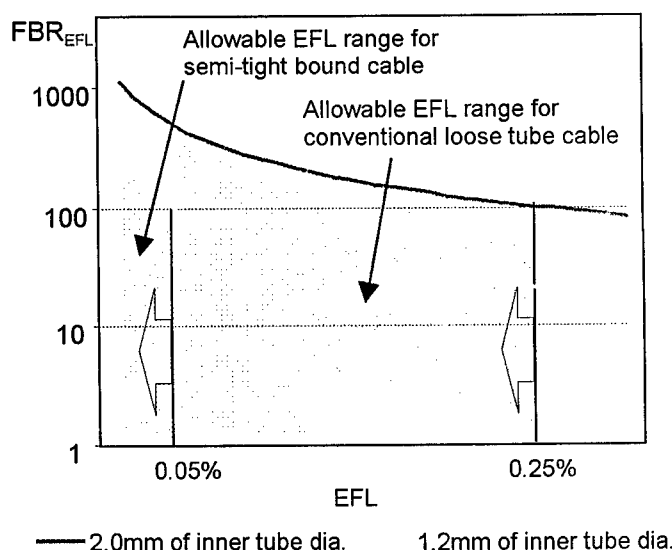


Figure 4. Fiber bending radius vs. excess fiber length

Cable design

The tensile window, TW, providing the fiber strain free region is given by the following equation 8¹ and the semi tight bound cable has about ± 0.1 percentage of tensile window value when the stranding structure is designed as having its lay length of 75mm.

$$TW = \sqrt{1 \pm \frac{\pi^2}{P_o^2} (D_{IT} - D_{FG}) \cdot (2D \pm (D_{IT} - D_{FG}))} - 1 \quad (8)$$

where

P_o is the lay length of the helically stranded units,

D is the equivalent diameter formed by the centers of stranded units.

And the thermal expansion coefficient, α_{cable} , of cable is calculated by the equation 9.

$$\alpha_{\text{cable}} = \frac{\sum_{i=1}^n \alpha_i \cdot E_i \cdot A_i}{\sum_{i=1}^n E_i \cdot A_i} \quad (9)$$

where

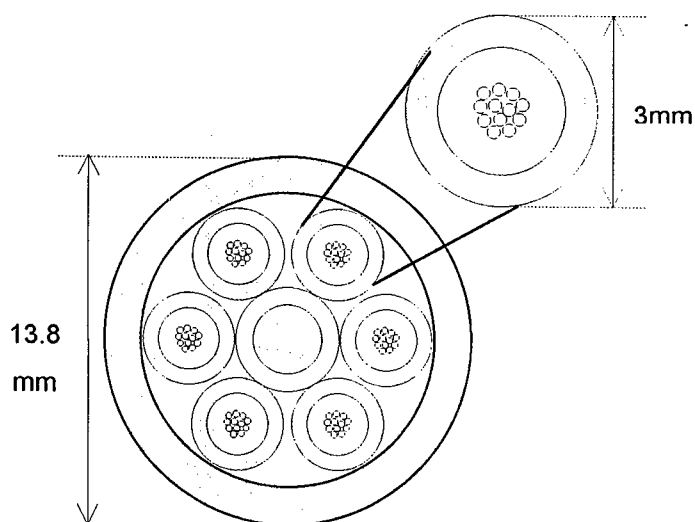
α_i is thermal expansion coefficient of cable elements,

E_i is young's modulus of cable elements,

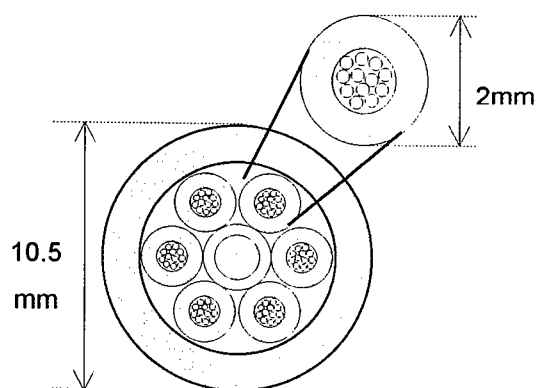
A_i is cross section area of cable elements,

Under the extreme temperature environments of -40°C and $+70^\circ\text{C}$, the 0.13 percentage of cable contraction and 0.12 percentage of cable expansion is obtained for the semi tight bound cable by the above equation 9. Accordingly, the maximum fiber strain under the temperature extreme is estimated less than -0.03 percentage and $+0.02$ percentage for the new cable if the tensile window of ± 0.1 percentage is regarded.

The semi tight bound unit and finished cable configuration are compared and shown in figure 5. When this new design concept is extended to the low and high fiber count cable of the same structure family, the cable outer diameter reduction of roughly 30 percentage is achieved and they are compared in figure 6.



(a) Conventional 72-fiber loose tube cable



(b) 72-fiber semi tight bound cable

Figure 5. Comparison conventions cable and semi tight bound cable

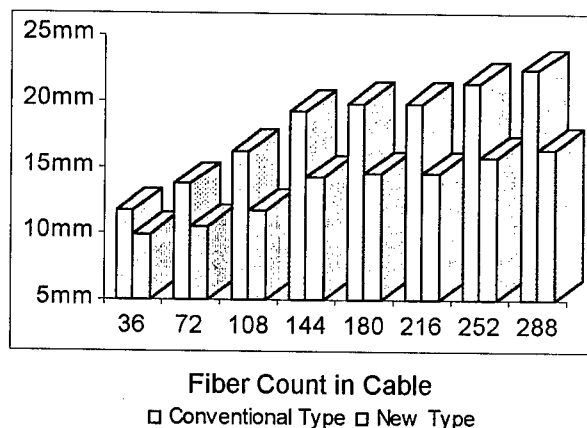


Figure 6. Outer diameter of conventional cable and new cable

CABLE PERFORMANCE

Cabling

The 72-fiber semi tight bound cable of duct type was produced for the evaluation of optical, mechanical and environmental performance.

As this new cable has no buffering area, the excess fiber length more than about 0.05 percentage can cause the fiber strain and microbending loss during the process. To avoid this kind of fiber strain and microbending, the length difference between the tube layer and optical fiber was controlled within 0.05 percentage by the fiber pay-off tension, the cooling speed of tube material and winding tension of tube in the tubing process and dynamic tension of tube pay-off in the stranding process. Then, the successful stable process conditions was confirmed by the attenuation distribution during in the whole manufacturing process which is shown as figure 7.

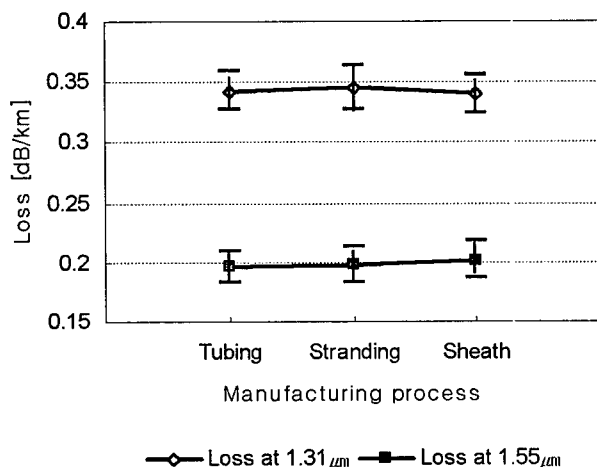


Figure 7. The attenuation distribution during the cabling process

Temperature Cycling Performance

Two $-40^{\circ}\text{C}/+70^{\circ}\text{C}$ of temperature cycle were completed. Figure 8 shows the attenuation changes (relative to the initial attenuation measured at 23°C) and the corresponding standard deviations for 72 fiber counts cable. Although the fibers are bound semi-tightly within the secondary coating layer during the expansion and contraction due to temperature change, almost no shift in the mean attenuation at temperature extreme was measured, and the

individual value of attenuation change was also less than 0.1dB/km, well within expectation and Bellcore standard.

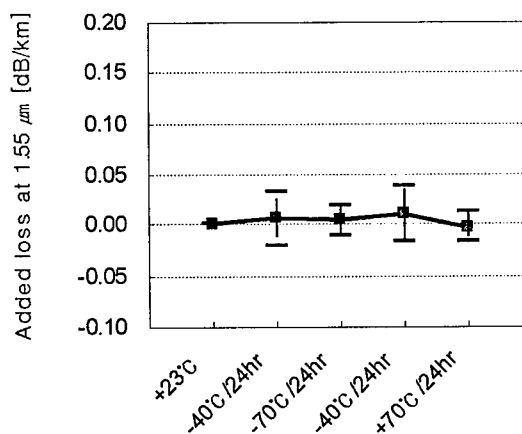


Figure 8. Temperature cycling performance of semi tight bound cable

Tensile Performance

The cable and fiber elongation versus the tensile load is shown in the figure 10. The length of cable under test was around 120m and elongation measurements made on the loops of 4 fibers was about 0.1 percentage at 1500 N and 0.3 percentage at 2700 N and no considerable added loss was measured at these tensile load. The fact that there is no fiber excess length in the cable explains the close relation between the fiber and cable elongation.

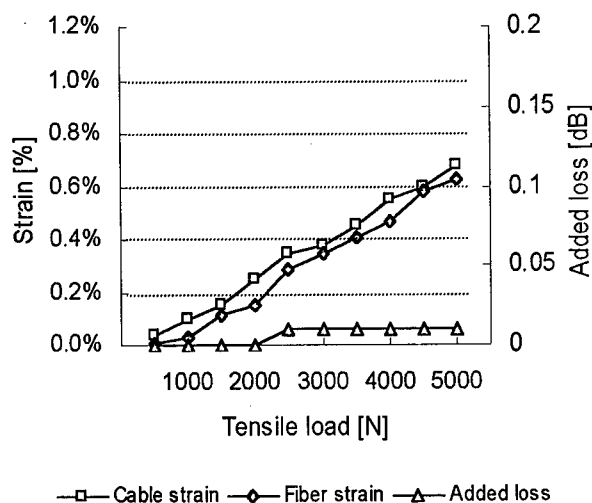


Figure 10. Tensile performance of semi tight bound cable

Impact

The cable withstands on the 20 times impact energy of 3N-m without any increase of attenuation and with no mechanical damage of the cable elements and fibers.

Compression

A load of 2500 N was applied to the cable through 100mm plates without any increase in attenuation and with no mechanical damage of the cable elements.

Mechanical and Environmental Characteristics

All test methods, conditions and results are shown in table 1.

Table 1. Evaluation test results of semi tight bound type optical fiber cable

Test item	Result	Test method
Temperature cycling (-40°C ~ +70°C, 2 Cycles)	Loss increase < 0.01dB/km (mean) < 0.05dB/km (max.)	EIA/TIA- 455-3A
Cable aging (+85°C, 168hrs)	Loss increase < 0.01dB/km (mean) < 0.03dB/km (max.)	EIA/TIA- 455-3A
Tensile strength (2700 N)	Loss increase < 0.01dB Fiber strain < 0.3 %	EIA/TIA- 455-33A
Impact (3 N-m, 20 Cycles)	Loss increase < 0.01dB	EIA/TIA- 455-25A
Compression (250N/cm)	Loss increase < 0.01dB	EIA/TIA- 455-41
Cyclic flex (100 Cycles)	Loss increase < 0.01dB	EIA/TIA- 455-104
Cable twist (2 m, 2 turns)	Loss increase < 0.01dB	EIA/TIA- 455-85A
High temp. cable bending (+60°C, 4 turns)	Loss Increase < 0.01dB	EIA/TIA- 455-37A
Low temp. cable bending (-30°C, 4 turns)	Loss Increase < 0.01dB	EIA/TIA- 455-37A
Water penetration (1m, 24hours)	No water leakage	EIA/TIA- 455-82A
Filling compound flow (80°C)	No compound flow	EIA/TIA- 455-81

CONCLUSION

The buffer area of conventional loose tube cable has been exploited from the viewpoint of fiber density and cable size and a down sized cable having semi-tight bound structure has been designed.

This newly designed cable has been submitted to various tests. And the cable has been evaluated as retaining higher than 2700 N tensile load rating and sufficiently reliable performance under the temperature range of -40°C to +70°C and all other mechanical and environmental test condition.

As result, this newly designed cable has been confirmed to meet or exceed the common industry standards.

ACKNOWLEDGEMENTS

The authors would like to extend their application to Mr. E.G. Hwang, Mr. J.H. Kim and Mr. S.Y. Park for their contributions in the secondary coating process and the testing and collection of the data.

REFERENCES

1. Jana Horska, "Design of Loose Tube Fiber Optic Cable with Adjusted Contraction and Strain Windows", proceedings of the 43rd International Wire and Cable Symposium, pp 50-58, 1994
2. Bellcore, "Generic Requirements for Optical Fiber and Fiber Optic Cable", Generic Requirements GR-20-CORE, Issue 2, July 1998



Euy-Don Park

LG Cable Ltd.

643, Jinpyung Dong, Kumi City, Kyungbuk
Korea

Euy-Don Park is received B.E. and M.E degrees in Electronics Engineering from Kyungbuk University in 1986 and 1991 respectively. He joined LG Cable Ltd. in 1986 and has been engaged in the design and development of optical fiber cable. He is now a general manager of optical cable technology team in Indong Plant.

ULTRA FLEXIBLE & HIGH FIBER COUNT OPTICAL CABLE FOR METROPOLITAN DUCT USING SLOTTED ROD WITH SEGMENTED-RIB

Yoshinori Kurosawa, Kenji Omura, Osamu Arai, Takahiro Sato, Isao Abe
and Hisanori Nakai

Hitachi Cable, Ltd.

5-1-1, Hitaka-cho, Hitachi-shi, Ibaraki-ken, 319-1414, JAPAN

ABSTRACT

We have developed a new flexible high fiber count optical cable. This cable features a slotted rod comprising a rib, which is slit at intervals of several millimeters, to effectively relax longitudinal tensile or compressive stress of the rib when the cable is bent. We calculated and measured flexural rigidities of several slit slotted rods and cables. Furthermore, trial cable was manufactured, and its optical and mechanical performances were examined.

1. INTRODUCTION

Digital network systems utilizing optical fiber transmission are increasing in metropolitan cities where new duct construction is strictly limited. A high count optical fiber cable using a slotted rod is necessary to construct optical fiber network trunk lines in metropolitan cities in Japan.¹⁾ In these cities, the cable duct routes are typically very complicated and comprise many bends. Therefore, installation of a high fiber count cable can be difficult due to the friction force occurring at each corner as a result of the cable's flexural rigidity.²⁾

To overcome this situation, a new flexible and high fiber count optical cable is necessary. The ribs of the slotted rod are slit at intervals of several millimeters to prevent longitudinal

tensile or compressive stress of the rib when the cable is bent.

In this paper, we describe the examination of the flexural rigidity of optical fiber cables and performance of flexible 1000-fibers optical cable.

2. FLEXURAL RIGIDITY

Flexural rigidity of the slotted rod type optical fiber cable increases rapidly in proportion to cable size. To maintain mechanical reliability, the dimensions and material of the sheath and central strength member must not be altered. Therefore, a modified slotted rod has been invented.

2.1 CALCULATION OF FLEXURAL RIGIDITY

Flexural rigidity of the slotted rod is dependent on the 'rib' component. This 'rib' component is made from hard high-density polyethylene to help maintain a constant groove shape along the cable length. The inside core part of the rod is made from low-density polyethylene to maintain integrity with the central strength member.³⁾

A calculation model of the slotted rod type optical fiber cable is shown in Fig. 1.

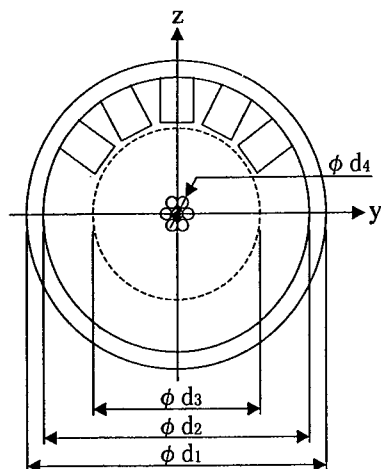


Fig.1. Calculation model of the slotted rod type optical fiber cable

Diameter of sheath is d_1 , outer diameter of slotted rod is d_2 , inner diameter of slotted rod of which low density polyethylene is d_3 , and the diameter of a section of the central strength member which is composed of seven twisted wires is d_4 . The Young's modulus of each is E_1 , E_2 , E_3 , and E_4 , respectively.

2nd moment of area of No. n slot of total m slots is expressed as:

$$I_{zrn} = \frac{1}{2}(I_{yr_1} + I_{zr_1}) - \frac{1}{2}(I_{yr_1} - I_{zr_1}) \cos\left\{-\frac{720(n-1)}{m}\right\}$$

2nd moment of area of sheath : I_{zs}

2nd moment of area of outer slotted rod (rib part) : I_{zo}

2nd moment of area of inner slotted rod (low density part) : I_{zi}

2nd moment of area of strength member : I_{zm} are expressed as follows:

$$I_{zs} = \frac{\pi d_1^4}{64} - \frac{\pi d_2^4}{64}$$

$$I_{zo} = \left(\frac{\pi d_2^4}{64} - \frac{\pi d_3^4}{64}\right) - (I_{zr_1} + I_{zr_2} + I_{zr_3} + \dots + I_{zr_m})$$

$$I_{zi} = \frac{\pi d_3^4}{64} - I_{zm}$$

$$I_{zm} = \frac{7\pi d_4^4}{64}$$

Consequently flexural rigidity of the cable : EI is expressed as:

$$EI = E_1 \times I_{zs} + E_2 \times I_{zo} + E_3 \times I_{zi} + E_4 \times I_{zm}$$

Flexural rigidities of the 1000 fiber cable are shown in Table.1 and its structure is

shown in Fig.2. The results suggest that the rib component shares a large proportion of the total flexural rigidity in the cable.

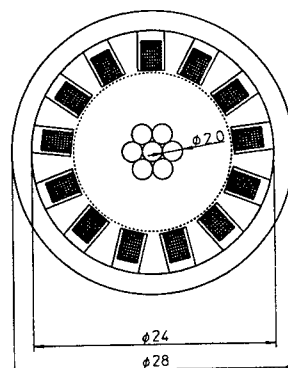


Fig.2. Structure of the 1000 fiber cable

Table.1 Flexural rigidities of the 1000 fiber cable

Item Part	Young's Modulus (kg/mm ²)	Flexural rigidity ($\times 10^5$ kg·mm ²)	Share Rate (%)
Sheath	50	7.02	43.9
outer slotted rod (rib part)	110	6.99	43.8
inner slotted rod	29	0.85	5.3
Strength Member	20000	1.11	7.0
Total	-	15.97	100

2.2 MEASUREMENT OF FLEXURAL RIGIDITY

We measured the flexural rigidities of two kinds of slotted rods with several slit conditions to optimize slit design. Structures of slotted rods are shown in Fig.3. The three-point bending test method is shown in Fig.4. In the three-point bending test, the relation between load P and sag length v is expressed as

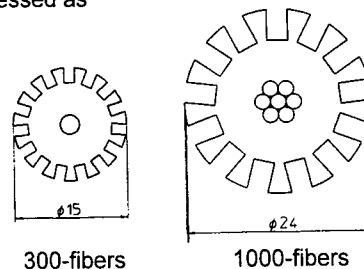


Fig.3 Structures of slotted rods

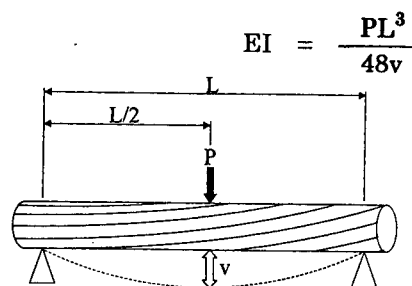


Fig.4 Three-point bending test

Measurement results of flexural rigidities are shown in Table.2. The deeper the slits or the shorter the intervals, the lower the flexural rigidity. We demonstrated in the bending test that the flexural rigidity of the slit rod was about 50% less than that of the conventional non-slit rod.

3. TRIAL CABLE

1000-fiber trial cable was manufactured on an experimental basis in light of the above, and was tested under several conditions.

3.1 CABLE STRUCTURE

The cable is designed to accommodate 1000 single mode fibers (one hundred and twenty-five 8-fiber ribbons which are 0.3mm thick and can be easily divided into two 4-fiber ribbons) in thirteen slots of the slotted core. (Fig. 5)

The ribs of the slotted rod were slit with a depth of 4mm and pitch of 6mm. Flexural rigidity of the trial cable was 30% less than that of the conventional cable,

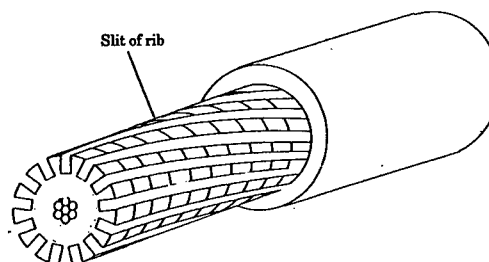


Fig. 5 1000 fiber count trial cable

3.2 CABLE PERFORMANCE

The characteristics of the trial cable were investigated through several tests.

Transmission and mechanical performances of the cable are shown in Table.3.

The trial cable has an attenuation of 0.23dB/km(max.), 0.20dB/km(average), and 0.19dB/km(min.) at 1.55 μ m.

The attenuation change during the temperature cycle test over the range of -30°C to 70°C was less than 0.1dB/km.

Results of mechanical tests such as the tensile test, bending test and lateral force test are also good.

Table.2 Measurement result of flexural rigidity

Slotted rod	Slit condition		Flexural rigidity (calculation) [$\times 10^5 \text{ kg} \cdot \text{mm}^2$]	Flexural rigidity (measurement) [$\times 10^5 \text{ kg} \cdot \text{mm}^2$]	Decrease rate of Flexural rigidity (measurement) [%]
	depth [mm]	pitch [mm]			
300-count (S)	Slit less		2.20	1.57	—
	1	2	1.54	1.04	34
		4		1.14	27
		6		1.23	22
	2	2	1.03	0.76	52
		4		0.81	48
		6		0.90	43
1000-count (S)	Slit less		8.94	6.70	—
	4	3	2.31	3.15	53
		6		3.35	50

Table.3 Trial cable performance

Item	Condition	Attenuation increase
Attenuation	At 1.55 μ m	<0.23dB/km
Temperature Cycling	-30°C to 70°C	less than 0.1dB/km
Tensile force	10000N	No increase
Bending	Bending radius 240mm \pm 90 deg	No increase
Lateral force	1960N/10cm for 1 min	No increase

4. CONCLUSION

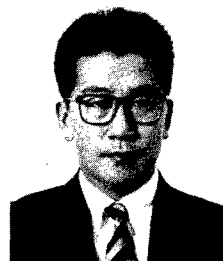
A new flexible 1000-fiber count optical cable has been developed, which demonstrated strong performance. Its performance results are as follows:

- (1) the flexural rigidity of the slit rod was 50% less than that of the non slit conventional rod,
- (2) the flexural rigidity of the cable was 30% less than that of the non slit conventional cable,
- (3) the trial cable shows good transmission and mechanical performances in several tests.

REFERENCES

- 1) S. Tomita, et al. "Ultra High-Density Optical Fiber Cable with Thin Coated Fibers and Multi-Fiber Connectors," 42nd IWCS, pp.5-15, (1993)
- 2) H. Iwata, et al. "Study on advanced function of optical fiber cable for access networks." Technical Report. of IEICE Vol.97 No.536 (1998)
- 3) M. Okada, et al, "Study on foamed polyethylene slotted rod," IEICE'98, March, B-10-71, (1998)

Yoshinori Kurosawa
Hitachi Cable, Ltd.
5-1-1, Hitaka-cho,
Hitachi-shi, 319-1414
Japan



Mr. Kurosawa received his B.E. degree in Mechanical Engineering from Waseda University in 1985 before joining Hitachi Cable, Ltd. He has been engaged in research and development of optical fibers and cables. He is now a senior researcher in the 4th Dept., Optoelectronic System Laboratory.

VERSATILE OUTSIDE PLANT SOLUTION FOR OPTICAL ACCESS NETWORKS

W. Griffioen, A. van Wingerden, C. van 't Hul

NKF Kabel, Delft, The Netherlands

ABSTRACT

A new outside plant solution for optical access networks is presented having versatility not offered by present technology. The number of splices has been reduced, midspan access has been made possible at any place and any time and investments grow with demand. Experimental trial and pilot are reported. Use in shared networks, where different telecom operators can rent access links, is also presented. As spin-off the technique has also advantages in backbone networks because of the high fiber density and because latest-technology fibers can be installed during expansion.

INTRODUCTION

While optical fiber is now being used on a large scale in telecom backbones (see Figure 1), copper twisted-pair still dominates in the access network. In the backbone the exchange offices are connected by simple point-point links. In the access network, however, the connection from exchange office to customer passes many splices and branches. Splicing and branching in copper twisted-pair has been done for more than a century, but for optical fiber (where a minimum of splices is preferred) the current technology does not suffice. Optical access networks require a high degree of versatility: It is not known when and where connection is asked for, installation shall be fast, new connections shall not disturb existing ones, both business and consumer market may ask for solutions and redundant connection may be required. The architecture for optical networks has to evolve in an environment where techniques for passive optical networks are still in development. Also excessive digging shall be avoided and trench space becomes more and more limited.



Figure 1 *Laying of HDPE protective tubes in the Netherlands for the optical backbone-network.*

In this paper a unique concept for the optical access network outside plant is presented. It is a further development of the "copper-in-tube" solution for "greenfield" access networks for the consumer market, prepared for future FTTH.¹ The new concept is suited especially for optical overlay networks for business customers. It will be illustrated by results from a technical trial and pilot projects. Some remarks will be made about advantageous use in long-distance backbone networks. Finally a network design will be shown where the concept is used in a shared network, where different telecom operators can rent links to access their customers.

THE NEW CONCEPT

The new concept for optical access networks consists of bundles of individual guide-tubes running through a protective HDPE duct network. A trunk duct runs through the streets and smaller ducts branch to the subscribers. Low-cost splittable "clip-on" branching connections are used which can be placed at any place and any time (see Figure 2). Miniaturized optical cables (2-48 fibers) can be installed without splice into the guide-tubes, e.g. by simply pushing or using compressed air. Two types of cables are used, one with hermetic welded steel-tube (same construction also used in OPGW cables) and a novel non-metallic multilayer design (based on cone extrusion process).² Both constructions offer excellent resistance to outside plant conditions and handling. The bundle of guide-tubes does not entirely fill up the protective duct to offer sufficient mechanical protection,³ to make all tubes accessible at any place and for ease of installation of the bundle.

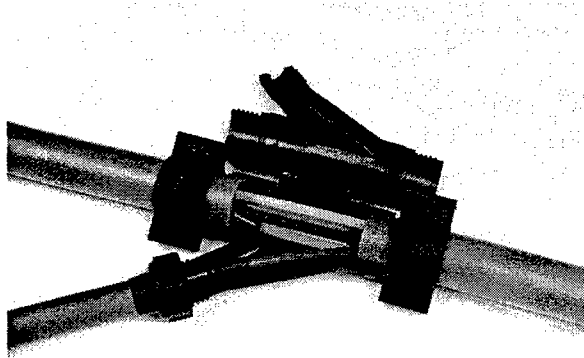


Figure 2 Clip-on Y-connector for branching a guide-tube. A mini-cable passes here without splice.

The concept can be completed with optional joint boxes to connect cables from feeder-, distribution- and drop-part of the access network. Separate protective ducts may be used for these parts of the network but integrated solutions are also possible. The new concept is less costly than traditional techniques for optical access networks. It solves today's problems connecting business customers and bringing FTTH within reach.

ARCHITECTURE

With the modular building blocks of the new concept almost any network can be created. This paper shows only a limited choice. In Figure 3 an example is shown of an optical access network

for business customers with redundant 2-fibre connections. A primary ring leaves the local exchange office. At (primary) nodes in this ring secondary clamp-shells are connected. The primary nodes can be fed e.g. by individual 48-fiber cables (see Figure 4). Note that no window-cuts are made in the network. The clamp-shells run close to the customers to which a drop can be made. It is possible to connect a number of customers (as many as the guide-tubes in the clamp-shell) directly to the primary node. This eliminates one layer of nodes compared to traditional technology. Also the number of protective ducts is less. In e.g. a 40 mm protective duct there is space for 10 guide-tubes with 2-fibre cables (see Figure 4). For the same number of customers in the traditional technology a number of additional protective ducts is needed to guide the drop cables from (pre-determined) splice points in the clamp-shell to the arbitrarily located branches.

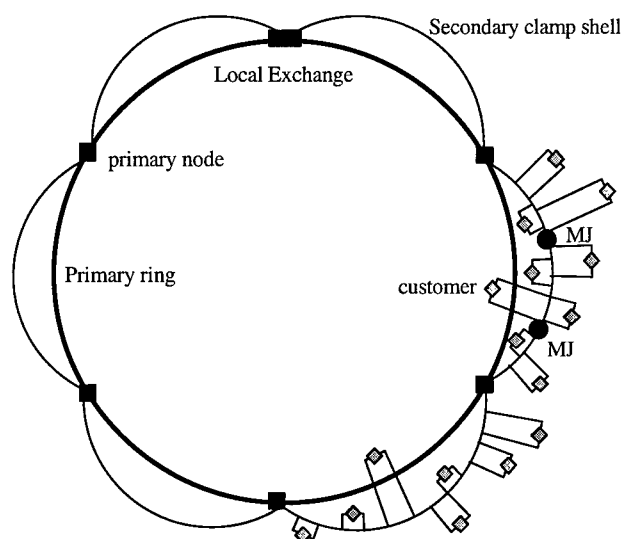


Figure 3 Example of architecture of the new concept for a primary ring with secondary clamp-shells and redundant connected customers.

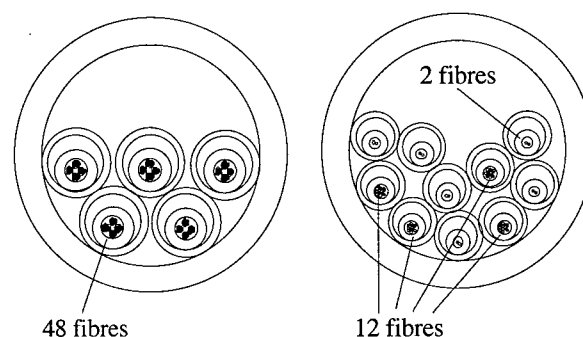


Figure 4 Example of tubes and cables used in primary-ring and secondary clamp-shell, respectively.

It is also possible to enlarge the number of customers per protective duct in the secondary clamp-shell even further by introducing (again) splice points (MJ's) in the shell. In Figure 5 a detail is shown of a section of such a shell. Four guide-tubes are used to feed the different MJ's by 12-fiber distribution cables. They are spliced at these MJ's to six 2-fiber drop cables which are guided to the branch-points at the customer-drop through the six remaining guide-tubes (see also Figure 4). With only one 40 mm protective HDPE duct now up to 30 customers can be connected in this way. Compared to the traditional cabling, where a number of extra 40 mm protective ducts were needed along the clamp-shell to reach the branch-points, a tremendous saving of protective ducts is achieved (up to a factor of 15!). As an additional advantage the distance from the last splice point to the customer becomes less. This allows one-shot blowing to the customers in more cases.

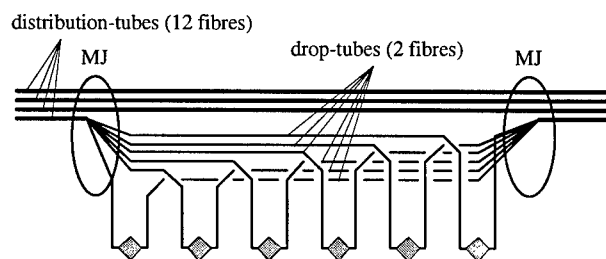


Figure 5 Detail of a section of a secondary clamp-shell with splice-points (MJ's).

The architecture shown is an example based on architecture used in traditional technology. The new concept also opens new ways to plan networks, e.g. the use of more and shorter clamp-shells and/or increased trench sharing of primary and secondary networks (the longer primary routes are only economical when using the new concept). Here the advantages of eliminating a layer of nodes can be combined with the advantages of shorter blowing lengths and extra saving on protective ducts.

ADVANTAGES

Typical advantages of the new concept are:

- Costs grow with demand. Parallel (filling tubes) and serial (connecting bundles of tubes; saves digging) upgradeable.
- No (expensive) pre-determined splice boxes with cable-overlength, low-cost branching.
- Much more customers per protective duct, less trench space.

- Mid-span access at any time (living fibers not disturbed) and any place.
- Joint boxes are more compact than current splice boxes (no "window cut") and can be placed at a later stage.
- Limited number of splices.
- Less splices at reparation (the fewer customers, the fewer fibers).
- Fast installation technology, short response time.
- Spare tubes can be used for other purposes, e.g. localization wires.
- When a customer moves or ends its subscription the guide-tube is easily used again.
- Match with installed base of HDPE ducts for optical cables, even when already occupied.
- Free space in protective ducts offers excellent mechanical protection.

INSTALLATION AND TRIAL

The different installation steps have been carried out in a technical trial in Delfzijl. Here a secondary clamp-shell has been built including the connection to the primary nodes and the customer's termination. The (optional) MJ's between secondary feeder and tertiary distribution and drop have also been built. The installation of tubes and cables is performed using the blowing technique.^{4,5} The required minimum installation lengths listed below have been tested in a trajectory with a bundle of direct-buried (40 cm deep) protective HDPE 40 mm ducts in a 300 m straight route, connected by loops to obtain longer lengths. The tests shall be passed in all weather conditions, also with reels of tube or cable unprotected in (artificial) rain. In other tests much longer lengths have been reached, also when the ducts were laid with more bends, above ground and on a hot and sunny day.

- Blowing of a bundle of ten tubes of 7 mm and five tubes of 10 mm. Required 1000 m.
- Blowing of 2-fibre cables in 7 mm tubes (in bundle). Required 1000 m.
- Blowing of 12-fibre cables in 7 mm tubes (in bundle). Required 800 m. Cascading possible.
- Blowing of 48-fibre cables in 10 mm tubes (in bundle). Required 1000 m. Cascading possible.
- Dig-up, lifting, at several places until cables break. No damage of cables after the anchoring-points of primary nodes, MJ's or customer's termination boxes.
- Dig-up, cutting down. Same as above.

PILOTS

In the pilots made with the technique of "copper-in-tube" the customers were connected by copper twisted-pair.¹ Nevertheless all handling and components of the new concept for optical access networks have been extensively tested because migration to FTTH had to be demonstrated. Pilots of the new concept are scheduled for the autumn of 1999 and will be reported during this symposium. By that time the installation will commence of the first "shared access network" (see further in this paper) where the technique presented in this paper will be used exclusively.

BACKBONE NETWORKS

The presented concept offers, as a spin-off, also advantages when used in long-distance backbone networks. Of special interest here is the high fiber-density, which can be achieved, e.g. 240 fibers in a 40 mm protective HDPE duct (see Figure 4). This will help to limit the wild growth of HDPE ducts in long-distance networks,⁶ see Figure 1. Splicing separate cables at different locations can reduce repair time. The repair time is, of course, even less when all tubes are not yet occupied. The investments grow with demand.

But, maybe most importantly, the latest-technology fibers can be installed during expansion. This is no luxury because fiber technology is still improving. New fiber types for DWDM transmission with larger effective area or flatter dispersion have recently been developed and it seems that the final optimal design is not yet there.⁶ For e.g. soliton transmission even other approaches, like dispersion-tapered fibers might once reach the market.

SHARED NETWORKS

A division of NKF uses the presented concept to lay shared optical access networks. Access is offered to different telecom operators who can rent links within the network to bridge the last mile to their customers. The versatility of the presented concept matches well with the needs of such networks. A shared network avoids multiple networks being built one by one which is occurring now in the deregulated telecom market. A shared network, however, requires a special and more expensive architecture.

An example of architecture for shared networks is given in Figure 6. The points where the networks of the telecom operators are connected to the shared network must be accessible by all parties, each having their own burglar-free space. Such points are present at all customer terminations and at the boundary of the shared network. The latter points require separate "telecom houses" which might have active equipment inside. To avoid single-points-of-failure at least two such houses are needed. To secure that ducts of the telecom operators never lay in the same trench as those of the shared network (which shall be avoided for full redundancy) a "circular road" of tubes surrounds the shared network. These tubes are rented to telecom operators to reach the telecom houses.

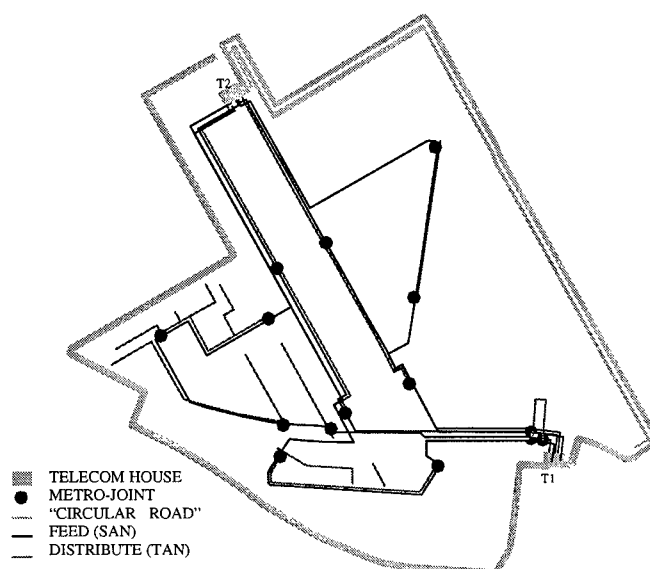


Figure 6 Example of architecture for a shared network.

CONCLUSIONS

The presented new outside plant solution offers the versatility, which is required for optical access networks. Examples of architecture demonstrate how the number of customers increases compared to traditional technology. The technique has been proven in field trials and pilots. The new concept can also be used for the long-distance backbone network. Finally the same technique can also be used in shared access networks where different telecom operators rent links to their customers.

ACKNOWLEDGEMENTS

The authors wish to acknowledge Willy Greven, Frans Bakker, Jeroen van Heck, Kees van Trigt, Hennie Rikken, Marko Lubberdink, Jan van der Stap, Albert Grooten, Bert van de Tuuk, Arnie Berkens, Esther Schulting, Sito Zandberg, Jan Jonker, Rick van der Werf, Jussi Ravela, Markku Heino and Gerard Plumettaz for their valuable contributions.

REFERENCES

1. W. Griffioen, H. Nijstad, A.T.M. Grooten, A. van Wingerden, G. Brown, D.F. Hawkins, G. Plumettaz, A new, extremely versatile, access network cabling concept for migration to optical fiber, *Proc. 45th IWCS* (1996), 485-489.
2. M. Heino, J. Ravela, M. Suvanto, R. Phillips, T. Vainio, "Novel non-metallic multilayer fiber optic cables based on cone extrusion process", *This Symposium*.
3. K. Nygård Skelman, E. Siönäs, S. Edman, G. Danielsson, The equipment and cables used in the optical fibre network at Banverket, Sweden, *Proceedings Interwire*, Atlanta (USA), November 1992.
4. W. Griffioen, "Installation of optical cables in ducts", Plumettaz, Bex (CH) 1993.
5. G. Plumettaz, A new universal tool for the placement of microcables in the local and business access network, *Proc. EC'99* (1999) 76-80.
6. Innovation rules as fibre makers battle for business, *Fibre Systems*, March 1999.

SPEAKER



Willem Griffioen received a MS degree in Physics and Mathematics from Leiden University (Netherlands) in 1980. Worked there until 1984. Joined KPN Research, St. Paulusstraat 4, 2264 XZ Leidschendam, The Netherlands. Responsibilities R&D of Outside-Plant and Installation Techniques. Worked at

Ericsson Cables, Hudiksvall (Sweden) and at Telia Research, Haninge (Sweden) in the scope of exchange/joint projects with KPN Research. Received Ph.D. (Reliability of Optical Fibers) in 1995 from the Technical University of Eindhoven (Netherlands). Currently, since 1998, he is product manager at NKF Kabel, Schieweg 9, 2627 AN Delft (Netherlands).

DEPLOYMENT OF A LONG DISTANCE OPTICAL CABLE NETWORK IN THE CANALS AND RIVERS RIGHT OF WAY

**David J. BENZEL⁽¹⁾, Jean-Pierre HULIN⁽¹⁾, Daniel RIVARD⁽²⁾, Antoine VEYRAT⁽²⁾,
Véronique STAPPERS⁽³⁾, Bertrand JOLY⁽³⁾, Rod NEWMAN⁽⁴⁾, François RICHAUME⁽⁴⁾**

(1) Alcatel Cable and Components - Calais, France

(2) LDCable - Paris, France

(3) Alcatel Cable Interface - Bezons, France

(4) MKI - France

ABSTRACT

Deregulation in the field of telecommunications in Europe has encouraged the arrival of new operators who have to build their own networks by leasing fiber from existing networks or by installing their own cables. Because of the limitations on where such networks can be installed, these operators have had to resort to alternative Rights of Way (ROW) for the installation of their cable networks. At the end of 1997, LD COM and *Les Voies Navigables de France (VNF)* investigated the possibility of using their network as a new "right of way" for telecommunications.

This paper describes the new high-count fiber optic cable solution specially designed and developed by ALCATEL to meet the performance requirements of a buried underwater cable, with up to 864 fibers and associated interconnection devices. It also discusses the underwater installation technique, which enabled rapid installation, and has been optimized to guarantee long-term reliability of the cables, that are deeply buried at the bottom of the river. The results of the installation of 1000 kilometers of cable, and of tests on the installed cables, are given in the final part of the paper.

INTRODUCTION

Many new independent telecommunications operators have recently been establishing themselves in Europe. These operators were initially seeking long distance networks and Metropolitan area networks. However, constructing a long distance network is not easy, and the solutions for installing cables in major cities are limited in most countries around the world. We are referring, here, to "rights of way". Motorways and

railways, power utilities, subways....., have all promoted their "rights of way" from the start, by installing cables and renting out dark fibers to operators. VNF, which manages the 8,000 kilometers of French rivers and canals, saw the opportunity of using its navigable waterways as a useful new ROW, providing that a cost-effective installation procedure, as well as a cost-effective cable solution, could be developed.

Early in 1998, LD COM signed an agreement for the deployment of a long distance telecommunications network in the French Canals & Rivers system. LDCOM, MKI France and ALCATEL joined forces to develop, evaluate and implement a new, reliable, rapid and low cost solution for M.A.Ns and long distance networks. The installation was specially set up by LD CABLE and TRAVOCEAN (two subsidiaries of LD COM). A new type of cable was required and many design factors had to be taken into consideration in order to find a cost-effective underwater cable. These included (among other factors) fiber packaging, cable density, core protection against water and hydrogen ingress, tensile strength, and mechanical resistance. In this paper we will discuss cable test results carried out to verify the cable design. Special underwater splicing techniques will be also described, and, in particular, a submersible splice box used for repairs or to avoid splices on the riverbank.

The project started in April 1998 with the first installation and discussion of the cable design; the first cable trials and installations took place just three months later, in June. At first this project was implemented to cover the Paris area, and the cable was installed in the river Seine during the summer and autumn of 1998.

LD COM and MCI Worldcom worked together to finance this project. This enabled the 2 operators to have their own infrastructure. MKI France carried out the general network architecture (submerged and terrestrial), subsequently doing the research studies and work for the landing sites (civil works and splicing).

PROJECT PARAMETERS AND CONSTRAINTS

The project was subject to many specific parameters and constraints, essential to ensure compatibility between the cable and its installation technique. The customer specifically required a cable of very high fiber count (up to 864 fibers) in a relatively small cable diameter (45mm max), so that it would fit through the cable installation equipment. Since the cables were to be installed using river barges, the overall cable weight, reel size, and cable lengths had to be closely analyzed. In order to meet the tight time constraints of the project, and to minimize the cost of the final product (which had to be similar to a standard terrestrial application), a combination of existing designs and processes was chosen.

The cable also had to be suitable for this new ROW environment. Being installed underwater, and buried at the bottom of the river bed, the cable had to have a hermetic barrier to guard against water ingress and its associated problems. It also had to be sufficiently mechanically robust to withstand elevated installation tension due to possible unforeseen barge movements, and the possibly rocky nature of the riverbed.

There were also many logistical issues to be resolved. The cable lengths were engineered to fit the exact lengths necessary to match each splice point. Due to limited storage on the installation sites and barges, the cables had to be delivered in a very short space of time, and often at extremely short notice.

Many criteria also relate to the network deployment in this right of way. Risks for the cable must be minimized, as it is installed in a restricted area. The installation and protection operations are therefore more important than for terrestrial installations. As far as festoons are concerned, their number must be minimized, the landing points must be chosen, and maximum cable lengths selected, taking into account the maximum safe manufacturing length and the maximum amount of cable that can be safely transported on a reel. The methods of laying and protection must be selected, using those that best

meet the needs of the system, the river environment, and other natural and man-made features.

CABLE DESIGN

In order to meet the quick delivery requirements of this new cable design, and to ensure maximum reliability in its construction, a new and innovative combination of existing cable designs and manufacturing techniques was chosen to satisfy the customer's requirements. The basic requirements were for 144 modules, with up to 864 fibers, in a single cable. The cable cross-sections are in Figure 1.

Loose tube core

A traditional loose tube cable core was selected using PBT tubes, but, in order to meet the high fiber count and small diameters, the tubes contain up to 24 fibers. These are SZ stranded and filled with a waterblocking compound to resist water penetration into the cable core. However, since it is well known that gels and plastics are not completely water tight, a welded aluminum tube was chosen to provide the hermetic moisture barrier necessary in an underwater cable. This is one of the most critical points of the design, since it allows the fibers to have reliable protection against H₂ and OH degradation. Without the application of this hermetic barrier, the reliability of the cable design could not have been achieved.

Armored Protection

The cable core was jacketed with a PE sheath to protect the aluminum tube from corrosion, and to insulate it from the armoring layer. The armor layer consists of HDPE upjacketed galvanized steel wires, helically stranded around the jacketed core. The steel wires are necessary to provide the cable modulus and tensile strength required for such an installation (1000 daN). They also provide a mechanical robustness to protect against crush, torsion, impact and unforeseen mechanical stress that may occur during the cable's installation or its life at the bottom of the river. The steel wires are upjacketed in order to reduce the friction between them and the installation components.

Cable	Weight kg/km	Diameter mm	Tension daN	Crush daN/cm	Static Bend Radius mm
144	600	19	1000	450	280
288	830	24	1000	450	360
6x144	2430	42	1000	450	630

PROJECT IMPLEMENTATION

There are five main steps to be followed for this type of project.

Desk Study

A preliminary report setting out the proposed route and landing points must be prepared, after gathering all the existing data on river banks, coordinates, geographical and geological details. If no such information is available, a complete survey must be conducted. This must subsequently be discussed with the landowners concerned, in order to make the preliminary choices.

Survey and final project design

A complementary survey is made to finalize the route in the river and the final landing points. The final route is agreed by all parties involved: customers, VNF, other administrations, and landowners. An agreement is made with VNF and potential customers for the protection of the cable along the route (buried depth or other means of protection when burial is not preferable or possible)

Landing point protection

During this phase the ducts for each landing point, which will make the connection to the splice chambers, are installed. This work is carried out by construction companies, and this phase permits a final survey of the area prior to cable installation.

Cable Installation

The cables are installed at a rate of about 1000m per day at a depth of between 0.5 and 1.5m, depending upon the dredging level and the quality of the river bed. Small teams are in charge of the landing points and areas where burying is not permitted. For example, certain lengths must be placed in ducts in areas where burial is not permitted or not possible. The cable is then secured in the splice chambers and is spliced. These operations are described in more detail later in this paper.

Maintenance

The final step in any project is to ensure its continued operation. Specific equipment has been developed to repair submerged cables. Part of this equipment is a submergible splice box that can be used to repair a cable, or even to make a planned underwater cable splice when a landing point is not possible or difficult to obtain. Responsibility for repair work is shared between the cable owners and the network operators. In some cases the maintenance contract stipulates repair within 60 hours of notification. Currently, LDCable is responsible for over 300 km of cable.

INSTALLATION TECHNIQUE

The installation technique was developed in conjunction with the cable design. Travocean (a sister company of LDCom) was given the task of developing an installation technique that could install a cable directly in the riverbed, efficiently and economically. After several joint discussions, it was decided that the cable had to be buried at the bottom of the riverbed at a depth of at least 50 cm in order to provide adequate protection. Thus an underwater trenching technique was developed, with all the equipment being supported by barges floating on the river. The trench is dug by an underwater plow. The cable is then fed into this trench from a barge floating on the surface. The plow is pulled by a winch situated on a separate barge. The ensemble is correctly positioned by use of a Global Positioning System (GPS).

Installation Equipment

The installation equipment consists of three main parts: the plow, the winch barge, and the cable barge. The Plow is a submerged sled consisting of a vibratory plow, which makes a furrow of 600x75 mm in the riverbed. Immediately behind this plow is a guide which buries the cable approximately 50 cm below the bottom of the riverbed.

The Winch Barge is a separate barge containing a winch that is attached, via a cable, to the plow sled. Once correctly positioned, the winch is used to pull the plow that buries the cable. The barge also has two pylons, used to fix the barge in place once the GPS has positioned it. This anchors the barge to prevent it moving while the winch is in operation.

The Cable Barge is a separate barge, used to hold the cable reels. The reels are supported by a pay-off system, which includes a tension control system, to

ensure correct control of the cable pay-off tension during installation. This barge is situated just above the plow, and the cables are fed down to the plow by a guide. This barge is also connected to the winch, which pulls it at the same time as the plow. This equipment, with the different phases of installation, is shown in Figure 2.

Installation Process

Installation begins with the cables loaded on to the cable barge, and guided down to the plow, by divers working underwater. The Winch Barge and plow sled are positioned by GPS.

A tugboat is usually used to position the winch barge. The pylons are then lowered into the riverbed to anchor the winch barge in place. The winch is then used to pull the cable barge and plow sled, which buries the cable.

When the cable barge is alongside the winch barge, the winch is stopped and the cable barge is anchored. The pylons on the winch barge are raised, and the winch barge is repositioned by a tugboat. During this process the winch cable is unreeled without tension. When the barge is repositioned, the installation process recommences as before.

When the cable installation is finished, the ends of the cable are brought into the splice chambers by means of conduits. This is called the landing point. Figure 3 shows the position of the installed cable and the landing points.

SPLICING TECHNIQUE

The cable is installed in lengths called 'festoons'. Each one consists of a length of cable buried in the riverbed, with each extremity brought up on to the riverbank and into a splice enclosure. A small splice chamber is installed in the riverbank with conduits leading down into the river. The cable is brought from the bottom of the river into these conduits and into the splice chamber. The metal wires are anchored and grounded, and the cable is spliced in a standard terrestrial splice closure (watertight). Standard splicing techniques and equipment are used. However, specific modifications were made by Alcatel Cable Interface and MKI France to improve the watertightness of the splice closures.

In some cases it is necessary to install the splice closures under water at the bottom of the river. In this event, a special closure is used, adapted to underwater conditions. This SSC (submersible splice

closure) can withstand 6 bars outside water pressure, with a 10 bar flash test, and 500 daN max cable pulling strength. The installation range is -30° to +70°C.

FIELD RESULTS AND CABLE TESTS

Several tests were conducted on the cable, both in the laboratory and in the field, in order to ensure that the cable design was well adapted to the installation conditions and equipment.

Laboratory Tests

Several types of mechanical, optical, and aging tests were carried out to test the cable design's conformity to the design specifications. A series of mechanical tests were performed to test the cable's performance for crush, impact and bending. The specification values were chosen as representative of the installation conditions to which the cable would be subjected. The climatic tests were designed to ensure that the cable would function correctly in the range of temperatures found in rivers, from 0°C to +60°C. An aging test was also performed to simulate the cable characteristics after 20 years of service. The temperature cycle and aging tests were performed in the water, in order to represent the actual service conditions of the cable. A traction test was performed to ensure that the cable would resist installation tensions, both those resulting from standard installation practices, and those which could result from sudden barge movements or cable blockages during the installation that could sharply increase the cable tension. The following table gives a short summary of these tests.

Test	Specification	Results
Traction	1000 daN, no attenuation change	Pass
Temperature Cycle	-10/+70 .1 dB attenuation change	Pass
Crush	45 daN/cm 0.05 dB	Pass
Bending	15x OD static 20xODdynamic 0.1 dB max change	Pass
Attenuation during installation	No attenuation change	Pass
Attenuation after installation	No attenuation change	Pass
Aging in Water	15 days 85°C 0.1 dB	Pass

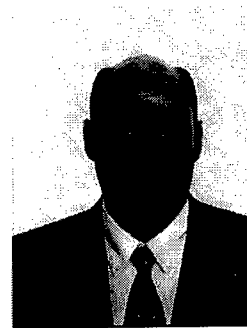
Field Tests

In addition to the laboratory tests, several tests were conducted in the field during and after installation to ensure that the installation equipment and technique were completely compatible with the cable design. During the installation, several cables were monitored with *Outdoors*, which measured the fiber attenuation. No anomalies were found to occur during or after the installation, thus proving that the installation equipment and method were compatible with the cable design. In addition, the final inspection tests, after the cables were installed and spliced, were found to be acceptable, with no attenuation problems, and to be within the splice loss budget. As an additional safeguard, an automatic monitoring system was installed for a period of 2 months, which measured several fibers, representing a total length of 20 cable kilometers. No attenuation changes were noted.

CONCLUSION

In order to satisfy a customer request for the installation of a cable network in a new right of way, a new cable design was created, compatible with the installation equipment, the installation technique, and the environment. This cable was designed for installation in rivers, canals, and all navigable waterways. To make development of this cable possible within a very short period of time, a partnership was created with the customer, which allowed the cable design to evolve in parallel with the development of the installation techniques. The design took into account the special environment in which this type of cable would be placed, and the type of installation techniques to which it would be subjected. Tests were carried out to simulate the cable's mechanical and environmental stresses, and these were validated by field tests proving the validity of the cable design.

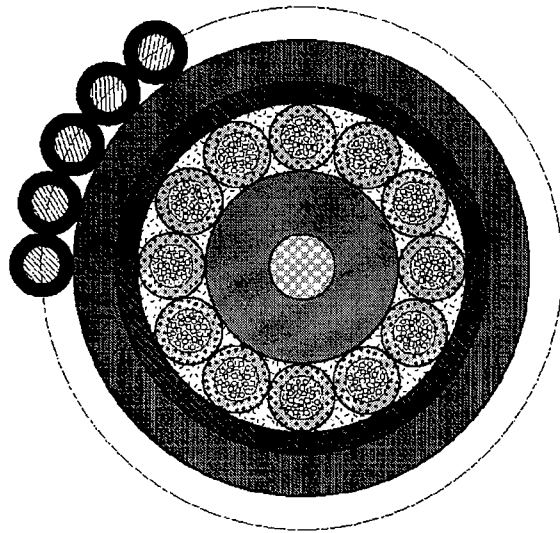
As a result, a very effective and efficient cable was developed, and customer satisfaction was achieved. This is evident by the customer partnership, which is still operating today, and by the continuing successful deployment of this cable in France.



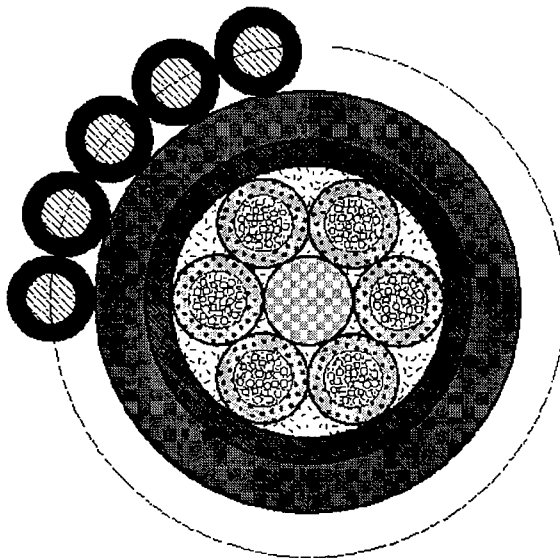
David J. BENZEL, Alcatel
536 quai de la Loire
62225 Calais Cedex, France

David Benzel was born in Buffalo, NY USA in 1965. He received his degree in Electrical Engineering from Clarkson University in 1987. He has held several positions in Field Engineering, Plant Engineering and Product Development since joining Alcatel in 1991. Since May 1997 he has held the position of Technical Manager in the manufacturing facility in Calais.

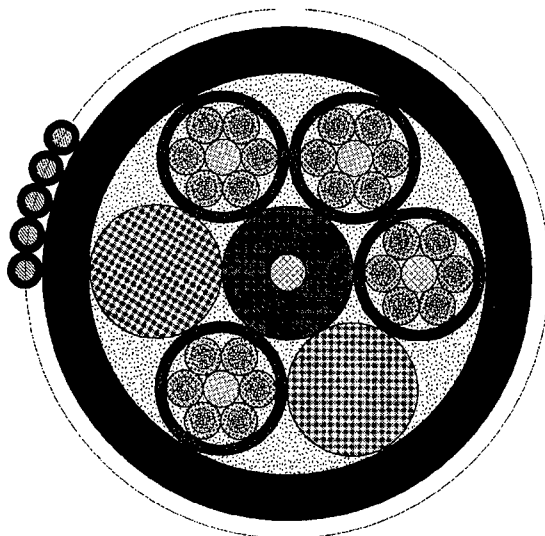
Figure 1
River cable cross sections



288 fibers



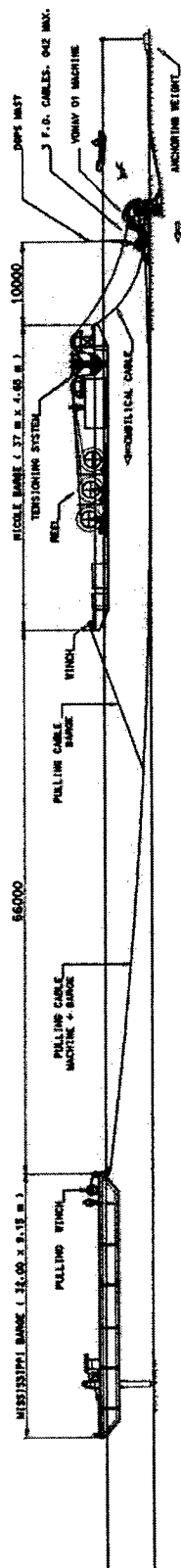
144 fibers



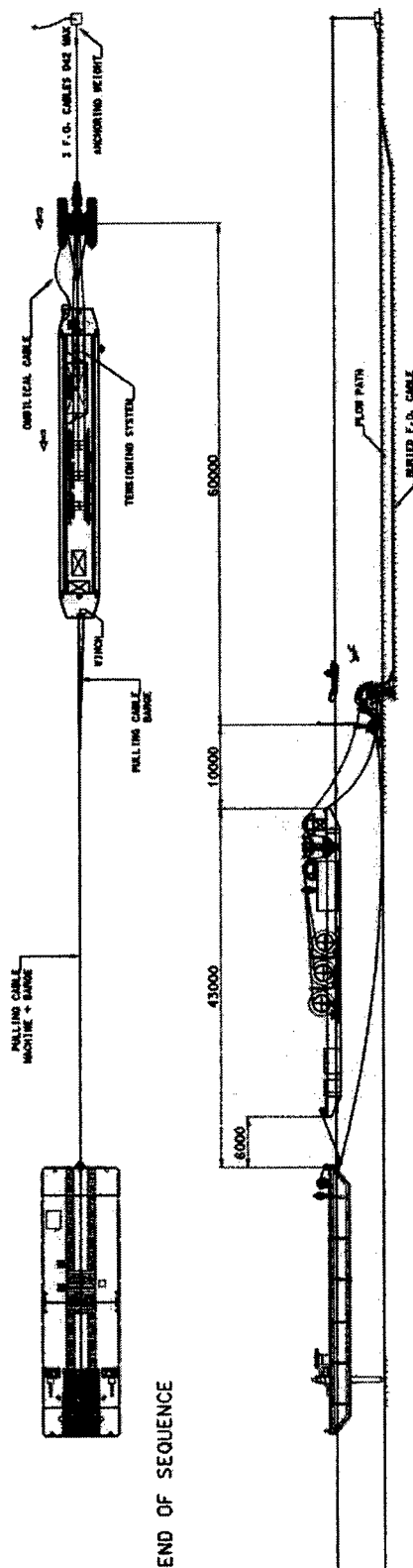
864 fibers (6 x 144)

Figure 2 Installation equipment and phases

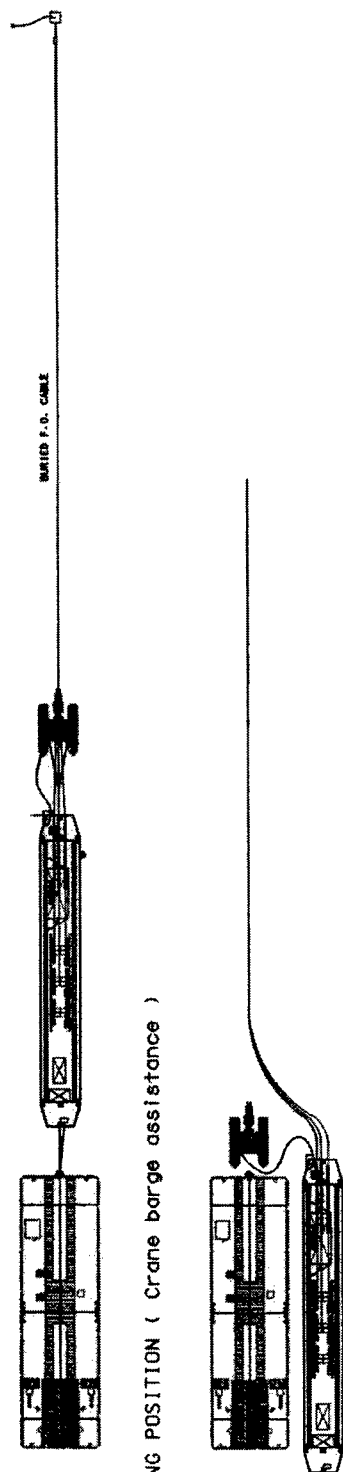
1 - START OF SEQUENCE



2 - END OF SEQUENCE

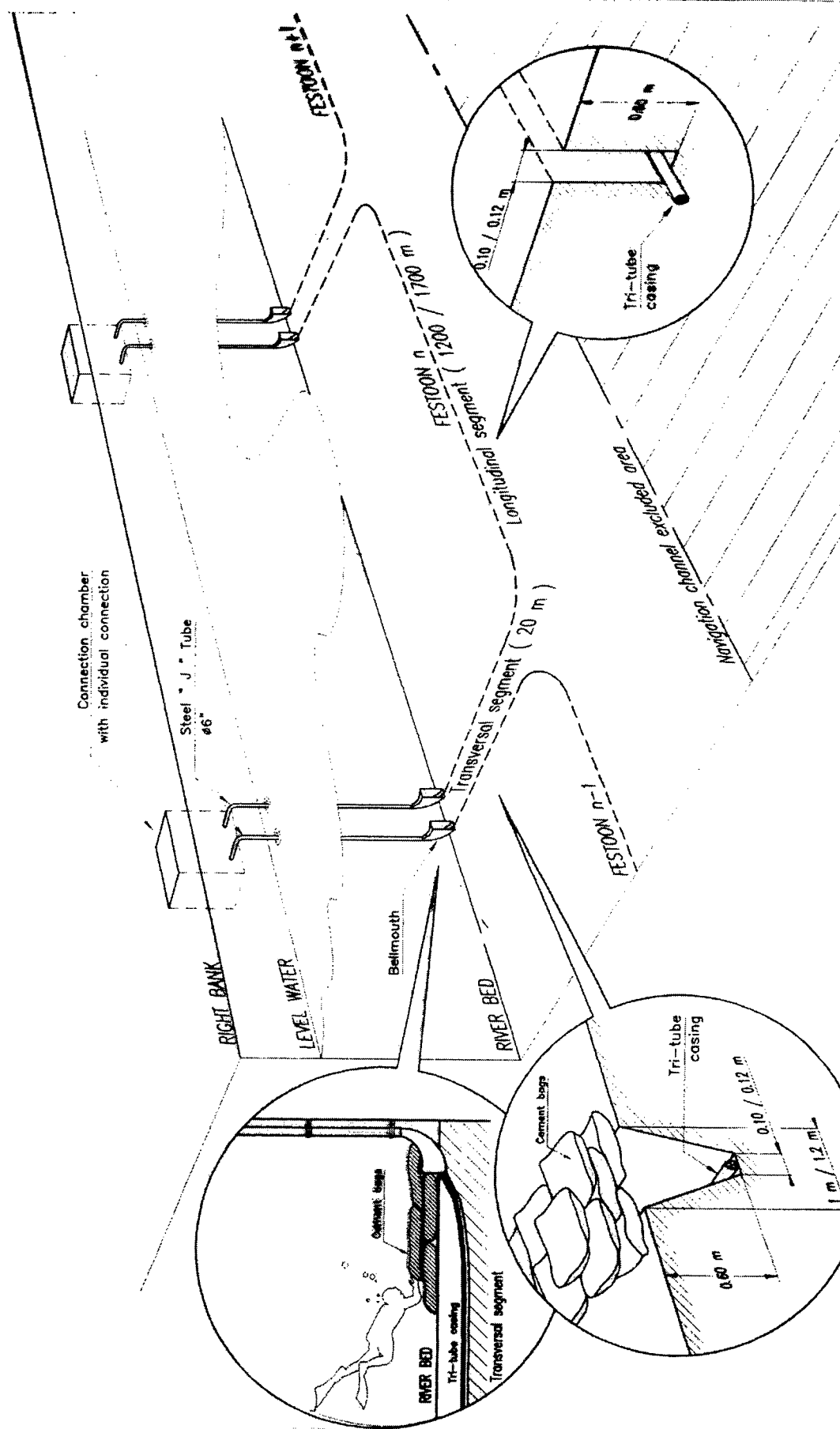


3 - RECOVERING POSITION (Crane barge assistance)



SPECIFICATION OF PARIS PROJECT LINK

Figure 3
Cable position and landing points



A theoretical study on cable design for blowing installation in consideration of pushing force at duct inlet

Itaru Sakabe, Yuji Kitamura, Wataru Katsurashima and Gen Morikawa

Yokohama Research Laboratories, Sumitomo Electric Industries, Ltd.

1, Taya-cho, Sakae-ku, Yokohama, 244-8588 Japan

Phone: +81-45-853-7164 / Fax: +81-45-851-5300 / E-mail: sakabe@yklab.sei.co.jp

Abstract

An estimation theory of cable blowing installation distance as functions of air viscous drag force and mechanical pushing force was established. According to the theory, the pushing force induced by driving wheels improves installation ability and the effect is enhanced with stiffer cable. A 300-count fiber cable, which was designed using the derived theory, was successfully installed up to 1500m distance in 50min. at a constant velocity as high as 30m/min. with 0.65MPa compressed air.

1. Introduction

As intelligent networks using optical fibers spread, the cost reduction of cable installation is becoming increasingly required as well as that of optical fiber cables. In the field of underground networks, cable blowing installation is one of the most effective method to reduce both labor costs and installation time. The blowing installation is a method to install a cable into a duct by using air flow. And it is desirable for optical fiber cable installations in the aspect of reliability because of the low installation tension. Therefore, the blowing installation has been put into practice, however, the cable blowing theory which describes the relationship between installable distance and cable design has not been enough analyzed quantitatively.

A set-up for cable blowing installation is shown in Fig.1. Propelling force F affecting to

cable consists of

- (i) A blowing force F_{blowing} caused by viscous air flow
- (ii) A pushing force F_{pushing} caused by driving wheels at inlet of duct

and shown by $F = F_{\text{blowing}} + F_{\text{pushing}}$.

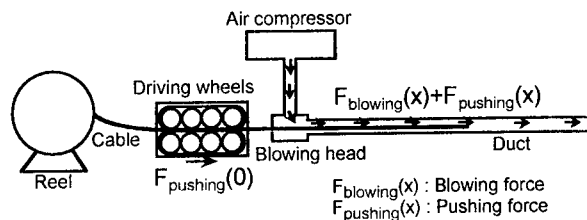


Fig.1. Set-up for cable blowing installation

The blowing force F_{blowing} caused by air flow has been already studied[1], however, the effect of pushing force F_{pushing} has not been considered in the cable blowing installation, though there are some studies of pushing force by itself [2,3]. The pushing effect is not so large in thin optical fiber unit blowing installation, however, it is thought to be large in the cable blowing installation because of its higher stiffness.

In order to theoretically estimate installable distance, we derived the distribution of pushing force F_{pushing} and added it to the blowing force F_{blowing} .

The blowing force F_{pushing} is derived and verified in Sec. 2 and the propelling force F considering the blowing force F_{blowing} will be estimated and verified in Sec.3.

2. Theory of pushing installation

2.1. Derivation of propagation of pushing force

When a cable is pushed into a duct, the cable would buckle and be pressed to the duct wall. Then, extra friction force is caused by the cable buckling in addition to normal friction caused by gravity. The schematic figure of cable pushing into a duct is shown in Fig.2.

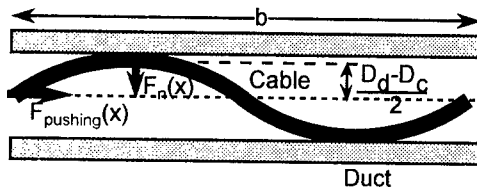


Fig.2. Forces acting on a cable pushed into a straight duct

The locus of periodically buckled cable which is pushed into a duct can be approximately expressed by Eq.1 on boundary conditions $y(0)=0$, $y(b/4)=(D_d-D_c)/2$ and $y'(b/4)=0$.

$$y = \frac{D_d - D_c}{2} \sin \left(\sqrt{\frac{F_{\text{pushing}}(x)}{EI}} x \right) \quad (1)$$

$$b = 2\pi \sqrt{\frac{EI}{F_{\text{pushing}}(x)}}$$

where D_d means an inner diameter of duct, D_c is a cable outside diameter, EI is a cable bending stiffness and $F_{\text{pushing}}(x)$ is a pushing force.

The cable can be propelled while the pushing force $F_{\text{pushing}}(x)$ is larger than the extra friction force $\mu F_n(x)$ on all points of the cable.

$$F_{\text{pushing}}(x) = \mu F_n(x) \quad (2)$$

Also, using Eq.2, the normal force per unit length when the cable stops is expressed as Eq.3,

$$\frac{dF_n(x)}{dx} = \frac{D_d - D_c}{\pi^2 EI} F_{\text{pushing}}(x)^2 \equiv \beta F_{\text{pushing}}(x)^2 \quad (3)$$

$$\beta \equiv \frac{D_d - D_c}{\pi^2 EI}$$

where β is a buckling coefficient depends only on cable diameter D_c , duct inner diameter D_d and cable stiffness EI .

Using Eq.2 and Eq.3, the distribution of pushing force $F_{\text{pushing}}(x)$ is expressed by Eq.4 as a function of distance x from inlet of duct,

$$F_{\text{pushing}}(x) = \frac{F_{\text{pushing}}(0)}{1 + \mu \beta F_{\text{pushing}}(0)x} \quad (4)$$

where $F_{\text{pushing}}(0)$ is a pushing force at inlet duct and it is a generally constant value.

The pushing force $F_{\text{pushing}}(x)$ is a function of distance x and it decreases with distance from inlet of duct. The distribution of pushing force per unit length is derived from Eq.4. It is a function which is decreased sharply regarding to distance x from inlet of duct.

$$\frac{dF_{\text{pushing}}(x)}{dx} = \frac{\mu \beta F_{\text{pushing}}(0)^2}{\{1 + \mu \beta F_{\text{pushing}}(0)x\}^2} \quad (5)$$

2.2. Verification of derived pushing force

In order to confirm the validity of the expression of pushing force such as Eq.4 and Eq.5, we measured pushing installation limit using five kinds of slotted rod type cable as shown in table 1 and two kinds of duct which are different with inner diameter and friction coefficient as shown in table 2.

Table 1. Cable used for pushing installations

	Fiber count	O.D. (mm)	Weight (kg/m)	Stiffness (kg·m ³)
Cable A	32	12.0	0.10	0.07
Cable B	96	12.3	0.11	0.07
Cable C	100	13.5	0.19	0.46
Cable D	200	18.8	0.34	0.18
Cable E	300	23.0	0.40	2.70

Table 2. Duct used for pushing installations

	I.D. (mm)	μ
Duct A	30	0.1
Duct B	30	0.12
Duct C	30	0.5
Duct D	50	0.1
Duct E	50	0.5

Assuming that the cable stops when the lowest pushing force at the cable tip is equal to the frictional resistance μmg (the product of friction coefficient μ , cable unit mass m and g), the theoretical pushing installation limit l is calculated from Eq.6.

$$l = \frac{1}{\mu \beta} \left\{ \sqrt{\frac{\beta}{mg}} - \frac{1}{F_{\text{Pushing}}(0)} \right\} \quad (6)$$

Also, the pushing installation limit is visualized by Fig.3 as a function of pushing force per unit length.

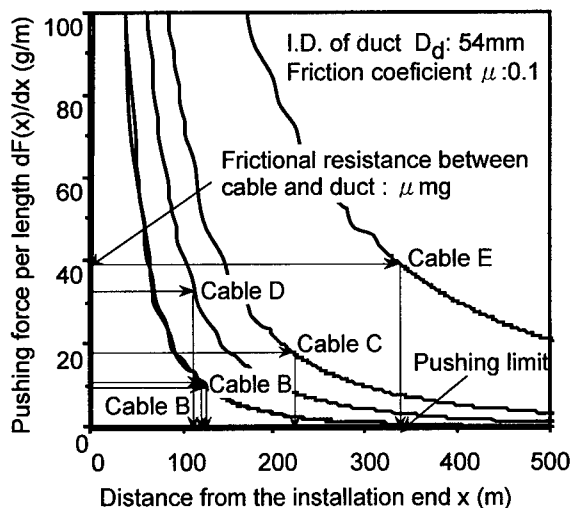


Fig.3. The pushing force per unit of length

The pushing force is sharply decreased with

the distance x from inlet of duct. The cross point of pushing force curve and frictional resistance is a pushing installation limit. For example, Cable C and Cable E are estimated to be installed 230m and 340m by only pushing. The higher the cable stiffness, the larger the pushing force.

These experimental results installed cables in table 1 into ducts in table 2 by pushing are shown in Fig.4.

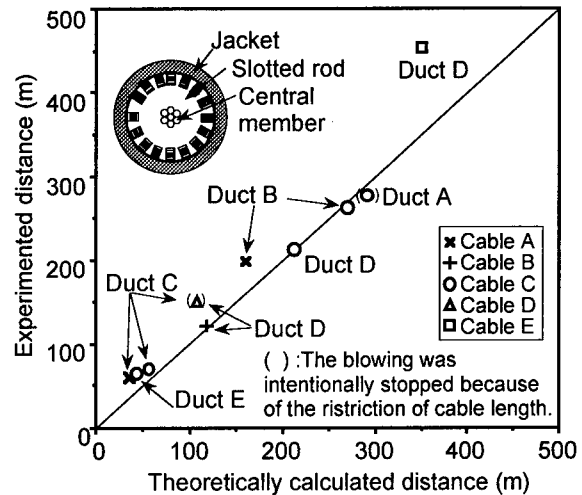


Fig.4. Pushing installation distance compared with theoretical value and experiment value

Theoretically calculated limits of pushing installation distance precisely agree with experimental values. Pushing effect become well described by Eq.4 and Eq.5.

3. Blowing Installation theory considering pushing force

3.1. Addition of pushing force F_{pushing} to blowing force F_{blowing}

In this chapter blowing installation distance in consideration of pushing force is analyzed. Blowing force $F_{\text{blowing}}(x)$ is expressed by Eq.7.

$$F_{\text{Blowing}}(x) = \frac{\pi D_d D_c}{4} \{ P_{\text{in}} - P_1(x) \} \quad (7)$$

$$P_1(x) = \sqrt{\frac{D_d^{19/4} x P_{\text{out}}^2 + D_c^{19/4} (L-x) P_{\text{in}}^2}{D_d^{19/4} x + D_c^{19/4} (L-x)}}$$

where D_c means an outer diameter of cable, D_d is an inner diameter of duct, L is a duct length, P_{in} is a pressure at the installation end and P_{out} is a pressure at outlet of duct.

A fundamental equation that adds pushing force to blowing force is expressed by Eq.8.

$$F_{Blowing}(x) + \frac{dF_{Pushing}(x)}{dx} x = \mu mgx \quad (8)$$

Assuming that the pushing force on the cable takes the lowest value at cable tip, Eq.8 is expressed by Eq.9.

$$F_{Blowing}(l) = \left[mg - \frac{\beta F_{Pushing}(0)^2}{\{1 + \mu \beta F_{Pushing}(0)l\}^2} \right] \mu l \quad (9)$$

Using Eq.9, we can estimate blowing installation distance.

3.2. Experimental results of blowing installation

In order to confirm the validity of the relation expressed by Eq.9, we conducted a limit installation length measurement. We constructed a straight polyethylene duct of I.D. 54mm and 1500m length. Lubricant oil was applied to the duct. At first, we installed two kinds of cable (Cable C and Cable E in table 1) into the duct without air flow. After the cable stopped, we started to inlet air flow at constant pressure. The blowing installation limit was judged when the blowing velocity fell below 3m/minute. When the cable stopped again, we raised air pressure and measured installation limit.

The experimental results of cable C and cable E are shown in Fig.5 and Fig.6 respectively as the relationship between integrated propelling force and the limit installed distance.

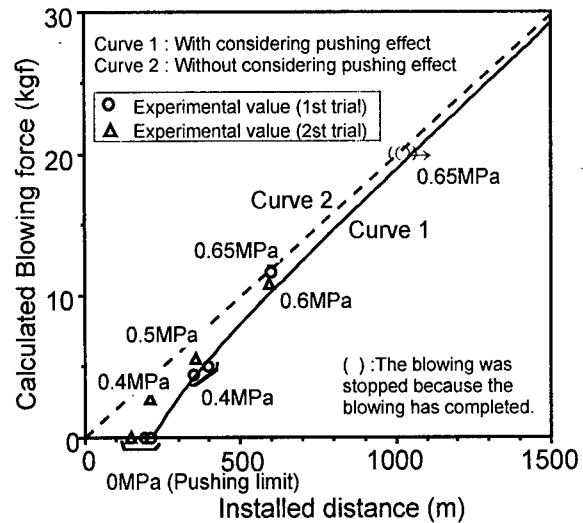


Fig.5. Blowing characteristics of Cable C

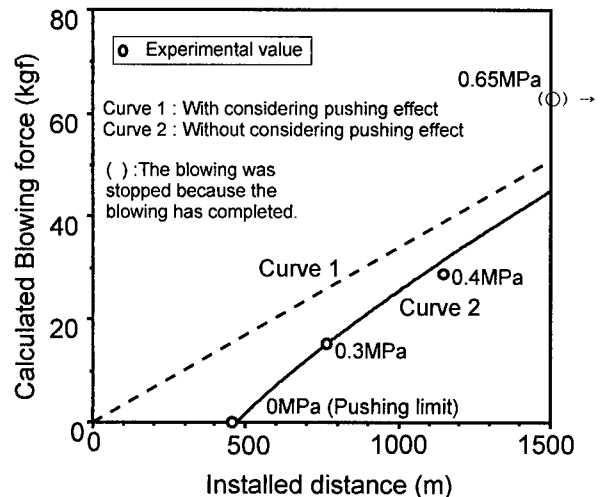


Fig.6. Blowing characteristics of Cable E

Curve 1 and Curve 2 in Fig.5 and Fig.6 mean calculated blowing curves with consideration of the pushing force and without consideration of the pushing force respectively.

From Fig.5 and Fig.6, we have confirmed that the experimental results agreed with the calculated curve 1. And the pushing installation distance of stiffer cable E is larger than that of cable C as shown in Fig.4. This property is also kept in blowing installation. And stiffer cable E has ability to be blown through 1500m at the constant velocity as fast as 30m/min with 0.65MPa compressed air.

It can be presumed that a higher count fiber cable such as 1000-count fiber cable shows a

higher pushing effect because of its higher stiffness.

4. Cable design for blowing installation

The relationship between cable stiffness and pushing installation distance can be calculated using Eq.6 as shown in Fig.7. From this figure, the minimum cable stiffness to achieve required pushing distance is known. For example, in order to install a cable through 250m by only pushing at the inlet duct, a 300-count fiber cable needs stiffness larger than $1.2 \text{ kgf} \cdot \text{m}^2$.

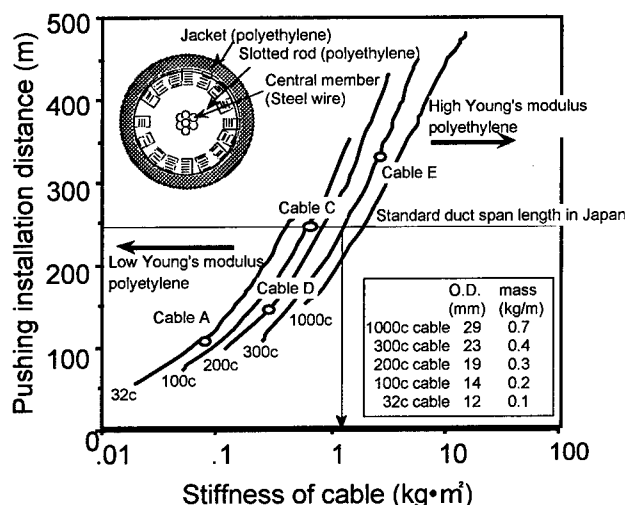


Fig.7. Pushing installation distance calculated as a function of cable stiffness

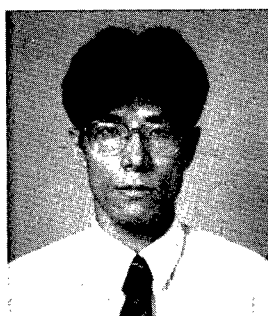
5. Summary

We have derived the distribution of pushing force. Our model which considered the effect of the pushing force enabled the blowing distance to be precisely estimated. The pushing effect was kept even in the blowing installation the same as the pushing installation. And stiffer cable has more excellent pushing and blowing installation property. A 300-count cable succeeded to install up to 1500m distance at a constant velocity as high as 30m/min with 0.65 MPa compressed air.

References

- [1] S. A. Cassidy and M. H. Reev, "A radically new approach to the installation of optical fibre using the viscous flow of air," Proceedings of IWCS '83, pp.250-254, (1983).
- [2] W. Griffioen et al., "Versatile Access Network Cabling Concept for Migration to Optical Fiber," Proceedings 45th IWCS '96, pp.485-489, (1996).
- [3] I. Sakabe et al., "A study of blowing velocity of optical fiber unit in a blowing installation," J. of Lightwave Technol., vol.7, No.2, '89, pp.297-302, (Feb. 1989).

Speaker Biography



Itaru Sakabe

Sumitomo Electric Industries, Ltd.
1, Taya-cho, Sakae-ku
Yokohama, Japan

Itaru Sakabe received his M.E. degree from Electro Communication University in 1993. He joined Sumitomo Electric Industries, Ltd. and then has been engaged in the development and design of communication cables. Mr. Sakabe is an engineer of Optical Network R&D Dept. in Yokohama Research Laboratories and a member of IEICE Japan.

OPTICAL FIBER CABLE LINKS WITHIN GAS PIPELINES AS AN ALTERNATIVE TELECOMMUNICATIONS ROUTE TECHNOLOGY

Paul E. Gregor, Lothar Kuhn, Dr. Alexander Weiss

Alcatel Kabel AG & Co, Mönchengladbach, Germany

ABSTRACT

A successful introduction of an alternative laying procedure for optical fiber cable systems has been achieved. Instead of buried cable installation gas pipelines of the non subscriber access have been selected to incorporate those dielectric cables in order to avoid or to minimize the unfavourable high expenditures for conventional cable laying procedures. Based upon practical experiences collected within several realized projects an acceptable technology to be used regularly can be offered. This contribution describes the most important technical criteria needed, like special components for cable entries and exit devices, adequate cable design and the laying procedure.

Evidence is given that under certain conditions the total costs for erection of underground OF cable systems can be put down on to 50% compared to conventional techniques.

INTRODUCTION

Optical fiber underground telecommunications cable systems are being installed with strong increasing tendency by new network carriers based upon the new telecommunication law in many European countries. Those networks shall be erected for broadband and system independent applications considering most reliable technology and a long life-time. More than 50% of the overall costs for conventional performed cable systems are caused by the cable laying procedure and necessary supporting measures. In order to reduce those high expenditures huge activities are being created to improve conventional installation methods or to find alternatives with highest profitability compared to normal laying methods. Among various possibilities existing pipeline

networks constitute a real challenge to become carrier of needed optical fiber cable links, because only the installation measure for cables has to be done to provide the necessary components for cable entries and exits. The special cable design and the adequate laying procedure is available. Within the different pipeline families those for gas transport with an extension in Germany of about 300.000 km offer the most promising solution to realize desired cable networks in national, regional and urban fields. This contribution describes general considerations and the actual situation of gas pipeline/optical fiber technology based on experiences of several practical executed projects. Moreover it expresses necessary measures for pipeline repairing work in case of already integrated cables and states future aspects and possibilities to increase profitability remarkable.

GAS PIPELINE STRUCTURES

In typical gas pipeline grids in Germany the transport level is designed to be operated at high pressures up to 100 bar and the distribution level up to 18 bar gas pressure but frequently operated only up to 4 bar. Finally the subscriber access network operates up to 100 mbar employing DN 100 (100 mm diameter) pipe dimensions. Transport level pipelines are of metal construction and designed for diameters between DN 200 and DN 400 using a wall thickness of 5.5 mm typically. According to DIN 2470, part 1 St 37.0, No.1.0254 a steel quality has been specified considering a certification 3.1 B according to DIN 50049. These pipelines are corrosion protected by polyethylene in conformity to DIN 30670 and require certification 2.2 according to a.m. DIN. It should be pointed out that there is an increasing tendency for use of plastic pipes for operating

pressures up to 4 bar. Application is basically given for the access network.

Within the network structure firm installed closing devices become incorporated as those are needed for operation and supervision purposes of pipeline systems. Normally such devices are mounted in the transport range and at branching locations.

The natural gas consists of approx. 87 % methane, 11.0 % nitrogen, 1.4 % ethane, 0.4 % carbondioxyde, and some remaining portions of different gases as trace element. The gas temperature is about 11°C. The speed of the gas stream depends from the actual consumption and the pressure and has been measured up to 10 m/s for low pressure levels. For high pressure systems 10 to 15 m/s are typically

The inner surface of the pipeline can be corroded significantly. This had been considered for the cable design by applying a sheath with enlarged wall thickness.

CABLE DESIGN

For this application the gaspipe environment had to be considered. It requires a sheath protected against natural gas with low friction –coefficient. To prevent gases from permeating into the cable a metal tape shall be applied. The core design can be chosen freely.

The cable dimensions are not restricted to much, because the gas flow will not suffer.

Finally the cable shall be pressure resistant.

Chosen design

The cable shall be installed in pipe for natural gas. These pipes usually are made of steel or HDPE. They have to support pressures up to 20 bars. The temperature will not exceed a range of 0°C to 20°C. Figure 1 shows this design. It is jelly-filled, to resist to gas pressure up to 18 bar. With respect to the high pulling load during cable laying the tensile strength of cable has to be designed for a minimum of 6000 N obtained by aramid yarns applied helically. As metallic tape a copolymer coated aluminum tape has been chosen. The outer sheath material is a special type of HDPE, which is stable against natural gas. The sheath wall thickness is 2.6 mm for enlarged stability. Here it had been considered that inside the pipe the wall may be very rough having sharp edges of steel. The sheath must withstand being scratched along such an edge.

The chosen HDPE has also a low friction coefficient and is a hard material.

In figure 1 a cross section of the OF cable type A-DF(ZN)(L)2Yis drawn.

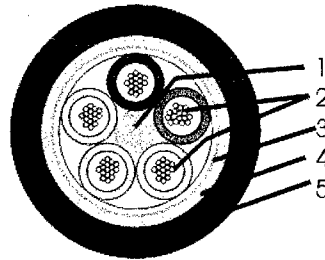


Fig.1: cross section of optical fiber cable

- 1 = central element (FRP)
- 2 = buffer tubes with fibers
- 3 = strain bearing elements
- 4 = copolymer coated aluminum tape
- 5 = high density polyethylene sheath

Permeation of gas

The natural gas contains a maximum of 0.5% hydrogen and nearly no moisture.

Optical fibers were tested according to Norwegian hydrogen specifications requiring 10 bar hydrogen pressure for 1000 h. This test was passed without changes in attenuation at all relevant wavelengths, including 1240 nm; therefore the behavior in a gaspipe environment can be considered being without risk due to hydrogen.

As protection against gas permeation the metallic tape has been selected. It acts as moisture barrier, but also as hydrogen barrier.

Figure 2 is showing the moisture transmission rate through polyethylene dependent of its density. Here the selected HDPE is the best solution.

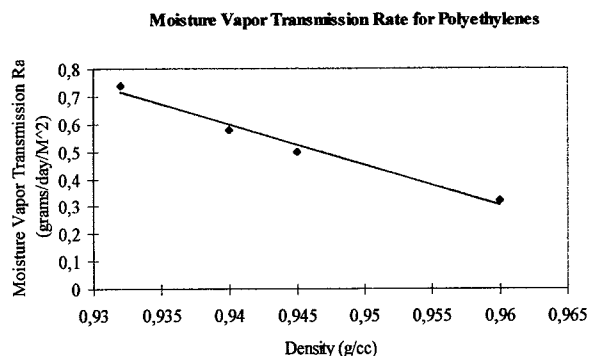


Fig. 2: Moisture vapor transmission rate for polyethylene

Up to natural gas pressure of approximately 40 bars and 80°C the selected HDPE is stable. At higher pressures it dissolves gas in its polymer matrix; then the HDPE is not suitable any more and has to be replaced, for example by polyamide.

DESIGN CONSIDERATIONS FOR CABLE ENTRIES AND EXITS

The cable entry/exit device is shown in figure 3. It consists of a metal steel dome of 300 mm height applied vertically to the gas pipeline by welding and covered by a removable plate which will be welded later after laying process has been finished. In order to enable easy introduction of cable into the pipeline a branching side pipe of 80 mm diameter has been applied under a suitable angle to the dome. Within this side arm the very important sealing device is located. It consists of a combination of special rubber rings and stainless steel rings which are held together by using steel screws of particular material. The selected dimensions and the type of rubber have to fulfil long term stability considering the high gas pressure at the inner wall of the branching arm and on the surface of the OF cable.

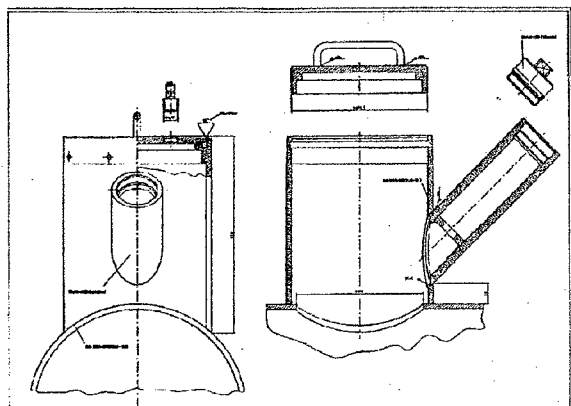


Fig. 3: Cable entry/exit device for gas pipelines

An ethylene-propylene-diene compound has been inserted within projects since it presents high stability against aggressive chemicals. Moreover it is resistant against thermal and mechanical loads within a temperature range of -40 °C up to + 140 °C

The primary objective was to achieve an absolute long term gas tightness together with stable behavior of the attenuation values of the OF despite of the pressure.

Within a first trial in laboratory the sandwich construction of sealing device had been tested at a pressure of 18 bar using helium over a period of 12 weeks. The examined OF link had a length of 11 km obtained by splicing the fibers. As a main result a safety factor of about 5 times regarding tightness of sealing construction had been achieved.

According to increasing customer demand cable links within higher pressure systems are required to be developed. Consequently entry/exit constructions for those projects had been executed and are under examination. With respect to an operational pressure level of 40 bar a suitable design lay out had to be calculated accordingly. Figure 4 exhibits the configuration for those high pressure devices including the sealing component with additional safety screw. Some of the most important data are given below:

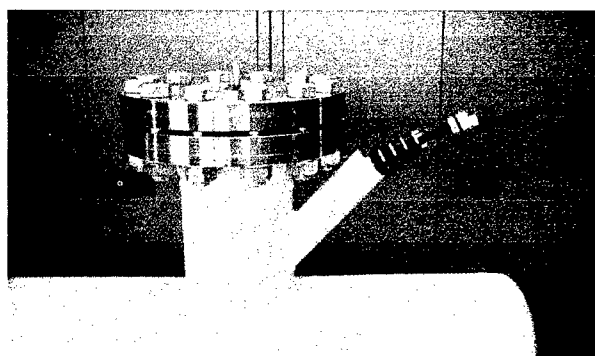


Fig. 4: Cable entry/exit construction device for higher pressure systems

- thickness of flange : 50 mm
- maximum diameter of dome : DN 200
- maximum pressure : PN 100 (bar)
- specification : DIN 2637
- screw material : steel, C22.8
- tensile strength, screw classification: 8.8

The whole test configuration for long term high pressure tests is shown in figure 5. A test pipeline of 4m in length is combined with an cable entry and exit component operating with 100 bar pressure over a period of 16 weeks, up to now without gas escape and change of fiber attenuation.

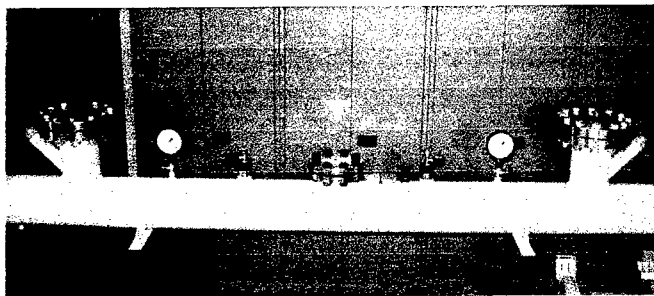


Fig.5: Test configuration of pipeline link with entry/exit components and integrated OF cable for 100 bar gas pressure level

DESIGN CONSIDERATIONS FOR LAYING COMPONENTS

It is a matter of fact that in the course of pipeline links and due to the geographical topology several narrow corners and sharp angles are existing. On the other hand it is desired to reduce the number of cable input and output locations for improvement of profitability. Thus cables should be blown into pipeline sections using only one entry point and only one exit place. Therefore the pulling tool connected to the head of cable has to be relatively short and should be able to be compressed. In figure 6 the design of such a tool is shown.

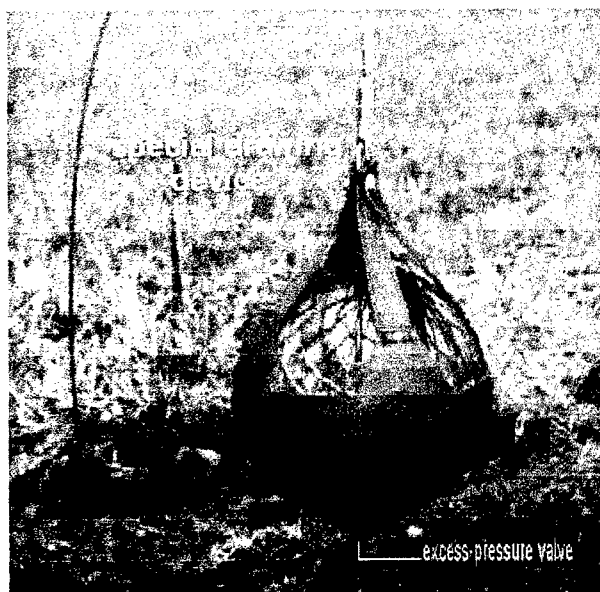


Fig.6: Special cable drawing device

It consists of a weak balloon of adequate diameter which is covered by a leather coat in order to protect the inner part towards the rough environment during the whole laying process.

Prior to the laying procedure the pipeline quality of inner surface smoothness is always unknown in case of older links. The friction load and the additional influence caused by pipeline curves on to the cable sheath increases the total load eventually. In order to make sure that not more than the maximum permitted pulling strength of the cable is applied the drawing device is combined to an excess pressure valve as shown in figure 6.

LAYING PROCEDURE FOR OPTICAL FIBER CABLES INTO THE GAS PIPELINE

In figure 7 a pipeline section is shown in principle including the necessary cable entry respectively exit components and the tools needed for the cable blowing process. Following steps have to be executed:

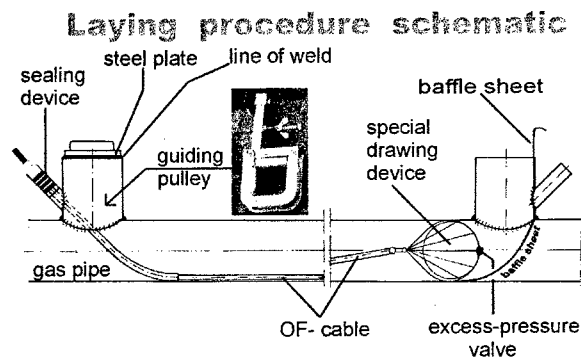


Fig 7: laying procedure in principal

- Introduction of the drawing balloon through the vertical placed entry device.
- Connection of the blowing-in-balloon to the OF cable via conventional steel grip.
- Insertion of special cable guiding rolls according to figure 7 into the dome
- At the far end of the pipeline section a baffle sheet to be inserted into the exit component. This tool bridges the bottom of the pipeline beginning approx. 1m before end of section and

the upper end of the exit device.

This measure is necessary to enable an easy receive of the cable end.

- After closing the holes at the near end laying operation can be executed by release of gas stream. Depending from the achieved speed of cable laying (typical value up to 100m/min) gas pressure can be matched accordingly. In case of an unwanted interruption of laying action the location of cable head has to be identified using the outer meter marking of cable. An additional input/output component becomes necessary.
- After finishing the laying process and reduction of gas pressure on to a level of below 10 mbar laying tools shall be removed and the final bended guiding steel tube between branching arm and the bottom of the pipeline has to be mounted at the near and the far end. In case of long cable length placed in figure-8-shape beside the cable route for instance for customer access it is advantageous to cut the guiding tubes into two halves in order to enable a fast adoption.
- Insertion of sealing packages. Respecting an favourable installation same procedure should be applied.
- Mounting of cable bending protection beginning at the end of the branching arm by employing corrugated plastic tubes with high impact resistance.
- Welding of the upper cover plate onto the dome.
- Performance of corrosion protection.
- Finally gas tightness shall be verified sufficiently and quality of new corrosion cover shall be examined by dielectric strength test

METHODS FOR CLOSING GAS STREAM IN PIPELINES OCCUPIED BY CABLES

Very often gas enterprises have to close the pipeline at certain location along the link, for instance to realize a new branching location or for repair work. In such a situation special bellows are introduced into the pipe through a small hole and filled with air afterwards to fill the whole cross section of the pipe. Normally two of those bellow

are installed close together to get a sufficient tightness.

In case of a pipeline with an integrated cable needed tightness can not be reached without additional measures because small interstices occur in the vicinity between cable and bellow. In order to solve this problem tests have been made. In figure 8 the overall test configuration is shown which represent the above described situation at site.

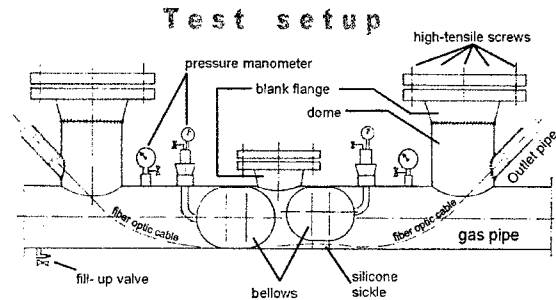


Fig. 8: Gas tightness test set up for pipelines with integrated OF cable

The evaluated solution consists of a weak synthetic shape according to figure 9. Through a hole in the pipeline this synthetic element is attached around the cable. The remaining space of the pipe is again of cylindrical structure and the used bellows can act as under normal circumstances. However attention has to be paid that a suitable synthetic compound is taken to produce the particular component. This material has to stick firm to the rough inner surface of the pipe and to maintain removeability necessary.



Fig.9: Special tool to obtain tightness in pipeline occupied by OF cable

CONCLUSION

Reliable knowledge about erection of optical fiber links in gas pipelines have been collected within practical projects.

Particular the special laying method, design of components for cable entries and exits together with an OF cable which withstands the high mechanical loads during laying procedure are available.

The overall costs of this new route technology can be dropped down to 50 % compared to the conventional underground method under certain conditions (considering only one entrance point and one end point).

A big advantage is moreover the short time for erection of the total cable system and minor problems regarding right of way discussions with owner of the route in question.

Together with realization of high count fiber broadband telecommunication links cables offer a second service respecting supervision of pipeline damages by using special multimode fibers integrated in the cable core upon request.

References

1. Gregor, Haag, Braun 'Optical Fiber Cable Links within drinkwater pipes as an alternative telecommunication route technology International Wire and Cable Symposium, proceedings 1998
2. Sander, Siever, Kuhn, P Gregor 'Lichtwellenleiterkabelstrecken in Gashochdruckleitungen' gwf, Gas . Erdgas 139 (1998) Nr. 10
3. DIN VDE 0888: Optical Fibers for telecommunications and data processing installations, Berlin Offenbach: vde- verlag
4. DIN EN 187000: Specification of optical fiber cables, Berlin Offenbach : vde- verlag
5. DIN EN 188000: Specification of optical fibers, Berlin Offenbach : vde- verlag
6. IEC 60793-1: Optical fibers, Part 1: Generic Specification, Berlin Offenbach : vde- verlag

7. IEC 60794-1: Optical fiber cables, Part 1 Generic Specification, Berlin Offenbach : vde- verlag

AUTHORS

Paul E. Gregor

Alcatel Kabel
Bonnenbroicher Str. 2-14
41238 Mönchengladbach
GERMANY



Paul E. Gregor was born in 1941. After study at Ingenieurschule Duisburg, Germany, he joined AEG Kabel, today Alcatel Kabel in 1966, where he had been involved in development projects for symmetrical and coaxial telecommunication cables. About for a decade he took over the responsibility as head of design department for cable technologies. At present he is responsible for the technical sales and is acting as a member in national and international standardisation bodies, like DKE & ISO/IEC

EXPERIENCES FROM CONSTRUCTION AND OPERATION OF FIBER OPTIC CABLE PLANTS IN SEWER SYSTEMS

Helmut G. Haag, Wolfgang Liese, Klaus Nothofer, Wolfgang Teschner, Alexander Weiss *
** Wolfgang Stapel

* Alcatel, Mönchengladbach, Germany

** HSE – Hamburger Stadtentwässerung, Hamburg, Germany

ABSTRACT

The race is on to create new fiber optic access networks throughout Europe. It is driven by the booming demand for internet services, the liberalization of the markets with a host of new players and finally the lack of capacity of the traditional access networks.

New players rush ahead and build their own fiber optic access networks. Cost and time are of essence. The sub street level space for new cables has become a limited resource in many cities.

Sewers provide excellent opportunities for access networks. They reach about every corner of the city and pass all potential customers. Utilizing sewers avoids bureaucratic digging approvals and reduces the cost below traditional digging installations.

The paper reviews the technique and experience gained from sewer installations during planning and construction of the sewer access networks, reviews the design of dedicated cables, and components and describes the cable laying robot and observations from operations.

INTRODUCTION

The race is on to create new fiber optic access networks throughout Europe. This is driven by three factors: the booming demand for internet services, the liberalized markets, which have introduced a host of new players and finally the nearly non – existent capacity of access networks which are not dominated by former telecom monopolists.

New players must go ahead and build their own access networks, but cost and time are of essence. The competitive environment today demands for connection services within 1 day to 4 weeks. Service providers build therefore their own access backbone rings and parts of the distribution network in advance in order to meet these high expectations. Only for the last odd hundred meters of distribution line and customer drop do they rely on building on demand to connect a customer. Another important development is, that new players access with their networks the final distribution points of the former telecoms to use at least temporary their copper lines to the subscribers.

New cost and time efficient installation methods are needed. In addition, transparency of the cable plant for all future applications as well as highest possible availability are requested. Reviewing the cost and time requirements of conventional ground digging installations reveals, that the overwhelming effort (approx. 75 %) is related to civil works, including the permission to dig.

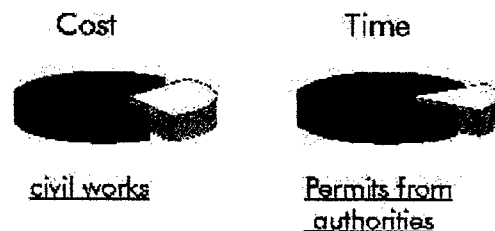


Fig 1. Cost and time effort for cable plants constructed by conventional digging

Utilization of the existing infrastructure of the public sewer systems is an answer to this call. A complete cabling system from cables,

components and gear is engineered to meet the special demands of such networks: FAST- fiber access by sewer tubes. It must be emphasized here, that both, the special requirements of the installation requirements for the new access networks under time constraints and the stringent requirements of the sewer operation must be met equally well and integrated into a unified cable / sewer plant. Both requirements will be reviewed separately in the following.

TODAYS ACCESS CABLE PLANTS

The main purpose of the access network is to collect all traffic from the various services and locations, combine it and transport it over the backbone portion to central points of the network for further processing like switching or long distance transport. As soon as higher data rates are employed only fiber optic links are capable to handle the high bitrates economically. On the other hand, high bitrates are required today only for selected services, mainly dealing with the transmission of data and pictures. Fiber in the distribution- and drop part of the access network is therefore generally installed "on demand" rather than as a pre-installed base providing a full area coverage. The implications for the cabling system are, that all parts of the cable plant will experience a more or less continuous growth, meaning, that fiber and cable capacity will increase in time. Frequent handling of cables and fibers in closures and cable termination equipment must be anticipated. Future growth of the cable plant requires changes of the construction if possible under full operation of the network. Rerouting of traffic in ring structures of backbone, distribution and even customer drop must be included already in the early stages of the network concept development. Cables designed for midspan access in bundle construction support high network availability, by avoiding transient attenuation during construction work on the cable plant. Transients may cause failures in the network. Closures and cable termination technology in the racks are designed for midspan access and equipped with customer circuit fiber management cassettes to permit network expansions under full operation. Since the exact location of the next high bitrate customers can be anticipated only within a few hundred meters, today's new cable plants provide for potential customer connection points all 100 to 500 m. In these locations only spare cable is installed today.

Upon later demand a suitable bundle of the cable will be opened, a closure or other termination equipment will be set and the customer connected via his customer circuit cassette. These practices differ largely from those of traditional networks. Especially planning, e.g. the splice plans for new customer connections with rerouting capabilities in the ring structures for hundreds of customers should not be attempted by small, new players. Integration of a cable plant into the sewer system adds to the challenge, as will be shown below.

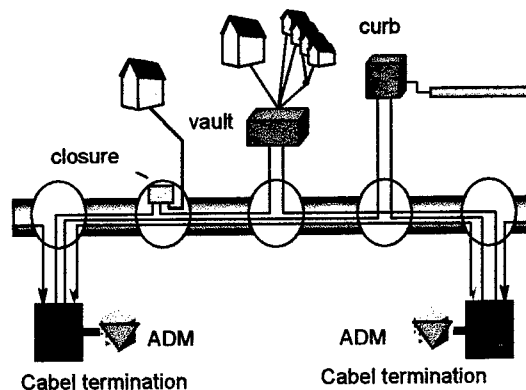


Fig 2. Sewer canals and manholes are well suited for the needs of access networks: backbone and distribution cables in a sewer

A highly structured approach, e.g. provision of empty ducts for future growth, separate cables for backbone and distribution, eases the planning, maintenance, future expansion and operation of the networks.

Typical cables in the cities have today fiber counts of 144 fibers and small diameters (e.g. 12 – 16 mm).

INTEGRATING CABLE PLANTS IN SEWERS

Sewers serve the public interest to collect and conduct waste water, including sometimes storm drainage. The infrastructure base is tremendous. In Germany e.g. about 500 000 km of public sewer lines are built. A city with 1 Mio inhabitants, such as Hamburg, has about 1600 km of public sewers, excluding the smaller house connections. About 200 000 manholes, 500 work sites, measuring stations, pumping stations etc. are spread over the city. All of this is an extremely valuable resource, which matches the need of

communications cable plants, since it covers all of the city, passing every doorstep of all dwellings.

Canal sizes in the public sewer range from 200 mm diameter to canals, which can be entered by boat. The majority of public canals ranges from 200 to 350 mm. They provide sufficient cross section for the installation of one or more small cables. These cables may provide revenue for the sewer owner or may be laid into the canal on the base of reimbursement for increased sewer maintenance cost, depending on the legal position of the sewer owner.

The high investment cost for sewers is typically a factor 3 -10 higher than for telecommunications cable plants. This, the environment as well as the operation and maintenance of sewers require special attention:

- Cross section reduction of the sewer canal by cable or duct installations must be only few percent
- Inspection and possible repair of canal before cable installation as preparation step
- Absolutely no jeopardizing of structural soundness of the canals: avoid drilling of holes, cutting or milling of the canal surface
- Installations must not jeopardize the normal functions and maintenance of the canal and manholes
- Repair concepts and methods must be available for cable- and sewer networks
- Closures and other installations in the manholes must not prevent accessibility and working safety
- High pressure cleaning (e.g. 120 bar) of the canals require crush and high impact resistant cables
- Cables and equipment must be resistant to the special environment:: abrasion; chemicals, such as kerosene, high and low pH, rodents and bacteria attacks
- The electrical safety requirements must be considered: grounding; potential explosion classes; lightning situations

An early cooperation between the engineering and operation departments of the cable network and sewer network side is mandatory for a successful project. The standardization and procedure development of technical-, safety-, legal- and political issues has started.

In the following sections a cabling system approach is reviewed, which was designed specifically for the installation in sewers.

SEWER CABLES AND ACCESSORIES

A single technical platform of cables and cable fixation elements is used to build access networks, regardless of the duct size of the installation: small and man accessible sewers as well as conventional duct systems use the same cables and – if required – fixation technique. Therefore it is possible to go from small to large canals and switch also into conventional ducts. The system was designed to be highly modular to address the dynamic growth of access networks. It is for example possible to install in the sewer canal only one single cable and add later up to 8 further cables for flexible growth with network demands.

The extreme chemical and biological conditions of sewers together with the demand for high crush and impact resistance require proven cable materials and constructions. All cables have a PE based jacket for high chemical resistance. Bundle construction adds to the crush resistance and provides safe handling in closures for midspan access technique and customer circuit applications. Bundles with up to 24 fibers are color coded by 12 base colors with additional ring identification for safe installation practices. Welded stainless steel jackets with helical corrugation form a hermetic mechanical outer sheath to shield the cable from rodents and chemical attacks as well as from impacts during the sewer maintenance and cleaning operations. Stiffness of the cables and miniature tubes are optimized for installation through the robot system.

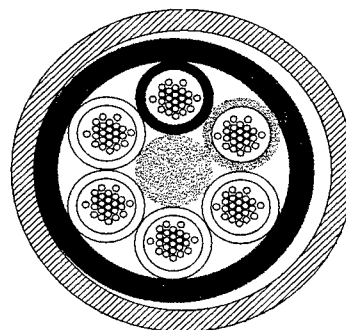


Fig 3. Cable cross section of sewer cable with 144 F and welded corrugated steel jacket

Cables can be implemented in the sewer as "cable - direct" (CD) installed in fixtures. They have up to 6 bundles, each carrying 24 fibers. The outer steel jacket can be removed by a special cutter, leaving a complete cable for maximum installation flexibility. Outer diameter over the steel jacket is only 11,5 mm for application in the smallest sewers (200 and 250 mm).

For fiber counts up to 72 F cables of 8 and 10 mm diameter can be inserted into a miniature stainless steel duct of 11,5 mm, alternate 16 mm outer diameter: "cable - in - minitube" (CIMT). This method is also suitable for all canals larger than 250 mm.

In addition a central tube cable with 4 -24 fibers and an outer diameter of 8 mm serves the customer drop.

The CIMT solution permits the pre-installation of miniature ducts, which can be filled on demand with cable for rapid installations, such as expansion of the distribution and customer access grid. Together with the capability to install up to 9 cables or miniature tubes in a sewer this approach offers a maximum flexibility for network planning and capacity migration of the access network.

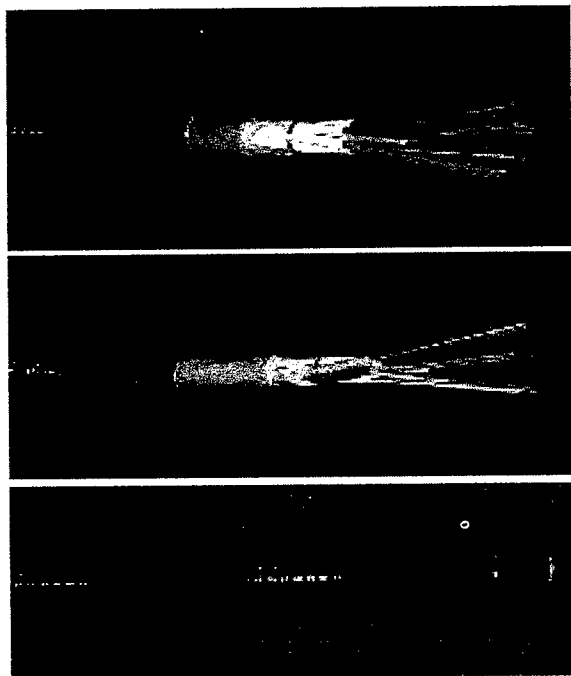


Fig 4. Sewer cables 144 F for CD and 60 F for CIMT installation with empty duct

For all connection, branching and distribution functions as well as customer circuit management a closure housing from stainless steel was developed for protection class IP68. The closure is placed in the manholes next to the entry ladder. For maintenance works and network expansion the closure is lifted from the manhole and splicing is performed outside the sewer manhole.

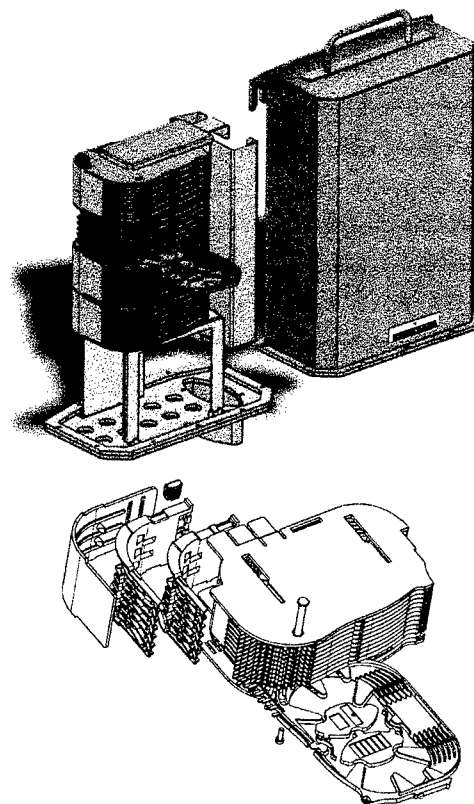


Fig 5. Closure and FibreArt fibre management module

A 80 x 20 mm access port permits cable entry in midspan access technique: the cable jacket is opened to provide handling of the selected fibre bundles. All other parts of the cable are kept and stored in a loop, leaving again through the entry port. This saves splicing of all other fibres, which are routed straight through this closure location. Further ports provide access for smaller cables.

The housing is extremely flat in order to match the depth of the ladder in the manhole for safety considerations.

Splice capacity can easily be adjusted to the local requirements by adding modules.

A novel fiber management module "FiberArt" has been designed. The compact module of approximately 16 x 12 x 10 cm carries 12 trays with up to 144 F splices. Identical splice cassettes are used for splice storage, excess fiber storage and single circuit management. On the back of the module the fiber branching from the bundles to the selected cassettes is performed. As a novelty the module avoids the threading of fibers through holes by employing only open fiber channels to route the fibers. The module is also applied to all other cable termination and fiber management equipment of the network.

The housing is also suited for electronic equipment, such as for traffic control boards.

INSTALLATION OF THE CABLES IN THE SEWER

Installing cables in the sewer must keep the sewers unaffected. Various materials, such as plastic tubes, concrete, ceramic and brick is used in the construction of canals and the wall thickness varies between millimeters and several centimeters. The best solution is therefore to use a method which is independent of the specifics of the canal construction. Steel bracings, which operate similar to conventional hose clamps are the best choice. The bracings are inserted into the small tubes and expanded to press against the sewer wall. This avoids drilling, milling and cutting and a single technique can be employed, regardless of the canal materials.



Fig 6. Cable installation in small canal with steel bracings

The bracings are equipped with clips, which accept the steel jackets of the cables or the miniature tubes. A robot is used for installations, where tubes become too small for man to enter.

Bracings with clips for sewers of 200 and 250 mm diameter accept 11,5 mm components. Above 250 mm canals can also be equipped with 16 mm components. Depending on the sewer diameter between 3 and 9 cable components can be fixed in the clips of one bracing. The cable components are positioned close to the top of the sewer tube and can be adjusted to avoid inlets from the houses.

Large canals are entered by man and cables are installed by hand with the steel clips, which are mounted on a small bracket on the walls.

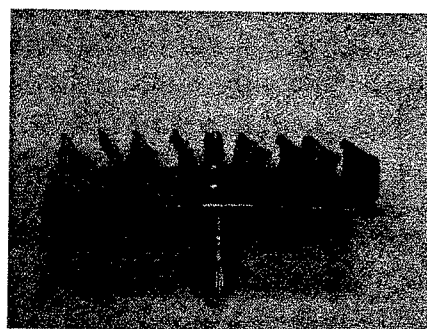


Fig 7. Clips with anchor for manual installation of cables in large canals

The transition sections from the canals to the vertical manholes require protective devices to maintain the minimum bending radius of the cables. Further protection may be required, routing the cables from the entry side to the outlet side of the canal in the manhole. Flexible steel profiles have been devised to add the required protections. A cable storage box takes the excess cable needed for the connection of a closure at a later time or to lift the closure to the street level for maintenance and additional customer connections. The solutions apply also to many non-standard manholes.

Other solutions are available, when closures are to be mounted in concrete vaults of the pavement or for curb applications.



Fig 8. Brick manhole with closure, cable storage box and flexible cable ducts

Installation of the cables in the manholes has been a major challenge in all projects conducted so far, since over about one century the constructions of sewers have changed considerably. It was necessary to devise flexible equipment, which can be adopted to a large variety of different situations in the manhole area.

ROBOT SYSTEM AND INSTALLATION PROCEDURE IN SMALL CANALS

A robot must be used to install the cables in the small canals. The robot is based on a module, which has been used worldwide in many systems



Fig 9. Roboter ready to be lowered into sewer

for sewer repairs since the eighties. This module has been adapted with tools, software and hardware modifications for the different tasks of the cable installation.

The control room on the command vehicle combines all computer control and TV inspection equipment. The operator controls the semi automated steps of the cable laying process.

After network planning and the selection of a cable route in the sewer the canals must be cleaned and inspected by TV for the state of repair. Minor repairs are performed before the cable installation. In case of serious damage the canal can either be repaired before cable installation or a new route must be selected, often in the next street block, only few meters away.

The cable installation starts with the installation of the bracing which holds the clips for the cables. Based on the video records the bracings are installed so that they avoid joints in the sewer and the inlets of houses. As a second step up to three cables or miniature tubes are pulled into the sewer. In the final step these elements are pushed by the robot upwards to engage in the clips. A final TV inspection at each bracing position serves as final documentation. All positions of the bracings including their orientation (clock position) are recorded in data format for a complete documentation. This data set forms the base of operation and maintenance records of the sewer - and cable network.

All necessary systems for the cable installation are included in the compact truck and trailer. The footprint needed for a construction site is reduced to few 20 m at a time. Since it is possible to install over 100 m per day the work site moves with the progress of the installation.



Fig 10. Moving sewer construction site

For work sites operating only temporarily a simplistic approval process is in place, avoiding the long approval times of conventional street digging. Digging is only required for customer access.

EXPERIENCES FROM SEWER CABLE INSTALLATIONS

Installation of cables in sewers has been done for some time in various major cities in the world. Only recently however, fuelled by the need for fast installation methods, a systematic development of technology has started. So far all major German cities above 750 000 inhabitants have cables installed in the large sewers. Only an estimated 20 % of all cables are so far installed in small canals by robot. Here lies an untapped potential, since digging is restricted by many city authorities for certain time periods due to tourist events or to avoid repeated opening of the street surfaces within few years time.

The city of Hanau with approx. 80 000 inhabitants serves as an example, where a digging permit could not be obtained. For the access backbone a

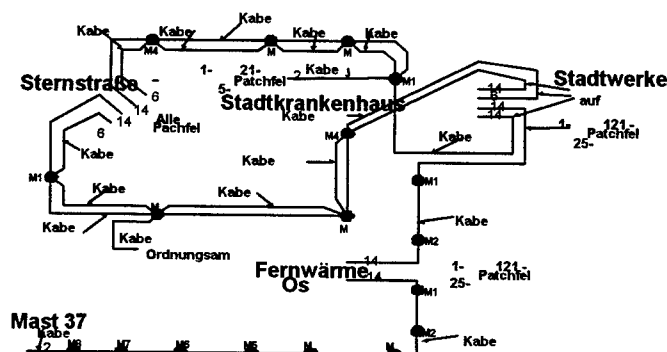


Fig 11. Cable plan for access backbone in sewer

first ring was completely installed in the sewer with a total length of approx. 4 km.

Frequent changes from large canals to small sewers were necessary for the route to be followed. In parallel one cable 144 F, one miniature tube with 60 F and one empty tube were installed. About 45 manholes were passed, 25 were equipped, in parts with spare cables for future applications. 8 closures were installed on this section for connection and customer access.

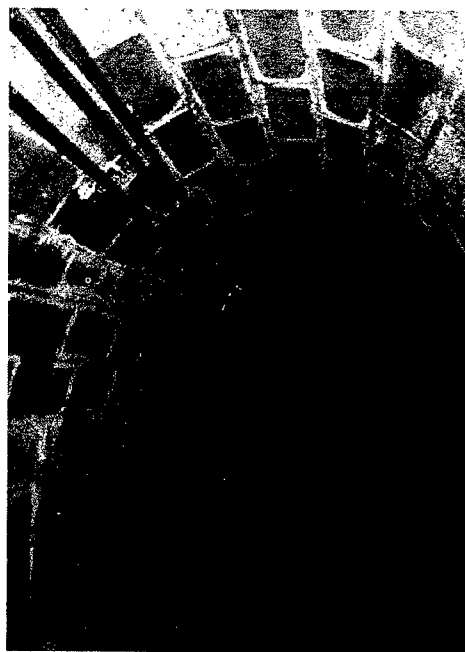


Fig 12. Sewer cable and miniature duct installation in an older large brick canal

The construction time for the complete sewer backbone was completed well below 2 months. The cable plant cost were 20 % below those for conventional digging.

In all stages of the project a close cooperation between the departments of the sewer and cable company as well as with the construction company is mandatory to provide seamless integration of the different trades.

The sewer system contained a large variety of different manhole constructions, since parts of the sewer date back to the turn of the century. Even under these unfavorable conditions was it possible to use prefabricated materials for a rapid installation in the manholes.

Although the robot is watertight an operation requires availability of TV sight. Typically only a small load of the canals were observed here, where the sewage passed under and around the robot. This caused no problem.

In the city of Hamburg some sewer canals are heavily loaded at certain periods over day. Even under night the load was too heavy to provide TV-camera sight, so that the canals had to be blocked off for periods of the robot operation. The procedure avoided the last resource: pumping the

sewage in a bypass line around the canal under work.

By now cable installations in sewers have reached a good routine, as e.g. in Hamburg. A separate company has been founded by the sewer owner and operator to make engineering and installation know-how also available to other, smaller communities, who may lack the necessary resources.

The technology has been tested in pilot installations in various cities in Europe. Additional tests have been performed to review the installation under lightning strokes, under cleaning with high pressure water jets and various cleaning conditions. Optical transient measurements were conducted repeatedly under cleaning operations without any significant change in attenuation. All tests were passed so far without the necessity to provide changes to the cabling system.

Experiences from the field installation show no contraption of dirt on the installed lines after over one and a half years of installation.

Major associations and institutions of the sewer and installation profession have started to act on this novel technique. The GSTT (German society of trenchless technologies) has implemented a working group to give recommendations for cable installations in existing duct (sewer) systems.

These are clear indications that cable installation in the sewer is today a reality, which is here to stay.

CONCLUSION

Today's booming demand for high bitrate communication links calls for faster and very flexible installation methods, cables, accessories and equipment.

Sewers are ideally suited to address the demand to reach to every doorstep, to allow for flexible migration path of cable and fiber capacity. Together with well designed equipment a rapid deployment of fiber optic cables on the route to the customer is possible and cost levels can meet and beat those of conventional digging installations in the cities.

With the equipment and procedures outlined in this paper we have opened up a new, fast lane to construct data highways in the crowded spaces of the cities.

ACKNOWLEDGMENT

The engineering and development work described here was started in close co-operation between: KA-TE System AG, Zürich- Switzerland; IK-T - Innovative Kommunikationen - Technologien, Regensburg - Germany; Alcatel Kabel, Mönchengladbach - Germany. HSE -Hamburger Stadtentwässerung, Hamburg - Germany joined the development group and added significant improvements from the practice of sewer operations.

AUTHOR



WOLFGANG LIESE
Alcatel Kabel
Bonnenbroicher
Str. 2-14

41238 Mönchen-
gladbach

GERMANY

Wolfgang Liese was born in 1947. He is Product Manager for Sewer Cable Technology of ALCATEL. Obtaining his PhD in Physics from University of Hannover he spent 13 years in Canada with various technical development projects, including fiber production. In 1991 he joined ALCATEL in Hannover, where he held Technical and management positions in Marketing and Engineering of cables, local area networks and access networks. He is involved in the development of sewer cable technology since its beginning in 1996. His professional memberships include ATV (German technical association for sewer technology) and the working group for "Cables in sewer canals" of GSTT, German Society for trenchless technologies.

INSTALLATION SOLUTIONS FOR AN OPTICAL TRANSPORT NETWORK BASED ON AERIAL CABLES AND RAILWAY INFRASTRUCTURE

P. Bonanni, S. Ghirardini
Infostrada – Milano - Italy

G. Clerico
Pirelli Cavi e Sistemi – Milano – Italy

E. Cottino, F. Mancarella, U. Morganti
Sirti. S. p. A. - Cassina de' Pecchi (MI) – Italy

ABSTRACT

This paper gives a general view of the technical solutions that Sirti and Pirelli Cavi e Sistemi had to arrange in building up the optical transport network for Infostrada, one of the new Italian telecommunication operators. The network is based on aerial optical cables and on the already existing Italian Railways infrastructure. A detailed description of the adopted solutions is here reported; related installation time and cost diagrams are given for comparison.

infrastructure serving over than 8,000 towns. From this start point a strategy for overall cost minimization, without affecting transmission quality, led to a short term plan for laying about 6,000 km of new fiber optic cable, 400 of which would be in metropolitan areas.

This paper deals with the whole set of solutions that Sirti and Pirelli Cavi e Sistemi had to arrange in order to meet Infostrada's requirements for a long distance optical network based on the FS' telecommunication infrastructure.

INTRODUCTION

The recent liberalization of the European telecommunication market has encouraged new operators to enter such business opportunity. At the same time, new operators have forced traditional turn-key system integrators towards new design and construction techniques in order to meet the requirements of short-term installation and cost saving solutions.

It is of paramount importance for new operators to have a proprietary network infrastructure, which ensures operative and technological autonomy, and to be competitive and timely.

Infostrada, one of the Italian new operators, has signed an agreement with FS, the Italian Railways, to acquire the right of way along over 16,000 km of railway infrastructure and the right to use some of the already existing FS' optical network fibers: that is a ready-to-start network

TECHNICAL BACKGROUND

The project made up by Sirti in collaboration with Pirelli Cavi e Sistemi in order to comply with Infostrada's requirements arranges the installation of a fiber optic self-supporting aerial cable along the railway electrical traction poles.

The cable plant has been designed according to the following assumptions:

- availability of the poles along the electrical traction line
- short term network build
- low cost

The choice of laying the optical cable along the railway lines has offered undoubted advantages, but it has also implied some constraints.

So, for instance, the proximity of the railway electrical traction line has imposed the use of an all-dielectric optical cable in order to avoid induced voltage risks and the need of expensive

earthing systems. Moreover, cable dead-ends and suspensions have been studied in order to guarantee quick and safe installation procedures during the normal railway operations. The cable was laid 7 meters high with respect to the rail level to prevent as much as possible accidental faults (i.e. cable damage caused by breaking out of the contact line), vandalism or sabotage acts. The optical network elements (cables, dead-ends, in-line suspensions ...) have been provided by Pirelli Cavi e Sistemi and have been installed by Sirti according to the following description.

OPTICAL CABLE

A 72 optical fibers cable was studied and developed by Pirelli for the Infostrada's network. The cable is equipped with ITU-T G.652 single mode optical fibers. The cable core consists of 6 PBT filled loose tubes, which are stranded according to the S/Z technique around the fiber

glass central element; each tube contains 12 optical fibers. The core is filled and protected with an inner polyethylene sheath, around which there is a double layers crown of aramid yarns as strength member; the external protection is made of a polyethylene sheath (figure 1).

Pirelli adopted appropriate techniques during the manufacturing process to match the design target performance reported in table 1 and to avoid slipping between the strength element (aramid armour) and the outer sheath.

Shot-gun protection, where required, was obtained by applying two aramid tapes with suitable thickness between the inner sheath and the dielectric armour. Such a protection proved to be effective as experimentally verified by a shot gun test on cable samples from a 25m distance according to IEC 794-2 method: bullets did not pierce the aramid protection tapes.

For in-tunnel cable spans a LSZH (Low-Smoke Zero-Halogen) version of the cable was used.

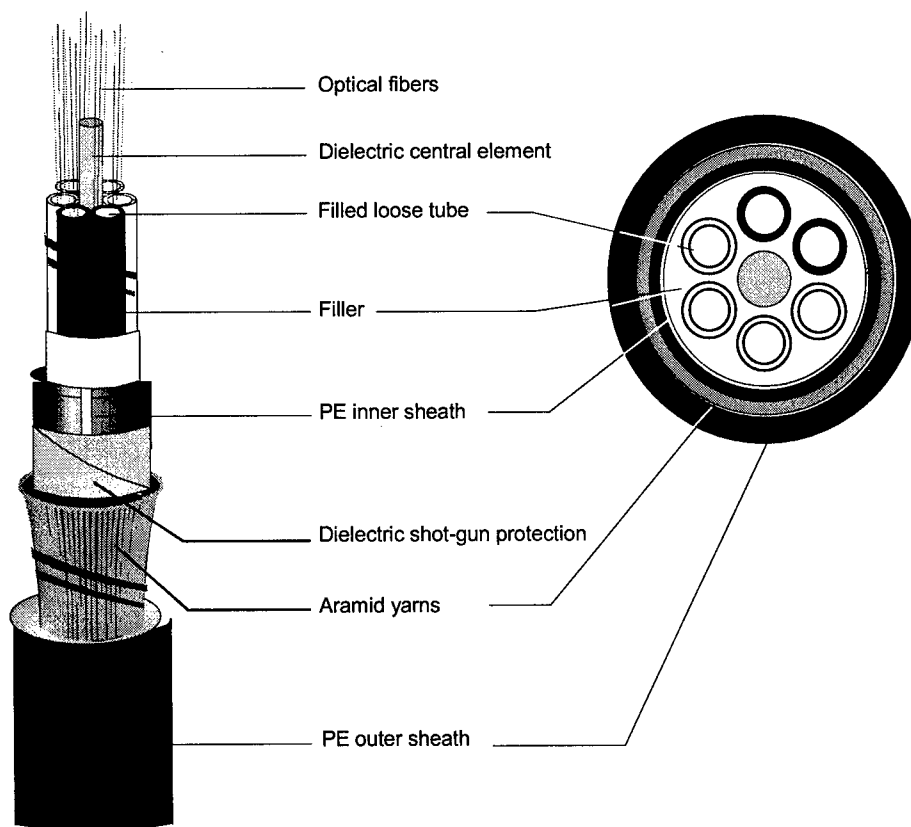


Figure 1 – Structure of the 72 fibers ADSS cable

FEATURES	Unit	VALUE
Maximum working tension (Tmax)	N	4000 (normal) 4500 (shot-gun version)
Max. cable elongation at Tmax	%	0.6
Max. fiber elongation at Tmax	%	0.0
Min. bending radius	mm	300 (dynamic) 200 (static)
Crush resistance	N/cm	>400
Torsion resistance	°	±360
Operating temperature range	°C	-30/+60

Table 1 - Main features of the 72 fibers ADSS cable

INSTALLATION ACCESSORIES: DEAD-ENDS, IN LINE SUSPENSIONS, CROSSES

Pirelli has provided the dead-ends of suitable length and size in order to guarantee cable tension without damage even in presence of high stresses.

Reinforcing rods are inserted under the tension clamps to better share mechanical stresses and avoid sheath damage even under worst case conditions.

The dead-end application technique is simple and quick, as no special tools are required.

Functionality tests have been carried out on these accessories such as slip load up to twice the maximum working tension.

In-line suspension is made essentially of an aluminum alloy fusion, which can be opened, and of a rubber insert split in two halves. The rubber insert assures a good grip to the clamp without damaging the cable sheath.

This type of suspension has proven to be particularly suitable for the considered application: it is easy to mount and it allows for safe installation even in the case of powered contact line.

Proper cross organizers of galvanized metal have been developed to get allocation of cable extra-lengths at the head-ends and at the joint sites, for maintenance purposes. A typical installation scheme is reported in figure 2.

Finally, 6 couples of splice and jumper organizers are used for each cable tube for cable termination and connection to the transmission equipment.

INSTALLATION PLAN

The installation activity for Infostrada's network typically consisted of 2 phases:

Phase 1: Executive project plan

The executive project plan allowed for efficient work planning, critical activities forecasting and time reduction, leading to high quality and reliable work results without affecting costs.

A precise inspection of the link alignment had to be carried out in order to check the cartography but also the local situation in terms of ground morphology, line and termination poles, level crossings and overpasses, bridges, viaducts, etc.. All the data were collected by specialists of the railway environment. They were analyzed in order to set up an efficient building yard organization and to forecast loads and stresses which would be applied on the electrical traction line.

Phase 2: In-field installation

FS, the Italian Railways, has strict specifications concerning works on the railway ground, especially in the presence of rolling stock.

The so-called "Protection building yard" had to be arranged according to the works to be done, the means to use and the traffic conditions.

On main railroad lines (i.e. Milano-Bologna and others) time slots without traffic were not available; therefore works were carried out from outside the electrical traction line poles in order to avoid interference with ordinary train circulation.

After an accurate study of the various operational techniques, Sirti arranged for its building yards a

precise sequence of operations, in order to work under maximum safety conditions keeping optimal work speed.

Typically, one cable dead-end every 500 meters and in-line suspensions at each pole were installed. The cable was generally fixed at the top of the pole (at about 7 meters height), with 60 meters long spans.

Cable extra-lengths of about 20 meters were stored within cross organizers at dead-ends and at the cable joints poles for future maintenance and repair purposes.

During works along the line, safety and antislippery ladders tightly fixed at the poles were used in order to allow personnel to stay on the pole even in the presence of trains running through at up to 160 km/hour speed.

Inside the railway tunnels, the cable was fastened to the sidewall at 3 meters height by means of ad-hoc 2 meters spaced plastic supports.

By means of these solutions, Sirti could install about 1,500 km of aerial optical cable a year on in-service Italian Railways lines.

COST AND TIME ANALYSIS

Generally, the choice of a new network installation solution has to be carefully evaluated in terms of cost and time implications.

In the case of Infostrada, the problem was to analyze and arrange a whole set of solutions, in order to carry out the new network installation by adding 6,000 km of new optical cable to the already existing FS' 3,000 km long private in-duct optical network.

Figure 3 shows the results of a general analysis carried out in order to compare different installation techniques for the new optical transport network.

The analysis considers the following four installation conditions for a pilot-link of about 100 km of a 72 optical fibers cable:

- aerial installation along the railway using the existing poles (1);
- in-duct installation along the railway line (2);
- in trench installation along a superhighway

emergency lane (3);

aerial wrapped installation around ground wires (4);

The analysis accounts for costs due to design, civil works, cable laying, cable junction / termination and network preliminary testing.

It is worth noting that aerial solutions (1) and (4) are the best choices in terms of reduced installation time and cost, thanks to the reduced incidence of civil works with respect to in-duct or in-trench cable laying (see figure 4).

CONCLUSIONS

Railway infrastructure has proven to be well suited to build up a new optical transport network. The decision to exploit this infrastructure, together with innovative technical solutions and aerial cable installation, allowed the establishment of Infostrada's long distance network in short time and at low cost.

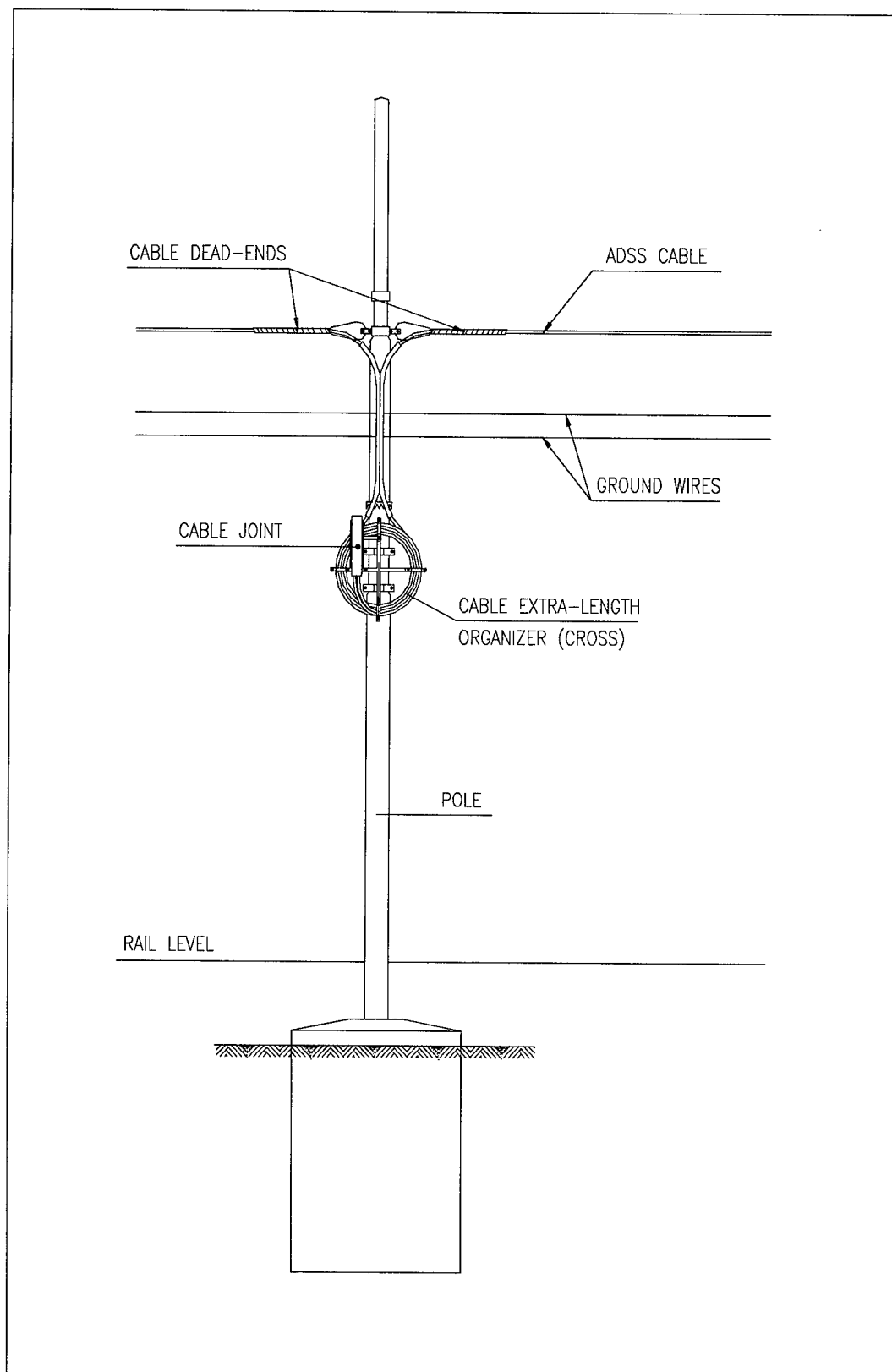


Figure 2 – Installation scheme of the optical cable on the railway poles

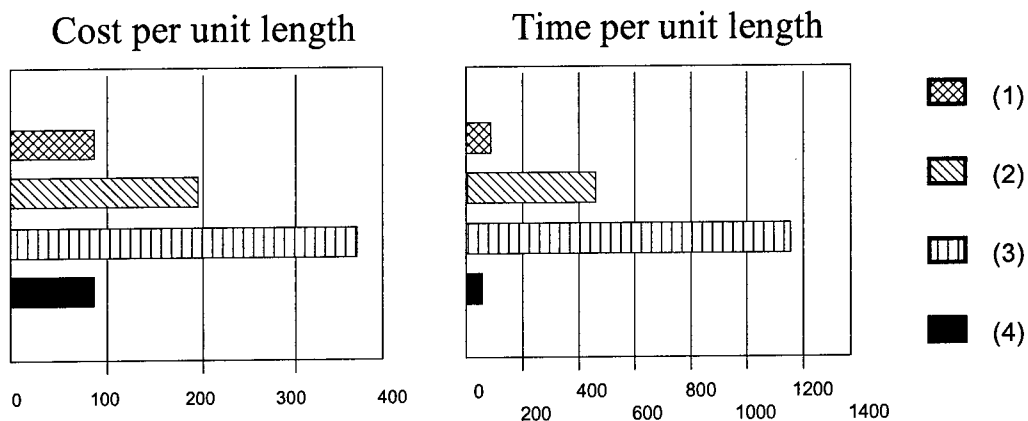


Figure 3 – Comparison among four installation conditions

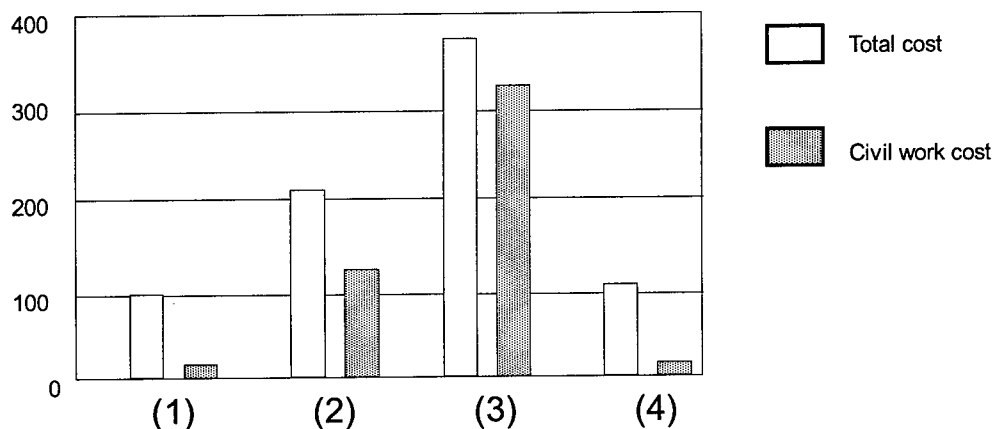
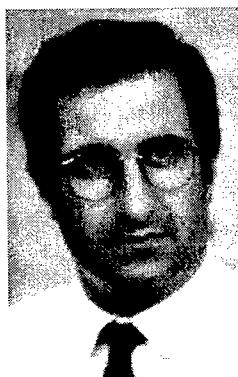


Figure 4 – Incidence of civil works on the total costs for the four considered installation conditions



Edoardo Cottino

Cables and Optical
Tech. - R&D Dep.
SIRTI S.p.A.
Via E. Fermi, 2 - 20060
Cassina de' Pecchi (MI) -
ITALY

Edoardo Cottino was born in Turin, Italy, in 1957. He received his degree of electronic engineering from the Polytechnic of Turin in 1982. He joined AET Telecomunicazioni in 1983 in the fiber optic laboratories, and moved to SIRTI in 1995, where he currently holds the position of manager of the Cables and Optical Technologies R&D Division. Dr. Cottino is a member of SPIE and his present responsibilities include ITU-T activities.

SMALL-SCALE RHEOLOGICAL TESTS TO DESCRIBE WIRE AND CABLE EXTRUSION

Scott H. Wasserman

Union Carbide Corporation, Somerset, New Jersey

ABSTRACT

Rheological tests are often used to measure melt-state flow properties of polymer compounds, delineating details of molecular structure and/or predicting extrusion performance. Here, the focus will be on the performance and behavior of wire and cable compounds in the extruder and die. Two related rheological techniques - dynamic oscillatory shear (DOS) and creep-recovery - will be described in terms of their ability to capture important viscous and elastic behavior that affects, for example, motor load, die swell, and thermal sensitivity.

It is shown that one can use specific rheological parameters to identify the capability of commercial jacket and insulation compounds to extrude well. This is particularly valuable for determining the extrusion quality of a new product or formulation. Rheological tests are done with as little as 25 g of sample, are completed in minutes, and enable one to differentiate among compounds made by different polymerization processes, catalyst systems, or formulations.

INTRODUCTION

An extensive evaluation of parameters that are calculated from DOS and creep-recovery tests was undertaken to determine the relative strengths and weaknesses for predicting extrusion performance. Zero-shear viscosity, recoverable elastic compliance, flow activation energy, and the Relaxation Spectrum Index (RSI)¹ were all evaluated. The RSI, a parameter that quantifies the breadth of the relaxation spectrum or distribution of melt relaxation times (see Figure 1), has been shown to be

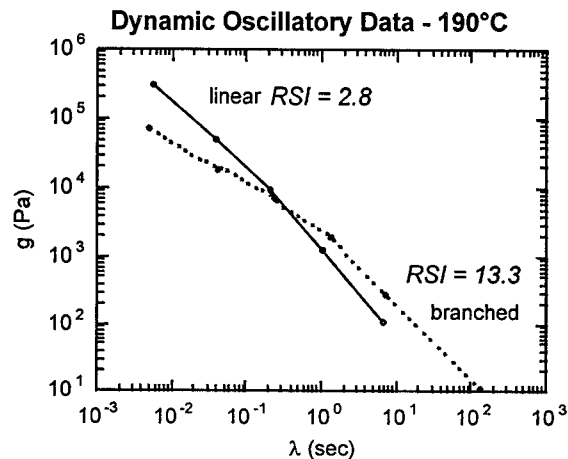


Figure 1. Relaxation spectra and RSI values for LLDPE (linear) and HP-LDPE (branched) of 2 MI.

a reliable and sensitive indicator of processing performance, such as head pressure and motor load in extrusion. The RSI can also be used to evaluate the extrusion stability of a polymer compound and is useful for designing cost-efficient process stabilization packages.² The flow activation energy, E_a , calculated from DOS tests at multiple temperatures, is a well known parameter for capturing the temperature sensitivity of polymer melts. The recoverable compliance, J_r , and the zero-shear viscosity, η_0 , are both calculated from creep recovery tests. J_r is sensitive to the elastic behavior of the polymer melt, for example the elastic recovery process that gives rise to die swell, while η_0 is a useful indicator of low-shear viscous behavior, such as the tendency to resist sag on the conductor in a wire or cable construction when exiting the cross-head die.

Rheological measurements have specific sensitivities to the elastic or viscous behavior (or both) that a polymer melt

exhibits during extrusion and between the coating die and water bath (or other quench method). The elastic properties of a polymer melt reflect its ability to store energy that is applied by stresses during processing; the viscous properties of the same melt reflect its ability to relax from the same applied energy. To illustrate, Figure 2 shows a ball that is bounced from some height. The higher the ball bounces back once dropped, the more elastic its behavior; the difference between the original height and the height of the bounce corresponds to the amount of energy lost, or viscous behavior.

In fabrication processes, the levels of elastic and viscous behavior displayed by a polymer melt are directly related to the time scale used to observe the behavior. To be more specific, the longer the time scale of the process or observation, the more elastic, and the less viscous, the behavior of a particular polymer will appear. This concept is captured by a quantity called the Deborah number, De , expressed as:

$$De = \tau/t_p \quad (1)$$

where t_p is the time scale of the process and τ is a relaxation time that is characteristic of the polymer melt under the conditions (i.e., temperature, pressure, shear history) of the process. The characteristic relaxation time is specified by the molecular structure of the polymer (i.e., MW, MWD, LCB) and the same conditions listed above, while the process time scale is specified by the process. For example, when leaving the

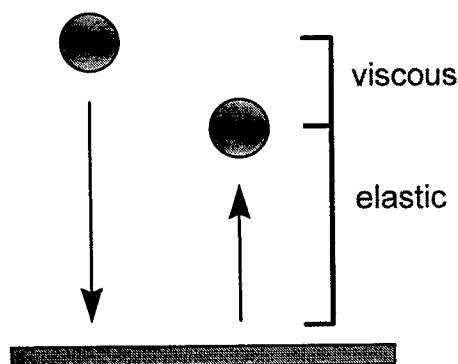


Figure 2. Simple illustration of viscous and elastic behavior shown when dropping a ball.

cross-head die, the polymer compound comprising the jacket or insulation can only relax during the time it takes to reach the water trough. Widening the gap between the die exit and the water trough will increase the process time scale, and decrease the De for that process. Alternatively, if one was to increase the melt temperature in the extruder, the characteristic relaxation time will decrease, also decreasing De .

Measuring the characteristic relaxation times of a polymer melt under specific conditions, therefore, will provide critical information about the elastic and viscous behavior one could expect during a particular process. Higher De values (i.e., $De \geq 1$) suggest a low level of stress or energy relaxation, so a high level of elastic memory will be retained by the polymer composition following quenching, which could lead to shrinkage of the polymer coating, for example. A high level of molecular orientation in the flow direction will also be retained, which sometimes can give benefits in solid-state properties such as impact strength.

For the reasons illustrated above, it is critical to measure the molecular rheological properties of a polymer composition to predict the behavior during and following wire or cable fabrication. Key measurements will be highlighted below, followed by some illustrative case studies in which rheological measurements were used to predict processing behavior.

EXPERIMENTAL

Dynamic oscillatory shear and creep-recovery tests have been used to provide key rheological parameters in the prediction of processing behavior for many polymer systems for wire and cable applications. Such low deformation tests are considered to be the best for detecting differences in features of molecular structure such as polydispersity index (PDI) and levels of long chain branching (LCB). Key calculations and appropriate test conditions are highlighted below, along with some commercial jacketing and insulation formulations used in this work.

Dynamic Oscillatory Shear

In dynamic oscillatory shear (DOS) a controlled stress or shear rate is applied by a motor to a melt sample confined between two parallel plates (one parallel plate is sometimes replaced by one with a 1-2° cone). The response of the sample to the deformation is detected by the plate opposite that attached to the motor, with torque measured when shear rate is applied or with strain measured when stress is applied. The response of the samples in a frequency sweep test is converted to dynamic storage and loss moduli (G' or G'' , respectively) as functions of frequency. While useful at that point, the experimental data are more conveniently interpreted in terms of the distribution of relaxation times, or the relaxation spectrum. The calculation of the relaxation spectrum from the dynamic moduli data can be accomplished by any number of commercial software packages or custom written computer code.

For the current work, and as standard practice at Union Carbide, DOS tests for polyethylene (PE) are run in parallel plate mode at 190 °C with a controlled strain of approximately 2% (ascertained to be low enough to give linear viscoelastic behavior, but high enough to give an acceptable signal to noise ratio). The frequency sweeps are specified to range from 0.1 to 100 1/sec and a nitrogen atmosphere is provided to prevent thermo-oxidative degradation during the test.

RSI. The relaxation spectrum is calculated by a simultaneous fit of the storage and loss moduli to a series of exponential relaxations according to:³

$$G'(\omega) = \sum_{i=1}^N g_i \frac{(\omega\lambda_i)^2}{1 + (\omega\lambda_i)^2} \quad (2)$$

$$G''(\omega) = \sum_{i=1}^N g_i \frac{\omega\lambda_i}{1 + (\omega\lambda_i)^2} \quad (3)$$

Each of the N individual relaxation modes in the above relations are described by a distinct strength g_i and relaxation time λ_i .

Increasing the breadth of the molecular weight distribution (MWD) or level of branching in the polymer system is reflected by an enhanced spectrum, particularly at long relaxation times. In order to differentiate polymers with different or changing relaxation spectra, we have introduced a quantity known as the Relaxation Spectrum Index (RSI). If the first and second moments of the spectrum are:

$$\begin{aligned} \lambda_I &= \sum_i g_i / \sum_i g_i / \lambda_i \\ \lambda_{II} &= \sum_i g_i \lambda_i / \sum_i g_i \end{aligned} \quad (3)$$

the RSI is defined as their ratio:

$$RSI \equiv \lambda_{II} / \lambda_I \quad (4)$$

Equations 3-4 are analogous to those used to calculate the polydispersity index (PDI) which describes the breadth of the MWD from size exclusion chromatography (SEC). The RSI has proven to be a sensitive indicator of differences in molecular structure, especially where those differences affect the breadth of the relaxation spectrum. The RSI is a dimensionless quantity, but varies with T and MW (or MI, for example).

Flow Activation Energy. A traditional use of DOS tests has been to calculate the flow activation energy, E_a . E_a describes the temperature sensitivity of the zero-shear viscosity, with higher E_a indicating a greater decrease in viscosity with increasing temperature. E_a is calculated from DOS tests run at multiple temperatures. The shift in frequency between data at particular test temperatures and those at a convenient reference temperature (aT) are fit to an Arrhenius expression:

$$a_T(T) = \exp \left[\frac{E_a}{R} \left(\frac{1}{T} - \frac{1}{T_0} \right) \right] \quad (5)$$

where T is the test temperature, T_0 is the reference temperature, and R is the ideal gas constant (i.e., 1.987 cal/mol.K). Typical E_a values are shown in Table I. In general, we use a series of four tests run at test

	HDPE/ LLDPE	PP	HP-LDPE
Ea (kcal/mol)	5.5-8.5	9.5-10.0	14.5-20.0

Table I. Typical flow activation energy values for common polyolefins.

temperatures of 175, 190 (reference) 210, and 230 °C, or higher as required by melt temperatures for polymers such as PP.

Creep Recovery

The creep-recovery test apparatus is very similar to that for DOS, except that all tests are run with constant stress applied by the motor and the strain response of the sample recorded by a detection device. In creep-recovery, the constant stress is applied for a predetermined time during which the strain eventually reaches steady-state (constant rate of change with time). At the end of that creep step, the stress is released and the sample is allowed to recoil, or recover, with no applied stress. The recovery step can be continued until no change in strain is detected or until a predetermined time has elapsed. The complete experiment is shown schematically in Figure 3.

Typical conditions for PE are 1 kPa stress applied for three minutes, followed by 15 minutes of recovery, all at 190 °C. The two key parameter calculated from the creep-recovery test, the zero-shear viscosity, η_0 , and the recoverable compliance, J_r are

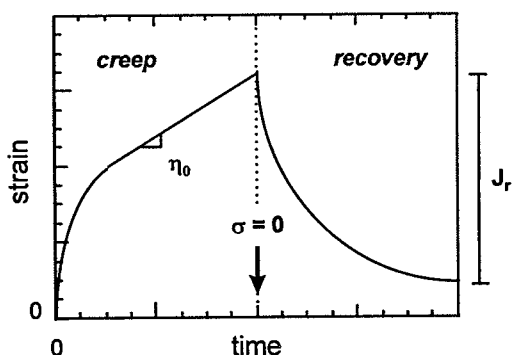


Figure 3. Schematic representation of a creep-recovery test and its useful parameters.

calculated directly from the creep and the recovery steps, respectively. The zero-shear viscosity is calculated from the slope of the steady-state creep curve and the applied stress:

$$\eta_0 = \sigma / (\partial \gamma / \partial t) \quad (6)$$

where σ and γ are the applied stress and the measured strain, respectively. J_r is measured from the recovery curve according to:

$$J_r = (\gamma_{\max} - \gamma_{\min}) / \sigma \quad (7)$$

where γ_{\max} and γ_{\min} are the initial (maximum) and the asymptotic minimum strain values, respectively, during recovery. Specifying a recovery time does not guarantee that recovery will reach steady-state but does ascertain that all samples experience the same experimental time scales.

Test Samples and Conditions

For the current study, rheological data for three commercial jacketing compounds were generated and compared to extrusion and die swell data. The compounds are listed in Table II, along with nominal melt flow index (MI, 2.1 kg/190°C conditions) and density (23 °C) values. Die swell values were recorded during MI tests by measuring the extrudate diameter and dividing by the standard die diameter in the melt indexer (i.e., 0.0825"). Extrusion data were measured during application of a 25 mil (0.6 mm) coating onto 14 AWG copper wire using a 2.5" Davis-Standard extruder with a line speed of 260 ft/min.

Product	Code	MI (g/10 min)	Density (cc/g)
DFDG-6059BK	LLDPE	0.55	0.932
DHDA-8864BK	MDPE	0.60	0.941
DGDK-3479BK	HDPE	0.20	0.955

Table II. Identification of samples included in the present study.

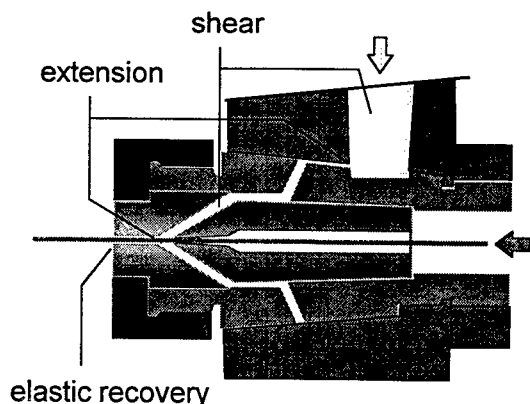


Figure 4. Schematic illustration of a cross-head die, showing sites of rheological phenomena.

DISCUSSION

As suggested in the earlier discussion, there are a large number of phenomena involved in the wire and cable coating process for which rheological testing can be used to provide information. Here, focus is given to three particular areas: relationship between rheology and extrudability; predicting die exit phenomena; and the broad area of melt process stability.

Extrudability

Before a wire or cable formulation even reaches the conductor, it should be extruded under conditions that attempt to minimize the head pressure, motor load, and melt temperatures. Such broad scale rheological phenomena require that one understands both the shear and the extensional properties of the formulation being processed. Extensional deformations arise wherever a sudden contraction in channel size occurs, such as the entrance to the cross-head die from the extruder, as shown in Figure 4. For the purposes of this paper, the measurement of extensional properties will not be discussed. Shear deformations are prevalent wherever a polymer melt flows past a fixed surface, such as along the extruder screw and barrel and within the channels of the cross-head die, as indicated in Figure 4.

Due to the prevalence of shear deformations in the extruder and cross-head die, DOS tests are specifically useful for predicting bulk extrusion performance. In particular, the RSI is a useful predictor of key extrusion parameters such as head/breaker plate pressures and motor load. Figure 5 shows both motor load and breaker plate pressure relative to RSI for samples HDPE, MDPE, and LLDPE. When comparing RSI values for samples of different MI, as in Figure 5, it is necessary to normalize the RSI values to a common MI, say 1.0 MI, in order to remove the MI effect from the data interpretation. A very reliable normalization leads to:⁴

$$nRSI = RSI_{1.0 MI} = RSI \cdot MI^{0.611} \quad (8)$$

In Figure 5, RSI (normalized to 1.0 MI) successfully emulates the decrease in both motor load and breaker plate pressure for the three commercial product samples.

Die Exit Phenomena

In Figure 4, the region in which the coated conductor first leaves the cross-head die is noted to be the location for elastic recovery.

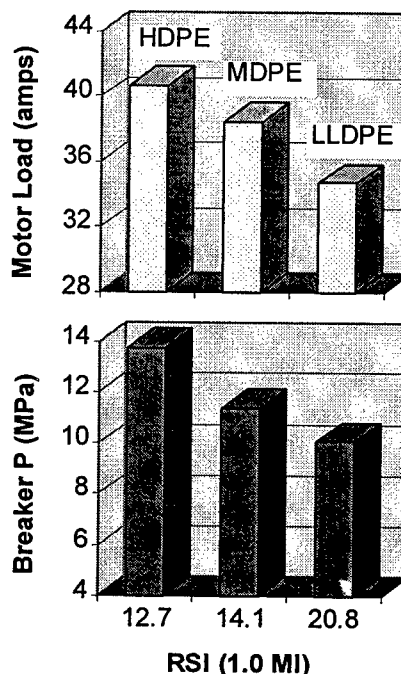


Figure 5. Relationship between RSI (at 1.0 MI) and extrusion parameters.

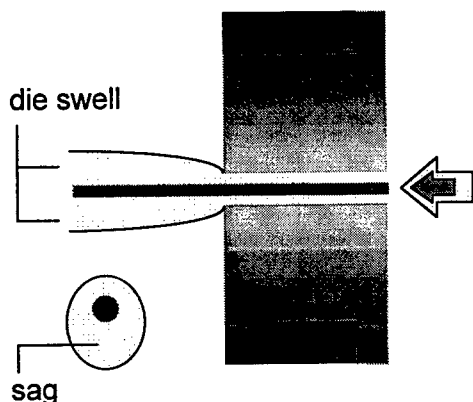


Figure 6. Schematic illustration of cross-head die exit showing die swell and sag on conductor.

In fact, the disappearance of shear stress at the die exit is analogous to the transition from creep to recovery in the creep-recovery test. This is why J_r is powerful for predicting die exit phenomena. The higher J_r , the more elastic the polymer melt. Further, high J_r suggests more energy applied during extrusion is stored and more "memory" remains in the melt upon leaving the cross-head die, so a greater degree of die exit phenomena can be expected.

Figure 6 shows a magnified view of the die exit with die swell. In relatively low-speed coating processes (i.e., hundreds of ft/min) or during other profile extrusion, the extent of die swell is controlled by the rate of extrusion or "draw down." For the coating of high-speed telephone singles, on the other hand, the line speed is so high (i.e., thousands of ft/min) that little die swell is allowed to occur, suggesting that any stored energy remains in the coating after quenching.

In tube-on extrusion in which a conical coating is drawn onto the wire or cable outside of the die, the thermal properties of the polymer compound, such as E_a , also become critical. In that process, draw down of the coating occurs as temperature is decreasing and prior to contacting the wire or cable. A compound with high E_a can be subject to coating instabilities due to a greater drop in viscosity.⁵

Upon leaving the die and before entering the water trough or other quench, the wire or

cable coating is subjected in the transverse direction to the effects of gravity. In fact, that condition is akin to the application of a very low shearing force, so the zero-shear viscosity can be used to predict the degree to which one expects the polymer coating to sag on the conductor (see Figure 6). A high η_0 suggests that the polymer melt has a high resistance to low-shear deformation, so it will be less susceptible to sag. Often, the molecular characteristics that lead to high η_0 also lead to high J_r , so a balance needs to be arranged between opposing rheological phenomena during product development.

To illustrate the connection between rheology and die exit phenomena, J_r and die swell data for our three test products are compared in Figure 7. Often, it is useful to use lower-stress test conditions in order to reach steady state behavior; here we used 0.1 kPa stress with 15/25 min creep/recovery. J_r reproduces the higher die swell for MDPE, relative to LLDPE and HDPE, but J_r for HDPE is also lower than that for LLDPE, while their die swell values are the same. The literature confirms that extrudate swell and J_r are related by:⁶

$$\text{extrudate swell} = \left[1 + \frac{1}{2} (\sigma J_r)^2 \right]^{1/6} \quad (9)$$

where σ is the applied stress, so the failure of our die swell measurement to detect differences between LLDPE and HDPE

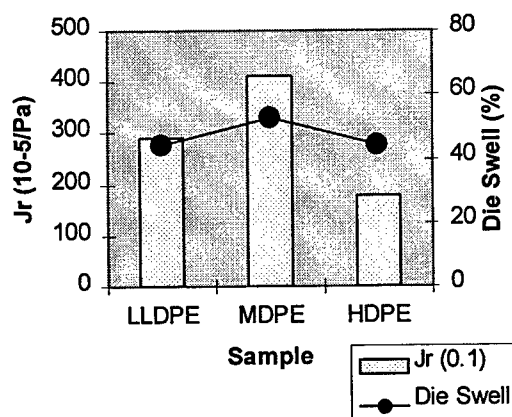


Figure 7. Comparison of die swell and J_r values measured for current products.

would have led to incorrect expectations during processing. This is probably due to the fact that the stress level during the die swell measurement is far below that experienced in extrusion (measurements based on the short die of the melt indexer are complicated by die entrance effects, as well). Note also that based on MI alone, one would have no reason to suspect a difference between LLDPE and MDPE, so Jr is a valuable parameter to use to predict die swell expected to occur during processing.

Melt Process Stability

Key to the complete formulation of wire and cable compounds is the stabilization package, which might consist of primary antioxidants, such as hindered phenolics or hindered amines, phosphite or thioester stabilizers, synergists or metal deactivators. The stabilization package is designed to protect the particular molecular structure for the targeted product application. Stabilization is key in all aspects of the fabrication process, including post-reactor extrusion and product finishing. Since all extrusion and compounding processes subject the polymer compound to mechanical and thermal stresses, one can simulate those deformations and study their effect on the molecular structure as detected by rheological tests. For example, we often use multiple passes through a laboratory-scale extruder to simulate the most severe processing histories, and then use DOS to follow the evolution of molecular structure.⁷

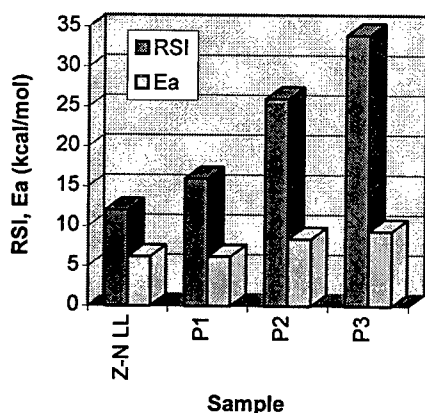


Figure 8. RSI and Ea values for Z-N LL after multiple passes through an extruder.

Figure 8 shows the change in the RSI and Ea for a Ziegler-Natta LLDPE film resin (Z-N LL) subjected to two passes through an extruder at 210 °C and one at 260 °C, with a sample taken before processing and after each pass.⁸ While Ea shows no change between the virgin material and the first pass sample, and consistent but small increases with successive processing, the RSI shows significant increases with each successive extrusion pass. We concluded that the RSI was the most sensitive test to be used to monitor change in molecular structure due to processing-induced degradation.

Based on such findings, we believe that DOS are valuable for use in designing stabilization packages. For example, one could subject a polymer compound to simulated processing conditions and adjust the stabilization package such that the rheology shows no significant shifts in molecular structure. In this case, DOS test are superior to creep-recovery, since the resulting relaxation spectrum can provide information on how the molecular structure is changing, be it chain scission, chain enlargement, or the formation of long-chain branches (LCBs).

Figure 9 shows the results from a study of the stabilization requirements for polyethylene made from a number of different catalyst systems.⁹ Here the results for LLDPE base resins made with Ziegler-Natta (Z-N) and chromium based (Cr) catalyst systems are provided along with those for a HP-LDPE. Multiple pass extrusion trials were completed with each of the base resins using three degrees of stabilization: unstabilized resins; resins stabilized with a hindered phenolic primary antioxidant (PAO); and "fully" stabilized with the PAO and a phenolic secondary antioxidant. The Z-N LLDPE shows an enormous increase in RSI when unstabilized, suggesting that chain enlargement or LCB formation was the dominant degradation mechanism. Increasing the potency of the stabilization package significantly reduced the extent of degradation. The Cr-catalyzed sample showed proportionally less degradation and

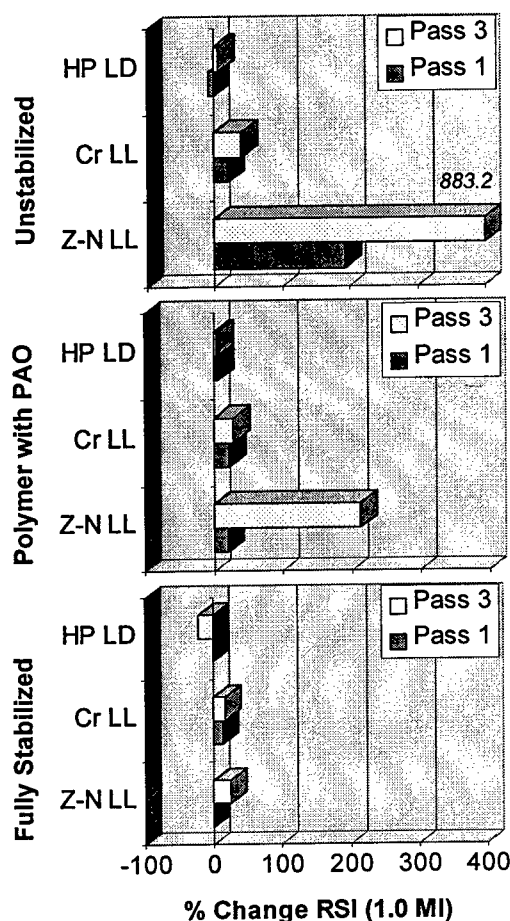


Figure 9. Percent change in RSI after extrusion passes for commercial LL and HP-LDPE.

the HP-LDPE showed even less. In fact, when fully stabilized, the dominant degradation mechanism for the HP-LDPE became chain scission, since the RSI became lower than that prior to extrusion (see data after the third pass).

CONCLUSIONS

Small-scale rheological tests have been discussed relative to their ability to predict critical phenomena in wire and cable coating processes. In extrusion, the RSI and E_a from DOS tests are indicative of pressures and motor load that one will experience in processing. When examining die exit phenomena, creep-recovery tests and the

related J_r and η_0 parameters are useful for predicting strictly elastic (die swell) or viscous (sag) behavior, respectively. Additional die exit phenomena, such as melt fracture and coating instabilities, are also critical and are probably related to thermal and elastic recovery phenomena at the die exit. Finally, the use of DOS in the study of polymer degradation and stabilization was illustrated. Such tests are an integral part of the design process involving stabilization packages in wire and cable compounds.

ACKNOWLEDGEMENTS

The author wishes to thank Mr. Dan Weaver for the die swell data and the cross-head diagram, and Dr. Tong Chen for the extrusion results, and Union Carbide for permission to present this paper.

REFERENCES

- 1 see S. H. Wasserman, "Characterizing the Melt Relaxation Behavior of Metallocene Polyethylenes," in *Metallocene-Catalyzed Polymers: Materials, Properties, Processing & Markets*, Plastics Design Library/SPE, New York, pp. 185-192 (1998).
- 2 S. H. Wasserman, G. N. Foster, D. J. Yacka, "Dynamic Melt Rheometry Used to Study the Degradation of Metallocene Polyethylene," *Proc. SPE ANTEC '98*, Atlanta, GA, pp. 992-996 (1998).
- 3 J. D. Ferry, *Viscoelastic Properties of Polymers*, 3rd ed., John Wiley & Sons, New York, 1980.
- 4 Wasserman, *Metallocene-Catalyzed Polymers: Materials, Properties, Processing & Markets*, pp. 185-192.
- 5 P. B. Kuyl, "Non-Isothermal Viscoelastic Flow Simulation of a High Speed Wire Coating Process," *Proc. SPE ANTEC '97*, Toronto, Canada, pp. 298-302 (1997).
- 6 R. Schroff and H. Mavridis, "New Measures of Polydispersity from Rheological Data on Polymer Melts," *J. Appl. Polymer Sci.*, 57, 1605 (1995).
- 7 S. H. Wasserman and G. N. Foster, "Rheological Detection of Structure Modification Due to Extrusion Processing in Polyethylene," *Proceedings of the XIIth Intl. Congress on Rheology*, Quebec City, Canada p. 48 (1996).
- 8 Ibid.
- 9 Wasserman, et al, *Proc. SPE ANTEC '98*, pp. 992-996.



Dr. Scott H. Wasserman
Union Carbide Corporation
1 Riverview Drive, P. O. Box 450
Somerset, NJ 08875 USA

Dr. Wasserman received his B. ChE. degree from the University of Delaware in 1988 and his Ph. D. in Chemical Engineering from Princeton University in 1994. In October, 1994, he joined Union Carbide in the polymer materials science group, with responsibility for melt rheology, the area of his doctoral research. Since, 1998, Dr. Wasserman has been a member of the Telecommunications group of Union Carbide's Wire and Cable business. His current work focuses on product development in areas including cellular insulation, fiber optic cable jacketing, and additives fundamentals.

Materials Advances in Next Generation Loose Tube Cables

Brian G. Risch, George Dallas, and Matthew Barber

Alcatel
O.F.C.C.C
P.O. Box 39, Claremont, NC

ABSTRACT:

Properties of materials are compared for a new type of high density, semi-tight buffered, loose tube cable design. An improved class of PVC and a proprietary flexible polyolefin compound are presented that offer advantages over conventional, phthalate based, PVC buffering compounds for high density, flexible loose tube cables. These materials are compared in terms of general mechanical properties, post extrusion shrinkage, coefficient of thermal expansion (CTE), waterblocking gel and fiber coating compatibility, as well as long term reliability.

INTRODUCTION:

Due to increases in demand for high capacity telecommunications systems, access and distribution sections of networks are facing greater space and cost constraints. In order to fit a higher fiber density into existing cable right of ways, new, higher fiber density cables are being developed.^{1,2} With these new cable designs, comes a need for new buffering materials. Proper choice of buffer materials, cable design, and process can lead to cable designs that achieve higher overall fiber density, smaller cable O.D., and reduced cable weight while maintaining good cable mechanical performance and reliability. These new designs require improved materials that optimize cable performance and ensure long-term cable reliability. This paper outlines the physical and mechanical properties of materials that are desirable for high density, flexible buffer tubes.

Flexible PVC buffering compounds offer the advantage that their low modulus results in reduced contact and buckling forces for flexible buffer units as well as reduced chances of damaging optical fibers during access. However, plasticizers in PVC can be leached out of the buffering compound especially in

the presence of filling gels. When the plasticizers are leached from buffering compounds buffer tube modulus increases and buffer tube low temperature performance decreases. Additionally fiber coating reliability can be reduced due to plasticizer migration and a resulting reduction in fiber coating adhesion. In accelerated aging tests phthalate type plasticizers were found to be less extraction resistant from flexible PVC than trimellitate type plasticizers. Furthermore, the type of gel used to fill the buffer tubes was found to strongly influence the extraction effects. Polyolefin or mineral oil based gels were found to have the strongest effect on plasticizer extraction while silicone based gels were found to minimize this effect. Trimellitate plasticized PVC compounds combined with silicone gels were found to offer the best overall reliability for a PVC based flexible buffering material combination.

The flexible polyolefin compounds that are presented in this paper totally eliminate the risk of plasticizer migration because plasticizers are not included in the polymer formulation. These compounds were also found to have a combination of lower CTE, lower post extrusion shrinkage, and lower low temperature modulus than PVC compounds. Essentially, the flexible polyolefin materials were more mechanically stable over the operating range of -40°C to 70° than the flexible PVC compounds. This combination of properties provides a lower risk for low temperature attenuation problems. These polyolefins also contain an antioxidant package that gives them thermo-oxidative stability high enough for a projected lifetime of more than 30 years. With the use of the new buffering materials presented in this paper, high fiber density can be achieved without compromising the high standards of cable reliability that are expected within the industry.

EXPERIMENTAL:

Dry Heat Aging:

Buffer tube samples were wrapped in 3.5" coils for 10 turns and placed in ovens at 150°C, 145°C, 140°C, 135°C, 125°C, 110°C, 105°C, 100°C, and 85°C. The temperature of these ovens was periodically monitored with thermocouples.

Tube Tensile Testing:

Buffer tube tensile testing was determined using a procedure as described in ASTM 348 except that the buffer tubes did not have a gauge section of reduced diameter. A Monsanto model 2000 mechanical tester was used for all tests. A gauge length of 20mm was used with a crosshead speed of 50mm/min.

Tube Shrinkage Determination:

Buffer tube shrinkage tests were carried out according to U.S REA Bulletin 1753F-601 and France Telecom CM-28 in a talc bed. Multiple test temperatures (85°C, 95°C, 100°C, and 115°C) as well as test times (30min., 1hr., and 24hrs.) were used to determine both time and temperature dependence on shrinkage.

Oxidative Induction Time Determination:

Oxidative Induction Time (OIT) determinations were carried out according to ASTM D3895³ except that aluminum sample pans were used instead of copper since copper has been shown to catalyze some degradation reactions in polyolefins resulting in reduced OIT values as well as variability of test results depending on the state of oxidation of the pan's surface.^{4,5, and 6} A TA 910 DSC was used for OIT determination. OIT values were determined at 200°C.

Dynamic Mechanical Thermal Analysis:

Dynamic Mechanical Thermal Analysis (DMTA) scans were produced using a TA Instruments DMA 2980. Temperature sweeps were performed at a constant frequency of 1hz. and a heating rate of 2°C per minute from -150°C to 140°C.

Coefficient of Thermal Expansion:

Coefficient of Thermal Expansion (CTE) measurements were performed using a TA Instruments DMA 2980 in the static force mode. A static load of 0.01N was used. A heating rate of 2°C per minute from -150°C to 140°C was used to produce test results.

Fiber Strip Force Measurement:

Fiber coating strip force measurements before and after aging were measured according to the procedure outlined in Bellcore GR-20. Ten tests were performed on each fiber at each condition and a total of 6 fibers were tested at each condition. The stripping tool was measured after each 6 fibers against a reference fiber to ensure that wear of the stripping tool did not influence test results.

RESULTS:

Figure 1 shows the modulus vs. temperature data obtained from a phthalate plasticized PVC compound, a trimellitate plasticized PVC compound, and a flexible polyolefin compound. The data reveals that the temperature dependence of modulus for the PVC compounds is higher than that for the polyolefins. Although the PVC compounds have a lower room temperature modulus than the polyolefin compound, the low temperature modulus of the polyolefin compound is less. The modulus of the phthalate plasticized PVC varied the most with respect to temperature. As a consequence of the improved temperature stability of modulus for the polyolefin compound, cable properties and reliability will vary less with temperature when this compound is used for buffering.

Figure 1: Modulus vs. Temperature for Flexible Buffering Materials

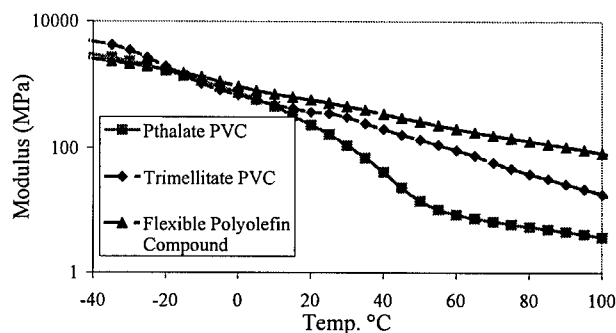


Figure 2 shows CTE vs. temperature for a phthalate plasticized PVC compound, a trimellitate plasticized PVC compound, and a flexible polyolefin compound. The CTE for the flexible polyolefin compound and the trimellitate plasticized PVC compound is reduced relative to phthalate PVC compound which will lead to reduced fiber stress as a function of thermal cycling for a given cable design.

Figure 2: CTE Data for Flexible Buffering Materials

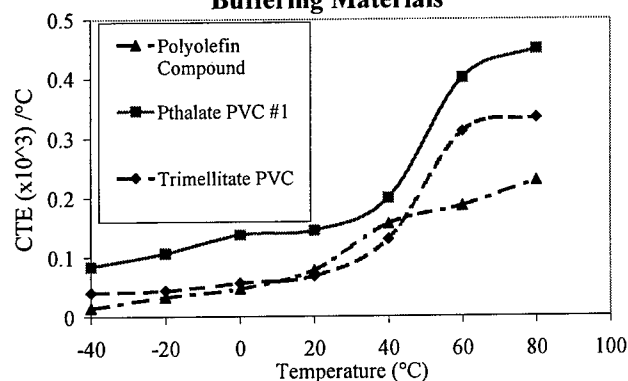


Figure 3 illustrates the post extrusion shrinkage behavior for flexible buffer tubes produced from PVC compounds and the flexible polyolefin compound. The shrinkback of the polyolefin compound is less than 0.5%, ten times less than that of the PVC compounds. Combined with the lower coefficient of thermal expansion for the polyolefin compound, the reduced buffer tube residual orientation (as indicated by reduced shrinkback) results in a more dimensionally stable buffering unit.

Figure 3: Post Extrusion Shrinkback of Flexible Buffering Units: Effect of Material Choice

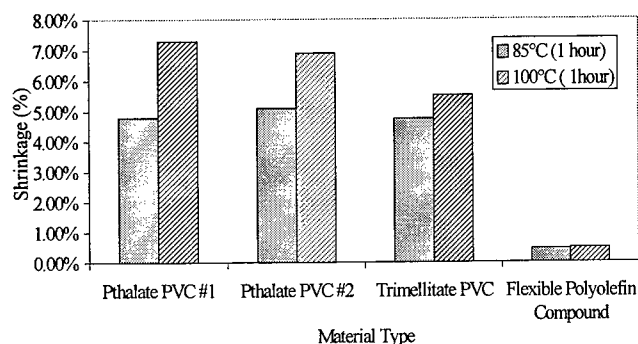


Figure 4 and 5 are comparison plots of initial mechanical properties of flexible buffering materials at room temperature. The two phthalate plasticized PVC compounds show the lowest initial modulus. Phthalate PVC #2 shows a higher break stress and elongation than phthalate PVC #1, and the

trimellitate PVC shows the highest tensile strength, modulus, and stress at 10% elongation of the PVC compounds. The flexible polyolefin material shows the highest modulus, stress at 10% elongation, and ultimate elongation, but because of substantial reduction in strain hardening behavior, this material shows a peak stress comparable with Pthalate PVC #1.

Figure 4: Initial Mechanical Properties of Flexible Buffer Tubes

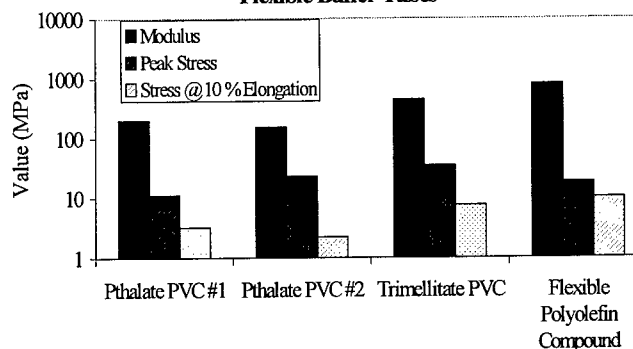
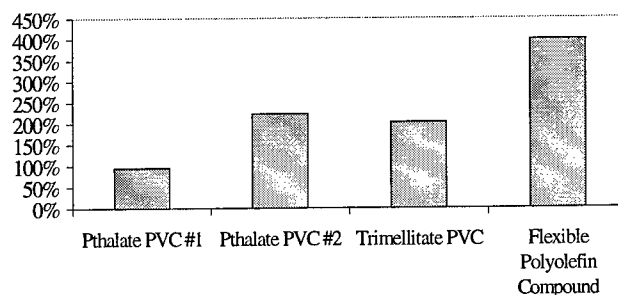


Figure 5: Flexible Buffer Initial Elongation



Figures 6&7 show the effects of aging at two different temperatures on flexible buffer tube materials. Under both aging conditions the phthalate plasticized PVC compounds showed a substantial increase in modulus and decrease in elongation after aging. This effect is due to migration of plasticizer from the compound. Both the trimellitate plasticized PVC compound and the polyolefin compound showed relatively little change in mechanical properties.

Figure 6: Comparison of Flexible Buffering Unit Properties after Aging at 105°C for 45 Days

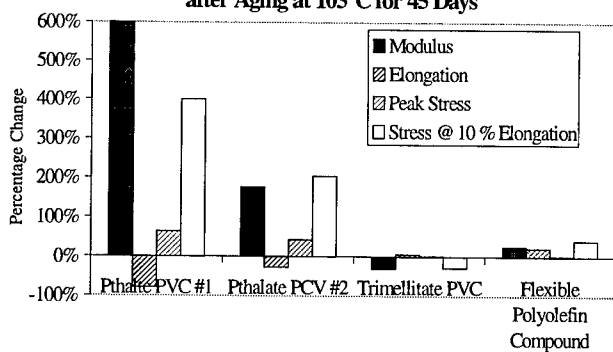
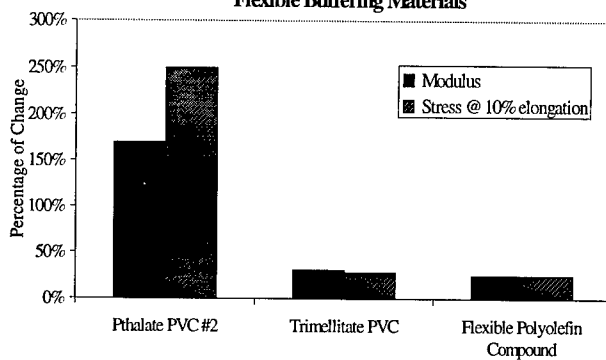


Figure 7: Effect of Aging @ 125 °C for 14 Days on Flexible Buffering Materials



OIT measurements were performed on the flexible polyolefin buffering compound. The OIT value for the compound exceeded 100 minutes. The long term stability of this material should be comparable to the grade of impact modified polypropylene presented in an earlier paper.⁷ Based on data from reliability testing done in this study and that from similar materials in earlier tests, a service lifetime in excess of 30 years can be expected under normal operational conditions.

Figures 8&9 illustrate the effects that gels can have on the aging of phthalate PVC based buffer tubes. The results for aging in the silicone gel were found to be essentially identical to aging results of tubes aged without gels. The explanation for the sharp increase in load at 10% elongation is explained by extraction of the plasticizer from the gel. The presence of plasticizer in the gels was verified by FTIR analysis after the aging tests. The results for change in both elongation and modulus indicate that the polyolefin gel has the poorest compatibility of the gels tested for use with flexible PVC compounds.

Figure 8: Retention of Elongation for Phthalate PVC #2 Aged @ 85°C as a Function of Gel type

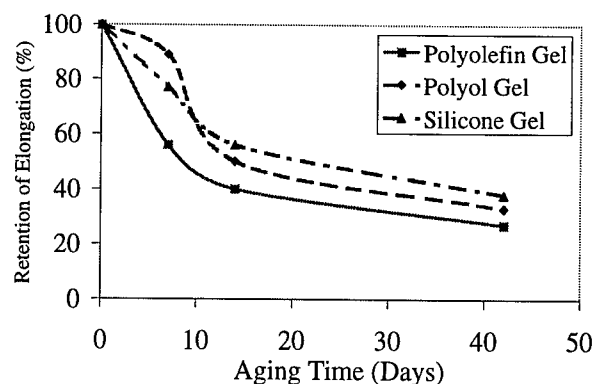
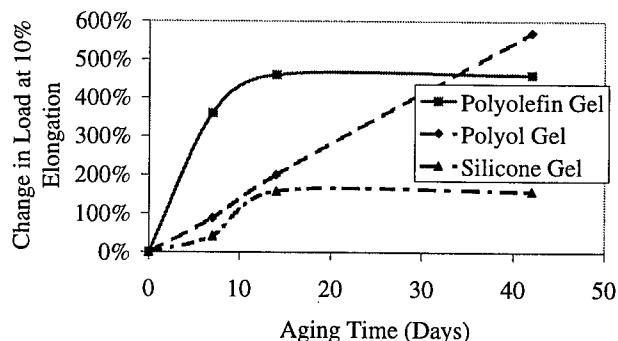


Figure 9: Change in Load at 10% Elongation for Phthalate PVC Tubes Aged in Gel @ 85°C



Due to the fact that aging of the PVC buffer tubes can cause migration of plasticizers to fiber coatings, fiber strip force measurements were performed on aged and unaged fibers. Strip force measurements were recorded after 45 days aging at 110°C and after 6 months at 85°C. Figure 10 illustrates the effect of aging on fiber strip force for PVC and flexible polyolefin buffer tubes aged at 110°C for 45 Days. Figure 11 illustrates the effect of material and gel type for buffer tubes aged at 85°C for 6 months. The trimellitate PVC compound showed less extractability and less of an effect on fiber strip force than the phthalate PVC compound even when the Phthalate PVC buffer tube did not contain gel. PVC compounds tended to show more effects on fiber strip force in gel filled tubes. The choice of gel, however, had no effect on strip force for the polyolefin compound, due to the lack of plasticizer interaction. The slight increase in strip force seen after aging is due to additional thermal

curing of the U.V. coatings that was verified by FTIR analysis.

Figure 10: Change in Strip Force Due to Aging @ 110°C for 45 Days

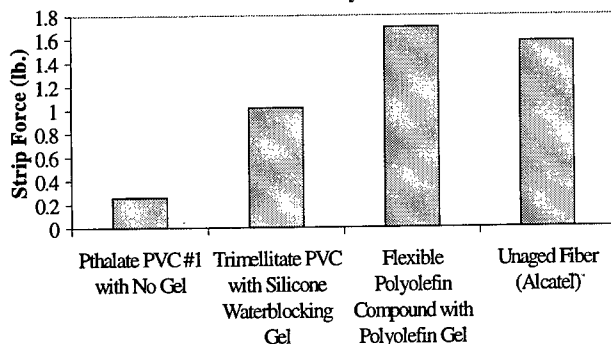
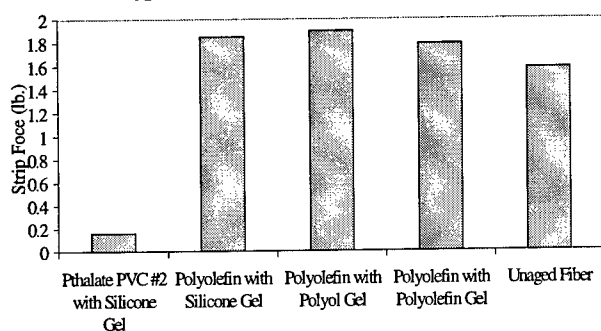


Figure #11: Effect of Flexible Buffering Material and Gel Type on Fiber Strip Force After 6 months @ 85°C



CONCLUSIONS:

The reliability and cable performance of buffer tubes for near-tight buffering applications has been shown to be a strong function of material selection. Phthalate plasticized PVC compounds have been shown to be a poor material choice for near-tight buffered cable designs due to poor low temperature ductility, a relatively high CTE, poor aging performance, poor gel compatibility, and a strong interaction of plasticizers with fiber coating. Additionally, waterblocking gel was shown to have a strong effect on both fiber and buffer tube long-term reliability. Two alternative materials were presented that offered superior performance to phthalate plasticized PVC compounds. An extraction resistant trimellitate PVC compound was found to have a lower CTE than phthalate PVC compounds as well as superior aging performance. A proprietary flexible

polyolefin compound was also presented that totally eliminated the problems associated with plasticizer extraction in PVC compounds while providing superior CTE properties as well as greater temperature stability of modulus.

ACKNOWLEDGEMENTS:

We would like to thank Thierry Auvray and Danny Ammons for assistance in coating strip force measurements and tube tensile testing. We would also like to thank Wayne Cheattle for his assistance on dynamic mechanical testing and CTE measurements.

REFERENCES:

- ¹ Garcia, M., et. al., *Proc. 47th International Wire and Cable Symposium*, 1998, 57-65.
- ² Pastruszka, et. al., *Proc. 48th International Wire and Cable Symposium*, 1999, In Press.
- ³ ASTM Method D 3895, "Test Method for Oxidative Induction Time of Polyolefins by DSC", American Society for Testing and Materials.
- ⁴ Kuck, V.J., *Proc. 6th Intern. Conf. Plastics in Telecomm.* 1992, 3, 1-10.
- ⁵ Patterson, G.H., and Riga, A.T., *Thermochim. Acta*. 1993, **226**, 201-210.
- ⁶ Riga, A.T., *Proc. 20th North Amer. Therm. Anal. Soc., Conf.* 1991, 517-521.
- ⁷ Risch, B.G., Auton, J. and Tatat, O., *Proc. 47th International Wire and Cable Symposium*, 1998, 698-704.

Speaker:



Brian G. Risch
Alcatel OFCCC
2512 Penny Rd.
P.O. Box 39
Claremont, NC 28610

Brian G. Risch is the Materials Technology Manager at Alcatel Telecommunications Optical Fiber Cable Competence Center. He holds a B.A. degree in Physics from Carleton College and a Ph.D. in Materials Science and Engineering from Virginia Polytechnic Institute and State University. His Ph.D. research was in the area of polymer crystallization and structure property relationships in polymers. Directly after he finished his Ph.D. he worked for ORD laboratories in the area of optical polymers developing new polyurethane and polythiourethanes for high performance ophthalmic lens applications. Since 1996 Brian has worked for Alcatel's Optical Fiber Cable Competence Center (OFCCC) in the area of thermoplastic cable materials. His specialization has been in the area of and crystallization behavior and materials reliability for thermoplastic cable materials.

Co-Authors

Matthew Barber is a Project Manager in the Alcatel Optical Fiber Cable Competence Center. He holds B.S. and M.S. degrees in Mechanical Engineering from Virginia Polytechnic Institute and State university.

George Dallas holds a B.S. degree in Chemistry from Hartwick College, an M.S. degree in Chemistry from San Jose State University, and a Ph.D. in Materials Engineering and Science from Virginia Polytechnic Institute and State University. George has 12 years experience in materials research and analysis and compounding and began working in Alcatel's Optical Fiber Cable Competence Center since 1999.

IMPROVED POLYETHYLENE AND EXTRUSION PROCESS FOR HIGH QUALITY SLOTTED CORE PROFILES

Ruth C. Dammert¹, Laila Rogestedt¹, Eeva-Leena Heino², Hans-Bertil Martinsson¹,
Tommi Vainio³ and Jukka Hillberg³

¹⁾ Borealis AB, Stenungsund, Sweden, ²⁾ Borealis Polymers Oy, Porvoo, Finland,
³⁾ Nextrom Oy, Vantaa, Finland

ABSTRACT

A polyethylene resin, intended for slotted core profiles, must meet several requirements, i.e. exhibit good melt processability, dimensional stability, mechanical properties, low shrinkage and smooth surface. A bimodal high density polyethylene (HDPE) was studied in this paper. The slotted core profiles were produced using a crosshead based on rotating die technology. Uniform air cooling with correct cooling gradient was found to give a good dimensional stability of the profile. A material suitable for slotted core profiles must possess a pronounced shear thinning behavior. With optical microscopy it was possible to identify the area where the most of the built in stresses are located. Dimensional variations in axial, radial and tangential directions of the slotted core profile were measured with thermomechanical analysis (TMA). The coefficient of linear thermal expansion (CLTE) was determined by TMA, as well.

In the bimodal HDPE, described in this study, a good balance between properties of importance for slotted core elements has been obtained.

INTRODUCTION

New optical access network cables represent a new challenge for slotted core extrusion. The requirements of the slotted core elements are very tight. This puts severe demands on the materials used in these elements. The primary

materials used for slotted core element extrusion are high density polyethylene (HDPE) and polypropylene (PP).

The polymer material in slotted core elements should, in molten stage, exhibit a good melt processability, but also a good dimensional stability to keep the slotted profile shape stable, i.e. the ridges of the slotted core do not collapse even at high extrusion line speeds. The material should own good mechanical properties at solid state. Low shrinkage during cooling is one of the key properties, as well. Moreover, the surface of the slotted core element must be smooth.

The dimensional stability of the plastic material used is of main importance in fiber optical cables. Plastic materials have in general much higher thermal expansivity than glass, which can cause heavy stresses on the brittle glass fibers. Depending on the level of the stresses, the effect can be microbends of the glass fibers which can cause signal attenuation of the cable. In severe cases the fiber can even break. In addition to dimensional changes from the thermal expansivity of the material, built in stresses from the processing of the cable can cause permanent deformations of the profile.

When a plastic material is processed into a complicated shape, like in a slotted core profile, the risk to introduce stresses into the material is quite high. These stresses can later on be released, when the cable is exposed to higher temperatures during its service life. Release of stresses can cause permanent deformation of the cable.

An HDPE, presented in this paper, is based on the new technology for bimodal polyethylene, Borstar™, developed by Borealis (Borstar is a trade mark of Borealis A/S, Denmark). A bimodal process provides the possibilities to tailor-make materials due to its multi reactor system. An optimized molecular weight as well as comonomer distribution can be obtained in each reactor.

Slotted core extrusion process optimization deals with finding the optimum balance between melt temperature profile in the extruder and crosshead, tool design, processing rate, cooling characteristics, and the rheological properties of the resin(s). In this work a crosshead based on rotating die technology was used to produce the slotted core element. This rotating die method makes it possible to manufacture both helical and SZ slotted cores with the same machinery. The process is a one pass tandemized process consisting of a round prelayer extrusion over the strength member combined with the main profile extrusion with the rotating die. Primary attention was paid to the profile extrusion step. It is essential to use the rotating die equipped with a position control algorithm with feedback option from measuring devices to achieve accurate slotted core trace. This will enable reliable and trouble-free ribbon assembly in the next step. In addition, it was found that uniform cooling with correct cooling gradient guaranteed the dimensional stability of the profile. For this purpose controlled air cooling has been used successfully. Optimized mass distribution and homogeneous flow conditions in the crosshead enable low melt temperatures with good surface quality.

By the choice of optimized process parameters for the slotted core element and the right material the processability, the built in stresses and the dimensional stability of the profile can be controlled.

SLOTTED CORE ELEMENT PROCESS

New optical access network cables represent a new challenge for slotted core extrusion. Large feeder area cables have extended slotted core diameters to up to 25 mm, and distribution aerial cables require low pitch SZ slotted core elements with accurate trace control. Nextrom's slotted core extrusion line incorporates a new rotating crosshead to manufacture both helical and SZ

slotted core elements (\varnothing 6...25 mm) with the same machinery. The inertia of rotating mass can be kept minimal, which makes rapid reversing of rotation (SZ-operation) and the control of rotation easier than in the RCM method (rotating central member). The rotation trace of the die can be expressed as parameters of mathematical functions as well as a combination of two different functions. In free-form trace mode, the user can program the rotation trace with 64 XY-points over each lay length.

A typical two-step, one pass slotted core element extrusion line configuration is presented in figure 1.

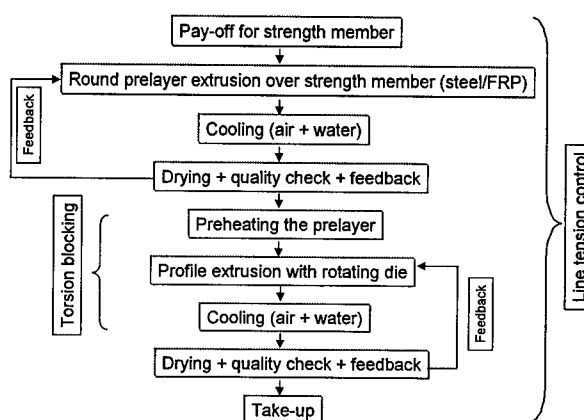


Figure 1. Description of the slotted core extrusion process with tandemized prelayer extrusion.

Two extrusion groups are needed for larger element diameters (typically $> \varnothing$ 8...10 mm) because extrusion in one single step would lead to biased profile geometry due to cooling problems and inhomogeneous crystallization of thick wall which could cause warping. The extruder sizes in the prelayer extrusion group are typically \varnothing 30 mm and \varnothing 60 mm for adhesive and prelayer, respectively. In the profile extrusion group the extruders are usually \varnothing 20 mm and \varnothing 80 mm for color striping and profile extrusion, respectively. The adhesive material to attach the plastic to the steel wire or rope is typically a polyolefin-based copolymer which contains functional polar groups.

The important process characteristics of the extrusion line performance for slotted core element are:

- tension control
- adhesion of plastic to steel wire
- adhesion between different plastic layers

- torsion blocking of the filler element (in SZ mode)
- die and mass distribution design
- low friction sealing of the rotating die in the crosshead
- rotation control of the rotating die
- cooling for optimum adhesion, profile stability, and line speed

Most of these requirements deal not only with machine design but also with process know-how and material knowledge.

Air cooling

An air-cooling unit, equipped with inverter controlled double stage axial fans, provides a maximum air speed of 40 m/s at the cooling channel. This unit was specially developed to ensure a uniform cooling environment for the slotted core profile. It can also be used for large size pre-layer cooling to minimize the jacketing tear-off from the steel wire or fiber reinforced plastic (FRP). Variations in air velocity and/or air temperature can be employed to alter the heat transfer rate to provide optimal relaxation conditions for the plastic and stable dimensions of the profile. Cooling characteristics have a pronounced effect on the adhesion of the plastic to the prelayer and to the dimensional stability of the slotted core profile.

EXPERIMENTAL

Materials

A bimodal polyethylene (PE) resin, designed as BIMO, was studied. A commercial unimodal grade (UNI), used in slotted core profiles, was included for comparison. The basic data, including mechanical properties, on the materials used in the study is found in table 1. The bimodal grade is an HDPE. The unimodal grade is a blend of a unimodal high density and a low density polyethylene (LDPE). Higher densities are usually preferred since they provide stiffness to the material.

Table 1. Data on materials used.

	Unit	BIMO	UNI
MFR ₅	g/10 min	0.4	1.1
Density	kg/m ³	946	928
Elongation at break	%	753	1091
Stress at break	MPa	39.2	23.1
Young's modulus	MPa	1018	574

Mechanical properties were measured in a tensile tester at 50 mm/min according to ISO 527/5A. Samples were taken from compression molded plaques. The molding was performed according to ISO 1827-2-B at 200°C. The same sample type was used for Young's modulus.

Characterization of the materials

Molecular weight distributions (MWD) were determined with Waters 150C GPC in 1,2,4-trichlorobenzene (TCB) at 135°C.

Capillary rheometer measurements were made on Göttfert Rheograph at 190°C. A round hole die with L/D ratio of 30/1 was used. Because of high L/D ratio no Bagley correction was made. Viscosity measurements were carried out at shear rates from 10 - 5000 1/s, but the appearance of melt fracture limits the range, so that the highest useful rates lie between 100 - 550 1/s depending on the material.

Dynamic measurements were performed on Rheometrics RDA II at 190°C under nitrogen atmosphere using a plate and plate test fixture with a diameter of 25 mm. The frequency range was 0.01 - 500 rad/s.

An Exstar 6100 TMA (Seiko Instruments) was used for the thermal expansivity measurements. The coefficient of linear thermal expansion (CLTE) was measured on pressed plaques (3 mm thick) in an helium atmosphere (150 ml/min) and with liquid nitrogen cooling. Circular samples of 5 mm diameter were punched out of the plaques and placed in the TMA instrument. A 3 mm circular, flat ended, quartz probe was used during the measurements. The heating rate was 2.5°C/min and a load of 5 grams was applied to the samples. The experiments were run in three cycles, heating-cooling-heating, between -20°C and +50°C, all with the same heating/cooling rate. The data was taken during the second heating cycle to eliminate the thermal memory of the samples. The data presented is the average of two measurements. The CLTE was calculated as the "local CLTE", that is the derivative of the length change to the temperature divided by the initial sample length at each temperature.

Characterization of the slotted core profiles

Optical microscope pictures were taken in a Nikon SMZ-U with a polarizer at a magnification of approximately 9 times. Thin cuts, 100 µm, were prepared by slicing in a microtome (Leica Polycut E). To prevent the shape of the profile to

collapse during slicing, the profile was molded into a solid shape using a hard (cold cured) molding compound. All samples were taken at the same position in the profile (at the turning point).

The same TMA instrument as described above was also used for the dimensional studies of the slotted core profile. Slices from the profile was cut with a scalpel in the radial, the tangential and the axial (machine) direction. The samples had the size of the ridges of the profile and the approximate thickness of 1.3 mm. A circular, flat ended, 1 mm quartz probe was used in this case (due to the smaller samples). The applied load was reduced to 1 gram and the heating rate was increased to 10°C/min. To follow the absolute dimensional change during a temperature cycle, the temperature interval was extended to -40°C to +60°C.

A scanning electron microscope (Jeol JSM-840) was used to study the surface finish of the slotted core profile.

Process conditions

The experimental set-up of the test runs is listed in table 2.

Table 2. Process conditions of the test runs.

Product characteristics	SZ slotted core element
Outer diameter (mm)	10
Number of slots (-)	5
Strength member material	Stainless steel
Diameter of strength member (mm)	2.3
Diameter after 1 st extrusion group (mm)	4.95
Slot width (bottom/top) (mm)	2.4/2.7
Slot depth (mm)	2.3
Process values	
Line speed (m/min)	15
Operation mode	SZ sine wave
Lay length (mm)	150
Rotation angle (°)	290
Line tension (N)	900
Melt temperature (°C)	180
Air cooling temperature (°C)	20
Water cooling temperature (°C)	60...20

Before entering to the rotating crosshead the prelayer was cooled down to about 45 °C. The experimental study concentrated only to the slotted core profile extrusion.

RESULTS

Cross-section profiles

The cross-section profiles of the SZ slotted core elements prepared with BIMO and UNI are shown in figure 2, appendix 1. The bimodal grade gave better shape of the profile both on the helical part and at SZ reversal point.

Dimensional stability

Figure 3 (appendix 1) shows the appearance of slices of the profile of different materials under polarized light in a microscope. Color patterns is an indication of stress in the material. Both the bimodal material (BIMO) and the unimodal reference (UNI) seem to have quite low stress level. The local stresses are mainly located at the thin areas at the inner of the slots. The stress seen in connection to the stripes is most probably an effect of the sample preparation. Two other materials studied as references, with low and high stress levels, respectively, are also presented. The material parameters that control the stress level are mainly the molecular weight and the molecular weight distribution. These do also control the rheological behavior of the material and tend to work contradictory. Finding the optimal parameters is consequently of main importance for the overall performance of the material. Except for the material parameters, the processing conditions will also play an important role for the stress level of the material.

Coefficient of linear thermal expansion

CLTE as a function of temperature is presented in figure 4. Data was taken between -15°C and +50°C. As can be seen the CLTE is both temperature and density dependent. Due to its higher density, the bimodal material, BIMO, has a lower expansivity than the unimodal reference, UNI. This is a positive aspect, since dimensional stability, as mentioned earlier, is very important in fiber optical cables. The data presented correlate well with literature data on expansivity.¹

The CLTE is a material property which determines the expansivity of the material. In a processed plastic article, the expansivity is determined by both the inherent expansivity of the material and the expansivity due to residual stresses from the fabrication process.

Residual stresses can give positive (expansion) and negative (shrinkage) permanent deformation. Compressive stresses give an expansion whereas tensile stresses give shrinkage.

Shrinkage is often seen in highly oriented material, e.g. in article produced with a high extrusion rate or with high draw down ratios.

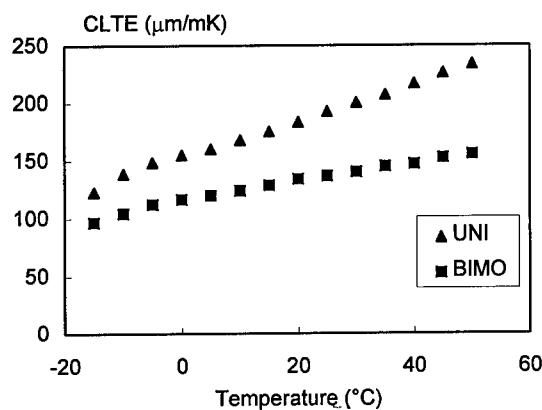


Figure 4. CLTE as a function of temperature.

Built in stresses

Figure 5 shows the TMA curves for a three cycle run between -40°C and $+60^{\circ}\text{C}$ (heating - cooling - heating). The dimension change in relation to the initial sample thickness (TMA %) is plotted against the temperature. This gives the total dimension change of an article during the heating cycles. During the first heating cycle built in stresses can be released, which will cause a dimension change overlaid on the inherent expansivity of the material. If the stresses are released the following cooling and heating cycles will only depend on the inherent expansivity of the material and consequently following similar curves in the TMA plot. Figure 5 shows an example of this in tangential direction of the slotted core profile of BIMO. The total expansion of the material in this direction, when cycling between -40°C and $+60^{\circ}\text{C}$, is in the order of 3 %. The sudden increase in expansion after 40°C represents release of some compressive stresses with a permanent positive expansion around 1.5 %. In this study, the permanent deformation was found to be almost negligible in the axial direction and a small permanent expansion in the radial direction. Overall, the stresses built in was quite small in this profile studied which can partly be explained by the mild processing conditions. Higher line speeds can give some permanent shrinkage.

With this technique dimensional stability of a profile during cooling and heating can be studied. It gives an picture of the shrinkage/expansion potential of the profile in different directions and

can be useful to predict the performance in big scale. The absolute value of the permanent deformation is just approximate due to the small sample size. In addition, in a real cable the total dimension change is also affected by the overall construction.

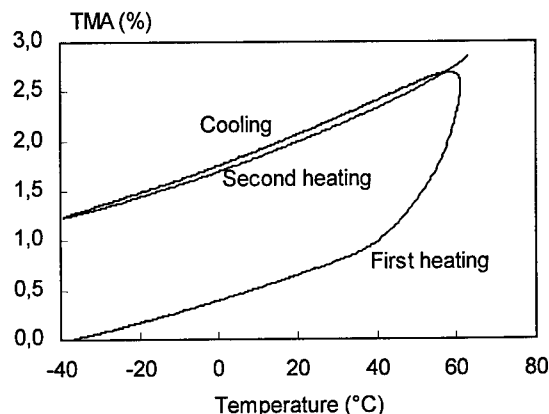


Figure 5. TMA curves for a three cycle run between -40°C and $+60^{\circ}\text{C}$ (heating - cooling - heating) for BIMO.

Surface finish

To avoid wear or damage of the brittle glass fibers, the surface finish of the slotted core profile must be of as good quality as possible. We have studied the surface finish in an electron microscope (Jeol JSM-840). In figure 6 (appendix 2), micrographs of the surface of the ridges of the profiles are presented at a magnification of X20. It is clearly seen that the surface quality is better in the bimodal sample, BIMO, compared to the reference, unimodal.

DISCUSSION

Molecular weight distributions of the materials are compared in figure 7. A much broader MWD of bimodal polymer compared to unimodal resin UNI is clearly seen.

Dynamic measurements give complex viscosity (η^*) as a function of frequency (ω). According to Cox-Merz rule the complex viscosity function, $\eta^*(\omega)$, is same as the conventional viscosity function, $\eta(\dot{\gamma})$, if frequency is taken in rad/s. The validity of the above rule is seen in figure 8 where $\eta^*(\omega)$ from dynamic and $\eta(\dot{\gamma})$ from capillary measurements have been put into the same figure. Dynamic measurements give information about viscous behavior at low shear rates from

0.01 to 500 1/s while the useful range of capillary results is from 10 to 500 1/s.

Bimodal polymer BIMO owns relatively high viscosity and pronounced shear thinning (figure 8), which comes from high molecular weight and broad molecular weight distribution (figure 7). In spite of narrow MWD also UNI shows high shear sensitivity. This is due to long chain branching given by the LDPE in the blend.

The point where melt fracture was in capillary measurements first observed has been marked into figure 8. This gives an information about possible roughness in the extrusion process. In spite of lower viscosity UNI exhibits melt fracture at lower shear rates compared to BIMO.

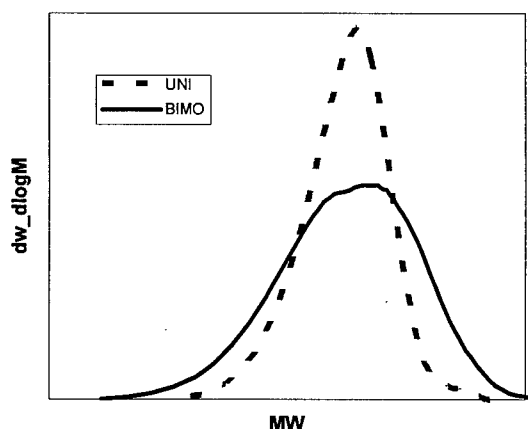


Figure 7. GPC curves of BIMO and UNI.

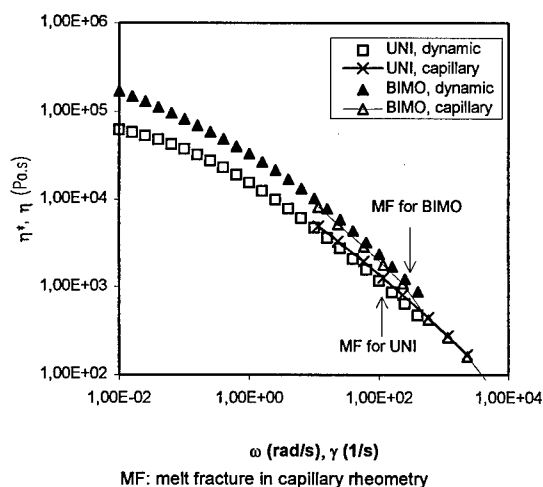


Figure 8. Viscosity functions of BIMO and UNI.

CONCLUSIONS

A bimodal HDPE has been studied in the present paper. Viscosity measurements, both capillary and dynamic, have been carried out. It was observed that the material suitable for this application should exhibit high melt strength to avoid deformation after die exit. On the other hand, it should have good flowability without melt fracture tendency at processing shear rates. To get a good balance of the above mentioned properties, it was found that the material must possess a pronounced shear thinning behavior, which means high viscosity at low shear rates but low enough viscosity at high shear rates.

The process optimization of the slotted core profile deals with finding the best possible balance between melt temperature, tool design, line speed, and cooling. It was found that uniform cooling with correct cooling gradient guaranteed the dimensional stability of the profile.

Different analytical techniques have been used to study the dimensional stability of the slotted core profile during heat cycling. Optical microscope, with polarized light, is a tool for studying the overall stress distribution in the profile. Careful sample preparation is essential to separate true stresses from stresses introduced during the preparation procedure. The samples used in this study, BIMO and UNI, showed quite low stress level, although not completely stressfree.

TMA was proven to be useful to study both the inherent expansivity of the material, determined as the CLTE, and the permanent deformation due to built in stresses from the fabrication process. In this case the built in stresses was quite low. The bimodal sample, BIMO, has a lower inherent expansivity than the unimodal reference, UNI, due to its higher density.

In the bimodal HDPE, described in this study, a good balance between properties of importance for slotted core elements has been obtained.

REFERENCES

1. Encyclopedia of Polymer Science, Wiley, 2nd ed., Vol 16, p.737.

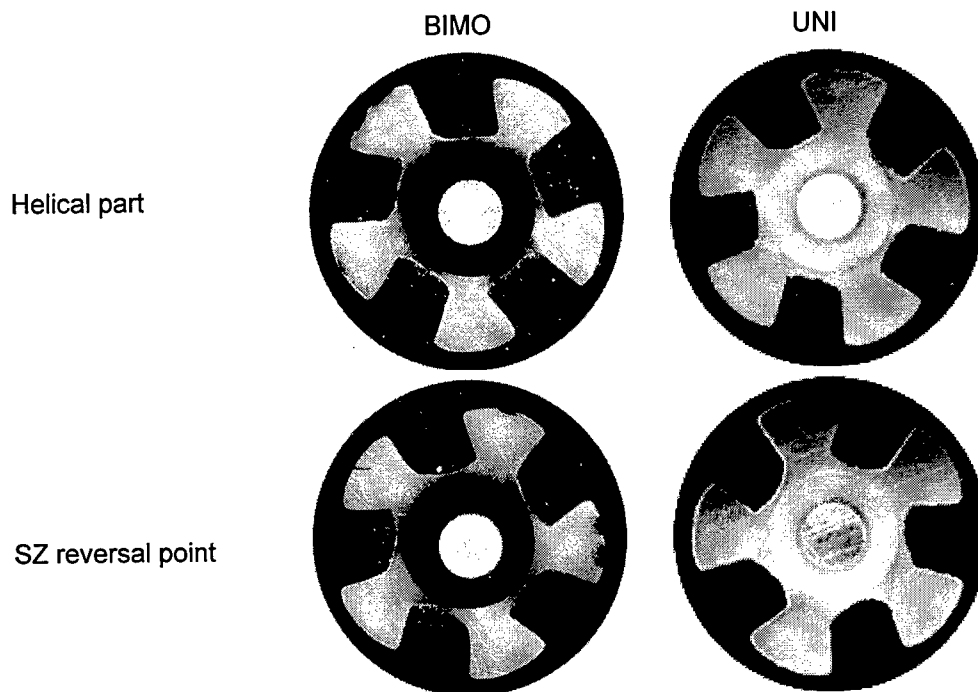


Figure 2. Micrographs of the cross-sections of the SZ slotted cores.

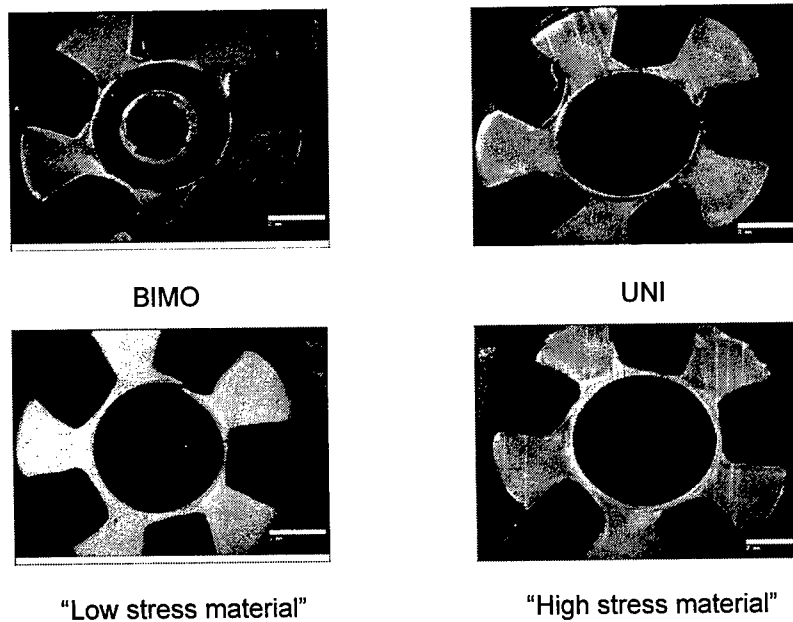
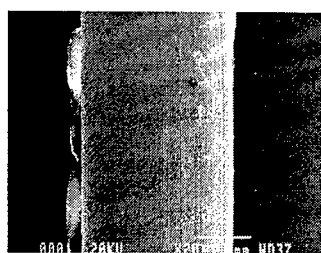
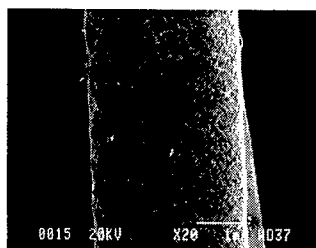


Figure 3. Micrographs (polarized light) showing the built in stresses of the profiles.



BIMO



UNI

Figure 6. Micrographs (electron microscopy) of the surface of the ridges of the profiles.

PRESENTING AUTHOR



Ruth C. Dammert
Borealis AB
S-444 86 Stenungsund
Sweden

Ruth Dammert received her M.Sc. degree in organic chemistry from University of Helsinki, Finland, in 1986. After research work at Sandoz A.G., Basle, Switzerland, and at University of Zürich, Switzerland and at University of Helsinki, Finland, she joined Borealis (Neste at that time) in 1989 and has since then mainly been involved in the development of materials for cable applications.

FIBERGLASS REINFORCED AERIAL SERVICE WIRE: MATERIALS INVESTIGATION and FAILURE ANALYSIS

Osman S. Gebizlioglu, Kenneth W. Moyers, Trevor N. Bowmer

Telcordia Technologies
Morristown, New Jersey 07960

INTRODUCTION

ABSTRACT

Fiberglass reinforced aerial service wire (FRASW) has been widely used in telecommunications applications where metallic (steel) based F-type drop wires were used previously. Although FRASW products have transmission performance advantages, their sag behavior under heavy ice loading during the late winter storms of 1996 has raised concern on their overall reliability. An investigation of the FRASW mechanical performance was conducted to identify product and material properties that are critical to minimizing sag under ice loading. This investigation included tensile load tests conducted on long FRASW samples, mechanical analyses of samples deformed under these tensile loads, and materials analyses of the FRASW components. A detailed account of the tensile load tests is presented in a companion paper authored by L.M. Slavin¹ et.al and published in this proceedings volume. In this manuscript, we present our results of failure analyses and materials studies to show that FRASW products develop kinks that consist of buckled copper conductors under the retractile force exerted by the wire jacket upon unloading of the service wire. The results of the entire study formed the basis for improved product performance requirements in the Telcordia generic requirements document GR-1069-CORE issued in December 1998.

Fiber glass reinforced aerial service wire has replaced steel-based F-type drop wire due to its lightweight and improved transmission performance. However, FRASW products exhibited excessive sag under ice loading during winter storms of 1996 in the Northeastern United States. Heavy ice build-up and wet snow deposited on aerial service wires over extended durations caused excessive sagging and led to hazardous conditions where sagging service wires interfered with traffic and snow plows. Most of the affected service lines were of the fiberglass-reinforced type. Field observations suggested that substantial wire stretch/creep and inadequate installation practices were most likely contributors to excessive sagging under load. These observations further indicated that the FRASW mechanical characteristics need to be better defined and understood, especially under extended and repeated loading conditions. Thus, we performed a detailed investigation on the mechanical response of the FRASW product to a range of loading scenarios. In this paper, we present the results of failure analyses on FRASW products that were subjected to "long gauge-length" tensile loads at Telcordia's outdoor test facility in Chester, New Jersey. A companion paper in this volume presents detailed results of these tensile tests, full-scale simulations, and their comparisons.¹

MATERIALS and PHYSICAL DESIGN ANALYSIS

The long gauge-length testing program was aimed at quantifying the behavior of the composite FRASW product that consists of the following component parts: fiberglass strength members, PVC jacket, and insulated copper wires. However, in order to understand the observations and results, it is essential to investigate the individual materials, construction, and physical relationship of the components within the completed FRASW product as well as to perform post-mortem analyses of tested samples.

Product Design

Figure 1 depicts a schematic cross-section of the FRASW product, including significant geometrical parameters. This schematic diagram also indicates the location of the fiberglass reinforcement bundles and shows that they may be of various geometrical configurations: circular (C), elliptical (E), or "butterfly" (B). The shape of the fiberglass bundles, in combination with the specific dimensions, determines the cross-sectional area and circumference which directly relates to the tensile strength and interfacial strength associated with the jacket and reinforcement.

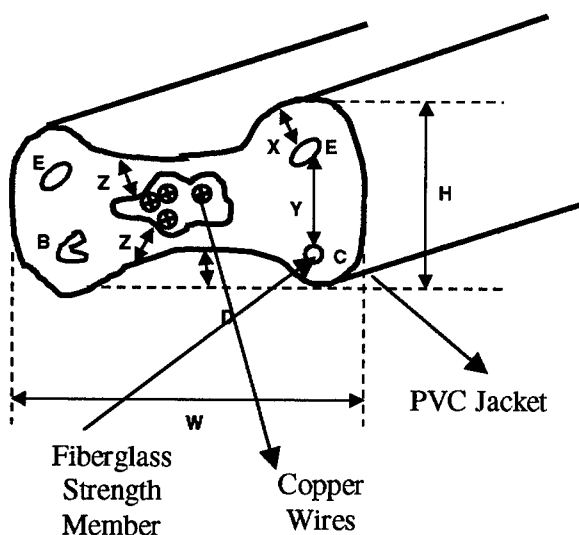


Figure 1. Geometrical Parameters of the FRASW Cross-section

The results of a corresponding survey of various FRASW products with regard to the physical cross-sectional characteristics are provided in Table 1. In particular, the information on fiberglass should prove useful about the ability to withstand tensile loads and transfer shear forces from the clamp through the PVC jacket to the fiberglass strength members. Thus, it is worth noting that the product with the minimum cross-sectional area ("W-C") also displayed the greatest vulnerability in the strength tests of the long gauge-length test program as demonstrated by the FRASW breakage at the 365-lb load.

An important segment of the strength testing program described in the companion paper involved repeated loading tests where test samples of the long gauge-length tests were subjected to cyclic loading in contrast to the constant load "product" test requirement in the existing generic requirements TR-1069. The rate of failures in the case of repeated loading was higher. Although the difference in the failure rates is not significant, the trends suggest the advisability of incorporating and maintaining a cyclic loading test in GR-1069 for both the "product" and "qualification" tests. The apparent weakening of the FRASW products due to the unloading/loading cycles is consistent with earlier Telcordia experiences where samples of FRASW returned from the field, following previous usage and exposure to heavy storm loadings, had considerably greater difficulty passing the TR-1069 qualification test than new product for which the tests had originally been intended.

Post-Mortem Analyses

Post-mortem analyses of tested products, including visual examination of test wire "cross-sections" and clamp sections, yield useful information and allow us to relate observed mechanical response of the wire and its potential vulnerability to storm loads.

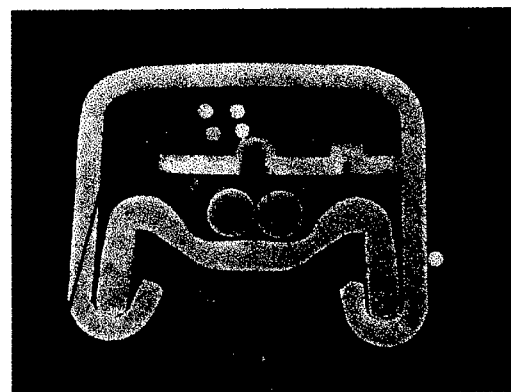
Figure 2 illustrates a cutaway view of a clamp cross-section following the strength and loading test and shows the transverse compression and

lateral extrusion of the FRASW jacket resulting in the PVC jacket tending to fill the available width of the clamp. This effect is accompanied by a corresponding reduction in the wire thickness, allowing the wedge movement that takes up the slack and leading to the observed clamp deflection.

The thinning of the jacket may potentially lead to the development of a short circuit between the clamp shim or shell and the copper wires as pointed out in Figure 2. Such electrical failures correspond to a dielectric strength breakdown, as occasionally experienced during the strength and elongation load testing program. The micrograph also shows the typical non-symmetrical position of the shim and FRASW within the clamp, resulting in a large PVC jacket extrusion to one side of the clamp, and possible uneven retention of the fiberglass strength members and reduced FRASW strength under tensile loading.

Table 2 indicates several other clamp-related failures such as clamp breakage or wire slippage through the clamp. This is particularly true for the 6-pair FRASW product/system, for which 2 out of 3 samples (using several different wire and clamp supplier products) exhibited such problems. These results -- and consideration of the overall importance of the clamp in the FRASW system -- emphasize the need for appropriate generic requirements controlling this important hardware item, as well as clarification of mechanical testing details in GR-1069 and appropriate field installation information. The present generic requirements document, TR-TSY-000267, *Drop Wire Clamp for Single Pair Aerial Service Wire*, Issue 1, July 1986, does not apply to the multi-pair FRASW type product.

Special analytical laboratory techniques will allow a detailed understanding of the local gripping stresses that develop between the clamp and FRASW. Such techniques are currently under development by Telcordia and would yield information that is required to define generic requirements for clamp and/or wire products.



PVC jacket extruded to side

Perforated shim contacting conductor

Figure 2. Clamp Cross-section

The present test program revealed a potentially serious issue related to the wire response after the removal of large tensile loads such as severe winter storm loads due to ice build-up and/or wet snow deposits, and/or temporary removal of the drop from the support hook(s). The appearance of small kinks or bulges in the wire, at approximately 1-foot intervals, often followed the removal of the load to the 40-lb. pre-load level. This effect became significantly pronounced upon the total load removal to perform the dielectric strength test, thereby raising serious concern about the re-use of existing drops that may have been subjected to high loads. Such an effect could correspond to the re-sagging of an existing drop in order to remove the increase in sag following a severe storm. The bulging phenomenon is due to the permanent (plastic) elongation of the copper wires within the PVC jacket, which, upon release of the load, is subjected to a compression imposed by the retracting fiberglass-reinforced PVC jacket. This compression (retraction of the reinforced jacket) causes the wires to buckle and form local kinks within the relatively loose fitting sheath along the FRASW. The wire bulging effect is illustrated in Figures 3 through 5.

Figure 3 illustrates a local bulge caused by the elastic recovery of the fiberglass-reinforced PVC jacket in a previously stretched copper wire.

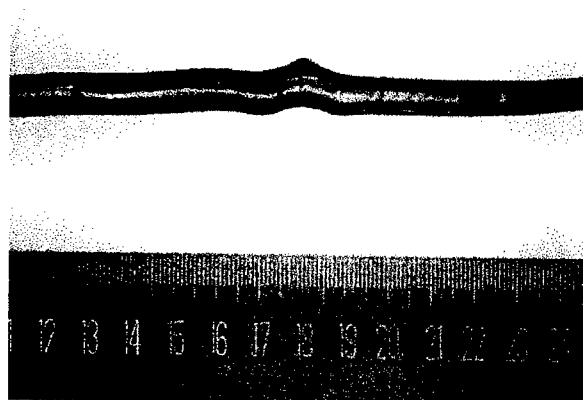


Figure 3. FRASW Bulging Due to Internal Copper Wires

Figure 4 shows a highly magnified cutaway cross-section clearly showing the copper wires pushing against the inside of the jacket, creating a large void.

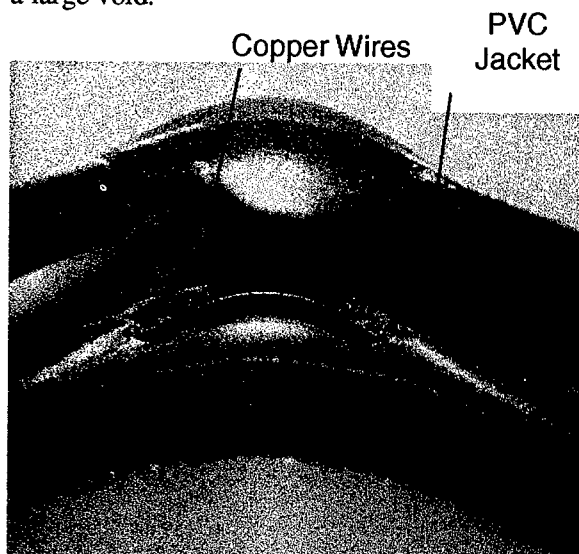


Figure 4. Copper Wires Pushing Through FRASW Jacket

Figure 5 vividly shows insulated copper wires penetrating the jacket of a FRASW sample previously subjected to a severe (breaking) tensile load, in excess of the load levels deployed in the present test program. However, similar effects have also been seen during the present strength and elongation tests; for instance, a relatively thin-walled product (with a small dimension "z" in Fig. 1 and Table 1) is

expected to be particularly susceptible to this bulging/kinking effect.

As discussed earlier, such effects must be carefully considered before a re-sagging scheme is implemented in the field. In particular, extensive field testing, including simulations are recommended to support an effective and reliable installation practice. For example, it is possible that the effect of Aeolian vibration or cable gallop may lead to subsequent penetration of the jacket after bulges have been initiated during a storm condition. At that point, deterioration of the conductors would accelerate due to direct exposure to the environment (e.g., rain, insects).

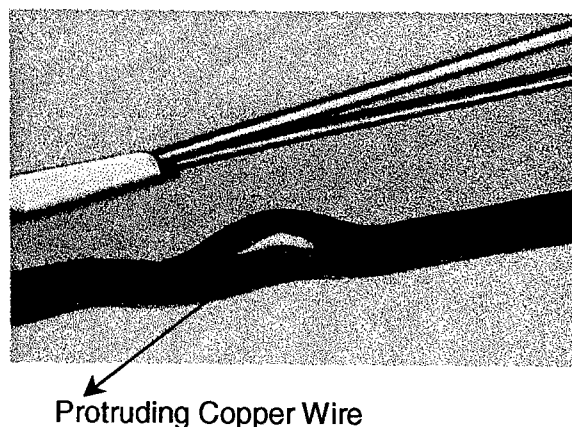


Figure 5. Copper Wires Penetrating Jacket

Table 3 summarizes the presence of the bulging effect as recorded for some of the samples that have undergone the long gauge-length strength and elongation testing or have been used for the full-scale simulations. The extent of the effect is qualitatively indicated as "mild", "moderate" or "severe" depending upon observations made following the completion of the testing program and complete removal of the load. It should be noted that the absence of any comment in Table 3 is not an indication of the absence of the bulging effect, but merely the lack of availability of the information for that sample. It is apparent that the effect is present in both the 2-pair and 6-pair configurations. For 2-pair or quad FRASW, the applied loads were in the range of 335 - 365 lbs. for the long gauge-length tests and on the order of 200 - 250 lbs for the full-scale simulations. For 6-pair FRASW, the

corresponding loads were in the range of 470 - 500 lbs for the long gauge-length tests and on the order of 250 - 350 lbs for full-scale simulations.

The Role of Thermal Expansion

In general, thermal expansion (or contraction) does not have a major effect upon the sag of the FRASW under practical field conditions. The relatively large elongation characteristics of the wire and clamp system under tension due to storm loads will tend to dominate the effects associated with realistic temperature fluctuations. Nonetheless, longitudinal thermal expansion of the wire should be considered as part of the overall product behavior and be reflected in the predictive model¹ and specified as well in generic requirements.

Previous investigations have assumed that the effective coefficient of thermal expansion (CTE) of the FRASW composite is essentially that of the reinforcing strength member. For instance, the fiberglass reinforcing member is reported to have a CTE of approximately 7×10^{-6} in./in./°C.³ We also attempted to directly measure the effective CTE of an inch-long FRASW sample by using the ASTM D696 test method in our laboratory. However, the results indicate a magnitude (14×10^{-6} in./in./°C mean, with 5×10^{-6} in./in./°C standard deviation) that is significantly greater than that reported for the fiberglass member. It is believed that the use of a short sample of such a composite product may not be appropriate for determining the overall thermal expansion properties. In a short sample, the individual elements (e.g., fiberglass, copper wires, and PVC jacket) will not act in unison, in contrast to a long FRASW sample in a field installation where the individual elements, away from clamps, would tend to elongate together. Thus, the measured CTE in the laboratory test may be dominated by the response of the local element in contact with the probe. If the ends of the sample could be effectively fixed so all elements act together, this problem might be alleviated. Furthermore, there is an absence of tension in the sample initially. When heated, there should be some low-level induced tension

in the fiberglass due to the greater thermal expansion of the PVC and copper elements. Thus, the initially relaxed fiberglass may have too large a slack to significantly restrain the complete FRASW assembly, even if all the individual elements were acting in unison. In field applications, the wire has an initial load (e.g., 40 lbs.) increasing to possibly 200 - 300 lbs. or greater under storm conditions. In this case, the initial slack in the fiberglass would be less of a factor, and it would be anticipated that the fiberglass would then more effectively restrain and control the overall expansion of the FRASW composite, consistent with previous assumptions.

Appropriate techniques for measuring the effective CTE for the composite FRASW product, under conditions representative of field application, are currently under development by Telcordia. Thus, at present it is considered judicious not to provide a specified quantitative limit in GR-1069 for the CTE that may not be readily verified by an existing test procedure. In the future, when the testing issues discussed above are resolved with respect to the composite FRASW product, appropriate quantitative requirements and/or objectives may be specified.

SUMMARY & CONCLUSIONS

In this paper, we presented the results of failure analyses and materials investigations, which were conducted as part of a detailed characterization study of fiberglass reinforced aerial service wire (FRASW). This characterization study was performed to better understand the thermo-mechanical behavior of this widely used product, particularly, in winter storm conditions. Thus, this study consisted of extensive mechanical testing and analysis of wire samples from a variety of suppliers. The failure analysis program presented in this manuscript included microscopy of the test samples from the long gauge-length testing in which relatively long lengths -- approximately 125 in. (310 cm) between clamps -- of FRASW were subjected to static tensile loads applied by weights suspended from the wire. The test procedure adopted in the long gauge-length program allowed verification of the strength of

the wire product, as well as independent measurement of the elongation properties of the wire and clamp system, including the effect of repeated loading and generated a large number of samples for failure analysis.

Samples of the FRASW, components of the product such as copper wire and PVC jacket, and clamps were examined to develop a fundamental understanding of the wire mechanical response to loads of extended duration. These results indicate potential vulnerabilities of the clamp and clamp/wire interface, including an important effect in which kinks or bulges result from a temporary application of a significant tensile load as discussed in this manuscript. A complete understanding of this response requires a detailed analysis of the retraction behavior of the wire jacket along with the buckling and kinking of the copper wire under the retractile force of the reinforced jacket. The results of failure analyses led to the development of requirements on the extent of kinking of the wire product upon removal of the long-term mechanical loads.

REFERENCES

1. L.M. Slavin, K. Hsing, E.E. Scerbo, L. Hore, "Fiber-Reinforced Aerial Service Wire: Mechanical Behavior and Installation Guidelines", IWCS Proceedings, in press, 1999.
2. J.-H. Walling, "About the Influence of Residual Elongation and Thermal Expansion on the Sagging Performance of Glass Fiber Reinforced Aerial Service Wires", IWCS Proceedings, 1997.
3. "Span Rules for Aerial Service Wire", Bellcore TM-TSV-021752, August 11, 1992 and "Fiberglass Reinforced Aerial Service Wires", AT&T 636-300-127, Issue 1, AT&T Practices, August 1991.

BIOGRAPHY



Osman S. Gebizlioglu

Telcordia Technologies
445 South Street
Room # 1A-140B
Morristown, New Jersey 07960

Osman S. Gebizlioglu is a Senior Consultant in the Fiber Optic Network Technologies Group at Telcordia Technologies, Formerly Bellcore. He holds B.Sc and M.Sc degrees in Chemical Engineering from the Middle East Technical University, Ankara, Turkey. After receiving his Ph.D in the Polymer Materials Program of the Chemical Engineering Department at Princeton University, Princeton, New Jersey, he was a Monsanto Postdoctoral Fellow in Mechanical Engineering at M.I.T, Cambridge, Massachusetts. Since he joined Telcordia Technologies in 1987, he has been involved in the investigations of performance / reliability issues in optical fibers, fiber optic cables, components and devices. He is also involved in TIA Standards groups, and he chairs the TIA working group on adhesives reliability in fiber optic connectors. He holds three US patents.

Table 1. Geometrical Characteristics of FRASW Cross-section

Physical Design of FRASW Drop Cable Jackets						
FRASW Cable (Supplier)	Jacket Thickness (mm)			Fiberglas Bundles B= Butterfly Shaped E= Elliptical Shaped C= Circular Shaped CF = Circumference XF = Cross-Section		Cable Shape and Design WxH (width x height) in mm D (Dip in center) A = CrossSectional Area in mm ²
	X (mm)	Y (mm)	Z (mm)	CF (mm)	XF (mm ²)	
W-C 2-pr FRASW 1993	1.1±0.2 (1↔1.5)	0.1↔0.2	0.5↔0.75	B (2E-0.41) 21.5 (4 x ~5.4)	B (2E-0.41) 3.8 (4 x ~0.94)	WxH = 8.8 x 5.8 mm D = 0.1-0.2 mm = 3-5% A = 50 mm ²
W-C 2-pr FRASW 1996	0.8±0.2 (0.3↔0.9)	0.4±0.2	1.0±0.2	E/B(0.4→0.6) 14.8 (4x 3.2→4.5)	E/B(0.4→0.6) 2.8 (4 x 0.7±0.05)	WxH = 10.1 x 4.6 mm D = 0.2 mm = 4% A = 45.9 mm ²
W-C 6-pr FRASW 1997	1.0±0.2	1↔1.5	0.6↔1.0	E/B (0.4) 21.7 (6 x ~3.6)	E/B (0.4) 4.43 6x(0.71↔0.77)	WxH = 13.2 x 7.5 mm D = -0.15 mm = -2%(bulge) A = 99-100 mm ²
W-D 6-pr FRASW 1992	1.2±0.3	1.5	1.3±0.3	E (0.42) 14.9 (4 x 3.73)	E (0.42) 3.17 (4 x 0.79)	WxH = 13.0 x 6.5 mm D = 0.1 mm = 3% A = 84mm ²
W-D 2-pr FRASW 1998	1.1±0.2 (0.9↔1.5)	0.1↔0.2	0.7↔1.2	E(0.75±0.25) 13.8 (4 x ~3.4)	E(0.75±0.25) 3.5 (4 x ~0.87)	WxH = 9.25 x 4.0mm D = <0.1mm = <5% A = 37 mm ²
W-D 6-pr FRASW 1998	1.1±0.2 (0.9↔1.4)	1.0±0.1	0.7↔1.4	E(0.5↔0.85) 17.4 4x(4.3↔4.4)	E(0.65±0.2) 5.12 4x(1.2↔1.4)	WxH = 12.5 x 6.2 mm D = 0.1 mm = 3% A = 77.5 mm ²
W-D 2-pr FRASW 1998	1.0±0.2 (0.6↔1.2)	0.1↔0.2	0.7↔1.2	E(0.5↔0.7) 14.7 4x(3.5↔3.9)	E(0.5↔0.7) 3.65 4x(0.76↔1.14)	WxH = 9.0 x 4.5 mm D = 0.25 mm = 11% A = 39 mm ²
W-E 2-pr FRASW 1994	1.5±0.4 (1.0↔2.0)	0.2↔0.3	0.8↔1.4	E(0.6↔0.8) 15.8 4x(3.8↔4.2)	E(0.6↔0.8) 4.55 4x(1.05↔1.26)	WxH = 10.0 x 5.0 mm D = 0.1mm = 4% A = 49 mm ²
W-E 2-pr FRASW twisted 1998	0.5↔2.0 varies greatly	0.05↔0.1	0.6↔1.0	E(0.4↔0.6) 15.4 4x(3.7↔4.0)	E(0.4↔0.6) 3.58 4x(0.8↔1.12)	WxH = 9.0 x 4.5 mm D = <0.1 mm = <5% A = 50 mm ²
W-F 2-pr FRASW 1993	1.0±0.2 (0.6↔1.5)	1.0±0.2	0.5↔1.0 (0.7±0.2)	E(0.4↔0.8) 15.2 4x(3.5↔4.0)	E(0.4↔0.8) 3.67 4x(0.6↔1.18)	WxH = 8.5 x 4.5 mm D = 0.25 mm = 12% A = 37.5 mm ²
W-B 2-pr FRASW quad 1996	0.9±0.1 (0.8↔1.1)	0.15↔0.2	0.5↔0.7	~C(0.8↔1.0) 13.2 4x(3.1↔3.6)	~C(0.8↔1.0) 3.44 4x(0.8↔1.02)	WxH = 9.2 x 4.8 mm D = 0.5 mm = 21% (dumbbell) A = 41.5 mm ²
W-B 2-pr FRASW quad 1998	0.8 ±0.1 (0.7↔1.0)	0.2↔0.4	0.5↔0.6	~C(0.8↔0.9) 13.7 4x(3.3↔3.6)	~C(0.8↔0.9) 3.7 4x(0.86↔1.04)	WxH = 9.0 x 4.5 mm D = 0.55 mm = 24% (dumbbell) A = 38 mm ²

Table 2. FRASW Breakage Rates

FRASW Breakage Rates		
	Breakage Rate, All 2-Pair Products (No. Failures / No. Tested)	Breakage Rate, "Weakest" 2-Pair Product (No. Failures / No. Tested)
Long Gauge-Length Tests (includes repeated loading)	4/14 (29%)	2/3 (67%)
Previous Experiences	8/52 (15%)	8/15 (53%)

Table 3. Kinks and Bulges After Load Removal

Presence of Kinks in FRASW Following Testing			
Test No.	Long Gauge-Length Test	Full-Scale Simulation	Remarks
1	severe	moderate	
2			
4		moderate	
5		mild	
6	moderate	moderate	
7			
8	mild	mild	
9	mild		
10	severe	moderate	
11	moderate	moderate	universal (water block)
12		moderate	
13		moderate	
14	severe	mild	6-pair reused wire
15			aged sample
16	moderate		6 in. tails
17			
19			
20	moderate	moderate	quad
21		mild	2-pair (simulation)
22		mild	6-pair
23			Instron

TEST METHODS FOR ARAMID YARN: THEIR IMPACT ON FIBER OPTIC CABLE DESIGN

*Alan S. Koralek¹, Albert L. Finnimore¹, Dexter L. Atkinson¹, Donal C. Breen²,
Helena A. McGuinness³, and A. Gerry O'Donnell³,*

¹E. I. DuPont de Nemours & Company, Inc., Richmond, Virginia

²DuPont International, S.A., Geneva Switzerland

³DuPont (UK), Ltd.

ABSTRACT

Since its infancy, fiber optic cable industry growth has occurred at explosive rates. Driving that growth has been the ability of fiber optics to reliably transmit year after year more information at lower cost than was previously possible. While improvements in hardware and waveguide technology are principally responsible for those gains, improvements in other cable components and effective use of them have contributed as well.

From the beginning, aramid yarns have been incorporated into cables as a "load-bearing member" whose function is to limit waveguide strain. Along with high modulus, aramid yarns possess good creep resistance, low thermal expansion and high electrical resistance – all of which provide value to the cable designer. Improvements in aramid yarn properties and processability, and knowledge about how to more effectively utilize those, have complemented the growth of the cable industry.

Strength members are an integral part of fiber optic cable and must be carefully considered in the design of the cable. The strength member serves a critical function, controlling the strain in the waveguide during the installation of the cable and, in the case of aerial cable, throughout its service life.

Consequently, a key property of the strength member is its resistance to stretch under tensile loading. Several methods of defining the stretch resistance of reinforcing materials are currently being used, and the results of testing by those methods are quoted by suppliers of materials used as strength members. Those methods – twisted yarn modulus, untwisted yarn modulus, yarn LASE, yarn FASE, and impregnated strand modulus – produce significantly different, and sometimes confusing, results.

This paper describes each of those methods, provides stress-strain data on aramid yarns from each of those methods and then incorporates that data into the design of both in-ground and aerial cable. A clear demonstration is presented of the impact of the methodology used to determine material stretch resistance on cable properties and of why the cable designer needs to exercise caution when comparing stretch resistance data generated by one method with data generated by another. Also discussed in this paper are other properties of aramid yarns, including their creep and thermal expansion characteristics, and low specific gravity. This outstanding combination of properties, combined with ever-improving processability continues to make aramid yarns an attractive consideration for use in fiber optic cable.

INTRODUCTION

Kevlar® aramid yarn was first commercialized in 1972. Among its earliest and sustained applications has been its use as a load-bearing member in fiber optic cables.

High resistance to stretch under tensile load, low creep, near-zero coefficient of thermal expansion and low specific gravity are all attributes of aramid yarns which are valued by the cable industry; and it is those properties that the yarn producer has and continues to improve to meet the changing needs of the industry. Typical properties of yarns currently used in fiber optic cables are given in Table 1.

Low creep, thermal expansion, and density are important properties, particularly in aerial cables which are continuously under tensile load and which undergo large variations in exposure temperature. However, the excellent resistance to stretch under tensile load is probably the property of aramid yarns most important to the cable designer.

Surprisingly, perhaps, the methods of quantification of stretch resistance by yarn suppliers is not uniform and has led to some confusion for the designer. It is the aim of this paper to describe the methods by which stretch resistance is measured, to provide data from several of those methods, to show the impact of those different test methodologies on cable design, and to provide the cable designer with better insight on the interpretation and use of published yarn data.

TEST METHODS

Several different methods for defining the stretch resistance of aramid yarns are currently in use. Among them are yarn modulus, yarn LASE, yarn FASE and impregnated strand modulus. A brief description of each is provided below.

Kevlar® is a DuPont Registered Trademark

Yarn Modulus

Yarn modulus is the ratio of the change in tenacity, expressed in millinewtons per tex (mN/tex) to the change in strain, expressed as a fraction of the original length. Rather than being normalized on a yarn weight per unit length (e.g. tex) basis, yarn modulus can also be expressed normalized on a yarn area basis - for example, in gigapascals (GPa), where $1 \text{ GPa} = 1 \text{ N/mm}^2$. The relation between the two values is:

$$\text{Modulus (in GPa)} = \text{modulus (in N/tex)} \times \text{yarn density (in g/cm}^3\text{)}$$

Yarn modulus is highly dependent on test methodology. Variables which strongly influence it are yarn twist, strain rate, gage length, test fixtures (clamps) and, because of non-linearity in the stress-strain curve, the location on that curve at which the slope is measured. DuPont utilizes the methodology prescribed in ASTM D885-98[1] when measuring and reporting the modulus of Kevlar® aramid yarn. Unless otherwise stated, the yarns tested are pre-twisted, as specified in ASTM D885-98, to a twist level (in turns per meter) of 1055 divided by the square root of the linear density, expressed in tex. The application of this small amount of twist reduces testing variability, but at the same time reduces the modulus value. ASTM D885-98 prescribed testing conditions are summarized in Table 2. The modulus values for Kevlar® obtained in the ASTM D885-98 test reflect those in the linear portion of the stress-strain curve. (Figure 1)

Yarn LASE and FASE

Yarn LASE (Load At Specified Elongation) or FASE (Force At Specified Elongation) test results describe the load (in newtons or pounds force) that will stretch the yarn to a specified elongation. A yarn LASE test was introduced by DuPont in 1990 in response to a desire to have a test indicative of in-cable performance, where yarns are utilized in an untwisted state and at relatively low strain.

In that LASE test, untwisted yarns are loaded to 6.2 mN/tex before clamping them in the tensile testing apparatus. They are then strained at a rate of 10% per minute, one-fifth the strain rate used in ASTM D885-98. A line is drawn on the stress-strain curve through the points

corresponding to a stress of 0.89 cN/tex and a stress of 5.29 cN/tex and is then extrapolated backwards to 0 load to define zero strain (See Figure 2). Strain levels 0.1%, 0.2%, 0.3%, 0.5%, and 1.0% from that established origin are located and the corresponding load levels are defined as LASE_{0.1%}, LASE_{0.2%}, etc. The information developed in that test describes the yarn stress-strain characteristics in both the nonlinear and linear regions.

Other yarn test procedures have been utilized within the fiber industry. The most commonly utilized alternative is a FASE test built off of the ASTM D885-98 tensile test procedure. In that method, a substantially higher pretension (20 mN/tex) is employed, the strain rate utilized is 50% per minute and zero strain is defined at the pretension load of 20 mN/tex. The test can be run on untwisted or twisted yarn. While the data produced by this test also describes the non-linearity of the aramid yarn stress-strain curve, it does so to a lesser degree, since stresses lower than 20 mN/tex are truncated from the curve. As will be made clear later in this paper, one cannot compare results generated by the FASE test procedure with those on another product generated by the DuPont LASE procedure.

Impregnated Strand Modulus

In this test, a yarn or roving is impregnated with a compatible thermosetting resin system, which is then cured. The resulting composite strand is then tensile tested. A stress-strain curve is established, and the chord modulus is defined in the linear portion of the stress-strain curve, calculated in gigapascals, based on the area of fiber in the composite strand. The test differs from the yarn modulus test in two important ways: strain is measured with a clip-on extensometer, rather than by cross head displacement, and strain rate is usually low (~5%/min). The impregnated strand test used by DuPont conforms to SACMA SRM 16R-94[2] and ASTM D2343[3], which were established to provide an understanding of the performance of fibers, yarns and rovings in composites. While useful in describing the stretch resistance of composite strength members (for example rigid CSM), the impregnated strand test is not a good descriptor of stress-strain behavior of peripherally served strength members.

RESULTS OF YARN TESTS

Yarn modulus LASE, FASE, and impregnated strand testing was carried out on 3160 dtex Kevlar® 49 yarn and on 7900 dtex Kevlar® 49 roving. The former is commonly used as a strength member in duct cable and the latter is commonly used in aerial cable.

Yarn and Roving Modulus

Testing according to ASTM D885-98 was carried out on untwisted and twisted 3160 dtex yarn, using Instron 4D clamps. Results are shown in Figure 3, along with those obtained on that same yarn using larger capacity 4E clamps and a longer (635mm) gage length. The 4D and 4E clamps are shown in Figure 4. The moduli of untwisted 3160 dtex yarn were about 5% higher than those for 1.1 twist multiplier twisted yarn. Utilization of the larger capacity 4E clamps and the longer gage length increased modulus values by about 10%. All the noted differences were statistically significant.

Testing was also carried out on 7900 dtex Kevlar® 49 roving. The effects of twist as well as clamps and gage length were similar to those seen with the 3160 dtex yarn (Figure 5). Again, the differences were statistically significant.

Further testing showed that gage length, alone, has a measurable effect on yarn modulus (Figure 6), again demonstrating the need to fully understand what testing parameters were employed in the generation of data. In those tests, strain rate effects were found to be small.

LASE/FASE

Testing was carried out on both the 3160 dtex and 7900 dtex Kevlar® 49 products using the DuPont LASE test in which zero strain is established by the extrapolation procedure described earlier. In addition to the standard pretension of 6.2 mN/tex, pretensions up to 40 mN/tex were employed. Figures 7 and 8 show the results of those tests and the influence of the pretension value.

In addition, testing was done using the FASE test procedure based on ASTM D885-98, where 0% strain is defined at the pretension load. Untwisted yarn and roving were used in this test, and the effect of pretension level and strain rate

was investigated. As expected, FASE values obtained using this test procedure are highly dependent on pretension value and only slightly dependent on strain rate. The effect of pretension level is shown in Figure 9.

In another experiment, a direct comparison was made between LASE values obtained by the DuPont method, utilizing a pretension of 6.2 mN/tex and a strain rate of 10%/min and FASE values utilizing a pretension of 20 mN/tex and strain rate of 10%/min. For 3160 dtex Kevlar® 49, FASE values obtained with 0% strain defined at the pretension load of 20 mN/tex were about 15 N higher than were those obtained using the DuPont LASE method in which 0% strain is defined by extrapolation of the initial modulus to zero load. For 7900 dtex roving, the differences were found to be about 44 N. Those results are shown in Table 3.

Impregnated Strand Modulus

Impregnated strand moduli were obtained for both the 3160 and 7900 dtex Kevlar® 49 products. Results are shown in Table 4, where they are also compared to twisted yarn moduli. The impregnated strand test inflates modulus values by about 25% when compared to results obtained on twisted yarn or roving tested according to ASTM D885-98.

IMPACT ON CABLE DESIGN

Stretch resistance data described in the previous sections was used to define the quantity of yarn required to meet imposed cable design constraints.

3160 dtex yarn was used in a loose-tube duct cable and 7900 dtex roving in a 366 meter span aerial cable.

Ducted Outdoor Cable

Design constraints on a 36 fiber, 12mm outer diameter, all dielectric cable for use in underground duct systems were established to be 0.5% cable strain at an installation tensile load of 2700N. The number of 3160 dtex Kevlar® yarns that would be needed to meet the constraint was calculated using the yarn modulus, LASE, and impregnated strand data

presented earlier in this paper. Required yarn weights ranged from 6.0 kg/km to 7.6 kg/km. Results can be found in Table 5.

Aerial Cable

A similar study was performed on a 96 fiber all-dielectric self supporting cable. Installation design constraints for a 366m span were 1% sag at 0.5% cable strain. DuPont proprietary software was used to calculate the required number of ends of 7900 dtex Kevlar® roving, based on roving stiffness values obtained using the various methods described in this paper. Calculated roving weights varied by more than 50% - from 26 kg/km if one used the data from the impregnated strand test to 40 kg/km if one used the data obtained from the DuPont LASE test. Results are summarized in Table 6.

CONCLUSIONS

Yarn modulus, LASE, FASE, and impregnated strand modulus tests produced significantly different values of yarn stiffness. It is clear that those property differences, described in this paper, are not inherent to the products tested, but are merely artifacts of test methodology. Cable performance is dependent on the load-bearing member's intrinsic stiffness, and not on the methods used to measure the yarn properties. Cable performance must be monotonically related to the quantity of load-bearing material used, as shown in Figures 10 and 11. Improper interpretation of yarn properties can lead to cable performance below that desired or to utilization of more reinforcing material (and incurred cost) than is needed to meet performance requirements.

It is clear then that the cable designer needs to know not only the values quoted for yarn stiffness, but also the test methods used to develop that information. Only then can the designer develop the proper relationship between required cable performance and yarn properties.

Table 1**Properties of Kevlar® Aramid Yarn**

Type	Kevlar® 29	Kevlar® 49	Kevlar® 149
Density (g/cm ³)	1.44	1.44	1.47
Dtex (g/10000m)	1500	1420	1420
Tenacity (cN/tex)	201	210	155
Modulus (cN/tex)	5160	8430	9970
Elongation at Break (%)	3.4	2.4	1.4
Creep at 50% of Break Strength (%/decade of time)	.05	.02	.01
Coefficient of Thermal Expansion (10 ⁻⁶ cm/cm-degC)	-4.0	-4.9	-2.0

Table 3**LASE/FASE Comparison**

Stiffness Test	Strain(%)				
	0.1	0.2	0.3	0.5	1.0
LASE _{3160dtex}	15.6	38.6	64.0	116.1	243.5
FASE _{3160dtex}	28.0	52.7	78.7	131.6	260.3
LASE _{7900dtex}	28.5	75.7	135.5	261.4	551.3
FASE _{7900dtex}	60.6	116.8	179.0	306.1	608.1

Notes: LASE and FASE values in Newtons
 DuPont LASE test: 6.2 mN/tex pretension
 FASE TEST: 20 mN/tex pretension

Table 2**ASTM D885-98 Test Conditions**

Yarn Twist (turns/m):	1055 (LD) ^{1/2} Where LD=linear density in tex
Atmosphere:	24°C, 55% RH
Gage Length:	500mm (or 20 in.)
Rate of extension	250mm/min (or 10 in/min)
Clamps:	Not Specified
Modulus Range (mN/tex)	300-400

Table 4**Aramid Modulus
Impregnated Strand vs Twisted Yarn**

<u>dtex</u>	<u>Impregnated Strand Modulus</u>		<u>Twisted Yarn Modulus</u>
(g/10000m)	(GPa)	(cN/tex)	(cN/tex)
3160	133.5	9270	7850
7900	140.1	9729	7498

Table 5**Duct Cable****3160 dtex Yarn Needed to Meet Design Requirements**

<u>Stiffness Test</u>	<u>Predicted Number of Yarn Ends</u>	<u>Predicted Yarn Weight (kg/km)</u>
Twisted yarn modulus	22	7.0
Untwisted yarn modulus	21	6.7
DuPont Lase	24	7.6
FASE	22	7.0
Impregnated Strand Modulus	19	6.0

Note: Design requirement is 0.5% strain @2700 N/load

Table 6**Aerial Cable****7900 dtex Roving Needed to Meet Design Requirements**

<u>Stiffness Test</u>	<u>Predicted Number of Roving Ends</u>	<u>Predicted Roving Weight (kg/km)</u>
Twisted Yarn Modulus	45	36
Untwisted Yarn Modulus	42	33
DuPont LASE	51	40
FASE	42	33
Impregnated Strand Modulus	33	26

Note: Design requirement is 1% sag on 366M span with 0.5% cable strain

FIG.1:

**ASTM D885-98
3160 dtex Kevlar® 49
Stress-Strain Curve**

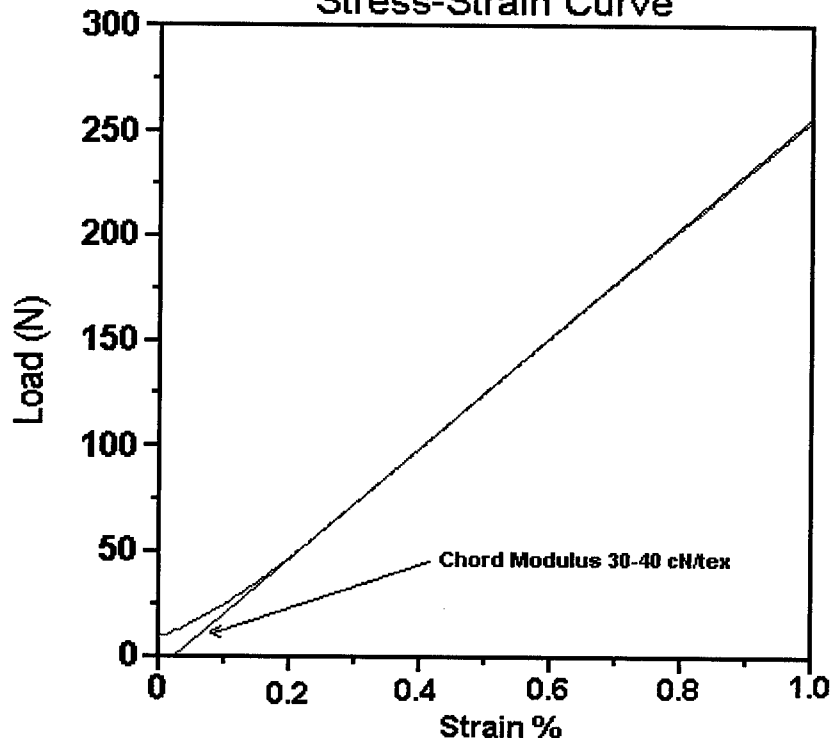


FIG.2: DuPont LASE Test

3160 dtex Yarn

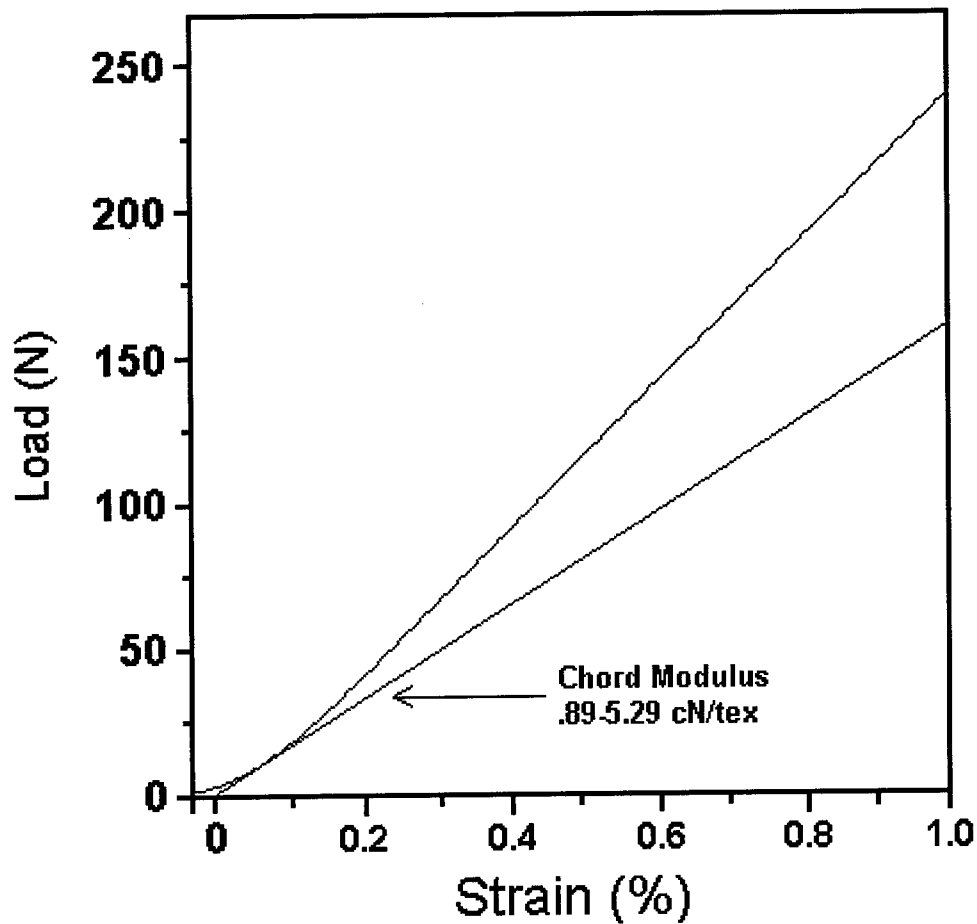


FIG. 3: Effect of Twist and Clamps on Modulus of 3160 dtex Kevlar®49 Yarn

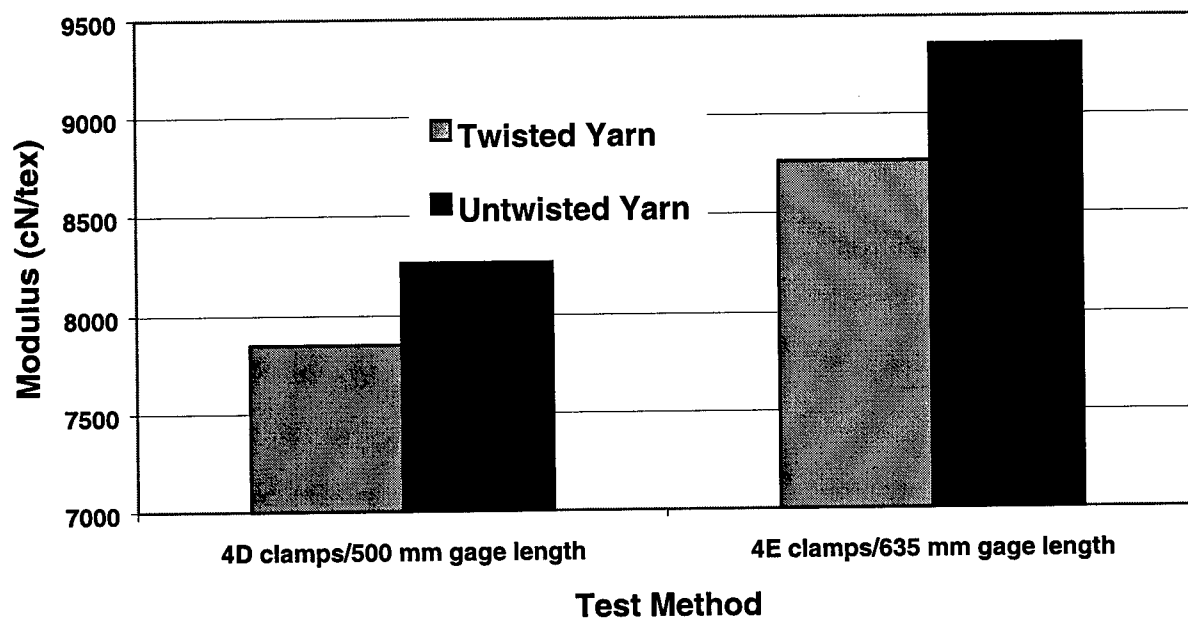


FIG.4: 4D Clamps (left) and 4E Clamps (right) with 25.4 mm Ruler

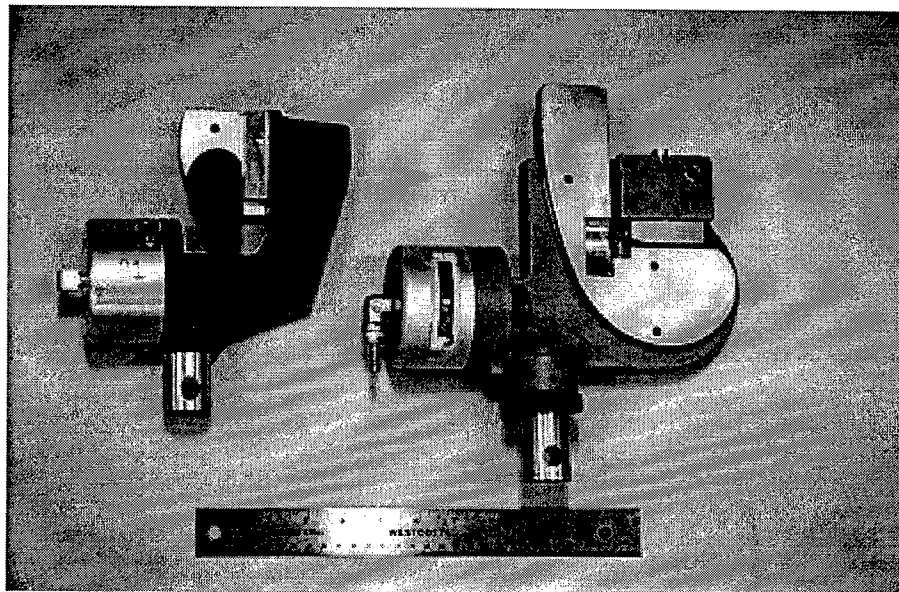


FIG.5: Effect of Twist and Clamps on Modulus of 7900 dtex Kevlar®49 Roving

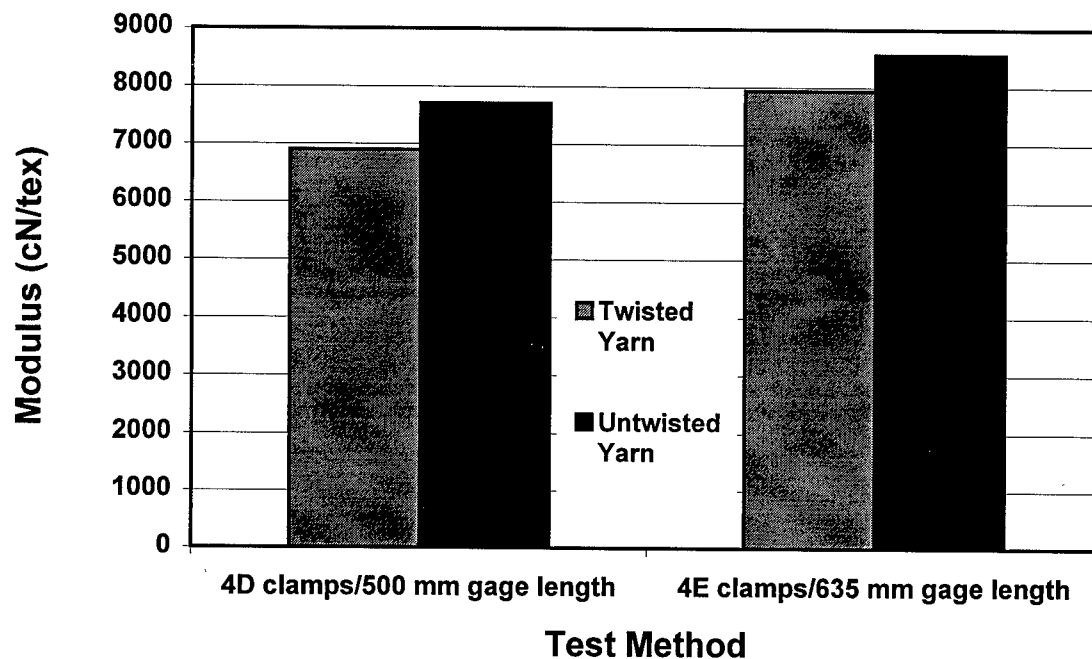


FIG.6: Effect of Gage Length on Modulus of 3160 dtex Kevlar®49 Yarn

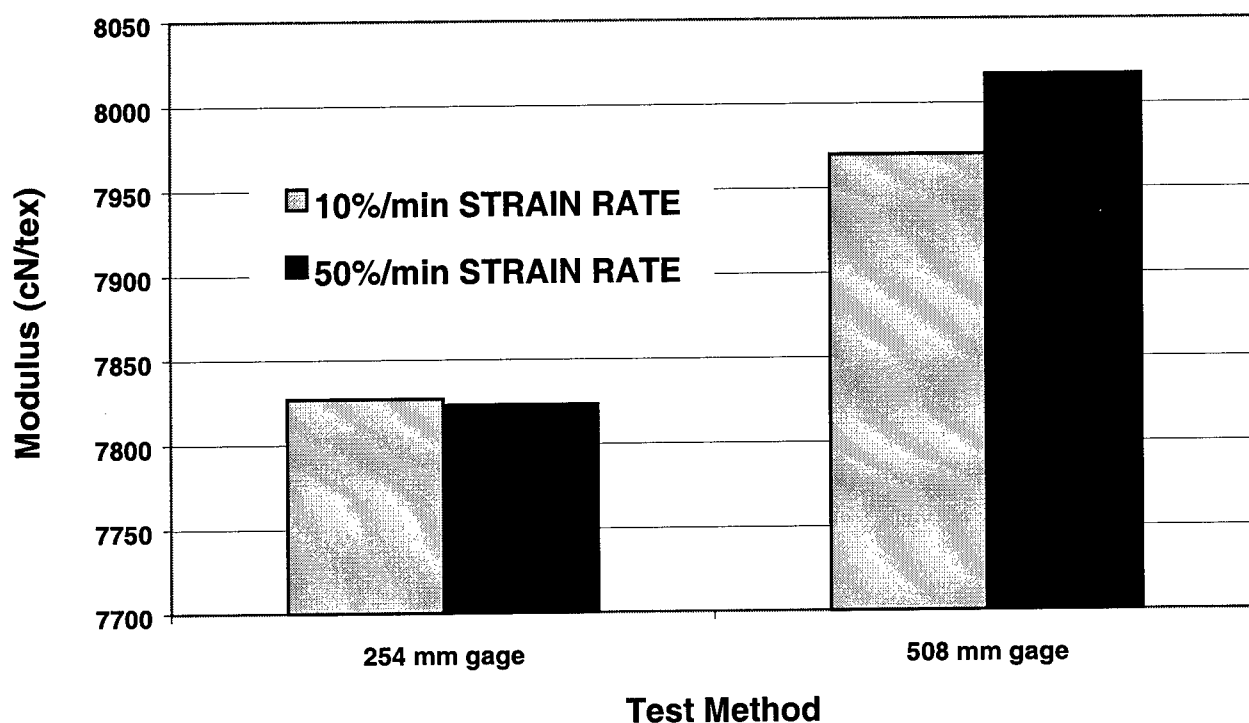
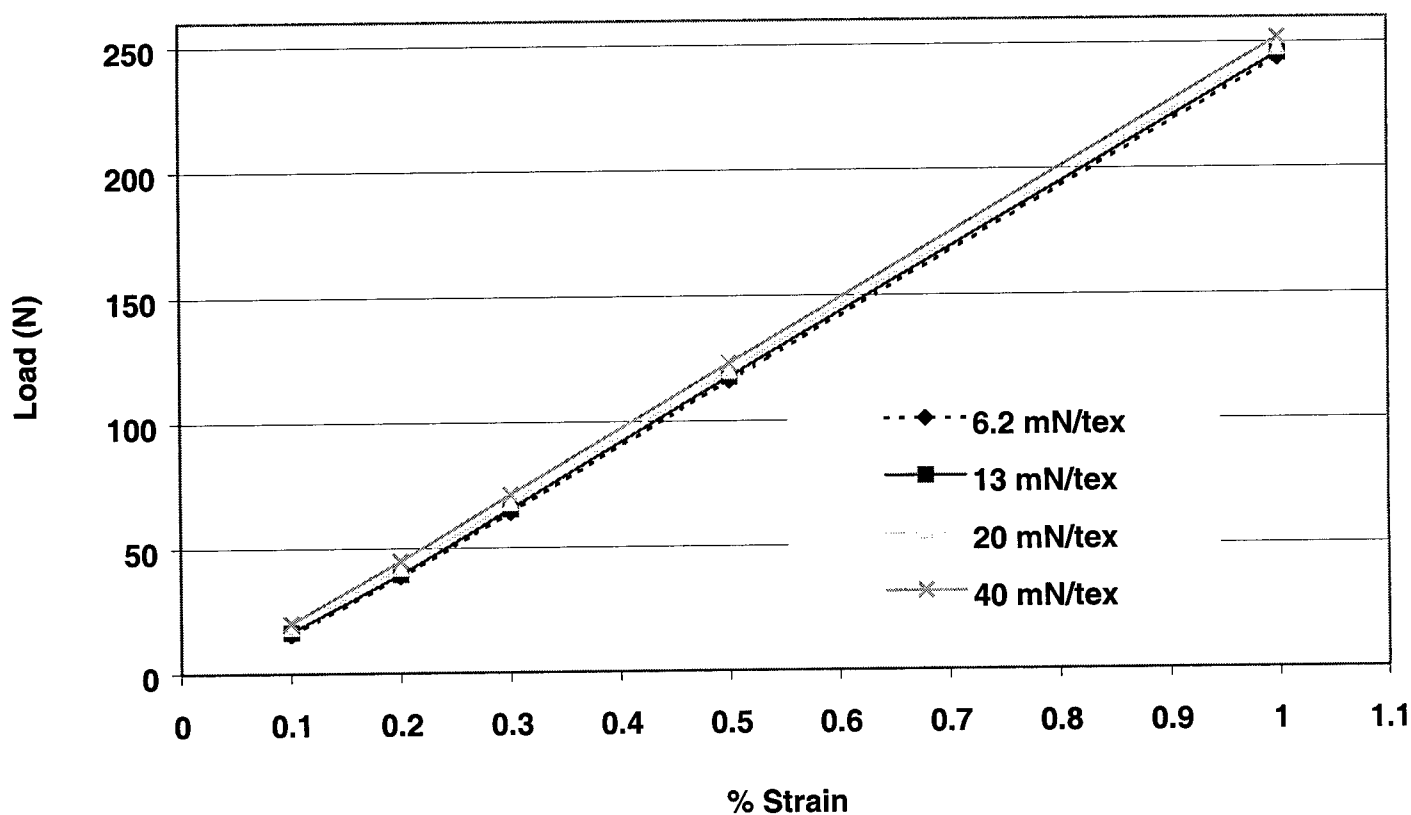
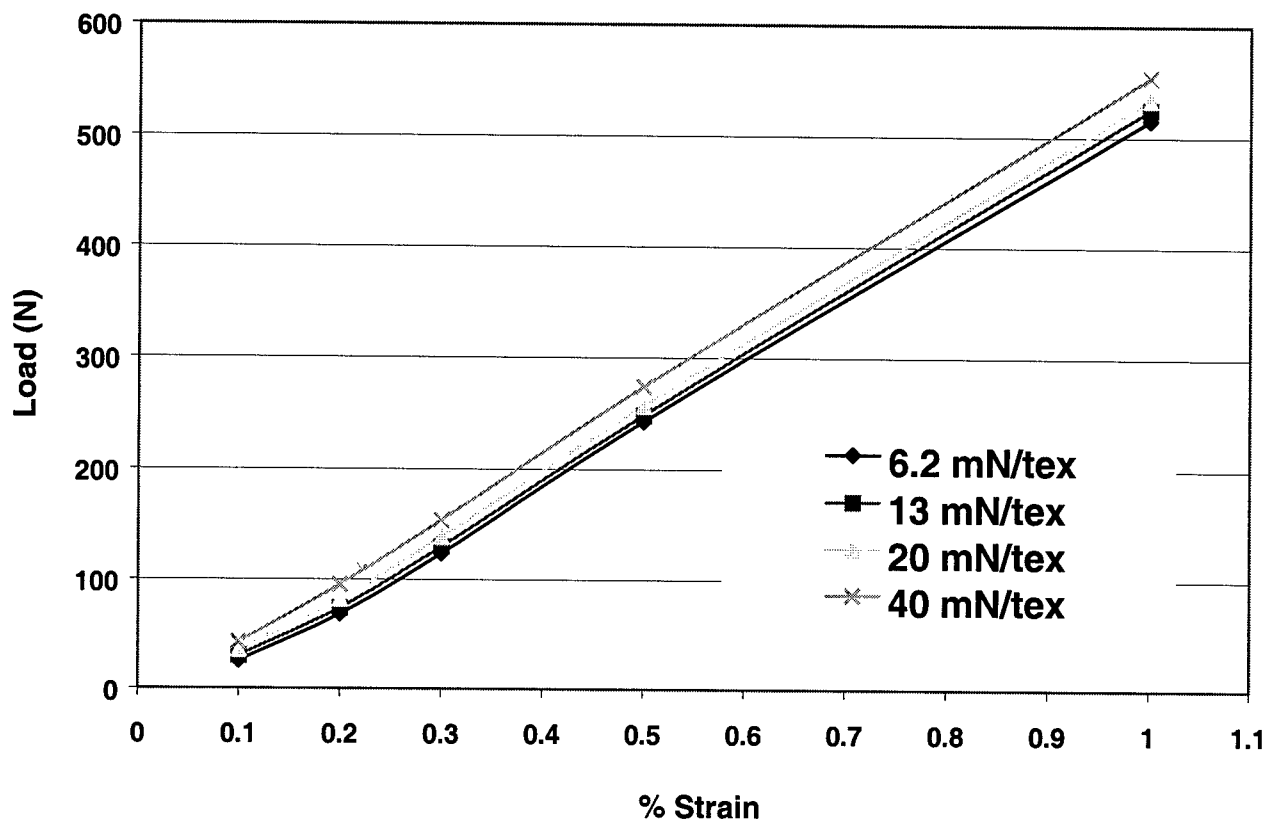


FIG.7: Effect of Pretension Load on DuPont LASE Test Results (3160 dtex Kevlar®49 Yarn)



**FIG.8: Effect of Pretension Load on DuPont LASE Test Results
(7900 dtex Kevlar® 49 Roving)**



**FIG.9: Effect of Pretension Load on FASE Results
(7900 dtex Kevlar® 49 Roving)**

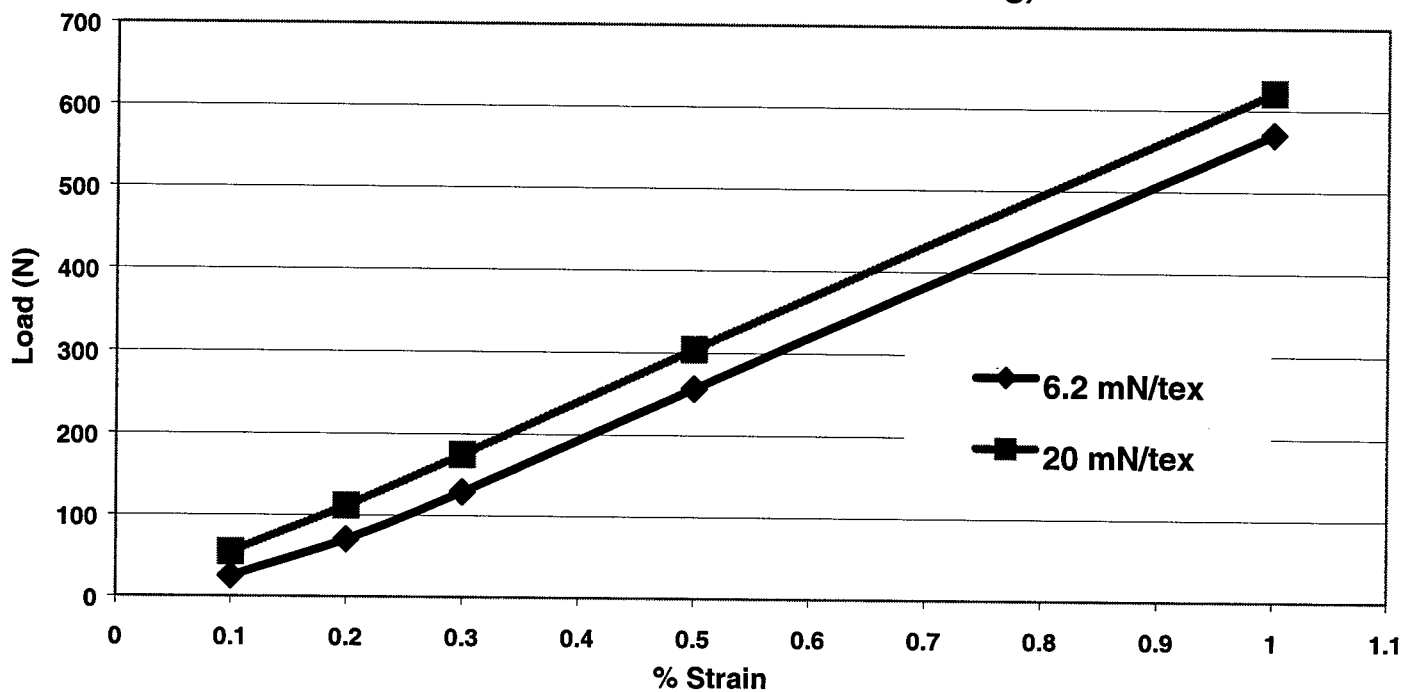


FIG.10: Impact Of Reinforcement Endcount On Duct Cable Performance

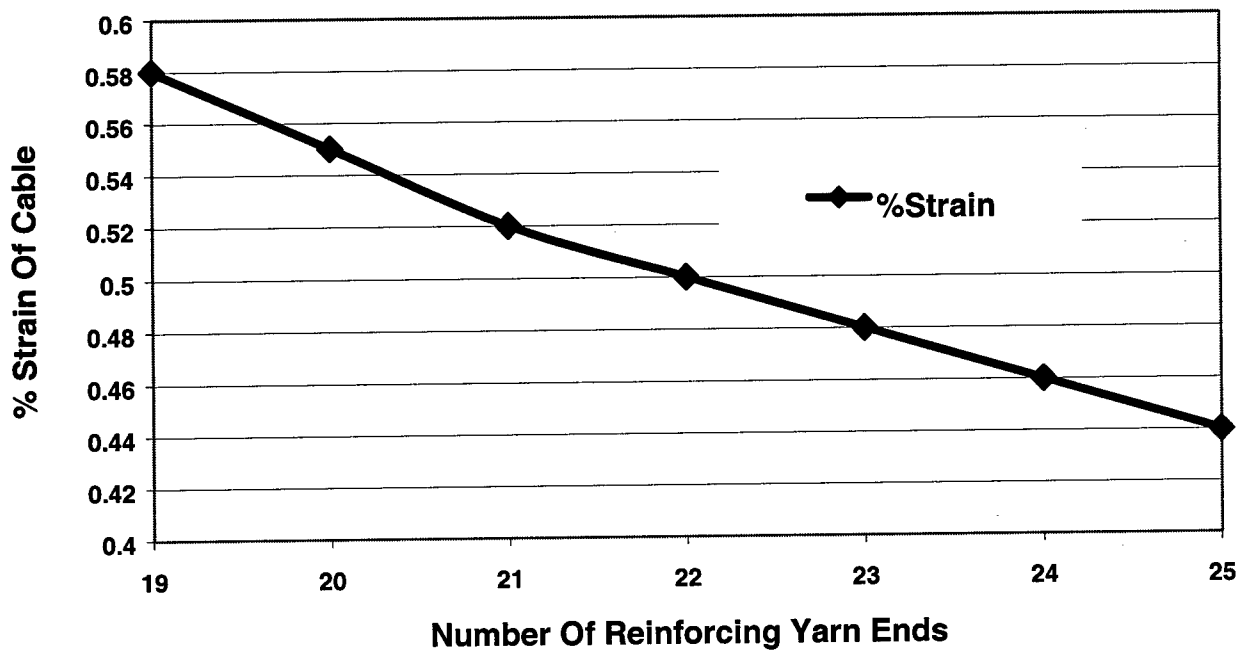
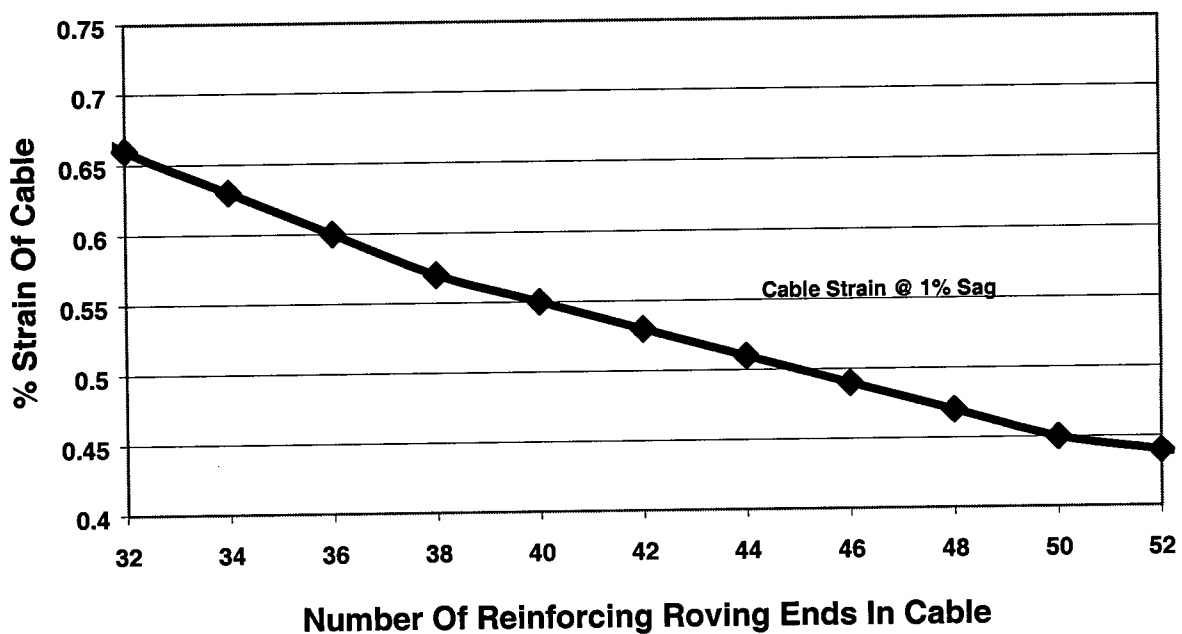


FIG.11: Impact Of Reinforcement Endcount On Aerial Cable Performance



REFERENCES

- (1) Standard Test Method D885-98, Standard Test Methods for Tire Cords, Tire Cord Fabrics, and Industrial Filament Yarns made from manufactured Organic-based Fibers, Annual Book Of ASTM Standards, Vol 7.01, American Society for Testing and Materials, West Conshohocken, PA.
- (2) Standard Test Method D3039/D3039M-95a, Standard Test Method for Tensile Properties of Polymer Matrix Composite Materials, Annual Book of ASTM Standards, Vol 15.03, American Society for Testing and Materials, West Conshohocken, PA
- (3) SRM4-94, Recommended Test Method for Tensile Properties of Oriented Fiber-Reinforced Composites, Suppliers of Advanced Composite Materials Association (SACMA), Arlington, VA

AUTHOR



Donal C. Breen
Du Pont de Nemours International S.A.
2, chemin du Pavillon
P. O. Box 50, CH-1218 Le Grand-Saconnex
Geneva, Switzerland

Donal Breen graduated with a BSc in Pharmacology from University College Dublin in 1982 and again in 1988 with a BSc Degree in Chemical Engineering from the same University. Between these two primary degrees, he worked in the pharmaceutical industry in the USA. He joined DuPont (UK) Ltd. in the start-up and commissioning of the Kevlar® plant in Londonderry, North Ireland. Between 1988 and 1999, he occupied a number of different positions including production, quality, and technology management. During this time he completed an MBA from the University of Ulster. In 1998 he transferred to DuPont de Nemours International S.A. where he holds the position of account supervisor for the application of Kevlar® in the Fiber Optic Cable industry.

ACKNOWLEDGEMENTS

The authors wish to thank Nell Ollis and Bill Harrison for their help in the preparation of this paper.

ANALYSIS OF UTP PATCH CABLE PERFORMANCE FOR HIGH BIT RATE APPLICATIONS

John Kincaid, Paul Vanderlaan, Carl Dole

Belden Electronics Division
Richmond, Indiana

ABSTRACT

Among the patch cable electrical performance requirements currently being standardized¹ by the Telecommunications Industries Association (TIA) for UTP structured cabling systems, return loss is identified as a key performance parameter. The mechanical structure of the patch cable is considered and the relationship between dimensional variation and the inductance, capacitance and high frequency (asymptote) characteristic impedance is examined. Possible changes in "s", conductor to conductor spacing, and "sd", virtual shield reference surface separation of the twisted pair are identified as contributors to inductance and capacitance variation and hence return loss variability. When conductor to conductor spacing is maintained constant it is shown that return loss variation is minimal due to the minor effect of "sd" variation. Empirical results for return loss of patch cable and patch cord implemented in a three-connector topology channel are presented.

INTRODUCTION

The importance of performance stability of UTP cabling has been a recent focal point of standards developers working in the Telecommunications Industries Association (TIA) subcommittee TR-42.1 (formerly TR41.8.1). Over the past year measurements of return loss variability (due to handling) of patch cords, and cabling links have been the subject of many contributions to working group meetings. Contributions by Sciacero² established the existence and severity of the variation. A test for qualifying the patch cord assembly is being considered for standardization. Other transmission parameters such as crosstalk, and attenuation have not exhibited such extreme variability and are not currently under investigation.

DESIGN

Handling-stability of patch cord return loss has been of concern as it may degrade the overall return loss performance of installed systems. Variation of performance has been observed in test leads and is of concern in cross-connect fields, equipment cords and workstation cords. This is due to patch cable design features as well as the type of handling to which the cable may be subjected. Variation due to cable design may include conductor separation within a pair, as well as core compaction or rearrangement due to lay length, and/or binder/jacket variables.

Handling of the patch cable may result in a mechanical rearrangement within the cable that in turn causes a change in reflected energy level. Coiling, stretching, looping, hanking and swinging are possible handling scenarios.

Figure 1 below plots the capacitance and inductance variation versus spacing distance in inches. Capacitance is in units of pF/ft and inductance is in $\mu\text{H}/\text{ft}$. This is a good engineering approximation³ which correctly shows the trends for multipair cables. Capacitance and inductance are both very sensitive to changes in "s" and less so to changes in "sd".

"s" and "sd" are defined in figure 2.

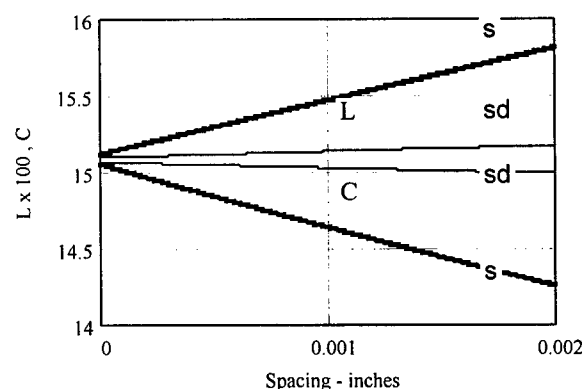


Figure 1. Inductance and capacitance variation

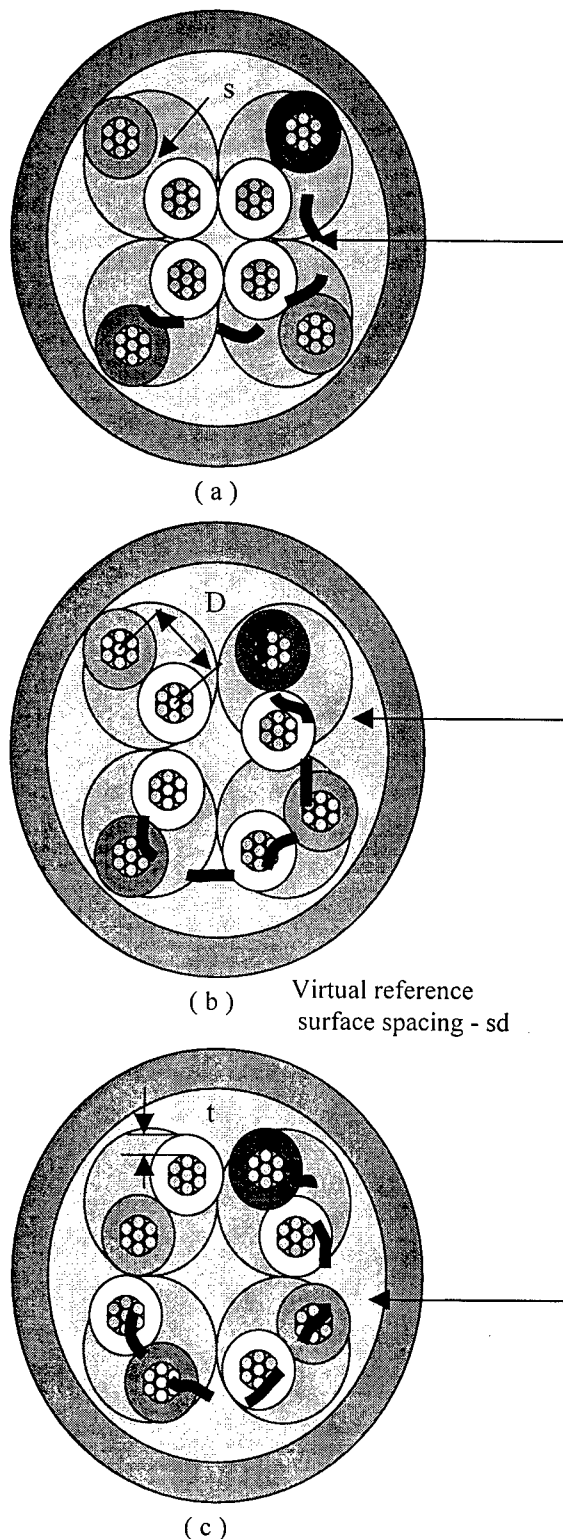


Figure 2. Cross section variability of patch cable

Referring to figure 2 three possible cross-sections for typical UTP four pair patch cable are illustrated. The conductors are stranded construction and the pairs are typically assembled with different lay lengths to minimize crosstalk. As the pairs are twisted longitudinally the locus of possible cross-section positions appears as four circles within the jacket. The jacket is a tubed construction and typically is not drawn tight about the twisted pair core to improve flexibility and aesthetics. As a consequence the core is seen to incorporate space for movement and rearrangement. Fillers and/or binders are typically not used due to a combination of cost, termination and flexibility considerations.

Figure 2(a) illustrates possible conductor to conductor separation "s". The virtual reference surface is shown as a heavy dash. Figures 2(b) and (c) define conductor to conductor spacing variable "D", insulation wall thickness "t" and additional possible rearrangements of conductors in the cross-section are illustrated.

It is noted that the virtual reference surface is not well defined due to the absence of a shield and naturally varies longitudinally as the core pair rearrangements take place. Figure 1 indicates the L and C variation due to this is minor compared to possible variation due to "s".

Variation of "s" is observed to occur unless specific design remedies such as conductor bonding, binder tapes, etc are used.

The consequence of varying L and C is variation in the local characteristic impedance. Figure 3 plots the variation of high frequency impedance asymptote versus "s" and "sd" variation. This is determined from the square root of the L, C ratio where the internal inductance is negligible. Impedance variation is seen to be strongly dependent on "s" variation and less so on "sd" as would be deduced from figure 1 results.

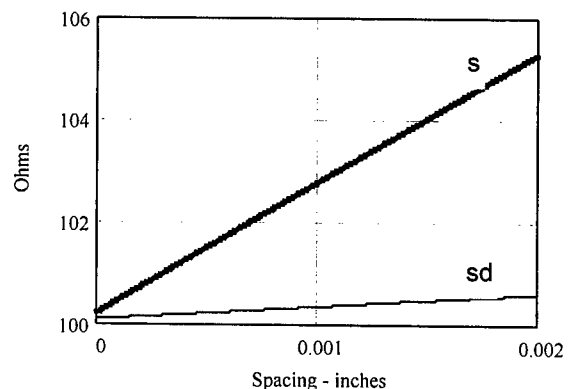


Figure 3. Impedance variation

PATCH CORD RL TEST

A test for qualifying the handling robustness of patch cord assemblies is in process of standardization by the Telecommunications Industries Association (TIA) subcommittee TR-42.1. Essential elements being considered are illustrated in figure 4. A standard return loss setup with network analyzer/S parameter set, balun, connecting hardware, and cord under test are specified. Critical issues are the calibration reference plane location, connecting hardware RL performance, differential and common mode terminations of the twisted pairs, and the mechanical cycling of the cord.

Network / S Parameter Analyzer

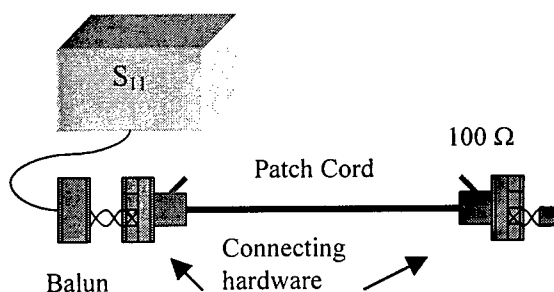


Figure 4. Patch cord return loss setup

The mechanical cycling includes a sequence of RL measurements involving forming the cord into approximate six inch diameter loops and rotations of the RJ-45 plug. The cord is qualified if return loss does not exceed specification limits across the frequency band.

RL TEST PROGRAM OVERVIEW

A test program was devised to study the return loss variability of patch cable with mechanical cycling under the following scenarios:

- Patch cable only
- Patch cord only
- Three connector channel topology involving connecting hardware, patch cords and horizontal cable
- Connecting hardware only

The patch cables and cords were minimum rated as Cat 5 enhanced and the designs included bonded as well as non-bonded conductor technology. The connecting hardware was also rated Cat 5 enhanced and the test frequency range was 1-350 MHz.

Patch cord test. Patch cords were tested as illustrated in figure 4. All pairs had differential impedance terminations at both ends and common mode terminations were also used at the measurement end. Low inductance chip resistors and short 100 Ohm twisted pair interconnects were used. The calibration plane was located at the balun terminals. Mechanical cycling involved the following steps:

- Straight configuration direct from packaging
- Six inch loops formed by hand
- Plug rotation increment of 360 degrees

Patch cable test. Patch cable testing was performed with the setup shown in figure 5. Test parameters were as in figure 4 except the connecting hardware was not required. Patch cords tested per figure 4 and later used in channel testing were also tested without the plugs at the end of the program according to figure 5. Mechanical cycling involved the same steps used in the patch cord test.

Network / S Parameter Analyzer

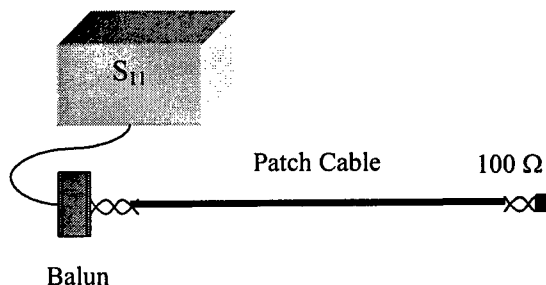


Figure 5. Patch cable return loss setup

Channel test. The channel was configured as shown in figure 6. Four cable segments are identified as #1-#4. Connecting hardware identified as A-C consisted of combination punchdown/RJ-45 Jack connections and were rated Cat 5 enhanced. The measurement calibration reference plane was located at the balun terminals. Common mode terminations were used at the measurement end and differential terminations were used on all pairs. Chip resistor terminations were used. The test protocol involving mechanical cycling, cable segment and patch cable design is specified in table 1.

Table 1. Channel Test Protocol Definitions

Reference Number	Segment #1		Segment #2		Segment #3		Segment #4	
	design	cycling	design	cycling	design	cycling	design	cycling
1	x	a	x	a	x	a	x	a
2	x	b,c	x	a	x	a	x	a
3	x	a	x	b,c	x	a	x	a
4	x	a	x	a	x	a	x	b,c
5	x	b,c	x	b,c	x	a	x	b,c
6	o	a	x	a	x	a	x	a
7	o	b,c	x	a	x	a	x	a
8	x	a	o	a	x	a	x	a
9	x	a	o	b,c	x	a	x	a
10	x	a	x	a	x	a	o	a
11	x	a	x	a	x	a	o	b,c
12	o	a	o	a	x	a	o	a
13	o	b,c	o	b,c	x	a	o	b,c

x – bonded conductor design : o – non-bonded conductor design

Network / S Parameter Analyzer

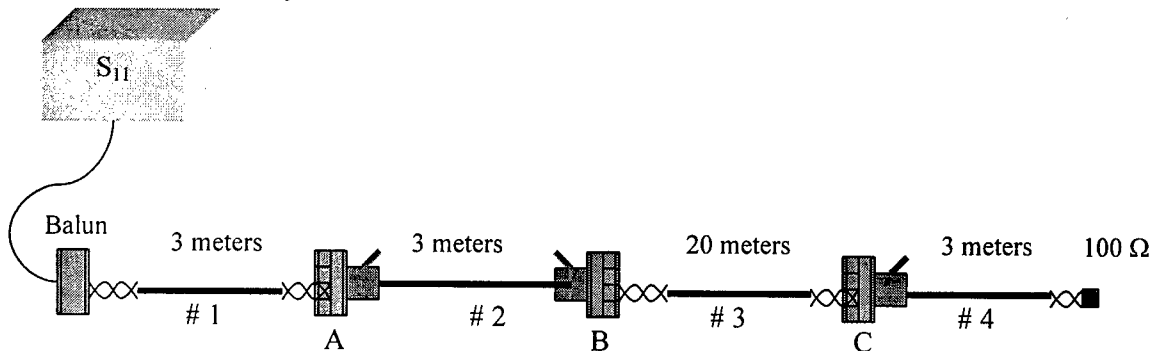


Figure 6. Channel configuration

Connecting hardware test. The combination punchdown/RJ-45 hardware used in the channel testing was tested separately for return loss. The setup shown in figure 7 was used. The calibration reference plane was located at the balun terminals. The test plug pairs were terminated with 100 Ohm chip resistors which were attached with minimal pair lead length. Common mode terminations were used on the measurement end and all pairs were measured.

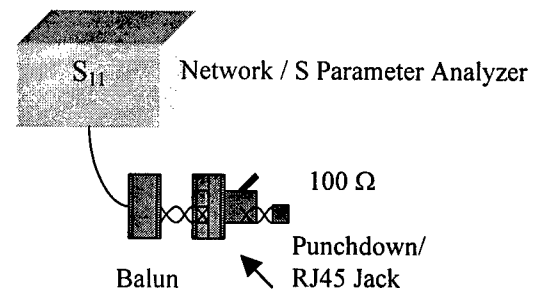


Figure 7. Connecting hardware return loss setup

RL TEST PROGRAM RESULTS

Patch cable and cord results. Figures 8-11 summarize the RL variation for design x and o. Results are shown for uncycled and cycled RL performance according to steps b,c. Only results for the green pair (split pair) are presented

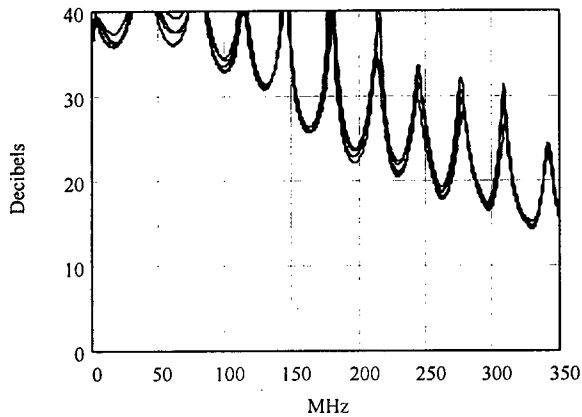


Figure 8. Cord RL variation, design x

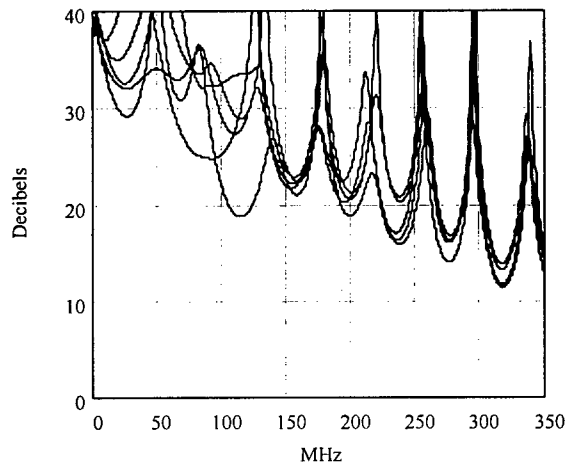


Figure 9. Cord RL variation, design o

Connecting hardware RL test results. The real and imaginary components of the reflection coefficient are plotted in figure 12. The green pair connection is seen to have significantly larger components than the other connections.

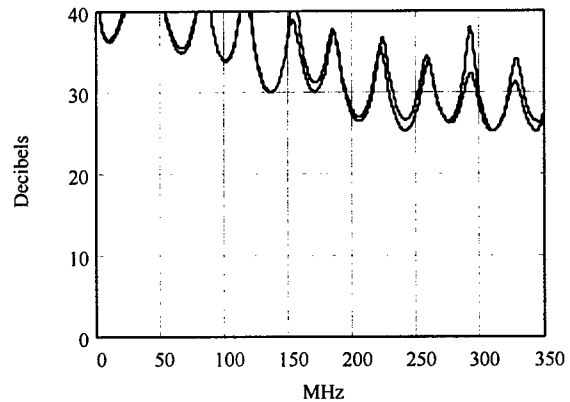


Figure 10. Cable RL variation, design x

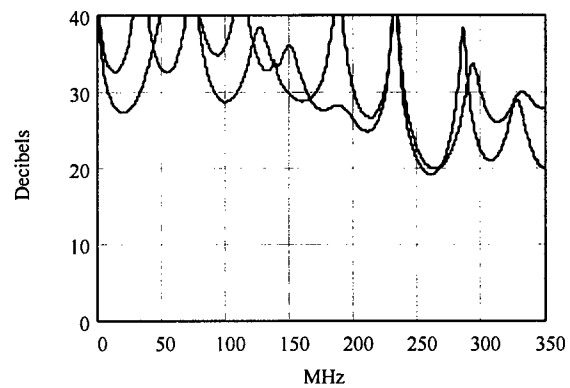


Figure 11. Cable RL variation, design o

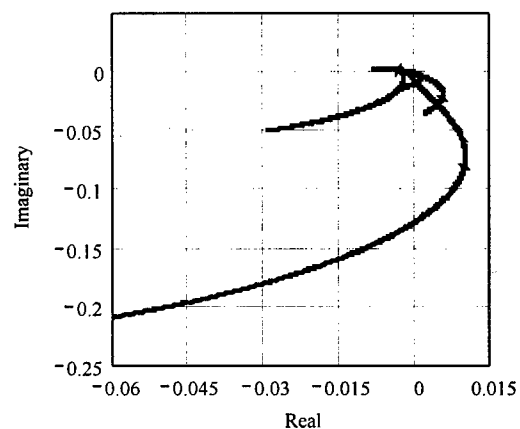


Figure 12. Connecting hardware real and imaginary components of the reflection coefficient

Channel RL test results. Figures 13, 14, and 15 summarize the channel performance for designs x and o corresponding to reference numbers 2 and 7. In this configuration the cycling occurs to the cable nearest the measurement end and consequently has a stronger effect than cycling farther into the channel. Figures 13 and 14 indicate performance for the green pair and figure 15 is for the orange pair.

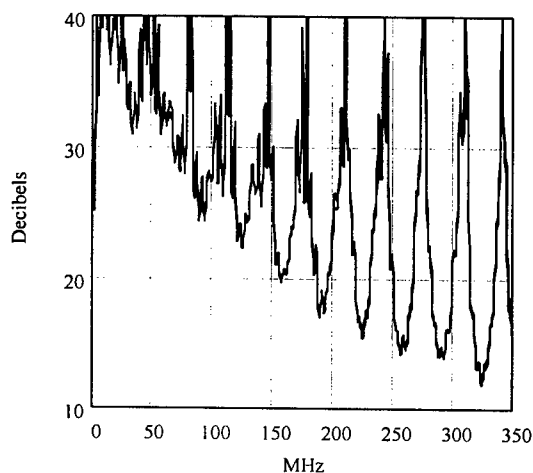


Figure 13. Channel RL variation for design x

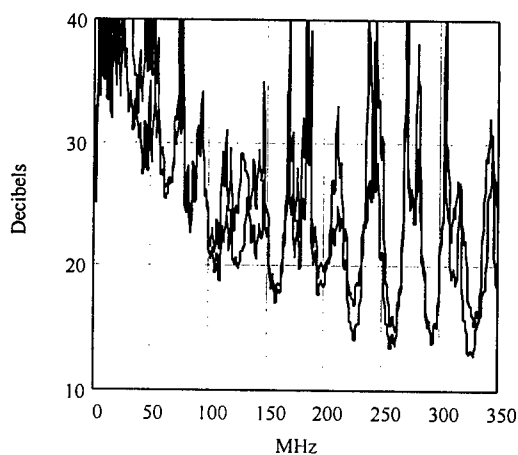


Figure 14. Channel RL variation for design o

Performance corresponding to reference numbers 5 and 13 are shown in figures 16, and 17 respectively. This configuration corresponds to cycling for each of the patch cord segments.

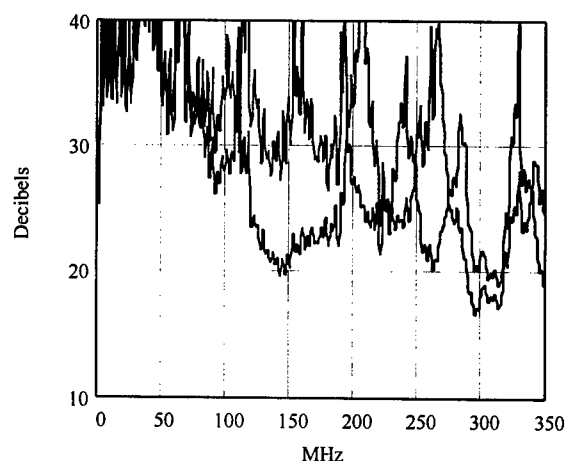


Figure 15. Channel RL variation, design o

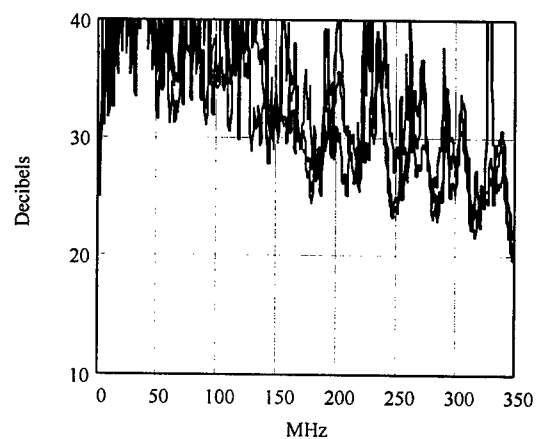


Figure 16. Channel RL variation, design x

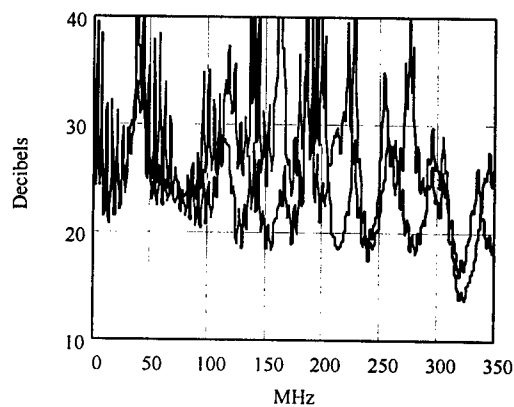


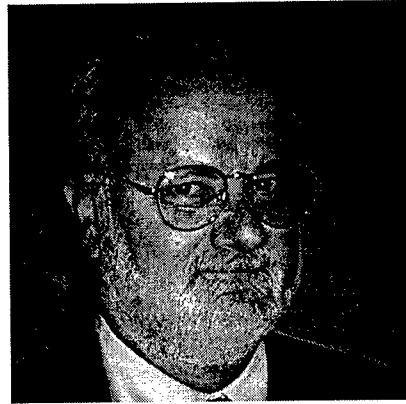
Figure 17. Channel RL variation, design o

CONCLUSION

Return loss variation with mechanical cycling of patch cables has been related to the possible movement of elements within the cable core. Conductor to conductor spacing variation and virtual reference surface movement have been related to changes in capacitance and inductance which in turn lead to variation in local characteristic impedance. Empirically it has been shown that bonding of the pair conductors together significantly reduces the return loss variation that may occur in patch cordage and channel applications. Mechanical cycling test procedures appear to successfully identify cable constructions which may exhibit excess return loss variation.

REFERENCES

1. *Commercial Building Telecommunications Cabling Standard*, TIA/EIA-568A-1995 and addenda in process of standardization.
2. TIA TR41.8.1 contribution on Patch Cord RL variation ,1999, J. Sciacero, MicroTest Inc.
3. H. Hughes, *Telecommunications Cables Design, Manufacture and Installation*, John Wiley & Sons, 1997



John Kincaid

John is a Senior Product Engineer at the Belden Engineering Center. He holds BSEE and MSEE degrees from the University of Oklahoma and has over 25 years experience with Belden. His experience encompasses engineering management and product development positions in the USA as well as in Europe. He holds nine patents. John is active in IEC and TIA cable standardization activities. He is the US Technical Advisor to IEC SC 46A on coaxial cables, and is Convenor of IEC SC 46A/WG3 on data and CATV cable. He is an expert on working groups 5 and 7 dealing with shielding and premises cabling issues.

(PO Box 1980; Richmond, IN, 47375)

TELECOMMUNICATIONS CONNECTING HARDWARE: SOLVING THE PERFORMANCE VALIDATION PUZZLE

Valerie Rybinski and Sterling Vaden

The Siemon Company, Watertown, Connecticut
Superior Modular Products, Swannanoa, North Carolina

ABSTRACT

Balanced twisted-pair telecommunications connecting hardware designs are engineered to satisfy the requirements of ANSI/TIA/EIA-568-A¹ and ISO/IEC 11801². Until recently, the most stringent transmission performance characterization had been defined in the frequency bandwidth of 1 to 100 MHz. However, as development progresses in the specification of telecommunications systems capable of supporting frequency bandwidths up to 250 MHz, standards bodies are finding that the existing qualification test methods are no longer sufficient to ensure consistent component performance validation. As a result, the specification of a test method that will ensure worst case performance characterization, backward compatibility with components of lower rated categories, and product interoperability between manufacturers has become a focal issue within the standards groups.

STANDARDS REQUIREMENTS

The ANSI/TIA/EIA-568-A and ISO/IEC 11801 commercial building telecommunications cabling standards specify laboratory methods for the validation of voice (category 3) and data grade (category 5) connecting hardware transmission performance. Requirements for higher bandwidth cabling grades (i.e. proposed category 6 and 7) are under development within the working groups of both TIA and ISO. Note that, although the Telecommunications Industry Association (TIA) and International Standards Organization (ISO) are not the only telecommunications standards governing bodies, they have the most significant impact upon telecommunications infrastructure design in North America. Table 1 shows the frequency range for which TIA and ISO categories of

connecting hardware are applicable. With a few minor exceptions, the TIA and ISO requirements for categories 3, 5, and 6 are well harmonized.

TABLE 1

TIA and ISO Bandwidths Specifications for Categories of Connecting Hardware

Category 3	1 - 16 MHz
Category 4*	1 - 20 MHz
Category 5	1 - 100 MHz
Category 5e	1 - 100 MHz
Category 6	1 - 250 MHz
Category 7**	1 - 600 MHz
* Category 4 is specified by TIA only. ** Category 7 is under development by ISO only.	

TIA and ISO specify transmission performance in terms of maximum attenuation and minimum return loss, near-end crosstalk loss, and far-end crosstalk loss to ensure that cabling components will support a given performance bandwidth. Table 2 provides a summary of applicable transmission performance parameters and their importance in relation to the implementation of high-speed data applications.

TABLE 2

Transmission Performance Parameters

<u>Attenuation</u> describes the drop or loss in signal power across the length of a transmission line. Maintaining low attenuation ensures that signal strengths will be high.
<u>Crosstalk</u> is undesired signal coupling from one pair to another. Too much crosstalk can result in increased bit error rates and/or undeliverable signal packets.
<u>Near-end Crosstalk (NEXT)</u> is crosstalk measured at the transmitter end of the cabling.

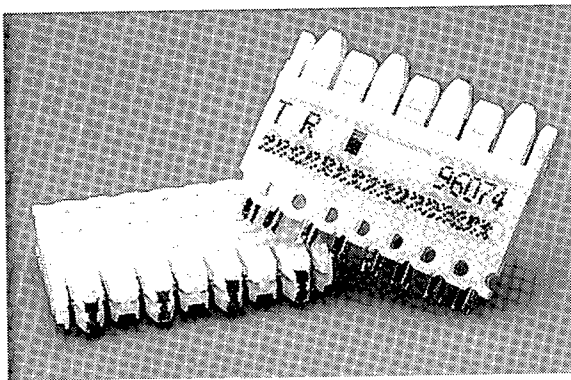
Far-end Crosstalk (FEXT) is crosstalk measured at the receiver end of cabling from a source at the transmitter end.

Return Loss is a measure of signal reflection that occurs along a transmission line and is related to impedance mismatches along the transmission line. Poor return loss can cause increased transmission errors, especially in applications that utilize full duplex encoding schemes.

CONNECTING HARDWARE STYLES

The most common types of connecting hardware recognized for telecommunications cabling are the insulation displacement connector (IDC) and the eight-position modular plug and jack outlet. An example of an IDC style connector is the 110 "punch down" block shown in figure 1.

FIGURE 1
IDC-Style 110 Connecting Block

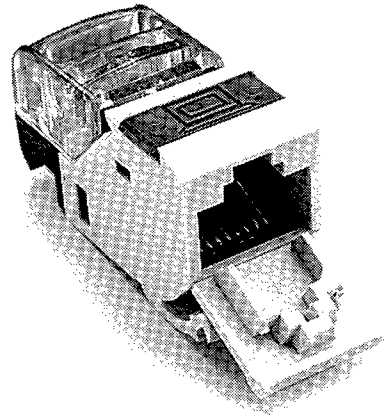


An example of an eight-position modular outlet connector is shown in figure 2. Note that most eight position modular outlets incorporate IDC style contacts for the purpose of terminating to the horizontal cabling.

Of these connector styles, both the TIA and ISO standards mandate that only an eight-position modular outlet may be used at the work area interface in a cabling system.

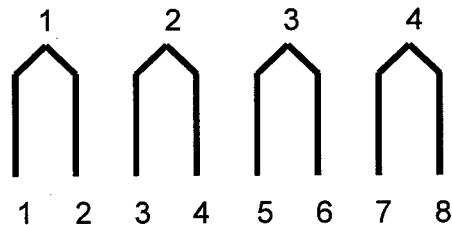
The designs of IDC connectors rely on fixed metal contacts to provide termination in a sequential manner as shown in figure 3. The IDC contact provides a "straight-through" connection. As a result, standards groups are not faced with a significant challenge in the specification of high frequency validation testing for these types of connectors since the

FIGURE 2
Typical Eight-Position Modular Outlet



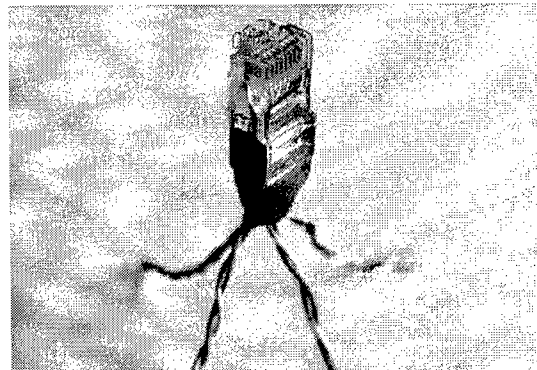
reference test leads are easily characterized and calibrated from the measurement.

FIGURE 3
Wiring Scheme for 4-Pair IDC Connector



Alternately, the transmission performance of an eight position modular jack interface must be evaluated when mated to an eight position modular test plug as shown in figure 4.

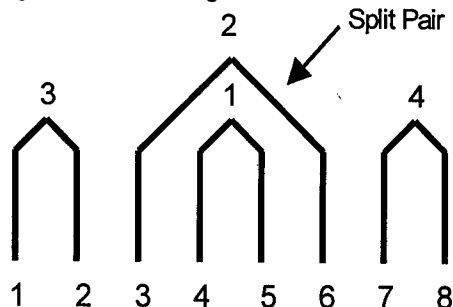
FIGURE 4
Eight Position Modular Test Plug



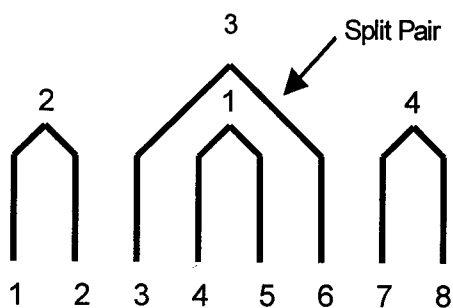
To further complicate matters, the standard wiring scheme of a modular eight position plug

incorporates a "split pair" into the termination scheme as shown in figure 5. Pair 2 is the split pair in a T568A wired modular outlet connector and pair 3 is the split pair in a T568B wired modular outlet connector.

FIGURE 5
Wiring Scheme for Eight-Position Connectors



T568A Wiring Scheme



T568B Wiring Scheme

Because balanced twisted-pair transmission relies on symmetry between the two conductors in each pair, any disturbance to the natural cable lay (such as splitting pairs when constructing a modular test plug) can adversely affect performance. In particular, separating or splitting the cable conductors in the plug termination process changes the inductive and capacitive relationship between the tip and ring conductors. One notable adverse effect of these disturbances is increased crosstalk. Other primary effects include increased signal reflections (return loss) and pair balance disturbance. More importantly, the magnitude of these effects is extremely difficult to control, even in a laboratory environment, because they are small and depend upon the exact conductor positioning.

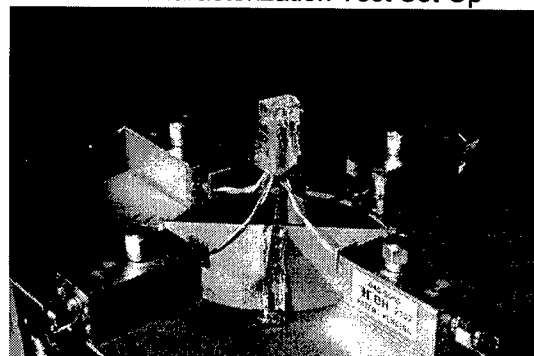
CATEGORY 5 AND LOWER TEST PLUGS

Historically, the typical eight position modular plug design supported category 3 applications.

As bandwidth requirements increased, the industry continued to support the same modular plug interface for higher categories of performance. The crosstalk contribution of the modular test plug was not a concern until the advent of category 5. Because category 5 requirements did not tolerate the amount of crosstalk present in the typical eight position plug design, modular outlet designs relied on an electrical circuit (typically incorporated into a printed circuit board) to compensate for the crosstalk of the plug. In order to validate worst case outlet performance, standards, for the first time, required modular test plugs to perform within a specified crosstalk range. This performance range provided a baseline against which manufacturers could test their modular connecting hardware and guarantee category 5 performance.

The category 5 test plug performance requirements rely on a simple characterization test referred to as the terminated open circuit or TOC method. Because of the difficulty in providing a matched load connection at the test plug contacts, the TOC method specifies 100 Ω load resistors to be applied at the output of the balun as shown in Figure 6.

FIGURE 6
TOC Characterization Test Set-Up



Currently, the TOC NEXT loss performance for the worst pair combination of a category 5 test plug, per Annex B.5.2 of '568-A and Annex A.3.1 of '11801, is specified between a lower range of 40 dB and an upper range of "greater than 41.5 dB". The advantage of the TOC method is that the procedure is relatively simple. One disadvantage is that, because current is not flowing through the length of the plug body, the method only quantifies the capacitive coupling mechanism within the test plug. Even so, the TOC test plug qualification method has been

considered sufficient for the characterization of category 5 and lower category modular outlets.

CATEGORY 6 TEST PLUGS

As development progresses in the specification of category 5e and category 6 component requirements, standards groups have found that compatibility with existing categories is no longer assured. As a result, the issue of specifying test methods that will ensure backward compatibility and product interoperability between manufacturers has gained prominence.

Backward compatibility implies that next generation cabling is not only superior to, but is also a superset of existing specifications. An electrical superset encompasses the total number of pairs supported and transmission performance. For example, four-pair category 5e and 6 cabling and components must meet or exceed all of the category 5 reliability and transmission requirements. Just as category 5 requirements are a superset of categories 3 and 4, category 5e and 6 components must at least be electrical supersets of category 5 to ensure that new standards will support all applications designed to operate over existing categories.

In particular, the concept of backward compatibility poses a dilemma for the specification of next generation connecting hardware. Because the same test plug criteria is applied to category 3, 4, and 5 connecting hardware, category 5 connectors are inherently compatible with lower category cabling. However, the precise degree of electrical compensation necessary to ensure compliance to the category 6 crosstalk (both NEXT and FEXT) requirements dictates that the electrical characteristics of the test plug be more completely specified than before. Obviously, to ensure that backward compatibility is maintained, the category 6 plug criteria must be a subset of the category 5 criteria (i.e. the category 6 performance range is a smaller range of the existing category 5 range). Furthermore, to ensure product interoperability, all manufacturers must be able to accurately assess test plug performance and design their products to deliver category 6 performance when mated to the specified range of test plugs. The challenge for standards groups is to develop a methodology that precisely characterizes both the real and imaginary

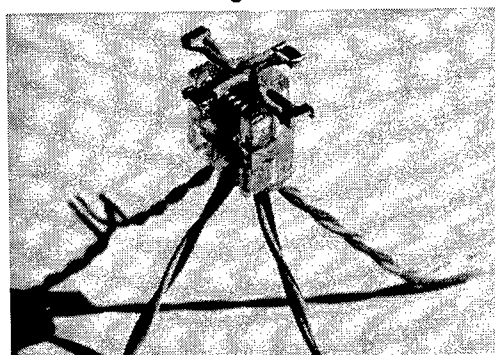
couplings of a test plug as completely as possible.

THE DE-EMBEDDING METHOD

Shortcomings known to be associated with the TOC method include the inability to characterize both inductive and capacitive coupling effects of the plug under test, which results in uncertainty in test plug characterization. Although not critical to the specification of plugs for validating category 3, 4, and 5 outlets, these shortcomings effectively disqualify the TOC method for use in category 6 outlet validation. The latest TIA research has led to agreement that a "de-embedded" plug characterization is the preferred test method for more completely specifying test plugs used to validate category 5e and 6 outlet performance.

The de-embedded NEXT loss test method specifies the construction of a reference jack that is characterized by its real and imaginary NEXT loss contributions. The measured reference jack NEXT loss values are then subtracted or "de-embedded" from a mated test plug/reference jack measurement. The result is a raw plug NEXT characterization that can be used to qualify (or disqualify) any plug for use in determining if specific outlet designs meet category 5e or 6 performance requirements. To characterize the reference jack, a de-embedding reference plug is constructed with test leads, terminated in precision 100 Ω resistor loads, extending through the front of the plug as shown in figure 7.

FIGURE 7
De-embedding Reference Plug

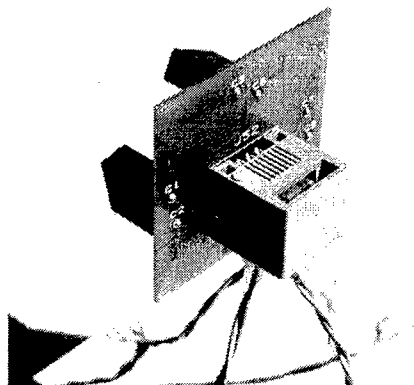


The crosstalk components of the de-embedding reference plug in Volts per Volt are recorded as NEXT_{ref_plug}.

The resistor loads are removed from the de-embedding reference plug and the plug is mated to a de-embedding reference jack as shown in figure 8. Note that the reference jack is terminated with 100 Ω resistor loads. The crosstalk components of the de-embedding reference plug mated to the reference jack, in Volts per Volt, are recorded as NEXT_{plug_jack}.

FIGURE 8

De-embedding Reference Plug mated to the De-embedding Reference Jack



The NEXT loss of the de-embedded reference jack (the "jack vector"), in Volts per Volt, is calculated using equation (1).

$$\text{NEXT}_{\text{ref_jack}} = (\text{NEXT}_{\text{plug_jack}} - \text{NEXT}_{\text{ref_plug}}) \text{ V/V} \quad (1)$$

Any test plug can be qualified by mating it to the de-embedding reference jack and recording the measured mated crosstalk (NEXT_{testplug_jack}). De-embedded test plug NEXT loss, in Volts per Volt, is calculated using equation (2).

$$\text{NEXT}_{\text{test_plug}} = (\text{NEXT}_{\text{testplug_jack}} - \text{NEXT}_{\text{ref_jack}}) \text{ V/V} \quad (2)$$

The logarithmic magnitude and phase of the de-embedded test plug NEXT loss is calculated using equation (3) and (4).

$$\text{NEXT}_{\text{mag}} = -20 \log \sqrt{\text{Re}_{\text{test_plug}}^2 + \text{Im}_{\text{test_plug}}^2} \text{ dB} \quad (3)$$

$$\text{NEXT}_{\text{phase}} = \tan^{-1} \left(\frac{\text{Im}_{\text{test_plug}}}{\text{Re}_{\text{test_plug}}} \right) \text{ degrees} \quad (4)$$

Note that the de-embedding calculations are approximations of the transmission matrix algebra, which neglect the effects of signal coupling due to reflections, attenuation, FEXT, and relative delay between the components in

the test. In order for the approximations to produce reasonably accurate results, these factors must be well controlled in the measurement set-up and reference devices.

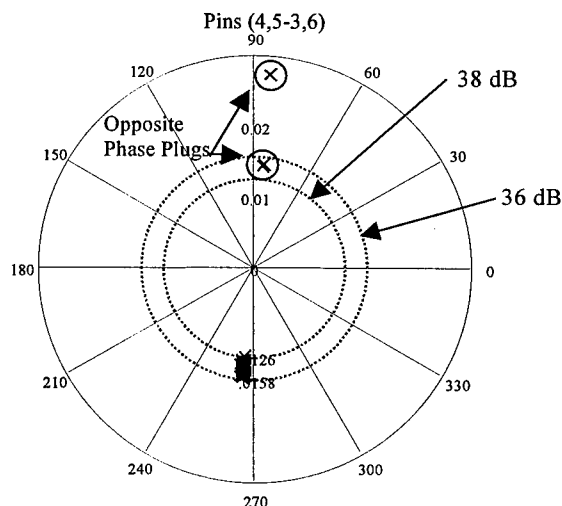
With some modifications to the reference test plugs and jacks, the de-embedding method can be applied similarly for the collection of test plug FEXT loss performance.

RESULTS

The most convenient method to assess NEXT loss performance for a sampling of test plugs is to plot de-embedded NEXT loss magnitude versus phase on a polar plot. Because of the positioning of the pair locations in both the T568A and T568B wiring schemes, each pair combination will tend to have its own de-embedded NEXT loss footprint, with symmetrical pairs tending to have symmetrical footprints. Because of the splitting of the conductors, the pairs terminated on pins 3,6 and 4,5 tend to have the worst NEXT loss performance. As a result, this pair combination is often subject to the most scrutiny. The polar plot in figure 9 depicts the de-embedded NEXT loss performance at 100 MHz for the split pair combination for a sampling of category 6 plugs.

FIGURE 9

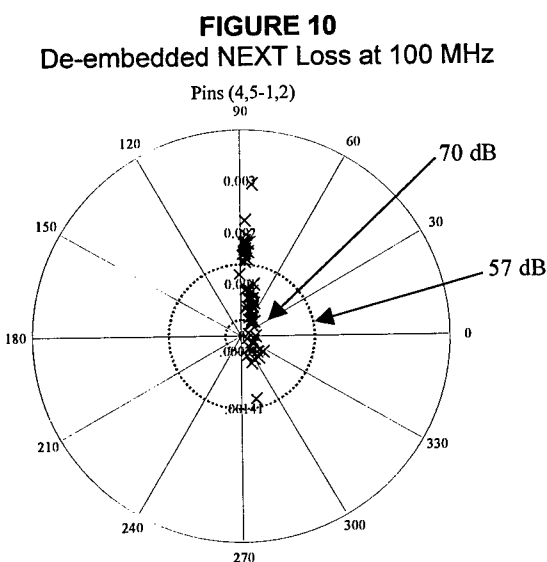
De-embedded NEXT at 100 MHz



Note the tight clustering of NEXT loss magnitudes in the approximate range of 36 to 38 dB and the consistent phase performance. This behavior is attributable to the fact that the capacitive coupling resulting from physically

splitting the conductor pairs is the dominant NEXT loss contributor. Also note that there are three plug samples in figure 9 that exhibit "upside-down phase". This shift is likely due to an error in the plug termination process and this phase variation would automatically disqualify these plugs for use in the validation of category 6 connecting hardware.

Secondary effects due to pair adjacency and differences in termination and physical location are the dominant coupling mechanisms for pair combinations other than the split pair. These other pair combinations exhibit a more random distribution of NEXT loss magnitude and phase as shown in figure 10. This polar plot depicts the de-embedded NEXT loss performance at 100 MHz for the pairs terminated on pins 1,2 and 4,5. Similar performance would be expected for the pairs terminated on pins 4,5 and 7,8 because of the wiring symmetry.



Note that the de-embedded NEXT loss magnitude is expected to be smallest and have the highest degree of phase variation for the outer pair combination terminated on pins 1,2 and 7,8. This is because the NEXT loss coupling function is almost entirely random in nature.

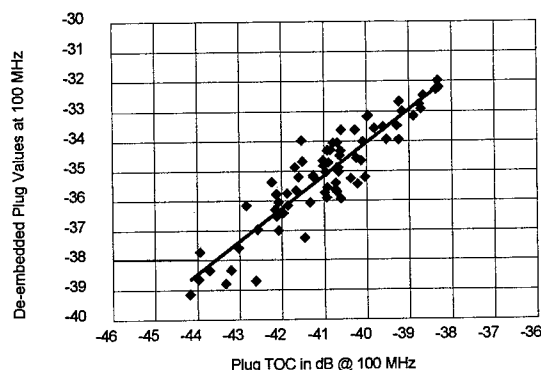
ESTABLISHING PERFORMANCE LIMITS

To ensure backward compatibility, the first step in establishing criteria for the qualification of test plugs used to assess category 6 performance is to determine the equivalent de-embedding NEXT loss to the existing category 5 TOC qualification criteria. This can be done by

plotting TOC versus de-embedded NEXT loss performance at a particular frequency of interest. A TOC versus de-embedded NEXT loss comparison plot for the pairs terminated on pins 4,5 and 3,6 is shown in figure 11.

FIGURE 11

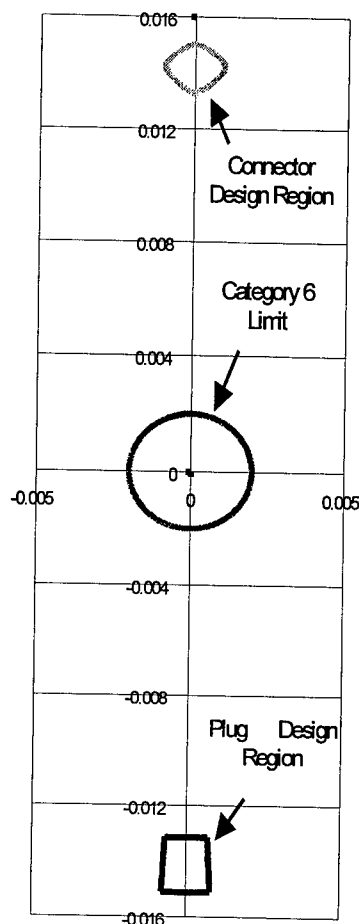
De-embedded Plug Data versus Measured Plug TOC on Pins 4,5-3,6



This data plot helps to identify a target de-embedded plug NEXT loss range of 34 to 38 dB for category 5. Because category 6 plugs are a subset of category 5, the category 6 de-embedded NEXT loss performance range will simply encompass a smaller region within the existing category 5 range. Once a target de-embedded range is established, statistical and vector evaluation techniques are used to hone in on a de-embedded plug range that is optimized for category 6 product compatibility. Plug performance ranges that are too stringent will result in a category 6 connector that is easy to design, but plugs will have unrealistic manufacturing tolerances. Plug ranges that are too lenient will mandate category 6 outlets with overly stringent design tolerances. Ideal plug qualification limits represent a compromise in that the manufacturing tolerances are shared equally between components.

The following example provides a statistical vector method for analyzing the combined test plug and connector NEXT loss performance contributions at 100 MHz for the pairs terminated on pins 4,5 and 3,6. Knowing that the proposed category 6 connecting hardware NEXT loss value is specified at 54 dB at 100 MHz³ provides a baseline for the vector evaluation technique. The first step is to plot the equivalent NEXT loss limit in Volts per Volt (.001995 V/V) on a polar chart as represented by the circle at the origin in figure 12.

FIGURE 12
Vector Evaluation of De-embedding Limits



Establishing a table for the entry of proposed de-embedded plug NEXT loss magnitude and phase entries will simplify the vector analysis process. A common sense approach combined with fine-tuning of the table entries will quickly enable assessment of the proposed test plug requirements. Table 3 presents optimized entries for the sample analysis on the pairs terminated on pins 4,5 and 3,6 at 100 MHz.

The target plug range, identified in Table 3 as having a NEXT loss magnitude of between 36.4 and 37.6 dB and a phase variance of $270 \pm 3^\circ$, appears in figure 12 as the trapezoidal outline in the lower region of the polar plot. The most critical values in the table are the difference between Re_{max} and Re_{min} and the difference between Im_{max} and Im_{min} . These values are calculated based upon the test plug range and represent the minimum and maximum values of the resulting category 6 connector design region. The connector design region for this

sample appears in figure 12 as the diamond outline in the upper region of the plot.

TABLE 3
De-embedded NEXT Loss Analysis

	Standard	Plug		
nits	R_o	R_{min}	R_{max}	$R_{max}-R_{min}$
dB	-54	-37.6	-36.4	-54.19
V/V	0.001995	0.013183	0.015136	0.001953

	Φ_{min}	Φ_{max}
Deg	267	273
Rad	4.660029	4.764749

Connector Variance

	$Re_{max} - Re_{min}$	$Im_{max} - Im_{min}$
V/V	0.00203021	0.001755831
dB	-53.85	-55.11

In specifying optimum de-embedded NEXT loss plug performance limits, there should be a balance between the size of the plug design range (the trapezoidal figure) and the connector design range (the diamond figure). This will ensure optimum allowance for variability in both the connector manufacturing process and the plug termination process. It has been suggested that a 58 dB value for the Im_{max} and Im_{min} difference is the limit of manufacturability in terms of printed circuit board techniques.

The statistical vector analysis method can be applied to any pair combination and any category of modular jack performance to develop optimum de-embedded NEXT loss criteria.

ONGOING RESEARCH

Although straightforward in theory, the de-embedding technique is complex in that the methodology requires precisely constructed measurement references and fixturing to ensure accurate jack vector calculations. Category 6 measurement difficulty is further compounded by the complexities of maintaining accuracy and measurement linearity beyond 100 MHz. One method to reduce complexity and increase consistency between test laboratories is to standardize on a singular jack design and its associated jack vector.

At this time, the qualification of other transmission parameters, such as FEXT loss and return loss, are being studied to determine their effect on test plug characterization. In the event that FEXT loss measurements are

needed, the de-embedded method can still be utilized, but may require a separate set of reference plugs.

Industry experts are also evaluating alternative methods of ascertaining plug NEXT loss and FEXT loss contributions. A variation of the de-embedding method, specifying requirements of the de-embedded performance of the test jack itself may hold promise. Another alternate method involves calculating crosstalk contributions from open and short circuit plug measurements (the TOC/TSC method). Although the theory is valid, the difficulty in specifying a true open and a true short at frequencies up to 250 MHz is likely to increase measurement uncertainty. Other methods that have been under study make use of alternative measurement approaches, such as modal decomposition network analysis, which utilizes matrix manipulation of balun-less measurements.

STANDARDS UPDATE

The TIA and ISO standards groups have made significant progress on the characterization and specification of next generation cabling and components. At this time, the proposed industry performance parameters for category 6 components and cabling are unlikely to endure major revisions. The ongoing emphasis of the task group committees is to specify laboratory and field qualification procedures, such as the de-embedded test methodology, that are suitable for extended bandwidth testing.

CONCLUSION

The de-embedded qualification technique results in more complete test plug NEXT loss characterization, improved measurement accuracy, and better repeatability between laboratory facilities when compared to previously adopted test methods. As a result, the de-embedded algorithm is a logical step forward in the specification of test methods for the validation of category 5e and category 6 connecting hardware performance.

REFERENCES

- [1] ANSI/TIA/EIA-568-A, Telecommunications Industry Association Standard, "Commercial Building Telecommunications Cabling

Standard", 1995.

- [2] ISO/IEC 11801, "Information Technology - Generic Cabling for Customer Premises", 1995.
- [3] TIA TR-42.7 Copper Cabling Systems Subcommittee Working Draft, "Transmission Performance Specifications for 4-Pair 100 Ω Category 6 Cabling", May 26, 1999.

AUTHORS

Valerie Rybinski received the B.S.E.E. degree from the University of Connecticut in 1991. Valerie is a senior electrical engineer at the Siemon Company in Watertown, CT. Her research activity is mainly in the field of balanced twisted-pair telecommunications cabling and connecting hardware.



Sterling Vaden received his BSEL degree from California Polytechnic State University in 1982. He has 15 years experience in the design of electronic connectors and holds several key patents in crosstalk reduction methods. He is currently Vice President of R&D for Superior Modular Products.

OPTICAL FIBER AND BALANCED CABLING LINKS -- THE PERFECT BASIS FOR FUTURE PROOFED GIGABIT LANs --

Stefan Mohr and Josef H. Kosilek

SIEMENS AG, Munich, Germany

ABSTRACT

Since the start of computer networking the discussion about 'the best' structure of generic cabling to provide the infrastructure for all kind of communication in telephony and data never stops. In many cases the exact definition of the criteria 'the best one' is not discussed very clearly or the opinions are very opposite. This paper describes in a technical and economic point of view the advantages of different structures and different types of generic cabling systems. Seen from the angle of today's networking and estimating the recommendations of future high data rate transmission systems there are clear clues to consider the pros and cons of different structures of generic cabling for LANs: complete optical fiber cabling systems or mixed media cabling systems with low-end or high-end balanced cabling up to the desktop of the user.

INTRODUCTION

Triggered by the rapid development in data processing and networking balanced cabling systems have worldwide established themselves for horizontal cabling subsystem of customer premises up to a frequency of 100 MHz. The technical requirements of these balanced cabling systems are defined in the standards EN 50173 and ISO/IEC IS 11801 /1, 3/. Thus, today it is possible to use balanced cabling systems very cost-effective for high bit rate data transmission like ATM (TP-PMD) with 155 Mbit/s and 100Base-TX with 100 Mbit/s from the switch in the distributor up to the workstation on the desktop of the user.

During the last two years a new motion comes into the discussion of customer premises cabling:

First, there is no doubt that the performance of data processing units will further grow so data rates of 1 Gbit/s will be required in the near future. Gigabit Ethernet is the answer to these requirements and seems to remain the most common transmission protocol to support high-end applications using a data rate of 1 Gbit/s at the workstation up to the desktop. Second, optical fiber cabling becomes more and more competitive caused by further development, decreasing costs and grown acceptance of use. Third, even the development of balanced copper cabling makes great strides too. Specifications up to 250 MHz and 600 MHz will be defined in the second edition of the cabling standards, hard to imagine five years ago /2, 4/.

All these facts provide restlessness while planning and installing structured cabling for future proofed Gigabit LANs. This paper will try to answer the questions being in the air. Among the structure of cabling the new characteristics of cabling and cabling components being established today by the requirements of the transmission systems and discussed by the standard bodies will be assessed from an European point of view.

MIXED MEDIA CABLING SYSTEMS

Structure

The concept of generic cabling was developed to provide to the customer a vendor independent way to interconnect his networking equipment, from simple data terminals and telephones connected to public switches to high-end workstations connected to powerful switches and routers. The most relevant standards for generic

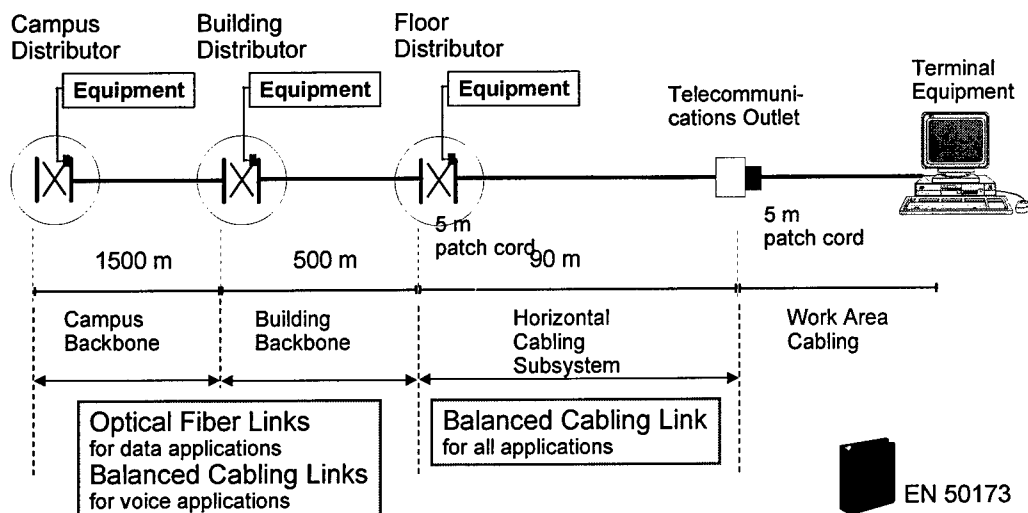


Figure 1 Structure of the generic cabling. Maximum distances and recommended media types.

cabling, EN 50173 and ISO/IEC IS 11801 have defined different subsystems and associated minimum performance.

The subsystems of a structured and generic cabling system are:

1. functional elements such as distributors and equipment rooms
2. the campus backbone cabling
3. the building backbone cabling
4. the horizontal cabling
5. outlets and work area components.

Today the European cabling standard EN 50173 recommends the use of optical fiber cabling in the campus backbone and building backbone subsystems of the generic cabling, see figure 1. In the horizontal cabling subsystem at least one telecommunications outlet shall be supported by 100 Ω balanced cable. Usually then the whole of the horizontal cabling subsystem is equipped with copper technology.

Campus Backbone Cabling

The continued success of Ethernet is due in large part to its installed base, scalability, ease of migration, low inherent cost and minimal increase of learning new technologies. Gigabit Ethernet links will quickly find their way into the backbone to relieve the bandwidth strain caused by the influx of high performance workstations equipped with 100 Mbps adapters. The shift in LAN traffic caused by the growth of corporate intranets and the migration to higher speed networks will place more demand on higher band-

width and faster switching. To be prepared for this next step of networking IEEE started to think about 10 Gbps Ethernet [7].

A few years ago many believed ATM would become the LAN protocol of choice. Many reasons can be attributed to ATM's lack of success. The primary reasons are cost, interoperability problems and integration difficulties between ATM and legacy networks and finally the switching technology is making Ethernet LANs more powerful, too.

Nevertheless the ATM protocol is capable of integrating voice, video, and data over a single network, while at the same time providing a scaleable, reliable and flexible solution. Various bit rates are available from 51 Mbps to 10 Gbps. In addition to high speed, ATM's extensive quality-of-service features are able to simultaneously handle a wide range of network traffic including constant bit rate, variable bit rate and available bit rate. The advanced features of ATM give it the ability to continuously monitor and control the flow of network traffic.

The main advantage of ATM is that it can be used to link the LAN, campus backbone, and WAN, thereby greatly simplifying corporate network architectures. Large meshed networks without any routing and many redundant paths can be build up to the workstations in ATM technology. However, if it is not feasible to implement a single protocol solution, ATM can coexist with legacy LANs such as Ethernet to connect the

workstations by implementing the ATM LAN Emulation /5/.

Gigabit Ethernet with 1 or 10 Gbps and ATM with up to 10 Gbps will be the future transmission protocols for network backbones almost independent of the network if it is in the middle range or world wide range. If the link lengths of the network backbone achieve 300 m **single-mode fiber** shall be the choice of the transmission media. For smaller networks and if there is no redundancy required the structure shall be in star topology, better and for larger networks recommended is the mashed structure of single-mode fiber cabling with as many as possible dark fibers for future network growth.

In conclusion, it is apparent that there are many driving forces drastically impacting data networking and forever changing the manner in which global companies operate. The network must be prepared today for tomorrow's high-speed bandwidth intensive applications that will put extreme demands on the corporate enterprise's ability to operate reliably and seamlessly in the business landscape to come. The corporate cabling infrastructure is the central nervous system of any business and must be kept healthy.

Building Backbone Cabling

As if in the concept of campus backbone cabling the same transmission and network technology

can be taken into consideration. The structure of the building backbone cabling shall be in star topology if redundancy is required a double star with different path is recommended. If the link lengths of the building backbone achieve 300 m **singlemode fiber** shall be the choice of the transmission media.

For smaller networks **multimode fibers** can be a good choice. To compensate the lower bandwidth of these fibers the IT manager should plan as many as possible dark fibers for future network growth and future bandwidth-hungry applications. There are two multimode fibers in the range. One is a 62,5 μm product that guarantees for example Gigabit Ethernet speeds across links up to 275 m at a wavelength of 850 nm and across 550 m links at 1300 nm. The fiber is designed for vertical building backbones and data-hungry fiber-to-the-desk applications like video-conferencing and computer-aided design (CAD). On the other hand is a 50 μm fiber that ensures link length up to 550 m in both the 850 nm and the 1300 nm transmission window.

The link lengths listed here correspond to the bandwidth limits for multimode optical fibers of 200 MHz \cdot km and 500 MHz \cdot km at 850 nm for 62,5 μm respectively 50 μm as required by EN50173(2000) and ISO/IEC 11801(2nd Edition). For the first time the standards make difference between 50 $\mu\text{m}/125 \mu\text{m}$ and 62,5 $\mu\text{m}/125 \mu\text{m}$ multimode optical fibers and the double higher

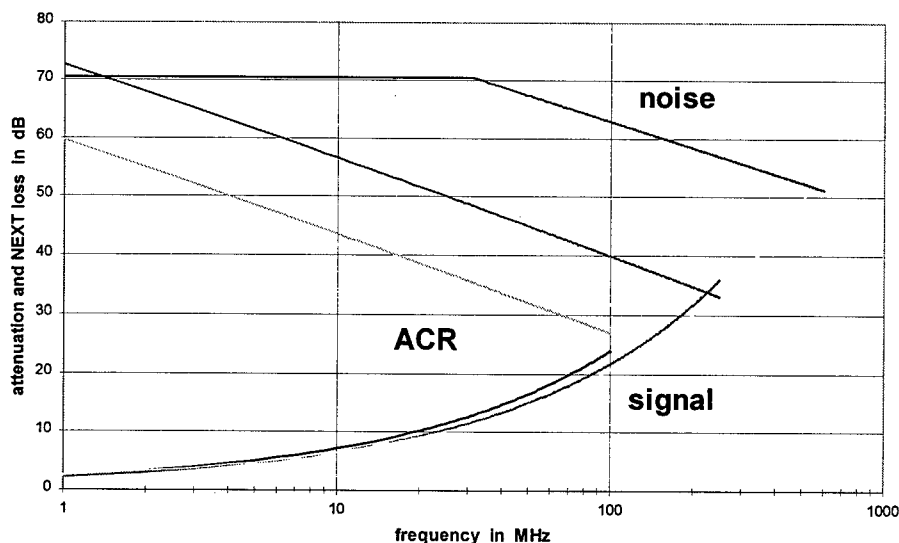


Figure 2 Electrical requirements attenuation and NEXT for balanced cabling channel class D (99), class E and class F.

bandwidth of 50 μ m/125 μ m multimode fiber is used by a transmission system. Nevertheless optical fibers are only specified at the wavelengths of 850 nm and 1300 nm, not yet at 980 nm. But the maximum bandwidth of multimode optical fibers lies between 850 nm and 1300 nm explaining the maximum link length in the range of the 980 nm wavelength. May be future applications will use this wavelength and increase the data rate up to 10 Gbps on **50 μ m multimode fiber**.

Horizontal Cabling

The mostly discussed subsystem of generic cabling is the horizontal cabling. During the last meetings of ISO/IEC and CENELEC working groups responsible for the cabling standards ISO/IEC IS 11801 and EN 50173 the next editions of these standards were discussed. Their publication is planned for the year 2000. The most attractive changes are the introduction of two new copper classes: class E and class F. So today three performance classes are available: class D (99), class E and class F, see figure 2.

For **class D (99)** the standard committees defined some new parameters required by Gigabit Ethernet. These are: PS NEXT, ELFEXT, PS ELFEXT. The specifications of Attenuation, NEXT, Return Loss were intensified /8/.

Class E is specified up to 250 MHz and will show the highest performance feasible with unshielded cabling /9/. Class E should be backwards compatible with class D, the modular jack interface shall be maintained at the work area, and category 6 components must be mechanically and electrically backwards compatible. If the components (i.e. plugs and jacks at the outlets) are able to be mixed, the mated combination shall at least meet the transmission requirements of the lower performing component. Class E gives a significant performance gain at least twice the usable bandwidth of class D channels (similar ACR at 200 MHz as class D at 100 MHz). Further arguments for class E balanced cabling links are low incremental installation costs, meanwhile standard components and systems and the possibility of verifying performance in the field. In western Europe 50% of cabling are specified up to 200 MHz or higher so there is an installed base too. Problems only force the missing interoperability between products of different vendors.

Class F is specified up to 600 MHz and these balanced cabling links are based on high-end screened S/STP cables /10/. Class F gives a significant performance gain at least twice the usable bandwidth of class E channels (similar ACR at 600 MHz as class E at 250 MHz). Since June of this year two category 7 connectors are specified making available the very high transmission performance on four pairs.

Which class is enough? That is the question to answer! Which performance will be needed in the future? Today in the age of 1 Gbps processors, the chicken and egg routine continues. Processing power ultimately drives innovation in user applications, specifically media-rich and collaborative functions. Transport technologies like switching and Gigabit Ethernet will likely catch on as the economic and sociological benefits of CAD/CAM, worldwide databases, distance learning and mediaconferencing are realized. If we consider that five years ago the high-end cabling choice was class D, when LAN data transmission rates were 10 and 16 Mbps, the additional capacity we built into our systems seemed more than adequate for the future.

Today this future has come. Gigabit Ethernet is reality and available on the market. Further we will see the promise of deploying even higher data rate technologies in the next five years as applications and processors address new creative and competitive business needs, and continue to consume more and more of the available bandwidth. So next generation cabling you would install shall meet the topology and not less than class D (99) performance as specified in EN50173 (2000) and ISO/IEC 11801/2nd Edition. This will guarantee the support of Gigabit Ethernet but without any additional capacity for future transmission systems.

Class E balanced cabling can be a cost-effective and future-proofing solution for your network. There is some additional capacity for new future transmission systems /7/. To guarantee performance, warranty and real value-add to the customer you need a total system solution from one vendor. The same applies to balanced cabling structures of class F. Here the additional bandwidth and capacity is enormous and data transmission systems with much more than 1 Gbps are conceivable /6/.

COMPLETE OPTICAL FIBER CABLING SYSTEMS

Till today, fiber optic cabling was considered as the primary media for campus and building backbones. But as applications demand for higher bandwidth, the question appears again to consider the extending of the fiber optic to the desktop as well. Optical fiber cabling becomes more and more competitive caused by further development, degreasing costs and grown acceptance of use. The reason for this change in the cabling philosophy are at one hand the introduction of new networking concepts (i.e. thin client) accompanied by a shift in the structure of the LAN traffic, and at the other hand the emergence of multimedia business applications. The spreading of fiber optic cables in the horizontal distribution was processed by a lot of technical and economical factors.

New products renew the acceptance on the market. New cables like break out cables, new tide buffer fibers and fiber ribbon solutions give the customer large advantages during installation. New optical connectors like MT-RJ are making the connection of optical fibers easier. The main features of these multi fiber connectors are high density, 2 or 4 fibers, small formfactors, guide pin concept and easy to install in combination with fiber ribbons.

Optical singlemode fibers have the largest bandwidth of all transmission media and offer the longest link lengths. Multimode fibers have almost the same bandwidth than category 7 balanced copper cables, but offer longer link lengths. This gives them much more flexibility in network design. Even with optical components the typical cabling system, which contains a wiring closet from where the horizontal cable has been deployed to the wall outlet, has migrated in the recent past to more efficient structures: centralized cabling approaches and fiber zone (open office) cabling.

With installed optical fibers all over the generic cabling structure of EN 50173 (figure 1), this means in the horizontal subsystem as well, a 1 Gbps transmission up to the desktop of the user is guaranteed in all circumstances. In this configuration the use of active components like hubs in the floor distributor is assumed. This structure has a favorable effect on using patch cords of any length in the work area up to the

workstation (open office environment). Also the maximum data rate supported by this cabling configuration is not limited to 1 Gbps. A maximum data rate transmission of about 5 Gbps will be possible in any cases. Requirements like lack of space, security aspects, EMC and an installation in manufacturing environment can easily be satisfied by complete optical fiber cabling systems, too.

However for the transmission of analogue telephone services or digital ISDN up to the desk top of the users, all cabling systems exclusively based on optical fiber need a balanced cabling system installed in the same area, at the same floor. The use of workstations for telephone services or private branch exchange equipment with optical interfaces can technically be realized but they are certainly not very common. New technology like voice-over-IP may change this very quickly. But the first system employed with legacy LANs, appearing on the market today, are not fully developed and can not be used as a simple telephone everybody is acquaint with.

An other point of view is the employment of active components, like hubs, switches or routers in the floor distributor. These components are more expensive when realized with optical interfaces than the same components with interfaces for balanced cable. This is the reason why complete optical fiber cabling systems installed in a centralized structure are very popular. These structures give optical fiber the chance to play off its main advantage, its flexibility.

Centralized campus-structure

The first kind of centralized cabling is already described in the European cabling standard EN 50173 and in the international standard ISO/IEC 11801 respectively. In this structure the campus backbone and the building backbone cabling build one transmission link, i.e. the two subsystems are connected with patch cords in a passive way exclusively and the active components in the building distributor can be cancelled. Thus homogeneous optical fiber links up to a length of 2 km can be constructed.

Deriving from the specifications mentioned before one can say that multimode optical fibers in the campus backbone cabling subsystem are not suitable for supporting high data rate transmission systems if maximum link lengths of

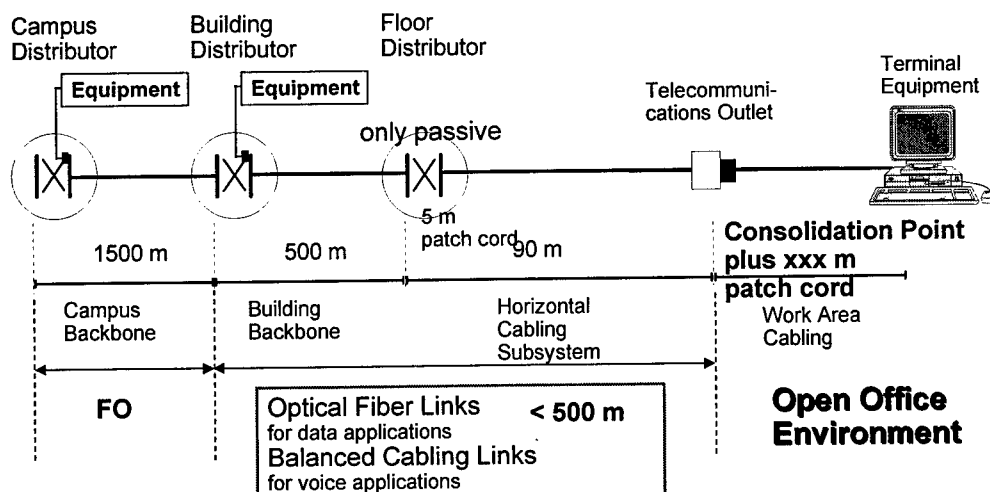


Figure 3 Structure of the generic cabling with centralized building-structure and open office cabling.

1,5 km or 2 km have to be guaranteed. Generally recommending only singlemode optical fibers should be installed in the campus backbone cabling subsystem. In this case even simple laser transmitters at a wavelength of 1300 nm guarantee a maximum link length of 10 km at data rates up to 1 Gbps.

Centralized building-structure

The construction of a centralized building-structure is shown in figure 3. Singlemode optical fibers are installed in the campus backbone cabling subsystem as mentioned before. The building backbone and the horizontal subsystem are combined to one transmission link, i.e. they are connected in a passive way exclusively and there are no active components in the floor distributor. In general this leads to a cost and administration reduction. Thus homogeneous optical fiber links up to a length of about 500 m can be constructed with 50 μ m multimode fibers. Today all LAN transmission systems based on multimode fibers support this link length in all circumstances. This is the reason why the cabling standards EN 50173 and ISO/IEC 11801 support this generic cabling structure in their 2nd Edition.

Full flexibility being as large as possible brings the combination of a centralized building-structure and a open office cabling. There are two possible strategies of open office cabling or fiber zone: a passive one with all optical equipment and an active one with electronic systems. The active design concept is an interesting mix between a collapsed backbone and a centralized

cabling scheme. Fiber zone cabling is a very effective way to bring fiber to a work area. It utilizes low-cost, copper-based electronics for Ethernet data communications, while providing a clear migration path to higher speed technologies.

Like centralized cabling, a fiber zone cabling scheme has one central distributor. Multimode fiber cables are deployed from this distributor to the work area. At the work area, the fiber cable is terminated in a multi-user outlet, and two of the fibers are connected to a workgroup hub. Connections between this hub and the workstations are made with long patch cords. In this concept, dark fibers provide a simple mechanism for adding user channels to the workgroup or for upgrading the workgroup to more advanced high-speed transmission system in an all optical way.

A centralized cabling structure design provides the same benefits as a collapsed backbone in active networks: condensed electronics and more efficient use of chassis and rack spaces. By providing one central location for all network electronics, maintenance is simplified, troubleshooting time reduced and security enhanced. Open office cabling is a cost-effective design that utilizes fiber in today's low-speed network while providing a simple migration strategy for tomorrow's high-speed connections.

CONCLUSION

The most flexible generic cabling system is the cabling with three separated subsystems as defined by ISO/IEC 11801 and EN 50173. This structure supports all possibilities for a physical and logical structuring of the network. One should install singlemode fibers in the campus backbone subsystem, multimode fibers in the building backbone subsystem and at least category 6 or high-end balanced cable in the horizontal subsystem of the generic cabling system. Meeting the requirements for very high flexibility this structure is the most cost-effective one, as well as active components have to be employed in all campus, building and floor distributors. Besides, in the horizontal cabling subsystem, the really biggest part of a generic cabling system, a homogenous transmission media can be installed. Thus, in the horizontal cabling subsystem up to the desktop of the user balanced cabling systems are able to support all common local area network transmission systems from analogue telephone, over low data rate services like ISDN and serial X.21 protocols, up to future high data rate Gigabit Ethernet with 1 Gbps or higher.

The construction of a Centralized Optical Fiber Cabling and/or optical links in the horizontal subsystem combined with the Open Office Cabling are second solutions being in an economic point of view the best one in some cases. Singlemode optical fibers are installed in the campus backbone cabling subsystem as mentioned before. The building backbone and the horizontal subsystem are combined to one transmission link, i.e. they are connected in a passive way exclusively and homogeneously equipped with 50 μ m multimode optical fibers of maximum combined link lengths of 500 m. There are no active components in the floor distributors and in general this leads to a cost and administration reduction. On condition that there is a well working telephone and data cabling infrastructure, i.e. category 5 cable, a multimode optical fiber cabling can be installed parallel as a high performance data cabling system in the same area. Alternative to the first solution employing balanced cabling, a Centralized Optical Fiber Cabling with 50 μ m multimode optical fiber systems is an equivalent solution if one will exclusively employ high data rate transmission systems like Fast or Gigabit

Ethernet with 100 Mbps respectively 1 Gbps up to the desktop of the user and using voice-over-IP for phoning and video-conferencing.

REFERENCES

- /1/ EN 50173: Information Technology - Generic Cabling Systems, 1995.
- /2/ Draft EN 50173 (2000), CLC TC 215, Dec. 1998.
- /3/ ISO/IEC IS 11801: Generic Cabling for Customer Premises, 1995.
- /4/ ISO/IEC 11801, Updated Draft Specifications for Class E and Class F, Cancun/WG3, Jan. 1999.
- /5/ 622 Mbps ATM transmission in balanced cabling networks, *S. Mohr et al.*, Proceedings of NOC'96, Heidelberg.
- /6/ 1 Gbps Data Transmission via Balanced Cabling: Measurement Results and Trends, *D. Schickelanz, A. Oehler*, Proceedings of NOC'98, Manchester.
- /7/ IEEE 802.3 Study Group TR 45.5.
- /8/ Development of Equal Level Far-End Crosstalk (ELFEXT) and Return Loss Specifications for Gigabit Ethernet Operation On Category 5 Copper Cabling, *C.T. Di Minico, P. Kish*, Proceedings of 47th IWCS, Philadelphia.
- /9/ Power Sum, Integral Power Sum and Vector Sum-Crosstalk, *M. Belanger et al.*, Proceedings of 47th IWCS, Philadelphia.
- /10/ High Grade Copper Data Cables and Connecting Hardware for Generic Cabling, *H. Haag et al.*, Proceedings of 47th IWCS, Philadelphia.

BIOGRAPHY

Stefan Mohr received his Diploma in Electrical Engineering in 1989 at the Technical University of Kaiserslautern working on coding schemes for noisy transmissions. In 1993 he obtained a Doctor's degree at the same university. He work on the characterization of optical fibers. He joined SIEMENS AG in the research and development department in 1993. Now he is working for the communication cables business unit responsible for generic cabling and hardware design.

Cabling Concept for Multimedia-Applications or Cabling for Multimedia

Does copper solve it all?

Karl Lesten - Jörg Bör

Kerpenwerk GmbH & Co., Stolberg, Germany

ABSTRACT

Nowadays, we are commonly used to the fact that a different cable design is used for the realisation of each individual communication service. There are telephone cables, data cables and coaxial cables for the transmission of TV-signals.

The principle of "structured cabling" represents the idea to do it all in one. One cable design for all communication services.

New cable designs with individual screened pairs according to Cat.7 draft ISO/IEC 11801 /2nd issue (600 MHz) together with new types of connectors open up new possibilities.

STANDARDISED STRUCTURAL CABLING

Today's cabling is based on actual standards as ISO/IEC11801. The preferred topology is star-designed. The cabling structure is divided into the three parts campus (backbone), riser and horizontal. In the backbone are often used fibre optics, the horizontal cabling almost is designed in copper.

Realising such a structured cabling concept with UTP Cat.5 (5e) cables according to ISO/IEC 11801 (100 MHz) and UTP Cat.6 according to the draft ISO/IEC 11801 /2nd ed. (200 MHz) together with RJ45 connectivity still means separate cabling for each multimedia-service such as telephone, data, TV. The reasons are as follows: Cat.5 cables and Cat.6 cables are not

able to do cable sharing. These cables are limited in bandwidth performance to 100 MHz and 200 MHz resp. Therefore, to reach the required frequencies for both, high data rated communication and TV signals, it is necessary to use additional transforming electronics able to reduce frequency by means of coding or multiplex.

Connecting high quality STP-cables with a standard RJ45, the great advantages of pair shielding can not be achieved by the cabling. The problems resulting from the connecting hardware are

- low return loss caused by reflections from the deviating impedance of the connector
- low near end crosstalk caused by the broken pair shielding in the connector

So a system consisting of horizontal cable, connecting hardware and connector cords was to develop, which is individually shielded over the entire length and where all components have the same impedance.

CABLES AND CONNECTORS

To reach minimum requirements according to ISO/IEC 11801 / 2nd ed. (600 MHz) it is obligatory to use individually screened pairs. This cable construction makes large bandwidths (up to 1000 MHz and even more) possible.

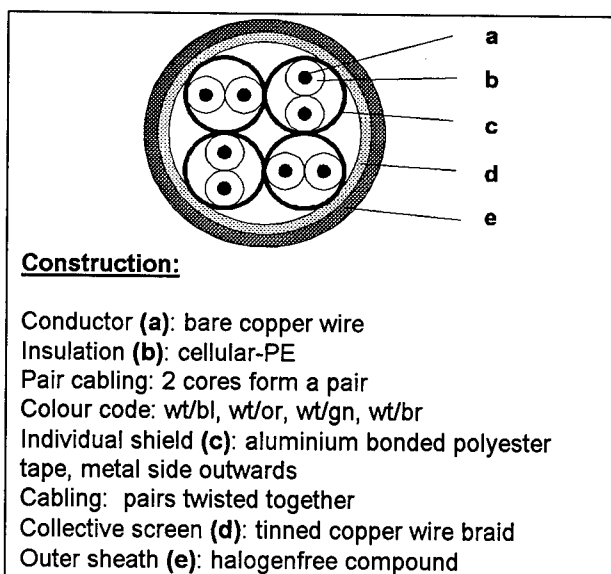


Fig. 1:
4-Pair-Cable

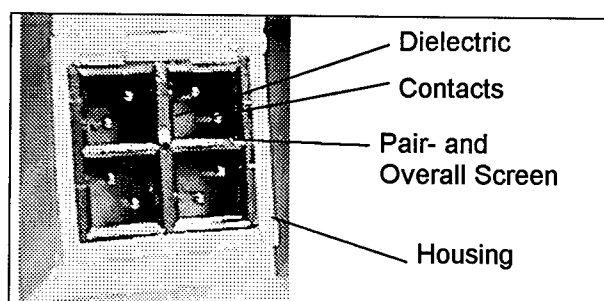


Fig. 2:
4-Pair-Connector

The individual screen (pair) and the overall screen (housing), the design (dielectric material) and the dimensions all together result in an excellent impedance of 100 ohm. If combined with an individually screened cable, most excellent transmission characteristics are achieved (impedance, attenuation, NEXT, PS-NEXT, ACR, EMC etc.)

This sophisticated technology allows the transmission of high data rates at high frequencies without additional electronics. Coding, decoding, modulation and demodulation are significantly reduced.

Pair screened connector cables with single-pair-plug, double-pair-plug and quad-pair-plug (each individually screened) complete the concept of cable- and connector sharing.

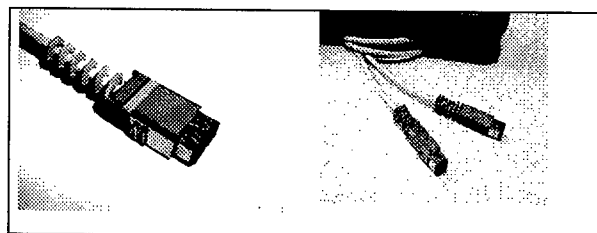


Fig. 3:
2-Pair-Connector and 1-Pair-Connectors

Structured Cabling according to Cat.7/ Class F, draft ISO/IEC 11801, 2nd ed. (600 MHz) means more than data transmission: Telephone-signals, TV-signals, Radio-signals, Audio-signals etc. are possible. The basic precondition to transmit all above mentioned signals at a max. length of 100 m is fulfilled.

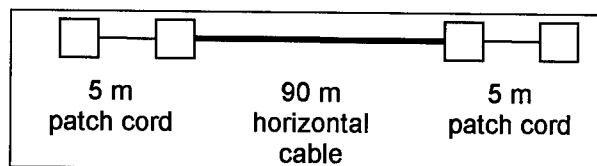


Fig. 4:
Transmission Channel

All UTP components (Cat.5 + Cat.6) including overall screened UTP components, (e.g. the RJ 45 modular plug) require separate cabling for each individual service. Neither cable- nor connector sharing is possible.

MULTIMEDIA APPLICATIONS

The multimedia idea (flexible usage of all four pairs in a cable) is based on the excellent electrical parameters of the individually screened components (cables and connectors) in a complete link. As examples the following figures show the attenuation, the near end crosstalk and the attenuation to crosstalk ratio of a channel link, designed with the system described above, measured up to a frequency of 1 GHz.

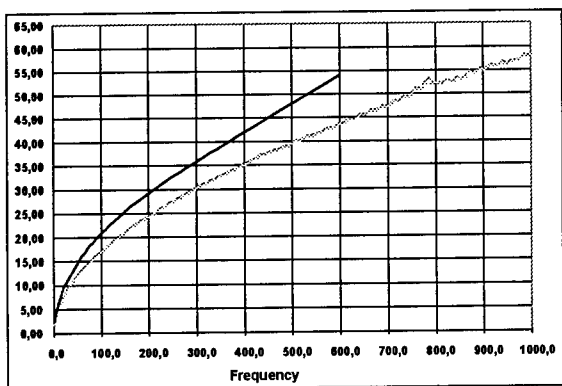


Fig. 5:
Attenuation of the Transmission Channel

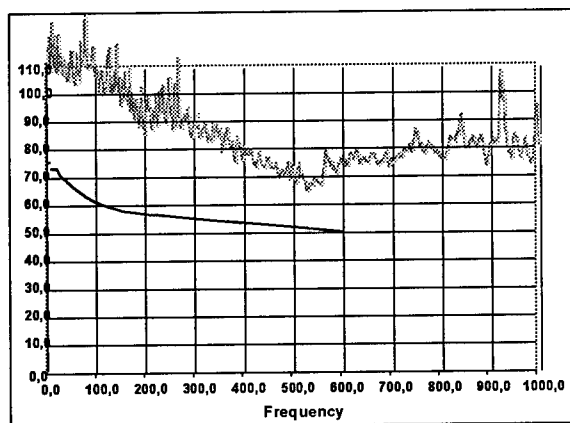


Fig. 6:
Near End Crosstalk of the Transmission Channel

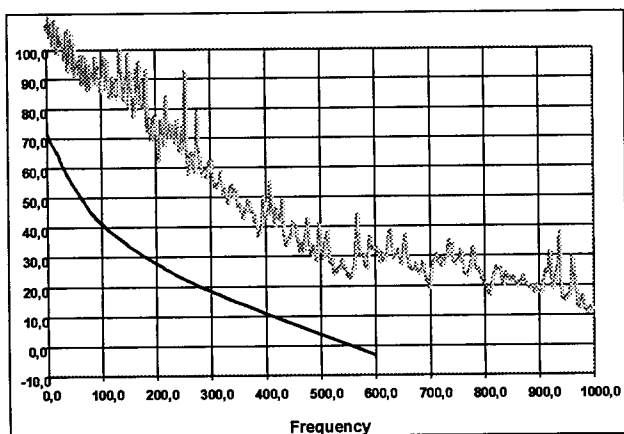


Fig. 7:
Different Applications running on individual pairs

Individual use of each ind. pair allows different applications to be realised from one port. Digital telephone signals need one pair. TV-signals also

need one pair. Data communication needs two or four pairs.

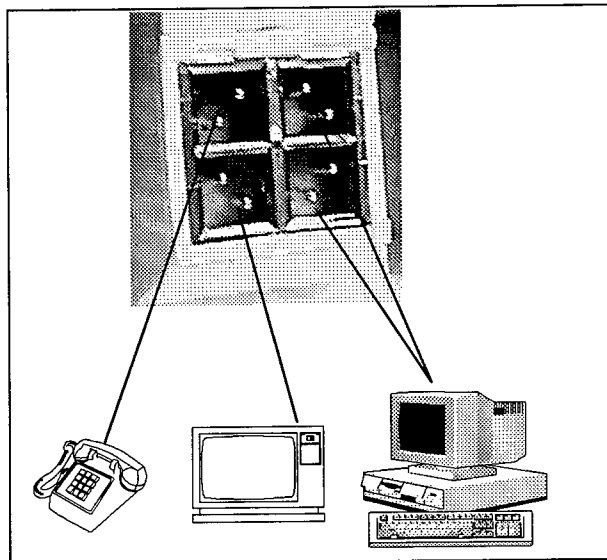


Fig. 8:
Different Applications running on individual pairs

The resulting network, based on the principle of structured cabling is very efficient. Data-, voice-, telephone- and TV-transmissions are all available from one cable, one outlet.

An essential profit from cable sharing is cost reduction as no coaxial cables or telephone cables are required.

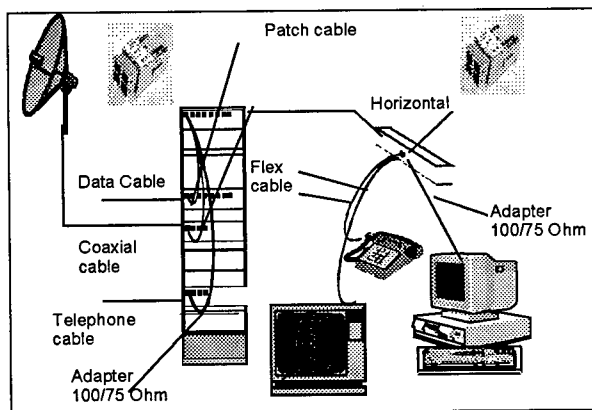


Fig. 9:
Example for Multimedia Cabling,
using the new System

TV-APPLICATION

The twisted pair link can transmit a TV-signal over a distance of 100 m. The matching from the 100 ohm twisted pair cable to the 75 ohm coaxial cable and vice versa is realised by means of a bi-directional adapter (balun).

The max. input level for a TV-signal is 105 dB μ V (depending on quality of signal and EMC). The min. input level of a TV-signal is \approx 60 dB μ V. The resulting attenuation of the total link (horizontal cable, patch-cord and all baluns) is:

$$105 \text{ dB} - 60 \text{ dB} = 45 \text{ dB}$$

This is improved by testing the total link as shown in figure 10. The max. possible frequency here is 800 MHz. For higher frequencies the length must be reduced.

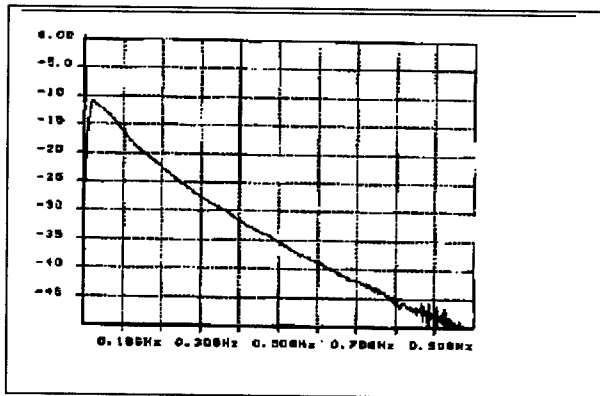


Fig. 10:
Test Result of the total Link (100 m)

In principle, TV-signals can also be sent over Cat.5 and Cat.6 cabling. However special electronics are required to reduce frequencies here. TV-transmission at TV-standard is not possible.

As individually pair-screened cables and connectors show excellent NEXT-values even at high frequencies, TV-transmission is well possible here at TV standards.

The structured cabling concept makes sense in all locations where flexible and combined use of above mentioned services is required.

A lot of projects are realised in this manner in hospitals, hotels, airports, universities, banks,

insurance companies, industry, small offices and even home offices, as there are for example shown in the following figures.

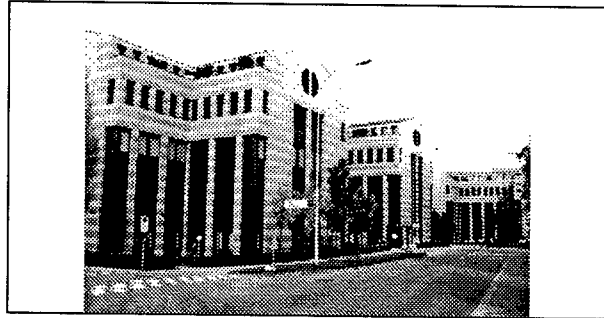


Fig. 11:
SGS-Bank, Switzerland

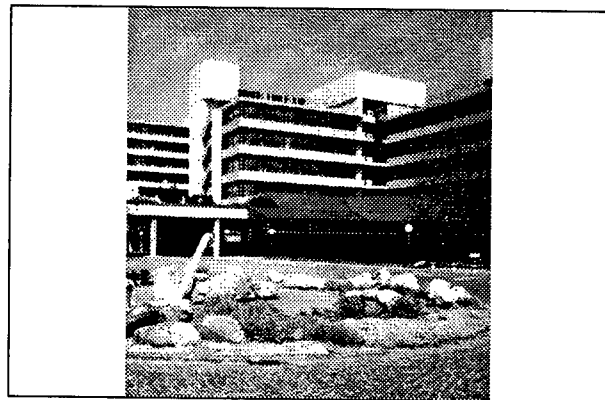


Fig. 12:
University of Konstanz, Germany

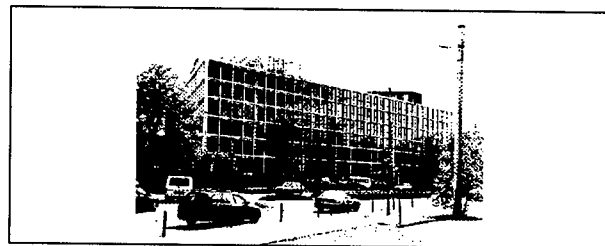


Fig. 13:
Rheinland Insurance Company, Germany

CONCLUSION

Individually screened twisted pair cables (PimF-Cables) together with a new connector generation open up new possibilities:

- large bandwidth (>1000 MHz)
- high frequencies and data rates without additional electronics
- all multimedia applications from one cable (cable- and connector-sharing)
- max. of 4 applications per cable (each pair = 1000 MHz)
- combinations of 4 different applications in one cable
- cost reduction due to cable-sharing (no telephone and coaxial cable)
- flexible and modular network management.

The installed base in Europe is already substantial.

AUTHORS

Karl Lesten

Karl Lesten was born in Jülich, Germany, in 1956. After his studies of communication techniques at the Fachhochschule Aachen he worked as a sales engineer for radio frequency products. 1986 he joined Kerpenwerk as a sales engineer for data cabling. Since 1989 he is the responsible product manager for data cables and systems.

Jörg Bör

Born in Hamburg, Germany in 1965, Jörg Bör finished his studies of electrical engineering at RWTH Aachen as Diplom-Ingenieur in 1991. After his graduation he started his professional career as a R & D engineer at Kerpenwerk GmbH & Co.

His activities at Kerpenwerk focus on the further development of symmetric copper data cables and the improvement of electrical transmission characteristics up into the gigahertz range. Currently, Jörg Bör is responsible for the electrotechnical development of Kerpenwerk.

Mailing Addresses:

Karl Lesten
Kerpenwerk GmbH & Co
Zweifaller Str. 275 - 287
D 52224 Stolberg
Germany
Phone xx49 / 24 02 / 17 - 468
Fax xx49 / 24 02 / 7 51 54
E-Mail karl.lesten@kerpen.com

Jörg Bör
Kerpenwerk GmbH & Co
Zweifaller Str. 275 - 287
D 52224 Stolberg
Germany
Phone xx49 / 24 02 / 17 - 440
Fax xx49 / 24 02 / 7 51 54
E-Mail joerg.boer@kerpen.com

COUPLING ATTENUATION – A NEW MEASURING TECHNIQUE TO QUALIFY THE EMC BEHAVIOR OF VARIOUS DATA CABLES

Dirk Wilhelm, Andreas Obst

GHMT, Bexbach/Saar, Germany

ABSTRACT

At present, generic cabling systems for horizontal subsystems are predominantly realized with symmetrically screened or unscreened copper conductor cables. However, unsymmetrical coaxial cables or twinax cables are still existing in older, established cabling structures. In order to develop a measurement technique for determining the coupling attenuation, two international working groups have been aiming at reaching an accepted standardization within the course of the next year. The purpose of their work consists in a reproducible test set-up applicable to the above-mentioned cable design features. This paper provides information on the comprehensive cycles of measurements performed and modified during pan-European round robin tests and additional analyses of GHMT.

INTRODUCTION

Within the European Union, the electromagnetic compatibility (EMC) of devices is regulated by the EMC directive 89/336/EEC which was enacted into law by a corresponding act in Germany on 1st January 1995 (EMVG). Any devices complying with this act may bear the so-called CE (conformité européenne) symbol. In other countries, the compliance with EMC regulations is examined similarly using other measures, e.g. by tests in accordance with FCC standards and the application of FCC notes. Initially, not much attention was given to the problem that these standards apply, almost exclusively, to active devices and deal, only insufficiently, with the issue of connecting such devices to form an entire system. With respect to copper-based data cables which are used in local area networks (LANs) and considering the continuously increasing bandwidths, a solid knowledge of the parameters relevant to EMC will be of crucial importance for determining the EMC characteristics of the entire cabling and thus the entire system.

SUBJECT

The theoretical basis of the injection clamp method and its benefits compared with the absorbing clamp method has already been presented in the proceedings of the forty-sixth IWCS. Following a retrospective summary, this technical paper will mainly discuss the measuring results achieved by means of both methods.

Test Setup of the Injection Clamp Method

The injection clamp method was developed by GHMT in 1994 and has been recorded by the IEC as a New Work Item Proposal since 18th June 1998. The proposal of the German National Committee is included in the IEC 46/86/NP document "Electrical test methods for data cables, coupling attenuation, injection clamp method". To illustrate the method of measurement, first of all the basic terms are described.

Primary system: The term 'primary system' was first of all used for coaxial lines – there consisting of the central carrier wire and the screen serving as return line. In case of twisted pair (TP) cables, the primary system consists of the electric characteristics of the signal-carrying two-core conductor. The screen, if existing at all, only has a protective function and is not included in the description of the primary system. Hence the primary system has been defined in such a way that there is no difference between screened and unscreened TP cables.

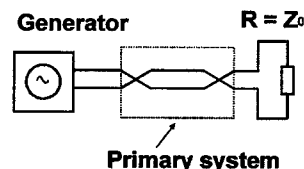


Fig. 1: Primary system of a screened / unscreened TP cable.

Secondary system: The secondary system describes the behavior of the cable within the framework of its electromagnetic environment. In case of coaxial cables, the secondary system mainly consists of the characteristics of the screen. However, TP cables may be available both as unscreened and as screened versions. Nevertheless, even unscreened cables have a secondary system. Just as screens only have a finite effect, unscreened TP cables accordingly only have a finite symmetry. Therefore there will inevitably be a reference value vis-à-vis earth.

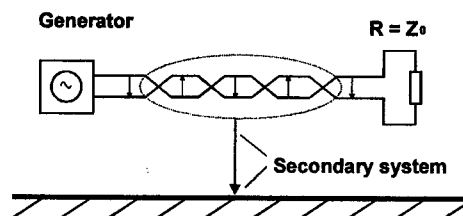


Fig. 2: Model of the secondary system in case of unscreened cables.

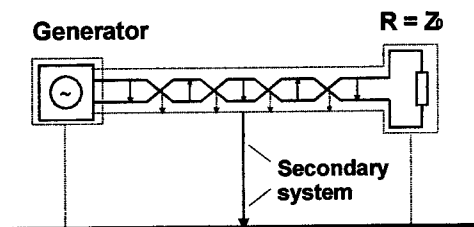


Fig. 3: Model of a secondary system in case of screened cables.

Traditional Method: Determination of the Screening Attenuation a_s

The methods of measuring the screening attenuation which have been specified primarily for coaxial cables (e.g. IEC 60096-1) can also be applied to TP cables. However, the TP cables which are optimized for a high degree of balance to earth must be pre-assembled coaxially (i.e. contrary to their design) – thus eliminating the asymmetry attenuation. Thus a key EMC parameter will not be taken into account.

Hence a universal parameter should be determined which evaluates both the attenuating effect of the cable screen and the even-mode suppressing influence of the twisted-pair symmetry.

Traditional Method: Determination of the Symmetry a_u of Twisted-Pair Cables

In case of the traditional methods of measuring the asymmetry attenuation a_u according to ITU 0.121 or prEN 50289-1-9, a even-mode wave is supplied to the test specimen terminated with respect to even-mode and odd-mode operation, and the resulting odd-mode wave is measured. The ratio of even-mode wave and odd-mode wave indicates the asymmetry attenuation of the test specimen.

The problems associated with this method consist in the fact that the method originally was designed for telecommunication lines with a lower bandwidth. In case of bandwidths of more than 600 MHz which are today aimed at for the transmission of data, there are significant dependencies on the measuring environment caused by parasitic earth couplings.

Definition of the Universal Descriptive Parameter

The new parameter to be defined should represent the EMC parameters of the cable independently of the cable type (symmetric / asymmetric). These relevant parameters are the screening attenuation a_s and the asymmetry attenuation a_u which have been outlined above.

The desired universal parameter – let us call it coupling attenuation a_{CA} – can now be represented as the sum of the two primary EMC parameters:

$$a_{CA} = a_u + a_s$$

As a rule, however, the two traditional methods of measurement cannot be compared with each other. Therefore the separately determined parameters must not be added up.

It can be recognized that the coupling attenuation actually is an attenuation, i.e. an insertion loss to be as high as possible between the primary system (signal path) and the secondary system (electromagnetic environment). This equation applies both to unscreened and to screened TP cables.

Measurement of the Coupling Attenuation by Means of the Injection Clamp

The new method takes into account not only the symmetry but also the screen quality of a cable. If possible, the test specimen must be connected, during the measurement, in the same way it is operated in the later production environment. In case of a TP cable, this means that the cable is connected symmetrically in accordance with its design – and not coaxially as in the previous methods used to determine the screening attenuation.

Both the symmetrically connected primary system and the secondary system, where asymmetric parasitic signals are injected, should be connected in accordance with the impedance.

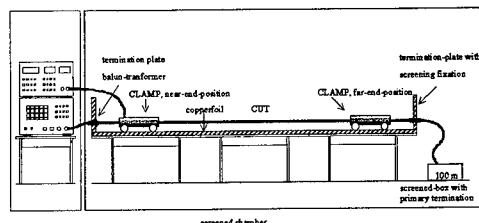


Fig. 4: Measuring setup to IEC 46/86/NP "Injection clamp method".

The test specimen shall be mounted and suspended across a length of 6 m and at a constant height above the test bench. A conductive reference plate has been installed on the test bench lengthwise in the direction of the specimen. The distance of the specimen as well as the external diameter of a possibly existing screen determine the characteristic wave impedance of the secondary system. Following the characteristics of the EM 101 injection clamp, an impedance of 150 Ω should be aimed at. Assuming that the width b of the ground plane is very much larger than the height h of the cable above the ground plane and that the screen diameter d can be regarded as small compared to the height h , the following equation applies:

$$Z = \frac{Z_F}{2\pi \cdot \sqrt{\epsilon_r}} \cdot \ln \frac{4h}{d}$$

(Z_F = field characteristic impedance: 377 Ω)

In order to realize a matched secondary system, the height h must amount to about $3d$. However, the exact height of the cable above the ground plane must be adjusted by means of a TDR in order to take into account the locally restricted dielectric influence of the cable sheath.



Fig. 5: Test setup with wooden bench and metallic reference level for a $150\ \Omega$ secondary impedance.

To ensure the correct termination of the secondary system in accordance with the impedance, HF-suitable terminating resistors between the ground plane and the cable screen are planned to be installed for both termination plates. A certain HF output power P_{1bal} will be fed to the primary system symmetrically connected by means of a balun. The decoupling of the output P_2 , reduced by the coupling attenuation, will be effected by means of an EM coupling run known from the EMC basic standard IEC 6100-4-6. On account of the detection of magnetic as well as capacitive field components, the EM 101 injection clamp is particularly suited for this. Using a scalar or a vectorial network analyzer, the displayed attenuation is as follows:

$$a_{clamp} = 10 \cdot \log \left| \frac{P_{1bal}}{P_2} \right|$$

The displayed attenuation must be corrected by means of the insertion losses of the balun, of the connecting cable, and of the injection clamp. The insertion loss of the EM 101 injection clamp shall be offset using a reference standard with a defined secondary circuit impedance of $150\ \Omega$. Thus it will be possible to exclude any environmental disturbance when recording the correction curve. However, it should be ensured that the cable to be tested also has a secondary impedance of approximately $150\ \Omega$ with respect to the ground plane.

Alternatively, the correction curve can be determined by means of a substitution method which requires three identical EM 101 injection clamps. The advantage of such a method consists in the fact that the calibration of the injection clamp can be carried out with the cable to be tested later on. Hence the secondary system is the same both during the calibration of the injection clamp and during

the measurement of the coupling attenuation. For the compensation, the clamps no. 1 and no. 2 enclose the cable while being positioned on the ground plane without any spacing between each other. Clamp no. 1 supplies the measuring signal to the cable, and clamp no. 2 serves for the detection. Within the framework of two additional measurements, the clamps no. 1, 2, and 3 will be exchanged non-cyclically. The insertion loss of each of the three injection clamps results from the solution of the linear system of equations.

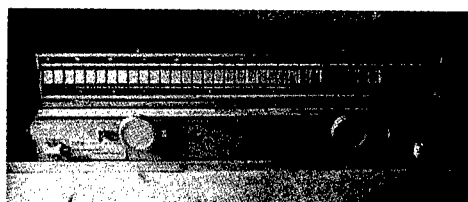


Fig. 6: Lütli EM 101 injection clamp with detector and absorber ferrites

Deviating Test Setup for the Absorbing Clamp Method

The absorbing clamp method is described in prEN 50289-1 "Communication cables – Specification for test methods", Part 6D "Electromagnetic performance". The draft has been prepared by the technical committee CENELEC TC 46X. On account of findings of the latest round robin test, the test setup presented in the draft of June 1999 is, however, no longer up to date.

Compared with the injection clamp method, the absorbing clamp method differs with respect to the test setup as follows:

- The cable is tested without any defined secondary circuit impedance and far away from all metallic equipotential surfaces. Therefore the radial distribution of the electric field may be heavily distorted by external dielectrics. For this reason, the wooden cable support of the test setup has meanwhile been replaced by a suspended cable.
- The recommended absorbing clamp of the MDS 21 type is a current transformer clamp which is not optimally suited for the different mode distribution in case of unscreened and screened cables.
- The calibration of the insertion loss of the absorbing clamp will be carried out according to the instructions of prEN 50289-1-6D. To that end, the current transformer of the absorbing clamp is positioned in front of a vertical reflector plate which serves as ground reference of the secondary circuit. The generator output is directly connected with the screen of the cable to be tested or – in case of unscreened cables – with the interconnected conductors.

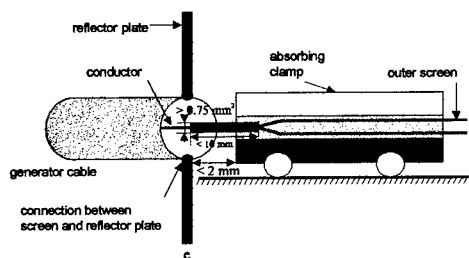


Fig. 7: Calibration setup according to prEN 50289-1-6D for the MDS 21 absorbing clamp.

The insertion loss of the test facility is determined by measuring the transmission loss and the subsequent correction of the return loss in the calibration setup. That way the response of the MDS 21 absorbing clamp is determined with respect to the output of an excited surface wave. The return loss in the test facility caused by the mismatch between the impedance of the surface wave and the impedance of the absorbing clamp will not be taken into account in the measurement.

Analyses carried out by GHMT have shown that the correction curve does not depend on the type of the screen or the diameter of the cable. This should be considered as a positive aspect because the work required for testing several specimens will be reduced significantly.

Figure 8 shows the correction curve of an MDS 21 absorbing clamp which was recorded in accordance with the instructions for the calibration method of prEN 50289-1-6D. In order to assess the fault tolerance, a second correction curve was recorded using the substitution method already presented above. The curves match surprisingly well with a maximum deviation of less than 2 dB.

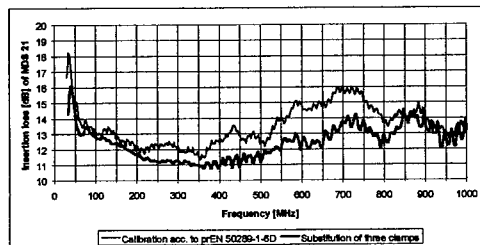


Fig. 8: Insertion loss of MDS 21 absorbing clamps recorded with different calibration procedures.

The manufacturer of the MDS 21 absorbing clamps encloses a common correction curve. From the point of view of GHMT, this curve represents only a rough-cut estimation. Figure 9 shows that different correction curves should be assigned even to three identical MDS 21 absorbing clamps (using the substitution method for the test). The correction curves of the three absorbing clamps differ by no more than 3 dB.

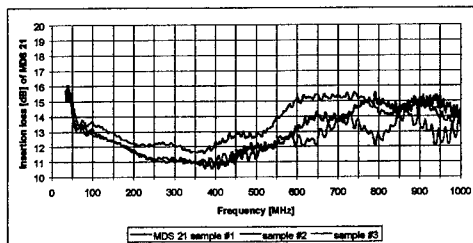


Fig. 9: Insertion loss of three MDS 21 absorbing clamps recorded with the substitution method.

The maximally measurable coupling attenuation defined by prEN 50289-1-6D amounts to 90 dB because the high insertion loss of the MDS 21 absorbing clamp limits the dynamic range of the network analyzer (as a rule: 115 dB). The additional utilization of an external pre-amplifier enlarges the useful dynamic range when the MDS 21 absorbing clamp is used.

The lower insertion loss of the EM 101 injection clamp should therefore be rated as an asset. The enlargement of the dynamic range amounts to no less than 6 dB in the frequency range from 30 MHz to 1 GHz.

Analyses carried out by GHMT have shown that the reciprocity with respect to the coupling of the measured signal via the EM 101 injection clamp leads to the same results when feeding the measured signal via the balun. This course of action is to be recommended if the useful dynamic range of the network analyzer is insufficient because of very high coupling attenuation values. The useful dynamic range is enlarged when the signal is fed by means of a clamp since a higher input can be applied to the EM 101 injection clamp than to the balun. Due to saturation effects, customary baluns have a non-linear curve shape at approx. +5 dBm while most network analyzers provide an adjusted output of over +20 dBm.

Error Sources during the Coupling of the Signal

The absorbing clamp method in accordance with prEN 50289-1-6D recommends the utilization of a balun for symmetrical coupling while the termination of the pairs at the near end, which are not being tested, remains undefined. In case of STP cables, the pair foils may, however, easily come off, and, in case of UTP cables, the twist of the pairs may open.

The injection clamp method provides for an even- or odd-mode termination of all pairs also at the near end. In practice, this can be realized by means of four baluns of which three are terminated, non-reflective, on the primary side by 50 Ω . In this configuration, the pair to be measured can be fed by easily changing the 50 Ω connecting port without any mechanical load. Figure 10 shows a cable adapter with four baluns 50 Ω / 100 Ω suitable for a frequency range from 1 MHz to 1.2 GHz. Using the four lockable chambers in the head plate, the four signal circuits are additionally decoupled in the connecting range exceeding 130 dB.

This decoupled supply of signals will be advantageous with respect to the currently discussed introduction of the power-sum coupling attenuation. In such a case, all four pairs can simultaneously be fed by means of a power splitter.

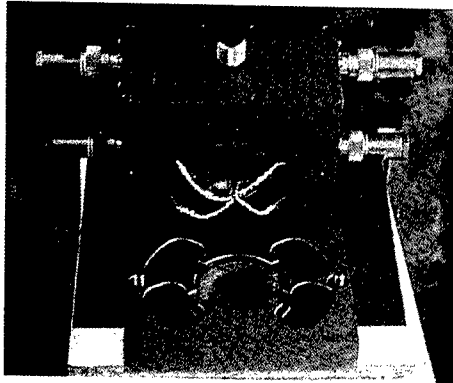


Fig. 10: Proposal for the symmetrical feeding of the test specimen. GHMT patent: Cable Reference Measuring Clamp

Using a substitution method which connects in series two out of the four baluns each in three non-cyclical measurements, the individual insertion loss of each balun can be calculated. We were able to prove that there are deviations of up to 7 dB in the range above 600 MHz between the frequency responses of the four baluns. In case of errors having this size, the correct determination of the insertion loss will absolutely be necessary for an exact calculation of the coupling attenuation. The same applies to the absorber method with one balun only. We urgently advise against determining the insertion loss based on an S_{21} transmission measurement of two baluns connected in series by simply halving the measured value.

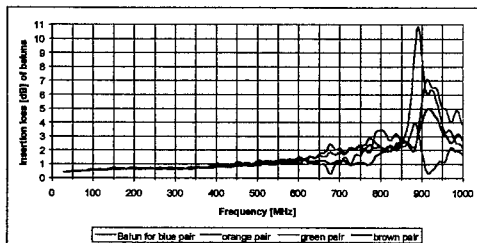


Fig. 11: Individual insertion loss of four baluns.

Error Sources in case of Far-End Measurements

The far-end measurements are carried out with an effective length of 6 m between the ferrite absorber and the absorbing / injection clamp. Considering the connecting area of the cable, the fed signal will be attenuated across a cable length of about 6.5 m before it is detected.

Both methods of measurement provide for a maximum inaccuracy of ± 1 dB for each component of the test facility. In case of symmetrical S-STP cables

having an attenuation which is approximately proportionate to \sqrt{f} up to a frequency of 1 GHz, it is therefore sufficient to use one pair for the determination of the symmetric attenuation. Ideally a central part of the length of the lay should be selected. The figure 12 shows a small difference of no more than 6.5 m x 8 dB / 100 m ≈ 0.5 dB for an AWG22 S-STP cable.

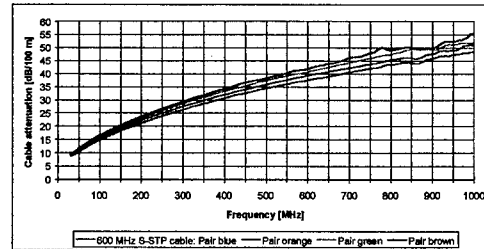


Fig. 12: Frequency response of attenuation for a four-pair AWG22 S-STP cable.

However, there will be problems in case of such cable types whose design does not account for the transmission of the odd-mode up to 1 GHz. In case of frequencies exceeding 100 MHz, resonance-like blocking zones could be proven in individual pairs which require an exact determination of the attenuation of all pairs in order to calculate the far-end coupling attenuation.

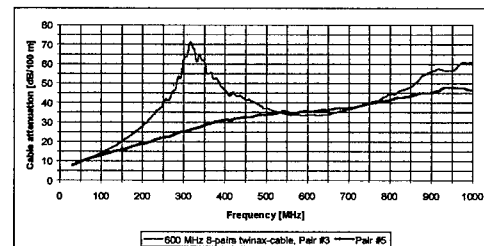


Fig. 13: Frequency response of attenuation for an eight-pair twinax cable (two pairs recorded).

Analog problems occur if the attenuation of the even mode is measured on symmetrical cables in order to determine the screening attenuation. By stranding the pairs and by the parallel connection of individual conductors to form a 50 Ω primary system, there will be periodical superimpositions of the frequency response (ideally proportionate to \sqrt{f}) of the coaxial attenuation. It should be considered whether the introduction of a smoothing unit may reduce disturbing resonance peaks.

GHMT Measurements to prEN 50289-1-6D (Absorbing Clamp Method) in a Round Robin Test

Figure 14 compares the test results of the coupling attenuation for the three cable types UTP, FTP, and S-STP of various manufacturers which are most frequently installed.

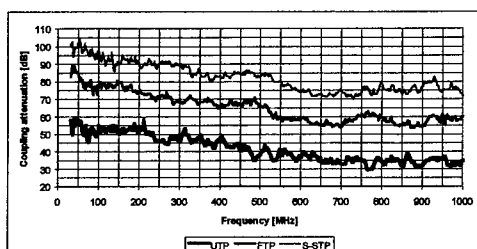


Fig. 14: Coupling attenuation of three different types of cables.

On account of the very small lengths of the lay and the homogeneous structure of the non-foamed polyethylene cores, the UTP cable has an immunity to interference which results only from the asymmetry attenuation a_U . The portion of the screening attenuation a_S within the coupling attenuation does not exist in case of UTP cables.

Distinctly outdistanced by the UTP cable, the FTP cable has an immunity to interference which is higher by about 20 dB. Since the cable core assembly of the FTP cable does not correspond to the very good earth symmetry of the UTP cable due to larger lengths of the lay and a more inhomogeneous foam skin core insulation, we can proceed from the assumption that the screening effect of the 40 μ m thick aluminum foil amounts to about 30 dB.

The very good coupling attenuation of the S-STP cable is mainly ensured by the excellent screening effect of the pairs enclosed in foils and the braided core. The portion of the asymmetry attenuation of the physically high-foamed S-STP cables is even of less importance than in the case of the FTP cable. The extremely long lengths of the lay (50 + 2 mm) of the pairs in metallized foil have also not been optimally selected with respect to the earth symmetry.

However, the assumption that pair-screened cables have the highest coupling attenuation for constructive reasons is contradicted by figure 15.

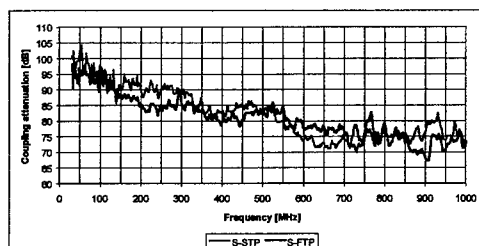


Fig. 15: Comparison of coupling attenuation (S-STP cable vis-à-vis S-FTP cable).

The represented S-FTP cable has the same core as the test specimen used in figure 14. Compared with the FTP cable, the coupling attenuation is, however, improved by well over 15 dB as a braid ensures an additional screening effect. With a distinctly more reasonable design, an S-FTP cable can therefore reach very good coupling attenuation values which correspond to those of the S-STP cable.

Measurements of other European Institutions to prEN 50289-1-6D (Absorbing Clamp Method) in the Round Robin Test

The presented results have been taken from a test cycle carried out by GHMT in March 1999 within the framework of a round robin test for the WG3 in the TC46 X. Seven institutions, among them test labs and cable manufacturers, tested the method of measurement to be introduced by using the same specimens. The analyses comprised seven different cable types.

The results of the round robin test showed that no reproducible test procedure exists at present. The results of all institutions differed very much from one another. That is why WG3 does not plan to publish the results.

The determined deviations are probably caused by individual simplifications of the test setup. Simplified test conditions such as the omission of the reflector plate or a bent cable routing are also listed in the standard. Hence the details of the prEN 50289-1-6D test instruction must not be simplified but specified more precisely. For the time being, the concept that the absorbing clamp method should be applied without in-depth practical and theoretical know-how of the test staff will remain an ideal. Solutions should be developed mainly for the following areas:

- **Correction for electrically short specimens.**

Part of the results of the round robin test were analyzed only for the range above 100 MHz as the defined effective test length of 6 m leads to irregular test conditions – in particular for data cables with high values of the nominal velocity of propagation (NVP). The demand to test electrically long cables at low frequencies failed on account of the dimensions of the existing screening chambers. In addition, analyses of GHMT have shown that a space-saving, meandering arrangement of the test specimen is not admissible because the transversal field components compensate each other. Hence the far-end and near-end measurements would differ.

- **Defined ground contact**

The reflector plate only serves as an equipotential surface of the secondary system if there is a low-resistance contact between the balun, the reflector plate, and the cable screen. This problem can be solved, e.g. in case of foil-screened cables, if an instruction concerning the preparation of the specimen would be part of the standardized test setup. In this respect, prEN 50289-1-6D leaves too many degrees of freedom to the user. The cable adapter developed by GHMT (cf. Figure 10) always provides for an optimal contact in the connecting area.

- **Defined secondary impedance**

From the point of view of GHMT, the lacking reproducibility within the course of the round robin test is caused by the secondary impedance which can significantly be influenced by ambient

conditions. We must examine therefore if a defined impedance – which can e.g. be realized by suspending the cable between supports at a well-defined distance – can optimize the method of measurement. For that purpose, GHMT has carried out tests and determined that dielectric inhomogeneities can also be determined by means of a TDR measurement when a ground plane is used. That is why cable supports made of wood or plastics cannot be used for both methods. The coupling attenuation of a test specimen can be evaluated correctly if the specimen is suspended straight-line above a ground plane and, if required, is fixed through cords.

Field Tests of GHMT to IEC 46/86/NP (Injection Clamp Method)

Figure 16 shows a comparison of screening attenuation and coupling attenuation measured by means of the same 100 m AWG23 S-FTP cable. The represented weighting curve is based on the assumption that the coupling attenuation is reduced by 20 dB/decade above 100 MHz while the weighting curve of the screening attenuation corresponds to a constant level. The difference of both weighting curves clearly corresponds (by neglecting complex coupling terms between the primary and secondary systems) to the asymmetry attenuation a_U – amounting to 30 dB at 100 MHz and to 10 dB at 1,000 MHz (i.e. a good correlation to practice). A separate measurement of a_U would be relevant to the evaluation of figure 16. However, this value cannot be determined up to 1,000 MHz because of the limiting upper critical frequency of the symmetry measuring bridges which are available.

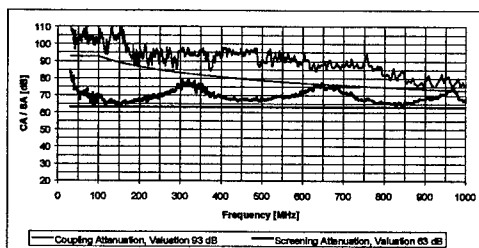


Fig. 16: Comparison of coupling and screening attenuation recorded for an S-FTP cable.

Comparison: Absorbing Clamp Method versus Injection Clamp Method

Finally it should be clarified whether the measurements of the coupling attenuation performed on a specimen by means of the absorbing and injection clamps are sufficiently matching. Figure 17 shows the comparison carried out by means of a 600 MHz AWG22 S-STP cable.

You can clearly recognize the higher measuring dynamic response of the injection clamp method in case of frequencies below 100 MHz (which is mainly resulting from the lower insertion loss of the EM 101 injection clamp. Roughly speaking, both methods of measurement have comparable frequency re-

sponses. The evaluation of the weighting curves, falling by 20 dB/decade above 100 MHz, leads to an offset of 1 dB. However, both weighting curves are only determined by the spike at 150 MHz. In case of high frequencies over and above 600 MHz, the two measured-value curves no longer follow the drop of the weighting curve. GHMT frequently observed this phenomenon in case of measurements performed on S-STP cables but not in case of measurements performed on UTP or FTP cables.

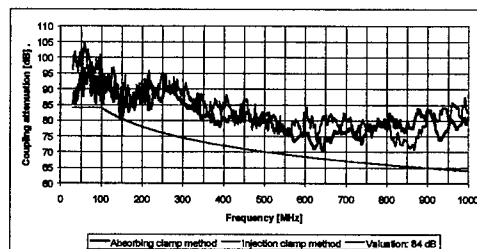


Fig. 17: Comparison of absorbing and injection clamp methods for an S-STP cable.

The frequency responses were represented for each frequency point out of the minimum number of four near-end and four far-end measurements. Although the attenuation of the far-end measurements of the four pairs has been corrected, there is a marked difference between near-end and far-end measurements in case of the absorbing clamp method. This offset of up to 10 dB which could not be expected was not ascertained in case of the injection clamp method. Using the injection clamp, the near-end and far-end measurements, with the attenuation being corrected, are on the same level because both screen contacts of the cable (effective length: 6 m) are terminated on the secondary side by a 150 Ω resistor within the reflector plate vis-à-vis the ground plane.

CONCLUSION

Only well-defined test conditions which do not neglect the individual characteristics of the environment, of the measuring equipment, and of the specimen will ensure a reproducible measurement of the coupling or screening attenuation. The absorbing clamp method to prEN 50289-1-6D in the currently adopted version of June 1999 produces measuring errors as a European round robin test showed. The injection clamp method which is being considered on the international level, however, requires a larger extent of testing activities which primarily concerns the alignment of a homogeneous secondary impedance. From the point of view of GHMT, the test results measured by means of the injection clamp method show a high degree of reproducibility as well as a sufficient dynamic response even without any pre-amplification.

OUTLOOK

GHMT aims at carrying out a new round robin test which proves the benefits of the injection clamp method independently of any specific test lab. Several European cable manufacturers already announced that they are ready to participate actively in such a test.

SPEAKER BIOGRAPHY



Andreas OBST (age: 33 years) is head of the laboratories for EMC and transmission measurements of LAN components at GHMT.

In 1993, he graduated at Technische Universität Hanover majoring in high frequency engineering. In the course of his diploma thesis at kabelmetal electro company in Hanover, he optimized elliptical shaped wave guides with corrugated sheath.

In 1994, he entered the product-engineering department of Alcatel Cable in Berlin. There he has been responsible for design, testing and quality features of symmetrical high-speed data cables.

At the beginning of 1997, he joined GHMT in his present position.

Mailing address

GHMT
Gesellschaft für Hochfrequenz-Meßtechnik mbH
In der Kolling 13
66450 Bexbach/Saar
GERMANY

Phone: +49 / (0) 68 26 / 92 28 - 0
Fax: +49 / (0) 68 26 / 92 28 - 99
E-mail: obst@ghmt.de

CO-AUTHOR

Dirk WILHELM (age: 33 years) studied telecommunications in Kaiserslautern, Germany and graduated as a Diplom-Ingenieur.

He is general manager of GHMT mbH, an independent test laboratory for the global certification of cables, components and active devices of LANs and WANs.

His technical field of responsibilities at GHMT mbH comprises the appraisal and analysis of electromagnetic compatibility of distributed facilities and systems.

Mailing address

GHMT
Gesellschaft für Hochfrequenz-Meßtechnik mbH
In der Kolling 13
66450 Bexbach/Saar
GERMANY

Phone: +49 / (0) 68 26 / 92 28 - 0
Fax: +49 / (0) 68 26 / 92 28 - 99
E-mail: wilhelm@ghmt.de

CORRELATIONS BETWEEN CROSSTALK AND SYMMETRY OF DATA CABLES

Jörg Bör

Kerpenwerk GmbH & Co., Stolberg, Germany

ABSTRACT

Increasing bandwidth of today's data transmission techniques requires a very high performance of cabling.

Thus cabling classes and correlating cable categories with their performance requirements are fixed in national, regional and international standards, which require to test many transmission parameters. Some of these properties depend on each other. But their physical correlations are hardly to describe in mathematical formulas which allow to reduce the number of performed measurements by calculating depending parameters from the results of correlating tests.

Referring to the experiences of a stable production process the cable manufacturers do not perform all required tests on every production length but only on random samples. Additional the knowledge of correlations between several transmission parameters can be used to reduce the number of tests in product quality control. Intended by the question whether it is possible to formulate a mathematical relationship, the correlations between crosstalk parameters (NEXT, FEXT) and symmetry parameters (LCL, LCTL) are investigated.

This paper presents an example of statistical analysis on one cable type and reflects over some approaches to find a mathematical formula. Possible reasons of deviations and the significance of the results for the aspired reduction of measurements are discussed.

IMPORTANT TRANSMISSION PARAMETERS OF SYMMETRICAL DATA CABLES

The most important parameters determining the transmission quality of symmetrical data cabling have been crosstalk, return loss and attenuation up to today. Now high speed applications as ATM or Gigabit Ethernet require further properties, for example FEXT, Delay Skew and LCL.

Attenuation

Each transmission line has losses, caused by transformation of electrical energy into caloric energy. The power ratio between output signal and input signal, measured in dB, is defined as attenuation.

Return Loss

Return loss is the power ratio of reflected signals to the input signal, measured in dB. Each change of characteristics along a transmission channel causes reflections. This might be a mechanical damage as well as a connector with another impedance than the cable. The reflected part of the signal does not reach the receiver. To receive a high output signal power reflections shall be as low as possible. This correlates to high return loss values.

Crosstalk (NEXT, FEXT)

Crosstalk is the signal power ratio of a disturbing pair to a disturbed pair, measured in dB. It is differed between near end crosstalk (NEXT), measured at the input end of a transmission line, and the far end crosstalk (FEXT), measured at the output end. The difference between equal level FEXT (EL-FEXT) and input output FEXT (IO-FEXT) is equal to the attenuation. To avoid

transmission disturbances the crosstalk should have a high dB value.

Crosstalk parameters are measured pair to pair, but it is useful to verify the power sum, calculated as the sum of signals received from all neighbour pairs. For example the power sum NEXT of a pair n is defined as

$$PS_n = -10 \log \sum_{\substack{m=1 \\ (m \neq n)}}^k 10^{NEXT_{n,m}/10} \quad (1)$$

where $NEXT_{n,m}$ is the NEXT of pairs n and m
 PS_n is the Powersum NEXT of pair n and
 k is the number of pairs

Symmetry (LCL, LCTL)

In symmetrical data cables the balanced mode is used for the data transmission. But there is also a common mode formed by unsymmetry of production or construction. This common mode propagates in the cable as disturbing wave. The power ratio of common mode to balanced mode is measured as Longitudinal Conversion Loss (LCL), measured in the input end of a pair. Measuring in the output end the Longitudinal Conversion Transfer Loss (LCTL) describes the common mode to balanced mode power ratio. To reach good transmission characteristics LCL and LCTL should have high dB values.

Delay Skew

Combining different pairs for data transmission as it is proposed in the standard draft Gigabit Ethernet for UTP cabling the speed difference of the pairs is becoming very important. The maximum delay time difference of a cabling is defined as delay skew.

CORRELATIONS BETWEEN TRANSMISSION PARAMETERS

The correlation between the parameters return loss and impedance is well known. A changing impedance along a transmission channel will cause signal reflections and the measured return loss decreases. Thus several standards define a formula to calculate a return loss parameter using input impedance derivations (e.g. structural return loss according ASTM D 4566)¹.

A similar effect is expected comparing crosstalk and symmetry parameters. A bad symmetry of a

pair causes a high common mode power level radiated out of this pair as well as received from other pairs. This results in a high crosstalk level between two pairs having bad symmetry.

Clearly exists a correlation between this properties as it was demonstrated for STP-cables on the 46th IWCS².

Regarding the crosstalk and symmetry parameters measured from the same end, it is expected that NEXT correlates to LCL and FEXT to LCTL, because the backscattering to the near end should be the same for the crosstalk signal as well as for the conversion signal.

CONSTRUCTIVE AND PRODUCTIVE PARAMETERS DETERMINING NEXT

There are several parameters causing NEXT of symmetrical data cables. They depend on cable construction as well as the production process. These parameters may be classified into the aspects distance, screening, pair shielding, pair-twist-ratio and symmetry.

Distance

The geometrical distance between two pairs determines the crosstalk between this pairs. This distance is fixed by the cable construction, but must be realised in an exact and stable production process, too.

Screening

The geometrical distance is overcome by the electrical neighbourhood caused by an overall screen. All pairs are positioned nearest to the screen, which transmits the disturbance signal from one pair to all other pairs. This does not depend from production effects.

Pair shielding

Pair shielding prevents electromagnetic waves from passing from one pair into another and reduce the crosstalk disturbance very efficient. Effective pair shielding needs a good and constant production process.

Pair-twist-ratio

Very important to reach a high crosstalk attenuation is the pair-twist-ratio. Considering pairs of the same twist, the vectors of the electromagnetic waves of every pair remain in the same direction relative to each other along the whole cable. Different twists will change the

direction along the cable. The result is a phase changing of disturbing electromagnetic waves. In good designed cables this phase shall inverse as often as possible. So the crosstalk applied in one segment of cabling length will be eliminated by the phase-inverted crosstalk applied in the next segment, as illustrated in Figure 1.

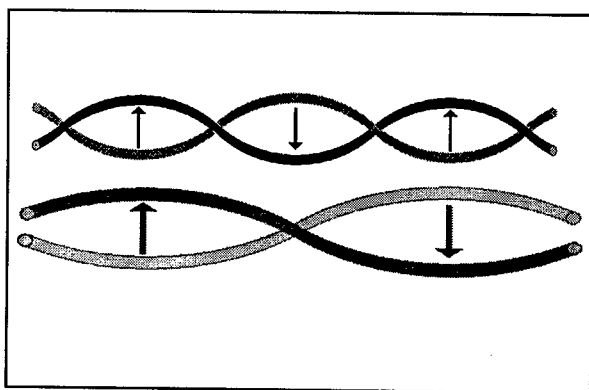


Figure 1:
Phase Changing between two Pairs

To reduce crosstalk by using a good pair-twist-ratio a cable must be constructed with optimal pair twists, but this optimal twists must be realised by an exact production process.

Symmetry

In symmetrical data cables the balanced mode is used for the data transmission. But there is also a common mode formed by unsymmetry of production or construction. This common mode propagates in the cable as disturbing wave. Similar to the communication of sending and receiving antennas the common mode of disturbing pair communicates with the common mode of disturbed pair.

Very precise producing is necessary to minimise this effect.

Due to the multitude and diversity of parameters influencing NEXT, the correlation between crosstalk and symmetry is hardly to formulate based on physical properties. So the aspired formula is tried to find by statistical analysis of performed measurements.

PERFORMED MEASUREMENTS

Referring to a fixed cable construction and a stable production process there should be a

linearity between correlating crosstalk and symmetry parameters. The statistical analysis of a lot of tests performed on one cable type confirms the correlation between this parameters, but reveals the mentioned problem to formulate it into a general mathematical formula.

The measured crosstalk parameter in this investigation is the near end crosstalk (NEXT), the corresponding symmetry parameter is the LCL. Both are measured in the input end of a pair. It is expected that the correlation is easier to find at the near end than at the far end parameters, because the attenuation of test samples does not influence the measurements.

In this investigation measurements of NEXT and LCL were performed in the frequency range from 100 kHz to 100 MHz on some thirty samples of a copper braid and foil screened four pair S/FTP-cable (figure 2). Not more than two samples belong to the same production charge, but all tested cables were manufactured in the same construction and production process. So the sampling is statistical independent and reveals typical effects of construction.

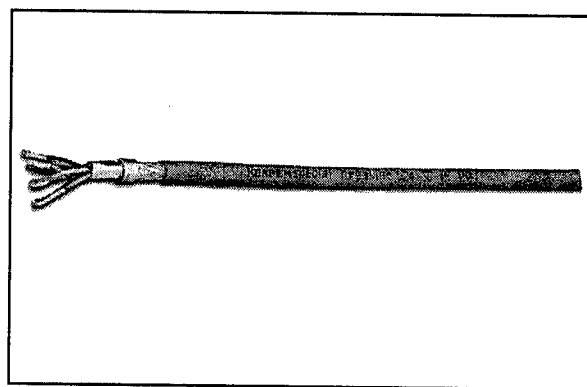


Figure 2:
The investigated S/FTP-Cable

EXPECTED RESULTS

To find the aspired mathematical relationship, the performed measurements are statistical analysed using three approaches which are introduced in the following paragraphs.

First Approach: The Difference Function

The power radiated by the common mode of a pair in the investigated four pair cable is received by the three other pairs and by the environment. The power radiated into the environment should

to be neglected, because the overall screen reflects radiated power back into the cable. For screened cables the effect of geometrical position of the pairs is to neglect, too. So it is expected that the third part of radiated common mode power from one pair will be received by each other pair, corresponding to a 9,5 dB difference.

Thus for each couple of pairs a difference function $D_{n,m}$ is defined according the following equation:

$$D_{n,m} = \text{NEXT}_{n,m} - (\text{LCL}_n + \text{LCL}_m - 9,5 \text{ dB}) \quad (2)$$

where $\text{NEXT}_{n,m}$ is the NEXT of pairs n and m
 LCL_n is the LCL of pair n
 LCL_m is the LCL of pair m

Second Approach: Frequency Dependency

The second approach takes into account the frequency dependency of NEXT and LCL. NEXT decreases with 15 dB per frequency decade, LCL with 10 dB per frequency decade.

Considering this fact, there should exist a correlation function $C_{n,m}$ describing the relationship between NEXT and LCL as follows:

$$C_{n,m} = \text{NEXT}_{n,m} - 0.75 (\text{LCL}_n + \text{LCL}_m) \quad (3)$$

where $\text{NEXT}_{n,m}$ is the NEXT of pairs n and m
 LCL_n is the LCL of pair n
 LCL_m is the LCL of pair m

In this correlation function $C_{n,m}$ there should be no frequency dependency.

Third Approach: LCL and Power Sum

The third approach regards only one pair to exclude effects of unequal power distribution to the different pairs. The LCL of each pair is compared with the power sum of the same pair.

For this approach a power sum difference function P_n is defined for each pair as

$$P_n = \text{PS}_n - \text{LCL}_n \quad (4)$$

where PS_n is the Powersum NEXT of pair n
 LCL_n is the LCL of pair n.

STATISTICAL ANALYSIS

On some single frequencies the values were checked to fulfil the numerical conditions for the gaussian statistical analysis. Figure 3 shows the distribution of the difference function values $D_{1,2}$ at 4 MHz, derived from measured values

according equation (2). In respect of the number of values, this is according a gaussian distribution.

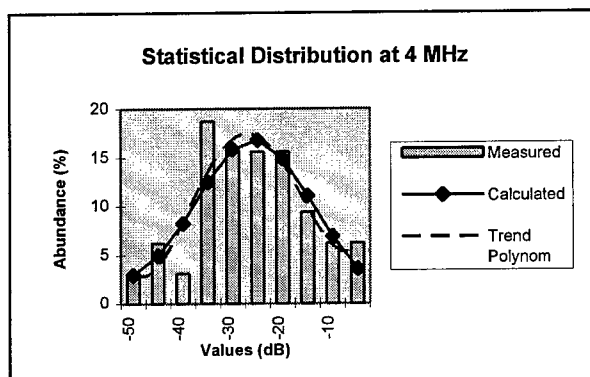


Figure 3:
Gaussian distribution of $D_{1,2}$ values at 4 MHz

First Approach: The Difference Function

The statistical distribution of the calculated difference function $D_{n,m}$ according equation (2) is shown in figure 4 for example for the pair combination 1-2. There is the mean value of the numerical difference between NEXT and LCL values of corresponding pairs versus frequency (black curve) and the trend line (shaded). The range signed by the grey curves is the confidence interval of 90 % (calculated by the standard deviation).

The periodic effects in the difference function are reflections from not optimal adapted far ends of the cable, resulting from the sample length of 100 m used in all measurements of this investigation.

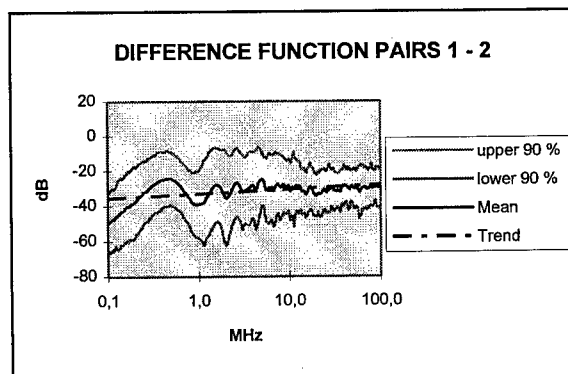


Figure 4:
Difference Function $D_{1,2}(f)$ of Pairs 1-2

The typical difference function for each couple of pairs is confirmed by the measurement results, but the high deviation does not allow to define a specific construction dependent constant for each pair combination of the investigated cable type. An uncertainty of 3 dB seems to be the maximum acceptable, but the result shows an uncertainty of about 15 dB.

Second Approach: Frequency Dependency

Figure 5 shows the statistical distribution of the calculated correlation function $C_{n,m}$ according equation (3) for example for the pair combination 1-2. The black curve presents the mean value of $C_{1,2}$ versus frequency, its trend line is shaded. The 90 % confidence interval is shown by the grey curves.

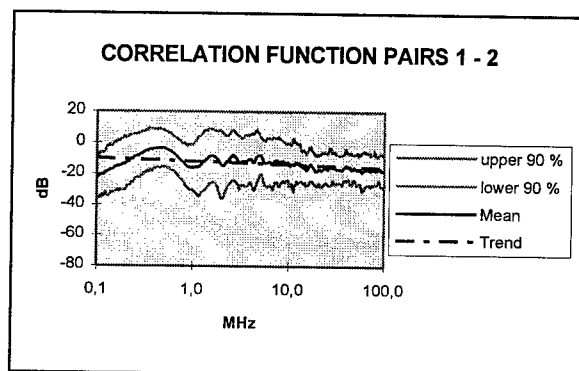


Figure 5:
Correlation Function $C_{1,2}(f)$ of Pairs 1-2

The correlation function $C_{n,m}$ versus frequency is rather constant as it is predicted above. But also in this approach a very high deviation is found and there is no reliable basic value for calculations deriving NEXT-values from LCL-measurements or LCL-values from NEXT-measurements.

Third Approach: LCL and Power Sum

In figure 6 the statistical distribution of the calculated power sum difference function P_n according equation (4) is shown for example for pair 1. Here the mean value of P_n versus frequency (black curve) and the trend line (shaded) can be seen as well as the 90 % confidence interval (grey curves).

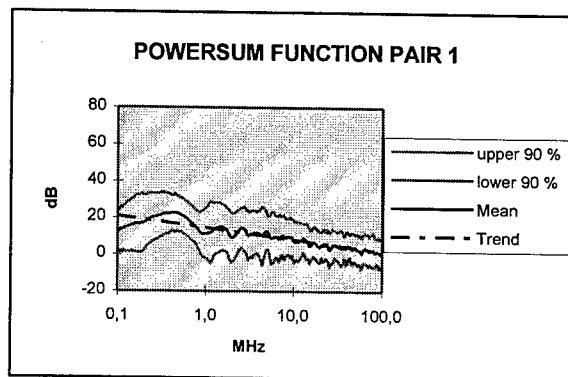


Figure 6:
Power Sum Difference Function $P_1(f)$ of Pair 1

The power sum difference function P_n decreases with 5 dB per decade, which confirms the experiences in frequency behaviour of NEXT and LCL as considered in the second approach.

The 90 % confidence interval of P_n is better, compared to the difference function $D_{n,m}$ and the correlation function $C_{n,m}$. But there is still a deviation of about 10 dB, which is not acceptable to base a mathematical correlation on this results.

DISCUSSION OF RESULTS

The presented statistical analysis of performed measurements confirms that there are physical correlations between NEXT and LCL. But in the approaches discussed in this paper it was not possible to formulate this correlation in a mathematical way. The high deviation signalises, that NEXT is influenced by other parameters, which are not considered.

This might be

- instable production effects,
- constructive uncertainties,
- reflection effects,
- measurement uncertainties, or
- physical properties not considered to influence the crosstalk.

Production and construction effects are to be excluded because of the great experience of thousands of kilometres in producing this cable in the same construction.

Measurement uncertainties should be negligible by using high quality measurement equipment with a very good performance. But considering the fact, that the most part of deviation is caused

by LCL, it can not be excluded that this parameter is an instable parameter in measuring. So the assumption is to be checked, that the reflection effects for crosstalk signals and common mode signals are the same. So the crosstalk and symmetry parameters of the far end, FEXT and LCTL, are taken into account. Thus a power sum for both ends of the cable is taken by calculating the powersum of NEXT and FEXT X_n and defining a symmetry powersum of LCL and LCTL Y_n . With the double end powersum

$$X_n = -10 \log \sum_{\substack{m=1 \\ (m \neq n)}}^k 10^{\text{NEXT}_{n,m}/10} + 10^{\text{FEXT}_{n,m}/10} \quad (8)$$

and the symmetry powersum

$$Y_n = -10 \log (10^{\text{LCL}_n/10} + 10^{\text{LCTL}_n/10}) \quad (9)$$

the power sum balance B_n is defined as follows:

$$B_n = X_n - Y_n \quad (10)$$

where $\text{NEXT}_{n,m}$ is the NEXT of pairs n and m
 $\text{FEXT}_{n,m}$ is the FEXT of pairs n and m
 LCL_n is the LCL of pair n .
 LCTL_n is the LCTL of pair n and
 k is the number of pairs.

The power sum balance B_n is analysed in the same way as the approaches introduced before. It is expected that the power sum balance is close to zero. This would confirm the approaches above, indicating that the far end must not be neglected.

The statistical analysis of the power sum balance B_n is shown for example in figure 7 for pair 1 with the mean value (black curve) and its trend (shaded) as well as the 90 % confidence interval (grey curves).

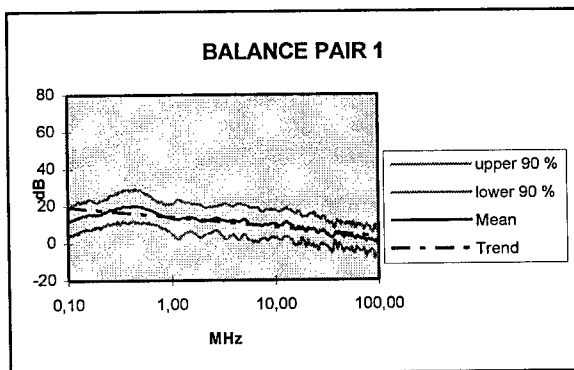


Figure 7:
Power Sum Balance $B_1(f)$ of Pair 1

The result of the power sum balance of crosstalk and symmetry parameters demonstrated in figure 7 shows the same characteristics as the power sum difference function P_n in values, frequency dependency and deviation. No effect from the far end is recognised. So diverse reflections to the near and the far end cannot be the reason for the high deviations noticed in the approaches above. This indicates, that other properties influence the crosstalk, which are not considered in this investigation.

CONCLUSION

The investigation confirms the correlation between crosstalk and symmetry parameters. But with today's equipment and experience it is not possible to create a mathematical correlation formula for calculating NEXT from LCL measurements. Properties which are not taken into account influence the results more than assumed.

The next steps to be done are the verification of reproducibility of LCL measurements testing different equipment and methods. After that the results of this investigation should be confirmed on other cable types and the distribution of crosstalk and symmetry parameters to the near and the far end of the cable is to investigate. The most important task is to find out, which further parameters influence the crosstalk and symmetry properties.

REFERENCES

- ¹ ASTM D 4566-94
Standard Test methods for Electrical
Performance Properties of Insulations and
Jackets for Telecommunications Wire and
Cable
- ² M. Backmann, Dr. C. Pfeiler, A. Waßmuth
„Crosstalk Model for Pair-shielded Data
Cables“ in Proceedings of the 46th IWCS, 1997

AUTHOR



Born in Hamburg, Germany in 1965, Jörg Bör finished his studies of electrical engineering at RWTH Aachen as Diplom-Ingenieur in 1991. After his graduation he started his professional career as a R & D engineer at Kerpenwerk GmbH & Co. His activities at Kerpenwerk focus on the further development of symmetric copper data cables and the improvement of electrical transmission characteristics up into the gigahertz range. Currently, Jörg Bör is responsible for the electrotechnical development of Kerpenwerk.

Mailing address

Jörg Bör
Kerpenwerk GmbH & Co
Zweifaller Str. 275 - 287
D 52224 Stolberg
Germany

Phone +49 / 24 02 / 17 - 440
Fax +49 / 24 02 / 7 51 54
E-Mail joerg.boer@kerpen.com

A DIGITAL COMMON-MODE NOISE CANCELLER FOR TWISTED-PAIR CABLE

David K. Fenton and Tet H. Yeap

University of Ottawa
Ottawa, Ontario
Canada

ABSTRACT

xDSL modems operate in frequency bands which coincide with many significant radio-frequency interference sources, particularly commercial AM radio. In these bands, the balance of most twisted-pair cables is low enough to allow substantial interference to transfer to differential mode, disrupting the transmitted information signal.

To compensate for this handicap, xDSL receivers will require a front-end circuit which uses the common-mode signal as a reference to cancel out as much differential interference as possible. Unfortunately, design of such a device is complicated by the statistical properties of the interference, as well as the complex interactions between differential and common-mode signals on the loop. If a digital canceller is desired, compensation for finite-precision effects poses an additional challenge.

This paper examines the feasibility of wideband digital noise cancellation for xDSL. Emphasis is placed on the stability of the adaptive algorithm, and on the number of bits of precision required.

NOTE: All power measurements given in this paper assume a loop termination of 100 Ω .

INTRODUCTION

For residential customers, the most crucial bottleneck in the speed of Internet file transfer is usually the voiceband telephone link to the home. To solve this bandwidth problem, local exchange carriers are currently deploying Asymmetric Digital Subscriber Line (ADSL) modems. These devices can operate over most existing loops. On shorter loops, higher-bandwidth services will eventually be offered using Very High Speed Digital Subscriber Line

(VDSL) technology, which has yet to complete the standardization process.

These new DSL technologies operate at frequencies which coincide with a variety of radio-frequency interference (RFI) sources, particularly commercial AM radio. Assuming that the wire pair is well twisted, such interference couples to the loop almost entirely in common mode. In turn, some portion of this common-mode signal then transfers to differential mode, disrupting the information signal. The differential-mode RFI can dwarf the desired signal: in worst-case conditions, the signal-to-interference ratio (SIR) on the loop can be as low as -40 dB.¹

To ensure correct reception of the information signal in such an environment, the receiver must carry out substantial interference cancellation or suppression. The two line codes currently under consideration for VDSL incorporate methods to cancel out moderate amounts of ingress noise. However, when the SIR is very low both modem types will be forced to lower their data rates in order to achieve sufficient noise margins.

To improve the SIR, and hence the bandwidth available over the link, a noise canceller at the receiver's front end can be used. The common-mode signal on the loop is a convenient reference for the differential RFI. Unfortunately, the correlation function between these two quantities is unknown, and can be quite complex. A variety of difficult hardware issues must also be addressed when building a canceller for xDSL applications.

A canceller can be designed to cancel either narrowband or wideband interference. If there are multiple narrowband interferers, a wideband device will be able to reduce all of them, although only one will be cancelled perfectly. Wideband cancellation also holds some promise

for impulse noise mitigation. On the other hand, multiple narrowband devices are required to handle multiple interferers, but very good noise reduction can be achieved because each canceller may be precisely tuned to a particular RFI threat. Since there may be a very large number of interferers in urban areas, this study concentrates on the design of a single wideband canceller. Any residual interference which exists at the noise canceller output must be suppressed by the VDSL receiver's equalization techniques.

This paper gives a brief overview of the xDSL noise cancellation problem, and studies the feasibility of wideband digital noise cancellation. Some simulation results are reported to illustrate why certain design choices have been made. The simulations are geared towards VDSL systems because these must operate at frequencies up to 20 MHz, where the channel attenuation is high and the cable balance is low. However, the results obtained can easily be applied to any DSL.

RADIO-FREQUENCY INTERFERENCE ON TWISTED-PAIR LOOPS

The RFI which couples to a twisted-pair loop may originate from many sources. These include transmissions from broadcast AM, amateur radio, shortwave radio, maritime and aeronautical mobile HF radio, and navigational aids. Of these, broadcast and amateur AM are usually the only two strong enough to merit cancellation.

Broadcast AM is by far the most ubiquitous and persistent form of interference. In North America, commercial AM stations occupy 10 kHz bands at centre frequencies from 540 - 1600 kHz, and typically have 50 or 5 kW transmitters. Worst-case conditions can be severe: loops in New York City are exposed to at least 22 stations with transmitter powers of 1 kW or more.² Tests performed in two Canadian cities found that 50% of loops carried at least one interferer with a differential-mode power of -53 dBm or higher.³ The 90th and 99th percentile figures were -37 and -20 dBm respectively. On average, the second most powerful interferer was only 1.3 dB weaker than the primary one.

Interference from amateur radio is rarely encountered, but can be devastating. These transmissions use 2.5 kHz slots in the nine

international amateur bands which fall between 1 and 30 MHz. Since the transmitter can be located arbitrarily close to the twisted-pair cable, the induced differential RFI may be very high: 40 metres from a 400 W transmitter, up to 100 mV_{rms} of differential voltage may be observed on the loop (giving an average power of -10 dBm).⁴ Furthermore, amateur transmissions are bursty in nature, and their carrier frequencies are not fixed. These factors make cancellation of amateur RFI more complicated than the reduction of comparatively stable broadcast AM signals.

For VDSL systems, the maximum value of the transmit power spectral density (PSD) mask will probably be set at -60 dBm/Hz, limiting the overall transmit power to 11.5 dBm. On a loop of length 1 km or less, the received signal power will be somewhere between -50 and -20 dBm. In the presence of a strong amateur interferer, the SIR on the loop could be -40 dB; in the more likely case of severe broadcast AM ingress, SIRs of -30 dB may be expected.

CABLE BALANCE AND MODES OF TRANSMISSION

Formally, cable balance may be defined by:

$$B = 20 \cdot \log_{10} \left| \frac{V_{cm}}{V_d} \right| \quad (1)$$

where V_{cm} is the common-mode voltage between the cable and ground, and V_d is the differential voltage across the wire pair. In general, most loops are likely to have a balance of 50 to 60 dB at frequencies under 150 kHz. Above that, the balance degrades by 12 - 15 dB/decade, and may be below 30 dB at across most of the VDSL band. One possible model for category 3 cable assumes a constant 50 dB balance below 150 kHz, falling according to:⁵

$$B(f) = 50 - 15 \cdot \log_{10} \left(\frac{f}{150 \text{ kHz}} \right) \quad (2)$$

at frequencies between 150 kHz and 30 MHz. This balance characteristic is shown in Figure 1.

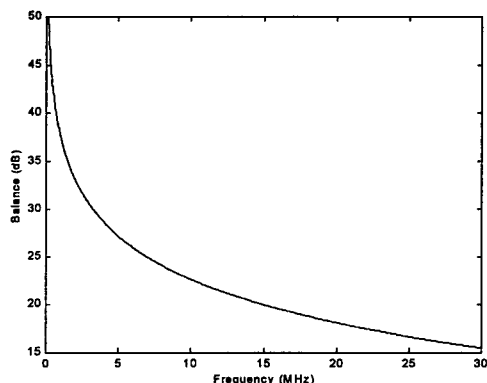


Figure 1: Typical balance characteristic for category 3 cable

While the balance is an accurate reflection of the relative interference power in the two modes of transmission, additional complications are introduced by the different propagation characteristics of the two channels. The differential signal experiences much more severe attenuation than the common-mode one, and travels about twice as fast. At 1 MHz, a differential signal on a 1-km AWG 26 cable is attenuated by 26.1 dB and travels at 0.65c; its common-mode counterpart is attenuated by 7.4 dB and moves at only 0.34c (for a more detailed explanation of this subject, see reference 6).

Knowing these characteristics, it is easy to see how impedance imbalances along the line will complicate the noise cancellation problem. Interfering signals that couple to the cable in common mode will be partly converted to differential mode at an impedance imbalance (which is more likely to be a diffuse "region" of imbalance than a nicely defined point). Over the length of the cable, the common-mode wave will lag behind the differential one. It will also attenuate more slowly, making it appear stronger relative to the differential signal. If multiple interferers couple to the cable at different distances from the receiver, and there are multiple impedance imbalances along the cable, it is clear that the differential and common-mode signals at the end of the loop could be related by a highly complicated correlation function. This means that it will not be practical to design a canceller which uses fixed filters; an adaptive solution is required.

ADAPTIVE NOISE CANCELLATION

The general structure of an adaptive noise canceller for communications over twisted-pair cable is shown in Figure 2.

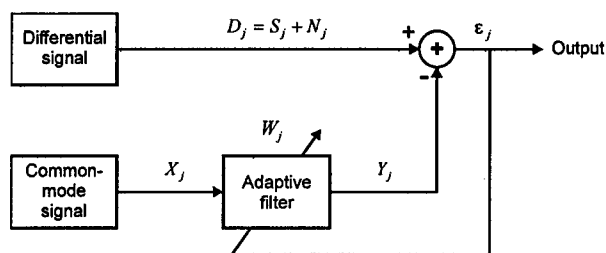


Figure 2: Adaptive noise canceller

The canceller is assumed to be digital, where j is a discrete-time index. The common-mode signal X_j is the reference noise for the system, and is assumed to be uncorrelated with the information signal. The differential input D_j is called the "desired signal" for the system; it is a combination of the attenuated and distorted information signal S_j and the induced noise N_j . X_j and N_j are correlated in some unknown manner, so the tap weights W_j of the adaptive filter can be adjusted such that the filter's output Y_j closely approximates N_j . If this operation is performed correctly, the output signal E_j will contain much less noise than the originally received signal D_j .

The simplest method of adjusting the adaptive filter weights is the widely used least-mean-square (LMS) algorithm. This iterative technique attempts to minimize the mean-squared error (MSE) between the desired response D_j and the filter output Y_j . When the system inputs X_j and D_j are wide-sense stationary, and the filter has M taps, the MSE may be viewed as an M -dimensional "error-performance surface" with a uniquely defined minimum point.⁷ The tap weights which correspond to this minimum point give the optimum estimate of D_j which can be generated using X_j ; this is called the Wiener solution.

The LMS algorithm seeks out the minimum point of the error-performance surface by calculating a series of instantaneous error gradients; at each

iteration, it assumes that ε_j^2 , the square of a single error sample, is an estimate of the mean-squared error.⁸ This approximation reduces system complexity, but means that the algorithm does not converge continually towards the minimum point. It follows a noisy path, occasionally steering in the wrong direction. Once it is close to the minimum point, it fluctuates about it but never converges to it exactly. For this reason, it is called a stochastic gradient algorithm, and one of its key limitations is the "gradient noise" caused by its random walk about the Wiener solution.

Defining the vectors for the common-mode input and the adaptive filter weights as:

$$\mathbf{X}_j \equiv \begin{Bmatrix} x_j \\ x_{j-1} \\ \vdots \\ x_{j-M+1} \end{Bmatrix}, \text{ and } \mathbf{W} \equiv \begin{Bmatrix} w_1 \\ w_2 \\ \vdots \\ w_M \end{Bmatrix} \quad (3)$$

the LMS algorithm at iteration j is described by the two equations:

$$\varepsilon_j = d_j - y_j = d_j - \mathbf{W}_j^T \mathbf{X}_j \quad (4)$$

and

$$\mathbf{W}_{j+1} = \mathbf{W}_j + 2\mu\varepsilon_j \mathbf{X}_j \quad (5)$$

where T denotes matrix transposition, and all matrix entries are assumed to be real. The parameter μ , frequently called the step size, controls the algorithm's stability and rate of convergence. A low μ reduces the undesirable gradient noise experienced at steady state, but slows down the algorithm's convergence. To guarantee convergence, μ should satisfy the relation:

$$0 < \mu < \frac{1}{\sum_{i=0}^{M-1} E\{|x_{j-i}|^2\}} \quad (6)$$

where E is the expectation operator, and the quantity in the denominator of the right-hand term is called the "tap-input power". For in-depth analysis of the LMS algorithm's performance, references 7 - 10 are recommended. In general, an adaptive noise canceller can achieve near-perfect cancellation of a single narrowband interference source. If multiple interferers are

present, the most powerful one will be almost perfectly cancelled but the remainder will be only partially suppressed. If all of the interferers have the same PSD and uncorrelated coupling paths to the loop, as is likely in the case of crosstalk noise, almost no cancellation at all will be achieved.

In non-stationary environments, the LMS algorithm can reliably track the time-varying minimum point of the error-performance surface, provided that the input data statistics vary slowly compared to the learning rate of the system.⁷

FINITE PRECISION ISSUES

The adaptive noise canceller suffers finite-precision errors from two sources:

- the analog-to-digital converter (ADC) quantization errors for the reference noise \mathbf{X}_j and the desired signal \mathbf{D}_j ; and
- the quantization error arising from the fact that the filter coefficients and output are represented by only a finite number of bits.

For optimum performance, the differential ADC's resolution should be selected such that its quantization noise does not raise the thermal noise floor significantly (so long as the common-mode ADC has the same resolution, its noise floor is not a major concern). Similarly, the number of bits used to carry out fixed-point math in the filter should be selected to keep the noise floor as low as possible.

Given that a received VDSL signal could have a dynamic range of 60 dB, an ADC with substantial resolution will be required. Recent submissions to the T1E1.4 subcommittee have suggested that low-power 12-bit 35-MSPS devices will likely be available by the time of VDSL deployment.¹¹ An ideal 12-bit ADC sampling at the Nyquist rate has a signal-to-quantization-noise ratio (SQNR) of approximately 74 dB. In a practical device, other noises, such as circuit noise, aperture jitter and comparator ambiguity, will usually reduce this SQNR value by 4 - 9 dB.¹²

VDSL testing assumes that the thermal noise floor is at -140 dBm/Hz. The total thermal noise power for a signal with a spectrum spanning from 1 - 17.5 MHz will therefore be about -67.8

dBm. To avoid raising this noise power by more than 0.5 dB, the bottom of the ADC's dynamic range must be placed 9.1 dB below the thermal noise power, ie. at -76.9 dBm.¹³ If practical limitations are assumed to reduce the SQNR of an ideal 12-bit ADC by 6 dB, the top of the ADC's dynamic range will fall at about -76.9 + (74 - 6) = -8.9 dBm. Since the peak-to-average ratio (PAR) of 30%-modulated AM stations is low, this upper limit is high enough to include the most severe broadcast AM threats. It also leaves enough overhead to accommodate the 15 dB PAR of discrete multitone systems, so long as the loop is at least 500 metres long. On shorter loops, the dynamic range of the ADC will need to be shifted up to capture the received signal. However, the SIR in these cases will be high enough to guarantee that noise cancellation is not a major concern.

There are two situations that a 12-bit ADC will not be able to handle without raising the noise floor undesirably: worst-case amateur radio interference, and digital frequency-division duplexing (FDD). Amateur interference with -10 dBm power will require that the ADC dynamic range be shifted up by several dB, unless front-end analog cancellation techniques are used to reduce the interferer power first. Digital FDD is an even more difficult problem. The maximum allowed transmit power of a VDSL signal is 11.5 dBm, so the transmitter will operate at 17.5 dBm to account for the hybrid transformer's insertion loss. Assuming a trans-hybrid loss of 12 dB, the transmit signal will arrive at the receiver with 5.5 dBm power. Adding the necessary PAR safety factor to this number makes digital FDD implausible for VDSL.

Because of these considerations, the authors favour the use of analog filters to conduct frequency-division duplexing. A narrowband analog noise canceller is also recommended to suppress the strongest interferer, followed by a wideband digital canceller to reduce the interference across the entire VDSL bandwidth.

The number of bits of precision required for the adaptive filter is a more sensitive issue. It can be shown that the expected value of the tap-weight vector at steady-state is:¹⁴

$$E\{\mathbf{W}_j\} = \mathbf{W}_{Wiener} + \frac{1}{2\mu} \mathbf{R}_X^{-1} E\{\mathbf{b}\} \quad (7)$$

where \mathbf{W}_{Wiener} is the optimum tap-weight vector, \mathbf{b} is a general term which represents all of the finite-precision errors experienced by the LMS algorithm, and \mathbf{R}_X^{-1} is the inverse of the common-mode input's autocorrelation matrix:

$$\mathbf{R}_X = E\{\mathbf{X}_j \mathbf{X}_j^T\} \quad (8)$$

Equation (8) is obviously not a flawless model: the tap-weight vector will not tend to infinity if μ is set to 0. However, in this application, the factor $1/2\mu$ is surprisingly unimportant. It will be shown later that \mathbf{R}_X can be considered singular for all practical purposes. Accordingly, if the finite-precision errors do not have zero mean, the LMS algorithm becomes inherently unstable and the tap weights quickly overflow their allocated storage. Once this has occurred, the filter must reset itself and re-converge.

Storage overflow can be prevented by leaking the LMS filter taps. This involves a simple modification of equation (6):

$$\mathbf{W}_{j+1} = (1 - 2\mu\alpha)\mathbf{W}_j + 2\mu\varepsilon_j \mathbf{X}_j \quad (9)$$

where α is another control parameter. For convergence, the condition

$$0 \leq \alpha < \frac{1}{2\mu} \quad (10)$$

must be met. Conceptually, adding the leakage factor $-2\mu\alpha\mathbf{W}_j$ to (6) is the same as adding a zero-mean white noise process with variance α to the reference noise input.⁷ This augments the autocorrelation matrix to $\mathbf{R}_X + \alpha\mathbf{I}$, ensuring that the lowest eigenvalue is greater than α and thus forcing the matrix to be positive definite.

The extra multiplication operations in leaky LMS add complexity to the algorithm, although it is possible to economize by leaking only one tap at each iteration.¹⁴ The MSE also rises slightly. However, these are small prices to pay to guarantee the stability of the algorithm.

DESCRIPTION OF THE SIMULATION

An uncoded QAM system operating at VDSL frequencies has been simulated to evaluate the

performance of a digital noise canceller. A QAM-16 signal is used in all cases, and the carrier frequency and data rate are selected to fill the entire bandwidth over which positive noise margin can be achieved (assuming an AWGN noise floor at -140 dBm/Hz and no crosstalk).

Ten broadcast AM interferers are generated in accordance with the threat models specified in the VDSL requirements document.¹⁵ Up to three amateur radio interferers are also generated with differential powers of -30 dBm. Their envelopes are interrupted periodically to characterize the major attributes of speech.

Testing is performed using ten loops with lengths between 500 metres and 1.5 km. The interference signals are coupled to the loop anywhere from 0 - 500 metres from the receiver.

At the receiver, analog bandpass filters are used to suppress all energy outside the transmitted signal's main lobe. Thermal noise is added, and analog-to-digital conversion is carried out. A 12-bit, 35 MSPS ADC is assumed, but only 11 bits are used to account for the device's imperfections. The ADC LSB step size is selected such that the thermal noise floor does not rise by more than 0.5 dB.

The adaptive filter is usually implemented with 150 taps; this ensures that signals which have diverged over almost 400 metres of cable can be re-aligned. When the noise couples to the line 500 metres away, a 200-tap filter is used.

The filter's step-size parameter μ is selected using the formula:

$$\mu = \frac{\beta}{\text{tap - input power}} \quad (11)$$

where β is a user-selected number between 0 and 1, and the tap-input power is calculated using the recursive relation:

$$\text{tap - input power} = 0.999 \times \text{tap - input power} + 0.001 \times \mathbf{X}^T \mathbf{X} \quad (12)$$

Throughout the simulation, a "benchmark" signal of the original transmitted signal is maintained. It undergoes channel distortion and receiver front-end filtering, but does not have any noise added to it.

The mean-squared error between the canceller output and the benchmark signal is computed. A second calculation is performed to measure the MSE between the received differential signal and the benchmark signal. Since the information signal energy is approximately the same at the input and the output of the canceller, the ratio of the two MSEs can be viewed as the reduction in noise energy achieved by the canceller. In the simulation results, this ratio is referred to as the "noise reduction", and is expressed in dB.

Noise reduction is not a sufficient performance metric by itself. As the size of μ increases, so does the level of gradient noise, which usually appears as a white noise floor. If μ gets too large, the gradient noise can very badly distort the differential signal. Accordingly, the noise floor's power density level was measured as a second performance measure. System performance was considered acceptable when this floor remained within 3 dB of the thermal noise floor. Values 3 - 5 dB above the thermal floor were considered marginal, while anything more than 5 dB above was deemed unacceptable.

SOME SIMULATION RESULTS

One of the first results observed during the simulations was the inherent instability of the LMS algorithm when truncation was used without leakage. The instantaneous autocorrelation matrix of the common-mode input was almost invariably found to be singular to the working precision of Matlab 5.0. Considering that Matlab can represent real numbers up to 1.8×10^{308} , and that the finite-precision errors arising from truncation were not likely to have zero mean, it is unsurprising that the algorithm was numerically unstable.

The iteration at which the first storage overflow occurred was heavily dependent on the number of bits used in the adaptive filter, but did not vary much with β (unless β was low enough to force μ below the minimum precision of the filter, in which case the tap weights stopped adapting). Sustaining 14 bits of precision for the internal operations of the adaptive filter, the first overflow of the tap weight memory occurred after only 25,000 to 35,000 iterations. As might be expected, using 15 bits of precision prolonged the survival of the filter to between 55,000 and 65,000 iterations. These numbers are clearly

unsatisfactory in a system which must process 35 million samples every second.

When rounding rather than truncation was used to shorten the double-precision numbers which resulted from fixed-point multiplications in the filter, the noise canceller proved to be quite robust. This was because the finite-precision errors due to rounding were evenly distributed about zero when the common-mode input contained signals over a wide range of frequencies. This reduced the importance of the ill-conditioned state of the autocorrelation matrix and kept the algorithm stable.

A series of tests were run to determine the best values of β for particular loops, as well as the number of bits of precision that would be required for reliable operation. The tests were run with no tap leakage. In general, it was found that β had to be kept below 0.2 if the noise floor was not to be raised significantly by gradient noise. For values up to 0.7, the filter usually remained stable, but above 0.7 the maximum tap weight often grew quickly and drove the system to overflow.

The following plots show the noise reduction achieved on five 1-km loops with different noise coupling characteristics. The points on the graphs are plotted according to the noise floor achieved: a circle means that the noise floor was contained below -137 dBm/Hz, a square indicates that it was between -137 and -135 dBm/Hz, and an asterisk represents a noise floor above -135 dBm/Hz. Figure 3 shows the noise reduction achieved as a function of β when full floating-point math was used. On the loop with the lowest input SIR (-21 dB), cancellation of about 33 dB was possible. It is interesting to note that all but one of the readings for $\beta \geq 0.2$ resulted in unacceptably high gradient noise, even with this level of mathematical precision.

When the internal fixed-point math of the filter was carried out using 16 or more bits of precision, the results were very similar to those shown in Figure 3. When 12 or fewer bits were used, the noise floor always rose unacceptably. The results for 15-, 14- and 13-bit representation fell in between these two extremes, and are shown in Figures 4 - 6.

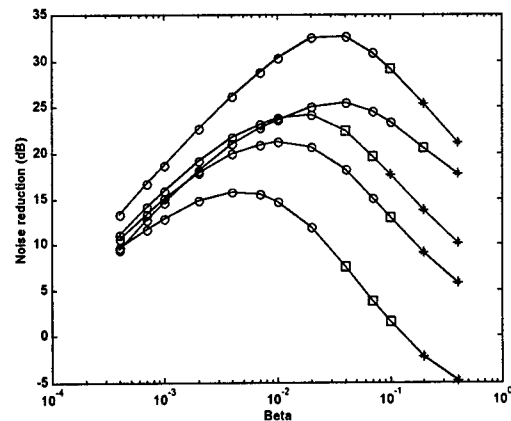


Figure 3: Noise reduction vs. β , IEEE floating-point math, five 1-km loops

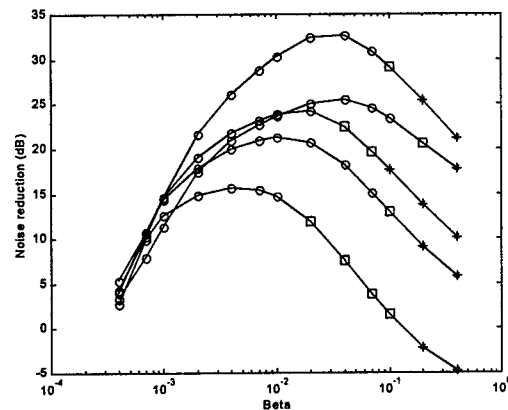


Figure 4: Noise reduction vs. β , 15-bit fixed-point math, five 1-km loops

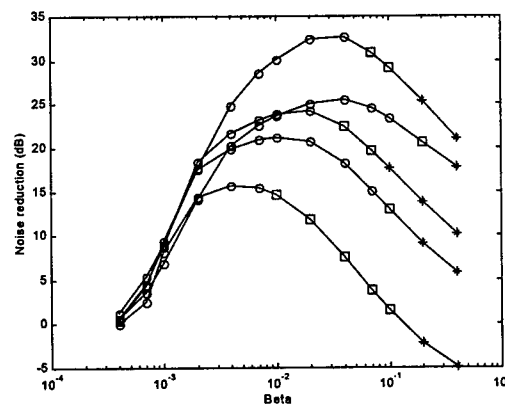


Figure 5: Noise reduction vs. β , 14-bit fixed-point math, five 1-km loops

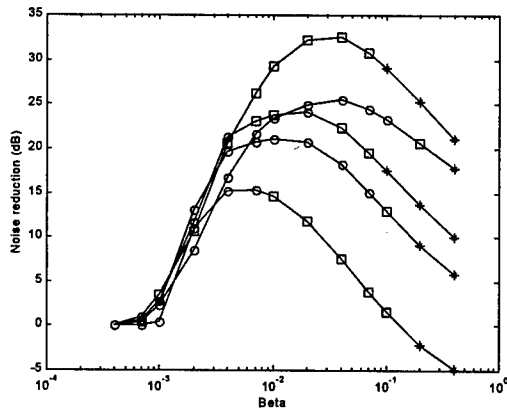


Figure 6: Noise reduction vs. β , 13-bit fixed-point math, five 1-km loops

It can be seen that the shapes of the noise reduction curves do not change much from the floating-point implementation. However, the noise floor does rise above -137 dBm/Hz for most points on the 13-bit plot. Accordingly, at least 14 bits should be used for the internal operations of the adaptive filter, even though its input and output are limited to 12 bits. For some extra margin against noise, a move to 15-bit representation would be prudent.

Plotting the value of β which gave the best noise reduction versus the input SIR, the following graph was obtained:

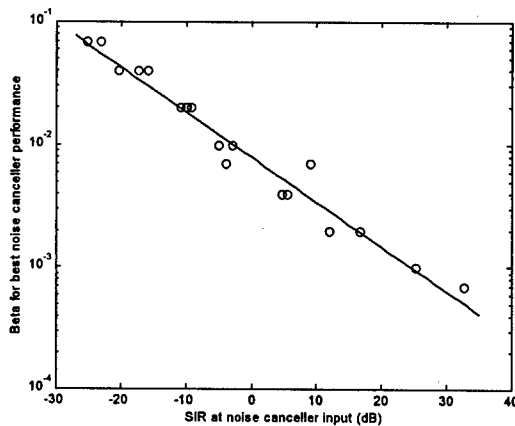


Figure 7: Optimal β vs. SIR of differential input

It can be seen that the logarithm of β demonstrates an approximately linear dependence on the SIR. The line shown on the plot is the best linear estimate for the points in the least-squares sense, and is described by:

$$\beta = 10^{(-0.0365 \cdot \text{SIR} - 2.1027)}, \quad -27 \leq \text{SIR}(\text{dB}) \leq 35 \quad (13)$$

If the receiver can develop a decent estimate of its differential SIR, this plot shows that it should be able to select an appropriate β for good cancellation performance.

The last result shown here pertains to the performance achievable with leaky LMS. Using the best value of β found for a particular cable, a million iterations of the leaky LMS algorithm were run for 14- and 15-bit math with both rounding and truncation. The tap weights were monitored for any steady increase which might indicate a susceptibility to overflow. The noise reduction figures that were achieved are depicted in Figure 8; the term "leakage factor" used in this graph applies to the expression $2\mu\alpha$ from equation 10.

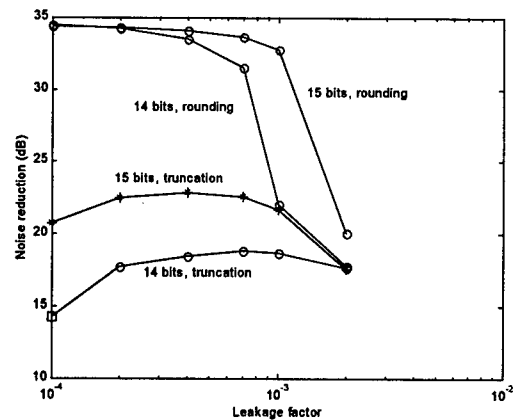


Figure 8: Noise reduction vs. leakage factor

Leakage of the filter taps did manage to stabilize the algorithm using truncation, preventing overflows for leakage factors of 0.0002 or more. However, the performance using truncation still fell over 10 dB below that possible with rounding. It is also interesting to note that leakage factors greater than 0.001 led to dramatic performance degradation for the implementations which used rounding.

When rounding was used, the tap weights were never observed to climb or fall steadily, even in a simulation run of several million iterations. This suggests that only a very small amount of leakage is necessary as insurance against instability. However, this hypothesis is still not proven; at the time of publication, long-term stability testing was just commencing.

Other scenarios which will be tested in the coming months include the performance of the canceller in the presence of impulse noise, as well as its capabilities when interference couples to the loop at several different physical locations. Performance in low-noise environments must also be evaluated to develop a set of rules governing when the canceller should be bypassed or shut down.

CONCLUSION

Wideband digital noise cancellation shows considerable promise as a solution to the interference problems experienced by xDSL. Simulation results show that the interference power can be reduced by over 30 dB in bad noise environments. This paper has also identified some of the problems and computational costs associated with digital cancellation, in particular:

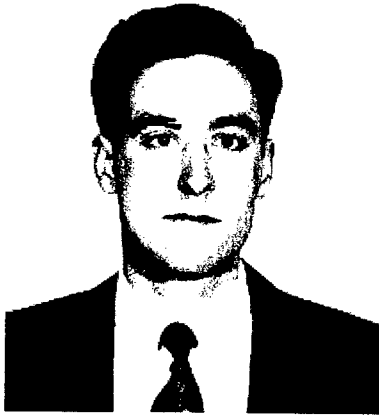
- a. the ill-conditioned nature of the common-mode input's autocorrelation matrix makes the canceller very sensitive to finite-precision effects. This implies that fixed-point circuits which simply truncate the double-precision bits created by multiplication operations cannot be used;
- b. reliable canceller operation is possible when the double-precision number is rounded rather than truncated after each multiplication. The finite-precision errors generated by rounding are much more likely to have zero mean, and can therefore counteract the high correlation between the common-mode input's samples;
- c. 12-bit ADCs are required for the two noise canceller inputs;
- d. 14- or 15-bit math will be necessary to bound finite-precision effects inside the adaptive filter within tolerable limits;
- e. low values for the adaptive filter's step size μ are required to keep gradient noise levels low and reduce the risk of instability;
- f. the values of μ leading to the best noise suppression performance can be approximately related to the SIR at the canceller's differential input by a simple equation; and
- g. a small amount of filter tap leakage will be necessary in order to ensure the

stable long-term performance of the canceller.

REFERENCES

1. David Jones, "Laboratory Measurements of a QAM-based VDSL Transceiver Being Used in Commercial Mass Market Service Deployments", *ANSI Contribution T1E1.4/99-313 (Broadcom Corporation)*, Ottawa, Ontario, 7 June 1999.
2. Mahbub Hoque, "Impact of RFI on Broadband Deployment and a few EMI Prediction Results Inside New York City", *ANSI Contribution T1E1.4/95-132 (Bellcore)*, Orlando, Florida, 13 November 1995.
3. N. Drew and K. Harris, "AM Ingress on xDSL Loops", *ANSI Contribution T1E1.4/99-132 (Nortel Networks)*, Costa Mesa, California, 8 March 1999.
4. Kevin Foster, "Practical Measurements of the Levels of Induced RFI from Amateur Radio Transmissions on Various Lengths of Dropwiring Commonly Found in BT's Access Network", *ANSI Contribution T1E1.4/95-097 (British Telecom)*, Silver Creek, Colorado, 21 August 1995.
5. Thomas Starr, John Cioffi and Peter Silverman, *Understanding Digital Subscriber Line Technology*, Prentice-Hall, 1999.
6. Richard A. Combellack, "Improving Range and Bandwidth of Telco Loop Plant", *Proceedings of the 47th International Wire and Cable Symposium*, Philadelphia, Pennsylvania, 16 - 19 November 1998.
7. Simon Haykin, *Adaptive Filter Theory*, Prentice-Hall Inc., 1996.
8. Bernard Widrow et al., "Adaptive Noise Cancellation: Principles and Applications", *Proceedings of the IEEE*, vol. 63, no 12, December 1975, pp. 1692-1716.
9. Bernard Widrow et al., "Stationary and Nonstationary Learning Characteristics of the LMS Adaptive Filter", *Proceedings of the IEEE*, vol. 64, no. 8, August 1976, pp 1151 - 1162.
10. Dennis J. Rauschmayer, "Crosstalk Reduction using Common-Mode Signal Correlation", *ANSI Contribution T1E1.4/96-069 (Pulse Communications Inc)*, Herndon, Virginia, 22 April 1996.
11. C. Conroy, B. Kim and J. Cioffi, "Some Implementation Issues Relevant to VDSL A/D Converters for Digital Duplexing", *ANSI Contribution T1E1.4/99-272R2 (VDSL Alliance)*, Ottawa, Ontario, 7 June 1999.
12. Robert Walden, "Analog-to-Digital Converter Survey and Analysis", *IEEE Journal on Selected Areas in Communications*, vol. 17, no. 4, April 1999, pp. 539 - 549.
13. David Jones, "Analog Front End Dynamic Range Requirements for Programmable Spectrum VDSL Systems", *ANSI Contribution T1E1.4/99-315 (Broadcom Corporation)*, Ottawa, Ontario, 7 June 1999.
14. John Cioffi, "Limited Precision Effects in Adaptive Filtering", *IEEE Transactions on Circuits and Systems*, vol. CAS-34, no. 7, July 1987.
15. John Cioffi, ed. "Very-high-speed Digital Subscriber Lines - System Requirements", *ANSI Contribution T1E1.4/98-043R8*, Plano, Texas, 30 November 1998.

BIOGRAPHY



Dave Fenton
S.I.T.E.
University of Ottawa
161 Louis Pasteur St.
Ottawa, Ontario K1N 6N5
Canada

Dave Fenton received his B.Eng. in Engineering Physics from the Royal Military College of Canada in 1992. He then served five years as a combat systems engineer in the Canadian navy before returning to university for graduate work. He is currently a Ph.D. student at the University of Ottawa. His primary research interest is digital signal processing for communications systems.

LASER WELDED METALLIC TUBES IN FIBRE OPTICAL CABLES

Jon S. Andreassen, Inge Vintermyr

Alcatel Kabel Norge AS, PO.Box 130 Økern, N-0509 Oslo, Norway

ABSTRACT

Laser welded metallic tubes with incorporated optical fibres has during the past years been used for a variety of cable designs. So far, fibres in metallic tubes are most frequently used in OPGW, submarine cables and special cable designs for military or industrial applications^{1,2,3,4,5}.

The tubes however are adequate for an even wider range of cables, from standard terrestrial cables to complex umbilical constructions for dynamic applications. The tube properties determine the proper cable design for the application in question, and it is consequently necessary to know certain characteristics of the tube.

The tube itself is a rugged construction, where in general the ratio between tube wall thickness and tube dimension determines the mechanical performance. Tubes may be manufactured in dimensions ranging from slightly below 1mm to more than 5mm diameter, and the maximum number of fibres per tube depends on design details such as fibre bend loss sensitivity, required fibre strain relief, fibre identification system, etc.

PROCESSING TUBES

The tube manufacturing starts with the forming of a flat metallic strip with a proper width for the tube dimension. The number of forming tools needed to obtain an adequate circularity may vary. The fibres and the filling compound are separately fed into the tube through small tubes ensuring protection against the laser weld beam. Finally, the tube is drawn down to the required diameter. This reduction is a cold deformation process enhancing the mechanical properties of the tube, in terms of higher yield strength.

A certain fibre excess length may be introduced into the tube, dependent on tube dimension and number of fibres.

Recently, Alcatel has manufactured 3.7mm stainless steel tubes with 48 fibres for a 192 fibre submarine cable⁶ where the fibre excess length is around 0.2%.

In principles, "infinite" continuous lengths may be manufactured, limited by the dimension of the pay off and take up systems. It is possible to stop and continue the tube process, allowing jointing of the metallic strip or fibres. For a 2.3mm outer diameter tube with a wall thickness of 0.2mm, up to 90km lengths are manufactured with a high yield.

In order to splice tubes, either for obtaining long lengths of cable core or as a repair option, a special procedure has been worked out, maintaining the outer diameter of the tube. Thus, the tube splice

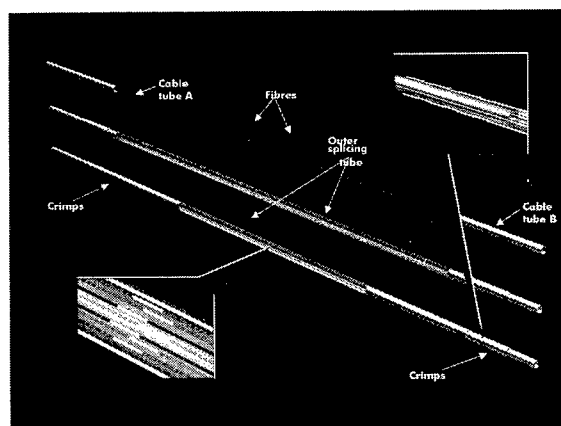


Figure 1 Schematic view on tube splice.

enters further cable processes without any special arrangements. This splice is based on a steel inner sleeve onto which the original tube is crimped, using a hydraulic pressure tool, as shown in Figure 1.

Such joints have been exposed to hydrostatic pressure tests of 1000bars without any leakage or collapse. The tube joint has a breaking load of minimum 80% of the tube itself.

APPLICATIONS

The metallic tube may in principles be applicable similar to any other polymeric tube, either into a stranded layer, or as a central tube. It is quite possible to obtain a fibre excess length into the tube itself in the tube manufacturing process, however by stranding the tube, the fibre strain relief can be expanded.

The stranded configuration is preferred for cables in vertical installations or for cables subjected to high axial elongation. Stranding small size tubes will result in an improved flexibility for the cable, as the bending stiffness will be reduced.

The compactness of a metallic tube fibre element makes it attractive for use in composite cables or umbilical cables for power and signal transmission. In many industrial applications, where harsh environments and severe mechanical exposures may be present, the small dimension, yet robust cable design is well suited. Also, for encapsulation of fibres for temperature sensing application, the metallic tubes are adequate due to small size, quick thermal response and mechanical performance avoiding other exposures to the sensor fibre.

For industrial or underwater applications, the metallic tubes are easy to incorporate in systems where gas or hydrostatic pressure tight penetrators have to be used. Due to the mechanical strength, the tube is not deformed in the penetrator or when exposed to pressure to the same degree as other fibre cable cores, which provides a good and durable tightness. This also applies to submarine cable joints for deep waters.

The most common material for such use is presently steel, however for special environments, other types of materials such as different Ni-Cr alloys can be used. Tubes from such alloys have for instance been used by Alcatel in Norway for cables for permanent installation into oil wells with a highly corrosive environment.

MECHANICAL PROPERTIES

One of the attractive features of the laser welded metallic tube is the robustness. This provides a good mechanical protection of the fibres, and may for many applications alone fulfil the mechanical requirements for the cable.

Hydrostatic Pressure

A tube will when exposed to a sufficiently high hydrostatic pressure collapse. When a hydrostatic pressure is acting on a tube, stresses will occur in the tube material. For safe and reliable operation, the maximum compressive stress introduced by the hydrostatic pressure should not exceed the yield stress for the tube material. For a circular tube with an initial radial deformation μ_0 , the hydrostatic pressure resistance can be evaluated from the following⁷:

$$\sigma_y > \sigma_{\max} = \frac{PR}{t} + \frac{6PR\mu_0}{t^2} \cdot \frac{1}{1 - \frac{P}{P_{CR}}}$$

Eq. 1

Where σ_y is the yield stress, σ_{\max} is the maximum stress introduced by the pressure, R is the tube radius and t is the tube wall thickness. The deformation μ_0 , is defined as the difference between original tube radius and minimum "radius" for an oval tube. It should be noted that the tube radius is the distance from the center of the tube to the middle of the tube wall. P is the hydrostatic pressure, and P_{CR} is a "critical pressure" which according to the above should be defined as:

$$P_{CR} = \frac{\sigma_y t}{R}$$

Eq. 2

By introducing a relative deformation, $\mu_0^* = \mu_0/R$, one sees from Eq. 1 that the pressure resistance is determined by the ratio between the tube wall thickness and the tube radius.

In Figure 2, the calculated collapse pressure versus t/R is shown for tubes with initial deformations up to above 10% are shown. For the calculations, an E-modulus of 200GPa and yield strength of 900MPa has been used. It should be noted that the tube manufacturing introduces a cold deformation of the tube material, which may increase the yield strength. Hence, the actual yield strength of the tube should be measured for more precise calculations. Also, the formulas do not take into consideration that the tubes are filled with a compound. If properly filled, this compound will lead to a counter pressure when the tube is subjected to radial compression. This

counter pressure will resist the collapse further. Also, for the calculations it has been assumed that the effect of the weld seam is negligible. It follows that calculations as shown below are considered to be rather conservative, however may be used as guidelines for tube dimensioning.

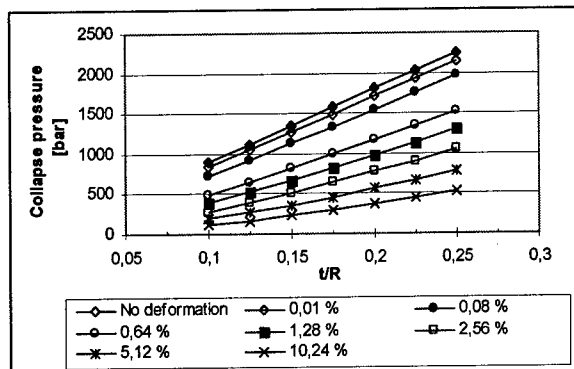


Figure 2 Collapse pressure vs. t/R ratio for various initial deformations.

One sees from Figure 2 that the ovality of the tube is of high importance for the hydrostatic pressure resistance. In Figure 3, the collapse pressure for a 2.3mm outer diameter tube with tube wall thickness ranging from 0.1mm up to 0.25mm is presented vs the initial deformation.

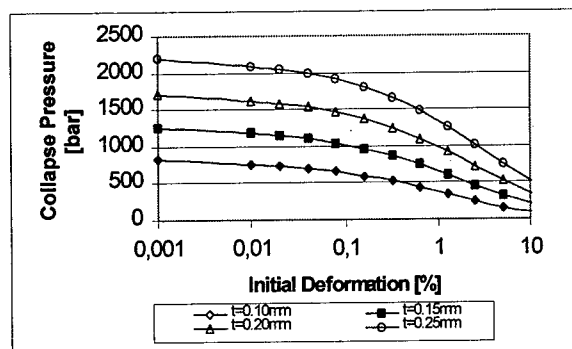


Figure 3 Collapse pressure vs. initial deformation for 2.3mm OD tube with different wall thickness

This reduction in pressure resistance has to be taken into consideration when evaluating not only tube quality itself, but also possible radial exposures during cable manufacturing and cable installation. If the tube for instance will be stranded, a certain deformation due to the curvature in the helical configuration will be introduced. Further, consequence of drum size, capstans and other cable handling machineries has to be considered.

Radial Crush

Assuming that a tube is exposed to a lateral load q per length unit, a deformation of the tube will take place. The reduction in diameter in the direction of the load will be ⁸

$$\delta = 0,149 \frac{q \cdot dz \cdot R^3}{E \cdot I} = 1,788 \frac{q \cdot R^3}{E \cdot t^3} \quad \text{Eq. 3}$$

Where the tube moment of inertia, I , is given by

$$I = \frac{t^3 dz}{12} \quad \text{Eq. 4}$$

By introducing the relative deformation, $\delta^* = \delta / (2R)$, one obtains:

$$\delta^* = 0,894 \frac{1}{t} \frac{q}{E} \left(\frac{R}{t} \right)^2 \quad \text{Eq. 5}$$

Again, the effect of the weld seam is assumed to be negligible.

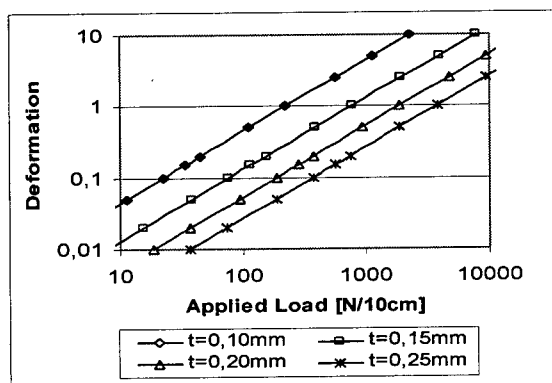


Figure 4 Deformation vs. applied lateral load for 2.3mm OD tube with different wall thickness.

In Figure 4, the relative deformation of a 2.3mm OD tube is shown for the same tube wall thickness as in Figure 3.

The expected radial forces that the tube will be exposed to, during manufacturing, cable installation

or cable operation has to be considered with respect to possible consequence on tube deformation. From the calculations of hydrostatic pressure resistance, it was clearly demonstrated that small deformations in terms of ovality of the tubes significantly reduce the strength of the tube.

Fatigue

For some cable applications, the operational conditions will lead to repeated loads in terms of variable axial tension or bending cycles. An aerial cable will be subjected to wind forces, introducing vibrations; similar to a hanging submerged cable exposed to water currents. Further, "dynamic cables" used for instance for remotely operated vehicles will be exposed to repeated off- and on-windings on the winch when operating the vehicles.

For every application, it is of importance to evaluate the operational conditions, so as to predict the corresponding load cycles. Next, when incorporating the tubes in the cable design one has to take into consideration the stresses that will be acting on the tube itself. These stresses will depend on design parameters such as lay length and layer diameter for stranded tubes and of course the axial stiffness and bending stiffness of the cable construction.

The fatigue strength of a material may be obtained from so called SN curves, that is plotting the lifetime or number of load cycles to failure versus applied load. Figure 5 show such data for a 2.3mm steel tube with a wall thickness of 0.2mm. Steel tube specimens were exposed to axial load cycles with an R-ratio equal to 0.1. ($R = \sigma_{\min} / \sigma_{\max}$). The number of cycles to failure was recorded for stress ranges from 400 MPa to 700 MPa. Some of the specimens were pre-strained by bending at 2% and 4% before cycling.

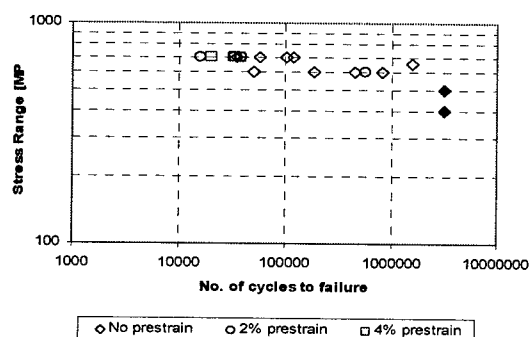


Figure 5 Fatigue diagram for 2.3mm steel tube. Tube wall thickness 0.2mm.

The filled markers in Figure 5 are actually test run outs, that is no fracture occurred. Some of the tube breaks were located in the termination sockets rather than on the mid span of the tubes, which probably makes the fatigue data somewhat conservative.

From the results, one sees that the slope is small, and that there seems to be a fatigue limit in constant amplitude loading at a stress range of approximately 500 MPa. The prestrain has only a small effect on the fatigue strength due to the small slope of the SN curve. This effect is less than 100 MPa.

The SN data can be fitted to the following expression:

$$\ln(N) = A - m \ln(\Delta S)$$

Eq. 6

where N is the number of cycles to failure, $A=144.1$ (Constant) and ΔS is the stress range in MPa. From the experimental study, m is estimated to 20.6.

From this, the following figures can be obtained:

Table 1

No. of cycles	Max. stress range
1000	780 MPa
10000	700 MPa
100000	620 MPa

By knowing the fatigue strength of the tube, the criteria for allowed stresses should be corresponding to the expected number of cycles, and the cable design should provide the fulfilment of these.

HYDROGEN DIFFUSION

The laser welded metallic tube adds a significant delay for the hydrogen diffusion into the surroundings of the optical fibres. Hydrogen may be present in the environment or generated within the cable as a consequence of exposing the cable to the environmental conditions, such as corrosion of cable armouring.

The hydrogen induced loss increase is of course dependent on the amount of hydrogen present in the fibre core. The diffusion path of hydrogen includes the tube wall, filling compound and fibre coating and cladding, before entering the lightguiding region of the fibre. Thus, there is a certain delay in "optical

response" on the environmental hydrogen concentrations, corresponding to the time needed for "building up" a hydrogen concentration at the regions of interest. Compared to the diffusion through the tube wall, the diffusion through all other materials within the tube are fast. Hence, it is assumed that the concentration of hydrogen molecules in the fibre core is in equilibrium to the partial pressure inside the tube at all times.

Considering a long cylinder, the general diffusion equation is⁹

$$\frac{\partial C}{\partial t} = \frac{1}{r} \frac{\partial}{\partial r} \left(r D \frac{\partial C}{\partial r} \right)$$

Eq. 7

where C is the concentration of the diffusing substance and D is the diffusion constant.

Considering a tube, and a constant diffusion coefficient, the steady state general solution of Eq. 7 for values of r between inner and outer radius of the tube is

$$C = A + B \ln(r)$$

Eq. 8

Assuming that at time zero, the inside partial pressure of hydrogen, p_i , in the tube is zero. However, the existence of hydrogen outside the tube initiates the diffusion process, and a hydrogen pressure inside the tube will build up, which when equilibrium is reached equalises the outer pressure. The time dependency of this build up can be expressed by:

$$\frac{dn}{dt} = \frac{d}{dt} \left(\frac{p_i V}{RT} \right) = \frac{2\pi P}{\ln \left(\frac{R_o}{R_i} \right)} (\sqrt{p_o} - \sqrt{p_i})$$

Eq. 9

where n is number of hydrogen molecules [mole], p_i and p_o are the inner and outer partial pressure, respectively, P is the permeability of hydrogen for the tube material, and R_i and R_o are the inner and outer radius of the tube. V is the free volume inside the tube, T is the absolute temperature and R is the molar gas constant. In Eq. 9, the relations given in Eq. 10 have been used, where K is the solubility and D is the diffusion coefficient

$$C = K \cdot \sqrt{p}$$

$$P = D \cdot K$$

Eq. 10

In terms of partial pressure, Eq. 9 turns into

$$\frac{dp_i}{dt} = \frac{RT}{V} \frac{2\pi P}{\ln \left(\frac{R_o}{R_i} \right)} (\sqrt{p_o} - \sqrt{p_i})$$

Eq. 11

For stainless steel (AISI 304), the permeability is given by¹⁰

$$P \approx 1 \cdot 10^7 e^{\frac{57800}{RT}} \left[\text{mole} (ms \sqrt{Pa})^{-1} \right]$$

Eq. 12

where the activation energy is given in J/mole, and R is the molar gas constant in J/(mole·K).

Regarding the volume, V, in Eq. 11, the volume inside the tube contains materials with different solubilities, such as glass, polymer coating and filling compound. For simplicity, however, all calculations here are based on the assumption that the "free volume" inside the tube is 90% of the total volume.

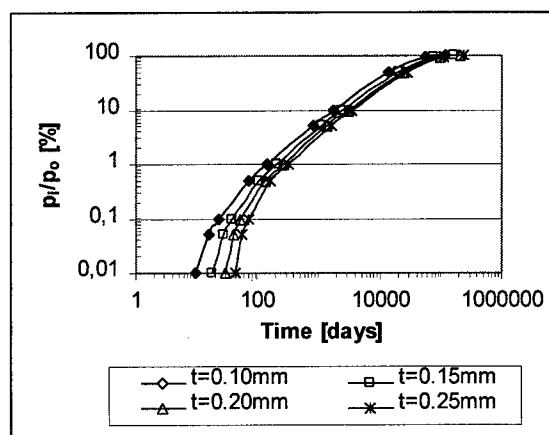


Figure 6 Relative H_2 pressure inside tube vs time. Outer pressure, $p_o = 1 \text{ bar}$, temperature = 20°C

One sees from Eq. 11 and Eq. 12 that the temperature is of high importance for the diffusion rate, both in terms of the $pV=nRT$ relation and the influence on the permeability for the material. The

tube wall thickness affects the path of the diffusion expressed by the $\ln(R_o/R_i)$ term as well as the volume V. In Figure 6 the internal partial pressure is shown versus time for a 2.3mm tube with various wall thickness, at a temperature of 20°C and an outer partial pressure of 1 bar. Time needed to build up a 100mbar pressure inside the tube is ranging from approximately 5 years for the 0.10mm tube wall to about 10 years for the 0.25mm tube wall thickness. More than some hundred years are needed for the inside pressure to reach 99% of the outer pressure.

In Figure 7, the inside partial H₂ pressure is shown versus time at different temperature for a 2.3mm tube with a wall thickness of 0.2mm, at an outer partial pressure of 0.1bar. Within the temperature range from 5°C to 70°C, the time needed to reach a certain pressure inside the tube varies by a few orders of magnitude, and the calculations clearly demonstrates the importance of temperature on the diffusion rate.

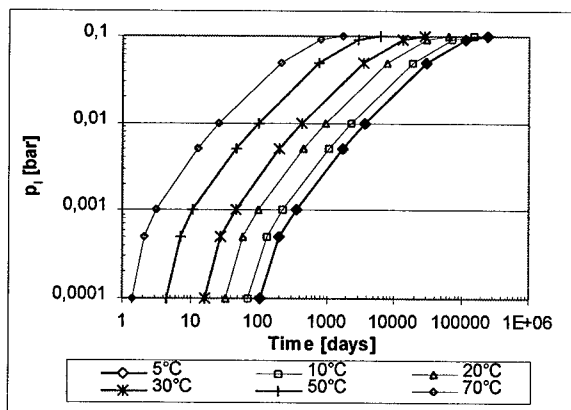


Figure 7 H₂ pressure inside tube vs time. Outer pressure, $p_o=0.1$ bar. Tube outer diameter = 2.3mm. Tube wall thickness = 0.2mm

At low temperatures, the diffusion is indeed very slow. At an outer pressure of 100mbar, it takes more than 10years to reach an inner pressure of 10mbar and about 80 years to reach 50mbar. Investigations on submarine cables installed along the Norwegian coast on "open" cable designs without any diffusion barrier¹¹, indicates that the hydrogen generated from corrosion of armour wires typically causes a hydrogen level of 100mbar order of magnitude.

For tube material according to AISI 316, the permeability is even lower¹²:

$$P \approx 2.3 \cdot 10^7 e^{-\frac{63496}{RT}} \left[\text{mole (ms } \sqrt{\text{Pa}})^{-1} \right] \quad \text{Eq. 13}$$

which compared to the standard material (AISI 304) reduces the hydrogen diffusion rate. In Table 2, a comparison between 2.3mm tubes with a 0.2mm wall thickness made from the two different steel materials is shown.

Table 2 Time needed to reach 10 and 50 mbar inside pressure at 5°C for outer partial H₂ pressures of 0.1 and 1bar. Tube diameter = 2.3mm, tube wall thickness = 0.2mm

p_i	$p_o=100\text{mbar}$		$p_o=1\text{bar}$	
	AISI 304	AISI 316	AISI 304	AISI 316
10 mbar	10 years	50 years	3 years	13 years
50 mbar	80 years	400 years	15 years	70 years

It follows that the hydrogen-induced loss in submarine cable applications at end of life will be very small, even without any further protective measures.

For high temperatures, the expected environmental conditions and the required lifetime of the application have to be considered together with diffusion properties of the steel tube itself.

CONCLUSION

Laser welded metallic tubes are applicable for a variety of cable designs and applications. Several steel types and alloys can be used for processing tubes, and the environmental conditions for the application determines the material choice.

The manufacturing process of laser welded tubes allows long continuous lengths. The robustness of the tube provides reliable cable production, and the available techniques for jointing tubes reduces the frequency of traditional cable splice houses on delivery lengths for long submarine cables.

The mechanical properties of steel tubes are excellent, in terms of high yield strength and ductility. The fatigue strength of the metallic tubes proves the applicability for dynamic cable applications as well as for permanently installed cables.

The hydrogen permeability of metallic tubes is sufficiently low for ensuring small hydrogen induced losses in submarine cables.

REFERENCES

1. G. Berthelsen, I. Vintermyr; "New low weight / small diameter optical fibre submarine cable for unrepeated system"; Proc. IWCS 1994
2. J-F. Libert, Y. Charles; "New submarine cable design for long-haul, high bit rate systems"; Proc. IWCS 1996
3. T. Yokokawa, et al; "Development of small size and high performance central stainless tube optical ground wire using colored thread binders for identification of fiber bundles"; Proc. IWCS 1996
4. C. Unger, G. Zeidler; "High fiber counts in aerial and submarine optical cables with metal tube design"; Proc. IWCS 1998
5. H. Ishisaki, et al; "Development of electro-fiber optic cable containing metal tube armored fiber for deep sea tow"; Proc. IWCS 1996
6. I. Vintermyr; "High fibre count submarine cable for unrepeated systems"; Proc. IWCS 1999
7. S. Timoschenko; "Strength of materials, Part II"; Third Edition, Van Nostrand Reinhold Company, 1958.
8. S. Timoschenko; "Strength of materials, Part I"; Third Edition, Van Nostrand Reinhold Company, 1955.
9. J.Crank; "The Mathematics of Diffusion", Second edition, Oxford University Press 1975, ISBN 0-19-853411-6.
10. J.T. Perng, C.S. Altstetter; "Effects of deformation on hydrogen permeation in austenitic stainless steels"; Acta metal. 34 pp.1771, 1986
11. S. Hopland; "Long term behaviour of hydrogen induced losses in installed fibreoptic submarine and underwater cables"; Proc. IWCS 1997
12. E.H. Van Deventer, V.A. Maroni; "Hydrogen permeation characteristics of some austenitic and nickel-base alloys"; J. Nuclear Materials 92 (1980) 103-111

SPEAKER BIOGRAPHY



Jon Steinar Andreassen
Alcatel Kabel Norge AS
PO Box 130 Økern
N-0509 Oslo, Norway

Jon Steinar Andreassen graduated from the University of Trondheim with a degree in physical electronics in 1985. He joined STK, now Alcatel Kabel Norge in 1986, and has been working with research and development of fibre optic cables, with special emphasis on reliability issues and cables for specialty applications.

EVALUATION OF BENDING STIFFNESS OF FIBEROPTIC SUBMARINE CABLE IN BOTH ELASTIC AND PLASTIC REGIONS

T. C. Chu

Tyco Submarine Systems Ltd.
250 Industrial Way West
Eatontown, New Jersey 07724

ABSTRACT

A theoretical model has been formulated to evaluate the bending stiffness of submarine cables in both linear elastic and nonlinear plastic regions. The predicted bending stiffness for a deep water fiber optic submarine cable is found to be in good agreement with the measured data from a four-point bending test. This model has been applied to evaluate the bending stiffness of various type cables within a fiber optic submarine cable family.

FORMULATION

Submarine cable normally consists of constituent materials in three different physical forms: straight cylindrical members, tubular members, and helically stranded members. Assuming negligible coupling friction among the members, the bending stiffness of the cable can be evaluated by the summation of bending stiffness of all constituent members:

$$(EI)_c = \sum_i E_i I_i \quad (1)$$

Where $(EI)_c$ is the cable bending stiffness and $E_i I_i$ is the bending stiffness of each constituent member. For a straight cylindrical member with diameter d and modulus of elasticity E , the bending stiffness is

$$EI = E \frac{\pi d^4}{64} \quad (2)$$

For a tubular member with outside diameter d_o and inside diameter d_i , the bending stiffness is

$$EI = E \frac{\pi(d_o^4 - d_i^4)}{64} \quad (3)$$

For a helically stranded strength member with diameter d , the bending stiffness is

$$EI = \frac{\cos \theta}{\frac{1 + \cos \theta^2}{E \pi d^4 / 32} + \frac{\sin \theta^2}{H \pi d^4 / 16}} \quad (4)$$

Where H is the modulus of rigidity and θ is the lay angle.

When cable is at small bending deflection, i.e. with large bending radius, the bending stiffness of the cable can be evaluated by the linear model where E and H are assumed to be constant. However, as the deflection becomes large, such as at looping and kink conditions, the linear model is no longer applicable since the cable constituent members are bent beyond the elastic limit into the plastic region. The modulus of elasticity in the plastic region is then a function of axial strain, $E = E(\epsilon)$. Such functional relationship has previously been determined by regression analysis from tensile test data for each cable constituent material¹. The test data can be approximated with an exponential function of the form:

$$\sigma(\epsilon) = a(1 - e^{-b\epsilon}) + c \quad (5)$$

Where $\sigma(\epsilon)$ and ϵ are the stress and strain respectively and a , b , and c are constant coefficients. The modulus of elasticity $E(\epsilon)$ for each material is then obtained by differentiating Equation (5)

$$E(\epsilon) = ab(e^{-b\epsilon}) \quad (6)$$

In the case of pure bending of a body, the axial strain ϵ is related to the bending radius R by

$$\epsilon = \frac{r}{R} \quad (7)$$

r is the distance between the element in the body and the neutral axis of the body.

Substitution of Equations (6) and (7) into Equation (1) yields the cable bending stiffness as a function of bending radius:

$$EI_c = \sum_i E_i \left(\frac{r}{R} \right) I_i \quad (8)$$

This is the equation for evaluating the cable bending stiffness in both elastic and plastic regions.

Equation (8) is applied to a deep water submarine cable and the result is compared with measured data from a four point bending test. The deep water submarine cable consists of a unit fiber structure protected by two layers of stranded high strength steel wires, a copper sheath, and a medium density polyethylene jacket as shown in Fig. 1. The unit fiber structure contains a copper clad steel wire (kingwire) with optical fibers helically wound and embedded in a buffering elastomeric material.

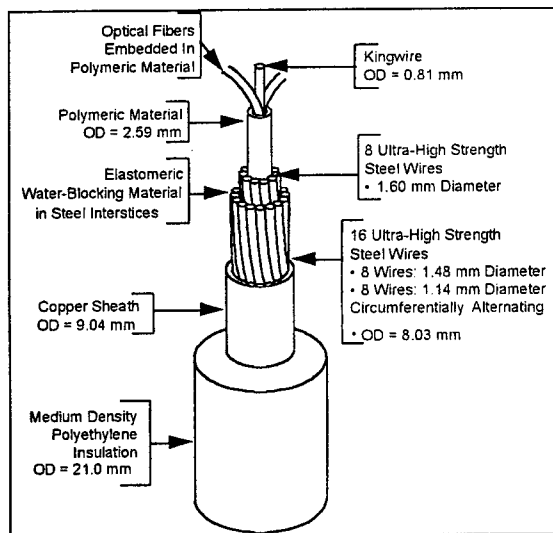


Fig.1 Deep water fiber optic cable

The cable constituent materials that contribute to the bending stiffness are the kingwire, stranded high strength steel wires, copper sheath, and polyethylene jacket. The tensile test data for these materials and corresponding exponential functions from nonlinear regression are shown in Fig. 2 to Fig. 5.

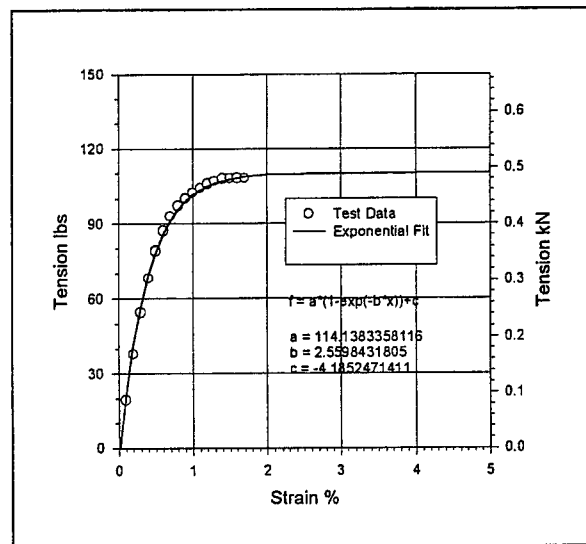


Fig. 2 Tensile test data and exponential function plotted for kingwire

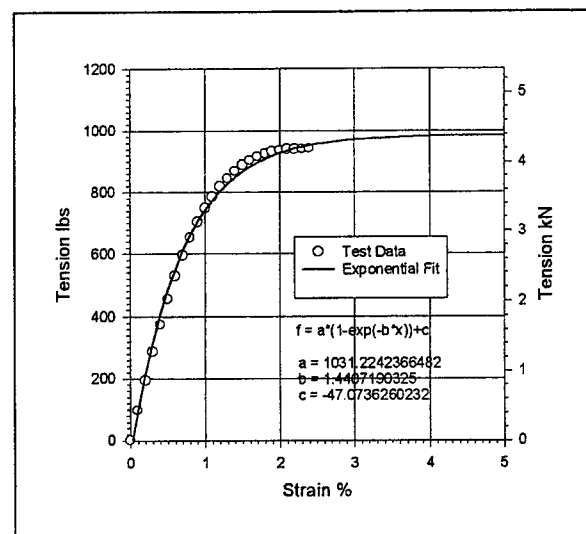


Fig. 3 Tensile test data and exponential function plotted for high strength steel wires

Since the copper sheath is swaged to the stranded steel wire package during cable manufacturing, high friction coupling is created for the steel wires by the copper sheath. A coupling factor C is introduced in Equation (8) to account for this coupling effect.

$$EI_c = EI_{kw} + C(EI_{steel1} + EI_{steel2} + EI_{steel3}) + EI_{cu} + EI_{mdpe} \quad (9)$$

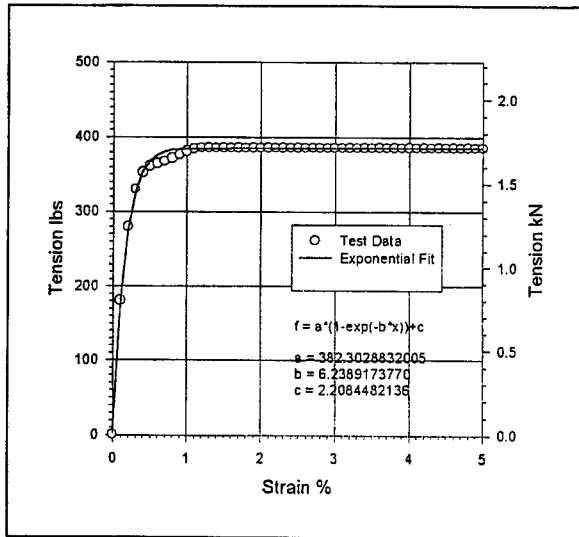


Fig. 4 Tensile test data and exponential function plotted for copper sheath

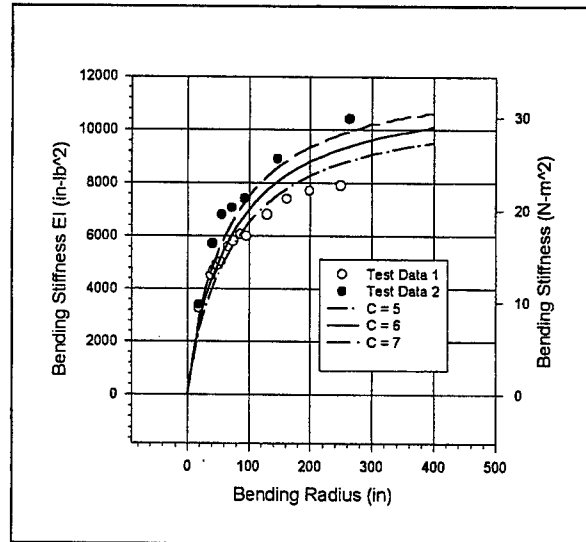


Fig. 6 Comparison of theoretical and measured bending stiffness for a deep water fiber optic submarine cable

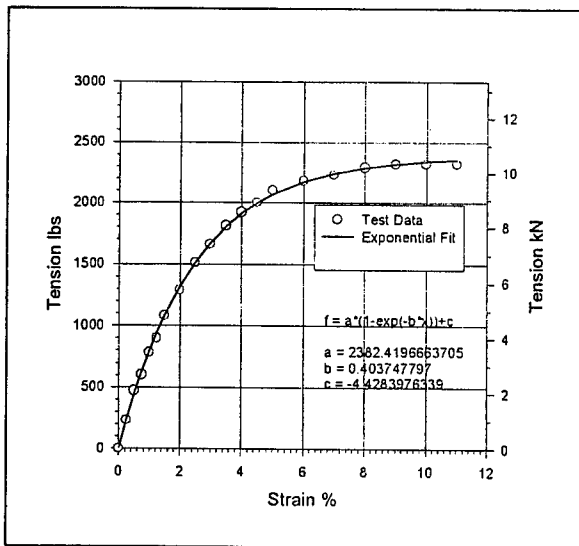


Fig. 5 Tensile test data and exponential function plotted for MDPE

Equation (9) is calculated for $C = 5, 6$ and 7 , and the results are plotted with the measured data from four-point bending tests in Fig. 6. This indicates that the theoretical model with $C = 6$ is a compromise average for the test data.

APPLICATIONS

The present model is applied to various cable types within the SL21 fiber optic submarine cable family, which includes deep water lightweight (LW) cable, special application cable (SPA), single armored (SA) and double armored (DA) cable. The LW cable is geometrically similar to the tested deep water fiber optic cable shown in Fig. 1 except that the diameters of the high strength steel wires in the SL-LW are slightly larger (1.88 mm, 1.76 mm, and 1.36 mm), which result in slightly larger copper OD (10.41 mm). The SPA cable has an additional metallic tape and second polyethylene (HDPE) jacket over the LW cable to provide additional abrasion protection and hydrogen sulfide protection. The SA has one armor layer applied over the Lightweight cable while the DA has two armor layers for additional protection. The configurations of SPA, SA, and DA are shown Fig. 7 to Fig. 9, respectively. The results of calculation for these cables with $C = 6$ are given in Fig. 10.

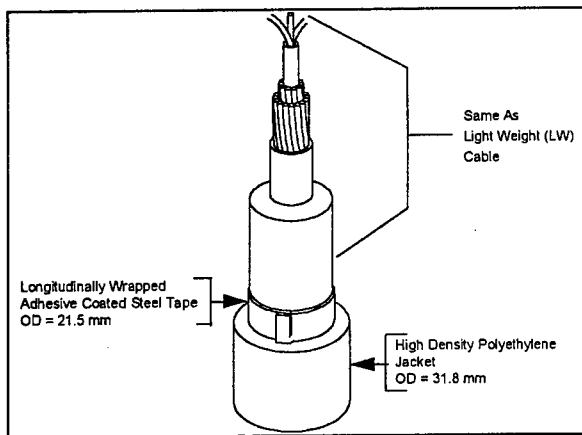


Fig. 7 Special Application (SPA) Cable

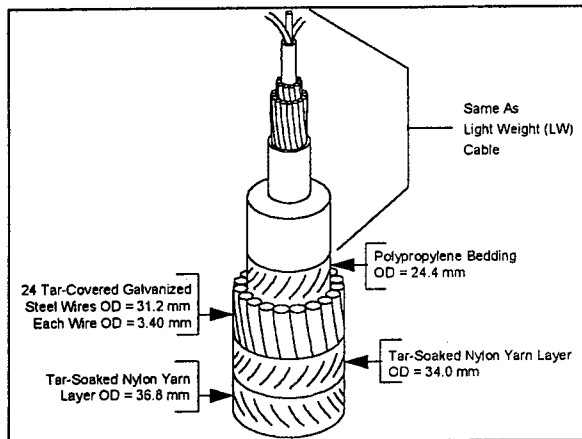


Fig. 8 Single armored (SA) cable

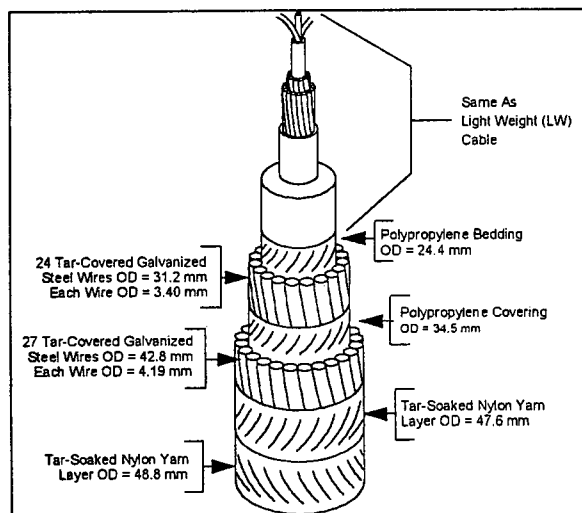


Fig. 9 Double armored (DA) cable

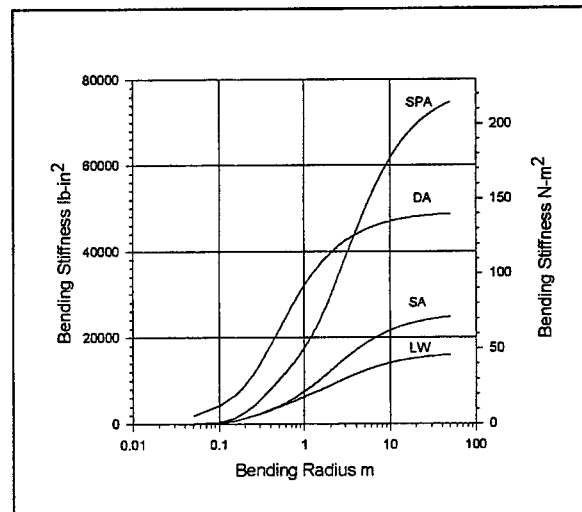


Fig. 10 Bending stiffness of different type submarine cables

The bending stiffness of the cable decreases drastically as the bending radius reduces. At normal handling radius of 1 to 2 meters the bending stiffness is much smaller than the value evaluated from linear elastic theory, which is represented by the asymptote of each curve in Fig. 11. Cable with smaller bending stiffness is more susceptible for looping and kink at a given torque as shown by the following relations ².

$$\tau = \sqrt{2PEI_c} \quad (10)$$

or

$$P = \frac{\tau^2}{2EI_c} \quad (11)$$

Where τ is the minimum torque required to generate a loop and P is the minimum axial tension required to prevent the formation of a loop. It is important for submarine cable to avoid looping at ocean bottom, especially for armored cable that generates large torque. The bending stiffness evaluated by the present model provides a more accurate estimate for the tension required to prevent the formation of loops and kinks.

CONCLUSIONS

A theoretical model has been applied to several fiber optic submarine cables to predict their bending stiffness in both the linear elastic and nonlinear plastic regions. Comparison between the theoretical and test data for a deep water

cable shows good agreement. The present model provides a more accurate tension estimate required to prevent the formation of loops and kinks during cable deployment.

REFERENCES

1. T. C. Chu and R. J. Rue, "Evaluation of Mechanical Properties of Various Fiberoptic Submarine Cables in Both Elastic and Plastic Regions," 47th International Wire and Cable Symposium, Philadelphia, 1998.
2. A. L. Ross, "Cable Kinking Analysis and Prevention," J. Eng. Ind. Vol. 99, 1977, pp.112-115.

BIOGRAPHY



T. C. Chu
Tyco Submarine
Systems Ltd.
Holmdel, NJ

T. C. Chu received his B.S.M.E Mechanical Engineering from Cheng Kung University, Taiwan, 1964, M.S.M.E. Mechanical Engineering from Syracuse University, 1967 and Ph.D. Aerospace Engineering from Cornell University, 1971. He joined Bell Laboratories in 1972 and retired from AT&T Bell Laboratories in 1997. He was responsible for the design and development of AT&T's SL and SL100 fiber optic submarine cable. He is currently a Distinguished Member of Technical Staff with the Cable Development Division of Tyco Submarine Systems Ltd.

FIBRE OPTICS FOR THE OFF SHORE INDUSTRY

Måns Isacsson, Kaj Sjölin & Joakim Jörgensen

Ericsson Cables AB Kabelvägen 1, 824 82 Hudiksvall Sweden

ABSTRACT

A 2.5 Gbit/s repeterless submarine fibre optic link has been designed and subsequently installed in the North Sea. The link connects four oil platforms with the Norwegian mainland. In total 500 km of submarine cable was installed. All cables used in the system except for the platform top-side cables are of ribbon design. The main cable is a 200 kN double armored cable with 24 to 48 fibres. Different solutions for platform connections, special cables, joints and branching units have been developed and installed.

INTRODUCTION

The platforms extracting oil and gas in the North Sea are relatively large production units, situated up to 300 km from the Norwegian mainland. One platform can extract more than 50000 barrels of oil per day and more than 200 persons can live and work on one single platform. The hazardous environment and the complicated production process demand a good communication between the platforms and the mainland. The best way to maintain a good communication is by a fibre optic link. Fibre optic links have a number of advantages compared to microwave links and satellite communication, commonly used in the offshore industry. Some of the advantages are:

- Higher capacity.
- No access time, which can be a problem using satellite communication.
- Very low downtime compared to radio systems.
- Long term cost effective in comparison with satellite communication.

These advantages have led to an increasing interest in fibre optics in the offshore industry during the last years.

Ericsson Cables in Hudiksvall, Sweden has on behalf of the Norwegian Oil Company Statoil provided a 2.5 Gbit/s repeterless submarine fibre optic link. The link connects the four oil platforms Heidrun, Draupner, Sleipner A, and Sleipner E in the North Sea to Tjeldbergsodden and Kårstø, on the Norwegian coast. Connection of four more platforms at a later stage has been prepared by installing branching units and prepared cable ends. The cable route is shown in figure 1. In total 500 km of submarine cable was installed.

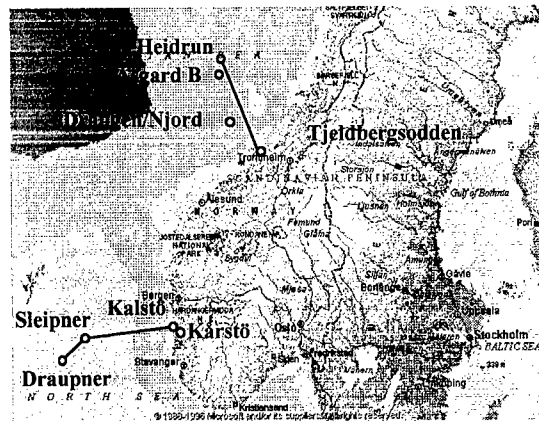


Figure 1; Route of the Installed fibre optic link.

The difference in engineering and installing a submarine cable link for the off shore industry and an ordinary submarine cable link is the fact that almost every connection to the platforms requires an individual design.

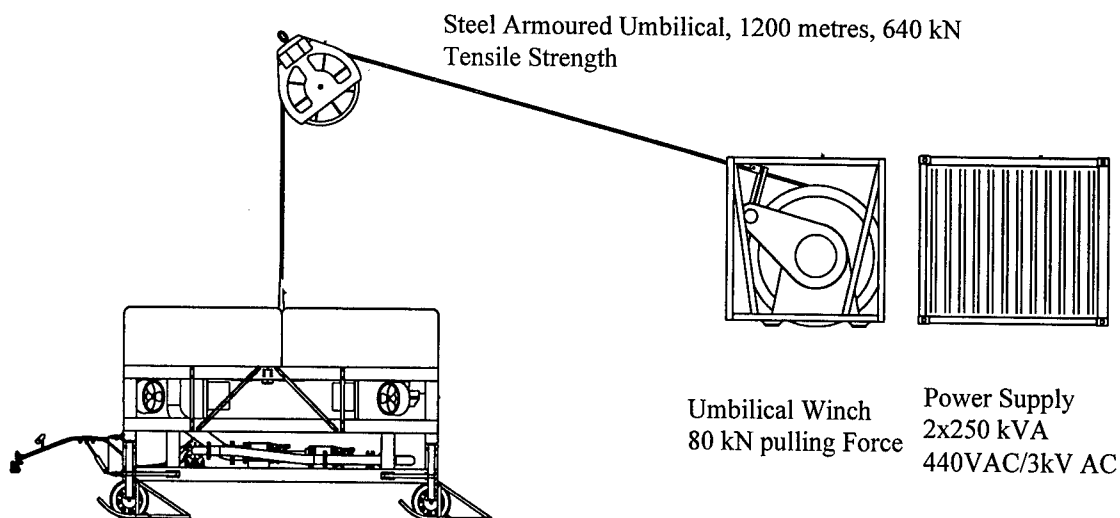


Figure 2; The remote operated trenching system provided by Uddevalla Dyk & Sjötjänst AB.

Also the high safety demands, especially in the safety zones close to the platforms, requires a very good positioning system for the cable ship and well-planned procedures for the work.

The Swedish Telecommunication Company, Swedia carried out the installation as a subcontractor to Ericsson Cables. The conditions of the seabed along the installation route were relatively well known, following a previous installation of a pipeline along the same route. Therefore a new survey was not considered necessary. The installation was performed using a cable ship with a digital positioning system. The ship was equipped with a Remote Operated Vehicle (ROV). As a protection against third party damage the cable was buried 0.5 to 1 m under the seabed. The burying of the cable was performed using a Remote Operated Trenching System (ROTS). The ROTS (figure 2) is a water jetting equipment manoeuvred from the cable ship. The ROV was used for different types of assignments such as survey, assistance of the ROTS, installation work etc. Both combined laying and trenching as well as separate were used.

In combined laying and trenching the trenching conditions determine the speed. The vessel is in this case put in a follow sub mode in which the navigation system keeps the distance to the ROTS constant and moves in the same direction and with the same speed as the ROTS. With good trenching conditions a speed of 900 m/h was achieved. In separate laying and trenching the vessel determines the speed during the lay and the touch down point of the cable is monitored using the ROTS or the ROV. In this case the ship have to come back to perform the trenching at a later stage.

Many different types of cables are used in the fibre optic system. All of the cables, except for the topside cables, are of ribbon design. The different cable types are:

- Submarine cables
- Indoor cables
- Land cables
- Platform top-side cables
- Hang-off cables
- Tunnel cable

OPTICAL CABLE PRODUCTS

Submarine Cable

The submarine cable used in the system is a 200 kN double armoured (DA) cable. The cross-section is shown in figure 3. The cable has a slotted core design and can contain up to 96 optical fibres (24 ribbons with four fibres in each ribbon). To prevent hydrogen and water from penetrating in to the cable core a copper tube is used (water and hydrogen can degrade the optical and mechanical performance of the optical fibres). The armouring consists of galvanised steel wires, encapsulated in bitumen. The outer diameter is 37 mm. Factory jointing of the cable core before armouring provides an unlimited delivery length without joint closures. To enable the connection of the Åsgard B and Draugen/Njord platforms branching units had to be developed. Joints performed off shore were made using Ericsson cable joints. The cable is also qualified for universal joint.

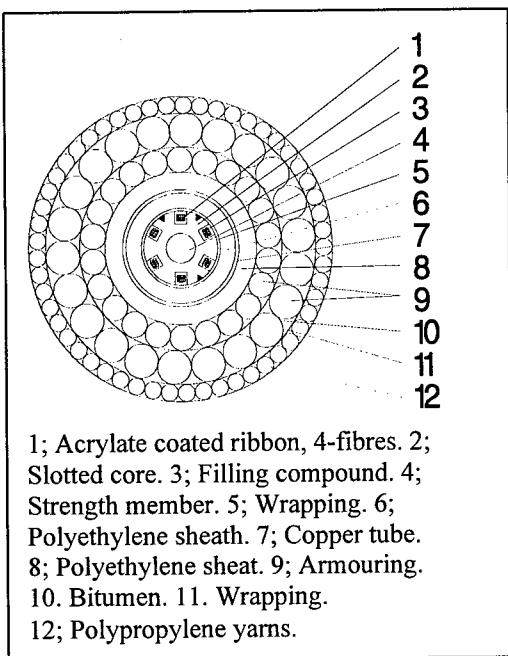


Figure 3; Cross section of the 200 kN DA submarine cable

Hang-off Cable and Arrangements for the Heidrun Platform

A sketch of the solution for the connection of the fibre optic cable to the Heidrun platform is shown in figure 4.

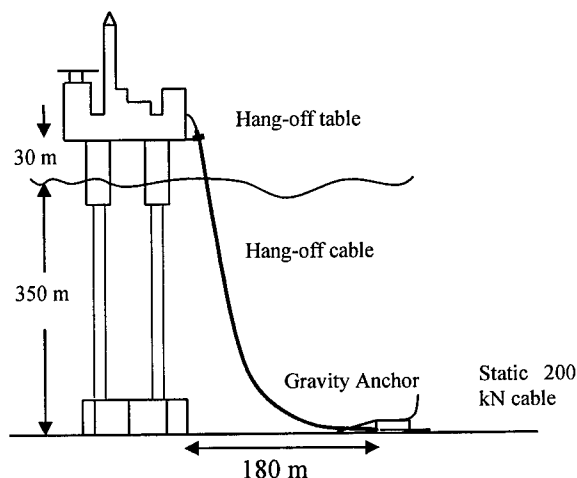


Figure 4; Hang-off Arrangement for the Heidrun Platform (not to scale).

The design of the hang-off cable (figure 5) is based on the design of the standard 200 kN DA submarine cable described above. In addition the hang-off cable has two extra layers of galvanised steel wires, bitumen, polypropylene (PP)-yarns and polyethylene (PE)-sheath. Some of the technical data for the cable are summarised in table 1. At the platform end the cable is secured to a hang off fixture, which has a semispherical bearing. The bearing enables the cable to move freely with a minimum of bending at the hang-off point. The other end of the cable is attached to a fixture which is locked in a 27000 kg heavy gravity anchor. The two outermost armouring layers are used to attach the cable to the fixtures. The Hang-off table and hang-off fixture are shown in figure 6.

Table 1; Technical data for the hang-off cable used on the Heidrun platform.

Outer diameter	72 mm
Weight in air	12.6 kg
Weight in water	8.7 kg
Tensile strength	400 kN
Axial stiffness	250 MN
Bend stiffness	400 Nm ²
Torsion stiffness	500 Nm ² /rad

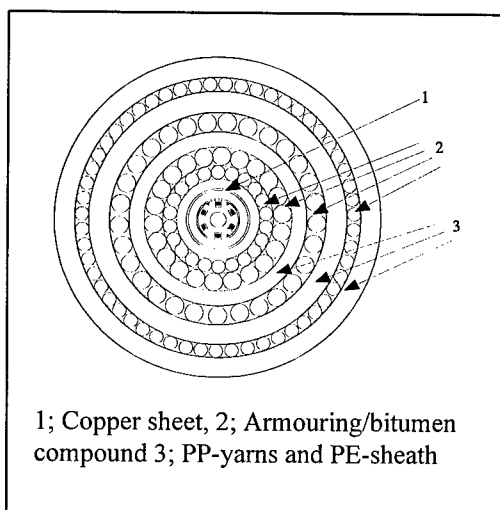


Figure 5; Hang-off cable for the Heidrun Platform.

The gravity anchor is needed to ensure that the positioning of the touchdown point and thereby the angle at the platform is kept within certain limits. It is also needed to ensure that no tensile force is introduced in the static 200 kN submarine cable, that could make it impossible to bury. The water depth and the positioning of the platform relative to the gravity anchor determines the angle of the cable at the hang-off point, the position of the touch-down point and thereby also the tensile force in the cable. The design of the gravity anchor and the device is shown in figure 7. The bow on the gravity anchor is for installation purpose only and is used to pull in the locking device in to the locking mechanism on the anchor. The bow is needed to enable the pull in to be performed from the ship.

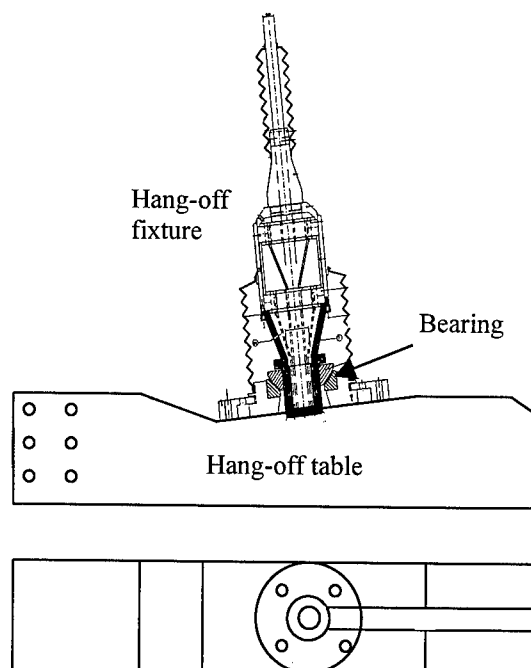


Figure 6; Hang-off table and fixture for the Heidrun platform

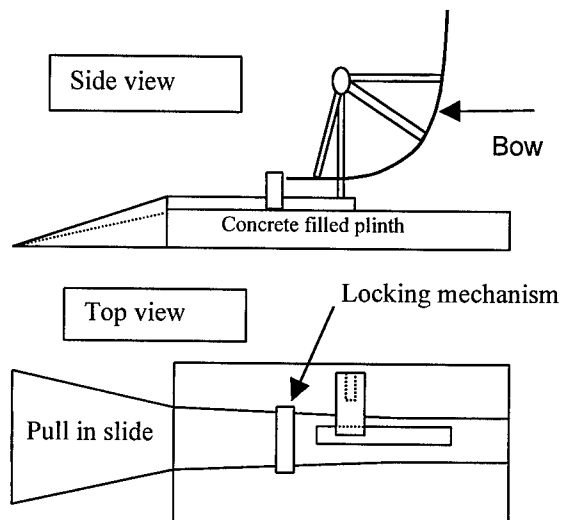


Figure 7; Gravity anchor for the Heidrun platform

The installation of the umbilical cable and the gravity anchor was carried out as follows.

- Before commencing the installation the hang-off fixture and the fixture to be locked in the anchor were mounted on the cable.
- The hang-off and the 200 kN submarine cables were jointed.
- The 27 000 kg heavy gravity anchor was lifted using the A-frame winch on the aft deck. The anchor was positioned on the sea bottom and the position was controlled using the ROV.
- The wires were cut by the ROV.
- The hang-off fixture was lifted to the platform and positioned on the hang-off table using a crane onboard the platform.
- The ship moved away from the platform and started to lay the cable beside the gravity anchor. The amount of cable put out at the position of the gravity anchor was larger than the length of the hang-off cable, to ensure that the fixture could be pulled in to the locking mechanism in the gravity anchor.
- The cable was monitored using the ROV while the ship moved sideways and positioned the 200 kN submarine cable in the bow on the gravity anchor.
- The tension in the cable was increased using the cable tensioner onboard and the fixture was pulled in to the locking mechanism of the anchor.
- The fixture was locked to the anchor by the ROV.

Integration of Fibre Optics in the Umbilical For the Åsgard B Platform

The fibre optics for the Åsgard B platform has been prepared and will be installed at a later stage. It was decided to integrate the fibre optic cable in to one of the umbilical for the sub sea production units. This solution was considered to be cost efficient since a separate installation of the fibre optic cable was avoided and the fibre optic cable could be made using a less complicated design. A sketch of the umbilical is shown in figure 8.

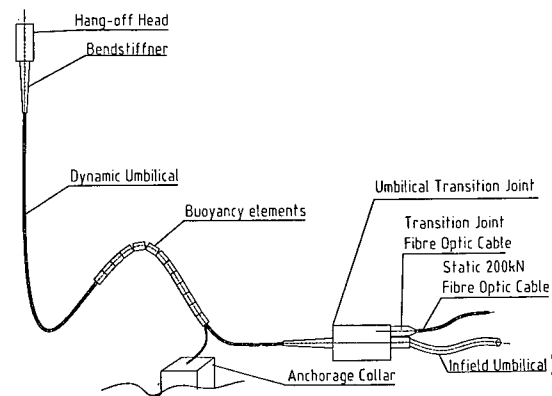


Figure 8; Umbilical cable for the Åsgard B Platform

Along the length of the umbilical, lead weights and buoyancy elements are used to give the umbilical the S-shape after installation. The S-shape allows the umbilical to move in a controlled way in rough sea states. The cross section of the umbilical is shown figure 9. The cable contain hydraulic tubes, power cables and the fibre optic cable. Each individual tube or cable can to move freely in the umbilical. The cross section of the integrated fibre optic cable is shown in figure 10.

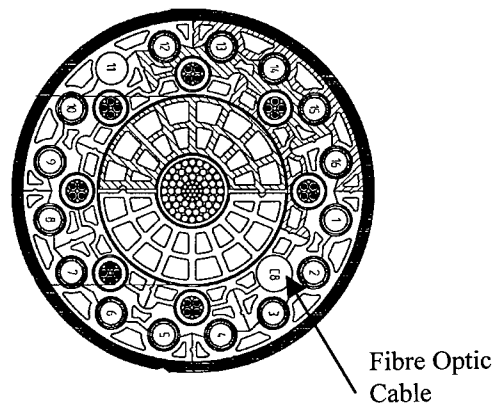


Figure 9; Cross-section of the Umbilical cable for the Åsgard B Platform

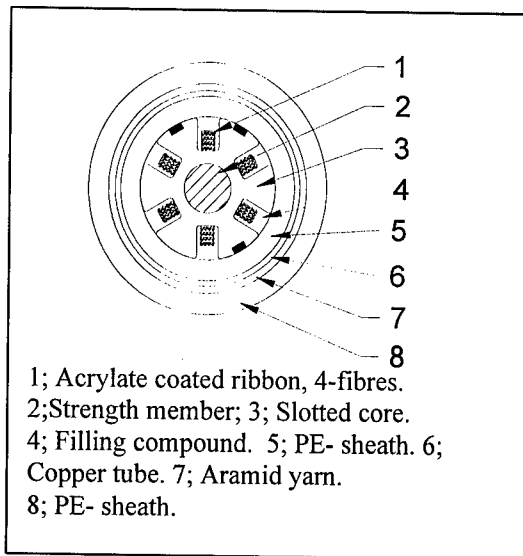


Figure 10; Fibre optic cable used in the dynamic umbilical for the Åsgard B platform.

The design is similar to the design for the cable core in the submarine cable but it has an aramid yarn armouring between the copper tube and the outer sheath. The outer diameter of the cable is 18 mm. On the platform end the umbilical is attached to a hang-off head. In the hang-off head each cable and tube has a separate hang-off arrangement designed to carry the weight of each individual cable or tube.

The hang-off arrangement for the fibre optic cable is shown in figure 11. Inside the hang-off fixture the outer sheath has been removed and the aramid yarn has been fixed using an epoxy casting.

The hang-off arrangement was, previous to installation, tensile tested to withstand loads in excess of 8 kN. The force corresponding to the weight of the integrated fibre optic cable is approximately 1.2 kN.

Break out of the fibre optic cable from the umbilical was performed, by integration of an auxiliary transition joint (figure 12) in to the main transition joint connecting the dynamic umbilical to the in field umbilical. In the transition joint the 18 mm dynamic cable was jointed to the static 200 kN submarine cable.

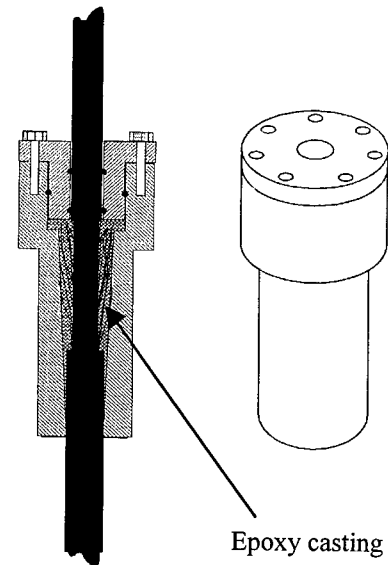


Figure 11; Hang-off fixture with epoxy casting for the fibre optic cable in the umbilical for the Åsgard B platform.

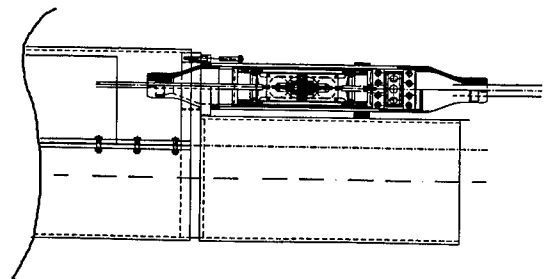


Figure 12; Transition joints for the umbilical and the fibre optic cable

Wave motion with corresponding variations in bend radius in the umbilical must be taken in to account when the cables and tubes in the umbilical are designed.

Due to the large number of cycles (on the order of 10^8 in twenty years) there is a risk for high cycle fatigue, if such effects are neglected. The minimum bend radius will occur at the touch down and hang-off points. Fatigue testing was performed, in order to verify the fatigue lifetime of the copper tube used in the fibre optic cable. Four point bend specimens were used in the tests. The results were used to estimate the number of cycles that the copper tube could withstand for different combinations of wave height and number of cycles. The results were then compared with the estimated number of cycles calculated for the umbilical. The results showed a good margin due to fatigue breaks in the copper tube during a lifetime of twenty years.

The Cable Used in the Tunnel at Kalstö

At Kalstö the submarine cable passed through a 1300 m long tunnel which after the cable installation was to be filled with water. The tunnel end is situated 70 m below sea level with ten metres of rock separating it from the sea. The cable used in this part was a standard submarine cable with an extra outer PE-sheath. The cross-section is shown in figure 13.

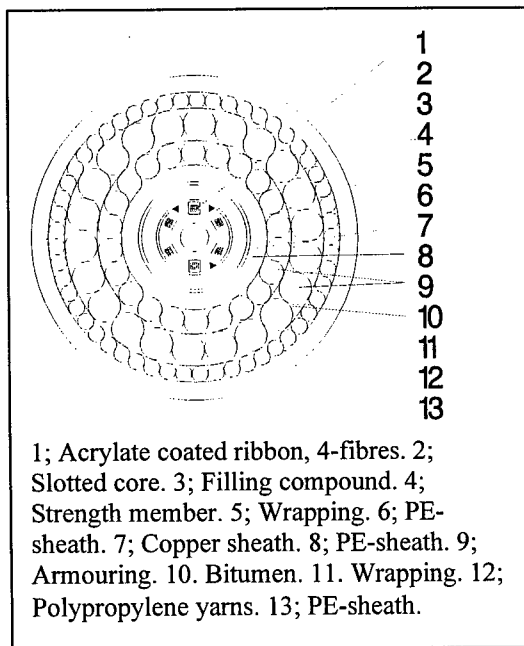


Figure 13; Cross-section of the cable used in the tunnel at Kalstö.

The extra sheath was needed to facilitate a good water seal between the cable and the drilling hole. The installation of the cable was carried out by drilling a hole from inside the tunnel and pulling the drill through the hole with the submarine cable attached to the end of the drill. The pulling was performed from the cable ship with a pulling wire attached to the drill by the ROV.

Branching Units

Branching units were used to enable the connection of the Draugen/Njord and Åsgard B platforms at a later stage. The design of the branching units is shown in figure 14.

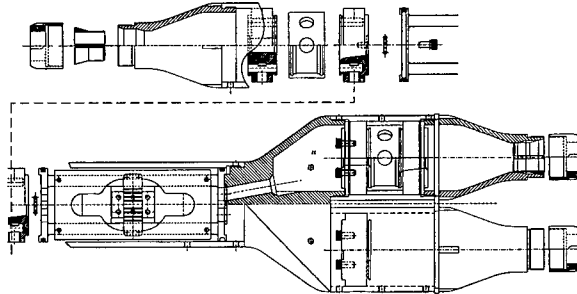


Figure 14; Branching Unit for the 200 kN DA cable

Pull-in through J-tubes at Draupner and Sleipner

The sleipner and Draupner platforms are of older design than the Heidrun and Åsgard B platforms and are situated in more shallow water. The water depth at these platforms is approximately 70 m and the platforms are standing on the seabed. This type of platforms which is not moving due to wave movements etc allows the use of J-tubes which is a tube ranging from the platform to the sea bed. On these platforms the 200 kN DA submarine cable was pulled in through existing J-tubes.

CONCLUSIONS

A 500 km ribbon fiber based 2.5 Gbit/s repeaterless submarine optic link has been designed and subsequently installed in the North Sea. The system includes various types of specially developed cable types, hang-off arrangements and locking devices for the off shore industry.



Mr Måns Isacson holds the degree licentiate in technology in solid mechanics from the Royal Institute of Technology in Stockholm, Sweden. He joined Ericsson Cables Telecom Cables Division in 1997 and is now working with engineering and development of submarine cable systems.

192-FIBRE COUNT SUBMARINE CABLE FOR REPEATERLESS SYSTEMS

Inge Vintermyr, Ragnar Vogt, Jon S. Andreassen

Alcatel Kabel Norge AS, PO.Box 130 Økern, N-0509 Oslo, Norway

ABSTRACT

During the last years there has been a great increase in the fibre count in both terrestrial and in submarine cables, especially in repeaterless cables used in coastal applications as part of terrestrial network. Until recently 48 fibres have been considered sufficient for a submarine cable. However, now more and more operators are requesting for 96 to 192 fibres in repeaterless submarine cables

In order to meet the new market demands, the existing URC-1 submarine cable with capacity for 48 fibres¹, has been further developed for 192 fibres.

The paper describes the design objectives, characteristics, design, qualification and current status of the URC-1 cable type with 192 fibres.

INTRODUCTION

Traditionally (in the early 1990's) fibre optic submarine cables for unrepeaters systems were designed to have a limited number of fibres with a typical maximum of 24 fibres (12 pairs). The systems were deployed on international links, and the capacity was mainly achieved by extensive use of terminal equipment with higher capacity than conventional land line systems. The line terminal design for unrepeaters systems were often close to the terminal equipment for repeaters systems, hence reflecting extensive use of multiplexing to achieve high bit rate transmission largely exceeding the capacity of land line systems.

Gradually, with growing capacity needs and development of new technologies (optical amplifiers extending the system range) the need for more fibres emerged in order to equip the cable with the sufficient number of systems to meet the increasing capacity demands.

Alcatel introduced its first 48-fibre submarine cable in 1994 based on the new steel tube technology for repeaterless cables¹.

However, with an increasing number of operators, unrepeaters systems were installed on more and more routes carrying heavy traffic, and often linked to trans-Atlantic type repeaters systems with hundreds of Gbit/s capacity using a mix of both high bitrate transmission and WDM (Wavelength-Division Multiplexing) on parallel systems.

Many new networks emerged, both in the US and Europe, with high capacity solutions as cheap bandwidth is the competitive edge for operators and also required to respond to bandwidth demanding new telecommunications services.

Some of the new actors in the unrepeaters area are carriers, for whom selling dark fibres is part of their core business.

In total, this created a demand for higher fibre counts in the submarine cables, often to directly match the land cable plants. Alcatel decided to further develop the 48-fibre steel tube cable of type URC-1 to have a maximum capacity of 192 fibres as the first stage to meet new requests in the market.

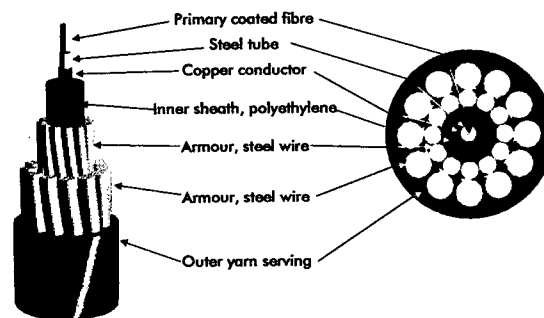


Figure 1 URC-1 cable with 48 fibres.

CABLE DESIGN OBJECTIVES

The main design objective for the cable has been to provide a reliable and cost effective protection for the transmission path, which is suitable for both present and future fibre types. Hence, a cable design has been developed to provide excellent physical protection for the fibres with very low stresses and environmental impacts on the fibre during all service conditions.

Hence, prior to the development of the 192-fibre cable a number of criteria for the new cable system were defined.

These can be split into two main categories:

1. Cable characteristics
 - Reliability
 - Optical characteristics
 - Bending/tensile characteristics
 - Bending and flexing characteristics
 - Hydrostatic pressure rating
 - Water blocking
 - Environmental characteristics
2. Handling and operational characteristics
 - Installation
 - Repair and maintenance

For both sets of requirements it was a clear target to achieve the same performance as for the existing cables and a limited need for new equipment for performing field jointing. Thus, to a large extent; maintain proven performance for both cable and joint.

Many of the market inputs specifically expressed great concern towards the maintenance and repair of cables with as many as 192 fibres.

Specifically, the repair time for a full field joint assembly with 192 fibres was specified to be maximum 24 hours. Further, the jointing technology should be easily transferable to jointers already familiar with submarine cable jointing of proprietary or universal type.

The qualification tests for cable and joints are based on relevant international specifications, Alcatel test methods and commonly specified tests by different PTO's

CABLE AND JOINT DESIGN

Cable Design and Characteristics

The cable core consists of 4-SZ stranded, 3.7 mm mm OD, laser welded stainless steel tubes, each with a capacity for 48 fibres².

Filler elements are placed in the tube interstices in order to provide extra protection and circularity. The fillers between the tubes (Q1, Q2, Q3 and Q4) are used to identify the tubes. The fillers between Q4 and Q1 is red. The filler between Q1 and Q2 is blue. The counting direction is from red towards blue. All fibres in each tube have unique colour coding for identification.

For electroding and fault finding purposes, two copper wires are integrated in the tube strand.

The cable design offers flexibility with respect to the fibre count as shown below.

1-48 fibres: One steel tube (e.g. standard URC-1)

49-96 fibres: Two steel tubes/ two filling elements

97-144 fibres: Three steel tubes/one filling element

145-192 fibres: Four steel tubes

For protection and electrical insulation a polyethylene sheath is applied over the stranded steel tubes to complete the cable core. The overall diameter of the cable core is 16 mm.

The cable core is armoured with one or two layers of galvanized steel wires with an outer yarn protection, or alternatively with a polyethylene outer jacket.

The single armoured cable with 5-mm armouring and the double armoured cable with 4.2/5.0-mm wires are shown below. The overall dimensions and the armour are identical to the similar URC-1 cable with 48 fibres¹.

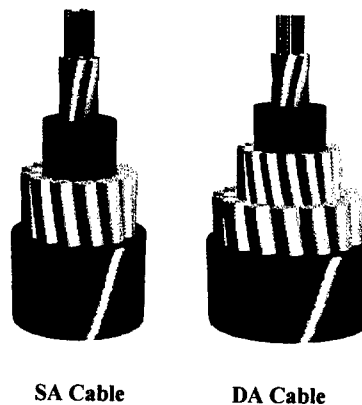


Figure 2 URC-1 cable with 192 fibres.

The main cable characteristics for SA and DA cable types referred to above are shown in Table 1. The cable characteristics for the 192-fibre cables are similar to the characteristics for the 48-fibre cable with one central steel tube.

Table 1 Cable characteristics for SA and DA 192 fibre cable types.

Characteristics	Unit	Value	
		SA	DA
Cable OD	mm	34	42
Cable weight in air	kg/m	2.6	5.1
Cable weight in water	kg/m	1.8	3.8
NTTS Load*)	kN	200	400
Min Bend Dia.**)	m	2.5	
Design Water Depth	m	1500	
Max Fibre count	-	192	
Temp range***)	°C	-20 - +35	

*) Maximum Transient Tensile Strength, 1 hour

**) Minimum bending diameter at the NTTS load

***) Nominal operating temperature range. Lower and higher temperatures on part of the cable segment will not have any effect on the transmission characteristics.

Joint Design and Characteristics

The URC-1 joint box with capacity for 48 fibre splices have been redesigned in order to handle 192 fibre splices. General design and physical dimensions for the 48- and the 192-fibre joint boxes are shown in Figure 3.

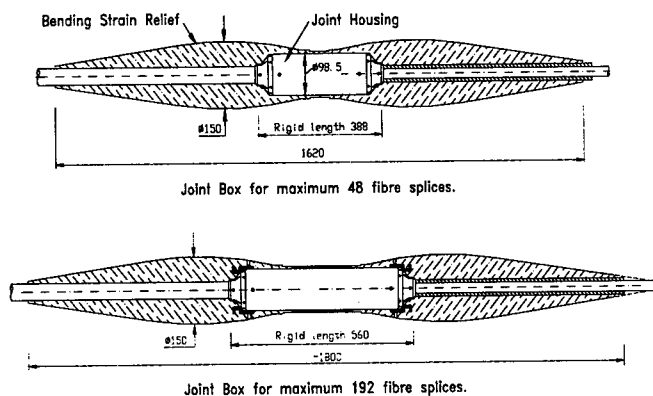


Figure 3 URC-1 joint boxes for 48- and 192-fibre splices.

Maximum outer diameter for both joints is 150 mm including the bend strain limiters. The rigid

lengths of the joint housings are 388 mm and 560 mm, respectively for the 48/192 joints. Furthermore, both joints are designed and tested for 3 m bending diameter.

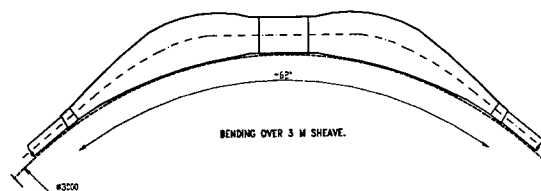


Figure 4 URC-1 joint box for 192 fibre over 3 m diameter sheave

The 192-fibre joint box has been designed with 4 fibre coiling chambers, each with capacity for 48 fibres. The coiling chambers are organised in such a way that two jointing teams can work simultaneously with fibre splicing. Furthermore, for the 192-fibre joint, re-coated fibre splices have replaced mechanical splice protectors. Jointing principles are shown in Figure 5, whereas fibre-coiling principles are shown in Figure 6. Final splice tray assembly is shown in Figure 7.

The required time for jointing with two teams (4 jointers + 1 supervisor) plus optical test personnel is typically:

- Mechanical assembly and optical verification: 8 hrs
- Fibre splicing: 10 hrs
- Mechanical completion and optical testing: 6 hrs

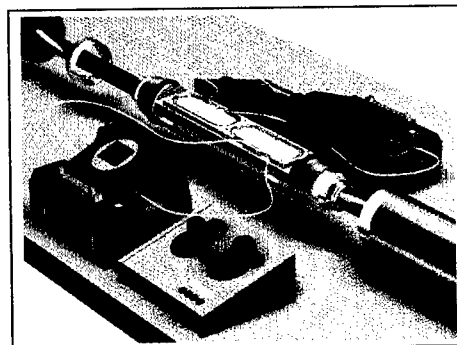


Figure 5 URC-1 192 fibre jointing principles with two fibre splicing teams.

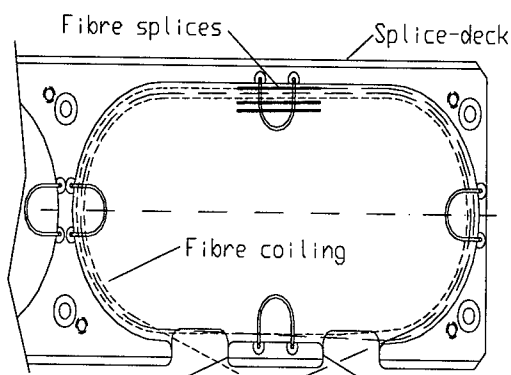


Figure 6 URC-1 192-fibre coiling principles.

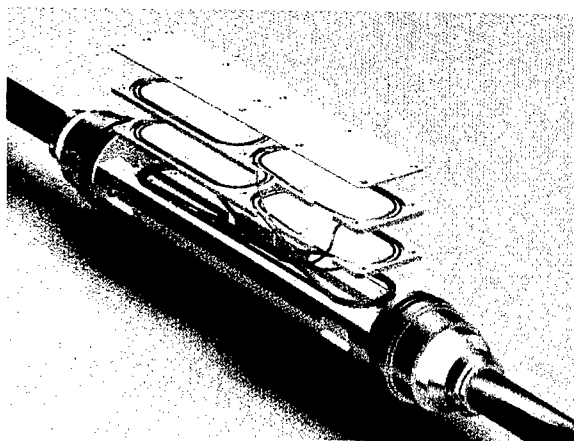


Figure 7 URC-1 192 splice tray assembly principles

TEST RESULTS

A wide range of tests has been performed on prototype cables in order to evaluate the optical, mechanical and environmental characteristics.

Furthermore, for the purpose of final confirmation of the cable characteristics, a sea trial has been performed in order to evaluate handling and installation characteristics, including required jointing time for 192 fibres.

Furthermore, three commercial cable lengths with 192 fibres have been manufactured, tested and installed with good results.

A summary of the obtained test results is reported below.

Optical Characteristics

Optical measurements on the prototype lengths, as well as the measurements on the first installation lengths, have shown that the cabled fibre loss is close to the attenuation for the received fibres.

The optical attenuation at 1550 nm for the 3 first commercial lengths (24 km, 8 km and 12 km) with 192 fibres are shown in **Figure 8**. The fibres were ordered in accordance with ITU-T G652 with @ 1550 nm specified to be maximum 0.195 dB/km.

As can be seen from **Figure 8**, the highest cabled fibre loss measured for the three 192-fibre cables (a total of 576 fibres) was 0.197 dB/km (only 3 fibres).

All 3 cable lengths were manufactured without cable joints. Failures occurring during the tube welding- or the tube-stranding process are normally repaired by means of the tube splice².

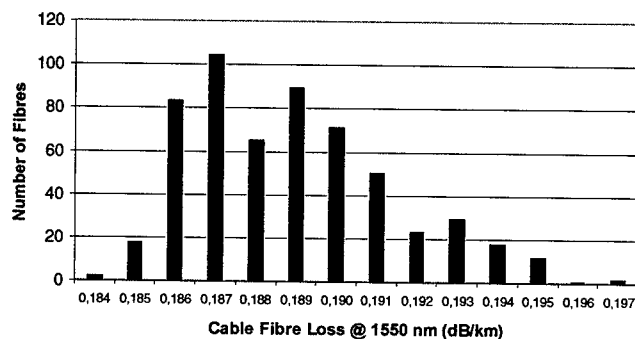


Figure 8 Cabled fibre loss @ 1550 nm.
Data collected from 3 cables with a total of 575 different fibres.

Mechanical Characteristics

Both cable and joint have been tensile tested over a 3 m sheave as shown in **Figure 9**.

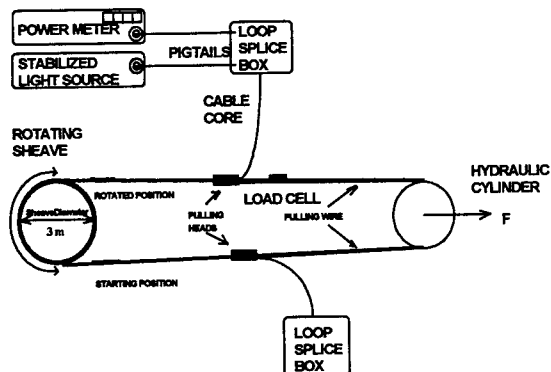


Figure 9. Mechanical test arrangement

Mechanical/optical test results for the SA cable during testing to 200 kN is shown in **Figure 9**.

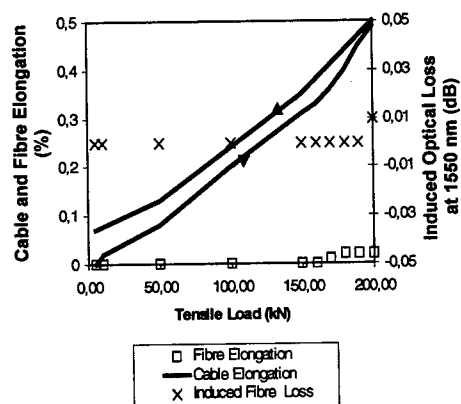


Figure 10. Tensile test results for the SA cable

From **Figure 10** it can be seen that the cable elongation is approximately 0.5% at a load of 200 kN (corresponding to the NTTS load for the SA cable). The fibre elongation is approximately 0.05% at this load. This is due to the combined effect of the fibre slack in the steel tube (0.2-0.3%) and the tube stranding effect ($\approx 0.2\%$).

The fibre loop did not show any significant change in attenuation during the tensile test.

Similar test results have been derived for the DA cable at 400 kN.

The joint box has been passed 6 cycles (from the sheave tangent point on one side to the tangent point on the other side) over the 3-m sheave at 150 kN without showing neither induced loss effects nor mechanical degradation.

Temperature Cycling Characteristics

A 2.5 km prototype length has been submitted to 7 cycles between -40°C and $+60^{\circ}\text{C}$.

No significant induced loss effects at 1550 nm were seen between -30°C and $+60^{\circ}\text{C}$. In the range of -30°C to -40°C , some minor effects could be measured. At -40°C the induced loss effects were measured to $\approx 0.003 \text{ dB/km}$.

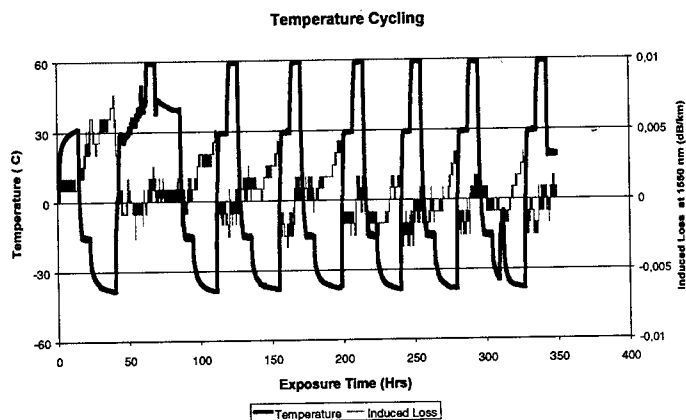


Figure 11. Temperature cycling

Ageing and Hydrogen Characteristics

In order to verify both hydrogen generation rate inside the steel tube as well as hydrogen permeation through the stainless steel tube, a 500 m steel tube length with optical fibres has been exposed to a hydrogen atmosphere at elevated temperatures. The fibres were measured during the test by means of spectral loss apparatus in order to measure hydrogen induced effects at 1240 nm.

The test arrangement is shown in **Figure 12**.

The tube length was exposed to 20 bar of hydrogen at 70°C for more than 100 days without showing

any significant hydrogen effects at 1240 nm, ref test results in Figure 13.

From the tests it was concluded that negligible amounts of hydrogen was generated inside the tube. Furthermore, the steel tube was found to be a good barrier against hydrogen permeation.

Calculations based on the test results have shown that the steel tube will resist more than 15 bar of hydrogen over a service life of 25 years at 10°C without any significant hydrogen effects.

The hydrogen level in the cable has been measured on a double armoured cable where the steel tube has been replaced by a non metallic core without any metallic diffusion barrier protecting the fibres.

The cable sample has been exposed in a water tank for more than 3 years.

The induced hydrogen effects at 1240 nm have been used to quantify the hydrogen level in the armouring. The test results are shown in Figure 14. The tests have indicated that the hydrogen level out in the armouring will be in the range of 0.1-0.4 bar. This also conforms with investigations reported by Hopland³ on installed cables without any metallic diffusion barrier over the fibres. Hence, it can be concluded that the measured protection level of more than 15 bar should provide hydrogen protection with a good margin.

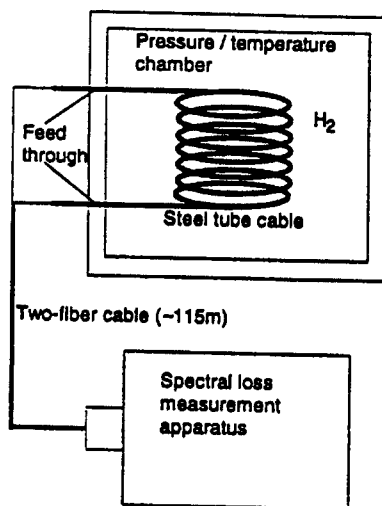


Figure 12. Hydrogen test arrangement

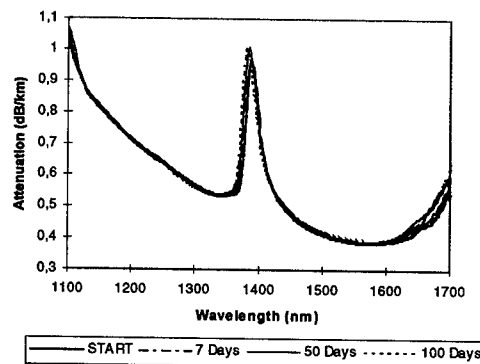


Figure 13. Spectral loss test results to detect hydrogen effects at 1240 nm

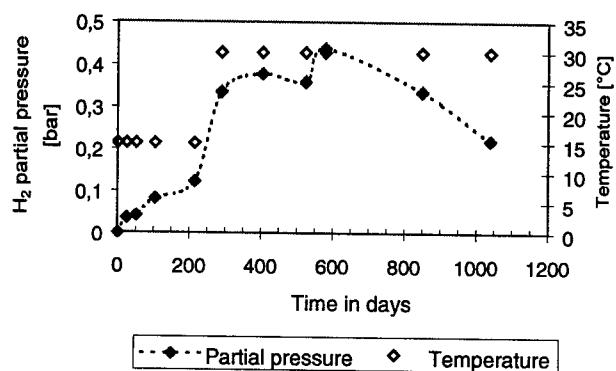


Figure 14. Measured hydrogen level in submarine cable versus temperature and exposure time.

Sea Trial

During the sea trial a 3-km single armoured cable length was laid, recovered and jointed to a 2-km double armoured cable.

The complete jointing operation was performed within a period of 24 hours. During this period 120 fibres were spliced and tested by one jointing team and thus confirmed that two jointing teams will be in position to make the 192 splices within 24 hours.

After jointing, both cables were laid and then recovered.

Throughout the sea trial, no optical loss increase was observed and no degradation of cable characteristics was observed.

CONCLUSION

The 48-fibre URC-1 cable type has been further developed for 192 fibres.

The SZ-stranded 192-fibre cable structure provides a high degree of protection to the fibres, which are maintained in a well sealed and stress free environment inside the laser welded steel tubes.

Qualification of cable and joints has been successfully completed with a comprehensive set of factory tests and sea trial.

The available splicing and jointing techniques allows for "unlimited" delivery lengths.

Tests and experience from installed cables have demonstrated the stability of the optical transmission characteristics of the URC-1 submarine cable under all service environments.

Furthermore, the sea trial has demonstrated that the 192-fibre joint can be performed during 24 hours.

REFERENCES

1. G. Berthelsen, I. Vintermyr; "New low weight / small diameter optical fibre submarine cable for unrepeated system"; Proc. IWCS 1994
2. J.S. Andreassen, I. Vintermyr, "Laser welded metallic tubes in fibre optic cables"; Proc IWCS 1999.
3. S. Hopland; "Long term behaviour of hydrogen induced losses in installed fibreoptic submarine and underwater cables"; Proc, IWCS 1997.



Inge Vintermyr
Alcatel Kabel Norge AS
PO Box 130 Økern
N-0509 Oslo, Norway

Inge Vintermyr graduated from the Norwegian Institute of Technology in 1989 with a Ph.D in Materials Science in 1989, and joined Alcatel Kabel Norge AS the same year. He has been working with research and development of steel tube based cables and umbilicals since 1991.

DEVELOPMENT OF SUBMARINE OPTICAL CABLE UNIT USING A LARGE EFFECTIVE AREA FIBER

Keiko Mitsuhashi, Tetsuo Hayano, Tsuyoshi Shimomichi, Tomio Abiru,
Keiji Oohashi and Matsuhiko Miyamoto

Fujikura Ltd., Chiba, JAPAN

ABSTRACT

We have developed a tight-type eight fiber optical unit that corresponds to the requirements of a high-speed, large-capacity, optical submarine cable system. Fibers with an effective area (A_{eff}) expanded to about $80 \mu\text{m}^2$ can be used for this unit and these fibers have a capacity of 160 Gbit/s per fiber pair. To maintain the transfer properties of the unit, it is more important to reduce the microbending loss rather than the macrobending loss.

INTRODUCTION

There is an increasing demand for telecommunications lines between the US and Japan, and expectations are high for the development of the Pacific crossing optical submarine cable that will employ fibers with a capacity of 160 Gbit/s per fiber pair that are compatible with the wavelength division multiplexing (WDM) system. The large effective area (LEA) fibers have been developed to enable long-distance transmission. The power density of the light decreases by when the A_{eff} is increased, and the non-linear effect of the light is decreased. The LEA fiber tends to cause a marked increase in macrobending loss, and it is anticipated that microbending sensitivity will be high in comparison with the conventional fiber. There has been a report on the application of the LEA fiber to a loose-type cable unit^[1], however, there has been no report on the tight-type unit.

We established the technique for grasping microbending properties of the LEA fiber, and then the correlation between the fiber parameters was investigated.

Moreover, the fiber coatings and the unit structure were optimized, and the microbending sensitivity of the fiber was reduced. Therefore, we developed a tight-type submarine optical fiber unit containing fiber with large A_{eff} expanded to about $80 \mu\text{m}^2$.

EVALUATION OF FIBER PROPERTIES

The technique in which the parameters relating to fiber core such as MFD, cut-off wavelength and macrobending loss are measured has been used in order to estimate the microbending properties of the optical fiber. But, the microbending properties of the optical fiber depend on Young's modulus and depend on the thickness of the fiber coating material. To estimate the microbending properties of the LEA fiber, we used the sand-paper drum winding test.

Microbending test method

To measure the microbending properties, we used a bobbin covered with sand-paper with particles. One layer of fiber was wound on to the bobbin at a regular tension (Fig. 1). The optical loss of the fiber was measured at a wavelength of $1.55 \mu\text{m}$ by OTDR. The loss of the fiber in a loose coil was also measured. The microbending loss was calculated by measuring the difference in loss between the fiber wound on to the bobbin and the loosely coiled fiber. This measurement employed a method similar to that used to measure the Microbending sensitivity of IEC793-1-C3B.

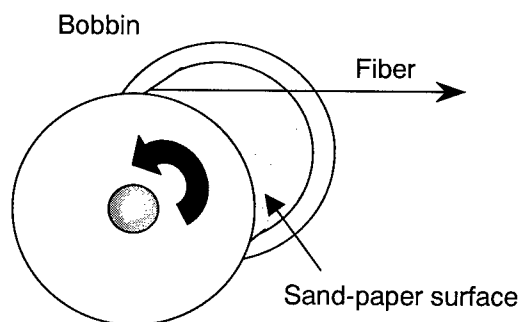


Fig.1 Illustration of microbending test

Microbending properties of LEA fibers

Figure 2 shows the relationship between the macrobending and the microbending loss of the fiber with a diameter of $250 \mu\text{m}$. We measured the macrobending loss by the method IEC793-1-

C11-Macrobending sensitivity. In figure 2, the open diamond indicates the usual fiber for WDM undersea use, and the solid square indicates the LEA fiber which has a capacity of 160 Gbit/s per fiber pair and is used for submarine non-zero dispersion-shifted fiber (NZ-DSF). As for the large Aeff fiber, it is understood that the properties deteriorate by more than one tenth for macrobending and microbending loss. The relationship between the mechanical characteristics of the dual-coated single-mode optical fiber and the microbending loss has been described in ref. [2]. In this study, we investigated the importance of the coating material and the coating diameter in improving the microbending properties of the LEA fiber.

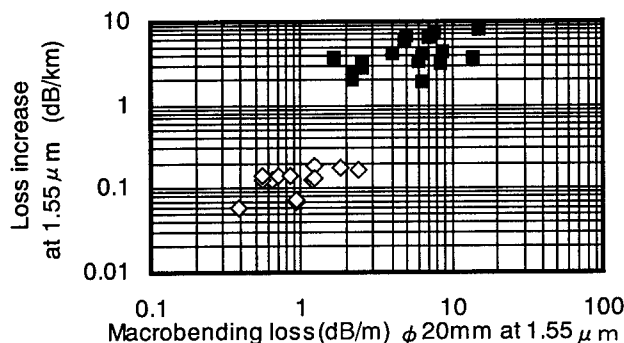


Fig.2 Relationship between microbending loss and macrobending loss

Investigation of the coating material

The microbending properties of the optical fiber depend on Young's modulus for coating materials. We made fibers using various Young's modulus coatings (with a coating diameter of 250 μm). Table 1 shows the coating structure of the fibers. All primary coating diameters are the same. Figure 3 shows the relationship between the Aeff of the fiber and the microbending loss.

There is a correlation of a certain extent between the microbending and Aeff in fiber A, while dispersion is also shown. (The fibers of larger Aeff show the greater microbending loss.) Both fibers B and C were coated with the structure for which a lower microbending loss was expected, and it is within the range of the dispersion of the microbending loss. It was found that improvement of the microbending properties was imperfect depending on Young's modulus in the range of this investigation.

Table 1 Coating structure of the fibers

Fiber type	Coating diameter (μm)	Primary Young's modulus (relative value)	Secondary Young's modulus (relative value)
A	250	1	1
B	250	1	1.5
C	250	0.7	1.5

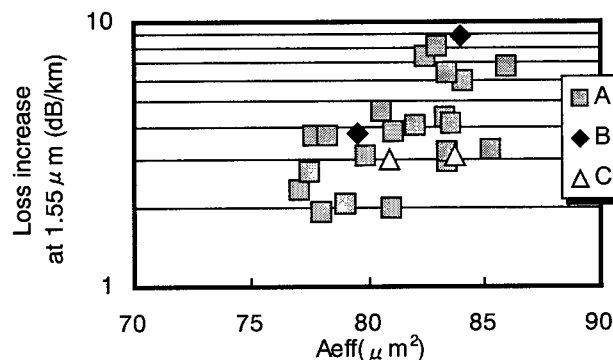


Fig.3 Relationship between microbending loss and Aeff

Investigation of coating diameter

Because it was difficult to reduce the microbending loss of the LEA fiber with a diameter of 250 μm , an increase in the coating diameter was investigated. We made fibers with diameters from 250 μm to 400 μm using the same preform and the microbending test was conducted. The results are shown in figure 4. The increase in the coating diameter effectively reduces the amount of microbending loss.

Figure 5 shows the relationship between the Aeff of the fiber and the microbending loss when the coating diameter was 250 μm and 400 μm . The coating with the 400 μm diameter has a much lower sensitivity to microbending than that of 250 μm .

Moreover, the larger the Aeff value of the fiber, the greater the microbending loss, indicating an increased sensitivity to microbending. However, the correlation was not totally convincing. Therefore, we searched for an additional parameter by which the effect of the microbending properties of the fiber were estimated.

Estimate of microbending loss

The optical loss due to the bending of the fiber is caused by a coupling between the LP_{01} mode and LP_{11} quasi-mode. The microbending loss can be estimated by an approximation equation(1) as a function of the propagation constants difference, $\Delta\beta_1 (= \beta_{01} - \beta_{11})$ [3][4].

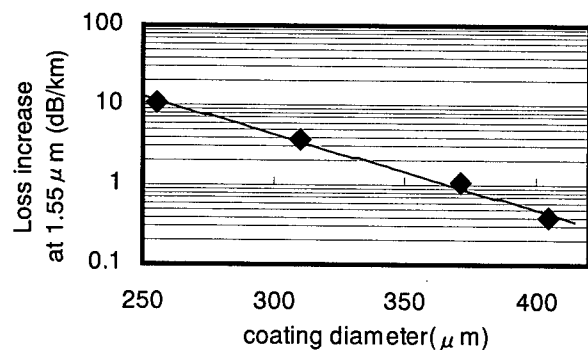


Fig.4 Microbending loss as a function of the coating diameter (A_{eff} @avg86 μm^2)

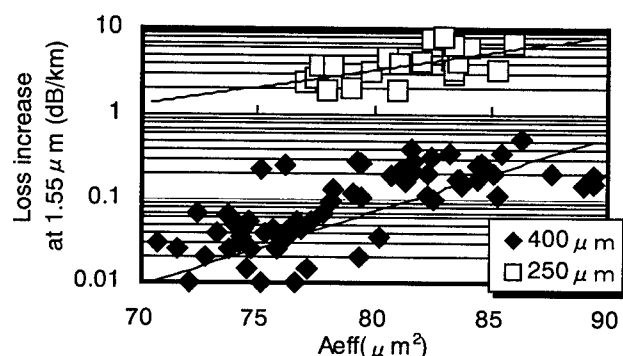


Fig.5 Relationship between microbending loss and A_{eff}

$$\alpha_{\mu B} = A/\Delta\beta_1^{2p} \quad (1)$$

We investigated the relationship between $\Delta\beta_1$ and the microbending loss. The propagation constant in each mode was calculated by using the refractive index profile. Relationship between $\Delta\beta_1$ and microbending loss is shown in figure 6. The solid curve in the figure is an approximation curve which was calculated by the equation (1) with a value of 5.3 for p . It seems that this equation is proper one.

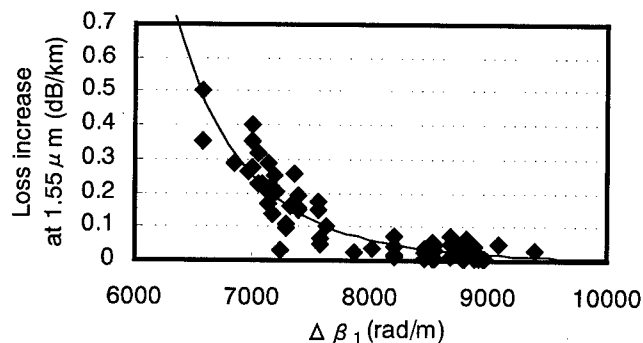


Fig.6 Relationship between microbending loss and $\Delta\beta_1$

FIBER UNIT

Structure of the unit

We investigated the use of the fiber of 400 μm in diameter in a tight-type unit. Figure 7 shows the structure of the undersea optical fiber unit that we have developed. Eight fibers were twisted around the core tension member. The UV cured resin was embedded in the inner layer and the outer layer enclosed the unit.

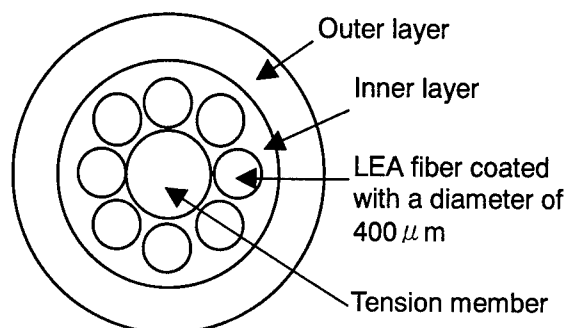


Fig.7 Cross section of the unit

Relationship between water pressure properties, macrobending and microbending loss

We conducted a test to determine the amount of transmission loss at a wavelength of 1.55 μm after applying a water pressure to a unit. Figure 8 illustrates the test apparatus. Figure 9 shows the results of this test. In this figure, there is no significant correlation between the pressure-attributed loss and the loss due to macrobending. A fiber unit having a large macrobending loss (over 20 dB/m) may yield a satisfactorily low loss when water pressure is applied. Figure 10 shows the influence of water pressure-attributed loss on microbending-attributed loss. Unlike the results in figure 9, there is a significant correlation between the pressure-attributed loss and the microbending properties.

When applying water pressure to a tight-type unit, the pressure is likely to induce a microbending stress rather than a macrobending stress. Thus, it may be possible to reduce transmission loss through reduced microbending loss of a fiber.

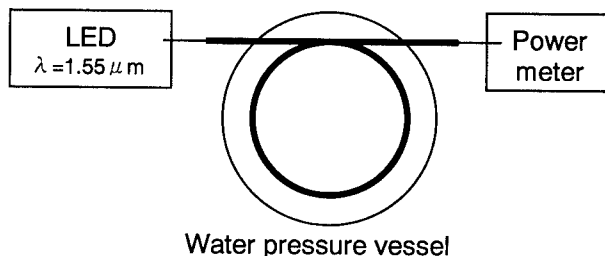


Fig.8 Illustration of water-pressure test

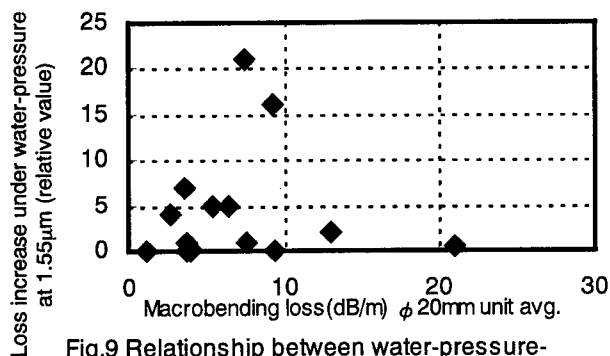


Fig.9 Relationship between water-pressure-attributed loss in the unit and macrobending loss in element unit

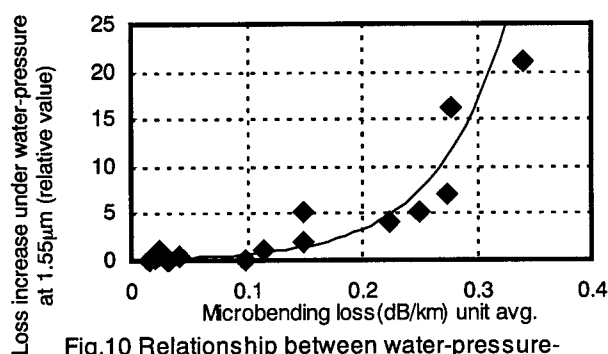


Fig.10 Relationship between water-pressure-attributed loss in the unit and microbending loss in element unit

Relationship between temperature properties and microbending loss

We examined transmission loss at a wavelength of $1.55 \mu\text{m}$ by changing the temperature in the range between -20°C and $+50^\circ\text{C}$. Figure 11 shows the change in transmission loss when the temperature changes from $+15^\circ\text{C}$ to -20°C and $+50^\circ\text{C}$. In case of small microbending loss, the loss changes were negligible. On the other hand, the loss increases became larger in the greater microbending loss region. Thus, a large amount of microbending properties may have a noticeable effect on transmission loss.

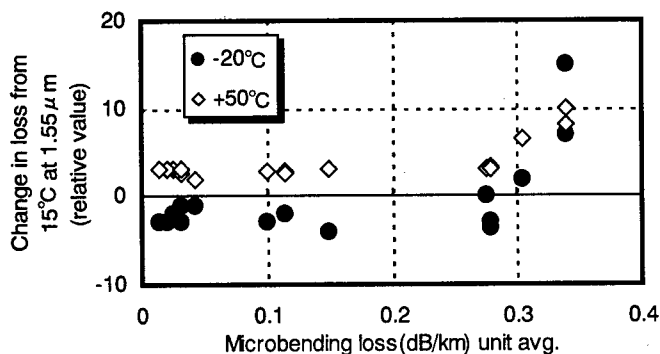


Fig.11 Relationship between change in loss and microbending loss in element unit

Optimal design of the tight-type unit

To reduce microbending propagation along the fiber, it is necessary to improve the design of the tight-type unit. We changed both Young's modulus for UV resin (used for the inner and the outer) and the diameter of the inner layer.

A lower Young's modulus and a larger radius in the inner layer appear to reduce the amount of transmission loss due to water pressure. On the other hand, these properties have an adverse effect on the mechanical properties of the unit when side pressure is applied. Figure 12 shows the measured dependencies of pressure-attributed loss on Young's modulus of the inner layer. This figure also shows the measured oblateness of the unit in the lateral pressure test. These two properties behaved oppositely. Figure 13 shows the plotted curve of Young's modulus of the outer layer. This figure indicates that a higher Young's modulus of the outer layer contributes to improved oblateness of the unit when side pressure is applied. Unfortunately, the combination of a very low inner layer modulus and a very high outer layer modulus will lead to unfavorable transmission loss due to temperature change and applied bending.

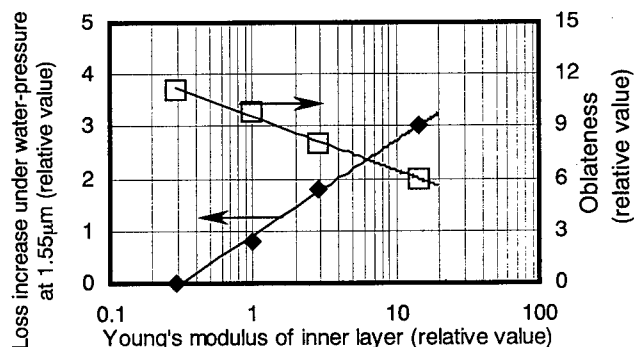


Fig.12 Unit properties as a function of Young's modulus of the unit inner layer

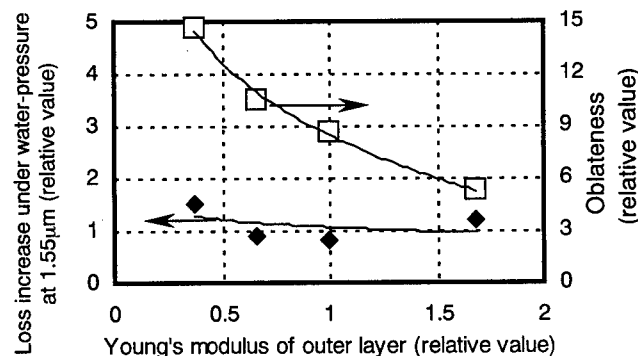


Fig.13 Unit properties as a function of Young's modulus of the unit outer layer

By taking the above findings into consideration, we successfully developed an optimal fiber unit. Table 4 shows the amount of transmission loss noted when testing the unit under various mechanical conditions. The results were satisfactory for all the tests we conducted.

Table 4 Properties of the unit

Test item	Test condition	Result
Tensile test	0.7% elongation	No increase
Bending test	50mmR×3turns	No increase
Lateral pressure test	4.90N/mm×300mm	No increase

Stability of PMD

Figure 14 shows the changes in the PMD of the fiber in the three stages of fabrication and at two temperatures. This figure indicates that our design of the coating structure and the unit structure has been effective in stabilizing the

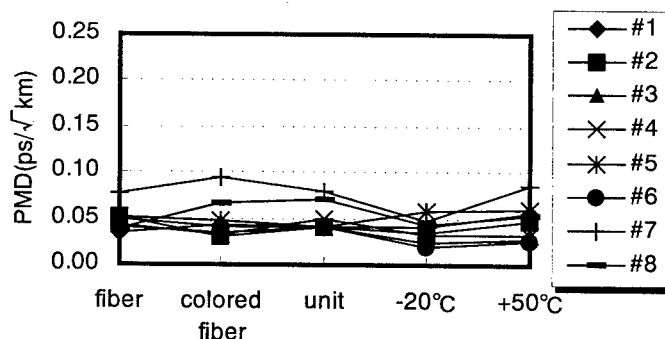


Fig.14 Change in PMD

PMD of the fiber.

CONCLUSIONS

We developed a tight-type eight fiber optical unit using fibers of $80\ \mu\text{m}^2$ in an effective area. It was important to reduce the amount of microbending loss of the fibers in order to reduce water pressure-attributed and temperature-related transmission loss. For this purpose, we took the following measures:

The diameter of the fiber coating was increased to $400\ \mu\text{m}$.

The design of the coating structure of the optical fiber unit was optimized.

Each fiber element was evaluated and controlled with respect to microbending.

We successfully developed a tight-type eight fiber optical unit having satisfactorily low transmission loss.

ACKNOWLEDGMENTS

The authors would like to thank KDD Submarine Cable System Inc. for providing the opportunity of this study.

REFERENCES

- [1] JF.Libert et al, "The new 160gigabit WDM challenge for submarine cable systems" *IWCS Proceedings*, pp.375-384 (1998)
- [2] K.Kobayashi et al, "Study of microbending loss in thin coated fibers and fiber ribbons" *IWCS Proceedings*, pp.386-391 (1993)
- [3] S.Horung et al, "Monomode fiber microbending loss measurements and their interpretation" *Opt. Quantum Electron.*, 14, pp.359-362 (1982)
- [4] K.Petermann et al, "Upper and lower limits for the microbending loss in arbitrary single-mode fibers" *J. Lightwave Technol.*, vol. LT-4, No.1, pp.2-7, Jan. (1986)

Keiko Mitsuhashi

R & D Dept.
Telecommunication
Cable Division
Fujikura LTD.

1440 Mutsuzaki,
Sakura, Chiba,
285-8550, JAPAN



Ms. Mitsuhashi graduated from Chiba University with a B.E. degree in 1986. After six years of work as an engineer for functional organic materials, she joined Fujikura Ltd. and has been engaged in research and development of optical fibers. She is now a senior engineer in the Telecommunication Cable Material Section and member of the IEICE of Japan.

Development of New Tight-Fit-Type Submarine Cable with Large Core Fibers for WDM System

Osamu Nagatomi, Kazuto Yamamoto, Hirofumi Wakamatsu, Ryo Kanda, Rokuro Morikawa

**Submarine Systems Division
Ocean Cable Co., Ltd.
Kitakyushu, Fukuoka, Japan**

1. Abstract

OCC has developed the new tight-fit-type submarine cable with large core area fibers for WDM system. Some kinds of large core fibers were evaluated and applied to the cable.

The cable qualification on land was implemented according to ITU-T recommendation G976. This paper describes the results of the sea trial of the cable.

This new tight-fit-type submarine cable (OCC-18W) will be able to be applied to the long-haul submarine cable systems with high bit rate such as Tb/s transmission in the very near future.

2. Introduction

Recently submarine cable with high capacity wavelength division multiplexing transmission system is growing livelier by being used for global communication networks. Consequently, the rate of the submarine cable links in the international network becomes very high.

One of the important factors for enhanced WDM is to suppress the nonlinear effects that are caused by the high optical power levels. For this purpose, it is necessary to adopt the fiber with large effective core area, so as to reduce the density of optical power.

On the other hand, optical fiber with large effective core area becomes sensitive to the external forces. Consequently, optical loss of fiber tends to increase that result in the difficulty to incorporate the large

core fiber into submarine cable. As one solution, the cable with loose-fit-type unit has been presented recently.

But loose-fit-type cable show the different movement between fibers and cable tension members respectively, when the submarine cable encounters large tension like under cable laying condition. Especially, it is very difficult to control the fiber movement at a discrete point in the cable termination.

This time, we have developed a new tight-fit-type submarine cable that is the most suitable structure to solve the above problem. In this cable, the trend fibers of which effective core area is from 68 to 82 [μm^2], twice as large as that of conventional ones, and of which chromatic dispersion slope is from 0.06 to 0.13 [ps/nm²/km], were applied. It was confirmed that the new tight-fit-type cable could be applied to submarine cable systems with big capacity by choosing the parameters of fiber appropriately.

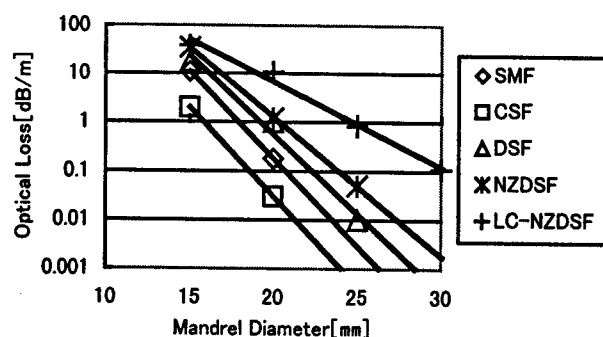
3. Fiber characteristics for WDM

3-1. Macro-bend characteristics

Until now the development of fibers used in optical submarine cable systems have been moving from SMF, CSF to DSF. Now with the development of WDM systems the introduction of NZDSF and LC-NZDSF are ahead.

Recently, with the introduction of WDM systems the

macro-bend characteristic is one of the important parameter at cabling, and the application of new fibers, like NZDSF and LC-NZDSF, has made this parameter worsen rapidly, as shown in Figure 1. Therefore the fiber applicability to the cable from its macro-bend characteristic has become a very important issue.



SMF	Single Mode Fiber
CSF	Cutoff Shifted Fiber
DSF	Dispersion Shifted Fiber
NZDSF	Non Zero Dispersion Shifted Fiber for WDM
LC-NZDSF	Large Core Non Zero Dispersion Shifted Fiber for WDM

Figure 1 Macro-bend Characteristics

This time, we studied 3 types of LC-NZDSF having the parameters as shown in Table 1.

Table 1. Fiber Original Characteristics

Type	Loss (dB/km) @1550nm	Aeff. (μm²) @1550nm	Dispersion (ps/nm/km) @1550nm	Slope (ps/nm²/km) @1550nm
1	0.202 to 0.227	80 to 87	-1.2 to +0.1	0.114 to 0.121
2	0.198 to 0.223	68 to 75	-3.3 to -2.3	0.117 to 0.124
3	0.234 to 0.303	69 to 85	-4.8 to -0.9	0.058 to 0.089

Each type can be described as follows,

Type 1: fiber with a large effective core area (Aeff.).

Type 2: fiber with smaller Aeff than type 1.

Type 3: fiber with smaller dispersion slope in comparison to type 1 and 2.

Macro-bend characteristics of the above-mentioned fibers are shown in Figure 2.

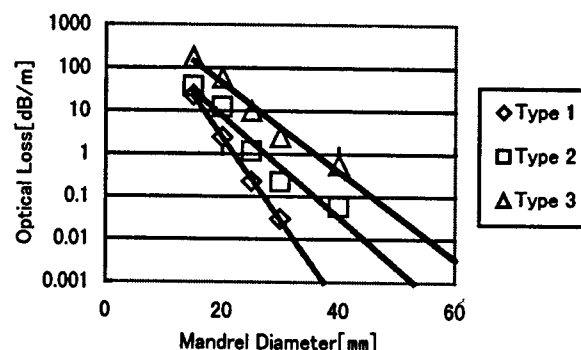


Figure 2 Macro-bend Characteristics of LCF

From Figure 2, it is understood that the following approximating equation that relates optical loss variation and mandrel diameter is valid.

$$\log y = -Ax + B \dots (1)$$

x: mandrel diameter [mm]

y: optical loss variation [dB/m]

In this equation, when the value of A is small the optical loss variation slope tends to be small. However, when winding around a large diameter mandrel optical loss tends to increase easily.

Moreover, relation between parameter A of each type fiber on Figure 2 and dispersion slope on Table 1 is shown in Figure 3. It is understood that if the dispersion slope is small, the optical loss tends to increase when winding on a large diameter mandrel.

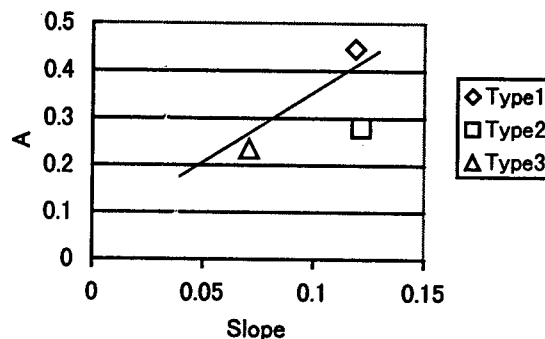


Figure 3 Dispersion Slope vs. Macro-bend Coefficient A

From the above results, we found that even if the fibers with small dispersion slope, required on WDM systems, are wound on large diameter mandrels, the optical loss tends to increase. Thus it was expected to be difficult to make the cable.

3-2.Cable evaluation

The above-described three types of fiber were cabled on the tight-fit structure (OCC-18W) as described in Figure 4 and their applicability to the cable was studied.

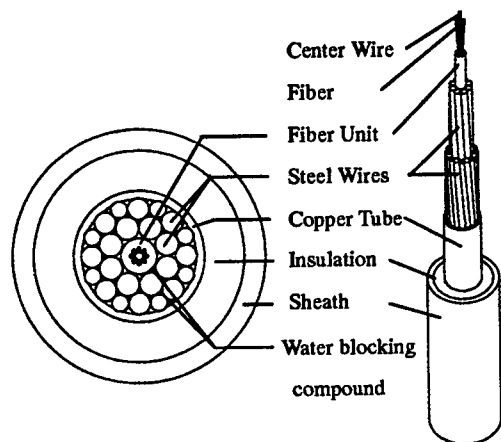
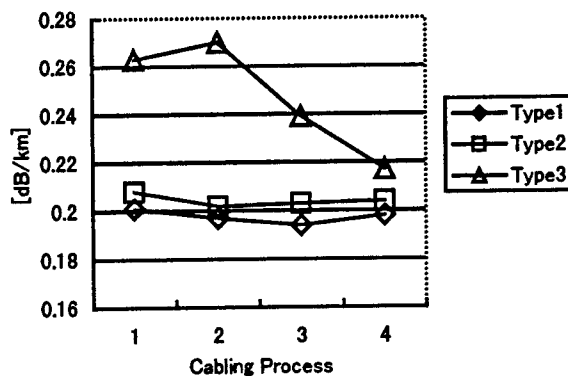


Figure 4 Structure of OCC-18W

3-2-1.Variations during cabling process

Type 1 to 3 fibers were applied to the above-described cable. Moreover, variations in the optical loss value as well as polarization mode dispersion value at each cabling process were measured. Typical values are shown in Figure 5 and Figure 6.

As described in Figure 5, optical loss after cabling indicates values under 0.220dB/km for each type of fibers. However, optical loss value of Type 3 fiber varies largely during each process showing its sensitivity.



[Cabling Process 1:Fiber Acceptance 2:Fiber Unit
3:Copper Tube 4:Sheath (LW)]

Figure 5 Optical Loss Change during Cabling

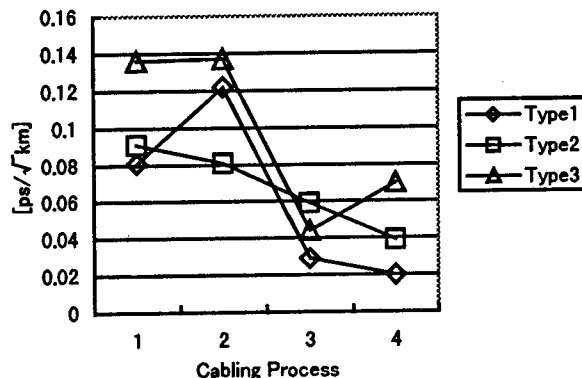


Figure 6 PMD Change during Cabling

For the PMD characteristics shown in Figure 6, all of the three types of fiber showed the same tendency at each process having finally values less than 0.08 ps/√km.

3-2-2.Temperature stability of the cable

To study the temperature stability all of the cables made utilizing three types of fiber were examined. Measured results are shown in Figure 7.

Observing the optical loss change behavior of the cable, there is a large hysteresis for Type 3 fiber while for Type 1 and 2 fibers this is not deserved.

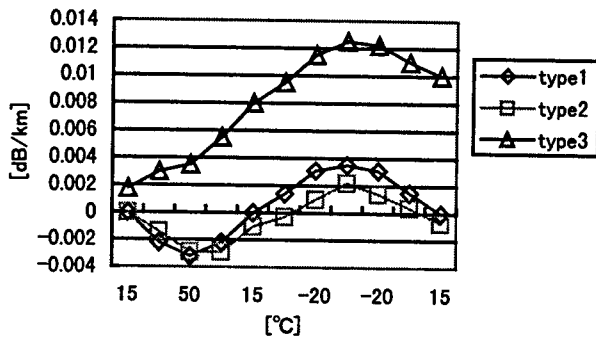


Figure 7 Temperature Stability

3-2-3. Fiber selection

From the fiber macro-bend characteristics, optical variations during cabling process, temperature stability and WDM systems requirements on dispersion values, we have selected Type 2 fiber as the applicable fiber for our new cable.

4. Long span cable manufacturing and evaluation

About 100km of cables using Type 2 fibers were manufactured. General evaluations were performed.

4-1. Variations during cabling process

Optical loss and PMD characteristics at each cabling process were the same as described in Figure 3 and Figure 4. Moreover, temperature stability also showed the same characteristics as in Figure 5.

4-2. Cable evaluation terms and results

For the core part of the OCC-18W cable, the LW cable, various evaluation tests were performed. Among those tests items the most important ones and the targeted specs as well as the conditions under which they are implemented and the results obtained are described in Table 2.

Table 2 Evaluation Terms and Results

Items	Targets	Condition	Results
Temperature stability	$\leq \pm 0.020$ dB/km	$-30^{\circ}\text{C} \sim 50^{\circ}\text{C}$	$-0.003 \sim 0.002$
Hydraulic pressure resistance	$\leq \pm 0.010$ dB/km	$78.4\text{MPa} \times 24\text{H}$	0.003 Loss up
Tensile test with twist restrained	$\leq \pm 0.020$ dB/km	NTTS $\times 1\text{H}$ +several times	0.002 Loss Gain
Tensile test with torque minimized	$\leq \pm 0.020$ dB/km	NOTS $\times 1\text{H}$ +several times	No Change
Tensile test with load to failure	$\geq \text{CBL}$	The load that any tensile member is failure.	83.7kN
Mechanical fatigue test	$\leq \pm 0.020$ dB/km	NOTS $\pm 10\text{kN} \times 48\text{H}$, Cycle period 15sec	0.002 Loss Gain
Sheave tests	$\leq \pm 0.007$ dB	NOTS $\times 50\text{times}$ +NTTS $\times 3\text{times}$	No Change
Crush resistance	$\leq \pm 0.002$ dB	20kN/200mm	No Change
Impact resistance	$\leq \pm 0.002$ dB	2kg $\times 1\text{m}$	No Change
Flexure resistance	$\leq \pm 0.002$ dB	0.9mR $\times 50\text{times}$	No Change
Water ingress limitation	$\leq 1.0\text{km}/2\text{weeks}$ @53.9Mpa	$\leq 100\text{m}/202\text{min.}$ @53.9Mpa	1200min
High-voltage test	$\pm 70\text{kV} \times 21\text{H}$	—	Good
Insulation integrity test	$\geq 2 \times 10^5$ M Ω	—	2.5×10^6
Cable inter-Layer adhesion Test	$\geq 0.5\text{kN}/25\text{mm}$	—	1.5kN/ 25mm
Cable stopper tests	$\leq \pm 0.002$ dB	NOTS $\times 90\text{min}$	No Change

4-3. Cable tensile characteristic

The results of tensile test with twist restrained, that is considered as the basic mechanical characteristic of submarine cables, is showed in Figure 8.

As this test was to confirm the influence of remaining fiber elongation, the load was applied several times.

From the results in Figure 8 it is understood that even for 8000m depth operations the cable can be safely laid and recovered.

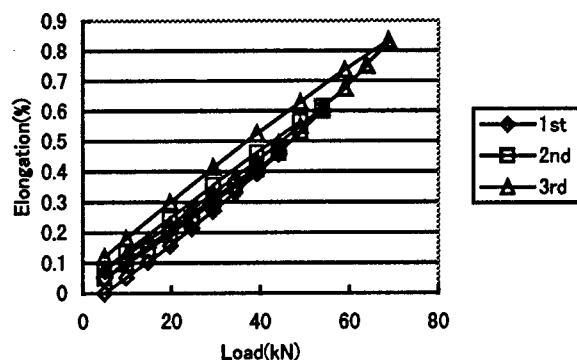


Figure 8 Tension-Elongation Characteristic

4-4 Cable parameters

Mechanical and electrical parameters of the LW cable obtained from the land evaluations are shown in Table 3.

Table 3 LW Cable Parameter

Item	Unit	LW
Outer Diameter	mm	18
Weight in Air	kN/km	6.4
Weight in Water	kN/km	3.9
CBL	kN	88
NPTS	kN	23
NOTS	kN	49
NTTS	kN	62
Stowage factor	m ³ /km	0.36
DCR(20°C)	Ω/km	0.9
IR	MΩ · km	2*10 ⁵
Typically Applied Depth	m	8000

From the results shown above, we concluded that optical characteristic as well as mechanical and electrical characteristics of the cable using Type 2 fiber indicated that this cable might resist to a sea trial.

5. Sea trial

5-1.Outline of sea trial

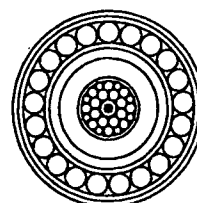
To confirm the cable characteristics in the sea as well as the cable coordination to cable ship equipment, a sea trial was carried out as final evaluation.

The test area was off the coast of Okinawa, Japan. 5000ton class International Cable Ship, the KUROSHIO-MARU was utilized.

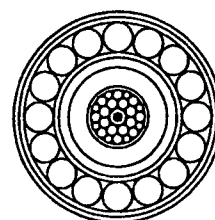
5.2 Sea trial cable

The cables used for the sea trial are shown in Figure 4 (LW), and Figure 9 (SAL, SA, DA).

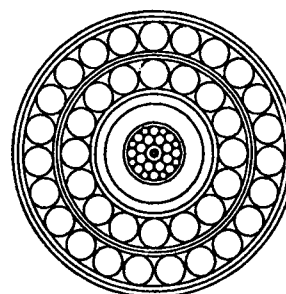
The cable parameters for armored cables are shown in Table 4.



SAL



SA



DA

Figure 9 Cross Section of Armored Cable

Table 4 Parameter of Armored Cable

Item	Unit	SAL	SA	DA
Outer Diameter	mm	29	32	43
Weight in Air	kN/km	21.7	28.6	59.9
Weight in Water	kN/km	15.5	21.3	46.3
CBL	kN	294	404	522
NPTS	kN	75	100	180
NOTS	kN	170	200	340
NTTS	kN	210	240	410
Stowage factor	m ³ /km	0.96	1.13	2.09
DCR(20°C)	Ω	←	←	←
IR	MΩ·km	←	←	←
Typically Applied Depth	m	2000	1500	400

5-3. Diagram of sea trial

Sea trial was implemented with the SLD described in Figure 10. The sea state was 3 at that time. The cable was laid from shallow waters heading to deep waters. During laying and recovery optical loss and fiber elongation were monitored continuously. PMD and dispersion measurements as well as fiber test through OTDR were carried out before and after laying.

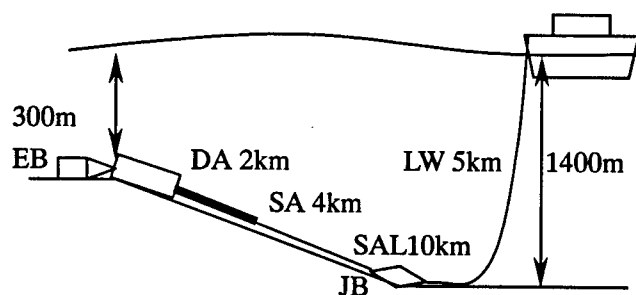


Figure 10 Diagram of Sea Trial

5-4. Results of sea trial

During laying-holding-recovery of the cable, optical loss value varied less than 1 mdB/km. Fiber elongation after recovery was less than 0.038 %, which means no influence to the fiber reliability. Moreover, after recovery no significant change on the cable mechanical and electrical characteristics shown in Table 3 and Table 4 was observed. OTDR

test and PMD measurement results were good performance shown in Table 5.

From these results we demonstrated the coordination of cables and JB to the ship equipment as well as their applicability to the real field.

Table 5 Optical Characteristics at Sea Trial

	Before Laying	Holding	After Recovery
Loss (OTDR) [dB/km]	0.200	0.201	0.201
PMD [ps/√km]	0.03	0.09	0.04

6. Conclusion

- 1) We studied the characteristics of several kinds of large effective core area fibers applicable to WDM systems and evaluated the characteristics of the cable manufactured using them. As the result, the most suitable fiber was selected.
- 2) Optical characteristics of the tight-fit-type cable obtained during cabling process, factory evaluation and field test confirmed their excellent stability.
- 3) The fiber utilized in this study combined with the appropriate DCF available nowadays can satisfy the large core, dispersion compensated and dispersion slope compensated requirements of WDM systems. Thus the applicability of the new cable to WDM systems is demonstrated.

We expect this new cable may contribute to the building of over Tera-bit networks planed for the 21st century.

7. Acknowledgments

We would like to thank the people of NTT World Engineering Marine Co., the KUROSHIOMARU and its crew for their cooperation in this work.

8.Reference

- [1]MASAHIKO KIUCHI "Development of small size
Optical Fiber Submarine Cable" IWCS'94 234-240

- [2]TAKATO NISHIDA "Development of repeater-less
optical fiber submarine cable system for extensive
application" IWCS'96 527-531

- [3]Y. CHARLES "A new high bit rate submarine product
range the OALC4 cable " IWCS'97 306-315

Speaker Biography



Osamu Nagatomi

Engineering Department
Submarine Systems div.
Ocean Cable Co.,Ltd.

1-105-2 HIBIKI-MACHI
WAKAMATU-KU
KITAKYUSHU 808-0021
JAPAN

Osamu Nagatomi was born in 1969. He received B.E. degree in 1993 and M.E. degree in 1995 from Kyushu University, Fukuoka, Japan. He joined Ocean Cable Co.,Ltd. And he has been engaged in research and development of optical fiber submarine cable. He is now an engineer of Engineering Department Submarine Systems division and a member of SNAJ of Japan.

MT-RJ OPTICAL CONNECTOR

Kazuhiro Takizawa, Natsuka Imazu, Toru Arikawa and Yasuhiro Tamaki

Fujikura Ltd. Cable Network Components Division
Sakura-shi, Chiba, JAPAN

ABSTRACT

The MT-RJ optical connector is designed as a new generation small form factor (SFF) connector to meet the demands of the rapidly growing fiber optic LAN for high density duplex fiber installation, reliability and ease of use. Good and reliable optical characteristics for both singlemode and multimode fibers were achieved through the use of the MT ferrule. The RJ-45 type latch of the MT-RJ connector provides ease and familiarity of use. The connector satisfies a series of mechanical and environmental reliability tests requirements based on the Telcordia (formerly Bellcore) and IEC standard specifications with typical insertion loss changes of less than 0.1dB. A field installable version of the MT-RJ connector is also developed for fast and easy fiber termination in the field without the need for adhesives or connector polish. Recent development efforts have produced stable low loss and low reflectance MT-RJ connector with an average insertion loss of 0.1dB and minimum return loss of 50dB for singlemode fibers.

1. INTRODUCTION

Recent years have seen widespread deployment of optical fibers in communication networks along with the development of various types of optical connectors¹⁾²⁾³⁾. These connectors link up the optical networks at different levels. In particular, recent trends toward FTTD(Fiber To The Desk) and FTTH(Fiber To The Home) to support bandwidth-intensive multi-service applications have led to the development of a new breed of small form factor (SFF) connectors. These connectors greatly increase fiber installation density over that offered by the industry standard SC duplex connectors, thereby reducing system costs. We

have developed the MT-RJ small form factor (SFF) connector having half the size of standard SC duplex connector, thus allowing the port density of network optoelectronic transceivers and patch panel to be doubled. The MT-RJ connector is based on proven MT ferrule technology⁴⁾⁵⁾⁶⁾ for reliable optical connection and feature a familiar RJ-45 latch design (IEC603-7) for sturdy and easy connection of both singlemode and multimode fibers.

To facilitate fast and easy termination of optical fibers in end-user premises networks, we have also developed a field installable type MT-RJ connector which does not require connector polishing or adhesive bonding. This field installable MT-RJ connector is developed based on the principle of mechanical splicing.

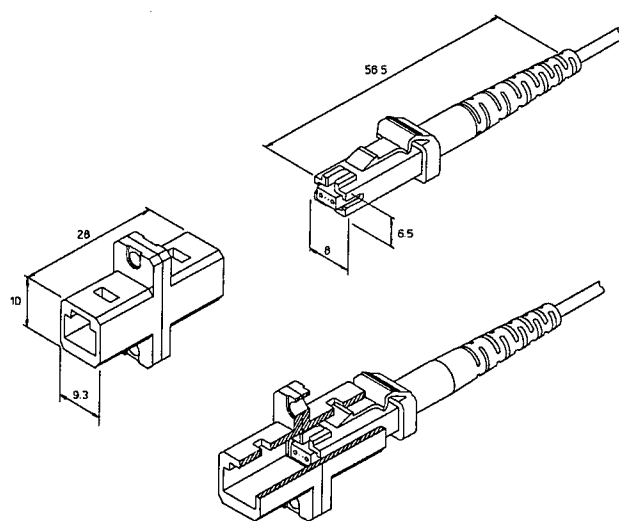


Fig. 1 Structure of MT-RJ connector

One of the most important factor in any optical connection is the optical loss performance of the connector. This has direct influence on system loss and demands careful consideration in selecting connectors for a specific application. Through our continual commitment to the development of the MT-RJ connector, we have achieved very low loss and low reflectance performances.

In this paper, we will first present the structure and the optical performance of the MT-RJ connector. Next, we will introduce a field installable version of the MT-RJ connector and the result of our development efforts in producing stable low loss and low reflectance MT-RJ connectors.

2. MT-RJ OPTICAL CONNECTOR

2.1 Structure of MT-RJ Connector

Fig. 1 shows the structure of the MT-RJ connector. The MT-RJ connector uses the mini-MT ferrule⁽⁷⁾⁽⁸⁾ to achieve precise fiber alignment for reliable duplex optical connection. The mini-MT ferrule is a miniature design of the MT connector widely deployed in optical communication networks in Japan for multi-fiber connections. Reducing the size of the MT ferrule for use in duplex-channel

Table 1 Comparison of dimensions between MT-RJ and SC-duplex connectors

	MT-RJ connector	SC-duplex connector
Fiber count	1~4	2
Cross section (mm)	W8×H6.5	W21.7×H7.4

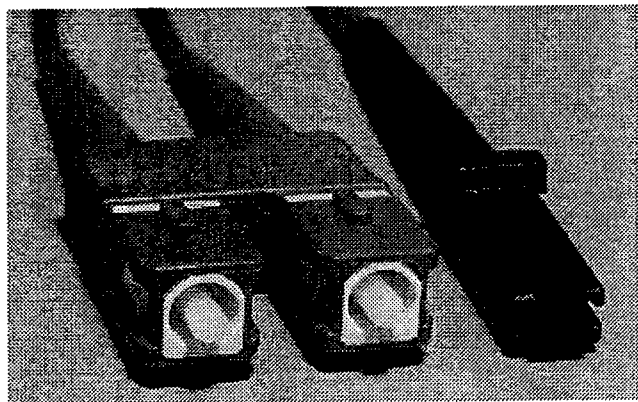


Fig. 2 Comparison between MT-RJ and SC-duplex connectors

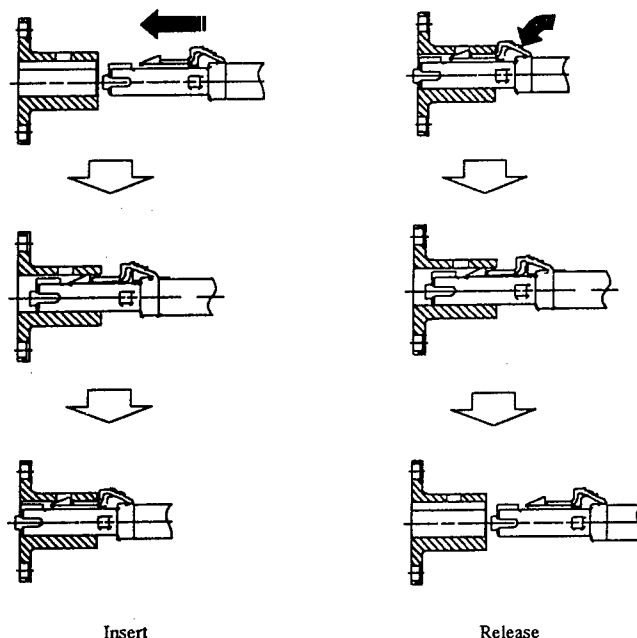


Fig. 3 MT-RJ latch mechanism

data networks has allowed the MT-RJ connector to attain a size less than half that of conventional SC duplex connector. Table 1 list the dimensions of the MT-RJ compared with conventional SC duplex connector. Fig. 2 shows the MT-RJ and duplex SC connectors placed side by side. The MT-RJ connector is smaller by half the width of the SC duplex connector and allows for twice the port packing density in patch panels, outlets and equipment interface.

The MT-RJ connector has a structure that is approximately the size of the standard RJ-45 connector (IEC603-7) used in LAN copper wiring. It employs the same type of latching mechanism to mate two connectors in an adapter or to couple a patch cord to a terminal jack with ease and efficiency. Fig. 3 shows the latching principle of the MT-RJ connector.

The MT-RJ connector employs physical contact (PC) technology to achieve low insertion loss, high return loss and high reliability without the use of index matching materials. The ferrule end-face is flat-polished in such a way as to allow slight protrusion of the fibers so that when the connecting ferrules are properly aligned and mated, the fibers are in physical contact. This eliminates any air gap in between that will degrade the transmission of optical signals across the connection.

2.2 Optical Performance and Reliability

In order to ascertain the field worthiness of the MT-RJ connector, optical performance tests and various reliability tests that address the mechanical and environmental tolerances of the connector were performed. The methods and conditions of testing are based on Telcordia (formerly Bellcore) and IEC standards and the results are summarised in Table 2. Detailed tests and results are discussed in the sections that follow.

Table 2 Summary of tests results of the MT-RJ connector

Tests	Methods and Conditions	Loss /Loss dev.	
		SM	MM
Insertion Loss	Random mating	0.13dB	0.02dB
Return Loss	Random mating	≥ 40 dB	≥ 30 dB
Durability	500 cycles	≤ 0.12 dB	≤ 0.08 dB
Temperature Cycling	Range : $-40 \sim +85^{\circ}\text{C}$ Duration : 10 cycles	≤ 0.05 dB	≤ 0.05 dB
Thermal Aging	Temperature : $+85^{\circ}\text{C}$ Duration : 96 hr	≤ 0.1 dB	≤ 0.05 dB
Thermal Aging	Temperature : -40°C Duration : 16 hr	≤ 0.1 dB	≤ 0.05 dB
Humidity	$+40^{\circ}\text{C} @ 93\% \text{RH}$ Duration : 96 hr	≤ 0.1 dB	≤ 0.05 dB
Humidity-Temperature Cycling	$-10 \sim +65^{\circ}\text{C} @ 93\% \text{RH}$ Duration : 10 cycles	≤ 0.1 dB	≤ 0.05 dB
Bellcore Service Life Test	Thermal Aging(85°C) → Humidity($60^{\circ}\text{C} @ 95\% \text{RH}$) → Temp. Cycling($-40 \sim 75^{\circ}\text{C}$) Duration : 14 days per process	≤ 0.2 dB	≤ 0.05 dB
Side Pull	Load : 20 N Directions : $8 \times 45^{\circ}$ intervals	≤ 0.12 dB	≤ 0.13 dB
Static Side Pull	Tensile load and duration: 1 N for 60min	≤ 0.03 dB	≤ 0.02 dB
Straight Pull	Tensile load : 40 N Duration : 120s	≤ 0.12 dB	≤ 0.05 dB

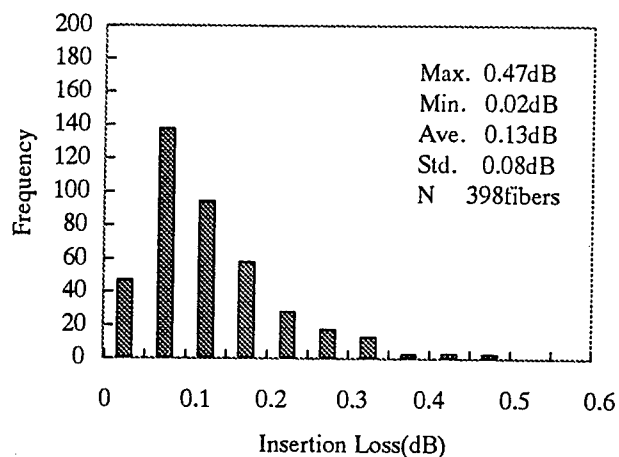


Fig. 4 Insertion loss of MT-RJ connector for singlemode fibers

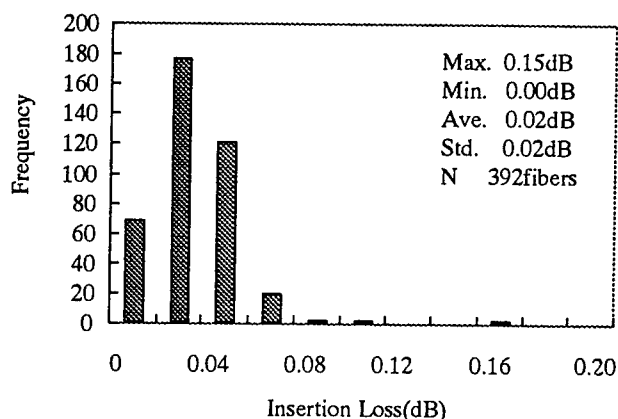


Fig. 5 Insertion loss of MT-RJ connector for multimode (GI) fibers

(1) Insertion loss

Fig. 4 and Fig. 5 show the insertion loss results of the MT-RJ connectors for $62.5/125 \mu\text{m}$ multimode(MM) GI fibers and $10/125 \mu\text{m}$ singlemode(SM) fibers respectively. The measurement was conducted at a wavelength of $1.31 \mu\text{m}$ without the use of index matching material. The average insertion loss is 0.02dB for multimode fibers and 0.13dB for singlemode fibers. These results confirmed the excellent low loss performance of the MT-RJ connector for connecting both singlemode and multimode fibers.

(2) Return loss

Fig. 6 shows the return loss result of the MT-RJ connector for singlemode fibers measured without the use of index matching materials. The return loss values are higher than 40dB. These values are typical of PC connectors with flat-polished

ferrule end-face. The fiber to fiber contact significantly reduces the back reflection at the connection interface due to Fresnel reflection caused by the presence of an air gap.

(3) Durability

Since a primary advantage of connectors is the flexibility to reconfigure fiber optic joints, connector durability and repeatability performance over multiple connection cycles are critical. Fig. 7 shows the result of the durability test conducted using singlemode fibers. The insertion loss was measured every 10 matings for a total of 500 repeated matings. Insertion loss deviation was less than 0.12 dB. This result has confirmed the repeatability and consistency of the MT-RJ connector in providing a stable optical connection.

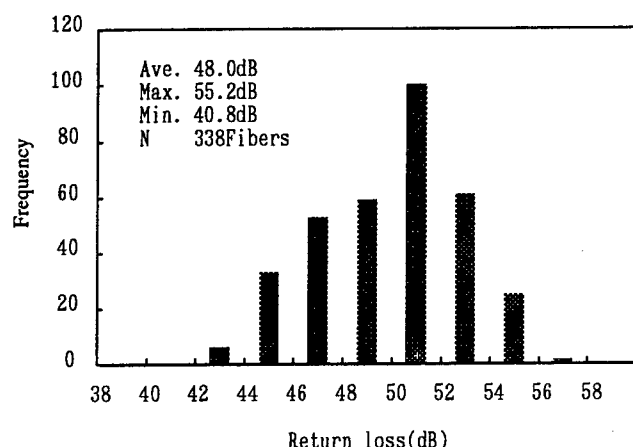


Fig. 6 Return loss of MT-RJ connector for singlemode fibers

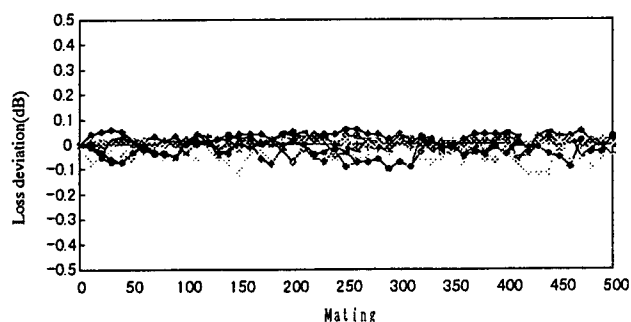


Fig. 7 Repeated mating loss characteristics of singlemode MT-RJ connector

(4) Temperature cycling

The MT-RJ connectors were subjected to a continuous varying temperature environment to determine its performance over a specified operating range. The insertion loss fluctuation of the connector was measured every ten minutes for a total of 10 cycles of temperature variation from -40°C to 85°C. The result for singlemode samples is shown in Fig. 8. The loss fluctuation during the test was well within 0.1 dB.

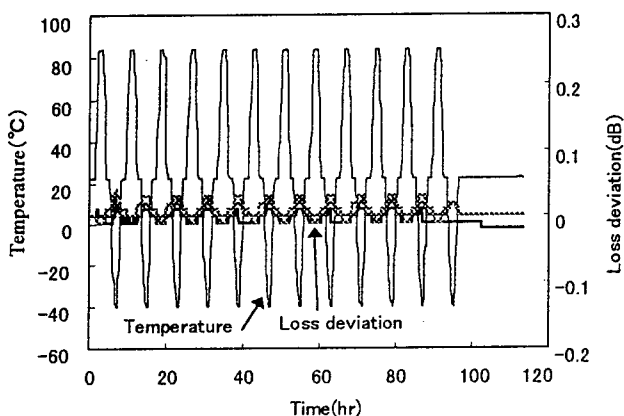


Fig. 8 Temperature cycling characteristics of singlemode MT-RJ connector

3. FIELD INSTALLABLE MT-RJ CONNECTOR

The field-installable MT-RJ plug and jack was developed to enable fast and easy connector assembly without the need for polishing, adhesive bonding or field electrical power supply. Based on pre-polished fiber stubs and mechanical splice technology⁹⁾, the field-installable MT-RJ connector can be easily terminated on any user-determined cable lengths to facilitate optical fiber installation in premises networks.

Fig. 9 and Fig. 10 show the structures of the field-installable MT-RJ plug and jack respectively. Both plug and jack have the same ferrule structure which consists of the mini-MT ferrule section and mechanical splice section. The mini-MT ferrule section contains factory-installed fibers and the

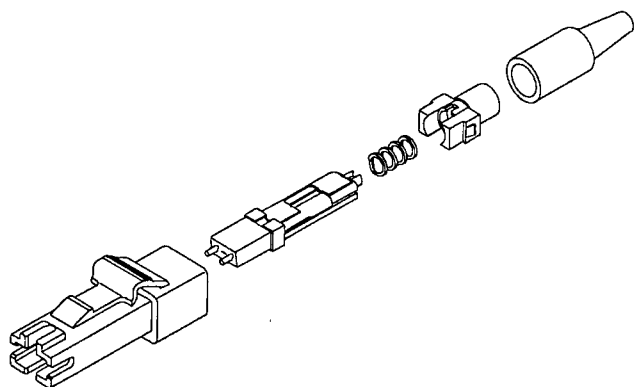


Fig. 9 Structure of field installable MT-RJ connector

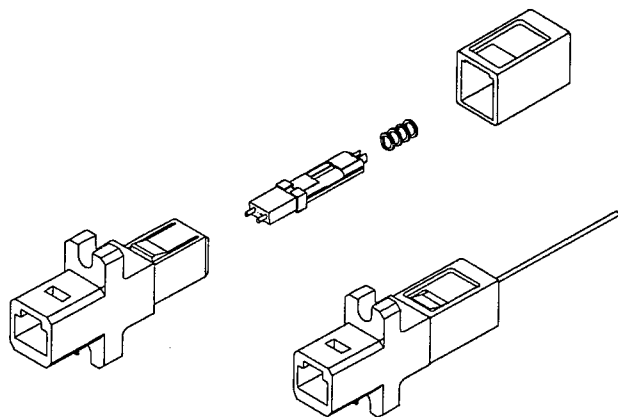


Fig. 10 Structure of field installable MT-RJ jack

end surface is pre-polished. Field terminated fibers are then mechanically spliced with the pre-installed fibers through the use of field assembly tools. Assembly of the connector is accomplished easily and efficiently with easy-to-use field tools. The assembly method is shown in Fig. 11. A wedge is inserted externally into the mechanical splice part to open it slightly, and bare fibers which have been cut with a mirror end-face are inserted. After the connecting fibers have come into contact with the pre-installed fibers in the ferrule, the wedge is removed and the fibers are thus mated. The average assembly time is about 2 minutes.

The average insertion loss of the field-installable MT-RJ connector is 0.08dB for multimode fibers and 0.25dB for singlemode fibers. Fig. 12 shows the loss histogram for singlemode connectors. The low loss result confirmed that the connector can be successfully employed in the field.

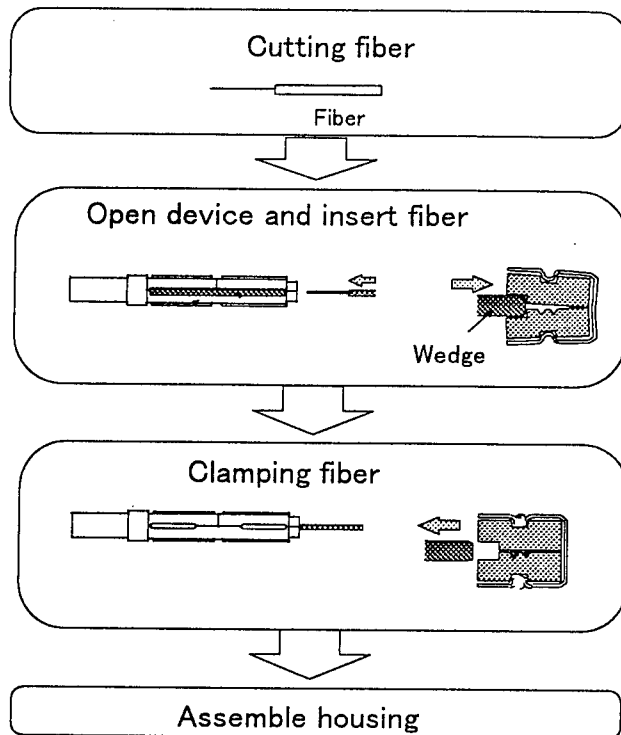


Fig. 11 Assembly method of field installable MT-RJ connector

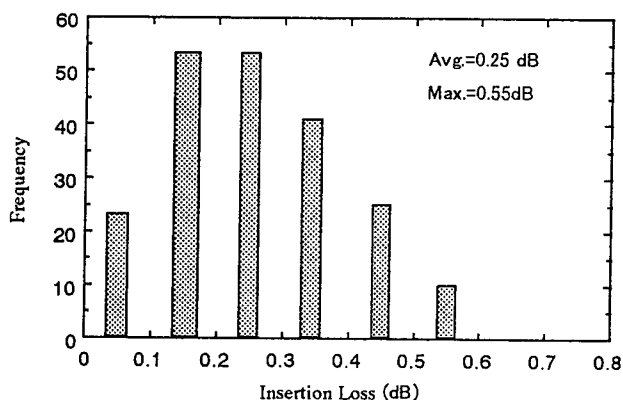


Fig. 12 Insertion loss of field installable MT-RJ connector (Singlemode)

4. LOW LOSS AND LOW REFLECTANCE CONSIDERATIONS

We are committed to further improve the optical performance of the MT-RJ connector for

applications which require very low optical transmission loss and low levels of back reflection. Our recent development efforts have produced very low loss and low reflectance singlemode MT-RJ connectors through precision molding and polishing techniques. Technical considerations and loss results are discussed in the sections that follow.

4.1 Low Loss

Considering the connection loss of the MT-RJ connector, transverse offset of the optical fiber core is the most important factor¹⁰. The relationship between transverse offset and connection loss is as follows.

$$L = -10 \log \{ \exp -(d/w)^2 \} \quad (1)$$

where L = connection loss (dB)
 d = transverse offset (μ m)
 w = mode field radius (μ m)

Fig 13 show the factors affecting fiber core alignment in the mini-MT ferrule of the MT-RJ connector. Connecting fibers are aligned through two precision guide pins on the male plugs that fit exactly into corresponding guide holes on the female plugs. The gap between the guide pins and the guide holes can affect fiber core alignment. The eccentricity of the fiber holes from their designed position in the ferrule also contributes to fiber core alignment offset. This eccentricity value is a very important parameter of the mini-MT ferrule and can be readily measured after the ferrule is molded.

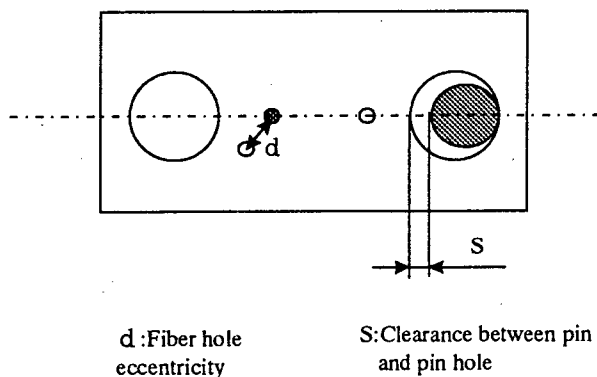


Fig. 13 Fiber core alignment offset considerations

Assuming that each transverse offset factor has a two-dimensional Gaussian distribution, the connection loss can be calculated. As a result, the random connection loss of a mated connector pair having an average fiber hole eccentricity of 0.25μ m is 0.08dB on average with 98 % confidence below 0.30 dB. Based on the above calculated results, we tightened our molding tolerance to produce mini-MT ferrules with fiber hole eccentricity below 0.25μ m and measured the connection loss for singlemode fibers. Fig.14 shows the loss measurement result. Low average connection loss of 0.10dB and maximum loss of 0.33dB were obtained.

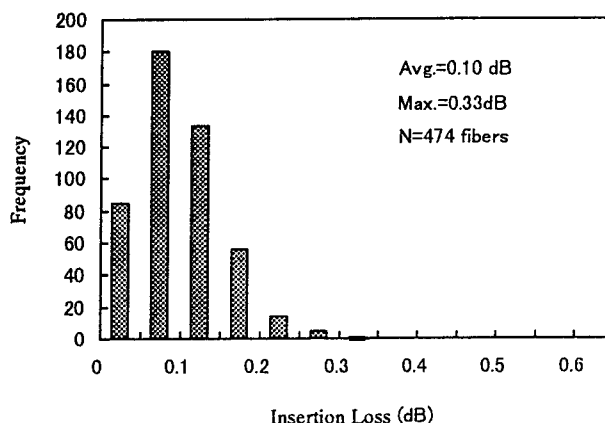


Fig. 14 Insertion loss of low loss singlemode MT-RJ connector

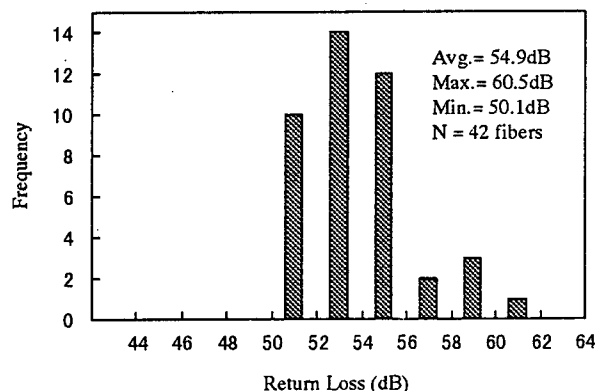


Fig. 15 Return loss of low reflectance singlemode MT-RJ connector

4.2 Low Reflectance

We have identified two limitations in reflectance performance of straight end-face connectors due to :

- 1) presence of a thin, high index damaged layer at polished end surface of fiber,
- 2) fiber end-face shape/angle not optimized for core to core contact

The first factor is a result of the polishing process. Current advanced PC polishing technique has reduced the average refractive index of the damage layer to a value close to that of the original silica and also the thickness of the layer to less than 0.1 μm . To remove this damage layer or further reduce the refractive index, polishing slurries and films with optimum chemomechanical properties and parameters that do not affect the properties of the contacting fiber surfaces have to be developed. Countering the second factor requires tighter control of the fiber end-face geometry to provide more consistent core to core contact when mated. For a 2-fiber ferrule, such an optimum end-face geometry is best realized with a flattened-dome fiber end surface profile.

We have directed our efforts toward improving the fiber end-face geometry by carefully examining and reviewing the polishing mechanics in current methods. The resultant improvement in precision polish was checked by accurately monitoring the polished fiber end surface profile. We then randomly mated the polished MT-RJ connectors and measured the return loss. The return loss is conventionally used to quantify optical back reflection at a connection interface and expresses a positive value of the reflectance in dB. Fig. 15 shows the return loss histogram. All return losses measured were above 50dB with an average value of 54.9dB. Thus without resorting to angle polish, we have successfully reduced the reflectance of the MT-RJ connector to below -50dB.

5. CONCLUSION

We have successfully developed the MT-RJ optical connector with less than half the size of the standard SC duplex connector. This small form factor connector features the use of a miniaturized MT ferrule for reliable optical connection and a sturdy and intuitive RJ-45 type latch for easy

connect. We have conducted a wide spectrum of optical, mechanical and environmental tests based on the Telcordia (formerly Bellcore) and IEC standards on the MT-RJ connector and the connector has met or exceeded the performance standard required of each test, confirming its applicability as an industry standard connector. In addition we have added to the versatility of the MT-RJ connector system a field installable type MT-RJ connector that enables fast and easy fiber termination in the field without polishing and adhesive bonding. Finally, our recent development efforts have produced stable low loss and low reflectance MT-RJ connector with an average insertion loss of 0.1dB and minimum return loss of 50dB for singlemode fibers.

References

- 1) S. Nagasawa et al. : "A High-Performance Single-mode Multifiber Connector Using Oblique and Direct Endface Contact Between Multiple Fibers Arranged in a Plastic Ferrule", J. Lightwave Technol., vol. 13, no. 6, pp. 987-994, 1995
- 2) H. Yokosuka : "Recent Progress in Fiber Splicing and Connector Technology", IOOC-95 Technical Digest Vol. 1, TuA2-2, 20-21, 1995.
- 3) K. Takizawa, et al.: Development of MT-RJ Optical Connector, Proceedings of the IEICE General Conference, SC-5-2 1999
- 4) Y. Kikuchi et al., "High Fiber Count Push-on Pull-off Connector," 43th IWCS Proceedings, pp. 627-632, 1994.
- 5) T. Satake et al., "Singlemode Multifiber Connector Performance," ECTC'96, pp. 494-499, 1996.
- 6) S. Nagasawa et al., "A High-Performance Singlemode Multifiber Connector Using Oblique and Direct Endface Contact Between Multiple Fibers Arranged in a Plastic Ferrule," J. Lightwave Technol., vol. 13, no. 6, pp. 987-994, 1995.
- 7) M. Takaya et al. : Designed Performance of a Miniaturized MPO type Connector for High-Density Optical Duplex Connection, IEEE Photon. Technol. Lett., vol. 10, No. 1, pp. 102-104, 1998
- 8) K. Takizawa, et al.: Development of Mini-MPO Connector, 46th IWCS, 1997
- 9) K. Takizawa, et al.: Field-installable Connector for Optical Fiber, 47th IWCS, 1998



Kazuhiro Takizawa
Fujikura Ltd.
1440 Mutsuzaki Sakura, Chiba, 285-8550, Japan

Kazuhiro Takizawa was born in 1968. He graduated from Yokohama National University with an M.E. degree in 1993. He joined Fujikura Ltd., and has been engaged in the research and development in the Cable Network Components Division. He is a member of the IEICE of Japan.

Design and Performance of Modular Jack Type Mini-MT Connectors

Masaaki Takaya, Shinji Nagasawa, Yasuji Murakami, and *Satomi Hatano

NTT Access Network Service Systems Laboratories
1-7-1 Hanabatake, Tsukuba, Ibaraki, 305-0805 JAPAN

*NTT Advanced Technology Corporation
2-1-1, Nishi-Sinjuku, Tokyo, 164-0431 JAPAN

Abstract

In this paper, we describe the design and performance of a modular jack type mini-MT connector that employs a compact 2-fiber ferrule in a newly designed housing. The basic mechanism for coupling the housings is similar to that of a conventional electric modular jack type connector. The connector has a locking mechanism to prevent accidental disconnection and a high packaging density of 2 fibers/cm². Fabricated connectors for single-mode 2-fiber ribbons exhibit a low insertion loss of 0.18 dB and a high return loss of more than 40 dB using a flat endface ferrule. In addition, they show an insertion loss of 0.20 dB and a return loss of 60 dB using an angled endface ferrule.

We have confirmed that this connector is highly effective for use in the duplex connection of advanced optical networks.

1. Introduction

It is essential to construct optical-fiber communication systems to provide broadband services to customers over a wide area. It is important to develop optical fiber joining techniques for these systems. There are three optical fiber joining techniques; fusion splicing, mechanical splicing, and connecting. Figure 1 shows the application of these techniques. Of these techniques, optical connection is useful where optical

fibers are frequently connected and disconnected. The connectors used in this approach must be inexpensive and provide low loss and high performance. Various optical connectors have been developed for this purpose. In NTT, the SC type, MU type, MT type, and MPO type connector are already in practical use [1]-[4]. The SC and MU type connectors are single-fiber connectors and they were developed mainly for equipment terminals. The MT and MPO type connectors are multifiber array connectors. They were developed mainly for subscriber cable joints.

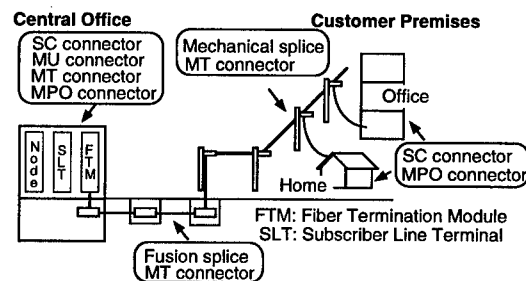


Fig.1 Applications of optical joining techniques

Recently small size duplex connectors have been needed as a replacement for SC connector in data communication systems. Typical examples are the LC type connector, the MT-RJ type connector, the VF-45 type connector, and the SC-DC connector [5]-[9]. Recent proposals include modular jack type connectors such as the LC type and MT-RJ type which can be connected and disconnected easily because they are similar to electric modular jack type connectors. Moreover, these connectors are inexpensive, small and have few components. They will be useful in subscriber buildings and premises.

However, there are some problems that

must be solved as regards their security and reliability when we use them in telecommunication systems. This connector is easier to operate than the SC connector, but it can be disconnected if the plug latch is touched unintentionally and it is possible for the fiber cord to become entangled with the latch during operation.

This paper proposes a new modular jack type mini-MT connector with a security locking mechanism. The connector provides stable direct endface contact for single-mode 2-fiber joints.

2. Example of practical configuration in subscriber building

Figure 2 shows an example of a practical configuration in a subscriber building.

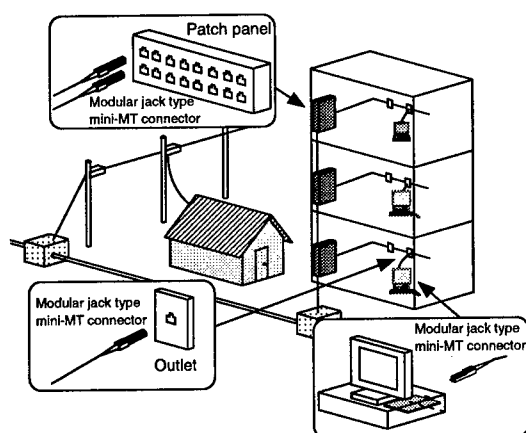


Fig. 2 Example of practical configuration in subscriber building

The modular jack type mini-MT connector can be employed with patch-panels used to switch optical connections. It can be also employed in outlets and desktop computers.

3. Target requirements for connectors

Table 1 shows the target requirements for modular jack type mini-MT connectors. The connectors must have excellent optical, mechanical, and environmental characteristics.

Table 1 Target requirement for the connectors

Tests		Conditions	Requirements
Optical tests	Insertion loss	With reference plug	< 0.50 dB
	Return loss	With reference plug	> 40 dB
Mechanical tests	Reconnection	500 times	$\Delta Li < 0.2$ dB
	Vibration	10~50 Hz, amplitude 1.5 mm, 2 hours, 3 directions	$\Delta Li < 0.2$ dB
	Straight pulling	49 N	$\Delta Li < 0.2$ dB
	Side pulling	20 N	$\Delta Li < 0.2$ dB
Environmental tests	Temperature change	-25~70 °C, 4 hours/cycle, 10 cycles	$\Delta Li < 0.2$ dB
	Temperature & humidity cycling	-10~65 °C, 93 % (at 65 °C), 1 day/cycle, 10 days	$\Delta Li < 0.2$ dB
	High temperature endurance	70 °C, 240 hours	$\Delta Li < 0.2$ dB
	Low temperature endurance	-25 °C, 240 hours	$\Delta Li < 0.2$ dB

ΔLi : Insertion loss increase

These characteristics are as good as those of conventional SC type connectors.

4. Connector structure

Figure 3 shows the structure of our new modular jack type mini-MT connector. The connector consists of two plugs and an adaptor.

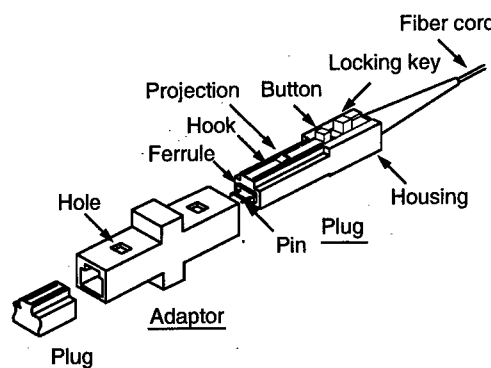


Fig. 3 Structure of modular jack type mini-MT connector

Each plug contains a plastic mini-MT ferrule in the connector housing. The ferrule endface houses two fibers, 0.75 mm apart,

between two guide-holes. The ferrule endface is polished flat and a slight fiber protrusion obtained to ensure direct fiber endface contact. The ferrules are aligned by fitting two guide-pins in one ferrule into the guide-holes of the other ferrule. On one side of the housing, there is an elastic hook with a button and a projection. The plug and adaptor are engaged by fitting the projection into a hole provided in the adaptor. The hook is buried in the housing to prevent the fiber cord from becoming entangled with it. There is a movable locking key behind the button. The connector is compatible with existing mini-MT type connectors using a specially designed adaptor.

It is easy to connect and disconnect the plugs. Connection is realized by pushing the plug into the adaptor. At this time it is unnecessary to release the locking key (the released state is as shown in Fig. 4 (a)). The hook is designed to provide enough elastic deformation to allow the plug to be inserted into the adaptor even if the key is in the locked position as shown in Fig. 4 (b). Disconnection is performed by releasing the locking key, pushing the button and pulling the plug. When the plug is connected and the key in position, the hook can not be bent and this prevents accidental disconnection.

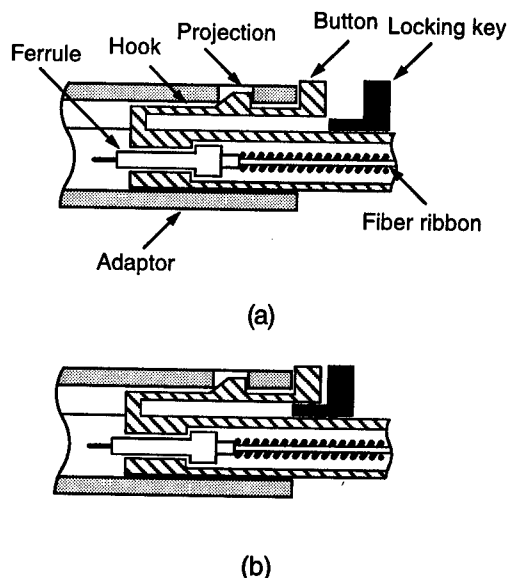


Fig. 4 Structure of the key in 2-fiber modular jack type mini-MT connector

- (a) released state
- (b) locked state

The plug is 7 mm wide and 6 mm high. The fiber packaging density for the connector is 2 fibers/cm². This is twice the density of the SC-type duplex connector.

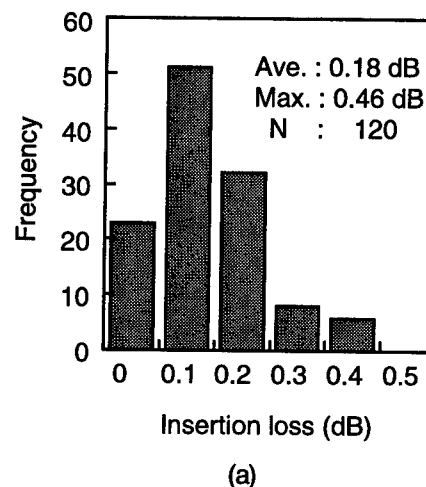
5. Connector performance

We constructed modular jack type mini-MT connectors for duplex connection based on the above design. The plugs that we used in this connector were assembled with 1.3 μ m zero-dispersion 2-fiber ribbons. The mode field diameter of the fiber was 9.5 μ m. Moreover the plugs were assembled with graded-index 2-fiber ribbons with a core diameter of 50 μ m. We then performed optical, mechanical, and environmental tests on these connectors when the connector locking mechanism was engaged.

A. Optical test results

We measured the insertion losses for random connection using an LED operating at 1.3 μ m.

Insertion loss histograms for the connectors with single-mode and multi-mode fibers are shown in Fig. 5. We measured the insertion loss with the multi-mode fibers in the steady state mode.



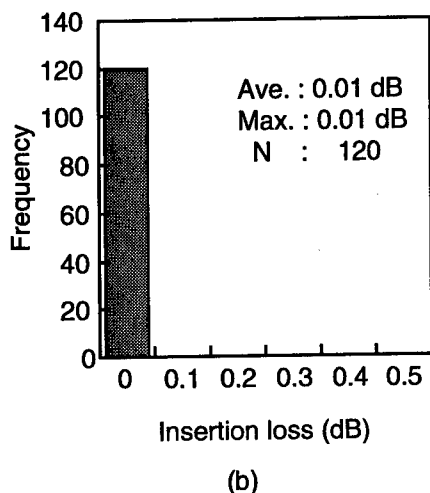


Fig. 5 Connector insertion loss
(a) single-mode fiber
(b) multi-mode fiber

The average insertion loss was 0.18 dB with the former type, and 0.01 dB with the latter type.

We measured insertion loss changes for the single-mode fiber connectors with and without index-matching materials. The relationship between insertion losses with and without index-matching is shown in Fig. 6.

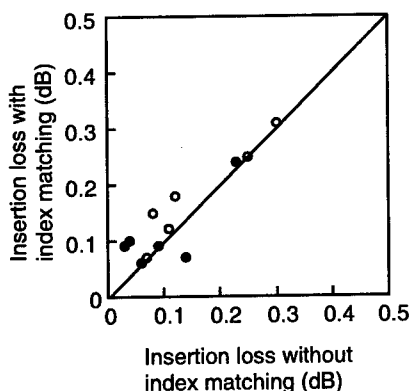


Fig. 6 Insertion loss changes for single-mode fiber connectors with and without index-matching materials

The insertion loss was almost the same in both cases. This shows that direct endface contact was obtained with these connectors. We measured the return losses of the single-mode connectors using an LD operating at

1.3 μm and found them to be more than 40 dB.

B. Mechanical test results

Figure 7 shows the insertion loss changes for 500 reconnections with single-mode and multi-mode fiber connectors.

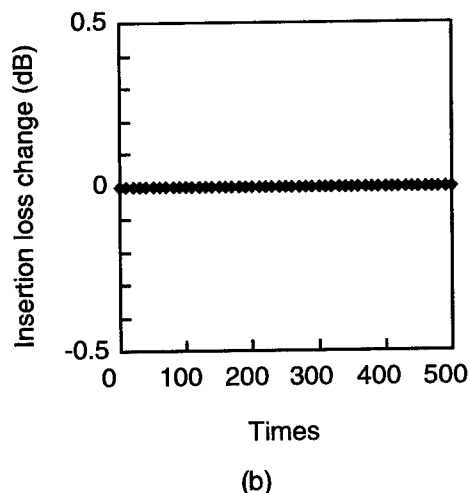
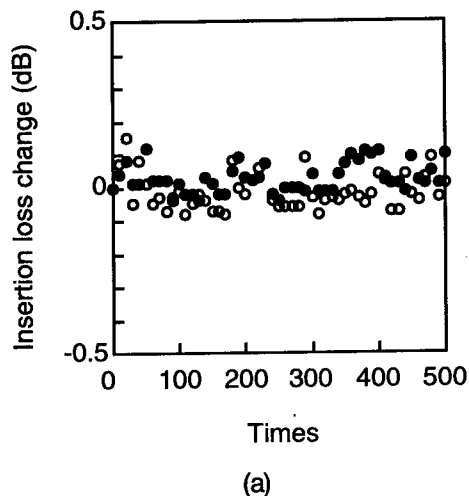


Fig. 7 Insertion loss changes of connectors for 500 reconnections
(a) single-mode fiber
(b) multi-mode fiber

The range of the maximum loss increase was less than 0.2 dB with the former type and 0.05 dB with the latter type, and there was no damage to the connectors. We also performed vibration tests. The frequency range was 10-55 Hz, and the vibration amplitude was 0.75 mm. We tested these

connectors for two hours in each direction. The insertion loss changes were less than 0.1 dB for both types of connector.

Tests were also undertaken in which pulling forces were applied to the connector plugs in several directions through fiber ribbons enclosed in a reinforced jacket as shown in Fig. 8.

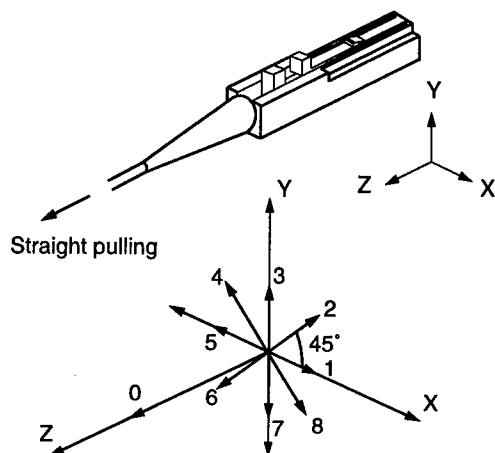


Fig. 8 Direction of pulling force.

We performed a straight pull test and a side pull test in eight directions. We pulled the cords at a point 25 cm from the connector plug. We applied a load of 40 N in the straight pull test and 20 N in the side pull test. The differences in insertion losses before and after the tests were less than 0.1 dB with the single-mode and multi-mode fibers, and there was no damage to the connectors. This result shows that direct endface contact is maintained when a load is exerted on the connector and that the connector is suitable for practical use.

C. Environmental test results

Next we performed two environmental tests on the connector. They were a temperature change test (-25°C to 70°C , 6h/cycle, 10 cycles) and a temperature and humidity cycling test (93% at 65°C , 24h/cycle, 10 cycles). The insertion loss changes were less than 0.2 dB during these tests for single-mode and multi-mode fibers.

These results indicate that the connector is stable as regards changes in temperature and

humidity. The results are summarized in Table 2.

Table 2 Results of mechanical and environmental tests on the connector.

Tests		Conditions	Results
Mechanical tests	Reconnection	500 times	$\Delta\text{Li} < 0.2\text{dB}$
	Vibration	10~50 Hz, amplitude 1.5 mm, 2 hours, 3 directions	$\Delta\text{Li} < 0.1\text{ dB}$
	Straight pulling	49 N	$\Delta\text{Li} < 0.1\text{ dB}$
	Side pulling	20 N	$\Delta\text{Li} < 0.1\text{ dB}$
Environmental tests	Temperature change test	$-25\sim 70^{\circ}\text{C}$, 4 hours/cycle, 10 cycles	$\Delta\text{Li} < 0.2\text{ dB}$
	Temperature & humidity cycling	$-10\sim 65^{\circ}\text{C}$, 93 % (at 65°C), 1 day/cycle, 10 days	$\Delta\text{Li} < 0.2\text{ dB}$

6. Structure and performance of connector with angled endface

In some systems, the optical connector must have a low return loss. For this purpose, we have developed a modified version of the modular jack type mini-MT connector. We polished the endface of the connector to an angle of 8 degrees to eliminate reflection.

Figure 9 shows the structure of the modular jack type mini-MT connector with an angled endface mini-MT ferrule.

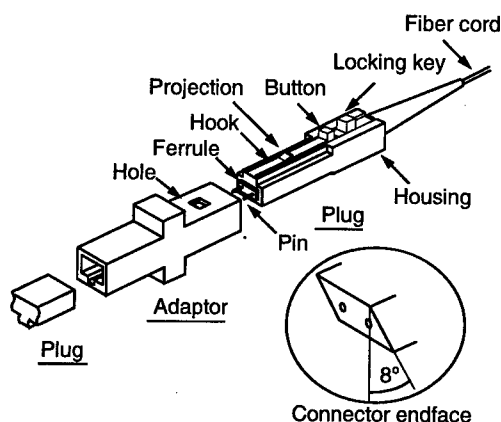


Fig. 9 Structure of modular jack type mini-MT connector with angled endface

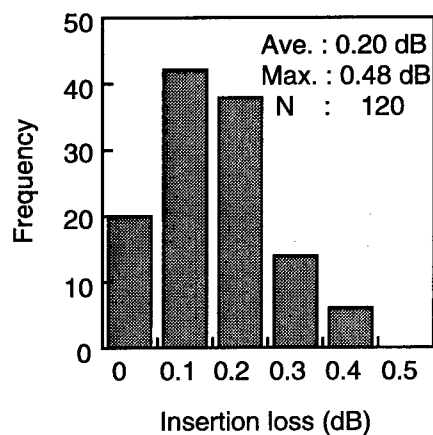
We constructed connectors with angled endfaces for duplex connection based on the above design. The plugs that we used in these connectors were assembled with $1.3\text{ }\mu\text{m}$ zero-dispersion 2-fiber ribbons. The

mode field diameter of the fiber was 9.5 μm . Moreover the plugs were assembled with graded-index 2-fiber ribbons with a core diameter of 50 μm . We then employed the same tests that we performed on the modular jack type mini-MT connectors with flat endfaces.

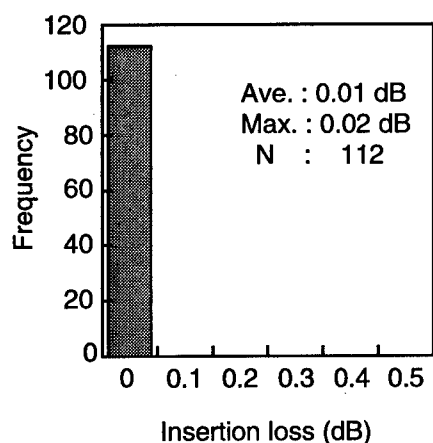
A. Optical test results

We measured the insertion losses for random connection using an LED operating at 1.3 μm .

Insertion loss histograms for the connectors with single-mode and multi-mode fibers are shown in Fig. 10. Again the insertion loss with the multi-mode fibers was measured in the steady state mode.



(a)



(b)

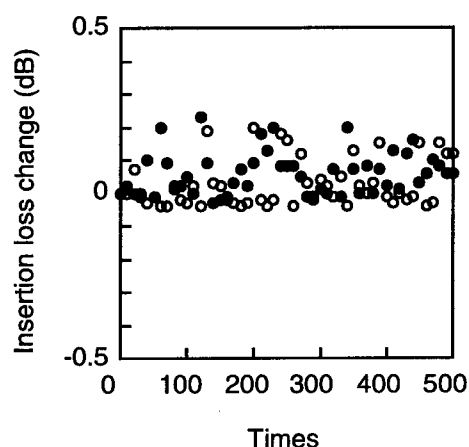
Fig. 10 Connector insertion loss
(a) single-mode fiber
(b) multi-mode fiber

The average insertion loss was 0.20 dB with the former type, and 0.01 dB with the latter type.

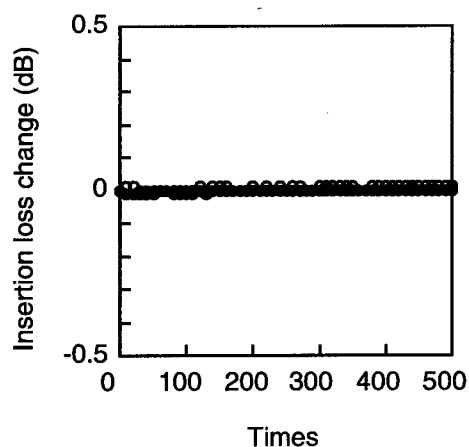
We measured the return losses of the connectors using an LD operating at 1.3 μm and found them to be more than 60 dB for single-mode fiber.

B. Mechanical test results

Figure 11 shows the insertion loss changes for 500 reconnections with single-mode and multi-mode fiber connectors.



(a)



(b)

Fig. 11 Insertion loss changes of connectors for 500 reconnections
(a) single-mode fiber
(b) multi-mode fiber

The range of the maximum loss increase was

less than 0.25 dB with the former type, and 0.05 dB with the latter type, and the connectors were undamaged. We also performed vibration tests with a frequency range of 10-55 Hz, and a vibration amplitude of 0.75 mm. We tested these connectors for two hours in each direction. The insertion loss changes were less than 0.1 dB for both connectors.

We also undertook tests in which pulling forces were applied to the connector plug in several directions through fiber ribbons enclosed in a reinforced jacket as described before. Again we applied a load of 40 N in a straight pull test and 20 N in a side pull test. The differences in insertion losses before and after the tests were less than 0.1 dB with both the single-mode and multi-mode fibers, and there was no damage to the connectors. This result shows that direct endface contact is maintained when a load is exerted on the connector and that the connector is suitable for practical use.

C. Environmental test results

Next we performed two environmental tests on the connector. The insertion loss changes were less than 0.2 dB during these tests for both single-mode and multi-mode fibers.

These results indicate that the connector is stable as regards changes in temperature and humidity. The results are summarized in Table 3.

Table 3 Results of mechanical and environmental tests on the connector

Tests	Conditions	Results
Mechanical tests	Reconnection	500 times $\Delta Li < 0.25$ dB
	Vibration	10~50 Hz, amplitude 1.5 mm, 2 hours, 3 directions $\Delta Li < 0.1$ dB
	Straight pulling	49 N $\Delta Li < 0.1$ dB
	Side pulling	20 N $\Delta Li < 0.1$ dB
Environmental tests	Temperature change test	-25~70 °C, 4 hours/cycle, 10 cycles $\Delta Li < 0.2$ dB
	Temperature & humidity cycling	-10~65 °C, 93 % (at 65 °C) , 1 day/cycle, 10 days $\Delta Li < 0.2$ dB

7. Conclusion

We have developed a modular jack type mini-MT connector with a secure locking mechanism.

We examined the insertion and return losses of these connectors. We obtained a low average insertion loss of 0.18 dB with a return loss of greater than 40 dB for a 2-fiber connector with a flat endface, and a low average insertion loss of 0.20 dB with a return loss of greater than 60 dB for a 2-fiber connector with an angled endface.

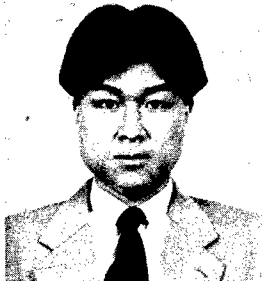
Our new connectors exhibit good levels of performance and are promising with regard to upgrading access networks for fiber to the home.

References

- [1] K. Kanayama, R. Nagase, K. Kato, S. Oguchi, T. Yoshizawa, and A. Nagayama, "Characteristics of an SC-Type Optical Fiber Connector with a Newly Developed Pre-Assembled Ferrule," IEEE Photon. Technol. Lett. Vol. 7, No. 5, pp. 520-522, 1995.
- [2] S. Iwano, R. Nagase, K. Kanayama, E. Sugita, E. Yasuda, and Y. Ando, "Compact and Self-retentive Multi-ferrule Optical Backpanel Connector," J. Lightwave Technol. Vol. 10, No. 10, pp. 1356-1362, 1992.
- [3] F. Ashiya, T. Satake, and S. Nagasawa, "Development of Multifiber Connectors and their Applications," E-FOC '87, pp. 304-308, 1987.
- [4] S. Nagasawa, Y. Yokoyama, F. Ashiya, and T. Satake, "A High-Performance Single-mode Multifiber Connector Using Oblique and Direct Endface Contact Between Multiple Fibers Arranged in a Plastic Ferrule," IEEE Photon. Technol. Lett. Vol. 3, No. 10, pp. 937-939, 1991.
- [5] Light Wave, pp. 39-51, May 1998.
- [6] C. DeCusaties, "Optical Data Communication : Fundamentals and Future Directions," Optical Engineering, vol. 37, No.12, pp. 3082-3099, 1998.

- [7] C. Vernon, "RJ-45 Style Duplex Fiber Optic Connector with 2.5-mm Ferrules," Optical Engineering, vol. 37, No. 12, pp. 3124-3128, 1998.
- [8] K.M. Wagner, D.L. Dean, M. Giebel, "SC-DC/SC-QC Fiber Optic Connector," Optical Engineering, vol. 37, No. 12, pp. 3129-3133, 1998.
- [9] R.K. Selli, S. Berglund, "Novel V-groove-based Interconnect Technology," Optical Engineering, vol. 37, No. 12, pp. 3134-3142, 1998.

Speaker Biography



Masaaki TAKAYA
NTT
Access Network
Service Systems
Laboratories
1-7-1, Hanabatake,
Tsukuba, Ibaraki,
305-0805
JAPAN

Masaaki Takaya is a research engineer at NTT Access Network Systems Laboratories. He joined NTT in 1992. Since 1993 he has been engaged in the research and development of multifiber connectors. Mr. Takaya is a member of IEICE of Japan.

A NOVEL POLISHING METHOD FOR PHYSICAL CONTACT (PC) CONNECTION OF MULTIFIBER CONNECTOR

Xu Jie, Takanobu Yamazaki, Naoko Shimoji, Katsuhiko Iwashita and Kenji Suzuki

The Furukawa Electric Co., Ltd. Ichihara, Chiba, JAPAN

ABSTRACT

A novel vibration polishing method of multi-fiber connector was developed by exclusively polishing the ferrule material to form fiber protrusion effectively. This method enabled us to obtain the desired fiber protrusion, for example, 5 μm , easily and the insertion loss difference of single-mode 12-fiber connector with and without index-matching material was less than 0.04 dB. Good optical characteristics were obtained. In the meantime, we confirmed when the fiber protrusion was as large as 5 μm , optical characteristics of 12-fiber connector without index-matching material remained stable during the reconnections of 500 cycles.

The results demonstrate that good and stable PC connection is achieved by this method.

INTRODUCTION

Along with the rapid development of the information society, there is a growing demand of transmitting large volume of data speedily. High-density and high-count optical cables have been developed to meet this need. Undoubtedly, multi-fiber connector that connects large number of

fibers in the cable is one of the most important components of large scale optical subscriber networks to facilitate the effective transmission of data. The development of multi-fiber connector is indispensable to such system.

Mechanically transferable (MT) connector and multi-fiber push-on (MPO) connector which uses the MT type ferrule have been developed^{1,2}. Both connectors have excellent characteristics. In MPO connector, the fiber endface is generally angle-polished and the optical fiber protrudes slightly from the ferrule surface to achieve the direct endface contact. By this polishing technique, Fresnel reflection is reduced without index-matching material and good optical characteristics are obtained. On account of these performances, MT connector and MPO connector have been widely used in recent years.

Good PC connection is indispensable to reduce Fresnel reflection and to obtain good and stable optical characteristics. However, there has remained a problem in the polishing process of multi-fiber connectors for high fiber count, such as 12 fibers. In this case, it is difficult to obtain good PC connection by conventional polishing method, because conventional method takes advantage of the hardness difference between plastic ferrule and fiber to achieve fiber protrusion of about 1 μm and it is not easy to

achieve even and sufficient fiber protrusion for all the 12 fibers.

This paper presents a novel vibration polishing method of multi-fiber connector. By this method, sufficient fiber protrusion can be easily formed in a short time regardless of ferrule and fiber materials by exclusively polishing the endface of ferrule surrounding the fibers. This method can be applied to angle-polished 12-fiber MPO connector and good optical characteristics are obtained.

POLISHING METHOD

In general, the essential factors to achieve PC connection include:

1. Fiber protrusion
2. Flat fiber-end plane
3. Perpendicularity of fiber-end plane to the guide pin axis

Good PC connection not only requires sufficient fiber protrusion but also the fiber ends to be in the same plane. Polishing method is critical to realize such endface geometry.

Conventional Polishing Method

The ferrule and fiber endfaces are simultaneously polished with polishing abrasive in the conventional polishing method. The endface of ferrule is polished deeper than the fiber endface due to the difference in the hardness of those materials and thus fiber protrusion is formed. By this method the fiber protrusion of about $1\mu\text{m}$ can be obtained easily, but as the number of fibers in the connector increases, the uneven protrusion between the fibers becomes a problem.

Novel Polishing Method

In this novel polishing method, the fiber

protrusion and the fiber-end flatness are obtained by completely separate polishing process. As a result, sufficient fiber protrusion is obtained while keeping the fiber-end position precisely even and therefore a good PC contact is realized.

At first, in order to align the fiber ends in the same plane at a right angle, the MT type ferrule is lapped by a special lapping wheel. And then only the ferrule material is polished by the vibration polishing machine to form fiber protrusion.

Fig.1 explains the fiber protrusion polishing process by the vibration polishing machine. The MT ferrule with highly flat endface is aligned by the guide pin with the assisting ferrule, which has empty fiber holes. At this time, abrasive is added between the ferrule ends. The assisting ferrule is then vibrated by the vibrator attached to it, and only the MT ferrule end-face is polished leaving the fiber-ends untouched because the fiber ends are free from the contact with the assisting ferrule. This polishing method leaves the fiber-ends unpolished without fail. A desired fiber protrusion can be obtained easily in a short time by suitably selecting the vibration frequency and the abrasive particle size.

In Fig. 2, it is clearly shown that the fiber protrusions of all the 12 fibers are about $5\mu\text{m}$ with very little variation.

This polishing process enables us to easily obtain a desired fiber protrusion regardless of the ferrule and fiber materials and at the same time to maintain precise end-face geometry with fiber-end in the same plane. This was made possible by separating the protrusion process completely from the end-face flat lapping process.

CHARACTERISTICS

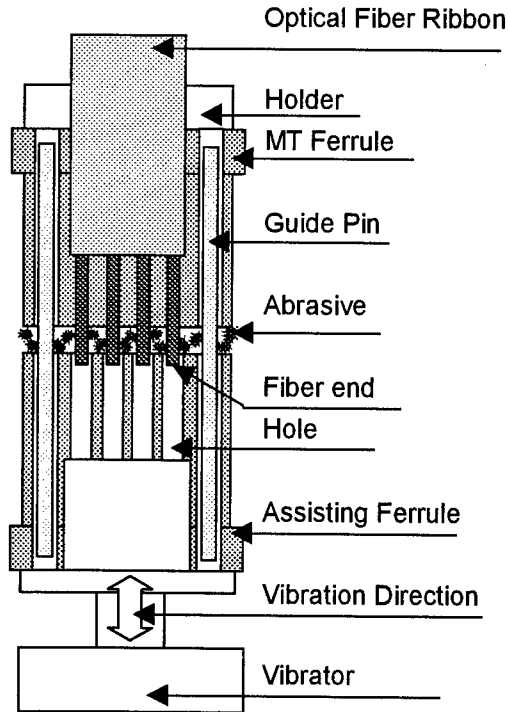


Fig. 1 The principle of the vibration polishing method

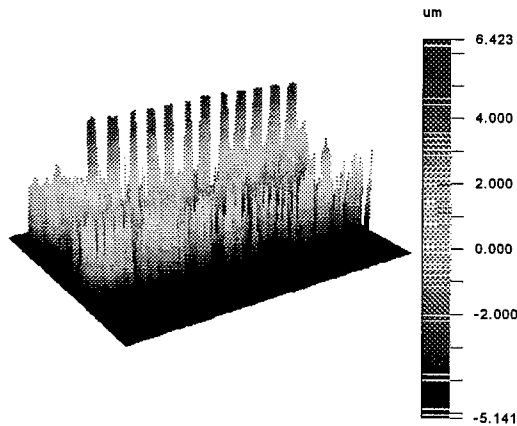


Fig. 2 The fiber protrusion of 12-fiber ferrule obtained by the novel polishing method measured by Roughness / step tester system

Optical Test Results

We examined the insertion loss and the return loss of single-mode 12-fiber MPO connectors angle-polished by the above vibration polishing method without index-matching material at 1310nm wavelength. The results are shown in Fig.3 and Fig.4. The mean insertion loss was 0.19 dB ($n=48$), and the mean return loss was 62.5 dB ($n=20$).

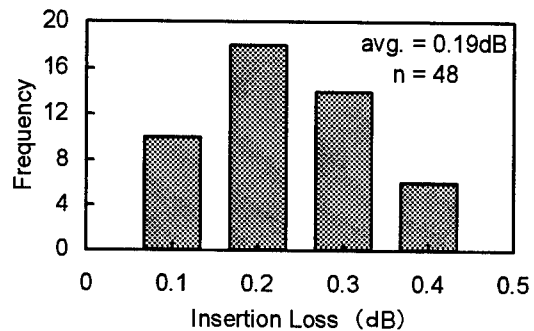


Fig. 3 Insertion loss without index-matching material for single-mode 12-fiber MPO connector polished by the novel polishing method

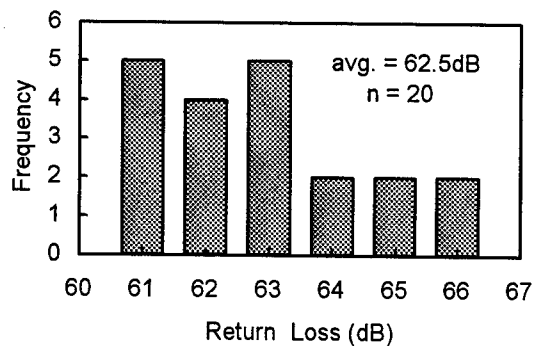


Fig. 4 Return loss without index-matching material for single-mode 12-fiber MPO connector polished by the novel polishing method

The insertion loss of multi-mode 12-fiber MPO connectors polished by this novel method was also tested without index-matching material as shown in Fig.5. The mean insertion loss was 0.11 dB ($n=144$).

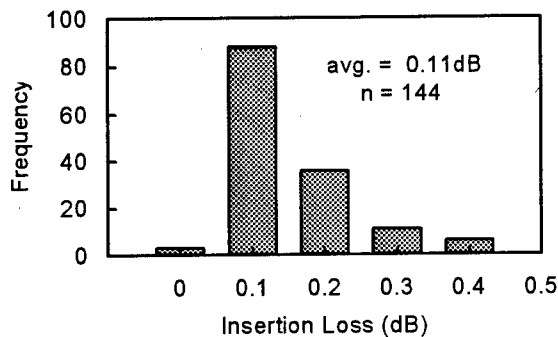


Fig. 5 Insertion loss without index-matching material for multi-mode 12-fiber MPO connector polished by the novel polishing method

These results demonstrate that both single-mode and multi-mode multi-fiber connectors polished by the novel vibration polishing method have good optical characteristics without index-matching material.

PC Connection Test Result

In order to testify whether good PC contact is achieved, we measured the insertion loss with and without index-matching material in single-mode 12-fiber MPO connectors polished by the vibration polishing method. As shown in Fig.6, the maximum difference of insertion loss with and without index-matching material was less than 0.04 dB ($n=48$).

The result indicates excellent PC connection is achieved by this novel polishing method.

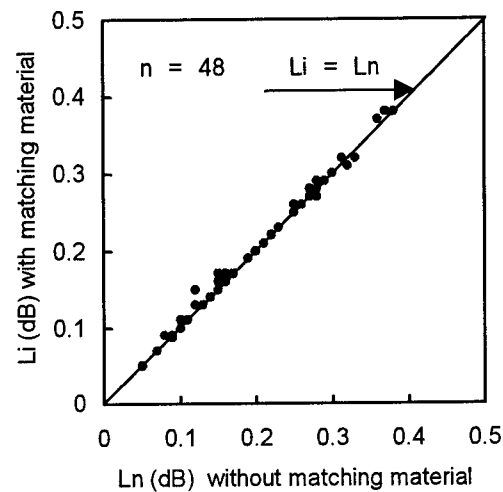


Fig. 6 Relationship between insertion losses with and without index-matching material for single-mode 12-fiber MPO connector polished by the novel polishing method

Stability Test Results

This vibration polishing method enabled us to easily obtain the desired fiber protrusion such as $5\mu\text{m}$. In this case, a question arises whether this protrusion is too large to maintain stable performance in practical use. Therefore we performed the connection-reconnection tests of the single-mode 12-fiber MPO connectors for 500 cycles. During the tests, the ferrules were connected under the compression force of 9.8N and the insertion loss and return loss for all the fibers were measured at every 25 cycles. According to our results, the insertion loss and the return loss for these fibers did not change significantly. For the sake of simplicity, only the results of the first, the sixth, the seventh and the twelfth fibers measured at every 100 cycles are shown in Fig. 7 and Fig. 8. The results demonstrate there are almost no change in optical characteristics in this reconnection test,

which means, the performance of the connectors with fiber protrusion of even $5\mu\text{m}$ is very stable.

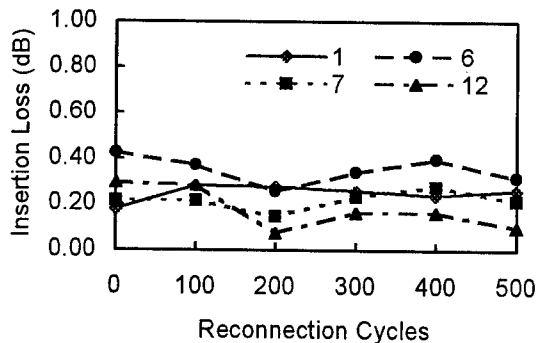


Fig. 7 Insertion loss for the first, the sixth, the seventh and the twelfth fibers in single-mode 12-fiber MPO connectors polished by the novel polishing method for reconnections of 500 cycles

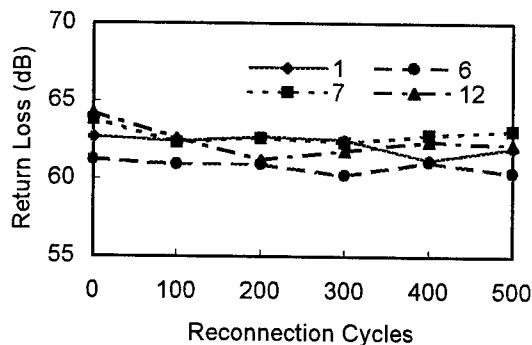


Fig. 8 Return loss for the first, the sixth, the seventh and the twelfth fibers in single-mode 12-fiber MPO connector polished by the novel polishing method for reconnections of 500 cycles

CONCLUSION

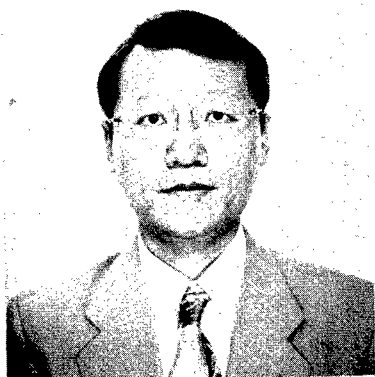
We developed a novel vibration polishing method of multi-fiber connector. By this method,

a desired fiber protrusion such as $3\mu\text{m}$ or $5\mu\text{m}$ can be easily obtained, and the difference of insertion loss with and without index-matching material in single-mode 12-fiber connector is less than 0.04 dB, demonstrating excellent PC connection. 12-fiber single-mode MPO connector angle-polished by this means has a low average insertion loss of 0.19 dB and a high average return loss of 62.5 dB at 1310nm wavelength. Multi-mode connector also has good optical characteristics. Meanwhile, we confirmed that when the fiber protrusion is as large as $5\mu\text{m}$, optical characteristics of 12-fiber connector without index-matching material remains stable during the reconnections of 500 cycles.

REFERENCES

1. S. Nagasawa, et al. " Mechanically Transferable Single-mode Multifiber connector ", Tech. Dig. IOOC' 89. 21C2-1, 99. pp. 48-49, 1989
2. S. Nagasawa, et al. " A High-performance Single-mode Multifiber Connector Using Oblique and Direct Endface Contact Between Multiple Fibers Arranged in a Plastic Ferrule ", IEEE Photon. Technol. Lett. Vol. 3, No.10, pp. 937-939, 1991

Speaker Biography



Xu Jie

The Furukawa Electric Co., Ltd
Production Engineering Development Center
6, Yawata-kaigandori, Ichihara,
Chiba 290-8555, JAPAN
E-mail: xu@ch.furukawa.co.jp

He received the M.E. degree in mechanical engineering from Tokyo Institute of Technology, Tokyo, Japan, in 1990. He joined The Furukawa Electric Co., Ltd. in 1990 and has been engaged in the research and development of the production facilities of optical fiber connector and semi-conductor wafer.

NEW PUSH-ON TYPE MT-CONNECTOR FOR OPTICAL FIBER

Kunihiko Fujiwara, Yukio Hayashi, Hiroshi Furukawa and Yoshikazu Nomura

Fujikura Limited
Cable Network Components Division
Sakura, Chiba, JAPAN

ABSTRACT

This paper presents a new push-on type MT-connector for fiber ribbons. This new connector comprises a pair of conventional MT-ferrules, with one of them held within a newly designed push-on type MT-connector. This new connector has a pair of built-in guide pins and a clip. It eliminates the need to insert guide-pins or assemble the clip during connection, and hence the fear of losing them during disconnection. The new push-on type MT-connector is also smaller than the MPO-connector (otherwise called the MTP). This smaller size increases the connection density. Very good optical characteristics and reliability are observed from this new push-on MT-connector, comparable to that of the conventional MT-connectors. The procedure for connection requires fewer steps than the conventional MT-connectors. Compared to the conventional MT-connectors, the overall connection time is halved.

INTRODUCTION

Mechanically Transferable (MT) connectors make swift connection/disconnection of multiple

fibers possible. Their importance in optical communications is demonstrated by the many varied versions of multi-fiber connectors available today, most whose key component is based on the MT-ferrule of the original MT connector. Examples are the mini-MT, MPO, mini-MPO, MT-RJ⁽¹⁾⁻⁶⁾ and their respective field-installable versions.

There are shortfalls in the conventional MT connector (and some MT-based connectors). The MT-connector while allowing quick connection/disconnection of multiple fibers requires insertion of guide pins and a clip spring during connection process. Although not tedious, this process requires relatively more time. The MPO addresses this shortfall with its "push-on" for connection and "pull-off" for disconnection. The MPO, however, has more parts than the conventional MT-connector. The cost is also expectedly higher. The physical size of the MPO is not ideally small. In fact, it is many times larger than the conventional MT-connector.

The new push-on type MT connector described in this paper attempt to address the shortcomings of the MT- and MPO- connectors. The new push-on type MT-connector has the convenience of push-on/pull-off actions with easy-to-use application tool for

connection/disconnection respectively. In addition, it has a connection footprint that is only 47% of MPO-connectors.

The next section describes the design, structure and operation of the new push-on type MT-connector. The optical characteristics and reliability of the new push-on type MT-connector are then described. This is followed by the conclusions.

DESIGN, STRUCTURE AND OPERATION

Physical design and structure

Fig. 1 is a schematic drawing of the push-on type MT-connector and Fig. 2 depicts how it looks like when in-use.

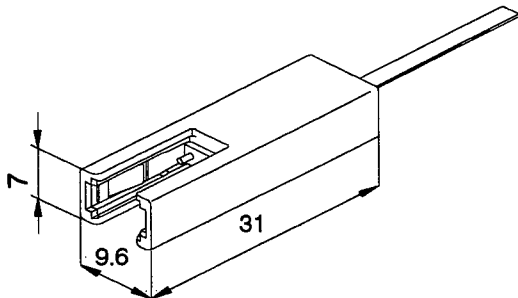


Fig. 1: Schematic drawing of the push-on type MT-connector.

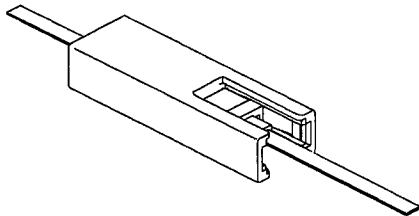


Fig. 2: A mated MT-housing and MT-ferrule.

The components in the new push-on type MT-connector are illustrated in Fig. 3. This new connector consists of a MT-ferrule, guide pins and a pin clamp, a spring, a clip and an external housing.

The external housing embraces all the other parts of this new connector. It also has an opening on one end from which the other MT-ferrule is guided into for mating with the MT-ferrule housed within. This external housing is made of molded plastic and is therefore inexpensive. The size of this plastic external housing is in fact the entire size of the connector. As can be observed from the dimensions in Fig. 1, this connector has a connection footprint only about 47% of the size of MPO-connectors. This smaller size allows for higher density on connector panels.

The function of the spring is to ensure a firm mating between the end-faces of the MT-ferrules. This spring seats within the clip. The clip is made by pressed metal sheet and again, this accounts for the overall cost economy. The clip functions to hold the two MT-ferrules together.

The guide pins are very essential for accurate alignment of MT-ferrules. In this new connector, the pins are fixed in the pin-clamp and housed within the external housing. This design eliminates the possibility of dropping the guide pins during disconnection as in the case of conventional MT-connectors.

The components described above plus the MT-ferrules are the only parts of the new push-on MT-connector. Its assembly is simple and no adhesive is required.

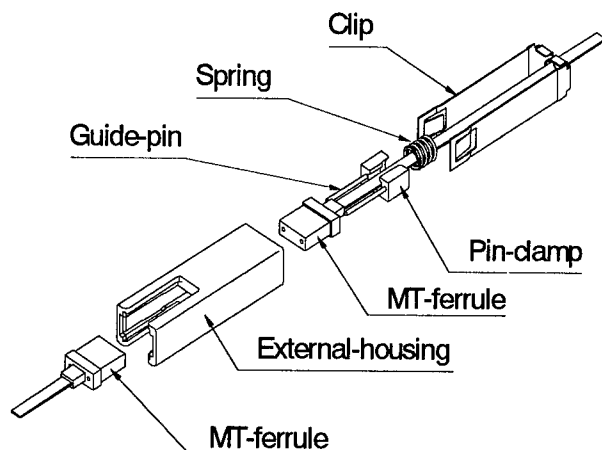


Fig. 3: Components of the push-on type MT-connector.

Application tool

The application tool is depicted in Fig. 4. The physical dimension of this application tool is small. It has an overall length of 100mm and a width of 7.5mm. It is a one-piece molded plastic and low-cost mass production is possible.

As illustrated in Fig. 4, the two ends on the application tool are dissimilar. One end is used for inserting a MT-ferrule into the external housing of the new connector for connection, the other is used for plucking the MT-ferrule out of the external housing for disconnection.

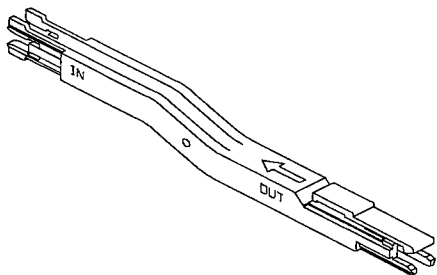
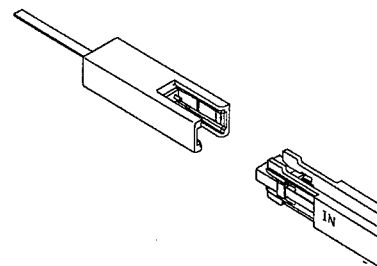


Fig. 4: Schematic drawing of the application tool

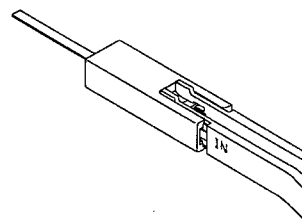
Procedures for connection/disconnection

The procedures for connection and disconnection of the new push-on type MT-connector are illustrated in Figs. 5 and 6 respectively.



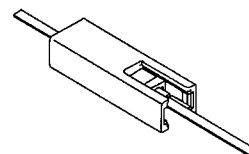
Step 1

Clamp the MT-ferrule between the jaws at the end of the application tool marked "IN"



Step 2

Insert the clamped MT-ferrule into the opening of the MT-housing until the MT-ferrule is firmly secured by the catches inside the MT-housing.



Step 3

Withdraw the application tool.

Fig. 5: Procedure for connection

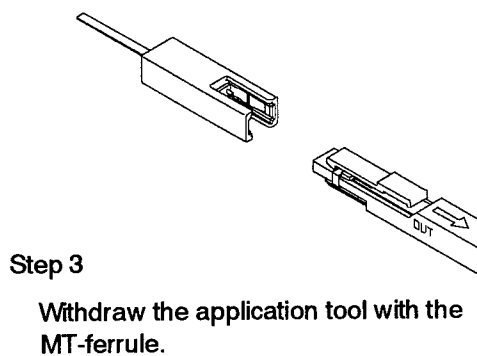
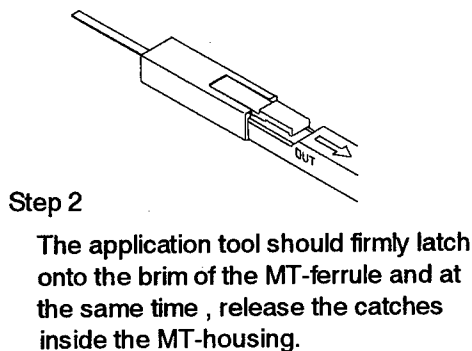
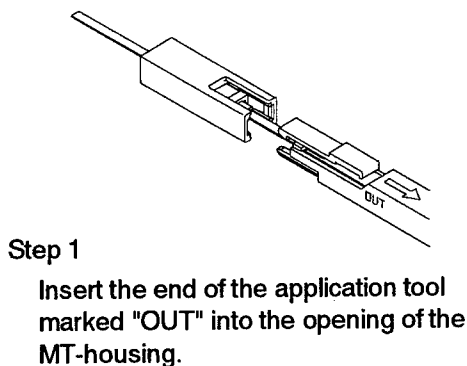


Fig. 6: Procedure for disconnection

PERFORMANCE CHARACTERISTICS

Connection loss

Connection losses of a number of fiber cores are measured at $1.31\mu\text{m}$ and the results are shown in the histogram in Fig. 7.

The average connection loss from the measurements is 0.15dB and the maximum connection loss is 0.41dB. A comparison with in-house conventional MT-connectors insertion

loss data shows the average difference between the two types of connector to be 0.08dB with a maximum of 0.18dB.

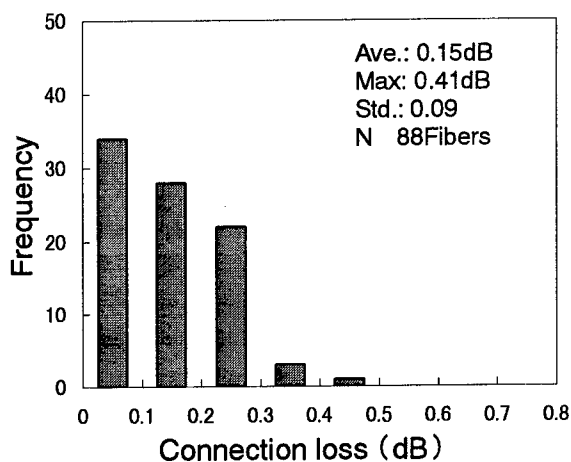


Fig. 7: Connection loss data

Repeatability

To assess the repeatability of this new push-on type MT-connector, repeated connections are performed for 500 times. The connection losses are again measured at $1.31\mu\text{m}$ and the results are shown in Fig. 8.

The difference between the maximum and minimum measured connection loss over the 500 repeated connections is 0.21 dB.

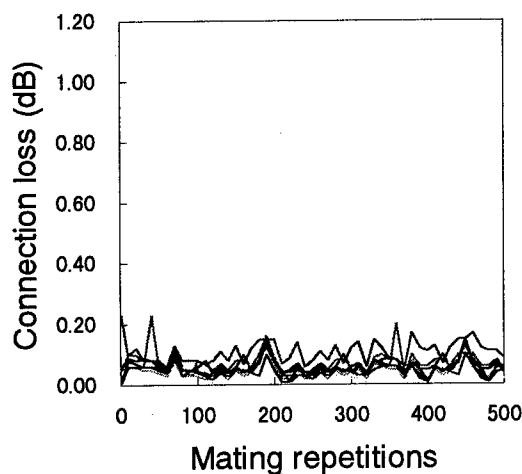


Fig. 8: Repeated mating loss data

Temperature cycling

The new push-on type MT-connector is also subjected to repeated temperature cycling between +70°C and -30°C, and the variations in connection loss are shown in Fig. 9.

The maximum deviation from initial value of connection loss is 0.2dB. Hence, the reliability of this new push-on MT-connector with regard to temperature variation is fully demonstrated here.

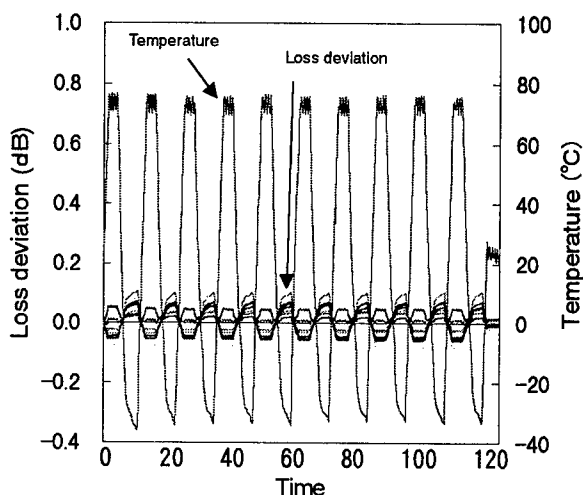


Fig. 9: Temperature cycling characteristics

Connection time

The working time required for connection is compared between the new push-on type MT-connector and the conventional MT-connector. The comparison is conducted under laboratory conditions. All MT-ferrules are flat-polished and matching grease is used in this comparison.

The steps for both the push-on type MT-connector and the conventional MT-connector are described in Table 1. There are only 3 required steps in the case of the new push-on type MT-connector while there are 5 steps in the case of the conventional MT-connector. The total amount of time required is 30 sec for

the formal and 60 sec for the latter. The two extra steps of inserting guide-pins and assembling the clip for the conventional MT-connector double the connection time.

Table 1

Steps	New Push-On	Conventional
1	Cleaning	Cleaning
2	Matching grease application	Guide-pins insertion
3	Connection	Matching grease application
4	-----	Connection
5	-----	Clip assembly
Time	30 sec	60 sec

CONCLUSIONS

We have described the new push-on type MT-connector for fiber ribbons. It is designed to take advantage of the multi-fiber connection capability of MT-connectors and improve on the shortfalls of conventional MT-connectors and MPO-connectors. It features simple push-on/pull-off action with easy-to-use application tool. It has good optical characteristics and reliability, comparable to that of conventional MT-connectors. The procedure for connection is also significantly simpler than conventional MT-connectors, needing only half the amount of time.

REFERENCES

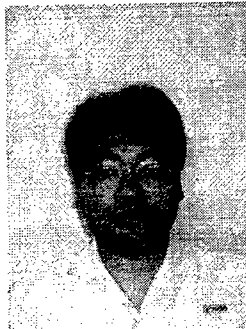
- 1) Y. Kikuchi *et al*, "High Fiber Count Push-on Pull-off Connector," 43rd IWCS Proceedings, pp. 627-632, 1994.
- 2) T. Satake *et al*, "Singlemode Multifiber Connector Performance," ECTC'96, pp. 494-499, 1996.
- 3) S. Nagasawa *et al*, "A High-Performance

Singlemode Multifiber Connector Using Oblique and Direct Endface Contact Between Multiple Fibers Arranged in a Plastic Ferrule," J. Lightwave Technol., vol.13, no.6, pp. 987-994, 1995.

4) M.Takaya *et al*, Designed Performance of a Miniaturized MPO type Connector for High-Density Optical Duplex Connection, IEEE Photon. Technol. Lett., vol.10, No.1, pp. 102-104, 1998.

5) K.Takizawa *et al*, Development of Mini-MPO Connector, 46th IWCS, 1997

6) K.Takizawa *et al*, MT-RJ Optical Connector, 48th IWCS, 1999.



Kunihiro Fujiwara

Fujikura Ltd.,
Cable Network
Components Division,
1440 Mutsuzaki,
Sakura, Chiba
285-8550, Japan

Kunihiro Fujiwara was born in 1971. He graduated from Scientific University of Tokyo with the M.Phys degree in 1996. He since joined Fujikura Ltd. and has been engaged in research and development in the Cable Network Components Division.

THE DEVELOPMENT OF WIDE RANGE OF WAVELENGTH WDM FUSED OPTICAL FIBER COUPLER

Tohru Takahashi, Kazuhiko Terui, Shiro Katsuki, Mitsuhiro Tabata and Hiroshi Maeyasiki

Showa Electric Wire & Cable Co., Ltd., Kanagawa, Japan

Introduction

The wavelength-division multiplexing (WDM) coupler, in general, is a device which isolates or combine optical signals of different wavelengths, and such couplers are being used as important components of fiber optic network systems. Demands for WDM devices of wider bandwidth are increasing, on the other hand, reflecting recent trends for higher speed and larger capacity optical communication.

To meet such demands, a fiber coupler fabrication machine which allows to make two standard type WDM couplers fused together in series was developed, and, using that machine, wide bandwidth WDM (WWDM) fused optical fiber couplers which are similar in size and cost as but superior in wavelength isolation characteristics over a wide wavelength range to conventional WDM couplers were fabricated. The WWDM coupler allows to freely design its bandwidth and isolation level by adjusting the central wavelengths of the two WDM couplers of series construction.

Two types of WWDM couplers were fabricated, the broadband type (wavelength cutoff level of 20 dB at bandwidth of 100 nm) and the high isolation type (wavelength cutoff level of 35 dB at bandwidth of 30 nm), and their characteristics are favorable. Their various environmental and mechanical characteristics are also favorable assuring satisfactory reliability.

Background

Wavelength-division multiplexing optical communication terminals are getting to be used, recently, to meet the ever demanding information communication services for high-speed and large-capacity data transmission, and the WDM couplers, the key component of such terminals, are being increasingly requested to be wider in bandwidth, smaller in size and lower in cost. Dielectric films built-in connectors and dielectric films built-in waveguides are available WDM components having reasonable wavelength isolation characteristics over a wide wavelength range, but they do not meet the demand as to cost (see Fig. 1)

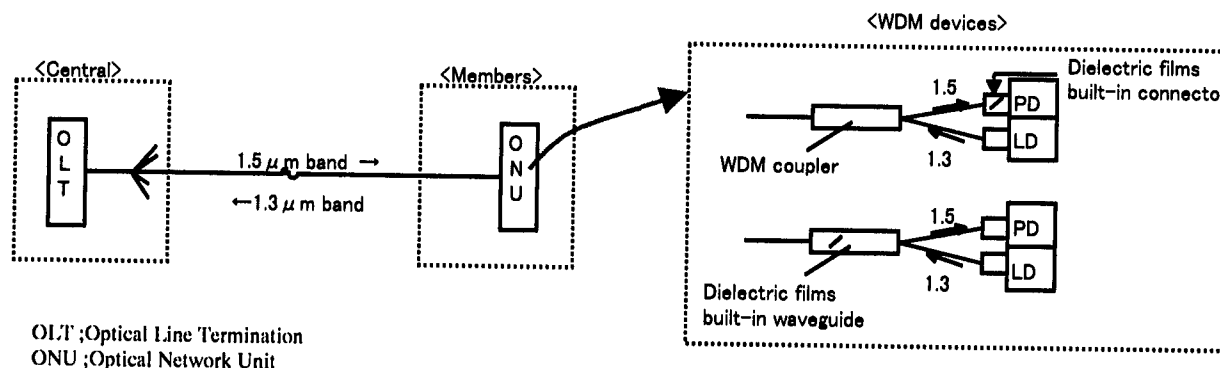


Fig.1 Current system configuration (Example)

The new WWDM coupler realizes a wide bandwidth WDM coupler, without using a dielectric films filter, by a series construction of two conventional WDM couplers. Such WWDM couplers are low in cost because material cost is similar to that of conventional WDM couplers, and small in size because they are finished in the form of single packages.

Construction

A schematic construction and typical wavelength characteristics of standard type WDM optical fiber coupler are shown in Figs. 2 and 3, respectively. In this coupler, the isolation level is inadequate at wavelength regions shown shaded in Figs. 2 and 3 for light sources having broad spectral ranges.

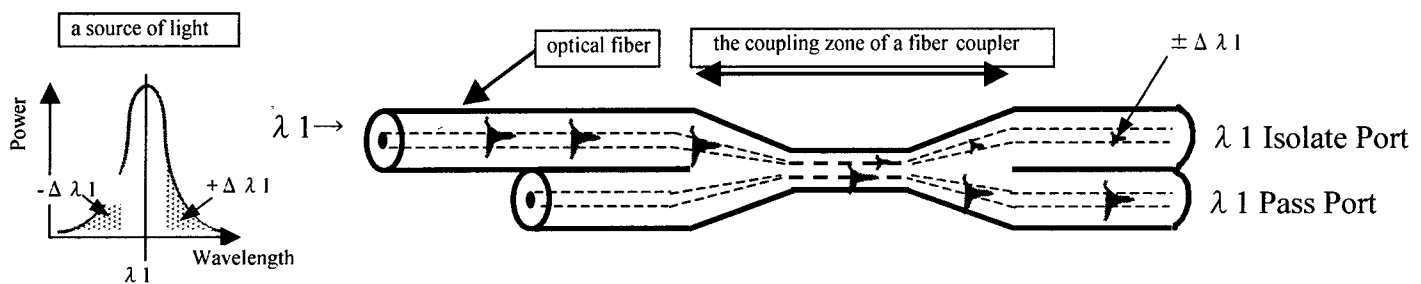


Fig. 2 Schematic construction of WDM optical fiber coupler

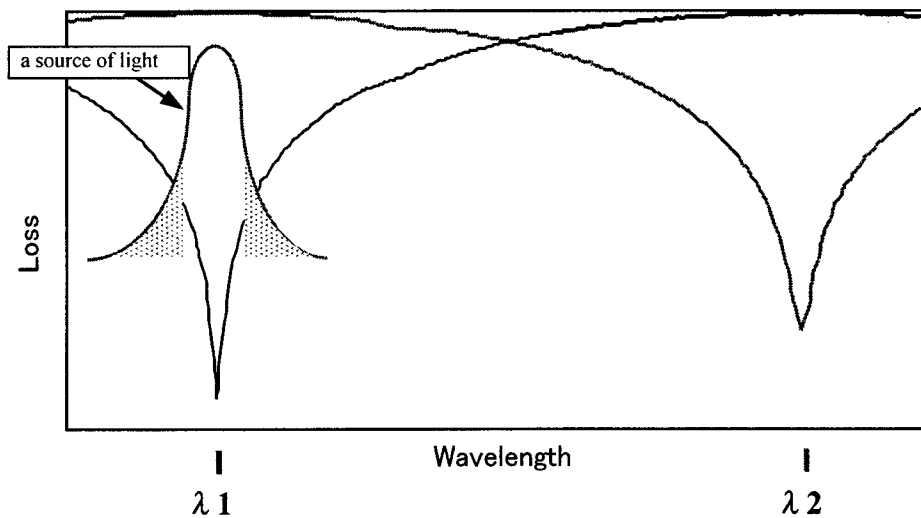


Fig. 3 Wavelength characteristics of WDM optical fiber coupler

The new WWDM coupler is developed based on the possibility of realizing a broadband or high isolation WDM optical fiber coupler by arranging two standard WDM couplers in series and adjusting the central wavelength of each WDM coupler. A schematic construction of the WWDM coupler is shown in Fig. 4.

When the central wavelength difference λ_d of WDM1 and WDM2 of Fig. 4 is defined as $(|+\Delta\lambda_1| - |-\Delta\lambda_2|)$, it is expected that a wide bandwidth WDM coupler is realized when λ_d is large, and a high isolation WDM coupler when small. The relationship between bandwidth and isolation level calculated theoretically is shown in Fig. 5.

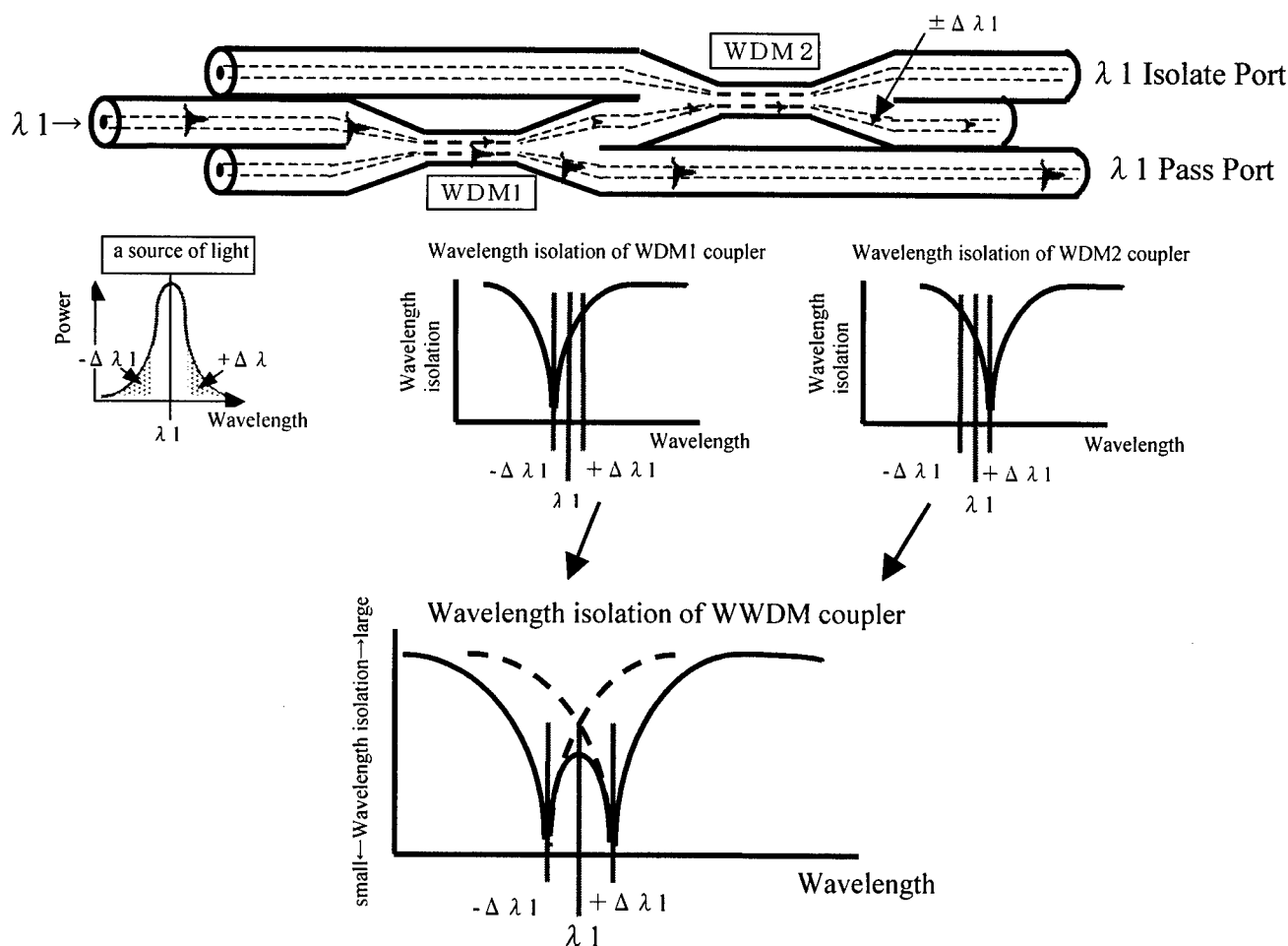


Fig. 4 Schematic construction of WWDM optical fiber coupler

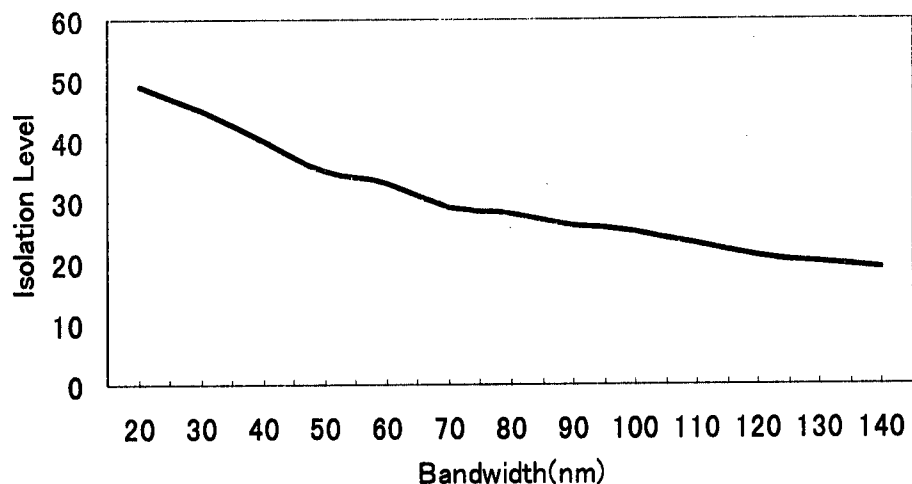


Fig. 5 Theoretical relationship between bandwidth and isolation level

The WWDM coupler of this construction allows to easily configure two different types of WWDM couplers by changing the configuration as shown in Figs. 6 and 7.

As discussed above, it is possible to realize a variety of WWDM couplers by adjusting λ_d and designing the coupler configuration.

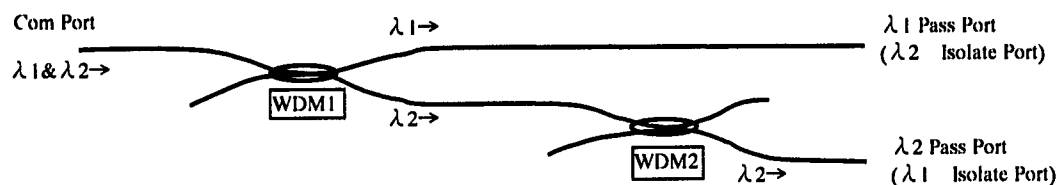


Fig. 6 Configuration ① (Broadband cutoff type for λ_1 - μm band)

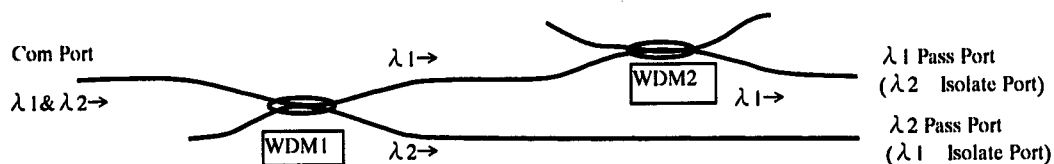


Fig. 7 Configuration ② (Broadband cutoff type for λ_2 - μm band)

Fabrication

For fabrication, a fabrication machine, which allows to produce a WWDM coupler of the construction shown in Fig. 4 and pack into a single package, was developed. The machine works on three SM fibers and automatically fabricates component WDM couplers of the WWDM coupler in turns using a micro-burner. External dimensions of a WWDM coupler fabricated by the dedicated machine are shown in Photo. 1. The packaged WWDM coupler

has a construction, like the ordinary WDM couplers, where a WWDM coupler bonded to a glass substrate is reinforced with a stainless steel pipe, and is therefore small in size (4 mm ϕ x 73 mm).

Three different types of WWDM couplers were fabricated: Broadband type for 1.3- μ m band, high isolation type for 1.3- μ m band, and broadband type for 1.5- μ m band. Wavelength characteristics of these WWDM couplers are shown in Figs. 8, 9 and 10, respectively.

As demonstrated above, the new WWDM coupler allows to easily fabricate a variety of WWDM couplers by adjusting λd and designing the coupler configuration.

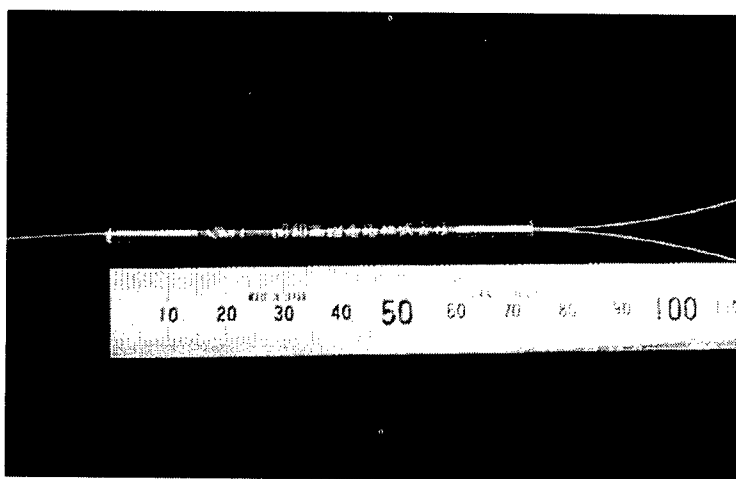
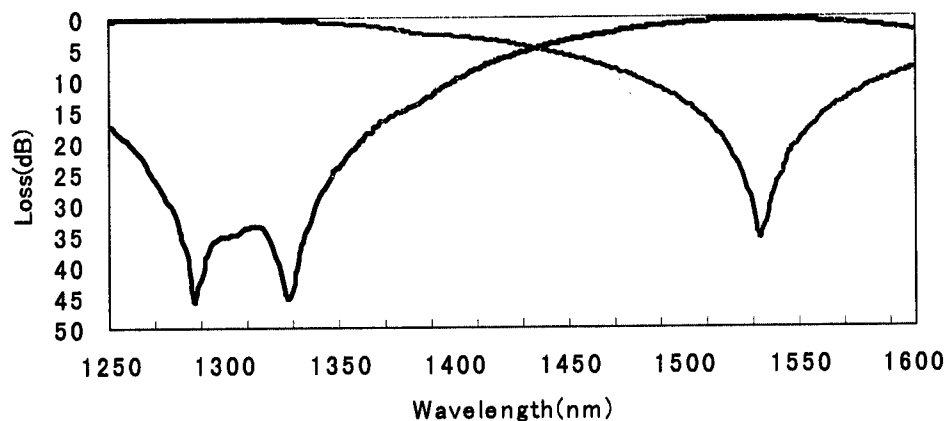
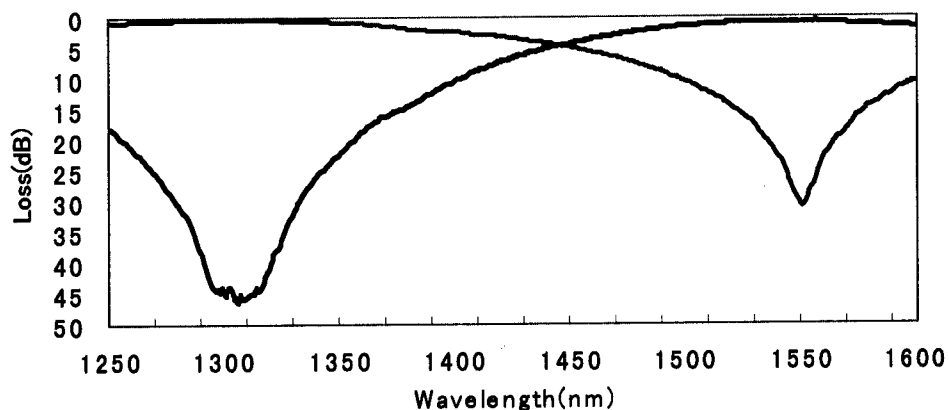


Photo. 1 External dimensions of WWDM coupler



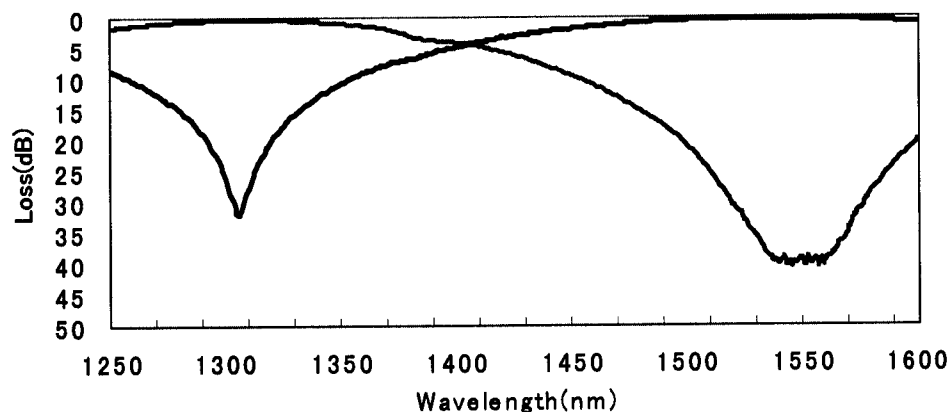
< Wavelength isolation of 19dB in the wavelength range of 1310 ± 50 nm >

Fig. 8 Wavelength characteristics of WWDM coupler (Broadband type of 1.3-μm band)



< Wavelength isolation of 35 dB in the wavelength range of 1310 ± 15 nm >

Fig. 9 Wavelength characteristics of WWDM coupler (High isolation type of 1.3-μm band)



< Wavelength isolation of 20 dB in the wavelength range of 1550 ± 50 nm >

Fig. 10 Wavelength characteristics of WWDM coupler (Broadband type of 1.5-μm band)

Reliability tests

Various environmental and mechanical tests were carried out on the WWDM couplers, and results are shown in Table 1. Each value in the table is the change between those obtained before and after the corresponding test. As seen in the table, every change is not more than 0.2 dB, demonstrating that the reliability of the WWDM couplers is satisfactory. It should be noted that each test was carried out under ordinary conditions of Bellcore and other standards.

Conclusions

A new type of WWDM optical fiber coupler of favorable characteristics, which achieves high isolation level in a wide wavelength range without using other components such as dielectric films filters, was developed. Having a single package construction with two ordinary WDM couplers arranged in series, the WWDM coupler is small in size and low in cost. Results of reliability tests carried out on the WWDM coupler were

favorable, in addition, demonstrating that its reliability is satisfactory.

When the WWDM couplers are used in wavelength-division multiplexing networks, it is possible to assume larger design margins for the light source because the WWDM couplers allow for larger wavelength variation tolerance for the light source, and it would in turn contribute to reduction of the total system cost.

Speaker's Biography



Tohru Takahashi received the B.E degree from Chuo University, Tokyo, Japan. In 1990, he joined Showa Electric Wire & Cable Co., Ltd. (SWCC), Kanagawa, Japan. He has been engaged in development of optical fiber devices.

Table 1 Results of Reliability Tests

Item	Condition	Change in insertion loss	
		average	maximum
Cable Retention Test	5 N load, 1 minute	<0.1dB	<0.2dB
Vibration Test	10 ~ 2000Hz random, 2 axles	<0.1dB	<0.2dB
Impact Test	100G, 2 axles, 3 cycles	<0.1dB	<0.2dB
High Temperature Storage Test	85°C, 500H	<0.1dB	<0.2dB
Temperature-Humidity Aging Test	85°C/85%RH, 500H	<0.1dB	<0.2dB
Thermal Shock Test	$\Delta T=125^{\circ}\text{C}$, 100cycles	<0.1dB	<0.2dB
Temperature Cycling Test	-40°C to 85°C, 42 cycles	<0.1dB	<0.2dB
Temperature-Humidity Cycling Test	-40°C to 75°C/85%RH, 5 cycles	<0.1dB	<0.2dB

(Volume of sample ; 11)

ULTRA-HIGH-DENSITY 4X1600 OPTICAL SWITCH

Yoshihisa Ito

Seiichi Naraoka

Makoto Okuda

Seiji Omizu

The Furukawa Electric Co., Ltd.
6, Yawatakaigandori, Ichihara, Chiba, 290-8555, Japan

1. ABSTRACT

Ultra-high-density 4x1600 optical switch has been developed. In this optical switch, axial alignment is achieved by butting optical fiber array composed of optical fibers aligned with V-grooves and mobile optical fibers each other. A pair of optical fiber arrays each of which have 800 fibers with interval of 127 μ m are piled up in a stair-step method. The new optical switch has twice as many optical fibers as the conventional 2x800 optical switch although its outside dimensions are equal to the conventional one (255x115x54 mm). Optical characteristics of the new optical switch are found satisfactory as shown in Table 2.

2. INTRODUCTION

Telecommunication cable for subscribers increasingly adopts optical fiber. Along with this trend, a remote optical fiber monitoring system is introduced for the purpose of checking of telecommunication cable.^{[1][2]} Figure 1 shows configuration of the monitoring system. A single measurement module of this system is capable of monitoring telecommunication cable composed of several thousands fibers. Optical switch performs switch-over in order to select an optical fiber in telecommunication cable to be monitored. It is currently required to raise fiber density of telecommunication cable and to reduce space for installation, which eventually requires reducing size of monitoring system.^{[3][4][5][6]} Targeting on the characteristics shown in Table 1, that authors have developed a new optical switch which doubles optical fiber density of the conventional system.

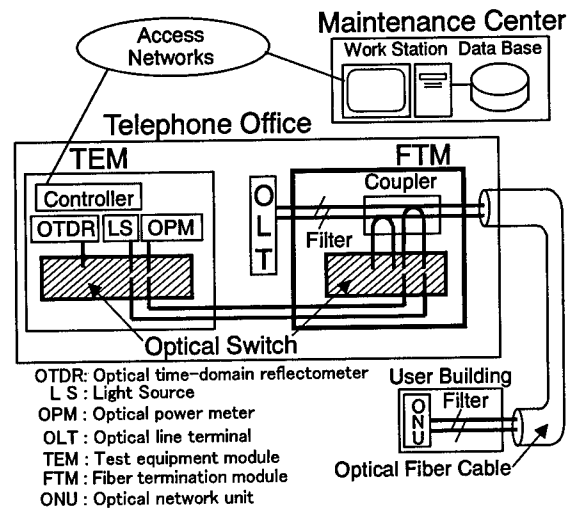


Figure 1 Configuration of monitoring system

Table 1 Target of newly optical switch characteristics

Item	Target
Insertion loss	<0.7 dB
Repeatability	<0.3 dB
Return loss	>40 dB
Switching time(adjacent port)	<1.5 sec
Switching time(maximum)	<3 sec
Life time	>5 million cycle

3. STRUCTURE

3.1. Structure of conventional optical switch

Figure 2 shows structure of the conventional optical switch that is composed of fixed optical fiber array, mobile optical fiber unit, fiber moving unit to move mobile optical fiber unit, and fiber holding-down unit. Optical fiber array is composed of 800 optical fibers aligned on plate V-grooved with pitch of 127 μ m.^[5] And a mobile optical fiber unit is composed of two optical fibers.

In this optical switch, optical fiber array and mobile optical fiber unit are placed opposite to each other. Position of mobile optical fibers is adjusted by fiber moving unit, so that a mobile optical fiber can face a target fiber of optical fiber array. Once the moving is done, fiber holding-down unit holds down mobile optical fibers onto the V-grooved plate to complete connection. Axial alignment is achieved by connecting with V-groove.

The conventional optical switch features dimensions of 255mm x 115mm x 54mm with above-mentioned structure to realize 2x800 optical switch.

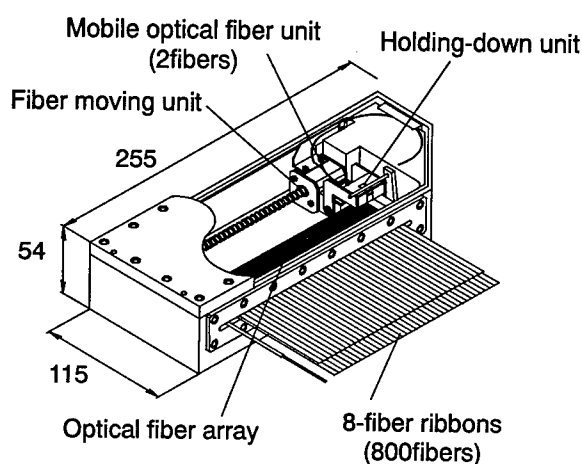


Figure 2 Appearance structure of conventional optical switch

3.2. Arrangement of optical fiber array

A new optical switch has been developed, aiming at doubling the number of fibers while keeping outer dimensions unchanged.

A pair of optical fiber arrays described above is piled up in a stair-step method to achieve the objective (Figure 3).

This basic design features two major advantages. Firstly, when optical fiber arrays are piled up in a stair-step method, it is possible to see upper and lower connections between mobile fibers and optical fiber arrays. A gap between mobile optical fiber and optical fiber array is set up for protecting edge of optical fiber at connection point. Adoption of stair-step arrangement enables up to control gap easily, and that prevents manufacturing efficiency from declining.

Secondly, this basic design is effective in reducing size of optical switch. Mobile optical fibers are pushed onto V-grooves with fiber holding-down unit to be connected with optical fiber arrays. The fiber holding-down unit needs to be mounted

above mobile fibers. This means it is necessary to reserve space which allows holding-down unit to move. When optical fiber arrays are piled up each other, dead space is created between upper optical fiber array and mobile fibers. Unit to hold down lower fibers can be mounted in that dead space, which makes optical switch more compacts in size.

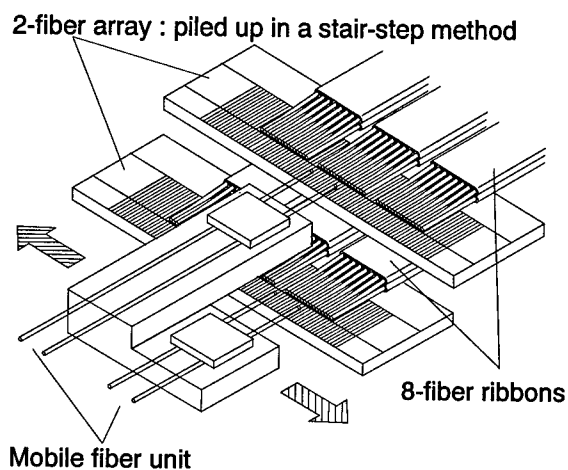


Figure 3 Basic configuration of new optical switch

3.3. Optical fiber holding down unit

Two mobile fibers are aligned with each optical fiber array. Each of the mobile optical fibers is pushed onto V-grooves with fiber holding-down unit to be connected with optical fiber arrays. With this configuration, it becomes hard to maintain adequate force to hold down upper and lower mobile fibers onto V-grooves.

Holding force is one of the critical parameters to determine optical characteristics. Inadequate holding force leads to such a problem as increase and fluctuation of insertion loss.

Figure 4 shows holding down mechanism. The holding down unit is composed of head to hold down fibers, rotating shaft to move head upward and downward, arm to connect head and shaft, and spring to generate holding force.

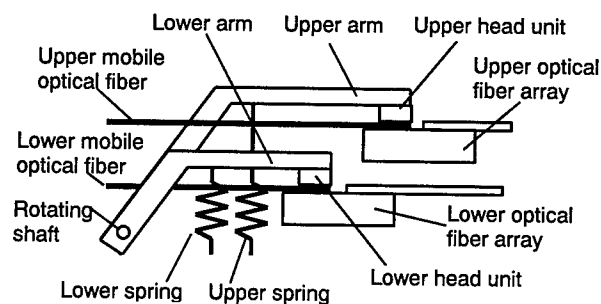


Figure 4 Configuration of holding-down unit

When upper and lower heads are supported with an arm and pulled with a spring, adjustment of one holding force inevitably affects the other holding force, which results in deterioration of insertion loss characteristics, which lowers manufacturing efficiency.

To overcome this problem, configuration has been modified. In the modified version, a head is supported with an arm, which allows each head to hold down mobile fibers independently. This configuration enables up to independently adjust holding force for upper and lower mobile fibers. Connection can be achieved with limited insertion loss and loss variance.

3.4. Structure of new optical switch

Figure 5 shows structure of newly developed optical switch. By adopting optical fiber arrays which are piled up in a stair-step method, the new switch doubles the number of optical fibers while keeping its outer dimensions the same as the conventional one: 255mm x 115mm x 54mm.

Upper and lower holding-down units are designed to feature independent holding down mechanism as described in Section 3.3. For moving mechanism of mobile fibers, the conventional design is adopted. Stepper motor is used as driving force, just like the conventional switch. Housing is also designed to feature air-tight sealing and charged with matching oil, like the conventional switch.^{[5][6]}

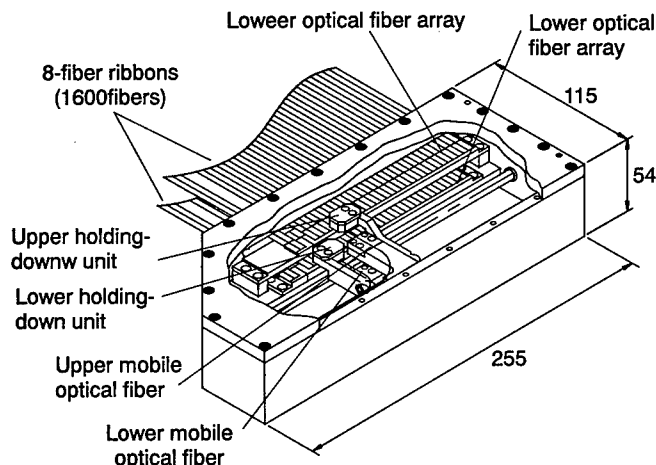


Figure 5 Appearance structure of new optical switch

4. CHARACTERISTICS OF NEW OPTICAL SWITCH

4.1. Insertion loss

Figure 6 shows histogram of insertion loss. Four mobile fibers were used to measure insertion loss, together with 800 optical fiber arrays that were connectable with the mobile fibers. In other words, insertion loss was measured for 3200 fibers in total. Insertion loss shown in Figure 6 includes insertion loss inside of optical switch and connector loss at inlet. Wavelength of light source used in the measurement was 1.31 μ m.

Insertion loss is found 0.407dB on average: with maximum of 0.69dB. These readings satisfy our target.

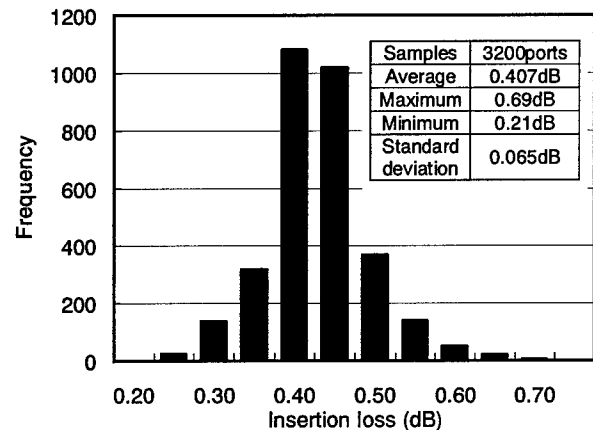


Figure 6 Histogram of insertion loss

4.2. Repeatability of insertion loss

Figure 7 shows fluctuation of insertion loss over 10000 times of switch-over. Every switch-over, insertion loss was measured at four mobile fibers. Wavelength of light source used in the measurement was 1.31 μ m.

Switch-over procedure during the measurement was I) connect a fiber to be measured, II) measure insertion loss, and III) switch over to another fiber. This procedure was repeated. As shown in Figure 7, fluctuation of insertion loss is found 0.1dB even at maximum.

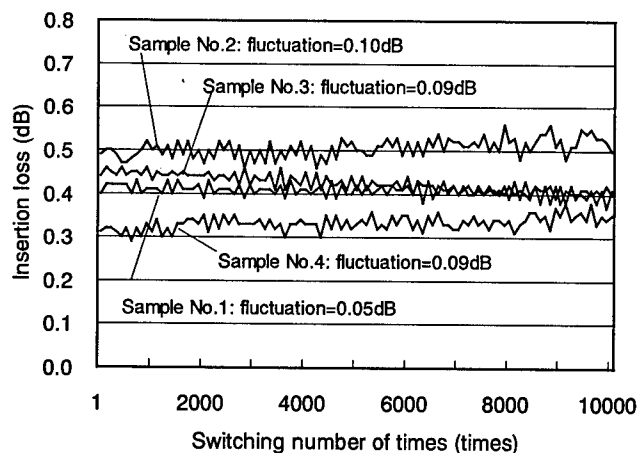


Figure 7 Repeatability of insertion loss

4.3. Return loss

Figure 8 shows histogram of return loss when 120 fibers sampled randomly are connected. Wavelength of light source used in the measurement was 1.31 μ m.

Return loss is found 46.68dB on average and 43.57dB at minimum. These findings satisfy the target characteristics.

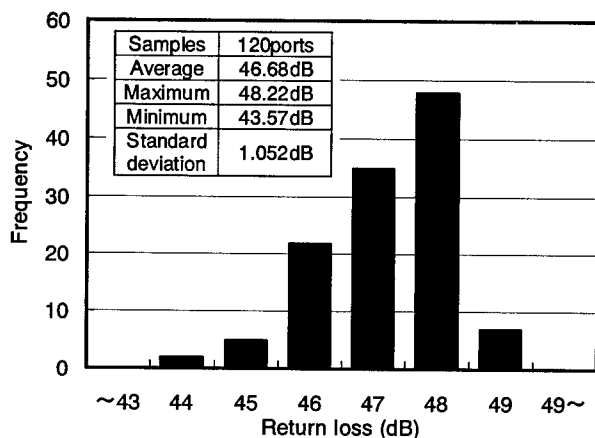


Figure 8 Histogram of return loss

5.CONCLUSION

Ultra-high density 4x1600 optical switch has been developed by arranging optical fiber arrays in a stair-step method.

The ultra-high density optical switch is found to feature insertion loss of 0.69dB at maximum, repeatability of insertion loss of 0.1dB, and return loss of 43.57dB at minimum. These optical characteristics are satisfactory, proven equal to the conventional optical switch.

Table 2 Summary of evaluation results

Item	Target	Results
Insertion loss	<0.7 dB	<0.7dB
Repeatability	<0.3 dB	<0.1dB
Return loss	>40 dB	>40dB
Switching time (adjacent port)	<1.5 sec	<1.1sec
Switching time (maximum)	<3 sec	<3sec
Life time	>5 million cycle	>5 million cycle

REFERENCES

- [1] N. Tomita, et al., "Optical fiber line support system", in NTT Rev., vol. 3 no. 1, pp97-104, 1991
- [2] N. Tomita, et al., "Future prospects of automatic fiber test systems for fiber-optic subscriber loops", in Tech. Dig. OECC'96, pp134-135, July 1997
- [3] Y. Enomoto, et al., "High density fiber termination module (FTM) for AURORA", in Tech. Dig. OECC'97, pp536-537, July 1997
- [4] Y. Enomoto, et al., "High density fiber termination module (FTM)", in Nat. Conv. Rec. IEICE, B-10-28, p350, March 1998
- [5] M. Okuda, et al., "2x800 optical switch using fiber butting method", in Proc. IWCS'97, pp51-56, November 1997
- [6] S. Naraoka, et al., "2x400 SMF optical switch with counterpart fibers in a V groove", in Proc. IWCS'96, pp894-899, November 1996

Speaker Biography



Yoshihisa Ito

The Furukawa Electric co., Ltd.
6, Yawatakaigandori, Ichihara
Chiba, 290-8555, Japan

Yoshihisa Ito was born in Yamagata, Japan, in 1969. He received the B.E. degree in electronics engineering from Utsunomiya University in 1992. He joined The Furukawa Electric co., Ltd., in 1992, and he has been engaged in research and development of optical fiber switch.

Automated Optical Fiber Cabling System for Intelligent Buildings

Kunihiko SASAKURA, Joji YAMAGUCHI, Takashi YOSHIKAWA,
Keiichi KOBAYASHI, and Kazumasa KANEKO

NTT Telecommunications Energy Laboratories
3-9-11 Midori-cho, Musashino-shi, Tokyo 180-8585, Japan
Phone: +81-422-59-2817 Fax: +81-422-59-4622

ABSTRACT

A newly automated optical fiber cabling system has been developed in order to reduce operation costs and in order to construct reliable optical networks for intelligent buildings. The system, which consists of optical cross-connection modules and a terminal, can achieve non-blocking optical connections by using a robot hand and micro-optical connectors. The optical cross-connection module can connect any of 100 input optical fibers to any of 100 output optical fibers. The terminal controls and manages up to 64 cross-connection modules via a modem connection to a public telephone network. The average cross-connection time is 1 minute. For single-mode fibers, the insertion loss of the cross-connection module is less than 1.0 dB and the return loss of the module is over 40 dB. Evaluation tests show that the system can construct cost-effective and highly reliable optical networks in intelligent buildings.

1. INTRODUCTION

With the rapid advances in high-speed and high-capacity multimedia communications, such as the Internet, optical access networks (as shown in figure 1) have been constructed using a π system⁽¹⁾ and a FTTH system based on an optical PDS (passive double star). Optical cabling, especially in intelligent buildings, increases along with a metropolitan optical network construction. In these buildings, a cable management system is important to ensure network reliability. However, the cabling is so complicated that the networks cannot be easily reconfigured and managed manually, and network operation costs are high. Moreover, manual configuration would result in misconnections caused by human error. To solve these problems, we have developed an automated optical fiber cabling system which consists of optical cross-connection modules and a remote terminal. This paper describes a new system concept. It also describes a prototype of the system and its configuration as well as experimental results obtained.

2. SYSTEM CONCEPT

The requirements of the optical fiber cabling system in the

buildings are as follows:

- (1) highly reliable and cost-effective optical fiber cabling and management;
- (2) high optical performance such as low insertion loss, high return loss, and transparency for optical wavelength;
- (3) self-holding optical connection even if the power supply is down;
- (4) over 100 non-blocking optical cross connections; and
- (5) cross connection for both single-mode fiber (SMF) and multi-mode fiber (MMF).

Several optical matrix switches such as the LD optical matrix switch⁽²⁾ and the thermo-optic optical matrix switch⁽³⁾ are proposed. However, these switches do not have a self-holding optical connection and their optical performances are worse than the ones of an optical connector. Furthermore, it is

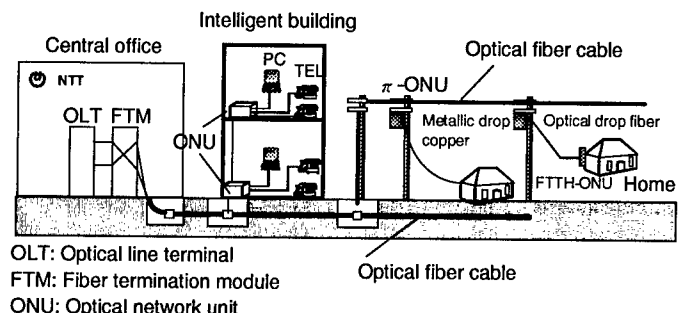


Fig. 1. Schematic diagram of optical access networks.

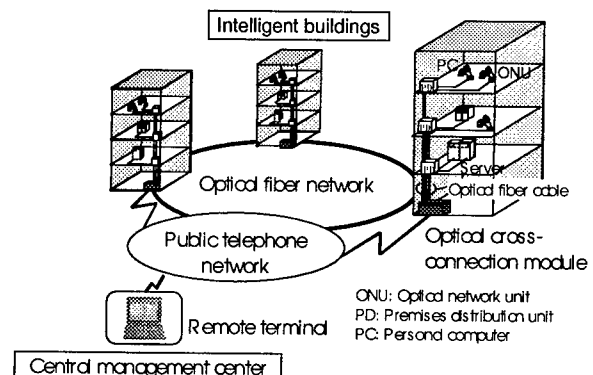


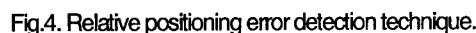
Fig. 2. Application of an optical fiber cabling system.

To reduce operation costs and to construct highly reliable networks in intelligent buildings, we have developed an automated fiber cabling system which can automatically cross connect by handling the optical connector. Figure 2 shows an application of the system for optical access networks. The system can cross connect and manage the optical network in buildings. The optical cross-connection modules are installed in intelligent buildings and a remote terminal is installed in a central management center. The terminal controls and manages optical cross-connection modules via a modem connection to the public telephone network. This centralized management results in networks that are highly reliable and that have low operating costs.

Using a robot hand, a plug with an optical fiber cord is connected to a jack with an optical fiber cord. So in order to achieve a highly reliable and compact optical cross-connection system, a reliable cross-connection operation that prevents the optical fiber cords from becoming entangled, a robot hand with a highly reliable position, and a micro-optical connector designed to miniaturize the system are required. The technical points for meeting these requirements are described below.

Cross-connection is achieved by exchanging one plug for another plug. In a simple plug exchange procedure, which directly connects a disconnected plug to another disconnected jack, the optical fiber cords of exchanged plugs get entangled to other optical fiber cords. So a cross-connection procedure without entanglement is devised⁽⁴⁾. Figure 3 shows the cross-connection procedure. Plugs are connected to jacks in a connection block. After a pair of exchanged plugs (P_m, P_n) are gripped by a robot hand and disconnected from a pair of jacks (J_m, J_n), a pair of disconnected plugs are wound to an alignment block using a rewind mechanism and a roller. This rewind procedure prevents the optical fiber cords from becoming entangled. A pair of plugs are connected to a pair of corresponding jacks for the cross-connection procedure. The devised procedure prevents the optical fiber cords from becoming entangled even if cross-connection operations are repeated.

Because an optical connection in the system is automatically achieved by connecting a plug to a jack with a robot hand, highly reliable positioning which is the precise position of a plug gripped by a robot is necessary. If the relative positioning error (Y, Z) between a plug gripped by the



robot hand and a jack is a critical value, the plug or the alignment sleeve in the jack may be broken. To reduce the error, photoelectric sensors as (shown in figure 4) are introduced. The error corresponds to the distance between the center of the sensor and the scanning center. And by detecting the center of the sensor, the error is simply calculated. The center detection procedure is as follows.

The sensor detects the reflection light from the plug endface. The level of the reflection light is in proportion to the incident area of the plug endface. A reference plug is scanned against the sensor in the Y direction. When the reflected light from the plug is more than a preset threshold level, the sensor detects to the left edge "a". After further scanning, the reflection light becomes less than the preset threshold level, and the sensor detects to the right edge "b". In a similar procedure, the sensor detects to the top edge "c" and the bottom edge "d" in Z direction. The center of the sensor is calculated from these edge points, and the offset values such as " y_{off} " and " z_{off} " are known by pre-measuring.

So the plug gripped by the robot hand can be precisely positioned to the target jack using the center of the sensor and offset values. Remained errors caused by the pitch error between each jack and positioning error of the driving mechanism are absorbed in compliance with the timing belt and robot hand.

3.3 Micro-optical connector

To achieve a high-density arrangement, we devised a new micro-optical connector which consists of a plug and a jack, both of which have a ferrule (a diameter of 1.25 mm) and are attached to an optical fiber cord diameter of 0.9 mm. The ferrule and the split alignment sleeve are the same ones as the MU optical connector⁽⁶⁾. Figure 5 shows a basic structure of a new micro-optical connector. The plug is designed for connecting a robot hand to a jack by hanging the step part of the plug on the leaf spring in front of the jack. The jack consists of a split alignment sleeve, a stopper, and a coil spring. The spring can absorb the assembly errors in X direction and can give a contact force between the plug and the jack. Each jack can be removed from a connection block by loosening the screw of the stopper. This jack-removal function has an advantage in maintenance. Environmental test also confirmed that the connectors have good optical characteristics.

4. PROTOTYPE AND CONFIGURATION OF THE SYSTEM

Figure 6 shows the configuration of the system. The cross-connection module can connect any of 100 input optical fibers to any of 100 output optical fibers. The module is 530 mm wide, 440 mm deep, and 380 mm high. The input and output optical interfaces in the module are the MU connectors. A robot hand can automatically connect any plug to a corresponding jack. Each plug and jack is attached to one end of a cord and an MU optical connector that is attached to another end of each cord. The jacks are arranged in two lines; the jacks in one line are shifted by a half pitch from those in the other line. Several mechanisms and a control unit for driving mechanism in X, Y, and Z directions are removed from the module without influence on any optical connections. In X and Y directions, it is driven by a pulse motor through pulleys and a timing belt. In Z direction, it is driven by a pulse motor through a ball screw. The resolutions in X and Y directions are 10 μm , and the resolution in Z direction is 1.25 μm . The operation program of the terminal has a graphical user interface and maintenance functions such as a self-test. The terminal controls and manages up to 64 cross-connection modules. In order to keep the optical fiber cabling system secured, the operations system is protected by passwords.

The cross-connection procedure in the system is as follows. The robot hand first disconnects a pair of target plugs and arranges them on the alignment block. The cord is rewound into the optical fiber storage cassette so that it does not get entangled with other cords during re-jumpering. The robot

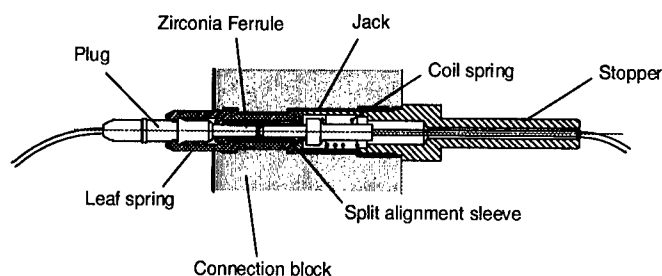


Fig. 5. Basic structure of the micro-optical connector.

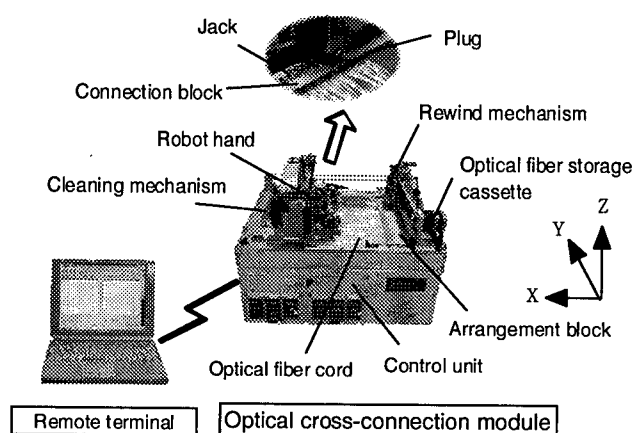


Fig. 6. System configuration.

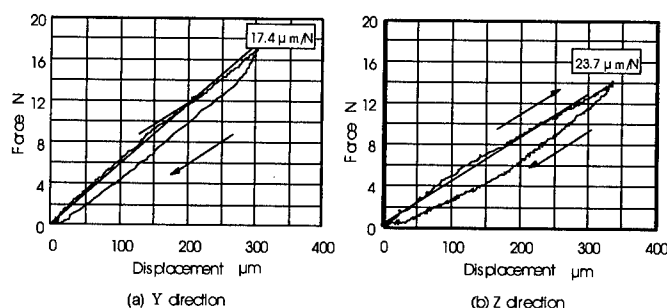


Fig. 7. Compliance characteristics.

hand grips one of the plugs that are rewound on the alignment block and connects it to a target jack in the connection block. The second plug is then connected in the same way and the new optical path information is stored in the database in the terminal. Before each connection, the endface of the plug is cleaned by using cleaning tape to get stable optical characteristics. The average cross-connection time is 1 minute. To achieve a highly reliable cross-connection procedure, a plug detection sensor and an excess insertion force detection sensor are introduced to a robot hand.

5. EXPERIMENTAL RESULTS

5.1 Positioning and compliance performance

The detection error of the photoelectric sensor, the

positioning error of the driving mechanism, the assembly error, and the machining error are measured in order to evaluate the relative positioning error. The total number of errors in Y direction is 94 μm and the total number of errors in Z direction is 35 μm . The deviations of positioning repeatability in Y, Z, and X directions are less than 5 μm . The errors in Y and Z directions are absorbed in the compliance mechanism. Figure 7 shows compliance characteristics. The experimental value in Y direction is approximately 17.4 $\mu\text{m}/\text{N}$ and the experimental value in Z direction is approximately 23.7 $\mu\text{m}/\text{N}$. As the total errors in Y and Z directions are 94 μm and 35 μm , the forces in Y and Z directions caused by the errors are estimated to 5.4 N and 1.5 N, respectively. These forces are less than the forces which break a plug or a sleeve in the connection or disconnection procedure. Furthermore, it is experimentally confirmed that cross-connection are completely carried out even if 100- μm relative positioning errors in Y and Z directions occur.

5.2 Optical characteristics

Figure 8 shows the optical characteristics of the module. There are three measured connection points; two connections of the MU connectors and one connection of the plug-jack. The average insertion loss for SMF is 0.27 dB and the average insertion loss for MMF is 0.18 dB. The average return loss for SMF is 45.4 dB and the average return loss for MMF is 24.1 dB. These characteristics are nearly equal to one characteristic of a single coupling connector.

Figure 9 shows insertion loss changes in 200 connections tests. The insertion loss increases to over 20 cycles when there is no cleaning. On the other hand, the insertion loss does not change so much until 200 cycles when there is cleaning. After the test, small worn pieces on the endface of the plug without cleaning were observed. It is supposed that the pieces degrade the optical characteristics. As a result, cleaning of the ferrule endface is effective for a stable cross connection.

The developed system rewinds the plug to the alignment block in order to prevent a rewound plug from getting tangled with other optical fiber cords. We investigated the influence of the optical characteristics on other optical connections in the rewinding procedure. Figure 10 shows insertion loss changes in a cross-connection procedure. In this experiment, the insertion loss change in the P4-J4 connection is monitored when P11 is exchanged for P3. The loss change is very little and there is no problem for actual usage.

5.3 Environmental test

A reliable optical connection should be ensured even if the temperature inside the installation room changes. In order to evaluate the relative position error caused by thermal deformation of the module, a thermal test was carried out. For ambient temperatures of 5 $^{\circ}\text{C}$, 25 $^{\circ}\text{C}$, and 45 $^{\circ}\text{C}$, the insertion loss change is less than 0.1 dB, and a reliable cross-connection is carried out in each ambient temperature.

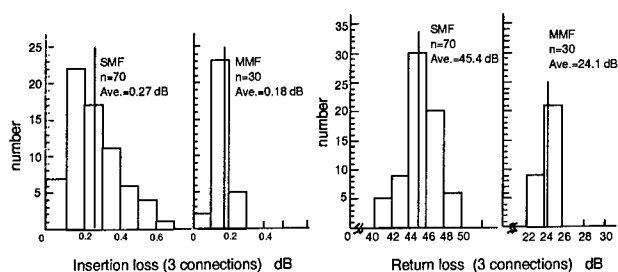


Fig. 8. Optical characteristics of the cross-connection module.

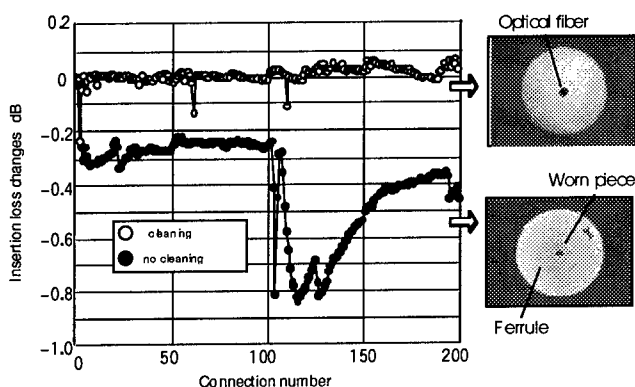


Fig.9. Insertion loss changes in 200 connections.

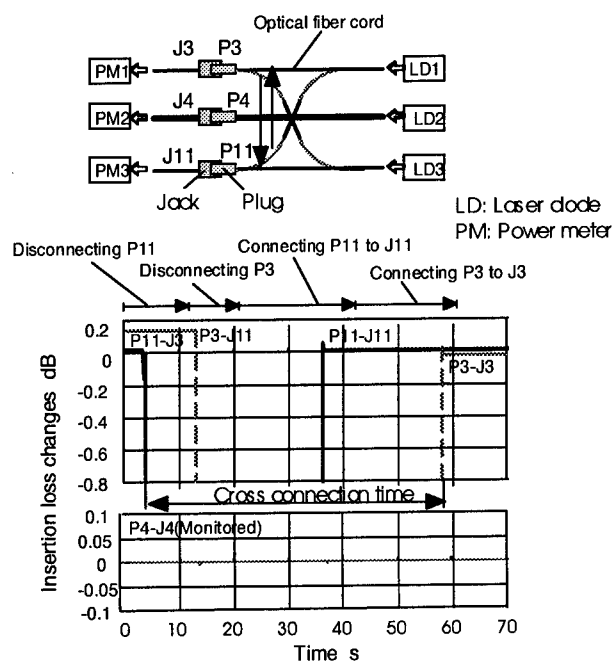


Fig. 10. Insertion loss changes in a cross-connection.

6. CONCLUSION

An automated optical cabling system, which can cross connect and manage 100 input and output optical fibers, has been developed. For single-mode fibers, the insertion loss is less than 1.0 dB and the return loss is over 40 dB. Highly reliable cross-connection is confirmed even if the temperature in the installation room changes from 5 °C to 40 °C. The system can reduce the operation costs, eliminate misconnections, and reconfigure the networks. Therefore, it is expected to construct cost-effective, highly reliable, and flexible optical networks in intelligent buildings.

REFERENCES

- (1) K. Ikeda, M. Tubokawa, K. Harikae, and H. Kitajima, "Deployment of New Optical Access Systems", 8th International Workshop on Optical / Hybrid Access Networks Conference Proceedings, March, 1997.
- (2) M. Ikeda, S. Oku, Y. Suzuki, and M. Okayasu, "Loss Less 4 x 4 Monolithic LD Optical Matrix Switches", International Topical Meeting on Photonic Switching, pp. 792, 2D1, 1992.
- (3) R. Nagase, A. Himeno, M. Okuno, K. Kato, K. Yukimatsu, and M. Kawachi, "Silica-Based 8 x 8 Optical Matrix Switch Module with Hybrid Integrated Driving Circuits and its System Application", IEEE J. Lightwave Technol., 12, No. 9, pp. 1631-1639, Sep., 1994.
- (4) J. Yamaguchi, N. Tamaru, T. Shoji, T. Kanai, Y. Nishida, and F. Ohira, "A 100x100 Optical Fiber Cross-connect System", Proc. 44th IWCS, pp. 232-238, 1995.
- (5) R. Nagase, E. Sugita, S. Iwano, K. Kanayama, and Y. Ando, "MSC-type Optical Connector with Small Zirconia Ferrule", IEEE Trans. Photon. Technol. Lett., 3, No. 11, pp. 1047-1054, Nov., 1991.



Kunihiro Sasakura
NTT Telecommunications Energy
Laboratories
3-9-11 Midori-cho, Musashino-shi,
Tokyo, 180
JAPAN

Mr. Sasakura received a B.E. degree from Shizuoka University, Shizuoka, Japan, in 1980. He then joined Musashino Electrical Communication Laboratories, Tokyo, Japan.

He has been active in the research and development of optical connectors, inspection systems for optical connectors, and more recently optical fiber cabling systems.

Mr. Sasakura is a member of the Japan Society for Precision Engineering.

NUMERICAL SIMULATION OF OPTICAL FIBER PREFORM NECK-DOWN FOR DRAW PROCESS OPTIMIZATION

Marc NICOLARDOT, Gérard ORCEL

ALCATEL, 53 rue Jean Broutin, 78700 Conflans Ste Honorine, France

ABSTRACT

Three aspects of the optical fiber draw process modeling are presented, in the domains of electromagnetism, thermics and mechanics.

They constitute an operational way for the optimization of the draw process, and can deal with realistic geometries and material characteristics.

The validation of each module is presented.

Thermal radiation and mechanical modeling are emphasized as key steps in these simulation procedures.

For the first time, the draw process has been modeled in a way consistent with experimental draw start-up and transient events.

INTRODUCTION

In order to optimize the optical fiber drawing process and to anticipate its evolution, it is necessary to model the preform neck-down during the various phases of the drawing process.

This paper presents the model of the draw process developed at ALCATEL and which is composed of electromagnetism, thermal and mechanical modules.

The electromagnetism and thermal modules are based on the commercial software SYSTUS. Molten glass mechanics is dealt with a home made software. Emphasis will be put on radiation treatment because it dominates heat transfer at high temperature. The neck-down geometry will also be detailed as the final result.

The modeled process is schematically represented Fig. 1. The heat sources (W/m³)

induced in the graphite susceptor are deduced from the electrical intensity in the coil by the electromagnetism module. The heat transfer between the furnace and the silica preform and the neck-down is simulated by the thermal module, and the result is the temperature map in the drawing furnace, in the preform and in the neck-down region. The mechanical module computes the transient geometry of the neck-down with the "small slope theory"¹ from the mean axial temperature profile in the neck-down, and the composition and temperature dependent viscosity of silica.

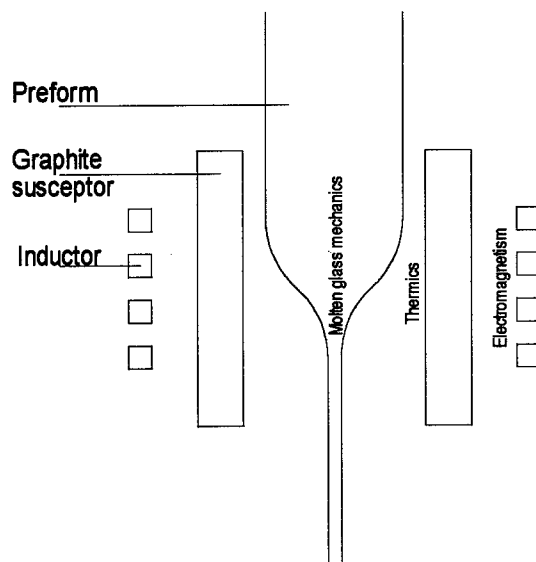


Fig. 1 Simulated draw furnace.

ELECTROMAGNETISM

Procedure

From the Maxwell equations, the axisymmetrical problem with a sinusoidal time dependence can be represented by the equation :

$$\sigma \frac{\partial A}{\partial t} + \text{Rot}(\mu^{-1} \text{Rot} A) = -\text{Grad} V - \text{Rot} H_c$$

with conventional notations ². This equation is solved by the finite elements method in the code SYSTUS, for the unknown vector potential **A**.

The boundary condition is that the component of the magnetic field **B** normal to the frontier of the studied domain is 0, or **A**=0 at the frontier.

From **A**, the magnetic field **B** and induced Joule power **P** can be deduced in the electric conducting parts of the furnace.

Then the geometry of the furnace can be optimized to have the greatest induced power in the graphite susceptor for a given maximum tension and a maximum intensity delivered by the MF generator. This can be done by optimization of the susceptor thickness, and by moving the other conducting parts away from the coil.

The magnetic energy :

$$E_{\text{mag}} = L I_{\text{max}}^2 / 2$$

leads to the equivalent inductance of the furnace **L**, and allows adaptation elements optimization by adjusting the whole impedance of the furnace.

Validation

Comparison with other softwares (Flux2D, Flux-expert) and different meshes leads to a 0.25% agreement for the Joule power. Results of SYSTUS have also been compared to analytical solution for an infinite solenoid. In this case, the agreement is 1% for the magnetic field **B** and 6% for the inductance **L**.

THERMICS

Description of the model

The thermal effects taken into account in the finite element procedure are:

- convective heat exchange between the inner furnace wall and the inert fluid inside the heating zone of the furnace, whose temperature has to be determined,
- the convective heat exchange between the preform and fiber surface, and the inert fluid,
- surface radiation between the inner furnace wall and the neck-down surface,
- local velocity of silica which induces a convection term,
- thermal conduction.

The boundary conditions are the temperature of the preform one meter above the furnace, radiative and convective heat transfer coefficient at the surface of the preform outside the furnace, radiative and convective heat transfer coefficient at the external wall of the furnace. The volume heat source in the graphite elements is the result of the electromagnetism simulation.

The result is the temperature map in the furnace elements, of the inert fluid, and in the preform and neck-down.

Radiation treatment

The previous thermal model requires an equivalent surface emissivity to characterize the radiative properties of the neck-down. Actually, radiation is a volume property of a semi-transparent material like silica, and is characterized by the refractive index $n(T, \lambda)$ and the absorption coefficient $\alpha(T, \lambda)$ (T is the temperature and λ the radiation wavelength).

Classically, radiation in a semi-transparent medium can be treated with an optically thin approximation, an optically thick approximation or numerically in a quasi exact way. Considering the size of the fiber and due to the large dependence of the absorption coefficient on wavelength, it is not clear what approach is the most suitable. Consequently, the three approaches were compared

The medium can be considered optically thick when the product of the characteristic dimension **L** by the mean absorption coefficient is much greater than unity. In this case, the radiation can be taken into account by an equivalent conductivity for internal exchanges and an equivalent surface emissivity for external exchanges. The surface emissivity is equal to the transmission coefficient at the glass/air interface. The contribution β of conductivity due to radiation is :

$$\beta = 16 n^2 \sigma T^3 / 3 k_r$$

where σ is the Stefan-Boltzmann constant and k_r is the Rosseland mean absorption coefficient, weighted by the temperature derivative of the Planck law³. Fig. 2 shows the equivalent conductivity and Fig. 3 the Rosseland mean absorption coefficient. The radiation contribution is negligible below 300°C. At 500 °C, the intrinsic and radiative contributions are both equal to 2 Wm⁻¹K⁻¹.

It should be noted that this limit case is never valid for an optical fiber due to the small values of the absorption coefficient near 1.5 μm . It is valid for a massive object like a preform near room temperature.

The other limit case concerns optically thin objects. There, the main effect is the emission of radiation from a given volume element and the radiation emitted by the surrounding elements and absorbed by this element is negligible. This approximation is valid when the product of the characteristic dimension L by the mean absorption coefficient is much smaller than unity.

The power emitted per unit volume is in this case :

$$Q_{\text{thin}} = 4 \text{ km } n^2 \sigma T^4$$

where km is the mean absorption coefficient weighted by Planck law, shown Fig. 4. This leads to the value $Q_{\text{thin}} = 2.14 \cdot 10^{10} \text{ Wm}^{-3}$ for silica at 1750 Celsius (Fig. 5).

Last, the exact way to compute the radiative balance uses the expression of the divergence of the radiative heat flux³ Q :

$$Q = \int_{\eta=0}^{\infty} k\eta \cdot (4\pi \cdot I_b\eta - \int_{\Omega=4\pi} \int_{r=0}^{\infty} I_b\eta(r) \cdot k\eta(r) \cdot \exp(-k\eta(r) \cdot r) dr \cdot d\Omega) \cdot d\eta$$

which is the sum of the contribution of all wave number η of the difference of the emitted radiation (like in the case of an optically thin medium) and the radiation received from all solid angles $d\Omega$ and all distances r , the multiple reflections being taken into account.

Fig. 6 shows the net power emitted by a 125 μm optical fiber in the case of homogeneous temperature $T=1750^\circ\text{C}$. The net power is a function of the radius in the fiber.

The mean net power emitted by a 125 μm fiber is a factor 21 lower than for the case of an optically thin medium.

Fig. 7 shows the case of a fiber with a 2 μm diameter. The mean emitted power is $1.2 \cdot 10^{10} \text{ Wm}^{-3}$. This case approaches the value $2.14 \cdot 10^{10} \text{ Wm}^{-3}$ of an optically thin medium. At the opposite, fig. 8 shows the case of a 20 mm diameter cylinder which behaves more like an optically thick medium.

In conclusion, a 125 μm diameter optical fiber at 1750 Celsius is just the intermediate case between optically thick and optically thin medium, and the exact way must be used to compute the net emitted radiative power.

The total net emitted power per unit length of fiber :

$$P_{\text{tot}} = \int_{r=0}^{R_{\text{fib}}} Q(r) 2\pi r dr$$

integrated over a cross-section of the fiber can be put in the form of surface emission :

$$P_{\text{tot}} = \varepsilon \sigma T^4 2\pi r$$

The value of the emissivity ε obtained in this way for a silica cylinder of radius R_{fib} at a temperature T (in Celsius) is given Fig. 9. The spectral value of the absorption coefficient have been measured by the CRMHT-CNRS⁴.

These values are used in the thermal model described above.

Results

The simulated temperature profile in a double hot zone furnace for the preform axis is compared to the experimental profile in Fig. 10. The agreement is about 10% for the temperature.

MECHANICS

The aim of this module is to compute the transient geometry of the neck-down during the draw process. This is done for a specified draw tension $F(t)$. Other input data are the preform feed rate $v_p(t)$ and the axial temperature profile $T(z,t)$. In addition to the neck-down geometry $R(z,t)$, the module computes the draw speed $v_f(t)$ and fiber diameter $D_f(t)$.

This module can also compute the draw tension $F(t)$ from a specified draw speed $v_f(t)$.

Physical relationships.

The three physical relationships used in the mechanical module are given for an approximately cylindrical thin slice of silica in the neck-down, localized between the coordinates z and $z+\Delta z$. The fiber has p components $i=\text{core, cladding, ...}$, of viscosity $\eta_i(T)$ and cross section area $S_i(z)$.

The relationship between the force $F(z)$ applied to the slice and the elongation rate is :

$$F(z) = \frac{3}{\Delta z} \frac{d(\Delta z)}{dt} \sum_{i=\text{core, cladding, ...}} \eta_i S_i(z)$$

The force balance for the slice of thickness Δz is :

$$F(z + \Delta z) - F(z) + \rho g \left(\sum_i S_i(z) \right) \Delta z = \rho \left(\sum_i S_i(z) \right) \Delta z \frac{d^2 z}{dt^2}$$

where ρ is the silica density and g the gravitation constant.

During the elongation, the volume of the slice ΔV is constant, thus :

$$\begin{aligned} \frac{d(\Delta V)}{dt} &= 0 \\ &= \frac{d\left(\sum_i S_i(z)\right)}{dt} \Delta z + \left(\sum_i S_i(z)\right) \frac{d(\Delta z)}{dt} \end{aligned}$$

These equations are solved by a one dimensional discretization along the z axis.

Draw start-up

Fig. 11 shows the evolution of the glass gob for a constant temperature profile $T(z)$ in the furnace. This evolution is driven by the weight of the drop itself.

Stationary state.

After about half an hour, a steady state is reached under constant draw tension. The computed geometry of the neck-down obtained from an experimental temperature profile shown Fig.12, can be compared to the geometry of an experimental neck-down on Fig.13. The agreement is very good, and this validates the mechanical module.

CONCLUSION

The procedures described above allow the simulation of the draw process. The optimization of the induction in the graphite parts of the furnace can be done with the electromagnetism module. The heat loss and the response time of the furnace can be optimized with the thermal module. The mechanical module allows the optimization of draw start and to predict the geometry of the neck-down in a very accurate way for new furnace design.

REFERENCES

- 1 - S. ROY CHOUDHURY, Y. JALURIA, "Generation of neck-down profile for furnace drawing of optical fiber", HTD-Vol. 306, 1995 National Heat Transfer Conference - Volume 4 ASME 1995.
- 2 - SYSTUS, Electromagnetism manual.
- 3 - Radiative Heat Transfer, M.F. Modest, McGraw-Hill, 1993
- 4- P. ECHEGUT, CRMHT-CNRS, to be published.

BIOGRAPHIES

Marc Nicolardot graduated from Ecole Centrale Paris in 1986 and received a Ph. D. in semiconductor physics in 1989 for his work on hot electron transport in quantum wells. He joined Alcatel R&D Center in 1990 and worked on band-gap engineering for opto-electronic devices. Since 1994, he has been working on optical fiber draw process modeling.

Gérard Orcel received his Ph. D. degree from the University of Florida in 1987. He held positions at GelTech and SpecTran before joining Alcatel in 1992. Since then, he has been involved in preform design, CVD and Draw technologies and coating development.

Fig. 2 Rosseland radiation contribution to thermal conductivity β for an optically thick silica object

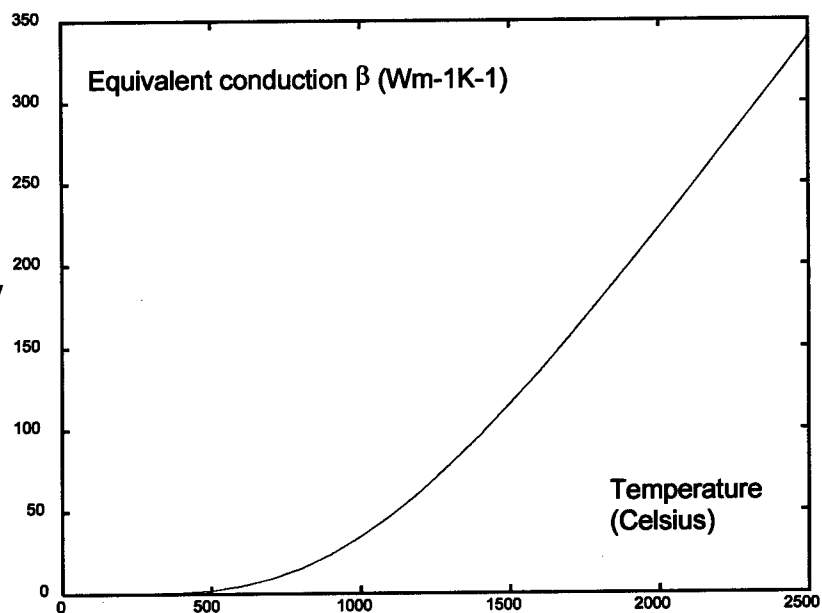


Fig. 3 Rosseland absorption coefficient for an optically thick silica object

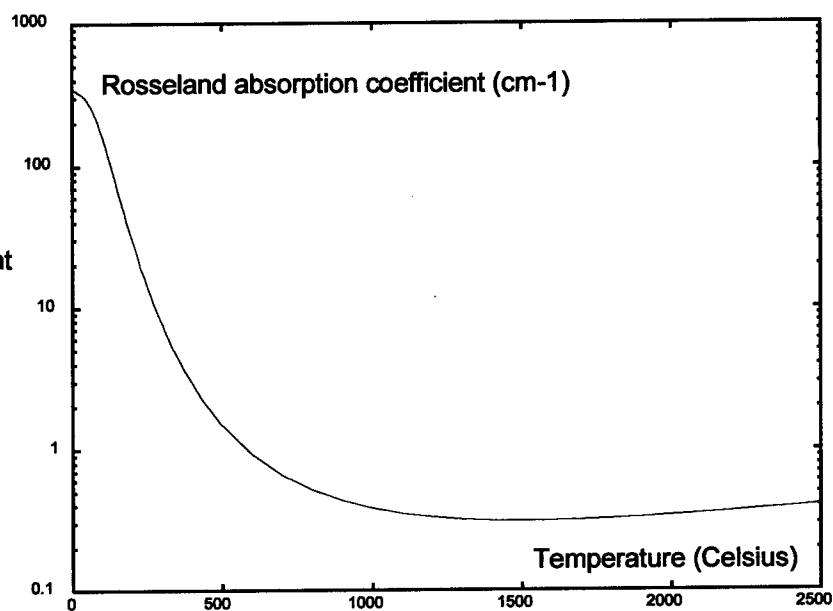


Fig. 4 Mean absorption coefficient weighted by Planck's law for an optically thin silica object

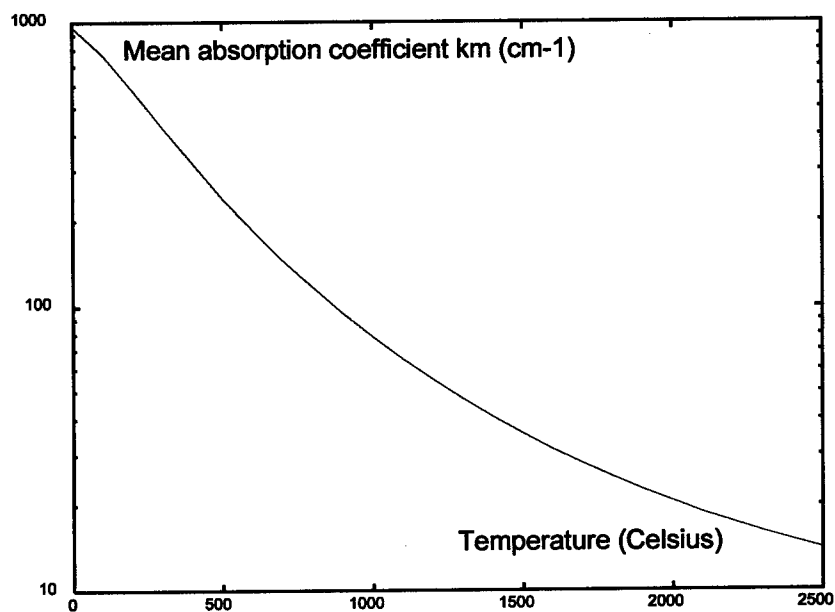


Fig. 5 Volume emitted power
for an optically thin silica object

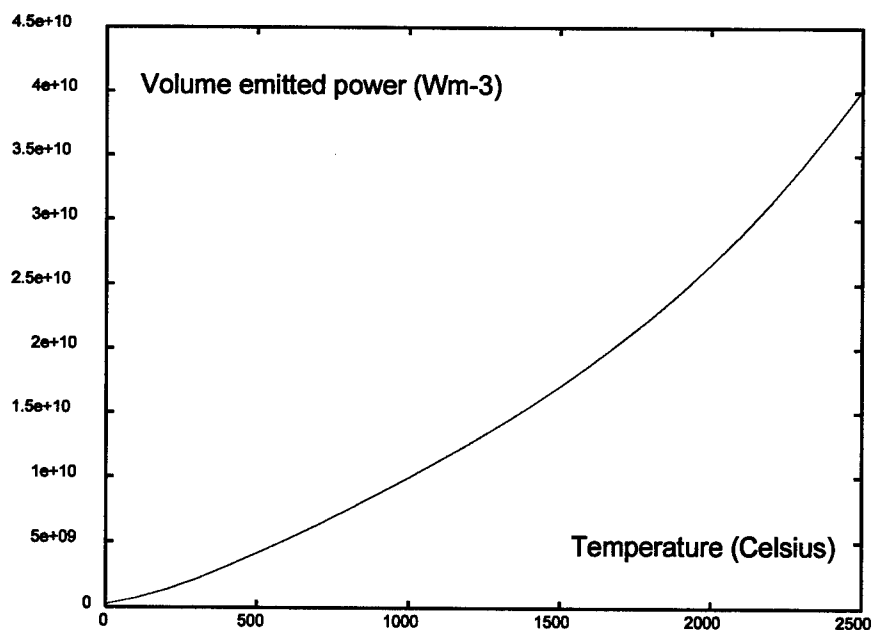


Fig. 6 Net emitted power density
as a function of the radial coordinate
for a 125 μm diameter silica
cylinder at 1750 Celsius

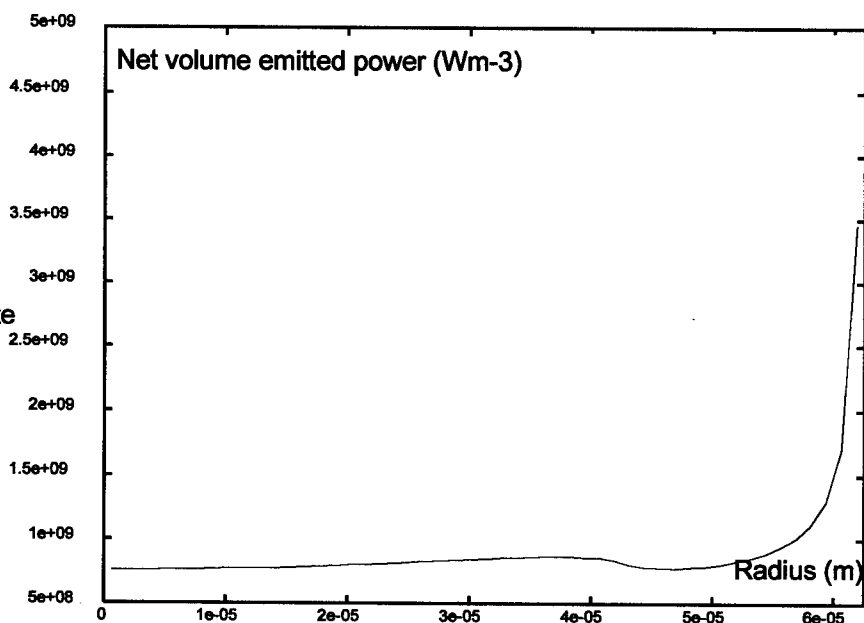


Fig. 7 Net emitted power density
as a function of the radial coordinate
for a 2 μm diameter silica cylinder
at 1750 Celsius

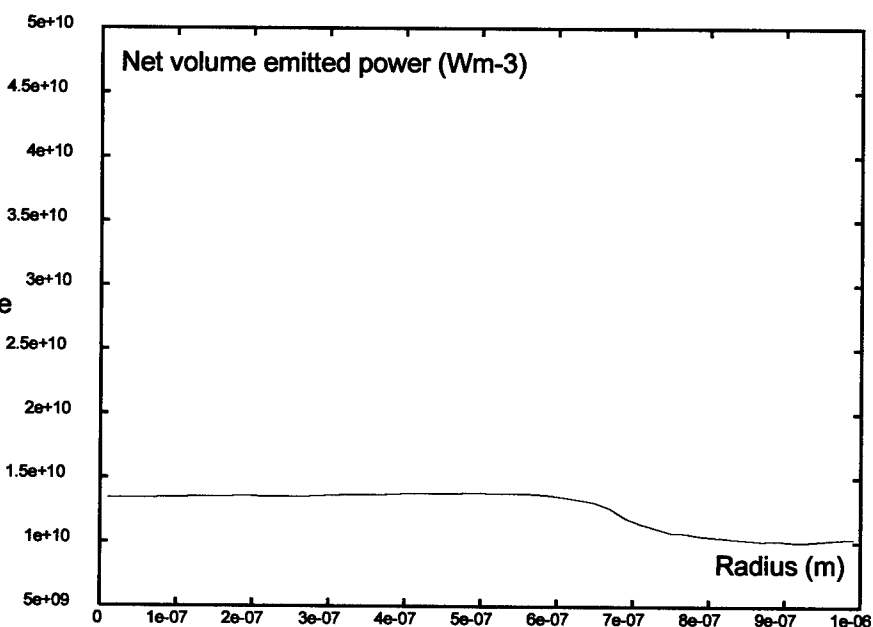


Fig. 8 Net emitted power density as a function of the radial coordinate for a 20 mm diameter silica cylinder at 1750 Celsius

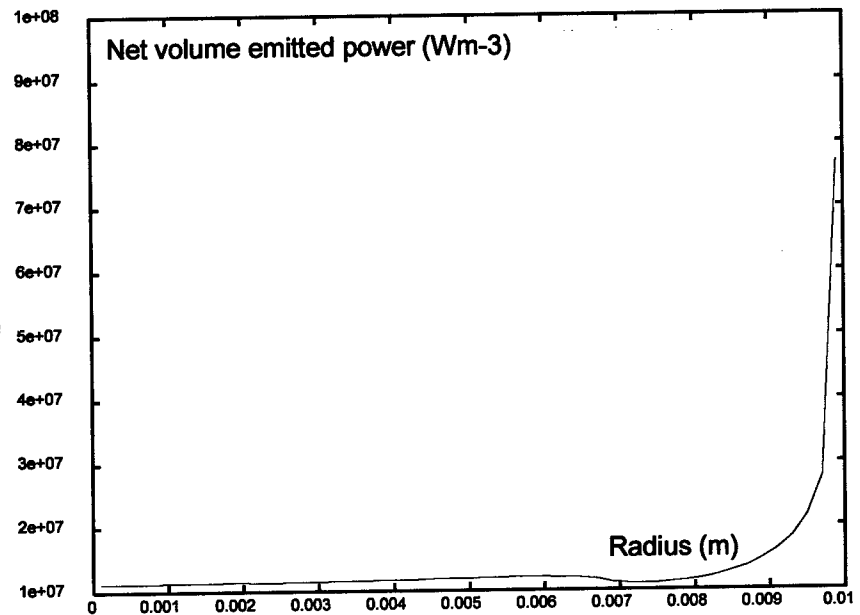


Fig. 9 Hemispherical emissivity of a silica cylinder of radius R_{fib} for different temperatures in Celsius

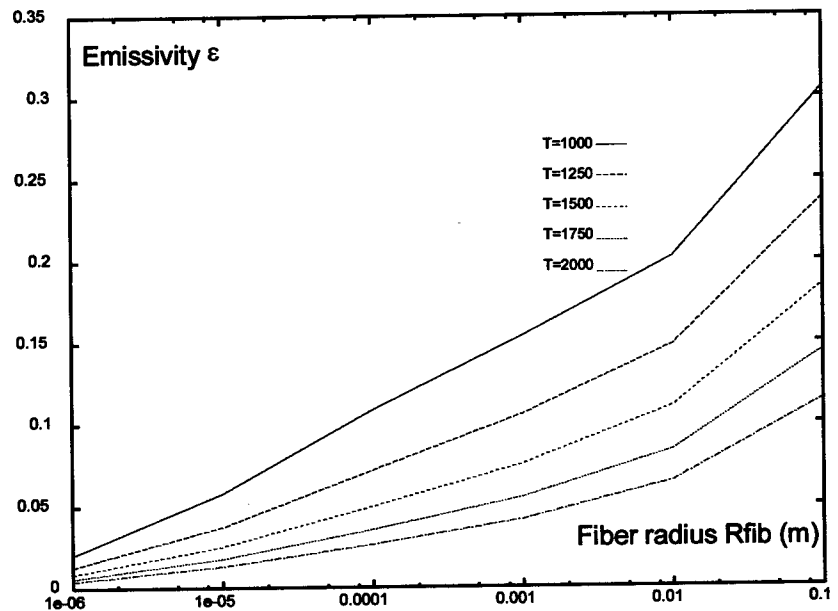


Fig. 10 Comparison simulation-experiment for a double hot zone furnace for 8 kW electrical power in each zone

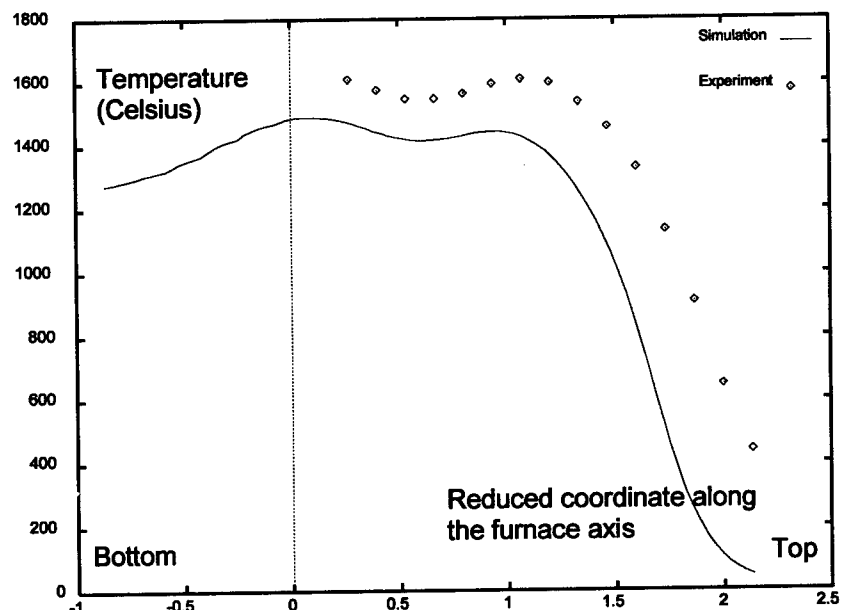


Fig. 11 Simulated evolution of the neck-down geometry $R(z)$ at $t=0s$, $t=9s$, $t=15s$, $t=17s$ and $t=18s$, for a constant temperature profile $T_1(z) = 1.2 * T_2(z)$ ($T_2(z)$ is shown Fig. 12)

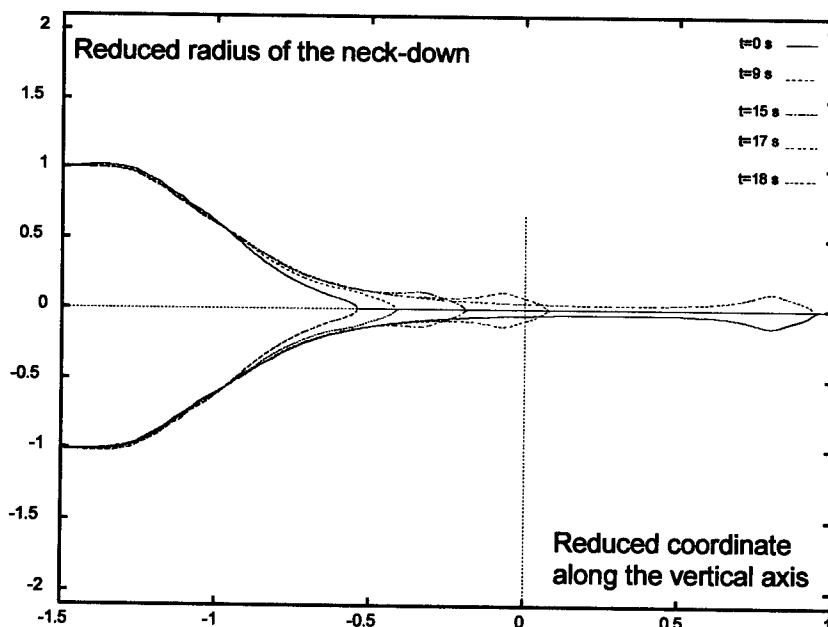


Fig. 12 Experimental temperature profile $T_2(z)$ along the axis of the furnace

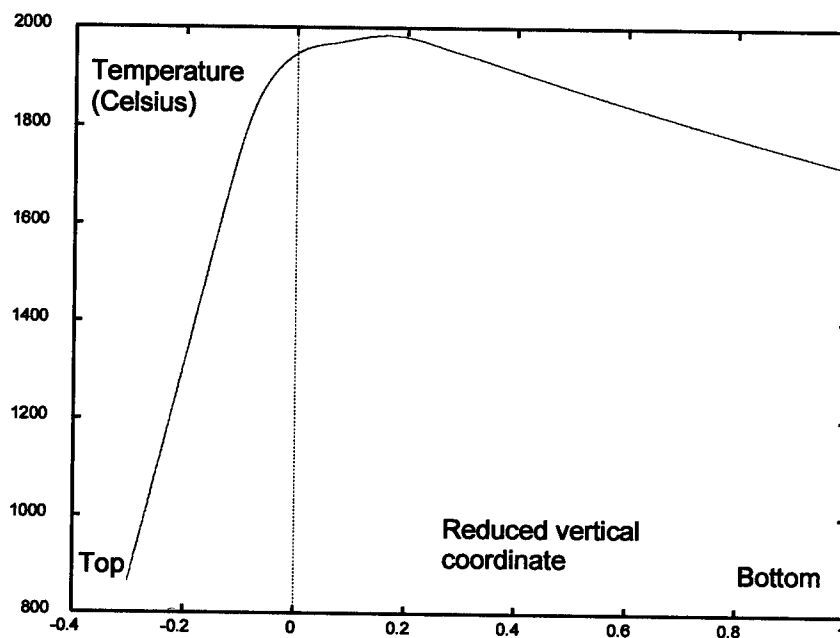
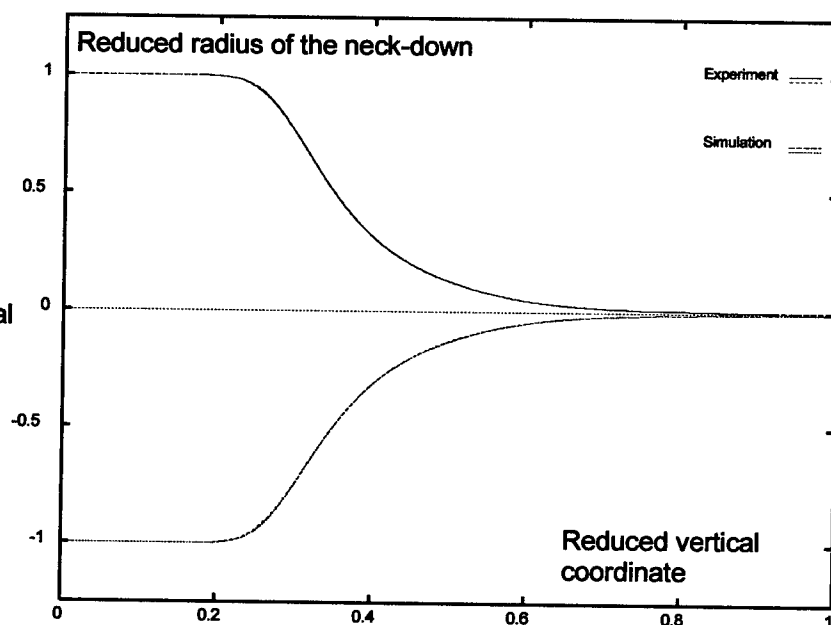


Fig. 13 Comparison of an experimental and a simulated neck-down geometry when the stationnary state is reached, for the temperature profile $T_2(z)$ shown Fig.12



STATISTICAL PROCESS CONTROL TECHNIQUES FOR ON-LINE MEASUREMENT OF AUTOCORRELATED PROCESS VARIABLES

Timothy G. Goddard

Lucent Technologies
Norcross, Georgia

ABSTRACT

Statistical process control (SPC) techniques have long been in use for determining the state of control of a manufacturing process. When applied to continuous monitoring of fiber-optic cable and ribbon process variables, care must be taken to account for correlation within the data. Autocorrelation, the correlation of a process variable with itself, is generally observed in on-line measurement of cable and ribbon process variables. If not addressed, it will distort the performance of traditional SPC control charts. The effect of autocorrelation on these charts can be eliminated by viewing process variables as time series, and fitting them to a class of models known as Autoregressive Integrated Moving Average (ARIMA). Control charts can then be designed that reflect the true state of control of the process variable of interest.

INTRODUCTION

Traditionally, fiber ribbon and cable producers have relied on end sample measurement of process quality variables such as ribbon thickness or cable jacket outside diameter to determine process capability in meeting customer specifications. More recently, both contact and non-contact sensors have been deployed that allow on-line measurement of variables such as thickness in ribbons and cables. Suppliers of these monitoring devices typically offer an SPC module for tracking process variables of interest, to determine whether they are in control. The specific method commonly employed is to use standard Shewhart control charts.

The Shewhart model of a stochastic process that is in control states that a process variable x_t measured at time t is the sum of the process mean, μ , and a random shock, ε_t .

$$x_t = \mu + \varepsilon_t \quad (1)$$

This model assumes that successive observations $t = \{1, 2, \dots, k\}$ come from a normal distribution, and are independent and identically distributed (*iid*). These charts work reasonably well when the normality assumption is violated to a moderate degree. However, violation of the independence assumption causes an excessive number of false alarms to be generated, even with low levels of correlation in the process data.

Unfortunately, the assumption of independence of observations in ribbon and cable production is not even approximately correct. Inertial forces inherent in these processes lead to correlation of successive measurements. When the time scale for sampling is much shorter than these forces, Shewhart type control charts will give a misleading view of the state of control of a process.

As an example, consider the on-line measurement of fiber-optic ribbon thickness, a key process variable affecting ribbon quality. For this example, on-line measurements were made on a 2 km section of ribbon as it was formed, with one thickness measurement generated for each consecutive meter of the sample. These measurements are plotted on a standard individuals control chart with a center line and 3.5σ upper and lower control limits in Figure 1 below. The ordinate in Figure 1 represents the observed ribbon thickness x_t . Values are

expressed in terms of the output voltage of the sensor, and are proportional to the actual thickness in microns.

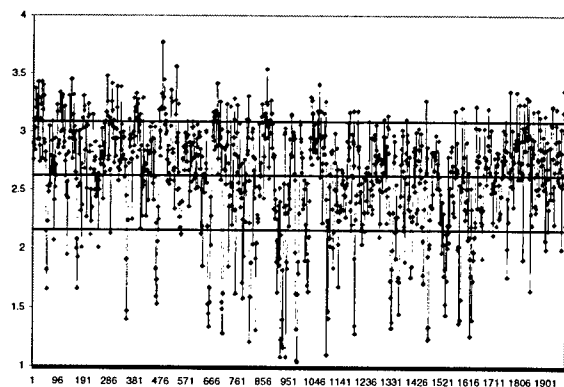


Figure 1: Individuals control chart for ribbon thickness data

Figure 1 shows that the process appears to be out of control. Numerous signals are observed at both control limits, and the process mean shows a visible drift. However, in subsequent random mechanical thickness testing the ribbon had minimal thickness variation across the entire sample, and was well within the specification limits for the product.

The apparent variation in on-line ribbon thickness measurement seen in Figure 1 is due to the presence of autocorrelation in successive samples. This type of correlation causes a gross under-estimation of the process variance, which results in an excessive number of false alarms in the control chart. The extent of the correlation of x_t with itself can be seen in Figure 2. Here the residuals ε_t from Equation (1) at time t are plotted in the abscissa against the residuals at $t+1$ in the ordinate. Figure 2 shows a high degree of correlation between consecutive points ε_t and ε_{t+1} .

In fact, unless the autocorrelation inherent in the on-line data is properly dealt with, standard run charts will be incapable of correctly representing the process control state.

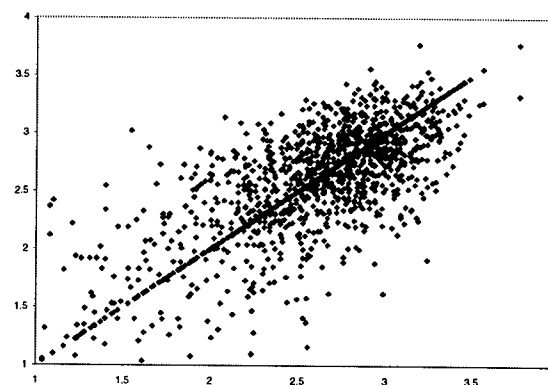


Figure 2: ε_t vs. ε_{t+1}

This paper will demonstrate a methodology for applying an SPC technique in fiber optic cable and ribbon manufacturing that allows control charts to be generated that give an accurate view of the state of control of a process. Specifically, on-line process data will be viewed as a time series. Then, it will be shown that the Autoregressive Integrated Moving Average (ARIMA) class of models can be used to describe the autocorrelation of a variable with itself. Once the correlational structure of the process variable of interest is accounted for, control charts can be designed on the residuals of the process data which will be *iid*. The statistical properties of these charts such as false alarm rate and average run length can then be calculated and used to specify the desired control limits.

In the next section the basic structure of ARIMA models will be presented along with the definitions of the autocorrelation function and partial autocorrelation function. The third section will focus on a discussion of the steps required to properly fit a particular ARIMA model to a time series. In the fourth section we will return to the above example of ribbon thickness to demonstrate the use of a fitted ARIMA model in designing a control chart for the ribbon thickness process variable.

LINEAR MODELS OF TIME SERIES

Elementary Concepts

A time series is a set of sequential, equally spaced observations. The particular system being viewed as a time series can be continuous, such as the extrusion of a core tube

through a die, or discrete, as in the number of cables produced in a week. Continuous systems can be viewed as discrete time series by making sample measurements at a specified interval.

A physical system that can be completely characterized by a mathematical model, so that some time-dependant characteristic of the system can be exactly known at any time, is known as a deterministic system. In reality, most systems are influenced by unknown factors producing variability in process parameters which cannot be captured functionally. These are known as stochastic systems or processes. Stochastic processes can be characterized by a probability or stochastic model, which calculates the probability that an observation from the process will be a certain value. The models for time series that will be discussed below are stochastic models.

Another important consideration in modeling time series is whether the process is stationary, or nonstationary. Stationary models assume the process is in equilibrium about a fixed mean, and has a constant variance and autocorrelation through time. An example of a stationary time series is the average daily temperature, which will vary by day and season, but will remain close to a fixed average from year to year. Nonstationary models of time series apply to processes where there is no natural mean over time. Examples here might include a stock market index, or the sales of a company. Nonstationary processes are frequently modeled for the purpose of forecasting values at future points in time.

Time series models of ribbon and cable manufacturing processes are assumed to be stationary. The goal is to develop a model for these processes that accounts for correlation between consecutive observations while presuming the process is in control about a fixed mean. If the process does shift, the model will no longer hold, and the shift will be detected. Next, we briefly cover the basic model structure that will be used to characterize the time series data of interest.

ARIMA Model Constructs

An effective class of models for characterizing time series is the set of autoregressive integrated moving average (ARIMA) models.

These models are discussed in detail by Box & Jenkins, and Montgomery.^{1,2} Below is a brief description of the structure of a generic ARIMA model.

Autoregressive Models. The autoregressive (AR) model is a stochastic model applicable to a number of regularly occurring processes. In this model, the current value of a time series is expressed as a finite linear sum of previous values of the series, and a random shock:

$$x_t = \xi + \phi_1 x_{t-1} + \phi_2 x_{t-2} + \dots + \phi_p x_{t-p} + \varepsilon_t \quad (2)$$

Here ξ is a constant and the model is said to be of order p . This model is similar to a standard regression model where a dependant variable is "regressed" on a number of independent variables. In the AR model the variable x_t is regressed on previous values of itself, hence the term "autoregressive".

Moving Average Models. Another time series model of practical importance is the moving average (MA) model. Here, the current observed value of a time series is linearly dependant on a finite number of q previous shocks:

$$x_t = \mu + \varepsilon_t - \theta_1 \varepsilon_{t-1} - \theta_2 \varepsilon_{t-2} - \dots - \theta_q \varepsilon_{t-q} \quad (3)$$

Note the sum of the weights $\{1, \theta_1, \theta_2, \dots, \theta_q\}$ need not equal 1, nor must they be positive.

Mixed Models. Sometimes elements of both AR and MA models are combined to form a mixed autoregressive/moving average (ARMA) model:

$$x_t = \xi + \phi_1 x_{t-1} + \varepsilon_t - \theta \varepsilon_{t-1} \quad (4)$$

Equation (4) is a first order ARMA model in both the p and q parameters.

Non-stationary models. The ARMA model described above is usually sufficient to characterize a stationary time series. However, if a process has no fixed mean this model will not be adequate. An effective procedure for transforming a non-stationary time series into one that is stationary is to transform the series by differencing consecutive observations d times. Therefore, an autoregressive integrated moving average (ARIMA) model is an ARMA model where d differencing passes have been made in the data.

Box and Jenkins introduced the standard notation for an ARIMA model. In their representation, a model is summarized as ARIMA(p, d, q) meaning that it has p autoregressive and q moving average parameters, which are calculated after the time series has been differenced d times. Note that the Shewhart model shown in Equation (1) is a sub-class of the ARIMA model with no differencing, and the number of p and q parameters equal to zero.

Quantifying Correlation

So far we have only stated that, in general, sequential time series data are correlated. A specific example was given in the first section which showed definite correlation between points at time t and $t+1$. Specifying an appropriate model requires that the correlation of observations that are k time periods apart (defined as the lag k) be known. A measure of this correlation is given by the autocorrelation function (ACF), ρ_k , for a stationary time series:

$$\rho_k = \frac{E[(x_t - \mu)(x_{t+k} - \mu)]}{\sqrt{E[(x_t - \mu)^2]E[(x_{t+k} - \mu)^2]}} \quad (5)$$

where $k = \{0, 1, 2, \dots, K\}$, x_t and x_{t+k} are the observations at lags 0 and k , and μ is the mean of the time series. In practice, the mean is unknown, and must be estimated from sample data. Therefore, the sample autocorrelation function, r_k , is used to determine the correlation at lag k , and is given by:

$$r_k = \frac{\sum_{t=1}^{n-k} (x_t - \bar{x})(x_{t+k} - \bar{x})}{\sum_{t=1}^n (x_t - \bar{x})^2} \quad (6)$$

An additional method for describing the dependency of data in a time series is via the partial autocorrelation function (PACF). The PACF differs from the ACF in that the effect of intermediate observations within a lag is removed. This yields a truer representation of the correlation between an observation at t and a specific lag k . Both the ACF and PACF for a sample can be generated for a designated number of lags using a number of commercially available statistical software packages. The ACF plot of 15 lags for the ribbon thickness sample from the introductory section is shown below.

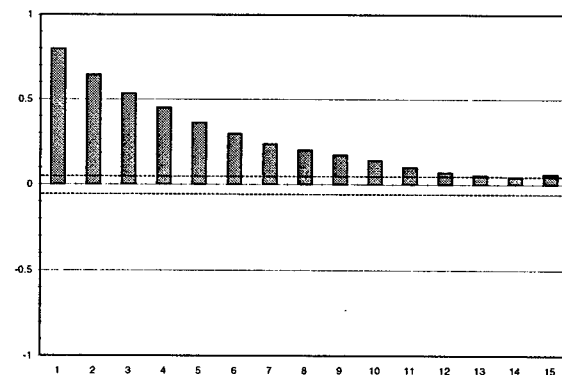


Figure 3: ACF for Ribbon Thickness Example

In this plot a value of 1.0 or -1.0 for a lag represents a perfect correlation or negative correlation respectively. A value of 0.0 represents no correlation. Figure 3 shows a significant degree of autocorrelation in the ribbon thickness data up to lag 12. This clearly violates the independence of observations assumption of the model given in Equation (1).

FITTING ARIMA MODELS

A systematic methodology for fitting an ARIMA model to a particular process consists of an iterative process of model identification, model parameter estimation and model evaluation. In what follows, we will discuss the basic

procedures associated with each of these steps, with references to detailed procedures. The calculations involved in the second and third steps can be cumbersome, however there are many commercially available software packages capable of performing them eliminating the need for manual computation.

Model Identification

The first step in specifying an ARIMA model is to identify the number of differencing passes needed. Initially a plot of a test sample or samples from a time series should be examined. Significant changes in the mean, μ , indicate that one or more differencing passes are required to make the process stationary. A log transformation on the data may also be required to stabilize the variance. Note that if the plot indicates there is only a slow drift about the mean, differencing the series can produce less stable coefficients.

Once the series has been transformed to meet stationarity requirements, the number of p and q parameters to be used in the model should be specified. Here, the shape of the plots of both the autocorrelation and partial autocorrelation functions are used to estimate the number of each type of parameter. Specific model recommendations based on the decay and number of significant lags for both functions are given by Pankratz.³ For virtually all time series the number of p or q parameters needed will be less than or equal to 2. This results in a parsimonious model with the greatest number of degrees of freedom among potential models.

Parameter Estimation

Once a candidate ARIMA(p, d, q) model has been identified any autoregressive or moving average coefficients must be calculated. Although the details are outside the scope of this paper, the general procedure is to specify coefficient values that maximize the likelihood or probability that the model fits an observed time series. This is accomplished via an algorithm (the quasi-Newton method) that performs a function minimization. Details of several different procedures for calculating model coefficients can be found by consulting McLeod & Sales or any standard text dealing with time series.⁴

Model Evaluation

The final step of the ARIMA model fitting process is to evaluate the quality, or "goodness of fit" of the model. This is usually accomplished by examining the residuals, ε_t , resulting from the difference in fitted vs. actual values. A well fit model will have residuals that are normally distributed, show no systematic trend with time (i.e. they are centered at a mean of zero and variation remains constant), and that they contain no serial dependency. The simplest method for evaluating these characteristics is to examine normal probability plots, histograms, scatter plots, and ACF plots of the residuals. Any trends or significant correlation levels indicate the model may be inadequate. If this is observed, one should return to step one, model identification, and begin the model selection process again.

RIBBON THICKNESS EXAMPLE

Now we return to the example presented in the first section of this paper. Remember that the individuals control chart constructed from the raw data indicated that the ribbon process was out of control. However, by studying the residual one-forward lag plot in Figure 2 we determined that there was a significant degree of autocorrelation in the on-line measurements of ribbon thickness. We were then able to quantify the degree of correlation by calculating the sample autocorrelation function for 15 lags (Figure 3). There was a high degree of correlation in the thickness measurements seen in the ACF plot, with $r_1 = 0.8$. This suggests that the out of control signals seen in the control chart are due to the correlational structure of the data and not necessarily significant thickness variability. Therefore, an SPC charting technique based on an ARIMA model would be appropriate.

Control Chart Design

Using the techniques discussed in the previous two sections, an ARIMA(1, 0, 0) model was fit to the ribbon thickness data using a commercially available software package⁵ to give:

$$x_t = 0.5275 + 0.7984x_{t-1} + \varepsilon_t \quad (7)$$

This model contains one autoregressive parameter that accounts for the correlation of data in our example. An individuals control chart was then constructed on the residuals of the ribbon thickness data based on Equation (7), with a center line at zero, and control limits specified by whatever tolerance is desired. For this example, the control limits were set at 3.5σ . The control chart is shown in Figure 4.

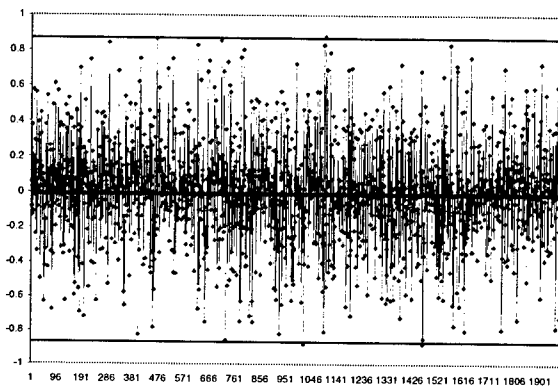


Figure 4: Individuals Chart for ARIMA(1, 0, 0) Residuals

In contrast to Figure 1, this chart shows the ribbon thickness to be reasonably in control as it was being formed. This agrees with the random mechanical testing performed after the ribbon sample had been made. The chart in Figure 4 shows no significant drift in the mean, and variability that is consistent throughout the sample. There are only a small percentage of points outside the 3.5σ control limits, with some of them expected based on the average run length (ARL) of the control chart. Note that the control limits were chosen to minimize the number of false signals, that is to maximize ARL_0 , the average run length until a signal is generated for an in control process.

Model Diagnostics

In Section Three we discussed the important step of model evaluation. This critical phase of the overall process is often either given cursory attention or overlooked altogether. Yet it is critical in determining whether the specified ARIMA model yields residuals which meet the requirements of independence. The control chart shown in Figure 4 was constructed based on the assumptions that the residuals were normally

and independently distributed. It is important that these assumptions are tested before using the model developed above. We now show how graphical methods can be used evaluate the residuals.

First we examine the distribution of the residuals. Remember, run charts are robust even when the normality assumption is violated. Still, it is worthwhile to determine whether there are any unusual patterns in the sampling distribution of the process. There are a number of possible tests for normality, and several specific charting techniques such as the normal probability plot. However, a very simple method for testing the normality of a distribution from a sample is to examine a histogram. The residuals from our ribbon thickness example are shown in this type of plot in Figure 5.

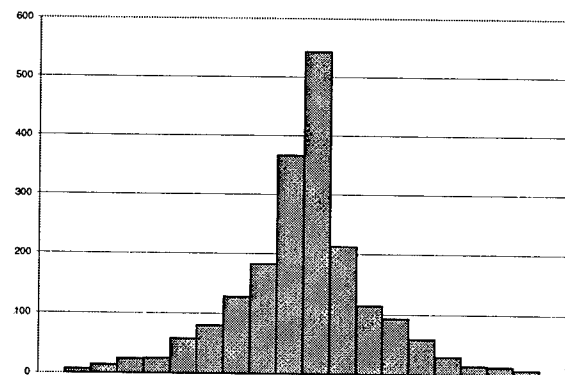


Figure 5: Histogram of ARIMA(1, 0, 0) Residuals

Here it can be seen that the residuals are reasonably normally distributed, with little or no skewness.

The second and more important assumption that must be checked is that of the independence of observations. In the first section the residuals resulting from the original Shewhart model were plotted in Figure 2. A strong degree of autocorrelation was seen between the residuals and their first lag. The purpose of the fitted ARIMA model was to account for this correlation and separate it from the random component of the model. Our fitted ARIMA model can be checked by re-examining the scatter plots, and the ACF of the residuals. In Figure 6 below we see a scatter plot of the σ_t vs. σ_{t+1} residuals from the ARIMA model. It can be seen that the

residuals and their one forward lag form a random cloud, with no systematic pattern or correlation. Figure 7 is a plot of the ACF of the ARIMA residuals for 15 lags. Again, no significant correlation between the residuals is seen.

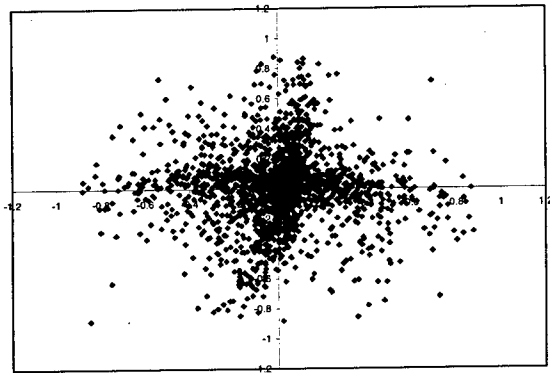


Figure 6: ε_t vs. ε_{t+1} for Fitted ARIMA Residuals

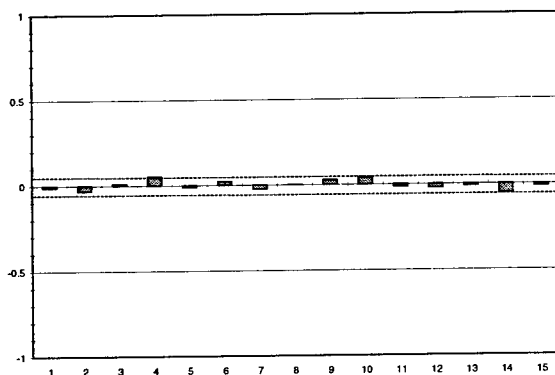


Figure 7: ACF for Fitted ARIMA Residuals

These straightforward charting techniques have been used to verify what we wished to know. The residuals from our fitted ARIMA model are indeed suitable for use in a Shewhart type control chart.

CONCLUSIONS

The fiber cabling industry has long benefited from the use of statistical process control charting techniques for monitoring and improving product quality. A primary method for implementation has been the use of individuals charts in conjunction with end sample

measurement on fiber optic ribbons and cables. This paper has illustrated a procedure for deploying run charts of on-line data capable of representing an accurate view of the state of control of key process variables. At high sampling rates these will generally be correlated, distorting the performance of standard charting techniques. It was demonstrated how the autocorrelation of on-line process data can be removed by viewing the process as a time series, and applying the ARIMA class of models to remove serial dependencies. The advantage of using such a procedure is that the state of control of key process variables are known throughout the length of ribbons or cables, not just inferred from end sample data. Another advantage of this procedure is that the high sampling rate translates to a low average time to signal, ATS_1 . Therefore a process departing a state of statistical control will be quickly detected.

REFERENCES

1. Box G.E.P. & Jenkins, G.M. , 1976. *Time Series Analysis: Forecasting and Control*. Holden-Day, San Francisco.
2. Montgomery, D.C., Johnson, L.A. & Gardiner, J.S. , 1990. *Forecasting and Time Series Analysis* (2nd ED). McGraw-Hill, New York.
3. Pankratz, A. , 1983. *Forecasting with Univariate Box-Jenkins Models: Concepts and Cases*. Wiley, New York.
4. McLeod, A.I. & Sales, P.R.H. , An Algorithm for Approximate Likelihood Calculation of ARMA and Seasonal ARMA Models. *Applied Statistics* (Algorithm AS), 211-223, 1983.
5. *Statistica V 5.1* , StatSoft Inc. , 1997, Tulsa, OK.



Tim Goddard is a Member of Technical Staff in the Outside Plant Manufacturing Engineering Group at Lucent Technologies, Norcross, Georgia. His responsibilities focus on process characterization and optimization in Enhanced AccuRibbon manufacturing. Tim graduated from the Georgia Institute of Technology in 1987 with a B.S. in Textile Engineering. After 5 years as a process engineer in the industrial textiles industry, he returned to graduate school at Georgia Tech. There he received his M.S. in Textile Engineering in 1994, and a Ph.D. in 1997.

NOVEL NON-METALLIC MULTILAYER FIBER OPTIC CABLES BASED ON CONE EXTRUSION PROCESS

Markku T. Heino, Jussi T. Ravela, Markku T. Suvanto,
Richard P.-G. Phillips*, and Tommi P. Vainio **

NK Cables Ltd., Helsinki, Finland
Nextrom Ltd., Ecublens, Switzerland *
Nextrom Ltd., Vantaa, Finland **

ABSTRACT

This paper describes new fiber optic cable designs based on multilayer extrusion accomplished with novel cone extrusion technology. The cables consist of coextruded multilayer structures, in which advanced thermoplastics with different functional properties are combined in a single processing step. The main components of the cone extruder (Conex®) are a rotating conical screw with helical channels (rotor), two stationary cones (stators), one on either side of the rotor, and a simple die. Each rotor can produce two layers, and multilayers are achieved by adding more nested stator/rotor/stator combinations. All layers are seamless since the material flows symmetrically around the core, and the thickness of each layer can be controlled separately. The processing conditions are optimal for thermoplastics (effective melting, short residence time, low shear for melt). This versatility makes cone extrusion a promising technique for the manufacture of non-metallic fiber optic cables such as needed in access networks.

INTRODUCTION

New lightweight, buffered, and stabilized non-metallic fiber optic cable designs for several end use applications are described. The new designs rely on the use of multilayer extrusion technology, which allows simultaneous processing of different advanced thermoplastics and manufacture of the cable in a single

processing step. A number of advantages are achieved over conventional cable constructions. Current non-metallic fiber optic cable designs comprise several discrete elements set around plastic buffer tubes – elements such as reinforcing aramide or glass fibers, composite strength members, water-blocking tapes, flooding compounds, binding yarns and an outer jacket. We have developed new concepts to simplify the customizing of cable designs. The idea is to use appropriate thermoplastic polymers or compounds exhibiting different functional properties, such as high strength, low moisture permeability, fire retardance, and wear resistance, as thin layers coextruded in a single processing step. Manufacturing of such multilayer cable constructions consisting of coextruded seamless layers is made possible by using the new cone extrusion technology called Conex®.

The technology is based on the original Finnish invention¹, which has been further jointly developed by Nextrom, NK Cables, Uponor and VTT (Technical Research Center of Finland) for cable, pipe and blown film applications.^{2,3}

A set of optical fibers or a previously made cable core is fed through the central hole of the cone extruder while the desired functional layers are coextruded on it. The multilayering, together with several other important basic features of cone extrusion, make it an advantageous and versatile processing method for novel fiber optic cables, as will be shown below.

DESCRIPTION OF THE CONE EXTRUDER

Basic construction

The three main components of the cone extruder are rotating conical screws (rotors), stationary conical parts (stators), and a simple die fixed to inner and outer stators (Figure 1).¹⁻³ The rotors are rotated by special gears, which also support the rotor/stator combination. Several helical channels on either side of the rotor serve to transport the material toward the die. The stator surfaces may be grooved, as well, to improve the conveyance of material. Each rotor can coextrude two layers, and any number of additional layers can be achieved by adding further nested stator/rotor/stator combinations.

One to four layers can be obtained with the two-rotor cone extruder presented in Figure 1.

The material flows symmetrically around the cable core with no melt distribution (no crosshead), resulting in a totally seamless product. The polymer melt flows for two adjacent layers merge at the rotor tip before the die. The die is short and simple, which makes it possible to maintain the helical flow field and material orientation in the product. Each layer has its own separate feeding equipment. The output is controlled by the feeding screws independently of the rotor speed, which is a major difference from the single-screw extruder. This gives wider scope for varying the thicknesses of individual layers and it also enables control of the melt temperature.^{2,4}

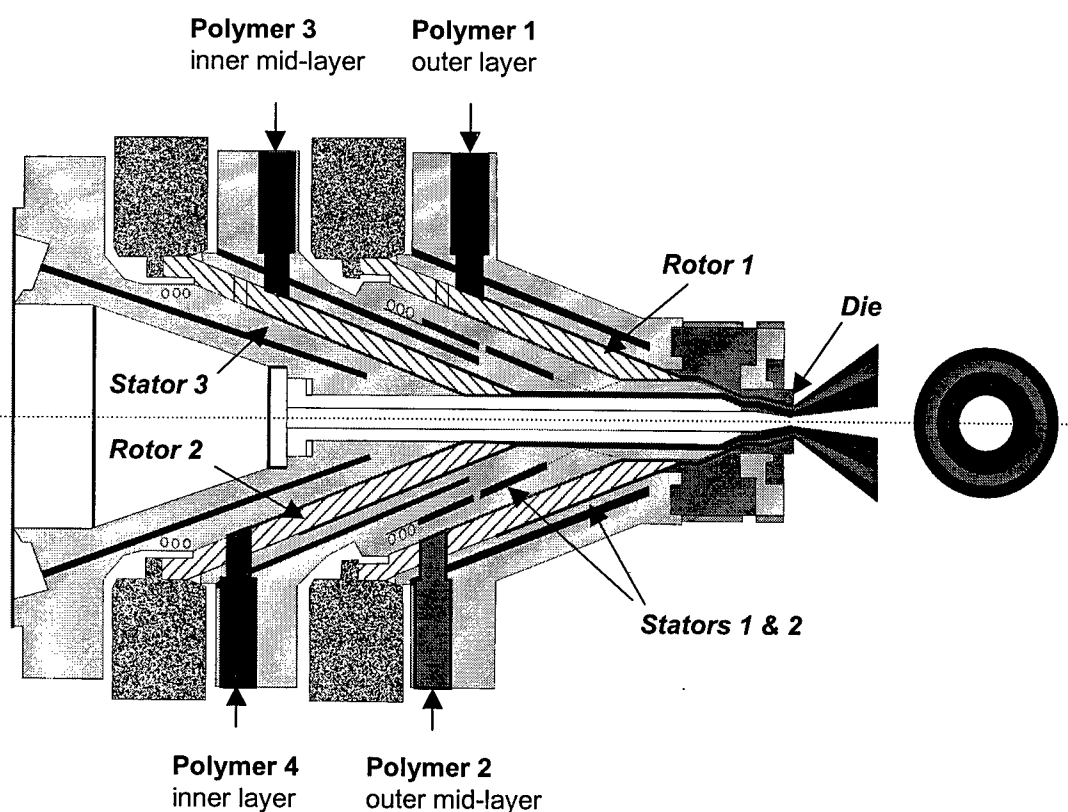


Figure 1. Schematic view of a two-rotor (four-layer) cone extruder.

Main features

Cone extrusion was developed as an optimal processing method for plastics. The method has several notable features.³

Features of cone extrusion:

- Multilayer concept
 - several layers coextruded in a single process step
 - combination of different materials and functional properties possible
- Axisymmetric flow (no cross-head)
 - no weld-lines
 - thin seamless layers of high quality
- Free access through the extruder
 - easy coating of any continuous object
- Optimal method for plastics processing
 - short residence time
 - narrow residence time distribution
 - high shear rate for solid plastic (effective melting)
 - low shear rate for melt
 - gentle processing especially for heat and/or shear sensitive polymers
- Output adjusted by feeding speed
 - separate feeders for each layer
 - possibility to vary layer thickness
- Helical flow field
 - controlled orientation of polymer melt and/or reinforcing fibers
- Extruder compact in size
 - easy to handle and dismantle
 - good energy balance
 - easy to clean

PERFORMANCE OF THE CONE EXTRUDER

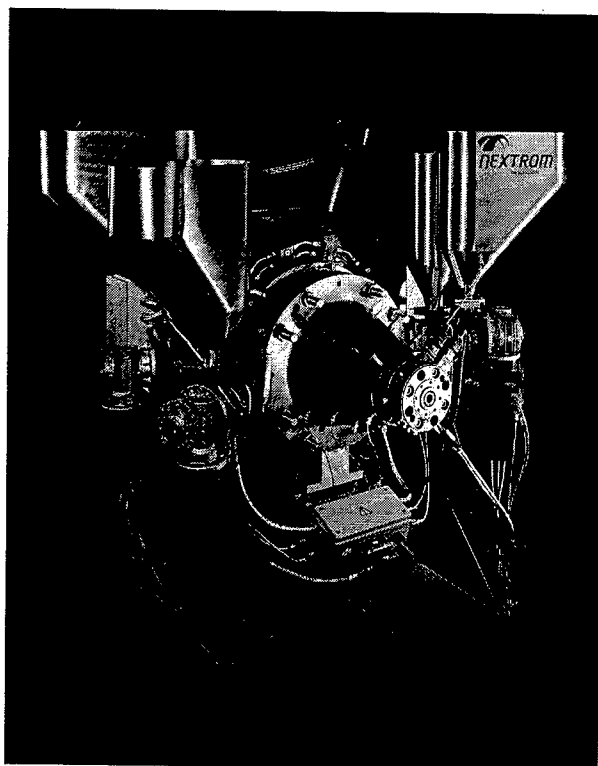
For purposes of this paper the performance of the cone extruder was experimentally demonstrated by bleeding tests with a two-layer laboratory machine (ModEx II), which can be equipped with several pressure transducers and thermocouples (Figure 2a). The angle of the cone is 15° with a maximum rotor diameter of 350 mm for a length of 325 mm. Three different materials were used for the experiment as examples: HDPE (HE 1110, Borealis), PA12 (Grilamid L20HL, EMS-Chemie), and a halogen-free fire retardant (HFFR) compound (Megolon S530, Scapa Polymeric). The measured typical outputs were 167 kg/h (HDPE), 174 kg/h (PA12), and 223 kg/h (HFFR).

The values show that ModEx II can compete well with a 60-mm extruder in processing of a monolayer product (same material on both sides of the rotor). Moreover, ModEx II can replace two 45-mm extruders in processing of a two-layer product. Consequently, a coextrusion unit where several extruders are distributed around a head (see Figure 2b) can be replaced by one Conex[®] machine. Three- or four-layer structures, in turn, can be achieved with a two-rotor cone extruder (see Figure 1) of the same size as ModEx II. Multirotor cone extruders with still more rotors can be constructed for a larger number of layers.

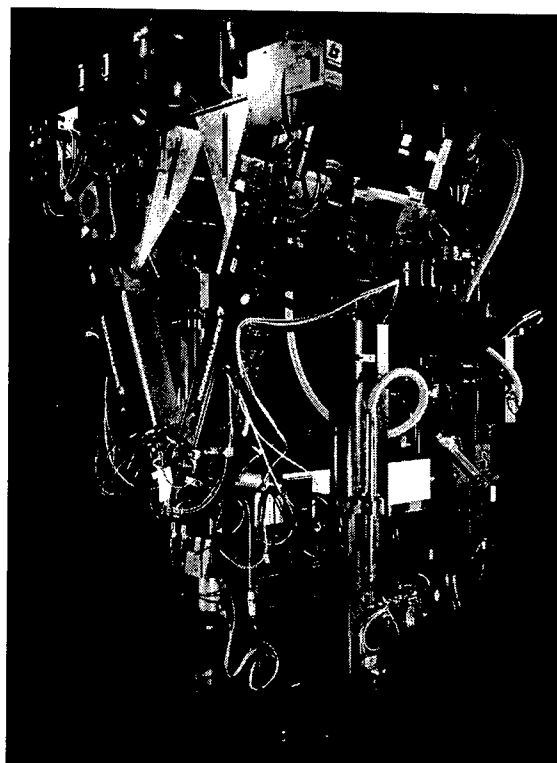
Table 1 shows the versatility of the cone extruder through comparison with a single-screw extruder. The cable examples 1 and 2 are discussed below.

Table 1. Versatility of cone extruder vs. single-screw extruder.

Layer structure	Example materials	Output (kg/h)	Cone extruder	Single-screw extruder
1 layer	HDPE ²	150	ModEx II (1 rotor)	1 x NMC 60-24D + 1-layer die
2 layers	HFFR1/HFFR2 (ref. Cable example 2)	100/100	ModEx II (1 rotor)	2 x NMC 45-24D + 2-layer die
4 layers	PA/LCP/adh/sheath (ref. Cable example 1)	60/60/20/60	ModEx II (2 rotors)	3 x NMC 45-24D + 1 x NMB 30-24D + 4-layer die



a)



b)

Figure 2: a) ModEx II, a two-layer (one-rotor) lab-scale cone extruder (cone angle 15°; max. rotor diameter 350 mm / length 325 mm) and b) a conventional coextrusion unit equipped with one NMC 60-24D and two NMA 30-24D single-screw extruders for manufacturing three-layer products.

The compact design of the conical extruder results in saving of space, elimination of melt distribution, and reduction of the total residence time. For instance, with HDPE at an output of 84.0 kg/h per layer, the total residence time in ModEx II was 48 s. There are even cases where the residence time can be as low as 34 s.² A special feature of the technology is control of the melt temperature. This can be adjusted by varying the rotor and/or the feeding screw speed, which control the energy created by viscous dissipation and the volumetric output, respectively.⁴ Melt temperature control is particularly important in processing thermally sensitive materials such as HFFR compounds. Another parameter, that is important to control when processing thermally sensitive material is the shear rate. Here, the conical shape is highly advantageous, as the shear rate is maximum at the beginning (about 100 1/s), where the material needs energy to melt, and minimum at the end (about 30 1/s), where, to avoid degradation, the melt should not be oversheared. The material

processability can be optimized by adjusting the cone angle, rotor dimensions, spiral angle, and geometry.

MULTILAYER FIBER OPTIC CABLE STRUCTURES

Central loose tube cables have performed well in all common installation modes: in direct buried, duct, aerial, and submarine applications. They are also easily modified and reinforced e.g. against harsh installation and environmental stresses. In one modification known as Spiral Space[®], the non-metallic core itself is designed and manufactured to carry more stresses and strain so that minimal amount of reinforcements is needed for easy installation conditions.⁵ The advent of access network cables and the slow but steady move towards Fiber To The Home applications creates a need for cables with new properties. We believe, that with new types of modification, the central loose tube is still a valid concept for these applications.

New cable features offered by cone extrusion

As an optimal and gentle processing method (see above), cone extrusion offers a major advantage for the manufacture of non-metallic fiber optic cables: a wide range of polymers with diverse functional properties can be processed simultaneously and combined in a single process step. Relatively wide variation in layer thicknesses is also possible which allows tailoring of the mechanical properties of the cables without significant effect on the final dimensions. Moreover, the cone extruder generates, with its rotors, a helical melt flow field, which makes it easier to orientate fibrous polymers and control their mechanical properties.

Possibilities offered by cone extrusion:

- combination of different functional properties and polymers
- completely new cable designs
- whole cable made by coextrusion in one process step
- versatility in multilayer sheathing
- structural elements composed of several layers

Examples of the new fiber optic cables:

- Small-dimension, lightweight non-metallic fiber optic cables
 - moisture buffering, reinforcement, and temperature stability
 - suitable for access network installations, made e.g. by blowing into tubes
- Non-metallic indoor & indoor/outdoor cables
 - optimized fire performance and mechanical properties
- Multilayer sheaths
 - combinations of different materials & properties
 - e.g. termite and rodent resistant, chemically resistant, and fire retardant constructions
- Shot gun resistant multilayer structures
 - (HDPE/PA12/PA12/PA12)⁶
- Several other non-metallic cables, cable cores and multilayer sheaths
 - for direct burying, duct, or aerial installations
 - a wide range of mechanical properties
 - for various environmental conditions

Example 1: Small-dimension, lightweight non-metallic fiber optic cables

A new type of access network systems is being presented elsewhere at this conference.⁷ The authors describe an ingenious way of installing and branching tubes and cables by blowing into a duct network. The cables required are lightweight, small-dimension / metallic and non-metallic cables with gel filling and normally up to 12 or 48 fibers. We now describe cables suitable for this purpose and their manufacture by cone extrusion technology.

Figure 3a shows the design of a multilayer fiber optic cable suitable for blown access networks. The cable, which consists of four functional layers, is made with a two-rotor cone extruder in one step. Polyamide (PA) or polybutylene terephthalate (PBT) is used for the thin innermost layer to give a smooth inner wall and good protection for the optical fibers. A special grade of thermotropic liquid crystalline polymer (LCP) is added as an intermediate layer to give the cable the required stiffness, strength, and stability. The LCP also exhibits good moisture buffering properties. This type of LCP can be extruded like thermoplastic polymers, but already in molten state the long, rigid polymer chains are oriented in the flow direction due to the elongational flow field. The orientation is maintained during cooling resulting in a composite-like fiber structure. A variety of different polymers can be used as an outer sheath to guarantee good installation properties for the cable, e.g. low friction to contribute to easy blowing into a small diameter tube. An extremely thin tie layer bonds together the LCP and sheath layers. To maintain and enhance the natural tendency of the cone extruder to generate a spiral flow field for the polymer melt, we introduced a rotating mandrel tip. This allowed better control of the fiber orientation and mechanical properties of the LCP layer, i.e. a good balance between strength and flexibility was achieved. The rotating tip created clear helical orientation in the inner layers (PA and LCP) and divided the LCP into extremely thin laminar phases with decreasing orientation angles from inside outwards.

Similar cable designs as described in this example may be used in other applications. For example, smaller ones may be used as stranded multilayer buffer tubes for special applications. A bigger one, in turn, may serve as a core for special cables such as OPGW.

Table 2. Description of layers in the cables of Example 1 (see text and Fig. 3a).

Number of layer	Layer	Function
1 (<i>innermost</i>)	polyamide	protection of optical fibers
2	LCP	mechanical strength & stability, moisture buffering
3	adhesive polymer	tie layer
4 (<i>outermost</i>)	outer sheath	protection, low friction

Table 3. Properties of a smaller 12-fiber cable.

Property	Typical value	Note
<i>tensile strength</i>	100 – 500 N	allowed strain of the fibers up to 0.3%
<i>minimum bending radius</i>	25 mm	with no damage to the components
<i>temperature range</i>	-40 – +70 °C	max. allowed attenuation increase < 0.05 dB/km
<i>crush resistance</i>	500 – 1000 N/100mm	with no damage to the components
<i>maximum weight</i>	< 10 kg/km	
<i>maximum diameter</i>	< 4 mm	

Table 4. Properties of a larger 48-fiber cable.

Property	Typical value	Note
<i>tensile strength</i>	500 – 1000 N	allowed strain of the fibers up to 0.3%
<i>minimum bending radius</i>	40 mm	with no damage to the components
<i>temperature range</i>	-40 – +70 °C	max. allowed attenuation increase < 0.05 dB/km
<i>crush resistance</i>	500 – 2000 N/100mm	with no damage to the components
<i>maximum weight</i>	< 25 kg/km	
<i>maximum diameter</i>	< 6 mm	

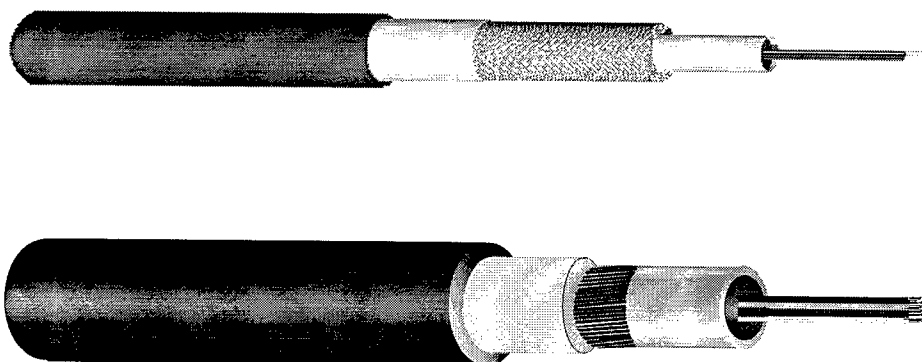


Figure 3. Schematic drawings of the cables of a) Example 1 (above; see Tables 2-4) and b) Example 2 (below; see Tables 5 and 6).

Example 2: Non-metallic indoor and indoor/outdoor cables

Cables employed in access network applications need to meet the traditional requirements set for both indoor and outdoor cables. Normally, a good combination of fire performance, mechanical properties, and thermal stability is required. We have developed new indoor and indoor/outdoor access network cables with multilayer structures based on cone extrusion technology. The example presented here describes one cable type with 12 or 24 fibers for indoor application. For this design the fiber count ranges up to 96 fibers. The basic features are provided by a multilayer sheath, which means that the same principles can be applied for all types of cable cores (central loose tube, stranded tubes, slotted core). In the stranded designs, the loose tubes may also consist of two layers to improve the fire performance.

Halogen-free low-smoke fire retardant (HFFR) materials are polyolefin-based compounds with high degree of mineral filling. The most common grades are based on aluminum hydroxide, which is sensitive to high temperatures. In processing of these compounds in a conventional extruder,

a lot of frictional heat is created due to the high filler loading. Cone extrusion has proven to be an optimal processing technology for these compounds thanks to its basic characteristics, low shear forces and short residence time for the melt. These features together with the multilayer concept makes it possible to use also materials, which have been traditionally difficult to process.

In our example (Fig. 3b, Tables 5 and 6) a pre-made cable core (polyolefin-based buffer tube with optical fibers and filling gel) surrounded by reinforcing fibers was fed through a two-rotor cone extruder and two HFFR sheath layers were coextruded on it. The multilayer feature makes it possible to utilize all four feeds to optimize material output for each individual layer and to include an adhesive layer if desired.

As suggested by our examples, cone extrusion is a versatile technology for making diverse multilayer structures comprising different materials and layer thicknesses. For access network applications it offers several possibilities to tailor non-metallic cable designs according to specific customer requirements.

Table 5. Description of layers in the cable of Example 2 (see text and Fig. 3b).

No. of layer	Material	Function
1 (innermost)	buffer tube (polyolefin)	fiber protection
2	tensile elements (fibers)	tensile strength
3	HFFR 2	high fire retardance
4 (outermost)	HFFR 1	mechanical properties & fire retardance

Table 6. Properties of an indoor cable with 12 or 24 fibers.

Property	Typical value	Note
Tensile strength	500 N	allowed strain of the fibers up to 0.3%
Minimum bending radius	100 mm	with no damage to the components
Temperature range	-15 – +70 °C	max. allowed attenuation increase 0.1 dB/km
Crush resistance	2000 N / 100 mm	with no damage to the components
Fire retardance	IEC 332-1 IEC 332-3, class C	
Outer diameter	10.5 mm	

CONCLUSIONS

A range of new lightweight non-metallic fiber optic cables is being developed. The idea is to simplify cable concepts and manufacturing processes by combining advanced thermoplastic materials with different functional properties through coextrusion in a single process step. This is made possible through novel cone extrusion technology.

Cone extrusion allows gentle combined processing of diverse materials. Many advantages are offered over conventional screw extrusion. In addition to the availability of multilayers, layer thicknesses can be easily varied and melt temperature and material orientation controlled. One particularly important feature is the symmetric material flow without melt distribution, which leads to homogeneous, seamless layers. Thanks to the versatility, cable designs can be tailored according to particular customer needs. Multilayer sheathing or multilayer structural elements for cables can be made, or the whole cable can be manufactured in a single extrusion step. Products consisting of one to four layers can be produced with the extruder described in this paper, while multirotor extruders can be constructed for more complex applications.

Two examples of new stabilized and buffered non-metallic fiber optic cables for access network applications have been presented above. Different combinations of functional properties such as mechanical strength, moisture barrier, fire retardance, and wear resistance were achieved by incorporating appropriate materials. Increasing demand for lightweight duct cables for access network as well as the need for optimal properties for indoor cables, make cables prepared by cone extrusion highly attractive.

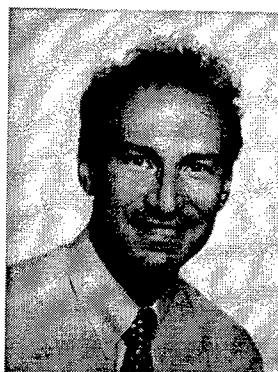
ACKNOWLEDGMENTS

Mr. Kari Kirjavainen, the inventor of the cone extruder, is thanked for his keen interest in and contributions to the development. Thanks are extended to all colleagues at NK Cables and Nextrom who have participated in the R&D work.

REFERENCES

1. K. Kirjavainen, Extrusion Method: Apparatus and Product, *Pat. No. WO 89/11961*, 1989.
2. K. Valta, S. Syrjälä, M. Karttunen, R. Phillips, and K. Kirjavainen, Cone Extruder: Novel Method For Multilayer Extrusions, *Plastics, Rubber and Composites Processing and Applications*, Vol. 27 (1998) No. 9, 400-406.
3. U. Hochstrasser, R. Phillips, and C. Petit, Conex: A Revolutionary Concept for Improved Multilayer Extrusion, *Wire Industry*, Vol. 66, (1999) No. 783, p. 187-190.
4. R. Phillips, Multilayer Conical Extrusion: A New Challenge for Film Blowing, *6th European Polymers, Laminations & Coatings Symposium*, Copenhagen, Denmark, June 7-8, 1999, p. 159-166.
5. T. Räsänen and J. Ravela, New Single Loose Tube Cable with Spiralling Channel in Finnish Field Trial, *39th International Wire and Cable Symposium*, Reno, USA, 1990, p. 412-417.
6. M. Hochuli, Ballistic Protection of Aerial Cables: A New Economical Solution with a Special Impact Modified Polyamide, *45th International Wire and Cable Symposium*, Reno, USA, 1996, p. 817-820.
7. W. Griffioen, A. van Wingerden, and C. van 't Hul, Versatile Outside Plant Solution for Optical Access Networks, *This conference*.

AUTHOR



Dr. Markku T. Heino
NK Cables
P.O. Box 419
FIN-00101 Helsinki
Finland

Markku Heino received the degree of M.Sc. in Chemical Engineering in 1990 and the degree of Dr. Tech. in Polymer Technology (Blends of Thermotropic Main-Chain Liquid Crystalline Polymers and Thermoplastics) in 1994 at Helsinki University of Technology, Finland. Before joining NK Cables (at that time Nokia Cables) in 1996 he worked as Research Scientist and Project Manager in the Laboratory of Polymer Technology at the Helsinki University of Technology. Currently, as R&D Manager at NK Cables (NK Communications), he is responsible for the R&D of polymeric materials for telecom cables.

Development of a Newly Designed Ultra High Fiber Count Ribbon Cable with Folder Units

Oh-Joon Kwon, Yong-Han Jeon, Sung-Hun Kim, Kwang-Joon Lew

Fiber Optic R&D Center, Daewoo Telecom, Gajwa-Dong, Seo-Gu, Incheon-city, Korea

Phone: +82-32-580-3869, Fax: +82-32-580-3396, E-mail address: ojkwon7@moon.daewoo.co.kr

ABSTRACT

A newly designed folder-unit type cable is introduced as a solution to produce high fiber count cable with easy, simple and low cost manufacturing method. The folder-units keep a flat shape before being inserted into a specially designed die in the stranding line. This flat shape gives merits in manufacturing and processing conditions as follows: 1. The folder-unit is manufactured very easily compared with U-groove. 2. The folder-unit pay-off reels are compact. 3. The stranding line is simple and small space is needed to install folder-unit pay-off machines. Especially, this flat shape makes it possible to wind much longer length on the much smaller pay-off drum as compared with U-groove type. This means we do not need to replace the folder-unit reels often and the total manufactured cable length, which can be accomplished continually at one time without a line stop, is much longer than that of U-groove type. These processing improvements were made to allow for the manufacture of the folder-unit type hybrid 2000-fiber ribbon cable. This prototype showed excellent performance characteristics during all tests.

INTRODUCTION

The emerging multimedia access network requires small diameter, high fiber count cable through the limited duct space specially, "in metropolitan areas" in the feeder line in the optical access network. To meet these requirements, it is necessary to induce ribbon type cable more than loose tube stranded cable. From the former published papers(1-2), we have found 30% or more increase of fiber density in ribbon fiber cable with better additive properties

when comparing with loose tube stranded cable.

Even though adopting these basic demands, it is clearly needed to reduce the manufacturing cost and to make the manufacturing process simple by changing the fundamental structural components or by using other methods.

To produce high fiber count ribbon cable, slotted rod and U-groove components are required. Various fiber counts U-groove & slotted core cables were previously proposed and developed.(3-7) Two kinds of cable types, U-groove and slotted core cable can be compared in manufacturing of the 1000-fiber count cable. The cable diameter, manufacturing difficulties of each component, and manufacturing cost of cable have to be considered. First, the cable consisted U-grooves has a little larger cable diameter than slotted rod cable. Second, when comparing the manufacturing difficulties of each component, both U-groove and slotted-rod, there are several factors which make difficult to manufacture of each component. U-groove is more influenced by gravity on the extrudate and by differential cooling problem which caused the deformation of extrudate than slotted rod. Otherwise, since slotted rod is extruded with pitch, it is very difficult to control the dimension of many grooves and the constant slot pitch. Finally, The manufacturing cost is one of the most important problem to be solved. If we use slotted rod, we do not need to invest to additional machines but in case of U-groove, U-groove pay-offs are additionally needed.

From the above, we can think slotted core type is better than U-groove in cable diameter and in cable manufacturing cost aspect. But both of components have problems to be solved in

manufacturing methods. To make high fiber count cable over 1000-fibers, U-grooves are necessary for outer layer. Therefore, we have developed a new method to overcome the problems of slotted rod and U-groove. In order to produce low and high fiber count cable with easy, simple and low cost method, we have introduced the folder-unit.

In this paper, we present the design, manufacture and testing of a slotted rod/folder-unit hybrid cable capable of incorporating up to 2000 fibers with 8-fiber ribbons containing 250 μ m OD fibers. A cross-section of the cable with the maximum complement of fibers is shown in Fig. 1. In this cable, the inner core is the core of the 1000-fiber cable with stacks of 10 ribbons in each slot. Ribbons in the 2000-fiber cable contain 8 fibers. 15 folder-units and 15 fillers are stranded around a 10-slot rod to construct a hybrid slotted rod core/folder-unit cable. Each folder-unit also contains a stack of ten 8-fiber ribbons. Each layer is wrapped with water-blocking tape. The key challenges in this development program are processing improvements, reducing manufacturing costs and attenuation performance. Improvements in processing and reduction in manufacturing costs were made by introducing folder-units. The challenge of good attenuation performance was met.

This paper will address the design and performance of a hybrid slotted rod/folder-unit cable by focusing on as follows: 1. cable design 2. manufacture of the folder-unit 3. optimization of cable stranding line 4. cable performance

CABLE DESIGN

A slotted core was selected as the inner core of the 1000-fiber cable since it has slightly smaller cable diameter than a folder-unit design. Folder-units are used as the second layer of the cable because they can be easily applied as a second layer. The 2000-fiber design consists of an inner slotted core with 10 slots and 15 folder-unit stranded around the slotted core. Each slot/folder-unit accommodated a stack of ten 8-fiber ribbons. Over both the slotted rod and the layer of folder-units are water-blocking tapes. The nominal cable diameter is 32mm. The overall polyethylene jacket is 25mm thick.

8-Fiber Ribbon

The 8-fiber ribbon which has 0.30mm and 0.32mm thickness were used. It has been known that thin ribbon wall increases sensitivity to microbending and reduces mechanical protection of the fiber. The 0.32mm thick ribbon fiber showed better attenuation performance during temperature test. But no significant differences were found in transmission and mechanical test.

Manufacture of folder-unit

When U-grooves or slotted core components are manufactured, several factors which make difficult to manufacture have to be considered. These factors have been previously discussed in several papers.(8) One of them is the effect of gravity on the extrudate.

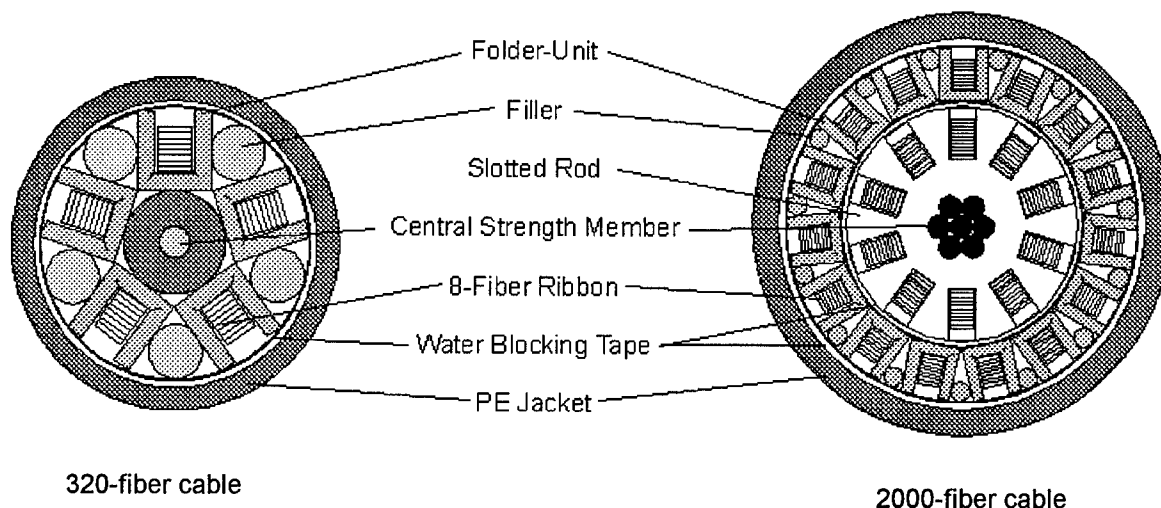


Fig. 1. Cross-sections of Folder-unit & Slotted rod/folder-unit ribbon cables

Both the U-groove and slotted rod are manufactured by profile extrusion which set-up horizontally. Because the each component material has relatively low melt strength, as the material exits from the extruder in a horizontal extrusion set-up, it can deform due to its own weight. When the component size is increased, this effect of gravity is also increased. This makes the slotted rod and the U-groove more difficult to manufacture. When comparing the U-groove and slotted-rod, U-groove is more difficult than slotted rod. In case of slotted rod, central strength member supports the molten material, so strength member decrease the effect of gravity. The differential cooling across the profile is another processing problem to be overcome for U-groove. For producing a lager U-groove, this problem can be more difficult to be solved. To prevent distortion of extrudate, it is necessary to minimize the stresses of extrudate. Otherwise, in case of slotted rod, since slotted rod is extrudated with pitch, it is very difficult to controll the dimension of many grooves and the constant slot pitch.

Since the folder-unit is manufactured in the form of flat type by vertical extrusion setup, even if folder-unit size increase, there is no manufacturing difficulties caused by the effect of gravity on the extrudate and the effect of differential cooling across the profile.

Fig.2. shows schematic of the folder-unit and Fig.3. is schematic of extrusion line for the folder-unit. The friction of ribbon-to-folder unit wall was considered. It is well known that low ribbon-to-ribbon friction is needed to allow slippage of the ribbons relative to each other when a cable is bent. This cable bends cause high fiber strains and large lateral stresses on the ribbon. These strains and stresses cause a fiber reliability issue and unacceptable attenuation increases.

Therefore, we introduced special design on folder-unit wall to reduce friction between ribbon and folder-unit wall. This designed wall provides less contact area to the ribbon and has an angle to increase slippage characteristics. It decreases the friction of ribbon-to-folder-unit wall so that the sensitivity of the fiber to microbending is decreased.

As shown in Fig. 3., the material exits from the extruder in a horizontal extrusion set-up. After cooling, the material passes through an annealing part. Since all polymer materials have elastomeric history, they have tendency to recover their own shape after processing. This causes shrinkage or distortion of processed material. The annealing part prevents this kind of shrinkage or distortion. We introduced specially designed compression rollers after annealing part. The rollers have two roles of making

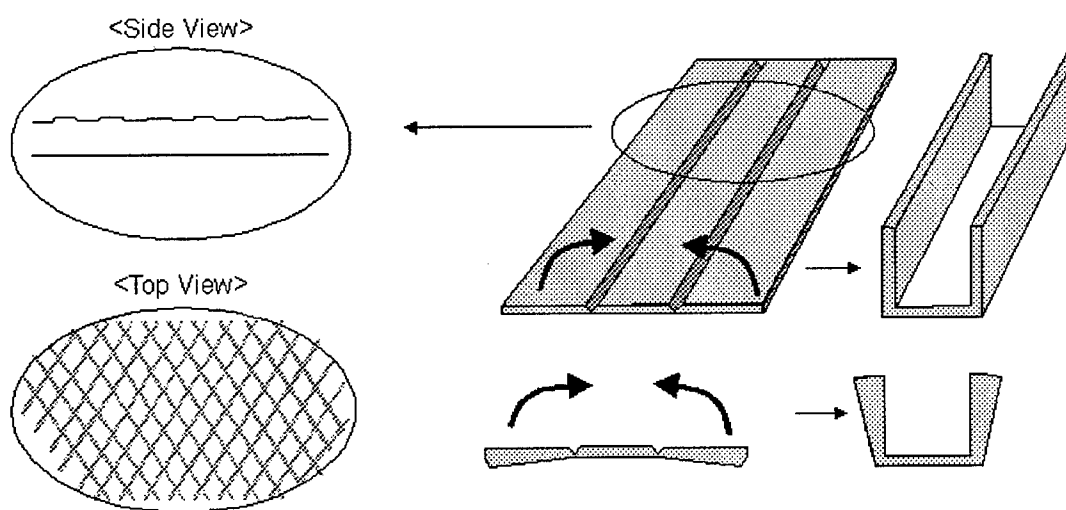


Fig. 2. Schematic of the Folder-Unit

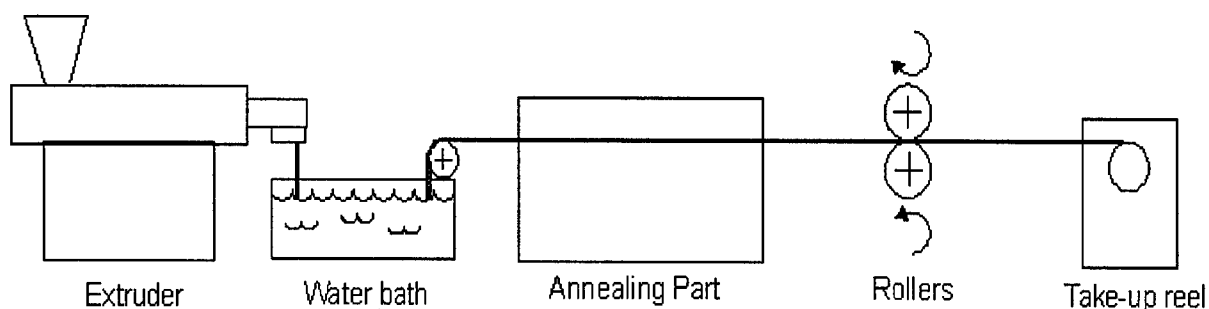


Fig. 3. Schematic of the Extrusion Line for the Folder-Unit.

special design on folder-unit wall and controlling the folder-unit thickness. We could control the folder thickness without difficulties using these rollers.

CABLE STRANDING PROCESS

The flat type folder-unit also allows a small reel to wind a long length of folder-unit and easy winding conditions. When U-groove is wound on reel, the reel size has to be considered to prevent deformation of U-groove shape. If we use relatively small reel to wind U-groove, there is a possibility deformation of U-groove. Compared with U-groove, the folder-unit is not needed to consider the reel size and the problem of shape deformation. This small size reel make possible minimize the size of pay-off machines and the space to install pay-off machines. There is almost no big difference in size between reel wound 2.5km folder-unit and ribbon bobbin. These advantages make much easier and

cheaper to manufacture cable than U-groove type cable. Fig. 4 shows the basic layout the stranding line for the hybrid 2000-fiber cable.

We have tried to simplify a folder-unit stranding process. The folder-unit stranding process must be precise. The layout was designed for the simplicity of organization and the easiness to control ribbon and folder-unit tension. Folder-unit and ribbon are inserted simultaneously into a specially designed die. This folder-unit is folded and formed while passing through this die. We optimized the process conditions to make folder-unit high fiber count ribbon cable in aspect of cost and simplicity of manufacture.

CABLE PERFORMANCE

Transmission Characteristics

The transmission characteristics were measured on 250 fibers after manufacturing. The mean attenuation at 1550nm was 0.20dB/km (Max=0.26dB/km).

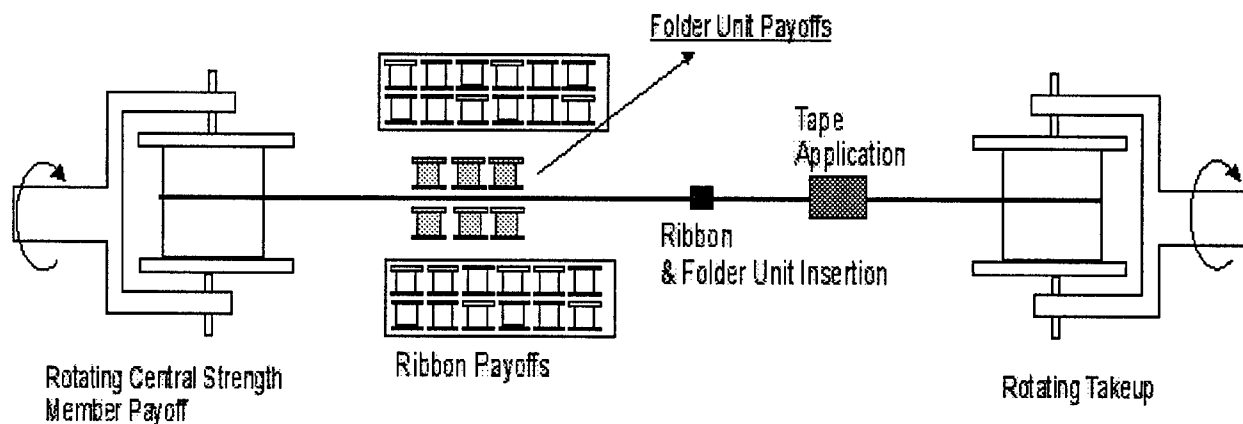


Fig.4. Stranding Line for the Hybrid slotted core/folder-unit 2000-Fiber Cable

At 1310nm, the mean attenuation was 0.34dB/km (Max=0.36dB/km). Fig.5. shows the results of the transmission performance.

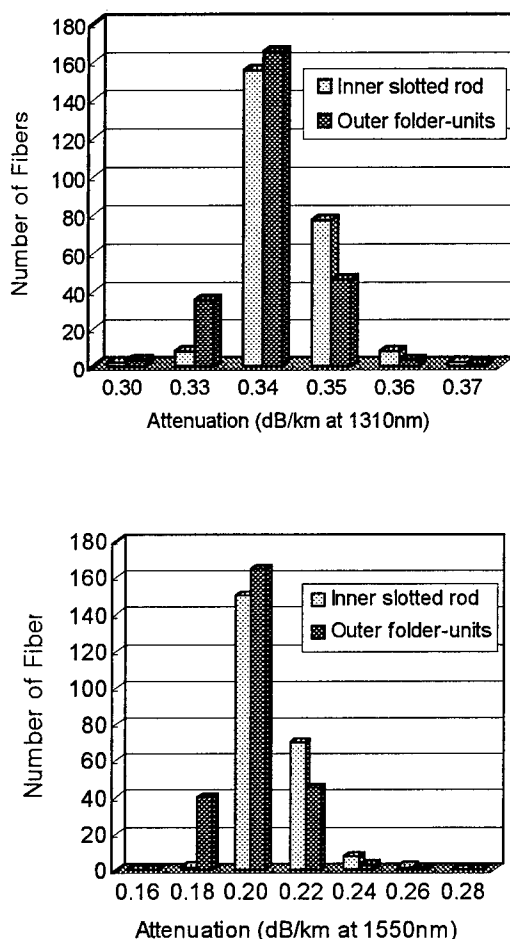


Fig. 5. Transmission characteristics of 2000-fiber cable

Temperature Characteristics

In the 320fibers in each ribbon stack, 30fibers were measured for attenuation change during temperature cycling test. With a filled folder unit and a filled slot, 15 fibers were measured respectively. Edge fibers in the top / bottom ribbons and center fibers in the middle ribbons were monitoring. Especially we focused on the

edge fibers. This cable was subjected to a series of temperature cycles in the range from -30°C to +60°C. But to investigate temperature limits of the cable, it was cycled through a temperature range of -40°C to +70°C. The cable had acceptable attenuation performance during temperature cycling. The maximum attenuation change in 1550nm at -30°C and -40°C was 0.07dB/km, 0.08 dB/km respectively. The mean 1550nm attenuation at -30°C, -40°C was 0.22dB/km and 0.23 dB/km. At +70°C, there was no significant increase in attenuation. The maximum 1550nm attenuation change and the mean 1550nm attenuation at +70°C was 0.05 dB/km and 0.23 dB/km.

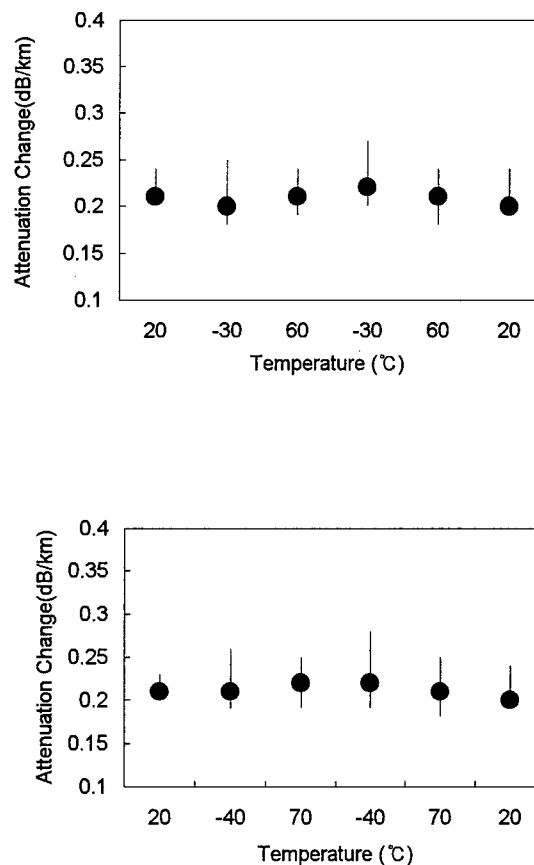


Fig. 6. Temperature characteristics of folder-Units in 2000-fiber cable

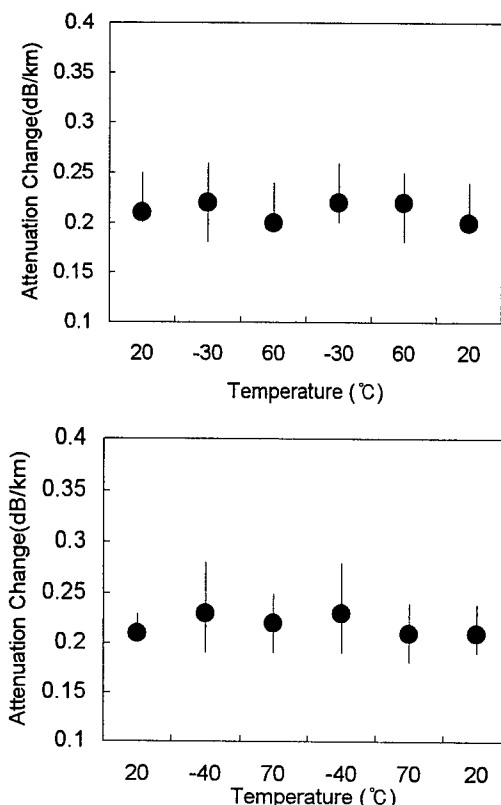


Fig. 7. Temperature characteristics of slotted rod in 2000-fiber cable.

Mechanical Characteristics

Attenuation change was measured at 1550nm during tensile, compression, twist, impact and bending tests.

Tensile strength

The cable was subjected to a test at elongations up to 0.25% of the original cable length, corresponding to a 20m. No increase in attenuation was observed for elongations up to 0.25%. Additionally, to check the elongation limits of the folder unit, it was elongated up to 0.52% and 0.70% using 320-fiber cable. The maximum attenuation change was 0.01dB/km and 0.02 dB/km respectively.

Cyclic Flex

400mm radius mandrel was used for the cyclic flex test. The load on the cable was set to correspond to 0.20% cable elongation. The test was done in the condition of 30cycles/ min. The

maximum attenuation increase observed was 0.02dB/km.

Compression

Lateral loads of 2000N/100mm, 4000N/100mm, 6000N/100mm were applied to the cable. Before measurements were taken, the load on the cable was maintained for 10 minutes. The resultant measurements showed no significant attenuation increase. Furthermore, permanent deformation of folder groove or slotted rod did not occur until a lateral force of 4000N/100mm was reached

Impact

Two kinds of test methods were used to measure attenuation increase and to check deformation or breakpoint of folder grooves. Each method is as follows:

-Method 1: 1M length of column weight corresponding to a load of 1kg, 2kg and 3kg were dropped from the 1M height. The impact points were 10 points with 300mm distance between points and the impact cycles were 3 times in each point.

-Method 2: 6kg column weight was used. The impact height was 150mm and impact cycles were 25 times.

The test results are shown in Table 2.

Fig 2. shows the scheme of test method 1.

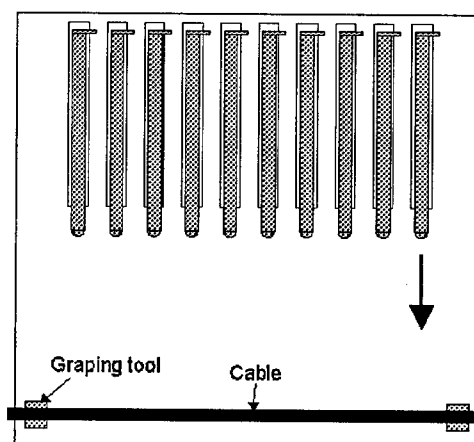


Fig. 8. The schematic of test method 1

Twist

The twist angle was $\pm 90^\circ/\text{m}$ with 25kgf tensile strength. The twist cycles was 10 times. No increase in attenuation was detected during the twist test.

Table 2. Impact Test Results of 320 & 2000-fibers cable.

Type		Max. Attenuation Change (dB/km)	
		320-fiber	2000-fiber
Method 1	1kg load	0.01	0.01
	2kg load	0.02	0.02
	3kg load	0.02	0.02
Method 2		0.01	0.02

CONCLUSION

A newly designed folder-unit type ribbon cable was manufactured as a solution to produce high fiber count cable with easy, simple and low cost manufacturing method. Since the folder-units keep a flat shape before inserting a specially designed die in the stranding line, this flat shape gives merits in manufacturing and processing conditions. This point makes possible high fiber count cable without difficulties. It is necessary to introduce kinds of U-groove components to make 2-layer structure which is very useful to consist of over 1000-fiber cable. Folder-units provided processing improvements and manufacturing cost effects. These were made to allow for the manufacture of the folder-unit type hybrid 2000-fiber ribbon cable. This prototype had excellent performance characteristics during all tests.

REFERENCES

- [1] William J. McCallum, Martin C. Light, Richard S. Wagman "Design and Development of a Compact High Fiber Count Ribbon Cable" *Proceedings of the 44th International Wire and Cable Symposium*, pp.8-14, 1995
- [2] Hideyuki Iwata, Masaru Okada, Jiro Sogame,

HiroYuki Akimoto, Shigeru Tomita, Yutaka Dein "Development of 2000-fiber cable with SZ-stranded U-grooves and Slotted Rod" *Proceedings of the 47th International Wire and Cable Symposium*, pp.34-40, 1998

- [3] Satomi Hatano, Yutaka Katsuyama, Toshinao Kokubun, Kazuo Hogari "Multi-hundred fiber cable composed of optical fiber ribbons inserted tightly into slots" *Proceedings of the 35th International Wire and Cable Symposium*, pp.17-23, 1986
- [4] D. Iwakura, I. Kobayashi, M. Hara, R. Takaoka, E. Konda, Y. Kamikura "Development of stacked ribbon SZ-slotted rod" *Proceedings of the 46th International Wire and Cable Symposium*, pp.793-801, 1997
- [5] R.S. Wagman, P.R. Bark, H.G. Cooke, C.K. Eoll, R.O. Livingston, G.A. Lochkovic, W.W. McAlpin e, F.M. Sears and S.S. Sodhi. "Design Concepts for a 4000-fiber cable with Thinly Coated Fiber" *Proceedings of the 43th International Wire and Cable Symposium*, pp.12-21, 1994
- [6] Shigeru Tomita, Michito Matsumoto, Tetsuro Yabuta and Takuya Ueno "Preliminary research into Ultra High density and High Count Optical Fiber Cables" *Proceedings of the 40th International Wire and Cable Symposium*, pp.8-15, 1991
- [7] Daisuke Iwakura, Ichiro Kobayashi, Masami Hara, Hideaki Kanzaki, Hideyo Hiramatsu, Yasuhiro Kamikura "Design of Ultra high density and high count 2000 optical fiber cable for easy branching" *Proceedings of the 47th International Wire and Cable Symposium*, pp.41-47, 1998
- [8] Frederick M. Sears, Peter R. Bark, Mary A. Clarke, Harriet G. Cooke, Christopher K. Eoll, Larry E. Herman, William S. Jackman, Ron O. Livingston, Shami S. Sodhi and Richard S. Wagman "Design and Performance of a 3200-fiber hybrid SCR/U-groove cable using 16-fiber ribbons" *Proceedings of the 45th International Wire and Cable Symposium*, pp.645-653, 1996

SPEAKER BIOGRAPHY



Oh-Joon Kwon
DAEWOO TELECOM Ltd.
531-1, Gajwa-Dong, Seo-Gu

He is senior engineer of Fiber Optic R&D Center. He graduated from INHA University with M.S.degree in the polymer science & engineering in 1997 and joined DAEWOO TELECOM.LTD. He is working as the cable designer in the cable part.

HFFR^a Cable Materials: Trends in Silane Coupling Agent Technology

^a halogen-free flame-retardant

Dr. Helmut Mack
Research • Development • Technical Service Silanes
DEGUSSA-HÜLS AG
SIVENTO DIVISION

"Much ado about nothing"
William Shakespeare

Abstract

Halogen-free flame-retardant (HFFR) cable materials occupy a rapidly growing and specialised area of cable production. Silane coupling agents greatly influence physical, electrical and burning performance of the final HFFR cable material.

Most important issues of HFFR technology will be covered. In addition to addressing traditional HFFR cable materials, the presentation will focus on new directions to get the maximum benefit from amino- and vinylsilanes in HFFR cable materials.

Basic Silane Chemistry

Silanes were introduced in the 1940s and have since become one of the most widely used coupling agents. Silanes offer tremendous advantages for virtually all market segments involving polymer-filler interactions; they improve physical and electrical properties and enable polymer composites to be used where they otherwise could not.

Aside from ups and downs the total volume of silane consumption has been increasing constantly over the last 15 years. By 1998, world-wide silane sales approximated \$ 600 million.

Silanes act as

- coupling agents ("molecular bridges") between inorganic materials (glass fibres, mineral wool, metals, mineral fillers such as aluminum trihydrate, magnesium dihydrate, silica, clay, talc, mica, and wollastonite) and polymers (elastomers, thermosets, and thermoplastics),
- surface modifiers

of inorganic and organic materials. Employment leads to hydrophobation, oleophobicity, organophilic adjustment of surfaces, improvement of wetting properties, better dispersion properties, and anti corrosion,

- crosslinking agents in the moisture curing process of silicones, polyurethanes, copolymers, and polyolefines, especially PE-LLD for cable sheathing applications (SIOPLAS[®] or MONOSIL[®] process),
- comonomers in polymer synthesis reactions such as free radical polymerisation,
- cobinders in scratch-resistant paints, coatings, and varnishes.

Silanes are typical organic substances, sensitive to hydrolysis, soluble in common organic solvents and, in a few cases, in water.

The effect of silanes as coupling agents is determined by their special molecular structure. The silicon as the center is combined with two different functional groups: organofunctional group Y and silicon-functional group OR (see Figure 1).

The organofunctional group Y that links with the polymer is bound tightly to the silicon via a short carbon chain. This group has to be carefully chosen to ensure maximum compatibility with the polymer system. Bonding to the polymer takes place by chemical reactions or physicochemical interactions. The silicon-functional groups OR, usually three alkoxy groups, can be stepwise hydrolysed liberating the corresponding alcohol. The small amount of water required for hydrolysis, is commonly supplied by trace moisture on the surface of the inorganic material or in the air,

from a pre-hydrolysis step, or from moisture inside the polymer. Upon hydrolysis the inactive silicon-functional groups OR are converted to the active silanol form. In successive curing steps these Si-OH groups can react with active surface OH groups of an inorganic substrate building up stable chemical Si-O-substrate bonds. The coupling effect of silanes can be explained as follows (see Figure 2).

Bonds are established through reaction or interaction of the organofunctional group of the silane, which link the silane – as bridge from the inorganic substrate – to the polymer. Here the polymer determines the identity of the organofunctional group of the silane.

General: Silanes in HFFR cable compounds

It is now almost 20 years since the first HFFR compounds were reported at the International Wire and Cable Symposium. Since that time there have been a number of major fire infernos around the world which have emphasised the need for materials with improved performance in a fire. The beneficial fire properties offered by HFFR cables are widely accepted around the world. Cables for installation in areas where smoke and acidic or toxic fumes present particular problems are a prime example.

The first generation of these improved HFFR materials possessed excellent fire and smoke properties, but were physically weak and were slow to process when compared with the PVC compounds which they were replacing.

HFFR compounds of consideration are those based on the incorporation of large amounts of aluminum trihydrate (ATH) or magnesium dihydrate (MDH) in ethylene vinylacetate copolymers (EVA) or EVA/polyolefine polymer blends.

In todays HFFR compounds silanes function as coupling agents, viscosity modifiers, and hydrophobing agents, resulting in improved physical and electrical properties (wet and dry) of the final HFFR compound.

A typical commercial HFFR compound range includes sheathing, insulating, bedding, and filling grades used in the manufacture of a variety of cables.

The general profile of European HFFR compound usage shows a dominance in

sheathing applications. 55% of the actual European HFFR compound production is consumed in the manufacture of telecommunication cables. Power cables consumed 40% and specialty cables 5 % (mining etc.) of the 1998 European HFFR compound production. It is estimated that this general profile of HFFR compound usage will maintain the current distribution.

Growth in HFFR compound demand primarily comes in existing PVC applications. A further factor assisting growth in HFFR compound demand is that HFFR materials are considered by cable manufacturers to be a route for increased profitability. Cable companies hope that the more specialized HFFR materials will enable them to increase their margins on cables by using these HFFR materials. Greatest penetrations have been achieved in markets where fires have raised concern by causing severe damage.

42,000 metric tonnes of HFFR compounds have been consumed by the European cable industry in 1998. The European market is fairly evenly divided between HFFR material sourced from "in house" plants (40% of usage) and HFFR material sourced externally (60% of usage).

Hydrated fillers such as ATH and MDH achieve their flame retardance by decomposing endothermically with the release of water close to the temperature at which the polymers themselves decompose, and do not have the smoke and corrosive gas problems associated with other types of flame retardant. The main limitation of ATH is its relatively low decomposition temperature (about 200°C), which has restricted its use in applications where processing temperatures are above this, notably many thermoplastics. Currently, great interest is being shown in MDH. The attraction of MDH compared to ATH lies in the much higher decomposition temperature (about 300°C). This allows its use in applications such as thermoplastics, which are processed at too high a temperature for ATH.

In order to produce an acceptable HFFR compound at high loadings of 60 to 65%, the filler particle sizes and shapes have to be carefully controlled. This is the prime goal of the ATH and MDH manufacturing process. MDH, for example, normally precipitates as small, thin, platelets with a high specific surface area. Larger, thicker, particles of considerably lower surface area are required for flame retardance applications.

Silanes may be used in cable compounds in a great variety (see Table 1).

Next to chlorosilanes for optical fibres, methacryl-, vinyl, amino-, epoxy- and mercaptosilanes are used as coupling agents in mineral-filled cable compounds. Vinylsilanes, mainly vinyltrimethoxysilane, DYNASYLAN® VTMO, are used for the production of moisture curable cable compounds.

Besides polymer, filler, silane and additive choice the compounding itself has a great influence on the final HFFR compound properties. Homogeneous dispersion of the filler in the polymer matrix avoiding filler agglomerates is essential.

The BUSS cokneader is known for its high filler loading capacity, controlled and equal shear mixing and precise temperature control. A wide range of HFFR formulations can be handled by varying dosage, speed, and temperature without retooling.

Twin-screw extruders equipped with counter-rotating screws allow high throughput and gentle handling of the polymer, but do not build up enough laminar shear needed for high filler loadings. Twin-screw extruders with co-rotating screws allow better filler dispersion. Generally the filler is incorporated via a second feeder after the polymer has been melted.

Internal mixers can be used, but it may be difficult to achieve the optimum parameter settings.

Aminosilanes in HFFR Cable Sheathing Compounds - Test Series A

The beneficial effects made possible by silane surface treatments make product modifications an area of very active research for ATH and MDH used in HFFR materials. DEGUSSA-HÜLS connect their know-how with the customers competence in the sense of "responsible care" for being able to offer silanes available throughout the world that work, are toxicologically safe and have improved properties.

The most serious disadvantage of ATH and MDH is the high loadings required for flame retardation. Such high levels result in severely compromised melt processability and poor physical properties.

Aminosilane bound surface treatments

surmount these problems by increasing the filler-matrix adhesion and reducing the surface energy of the filler.

This HFFR study was undertaken to demonstrate the advantages of using aminosilane treatments on ATH which is compounded into an EVA matrix (see Table 2).

The EVA selected for this study was supplied by EXXON CHEMICAL and contains 19% w/w vinyl acetate (density 0.943 g·cm⁻³, melting point 83°C). This EVA grade is particularly used by the cable industry. The flame retardant filler was obtained from ALUSUISSE, MARTINSWERK and is a fine precipitated uncoated ATH grade (specific surface area 4 m²·g⁻¹, d₅₀ 1.3 to 2.2 µm). The stabiliser was supplied by CIBA SPECIALTIES and due to its sterically hindered phenolic structure acts as a primary antioxidant showing rapid reaction with radicals.

The EVA polymer was dried 1 hour in an air ventilated oven. The silane was absorbed onto the EVA polymer for 1 hour at ambient temperature prior to compounding. The stabiliser was dry blended with the filler.

A BERSTORFF ZE 25 twin-screw co-rotating extruder was used for compounding. The screw design was optimised for HFFR compounding. Length/diameter ratio was 33 and the screw diameter was 25. Two hoppers with gravimetric dosers for polymer/silane and filler/stabiliser were employed. Test samples were made from extruded tapes.

Table 3 summarises the physical properties obtained for the EVA/ATH composites stated.

The use of alkylsilanes like DYNASYLAN® PTEO (*n*-propyltriethoxysilane) results in improved physical characteristics of the final HFFR compound compared to HFFR compounds where no silane is employed. Vinylsilanes like DYNASYLAN® 6490 (oligomeric vinyltrimethoxysilane, DYNASYLAN® VTMO) improve physical properties in the absence of peroxide, too. Alkyl- and vinylsilane dispersant type ATH treatment affords an increase in elongation, but a reduction in tensile strength relative to untreated ATH together with an increase in LOI and MFI. These effects can be associated with enhanced freedom of ATH dispersion and a reduction in ATH - EVA interaction. This clearly defines the role of an alkyl- or vinylsilane in an HFFR compound as a dispersant only which

reduces ATH surface energy. Due to the hydrophobic character of alkyl- and vinylsilanes, water uptake is significantly reduced leading to improved electrical properties of the final HFFR compound in humid environments.

Incorporation of aminosilanes results in increased tensile strength which is characteristic of enhanced ATH - EVA adhesion. The use of a peroxide is obviously not required. There is strong evidence for aminosilane grafting onto the EVA polymer during extrusion. Due to the polar character of the amino group, water uptake of the final HFFR compound is significantly higher compared to non-polar alkyl- and vinylsilanes.

Generally, good ATH dispersion in the polymer phase leads to excellent HFFR compound viscosities (MFI) and high tear strength.

The use of 3-aminopropyltriethoxysilane, DYNASYLAN® AMEO became an industrial standard for the production of reliable thermoplastic HFFR compounds within record time. As clearly demonstrated in Table 3 the employment of 3-aminopropyltriethoxysilane, DYNASYLAN® AMEO is no longer the ultimate aminosilane solution and HFFR industry can now move ahead.

The aminosilanes DYNASYLAN® AMEO-T and DYNASYLAN® 1204 show dramatic improvements in the final HFFR compound. The goal of excellent physical properties, resulting in high tensile strength in combination with high elongation at break, is perfectly achieved. The optimum performance can be achieved by employing either DYNASYLAN® AMEO-T or DYNASYLAN® 1204.

Moreover, the use of DYNASYLAN® 1291 provides the highest level of overall HFFR compound performance. DYNASYLAN® 1291 helps to reduce the water uptake significantly. Insulation breakdown of HFFR compounds can be minimised by employing DYNASYLAN® 1291.

Vinylsilanes in HFFR Cable Sheathing Compounds - Test Series B

Vinyl- and methacrylsilanes are employed in thermoplastic HFFR compounds. Coupling of the unsaturated silane to the polymer is achieved by peroxide. HFFR compounds based on unsaturated silanes are more sophisticated in production and require a higher level of

compounding and processing knowledge than aminosilane containing HFFR compounds.

Vinyl/peroxide ratio has to be watched very carefully. If not, grafting of the vinylsilane onto the polymer is not efficient or pre-crosslinking of the HFFR compound in the extruder or kneader occurs. Scorch is the consequence.

For thermoplastic HFFR compounds the use of vinylsilanes is of great interest for price reasons. DEGUSSA-HÜLS has commercialized a new generation of oligomeric vinylsilanes for HFFR compounds as a further development of vinyl-tris(2-methoxyethoxy)silane, DYNASYLAN® VTMOEO. Oligomeric vinyltrimethoxysilane, DYNASYLAN® 6490 and oligomeric vinyltriethoxysilane, DYNASYLAN® 6498 are tailored for HFFR compound applications.

Upon reaction with water a significantly reduced quantity of hydrolysis alcohol (corresponding to VOC) is released compared to the standard monomeric vinylsilanes. The characteristics of the new generation of vinylsilanes are a low viscosity and high boiling and flash points. Low silane volatilities have been realised. Easy handling and safe processing in standard extruders or kneaders is provided. No investment or change of equipment is necessary.

DYNASYLAN® 6490 and DYNASYLAN® 6498 are vinylsilane concentrates with a high vinyl activity leading to increased physical properties of HFFR compounds (see Table 4).

Series B of the HFFR study was conducted in the same way as series A to demonstrate the advantages of using oligomeric vinylsilane treatments on ATH which is compounded into an EVA matrix (see Table 5).

The dicumylperoxide selected for this study was supplied by AKZO CHEMICALS. Decomposition starts at approximately 170°C. The active oxygen content is approximately 5.8%.

To optimise vinylsilane/peroxide ratio a DYNASYLAN® 6490 screening has been conducted. Table 6 summarises the physical properties obtained for the EVA/ATH composites stated.

The use of oligomeric vinyltrimethoxysilane, DYNASYLAN® 6490 results only in slight improvements of the physical properties of the

final HFFR compound in the absence of peroxide. In the presence of peroxide the overall picture changes dramatically. The use of oligomeric vinyltrimethoxysilane, DYNASYLAN® 6490 gives quite dramatic improvements as the ATH couples to the EVA polymer, increasing physical properties and reducing water pick-up both through increasing crosslink density and also by rendering the compound hydrophobic.

Even at a low dosage level of 1.6 phr oligomeric vinyltrimethoxysilane, DYNASYLAN® 6490 performs very well. At these low silane dosages the vinyl/peroxide ratio has to be watched very carefully. At a silane dosage of 1.6 phr the peroxide dosage should not exceed 0.04 phr because of the risk of scorch! It is clearly demonstrated that an increased silane dosage reduces the risk of scorch significantly.

The properties of oligomeric vinyltrimethoxysilane, DYNASYLAN® 6490 clearly outmatch those of commonly employed monomeric vinyltrimethoxysilane, DYNASYLAN® VTMO or monomeric vinyltriethoxysilane, DYNASYLAN® VTEO (see Table 7). It is evident that oligomeric vinyltrimethoxysilane, DYNASYLAN® 6490 gives the best overall HFFR compound performance even at lowest silane dosages compared to monomeric vinylsilanes.

Correct use of oligomeric vinyltrimethoxysilane, DYNASYLAN® 6490 reduces compound viscosity and results in good melt flow rates (MFI) and a smooth, defect-free surface.

Conclusions

DEGUSSA-HÜLS' amino- and vinylsilanes perform as excellent coupling agents in ATH-filled, EVA-based HFFR compounds.

The use of aminosilanes in thermoplastic HFFR compounds leads to outstanding physical properties. New commercial aminosilanes such as DYNASYLAN® 1291 achieve improved mechanical and electrical properties, especially upon moisture and temperature stress. Since the type of organofunctional group is a critical factor in HFFR compounds, the use of DYNASYLAN® 1291 achieves the optimum performance.

Oligomeric vinylsilanes such as DYNASYLAN® 6490 offer safe handling and perform best in vinylsilane/peroxide based thermoplastic HFFR compounds. The goal of a perfectly dispersed discontinuous filler phase in

the continuous polymer phase is easily, quickly, and perfectly achieved through oligomeric vinylsilane surface modification. DYNASYLAN® 6490 offers excellent adhesion promotion, plus exhibiting a strong hydrophobic effect. Vinyl/peroxide ratio is crucial for success.

Careful silane use can afford optimal balance of physical, rheological and flame retardant properties of the final HFFR compound.

DEGUSSA-HÜLS' Technical Service Specialists are ready to help you develop your own applications for these products, achieving properties that can be obtained in no other way.



Dr. Helmut Mack
Research, Development
and Technical Service Silanes
DEGUSSA-HÜLS AG
SIVENTO DIVISION
P.O.Box 1260
Untere Kanalstrasse 3
D-79602 Rheinfelden
Germany

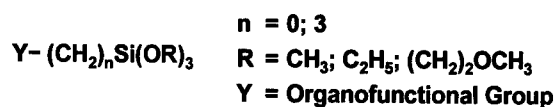
Tel.: +49 7623 80233
Fax: +49 7623 80571
E-mail: helmut.mack@degussa-huels.de

Dr. Helmut Mack received his Ph.D. in Chemistry from the University of Munich, Germany. He then joined the Technion in Haifa, Israel to develop novel high performance polymerisation catalysts. In 1996 he assumed a position at HÜLS AG, at their Silane Research, Development and Technical Service Center in Rheinfelden, Germany. His responsibilities include the technical business support of silanes in the filler, adhesives and sealants and filled elastomeric and thermoplastic field.

Addendum

Figure 1: Structures of Silanes

Most frequently quoted Silanes in Papers and Patents (1998)



DYNASYLAN®	Structure
AMEO (A-1100) 3-Aminopropyltriethoxysilane	
MEMO (A-174) 3-Methacryloxypropyltrimethoxysilane	
GLYMO (A-187) 3-Glycidyloxypropyltrimethoxysilane	

Figure 2: Basic Effect of Silanes - Coupling

Choice of Silane Coupling Agent for specific End Use

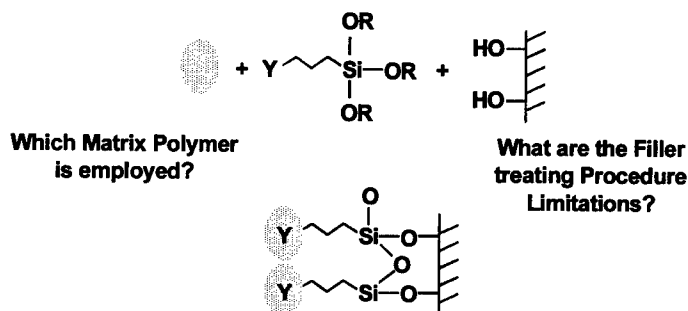


Table 1: DYNASYLAN® Silanes for Cable Compounds

Type of Cable Compound	DYNASYLAN® Silane	Organofunctional Group
mineral-filled (EPDM, EPR, EVA, PE)	VTMO	vinyl
	VTEO	vinyl
	VTMOEO	vinyl
	6490	vinyl
	6498	vinyl
	6598	vinyl
	6590	vinyl

Type of Cable Compound	DYNASYLAN® Silane	Organofunctional Group
moisture-cured (various PE types, mainly PE-LD and PE-LLD)	VTMO VTEO SILFINs	vinyl vinyl vinyl blends
mineral-filled HFFR (EVA, PP, polymer blends, EPDM, PE)	AMEO AMEO-T 1204 1189 1291 MEMO 5821 5823 GLYMO MTMO	amino amino blend amino blend sec. amino amino blend methacryl methacryl methacryl blend epoxy mercapto

Table 2: Study HFFR Compound Formulation

Study Formulation	Amount (phr)
ATH (MARTINAL® OL-104/LE)	160
EVA (ESCORENE® UL 00119)	100
Stabiliser (IRGANOX® 1010)	1.0
DYNASYLAN® Silane Coupling Agent	1.5

Table 3: Physical Properties of HFFR Compounds using different DYNASYLAN® Silanes

DYNASYLAN® Silane	Tensile Strength [N·mm ⁻²]	Elongation at Break [%]	Tear Strength [N·mm ⁻¹]	Water Uptake (14 d at 70°C) [mg·cm ⁻³]
PTEO	8.6	245	27.9	1.19
6490	12.3	210	19.1	1.36
AMEO	16.3	200	10.2	4.02
AMEO-T	17.3	220	10.9	3.85
1204	16.6	210	11.6	3.75
1291	16.6	226	12.4	2.40

Table 4: New Generation of oligomeric DYNASYLAN® Vinylsilanes

DYNASYLAN® Silane	VTMO	VTEO	VTMOEO	6490	6590	6498	6598
Viscosity (20°C) [mPa·s]	0.8	0.7	2.8	6	5.8	3.6	4.6
Flash point [°C]	22	38	115	87	110	>100	116
Boiling point [°C]	123	158	285	>220	257	240	255

DYNASYLAN® Silane	VTMO	VTEO	VTMOEO	6490	6590	6498	6598
% w/w "Vinyl"	18	14	10	24	10	21	10
Released amount of alcohol after complete hydrolysis of 1 kg [g]	650 (MeOH)	730 (EtOH)	820 (2-methoxy-ethanol)	400 (MeOH)	370 (MeOH)	490 (EtOH)	460 (EtOH)

Table 5: Study HFFR Compound Formulation

Study Formulation	Amount (phr)
ATH (MARTINAL® OL-104/LE)	160
EVA (ESCORENE® UL 00119)	100
Stabiliser (IRGANOX® 1010)	1.0
Peroxide (PERKADOX® BC)	varies
DYNASYLAN® Silane Coupling Agent	varies

Table 6: Physical Properties of HFFR Compounds using DYNASYLAN® 6490

DYNASYLAN® 6490 Amount (phr)	Peroxide Amount (phr)	Tensile Strength [N·mm ⁻²]	Elongation at Break [%]	Tear Strength [N·mm ⁻¹]
1.50	no peroxide	12.3	210	19.1
1.60	0.03	16.8	213	9.9
1.60	0.04	17.4	203	9.7
1.60	0.05	scorch!	scorch!	scorch!
1.85	0.03	16.9	213	11.4
1.85	0.05	17.6	210	10.2
2.10	0.03	16.4	212	10.1
2.10	0.04	17.4	204	9.0
2.10	0.05	17.9	199	8.9

Table 7: Physical Properties of HFFR Compounds using the same Vinyl Content

DYNASYLAN® Silane	Silane Amount (phr)	Peroxide Amount (phr)	Tensile Strength [N·mm ⁻²]	Elongation at Break [%]	Tear Strength [N·mm ⁻¹]
6490	1.85	0.03	16.9	213	11.4
VTMO	2.50	0.03	16.4	192	11.5
VTEO	3.20	0.03	14.3	201	16.4

CONTINUED DEVELOPMENT OF THE PLENUM-OUTDOOR TOTALLY DRY OPTICAL FIBER CABLE DESIGNS.

David A. Keller¹, Jack Rosko¹, Brian Risch², Randy Yoder¹, Bob Overton², Gilberto Camilo² Scott Munday², Bill Charuk¹, Dan Rouse¹

1) Alcatel-Berk-Tek, Fuquay-Varina, N.C., 2) Alcatel Cable, Claremont, N.C.

ABSTRACT

Totally Dry Campus Cables entered crossfunctional capability in three broad areas of Outdoor, Riser, Plenum environments from our 1998 IWCS paper/presentation¹.

The Plenum-Outdoor Cables, having cross-functional cable performance capabilities are beginning to meet the growing demand for the Internet capable desk-to-desk links.

Expanded fiber counts for these point to point building plenum links across an outside plant environment continues to illustrate the benefits of having a cable designed for Indoor and Outdoor use. The design continues to be as fire resistant/retardant meeting the highest rated cable flammability requirements. The cable links also meet specific outside performance and environmental stability requirements.

The 12 fiber central tube design was expanded to a 72 fiber LT design, meeting and exceeding strategic UL targets of peak flame, peak smoke, average smoke and GR-20-CORE targets of cold bend, compression, and temperature cycling attenuation. PVDF and PVC Plenum compounds were combined with water swellable elements to best meet these requirements. Improving on the earlier design, the most rigid industry standards were exceeded with the 72 fiber version.

Dry tubes having WS powder are continued with the 72 fiber design. Our work continues exploring optical fiber performance in 85 C, 85% humidity and water soak, additionally exploring the effect of swellable powder versus gel. The water swellable, totally dry version remained the choice for accessibility, cable preparation, and performance.

Four 72 fiber design variations were UL 910 tested and the results are presented and

compared. An optimum cable design and its performance in Peak Flame, Peak Smoke, Average Smoke, Compression and Cold Temperature bend is presented.

The Totally Dry 72 fiber Plenum-Outdoor Cable Design, preventing water ingress with dry water-swellable construction, exceeded UL, ICEA 640 and GR-20 rated performance including with peak flame of .5 feet, a peak smoke of .1 and an average smoke of .05, a Compression exceeding 300 N/cm, Cold temperature bend exceeding -50 C, and temperature performance exceeding -40 to +70.

INTRODUCTION

Campus Cables consist of Outdoor, Riser, Outdoor-Riser and Plenum Rated Designs which link, point to point,³ to and from a plenum environment, across a riser and an outside plant environment. Newly installed indoor cables should be as fire retardant as possible to lower the aggregate flammability of new or existing installations². The highest rated cable flammability test is the UL 910 Plenum, as illustrated from Chapin, Caudill, & Hoover³.

The Outdoor-Plenum designs continue to be market driven towards higher performance levels. From a Berk-Tek Adventum Case History, Customer Approved Draft, July 23, 1999, we quote the following:

The new loose-tube, outdoor-plenum fiber cable eliminates transition points, which lowered costs for a secondary school system LAN and WAN installation, located in the Midwest.

The cable was run from the outdoors directly into a plenum environment enabling the installer to generate some significant savings on the installation of a five-building LAN and WAN.

The cable was installed continuously from aerial to underground to an indoor plenum with no transition points in the fiber backbone for the school's 100BASE-T Fast Ethernet LAN and WAN. The same cable was also used in conduit between the buildings and ducts within the buildings.

The original specifications called for pulling outdoor cable and transitioning it at each building to an indoor cable. Installation could have also been in rigid conduit within the buildings and used all outdoor cable, a much more costly option.

A product designed to be installed in any campus environment-conduit, aerial or in plenum spaces, without the need for expensive transition points was the optimum option. Not having a transition within the buildings, which comprised a plenum environment, allowed maintenance of cable integrity throughout the installation. Eliminating splices further reduced failure points and installation costs.

The fiber cable was installed underground from the main building to the remote buildings and in some cases risered and lashed to poles. Being able to run Adventum underground, to the poles and then into the plenum environment saved time. The cable also was quoted as having good pulling installation characteristics, easy access, and good characteristics for hanging applications.

Because the cables had no gel-type filling compounds of any kind, cleaning was simplified, and cable preparation time was reduced. Although the cable is without any gel-type filling compounds in the cable core or buffer tube, the cable is fully water-blocked because it features a dry compound water-blocking scheme inside and outside of the buffer tube.

In counts ranging from six to 72 fibers, this is the first cable of its kind with a completely dry water blocking system in both the cable core and buffer tubes.

Due to its loose tube, plenum design, it is a product that can be used in virtually any indoor and outdoor application and is especially advantageous for campus LANs.

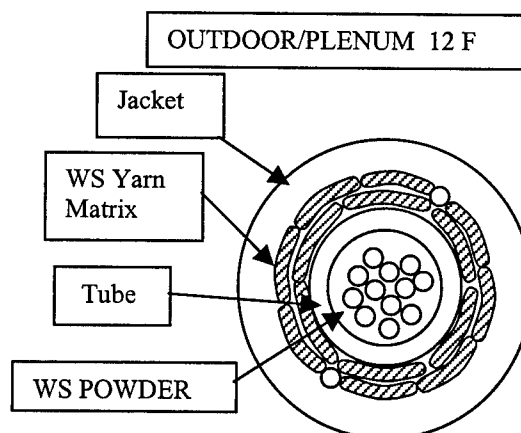
OUTSIDE-PLENUM DEVELOPMENT

Upgrading the Uni-Lite RD 12 F to Plenum Rating in 1997-1998 required rethinking the

material selection to meet the combined of GR-20, GR-409 and UL 910 specifications¹.

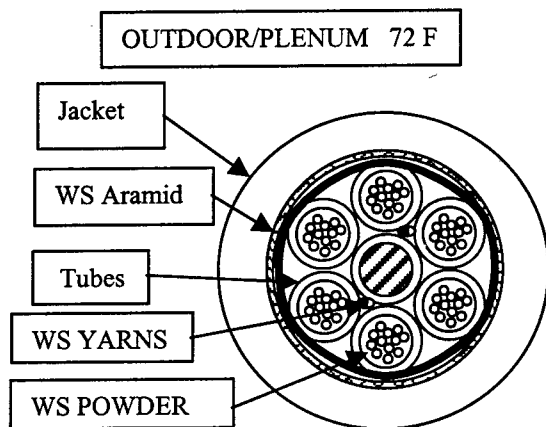
Highest UL 910 performance, tied to aggregate cable fuel content, was delivered by a dry tube without gel. The dry tube without gel also greatly enhanced the overall cable accessibility and cable splicing preparation. These positive attributes illustrated the need for a totally dry plenum indoor and outdoor cable¹.

Water swellable yarn matrix strength members were used between the jacket and tube, as in the reduced diameter Riser design. A plenum flame retardant and UV Resistant material was used for the jacket material. Water swellable powder was used to prevent water ingress inside the plenum flame-retardant tube¹.



Compared to the Plenum central tube design which has maximum fiber count of 12, the loose tube fiber count was increased to 72, utilizing the 6 @ 1 design. The characteristics of buffering and jacketing materials were also improved while the totally dry design characteristics were maintained.

In this design water swellable yarns were used to prevent water penetration within the interstices between the glass reinforced plastic central rod and the tubes. Water swellable binders were incorporated to hold the tubes in their reverse lay position and water swellable aramids were also used to finish the "totally dry" water ingress prevention capability. The resulting design is depicted in the following drawing (not to scale):

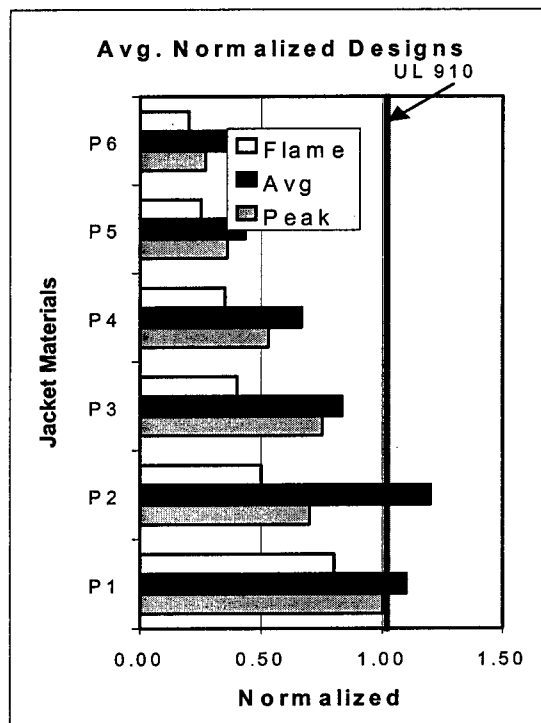


UL 910

The UL 910 capability was of critical importance. New targets for UL test performance, reward cable designs that have a statistically tighter flame, peak smoke and average smoke performance with less follow-on testing rigor and compliance protocol⁴. As was previously the case, UL also has a more relaxed dimensional tolerance specification listing protocol for cables which generate results at the lower end of the allowable ranges for flame, peak smoke and average smoke.

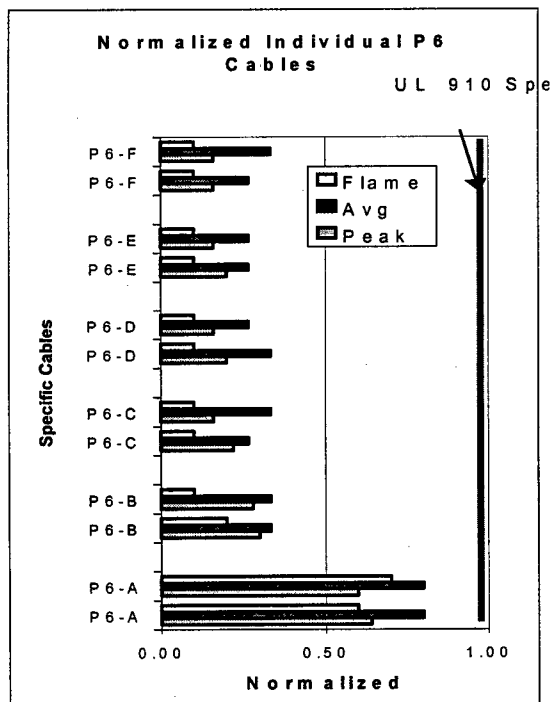
In review, the UL 910⁹ test is performed on a 7.6m x 0.3m horizontal cable array, enclosed in a tunnel (Steiner tunnel test). The array is subjected to a 90kW gas direct flame at the front end, over 1.5 meters length. The ventilation rate in the tunnel is 73m per minute.³

In the following chart, sets of horizontal columns illustrate the evolution of the plenum designs from P1 to P6. The columns display normalized results for the max flame, peak and average smoke from the UL 910 cable tests, performed in the Steiner Tunnel. Increased optimization of material selection has resulted in the best performing material assembly P6. This outstanding performance level has the most favorable listing protocol for the UL 910 qualification system⁴ and may also fare well given the on-going "permanent" plenum standards development within the NFPA. Of six Plenum designs submitted, P3, P4, P5 & P6 met UL 910 requirements as illustrated in the following chart:



The P6 design covers 6-72 fibers, thus requiring filler tubes in the lower fiber counts. Back-up materials may also be needed to match specific customer preference for cable accessibility and handling.

The "P6 A-F" performance listed as follows, represents 6 uniquely different cable designs submitted to UL.



In order to cover the full 6-72 fiber count design range, all of the cables passed the three specific UL 910 measurement parameters of Flame length, Peak smoke generation, and Average smoke generation as required by the UL 910 test. Each cable design was tested 2 times, pursuant to current UL procedure. The specific performance results of the P6 cables A-F are normalized. It is evident that P6-(B-F) performed very well at about 30% of the allowable range, with P6-A at about 80% of the allowable range. P6-A contained a dramatically different tube material, resulting in the variance.

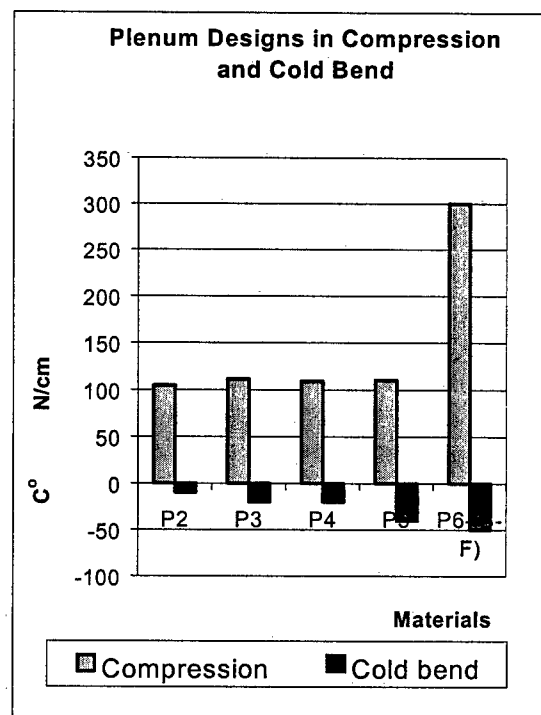
The cables were tested prior to the proposed new UL 910 Qualification Testing Procedure⁴, but it is interesting to discuss the possible impact the results would have had in the new procedure. To avoid a costly UL IPS (in production samples⁴) activity, the cable results would need to generate Cpk ratings of greater than 1.33 for Peak Optical Density and Average Optical Density.

Calculating the Cpk for cables P6 G-F renders a Cpk of 5.08 for peak optical density and 6.64 for Average Optical Density. The P6-A cable lowers the Cpk of the group Average Optical Density to 1.04, missing the 1.33 Cpk target. Had the P6-A been a valid sample of our proposed design, missing the Cpk target would have required either 1) more testing of the cable or 2) that the cable would be subjected to the IPS testing program⁴. As illustrated, 10 close following results do not repair the Cpk value sufficiently. The new proposed UL qualification program encourages designs having the narrowest standard deviation within the UL 910 flame results⁴. The optimum designs P6-B to F will likely fare well in future UL re-burns thus keeping the direct listing costs for the design family as low as possible. As stated above, the performance should also bode well within the on-going "permanent" plenum standards development within the NFPA.

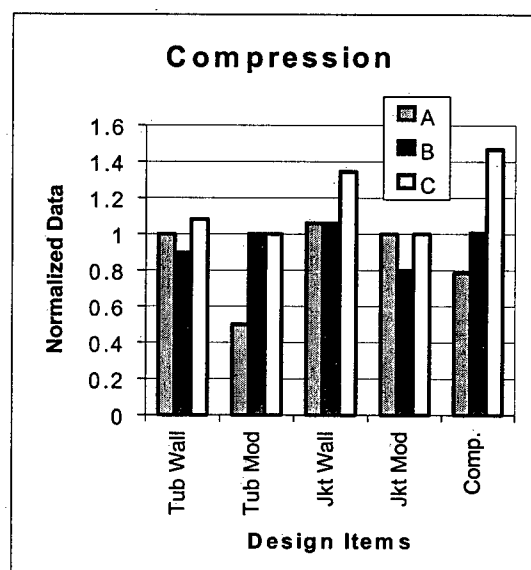
Compression, Cold Bend

The following graph includes information from our 12 Fiber designs¹ for Out-door and In-door performance and compares it to our latest 72 fiber Loose tube 6 @ 1 design. As is well known in the industry, shifting from a low modulus tube in a central tube design to a higher modulus tube in a 6 @ 1 design will provide improved

compression performance, which in this case exceeded 300 N/cm. An additional benefit is that the improved material, resulted in an improved cold bend performance to -50°C.



Looking at three of the P6 designs individually, we illustrate how changing the component design parameters, affects the overall compression performance as follows:



The input of the component design parameters for tube wall thickness, tube material modulus, jacket wall thickness, jacket material modulus and resulting compression were all normalized

against our nominal design. All three compression performances exceed the GR-20 CORE requirement of 220 N/cm.

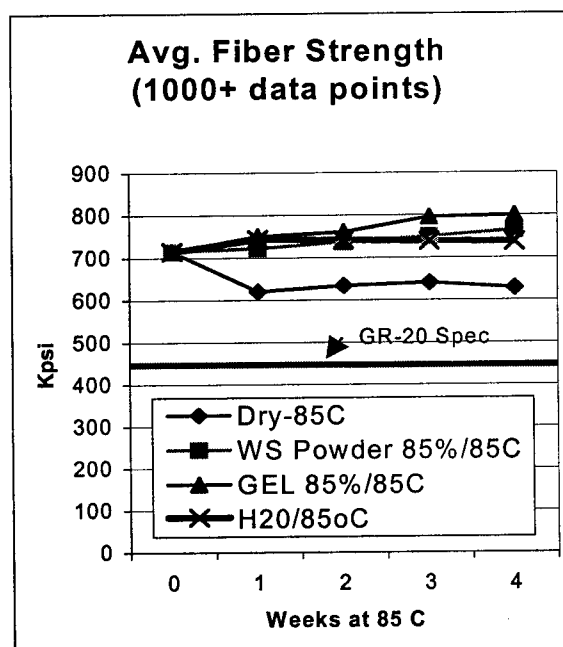
Design A of the three shown here performed at the lowest level due to a significantly lower tube modulus than the other two designs, B and C. Design C, having the highest material modulus and wall thickness, performed at a level exceeding 310 N/cm.

Water Soak

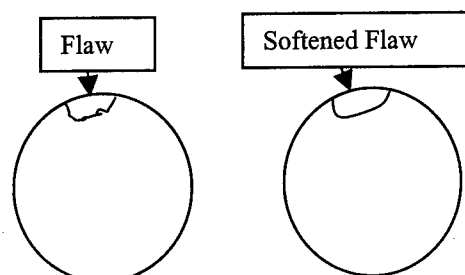
Our work continues exploring optical fibers performance in 85 °C, 85% humidity and water soak, additionally exploring the effect of swellable powder versus gel. The exploration of current generation optical fibers performance in 85 C & 85 % humidity¹ was expanded to tests involving several fiber types, other environments and additional performance criteria⁵.

The effects of aging on fiber strength was studied in four environments: 1) Dry 85 °C, 2) Water swellable powder 85 % humidity and 85 °C, 3) Filling Gel at 85 % humidity and 85 °C, and 4) water soak at 85 °C.

The results indicate that when the current generation of optical fibers are exposed to humidity or water under the test conditions investigated, a higher strength result over the 1000 measurements was observed as compared to fibers only exposed only to 85 °C. Results are illustrated in the following chart:

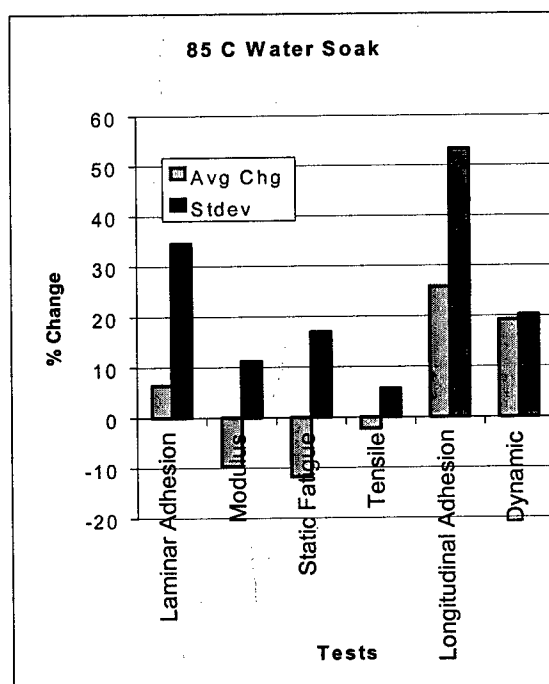


A possible explanation is "flaw softening" that occurs when the glass surface is exposed to humidity⁶. This conversion of sharp cracks to blunt pits is illustrated in an "exaggerated" depiction as follows:



Thus fibers aged under "dry" conditions can have poorer fiber strength relative to those aged in a humid environment. Over a more extended period of time the performance of all the scenarios may merge or the performance of fibers aged in a humid environment may decrease. Complete data will be available after the completion of ongoing testing⁵.

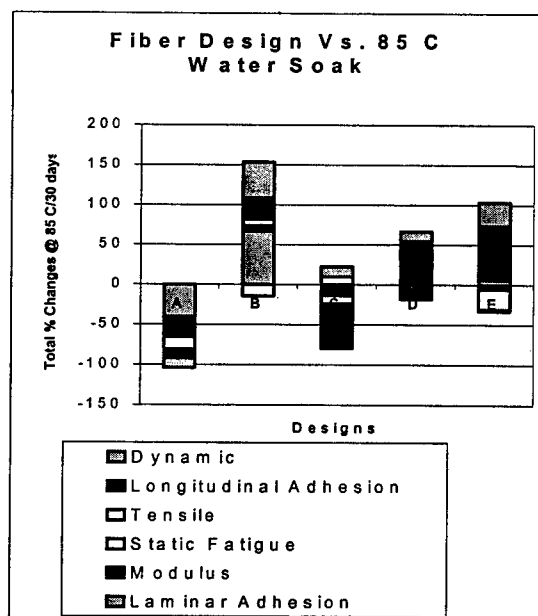
The fiber strength is one parameter that may be affected by exposure to water. The % change of other parameters of 1) Laminar adhesion, 2) Modulus, 3) Static Fatigue, 4) Tensile Strength 5) Longitudinal Adhesion 6) Dynamic Fatigue. are graphed as follows:



The data represents the aggregate average of the results from fiber designs that were used in the cable design as described in this paper. Other fiber designs available in the world market did not perform as well. As requested, we will be working with those vendors to modify their designs as needed. It can be seen that the % change of the parameters generally illustrates an improvement after exposure to water, but there are some large standard deviations in the measurements. Overall the fibers performances are well within the required tolerances for the lifetime expectancy of the cable.

Looking at the fiber designs on an individual basis, cumulative changes in 1) Laminar adhesion, 2) Modulus, 3) Static Fatigue, 4) Tensile Strength 5) Longitudinal Adhesion 6) Dynamic Fatigue are graphed.

From this graph we can see the overall cumulative % changes of Fiber design A & C, result in a net depreciation in performance, with B, D & E improving in the overall performance as follows:



TEST RESULTS

UL 910 PLENUM RESULTS

Parameter	Max.	Results
Flame	5 ft	.5/.5
Peak Smoke	0.5	.10/.08
Avg. Smoke	0.15	0.04/0.04

ICEA 640, GR-20 and GR-409 RESULTS

TEST	ICEA 640/GR-20	GR-409	12 F	72 F
Low Temp. Bend	20 x -30C	20 x -20 C	20 x -20 C	20 x -50C
Impact Resist.	25 cyc 2.2/2.9 N-m	25 cyc 2.2/2.9 N-m	25 cyc 2.2 N-m	25 cyc 2.94 N-m
Comp. Strength	220 N/cm	100 N/cm	170 N/cm	300 N/cm
Tensile Strength	1335/2700 N	1320 N	1335N	4450N
Twist	10 cyc 2 m	10 cyc 2 m	10 cyc 2 m	10 cyc 2 m
CycFlex	25 cyc	25 cyc	25 cyc	25
Temp. Cyc -Age	-40 +70C & 85 C Age	-20 +50C & 85 C Age	-40 +70C & 85 C Age	-40C to +70C & 85 C Age
Water Pen	24 hr unaged 1 hr aged	N/A	24 hr unaged 1 hr aged	24 hr unaged 1 hr aged

CONCLUSIONS

- 1) Optimized UL 910 performance for narrow standard deviation, results in listing benefits.
- 2) Higher modulus materials, layer thickness, and the 6 @1 design deliver compression in excess of 300 N/cm.
- 3) The current generation of optical fiber's performance remains very stable after exposure to a variety of environments, including 85 % humidity, at 85 C, with or without utilization of water swellable powder and Water soak at 85 C.
- 4) The dry interior tube, having water swellable powder, performs very well, and tests are continuing.
- 5) The 72 Fiber Outdoor-Plenum, successfully meets specific ICEA 640, GR-20-CORE and GR-409-CORE requirements.

REFERENCES

1. Keller, Rosko, Risch, Yoder, Munday, "DEVELOPMENT OF CROSS-

FUNCTIONAL TOTALLY DRY OPTICAL FIBER CABLE FOR OUTDOOR, RISER, AND PLENUM APPLICATIONS" IWCS, 1998, pp. 17-24.

2. Siegfried Richter, Rudiger Schmidt, "TESTING OF CABLES DESIGNED FOR FIRE RESISTANCE A COMPARISON OF U.S. AND EUROPEAN STANDARDS" IWCS, 1997, pp. 752-760.
3. J. T. Chapin, L. Caudill, J. R. Hoover, "COMPARISON OF FIRE BEHAVIOR OF COPPER AND FIBER OPTIC CABLE IN LARGE AND FULL SCALE FIRE TEST FACILITIES" IWCS, 1997, pp. 775-784.
4. Laura Schroepel, Thomas J. Guida, George J. Fechtmann, "REPORT ON THE APRIL 15, 1999 MEETING" Subject 444 Underwriters Laboratories Inc. 1285 Walt Whitman Road, July 9, 1999, pp. 1-9.
5. E. M. Vogel, B. J. Keon, C. R. Kurkjian, R. A. Frantz and H. H. Yuce, "MECHANICAL PROPERTIES OF COLOR CODED FIBERS", NFOEC, Boston, 18-22 October, 1995, pp. 237-247.
6. M. J. Matthewson and C. R. Kurkjian, "ENVIRONMENTAL EFFECTS ON THE STATIC FATIGUE OF SILICA OPTICAL FIBER", J. Am. Ceram. Soc., 71[3]1988, pp. 177-183.
7. Michael R. Ellwanger et al., "HIGH FIBER COUNT INDOOR/OUTDOOR FAMILY OF RIBBON CABLES" NFOEC, 1996, pp. 371-380.
8. Allan Kaiser et al., "INDOOR/OUTDOOR FIBER OPTIC CABLE" NFOEC Proceedings, 1996, pp. 347-355.
9. UL 910 STANDARD, November 23, 1998

SPEAKER

Jack Rosko, received his BSEE Degree from Union College in Schenectady, NY. He has worked for Berk-Tek since 1991 and is now Research & Development manager. Mr. Rosko has been involved in Fiber Optic Cable Design and Development since 1979. His previous work experience has been with Siecor, Phalo OSD, and Sumitomo Electric.

OTHER AUTHORS

David A. Keller, received his B.S. in Mechanical Engineering from the University of Kentucky in 1983. He has held positions in product and process development before and after joining Alcatel 1987. He holds the position of Senior Product Development Engineer at Alcatel-Berk-Tek's Data-Cable Division.

Brian G. Risch is the Materials Technology Manager at Alcatel Telecommunications Optical Fiber Cable Competence Center. He holds a B.A. degree in Physics from Carleton College and a Ph.D. in Materials Science and Engineering from Virginia Polytechnic Institute and State University.

Randy L. Yoder started working for Berk-Tek in 1980 in the Copper Data Cable Division in New Holland, Pa. His experience has included all areas of Process Development of Data Cables and Manufacturing Process Control.

Bob Overton joined Alcatel in 1991 and is a Senior Principal Scientist and Manager of the Coatings Technology Group in the Fiber Optic Competence Center. He has a BS in Chemistry from Mercer University and a Master of Science in Chemical Engineering - Polymers, from Georgia Institute of Technology.

Gilberto Camilo received a Physics Doctor degree at Campinas University, Sao Paulo, Brazil in 1991, and joined Alcatel Telecommunications in 1998 and is the Senior Researcher in the Coatings Technology Group.

Scott Munday received his A.A.S. degree in Mechanical Engineering Technologies from Catawba Valley Community College in 1992. He joined Alcatel in 1993 and now holds the position of Quality Assurance Technician.

Bill Charuk received a BS degree from The Pennsylvania State University in State College, PA. After service in the military, he worked for Siecor in various engineering and sales positions. Since 1997 he has worked for Berk-Tek as the Business Unit Manager for the Fiber Optic Group.

Dan Rouse received his A.A.S. degree in Laser and Electro-Optic Technologies from Central Carolina Community College in 1989. He joined Alcatel-BERL-TEK in 1990 and now holds the position of Quality Assurance Engineer.

FLAME RETARDANT CABLES WITH ENHANCED PERFORMANCE

David Benzel⁴, JeanPierre Bonicel², Jurg Hosner³,
Klaus Nothofer¹, and Alexander Weiss¹

¹ALCATEL Kabel AG & Co, Mönchengladbach, Germany

²ALCATEL Cable, Clichy, France

⁴ALCATEL Cable, Calais, France

³ALCATEL Cables Switzerland, Cortaillod, USA

ABSTRACT

Cables for harsh environments requiring special flame retardant properties have been developed and tested to prove their suitability for subway applications.

To pass severe fire conditions a corrugated, welded steel armoring turned out to be the best solution, offering a hermetically closed structure as protection in case of fire. Such cables offer the best solution for sensitive applications in restricted areas.

This cable design fulfills common specifications like IEC 332 and the Paris subway specification RATP K 209 A in France, which is one of the most restrictive specification and which was objective for the cable design described here. This design is discussed in comparison with other existing design solutions.

INTRODUCTION

As more and more fiber optic cables networks and links are installed all over the world it is of obvious interest to use all suitable rights of way (ROW), such as tunnels (for example the Euro-tunnel between France and the UK), subways, sewer tubes and others for installation. Each ROW requires a fully adapted cable design. For all inhouse, subway and tunnel applications the flame retardancy of the installed systems is one of the most important topics to focus on as fires can have disastrous consequences. As an example the fire in the Mont-Blanc tunnel in the European Alps in March 1999 shall be mentioned. Consequently, the whole system installed and its components are subject to very strict fire protection requirements given in different specifications, which cover cables, components and the whole system itself. Most of these specifications are derived from established specs for copper cables.

The difficulty arising when applying them to fiber optic cables is the significant amount of burnable plastic materials used in today's designs in the cable cores for the buffer tubes, which can not be replaced very easily. In parallel the trend towards high fiber counts (≥ 144) gives another big impact on cable design by leading to bigger sized cores with more buffer tubes.

Cables described here focus on the French RATP specification, which applies for many tunnels and for different metro companies in European countries.

Solutions for a suitable cable design are existing for up to 72 fibers. The intended higher fiber counts require introduction of other cable design elements.

FLAME SPECIFICATIONS

Existing flame specifications focus on different cases of fire influences. One is a fire due to a burning cable, focussing on the burning properties of the cable, like specified in IEC 331, IEC 332, sections 1 to 3. Some other focus on the influence of an external heat source, like French RATP K 209 A (Régie Autonome des Transports Parisiens) specification, often applied for subway cables, especially in France. Although the RATP specifies a cable design as well as flame and smoke tests most French customers refer only to flame and smoke portions of the spec. For the purposes of this paper references to the RATP K 209 A refer only to the flame and smoke requirements. Herein enough external energy is applied to destroy all burnable or decomposable components of the sample. All released gases will support the fire. To pass this specification the cable must be significantly better protected than for standard flame retardancy specifications. The consequences for the cable designs are important. For a cable according to IEC 332-3 the

energy released by the burning cable core must be compensated by the energy absorbing flame retardant sheath. For a RATP design the total amount of decomposable plastic, taking into account each material, also HFFR compounds used, must be minimized to pass the test.

Beside this fire protection standards some important standards covering material properties have to be considered. Normally the materials used shall be halogen free. The materials shall not decompose by fire or heat releasing acidic, basic or toxic gases. A further important aspect are the low smoke emission characteristics of the materials used.

CABLE DESIGN

Actual designs

Presently, most of the fiber optic cable designs use plastic buffer tubes for protecting the fibers. For the tubes a fillgel, commonly a polyolefine based one, and a plastic tube, for example PBT or PP are used, both being highly inflammable. Suitable flame retardant, alternative materials are not available for an acceptable price.

Therefore the cable fire protection is achieved by applying a special sheath design. Here, different kinds of solutions are well-introduced, like flame retardant sheath materials, cable wrappings, like for example micaTM tapes, glass yarns and others, also armor constructions with ZetabonTM steel or aluminum tapes, which are commonly applied in form of overlapped tapes.

For the different required flame protection levels and material requirements the sheath construction has to be adapted. Yet, the difficulty is to reach high protection levels due to the remaining burnable cable core with the buffer tubes. The behavior of a cable design during a fire is mainly adjusted by the sheath construction.

Figure 1 shows common designs for cables up to 72 fibers according to IEC 332-3 and for a cable according to flame and smoke tests given RATP K 209 A.

Both designs fulfill IEC 332-3. Higher fiber count designs that pass passing RATP can be made. Yet, the difficulty arising is the increasing amount of plastic used for the cable core making it more and more difficult to pass RATP. The new cable design gives an added protection that ensures passing of the burning tests. It can be concluded, that the larger the cable, the more difficult to meet the K 209 A spec. This is especially true above 144 fibers.

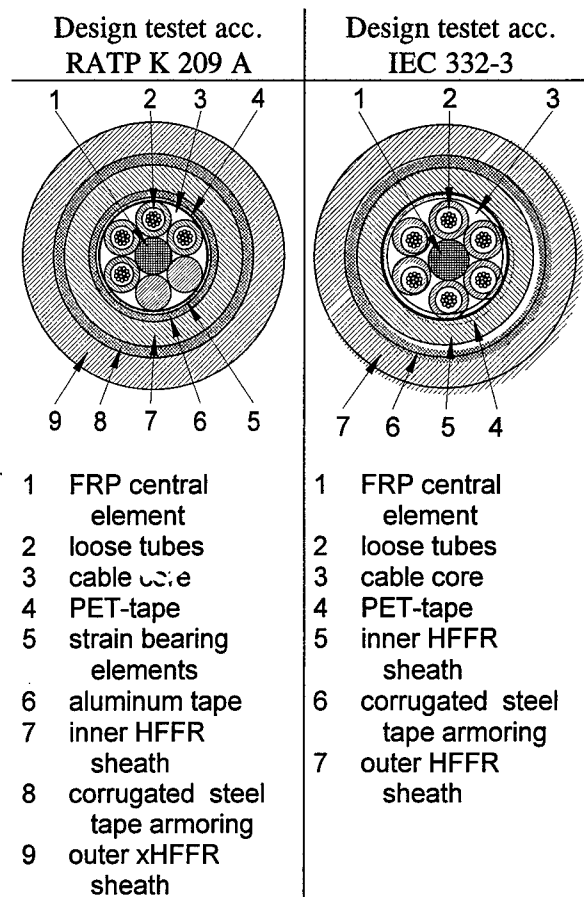


Fig. 1: Common IEC and RATP designs

High protection level design

To reach high fire protection levels at small cable diameters some main aspects have to be considered. First is to minimize the amount of plastic, including also the HFFR (sheathing) compounds, as they will be decomposed, too.

As a consequence the cable diameter shall be small; the fibers shall be placed in the smallest possible tubes. A cable filling compound may not be used.

To reach the highest level of protection a steel armoring shall be applied, consisting of a corrugated, welded steel tape. Aluminum is not suitable, because its melting point is approx. 660°C, which is lower than the temperatures occurring in a fire. Such an armor offers a hermetically closed cable core, which is not subject to direct contact to fire any more. In fact, the heat occurring will destroy the cable core, but the hermetically closed steel armor will prevent it from burning and releasing of gases.

The difference from traditional designs is the closed structure of the armor. In case of overlapped metal armoring molten plastic or decomposed gases will be released from the cable core. As they are burning the test will fail.

With the new design flame retardant cables according to the strictest RATP specs can be achieved with small cable size, even with high fiber counts; keeping the advantages of customary loose tube designs. As cable core, also other traditional designs are suitable, like slotted core or unitube cables. The core can have an outer sheath for easy installation of splice boxes outside the high protection area.

If required a HFFR plastic sheath can be applied on the steel armor. If not a stainless steel shall be chosen to avoid corrosion of the steel.

Cable construction acc. to RATP K209A

The above mentioned design requirements were applied to the new cable. The results of this evaluation is shown in Figure 2, giving the cross section of the cable designed for this application. It is suitable for up to 288 fibers in a conventional core. Fibers are placed in 24-fiber tubes. As core wrapping a PET-tape is used. An inner sheath was not required. RATP requires for a cross-linked outer sheath, therefore a crosslinked HFFR material has been applied. The sheath thickness shall be as low as possible, which is also an advantage for smoke density and opacity test behavior.

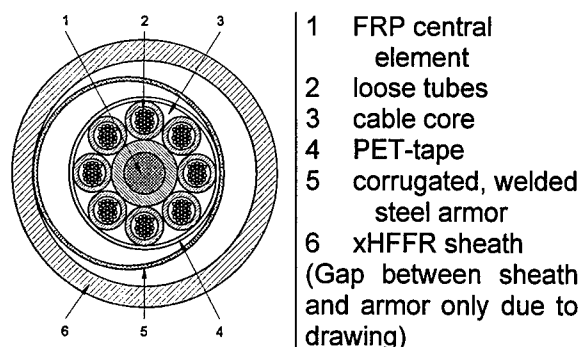


Fig. 2: Cross section of a 192 fiber cable

In case water tightness is required water swella-ble yarns or tapes shall be used.

MAIN PERFORMANCE PARAMETERS

Several cables were tested according to RATP fire protection requirements. The results were compared with results gained on traditional cables.

As expected it turned out, that the new design fulfills these requirements much better than the old ones. It does not burn at all; the steel tube acts as the predicted hermetically closed struc-

ture. It remains undamaged during all tests, therefore the inner cable materials were completely separated from the direct fire influence, but decomposed due to the heat. In fact, nothing will be released, because the steel tube remains undamaged.

The test according to IEC 332-3 has been passed, too.

The only directly destroyed material was the outer sheath, but due to its composition it does not support a fire.

All other cable tests beside the flame retardant characteristics were passed without failure. Due to the nature of the steel armor the cable the bending radius is limited to 15D.

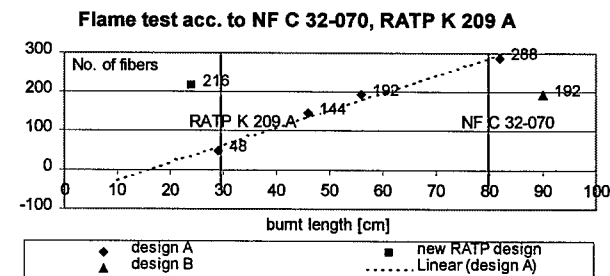
Special attention has to be paid to the smoke density test. The new design may fail in certain test setups, because the flame cannot reach and burn the cable core. If a test setup is used, that allows material to drop out of core due to heat this may insufficiently burn and release smoke. Use of a flame retardant silicone buffer tube fillgel will not influence the result as this material smokes, too.

Table 1: Main flame performance parameters

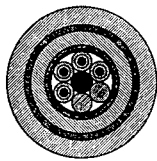
Test	Requirement	Result
flame test, category 1	burnt length ≤ 300 mm	240 mm
flame test, category 2	non-burnt length > 50 mm	365 mm
smoke density	$D_m < 350$	332 passed
smoke opacity	$VOF_4 < 100$	24 passed
acidity of smoke gases	ITC 800°C < 5	2.8

Flame test according to NF C 32-070 C1

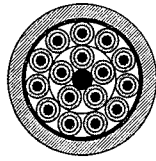
The main test to pass is the vertical burning test according to NFC 32-070 category C1, with requirements set by RATP K 209 A. The NF requires maximum 80cm burnt cable length, respectively 30cm for the RATP. The graph shows results for some cable designs:



The following two designs were tested additionally to the new one. Both designs have corrugated, overlapped steel armor and a HFFR sheath.



Design A
(see figure 1)



Design B

The graph demonstrates that the only suitable design is the new one with corrugated, welded steel armor, and design A for low fiber count. The higher fiber count designs A are not passing this test.

The trend line put through the results of design A indicates, that this customary design shows increase in burnt length with increasing amount of plastic in the cables (more tubes, larger upjacketed central element).

Design B is significantly worse, because the share of burnable material being much larger than for design A.

Based on this results the design conclusions are given. Small designs and separation of the core with a hermetically closed armor will allow to pass the test.

The difference responsible for the test results is the involvement of the cable core at the old designs in the flame test. It contributes a suitable amount of decomposed gases, which burn and lead to the failure of the test.

The new design and cables according to design A fulfill the IEC 332-3. They do not support a fire. Design B is failing this test, as the sheath is too thin.

Further test results

For subway and tunnel applications some other tests are also important to be passed for the installed cables.

The resistance to microorganisms is more related to the sheath material used, to avoid degradation of the cable sheath.

The situation is similar with the salt fog test. Salt fog occurs always in tunnels being close to the seaside or under the sea, like the Eurotunnel between France and Great Britain. It is also important for tunnels in areas where roads become salted in winter to melt snow and ice.

In parallel also other properties were tested, with good results.

Test	Requirement	Result
attenuation 1310 nm 1550 nm	for SM fibers ≤ 0.35 dB/km ≤ 0.22 dB/km	passed
tension test	$\delta\alpha_{\max}$ 0.1 dB/km, 2.5 kN	passed
crush test	$\delta\alpha_{\max}$ 0.1 dB/km, 2.0 kN / 10cm	passed
bending test	12.5 d no bends	passed
temperature cycling	$\delta\alpha_{\max}$ 0.2 dB/km, reversible	passed
salt fog test	CEI 68.2.11 (40 cm, 24h)	passed
resistance against microorganisms	NF EN ISO 846, A, B	passed

CONCLUSIONS AND OUTLOOK

To fulfill restrictive flame test requirements and high fiber count at the same time all required parameters of the specifications shall be considered to find the best performance and lowest costs cable design to pass. Traditional designs for IEC 332-3 are based on the balance between burning cable core and non-burning sheath design. Obviously the cores shall be designed as small as possible.

For RATP suitable cables this objective has to be extended to all plastic materials of a cable, also flame retardant ones. Passive cable elements, like fillers or upjacketing material for FRP central elements shall be flame retardant. As far as possible the cable core has to be prevented from direct contact with fire.

Most of the cable designs for high level flame retardant cables are armored. The commonly used steel or aluminum ZetabonTM type armor leaves space for flame contact to the cable core. It improves the cables flame test behavior, but is at high fiber count and low diameter cables, not sufficient when RATP K 209 A applies.

For this reason hermetically closed, corrugated, welded steel armor was chosen, which fulfilled best all these requirements. It offers absolute protection of the cable core and allows to keep the traditional loose tube cable core design. The number of fibers can be selected according to customer requirements.

Other designs may show a lack of safety in some properties, like the smoke density.

The closed armor is suitable for each tunnel or subway network, because it precludes all risks of fire or flame propagation related to the cable. The

design also allows the installation of several cables along a tunnel without increasing the risk of fire.

The way of installation can be chosen without regard to flame protected ducts or other tunnel installations. Beside the cable no special installation measures, like ducts with inner fire or heat barriers) must be taken to avoid the risk of fire.

The design is also suitable for inhouse installation by applying the principle of the steel armor to an indoor cable, for example by just using a steel tube filled with fibers.

It can be concluded that the developed cable design with the corrugated, welded steel armor is the best solution for flame retardant cables in areas with extended risk of fire and where the consequences of possible incidents can be disastrous.

ACKNOWLEDGEMENTS

The authors would like to thank Chantal Barioz for doing the whole set of flame tests, Nelly Drabczyk for the type test, furtheron Wilfried Konieczny and Heinz-Jürgen Hemken for manufacturing of the trial cables.

REFERENCES

- ▽ A very innovative technology for ROW application, J.P.Bonicel et al., IWCS 1998, Philadelphia
- ▽ Optimization of loose tube designs: the next step, P.Gaillard et al., IWCS 1998, Philadelphia
- ▽ Testing of cables designed for fire resistance. A comparison of US and European standards, S.Richter et al., IWCS 1997, Philadelphia

Alexander Weiss

ALCATEL Kabel AG&Co
Bonnenbroicher Str. 2-14
D-41048 Mönchengladbach
GERMANY



Dr. Weiss (38) obtained his degree of graduated chemist of the University of Tübingen in 1990. In the same year he joined AEG Kabel, now Alcatel Kabel. He is in charge of the cable development for F.O. cables since 1992. He is head of coordination center engineering for the European F.O. cable factories in ALCATEL CABLE.

THE DEVELOPMENT AND PERFORMANCE OF A CALIBRATION CABLE FOR THE NFPA 262/UL 910 PLENUM CABLE FIRE TEST

J. Thomas Chapin, Ph.D.
Lucent Technologies
Norcross, GA

Larry L. Bleich
Lucent Technologies
Omaha, NE

Pravin Gandhi, Ph.D., P.E., and Thomas Ebert, P.E.
Underwriters Laboratories
Northbrook, IL

ABSTRACT

In this paper, data are presented on the development and performance of a calibration cable for the Steiner Tunnel. An industry-led task group developed the desired characteristics of a calibration cable to assist in the verification of the NFPA 262/UL910 plenum cable fire test method and instrumentation. A review of existing materials against the requirements yielded several candidates that were manufactured into an extruded article and tested in the UL 910 apparatus. A polyvinylidene difluoride copolymer was selected.

The data generated with the calibration cable have resulted in a process control methodology to assist in the diagnostics of the fire test apparatus and equipment. The results indicate that the calibration cable has performed well through six manufacturing runs over a period of 14 months. This indicates that the concept of manufacturing a reproducible thermoplastic calibration cable to validate Steiner Tunnel performance has been realized. This is a first for any large-scale US or international cable fire test. It is expected that this approach of verifying other US and international large-scale fire tests is possible.

BACKGROUND

In the US, the National Fire Protection Association and Underwriters Laboratories issue standards related to fire protection. Until recently, the NFPA 262 and UL 910 plenum cable standards employed red oak as the calibration material. The oak timber product served as reference for measuring flame propagation and smoke generation behavior of the Steiner tunnel. Since red oak is a natural product, it is subject to lot-to-lot variation due to changes in the source of supply, age of the harvested wood and seasonal growth variables. These changes can affect density and hardness, which can affect its' response to relative humidity and corresponding reaction to fire. Further, the test standards specify that the red oak sample be placed at a different location in the test chamber as compared to a cable sample.

In this paper, the definitions for all acronyms and trademarks are found at the end of the paper.

UL 910 Steiner Tunnel Test

The most severe intermediate-scale horizontal tray fire test for cable in the US is UL 910¹ and

NFPA 262². It is specified for cable installed in horizontal, concealed spaces transporting environmental air (also known as plenum spaces) within buildings. A photograph of the UL Northbrook UL 910 facility is found in Figure 1

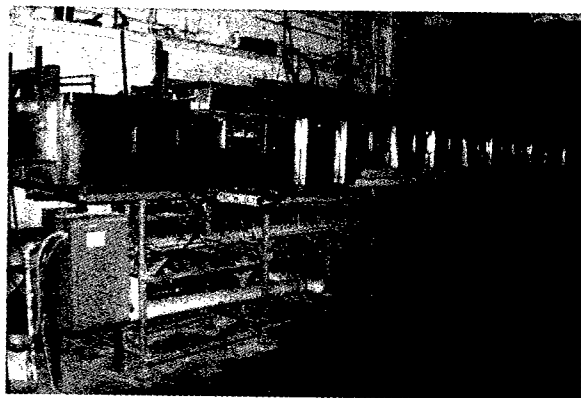


Figure 1 - UL 910 Facility at Underwriters Laboratories

In this method, a single layer of cables 11-1/4 inches wide and 24 feet long is strung on a steel ladder tray extending for the length of the tunnel. A diffusion gas burner flame 78kW (nominal) exposes 4-1/2 feet of the cable to the fire at the upstream end. Ventilation is supplied from the burner end at a linear flow rate of 240 feet per minute.

Cables for plenum installation in the US must meet the requirements of UL 910 test which are as follows: flame propagation distance (FPD) not exceeding 5 feet past the burner flame tip; a peak smoke optical density (POD) not exceeding 0.50; and an average smoke optical density (AOD) not exceeding 0.15. Additional measurements of heat release, smoke release rates, and flaming droplets can be made on cables. While these measurements are not required, they allow further comparison of cable performance and provide data for fire safety engineering calculations.

UL 910 Test and The Demand for Commercial Plenum Cable

The NFPA 262/UL 910 Standards have taken on greater significance with the increase in demand for high performance LAN (local area network) copper and fiber optic cable worldwide. For example, it is estimated that 22 billion conductor feet of LAN cable was manufactured in the US in 1997³ with 40% being plenum cable (coaxial,

twisted pair, optical fiber and low voltage power cable). This has generated a great concern about the tremendous amount of cable being installed in buildings and the risk of accumulated cable as cable is retired. Abandoned cable in these spaces will increase the net fuel load in the building.

This demand for plenum cable has triggered an increase in research and development into new cable constructions and materials. The drivers for innovation and cable redesign include increasing transmission performance, increasing fire performance, new installation practices, improved termination techniques and lower cost. To sustain this R&D effort, cable manufacturers, independent testing laboratories and raw materials suppliers require high reliability and consistency for this Standard. Intra- and inter-laboratory agreement year round is essential.

In 1997, UL convened an Industry/UL forum called TAPCOM – Technical Advisory Panel for Communications Cables, focused on plenum cables. This committee met to discuss the variation in fire performance of commercial plenum cables. Three areas of variation were considered: 1) variation in cable raw materials, 2) variation in cable design and manufacture and 3) variation in UL 910 tunnel performance. Within this TAPCOM forum, an Ad-Hoc Committee was formed⁴ to develop requirements for a UL 910 calibration cable to assist in verifying the operation parameters of the Steiner Tunnel.

The design requirements for a suitable calibration cable were developed and are listed below:

- ◆ **Design:** Resemble a typical LAN cable (longitudinal form with a circular cross-section with a copper conductor);
- ◆ **Material:** A thermoplastic (extrudable), non-compounded material, readily available, minimal lot-to-lot variation and easily characterized;
- ◆ **Manufacture:** Calibration cable must be simple to manufacture;
- ◆ **Fire Performance:** Construction of cable should provide a POD > 0.3, AOD > 0.10 and FPD of approximately 3 feet in the UL 910 test.

PROTOTYPE MATERIALS

To this end, a new calibration "cable" was developed using a thermoplastic material and a copper central conductor for support. The candidate materials selected are found in Table 1 and the supporting information cited are found at the end of the paper.

Table 1 Candidate Thermoplastic Materials

#	Description	Chemistry
1	Halar 985 ^A	ECTFE ^B
2	Halar 300LC	ECTFE ^B
3	Solef 11008/0003 ^C	PVDF - VF ₂ /HFP ^D copolymer with smoke suppressant
4	Solef 32008/0009	PVDF - VF ₂ /CTFE ^E copolymer with smoke suppressant
5	Solef 32008/0000	PVDF - VF ₂ /CTFE ^E copolymer without smoke suppressant

The prototype samples were manufactured with a 12 AWG copper conductor and an outside diameter (OD) of 0.225 inches.

Prototype Cable Fire Results

The cables were burned at the UL 910 facility in Northbrook and the results compared to the initial design requirements. The results are found in Table 2.

Table 2 Prototype UL 910 Results¹

Cable	FPD, ft	POD	AOD	Tests
Halar 985	1.5	0.35	0.13	4
Halar 300LC	1.5	0.40	0.14	1
Solef 11008/0003	2.0	0.04	0.02	1
Solef 32008/0009	0.5	0.17	0.07	1
Solef 32008/0000	1.5	0.26	0.12	2

¹ Results are averaged where multiple tests were conducted.

Based upon the overall criteria for an acceptable design and the fire test results, Solef 32008/0000 was selected as the calibration cable material.

Characterization of PVDF Copolymer

The Solef 32008/0000 material is produced without smoke suppressant. The copolymer is composed of 80% VF₂ and 20% CTFE on a weight basis. A trace amount of polyethylene (0.3 parts per hundred) is added as a processing aid. Typical physical and chemical properties are found in Table 3.

Table 3 Typical Physical and Chemical Properties of Solef 32008/0000

Property	Value
LOI ^F	52%
DSC ^G	T _M 167°C
Hc ^H	6250 BTU/lb.
TGA ^I	355 C onset of weight loss
MFI ^J	4.6 – 4.9 g/10 min.
%C	34.21
%H	2.62
%Cl	6.22
%F	56.52

Application, Manufacturing and Fire Experience of the Calibration Cable

Once the material, cable design and initial manufacturing requirements were established, the calibration cable was identified as "910ST" (UL 910 Steiner Tunnel). A photograph of the 910ST cable is found in Figure 2.

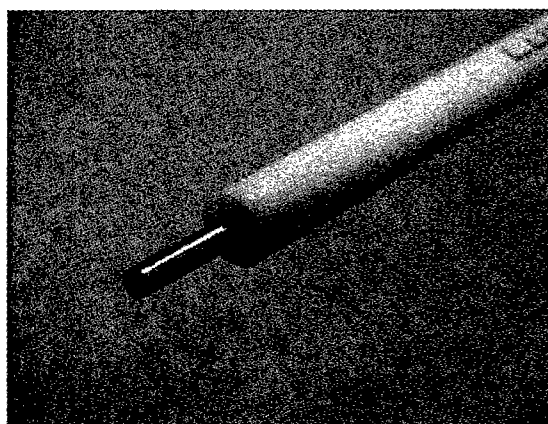


Figure 2 Photograph of 910ST Calibration Cable

As a result of the large volume of cable required for the investigations (cited below), a study was undertaken to assess the variation in fire performance of the 910ST calibration cable with successive lots of Solef raw material and production runs of the calibration cable itself.

From the outset, the calibration cable prototypes were manufactured with a small concentration of white color concentrate. It was initially felt that the colorant would not have a significant effect on UL 910 performance. Colorant was added at the extruder at a level of 3 parts by weight per hundred parts of Solef 32008/0000. For a period of one-year (October 1997 – October 1998) a total of 165,000 feet was produced and used in the above investigations. The average and standard deviations obtained for the cable are shown in Table 4.

Table 4- 910ST Cable Performance

Property	Average	Standard Deviation
FPD	2.0 ft.	0.5 ft.
POD	0.31	0.06
AOD	0.12	0.015

Once the design and manufacturing process was established, several applications for 910ST cable were identified:

1. A design of experiments (DOE) investigation of the variables associated with the operation of the Steiner Tunnel.
2. Development of statistical process control (SPC) charts for the Steiner Tunnel.
3. Harmonization of Steiner Tunnels located in the US, UK and Japan.

DOE INVESTIGATION

A DOE was conducted using the 910ST cable to investigate the influence of operational variables on the UL 910 results. In this study seven variables were studied. These were: A - room pressure; B - position of the draft plate; C - static pressure required to establish the air flow in the tunnel; D - cleanliness of the smoke measurement system; E - variation in the number of cable lengths used in the test; F - tunnel temperature at the start of the test; and G - lay of cables on the cable tray. The tests were conducted in duplicates and included the basic and reflected matrices to determine the key factors that influence fire performance results in UL 910 test.

The main finding of the DOE was that the static pressure setting used in establishing the air flow rate and the draft plate position were significant in influencing 910ST cable's fire performance.

These results for the FPD, POD and AOD are presented in Figure 3, Figure 4 and Figure 5. In these figures, the variables investigated are represented on the x-axis. The y-axis - score ($S^2/8$), represents the relative importance the test variable investigated. Higher value indicates greater influence of that variable on the test result.

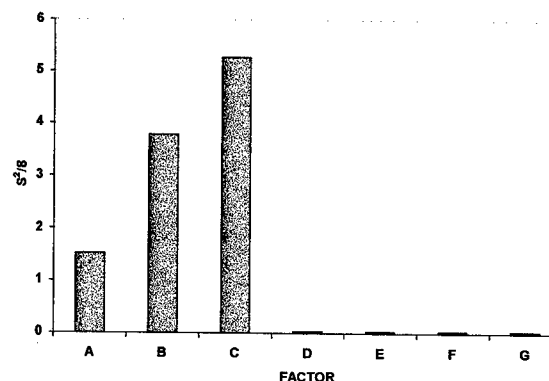


Figure 3 – Influence of Variables on FPD

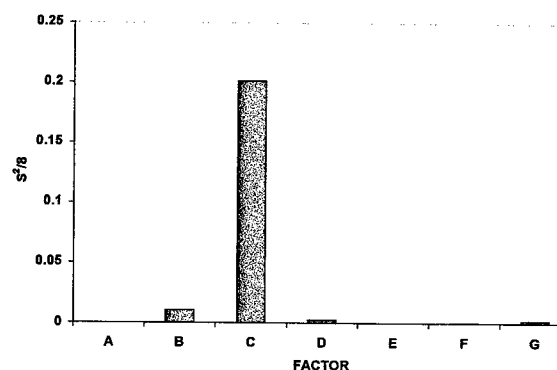


Figure 4 – Influence of Variables on POD

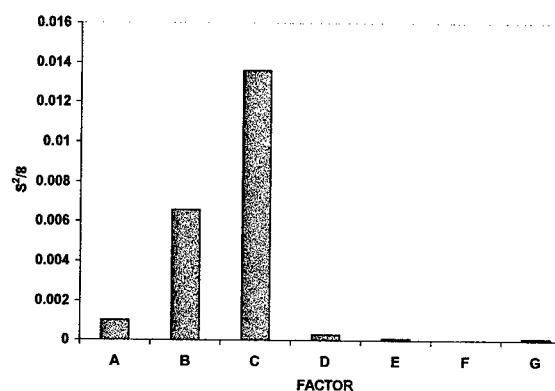


Figure 5 – Influence of Variables on AOD

The figures show the relative importance of tunnel operational variables on fire performance.

DEVELOPMENT OF STATISTICAL PROCESS CONTROL CHARTS

Additional data on 910ST cable were developed (average and standard deviations shown in Table 4) to develop SPC charts. These charts are used to verify that variations in the results are random and not due to any systemic problems with the Steiner Tunnel. An example of a SPC chart is found in Figure 6.

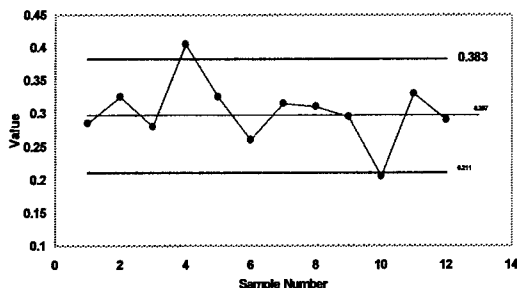


Figure 6- Typical Statistical Process Control Chart for the 910ST calibration cable POD for the UL Steiner Tunnel

A second batch of 910ST cable was produced in which the white colorant was replaced with a white color concentrate from another source. This resulted in a significant increase in the smoke generated with an average POD of 0.62, and an average AOD of 0.20. The FPD value was unchanged. In order to ensure consistency in successive manufacturing runs of the 910ST calibration cable, it was decided that the Solef 32008/0000 should be precolored with the original color concentrate and pelletized prior to extrusion.

FPRF INTERNATIONAL NFPA 262/UL910 HARMONIZATION PROJECT

The globalization of plenum cable is accompanied by the construction of Steiner Tunnels in Europe and in Japan. In order to ensure consistent fire performance in each facility the US Fire Protection Research Foundation initiated the International NFPA 262/UL 910 Harmonization Project in August

1998. The following independent testing laboratories are participating: UL and ITS in the US, BRE/FRS and LPC in the UK and JECTEC in Japan. The 910ST calibration cable is being used as the calibration standard in this project along with several commercial telecommunications cables.

CONCLUSIONS

A commercially manufactured calibration cable was developed for the NFPA 262/UL 910 plenum fire test. This is the first example of a thermoplastic extruded product to be used in a large-scale cable fire test method. The cable is composed of a PVDF copolymer with a white color concentrate added. The calibration cable has been named "910ST" and has been in use for the past two years with good performance. A key factor in its' performance is the maintenance of high quality control with regards to the PVDF raw material and subsequent pre-coloring prior to cable extrusion.

The 910ST calibration cable has been successfully used in several key Steiner Tunnel calibration projects in the US, Europe and Japan. The use of this calibration cable in statistical process control of the Steiner Tunnel has resulted in a higher level of confidence in the fire performance results of the NFPA 262/UL 910 Standard.

FUTURE WORK

This approach will be considered for other domestic and international large-scale cable fire tests.

ACKNOWLEDGEMENTS

A special thanks is due to the following people who have provided valuable technical support and guidance over the course of this work: V. J. Vasudevan, P. E. Neveux, M. R. Ratnam and G. Miller Lucent Technologies, P. Pastor and Larry Plencner UL, Northbrook, Ill., USA, J. Walnock of DuPont, Wilmington, DE, USA

ABBREVIATIONS AND TRADEMARKS

- ^A Halar™ is a Trademark of Elf Atochem
- ^B ECTFE - Ethylene-chloro, trifluoroethylene copolymer.
- ^C Solef™ is a Trademark of Solvay SA.

^D PVDF - VF₂/HFP copolymer – Vinylidene fluoride/hexafluoro propylene copolymer.
^E PVDF - VF₂/CTFE copolymer – Vinylidene fluoride/chloro, trifluoro ethylene copolymer.
^F LOI - Limiting oxygen index
^G DSC - Differential Scanning Calorimetry, T_M melting temperature (peak)
^H Hc – Heat of combustion
^I TGA - Thermogravimetric analysis
^J MFI - Melt Flow Index
 BRE/FRS – Building Research Establishment/Fire Research Station
 ITS – Intertek Testing Services
 JECTEC – Japan Electrical Cable Technology Center Inc.
 LPC - Loss Prevention Council
 UL – Underwriters Laboratories Inc.
 FPRF – Fire Protection Research Foundation (formerly NFPRF, National Fire Protection Research Foundation)

REFERENCES

- ¹ UL 910 *Test for Flame-Propagation and smoke Density Values for Electrical and Optical Cables Used in Spaces Transporting Environmental Air*, Fifth Edition November 23, 1998.
- ² NFPA 262 *Standard Method of Test for Flame Travel and Smoke of Wires and Cables for use in Air-Handling Spaces*, 199 Edition
- ³ Source: information from Underwriters Laboratories, Melville, NY
- ⁴ UL TAPCOM Calibration Cable Committee Members were: P. D. Gandhi/UL, T. Ebert/UL, J. T. Chapin/Lucent Technologies, D. Rockosi/Elf Atochem, Kerry Newmoyer/Berk-Tek, D. Kiddoo/AlphaGary, S. Nave'/Siecor, D. Biggins/Solvay.



J. Thomas Chapin is the Technical Manager of the Premises Cable Materials Platform Group at Lucent Technologies, Bell Laboratories in Norcross, Georgia. He is responsible for managing the materials activities associated with the development and manufacture of copper and fiber optic premises cables. He joined AT&T Bell Laboratories in 1980 after working at The Upjohn Company for three years. He received his BS in Chemistry and Ph.D. in Polymer Science from the Institute of Materials Science at the University of Connecticut in 1977. Since 1980 he has worked in the areas of outside plant materials failure phenomena, optical fiber coating and fiber optic cable development, and fire and corrosion research. He has 13 patents and over 30 publications.

Panel Discussion Abstract—Session 13

WIRELESS: GOOD ENOUGH TO BACK UP OR REPLACE LANDLINES?

Reiner J. Gerdes

TransTel Group, Inc., Norcross, Georgia

ABSTRACT

Copper or fiber-based cable plant provides the link from the customer to the public switched telephone network. In most cases, a single cable connects the customer to the nearest telephone company central office. However, telephone cable is vulnerable to cuts, vandalism, and failures of the associated switching equipment. For businesses, any failure of this equipment can lead to severe economic losses. Failures in public safety installations can place human lives at risk.

Wireless networks exist in all parts of the world and are growing rapidly. This growth continues although wireless technologies do not offer the quality of transmission of the land-based network. In addition, there is a perception of lessened reliability.

In reality, the reliability of wireless networks is quite good. To a certain extent, wireless networks are inherently less vulnerable than land-based networks. The reason is the distributed nature of the "wireless local loop". The failure of a single cell site does not necessarily impact service to the customer as was shown in several natural disasters.

The transmission quality of wireless transmission is still inferior and likely to remain so when compared, for example, to that of fiber. For voice traffic, the quality is improving and considered acceptable. Data transmission with a throughput of up to 115 kbps is achievable but also dependent on received signal strength, modems used, and information being transmitted.

The combination of reliability, acceptable overall quality, and ubiquity make wireless transmission a good choice for backing up land-based facilities or even replacing it in certain applications. Equipment manufactured for backing up cable plant and PBX's will be discussed that illustrate several backup and land-line replacement scenarios.

BIOGRAPHY



Dr. Reiner J. Gerdes
TransTel Group Inc
5555 Oakbrook Pkwy
Suite 110
Norcross, GA 30093

Reiner J. Gerdes started to work in telecommunications at age 15 to help his parents put himself through high school. During the long and hard hours working night shifts on a telephone cable jacketing line, he could not help but becoming overly familiar with telephone cable. He swore to himself to do everything possible to stay away from this aspect of telecommunications once he finished high school.

In the following 20 years, he managed to do just that. He studied at the École National Supérieur de Chimie in Paris, France, finished college, received his doctorate in physical chemistry from the Technical University Hannover, Germany, and did research and teaching at Georgia Tech.

When an opportunity arose to choose between academia and telecommunications, he chose the latter because it promised more excitement and interesting work. Eventually he became director of Contel Labs. From the point of view of this position, working with telephone cables was relatively palatable if not challenging. However, when he chose to retire from Contel, he decided that telephone cables would do just fine without him. He became and still is president of TransTel Group Inc., a manufacturer that specializes in equipment for wireless access to the public switched telephone network.

Panel Discussion Abstract—Session 13

CELLULAR DIGITAL PACKET DATA TECHNOLOGY

David Gambrell

GTE Wireless, Alpharetta, Georgia

ABSTRACT

Wireless data communications is being used extensively in commercial, industrial, and agricultural segments throughout the world. Cellular Digital Packet Data (CDPD) wireless services provides a cost-effective way of providing wireless IP connectivity to meet the data transport needs of these business segments.

Topics included in this discussion include an overview of CDPD technology, comparisons of CDPD with other wireless data technologies, business applications using this technology, and CDPD's future direction. The discussion will also relate the applicability of wireless data technologies to those of wireline data technologies.

BIOGRAPHY



David Gambrell
Manager-Business Solutions Engineering
GTE Wireless
One GTE Place
Alpharetta, GA 30004
Mail Code GA2A2DTE
dgambrell@mobilnet.gte.com

David Gambrell is Business Solutions Engineering Manager for GTE Wireless, Headquartered in the Atlanta, Georgia area. Mr. Gambrell is responsible for the development and implementation of wireless data technologies for GTE Wireless. He has written numerous White Papers for GTE Wireless on the subject of CDPD and other wireless data technologies. He has over 19 years of data communications experience in the development of fiber optic, frame relay, ATM, ISDN, and wired and wireless IP data networks for the telecommunications industry.

Panel Discussion Abstract—Session 13
BROADBAND AND MIDBAND WIRELESS ACCESS

Robert Merrett

**British Telecom, Advanced Communications Engineering
Ipswich, United Kingdom**

ABSTRACT

The flexibility of the new generation of broadband and midband wireless access systems opens up opportunities for new entrants and incumbent operators. Broadband systems provide a multi service access medium to a multi service platform and can support bandwidth on demand. Because of their cost structure the target market will normally be centered on small to medium enterprises. Midband systems are IP based and the cost structure is such that it is possible to serve top end residential and very small business. Both systems avoid the limitations of the narrow band wireless access systems; namely, the

inability to efficiently carry bursty data and to offer simple upgrade paths. However, as with all wireless access systems, the economic viability in developed countries has to be examined on a cell by cell basis.

The objective of this review is to examine the service flexibility and the economic viability of the various broadband and midband wireless access architectures. From this it will be possible to define the conditions needed to make wireless access an effective means of increasing competition, and the conditions under which it will allow the incumbent to reduce the costs of meeting universal service obligations.

Panel Discussion Abstract—Session 14

LAN TWISTED PAIR CABLING – OVERVIEW OF CURRENT TIA STANDARDS ACTIVITIES

Masood Shariff

Bell Labs of Lucent Technologies, Holmdel, New Jersey

ABSTRACT

Cabling systems have gained rapid acceptance by industry since they provide a measurable hand-off between cabling system providers and network applications equipment providers. As a result of cabling standards, first published as TIA/EIA-568 in 1991, common target architecture requirements and design specifications have been established for building architects, cabling system designers, and applications developers. TIA has indicated that the TIA-568-A standard is currently the best selling standard published by TIA.

Following the publication of TIA-568-A with the associated channel and link field testing document TIA TSB-67, the TIA TR42 cabling systems and infrastructure committee has embarked on aggressive new directions to support bi-directional parallel transmission schemes used by Gigabit applications. TIA TSB-95 was approved for publication and complements TIA TSB-67 to test installed category 5 cabling for Equal Level Far End Cross-talk (ELFEXT) and Return Loss. This testing is needed to ensure that installed category 5 cabling can support 1000BaseT Gigabit Ethernet.

In parallel with the development of TSB-95, TIA developed an enhanced specification for twisted pair cabling called category 5e. This document, now in the final default ballot cycle, is referred to as SP-4195 and will be published as Addendum A-5 to TIA-568-A. Unlike TSB-95, Category 5e includes enhanced component specifications to ensure that 1000BaseT is supported under worst case channel configurations including 4 connections, installation variability, and worst case addition of components.

Cabling systems have to keep pace with the doubling of processing power every 18 months and towards this goal, next generation category 6 cabling is being developed both in TIA and ISO. The category 6 channel doubles the

bandwidth of category 5 by requiring positive power-sum ACR at 200 MHz. This increased bandwidth facilitates both simpler electronics and faster data rates in the future. Category 6 also has the firm objective of being backward compatible to existing categories of cabling and support interoperability between components from different manufactures.

Standards are living documents and TIA requires standards to be revised every 5 years. The "B" revision of TIA-568 will be published as a series of 3 documents, TIA-568-B.1, TIA-568-B.2, and TIA-568-B.3. This division is to improve the alignment of the documents for designers, testers, end users (B.1), copper cabling systems manufacturers (B.2), and fiber cabling systems manufacturers (B.3).

Masood Shariff is a Distinguished Member of Technical Staff at Bell Laboratories of Lucent Technologies in the SYSTIMAX® Structured



Connectivity Solutions Research and Development Department, in Holmdel, New Jersey, U.S.A. Masood is chair of TIA TR42.7 responsible for copper cabling systems specifications including category 5e and category 6. Masood is a member of IEEE and BICSI, and serves as one of the editors of the BICSI Telecommunications Distribution Methods Manual.

Panel Discussion Abstract—Session 14

Development of a PSNEXT, PSELFEXT and Return Loss Model for Category 5e Channels

Paul Kish

NORDX/CDT, Inc.
Point-Claire Quebec Canada

ABSTRACT

The TIA TR-42.7 subcommittee has been working on the development of a specification for enhanced Category 5 cabling for about 2 years. What started off initially as a relatively straightforward undertaking burgeoned into a major development effort that was necessary to ensure satisfactory channel performance. It took a lot longer than anticipated to finish the technical work on the Category 5e standard. In the long run, the delay will be beneficial for the industry since many of the problems and issues, such as return loss, have been resolved up front, and should not come back to haunt us. This is a hard learned lesson from the growing pains associated with the evolution of Category 5 in the early years before 1995.

A task group within the TIA TR 42.7 subcommittee was involved in modeling channel performance for Near End Crosstalk (NEXT) and Equal Level Far End Crosstalk (ELFEXT) coupling loss. The NEXT loss needs to be considered from all cabling components in close proximity to the near end disturbers (transmitters on adjacent pairs). The further away the component is located from the disturbing source, the less significant is the effect on overall NEXT loss. In practice, it has been found that components (e.g. connectors) that are located more than 20 meters from the near end need not be considered. In the worst case, the TIA model assumes that the resultant NEXT from the combined length of cable and cords add together as a voltage sum, i.e. in-phase, with the NEXT from two near end connectors. The following equation applies for pair-to-pair channel NEXT loss in dB:

$$NEXT_{channel} = -20 \cdot \log \left(10^{\frac{-NEXT_{cable}}{20}} + 2 \cdot 10^{\frac{-NEXT_{conn}}{20}} \right)$$

The crosstalk coupling path in the case of Far End Crosstalk (FEXT) at any point along a channel includes the attenuation of a portion of the cable transmit pair and a portion of the cable receive pair circuit. Each coupling point is attenuated by approximately the same amount and therefore contributes equally to the total FEXT coupling loss as measured at the far end. By definition, ELFEXT = FEXT - Attenuation is a ratio of the FEXT Loss relative to the level of the receive signal.

In the worst case, the TIA model assumes that the ELFEXT from the combined length of cable and cords add together as a voltage sum, i.e. in-phase, with the crosstalk from four connectors. The following equation applies for pair-to-pair channel ELFEXT loss in dB:

$$ELFEXT_{channel} = -20 \cdot \log \left(10^{\frac{-ELFEXT_{cable}}{20}} + 4 \cdot 10^{\frac{-ELFEXT_{conn}}{20}} \right)$$

Finally, the TIA crosstalk model takes into account the added noise due to multiple disturbers operating simultaneously on all pairs at both ends of the channel. This is the actual case for systems that use parallel, full duplex transmission such as 1000BASE-T. The TIA model assumes that these noise sources add as a power sum. The resultant Power Sum NEXT and FEXT are given by:

$$PSNEXT_{channel} = -10 \cdot \log \left(10^{\frac{-X1}{10}} + 10^{\frac{-X2}{10}} + 10^{\frac{-X3}{10}} \right)$$

$$PSELFEXT_{channel} = -10 \cdot \log \left(10^{\frac{-X1}{10}} + 10^{\frac{-X2}{10}} + 10^{\frac{-X3}{10}} \right)$$

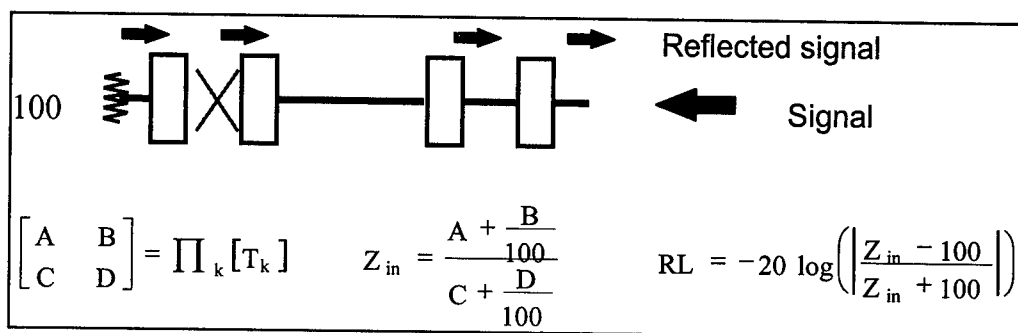
Where, X1, X2, and X3 are the pair-to-pair measurements between the selected pair in dB and the other three pairs.

One of the main reasons for the delay in the Category 5e standard has been the issue of return loss performance. It was pointed out to the TR 42.7 committee at the end of last year that channel return loss failures in the field (tested to the draft 5e standard) were a major cause of concern.

An investigation by a TIA task group led to the conclusion that impedance mismatch between components (cables, cords and connectors) was one of the main factors contributing to channel return loss failures. Another factor was the instability in patch cord impedance due to handling.

The latest Category 5e draft standard contains much tighter return loss requirements on all components as well as a new patch cord mechanical stress test. These requirements were validated using a channel return loss model and experimental data.

The channel return loss performance was modeled using a cascaded transmission line model containing nine sections. Each section is modeled by its own transmission matrix $[T_k]$. The return loss is determined from the resultant transmission matrix using the equations shown in the figure below.



where,

$$A = \cosh(\gamma \cdot \ell)$$

$$B = Z_0 \cdot \sinh(\gamma \cdot \ell)$$

$$C = \frac{\sinh(\gamma \cdot \ell)}{Z_0}$$

$$D = \cosh(\gamma \cdot \ell)$$

$$\gamma = \alpha + j\beta$$

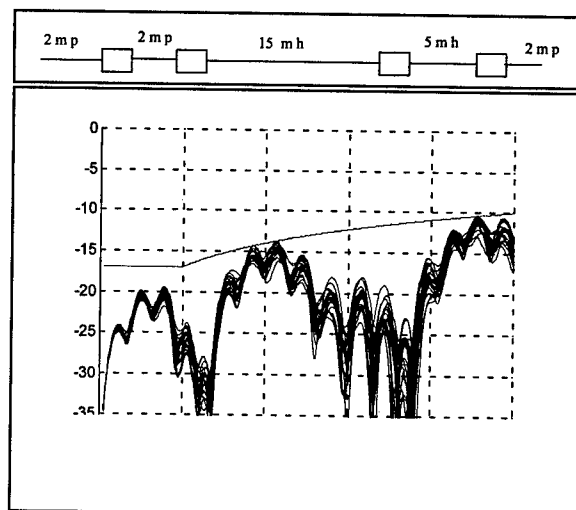
$$\alpha = \frac{\text{Atten(dB)}}{20 \cdot \log(e)}$$

$$\text{Atten(dB)} = k_1 \cdot \sqrt{f} + k_2 \cdot f + \frac{k_3}{\sqrt{f}}$$

$$\beta = \frac{2\pi f}{V_p}$$

EXAMPLE CATEGORY 5e MODELING RESULTS

20 dB con, 22 dB peak RL patch, with 20 different cables whose 100 meter RL met the proposed cable RL requirement. Just meets Channel limit



reference: 3/8/99 By: Jim Sciacero Microtest

What is the most important addition to the enhanced Category 5 standard?

The patch cord return loss test is very important. The patch cords are often the weak link in a cabling system. The new patch cord return loss test requires that the patch cord be tested before and after mechanical handling, to ensure that the impedance remains stable and within tight limits. A deviation of greater than ± 5 Ohms about a nominal impedance of 100 Ohms can result in a failure.

What is the significance of the enhanced Category 5 standard?

The new transmission parameters and requirements are a major improvement over Category 5. These performance improvements will enable Category 5e cabling to support gigabit applications such as 1000BASE-T for worst case channel topologies that can include up to four connectors and 100 meters of cabling. The most demanding requirements are on the cable and cabling return loss performance. A higher return loss in dB, requires a more uniform cable impedance (more precise manufacturing process) and better impedance matching between components. This will translate into a cleaner signal and more reliable performance (fewer data errors).



Paul Kish graduated with an M.A.Sc. degree in electrical engineering from the University of Waterloo, Ontario, Canada in 1972. He has held a number of positions at Northern Telecom including Manager of the Cable Development Laboratories, Manager of Cable Design and Product Manager for IBDN Cabling.

Paul Kish is currently Senior Product Manager, IBDN Systems and Standards with NORDX/CDT and is also the current chairman of the TIA engineering committee TR-42 responsible for "Telecommunications Cabling Infrastructure Standards".

Panel Discussion Abstract—Session 14

NEW DEVELOPMENTS IN TWISTED PAIR CABLE STANDARDS

Rob Wessels

CommScope Inc. of North Carolina, Hickory NC

ABSTRACT

In the not too distant past we measured data throughput over twisted pair cables in kilobits per second. Current applications such as 1000 BaseT transmit information at rates in excess of a Gigabit per second. As Moores Law continues to define our advances in LAN transmission speeds it is very apparent that updated cabling standards are needed. Category 5 cable was developed in the early 1990's to provide a transmission media that would support increases in network transmission speeds. During the development of a twisted pair standard for Gigabit Ethernet the IEEE 802.3 committee recognized the need for additional parameters to be characterized for twisted pair cabling. Additional headroom for existing parameters was also desirable. In response to these needs several standards bodies have initiated work to develop new cables for existing and future applications. These groups include ANSI/TIA/EIA-TR42, NEMA, ICEA and ISO/IEC.

To respond to this challenge draft standards were developed for Category 5E and Category 6 UTP cable. Category 7 shielded cables are also being characterized by several standards organizations. Category 5E cable retains the 100 MHz bandwidth of Category 5 but has tighter requirements for Near End Crosstalk (NEXT) and adds several new measurement parameters. Category 6 cable is characterized to a frequency of 250 MHz and requires improved NEXT and attenuation relative to Category 5E. In addition Category 6 cables must meet several new measurement parameters. Category 7 type cables have bandwidths ranging up to 750 MHz. New challenges in the measurement of balanced cables have surfaced during the development of these standards.

Increased data throughput is not accomplished by simply increasing cable bandwidth. Applications such as Gigabit Ethernet utilize full-duplex transmission schemes combined with complex encoding and splitting of data streams for transmission over multiple pairs. To facilitate

the use of these techniques digital signal processing (DSP), including echo cancellation, crosstalk cancellation and signal equalization is used. In order to support these signaling schemes, new measurement parameters have been defined. The parameters include Return Loss (RL) and Power Sum Crosstalk (PSUM FEXT/NEXT). Also characterized are pair to pair NEXT, FEXT, attenuation, delay skew, propagation delay and characteristic impedance. For Category 6 cable standards balance requirements are being established.

The importance of patch cords in channel performance has been very evident. Patch cable requirements are also addressed in the new standards. A major discontinuity between North American and international standards is the attenuation allowance for patch cable. This will continue to be an issue as attempts are made to harmonize cabling standards worldwide.

It is hoped that with the publishing of these new cable standards additional LAN applications will become feasible. There haven't been any indications that the growth in LAN technology will be slowing down. These new standards will facilitate technology growth well into the future.

AUTHOR

Rob Wessels received his Bachelors of Chemical Engineering degree from the Georgia Institute of Technology in 1982. He also received an MBA from Georgia State University in 1989. Rob is currently Vice President of Engineering for CommScope.

Panel Discussion Abstract—Session 14

INSTALLATION EFFECTS UPON CABLING PERFORMANCE

Paul Vanderlaan

Belden Electronics Division, Richmond, Indiana

ABSTRACT

There are two critical components to the successful completion of a data highway. First and foremost the quality of the components must perform to the minimum system requirements. Second, the installation of the components must be done in such a manner not to degrade the overall system performance. The installation requirements of category 5 brought new inventions and a new awareness to the telecommunications industry. Category 5e and category 6 promise to do the same.

Category 5 required a new installation technique. The channel electrical specifications as called out in TIA/EIA TSB67 revolved around near-end crosstalk (NEXT) and attenuation. Installers familiar with the old category 3 type material had to adjust their termination style in order to meet these installed requirements. These installers were given only minimal guidance as described in ANSI/TIA/EIA-568-A. These guidelines were vague at best and sometimes, depending on the conditions, not feasible to incorporate.

Through the development of category 5e and category 6 cabling, several different segments of the industry have made some surprising discoveries. These discoveries have been prompted by some of the new requirements, the increased frequency bandwidth of category 6, and the ability of hand held test manufacturers to verify these new parameters with increasing accuracy. Many of these discoveries will have a direct impact upon the cabling practices of today.

The standards groups are attempting to address these issues by incorporating these installation guidelines into the proposed TIA/EIA-568-B.1 document. Attempts are underway to re-qualify requirements such as pair untwist, cable bend radius, jacket removal, conduit fill, and pulling tensions on cables. New items under

investigation include pulling methods for large cables, service loops, patch cable management, and bundling techniques.

Although neither comprehensive nor exhaustive, the TIA/EIA committee is attempting to provide a set of guidelines for cable installation and termination. By the diverse nature of the industry, some of these guidelines will have to be generic in nature. However, the intent is to provide the installer with a new set of guidelines and the end user a list to verify his or her installation as new systems are installed in the next millennium

AUTHOR



Paul Vanderlaan is a Product Development Engineer at the Belden Electronics Division, IN and received his B.S.E.E. degree from Purdue University in 1992. Paul has over 7 years of experience with Belden developing high performance cable. He holds two patents and represents Belden at the TIA standardization meetings.

Panel Discussion Abstract—Session 14

NEW DEVELOPMENTS IN CONNECTING HARDWARE SPECIFICATIONS

Valerie Rybinski

The Siemon Company, Watertown, Connecticut

ABSTRACT

Like a roadway without bridges and bypasses, cables without compatible connecting hardware can not support the data flow of tomorrow's information transfer needs. In particular, next generation connecting hardware will not only exhibit superior electrical performance over ANSI/TIA/EIA-568-A and ISO/IEC 11801 category 5 requirements, but they will also be required to be backward compatible with the existing categories of components.

As development progresses in the specification of category 5e and category 6 component requirements, standards groups are finding that electrical compatibility with existing categories is no longer assured. As a result, the issue of backward compatibility and product interoperability has come under increased scrutiny. Standards groups have agreed that the specification of next generation connecting hardware requirements that support backward compatibility and product interoperability can be realized by adopting an improved test plug qualification method and precisely specifying a complete range of transmission parameters.

Supporting increased bits rates necessitates that next generation solutions take advantage of full-duplex transmission schemes in addition to the standard methods of encoding, transmitting over multiple pairs, and utilizing digital signal processing techniques. In order to support these signaling schemes, TIA and ISO will define connecting hardware near-end crosstalk, far-end crosstalk, attenuation, return loss, delay skew and propagation delay performance. Connecting hardware crosstalk requirements will be specified both with and without common mode terminations, thereby guaranteeing compatibility with all types of equipment terminations. It is expected that the new transmission parameter of balance will also be introduced for category 6 performance specification to help ensure that cabling

components do not emit unwanted electromagnetic radiation and are not susceptible to electrical noise.

In addition, the standards groups have recently finalized patch cord performance specifications. The first modular patch cord NEXT loss test procedure, which is defined by a compatibility assessment between an outlet and a modular cord, will be published in October of 1999.

Currently, standards groups are focusing the majority of their development efforts on performance improvements beyond what is currently specified in ANSI/TIA/EIA-568-A and ISO/IEC 11801. Looking forward, it is expected that these new specifications will emerge as a true superset of existing requirements and supported applications. By achieving global harmonization and providing even greater performance advantages, next generation cabling standards will ensure that new telecommunications technologies will be supported well into the millennium.

AUTHOR



Valerie Rybinski received the B.S.E.E. degree from the University of Connecticut in 1991. Valerie is a senior electrical engineer at the Siemon Company in Watertown, CT.

Panel Discussion Abstract—Session 14

NEW DEVELOPMENTS IN CONNECTING HARDWARE MEASUREMENT PROCEDURES

Sterling Vaden

Superior Modular Products, Swannanoa, NC

ABSTRACT

TIA and ISO standards are being tightened for Category 5 and new category 6 and 7 standards are under development. These standards are pushing the industry to develop new measurement techniques in order to ensure that cabling components comply with the new requirements.

As is so often the case, performance requirements are being specified for which there is no standard measurement procedure that has been established that yields a known level of accuracy. The engineering committees are therefore faced with the task of developing adequate measurement methodology. This has historically been done after new standards requirements have been developed.

With the development of the Cat5e standard, the TIA connecting hardware working group has undertaken the difficult task of establishing a new measurement procedure for modular plugs which are used subsequently to qualify modular connecting hardware. This measurement procedure is generically known as de-embedding.

De-embedding has been used successfully in the RF and microwave fields to characterize components that are difficult or impossible to measure individually. The method involves measuring one part of an assembly, measuring the whole assembly, and then mathematically subtracting the known part from the whole to obtain values for the unknown part.

In the case of modular connecting hardware, the connector exists in the link or channel as a plug and jack mated pair. The link and channel performance requirements are developed from the performance of this mated pair connection. It has long been recognized that the performance of the mated connection is highly influenced by the modular plug, hence the requirement for

determining modular plug performance independently from the jack. In a real sense, the values specified for modular plug performance in the Cat 5, Cat 5e draft, and the proposed Cat 6 standards are the bedrock on which connecting hardware performance is built.

It is of the highest importance then that these plugs can be measured accurately and without elaborate means. It is for this reason that TIA has developed a method of de-embedding that does not require the manipulation of 16 X 16 or 8 X 8 matrix equations and transforms. Since the basic dimensions of the modular plug interface are highly standardized, a method that relies on these standardized characteristics allows simplified mathematics to be used to arrive at the most important electrical parameters of the modular plug.

At the present time near end crosstalk NEXT has been established as the primary qualifier of modular plug performance. The TIA connecting hardware working group is continuing to develop performance criteria for FEXT and return loss. In addition, variations of the de-embedding method are being considered for category 6 connector qualification.

AUTHOR



Sterling Vaden received the B.S.E.L. degree from Cal Poly in 1982. He is currently Vice President of Research and Development at Superior Modular Products in Swannanoa, NC.

Universal Fiber Optic Cable with Pultruded Core

R. UTESCHILL AND R. KLUG

IPT – Innovative Pultrusions Technologie, Kapfenberg, Austria

1. Abstract

TOP CABLE is used in communication transmission networks. It can be used as an aerial, buried or duct cable. The fiber tubes are enclosed by a glass fiber reinforced plastic (GRP) tube for stress and pressure relief and protection of the core. The GRP tube carries a polyethylene (PE) jacket. A fiber optic cable constructed accordingly has a small diameter, low weight and is all dielectric. As an aerial cable it is self-

supporting and shotproof. It is injectable into pipes and can easily be made flame resistant. Due to its wide variety of features, the same cable can be used for all the above purposes and is thus ideal in areas where the route of the cable is not exactly known beforehand. Several hundred kilometers have already been installed in South East Asia.

2. Introduction

Since the advent of fiber optic cables, numerous very specialized constructions have been developed to meet an extremely wide variety of technical, environmental, production and transmission requirements.

Just as an example, a network provider in a developing South East Asian country might want to establish a fiber optic link over a distance of 400 km, where in parts of the area medium voltage overhead power lines should be used to cross a rather harsh mountainous region, parts of the distance should be overcome on primitive wooden poles through virgin jungle while through occasional swampy areas sprinkled in between, the cable seems safer being immersed directly in the mud. In and around several villages and small towns on the way needing access to the

While each of these cable types probably represents an optimum solution to a particular situation, there are cases where a much broader adaptation to diverging requirements is an absolute must.

link, the cable should be buried directly for safety reasons and, on top of that, a certain amount of flame resistance is required within the numerous terminal buildings. It is no problem to find cable designs perfectly meeting any of these requirements separately, however, since cable laying and splicing should be done by the local workforce trained only in short crash courses, the use of just one single type of cable is a valuable asset, not to speak of later repairs and/or replacements, where logistics become an additional problem.

It is easy to imagine similar situations under less exotic circumstances, where a versatile construction, meeting a multitude of demands at the same time, would be highly desirable for the customer. From the point of view of the manufacturer, a

universal solution to this complex spectrum of requirements might offer the additional attraction to realize significant economies of quantity, which in turn would make a product like this even more competitive.

3. Our design solution:

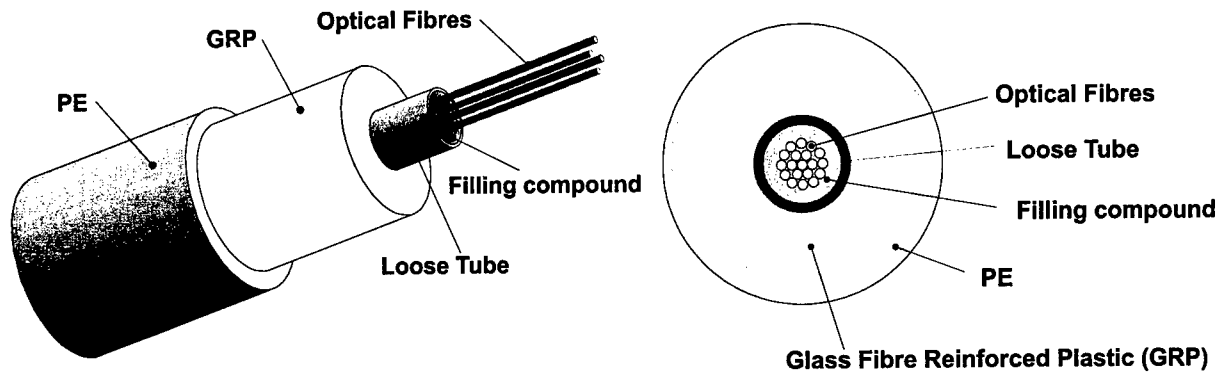


Fig. 1: Basic design according to central loose tube concept

Fig. 1 shows the basic idea behind our product design: A central loose tube housing up to 24 standard single or multimode fibers is surrounded by a massive, extremely rugged GRP tube. This thick-walled GRP tube is pultruded in a specially developed process ensuring perfect protection of the fibers and their transmission characteristics from all mechanical, chemical and other environmental stresses. An outer jacket

provides surface protection of the GRP. Usually PE is perfectly sufficient for this purpose, although other materials such as FRNC (flame retardant non corrosive) or LLDPE (linear low density PE) compounds may offer additional performance features (see 5.4 and 5.5). For fiber counts above 24 and/or increased strain requirements SZ stranded core constructions, fig. 2, are available, too.

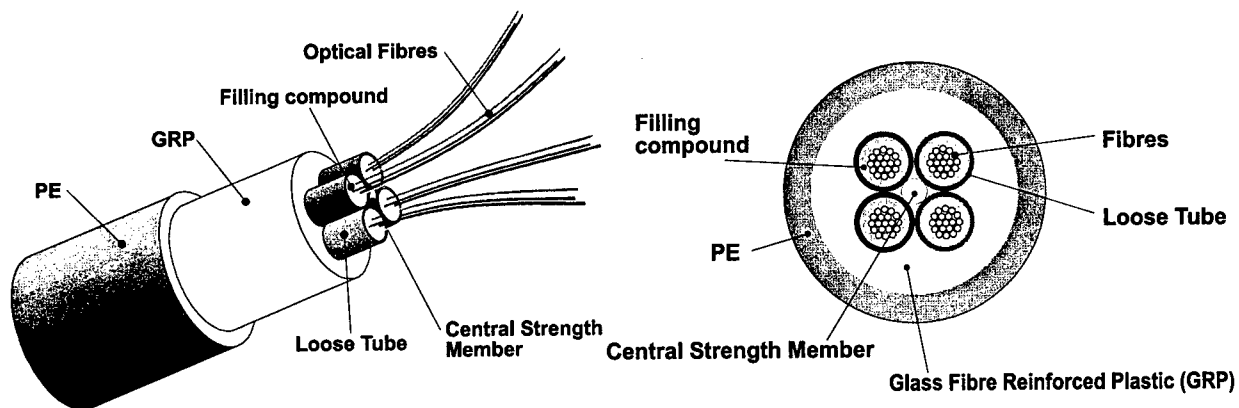


Fig. 2: Basic design according to (SZ) stranded loose tube concept.

4. Standard designs

For a newly developed product it is particularly important not to get lost in a maze of different special versions of, in principle, the same thing. This is all the more valid for a design which, by its very concept, aims at all-round application. At

present we try to restrict the product range to essentially 4 types of the central tube design (fig. 1). Their main parameters are given in fig. 3. For the stranded tube design no standard types have as yet crystallized.

VERSION:		STANDARD		EXTRA	
parameter		excess load 15 N/m		excess load 25 N/m	
number of fibers		≤ 12	> 12, ≤ 24	≤ 12	> 12, ≤ 24
loose tube outer diameter	mm	2,9	3,5	2,9	3,5
diameter over GRP	mm	6	6,6	7,6	8
nominal GRP cross section	mm ²	21,7	24,6	38,8	40,6
modulus of elasticity	kN/mm ²	45	45	45	45
coefficient of thermal expansion	1/K	8x10 ⁻⁶	8x10 ⁻⁶	8x10 ⁻⁶	8x10 ⁻⁶
PE-sheath, approximate value	mm	2	2,2	2,2	2
cable diameter	mm	10 ± 0,3	11 ± 0,3	12 ± 0,3	12 ± 0,3
min. bending radius	mm	250	275	300	300
cable weight, approximately	kg/km	100	120	155	155
tensile force at 100m span&exc.load	N	4620	4850	7810	7880

Fig. 3: 4 standard designs, central tube type

5. Essential performance aspects

5.1 Handling

Cable and preparation is faster and easier than one might think. From our experience with this newly developed product, special, though quite simple, tools are required for fast stripping of the GRP tube, see fig. 4. The procedure is to remove the jacket using standard cutters; since there is no

adhesive, this is a very simple step. Then, a ring shaped groove is made around the GRP tube, using a glass saw. Next, the tube length to be removed is cleaved longitudinally, starting at the cable end and proceeding towards the ring groove; this can be done with any kind of knife.

After cleaving, the GRP tube can be peeled off like the segments of a banana skin. Once the fibers' loose tube(s) is (are)

accessible, there is no difference in handling as compared to other standard fiber optic cables.

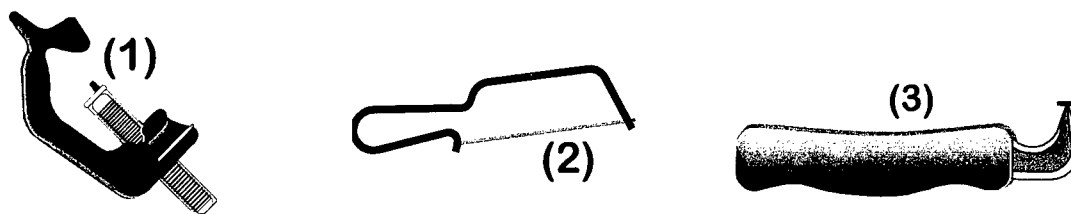


Fig. 4: GRP stripping tools

- (1) cable cutter
- (2) glass saw
- (3) cleaving knife

Another frequently addressed problem is the springing back of an unfastened cable end from the drum. This is, admittedly, a (safety) problem – however, the remedy is as simple as effective: keeping the end fastened to the drum as long as possible, either by the usual string or by clamping it to the drum's flange with U-clamps in the

same way as it has been done since ages for any other type of cable, too. Though some people seem to worry, we have not had one single accident since the beginning of our activities with this cable simply by obeying this generally accepted rule of good workmanship in handling of cables.

5.2 General GRP properties

Below, fig. 5, are given the presently used material constants of our GRP. Since the beginning of our developmental work, the tensile modulus has been increased considerably due to progress in getting the resin in between the glass fiber rovings, thereby increasing the relative amount of

glass, and we still deem further, though only marginal improvements to be possible. In many other respects, this material already corresponds to an optimum as seen from the cable designer's point of view.

GRP-properties		
glass type	E	
spec. Weight	2,1 g/mm ²	
coeff. Of expansion	8x10 ⁻⁶ 1/K	
tensile strength	1,30 kN/mm ²	DIN 53455, EN 61
elong. at break	> 2,4 %	
elastic (tensile) modulus	45,0 kN/mm ²	DIN 53457, EN 61
compressive strength	0,95 kN/mm ²	
flexural strength	1,85 kN/mm ²	EN 63
water absorption	0,02 %	70 ° C/168h, DIN 53495
temp. Stability	-50.... +120 ° C	

Fig. 5: General GRP-properties as used

5.3 Duct and directly buried application

As shown in fir. 6 below, this cable passes all usual tests applicable to this basic area of application. It must be added, however, that water blocking properties for the whole cable cross-section can at present

only be guaranteed for the central tube design, fig. 1. Trial lengths of dry watertight stranded constructions (1) have already been done but qualification tests are not finished yet.

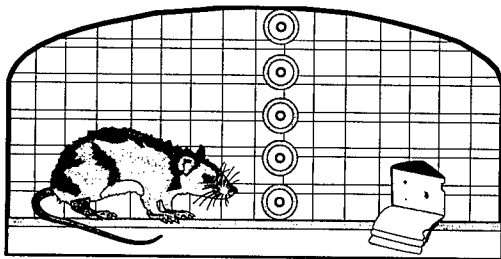
miscellaneous performance tests		
Test	Result	Conditions (IEC 794-1)
temperature cycling	-55... +85 ° C	6 steps à 24h, nac, nfb, ncd
bend	,min. diam. 200 mm	≤ 12 F, nac, nfb, ncd
repeated bending	20 x D	≤ 12 F, nfb
kink	,min. diam. 200 mm	≤ 12 F, nac, nfb, ncd
torsion	10 x ± 360 °	≤ 48 F, cl 2m, nac, nfb, ncd
impact	30 Nm	≤ 12 F, hammer radius 12,5mm, nac
crush	3000 N	≤ 12 F, 0,1m shoe length, nac, nfb
tensile performance	3000 N	≤ 24 F, nac, nfb, ncd
snatch	300 N, 0,1 m height	6F, 4,5m span, 0,3m sag, nfb, ncd
long term vibration	10 ⁸ cycles	48F, 2000N, nac, nfb, ncd (VDE0212)
water penetration	1 m water col.	Cl 3m, dry end after 48h

Notes: cl...cable length; nac...attenuation change ≤ 0.05 dB; nfb...no fiber break, ncd...no cable damage

Fig. 6: Miscellaneous performance tests

5.4 Indoor applications

From its basic design features, this cable is obviously not an indoor distribution cable. However, as a riser cable, leading e. g. to floor distribution boxes, it is perfectly suited. This is the application we have in mind when recommending it for indoor use.



For indoor applications the requirements are usually very similar as for duct and direct buried laying; the essential additional feature is flame retardancy. This is tested according to IEC 332-3(C) / ÖNORM E 3652 / VDE0472 T.804(C) and TOP CABLE, equipped with FRNC jacket, meets the requirements. Since the diameter of the cable remains the same for both PE and FRNC jacket, there is virtually no difference in handling and the two versions are simply distinguished by the jacket's color (black: PE, green: FRNC).

Fig. 7: Test setup for rodent attacks (↗) and results (↘)

Forschungsinstitut für Versuchstierzucht und -haltung, Himberg	AUSTRIA
Brown Rat (<i>Rattus norvegicus</i>)	10 weeks (max. 72 hrs without food) (max. 24 hrs without water)
Justus - Liebig - University, Gießen	GERMANY
Brown Rat (<i>Rattus norvegicus</i>) House Mouse (<i>Mus musculus</i>) Field Mouse (<i>Apodemus sylvaticus</i>) Fat Dormouse (<i>Glis glis</i>)	1.Period: 4 days 2.Period: 4 days 3.Period: 11 weeks
All India Co-Ordinated Research Project On Rodent Control, Jodhpur	INDIA
Field Rat (<i>Rattus melta</i>) Indian Gerbil (<i>Tatera indica</i>) Bandicoot Rat (<i>Bandicota bengalensis</i>)	appr. 5 weeks

In both indoor and outdoor applications, the ability of a cable to withstand attacks of rodents and termites may be decisive for its widespread use. TOP CABLE has therefore been subjected to numerous tests involving rodent attacks with excellent results, see fig. 7. Usually, the jacket is bitten away within several hours; as expected, the GRP tube remains untouched. It seems that its smooth, hard surface offers too little attraction for the animals. Similar results are obtained with termites.

5.5 Aerial application

From its very favorable ratio of load-bearing to non-bearing cross-section and also from the relation between elastic modulus and weight per cross-sectional unit, it might be supposed that this cable is an ideal candidate for aerial applications. Our tests fully confirmed this conjecture.

This cable may be used as it is for aerial applications up to medium voltage (≤ 30 kV) overhead power lines; fig. 3 gives parameters for typical cases. Vibration tests were passed, see fig. 6. An investigation on dry-band arcing effects (2)

Installing this cable as an aerial cable does not require special precautions as compared to other ADSS types. For dead ends the usual helical preformed fittings are recommended, up to 150 m span length without reinforcement. Between dead end sections, apart from the usual suspension clamps specially developed pulleys (Mosdorfer) can be used, which during laying are working as simple rollers. By pushing a lever, the pulley is blocked for

Starting from our initial design, the only improvement we found necessary was not to use any adhesive between jacket and GRP – which tended to lubricate these two components at higher temperatures rather than bonding them together.

as they would have to be expected e. g. when used on 380 kV systems is on its way and we expect to propose viable solutions for this application towards the end of this year.

normal operation. In case of a predetermined differential excess load on the pulleys (in the order of 500...700 N), the braking mechanism gives way to stress relief of the cable. Later, when the cause of the differential excess load has been removed, the cable itself reestablishes load equalization again and the pulleys may be blocked anew. Mounting of these fittings on all usual types of poles is possible.

This cable is shotproof, a very special feature for an all dielectric cable indeed, and quite important e. g. in Austria as well as in Australia. In tests performed up to and including grain size 2,9 mm diameter (Winchester Super Speed cal. 12/70), fired

from a distance of 15 m using a shotgun Baikal Mod. IJ-25, the grains enter or even graze through the jacket, but never injure the GRP tube itself, thus fully protecting the fibers.

5.6 Underwater applications

TOP SEA is a further development of our proved cable. This special product is safely

This new technology makes a copper sheath unnecessary. Therefore TOP SEA is lighter and thus can be laid better and more economically compared to competing

For easier understanding – that is what TOP SEA looks like! The most particular

protected by an aluminum layer against decomposition by penetrating hydrogen.

products. At present tests are being carried out by the Research Institute Seibersdorf, Austria.

feature is that the aluminum layer is coated on below the exterior HDPE-layer.

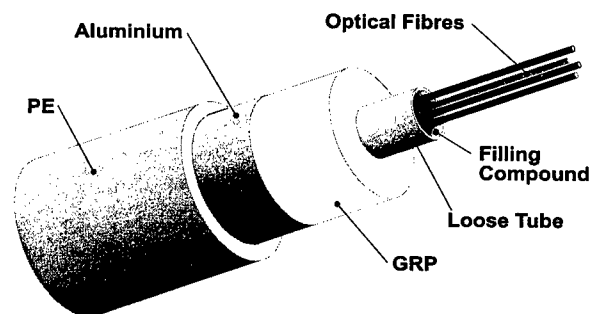


Fig. 8: TOP SEA Cable

5.7 Ground wire application

TOP GW is a new generation optical fiber composite ground wire. Based on ADSS this cable, through researching, testing and developed the new type of OPGW, called

The cable core consists of either a single central loose tube or a loose tube bundle stranded around a central strength member. The fibers in the loose tubes can be singlemode and/or multimode. A cold fill thixotropic tube filling compound provides both water blocking and prevention of mechanical damages. The cable core

TOP GW. It is one kind of very worthwhile substitute of traditional OPGW.

elements are protected against mechanical damages by a pultruded glass fiber reinforced plastic tube (GRP). The GRP sheath provides excellent protection against tensile and compression forces that may be incurred during installation and service. It also resistance against rodents, termites and bullets.

Coupled with the pultruded Aluminum outer sheath, it is more uniformly, concentrically and tightly around the cable core elements than welded Aluminum tube. The cable is capable of withstanding

harsh environmental conditions. The standard cable is sheathed with different thickness of Aluminum, on demand for special applications.

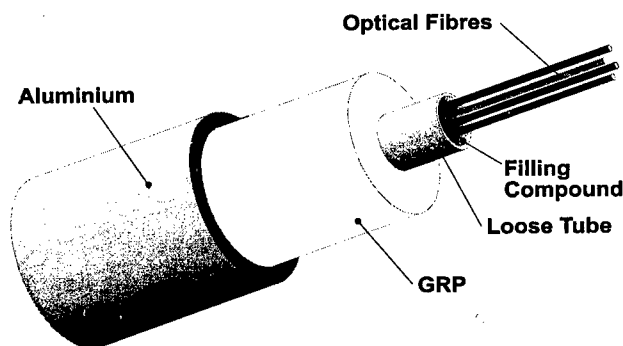


Fig. 9: TOP GW Cable

6. Conclusions

Several thousands of kilometers of this cable have already been installed during the past years in South East Asia, and several hundreds of kilometers in other countries all around the world, each single project being a full success. This brings us to the conclusion that this cable actually fills a market-niche where a low cost, rugged and extremely versatile cable design is required. We are very keen to

extend the field of potential applications of this novel product to other areas; some of them have already been mentioned in this paper (dry longitudinally watertight stranded type: on HV power lines; as a submarine cable), but there might be others yet. Continued contacts with our customers will show where the market leads us and this cable.

Speaker



Raoul Uteschill
IPT – Innovative
Pultrusions Technologie
Burgstallweg 25
A-8605 Kapfenberg
Austria

ALL-DIELECTRIC SELF-SUPPORTING CABLES (ADSS) WITH BALLISTIC PROTECTION FOR USE IN THE COUNTRYSIDE

Sônia S. Natume, Alexandre M. Simião, João M. I. Furtado, Leonardo Silvério

Furukawa Industrial S.A. Produtos Elétricos, Curitiba, Paraná, Brazil.

ABSTRACT

This paper describes the performance of ballistic protection on aerial optical fiber cables, All Dielectric Self-Supporting (ADSS) type, that can be damaged by hunters while adjusting their guns or shooting birds in the countryside. Considering the high cost to repair optical fiber cables systems and the problems with transmission loss, an alternative is to use tapes with high modulus and tenacity fibers, with lower weight and more efficient ballistic protection when compared to usual woven aramid tapes¹.

Tests with plates were performed, to define the best cable configuration and a good correlation was found on plates and cables shot-gun test results. Prototype cables were manufactured and checked in dimensional, mechanical and environmental characteristics².

INTRODUCTION

Aerial telecommunication cables offer to operating companies, advantages in installation cost when in comparison with the usual direct buried or in ducts optical fiber cables. On the other hand aerial cables require additional protection according to the service environment¹.

As in some Brazilian regions like South and Central-West, and Argentina there were claims about damages on aerial optical fiber cables without antiballistic protection, which were caused by hunters or vandals, it is important to develop cables with specific materials to avoid the optical fiber damage by lead pellets.

The common antiballistic materials used in this kind of cables are:

- steel tapes which increase the cable weight, and require grounding;
- polyamide which can decrease the cable flexibility;
- woven aramid tapes which are good ballistic protection but they are heavy (400 to 600 g/m²) and can absorb moisture increasing the cable weight.

Alternative materials were used to take into account the followings parameters: low weight, non hygroscopic and excellent ballistic performance. These materials avoid any gap between high modulus fibers and hold them firmly in place during the shotgun impact, reducing the penetration/trauma of the lead pellets on the cable.

CABLE DESIGN

In order to define the best antiballistic cable design it was necessary to consider some factors like :

- the distance from the gun to the cable;
- the type of gun, type of pellet and it's size;

These parameters were defined in accordance with international standards as GT.ER.f6.020 Ed.01(Grupo Telefónica – "Resistencia al disparo por arma")³. and IEC/CEI 794-1(3.15 Method Shot-gun damage)⁴. Both consider 20m of distance between gun and cable.

Fig.01 illustrates the basic design of the aerial antiballistic optical fiber cable.

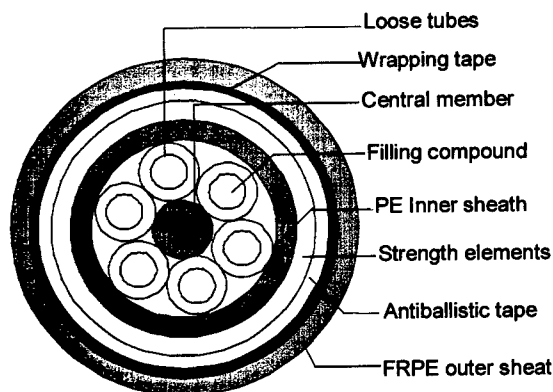


Fig. 01 – Aerial antiballistic cable type ADSS - cross section

With this cable design was possible to have a good contact between the outer sheath and reinforced strength elements, and an excellent mechanical properties were obtained.

Antiballistic tapes were applied helically over the reinforcement fibers. Although these tapes might not be considered as reinforcement elements in the cable.

ANTIBALLISTIC MATERIALS

Antiballistic tapes considered in this work were manufactured with two different types of high modulus and tenacity fibers, as described in Table 1⁵:

Table 1 – Fiber characteristics

Properties	Fiber 1	Fiber 2
Density (g/cm ³)	0.97	1.44
Tensile strength (GPa)	3.0	2.9
Elongation (%)	3.4	3.6
Modulus (GPa)	100	83

These fibers are arranged in tapes to improve the impact absorption. The tape characteristics are described in Table 2:

Table 2 – Tape characteristics

Properties	Tape 1	Tape 2	Tape 3	Tape 4
Fiber type	1	2	2	2
Thickness (mm)	0.18	0.30	0.53	0.41
Area density (g/m ²)	150	230	400	310

Tapes 1 and 2 have pre-tensioned fibers, avoiding gaps between the fibers. Therefore, the best impact resistance is obtained with highest energy dispersion at the impact point, and as a consequence, a significant reduction of the lead pellet penetration was obtained on the cable core (see Fig.02).

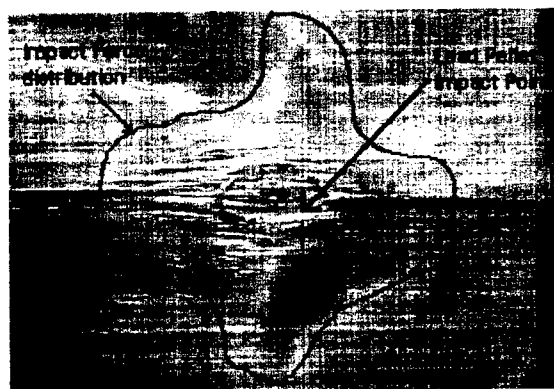


Fig. 02 – Antiballistic tape 1 damaged by a lead pellet.

Tapes 3 and 4 are usual woven tapes, that concentrates the impact force in a small area causing bigger lead pellet penetration as shown in Fig. 03:

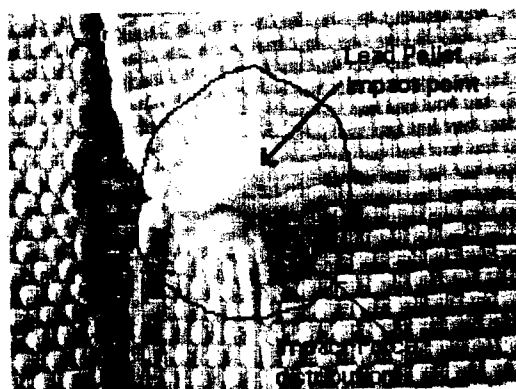


Fig.03 –Antiballistic tape 3 damaged by a lead pellet.

SHOT-GUN TESTS

In order to define the best material to protect the cable against shot-gun damage, tests with different plates and prototype cables were performed as described below.

Shot-gun test for plates

Test with plates were performed positioning the plates in contact with a clay backing, and measuring the penetration/trauma, due to the lead pellets impact.

Shot-gun test conditions were:

- distance from gun to cable: 20m;
- gun type: 12 gauge cylindrical, CBC pump;
- shot size: 5 (See Table 3);
- shot type: lead.

The experimental used a clay backing thickness with 150mm, and was made with controlled temperature at $35 \pm 2^\circ\text{C}$, maintaining the texture of the clay in order to give reproducible results^{6,7}.

Table3 – Cartridge characteristics

Property/shot type	# 7	# 5
Pellet unit weight (g)	0.080	0.150
Total n° of pellets	259	188
Pellet diameter	2.2	2.7
Speed (m/s)	370	390

According to the data showed in Table 3, lead pellet # 5 is more critical than #7 in terms of the impact force to damage the cable core. For this reason only the lead pellet #5 was chosen for the plate shot-gun test.

Plate configuration. In order to simulate the cable design, there were used

polymeric layers and the same number of layers of antiballistic tapes.

The construction of the plates are described in Table 4.

Table 4 – Plate construction

Plate A	Plate B	Plate C	Plate D
FRPE	FRPE	FRPE	FRPE
Tape 1	Tape 2	Tape 3	Tape 4
PE	PE	PE	PE

Test results. The antiballistic barrier efficiency factor is defined as the ratio of the percentage of lead pellets stopped by antiballistic tapes and the respective tape density. As shown in Fig. 5, the best results were obtained for Sheaths A and B with very similar values. For Sheaths C and D the antiballistic barrier efficiency factor was a half.

The penetration/trauma, is another important parameter to measure the protection for optical fiber. The best results were found for Sheaths A and B, fairly because of the improved tape construction that gives better distribution of the impact energy comparing to common woven tapes (See Fig.02 and Fig.03).

Sheath D presented the worst results, both antiballistic efficiency and trauma. Based on these results, was chosen Tapes 1, 2 and 3 to manufacture prototype cables.

Table 5 – Plate shot-gun test results

	Plate A	Plate B	Plate C	Plate D
Fiber type	1	2	2	2
Tape type	1	2	3	4
Holes in 1 st layer of FRPE	56	65	60	49
Holes in antiballistic tape	20	3	7	19
Holes in 2 nd layer of PE	8	1	4	16
Traumas + holes on the clay backing	17	16	31	37
Holes on the clay backing	8	1	4	16
Depth of trauma on the clay backing (mm)	3.34	3.10	4.12	4.22
Lead pellets stopped by antiballistic tapes (%)	64	95	88	61
Area density of the tapes (g/m ²)	150	230	400	310
Antiballistic barrier efficiency factor	0.43	0.41	0.22	0.20

Tests with cables

Cable samples were tested in the same conditions of plates (20m / 12 gauge / lead pellet), with exception of:

- lead pellet size: #7 and #5;
- cable sample length: 3m

Samples were in a vertical position, with 5 kg tension the sample in a shot-gun test. Test was made with only one gun shot.

The shot-gun damage evaluation was made by visual inspection, observing whether there were holes on the inner sheath as specified by GT.ER.f6.020³, and whether the cable sample remained optically continuous after the test, as specified by IEC/CEI 794-1⁴.

Table 6 presents the cables shot-gun test results, considering the same configuration as shown in Fig.01, but changing the tape layer (type and quantity) on the cable core to define the best option in terms of antiballistic barrier.

Tests with prototype cables presented very similar results in terms of percentage of lead pellets stopped by antiballistic tapes when compare to plate shot-gun test.

Cables A, B and C presented very similar results in antiballistic barrier efficiency factor, but Cable A presented better characteristics than others, because of less antiballistic material (g/length), Cable A presented no holes on the inner sheath and no damage on the optical fiber.

For Cables B,C and D the percentage of lead pellets stopped by antiballistic tapes was 100%, but the amount of antiballistic layers used in this case are at least 50% higher than Cable A, which increases significantly the cable cost. In terms of cable linear weight, Cable A is 5 to 18% lighter than the others, as shown in Fig.05

Cable E showed almost the same percentage of lead pellets stopped by antiballistic tape comparing to Cable A but with significant increase in cable diameter and weight, see Fig.05.

All samples remained optically continuous, despite of loose tube trauma as shown in Fig.04.

Table 6 - Cable shot-gun test results

Cable sample	Tape type	Lead pellet size	Holes on outer sheath	Holes on the last tape layer	Lead pellets stopped by antib. tape (%)	Antib. layer (g/length)	Antib. barrier efficiency factor *	Holes on the inner sheath
Cable A	1	# 5	6	2	66	10	6.6	0
		# 7	5	2	60		6.0	0
Cable B		# 5	4	0	100	15	6.7	0
		# 7	8	0	100		6.7	0
Cable C	2	# 5	6	0	100	15	6.7	0
		# 7	5	0	100		6.7	0
Cable D		# 5	9	0	100	20	5.0	0
		# 7	6	0	100		5.0	0
Cable E	3	# 5	11	4	64	35	1.8	0
		# 7	4	1	75		2.1	0

Note: All samples remained optically continuous.

* Antiballistic barrier efficiency factor is the ratio of Lead pellets stopped by antib. tape and Antib. layer.

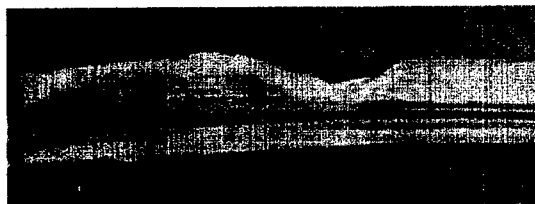


Fig. 04 – Transverse section of loose tube damaged in a shot gun test, with no optical fiber damage.

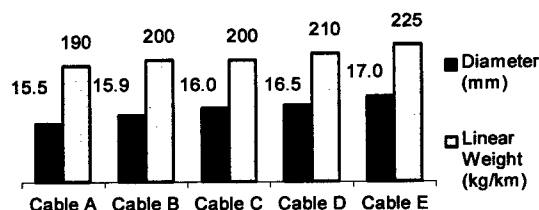


Fig.05 – Cable diameter and Linear weight comparison

MECHANICAL AND ENVIRONMENTAL TESTS

Mechanical and environmental tests were performed on prototype Cable A, that presented the best antiballistic barrier efficiency, for 200m span.

Tests were made in accordance with Brazilian standard NBR 14610 Ago. 1998⁸.

Test results are in Table 7 and all the results approve Cable design A.

Table 7 – Results of the mechanical and environmental tests of Cable A, aerial optical fiber cable with antiballistic protection

Test	Reference	Conditions	Results
Shot-gun damage	IEC/CEI 794-1:1996	Distance = 20m ; lead pellet size = #7 or as specified. Shall be optically continuous.	Pass. Optically continuous
Shot-gun damage	GT.ER.f6.020 ed.01	Distance = 20m; lead pellet size = #5 or #7. With no holes on the inner sheath.	Pass. NO HOLES ON THE INNER SHEATH.
Flame test	NBR 14160	Sample length = 600mm time exposure = 65s self-extinguish the flame and attenuation change < 0.1 dB	Pass. No attenuation change.
Fiber Strain	NBR 14160	No fiber deformation and attenuation change. Load = 3 times cable weight (540 kgf)	Pass. Load = 900 kgf.
Ultimate tensile load	NBR 14160	Load = 13.5 times cable weight (2,500kgf)	Pass. Load = 2,750 kgf
Bending	NBR 14160	Mandrel radius = 90mm; 5turns; attenuation change < 0.1 dB and No cracks or damage on the outer sheath.	Pass. < 0.03 dB no cracks or damage on the outer sheath.
Cyclic Flexing	NBR 14160	Mandrel diameter = 180 mm 50 cycles; Attenuation change < 0.1 dB; No cracks or damage on the outer sheath.	Pass. < 0.02 dB
Compressive Load	NBR 14160	Min. 1000N / 1 time cable weight. Attenuation change < 0.1 dB. No cracks or damage on the outer sheath.	Pass. Load = 3,200 N < 0.01 dB
Twist	NBR 14160	L = 150 mm; 50 cycles; 10 cycles/min. Attenuation change < 0.1 dB, No cracks or damage on the outer sheath.	Pass. < 0.02
Temperature cycling	NBR 14160	-20 °C a +65 °C (4 cycles x 48h) Attenuation change < 0.05 dB	Pass. < 0.02 dB
Impact	NBR 14160	Load = 6kgf, 25 cycles with no fiber break.	Pass. Load = 8kgf.
Creep	NBR 14160	10 days, Load = 3 times cable weigh (540 kgf) with max. 0.2% in cable strain.	Pass. 0.14% strain.

*measurement wavelength : $\lambda = 1310 / 1550$ nm.

CONCLUSION

Shot-gun tests showed a good correlation between plates and cable shot-gun tests. Thus the tests with plates are cost-effective and confident option for the choice of material and cable design. Furthermore, tapes 1 and 2 are more effective antiballistic barriers than the common woven antiballistic tapes 3 and 4.

Shot-gun tests were made with different cable designs, in terms of antiballistic tape type and quantity. Cable A presented the best antiballistic efficiency with the lowest cable linear weight and diameter. Antiballistic barrier efficiency of 60% was enough to prevent damage in the inner sheath and optical fiber in a Cable design A with competitive cost.

SPEAKER BIOGRAPHY

According to the Brazilian standards, this configuration meets and exceeds the mechanical and environmental characteristics.

Furukawa Industrial S.A. Produtos Elétricos offers the customers this cable design as a reliable and competitive option for aerial installations guaranteeing the advantages in terms of antiballistic performance, with lower weight, good flexibility and excellent mechanical properties.

ACKNOWLEDGEMENTS

The authors would like to acknowledge the support of their colleagues and suppliers in carrying out this work. Special thanks go out to Raquel Andrade, Ana Lúcia Veiga and Janúncio Medeiros for the valuable contribution.

REFERENCES

- [1] Abadía, V.; Baguer, L.; Calvo, F.; Villarig, M. "Ballistic Protection of Aerial Cables"; Spain.
- [2] Lang I.D.; Davies M.V.; Poole N.J.; Cockrill K.J.C. "Evaluation of Impact Testing for Simulated Shotgun Damage of Optical Fibre Cable". 35th IWCS, 1995, pp. 540 – 545.
- [3] GT.ER.f6.020 Ed.01. "Especificación Unificada de Requisitos de Cables de Fibras Ópticas Aéreos.(Telefónica de Argentina).
- [4] CEI/IEC 794-1:1996. Optical Fiber Cables.
- [5] Bensink, S. J. B.; "Aramid Tapes as Anti ballistic Protection of Aerial Optical Fibre Cables". 30th IWCS, 1990, pp 362 – 367.
- [6] Camara S.; Cortines C.G.. "Evaluation of Antiballistic Sheathings for Aerial Fiber Cables". 31th IWCS, 1991, pp 540 – 544.
- [7] Hochuli M.. "Ballistic Protection of aerial Cables a New Economical solution with a Special Impact Modified Polyamide". 36th IWCS, 1996, pp 817 – 820.
- [8] NBR 14160. Cabo óptico dielétrico aéreo auto-sustentado : Ago 1998.



Sônia Suzuki Natume
Furukawa Industrial S.A. Produtos Elétricos
Rua Hasdrubal Bellegard, 820 – CIC
CEP 81450-140 Curitiba-Pr-BRAZIL

SÔNIA Suzuki Natume joined Furukawa Industrial S.A. after receiving her B.S. degree as a Chemical Engineer from Federal University of Parana (UFPR)". Ever since she has been working in the R&D of materials for telecommunication cables.

Evaluation of Damping Effectiveness of Impact Dampers on ADSS Cable

David C. Sunkle, Dennis F. McKenna, and John J. Olenik

Preformed Line Products, Cleveland, Ohio

ABSTRACT

All Dielectric Self-Supporting (ADSS) fiber optic cables have a tendency to experience severe vibration due to their low self-damping characteristics. To reduce these vibration levels and prevent damage to the ADSS cable and possible loss of critical optical signals, dampers are a required component of an effective aerial fiber optic system. One of the most common dampers for ADSS cables is the impact-type damper. This paper will discuss how the damper functions and laboratory and field measurement techniques to determine the effectiveness of this type of damper. The paper will also discuss limitations of this damper.

The analysis technique used for laboratory evaluation of the impact damper includes damper energy dissipation measurements following the IEEE 664 Standard. These laboratory evaluations are then compared to results from field vibration studies conducted on similar size cables. For the field vibration studies, actual measurements are taken using specialized vibration recorders to determine how severe the vibration is in the field. These readings are taken both with and without dampers installed to provide a means for evaluating the effectiveness of the damper in reducing field vibration levels.

INTRODUCTION TO AEOLIAN VIBRATION

In overhead construction, the fiber optic cable is exposed to wind-induced motions and therefore vulnerable to damage. When overhead cables fail mechanically, the failure location is confined almost exclusively to places where hardware is attached.

Damage caused by aeolian vibration is generally long term in nature. Early detection of cable motion saves not only unpredictable disruptions,

but also considerable time and money devoted to extensive line repairs.¹

To safeguard the investment in an overhead communication system, consideration should be given to preventive cable damping during the design stages of the line.² This consideration should include whether or not dampers are required.

Aeolian Vibration

Aeolian Vibration occurs almost constantly on overhead cables of circular cross-section. Depending on the cable characteristics and environmental exposure, the vibration may vary from an extremely severe level to one detectable only with highly sensitive instruments such as strain gauges or field vibration recorders. Figure 1 is a typical trace from a field vibration recorder.



Figure 1 – Typical Field Vibration
of 9 mm Shield Wire

Aeolian vibration is caused by the laminar wind flow across a cylindrical shape, such as an overhead fiber optic cable. The formation of alternate vortices (eddies) across the cable creates alternating pressures which move the cable at right angles to the direction of the wind flow, also known as vortex shedding. Although the cable motion may be readily apparent from the ground when serious vibration exists, the peak-to-peak amplitude rarely exceeds the diameter of the cable.

The frequency at which vortex shedding occurs on cables can be closely approximated by the following relationship, based on the Strouhal Number:

$$\text{Frequency (Hertz)} = \frac{185V}{d}$$

Where: **V** is wind velocity normal to the cable in m/s

d is the cable diameter in mm

185 is the Strouhal Number which is an aerodynamic constant

When the frequency of the forces created by the vortex shedding corresponds closely with one of the natural frequencies of a span of cable, aeolian vibration is initiated. The vibrations take the form of discrete standing waves with forced nodes at support structures and intermediate nodes spaced at intervals along the span.

The natural vibration frequencies of a tensioned cable are calculated by the following expression:

$$\text{Frequency (Hertz)} = \frac{n}{2S} \sqrt{\frac{T}{w}}$$

With $L = \frac{S}{n}$

The equation converts to: $\frac{1}{2L} \sqrt{\frac{T}{w}}$

Where: **n** is the number of standing wave loops in the span (1,2,3...)

S is the span length in m

L is the standing wave loop length in m

w is the cable mass per unit length in kg/m

T is the cable tension in N

Using the equation for the vortex frequency predicted by the Strouhal Number, it can be seen that frequency increases with a decrease in cable diameter, assuming a constant wind velocity. Therefore, on a power line exposed to laminar wind, ADSS cables will vibrate at higher frequencies and accumulate more vibration cycles per day than the larger diameter phase conductors. It can also be seen that long-span cables have many more resonant frequencies; therefore, long-span construction will accumulate

larger numbers of vibration cycles per day than short-span construction.

The characteristics associated with aeolian vibration are listed in the table below and are shown in Figure 2.

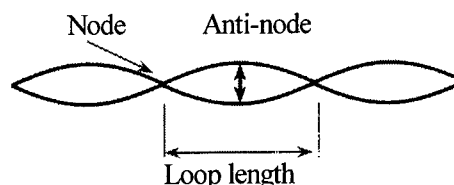


Figure 2 – Loop Geometry

Characteristics of Aeolian Vibration

Wind Speed	Frequency Vibration	Loop Length	Amplitude
1 to 7 m/s	5 to 140 Hz	.6 to 9 m	<cable diameter

Factors Contributing to Aeolian Vibration Damage

The effects that line design parameters, environment, and stress have on the severity of aeolian vibration are listed below.

1. The air movement most conducive to aeolian vibration occurs in open, flat terrain where there are few obstructions to the flow pattern of the wind.
2. High cable tensions reduce the self-damping of aerial cables; therefore, less energy is dissipated and higher vibration levels result.
3. High cable tension raises the base stress level of the cable and reduces the range of wind-induced stress that can be safely tolerated by the cable-hardware system.

The damage resulting from aeolian vibration may be divided into two broad categories, fatigue and abrasion. Both types of damage are progressive and long-term in nature and can occur simultaneously.

ADSS cables have very low self damping characteristics; therefore, dampers are required in most cases.³

Types of Dampers

In order to prevent damage, two types of dampers are used to suppress aeolian vibration - tuned dampers and impact dampers.

One of the most widely used tuned dampers is the Stockbridge type, Figure 3. The Stockbridge type damper is extremely effective on larger diameter conductors. The Stockbridge type damper is a dynamic absorber with two principal modes of response. The frequency range of these modes varies with damper size, with the frequency higher for lighter weight sizes. A tuned damper will usually have a determined frequency response range. This response range essentially covers the conductor vibration frequencies usually associated with conductors strung at moderate tensions and exposed to moderate wind speeds. The Stockbridge type damper generally is attached to the cable via a bolted clamp.

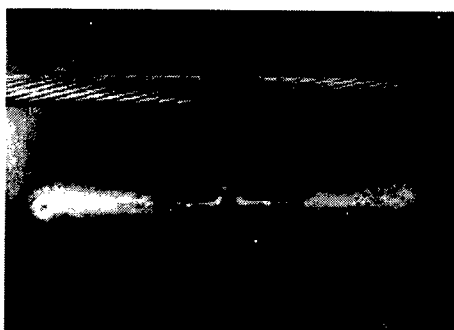


Figure 3 - Stockbridge Type Damper

The Spiral Vibration Damper (SVD) is one of the most common impact dampers available today, Figure 4. The SVD is very effective at the high frequencies associated with small diameter distribution conductors, static wires, and fiber optic cables. The SVD reduces aeolian vibration by dissipating vibration energy by impacting the cable or conductor. As mentioned above, this type of damper is extremely effective on smaller diameter conductors, but loses some of its effectiveness on larger cable. This reduction is due to the mass/frequency relationship between the damper and the conductor. This damper is attached to the cable by a tight plastic helix.

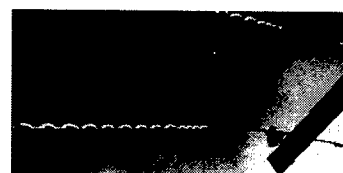


Figure 4 - Spiral Vibration Damper

PERFORMANCE OF IMPACT DAMPERS

Impact dampers, such as the SVD, have historically been used on distribution conductors to reduce abrasion. They have also been used heavily in the past twenty years on overhead shield wires to reduce fatigue failures due to high frequencies associated with shield wire applications. In total, there are over two million of these types of dampers installed on power lines in the United States.

Over the past ten years, this product has been used extensively on optical ground wires. The performance of the SVD has been well documented on these particular cables using field vibration measurements.⁴ In this type of analysis, actual field data is reduced and evaluated to verify the vibration levels are below the fatigue endurance limits. Field testing of cables is extremely expensive and time consuming.

With the advent of all-dielectric self-supporting cables and various types of optical ground wire, it became necessary to develop a proven laboratory evaluation technique to determine the effectiveness of the SVD. In the next section of this paper, the laboratory technique developed to evaluate the performance of impact dampers will be discussed.

Laboratory Evaluation of Impact Dampers

Laboratory measurements of the power dissipated by conductor vibration dampers are used by engineers to test designs and to determine a damper's suitability for use. Several different methods have therefore been developed to determine the dissipation characteristics of the variety of dampers available.

Four basic test methods have been described in IEEE Standard 664-1993. These are the power, inverse standing wave ratio, decay, and forced response methods.

These methods require pure sinusoidal vibration to accurately determine the dissipated power and therefore have been used almost exclusively with Stockbridge type dampers. Impact type dampers, such as the SVD, add an almost random component to the conductor motion during vibration which, until recently, precludes the use of the above test methods except for the decay method.

The advent of modern electronics and inexpensive computing power have now made testing impact type dampers practical. By removing all components other than that of the driving frequency from the measuring transducers signals through the use of filters or Fast Fourier Transform (FFT) analyzers, several of the above methods may be used.

Testing

Laboratory damper efficiency testing of an impact type Spiral Vibration Damper was performed by the power method based on IEEE Standard 664-1993. A length of ADSS was installed in a laboratory vibration span at a constant tension equal to the installation tension of the ADSS cable and maintained by a pivoting balance beam. Square faced, rigid clamps, to minimize energy losses in the terminations, were installed at each end of the cable resulting in a test span of 30 m. A Spiral Vibration Damper was installed on the ADSS approximately 130 mm from the same rigid clamp, Figure 5. A vibration shaker was installed to excite the ADSS. An impedance transducer, a combination load cell and accelerometer, was installed between the shaker armature and the test cable to measure the force and acceleration imparted to the test cable. Figure 6 is a schematic of the test setup.

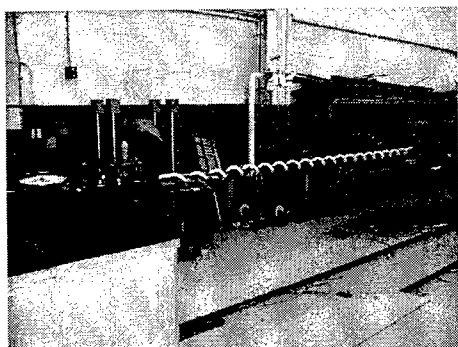


Figure 5 – SVD Installed on Laboratory Test Span

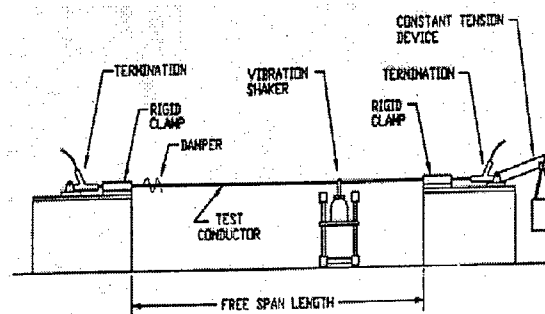


Figure 6 – Laboratory Test Setup

The signals from the amplifiers were sent through a tracking filter which removed all frequency components other than the driving frequency and then viewed with an oscilloscope. The force and acceleration signals from the impedance transducer were sent to an FFT analyzer which displayed the frequency spectrum of each signal and the phase angle between the two signals.

Measurements to determine the dissipated power were taken at tunable harmonics within the specified frequency range of $.185/D$ to $1.295/D$, where D is the conductor diameter in meters. At each frequency the shaker input was adjusted to a specific level in order to obtain a wave velocity of 200mm/s. To measure the antinode amplitude of the first free vibration loop from the damper, a miniature accelerometer was installed on the conductor and the signal sent to the FFT analyzer. The force, acceleration and conductor amplitude were then obtained from the FFT analyzer display. The dissipated power and the theoretical wind power input for a set span length were then calculated and plotted.

The dissipated power was calculated from the following equation:

$$P = \frac{F \cdot A \cdot \sin(\Theta)}{4 \cdot \pi \cdot f}$$

and the wind power input was calculated from:

$$P = D^4 \cdot f^3 \cdot \text{fnc}(Y/D) \cdot L$$

Where:

P is power (W)

F is the measured force at the shaker (N)

A is the measured acceleration at the shaker (m/sec^2)

Θ is the phase angle between the force and acceleration signals

f is the frequency of vibration (Hz)

D is the conductor diameter (m)

L is the span length (m)

Y is the antinode amplitude (m peak-peak)

fnc(Y/D) is a function of conductor antinode amplitude

Test Results

The results of two ADSS cables are presented below.

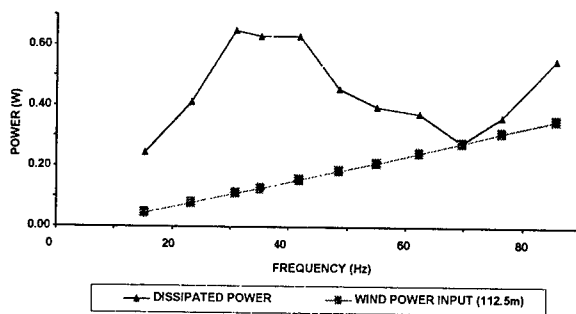


Figure 7 – 14.9mm ADSS Laboratory Results With Two SVD's

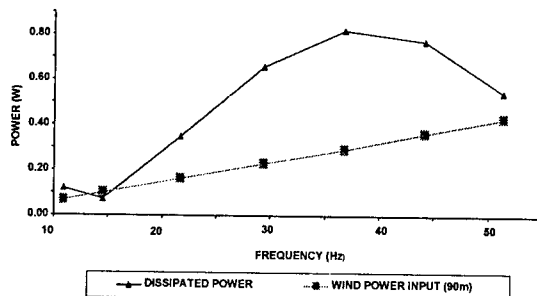


Figure 8 – 23.8 ADSS Laboratory Results With 1 SVD

On the 14.9 mm ADSS, the results indicate the energy being dissipated by the damper is equal to, or greater than, the theoretical wind energy input.

On the 23.8 mm ADSS, the results indicate the energy being dissipated by the damper exceeds the wind energy input at all frequencies except 15 Hz. This deviation is not deemed significant to the overall performance of the damper. Therefore, theoretically, these ADSS cables, with Spiral Vibrations Dampers installed, should not experience damaging levels of vibration.

Confirmation of Laboratory Data

To validate the data given in Figures 7 and 8 from the laboratory evaluation, a comparison to actual field vibration data was made. In the late 1980's, extensive field testing was conducted at two Northeastern Power Utilities on similar size ADSS cables. For these studies, vibration recorders were mounted to installed ADSS cables.

Field Vibration Testing of ADSS Cable

Various types of test equipment have been used to assess the dynamic characteristics of transmission and distribution lines in the field. These include electronic, mechanical, and optical devices.

Electronic equipment includes strain gauges, accelerometers, and velocity pickups. Mechanical equipment includes live line recorders, Jaquet Cycle Counters, Zenith, or other vibragraph recorders, and deformation markers. Optical equipment includes motion picture cameras or video tape.

Since 1965, the field vibration recorder has been the principal tool used at Preformed Line Products Company to gather field vibration data⁵

The field vibration recorder is an electromechanical instrument which measures cable bending near the mouth of a suspension clamp. The body of the instrument is fastened rigidly to the suspension clamp and the bending amplitude is sensed by a deflection arm attached to the cable. Motion of the deflection arm is measured by the recorder every 15 minutes over a two-week period.

The resulting data can be assessed in several different ways, but the important aspect is that the data gives a good measure of vibration activity over a 2-week period. Preformed Line Products Company has conducted approximately 1,000 field vibration studies during the past 25 years. Work done by our engineers and published in IEEE papers^{5,6}, resulted in a method to convert the displacement recorded to bending strain for aluminum and steel base cables. This relationship, however has not been developed for ADSS cables.

ADSS Field Test Setup

Two test sites were utilized, one which had a 15 mm and another which had an 18.5 mm ADSS cable installed. For the field vibration study, vibration recorders were installed as given in Figures 9 and 10. During these studies, simultaneous measurements were taken for both damped and undamped ADSS cables. The results are given in Figures 11 and 12. The vibration studies indicated that the dampers effectively reduced the vibration to acceptable levels.

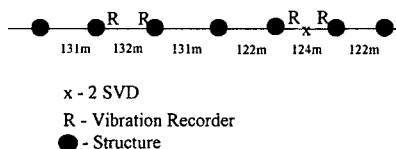


Figure 9 – Schematic of 15 mm ADSS Field Test Site

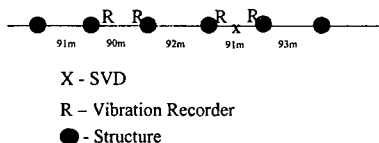


Figure 10 – Schematic of 18.5 mm ADSS Field Test Site

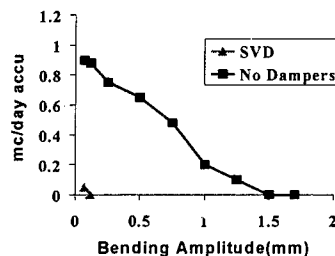


Figure 11 – Field Test Results on 15 mm ADSS Cable

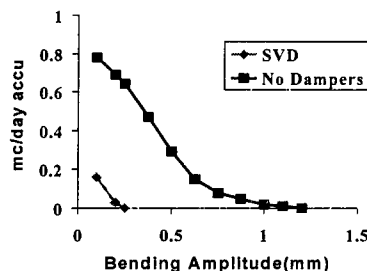


Figure 12 – Field Test Results of 18.5 mm ADSS Cable

Comparison of Laboratory Analysis to Field Analysis

On the smaller size ADSS cable, there is an acceptable correlation when comparing the test results given in Figure 7 to the field vibration data in Figure 11. The data given in Figure 7 indicates that the dampers should successfully protect 112 m of cable. The field vibration data indicated that the dampers were extremely effective in reducing the vibration in 120 m of cable. In fact, the correlation indicates that the laboratory test is more severe than the field test. In other words, a damper will perform better in the field than is projected by the laboratory test analysis.

The analysis of the larger diameter cable, once again, shows the damper is very effective at reducing the vibration activity level. This is shown in Figure 8. The field analysis given in Figure 12, indicated that the vibration performance predicted by the laboratory analysis is quite accurate, and therefore, once again, a good correlation. Due to availability, different cable diameters were used in this comparison. It is believed the comparison is still valid.

CONCLUSION AND SUMMARY

A laboratory test method has been developed and utilized for prediction of performance of impact dampers on ADSS cables. This laboratory method compares quite favorably to field vibration data which had previously been conducted on ADSS cable. This analysis shows that if an impact damper performs well in the laboratory, it can be expected to perform even better in the field.

FUTURE WORK

There is a need to conduct further testing on ADSS cable with impact dampers, particularly on larger size ADSS cables. To further investigate the performance of impact dampers on ADSS cables, a testing program is planned for the winter of 1999.

REFERENCE

- ¹ D'Agati, J.R., and Champa, R.J., "Field Inspection of Overhead Conductor Supports," presented at IEEE T&D Committee Meeting, Seattle, Washington, October 3, 1974.
- ² Poffenberger, J.C., Champa, R.J., and D'Agati, J.R., "Damping Devices and Hardware," Electric Light and Power, Vol. 50, No. 20, pp. 65-69, 88, October 1972
- ³ Sunkle, David C and Christian, David F "The Effects of Tension on Vibration of All-Dielectric Self-Supporting Fiber Optic Cable," presented at the Seventh International Conference on Transmission and Distribution Construction and Live Line Maintenance (ESMO-95 CP-23), Columbus, Ohio, October 29 – November 3, 1995
- ⁴ Sunkle, David C. and Champa, Raymond J. "Testing of Fittings and Aerial Fiber Optic Cables," presented at the 1991 Distribution 2000

Conference Insulated Line and Cable Systems, Sydney, Australia, May 29-31, 1991

⁵ Poffenberger, J.C. and Swart, R.L., "Differential Displacement and Dynamic Conductor Strain," IEEE Trans. Power Apparatus and Systems, Vol. PAS-84, pp. 281-289, April 1965.

⁶ Komenda, R.A. and Swart, R.L., Interpretation of Field Vibration Data, "IEEE Trans. Power Apparatus and Systems," Vol. PAS-87, pp. 1066 – 1073, April 1968.

AUTHOR

David C. Sunkle, P.E., Preformed Line Products, 660 Beta Drive, Mayfield Village, Ohio 44143



David is a degreed Mechanical Engineer and a Registered Professional Engineer. He has been with Preformed Line Products for 21 years and is presently the Product Engineering Manager. His responsibilities include development, evaluation, and approval of all products developed by PLP-U.S.

He has been active in IEEE and CIGRE technical organizations dealing with cable mechanics. He is presently the Secretary for the CIGRE Task Force on Galloping, and is a member of Working Groups on Fiber Optics for both IEEE and CIGRE.

Verification by Means of Temperature Characteristic Test and Cable Laying Test on Optimum Design in Fiber Excess Length of Slotted Type Optical Cable

Norifumi Kimura, Yasushi Sudo, Takuya Ohsako,
Hiroshi Keruma, Kazumasa Nemoto

Ocean Cable Co., Ltd.
Engineering Development Department
Tochigi, Japan

ABSTRACT

While optical access network construction is in progress, more multimedia information typified by Internet had been increasing rapidly. Technologies such as WDM for expansion of transmission capacity have been developed in order to cope with such a rapid increase.

Under these circumstances, we have conducted investigations about the relationship between fiber excess length and temperature characteristics. And we found that fiber excess length had an influence on the reliability of optical fiber cable under actual environment.

We have concluded that an optical fiber excess length ratio is one of the factors that have an important influence in optical fiber cable performance. Therefore we have verified that optical fiber cable characteristics of higher reliability can be obtained by controlling such a ratio properly.

INTRODUCTION

Construction of optical access networks is currently underway, but communication networks as represented by the Internet are also experiencing significant growth. Technologies like WDM (Wavelength Division Multiplexing) are being developed to cope with the rapid increase in communication capacity, eventually leading to even more sophistication in transmission technology. Highly reliable optical fiber cables capable of sustaining stable transmission without offsetting the transmission characteristics under any environment are indispensable in constructing such networks.

Other important factors besides reliability are also demanded of optical cables comprising networks. Low cost is one of such factors. In aerial cables, the introduction of SZ slotted-core ribbon cables allowing mid-span access operation is insisted to be advantageous in the context of overall cost.

Upon consideration of this background, we evaluated means of ensuring the reliability of SZ slotted-core optical fiber cables. From among the many elements influencing the reliability of the cables, the fiber excess length included were evaluated as a factor directly influencing the characteristics of optical cables.

CABLE DESIGN AND MANUFACTURING

Cables utilized in the study were of 100-fiber SZ slotted-core optical fiber cable design, respectively designed to accommodate five 4-fiber (single mode) ribbons within each of the five slots of the slotted rod. The parameters of this cable are as indicated in Table 1. In this study, adjusting the fiber excess length to 0, 0.1, and 0.2% respectively. A cross-section of a 100-fiber SZ slotted-core optical fiber cable is shown in Figure 1. As illustrated in the figure 1, the topmost layer of the stacked ribbons is indicated as ribbon No. 1 and the bottommost layer as ribbon No. 5.

Table 1 Cable Dimension

Fiber count	100
Supporting wire	7/2.0 steel Wire
Fiber ribbon	4-fiber ribbon
Ribbon number	5/Slot
Cable diameter	14 mm

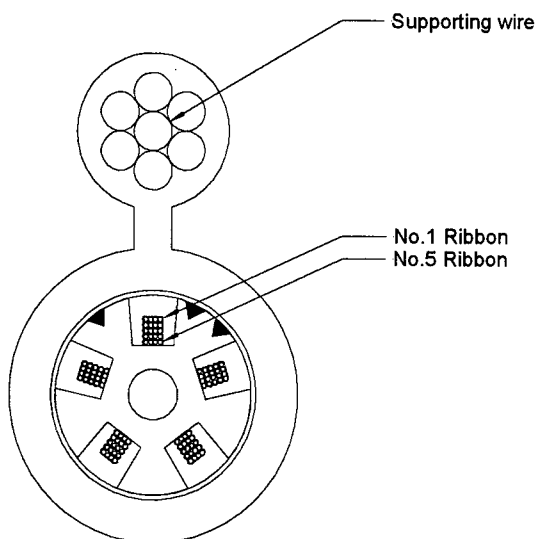


Figure 1 Cross-section of the 100-fiber SZ slotted-core optical fiber cable

CABLE CHARACTERISTICS

Temperature characteristic test

The three cables manufactured for the test were each wound on an 800 mm diameter drum and subjected to temperature characteristic tests in the range of -30 to 70 degrees Celsius. Measurements of the fibers were taken using ribbons No. 1 and No. 5 looped at both ends. The results obtained in Figures 2, 3, 4, and Table 2. According to Table 2, the increase in attenuation was significant in cable with 0% fiber excess length indicating an attenuation change of 0.14dB/km, while cables with 0.1 and 0.2% fiber excess length both indicated attenuation change of 0.07dB/km. It was also confirmed that the attenuation in fibers with 0.2% fiber excess length increased when subjected to low temperatures, and the attenuation in fibers with 0% fiber excess length increased under high temperatures.

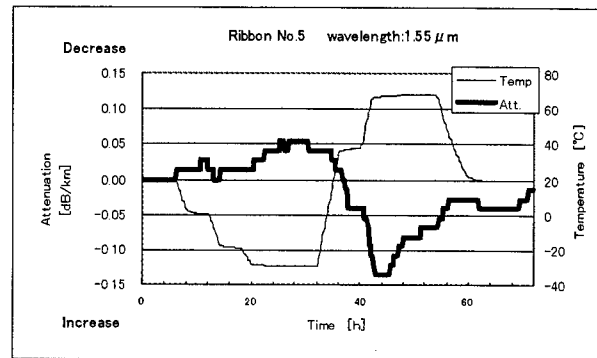


Figure 2 Temperature characteristics test, Fiber excess length 0.0%

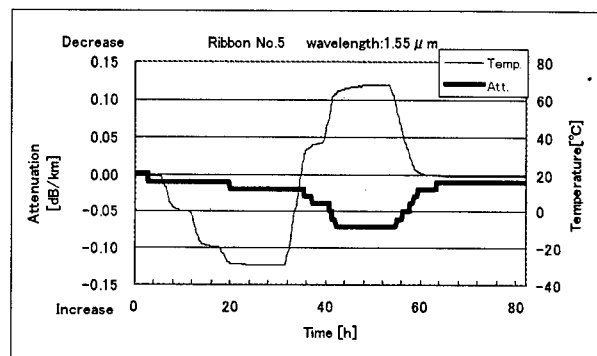


Figure 3 Temperature characteristics test, Fiber excess length 0.1%

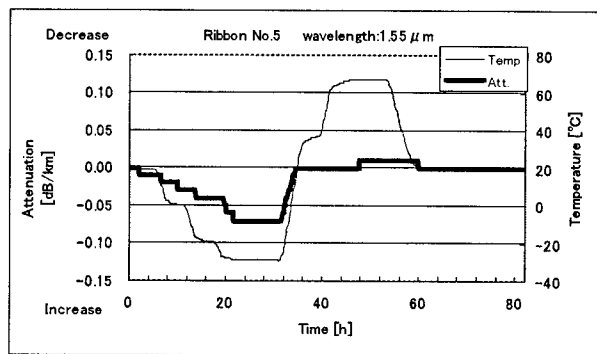


Figure 4 Temperature characteristics test, Fiber excess length 0.2%

Table 2 Maximum increase in attenuation at Temperature characteristic test

Ribbon No.	Fiber excess length		
	0%	0.1%	0.2%
1	0.095 dB/km	0.02dB/km	0.0 dB/km
5	0.14 dB/km	0.07dB/km	0.07dB/km

Apparently, the temperature increase extended the slotted rod including the fibers, causing them to stretch and thus resulting in the increased

attenuation in fibers without any allowance. When the fibers are provided with 0.2% fiber excess length, the loosely accommodated fiber ribbons were frequently bent due to the contraction of the slotted rod under low temperatures, causing the additional attenuation change in these cables.

Fiber strain after the cable manufacturing process

The strain of fibers was measured on each fiber of No.1 and No.5 ribbons with the cable wound on 800 mm drums. The results obtained using BOTDR (Brillouin Optical Time Domain Reflectometer) were compared with a sample ribbon from the same manufacturing lot as those included in the cables. The measurement result for one sample is shown in Figure 5, and the results are as indicated in Table 3 and Figure 6.

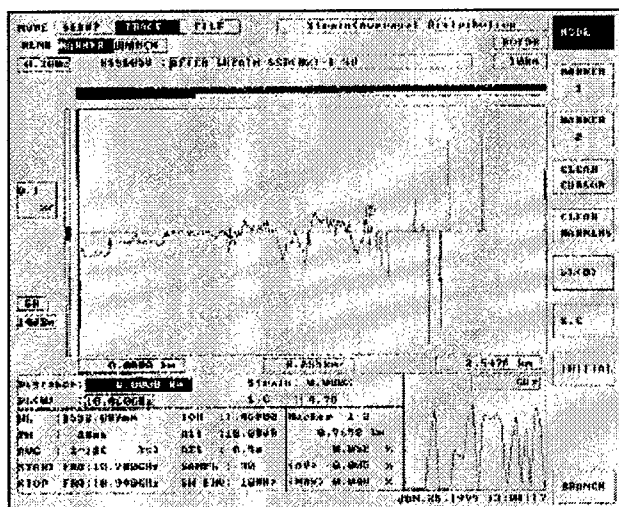


Figure 5 Chart of BOTDR

Table 3 Fiber strain (%), after manufacturing process (wound on drum, diameter=800mm)

Ribbon No.	Fiber color	Fiber excess length		
		0%	0.10%	0.20%
No.1	BLUE	-0.155	-0.011	-0.02
	WHITE	-0.106	0.002	-0.009
	BROWN	-0.115	-0.008	-0.015
	GLAY	-0.096	-0.029	-0.029
No.5	BLUE	0.005	0.052	0.046
	WHITE	0.014	0.029	0.032
	BROWN	0.035	0.03	0.029
	GLAY	0.049	0.019	-0.028

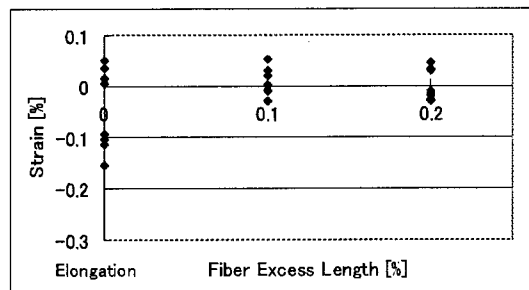


Figure 6 Fiber strain (BOTDR, After manufacturing process, cables are wound on drum, diameter is 800mm)

According to the Figure 6, the strain on the fiber is significant when the fiber excess length is at 0% with the maximum strain reaching 0.15%. The maximum for fibers with 0.1 and 0.2% of fiber excess length was in the order of 0.05%.

Fibers included in cables wound on drums are generally subjected to strain from bending, but it was confirmed that providing the fibers with fiber excess length eased the strain.

Tensile performance test

The tensile performance of cables was tested using phase method for averaged strain measurement concurrently observing the attenuation of the optical fiber under assumption that cables are subjected to tension during the installation and strong wind conditions after the installation. The result of the test is indicated in Figure 7.

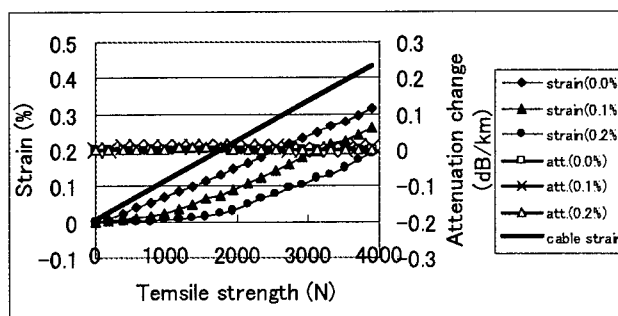


Figure 7 The result of Tensile performance test

Under a tensile stress of 4,000N, the attenuation did not increase in any of the three types of cables, but the strain was increased when the cable strain reached fiber excess length.

FIELD TEST

Fiber strain, after installation

To confirm the long-term reliability, the cables were actually installed in a field site. The overall length of the installed cables was approximately 730m with a span of approximately 50m, 1% cable excess length and twisting rate of once per 10m. One end of each cable was brought indoors and connected to the measurement instrument. The other end was terminated within the end-box by connecting the two outer fibers and the two inner fibers of ribbons No. 1 and No. 5 together respectively. The connection diagram is indicated as Figure 8.

Immediately after the installation of the cables, the strain was measured using BOTDR when the temperature was 20 degrees Celsius. The results of the measurement are as indicated in Table 4 and Figure 9. Upon comparison of the results with figures indicated in Figure 6, the strain was varied among the three types of cables when wound on drums but the difference was almost non-existent after installation.

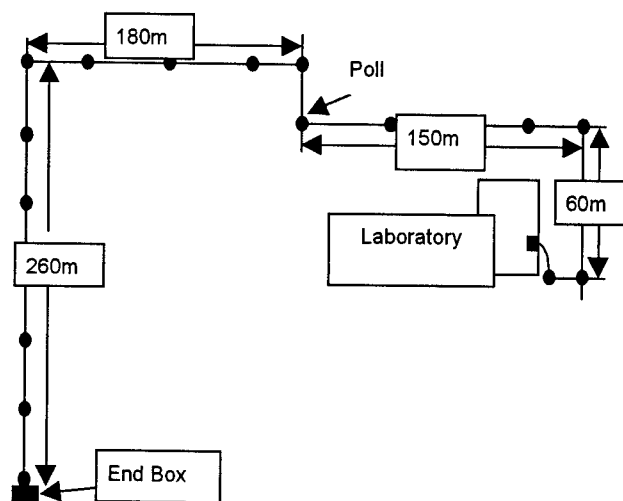


Figure 8 Connection Diagram

Table 4 Fiber strain, after installation, 20 degrees Celsius

Ribbon No.	Fiber color	Fiber excess length		
		0%	0.10%	0.20%
No.1	BLUE	0.009	0.000	0.008
	WHITE	0.033	0.033	0.029
	BROWN	0.035	0.039	0.041
	GLAY	0.033	0.039	0.038
No.5	BLUE	0.029	0.034	0.023
	WHITE	0.025	0.028	0.032
	BROWN	0.028	0.031	0.036
	GLAY	0.031	0.036	0.043

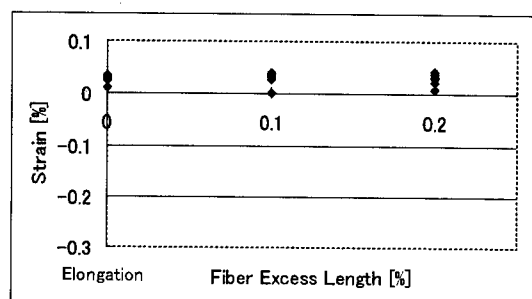


Figure 9 Fiber strain (BOTDR, After installation, 20 degrees Celsius)

Cable characteristics in field test

With the cables installed at a field site, the attenuation was measured continuously with the outer loop of ribbons No. 1 and No. 5 while the inner loop of ribbon No. 1 was used for the continuous strain measurement by phase method.

Of the measurements obtained, the change in attenuation for two hot days are provided in Figure 10 along with the change in strain over the same period of time in Figure 11. According to these results, the attenuation and strain were quite uniform for the three types of cables. The linear coefficient of expansion for the fiber ribbon is approximately 1.0×10^{-5} , causing the ribbons to extend by 0.01% when the temperature increases by 10 degrees. Accordingly, the change is presumed to be caused by the thermal expansion of the fibers.

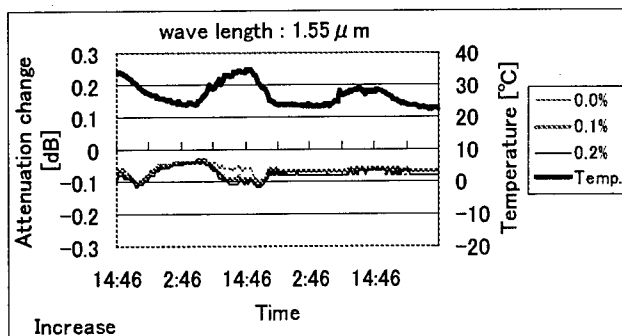


Figure 11 The result of field test (Attenuation change)

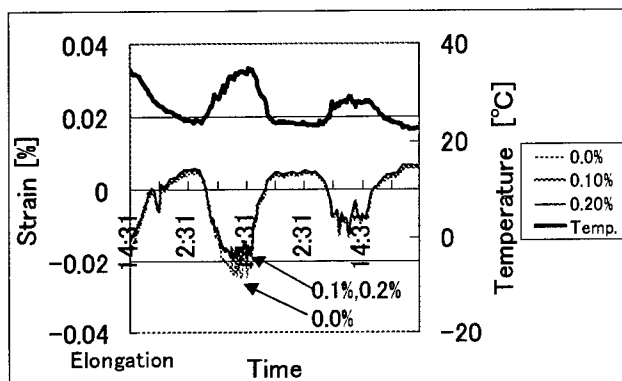


Figure 12 The result of Field test (Fiber strain)

As the linear coefficient of expansion for the slot is approximately 1.9×10^{-3} , the difference of strain between the slot and the fibers is merely 0.009% with a thermal change of 10 degrees Celsius, resulting in the uniform attenuation and strain for the three cables despite the difference in the fiber excess length.

However, the characteristics of the cables may be influenced by the difference in fiber excess length when subjected to higher temperatures and more extreme conditions including strong winds caused by typhoon or tropical storms and the low temperatures during the winter season. The testing shall be continued to confirm this possibility.

CONCLUSIONS

It was confirmed that the fiber excess length of optical fibers was one factor significantly affecting the temperature characteristics of optical fiber cables. Therefore we have verified that optical fiber cable characteristics of higher reliability can be obtained by controlling such a ratio properly.

However, the strain of fibers included in slotted-core ribbon cables actually installed under field conditions was insignificant, and the attenuation

and strain of cables were fairly uniform in the temperature range of 15 to 30 degrees Celsius despite the difference in the fiber excess length. Tensile testing simulating strong winds was also performed. The fiber excess length did not affect the attenuation, but the strain was increased when the cable strain reached fiber excess length.

Measurements will continue into the winter season to evaluate the characteristics of the cables under low temperatures. Furthermore, the deterioration due to aging will be determined by continuing the test over a period of several years.

REFERENCE

1. H. Ishikawa, et al., "A STUDY ON BEHAVIOR OF FIBER RIBBONS IN SZ-GROOVED SPACER AND ITS APPLICATION TO AERIAL CABLE", IWCS, 1997
2. D. Iwakura, et al., "Development of stacked ribbon SZ-slotted rod cable", IWCS, 1997
3. N. Okada, et al., "Study of the SZ-slotted rod type optical cable with the 4-fiber ribbons for aerial applications", IWCS, 1997
4. D. Iwakura, et al., "Long-term field test of AZ-slotted rod cable having excess fiber ribbon length", IEICE B-10-6, 1999 (in Japanese)



NORIFUMI KIMURA

E-mail : kimura-norifumi@n-occ.co.jp
KAMINOKAWA PLANT Ocean Cable Co., Ltd.
3967 Kaminokawa-machi Kawachi-gun Tochigi 329-0611
Japan

NORIFUMI KIMURA was born in 1973. He received the B.E. degree in naval architecture and the M.E. degree in earth system science and technology engineering from Kyushu University in 1995 and 1997, respectively. He joined Ocean Cable Co., Ltd. in 1997 and engaged in engineering development department of Cable. He is an engineer of the KAMINOKAWA PLANT.

STUDY TO DETERMINE THE DRAG COEFFICIENT FOR SUBMARINE CABLES

Ph.DUPIRE – Y.CHARLES – JF LIBERT

ALCATEL SUBMARINE NETWORKS
536 Quai de la Loire BP 849
62 225 CALAIS FRANCE

ABSTRACT

The drag coefficient C_D is an important parameter which is essential to know when laying or recovering submarine fibre optic cables. In particular, it allows calculation of the hydrodynamic constant H which determines the critical angle, the distance between the cable laying point and the vessel, and the cable recovery tension.

The drag coefficient C_D characterises the frictional forces exerted by the water on the cable in a transverse direction. It is a function of the Reynolds number and of the amplitude of the vibrations caused by the hydrodynamic forces acting on the cable. The frequency and amplitude of these vibrations depends, in particular, on the cable's length and its rigidity. Moreover, it is clear that the cable does not react to vibrations in the same way in the case of laying and of recovery, due to the fact that the recovery tensions of the cable are much greater than those measured during laying. It is therefore valid to make a distinction between these two cases when selecting the drag coefficient C_D , although this point is not, to the best of our knowledge, dealt with in the literature.

INTRODUCTION

After a reminder of the standard equations, and the parameters on which the drag coefficient C_D depends, a review of various methods used in the literature

to determine the drag coefficient C_D value, will be presented. Selection of values for the C_D parameters will be made and justified by both theoretical inputs and practical experiments.

1- BASIC EQUATIONS

The hydrodynamic constant H , which is equal to a cable segment's transverse sink speed under its own weight in water, is expressed in relation to the characteristics of the cable and the drag coefficient C_D in the following way [1][2]:

$$H = \sqrt{\frac{2w}{C_D \rho d}} \quad (1)$$

where w is the cable's weight per unit of length in water, d is the cable diameter and ρ the sea water density.

The drag coefficient C_D translates the friction exerted by the water on the cable in a direction perpendicular to it. It enters the expression of the transverse frictional force (perpendicular to the cable) per unit of length F_N which is exerted on the cable (see fig 4):

$$F_N = 0.5 C_D \rho d (V_N)^2 \quad (2)$$

where d is the cable diameter, and V_N is the flow speed component perpendicular to the cable.

The laying angle or critical angle α (the cable's angle in relation to the horizontal level) is expressed in relation to the vessel speed V_s and the hydrodynamic constant H :

$$\cos \alpha = \sqrt{1 + \frac{1}{4} \left(\frac{H}{V_s} \right)^4} - \frac{1}{2} \left(\frac{H}{V_s} \right)^2 \quad (3)$$

Where the laying angle is sufficiently small ($\cos \alpha \cong 1$, $\sin \alpha \cong \alpha_0$), the hydrodynamic constant can also be written in the following way:

$$H \cong \alpha_0 V_s \quad (4)$$

These latter two equations (3) and (4) can be used to calculate the hydrodynamic constant H using measured values of the laying angle α and the vessel speed V_s . Where the vessel speed is not high enough to enable the approximation which gives equation (4) to be applied, equation (3) must be solved. The value of the drag coefficient C_D can then be deduced using equation (1).

The expression of a cable's recovery tension T_s under stable conditions should also be noted:

$$T_s = \frac{wh}{1 - \left(\frac{\tan^2(\alpha/2)(\cos \alpha + \cos \alpha_s)}{1 - \cos \alpha \cos \alpha_s} \right)^{1/\gamma}} \quad (5)$$

where $\gamma = \frac{2 - \sin^2 \alpha}{\sin^2 \alpha}$, and where α is the critical angle, α_s is the cable's angle in relation to the horizontal level on the boat, w is the cable's weight in water per unit of length, and h is the water's depth.

2- DRAG COEFFICIENT VARIATIONS

2-1 Effect of cable vibrations

The bibliographical study presented in the report by J.A. Humphries [3] shows that the drag coefficient C_D varies depending on the amplitude of the vibrations to which the cable is subjected.

Much work has been done in relation to these vibrations and their effect on the drag coefficient C_D , mainly using towing tests. The results of these tests are quite varied: the C_D values found vary between 1.2 and 3.2, and between 1.5 and 2.0 for longer cables (which are therefore subjected to a greater tension). The reason for this variation in the results would appear to be the differences in the vibration amplitudes measured on the cables. These amplitudes depend on the cables' structure (rigidity, surface condition...) and therefore vary from one cable to another. However, the results show a general tendency, which is that the drag coefficient C_D increases as the amplitude of the vibrations increases or when cable tension decreases.

It should also be noted that Griffin [4] presented a model which estimates the value of the drag coefficient C_D . However, experiments performed at B.H.R.A. [5] show that this model clearly has a tendency to over estimate the coefficient. Moreover, according to Humphries, estimation of cable vibration amplitude remains highly empirical.

2-2 Effect of Reynolds number

For a rigid cylinder (*i.e.* which does not vibrate) in the presence of fluid flow, the Reynolds number N_R is defined by the relationship

$$N_R = Vd/\nu \quad (5)$$

where d is the cylinder diameter, ν is the fluid's kinematic viscosity coefficient (here, sea water with $\nu = 1.5 \cdot 10^{-6} \text{ m}^2/\text{s}$), and V is the fluid speed. The Reynolds number characterises the fluid's behaviour around the cylinder, like, for example, the formation of vortexes in the cylinder's wake, their evolution, etc... In the case of a cable, and under standard laying and recovery conditions, the Reynolds numbers associated with the various configurations remain within a zone called sub-critical ($N_R \leq 3 \cdot 10^5$), where the drag

coefficient C_D is relatively constant and equals 1.2 [3]. The minimum value of C_D to be used in equation (1) and which corresponds to the case of a rigid cylinder, is therefore 1.2.

3- CALCULATION OF COEFFICIENT IN THE CASE OF LAYING.

Over the last thirty years, several methods for calculating the value of the hydrodynamic constant and the drag coefficient C_D have been developed. These are more or less complex calculations based on experimental data (critical angle, or sink time). Here, we present a brief summary of some known methods and results.

3-1 Towing tests

The towing of a cable at a constant speed, in the sea or in a tank, is one experimental method used to simulate cable laying in order to calculate the value of the drag coefficient C_D . Most often, the method is comprised in measurements of the cable laying angle α and the vessel speed V_s during cable towing.

E.E. Zajac [1](1957) uses the results of this type of test on a 19 mm diameter cable in order to calculate the drag coefficient C_D . He also performs an estimated calculation of C_D using published values relating to fluid flow around an immersed cylinder. Using these two methods, he obtains values for C_D of between 1 and 1.55.

G. Betherlsen and I. Vintermyr [6](1994) present C_D values obtained using towing tests performed in a tank on small lengths of cable (< 160 m), with and without armouring. The results of these tests also give C_D values between 1.1 and 1.2. Finally, other towing tests on armoured cables with a polyethylene sheath were performed in the Norwegian fjords [7](1993), on lengths of armoured cable with polyethylene sheaths measuring approximately 360 m, at speeds lower

than 3 knots. The results give C_D values between 1.5 and 2.6, depending on the cable's armouring (with a value of 2.6 for the lightest cable, as expected).

This method is fairly controversial, because it is difficult to compare towing to laying (or to recovery). Depending on the length of cable tested and the vessel speed, the tensions in place (and therefore, the vibrations induced in the cable) may vary greatly, thus giving higher or lower C_D values, and a significant variation in the results. In addition, estimation of the vibration amplitude according to the situation remains highly empirical. It is therefore preferable to base calculation of the coefficient C_D on measurements taken during tests performed in an actual laying situation.

3-2 Tests performed in actual laying situation.

C.E. Roden [2] (1964) presents a result obtained using a measurement taken during a sea laying test for a non-armoured cable. He obtains a C_D value of around 3. Despite the few details which are given regarding the method used, one may assume that he calculates the coefficient based on the cable descent time, and not based on measurement of the laying angle. However, it is difficult to draw a conclusion from these results, in the absence of a complete description of the tests and of the measurement accuracy.

D.I. Curtis (1991)[8] presents a method based on direct and precise measurement of the laying time of repeaters, in deep water. Based on measurements taken in an actual laying situation (constant speed, correct slack...) using around forty repeaters, he calculates a repeater's average sinking speed. He then simulates laying of the repeater using a digital model, and adjusts the drag coefficient C_D value in the model, in order to match the experimental results. The C_D value obtained for a non-armoured cable (NL LW) is 2.2.

3-3 Selected Method.

Among the different theories and techniques listed above to estimate the value of C_d , the method presented by Curtis [8] appears to be a satisfactory choice, since it is based on a very precise measurement of the laying time for a repeater, and on a simulation model validated by this same measurement. This method gave a drag coefficient C_D values close to 2.2.

Since this approach, several sea trials on different cable types : 21.5 mm , 17 mm and 14 mm confirmed that this value of C_d is the correct choice for submarine cable deployment. The measurements for each of these cables gave respectively for value of C_d 2.20 ; 2.25 and 2.20

On the other hand, it is strange that none of the authors mention the need to recalculate this coefficient for recovery. During this operation the cable is subjected to greater tensions than during laying, due to the hydrodynamic frictional forces which add to the weight of the cable and consequently, the drag coefficient C_D value should be lower than the value calculated for laying.

4- CALCULATION OF COEFFICIENT IN THE CASE OF RECOVERY.

The determining factor for the drag coefficient C_D value is the amplitude of the vibrations to which the cable is subjected, in other words, the cable tension. In the case of recovery, the tension at the level of the cable ship is clearly greater than that which is present during laying, due to the hydrodynamic frictional forces which tend to run counter to the recovery of the cable. We can assume that the cable's behaviour is therefore « intermediate » between that during laying and that of a rigid cylinder. The coefficient C_D for recovery will therefore be lower than that which is used for cable laying 2.2 ; retaining a lower limit of 1.2.

As far as we know, no analytical solution expressing the amplitude of the complex vibrations to which the cable is subjected, depending on its tension, has been published. For this reason, calculation of the drag coefficient C_D value for recovery is based on various measurements taken during laboratory tests and sea trials.

In order to make an appropriate calculation of the coefficient value, laboratory tests were performed in a tank, on short lengths of LW cable, to measure the transverse frictional force which is exerted on the cable when it is subjected to transverse currents [5]. The results (see fig. 1) show that the coefficient in fact decreases when the tension increases. With the greatest tension applied during the test (3.5 kN), it would appear that the drag coefficient C_D has a value varying between that of a rigid cylinder (1.2), and that of laying (2.2). The average value of the drag coefficients C_D calculated for this tension is 1.6. It therefore seems natural to chose a value of 1.6 for the drag coefficient C_D during recovery.

This choice has been confirmed by recovery tests performed at sea on the 17 mm LW cable, at a depth of 5 km (February 1997). The recovery tensions calculated with a drag coefficient C_D of 1.6 on the one hand, and 3.0 on the other, are compared with the tensions measured on board, for various recovery speeds (see fig. 2). The results correspond satisfactorily when the calculation is made with a C_D equal to 1.6, but one sees that the calculation made with a C_D equal to 3.0 (the value commonly used for laying and recovery) gives estimated recovery tensions which are much too high when compared with the measured tensions.

An other experiment which demonstrates that the selected value of 1.6 for C_d is correct has been performed. On figure 3, are plotted the average recovery tensions measured during the recovery in a 5000 metre water depth of the LW 17 mm cable with regard to different speeds (from 0.8 to 1.5 knots),

and given recovery angle (between 75° and 85°). When comparing these measured figures to the theoretical curves using respectively a Cd of 3.0 and 1.6 it clearly appears that the theoretical curve with Cd=3.0, even with a recovery angle of 90°, which is supposed to reduce the cable tension, over estimates the recovery load, while the theoretical curve obtained with a Cd of 1.6 is far better in conformance with practical experiment.

CONCLUSION

The drag coefficient C_D increases with the amplitude of the vibrations to which the cable is subjected. The diversity of the results reported in the literature shows that it is highly preferable to calculate its value under actual laying or recovery conditions, which necessarily implies sea trials. Moreover, since the amplitude of the cable vibrations is closely linked to the tension exerted on the cable, it is essential to distinguish separate coefficient values in the case of laying and in the case of recovery.

The various tests performed confirm that the selected values of Cd 2.2 for laying and 1.6 for recovery are fully realistic. Furthermore they are in a better accordance to actual laying and recovery operations than when a single Cd value of 3.0 is used.

ACKNOWLEDGEMENTS

The authors wish to acknowledge Peter Worthington for his valuable contribution.

BIBLIOGRAPHICAL REFERENCES

- [1] E.E. Zajac, « Dynamics and kinematics of the laying and recovery of submarine cables » Bell System Technical Journal. Sept 1957.
- [2] C.E. Roden, « Mécanique des câbles sous-marins et règles recommandées pour leur pose » (*the mechanics of submarine cables and recommended rules for*

laying), Bell Telephone Laboratories, U.S.A. 1964.

[3] J.A. Humphries, « Fibre optic cable drag measurements, Phase I : Literature Survey » BHRA Report, March 1987.

[4] Griffin « Vortex induced vibrations of marine cables and structures » NRL Memo Rep. 5600, 1985.

[5] D.H. Walker, K.I. Bushell, B.A. Bruce, « Fibre optic cable drag measurements, Phase II : Experimental Work » BHRA Report, March 1987.

[6] G. Berthelsen, I. Vintermyr, « New low weight/diameter optical fibre submarine cable for unrepeatered system » International wire & cable symposium proceedings, 1994, 249-255.

[7] S. Hopland, « Investigation of cable behaviour in water during laying of fiberoptic submarine cables » International wire & cable symposium proceedings, 1993, 734-739.

[8] D.I. Curtis, « The hydrodynamic constant of cables and the sink speed of repeaters under different laying conditions » STC ER 1991:010.

[9] B.S. Massey, « Mechanics of fluids », Van Nostrand Reinhold, 1975.

BIOGRAPHY

Philippa DUPIRE received her Doctorat of Sciences for Engineer" from Le Mans (France) in 1996. She is working on research and development for Alcatel since 1997.

Yves CHARLES is graduated from the Ecole Universitaire de LILLE (France). He joined Alcatel in 1993 where he is in charge of submarine cable design and product qualification.

Jean François LIBERT received his engineering degree from "Hautes Etudes Industrielles" of LILLE (France). He joined Alcatel in 1988. He is Now Technical Manager for Optical Submarine Cable.

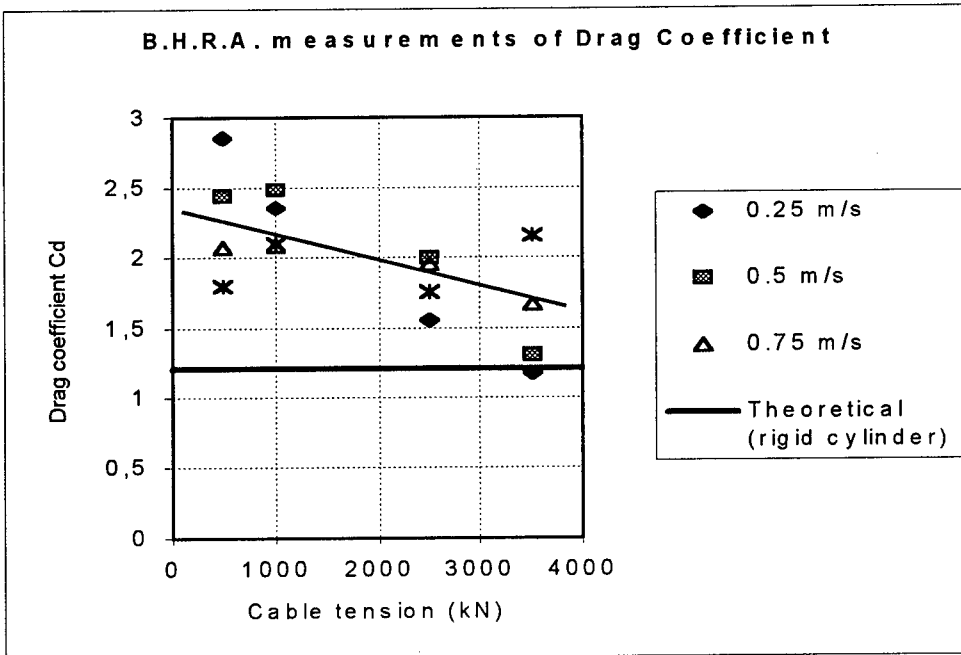


Figure 1 : Variations of Drag Coefficient C_d .
This figure demonstrates that C_d is not a constant.

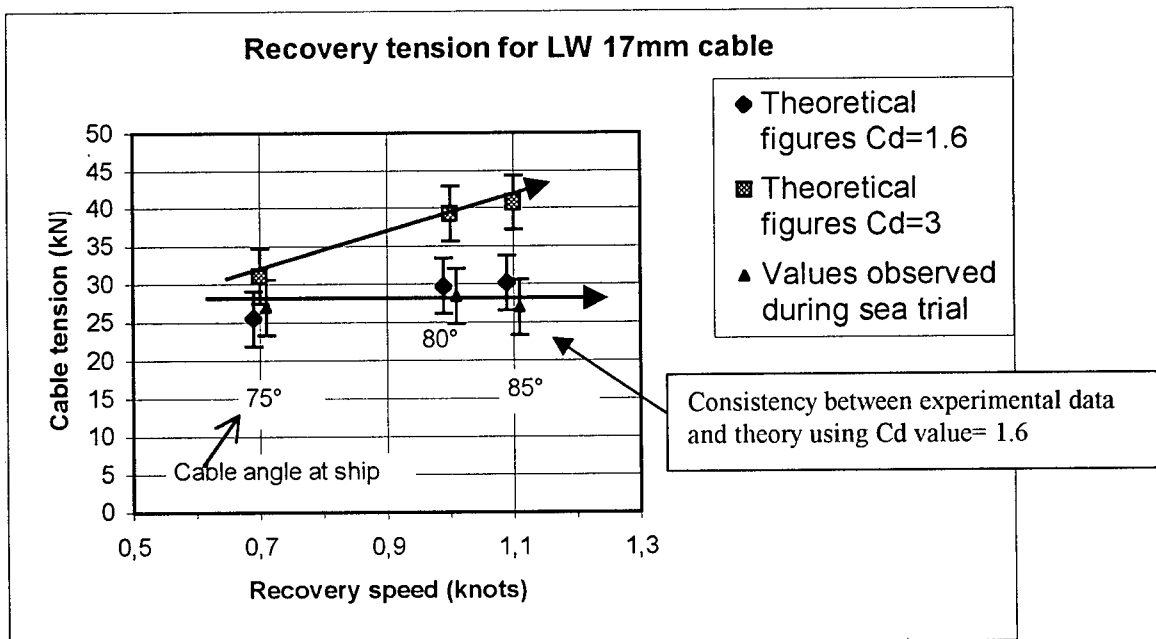


Figure 2 : Correlation of actual recovery cable tension with theoretical curves with $C_d=1.6$ and 3.

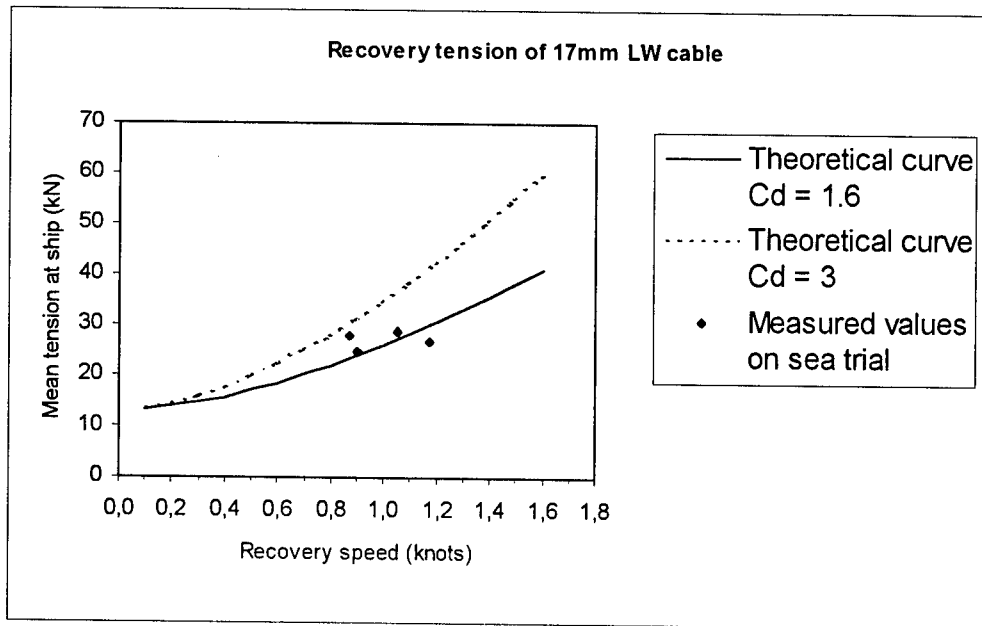


Figure 3 : Accordance of selected $C_d = 1.6$ with different recovery speed conditions.

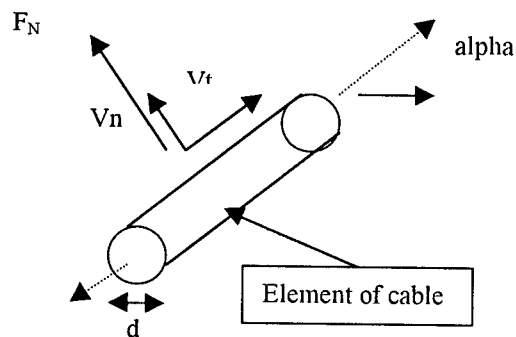


Figure 4 : Frictional force exerted on cable element.

OPMA - A HIGH MECHANICAL AND HEAT PERFORMANCE ALTERNATIVE OPTICAL CABLE FOR AERIAL APPLICATION

**Marco A. Scocco¹, Edvaldo C. Mendes¹, Marcello V. Giacaglia¹,
Dionisio A. Fulop², Marcínia Naur³,
Jaime R. da Mota³**

¹ Pirelli Cabos S.A, Sorocaba, Brazil

² Telefonica, Telecomunicações de São Paulo, São Paulo, Brazil

³ Telemar-MG, Telecomunicações de Minas Gerais, Belo Horizonte, Brazil

ABSTRACT

This paper presents the development of a high mechanical and heat performance alternative optical cable for aerial application, denominated OPMA Cable - Optical Metallic Armored Cable. Due to its innovative design, the OPMA cable presents an enhanced optical and mechanical performance and reliability when submitted to high temperature or fire, as well as to the shots of hunters' firearms, when compared with all dielectric self-supported optical cables.

Results of OPMA performance in laboratory tests are presented, as well as results of field trial experiments carried out together with two important Brazilian Telecommunication Operators: Telemar and Telefonica.

INTRODUCTION

The transport networks have been presenting a constant growth of transmission rate for each optical fiber, while the access networks are characterized by the use of cables with a larger number of fibers. In both cases, the reliability of the optical cable, with respect to the preservation of its optical and mechanical characteristics, when submitted to normal or extraordinary external factors, needs to be increased, to minimize interruptions of the optical link.

Many telecommunications operators need to install optical cables for their transport and access networks, passing through rural areas. In

these areas accidents frequently occur with optical cables, because of fire caused by natural or forced burning of local vegetation and also caused by hunter's shots.

Among the options for optical cable installations, the aerial types present a good cost/benefit relationship, mainly when it is possible to use the infrastructure of the electric power transmission and distribution lines. Typically the OPGW cables (composite optical ground wire) and ADSS (all dielectric self-supporting) optical cables are used.

Another important aspect of aerial optical cables is the installation conditions such as maximum distance between poles, sags, climatic conditions, etc., which must be taken into account in the aerial network project.

In the market there are different types of all dielectric aerial optical cables, which have several advantages over the traditional solutions of metallic sheathed cables. However, dielectric solutions show a low performance relatively to fire and gunshots resistance.

OPGW cables are also used in transport networks using their own pole lines, to take advantages of their exceptional optical and mechanical features. However, for this kind of installation, this alternative is not always the best solution from the economical point of view.

Ahead of these facts, the present development provides a technically and economically viable alternative for aerial optical cable project, so as

to assure the optical cable works according to the project's conditions and, therefore, guaranteeing the mechanical and optical integrity of the optical fibers within the foreseen mechanical stress and temperature limits.

CABLE DESCRIPTION

This optical cable consists basically of a dielectric optical core with loose tube construction protected by a flame resistant polymeric sheath, and covered by a helically applied layer of metallic wires.

The optical cable core may contain up to 144 optical fibers. The armoring wires may be of steel-aluminum clad, aluminum alloy or a mixture of them, designed for aerial installation in spans up to 500 m. A cross section of a typical OPMA cable is illustrated in figure 1.

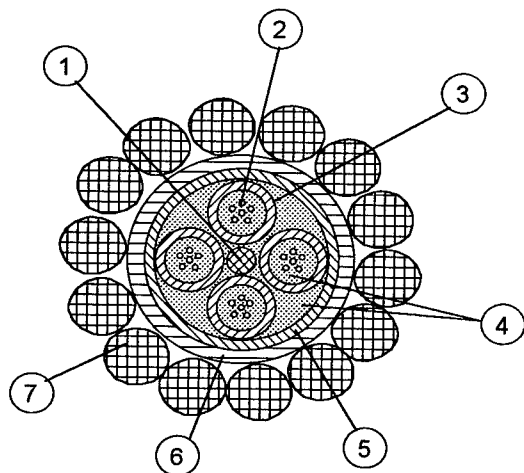


Figure 1 - OPMA cable cross section

- 1) central strength member
- 2) optical fibers
- 3) loose tubes up to 12 OF per tube
- 4) filling and flooding compounds
- 5) tapes
- 6) flame resistant sheath
- 7) armoring

The main characteristics of this cable applied for spans up to 500 meters and up to 48 OF are shown in Table 1:

Table 1 - Main characteristics of OPMA cable

unitary weight:	500 kg/km
maximum external diameter	13.5 mm
temperature range	-20°C to +65°C
linear thermal coefficient	$12 \times 10^{-6} 1/^{\circ}\text{C}$
modulus of elasticity	164500 MPa
rated tensile strength	54 kN
maximum operating tension	25 kN
every day stress for sag of 1.5 % and wind of 100 km/h	20.6 kN

TYPE TESTS

The qualification tests were carried out according to Brazilian Standards [1]~[3], comparing the performance of OPMA cable related to ADSS and OPGW cables, depending on the characteristic to be evaluated.

Optical

The optical characteristics are directly related to the performance desired for the optical fiber that compose the cable and are demanded in such a way for OPGW cables as for the ADSS and, for extension, also must be for the OPMA:

- attenuation
- uniformity of attenuation
- cut-off wavelength

Mechanical

The mechanical features are related to the construction design of the cable (external diameter, weight, thermal coefficient of the materials, etc.) and with its application (maximum span, maximum wind, maximum and minimum temperatures, form of installation, etc.).

Many mechanical features are demanded in such a way for cables OPGW as for the ADSS, however with slightly different performance requirements:

- aeolian vibration
- compression
- impact
- tensile performance
- repeated bending
- minimum bending radius
- creep

- torsion
- sheave

Environmental

These features have relation with the effect of the environment of use of the cable (temperature, humidity, solar radiation, etc.) on its performance:

- thermal cycling
- water penetration
- inflammability

Specific

Some features required for OPMA cable and currently not demanded for OPGW and ADSS cables were evaluated according to IEC Standards:

- fire resistance [4]
- shotgun resistance [5]

These tests were performed using standard ADSS and OPMA cables to allow a performance comparison.

The fire resistance test (see figure 2) was carried out with the cable under axial operating load in order to simulate the installation conditions. This condition is considered more severe related to IEC Test Method. During the test was measured the optical attenuation and the time to a first break of any fiber.

In the case of shotgun resistance test (see figure 3) it was used a 2 mm lead shot size, varying the shot distance from the typical IEC value of 20 meters to 3 meters.

The cable sample was installed using also the axial load tension. After shots it was observed the perforation of the cable by the shots and the exposition of the cable core.

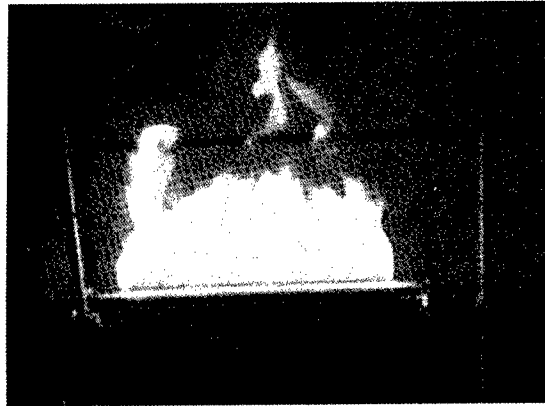


Figure 2 - OPMA Cable - IEC 60332-3 Fire test

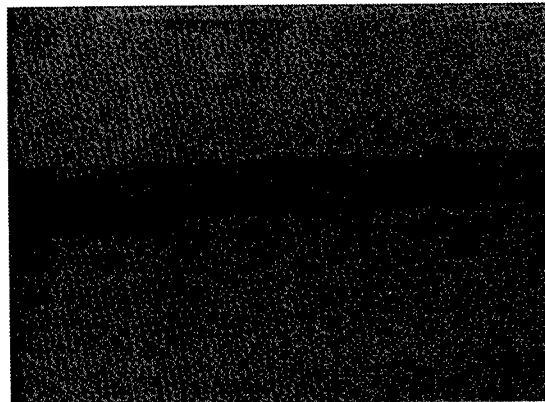


Figure 3 - OPMA Cable after shotgun test (3 m distance)

Results

The optical, mechanical and environmental type tests carried out demonstrate an excellent performance of OPMA cable according to the acceptance criteria presented in ABNT and Telebras Standards.

In the fire resistance test the OPMA cable presented a better heat performance related to ADSS. The time under fire until the break of optical fibers was typically twice that obtained with ADSS cable.

In the shotgun resistance test the OPMA cable withstood the minimum shot distance of 3 meters without perforation of optical core or fiber damages. The standard ADSS cable when submitted to the same test conditions presented optical core perforation for distances lower than 10 meters.

FIELD-TRIALS

The objective of the field-trials were to evaluate the technical and operational performance of the cables in compliance with Brazilian Telecom installation standards, comprising an uninterrupted period of 90 days of structural and optical evaluation of the cable and its accessories. Two important Brazilian Telecommunication Operators had provided the installation sites for field trials: Telemar and Telefonica.

The first alternative OPMA cable, for spans up to 250 meters, had been installed on an intermediate stretch of the path between the cities of Vera Cruz and Marília (São Paulo State - Brazil). The accessories had been specially developed by PLP (Preformed Line Products - Brazil) and provided to the installation.

In a total path length of 8.5 km, initially addressed for ADSS cables for spans up to 80 meters, about 3 km of cable OPMA was chosen to be installed in the stretch that presented the highest inclinations between poles. Also some poles had been removed to increase the span up to 250 meters.

In figure 4 is showed a typical OPMA installation using own concrete poles with 12 meters high.

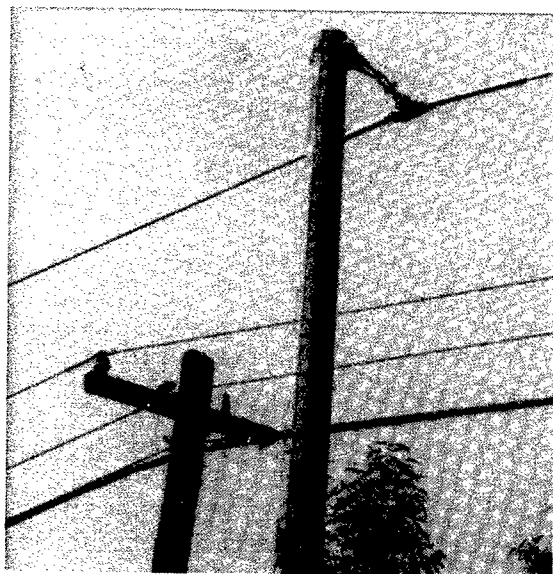


Figure 4 - Detail of OPMA installation

Measurements of optical attenuation had been carried out soon through after the installation of the cable and at the end of the period of evaluation in the whole path.

Other important aspect of this installation is the need of steel cords for the reinforcement of the concrete poles with dead end assemblies, as well as the necessity of electrical grounding of the cable.

Another OPMA cable for spans up to 500 meters was installed in Monte Azul City (north of Minas Gerais State - Brazil). Telemar elaborated the design of installation using an own pole line with spans up to 557 meters. In this case Telemar had been used preformed accessories of the same type applied for OPGW cables.

To the end of the period of field evaluation the cables presented fully satisfactory structural and optical performance for the applied conditions of use. However, the optical cables were not submitted yet to a natural or forced fire until the preparation of this paper.

CONCLUSION

The present development provides a technically and economically viable alternative for aerial optical cable project, so as to assure that the optical cable works according to the project's conditions and, therefore, guaranteeing the mechanical and optical integrity of the optical fibers, within the foreseen mechanical stress and temperature limits.

The results obtained, in comparison with standard dielectric self-supported optical cables, specially for shot and flame resistance tests, lead this alternative optical cable to be a more reliable and cost-effective solution, mainly for installations that need to pass through rural areas.

The field tests are still under evaluation and study, for better evaluation. The establishment of a specific standard for this type of cable is in course.

ACKNOWLEDGEMENTS

The authors acknowledge the support and permission of Telefonica, Telemar and Pirelli Cabos to elaborate and present this paper. We also thank PLP Brazil in developing the accessories for the cable.

REFERENCES

- [1] ABNT Standard NBR 14160 – "All dielectric self-supporting aerial cables - Specification" – Aug 1998
- [2] ABNT Standard NBR 14074 – "Composite overhead ground wire with optical fiber (OPGW) - Specification" – Apr 1998
- [3] Telebras Standard SDT 235-350-715 – "Specification of all dielectric self-supporting aerial cables" – Issue 3, May 1998
- [4] IEC Standard 60332-3 – "Tests on electric cable under fire conditions – Part 3: Tests on bunched wires or cables" – 1992
- [5] IEC Standard 60794-1-2:E13 – "Shot-gun damage" – First edition – 1999

Authors

Marco Antonio Scocco was born in São Paulo-SP, Brazil in 1957. He received B.Sc. degree in Physics from University of Sao Paulo and M.Sc. in Electronic Engineering from Engineering School of the same University in 1990. He is currently the Telecommunication Engineering Manager of Pirelli Cabos S.A. He is a member of ABNT Standard Commission.

Edvaldo Chaves Mendes was born in São Paulo-SP, Brazil in 1960. He received M.Sc. degree in Mechanical Engineering from Federal University of Santa Catarina in 1986 and joined Pirelli Cabos S.A. He has been engaged in development engineering of aerial optical cables and is responsible of Telecommunication Laboratory. He is a member of ABNT Standard Commission of aerial optical cables.

Marcello Valente Giacaglia was born in São Paulo-SP, Brazil in 1963. He graduated Electrical Engineering from University of Sao Paulo at São Carlos in 1990 and joined Pirelli Cabos S.A. He is a Sales Manager of Telecommunication cables.

Dionisio Alberto Fulop was born in Santo André-SP, Brazil in 1949. He graduated Electronic Engineering from Industrial Engineering Faculty (FEI) in 1973 and joined Telefonica. He has been engaged in technical support on materials specification and standardization for External Telecommunication Networks. He is a member of ABNT Standard Commission of telecommunications copper (chairman) and optical cables.

Marcínia Naur was born in Diamantina-MG, Brazil in 1951. She graduated Electrical Engineering from Minas Gerais Catholic University (PUC) in 1974 and joined Telemar-MG in 1975. She is currently the manager of Telecommunication Backbone of Minas Gerais State, Brazil.

Jaime Ribeiro da Mota was born in Bonfim-MG, Brazil in 1948. He is a Telecommunication Technician from UTRAMIG School of Minas Gerais in 1983. Since 1968 he is working at Telemar-MG. He has been engaged in design and set up of Long Distance Telecommunication Backbone of Minas Gerais State, Brazil.

Effect of Thermal Aging on High Frequency Transmission Characteristics of Coaxial Drop Cables

S.-H. Chou, J.-C. Lin, H.-F. Lin, Y.-H. Hwang, C.-H. Hsieh,
H.-P. Hsu, Y.-c. Lin, Y.-K. Tu

OSP, Telecommunication Laboratories, Chunghwa Telecom, Taiwan, R.O.C.

ABSTRACT

Thermal effect on high frequency transmission characteristics of coaxial drop cable, including characteristic impedance, attenuation, structural return loss and velocity of propagation, has been studied in this study. By choosing drop cables of different sizes, RG-59 and RG-11 were aged at three different temperatures in the oven for a period of 25 weeks. The results show that 100°C is an unacceptable temperature for all samples, especially for the smaller cable RG-59. Except cable dimension, cable design is another important factor. Thermal effects result in the increase in attenuation, and the decrease in characteristic impedance, structural return loss and velocity of propagation. Based upon capacitance results, the deterioration of transmission characteristics can be attributed to insulation properties changed.

INTRODUCTION

Coaxial cables have been used in video and broadband applications for a long time. For example, the networks of telecommunications and cable television (CATV) companies similarly use coaxial cables to connect customers to fiber distribution networks for delivery of broadband services.

One of the main advantages of coaxial drop cables is high bandwidth [1-6]. The performance of coaxial drop cable can be characterized by examining the electrical parameters. The requirement of initial electrical performance has been clearly described in Bellcore Specification [7]. However, there exist no transmission requirements after thermal aging by Bellcore.

Coaxial drop cables are designed to carry high frequency radio waves (5 MHz to 1 GHz) from some distribution point to the user [8]. The determination of cable electrical performance involves the measurements of low frequency parameters and high frequency parameters. The former, so-called low frequency parameters, includes conductor resistance and capacitance because they are measured at DC and at the frequency of 1 kHz, respectively. On the other hand,

the latter, named high frequency parameters, includes characteristic impedance, attenuation, structural return loss and velocity of propagation. The reasons are that velocity of propagation is measured at 200 MHz and the others are required to measure over a wide frequency range from 5 MHz to 1 GHz.

The life expectancy of coaxial drop cables [1-2] and coaxial distribution cables [3-4] has been discussed in the literature. Key et al. studied the reliability of coaxial cables drops in the CATV industry and reported that installed CATV coaxial drop cables had an average useful life of only three years, clearly showing that the drop portion was responsible for the majority of service problems [1]. Unfortunately, in these reports, [2-4] except cable's attenuation, transmission characteristics were not discussed in detail. However, an understanding of the thermal effect on high frequency transmission characteristics of coaxial cables is necessary in order to understand the life expectancy of coaxial drop cables. This understanding has not yet been reached.

There will be four famous properties, characteristic impedance, attenuation, structural return loss and velocity of propagation, discussed in this study. First of all, characteristic impedance can be calculated from the outside diameter of center conductor, the inside diameter of outer conductor and the dielectric constant of the insulation. In general, the characteristic impedance varies as a function of the frequency of the applied signal and is unrelated to length. At very high frequencies, the value of this parameter approaches to a fixed value. Most cables today are commonly either 50 ohm or 75 ohm impedance [5].

Secondly, attenuation is an expression of how much signal energy is lost due to conductor and dielectric losses, which have been described in the literature [1-4]. In general, lower transmission loss of coaxial cable can be obtained through the increase in the conductor size, the reduction of the dielectric constant of the insulation, the increase in the insulation diameter and so forth [5]. For higher frequency applications, larger size cable is necessary. For example, bandwidths operating above 330 MHz would tend to require RG-11 cables in place

of RG-59 cables [9]. Because RG-11 cables have larger conductor diameter and insulation diameter, comparing with RG-59.

Thirdly, structure return loss is used to describe the portion of the total return loss which is due to these structural changes along the cable [7]. Structural variations of the cable in a periodic and random manner produce reflections of signals within the cable and reduce the signal strength.

Finally, velocity of propagation is the speed of an electrical signal down a length of cable compared to the speed of light in a vacuum, expressed as a percentage. For practical cables, the velocity of propagation depends on the properties of the dielectric materials surrounding the conductor [10]. At high frequencies, the velocity of propagation tends towards a constant value. This parameter is usually required to measure at a certain frequency.

Except these four high frequency parameters, the capacitance is also discussed in this study. The higher the dielectric constant of the insulation, the higher the capacitance [10]; therefore, this parameter is useful to inspect the changes in the insulation material properties.

It is well known that exposed to the service environments with time, in particular at high temperature, the cable transmission performance can be adversely affected. The objective of this work is to study the thermal effect on the electrical performance of coaxial drop cable, especially at high frequency range. This study further compares the thermal effect on the electrical performance of coaxial drop cables supplied from different manufacturers.

EXPERIMENTAL SECTION

RG-59 and RG-11 coaxial drop cables were chosen to evaluate the thermal effect on cable electrical performance. Three manufacturers (identified as C, T, and W) supplied both of cables RG-59 and RG-11; six samples (referred as C-59, C-11, T-59, T-11, W-59 and W-11) therefore were used in this work. All samples have 75 ohm impedance and are with standard shield. Typical values of nominal diameters in drop cables are listed in Table 1.

The samples cut into 100 meters in length were prepared to be aged at three different temperatures, 55, 85 and 100°C in the ovens, and then removed from the aging environments after 1, 4, 8, 16 and 25 weeks for electrical tests.

Table 1. Nominal diameters in drop cables

Drop cable	RG-59	RG-11
Center Conductor	0.81 mm	1.63 mm
Dielectric	3.71 mm	7.11 mm
Jacket	6.10 mm	10.16 mm

Cable transmission measurements were performed by DCM CMS-COAX system. The system consists of a control subsystem, coaxial test panel, LCR meter, network analyzer, and associated connectivity and control cabling. Furthermore, standard accessories should include 75 ohms calibration kits for high frequency measurements.

By combining the control subsystem, coaxial test panel and network analyzer, the system is available to test high frequency parameters, whereas the combination of the control subsystem and LCR meter can offer a system for low frequency measurement.

Based upon Bellcore requirements, the report for attenuation measurements would include twelve frequency points, 5, 55, 211, 270, 300, 330, 400, 450, 550, 750, 870 and 1000 MHz. On the other hand, for characteristic impedance and structural return loss measurements, except twelve frequency points as shown above, ten more points were selected to display the data, 108, 150, 350, 500, 600, 650, 700, 800, 900 and 950 MHz. Furthermore, the data of velocity of propagation were measured at center frequency of 200 MHz.

For an accurate determination of all electrical parameters, calibration is required before a measurement. Kelvin clips are used for low frequency calibration and measurement. Furthermore, for high frequency measurements, as described in instrument manual, it is necessary to install an N connector at each end of the cable. All data were stated as the average of values at three individual measurements to ensure the accuracy of measurements.

RESULTS AND DISCUSSION

Characteristic impedance measurement. Initial characteristic impedance data are illustrated graphically in Figure 1, which shows the data for all six samples obtained by 22 frequencies as mentioned above. As expected, at high frequencies, the values of this parameter tend to a constant between 74.2 ohm and 77.5 ohm for all six samples. RG-59 samples have a little higher values, whereas RG-11 ones do lower values. However, the values at low frequency side (5 MHz) are somewhat high, comparing with the constant at higher frequencies, even up to 78.6 ohm.

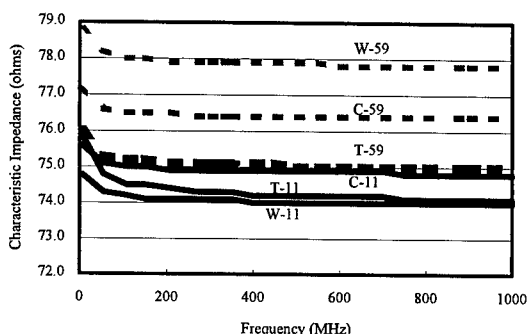


Figure 1. Initial characteristic impedance for six samples

Because characteristic impedance for a given cable is a constant at high frequencies, the values of this parameter at 500 MHz were chosen for further discussion to find out the thermal aging effect. Figure 2 shows the changes in characteristic impedance at 500 MHz for T-59 samples aged at three different temperatures during 25 weeks of aging time. The data were obtained by comparing the values after thermal aging with initial value.

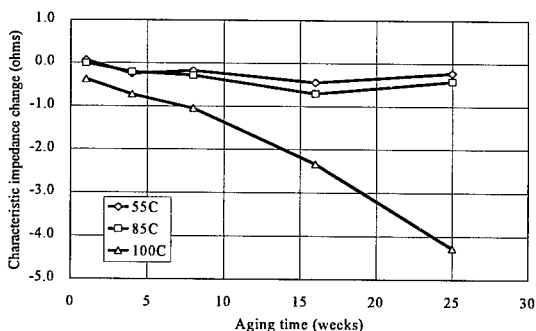


Figure 2. Characteristic impedance change at different aging temperature for T-59

For the samples aged at 55 and 85°C, the values shown in Figure 2 remain almost unchanged over 25 weeks of aging time. Furthermore, when the sample was aged at 100°C, the ones obviously change in demonstrating monotonous decrease over the aging time, from 75.0 ohms down to 70.8 ohms. The result clearly concludes that although 85°C is not high enough to affect this cable parameter, 100°C is an unacceptable temperature to the sample T-59, the change up to 4.3 ohms.

As described for the sample T-59, the others also showed similar performance when the samples were aged at lower temperatures, 55 and 85°C. However, there would be a great importance in the data obtained

from the samples aged at 100°C. Figure 3 is a plot of characteristic impedance changes vs aging time for all six samples aged at 100°C.

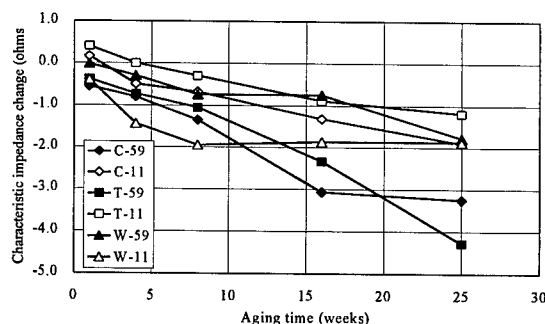


Figure 3. Characteristic impedance changes for six samples aged at 100°C.

Negative slopes for all samples clearly prove that characteristic impedance of coaxial drop cables, no matter what the sample is, definitely decreases with aging time when the samples were aged at 100°C.

Characteristic impedance of the samples C-59 and T-59 shows a monotonous decrease with aging time, whereas ones of C-11, T-11 and W-59 only changes slightly. However, W-11 shows different feature, which having the greater part of change during the first 8 weeks and then changing near to equilibrium.

The result indicates that characteristic impedance of coaxial drop cable decreases with aging time at high aging temperature. At 100°C, thermal effect on characteristic impedance performance can not be neglected. Again, based upon characteristic impedance measurement, C-59 and T-59 can not provide good resistance to thermal aging effect.

One more issue need to be mentioned is that the value of characteristic impedance always drops after thermal aging; therefore, in order to meet the requirement even after aging, to increase initial characteristic impedance is a useful method.

Attenuation measurement. Initial attenuation data are illustrated graphically in Figure 4, which shows the data for all six samples obtained by 12 frequencies as mentioned above. Several features are shown in this Figure. Firstly, the attenuation of signal in the cable increases with the operating frequencies. Secondly, three RG-11 samples have very similar attenuation data, whereas three RG-59 ones also display great resemblance. Thirdly, no matter what the supplier is, initial attenuation values strongly depend on the cable dimensions. Finally, comparing to RG-59, RG-11 has

better attenuation performance due to larger cable dimension.

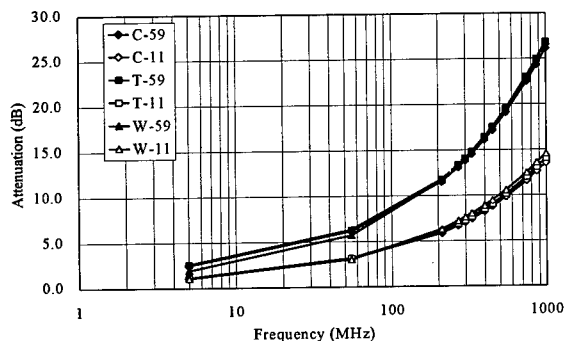


Figure 4. Initial attenuation data for six samples

A plot of attenuation change (%) vs log (operating frequency) is used to discuss the thermal effect on cable attenuation. W-11 samples are chosen as an example. The attenuation change data for W-11 aged at 55, 85 and 100°C are presented in Figures 5-a, 5-b and 5-c, respectively. Attenuation change (%) was obtained by initial attenuation datum subtracted from the values after thermal aging, and then divided by initial attenuation datum.

Three factors, operating frequency, temperature and aging time, would be discussed according to the data shown in these figures. For operating frequency, although attenuation changes increase as increasing the operating frequency, attenuation changes show just a somewhat monotonous increase with the frequency as higher than 100 MHz.

Concerning the combination effect of aging temperature and aging time, no effect was observed when the sample was experienced at 55°C up to 25 weeks, whereas thermal effect was clearly shown at 85°C and 100°C. For the first four weeks, the attenuation changes were about 3% and 12% for the samples aged at 85°C and 100°C, respectively. It means that the higher the aging temperature, the larger the attenuation change. On the other hand, when the sample was aged at 100°C, the changes were about 12% and 91% in tune for the samples aged for 4 weeks and 25 weeks. It clearly indicates that the longer the aging time, the larger the attenuation change. The results ensure that temperature effect is the main factor to influence cable's attenuation.

The attenuation changes for all samples aged at 55°C, similar to W-11 sample, will not be discussed here.

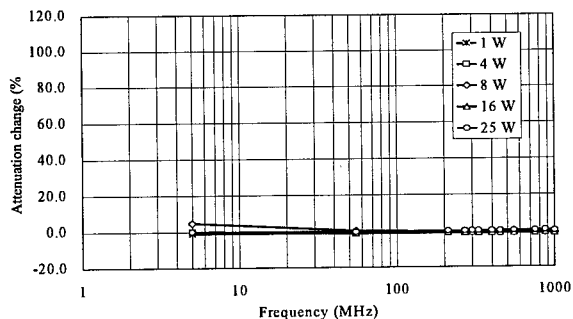


Figure 5-a. Attenuation change for W-11 aged at 55°C.

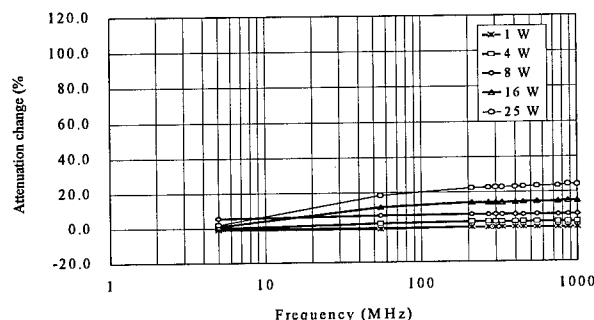


Figure 5-b. Attenuation change for W-11 aged at 85°C.

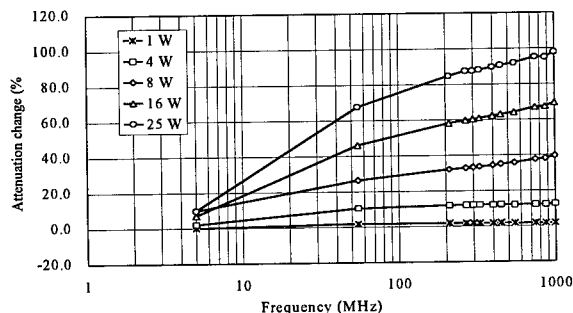


Figure 5-c. Attenuation change for W-11 aged at 100°C.

Nevertheless, the attenuation changes for six samples aged at 85°C and 100°C for a period of 25 weeks are displayed in Figures 6-a and 6-b, respectively. It needs to be noted that there are completely different scales in these two figures.

When the samples were aged at 85°C, the values of attenuation change for W-11 are the largest and for C-11 are the smallest. For the samples aged at 100°C at a testing frequency of 1 GHz, T-59 and C-59 exhibit the worst cases for the cable attenuation property,

unbelievably near to 300% or higher. It is clear from the data that an increase in temperature would cause attenuation to increase significantly.

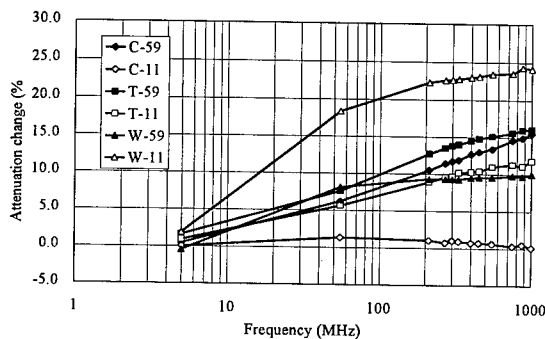


Figure 6-a. Attenuation changes for six samples aged at 85°C after 25 weeks

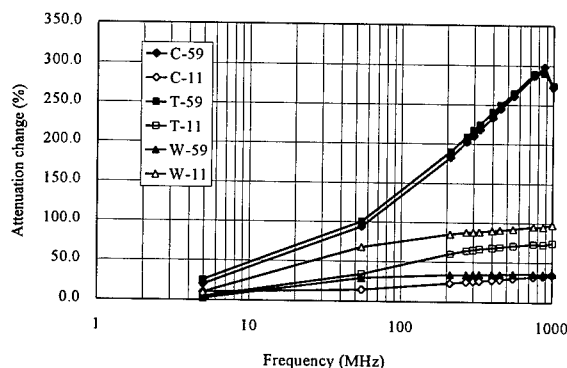


Figure 6-b. Attenuation changes for six samples aged at 100°C after 25 weeks.

In Figure 6-b, the data for T-59 and C-59 drop slightly at high-frequency side, resulting from instrument limitation. The accuracy of attenuation measurements can be varied over different amplitude range and different frequency range. The attenuation data measured at the frequency point near to 1GHz have very large fluctuation. It is due to the instrument limitation for high attenuation values over 78 dB; the accuracy of attenuation measurements is up to ± 10 dB over the range from 65 to 78 dB at testing frequency from 100 MHz to 1 GHz. The attenuation data for T-59 and C-59 approach to 100 dB at high-frequency range; therefore, large fluctuation is unavoidable.

However, for the samples aged at 100°C for a period of 25 weeks, T-59 and C-59 exhibit the attenuation change near to 300% at a testing frequency of 1 GHz, whereas C-11 and W-59 have similar values about 35%. The data clearly explains that cable dimension is a factor to

influence attenuation performance, but cable design such as quality of cable materials used is also an important factor.

Another important issue is shown in Figures 7-a and 7-b. Comparing the data for T-59 with ones for C-59, these figures show that both have very similar attenuation property; they however do not exhibit the same tendency to change the attenuation property when the samples were aged up to 16 weeks. After a period of 16 weeks, attenuation change for T-59 increases rapidly up to 162% at a testing frequency of 1 GHz, whereas one for C-59 just increases near to 46%. The result explains that the cables from different manufacturers indicate different transmission characteristics due to different cable design or different quality of cable materials used. The result shows that up to 25 weeks aging time, if a 10% increase in attenuation at a testing frequency of 1 GHz is considered, 55°C is acceptable for all samples, 85°C is only for C-11, and 100°C is not acceptable at all.

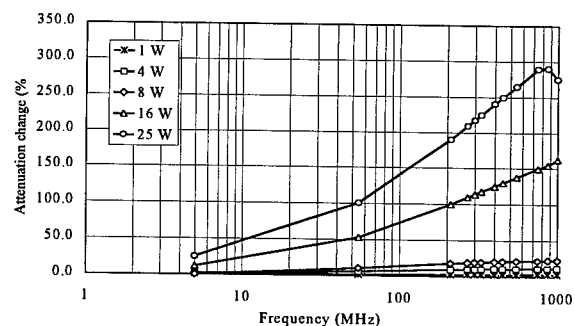


Figure 7-a. Attenuation change for T-59 at 100°C

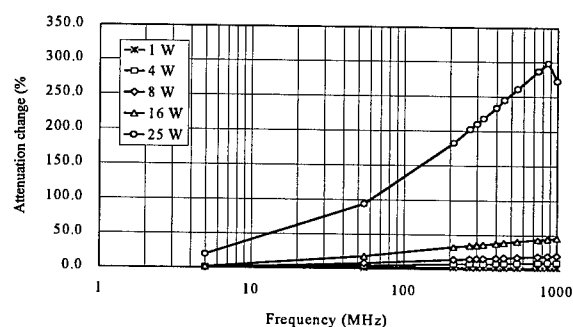


Figure 7-b. Attenuation change for C-59 aged at 100°C.

Structural Return Loss (SRL) measurement. It has to be noted that SRL measurements exhibit high inaccuracy. In this study, the standard deviation of

values at three measurements is about 0.6 dB. However, unusual values up to 6 dB could be observed at a few frequency points. SRL is an important performance for broadband applications; therefore, SRL measurements are still completed in this work.

Except the samples T-59 and C-59 aged at 100°C, all other samples have no valuable observations, even aged for a period up to 25 weeks. The SRL data for C-59 and T-59 are illustrated graphically in Figures 8-a and 8-b, respectively, measured at 22 frequency points as mentioned above. The data of the samples, including initial values, and aged for 8 weeks and 25 weeks, are shown in each figure. The data for C-59 sample seem unchanged after aged 8 weeks and slightly decreased for a period of 25 weeks. However, when the T-59 sample was aged for 8 weeks, a slight decrease of SRL values was observed. Furthermore, after aging 25 weeks, a decrease in SRL performance is significantly.

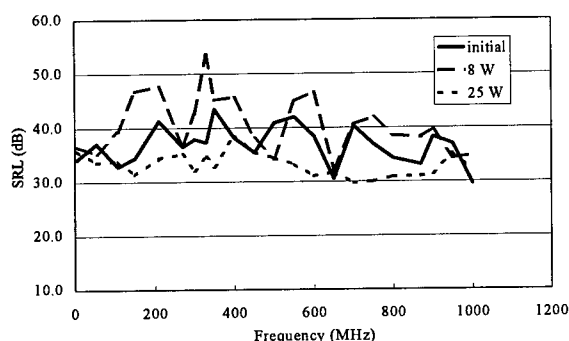
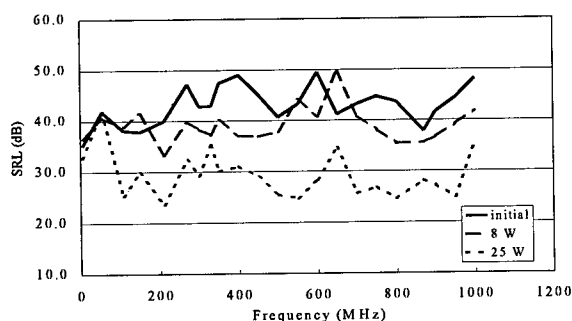


Figure 8-a. SRL data for C-59 aged at 100°C.

Figure 8-b. SRL data for T-59 aged at 100°C.



It seems difficult to draw conclusions from SRL data. However, SRL measurements are not so sensitive as attenuation measurements, even as characteristic impedance. It is still clear to prove that the samples T-59 and C-59 could not provide a good SRL performance

when the samples were aged at 100°C. In conclusion, concerning SRL performance, up to 25 weeks aging time, 100°C is still acceptable for the samples, except T-59 and C-59.

Velocity of propagation (VP). For some reasons, VP measurements were completed only when the samples were aged for 4, 8, 16 and 25 weeks. The standard deviation of VP values at three individual measurements is always zero; VP therefore is a reliable parameter. Table 2 list the values of VP change, obtained by comparing to VP data after aged for 4 weeks subtracted from ones after aged for 25 weeks. During the aging time between 4 weeks and 25 weeks, VP values remain almost unchanged when the samples were aged at 55 and 85°C. However, VP values of the samples T-59 and C-59 decrease significantly, ones of W-11 are next, and the others are very stable. The conclusion again is that T-59 and C-59 have the worst reliability of VP.

Table 2. The values of VP changes after thermal aging for six samples

Aging temperature	55°C	85°C	100°C
C-59	+ 0.0	+ 0.0	- 2.1
C-11	+ 0.1	+ 0.1	- 0.2
T-59	+ 0.1	+ 0.0	- 1.8
T-11	+ 0.1	+ 0.1	- 0.2
W-59	+ 0.1	+ 0.0	- 0.2
W-11	+ 0.1	+ 0.0	- 0.6

Capacitance measurements. Finally, capacitance will be discussed briefly, which is related to the insulation material properties. Cable capacitance is the only discussed parameter defined low frequency parameter, measured at a test frequency of 1 kHz.

There is no thermal effect on capacitance when the samples were aged at 55 and 85°C for the aging time up to 25 weeks. The capacitance data for the samples aged at 100°C are shown in Figure 9. The data show that an increase in capacitance was observed for T-59 after aging 8 weeks and for C-59 after aging 16 weeks.

It is well known that the higher the dielectric constant of the insulation, the higher the capacitance; furthermore, the lower the insulation property. Therefore, an increase in capacitance states clearly a decrease in insulation material properties.

Based upon the results of high frequency parameters, 100°C is an unacceptable temperature for coaxial drop cables, including series RG-59 and RG-11. The main reason is that 100°C is too high for the insulation material.

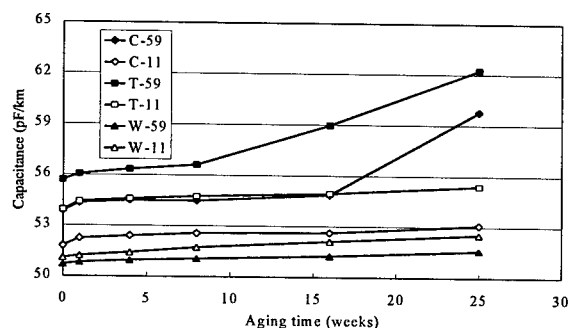


Figure 9. Capacitance data for six samples aged at 100 °C.

CONCLUSION

The performance of coaxial drop cable under thermal aging process can be qualified by the changes in high frequency transmission characteristics. 100°C is definitely an unacceptable temperature for cable transmission characteristics, exhibiting the increase in attenuation, and the decrease in characteristic impedance, structural return loss and velocity of propagation. By choosing drop cables of different size, the results show that drop cables having larger size, such as RG-11, provide better resistance to thermal aging effect. On the hand, comparing T-59 and C-59 with

W-59, it clearly explains that cable dimension is not the only factor to influence thermal effect on coaxial drop cable. Due to different cable design and different quality of cable material used, cables supplied from different manufacturers provide completely different thermal aging effect.

REFERENCE

1. P.L. Key, S.A. Schwarz, J.N. D'Amico, L.M. Hore, R.J. Schmieder and P.H. Whipple, *NFOEC*, III, 103, 1994.
2. J.N. D'Amico, T.N. Bowmer, O.G.Chavez and L.M. Hore, *Proc. 44th IWCS*, 720, 1995.
3. L. M. Hore and O.G. Chavez, *Proc. 47th IWCS*, 299, 1998.
4. L.M. Hore, V.J. Ferraro, O.G. Chavez and J.N. D'Amico, *Proc. 45th IWCS*, 946, 1996.
5. J. Weir, *Outside Plant*, 70, August 1996.
6. M. Davis, *Outside Plant*, 58, May 1996.
7. GR-1398-CORE, *Bell Communications Research, Generic Requirements*, Revision 1, 1996.
8. J.N. D'Amico and G.F. Apger, *Proc. 45th IWCS*, 977, 1996.
9. B. Davies, *Outside Plant*, 29, August 1996.
10. DCM Technical Paper.

CABLING OF DISPERSION COMPENSATING FIBRES

Lars Grüner-Nielsen and Stig Nissen Knudsen

Lucent Technologies Denmark
Brøndby
Denmark

ABSTRACT

Cabling of dispersion compensating fibres (DCF) has been examined for the first time. The micro and macro bending performance has been evaluated and compared to standard non-shifted single mode fibres (SSMF). At 1550 nm, it is found that the macro bending performance of DCF is comparable to SSMF. At 1550 nm, the micro bending performance is better for DCF than SSMF. The wavelength dependence of both macro and micro bending loss is much steeper for DCF than SSMF. The DCF has been cabled in a loose tube cable with good result. Compared to measurement on fibre spools, the attenuation dropped both at 1550 and 1580 nm on all fibres. On five out of six fibres, the PMD dropped as well. The cable was temperature cycled between -40 and 70°C without any significant change in attenuation.

INTRODUCTION

Use of dispersion compensating fibres (DCF) is now a well-proven and commercially available technique for compensating the dispersion of standard non-shifted single mode fibres.¹ So far, the DCF have primarily been used in modules for discrete dispersion compensation at the repeater stations. For some applications, for example submarine cables, it could however be more advantageous to deploy the fibre in the cable plant. Until now there has been no reports on the cabling sensitivity of DCF.

There are three main concerns when evaluating a new fibre type for cabling:

1. Macro bending sensitivity
2. Micro bending sensitivity
3. Change in PMD during cabling

Macro bending sensitivity is an inherent concern for DCF. This is because DCF rely on a high contribution from wave-guide dispersion. DCF

designs where the field is only loosely bound to the core will lead to high negative dispersion but also to high bend loss sensitivity.²

Another challenge is to obtain low polarisation mode dispersion (PMD). DCF are more than one order of magnitude more sensitive to core ovality than conventional telecommunication fibres due to the high core index used.³ Therefore, extreme care has to be taken to avoid core ovality. At the same time, the mode coupling can be stimulated by introducing oscillatory twist into the fibre during draw. Enhanced mode coupling not only reduces the PMD, but also gives a more stable PMD value.⁴

FIBRE PROPERTIES

Six DCF fibres were selected for the cabling experiment. All fibres have a standard 245 µm dual layer D-LUX100® acrylate coating. Fibre 1-4 were colour coated with a UV curable ink to a diameter of 255 µm. All DCF fibres belong to the newly developed full slope compensating type.⁵ Data for the fibres are summarised in Table 1.

DCF no.	Loss at 1550 nm dB/km	Loss at 1580 nm dB/km	Dispersion at 1550 nm ps/(nm·km)	Dispersion slope at 1550 nm ps/(nm ² ·km)	RDS %/nm	FOM ps/(nm·dB)	PMD ps/√km
1	0.520	0.521	-91.7	-0.31	3.36	176	0.08
2	0.547	0.580	-96.8	-0.35	3.66	177	0.05
3	0.532	0.553	-87.3	-0.28	3.16	164	0.06
4	0.501	0.488	-94.7	-0.33	3.51	189	0.08
5	0.469	0.438	-89.9	-0.29	3.22	192	0.09
6	0.586	0.689	-105.4	-0.39	3.73	180	0.06

Table 1. Data for the selected fibres

RDS is the relative dispersion slope, which is defined as the dispersion slope divided by the dispersion. The RDS is an important parameter as the condition for simultaneous dispersion and dispersion slope compensation is that the RDS of the DCF equals the RDS of the compensated

fibre.⁵ The RDS of non-shifted standard single mode fibres is around 3.4 %/nm.

FOM is the figure of merit of DCF, which is defined as the ratio of dispersion to attenuation.

Macro bending resistance

The macro bending resistance of the six DCF was evaluated. The bend loss was measured for three turns around a 20 mm mandrel, three turns around a 30 mm mandrel as well as for 100 turns in a loose coil with a diameter of 50 mm. For comparison, three standard non-shifted single mode fibres (SSMF) were evaluated as well. Cut-off and mode field diameter (MFD) for the three SSMF are summarised in Table 2.

Fibre	Cut-off nm	Mode field diameter µm
SSMF A	1299	9.11
SSMF B	1254	9.32
SSMF C	1188	9.55

Table 2. Properties of the tested standard matched cladding fibres

Fibre B has a typical cut-off and MFD, while fibre A has a high cut-off and low MFD and fibre C a low cut-off and high MFD.

The measured bend loss at 1550 nm as a function of bend diameter is shown in Figure 1.

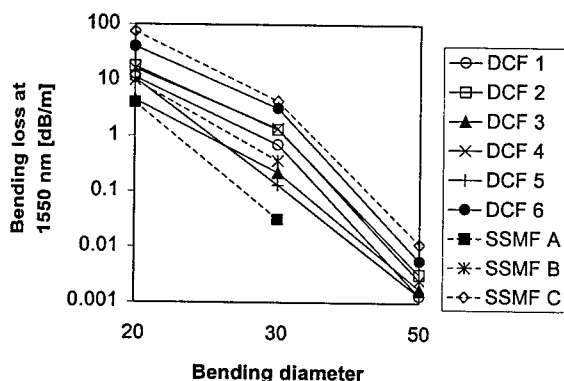


Figure 1. Result at 1550 nm of the macro bending test

It is interesting to observe that the most bend sensitive SSMF fibre has higher bend loss than any of the six DCF. The most bend sensitive SSMF (SSMF C) is as expected the fibre with low cut-off and high MFD. The wavelength dependence of the bend loss for a bend diameter of 50 mm is shown in Figure 2 for the most bend sensitive DCF and SSMF fibre.

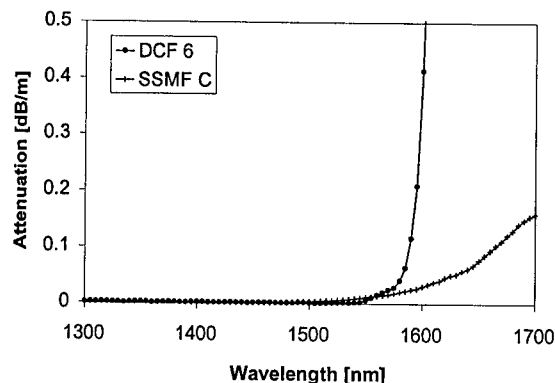


Figure 2. Macro bending results for a diameter of 50 mm

Very different wavelength dependence is observed for the two fibre types. The DCF has a steep wavelength dependence compared to the SSMF.

Micro bending resistance

The micro bending resistance of the fibres has been evaluated using the test method IEC 793-1-C3C.⁶ The fibre is placed under load in a loop of diameter 98.5 mm between a rubber sheet and a wire mesh (70, woven).

The induced excess loss at 1550 nm as a function of load is shown in Figure 3 for the nine fibres.

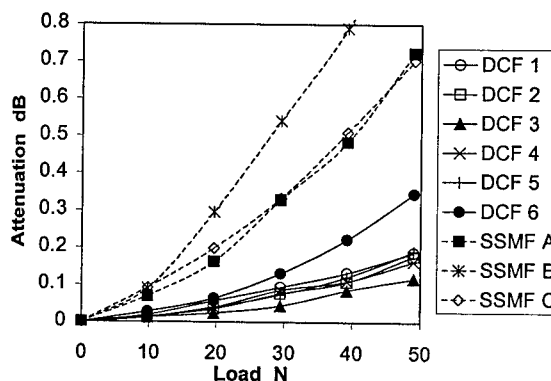


Figure 3. Results at 1550 nm of the micro bending test

All six DCF are seen to be less micro bending sensitive than any of the SSMF are. There seems to be a reasonable correlation between the macro and micro bending sensitivity of the DCF. The wavelength dependence of the micro bending loss for a load of 49 N is shown in Figure 4 for the most micro bending bend sensitive DCF and SSMF fibre.

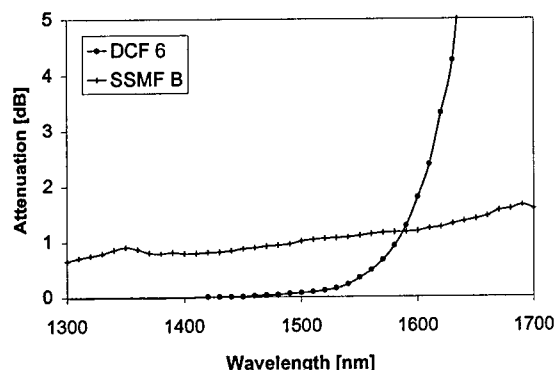


Figure 4. Micro bending results for a load of 49 N

As for the macro bending sensitivity, a very different wavelength dependence is observed for the two fibre types. While the SSMF has hardly any wavelength dependence for the micro bending loss, the DCF has a quite steep wavelength dependence, but not as steep as for the macro bend loss.

DESCRIPTION OF CABLE

The fibres have been cabled in a loose tube cable. A cross sectional drawing of the cable is shown in Figure 5. The cable has three tubes and three dummy elements. There is one tube with four coloured fibres and two tubes with only one (uncoloured) fibre per tube to test the effect of having more fibres per tube.

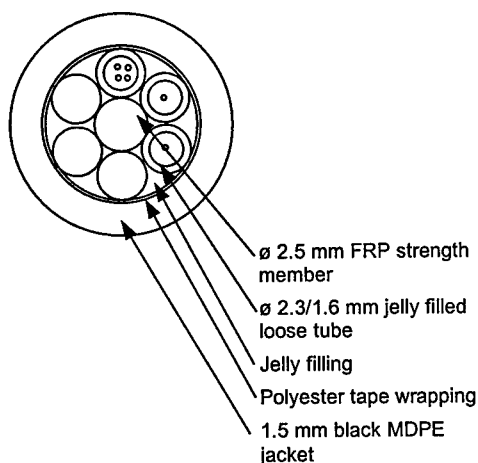


Figure 5. Cross sectional drawing of the cable

The tubes are made of polyester (polybutylene terephthalate) and filled with a thixotropic jelly. The tubes have an outer diameter of 2.3 mm and an inner diameter of 1.6 mm. The excess

fibre length relative to the tube is between 0 and 1 % after cabling. The tubes are S-Z stranded around a central fibre reinforced plastic (FRP) strength member. The stranding pitch was 80 mm. This geometry gives the fibre an equivalent bend radius of 70 mm. The allowable cable elongation and contraction, with stress free fibres, becomes around ± 8 %. The tubes are surrounded by a polyester tape and a black medium density polyethylene (MDPE) jacket. The jacket thickness is 1.5 mm.

RESULT OF CABLING EXPERIMENT

The length of the cable was 2.1 km. Measured attenuation, dispersion and PMD after cabling are shown in Table 3. The changes due to cabling are also shown. The measurements on the fibres before cabling shown in Table 1 were done on 3 km lengths on fibre spools. The data for fibres 1-4 in Table 1 are after colouring. The fibre spools had a core radius of 90 mm.

Fibre no.	Tube no.	Loss at 1550 nm dB/km	Loss at 1580 nm dB/km	Dispersion at 1550 nm ps/(nm ² ·km)	Dispersion slope at 1550 nm ps/(nm ³ ·km)	PMD ps/√km
After cabling						
1	1	0.519	0.493	-91.6	-0.31	0.04
1	1	0.529	0.509	-96.7	-0.37	0.03
1	1	0.503	0.465	-86.9	-0.28	0.03
1	1	0.491	0.456	-95.1	-0.34	0.02
1	2	0.464	0.425	-90.6	-0.30	0.04
1	3	0.543	0.624	-106.8	-0.41	0.11
Change due to cabling						
1	1	-0.001	-0.028	0.1	-0.01	-0.04
2	1	-0.018	-0.071	0.1	-0.01	-0.02
3	1	-0.029	-0.088	0.4	-0.01	-0.03
4	1	-0.010	-0.032	-0.4	-0.01	-0.06
5	2	-0.005	-0.013	-0.7	-0.01	-0.05
6	3	-0.043	-0.065	-1.4	-0.01	0.05

Table 3. Result of cabling

It is observed that the attenuation drops on all fibres both at 1550 nm and at 1580 nm. The average drop is 0.018 dB/km at 1550 nm and 0.050 dB/km at 1580 nm. The effect of cabling on the attenuation between 1300 and 1700 nm for DCF 4 is shown in Figure 6. It is observed that the bend loss edge moves to longer wavelengths. The drop in attenuation is a sign of the fact that the fibres lie better in the cable than on the fibre spool even though the bend radius has dropped from 90 to 70 mm.

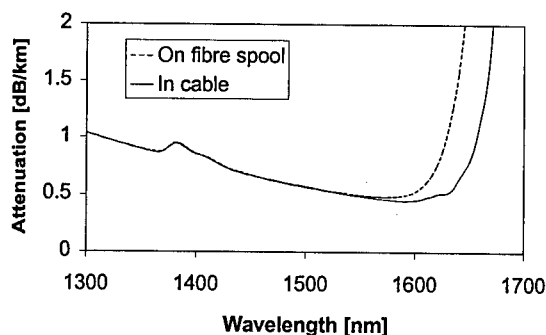


Figure 6. Effect of cabling on the spectral attenuation of DCF 4

As expected there is only a negligible change in the dispersion.

It is remarkable that the PMD drops on five of the six fibres after cabling. This is a sign of the efficiency of the oscillatory twisting during fibre draw. The same effect has been observed earlier on standard transmission fibres with oscillatory twist.⁴

No difference is observed between the fibres in the four-fibre tube and the single-fibre tube. This is a further evidence of the low micro bending sensitivity of the DCF.

TEMPERATURE CYKLING

The cable has been temperature cycled between -40 and $+70^{\circ}\text{C}$ according to Bellcore GR-20-CORE.⁷ The used temperature cycle is shown in Figure 7.

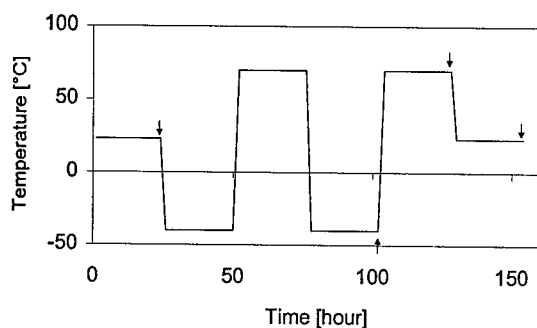


Figure 7. Temperature cycle. Arrows indicate time of attenuation measurement

The attenuation was measured with an OTDR from the outer end of the cable. The change in attenuation during cycling is shown for all six fibres in Figure 8.

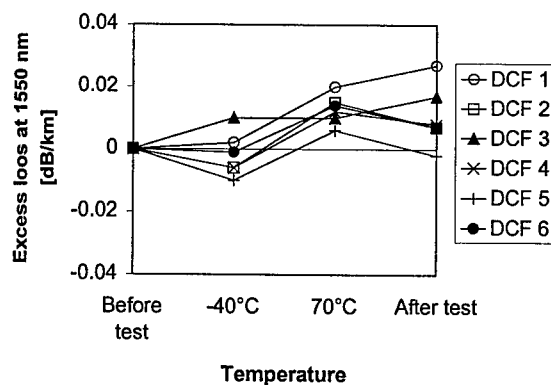


Figure 8. Measured attenuation change during temperature cycling

Only negligible changes in attenuation are observed.

CONCLUSION

For the first time it has been shown that dispersion compensating fibres (DCF) can be cabled without problems. In a loose tube cable with an equivalent bend radius as low as 70 mm, the attenuation dropped both at 1550 and 1580 nm compared to the measurements on the fibre spools. Generally PMD also dropped, which shows the efficiency of the mode coupling introduced by the oscillatory twist frozen into the fibre during draw.

No significant change in attenuation was observed during or after temperature cycling between -40 and $+70^{\circ}\text{C}$.

The macro bending resistance at 1550 nm of the examined DCF was comparable to standard non-shifted single mode fibres (SSMF) and found to be comparable. However, the wavelength dependence of the macro bending loss was much steeper for DCF than for SSMF.

The micro bending resistance at 1550 nm of the DCF was better than for SSMF. Again, the DCF had much steeper wavelength dependence than the SSMF. The wavelength dependence of the micro bend loss for the DCF was not as steep as for the macro bend loss of the DCF.

ACKNOWLEDGEMENT

Draka Denmark Optical Cable is acknowledged for the manufacture of the cable and loan of the temperature chamber.

REFERENCES

- ¹ L. Grüner-Nielsen, B. Edvold, D. Magnussen, D. Peckham, A. Vengsarkar, D. Jacobsen, T. Veng, C. C. Larsen and H. Damsgaard; Large volume manufacturing of dispersion compensating fibres; Technical Digest of OFC'98, paper TuD5, pp. 24-25, 1998
- ² A. Joseph, Antos and David K. Smith; Design and Characterization of dispersion Compensating Fiber Based on the LP₀₁ Mode; Journal of Lightwave Technology, Vol. 12, No. 10, pp. 1739-1745; 1994
- ³ J. Chesnoy, P. Nouchi, J. Y. Boniort, C. Brehm, C. Le Sergent and P. Sansonetti; Optimum dispersion compensating fiber: Birefringence and PMD simulation and fiber process improvement; Proceeding of International Wire and Cable Symposium, IWCS'95, pp. 343-346; 1995
- ⁴ A. F. Judy; Improved PMD stability in optical fibers and cables; Proceeding of International Wire and Cable Symposium, IWCS'94, pp. 658-664; 1994
- ⁵ L. Grüner-Nielsen, S. Nissen Knudsen, T. Veng, B. Edvold and C. C. Larsen; Design and manufacture of dispersion compensating fibre for simultaneous compensation of dispersion and dispersion slope; Technical Digest of OFC'99, paper WM13, pp. 232-234, 1999.
- ⁶ IEC 60793-1-4 Amendment 1; Optical fibres - Part 1: Generic specification - Section 4: Measuring methods for transmission and optical characteristics; 1996
- ⁷ Bellcore GR-20-CORE; Generic Requirements for Optical Fiber and Fiber Optic Cable; issue 1; 1994

BIOGRAPHY



Lars Grüner-Nielsen got his master degree and Ph.D. from the Technical University of Denmark in 1983 and 1998, respectively. From 1983 to 1994, he worked at the Danish cable company NKT's R&D department for optical cables. Since 1994, he has worked at the R&D department for specialty fibres at Lucent Technologies Denmark. His current activities are focused on development, production and application of dispersion compensating fibres.

INTERMITTENT WATERBLOCKING FOR SUBMARINE CABLE APPLICATIONS

Ted A. Bookwalter, Richard K. Jones, Joseph B. Wojno

Alcatel Submarine Networks Inc., Portland Oregon

Abstract

Intermittent axial waterblocking within the steel strength-member strand of submarine cables dramatically reduces the water penetration into the cable. Intermittent water blocking may also be applied to terrestrial cables.

Waterblocking is generally required within submarine cable to limit the distance water will ingress into the cable in the event of external damage to the cable. The water blocking also limits the length of the cable that must be replaced during a marine repair, reducing costly repair time.

This paper presents the theoretical performance of an intermittently water blocked cable with respect to axial water penetration.

INTRODUCTION

Intermittently blocked cable has the advantage of using less raw material and also utilizes the material much more effectively in arresting the penetration of water. This is due to the unblocked portions acting as reservoirs, which take time to fill, thus providing a 'capacitance' effect. This increases the time to penetrate a given length of cable in comparison with a fully water blocked cable.

THEORETICAL DETERMINATION OF WATER PENETRATION

The following analysis considers the magnitude of the water ingress into unblocked, 'fully' blocked, and intermittently blocked cables.

The flow of water along the strand wire interstices is assumed to be governed by the Poiseuille Law:

$$Q = \frac{\pi \Delta P a^4}{8 \eta L} \quad 1)$$

where:

Q = transmission rate m^3s^{-1}

ΔP = pressure drop along cable (Pa)

a = radius of capillary (m)

η = viscosity of water (Nm^{-2}s)

L = length of cable (m)

The penetration of the water 'front' along a single capillary path in the cable as a function of time can be derived from equation 1), assuming that the back pressure developed by compressing the air within the cable is a second order effect.

$$L(t) = \frac{a}{2} \sqrt{\frac{\Delta P t}{\eta}} \quad 2)$$

where:

$L(t)$ = Distance penetrated in time t

t = time (secs)

$\Delta P = P_o - P_i$

P_o = Hydrostatic pressure

P_i = Initial pressure within cable

In general $P_o \gg P_i$, thus equation 2 reduces to:

$$L(t) = \frac{a}{2} \sqrt{\frac{P_o t}{\eta}} \quad 3)$$

It is evident that the penetration distance of water into the cable, for a given time and applied pressure, is dependent on the magnitude of the equivalent radius of each single leak path within the cable.

Theoretical Assessment of an Unblocked Cable

With an unblocked cable it is possible to determine the radius of a capillary which has the same flow characteristics as a single strand wire interstice. This equivalent capillary radius is derived from:

$$a_s = \frac{2 \times \text{cross sectional area}}{\text{wetted perimeter}} \quad 4)$$

For a submarine cable containing a uni-lay wire nest around a center optical module, the average equivalent hydraulic radius for a single interstice was found to be:

$$a_s = 7.7 \times 10^{-5} \text{ m.}$$

From this value of a_s , the water penetration into the unblocked cable with time has been calculated using equation 3. The result is shown in Fig 1, where it is observed that over a 14 day period with an applied hydrostatic pressure of 80 MPa, water penetrates ~ 12 km along the cable.

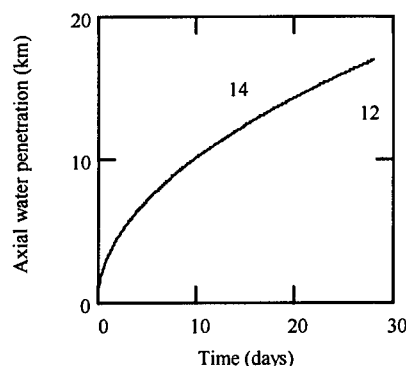


Figure 1. No strand water blocking compound
Hydraulic radius = 7.7×10^{-5} m
Hydrostatic pressure = 80 MPa

Axial Water Penetration into Blocked Cable

To limit the axial water penetration into the cable, water blocking compound is included within the cable to fill the strand wire interstices. The traditional method is to apply a strand vault blocking material all along the length of the cable. In practice this method does not prevent water penetration completely, but limits the distance to a manageable level. A typical requirement for a commercial submarine optical cable, is that water will not penetrate further than

1 km over a 14 day period, with an applied hydrostatic pressure of 80 MPa (~ 8 km depth). The maximum hydraulic radius that meets this penetration requirement may be calculated using equation 3, and is found to be 6.4×10^{-6} m. The axial water penetration as a function of time for this capillary radius is shown in Figure 2.

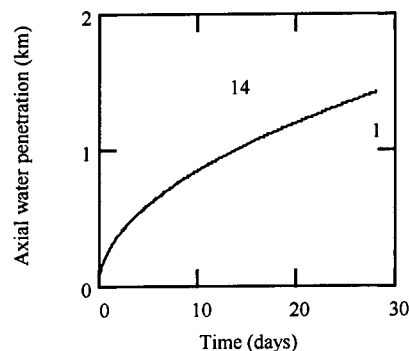


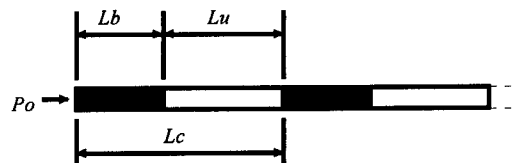
Figure 2. Water blocked cable
Hydraulic radius = 6.4×10^{-6} m
Hydrostatic pressure = 80 MPa

Intermittently Blocked Cable

An intermittently blocked utilizes the water blocking material much more effectively in arresting the penetration of water. This is due to the unblocked portions acting as reservoirs that take time to fill, thus providing a 'capacitance' effect. This increases the time to penetrate a given length of cable in comparison with a 'fully' water blocked cable.

A simple model may be generated to predict this effect as follows.

Consider the intermittently blocked cable as seen schematically below:



The axial leak path within the blocked portions (L_b) will be considered as 'prefilled' with water. Thus when water pressure is applied to a blocked section, the equilibrium transmission rate through the blocked region is immediately attained. This assumes that the time lag to penetrate a blocked portion of cable is zero, giving the worst case scenario. As before, the back pressure developed by the water penetration compressing the air within the cable will be assumed

to be a second order effect. The rate that the unblocked section fills with water is dependent upon the leak rate into the unblocked length from the adjacent blocked region.

Therefore the time for water to fill an unblocked section is given by:

$$T = \frac{L_u V_u}{Q_b} \quad 5)$$

where:

L_u = length of the unblocked cable section

V_u = volume/unit length of unblocked section

Q_b = leak rate through adjacent blocked section

Once the first unblocked section fills, then the next unblocked area commences filling, but now with two blocked sections in series. Therefore the time for water to fill the n th unblocked region is given by:

$$T_n = \frac{L_u V_u}{Q_b} \frac{n(n+1)}{2} \quad 6)$$

where n is the number of blocked/unblocked cells.

Substituting equation 1) yields:

$$T_n = \frac{4\eta L_u L_b V_u}{\pi a_b^4 P} n(n+1) \quad 7)$$

It is observed that the time taken to penetrate the cable is dependent on the relative lengths of the unblocked and blocked sections.

Defining the length of a 'cell' as:

$$L_c = L_b + L_u$$

and substituting in equation 7:

$$T_n = \frac{4\eta(L_c - L_b)L_b V_u}{\pi a_b^4 P} n(n+1) \quad 8)$$

The value of n is related to the penetration distance (L_p) by:

$$n = \frac{L_p}{L_b + L_u}$$

Substitution in equation 8) and rearranging gives:

$$L_p = -\frac{(L_b + L_u)}{2} \left[1 - \sqrt{1 + \frac{T_n \pi P a_b^4}{L_u L_b \eta V_u}} \right] \quad 9)$$

The optimum block/unblocked ratio is given when:

$$\frac{dT_n}{dL_b} = 0$$

Thus differentiating equation 8, this is achieved when:

$$L_b = \frac{L_c}{2} \text{ or } L_b = L_u$$

Therefore to obtain the maximum water blocking efficiency, a fill factor close to 50% should be implemented.

The water penetration into an intermittently blocked cable is shown in Fig 4 using equation 9. In this case the blocked and unblocked lengths are 50 m, and the radius of the equivalent leak path through each blocked section is 6.4×10^{-6} m.

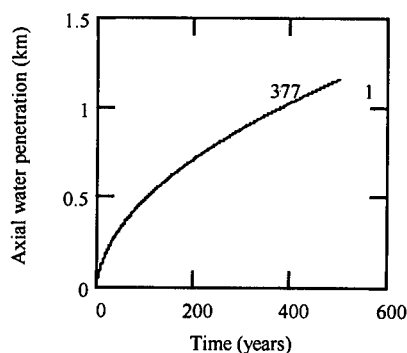


Figure 3. Performance of Intermittently Blocked Cable

From Figure 3 it is observed that water penetrates 1 km along the cable after ~ 350 years. In comparison, water will penetrate 1 km of fully blocked cable in only 14 days. Thus the water blocking performance is increased by a factor of ~ 9000 by the use of an intermittent block with a 50% fill ratio.

As before it is possible to calculate the maximum equivalent pore radius of the water blocked sections within an intermittently blocked cable to meet the design requirement.

BIOGRAPHIES

Thus rearranging equation 9):

$$a_b \leq \sqrt[4]{\frac{4\eta L_u L_b V_u L_p}{\pi T_n P(L_u + L_b)}} \left[1 + \frac{L_p}{L_u + L_b} \right] \quad 10)$$

For the intermittently water submarine optical cable previously considered, the radius of the leak path in the blocked regions must be $\leq 6.5 \times 10^{-5}$ m.

For the fully blocked cable it was shown that the radius of the equivalent leak path along the cable must be $\leq 6.4 \times 10^{-6}$ m to prevent water ingress beyond 1 km after 14 days at 80 MPa. Thus it is apparent that with an intermittently blocked cable, a larger leak path through the blocked regions can be tolerated, in comparison with a fully blocked cable, to meet the same water blocking requirement.

CONCLUSION

This paper has considered the performance of an intermittently water blocked cable with respect to axial water penetration resistance. It has been demonstrated that:

- The water penetration performance of the intermittently blocked cable will be significantly greater than with a fully water blocked cable.
- The intermittently blocked cable is much more tolerant of variability in the leak performance of the blocked regions.
- The optimum axial water penetration resistance is achieved when the lengths of the blocked and unblocked regions are equal.

Richard K. Jones
Alcatel Submarine Networks Inc.
Portland, OR 97203

Richard Jones received his Bachelors of Science degree with Honours in Physics from Nottingham University, Nottingham, England, in 1978. He joined STL laboratories in Harlow England in 1978 and transferred to Alcatel Submarine Networks in 1993, where he has held the position of Product Development Manager since 1996.

Joseph B. Wojno
Alcatel Submarine Networks Inc.
Portland, OR 97203

Joseph Wojno received a degree in Electronics Technology from Texas A&M University in 1986. He held several engineering positions in the development and manufacture of submarine cable manufacture, before joining Alcatel in 1989. He is currently working as a Manufacturing Engineer in Alcatel Submarine Networks.

Ted A. Bookwalter
Alcatel Submarine Networks Inc.
Portland, OR 97203

Ted A. Bookwalter received a Bachelors degree in Electronics Engineering from the Ohio Institute of Technology in 1979. He has held several positions in optical cable design, process development, and quality. He joined Alcatel Submarine Networks in 1993, and has held the position of Manufacturing Engineering Manager since 1996.

NOVEL COMPACT LOOSE TUBE CABLE INCORPORATING EVOLVED DRY WATERBLOCKING METHOD

Anne G. Bringuier, Siecor, Hickory, North Carolina
and
James R. Priest, Owens Corning, Granville, Ohio

Abstract

Cable constructions with dry core designs have been introduced to provide field personnel with craft-friendly and cost effective methods of accessing the cable core for reentries and mid-span access. The novelty of the cable introduced in this paper lies in its function for indoor and outdoor use and its compactness, i.e. decreased cable weight and diameter. The cable still retains its ease of connectorization through the use of standard loose tube fan-out kits for rapid, simple termination. The paper introduces a new method to waterblock a loose tube design using swellable impregnated fiberglass yarns.

Introduction

With local area networks penetrating further into the campus environment to connect buildings within short spans, cables suitable for use both indoors and outdoors are becoming increasingly popular. The installation contractors can use the same cable to go from one building to another, eliminating the need for transition splices at the entrance of the buildings and therefore saving time and money. Historically, indoor and outdoor cables have been very different in

construction, with tight buffer fiber cables used indoors and grease-filled tube cables used outdoors. The challenge was to design a cable to meet the demanding specifications for both UL requirements and outside plant use. Loose tube cables have been proven for the last 15 years as true exterior-rated products. This design was modified into a novel loose-tube cable that is able to meet the riser specifications for indoor use. One of the modifications involved the replacing the flooding compound located outside the buffer tubes with waterblocking fiberglass yarns. These yarns provide for a compact cable design with fewer components to remove during field installation and mid-span access, while still providing the necessary waterblocking.

Cable Design

The cable consists of two buffer tubes stranded with a dielectric strength member, a non-tensile swell yarn, a layer of water-swellable fiberglass yarns helically stranded around the core and a UV-resistant flame retardant jacket. The cable can accommodate 2 to 24 fibers. Figure 1 shows the cross-section of the 24 fiber cable. Figure 2 shows an isometric view of this cable.

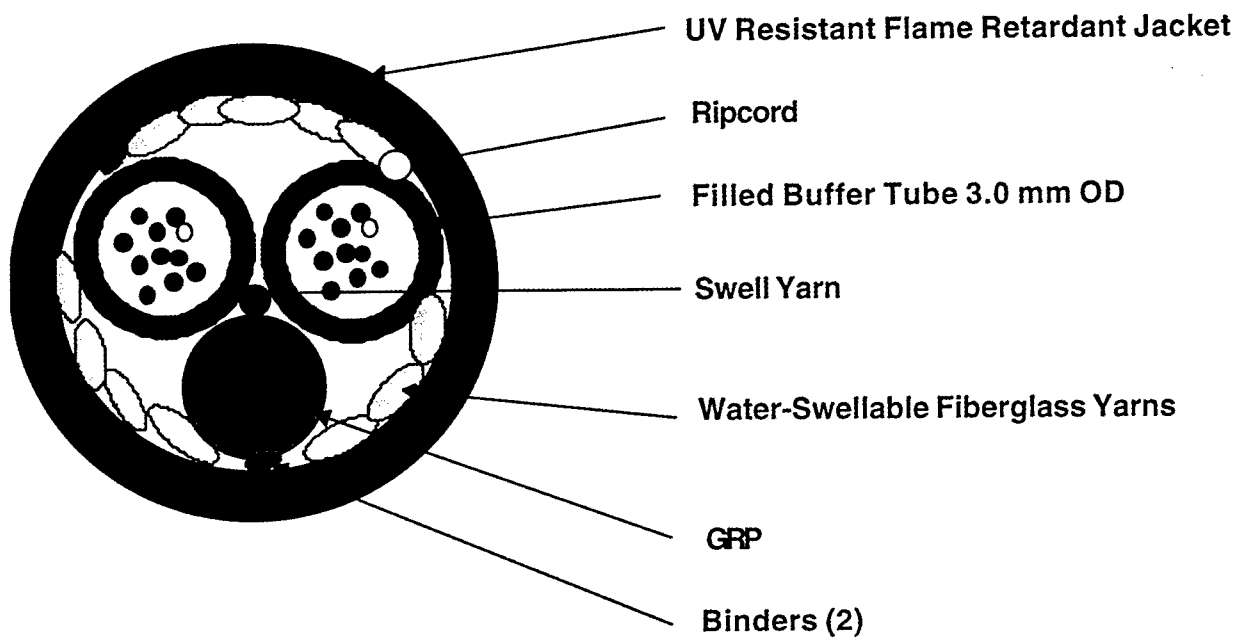


Figure 1: Cable Cross-Section

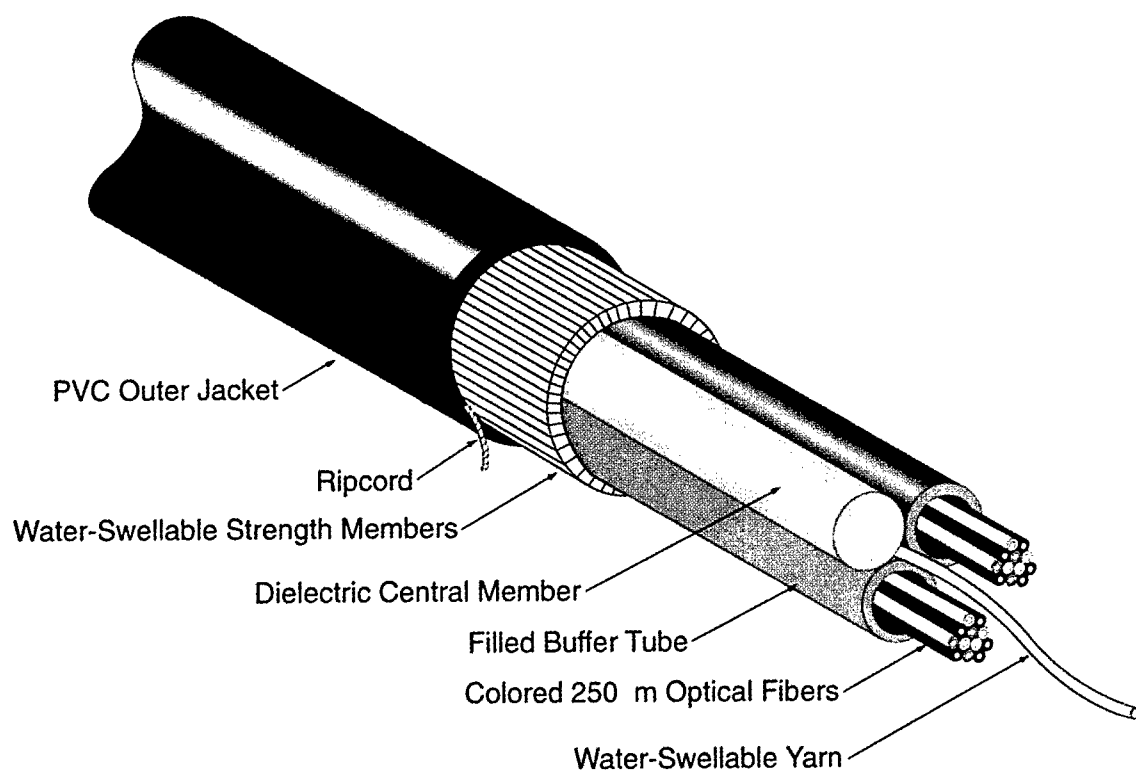


Figure 2: Isometric View

The UV and flame retardant jacket allows this cable to meet the UL riser (UL-1666) requirements, making this cable suitable for both indoor and outdoor applications. The cable uses a polyolefin tube chosen for its superior hydrolytic stability in hot humid environments and great flexibility in limited space applications. The 3.0 mm diameter buffer tube is compatible with standard loose tube fan-out kits for rapid, simple termination. The cable introduces a new waterblocking method for a loose tube construction, using a layer of highly flexible fiberglass strength members wrapped around the core. These yarns perform a dual role, acting as a tensile strength provider as well as a waterblocking barrier. An alternative jacket material of medium density polyethylene may be used for this cable where only outside plant requirements are needed.

Cable Performance

Indoor/outdoor cables were manufactured with fiber counts ranging from 12 to 24, and fiber

types ranging from dispersion-unshifted single mode fibers to 50/125 μm and 62.5/125 μm multimode fibers. The cables were tested to different environmental, optical and mechanical requirements.

Environmental

The cable was subjected to a temperature cycling and aging test consisting of four cycles between -40°C and $+70^{\circ}\text{C}$ with an 85°C heat soak for seven days after the first two cycles. Before heat soak, both 12-fiber and 24-fiber count designs exhibited maximum average attenuation differences of less than 0.05 dB/km for single-mode fibers and less than 0.60 dB/km for multimode fibers. The cables met major industry performance requirements for environmental testing including ICEA S-83-596, ICEA-640 and Bellcore GR-20 (Table 1). Attenuation results include a 0.05 dB/km allowance for measurement repeatability.

Test	Results	Method
Temperature Cycling <i>-40°C to $+70^{\circ}\text{C}$</i>	Maximum Change* (SM / MM in dB/km) <0.3/0.5	FOTP-3A
Cable Aging <i>85°C 168 hrs</i>	Maximum Change* (SM / MM in dB/km) <0.6/1.2	FOTP-3
Water Penetration <i>24 hours unaged 1 hour aged 168 hr @ 85°C</i>	No water leakage	FOTP-82
Jacket Shrinkage <i>110°C, 2hrs</i>	< 5%	FOTP-86
Filling Compound Flow @ 85°C	No compound Flow	FOTP-81
Material Compatibility	Buffer tube elongation >10% 45 days in 85°C water	ASTM D1205

* Note: SM attenuation measurements at 1550 nm

Table 1: Environmental test results

Fiber Strain Measurements

While the cables were temperature-cycled, absolute fiber strain measurements were taken using the BOTDR (Brillouin Optical Time Domain Reflectometer) method, providing further characterization of fiber behavior during cable contraction. The BOTDR measures Brillouin scattering to quantify the distribution of strain along an optical fiber. A spatial resolution of 5 meters along the optical fiber length was applied. The advantage of this apparatus is that it measures absolute values of strain rather than

relative values. The graph in Figure 2 represents the absolute strain measured along a fiber while a cable is in its fourth cycle going through -40°C and 70°C . Other strain measurements taken throughout the four cycles varied between -0.03 to 0.01% . These values confirm the superiority of a loose tube type design where the fiber remains in a stress-free state while the cable contracts and expands through extreme temperatures. Also during cable installation at 2700 N loadings, since the fibers are allowed to move within the buffer tube, the fibers will see considerably less fiber strain.

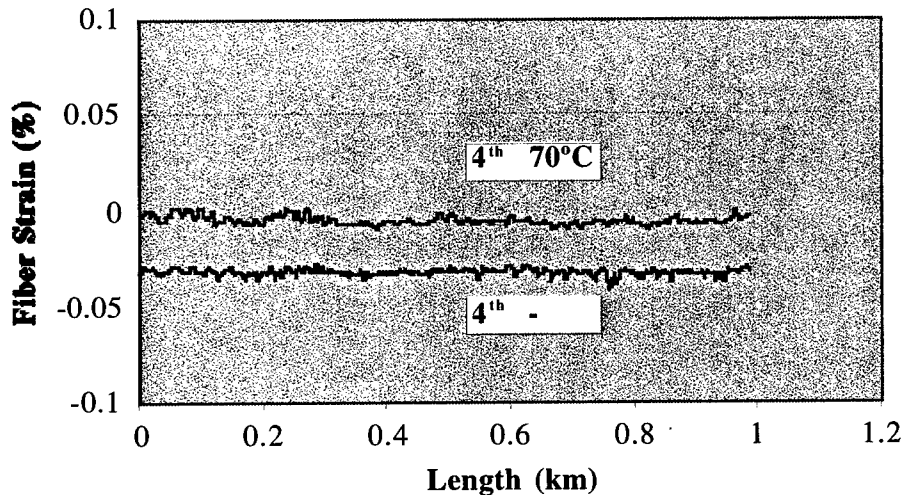


Figure 3: BOTDR Fiber Strain Measurements during Temperature Cycling

Mechanical

Both 12-fiber and 24-fiber cables were tested in compliance with the mechanical requirements of ICEA-S83-596 and RUS 7 CFR 1755.900. The results are shown in Table 2. Attenuation values were measured at 850 and 1310 nm for multimode fibers and 1550 nm for single mode fiber.

Test	Results	Method
High/Low Temperature Bend 10X cable OD (60°C, -30°C, 4 turns)	Maximum Change* (SM / MM in dB) <0.10/0.40	FOTP-37
Impact 25 cycles	Maximum Change* (SM / MM in dB) <0.10/0.40	FOTP-25
Compression 220 N/cm 10 minutes	Maximum Change after Load Removal* (SM / MM in dB) <0.10/0.40	FOTP-41
Tensile Strength 2700 N 1 hour	Maximum Change* (SM / MM in dB) <0.20/0.50 during loading <0.10/0.20 after removal	FOTP-33
Cable Twist 10 cycles	Maximum Change* (SM / MM in dB) <0.10/0.40	FOTP-91
Cyclic Flex 25 cycles 20X cable OD	Maximum Change* (SM / MM in dB) <0.10/0.40	FOTP-104

Note: SM attenuation measurements at 1550 nm

Table 2: Mechanical Test Results

Again all major performance levels were met.

Tensile Yarn Performance

In 1996, Owens Corning introduced AquaBlok[®] roving, a dual functional reinforcement that carried a superabsorbent powder along with its protective coating. One of the first swellable reinforcement products, AquaBlok was well received in various cable designs. Listening to customer feedback, the next generation of this product sought to improve on several areas including cleanliness, pliability and performance in ionic waters. The result of this development is called Instant Dry[®]. Instant Dry technology is a unique, patent-pending chemistry and application method that provides superior reinforcement. Reinforcements coated with Instant Dry technology have a uniform coating of superabsorbent polymer applied to each and

every fiber. The resultant strand is soft and pliable for better conformation in the cable and provides more uniform protection from water migration.

Physical Properties

The cable described in Figure 1 uses a 785 tex reinforcement. In order for the dual functional reinforcement to be acceptable, it must be equivalent or superior in physical strength to its non-waterblocking counterpart. Therefore, the new swellable fiberglass yarn was compared to a standard 785 tex roving for cable reinforcement. As seen in the force at specified elongation on Figure 3, there was no decline in physical properties.

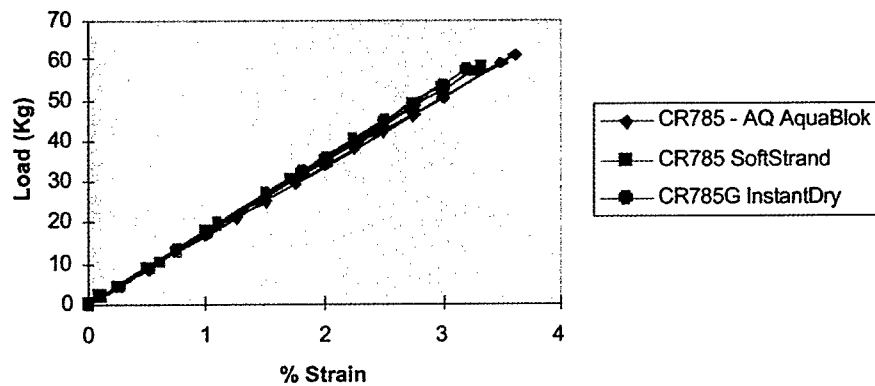


Figure 4: Force at Specified Elongation

In Table 3, the physical properties of a typical sample of CR785G Instant Dry are summarized. These are the average values of testing results.

Linear Density	785 tex
Tensile Strength	560N
Load at 0.5% Elongation	108N
Load at 1% Elongation	211N
Modulus of elasticity	3.20%
Loss on Ignition	6.00%
Strand Width (Dry, Under 1 lb load)	2.18 mm
Strand Thickness (Dry, Under 1 lb load)	.069 mm
1 minute absorbance in Deionized Water	800%

Table 3: Fiberglass Yarn Properties

Waterblocking Performance

Reinforcements coated with Instant Dry technology show vast improvements over previous and competitive products in the area of waterblocking. The new CR785G reinforcement displays the following benefits:

1. In standard water absorbency testing with deionized water, the Instant Dry coated strand absorbs water four times faster at the moment of contact.
2. After the first minute of contact the new material is two times faster in absorption than its predecessor.
3. Ultimately, products with Instant Dry coatings will exceed the absorbance of AquaBlok® products by two hundred percent. Figure 4 demonstrates the performance of CR785G with Instant Dry technology in water absorption over time.

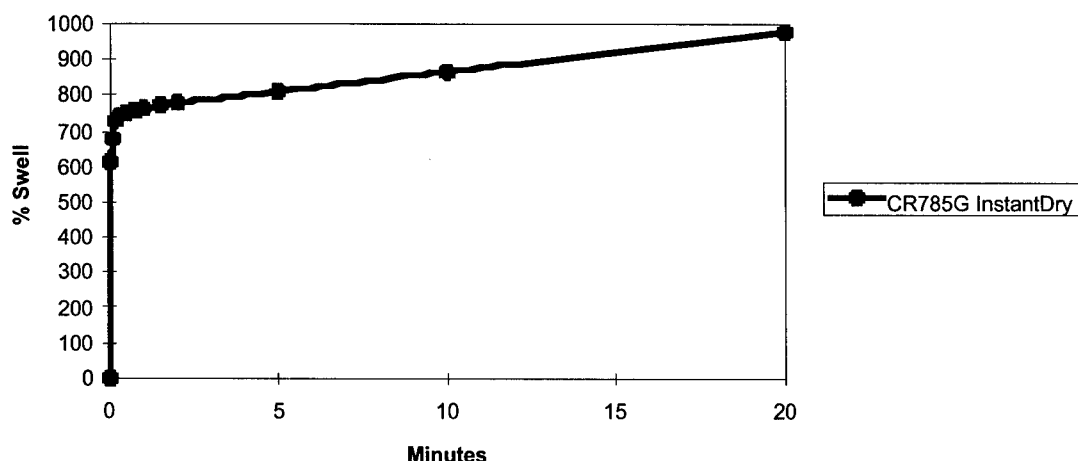


Figure 5: Water Absorption over Time

Due to the decreased ion sensitivity of the polymer coating over traditional superabsorbents, Instant Dry products have demonstrated good performance in highly ionic environments such as brackish and marine waters. A 1% saline solution was used to mimic a brackish environment. The CR 785G used in this cable

continued to demonstrate the instant absorption characteristics seen in fresh water environments. Once again, over a two hundred percent increase compared to the previous generation product was realized. The results of water absorbence versus time testing for exposure to a 1% saline solution can be seen in Figure 5.

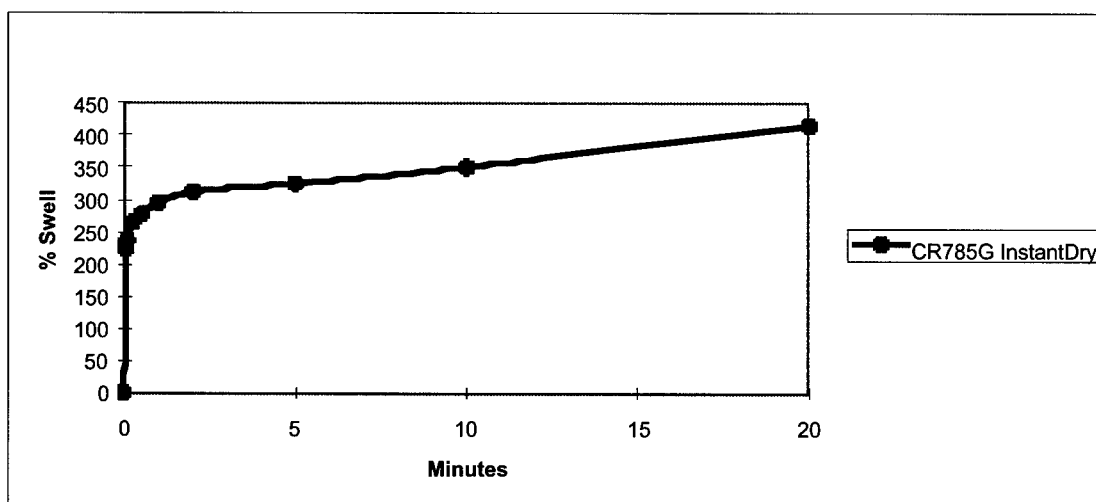


Figure 6: Water Absorption in 1% Saline

In sea water, the performance of Instant Dry coated products remains acceptable. Swell rates are instantaneous on contact and ultimately reach a final absorbence of approximately two hundred

fifty percent. Figure 6 demonstrates typical absorbence values versus time for exposure to synthetic sea water.

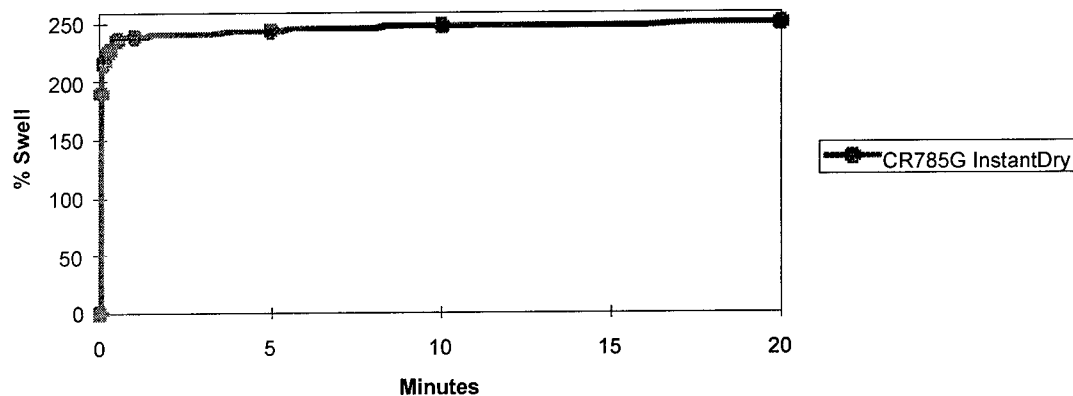


Figure 7: Water Absorption in Synthetic Sea Water

Finally, the ability of this new fiberglass to conform around the cable leads to a more uniform level of protection from water penetration and to a smaller cable outside diameter. The soft pliable strand serves easily and does not require extensive cleaning due to dusting or accumulation of fiber deposits. The combined advantages of the new fiberglass yarn are truly an evolved method for the prevention of water penetration as well as an advance in the promotion of the dry cable concept.

Conclusions

In summary, a robust loose tube indoor/outdoor cable was developed, containing up to 24 fibers in a compact dry core design. It employs a new swellable fiberglass with improved waterblocking performance and greater processing ease compared to previous versions. The design facilitates connectorization and mid-span access with no removal of water-swellable tape during cable splicing. The cable met all relevant industry requirements.

Authors

Anne Bringuier

Siecor

Research, Development & Engineering

PO Box 489

Hickory, NC 28603

Anne G. Bringuier received a B.S. degree in Materials Engineering from the Institut National des Sciences Appliquees (INSA) in Lyon, France, an "Advanced Studies Diploma (DEA)" in Macromolecular Science from the University of Lyon in 1985 and a M.S. in Polymer Science and Engineering from Pennsylvania State University in 1987. She worked at Raychem Corporation from 1987 to

1993 developing telecommunication closures. In 1993, she joined Siecor where she has been involved with materials selection and design activities for optical fiber cables. She has developed cable designs for both indoor and outdoor applications. Anne is currently a Staff Product Development Engineer in the Research, Development and Engineering Department



James Priest

Owens Corning

Science and Technology Center

2790 Columbus Road

Granville, OH 43023

James R. Priest is an Associate Scientist with Owens Corning at their Science and Technology Center in Granville, Ohio. He has been with Owens Corning since 1995. He is currently focused on the development of products and systems for telecommunications. Prior to this assignment his works primarily involved the development of polyester resin systems for

Owens Corning's AOC joint venture. He also has developed sheet molding compounds for use in automotive and low temperature/ low pressure applications. He received his B.S. degree in chemistry and biology from Ashland University in 1992.

Selecting proper superabsorbent tape for slotted core optical cables capable of blocking manhole water

Chieh-Mei Hsiao, Huei-Jen Chen, Jau-Ching Lii, Ting-Chung Chang,

His-Pai Hsu, Y.-c Lin, Yuan-Kuang Tu

OSP, Telecommunication Laboratories, Chunghwa Telecom, Taiwan, R.O.C.

ABSTRACT

Water-blocking tape was adopted in slotted core optical fiber cable to prevent water penetration. its main component is superabsorbent polymer (SAP). In particular, the water absorbing character of SAP depends on the ionic species and ion concentrations of the water absorbed. We analyzed the water absorbing properties of water-blocking tapes in different solutions such as 40 different area manhole waters, 3 different coastal ocean waters, substitute ocean water solution, and diluted substitute ocean water solutions. It was found that all test tapes were affected by ionic water and dwindled their water-blocking properties, but the swelling characteristic of these tapes correlated well with the salinity ratio of the test solutions. In other word, by matching the salinity of diluted substitute ocean water to that of the manhole water, the actual performance of the water-blocking tape in outside plant could be simulated by immerse it to that diluted substitute ocean water

1. INTRODUCTION

A slotted core optical fiber cable uses water-blocking tape to prevent water from penetrating it. It is free of the sticky water blocking grease compounds and is welcomed by field craftsmen. Several factors determine the effectiveness of a water-blocking tape : 1. The character of its main component⁽¹⁾⁽²⁾, superabsorbent polymer (SAP), such as water absorbing rate, water absorbing capacity, and gel property; 2. The structure of the cable, such as the cable internal cavities and the tape packing pattern; 3. The environment in which the optical fiber cable being deployed; and 4. The long term stability

of SAP. In particular, the water absorbing character of SAP depends on the ionic species and ion concentrations of the water absorbed. Therefore, the water prevention effect of an optical fiber cable will be different in waters containing different ionic species and ion concentrations.

We examined the water absorbing properties of water- blocking tapes with manhole water and diluted substitute ocean water solutions, and this help to understand the relationship between the solutions that affect the water absorbing properties of water blocking tapes. In the end, we are able to establish laboratory screening methods that could more accurately gauge the water blocking performance of SAP and slotted core optical fiber cables in outside plant environment.

2. EXPERIMENTAL

2.1 Test solutions

Test solutions included pure water, manhole water samples, ocean water samples, substitute ocean water and diluted substitute ocean water solutions. In Taiwan, 40 different area manhole waters and 3 different coastal ocean waters were randomly selected to examine the water-blocking tapes. Ionic components in each water were determined by DIONEX DX-100 Ion Chromatography, according to the US EPA300.6⁽³⁾ and 300.7⁽⁴⁾ methods. Six ionic species (Na^+ 、 Ca^{+2} 、 Mg^{+2} 、 Cl^- 、 K^+ 、 SO_4^{+2}) that are abundant in ocean water (>99%) were analyzed in this paper. Substitute ocean water was prepared according to ASTM D1141-90⁽⁵⁾. Substitute ocean water was then diluted to ratio 1000:1, 500:1, 100:1, 50:1, 10:1 as diluted substitute ocean water solutions.

The salinity is defined as the mass in grams of all ionic species present in 1 kg of ocean water. In this paper, the salinity of test solutions were calculated according to the concentrations of the six ionic species such as sodium, calcium, magnesium, chloride, potassium, and sulfate ions.

2.2 Water-blocking tapes

Water-blocking tapes from three suppliers were used. All had a sandwich structure with SAP in the middle and non-woven fabrics on the top and the bottom. Tape A and B had a loosely woven top layer and a densely woven bottom layer, while tape C had both layers loosely woven. Each contained different formulations of SAP.

2.3 Measuring method

The swelling height varied with time of each tape in each test solution was measured using cup and plunger method⁽⁶⁾.

One meter of the cables made with the aforementioned water-blocking tape were subjected to a 'T' test with 1 m water head. The test solutions included pure water, 10:1 diluted substitute ocean water, and substitute ocean water.

3. RESULTS AND DISCUSSION

3.1 Ionic concentration and salinity of manhole water and ocean water

Table 1 showed the similarity of the salinity from three ocean waters and substitute ocean water. The concentrations and salinity of major ionic components from different samples were almost the same. Table 2 presented the manhole water salinity ratio compared with substitute ocean water. Fig 1 showed the distribution of manhole water salinity ratio. The results showed that 59% manhole water quality were about the same as the ground water in most regions, having an ion concentrations approximately one two-hundredth of that of substitute ocean water or less. Higher ion concentrations were found in certain coastal regions, being around one hundredth of that of ocean water. The urban manhole waters were

thought to contain lower salinity. However it had not always the case. NA-2 and MA-6 had the salinity ratio 1/87 and 1/56 that were higher than those of usual coastal manhole water. On the other hand, NB-2 and MB-3 of coastal manhole contained the water salinity ratio only 1/617 and 1/586 that were much lower than those of common urban manhole. The highest salinity manhole MB-5 was found about 1/9 ratio of substitute ocean water. In fig 1, 16% manhole contained high water salinity ratio of substitute ocean water, being higher than 1/50, and these waters could had more serious effect to the water absorbed properties of water-blocking tapes.

3.2 Water absorbing properties of water-blocking tape

3.2.1 Pure water

The pure water absorbing rate and swelling height of water-blocking tapes A, B and C were measured and shown in fig 2.

Tape C had a fastest absorbing rate, being saturated with water in 3 min. Tape B was slower and saturated in 5 min. and Tape A slowest in 15 min. The maximum swelling height, an indication of the maximum volume of water absorbed, was about the same for all three tapes. In addition, fig 2 also showed that the height of the swelled Tape B gradually decreased with time, while swelled Tape A, and C maintained their height. It indicated that Tape B had a lower gel strength to hold absorbed water than that of Tape A, and C.

3.2.2 Substitute ocean water

The substitute ocean water absorbing rate and swelling height of water-blocking tapes A, B and C were measured and shown in fig 3.

During substitute ocean water test, the maximum swelling height reduced drastically. Tape A swelled to 14.6% of the height in pure water test, Tape B to 14%, and Tape C only 4.3%. Tape C had the worst ability to hold water that contained high ionic components. The time to reach maximum swelling height was 7 min for Tape A and B, 2 min for tape C.

3.2.3 diluted substitute ocean water

The diluted substitute ocean water absorbing rate and swelling height of water-blocking tapes A, B and C were measured and shown in fig 4, 5 and 6.

All test tapes were affected by ionic water and dwindled their water-blocking properties, and tape C showed the worst ability to hold water after the test. The maximum swelling height of these tapes reduced in diluted substitute ocean water, as its ion concentrations were increased. When dilution ratio is 10:1, Tape A only swelled to 29.1% of the height in pure water test, Tape B to 30.8% and Tape C 16.5%. When dilution ratio reached 1000:1, Tape A then swelled back to 89.2% of the height in pure water test, Tape B to 95.1% and Tape C 82.7%.

3.2.4 Manhole water

Repeated the same test with manhole water samples yielded similar results. Fig 7, 8 and 9 presented the test results from the different salinity ratio of 1/10 ~ 1/50, 1/50 ~ 1/100, and 1/100 ~ 1/500, respectively. When results from diluted substitute ocean water and manhole water samples were compared, it was found that the swelling characteristic of these tapes correlated well with the salinity of the test solutions. In other word, by matching the salinity of diluted substitute ocean water to that of the manhole water, the actual performance of the water-blocking tape in outside plant could be simulated by immerse it to that diluted substitute ocean water.

3.3 Water blocking properties of slotted core optical fiber

One meter of the cables made with the aforementioned water-blocking tape was subjected to a 'T' test with 1 m water head. The test solutions included pure water, 10:1 diluted substitute ocean water, and substitute ocean water. All three cables with tape A, B and C did not leak in 96 hr during pure water test. Cable with Tape C leaked in 24 hr when tested with 10:1 diluted substitute ocean water. Cable with Tape B started to leak in 24 hr when tested with substitute ocean water. Only cable with Tape A survived all three test conditions in 96 hr.

4. SUMMARY

The swelling height of water-blocking tape decreased drastically in solutions containing high ionic concentrations. The maximum swelling height of Tape C in substitute ocean water can only swell to 4.3% of the height in pure water. Manhole water samples from various regions of Taiwan were collected and analyzed. The results showed that 16% manhole contained high water salinity ratio of substitute ocean water, being higher than 1/50, and these waters could had more serious effect to the water absorbed properties of water-blocking tapes. It is proper to use the diluted substitute ocean water to gauge the actual water blocking effectiveness of deployed slotted core optic cable as long as its salinity is matched to that of manhole water. For long term, a slotted core optical fiber cable will benefit from using water-blocking tapes that can keep high swelling height and gel strength in high ionic strength solution.

5. REFERENCES

1. Douglas A. Skoog, Donald M. West, *Proc. 38th IWCS*, 463, 1989.
2. Clinton E. Clyburn III, Anne G. Bringuier, *Proc. 44th IWCS*, 29, 1995.
3. EPA Method 300.6, March 1987.
4. EPA Method 300.7, March 1987.
5. ASTM D1141-90, "Standard specification for substitute ocean water".
6. Naren I. Patel, *Proc. 47th IWCS*, 136, 1998.

SPEAKER BIOGRAPHY



Chieh-Mei Hsiao

OSP, T.L.
Chunghwa Telecom
P.O. Box 6-48, Yang Mei
Taoyuan, Taiwan 326,
R.O.C.

Chieh-Mei Hsiao received her M.S. degree in Chemical Engineering from Tsing Hua University. She joined T.L. in 1981 and presently worked as a research scientist and a member of outside plant laboratory in T.L.

Table 1 Ionic concentration and salinity of ocean water and substitute ocean water

Ionic concentration (ppm)	Ocean water from different areas			substitute ocean water
	A	B	C	
Cl ⁻	21293	19249	20724	19860
SO ₄ ⁺²	2462	2167	2262	2500
Na ⁺	9000	9173	10666	11070
K ⁺	338	310	360	350
Mg ⁺²	1166	1223	1416	1470
Ca ⁺²	572	559	646	450
Salinity (g/kg)	34.83	32.68	36.07	35.70

Table 2 Salinity ratio of manhole water

	Urban region			Coastal region		
No.	NA-1	NA-2	NA-3	NB-1	NB-2	
Salinity Ratio	1/161	1/87	1/218	1/80	1/617	
No.	NA-4	NA-5		NB-3	NB-4	
Salinity Ratio	1/177	1/241		1/99	1/112	
No.	NA-6	NA-7		NB-5	NB-6	
Salinity Ratio	1/180	1/240		1/60	1/79	
No.				MB-1	MB-2	MB-3
Salinity Ratio				1/420	1/87	1/586
No.	MA-1	MA-2		MB-4	MB-5	
Salinity Ratio	1/265	1/230		1/33	1/9	
No.	MA-3	MA-4		MB-6	MB-7	
Salinity Ratio	1/497	1/269		1/224	1/167	
No.	MA-5	MA-6		MB-8	MB-9	
Salinity Ratio	1/115	1/56		1/14	1/16	
No.	SA-1			SB-1	SB-2	SB-3
Salinity Ratio	1/106			1/19	1/34	1/51
No.	SA-2	SA-3		SB-4	SB-5	
Salinity Ratio	1/158	1/354		1/171	1/60	
No.	SA-4	SA-5		SB-6	SB-7	
Salinity Ratio	1/182	1/207		1/62	1/199	

salinity ratio = (salinity of manhole water) / (salinity of substitute ocean water)

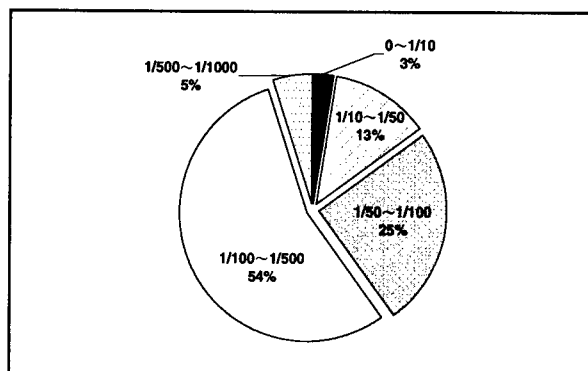


Fig 1 Distribution of manhole water salinity

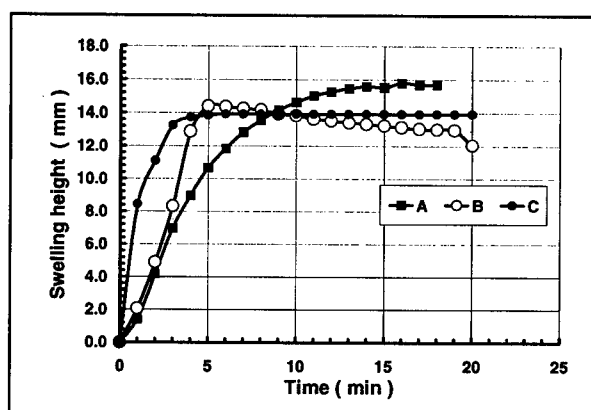


Fig 2 Swelling height of water-blocking tapes in pure water

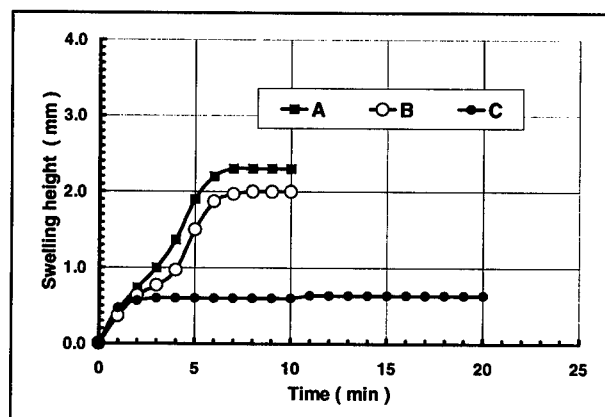


Fig 3 Swelling height of water-blocking tapes in substitute ocean water

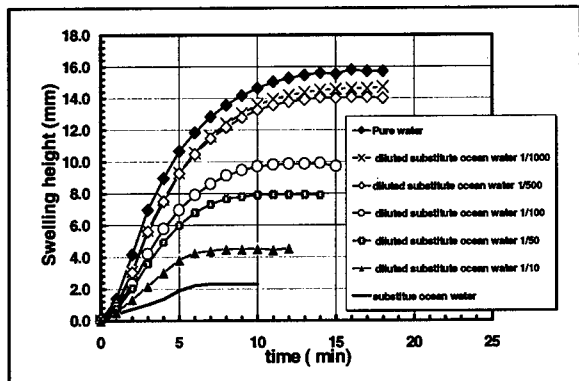


Fig 4 Swelling height of water-blocking tapes A in diluted substitute ocean water

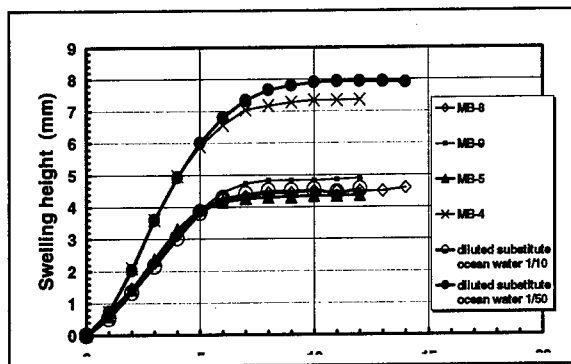


Fig7 Swelling height of water-blocking tapes A in manhole water (salinity ratio 1/10 ~ 1/50)

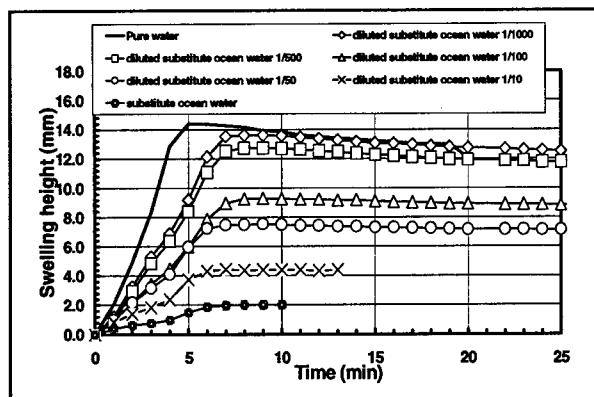


Fig 5 Swelling height of water-blocking tapes B in diluted substitute ocean water

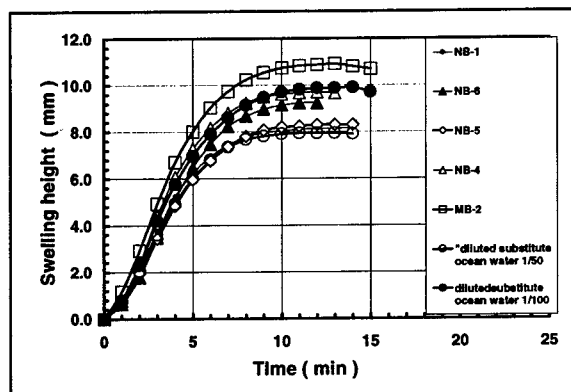


Fig8 Swelling height of water-blocking tapes A in manhole water (salinity ratio 1/50 ~ 1/100)

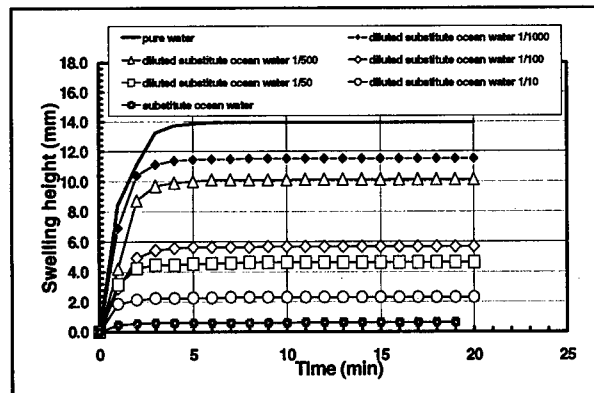


Fig6 Swelling height of water-blocking tapes C in diluted substitute ocean water

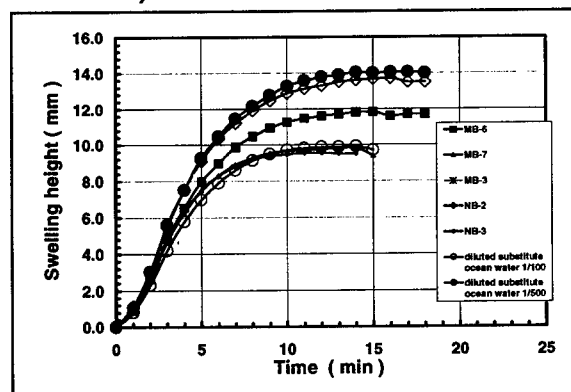


Fig9 Swelling height of water-blocking tapes A in manhole water (salinity ratio 1/100 ~ 1/500)

A POSITIVE DISPERSION SHIFTED SINGLE MODE FIBRE MADE BY PCVD PROCESS

Yanbin Huang, Raadjkoemar Matai, Weichang Yu and Shihui Wang

Yangtze Optical Fibre and Cable Co.Ltd. Wuhan, Hubei, China

ABSTRACT

A Positive Dispersion Shifted Single Mode Fibre (POSH) is designed for super transmission rate, high capacity and long-haul system, while moving the zero dispersion below 1520 nm and with lower positive dispersion in operation window to suppress the nonlinear effects, such as four wave mixing. The fibre made by PCVD process has the best performance simultaneous in optical and geometry properties. 8×2.5 Gb/s and 10 Gb/s transmission experiments have been done in China with this fibre which represented the highest level in China and got good results. In this paper the theory of nonlinear effects is introduced briefly. The dispersion shifted single mode fibre is regarded has four wave mixing effect is described compared with POSH fibre. The system test results of POSH fibre are presented in this paper as well.

INTRODUCTION

Information revolution is adventing worldwide in a very fast pace. Optical telecommunication system galloped to catch up with this revolution. As demands of bandwidth increasing aggressively, new types of fibre, erbium-doped fibre amplifiers and wavelength-division multiplexing technology throughout their networks to take advantage of long transmission distance, super bit-rate, and large carrier capacity system.

In long transmission distance, super bit-rate, and large carrier capacity system, single mode fibre is the first choice to be used. Conventional single mode fibre, matched cladding single mode fibre (MCSM) is working in 1310 nm-operation window. In this window, the fibre has attenuation about 0.34 dB/km, meanwhile, with zero dispersion in 1310 nm wavelength. It is not appropriate for long distance transmission as high attenuation. If the

fibre is transferred to work in 1550 nm window, the attenuation is low (0.19 dB/km), but dispersion is high (18 ps/nm.km). This is an obstacle for transmitting in high bit-rate. Although with the using of dispersion compensation fibre it can also realize the high bit-rate transmission, but it's only economically for the existing line. Traditional dispersion shifted single mode fibre (DSSM) has the lower attenuation (0.21 dB/km) simultaneously zero dispersion wavelength in 1550 nm operation window. This is capable for the fibre to transmit in long distance and high bit-rate. But it is only used in single-channel system, while producing serious nonlinear phenomenon in multi-channel system as zero dispersion on operation window. This does not meet the requirement of the tremendous growth of the bandwidth. A positive dispersion shifted single mode fibre shifts zero dispersion position below 1520nm, while with low positive dispersion in 1550nm-operation window. The fibre, which suppressed four wave mixing, a kind of nonlinear effects, grants the system long distance, high capacity and super bit-rate. It is reported that this kind of fibre is introduced in 8×2.5 Gb/s, 8 or 32×10 Gb/s commercial system. 100 channels WDM 10 Gb/s experiment system is also demonstrated with fibre like POSH, using gain-flattened, ultra-wide bandwidth amplifiers.

DISPERSION SHIFTED SINGLE MODE FIBRE AND NONLINEAR EFFECTS

There is a dispersion shifted single mode (DSSM) fibre/cable line in Xinjiang province China with the distance 168 km without regenerator in between. This is the only line actually in use in China with dispersion shifted single mode fibre. The line has been put into use from year 1996 and work very well up to now.

PCVD, plasma chemical vapor deposition process has the well-know advantages, such as, very thin

deposited layers, high process control ability which can provide precise refractive index profile and high efficiency of chloride material, etc. The fibre made by PCVD process has good performance, repeatability both in geometry and optical properties. It is optimal for the fibre, which has complexity refractive index profile, such as DSSM fibre, to be made by PCVD process.

With architecture of EDFAs emerging, which has been developed to meet the low attenuation 1550nm operation window optical network design requirements, the attenuation is not a limitation of the long distance transmission. In addition, the main limitation factor is dispersion. The DSSM fibre shifting the zero dispersion wavelength to the 1550 nm window takes advantage of the inherently low attenuation rate that silica-based fibres exhibit at higher wavelengths. The low attenuation allows longer link spans and limits the need for costly signal regeneration. But while introducing high output power erbium-doped fibre amplifiers (EDFAs) and multi-channel wave length division multiplexing (WDM), as zero dispersion on operation window, another obstacle of transmission occurred, which is named nonlinear effects. They are encountered when the intensity of the transmitted signal in the fibre reaches unacceptably high levels, combined with simultaneous transmission of multiple wavelengths. In this new regime of EDFAs and WDM, fibre nonlinear effects are growing in importance. If unchecked, these nonlinear effects will degrade system performance.

Nonlinear effects include self phase modulation (SPM), four wave mixing (FWM), cross phase modulation (CPM), modulation instability (MI), stimulated Raman scattering (SRS) and stimulated Brillouin scattering (SBS), etc. In multi-wavelength combining with EDFAs system, SRS and FWM are the main nonlinear effects.

Because SRS has high threshold (about 500 mW at 1550 nm), fibre functions as a Raman amplifier after the channel signal power reach the threshold in WDM system. In Raman gain bandwidth, the energy of high frequency is transferred to low frequency through stimulated Raman Scattering, amplifying the low frequency channel signal and attenuating the high frequency ones. And the bandwidth of Raman gain is considerably wide; even two channels with channel span 200 nm would be influenced by it. Thus SRS limits the

capacity to optical communication. To prevent the bad results of SRS, by limiting each channel's power, we could restrict the total output power of the multi-channel signal to no more than 500 mW.

The characteristic of FWM is the generating of additional channels that can sap power from and overlap with the original when multiple signals co-propagate through optical fibre. It originates from the nonlinear effects of multi-wavelength system causing by chromatic dispersion of optical fibre material. When the channel span and optical fibre dispersion is small enough, and the phase matching condition is satisfied, FWM would be the main factor of nonlinear effects.

The mathematics approach of FWM in optical fibre:

$$P_{NL} = \epsilon_0 \chi^{(3)} \cdot EEE \quad (1)$$

P_{NL} : faradic polarization vector; E : electric field; ϵ_0 : capacitivity; $\chi^{(3)}$: three factorial medium polarization rate.

Considering the four x-direction polarized light waves transmitting along z-direction with frequency $\omega_1, \omega_2, \omega_3$ and ω_4 , the combined electric field is

$$E = e_x (1/2) \sum_{j=1}^4 E_j \exp[i(k_j z - \omega_j t)] + C.C. \quad (2)$$

From (1) and (2), we get

$$P_{NL} = e_x (1/2) \sum_{j=1}^4 P_j \exp[i(k_j z - \omega_j t)] + C.C. \quad (3)$$

And from (3), we know there are many terms in P ($j=1,2,3,4$) that deal with the product of three electric fields. For example

$$P_4 = (3\epsilon_0 / 4) \chi_{xxxx}^{(3)} \{ [|E_4|^2 + 2(|E_1|^2 + |E_2|^2)] E_4 + 2E_1 E_2 E_3 \exp(i\theta_+) + 2E_1 E_2 E_3^* \exp(i\theta_-) + \dots \} \quad (4)$$

$$\text{Here, } \theta_+ = (k_1 + k_2 + k_3 - k_4)z - (\omega_1 + \omega_2 + \omega_3 - \omega_4)t \quad (5)$$

$$\theta_- = (k_1 + k_2 - k_3 - k_4)z - (\omega_1 + \omega_2 - \omega_3 - \omega_4)t \quad (6)$$

The terms in (4) that are directly proportion to E , cause SPM and CPM effects, others cause FWM. The parameter coupling efficiency depends on the relative phase between E_4 and P_4 , which is presented by θ_+ and θ_- . When the phase matches the channel wavelength and the relative phase is about zero, obvious FWM will appear.

Table 1: The typical characteristics of POSH fiber

Characteristics	POSH fiber	Characteristics	POSH fiber
Attenuation@1310 nm	0.381 dB/km	Disp.@1530 nm	2.8 ps/nm.km
Attenuation@1550nm	0.214 dB/km	Disp.@1565 nm	5.1 ps/nm.km
MFD@1310 nm	6.7 μm	RI fiber @1550 nm	1.472
MFD@1550 nm	8.3 μm	Temp. dependence @1550 nm -60°C/+85°C	$\Delta\alpha \leq 0.02 \text{ dB/km}$
λ zero	1485 nm	Slope	0.064 ps/nm ² .km
Region of NON-zero dispersion	1530 nm~1565 nm	PMD	0.09 ps/√km

Suppose we have two channel signals with wavelength λ_1 and λ_2 transmitting in system, if the input power is strong enough and the channel span small enough, we would get four wavelength signals. As Fig. 1 shows: In this process, the strongly pumped light with wavelength λ_1 would cause sideband in position of wavelength λ_2 . The sideband is defined as Stokes band or anti-Stokes

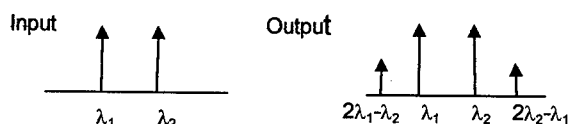


Fig. 1 Two Wavelength Channels FWM

band. The wavelength of sidebands is $\Omega_s = 2\lambda_1 - \lambda_2$ or $\Omega_s = 2\lambda_2 - \lambda_1$. FWM will be more complex when the channel gets three wavelengths. Fig. 2 illustrates the FWM process for three evenly spaced channels λ_1 , λ_2 and λ_3 . The mixing components occur at $\lambda_{xyz} = \lambda_x + \lambda_y - \lambda_z$. The total number of mixing components generated, m , is calculated as $m = 1/2 (N^3 - N^2)$. For a 2-channel system, this means there are additional signals to contend with. For a 3-channel system, this number is 9. And for an 8-channel system, this number increases to 224.

POSH and DSSM fibre has the same refractive index profile basically. The only different is the core and cladding dimension, and delta. The zero wavelength of POSH fibre is moved below 1520nm by manipulate the dimension of core and cladding and the delta value. Thus, it resides outside the EDFA's operating gain band, effectively reintroducing a controlled amount of dispersion into the system. The resulting dispersion for the POSH fibre is low enough to provide for long haul, high capacity and super bit-rate, yet not so low that FWM leads easily to system impairment.

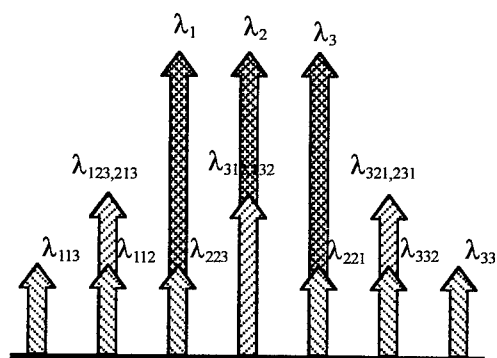


Fig. 2 Three Wavelength Channels FWM

There are many methods to abate the serious influence of nonlinear effects:

1. Lower the input optical power of optical amplifier.
2. Widen the space between wavelengths.
3. Degrade the system performance or shorten the relay distance to return to the old system.
4. Use the working wavelength with low dispersion.
5. Increase the effective CSA for signal transmission.

The last two methods are actually the direction for designing the POSH and Large Effect Area Positive Dispersion Shifted Single Mode Fibre.

POSH FIBRE

POSH fibre is made by PCVD process, which has the same process procedure as DSSM. So the fibre results in good performance, repeatability both in geometry and optical properties. The refractive index profile is manipulated accurately. We can get low slope and well controlled zero dispersion point, which is the key parameter in designing the fibre, and play a crucial role in system today. The typical characteristics of POSH fibre are depicted on Table 1. The typical dispersion of the POSH fibre is from 2.5 ps/nm.km to 5.2 ps/nm.km in operation window 1530 nm to 1565 nm. So it is named positive dispersion fibre.

In addition to nonlinear effects, system designers have voiced concerns about the ramifications of PMD as the installed based of optical fibre is upgraded to high bit-rate. Single-mode fibres actually support two perpendicular polarization of the original transmitted signal (fundamental mode). Perfect fibres, free from non-uniform geometry and stress, would propagate both orthogonal polarizations at exactly the same speed. However, practical fibres are not perfect and, such as, core ellipticity/deformation and asymmetries internal stress, which are called geometrical birefringence and stress birefringence respectively. As a result, the two perpendicular polarization may travel at different speeds and consequently arrive at the end of the fibre at different times (Fig. 3). The difference in arrival times, normalized with length, is known as PMD (Polarization Mode Dispersion). It can result in either the impairment of analog video picture quality in a system with multi-channel count or reduced span length for high bit-rate digital 1550nm operating region systems. The external reasons for PMD are formed environmental perturbation while fibre cabling and installing the cable.

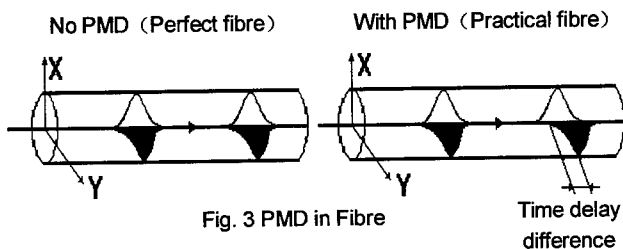


Fig. 3 PMD in Fibre

POSH fibre has superior geometry. And during drawing it introduces mode interference device, which eliminates the reflective index inhomogeneity caused by inhomogeneous stress. These make the POSH fibre has comparatively small PMD (typical value less than 0.1 ps/√km).

POSH FIBRE SYSTEM TEST

POSH fibre has been test on 8×2.5 Gb/s and 1×10 Gb/s transmission system.

8×2.5 Gb/s system diagram is demonstrated on Fig. 4. On the system there were 4 EDFAs: two line amplifiers (LA1 & LA2), one power amplifier (OBA) and one pre-amplifier. The system was consisted three spacing of POSH fibre with each spacing about 100 km. A optical spectrum analyzer was used to measure the spectrum of node A, B and C.

We compared the POSH fibre and DSSM fibre results from the system test and saw FWM

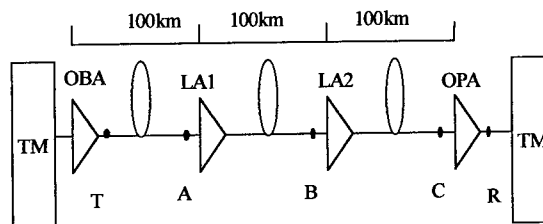


Fig. 4, 8×2.5Gb/s WDM system diagram

phenomena occurred on using DSSM fibre while no this effect on using POSH fibre (Fig 5/6).

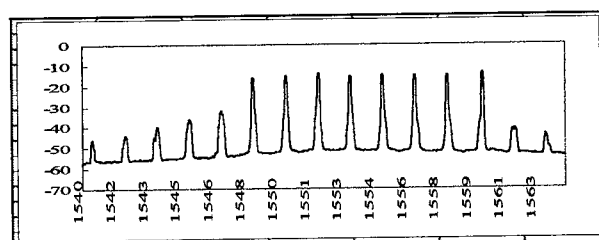


Fig. 5 DSSM fibre WDM test result

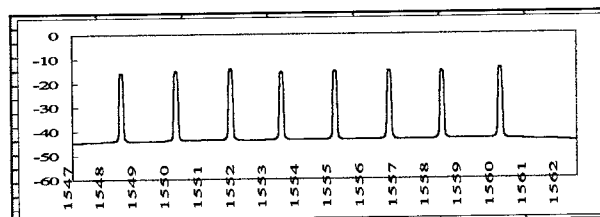


Fig. 6 POSH fibre WDM test result

Fig. 7 demonstrates the 1×10 Gb/s system configuration. The system includes five EDFAs and five spacing of POSH fibre. A polarization controller (PC) is added to the system on input terminal. The whole line is managed without any dispersion compensation. For the 1st, 2nd, 3rd and 5th spacing is about 100.8 km, and the 4th spacing is about 75.6 km. The fibre length of the system is 478.8 km, and total dispersion of it is 1083.1 ps/nm. Average attenuation is 0.21 dB/km. The parameters of the system are, transmission rate: 9.95328 Gb/s, dispatch wavelength: 1557 nm, signal pattern: 2³¹-1 stochastic pseudocode, receiver sensitivity: BER<10⁻¹². Fig. 8 shows the result obtained. The dispersion penalty is about 0.1dB. The polarization controller indicates PMD of POSH fibre has no distinct influence on transmission.

CONCLUSION

POSH fibre takes advantage of PCVD techniques, with low attenuation, zero dispersion wavelength controlled below 1520 nm. It introduces a small amount of positive dispersion at 1550 nm operating window, which can suppress FWM effectively. It meets the requirement continued very fast increasing of bandwidth demand. Combining EDFAs, the fibre is accommodated for multi-wavelength, high bit-rate, long distance and high

capacity in system. This also facilitates a cost-effective and flexibility network system.

ACKNOWLEDGEMENT

The authors gratefully acknowledge Wuhan Research Institute of Post Tele-communication, PTT. at the assistance on POSH fibre system test. Mr. ZhangMu, WuWei and all other colleagues of the authors are acknowledged for their supporting on this work as well.

REFERENCES

- [1] Liu Deming etc. "Fibre optics". National defense industry publishing house 1995
- [2] Yuan Rong. "Considering on designing WDM system". The eighth national optical fibre communication conference. p241~243
- [3] Corningfibre Library, r3118, LIGHTWAVE special report "Optical-fibre designs evolve"
- [4] Corning optical fibre Product Information, pi1050, "Corning SMF-LSTM CPC6 Single-Mode Dispersion-Shifted Optical fibre"
- [5] Corningfibre Library, pb1055, "CORNING® SMF-LSTM Optical fibre: The fibre That Goes The Distance"
- [6] Development of DWDM. Study on optical communications. 1998 2, p55
- [7] Dr. K. Kemeter, "Applications of standard single mode fibre in high speed optical transmission systems", The eighth national optical fibre communication conference.

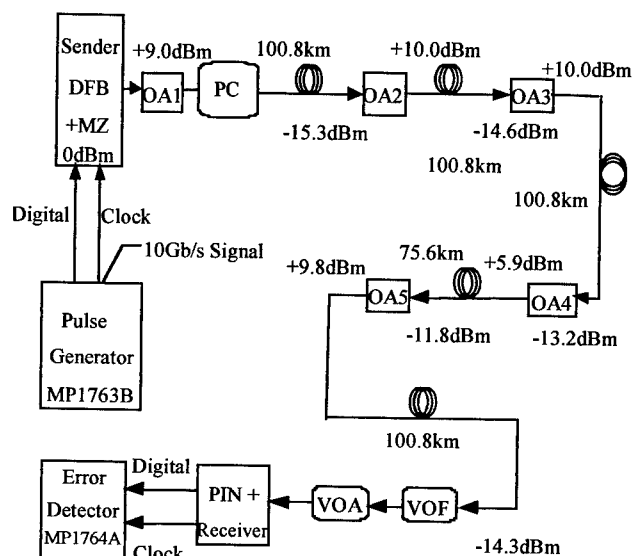


Fig. 7 10 Gb/s system construction

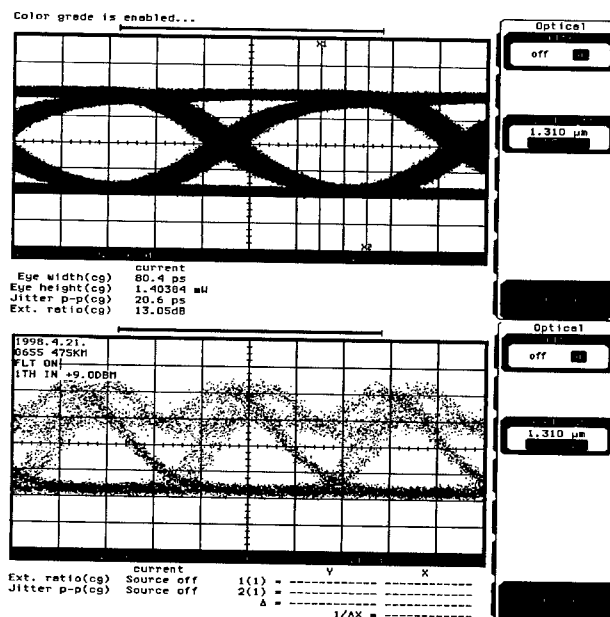


Fig. 8 POSH fibre 10Gb/s system test



Yanbin Huang
Chief Engineer of Fibre Dep.
Yangtze Optical Fibre and Cable
Co.Ltd. Wuhan, Hubei, China

Yanbin Huang was born in 1972. He received his bachelor degree of Silicon Engineer in 1993 at Wuhan University of Technology. In 1999, he obtained master degree of Economy. Since 1993, he has been with Yangtze Optical Fibre and Cable Co.Ltd., as a process engineer, responsible for PCVD production and development. He is in charge of the process group of Fibre Department now.

The Principle of Design and Manufacturing for a Large Effective Area Dispersion Shifted Single Mode Fibre made by PCVD process

Wu Wei R.Matai Zhang Mu John Cain

Yangtze optical fibre & cable co.Ltd. Wuhan, P.R. China

ABSTRACT

On the basis of the Refractive Index structure of normal single mode fibre, through changing its shape and dimension, the zero dispersion wavelength can be shifted according to what we expected. By this principle, we develop a kind of Large Effective Area Dispersion Shifted Single Mode fibre, it's made by PCVD process. For designing and manufacturing this kind of fibre, the structure of fibre refractive index profile and the method of producing are very important as they decide the fibre specifications like Attenuation, PMD value, Dispersion and MFD etc. In this paper, the way of how to design and how to make by PCVD process is presented.

INTRODUCTION

In the recent optical fibre market, more and more customers are getting interested on G.655 fibre as this kind of fibre has many unique characteristics and advantages.

Nowadays, G.655 Non-zero Dispersion Shifted Single Mode fibre has three types:

- ① Non-zero Negative Dispersion Shifted SM fibre, such as SMF-LS™.
- ② Non-zero Positive Dispersion Shifted SM fibre, for example, POSH® and TRUEWAVE™.
- ③ Large Effective Area Non-zero Dispersion Shifted SM fibre, For instance, LAPOSH® and LEAF™.

A Large Effective Area Dispersion Shifted SM fibre can both supply low attenuation and low dispersion transmission window, and can reduce the non-linear effect by Large Effective Area. So it can make the optical fibre telecommunication longer distance, larger capacity and higher bit rate.

We choose the positive dispersion in working window as its market demand on terrestrial application.

In production of this fibre, a very strict process

must be guaranteed. The shape and dimension of core and cladding should be obtained to the designed value precisely. Any deviation or error happens in process control, the fibre making efficiency and quality will drop down tremendously. We take the PCVD process to make the preform as it can duplicate any complicate shape of refractive index plot accurately and can reach the exact dimension. On the other hand, we find the drawing process may influence the optical parameters of this type of fibre strongly. So, when you make this kind of fibre, take one eye on the drawing process also.

PRINCIPLE

The factors which limit optical fibre data transmission capacity, rate and distance are : Attenuation, Dispersion, Non-linear Effect and PMD. So, during designing this kind of Large Effective Area Non-zero Dispersion Shifted fibre, we must completely consider items above and optimize them well.

DISPERSION

As we know, the dispersion of single mode fibre is mainly consist of material dispersion and waveguide dispersion. In the wavelength range for optical telecommunication (1.27—2.0 μ m), material dispersion presents positive dispersion, so called abnormal dispersion, longer wavelength gets larger dispersion value. From step single mode fibre refractive index structure, there are following formula [2]:

Material dispersion:

$$\Delta \tau_m = -\frac{\lambda_0}{c} \cdot \frac{d^2 n}{d\lambda^2} \cdot \delta\lambda$$

Wave guide dispersion:

$$\Delta\tau_w = -\frac{n\Delta}{c\lambda_0} \cdot v \cdot \frac{d^2(vb)}{dv^2} \cdot \delta\lambda$$

$$\text{Total dispersion} = \Delta\tau_m + \Delta\tau_w$$

b Normalized propagation constant

v Normalized frequency

λ_0 wavelength

n core refractive index

Δ core relative refractive index difference

These formula show that both kind of dispersion change by following the variation of wavelength, but the wave guide dispersion drift more rapidly if the fibre wave guide structure is changed. For DSSM fibre, the main factors to shift dispersion are Δ and V value of the fibre. By suitable adjusting the parameter of waveguide, correspond to the Δ and V value, the fibre zero dispersion wavelength can be moved according to what we want.

Higher Δ value or lower V value will give larger dispersion movement to negative direction.

In this case, for the Large Effective Area Dispersion Shifted SM fibre, we make the core like a quasi-parabolic shape. This shape of core can allow lower Δ and higher V value to the minimum requirement which can shift the dispersion to a certain level. Besides dispersion, this structure can also benefit the attenuation, MFD, and dispersion slope etc. quite a lot.

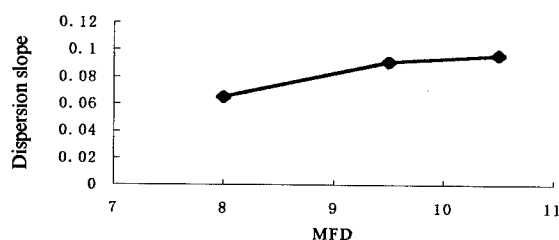


Figure 1 The G.655 fibre dispersion slope vary with MFD

Low Δ can improve the attenuation, MFD and dispersion slope, and high V value may reduce the bending loss sensitivity.

By the way, a special and well done refractive index profile of fibre cladding is very attractive to help the points mentioned above.

The quasi-parabolic core with a matched cladding can reduce the sensitivity influenced by the process tolerance in manufacturing process. It makes the technical process control much easier so that fibre making efficiency rise truly.

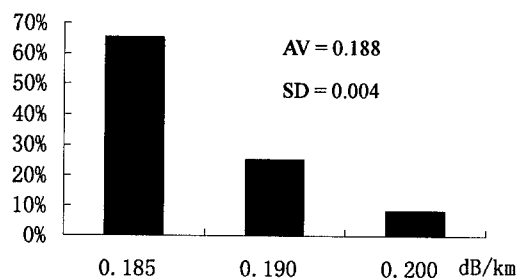


Figure 2.The MCSM attenuation distribution at 1310nm

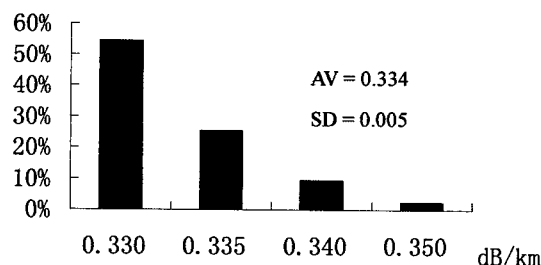


Figure 3.The MCSM attenuation distribution at 1550nm

ATTENUATION

The attenuation of single mode fibre is mainly caused by:

- ① Content of various contamination in fibre, including OH^- .
- ② Content of GeO_2 of fibre cone.
- ③ Homogeneity, flatness and defect of the waveguide and its interface.
- ④ Bending loss.

In production of MCSM fibre, we take some special ways on PCVD process and drawing process, so the MCSM fibre attenuation is improved quite much. (see Fig.2 and Fig. 3). Also, we apply same concept into DSSM fibre production.

During designing the Large Effective Area Dispersion Shifted SM fibre, besides suitable dispersion shifted, we try to lower the GeO_2 content in the fibre as much as possible.

The quasi parabolic refractive index profile structure let a certain large part of transmission light transfer along the path of core and cladding where relatively lower GeO_2 content is.

By PCVD perform making process, the wave guide plus its interface of fibre can be very homogeneous and smooth. Meanwhile the preform is forming a fibre during drawing process, a physical and chemical variation of waveguide happens in the heat zone of drawing furnace.

Because the GeO_2 and F^- in the core and cladding will diffuse each other, the final fibre refractive index profile shape is obtained in this step, so is the flatness of the interface. In this case, we know that the drawing process would change the fibre result quite a lot. Any process parameter setting should be well analyzed. The general principle to set the drawing process figure is that:

- Less or stable diffusion of GeO_2 and F^- in different wave guide interface.
- Less or stable thermal expansion in core and cladding.
- Less abnormal deformation in the heat zone where the preform is becoming fibre

Table 1. Comparison of different drawing condition for the Large Effective Area Dispersion Shifted SM fibre made by PCVD process

Drawing condition	Normal	Optimized
Attenuation at 1310nm	$\geq 0.38\text{dB/Km}$	$\leq 0.36\text{dB/Km}$
Attenuation at 1550nm	$\geq 0.22\text{dB/Km}$	$\leq 0.21\text{dB/Km}$
Attenuation at 1625nm	> 0.23	$\leq 0.23\text{dB/Km}$
Dispersion control	Normal	Easy and stable
Fibre making efficiency	Low	High

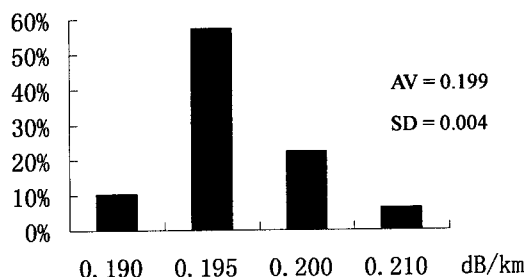


Figure 4. The Laposh fibre attenuation distribution at 1550nm

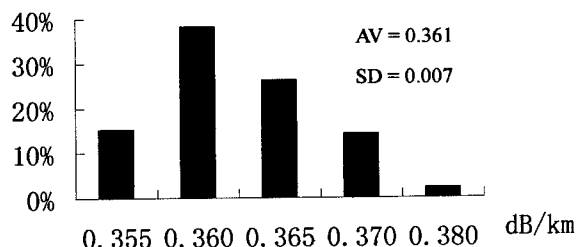


Figure 5. The Laposh fiber attenuation distribution at 1310nm

NON-LINEAR EFFECT

In recent transmission system, the main factor of non-linear effects is "Four wavelength mixture" (FWM). The non-linear effect is in direct proportion to light power and length, but in inverse proportion to Dispersion and Effective Area. In this case, there are 4 methods to recover the influence of non-linear effect:

- ① To Reduce input light power
- ② To Use the transmission wave length window with a certain dispersion
- ③ To Enlarge fibre Effective area
- ④ To increase the wavelength interval of each channel

Obviously, to use the window with certain dispersion and to increase Effective area are best choice to suppress the non-linear effect on fibre transmission. The Large effective area dispersion shifted SM fibre possess those advantages.

PMD

In DWDM high data transmission rate system, the PMD may strongly limit the distance of Non-retransmission.

The PMD is mainly caused by birefringence effect, for instance, non-circularity of Geometry in radius direction, anisotropy birefringence by stress and influence of environment.

To reduce the fibre PMD, the fibre core and cladding circularity must be obtained, the uneven stress from preform making and fibre drawing must be released.

By means of special process control during collapsing and drawing process.

By the way, it's very important to control PCVD process to let the GeO_2 and F^- diffuse evenly to get less deformation of core and cladding.

MANUFACTURING

We produce the Large Effective Area Dispersion Shifted SM preform by PCVD process so that the core and cladding can be done very smooth and exactly according to what we design, with this process, a very special and very smooth quasi-parabolic core combined with cladding is made.

By this kind of structure, the Δ value of core can decrease some how and the V value can be raised to a certain extent, Therefore, it allow more process tolerance in real mass production so as to increase the fibre making efficiency obviously. Secondly, it improves the mean value of dispersion, dispersion slope, MFD and bending loss. As we understand, there is inverse proportion relation among the MFD, dispersion slope (see Fig. 1) and bending loss. So this structure can optimize them very well. In

real mass production a good process control is extremely important, any a very small deviation on key wave guide parameter, like core diameter, Δ and parabolic α value, will drift the optical result heavily and cause a huge rejection of products. Luckily, PCVD process is easier to precisely control those points (see table 2).

In PCVD process we introduce applying Cl_2 to reduce OH^- in the fibre so that the Large Effective Area Dispersion Shifted SM fibre attenuation is very low and stable. (see Fig. 4 and Fig. 5)

Not only Attenuation, also the dispersion can be strongly influenced in drawing process. After the moment when PCVD preform making is fixed, the drawing process parameters must be optimized and stabilized.

Table 2 Main characteristics of the Large Effective Area Dispersion Shifted SM fibre made by PCVD process

Item	Value
Attenuation at 1310nm	$\leq 0.38\text{dB/km}$
Attenuation at 1550nm	$\leq 0.20\text{dB/km}$
Effective Area(typical value)	$80\mu\text{m}^2$
Bending loss at 1550nm ϕ 75mm, 100turns	$\leq 0.05\text{ dB}$
Bending loss at 1550nm ϕ 32mm, 1turn	$\leq 0.5\text{ dB}$ (Avg=0.01 dB)
Zero dispersion slope	$\leq 0.093\text{ ps/nm}^2\text{ km}$
Dispersion at 1530nm	$\geq 1.0\text{ ps/nm.km}$
Dispersion at 1550nm	4.0ps/nm.km
Dispersion at 1565nm	$\leq 6\text{ps/nm.km}$
Zero dispersion wavelength	$\leq 1520\text{nm}$
PMD	$\leq 0.2\text{ps} / \sqrt{\text{km}}$
Others	Meet the ITU-T Requirements

CONCLUSION

1. The fibre with Larger Effective Area, suitable Dispersion Parameter, low Attenuation and PMD may help the optical transmission system a lot.
2. For designing and manufacturing this kind of fibre, the structure of fibre refractive index profile and the way of producing are key points. The factors influencing Attenuation, Dispersion, MFD and PMD etc. must be considered and optimized completely.
3. We make the Large Effective Area Dispersion Shifted SM fibre with a special refractive

index structure of core and cladding, so the Effective Area is larger and the attenuation (including bending loss) is low, at the condition of good dispersion performance.

4. PCVD process can realize the refractive index profile close to designed value.
5. Not only the preform making, but also the drawing process may influence the fibre optical parameters very much.

REFERENCE

1. Physical Optics, Industry of National Defence, P.R.China, 1980.
2. DeMing Liu, Fibre Optics, 1995.

SPEAKER



Wu Wei
Yangtze optical fibre &
cable co. Ltd. (YOFC)
Wuhan, 430073
P. R. China

Wuwei was born in 1963. He graduated with a B.E. degree in optics engineering from Huazhong science and Technology University in 1985.

He worked at Post and Telecommunication Research institute of Wuhan, P. R.China from 1985 to 1988. In 1988 he joined Yangtze optical fibre and cable co. Ltd., P. R. China, Since 1988, He has been working in the optical fibre manufacturing. In 1999, he got a Master degree in Economics from HuaZhong science and Technology University. Since 1999. He has been the assistant manager of fibre Dept. of YOFC, P.R. China.

BENDING PERFORMANCE STUDY OF LARGE EFFECTIVE AREA G.655 FIBRE

Ming Cheng, Guohui Niu and Mu Zhang

Yangtze Optical Fibre and Cable Co. Ltd. Wuhan P. R. China

ABSTRACT

The bending performance of fibre is very critical to its ribbon making, cabling and has great influence on the performance during installing and after installations. We designed and fabricated large effective area non-zero dispersion shifted single-mode optical fibre (LEA-G.655 fibre) and studied the relation between macro-bending loss and other optical characteristics of this fibre. Upon the analysis of the test results we find that the fibres with certain parameters have very good optical characteristics and bend performance and are very suitable to the future DWDM applications.

INTRODUCTION

In order to increase the transmission capacity, enlarge the repeater spacing, broad band erbium doped fibre amplifiers (EDFAs) and dense wavelength division multiplexing transmission (DWDM) have been introduced. The signal powers inserting into a fibre can go up to a very high level, resulting in non-linearities and degrading the signal transmission in fibre. The non-linear effects are in proportional to nonlinear index (n_2) and optical power density (P/A_{eff}). In order to suppress the non-linearity, we should minimize $n_2 P/A_{eff}$. Due to the high transmission rate, P cannot be reduced. n_2 is related to the doped material and is difficult to change, so the most suitable way is to increase A_{eff} . Many fibre manufacturers use this concept to fabricate this fibre [1, 2]. We know that increasing A_{eff} without limit will induce many penalties to this fibre such as dispersion slope increasing and bending sensitivity increasing etc. For this reason A_{eff} should be kept at an optimized value. According to the general principle, macro-bending sensitivity increase with A_{eff} increase and A_{eff} is proportional to mode field diameter (MFD). For this reason, macro-bending

performance is related to MFD of fibre and at the same time MFD is related to other characteristics of fibre , so macro-bending performance of fibre is related to all of the fibre's characteristics. it is necessary to make clear the relations between the macro-bending loss and fibre characteristics and this is very important to the fibre design, fibre fabrication and its future applications.

FIBRE DESIGN AND FABRICATION

We designed and fabricated the large effective area G.655 fibres (LEA-G.655 fibre). The main characteristics of these fibres are displayed in Table 1.

Characteristics	Specified Values
Attenuation at 1550nm	≤ 0.20 dB/km
Total Dispersion for 1530-1565nm	1.0-6.0 ps/nm*km
Zero dispersion wavelength	≤ 1520 nm
Zero dispersion slope	0.093 ps/nm ² *km
Cutoff wavelength	≤ 1470 nm
MFD @1550nm	$9.5\sim 10.5$ μ m
A_{eff}	~ 80 μ m ²

Table 1: main characteristics of LEA G.655 fibre

We have done 8×10 Gbit/s WDM transmission test on these fibres. Error-free transmission in these fibres were achieved [3]. This means that this sort fibres can be put into practical use.

MACRO-BENDING TEST

According to ITU-T Recommendation G.655, the loss increase for 100 turns, loosely wound with 75 mm diameter mandrel and measured at 1550nm, shall not exceed 0.5 dB.

For SDH and WDM applications, the fibre may be used at wavelengths exceeding 1550nm. The 0.5 dB maximum loss shall apply at the maximum wavelength of

anticipated use.

In the near future DWDM wavelengths may expand to L-band (1570 nm –1625 nm), so we need to know the macro-bending performance of this fibre at the two bands (C-Band and L-Band).

Test 1. In order to make clear the relation between the fibre macro-bending loss and its optical characteristics, we deliberately designed and fabricated many test fibres. These fibres have a wide range of mode field diameters (MFD) and cutoff wavelengths (λ_c). MFD range from 9.26 μ m to 10.53 μ m and λ_c range from 1114 nm to 1450 nm, then the value of mode field diameter against cutoff wavelength (called MAC) ranges from 6.70 to 9.27.

These fibres were wound on 75mm mandrel 100 turns and the loss increases were measured. The macro-bending loss distributions are shown in Fig.1 ~ Fig.4.

From these figures we can find that a large part of these fibres have a zero or near to zero macro-bending loss. This means that this fibre has very small and stable macro-bending performance.

The typical values of macro-bending loss in the whole range of MAC (from 6.70 to 9.27) are in Table 2

MAC	1550 nm	1600 nm	1625 nm
6.70~9.27	0.008	0.009	0.012
<=7.8	0.006	0.008	0.011

Table 2: The average macro-bending losses of all fibres for 100 turns on 75 mm mandrel at three wavelengths

The test results show that the macro-bending loss of such fibres at 1550nm, 1600nm and 1625nm are 100% less than 0.05 dB no matter how much the MAC is (in the range of 6.70 to 9.27).

That is if the MAC is controlled within this range then this sort of LEA-G.655 fibre's macro-bending loss can be less than 0.05 dB.

We have chosen some fibres with same MAC and tested their macro-bending losses. The test results show that the macro-

bending losses increase with the increase of MFD, and increase with the decrease of cutoff wavelengths. That means, we should control MFD in a suitable range. Despite through the design of fibre RI profile we can increase MFD and simultaneously increase cutoff wavelength to acquire same MAC value, too big MFD that larger than 11 μ m, still have influence on the fibre bend performance and will bring some other penalties to this fibre, so the wise choice is to find a trade-off among all these fibre's characteristics.

Test 2. LEA-G.655 fibre macro-bending losses induced by winding one turn on 32mm mandrel were measured. The test samples are the same samples that in the Test 1. The variations of macro-bending loss against MAC are shown in Fig.5, Fig.6 and Fig.7

From these figures we find that the macro-bending loss of this fibre increase with the increase of the fibres MAC value and the trend is evident. We also find that the macro-bending losses are low and very stable for the fibre with small MAC values that less than 7.8.

The test results show that macro-bending losses of this LEA-G.655 fibre at 1550nm, 1600 nm and 1625 nm are 100 % less than 0.5 dB if the MAC are less than 8.5; Of course the macro-bending losses of some fibres are less than 0.5 dB despite their MAC values are larger than 8.5 (the MFD up-limit of these fibres is 10.53 and the λ_c low-limit is 1114nm).

The average macro-bending losses of these fibres are listed in the Table 3

MAC	1550 nm	1600 nm	1625 nm
6.70~9.27	0.086	0.155	0.195
<=7.8	0.022	0.045	0.074

Table 3: The average of all fibres macro-bending loss for one turn on 32 mm mandrel at three wavelengths

From the test results we conclude that as long as the fibre's MAC value is less than 8.5 (the MFD up-limit of these fibres is 10.53 and the λ_c low-limit is 1114nm) then the macro-bending performance of this fibre can easily meet the customer's requirements. If

we choose 7.8 as the up-limit of the fibre's MAC value then the fibre will have excellent bend performance.

From the above two tests we find that if we control fibre's MAC value to be less than 7.8 then excellent macro-bending performance can be easily obtained. For example we can control the MFD around 10 μm and λ_c around 1370 nm so the MAC is around 7.3. this can be easily realized by PCVD technology through the optical wave-guide design and the producing process control. That means we can ensure the fibre macro-bending performance without difficult.

Test 3. The LEA-G.655 fibre's macro-bending losses for 100 turns loosely wound on different diameter mandrels were tested and the results are shown in Table 4. The MFD of the sample is 10.05 μm , the cutoff wavelength is 1150 nm, then its MAC is 8.74 and relatively a big one (worse case).

Mandrel diameter	1550nm	1600nm	1625nm
35mm	4.507	8.393	12.306
40mm	0.836	2.531	4.843
45mm	0.249	0.328	0.389
50mm	0.138	0.209	0.224
55mm	0.038	0.043	0.084
60mm	0.030	0.032	0.036
65mm	0.016	0.018	0.021
70mm	0.013	0.014	0.017
75mm	0.008	0.011	0.013

Table 4: LEA-G.655 fibre macro-bending losses for 100 turns wound on different diameter mandrels

The test result shows that when mandrel diameters change from 75 mm to 45mm, the macro-bending losses increase gently and the values can easily meet with the requirement of ITU-T Recommendation (0.5 dB). When the mandrel diameters become 40mm and 35 mm, the macro-bending loss increases. We have done the same test with the same sort fibres from other manufacturers and found the same phenomenon. In practical single mode fibre installations, winding many turns of 40 mm or 35 mm is not permitted. Therefore this fibre can be used in much adverse situation than the practical situation.

CONCLUSION

LEA-G.655 fibre fabricated by PCVD technology can be put into future DWDM application in C-Band and L-Band. Its optical characteristics and its macro-bending performance can easily meet the customer's requirements. This fibre can be used in much adverse situation than nowadays practical installations and application.

ACKNOWLEDGEMENTS

We thank Mr. R. Matai for his instructions and beneficial discussions. We also thank Mr. Mo Xiaohong for his testing assistance.

REFERENCES

- [1] Y. Liu etc. "Single-mode dispersion shifted fibres with large effective area for amplified systems" IOOC95, PD-19, 1995
- [2] P. Nouchi etc. "New dispersion shifted fibre with effective area larger than 90 μm^2 " ECOC'96 MoB.3.2
- [3] M. Cheng etc. "LAPOSH fibre 8*10 Gbps WDM transmission test" China OFC Technical Conference 1999

SPEAKER BIOGRAPHY



Ming Cheng
Yangtze Optical
Fibre and Cable Co.
Ltd. (YOFC)
Wuhan 430073
P. R. China

Ming Cheng was born in 1962. He received his diploma in physics in 1983 at Wuhan University and MSc degree in solid-state physics in 1990 at Huazhong University of Science and Technology (HUST) in China. Since 1994 he has been with Yangtze Optical Fibre and Cable Co. Ltd. (YOFC), responsible for R & D related to optical fibre, fibre optics and optical fibre telecommunications.

Fig 1. Distribution of Macro-bending Loss at 1550nm (MAC up to 9.27)
75mm, 100 turns

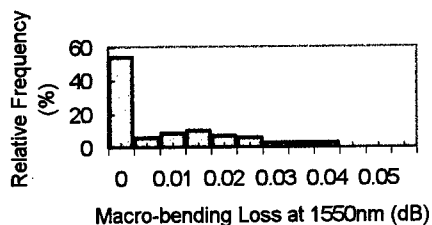


Fig 2. Distribution of Macro-bending Loss at 1625nm (MAC up to 9.27)
75mm, 100 turns

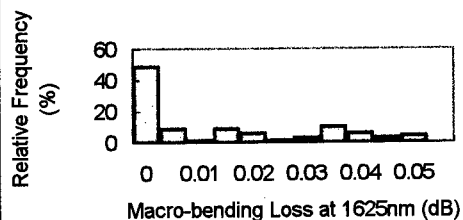


Fig 3. Distribution of Macro-bending Loss at 1550nm (MAC < 7.8)
75mm, 100 turns

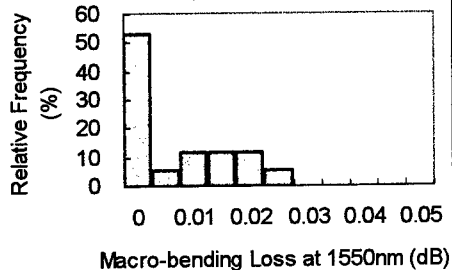


Fig 4. Distribution of Macro-bending Loss at 1625nm (MAC < 7.8)
75mm, 100 turns

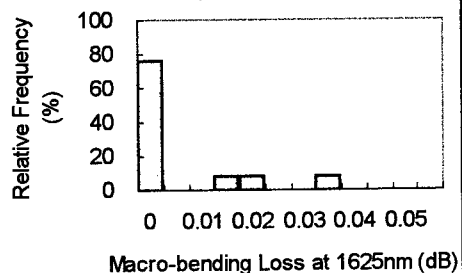


Fig.5 Macro-bending loss at 1550nm
32mm, 1 turn

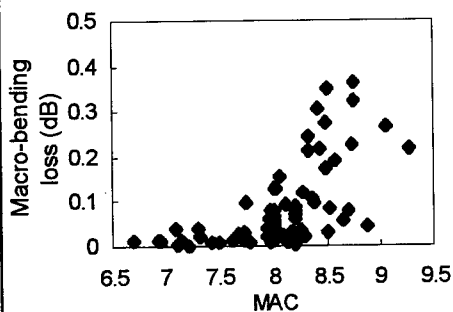


Fig.6 Macro-bending loss at 1600nm
32mm, 1 turn

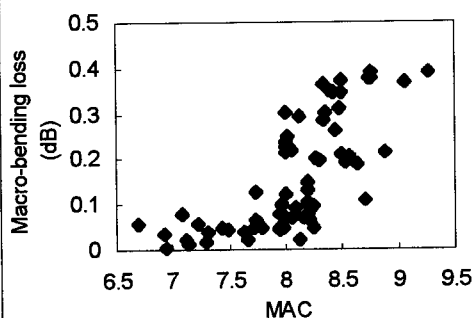
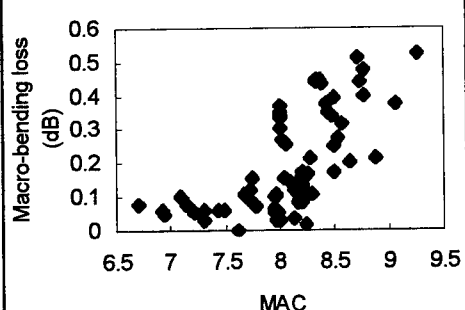


Fig.7 Macro-bending loss at 1625 nm
32mm, 1 turn



DYNAMIC MENISCI ON MOVING FIBERS

Anil Abraham and Constantine Polymeropoulos

Rutgers, The State University of New Jersey
Piscataway, NJ

ABSTRACT

This work is part of a research effort motivated by the coating process in the manufacture of optical fibers and describes measurements relevant to the upstream meniscus within an open cup applicator. Results, which include the variation of the apparent advancing contact angle and the meniscus length with fiber speed along with fluid properties, are presented and discussed using available correlations wherever possible. Conditions for air entrainment were identified and the effect of pressurizing the test section was qualitatively examined.

INTRODUCTION

The manufacture of optical fibers includes a stage where a protective coat is applied to the fiber in a cup applicator. Upon entering the applicator air entrained by the fiber is replaced by the coating liquid in the vicinity of an apparent dynamic contact surface between the air, the liquid and the moving fiber. At the applicator exit the fiber is drawn through a coating die forming a downstream meniscus as it is deposited on the fiber. The process is similar to other industrial coating processes for wire, magnetic tape, photographic film, etc. Control of the thickness and uniformity of the resulting coating are of interest, especially as the coating speed is increased.

The literature on coating flows is large but recent review papers^{1,2} can be consulted for discussion on the subject. There have been few published works on replacement flows using fibers³⁻⁵. Examples of other experimental works on replacement flows appropriate to the present study are with immersion of tapes⁶⁻⁹ or with rotating horizontal cylinders partially immersed in a pool of liquid. Air displacement by the wetting liquid depends on molecular interactions at the surface of the solid substrate, which have not yet been resolved. Macroscopically the contact surface near a smooth substrate generally appears to be well defined, but accurate measurements require high magnification since the curvature of the surface may vary rapidly near the solid substrate. It is for this reason that measurements refer to apparent contact angles. The dynamic contact angle increases with substrate speed

to near 180° where the advancing liquid can no longer displace all the air, resulting in air entrainment in the form of small bubbles. Results from asymptotic analysis in the limit of small capillary numbers have been in good agreement with measurements of the liquid/air interface shape and the velocity field in the vicinity of a plunging relatively large diameter cylindrical surface^{10,11}. However, because of the absence of a predictive general theory, most of the experimental data on the dependence of contact angle, meniscus depth, and incipient air entrainment have been correlated based on dimensional considerations.

Published work on the processes within optical fiber coating applicators has focused on the flow within the coating die, and on the relationships between flow parameters and coating fluid properties on the resulting coat thickness^{12,13}. Optical fiber production draw speeds may be currently in excess of 15-20 m/sec and require special pressurized applicator designs since the speed range is above the limit for air entrainment in open applicators. However, except for the description of a pressurized air bubble stripping applicator¹⁴ the upstream meniscus in high speed coating has received little attention in the literature.

This work is an experimental investigation of the upstream meniscus formed by a fiber entering a simulated coating applicator. Specifically, the meniscus shape, length and the dynamic contact angle were measured for water and two different glycerin/water solutions. Measurements were taken for a range of fiber speeds up to incipient air entrainment. The latter is of particular importance because it sets upper coating speed limits for open cup applicators. The capillary number range was between approximately 0.001 and 18, and the highest liquid viscosity was 1 N m/sec². The use of actual coating liquids awaits installation of the necessary curing equipment. The experimental apparatus was off a fiber production line and required relatively long lengths of fiber. Because of the fragility of uncoated fused silica fiber it was necessary to use coated fiber manufactured in a conventional draw tower. Most of the work was carried out with an open cup applicator, but a limited set of observations were recorded

regarding the difference in apparent air entrainment accompanying applicator pressurization.

EXPERIMENTAL APPARATUS

Figures 1 and 2 are schematic diagrams of the overall experimental apparatus and the test section, respectively. The fiber motion was controlled using a commercial optical fiber rewriter system with a speed range between approximately 0.02 and 17 m/sec. The test section was a plexiglass cylindrical cup, 4.4 cm inside diameter, 12 cm deep, and was equipped with flat glass windows for visualization of the meniscus. The fiber entrance and exit from the test section were through two 350 μ m diameter coating dies located in the upper lower surfaces of the test cup. Test liquids were supplied symmetrically about the exit die through four 3.2 mm diameter holes located at a radius of 5 cm. Diffuse backlighting was provided from a continuous incandescent light source, or a short duration (0.5 msec) spark source. Images of the menisci were acquired using a telescope equipped CCD camera and video tape recorder. The short duration images with the spark source also required a high-speed frame grabber. The taped images of the resulting menisci were analyzed using image processing and analysis software*. Since the fiber speeds tested resulted in advancing contact angle menisci, which were below the surface of the liquid, it was necessary to position the camera for viewing from a direction below the liquid surface with a camera angle of approximately 1°. The resolution of the optical system depended on the object distance used which ranged from 30 cm to 1 m resulting in magnification between 500 and 100 and pixel to pixel spacing between 5 μ m and 10 μ m depending on magnification. The edge of the meniscus and fiber were identified using Sobel edge detection. The error was estimated to be $\pm 2^\circ$ at the 95% confidence level, except for larger than approximately 160° angles where the error was $\pm 4^\circ$ because of difficulty in identifying the meniscus contact point.

The glass fibers used were drawn in house from fused silica rods and were coated with a single coat of UV curable polyacrylate. The fiber diameter was 218 μ m \pm 25 μ m and was monitored continuously using a fiber diameter monitor. Table 1 shows relevant liquid properties of the three test liquids used.

RESULTS AND DISCUSSION

Figure 3 is an example of a meniscus image around the fiber plunging at 0.17 m/sec into the

glycerine/water 2 solution. The fiber speed was larger than that for bubble formation, but the interest in this figure was the V shaped structure clearly visible on the fiber. The appearance of such structures was intermittent and spatially varying suggesting conditions of meniscus instability similar to the saw-tooth advancing wetting lines previously reported with plunging tapes^{6,9}.

Figure 4 shows the fiber speed for initial bubble detection within the test section. The solid line is the previous correlation $V_c = k\mu^n$ ^{4,8}. It should be noted that bubbles appeared suddenly in easily detected large numbers and within a narrow speed range for the two lower viscosity liquids tested. This was due to the relatively large fiber speeds at air entrainment for water and the glycerine/water 1 solution, resulting in large rate of bubble addition into the test liquid. For glycerine/water 2 solution the first appearance of bubbles was more difficult to determine because of the low rate of bubble generation with the much slower moving fiber.

Since the test section could be operated at elevated pressures (0-10 psi), qualitative observations were possible regarding the effect of pressurization on bubble formation. With fiber speed of approximately ten times larger than for air entrainment, the level of glycerine/water 2 solution was allowed to rise until the meniscus was located within the entry die (figure 2). Here, the small (65 μ m) clearance between the fiber and the die diameter allowed pressurization without fluid flowing through the die. At a gage pressure of approximately 60 kPa the bubbles were smaller, because of the increase in pressure, but also appeared to be of lower number density compared to what could be observed with the test section at atmospheric pressure. Confirmation of this observation will have to await a quantitative measurement of bubble formation. In addition, the effect of bubble size on the bubbles eventually within the fiber coat requires microscopic examination of fibers coated under different conditions. It appears reasonable however, that the meniscus shape within the entry die will have an impact on the advancing contact angle and on the displacement of air by the advancing surface.

The distance (meniscus depression) from the free surface to the apparent contact point was correlated using the relationship

$$We = (1.936)Re^{1.77}N_{pr}^{-0.346} \quad (1)$$

where the Weber number was based on the measured meniscus depression. The results are shown on fig. 5. The dynamic contact line was observed to experience a stick-slip behavior, especially at high

* Available from the National Institute of Health

fiber speeds, and the angles measured were mean values from different images. The results on fig. 6 show that the apparent contact angle initially increased rapidly with speed, it then reached a region of lower rate of increase, and then increased again more rapidly until air entrainment which was observed with angles near but lower than 180°. Similar behavior for water and glycerine solutions has been reported in previous work¹⁻⁴, with plunging tapes. Figure 7 shows measured angles, to the critical fiber speed for air entrainment, plotted against the following empirical correlation which is similar in form to one in ref. 8:

$$\theta_D = 2.786Ca^{0.07397}N_{pr}^{0.3546}\mu^{1.3997} \quad (2)$$

The collapse of the data points for the different fluids shows that it is possible to use expressions such as equations (1) and (2) for correlating meniscus measurements. However, this does not offer physical insight on the process under consideration.

CONCLUSIONS

An experimental investigation into the properties of advancing contact surfaces generated in an optical fiber coating applicator has shown the influence of fiber motion and fluid properties on advancing contact angle, meniscus depression, and incipient air entrainment. The results to the extent possible were correlated using relationships that were previously developed mostly for plunging tapes and to a lesser extent using fibers. Sawtooth instabilities similar to those observed with plunging tapes were observed at fiber speeds larger than the critical speed for air entrainment. The quantitative results were applicable to open cup applicators. The effect of pressurizing the applicator suggested the need for further investigation on the effect of pressure on air entrainment. Further work is planned using actual fiber coating fluids.

NOMENCLATURE

$Ca = \frac{V\mu}{\sigma}$	Capillary number
h	meniscus depression
$N_{pr} = \frac{\rho\sigma^3}{g\mu^4}$	Property number
$Re = \frac{hV\rho}{\mu}$	Reynolds number
V	fiber speed
$We = \frac{hpV^2}{\sigma}$	Weber number
Greek Symbols	
θ_D	dynamic contact angle

μ	viscosity
ρ	density
σ	surface tension

ACKNOWLEDGMENTS

The work was supported by National Science Foundation Grant CTS-9610102, and by the Fiber Optic Material Research Program at Rutgers University. Discussions with Professor Y. Jaluria are gratefully acknowledged. Mr. Jonathan To helped with the experimentation.

REFERENCES

1. Blake, T.E., (1993), "Dynamic Contact Angles and Wetting Kinetics", Ch. 5, *Wettability*, Berg, J.C. ed., Marcell Dekker, New York.
2. Kistler, S.F., (1993), "Hydrodynamics of Wetting", Ch. 6, *Wettability*, Berg, J.C. ed., Marcell Dekker, New York.
3. Inverarity, G., (1969), "Dynamic Wetting of Glass Fibre and Polymer Fibre", *Br. Polym. J.*, v. 1, pp. 245-251.
4. Ghannam, M., T., and Esmail, M.N., (1993), "Experimental Study of the Wetting of Fibers", *AIChE J.*, v. 39, pp. 361-365.
5. Ghannam, M., T., and Esmail, M.N., (1997) "Experimental Study on Wetting of Fibers with Non-Newtonian Fluids", *AIChE J.*, v. 43, pp. 1579-1588.
6. Burley, R., and Kennedy, B.S., (1976), "An Experimental Study of Air Entrainment at a Solid/Liquid/Gas Interface", *Ch. Eng. Sc.*, v. 31, pp. 901-911.
7. Burley, E., and Jolly, R.P.S., (1984), "Entrainment of Air into Liquids by a High Speed Continuous Solid Surface", *Ch. Eng. Sc.*, V 39, pp. 1357-1372.
8. Guttoff, E.B., and Kendrick, C.E., (1982), "Dynamic Contact Angles", *AIChE J.*, v. 28 pp. 459-466.
9. Blake, T.E., and Ruschak, K.J., (1979), "A Maximum Speed of Wetting", *Nature*, v. 282, pp. 489-491.
10. Dussan, E. B., Rame, E., and Garoff, S., (1991), "On Identifying the Appropriate Boundary Conditions at a Moving Contact Line: an Experimental Investigation", *J. Fluid Mech.*, v. 230, pp. 97-116.
11. Marsh, J.A., and Garoff, S., (1993), "Dynamic Contact Angles and Hydrodynamics near a Moving Contact Line", *Phys. Rev. Let.*, v. 70, pp. 2778-2781.

12. Paek, U.C., (1986), "High Speed High Strength Fiber Coating", *J. Lightwave Tech.*, v. LT-4, pp 1048-1059.
13. Paniliaskos, A., Hallett, W.L.H., and Garis, I.,(1985), "Prediction of Optical Fiber Coating Thickness", *App. Opt.*, v. 24, pp. 2309-2312.
14. Aloisio, C.J., (1984), "Coating Optical Fibers with Dual Dies Separated by a Pressurized Chamber", *Fiber and Integrated Optics*, v. 5, number 1,pp.81-97.

Table 1. Fluid Properties

Fluid	Density,kg/m ³	Viscosity,Nm/sec ²	Surface Tension,N/m
Water	1000	960x10 ⁻⁶	0.072
Glycerine/water 1	1031.768	0.0063	0.0683
Glycerine/water 2	1250	1	0.0683

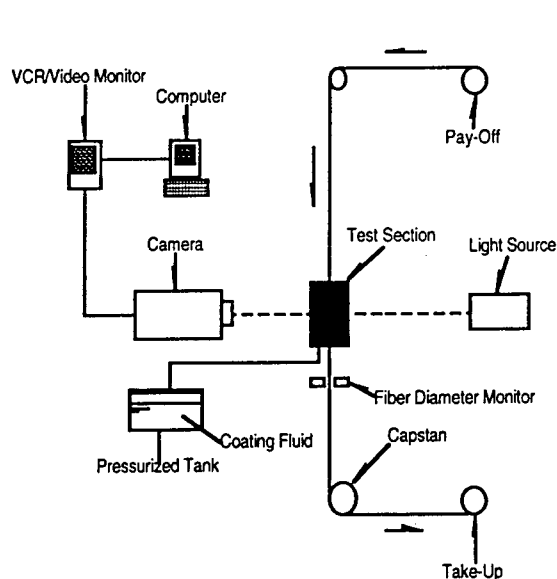


Figure 1. Experimental Apparatus

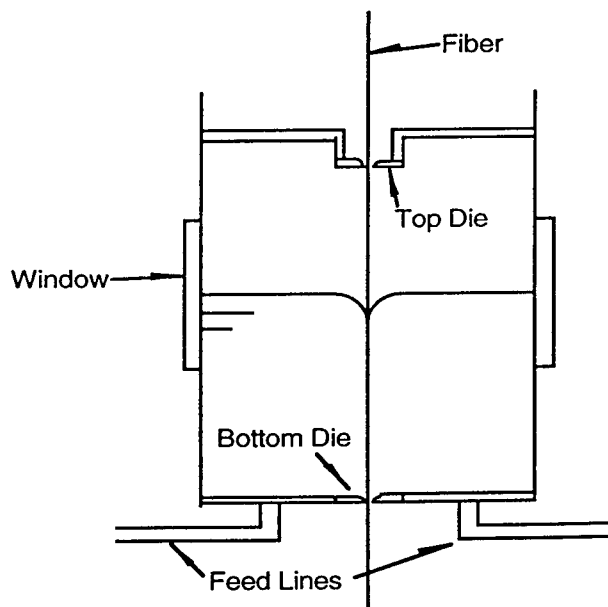


Figure 2. Test Section

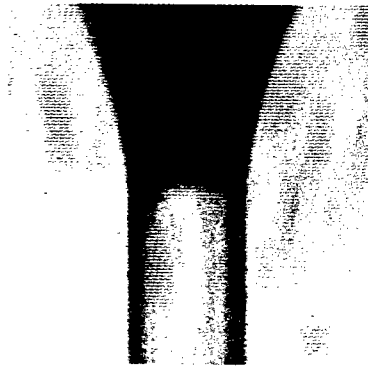


Figure 3. Image of contact region. $V = 0.17$ m/sec. Fiber diameter $218 \mu\text{m}$. Glycerine/water 2 solution.

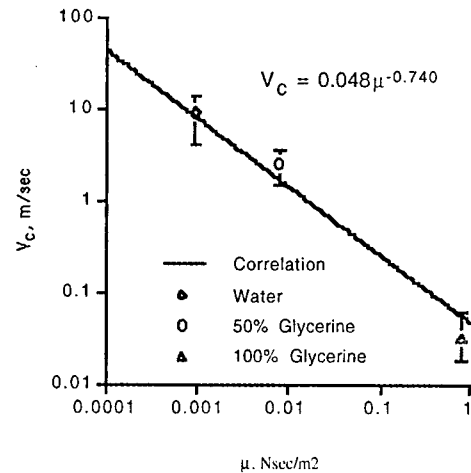


Figure 4. Air Entrainment Velocity vs. Viscosity

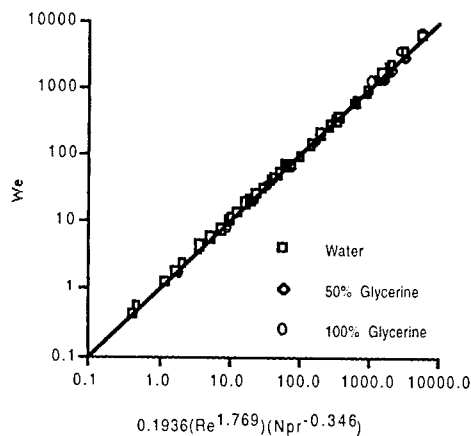


Figure 5. Correlation of the Weber Number Based on the Meniscus Depression

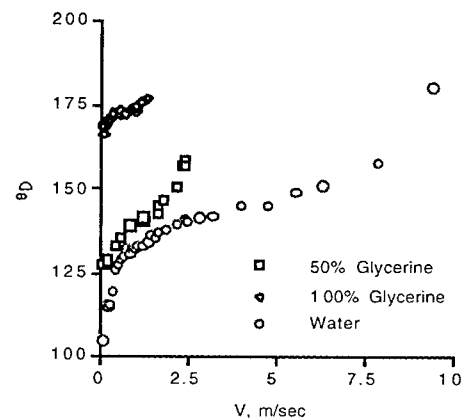


Figure 6. Dynamic Contact Angle vs. Speed

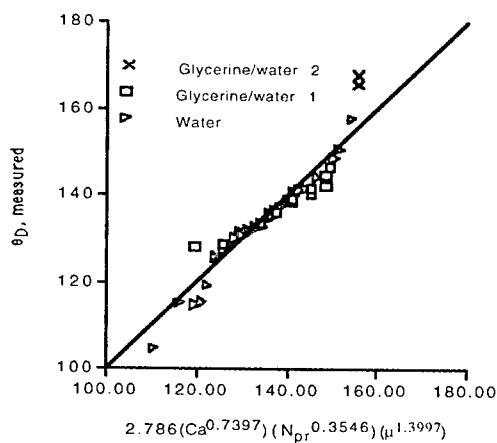


Figure 7. Correlation of the Dynamic Contact Angle Measurements



C.E. Polymeropoulos
Department of Mechanical and Aerospace Engineering
Rutgers University
97 Brett Road, Piscataway, NJ 08854-8058

Dr. Polymeropoulos is a professor of Mechanical Engineering at Rutgers and has been teaching and doing research in the general area of thermal processes.

EFFECT OF TEMPERATURE, STRAIN AND INSTALLATION ON PMD IN HIGH FIBER COUNT RIBBON CABLES

Shami S. Sodhi, Allen C. Gregory and Gary E. Grogan

Siecor, Hickory, North Carolina

ABSTRACT

Polarization mode dispersion (PMD) is an intramodal dispersion phenomenon that can limit the transmission distance and information carrying capacity of fiber. Over the past few years, several papers have been published on PMD of loose fiber cables¹ and a limited number of papers have been published on ribbon cables² (mainly slotted core ribbon cable design). This paper presents PMD measurements on high fiber count single tube ribbon cables using 12-fiber and 24-fiber ribbon designs. The effects of temperature and axial strain on PMD are examined, and PMD measurements on an installed cable are compared to initial fiber values.

Effect of temperature on a 216F ribbon cable

A 216F single tube cable sample using 12F ribbons was placed in a temperature chamber. The cable design is shown in Figure 1. The cable had a stack of 18 ribbons that were helically stranded. The fiber used was standard unshifted single mode fiber. Six out of 18 ribbons were concatenated (with corresponding fiber positions spliced to each other) resulting in twelve fiber links with six fibers per link. The cable was cycled through a temperature sequence of 23°C, -40°C, and +70°C. PMD measurements were performed on the above fiber links at these temperatures. The results are shown in Figure 2. PMD did not change significantly with temperature and the PMD quadrature average was less than 0.04 ps/√km at each of the above temperatures.

Effect of axial strain on a 216F ribbon cable

A different sample of the same cable was installed on a long length tensile tester. EIA-455 gives a general description of the tensile test

setup³. The same six "12F ribbons" were concatenated as before. PMD measurements were performed on these fiber links at various values of tensile load (up to a maximum load of 3007 N). The results are shown in Figure 3. PMD did not change significantly with increase in cable strain during the long length tensile test.

Effect of installation on a 432F ribbon cable

A 432F single tube cable using 24F ribbons in a duct installation was examined for PMD. The installed length was approximately 832 meters. The cable design is shown in Figure 4. The cable had a stack of 18 ribbons that were helically stranded. The cable consisted of standard unshifted single-mode fiber and non-zero dispersion shifted fiber with large effective area (LEAF[®] fiber). PMD was measured on several ribbons. The results are shown in Figure 5. The PMD quadrature average for both fiber types was less than 0.05 ps/√km. This was within reasonable agreement with the quadrature average calculated using the PMD of the input uncabled fibers (approximately 0.03 ps/√km).

CONCLUSION

The effects of temperature, strain and installation on the PMD of high fiber count single tube ribbon cables were examined. It was observed that for a 216F single tube ribbon cable using 12F ribbons, PMD did not change significantly with strain and temperature. PMD measurement on a duct installation of a 432F single tube ribbon cable using 24F ribbons resulted in a PMD quadrature average of less than 0.05 ps/√km. This was in close agreement to the quadrature average calculated using the input fiber PMD values of the uncabled fibers.

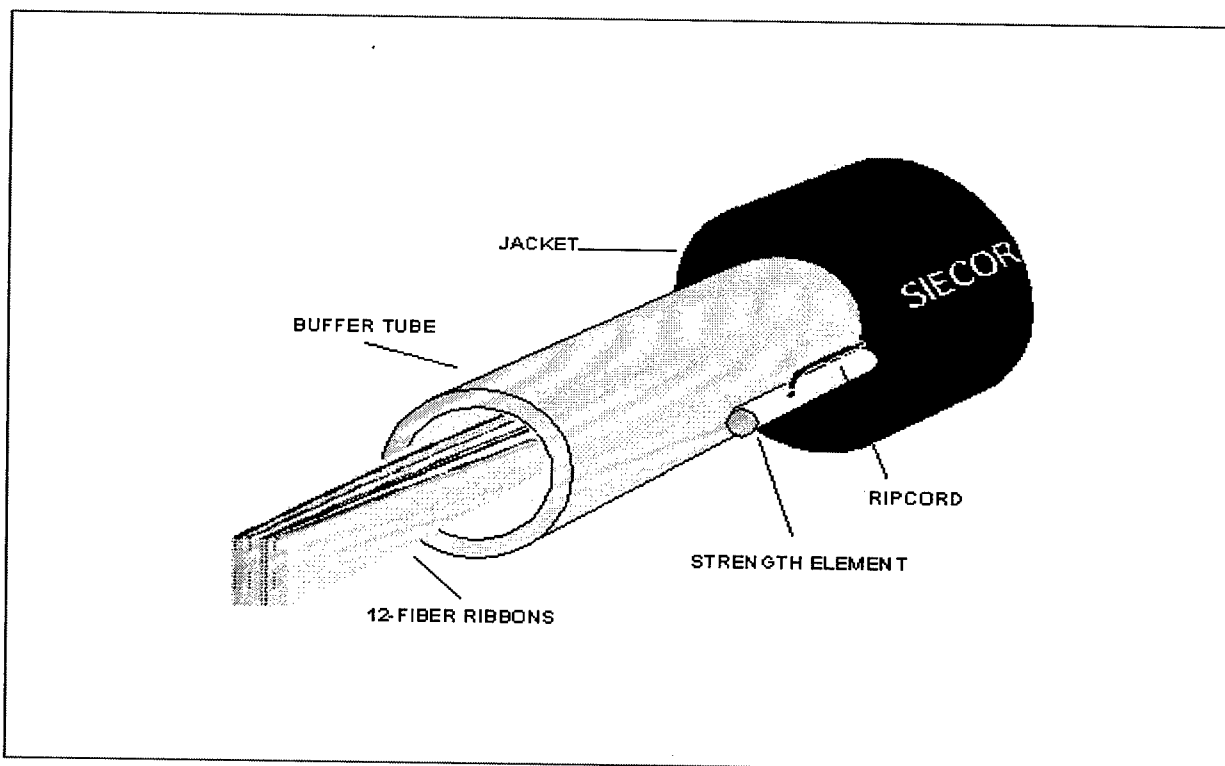


Figure 1. 216F Single Tube Ribbon Cable

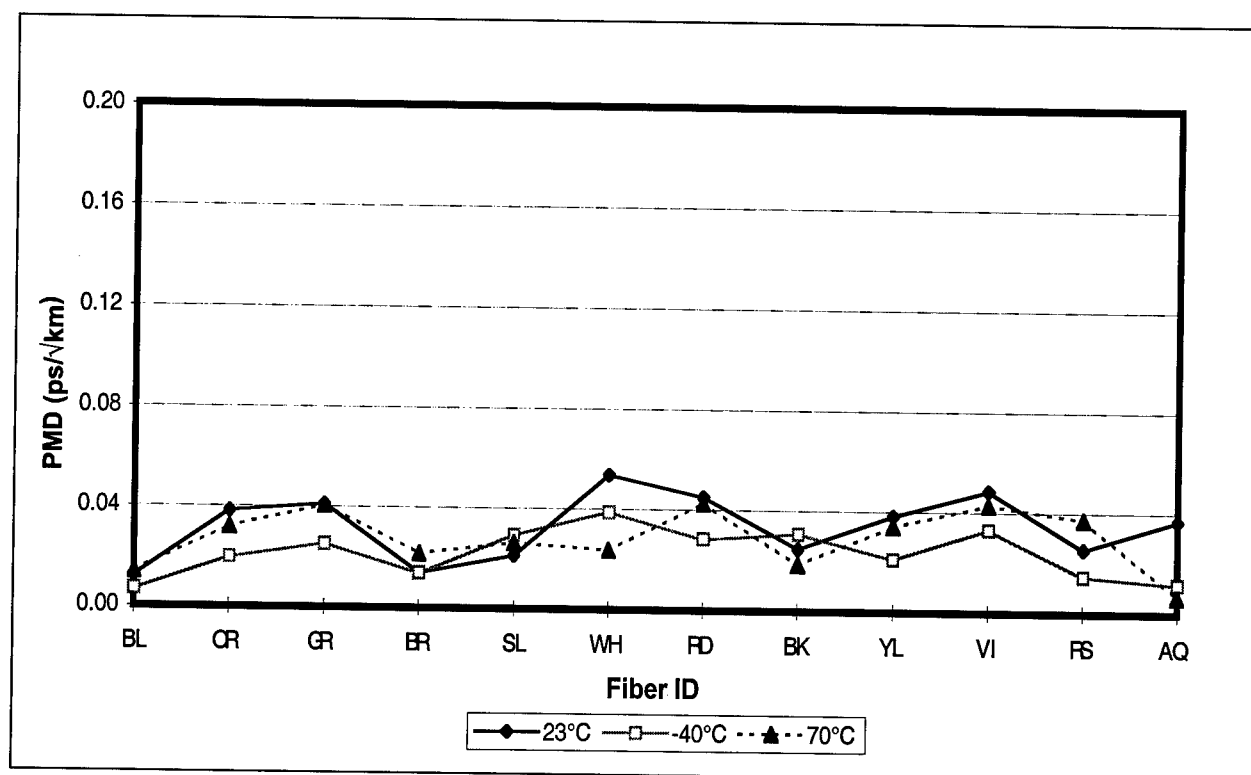


Figure 2. Effect of Temperature Cycling on PMD for a 216F Single Tube Ribbon Cable

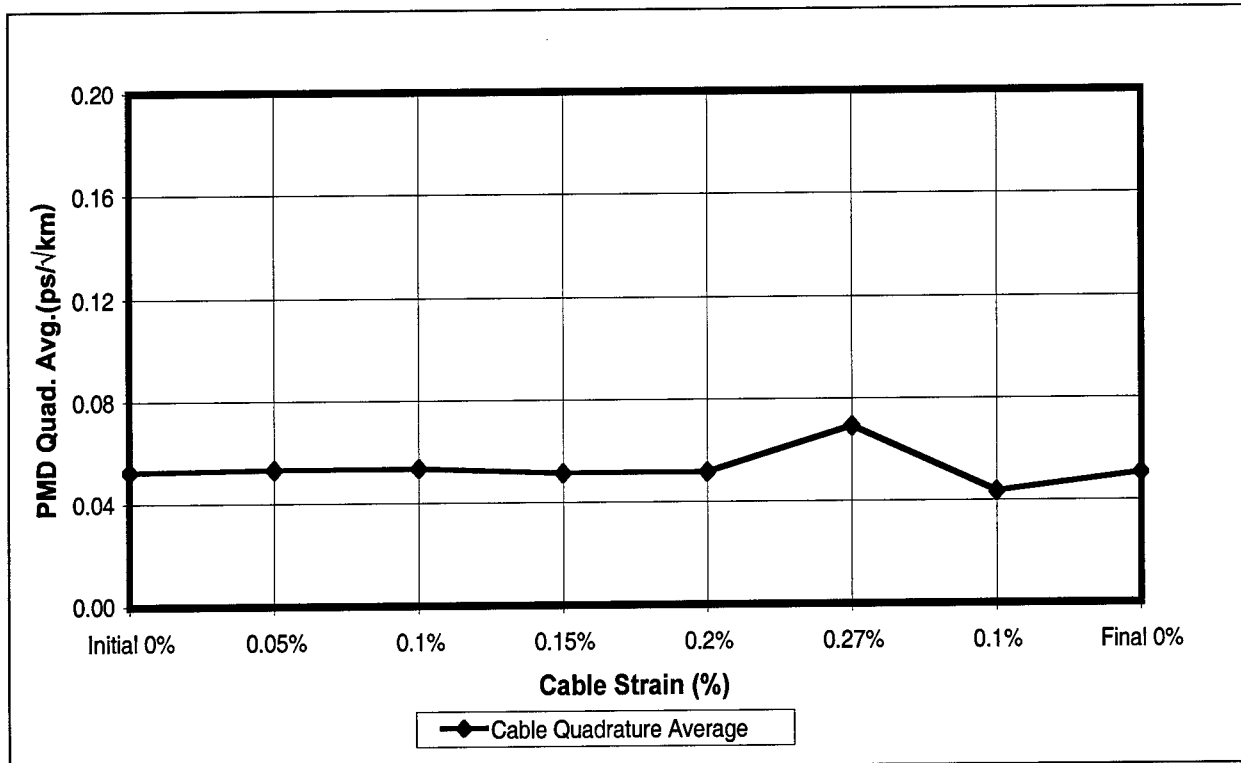


Figure 3. Effect of Strain on PMD for a 216F Single Tube Ribbon Cable

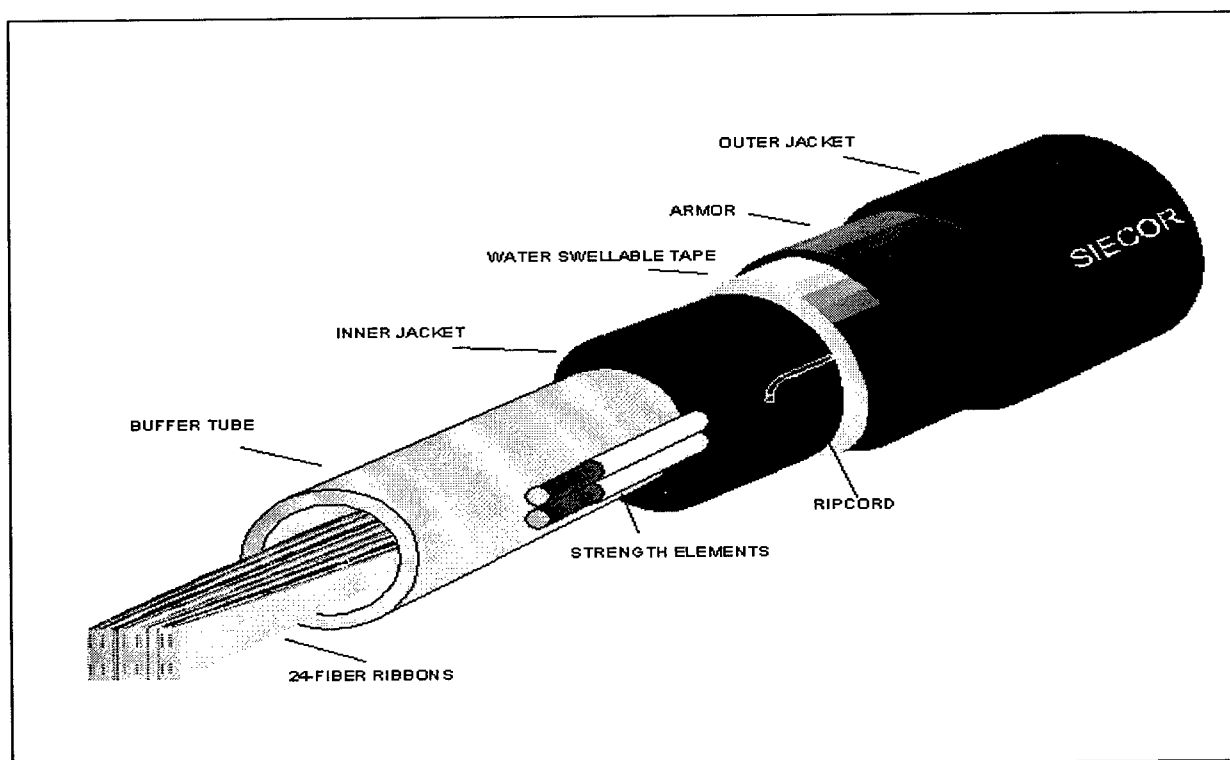


Figure 4. 432F Single Tube Ribbon Cable

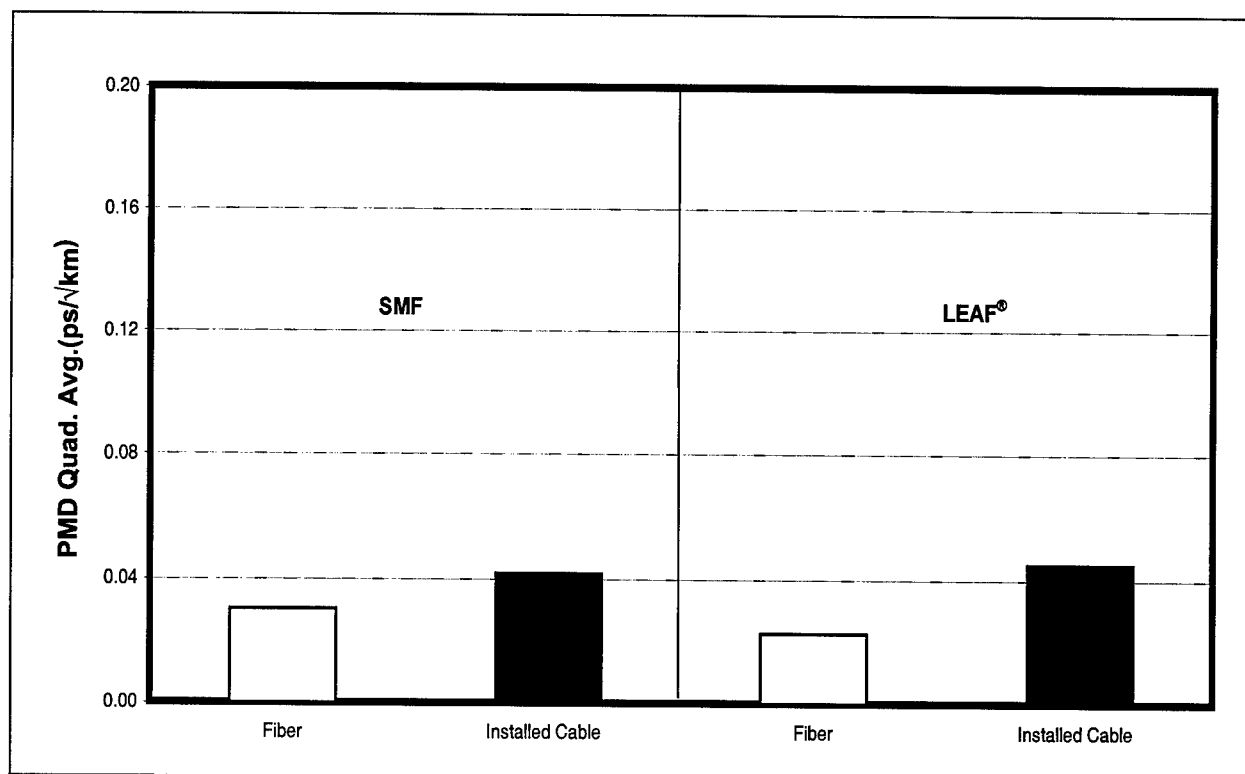
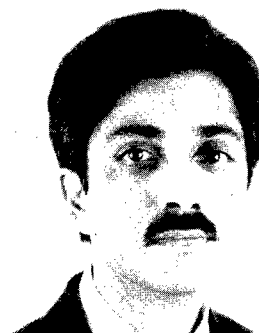


Figure 5. Effect of Installation on PMD for a 432F Single Tube Ribbon Cable

REFERENCES

1. A. Kapovits, "Measurement of Polarization Mode Dispersion in Installed Cables," OFMC 97, pp. 204-208.
2. A. Rossaro, P. Morra and M. Artiglia, "PMD Measurements performed on Installed Ribbon Cables," OFMC 97, pp. 118-121.
3. EIA-455-33A, "FOTP-33 Fiber Optic Tensile Cable Loading and Bending Test," 1988, Electronic Industries Association.



AUTHOR

Shami S. Sodhi
Siecor
P.O. Box 489
Hickory, NC 28603
USA

Shami S. Sodhi was born in Amritsar, India in 1964. He received his M.S. in Electrical Engineering from Virginia Polytechnic Institute and State University in 1989. Since 1989 he has been with Siecor in Hickory, N.C. and is presently Manager of Product Evaluation in the Research, Development and Engineering Department. He has authored and co-authored several papers and is a member of the IEEE.

RIBBON CROSS-SECTION MEASUREMENT METHODS COMPARISON

Gregory A. Mills and Ronald J. Speights

Siecor Operations LLC, Hickory NC

ABSTRACT:

Ribbon cross-sections are commonly used to check for ribbon dimensional tolerances of the pertinent geometric attributes. There are many methods used to measure ribbon cross-section parameters. We evaluated three of these methods with a focus on speed, ease of operation, repeatability, and expense. These methods involve different sample preparation and measurement procedures. The ones we chose are as follows:

Preparation methods:

1. Pot the ribbon in a curable resin and cut the sample with a diamond saw.
2. Cut the ribbon with a razor blade.
3. Hold the ribbon in a fixture, cut it with a diamond saw, and polish the ribbon.

Measurement methods:

1. Video Grey Scale Analysis (VGSA)
2. Digital computer imaging and analysis
3. Microscope and stage micrometer.

A full factorial experiment was used to compare these methods. The most repeatable method is a fully automated measurement system but the fastest and lowest cost method is to use a razor blade and microscope.

INTRODUCTION:

The fiber optic cable market has seen an increase in the use of ribbon cables due to the increased fiber packing density and reduced installation costs. For example, the diameter of a 432-fiber loose tube cable is approximately 24 mm and the diameter of a 432-fiber ribbon cable is approximately 20 mm. Lower installation cost is achieved by reducing the splicing time of a ribbon cable versus a loose tube cable with the same number of fibers by using mass fusion splicers.

There are two main issues relevant to ribbon splicing that need to be optimized. The first issue is the need to minimize the number of bad splices. Among other reasons, bad splices can be caused by fiber breaks and fibers not fusing together. The

second issue is the ability to achieve consistently low splice loss on all fibers in a ribbon. Tight dimensional tolerances on both the fibers and the ribbon are needed to achieve low splice loss and minimize bad splices.

A great deal of work has been done in the last 15 years to reduce the tolerance levels on fiber coating diameter, coating concentricity and core to cladding concentricity.¹ Currently, most single mode fiber manufacturers adhere to a core to cladding concentricity specification of less than 0.6 μm . This specification allows single fiber splices on single mode fiber to meet splice specifications of 0.05 dB average per cable. Since all the fibers in splicing a ribbon need to meet the same specification, the ribbon also has to meet tight dimensional specifications.

Additionally, the use of ribbon connectors needs to be considered. If a ribbon has poor geometry relative to fiber spacing and planarity, the fibers will not easily fit into the precise holes in the connector. A ribbon with poor geometry could cause problems such as fiber breaks or high attenuation depending on connector design and assemble procedure.

The specifications for ribbon geometry are identified for the industry in Bellcore GR-20 and ANSI/ICEA S-87-640-199 (draft). The pertinent geometric parameters identified by these documents are width, thickness, planarity, and extreme fiber distance (Figure 1).

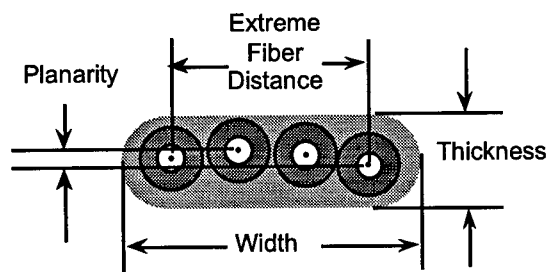


Figure 1: Ribbon Dimensions

This study will report work done in comparing three sample preparation methods to view ribbons cross-sections and three commercially available measurement methods.

EQUIPMENT & PROCEDURES:

Ribbon Sample Preparation Methods:

1) Pot and Cut

The ribbon sample is placed in a pre-made mold. A curable resin is poured over the ribbon. The resin can be heat curable, UV curable or an epoxy mix. The resin is allowed to cure and the sample is removed from the mold. A thin section is cut from the molded sample on a diamond saw. Depending on the resin selection, curing equipment and type of diamond saw, this method will cost in the range of \$10,000 to \$40,000.

2) Razor Blade Cut

The ribbon sample is placed on a plastic cutting board and the razor blade is pressed onto the top of the ribbon. The razor blade only cuts through the top half of the ribbon and scores the fibers. The ribbon sample is then broken in two. The material and equipment cost of this method is less than \$20.

3) Fixture Cut and Polish

A 1-2 meter ribbon sample is obtained and each end is inserted into a ribbon clip allowing 10-20 mm of ribbon to extend past the end of the clip. The ribbon clips are then placed into a precision holder for the cutting and polishing steps. The holder is clamped into a diamond saw and the ends of the ribbons cut. Next, the holder is placed on a polishing pad and the ends of the ribbons are polished. The cost of the materials and equipment is approximately \$30,000.

Caution: Safety should always be a major focus when preparing samples that involve using razor blades or any type of cutting equipment.

Ribbon Measurement Methods:

1) Video Grey Scale Analysis Bench (VGSA)

This method uses video gray scale analysis to find the center of the fiber cores and the outer ribbon edges. The sample is loaded into the VGSA bench, focused and aligned on the right-most core. Then "proceed" is clicked and the data is automatically calculated. The software optimizes lighting and performs a fine-focus before measuring each fiber. The VGSA measurement bench makes fully automated measurements of

planarity, ribbon height and width, and fiber spacing. A sample takes approximately 2-3 minutes to measure. The VGSA bench used in this study was developed by PK Technologies, Inc. The total cost of the bench range from \$70,000 to \$80,000.

2) Digital Computer Imaging

The ribbon sample is placed under a microscope and a digital camera and computer are used to capture and store the image. The operator manually picks points on the stored ribbon image. The data is then imported into a spreadsheet where ribbon width, thickness, planarity and extreme fiber distance are calculated from the coordinate data. The measurements take approximately 7 - 10 minutes. The microscope, digital camera and computer are commercially available and cost varies from \$15,000 to \$60,000 depending on manufacture and model. The software used in this study was NIH Image.²

3) Microscope Stage Micrometer

This method requires a microscope, a coordinate measurement system and a computer. The ribbon sample is placed under a microscope and focused. The sample is aligned using a rotary and X-Y stage. The operator manually picks points by moving the stage. Planarity, width, thickness and extreme fiber distance are then calculated from the coordinate data. It takes approximately 7 - 10 minutes to make these measurements and the total cost of a system could range from \$30,000 to \$70,000 depending on manufacture and model.

EXPERIMENT LAYOUT:

In order to compare the sample preparation methods and measurement methods, three experiments were run.

1) Full Factorial Comparison

The purpose of the first experiment was to make a visual comparison of how each sample preparation method performed with each measurement method. This was done in a full factorial experiment. Each combination was assigned a clarity rating of 1 - 5 depending on the clarity of the ribbon and fiber interfaces. The ability to locate the interfaces between coating layers and locate the fiber cores is critical when measuring ribbon dimensions.

2) Repeatability

In the second experiment, a repeatability study was performed to test the capabilities of the three measurement methods. Ribbon samples were measured multiple times for each measurement method to determine the measurement variability.

3) Operator Variance

In the third experiment three different people performed ribbon cross-section measurements on the same five ribbon samples to determine variation caused by testing operators.

RESULTS AND DISCUSSION:

Experiment 1 – Full Factorial Comparison

To determine which preparation and measurement method together give the clearest picture of the ribbon sample, a full-factorial experiment was run. In this experiment, we mismatched the cutting methods with the measurement methods and ranked their clarity on a scale of 1 – 5

- Clarity 1 All interfaces and/or fiber cores are easily distinguished.
Clarity 2 Most interfaces and/or fiber cores are easily distinguished.
Clarity 3 Some interfaces and/or fiber cores are easily distinguished.
Clarity 4 A few interfaces and/or fiber cores are easily distinguished.
Clarity 5 No interfaces and/or fiber cores are easily distinguished.

The best results were obtained with the Fixture Cut and Polish and the VGSA Measurement Bench. The razorblade also worked well with the VGSA Bench and Digital Imaging. The Pot and Cut Method with the VGSA measurement bench gave the worst results due to the software failing to find any of the fiber cores in the ribbon (Table 2).

Cutting Method	Measurement Method	Clarity Ranking (1 – 5)
Pot & Cut	VGSA Bench	5
Pot & Cut	Digital Image	4
Pot & Cut	Microscope	4
Razor Blade	VGSA Bench	2
Razor Blade	Digital Image	4
Razor Blade	Microscope	3
Fixture/Cut/Polish	VGSA Bench	1
Fixture/Cut/Polish	Digital Image	4
Fixture/Cut/Polish	Microscope	2

Table 1: Visual Clarity Comparison

Experiment 2 – Repeatability Study

To determine the repeatability of the three measurement methods, a detailed measurement capability study was performed. In this experiment, eight ribbons were measured thirty times each on each measurement method. After each measurement, the ribbon sample was removed from the measurement bench and replaced to simulate a new measurement. The pooled standard deviations were calculated for each measurement method (Table 2).

Ribbon Dimension	Measurement Method (All units are in μm)		
	Digital Image	VGSA	Microscope
Thickness	4.28	0.83	2.20
Width	4.81	1.02	6.20
Planarity	3.38	0.40	3.10
Average	4.16	0.75	3.83

Table 2: Pooled Standard Deviation of each Measurement Method

The digital image analysis yielded the highest variability. This variability is consistent across all three measurements and is associated with the digital image resolution and the clarity of edge interfaces. Thus a higher resolution image would yield lower variability, but this would increase the cost of a measurement system.

The microscope has lower average variation than the digital image, but only slightly. The thickness variation is about half the Digital image but the width variation is almost 50% higher. This is partly due to clarity of edge interfaced, but the high variability in the width is primarily related to rotational alignment of the ribbon sample on the microscope stage.

The VGSA method is by far the most repeatable of the three measurement methods. The average variation is less than 1 μm . The VGSA method is the method of choice if repeatability is a major concern.

Experiment 3 – Operator Variance Study

Operator variance is a concern in any measurement system. The desire is to have a system where variation induced by different operators is only a small part of the overall system variation. In order to quantify the effect of operator variation, an experiment was conducted using three operators to measure 5 ribbons, five times each. The pooled standard deviations for each of the three measurement methods are included below (Table 3).

Ribbon Dimension	Measurement Method (All units are in μm)		
	Digital Image	VGSA	Microscope
Thickness	8.47	0.73	1.2
Width	1.55	0.66	6.1
Planarity	1.75	0.06	2.9

Table 3: Pooled Operator Variance

The VGSA had the lowest deviations of all the measurement methods. This was achieved by eliminating the objective selection of the interface location, as in the other two methods.

CONCLUSIONS:

The lowest cost method for preparing a ribbon sample for a cross-section measurement is the razor blade method but the fixture/cut/polish yields the clearest cross-section on which to make dimensional measurements.

The most accurate and repeatable ribbon measurement system in this study is the VGSA Bench. This system minimizes both the ribbon measurement variation and variations due to operator.

ACKNOWLEDGEMENTS:

The authors would like to thank Jamie Sullivan, a co-op student working on her BS in chemical Engineering at Virginia Tech, for many hours of testing, data analysis and writing to make this paper possible.

We would also like to thank PK Technology for allowing us to evaluate their VGSA ribbon measurement bench in this study.

PRESENTOR:



Ronald J. Speights is a Process Development Technician in the Ribbon Development Group at Siecor RD&E in Hickory, NC. He has received an Associates degrees in Science – Pre-engineering as well as Arts/English. He also received a BS in Business Administration from Gardner-Webb University in 1996. He has been involved with ribbon products and UV processing since its earliest beginnings at Siecor. He has been in the RD&E organization since 1993.

¹ Colton, J.R. and Hallman, A.G., "Measurements on the uniformity of Fibre Cladding Geometry," Optical Fiber Measurement Conference, 1991 York, U.K., pp. 127 – 130.

² National Institute of Health Web Site
<http://rsb.info.nih.gov/nih-image/>

COMPUTATIONAL FLUID DYNAMICS (CFD) ANALYSIS OF RIBBON PROCESSING

Steven X. Shen

Alcatel Telecommunications Cable, OFCCC
Claremont, North Carolina, U.S.A.

ABSTRACT

An analysis was conducted to simulate the fluid dynamics within the ribbon coating polymer matrix applicator. The results of the analysis are used to verify and improve matrix flow conditions within the applicator. The technical approach was to use computer aided engineering techniques to simulate the matrix flow in the applicator cavity under various design geometries and operating conditions. The scope of the analysis concentrated on flow patterns at the center section of the applicator. A non-Newtonian viscosity model was developed and applied in this analysis. The model agreed well with the experimental data. The paper discusses various aspects regarding ribbon manufacturing to achieve superior ribbon quality, especially for the ribbon geometry, including: 1) Flow situation in the applicator chamber, 2) Pressure or centering/oscillating effects, and 3) Non-Newtonian 'Shear thinning' effect of the polymer matrix flow. The flow analysis was conducted by solving mass conservation, momentum conservation, and state equations simultaneously under an isothermal condition.

New applicator design concepts developed from this analysis are presented and discussed. The new design concepts incorporate the optimal flow situation based on the knowledge from this CFD analysis.

INTRODUCTION

General background

Optical fiber ribbons have become popular in various optical fiber cable designs for two primary reasons: 1) ribbonized optical fibers provide optimum packing density for compact cable dimensions, and 2) the organized ribbon structures enable high connectorization

efficiency, as many fibers can be spliced at the same time. One of the important requirements, among many others, for a high quality ribbon is to have controlled ribbon geometrical dimensions, such as planarity (P), height (H) and width (W) of the ribbon. These parameters are important in terms of obtaining low splicing loss for field applications and achieving high consistency in the design and manufacturing of optical fiber cables.

The key step in ribbon production is to apply the Ultra Violet (UV) curable resin coating onto a plurality of optical fibers, which are arranged in a parallel fashion, to form the ribbon. The matrix application die is the device used to perform this step of the process, and its quality directly affects final quality of the ribbon processed.

Ribbon process

The ribbon process is analogous to the coating process during optical fiber draw. Figure 1 shows a common ribbon coating process diagram. A plurality of optical fibers is arranged parallel to each other via the top sheave (1) and pass through the coating die (2). The coating matrix (UV curable acrylate) is applied to all the fibers while passing through the matrix applicator. The matrix-encapsulated fibers then pass through a series of UV lamps (3), where UV light cures the coating material. The individual optical fibers are now grouped and encapsulated. The finished ribbon is then taken-up on the reel (5) via the bottom sheave (4).

In addition to its grouping and identifying functionality, the ribbon coating provides extra protection to the optical fibers. The quality of the coating layer will also directly affect ribbon performance in the field applications, such as long term fiber/cable reliability as well as fiber accessibility and splice quality.

The focus of this analysis is to understand, verify and improve flow in the matrix

coating die design. The direct influence of the flow on the applicator die performance and eventually, on ribbon geometry will be assessed in the following terms:

- Flow in different die designs.
- Shear rate distribution and coating matrix viscosity change due to 'shearing thinning'
- Centering/oscillating force on ribbon due to coating fluid flow

The technical approach is to use computer aided engineering techniques to simulate the matrix flow in the applicator die cavity, with various die geometries and under different operating conditions.

The scope of the analysis concentrates on the 2D flow in the center cross section of the die cavity, which is perpendicular to the ribbon surface (Figure 2). Due to the symmetry only half of the die cavity will be modeled to make economic use of the computing resources. The "off center" case can be assessed by adjusting the gap between ribbon and die wall.

After the flow analysis, a set of new dies was designed to improve the quality of ribbon, especially the ribbon geometry. The new design incorporated the desired geometry configurations for producing high quality ribbon and optimal flow based on the flow analysis.

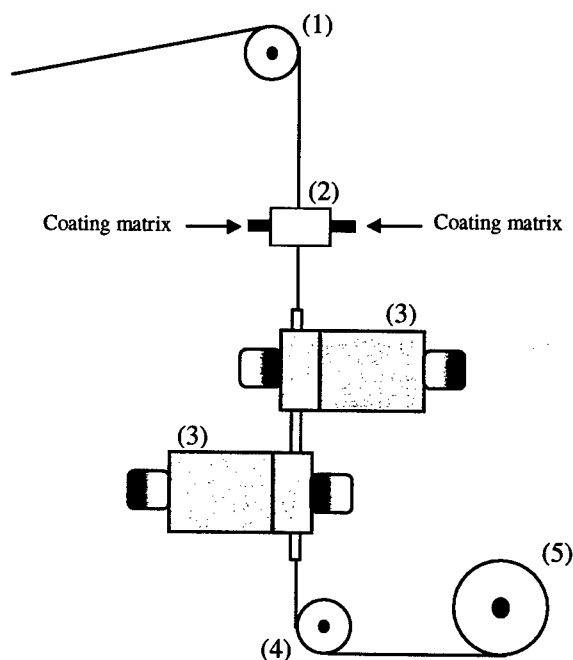


Figure 1. Schematic drawing depicts ribbon process.

ANALYSIS MODEL

Geometry

The flow field within the die is three-dimensional. This is particularly true in regard to the application of the acrylate along the edges of the 12-fiber ribbon. Nevertheless, the two dimensional (2-D) analysis presented here is an essential prerequisite to understand the flow in the three-dimensional dies.

The 2D-analysis model depicted in Figure 2 is a cross-section model well suited to predicting the application of the acrylate to the central region of the ribbon. A 2D model can be constructed and solved quickly. This means that a large set of 2D cases can be analyzed efficiently to evaluate the effects of changes in geometry and operating conditions. The payoff from the 2D analysis is substantial in terms of understanding the analysis process and the acrylate coating process.

The key geometry parameters are the coordinates of the vertices of the die cavity cross section. The other parameter (DB) is the thickness of the refinement of the model along the walls to capture boundary layer effects. The existing default values of the geometric parameters are set for the central cross section of the die design in Figure 2. Adjusting the distance between the fiber and the die walls simulates the off-center effects on the flow and the resulting pressure distributions. This is achieved by shifting the coordinate of X0.

Material properties

The viscosity is usually a function of temperature. A temperature independent value (nominal value) is specified and applied in different geometry cases (isothermal). The shear rate dependence of viscosity is applied only to the final optimal geometry to evaluate the shear-thinning effect on the flow in the double chamber die design. The nonlinear curve fitting from the experimental rheology data at ambient temperature is conducted to obtain the constants for the Carreau non-Newtonian viscosity model used in the flow analysis model¹. The Carreau model and four constants in the equation are given below (and Table 1 in next page):

$$\mu = \mu_{\infty} + (\mu_0 - \mu_{\infty}) \cdot [1 + (\lambda \cdot \theta)^2]^{\left(\frac{n-1}{2}\right)}$$

Table 1. Carreau model constants from nonlinear curve fitting

μ_0	μ_∞	λ	n
Nominal viscosity	Infinite shear viscosity	Time constant	Power constant
55	0.00001	0.000034	0.00003

The comparison between experimental rheology data and the data created by the Carreau model are plotted together in Figure 3. Good correlation is established.

The density of the matrix material is also treated as temperature and shear-rate independent for all the cases.

Applied Loading and Boundary Conditions

1. Die cavity wall

All velocity components of the acrylate matrix fluid are set to zero at the wall of the die cavity. This is a realistic no-slip boundary condition. The velocity parallel to the wall rises quickly across the boundary layer and special refinement is included in the model to represent this effect.

2. Matrix feed inlet

A uniform pressure is specified at the matrix feed inlet. Supposing a fully developed flow condition, a uniform pressure is judged to be permissible because the matrix feed inlet is sufficiently remote from the fibers. Also, the magnitude of the feed pressure is relatively small compared to the pressure build-up near fibers due to the high fluid speed.

When pressure is specified, velocity components exist as degrees of freedom to be determined. The degrees of freedom for kinetic energy and kinetic energy dissipation rate are not specified.

3. Fiber inlet

No flow is expected at the fiber inlet; neither gas entrainment nor matrix fluid leakage allowed. The pressure is also known to be atmospheric. The pressure boundary condition is specified at the fiber inlet. Review of the results indicates that the associated flow condition is sensitive to the fiber speed.

4. Fiber outlet

The velocity at the ribbon outlet varies from the speed of the fiber to zero at the die cavity wall. The boundary condition is specified best as a pressure condition (atmospheric

pressure).

5. Fiber contact boundary

The fiber contact boundary is a moving wall. The normal component of matrix fluid velocity is set to zero. The tangent velocity component of matrix fluid velocity is set equal to the speed of the fiber. In calculation, the kinetic energy degree of freedom is not set internally using the conventional formula for inlets and/or outlets.

6. Solution Procedures

The regime for this flow model is Non-Newtonian, steady state, laminar and incompressible. The fluid domain is fixed, *i.e.*, there are no free surfaces. All inlets and outlets are specified to be pressure boundary conditions. The flow regime is determined by calculating Mach number and generalized Reynolds number² for the acrylate matrix fluid. The energy equation is not solved as all the cases run in this study were isothermal.

A computational fluid dynamics (CFD) software is used to analyze the matrix die flow. Two-dimensional quadrilateral finite elements are applied. Isothermal conditions are assumed for all the cases. Turbulence kinetic energy and kinetic dissipation rate are not calculated due to the laminar flow regime. The convergence criteria are set such that all components of velocity and the pressure norms are less than 0.0005.

RESULTS

Many cases have been studied for the effect of die geometry changes and different process conditions (matrix feeding pressure, fiber draw speed, etc.). For brevity, only the flow situation in a double chamber die is presented in this section.

Flow situation in the new design geometry for the double chamber die

Figure 4 is the 2-D velocity streamline function plot. It is clear that a single vortex forms in each of the chambers due to the

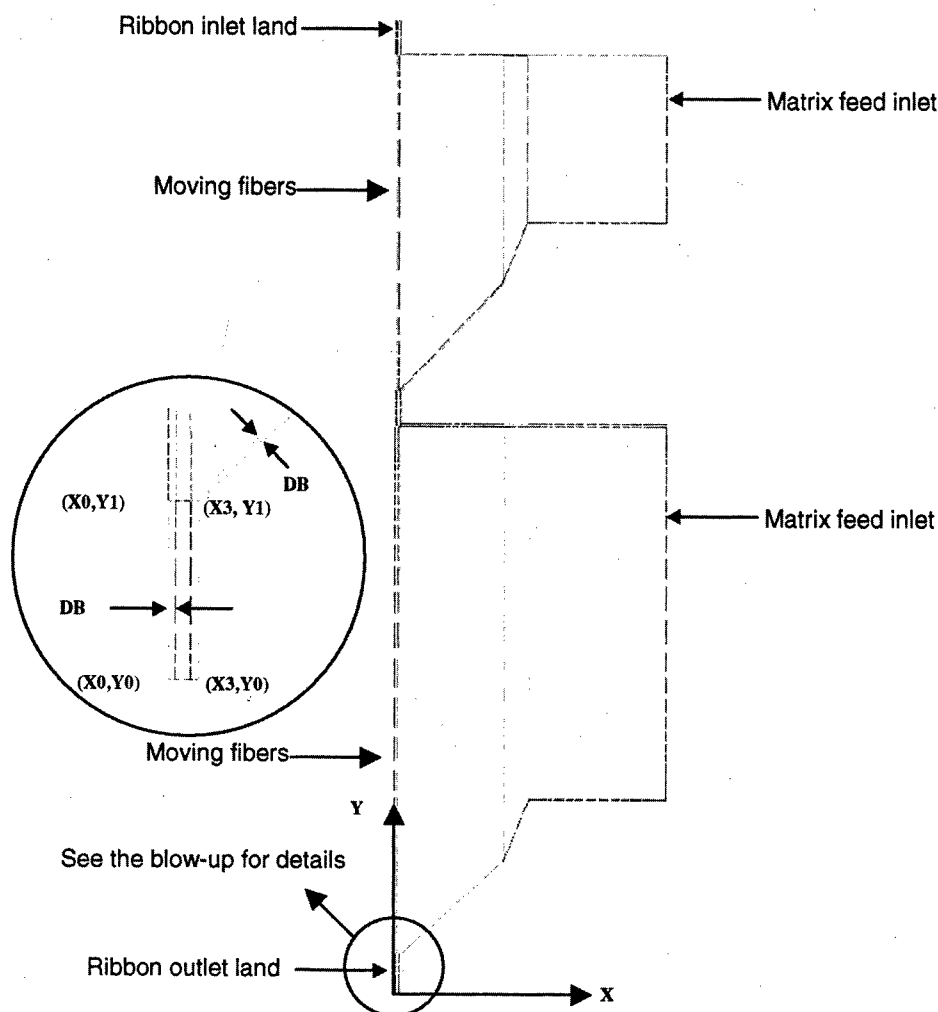


Figure 2. 2D-model geometry plot showing coordinates.

shearing of the fast moving fiber. The vortex in the upper chamber is smaller but rotates faster than that in the lower chamber. This is a direct result from momentum/mass conservation.

The flow is fully developed in the land regions (narrow outlet) and the pressure contour becomes flat. This result is consistent with a previous study³, in which the longer land model did not alternate the pressure profile. Figure 5 shows velocity vectors and pressure contour lines in the exit nozzle.

Generally, the flow situation in the double chamber die follows that of a single chamber, being laminar flow with one vortex in the cavity of each chamber. The flow in three narrow regions is fully developed laminar flow.

Rheology of the acrylate matrix and its effect

Figure 6 depicts the viscosity distribution in the narrow die exit region. This narrow exit region exhibited severe shear-thinning effects resulting in low fluid viscosity. The majority of fluid in the middle of the die chambers away from the stationary die-walls showed little viscosity changes. Again, this result is not surprising because the highest shearing rates are at the inlet/outlet regions.

A comparison of the flow situation in the narrow exit regions is shown in Figure 7. Comparisons of pressure distributions along the fiber between non-Newtonian and Newtonian

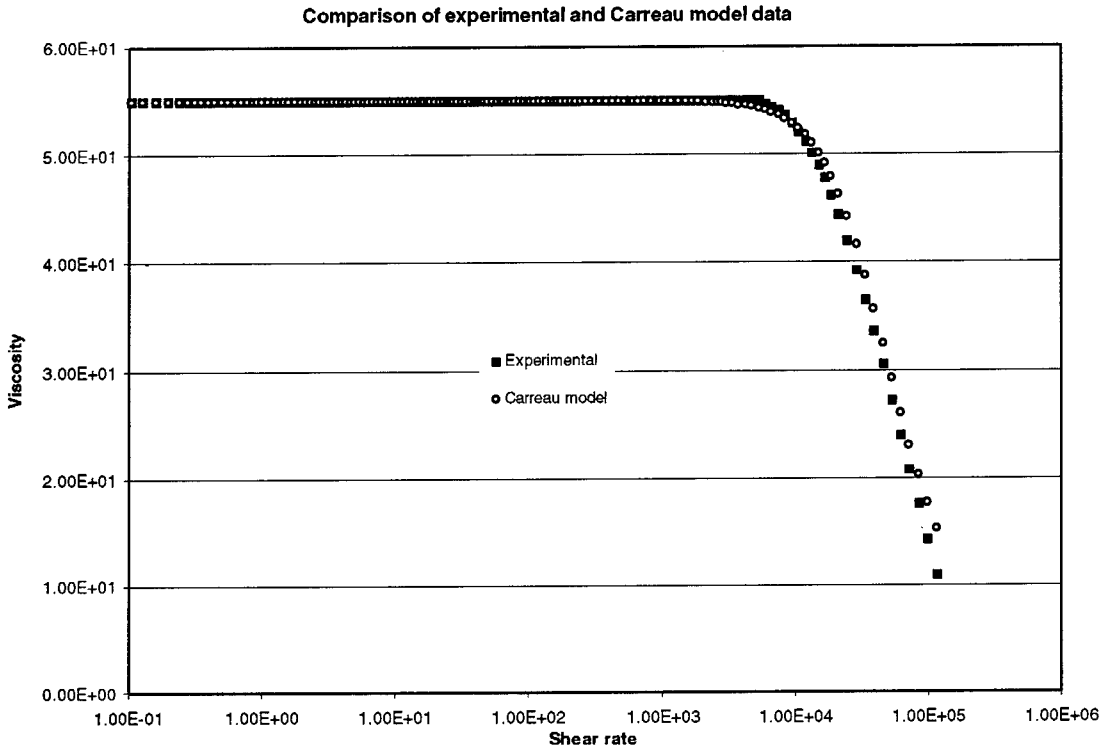


Figure 3. Comparison of experimental and Carreau model data

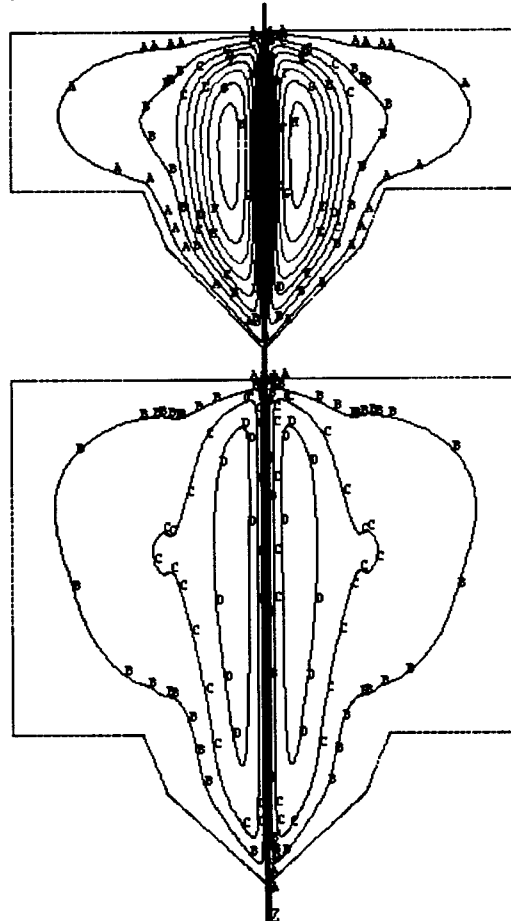


Figure 4. The plot of the 2-D stream function to show vortices in the double die chambers.

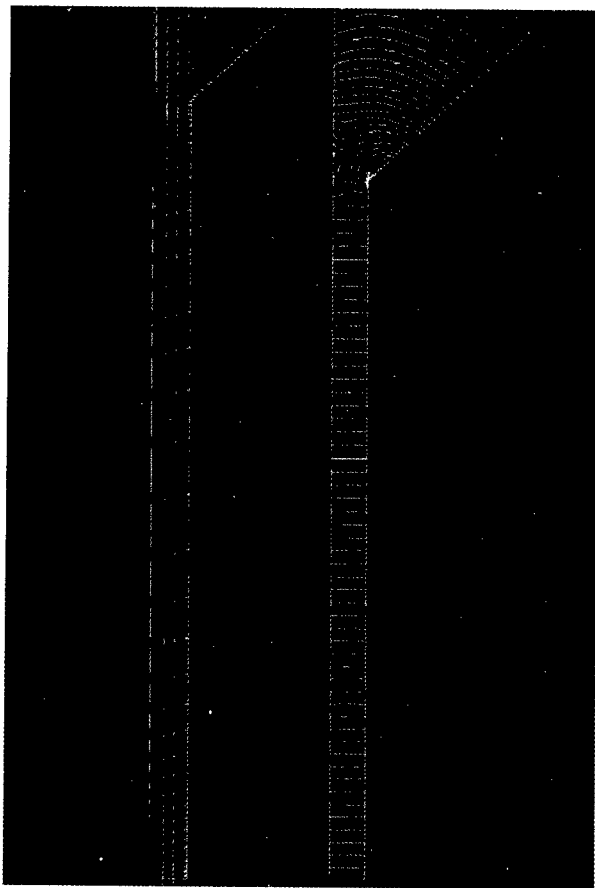


Figure 5. The velocity sum vector and pressure contour plots near exit region.

flow are given in Figure 8. The pressure spikes at the starting and ending location of each narrow land region is reduced and smoothed out. Also the axial (Y, parallel to the fiber drawing) direction velocity drop in narrow land region is reduced comparing to the case of constant viscosity fluid.

The effect of the shear thinning of the acrylate material reduces the friction between matrix and static die-walls, and thus, decreases the boundary layer thickness. As a result, more acrylate will flow at the fiber drawing speed around fibers and go through the narrow exit region more easily. This is beneficial to the coating process.

On the other hand, however, the rheology of polymer matrix can be a source of instability and cause vibration of fibers or even turbulence fluid flow, which is detrimental to the ribbon process. In any case, the effects of matrix shear thinning warrant more detailed analysis.

The fiber "off-center" effect on the matrix flow fields

The situation of fiber misalignment or "imperfect" condition is simulated by adjusting the ribbon or "moving wall" toward or away from the die walls. It is equivalent to an increase or decrease of the gap between fiber and the exit land. From study of the differences among these cases, the effect of fiber "off-center" on matrix flow can be demonstrated.

Figure 9 is the distribution of axial flow velocity (Y) component along the fiber, within a close vicinity of the fiber. Generally, the wider the gap, the better flow follows the fiber.

The pressure difference between different cases (fiber "off-center" positions) is shown in Figure 10. The differential pressure (differences between each fiber "off-center" position) represents the centering force acting on the fiber when fiber shifting to off-center positions. This centering or balancing force increases sharply with the off-center distance. From the process point of view, it helps to keep the fiber in the center of the coating die exit.

Ribbon trials

Based on the CFD analysis results, new dies were designed to obtain optimal flow and process conditions. Figure 11 shows superior ribbon geometry control with the new die design.

DISCUSSION

It is reasonable to assume that the velocity field of matrix flow near the fiber outlet is most important to the ribbon coating process in terms of coating quality. The best processing condition would be to have constant flow velocity which equals to the fiber draw speed within the narrow land region. The thicker the layer of flow with the velocity equal to the fiber draw speed, the better to the coating process. This observation needs to be verified through experiments. The pressure at the inlet land region alters from negative to positive as the gap between the fiber and inlet land increases. With large negative pressure air tends to be drawn into the die chamber following the fiber movement. In this case, bubbles will be created in the matrix.

It needs to be pointed out that the free surfaces formed between fiber and die inlet/exit

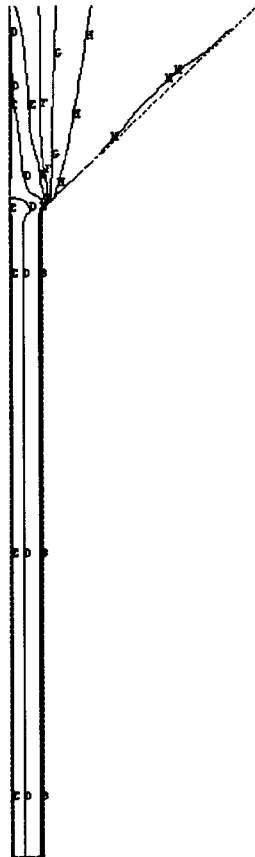


Figure 6. The viscosity distribution contour plot near exit land region.

land can move up and down in reality. This free surface movement may change the matrix flow pressure distribution completely.

The natural step for future analysis work is to develop a material model, which incorporates transport property dependency on local temperature as well as on local shear-rate. In order to study the air entrapment and its impact, detailed formulation of boundary conditions at fiber inlet/outlet, including free coating matrix-air surface meniscus, need to be developed. Some non-equilibrium (transient) phenomena associated with the process may need to be investigated to assess startup impact on process. More experimental data will also be collected to help fine-tune numerical model and to verify theoretical analysis results. The final goal will be to systematically apply CFD analysis results in design and process to reduce development cycle time and physical prototype cost.

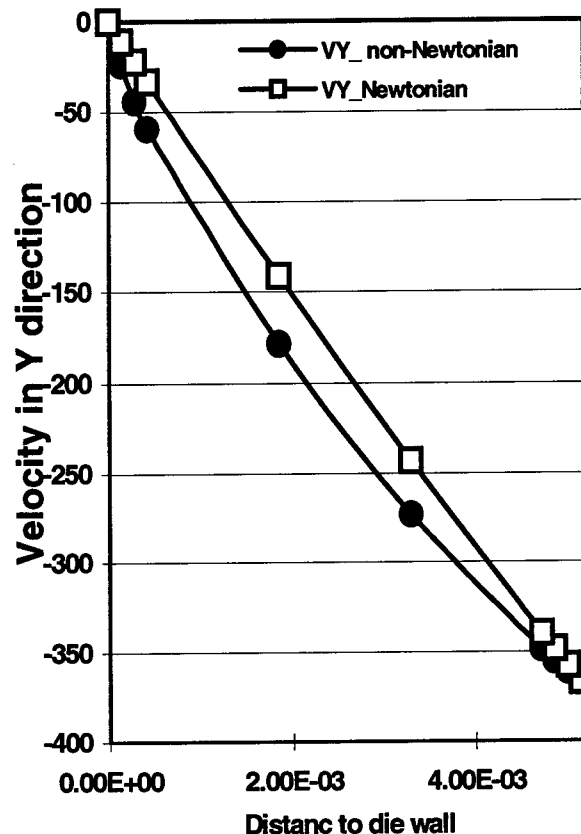


Figure 7. The Y component of flow velocity comparison between two regimes, Newtonian "□" vs. non-Newtonian "●".

CONCLUDING REMARKS

The flow situation in the double chamber die design follows that of a single chamber die, *i.e.*, one vortex in each chamber with fully developed laminar flow in the narrow exit regions.

The back flow in upper smaller chamber is faster than that in the lower large chamber due to the combination of fiber shear and momentum/mass conservation. The back flow forms a single vortex in the chamber and provides mixing for the fluid. The mixing is beneficial in terms of smoothing temperature fluctuations in the matrix.

The shear thinning of the acrylate occurs during the ribbon process. The pressure difference or the normal force acting on the fiber generated due to the matrix shear thinning is negligible in comparison with the fiber tension.

As a result of the shear thinning of the

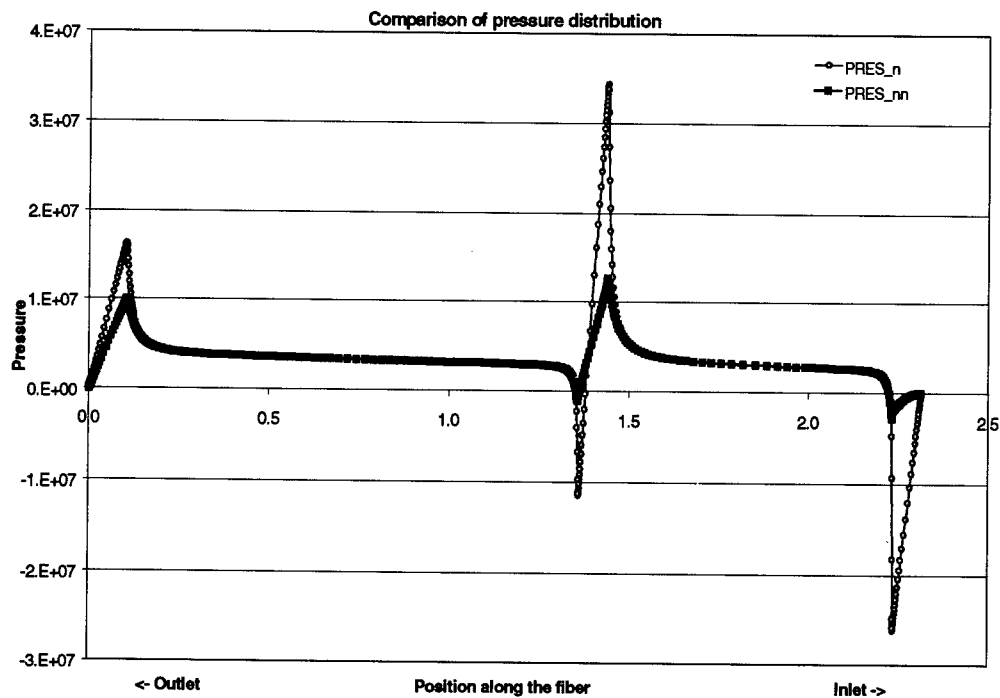


Figure 8. The comparison of pressure distribution along fibers.

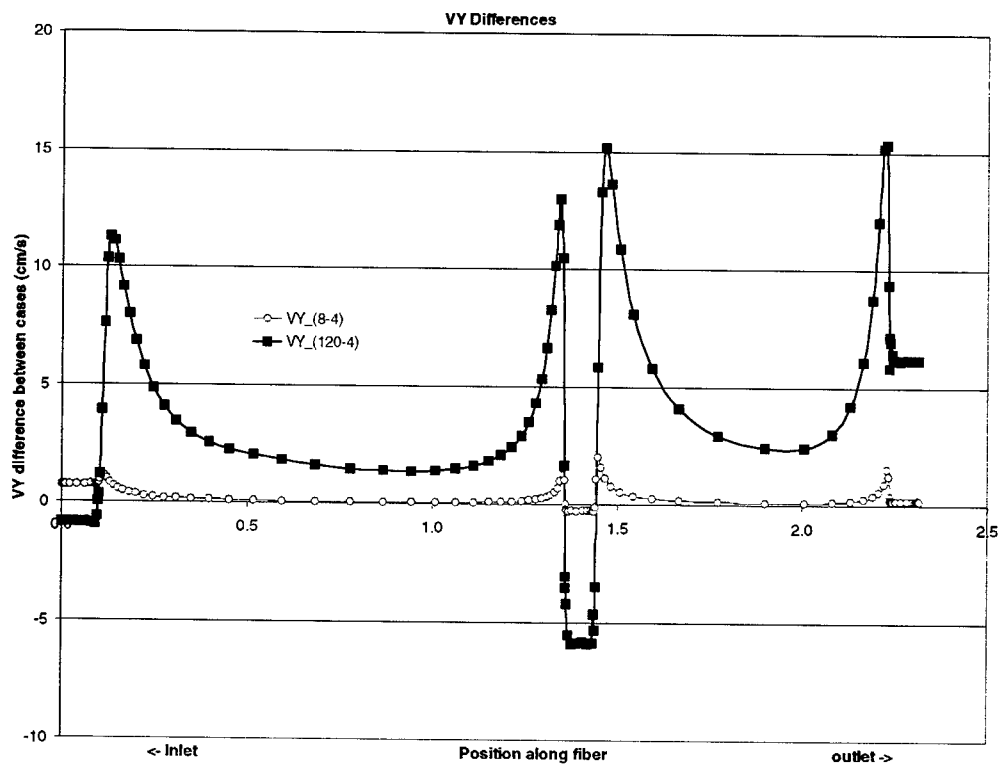


Figure 9. The distribution of flow velocity, which is parallel to fiber moving direction at different fiber "off-center" positions.

acrylate, the flow with speed following that of the fiber penetrates more into the bulk of the fluid. It is considered as beneficial to the coating process.

The pressure builds up at the exit location of each chamber. The high-pressure buildups at those locations create a centering force on the fiber. This centering force helps to self-align the fibers when they are off the centerline of the coating-die.

The pressure buildup and the flow velocity near the narrow exit regions (entrance, middle alignment and exit) are several orders higher than those at the matrix feed inlets. Comparing to the moving fiber speed and its shear effect on the matrix fluid, the matrix feed pressure and its location have very little influence on the whole flow field.

Finally, superior ribbon geometry control is achieved through applying the knowledge obtained from CFD simulation and analysis to new die designs.

REFERENCES

- ¹ ANSYS FLOTRAN Theoretical manual. ANSYS Inc. (1997).
- ² Metzner, A. B. and J.C. Reed, *Am. Inst. Chem. Eng. J.*, 1, 434 (1955).
- ³ S.X. Shen, *Matrix Die Flow Analysis, 2-D cross Section Examples*, MTI-TR-923, Mallett Technology, Incorporated, (1997).

ACKNOWLEDGEMENT

The author would like to thank Jeff Barker, Pierre Gaillard, Curt Hutton, Boyet Stevens, Pete Stupak and many others for their constructive criticisms, suggestions and comments, which made this paper more complete. The cooperation from the material development group and ribbon business unit during the experiment made this paper possible.

AUTHOR



Steven X Shen

2512 Penny Road, P.O. BOX 39
Claremont, North Carolina 28610
steve.shen@cable.alcatel.com

Steven X Shen received his Ph.D. from Vanderbilt University in 1995. He is a senior development engineer in the Optical Fiber Cable Competence Center of Alcatel. His research interests focus on new optical fiber cable designs and developments, and promoting computer aided engineering (CAE) solutions.

APPLICATION OF MONTE CARLO SIMULATION TECHNIQUES TO OPTICAL FIBER COMMUNICATION LINK MODELS

J. David Schell

3M Telecom Systems Division, Austin, Texas

ABSTRACT

Standards bodies typically model network links using worst-case link models in their standardization efforts. While these efforts have been exemplary, the worst-case model does not foster an understanding of the expected link performance or how tradeoffs of component specifications may increase link performance. Thus, limiting the network designer's choices in link implementations. A unique approach to this problem, providing a better understanding of the link performance, may be obtained by applying Monte Carlo simulation methods to the link models. To demonstrate the usefulness of this link modeling method, test results have been compiled to produce the necessary real world distributions as input to the simulation. The results of the simulation allow one to analyze the resultant link distance and power penalty probability distributions. One may then choose a confidence level required for the link performance as opposed to resorting to the worst-case scenario. Optimization of each component's key parameters may also be examined when utilizing this technique.

INTRODUCTION

The erupting demand for higher data rates at greater distances creates a unique opportunity for increasing the deployment of optical fiber for premises wiring. In particular, complete optical fiber network solutions allow for the seamless integration of network electronics, optical fiber cabling, and optical fiber interconnects. It is imperative that these optical fiber networks conform to published standards so that interoperability is maintained. One shortcoming of complying with these standards is the link distance limitations. These limitations originate from the worst-case link modeling efforts of the standards bodies. While these efforts have been exemplary, as demonstrated by the success of networking in general, the worst-case model does not foster an understanding of the

expected link performance or how tradeoffs of component specifications may increase link performance. It is not the intent of this paper to dispute the worst-case modeling philosophy in developing a standard. This philosophy has demonstrated its worth over the years by the number of successfully deployed network nodes. Rather, it is the intent to provide the network designer an alternative tool to examine link distance limitations and increase the link distance while maintaining a quantitative confidence that the link will perform as expected.

A unique approach to the worst case modeling, that also provides a better understanding of the link performance, may be obtained by applying Monte Carlo simulation methods to the link models. A Monte Carlo simulation may be utilized to better represent "real world" scenarios by allowing the network designer to use the actual probability distribution of each component's key parameters in the model. In the past, Monte Carlo simulations have typically been complex, expensive, and time consuming. However, with today's desktop computing power and inexpensive simulation software for spreadsheet modeling, simple, cost-effective and efficient Monte Carlo simulations are realizable.

The augmentation of Monte Carlo techniques to optical fiber communication link models allows the system designer to better understand the system performance and component tradeoffs. This paper reiterates the model utilized in the Gigabit Ethernet standardization effort and examines how the Monte Carlo simulation is layered onto the existing model. Simulation results, utilizing laboratory data, are presented and used to illustrate the usefulness of these techniques.

LINK MODEL

The IEEE 802.3z committee used the Gigabit Ethernet optical link model to validate the

standard's specifications. This model was developed within the optical PMD task force of 802.3z and contains the work of the task force's members and previous modeling efforts^{1,2,3,4,5,6}. Cunningham et al were the first to describe the model⁷. The first public description of the model is found in Cunningham's book⁸. This paper will not attempt to describe the model in all its detail, but will describe the key concepts and equations of the model.

The Gigabit Ethernet optical link model is based on optical power budgeting and can be described by the power margin

$$P_{margin} = P_{budget} - P_{penalties} \quad (1)$$

Where P_{budget} is the difference between the transmitter's output and the receiver's maximum sensitivity, and $P_{penalties}$ are the link power penalties

$$P_{penalties} = P_{ISI} + P_e + P_{eye} + P_{mn} + P_{RIN} + P_{mpn} + P_{attn} + P_{con} \quad (2)$$

These power penalties will be defined in the following discussion. All are described in units of dB.

The inter-symbol interference penalty (P_{ISI}) is the penalty that arises from bandwidth limitations of the link elements. Specifically, it is the reduction of the signal's modulation depth due to the spreading of the signal's pulses into the adjacent bit period's time window. P_{ISI} is determined by the baud period (T) and the channel exit response time (T_c) as described by

$$P_{ISI} = -10 \log \left\{ 1 - 1.425 \exp \left[-1.28 \left(\frac{T}{T_c} \right)^2 \right] \right\}^{-1} \quad (3)$$

The channel exit response time is the rise time for the analog output of the optical receiver as controlled by input signal to the receiver (T_e) and the receiver's own bandwidth (BW_r).

$$T_c^2 = T_e^2 + T_r^2 \quad (4)$$

Where T_r is related to the receiver's 3 dB electrical bandwidth by

$$T_r = \frac{0.35}{BW_r} \quad (5)$$

(Note that the 10-90% rise time is equivalent to 1.518 times the 20-80% rise time)

T_e is actually the optical fiber's exit response time as influenced by the laser's response time (T_L) and the 3-dB optical modal and chromatic bandwidths of the optical fiber (BW_m , BW_{ch})

$$T_e^2 = T_L^2 + \left(\frac{0.48}{BW_m} \right)^2 + \left(\frac{0.48}{BW_{ch}} \right)^2 \quad (6)$$

where

$$BW_{ch} (MHz) = \frac{441 \times 10^3}{L \cdot \lambda_{FWHM}} (D_1^2 + D_2^2)^{-1/2} \quad (7)$$

$$D_1 = \frac{S_0 \cdot \lambda_c}{4} \left[1 - \left(\frac{\lambda_0}{\lambda_c} \right)^4 \right] \quad (8)$$

$$D_2 = 0.3 \cdot S_0 \cdot \lambda_{FWHM} \quad (9)$$

and the transmitter rms spectral width is given by⁹

$$\lambda_\sigma = \frac{\lambda_{FWHM}}{2.355} \quad (10)$$

L (km) is the link distance, λ_{FWHM} (nm) is the transmitter spectral width at full width half max, λ_0 (nm) is the fiber's zero dispersion wavelength, λ_c (nm) is the transmitter's center wavelength, and S_0 (ps/km.nm²) is the fiber's dispersion slope at λ_0 .

The power penalty obtained from transmitting some amount of power, other than zero, during the "0" bit times is the extinction ratio power penalty (P_e). Because this penalty is included in the receiver's sensitivity measurements, P_e is set to zero in the model.

The receiver's eye opening penalty is determined by the required minimum eye opening (T_{eye}) for clock recovery, and the baud period (T). Deterministic and random jitter of the signal cause horizontal (time) eye closure.

When the sensitivity is measured at the center of the eye, the receiver may achieve the required bit error rate (BER) even with a nearly closed eye (horizontally). However, the clock recovery circuit has some amount of error, or jitter, in its sampling time that will cause a high BER in the above scenario. As a result, the receiver's eye must be opened to accommodate the clock recovery's jitter. To accomplish this opening of the eye, more power must be present at the input of the receiver, resulting in a power penalty. This is essentially a jitter power penalty and is given by

$$P_{eye} = -10 \log \left\{ \frac{2 \sin \left[\pi \left(\frac{T_{eye}}{T} \right) \right]}{\pi \left(\frac{T_{eye}}{T} \right) \left[1 - \left(\frac{T_{eye}}{T} \right)^2 \right]} - 1 \right\} \quad (11)$$

The power fluctuations between laser modes lead to an additional chromatic dispersion power penalty known as the mode partition noise penalty (P_{mpn}).

$$P_{mpn} = -10 \log \left\{ \left[1 - (Q \cdot \sigma_{mpn})^2 \right]^{1/2} \right\} \quad (12)$$

where Q is the digital signal to noise ratio as determined by

$$BER = \frac{1}{Q\sqrt{2\pi}} \cdot \exp \left(-\frac{Q^2}{2} \right) \quad (13)$$

and σ_{mpn} is the rms value of the mode partition noise as determined by

$$\sigma_{mpn} = \frac{k}{\sqrt{2}} \left\{ 1 - \exp \left[-\left(\frac{\pi \cdot D_1 \cdot L \cdot \lambda_\sigma}{T} \right)^2 \right] \right\} \quad (14)$$

Where T is the baud period and k is the mode partitioning factor ($0 < k < 1$).

Relative intensity noise (RIN) is the natural noise profile of the laser. RIN stems from the amplified spontaneous emission in the laser's cavity and is defined as the ratio of mean square noise intensity to the mean intensity of the laser's output. The power penalty due to RIN is

determined by Q , as previously defined, and the rms noise due to RIN (σ_{RIN}), and is given by

$$P_{RIN} = -10 \log \left\{ \left[1 - (Q \cdot \sigma_{RIN})^2 \right]^{1/2} \right\} \quad (15)$$

$$\sigma_{RIN}^2 = \alpha \left(\frac{0.48}{T_c} \right) 10^{RIN/10} \quad (16)$$

and RIN is the laser RIN in dB/Hz and α is equal to 0.7 and 0.6 for 1000BASE-LX and 1000BASE-SX respectively.

Modal noise is the intensity fluctuation of the signal exiting the fiber that is caused by the interference of different modes within the fiber. The interference is caused by mode selective loss generally due to fiber couplings. The power penalty associated with modal noise (P_{MN}) is quite complex, and beyond the scope of this paper. The 802.3z committee chose to statically set P_{MN} within the model, for each type of link specified in the standard. These values were determined from the work of Bates et al⁵, and the empirical observation of the committee.

The cabled optical fiber attenuates the signal in a manner that is proportional to the link distance (L) and inversely proportional to the transmitter's center wavelength (λ_c) as given by

$$P_{attn} = L \cdot \frac{R_\lambda}{C_\lambda} \left[\frac{1.28}{10^{-12} \cdot \lambda_c^4} + 1.05 \right] \quad (17)$$

Where R_λ is the actual cable attenuation (dB/km) (at 850 or 1300 nm) and C_λ is a scaling factor that equals 3.5 or 1.5 for 1000BASE-SX and 1000BASE-LX respectively. This equation takes into account the fact that the cable attenuation is usually specified at 850nm, 1300nm, or 1310 nm (for single mode) while the standards allow the transmitter's center wavelength to vary over a window of ~90 nm.

Each optical fiber interconnect will cause some amount of optical power loss. The 802.3z committee set the interconnect power penalty (loss) to a static worst case value of 1.5 dB in the link model. The network designer may find it more useful to vary the number of connections within any given length. Additionally, the designer may wish to evaluate the link with

interconnect solutions from different vendors, resulting in different penalties. One method to address this need is to perform a statistical analysis of the interconnect losses. Thus the interconnect power penalty (P_{con}) may be described by¹⁰

$$P_{con} = \mu_c n_c + 2\sqrt{\sigma_c^2 n_c} \quad (18)$$

Where μ_c is the mean interconnect loss in dB, σ_c is the interconnect loss standard deviation in dB, and n_c is the number of connectors in the link.

While not explicitly defined as a separate power penalty, duty cycle distortion (DCD) may be accounted for in the model by reducing the baud period T (increasing the data rate) by the DCD time allocation. In other words, $T_{eff} = T - T_{DCD}$. T_{eff} may then be substituted for T into equations 3, 11 and 14. The resultant power penalties are then adjusted to higher values due to the effects of DCD.

MODEL IMPLEMENTATION

A couple of strong points of the 802.3z model is that the parameters of the model are, for the most part, easily measured, and the model lends itself to implementation in a spreadsheet. The strength of this application is the ease with which the model is implemented and the versatility of the spreadsheet's functions. The weakness, however, is that the spreadsheet is designed for single value inputs, limiting the speed at which different scenario's may be examined.

MONTE CARLO IMPLEMENTATION

The spreadsheet implementation of the model lends itself to the application of Monte Carlo simulation techniques. A Monte Carlo simulation may be utilized to better represent "real world" scenarios by allowing the network designer to use the actual probability distribution of each component's key parameters in the model. The simulation then randomly picks the component's parameters based on the probability distributions, mimicking the randomness of the actual link components. Today, Monte Carlo simulations can be easily implemented with inexpensive simulation software for spreadsheets. Such a software package is Crystal Ball® by Decisioneering. Crystal Ball

allows the network designer to convert a single input value spreadsheet into a multi-input value spreadsheet (based on probability distributions).

The statistical distribution information is simply layered onto the original spreadsheet by clicking on the cell of interest then clicking on the "Define Assumptions" button. A window is displayed that provides a choice of distributions (normal, uniform, binomial, custom, etc.), followed by a window as illustrated in figure 1.

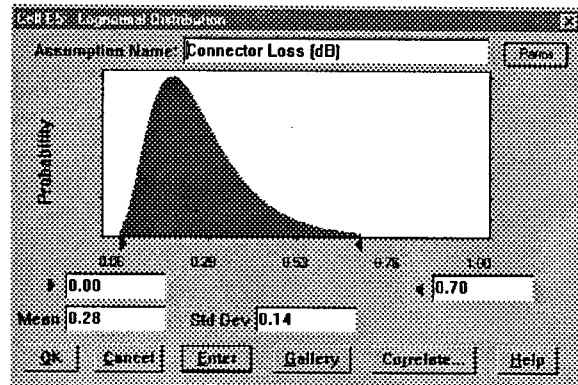


Figure 1: Distribution definition window.

The window of figure 1 illustrates the method of defining the different distributions. As can be seen, it is quite intuitive. A significant strength of this type of software package is the ability to define custom distributions based on measured data.

"Forecast" may be assigned to specific cells in a similar manner. The Forecast cells are the output of the simulation. These Forecast cells contain all the calculation results of the simulation, allowing the user to generate probability distributions of the simulation's output. Figure 2 illustrates the results from one such Forecast cell.

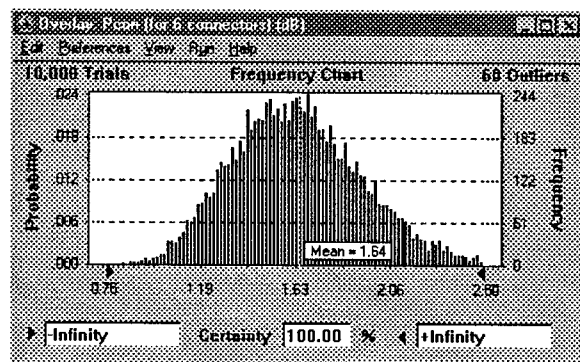


Figure 2: Forecast results window.

SIMULATION RESULTS

Combining the Monte Carlo simulation capability with the Gigabit Ethernet Link model provides a very powerful analytical tool. Thus, it was decided to perform a sensitivity analysis on the model, and then, based on the link model and measured laboratory data, evaluate the predicted link distances of a network system.

To perform the sensitivity analysis, the input parameters to the model were converted to uniform probability distribution functions (pdf), spanning the maximum allowed range. The uniform pdf was chosen because all values within the chosen range are equally likely to be chosen in the simulation, including the worst case. Additionally, the link distance was statically set to 275 meters. The sensitivity relative to the power margin (P_{margin}) was analyzed. The results of this simulation are displayed in figure 3.

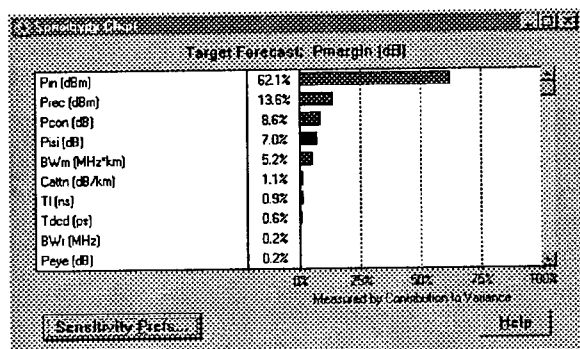


Figure 3: Sensitivity analysis of the link model's power margin

Not surprising is the fact that most of the variance in the power margin is due to the transmitter's launch power (P_{in}) and the receiver's maximum sensitivity (P_{rec}). The difference in P_{in} and P_{rec} constitutes the link's power budget. The analysis also confirms that the power margin is equally sensitive to the fiber's modal bandwidth (BW_m) and the power penalties of inter-symbol interference (P_{sl}) and interconnect losses (P_{con}). To further understand the model, the sensitivity relative to P_{sl} was analyzed. Figure 4 illustrates the results of the simulation. The fiber's modal bandwidth is a major contributor to P_{sl} . A distant second is the laser's rise time (T_L). Thus, if one wished to increase link distance, a logical route would be to improve the fiber's modal bandwidth. Fortunately, that is precisely what

the TIA FO-2.2 Task Group on Modal Dependence is examining. Their goal is to provide a modal bandwidth specification and test procedure to be used with laser sources that underfill the fiber's core, such as those used with Gigabit Ethernet.

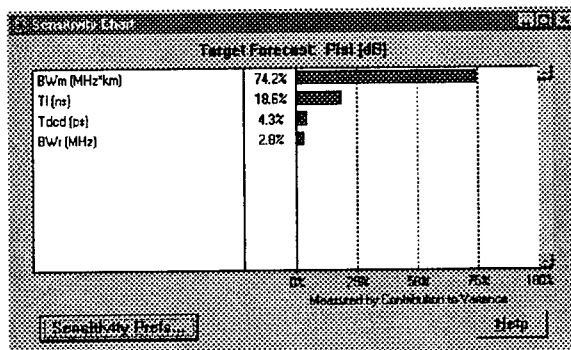


Figure 4: Sensitivity analysis of the inter-symbol interference power penalty.

Laboratory data for the 100BASE-SX Volition™ Network Solution, which is an end-to-end optical fiber network system, was analyzed. The probability distributions from the collected data were then used as inputs to the Monte Carlo link model. The optical fiber cabling data was obtained from 200 MHz*km cable. Six independent VF-45™ interconnect distributions were entered into the model. A macro was written that would run after each new calculation was performed. This macro would adjust the link distance such that a power margin of 0 dB was obtained. This link distance was then output to the forecast window. 10^5 simulations were run. The resultant link distances are shown in figures 5 and 6.

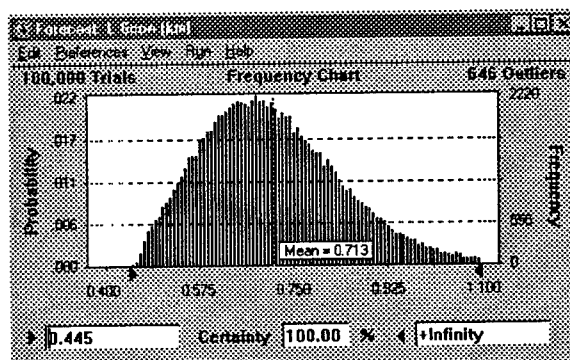


Figure 5: Link distance distributions.

As can be seen from figure 5, 100% of the links achieve a distance >275 meters (the standard's specification). In fact, 100% of the link distances are >445 meters. Further, the network designer

can determine from the given data a distance of >483 meters can be achieved with a 99% certainty level, see figure 6. Thus allowing the designer to increase the link distances with a quantitative confidence.

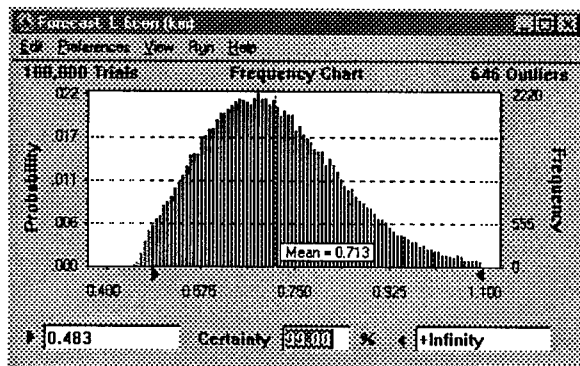


Figure 6: Link distance distributions for 99% certainty.

CONCLUSION

It has been shown that the Gigabit Ethernet link model, as developed by the IEEE 802.3z optical PMD task force, is a powerful tool for the network designer. Its usefulness continues to be proven by its utilization in Fibre Channel standardization activities. The model has also seen some early use in the new IEEE 802.3 High Speed Study Group (HSSG) that is in the early stages of standards development for 10-Gigabit Ethernet. Additionally, the model has been modified for use with LEDs by the 10/100 Optical Fiber Auto-Negotiation standards activities, led by the TIA FO-2.2 Task group 2.

Finally it has also been shown that overlaying a Monte Carlo simulation onto the spreadsheet implementation may enhance the model's power and usefulness. Hence, allowing the designer to examine the link's performance relative to any of the parameters. One such simulation of a real world networking system showed that the link distance could be increased 62% above the 1000BASE-SX specification. A word of caution, despite the tremendous distance predictions as a result of this simulation, it is not advisable to implement a network system using these predictions. The predictions in this paper are valid only for the implementation that was analyzed.

REFERENCES

[1] Gair D. Brown, "Bandwidth and Rise Time Calculations for Digital Multimode Fiber-Optic

Data Links," *Journal of Lightwave Technology*, VOL. 10, No. 5, May 1992, pp. 672-678.

[2] ANSI T1.646-1995, Broadband ISDN-Physical Layer Specification for User-Network Interfaces, Appendix B.

[3] James L. Gimlett and Nim K. Cheung, "Dispersion Penalty Analysis for LED/Single-Mode Fiber Transmission Systems," *Journal of Lightwave Technology*, VOL. LT-4, No. 9, Sept. 1986, pp. 1381-1392.

[4] Govind P. Agrawal, P. J. Anthony and T. M. Shen, "Dispersion Penalty for 1.3-mm Lightwave Systems with Multimode Semiconductor Lasers," *Journal of Lightwave Technology*, VOL. 6, No. 5, May 1988, pp. 620-625.

[5] Richard J. S. Bates, Daniel M. Kuchta, Kenneth P. Jackson, "Improved Multimode Fiber Link BER Calculations due to Modal Noise and Non Self-Pulsating Laser Diodes," *Optical and Quantum Electronics*, No. 27, 1995, pp 203-224.

[6] R. G. Smith and S. D. Personick, "Receiver Design for Optical Communication Systems." *Topics in Applied Physics: Semiconductor Devices for Optical Communication*, Volume 39, Editor: H. Kressel, New York: Springer-Verlag, 1982. pp. 89-160.

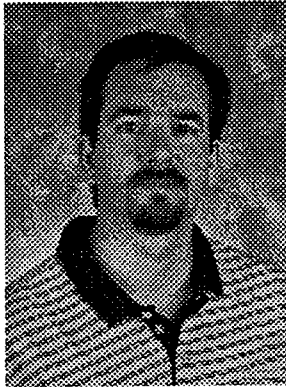
[7] David G. Cunningham, Mark Nowell, Delon C. Hanson, and Leonid Kazovsky, "The IEEE 802.3z Worst Case Link Model for Optical Physical Media Dependent Specification Development." An Internet White Paper, IEEE 802.3, <http://grouper.ieee.org/groups/802/3/z/public/presentations/mar1997/DCwpaper.pdf>, March 1997.

[8] David G. Cunningham and William G. Lane. *Gigabit Ethernet Networking*. Indianapolis, IN, Macmillan Technical Publishing, 1999.

[9] Joachim Vobis and Dennis Derickson, "Optical Spectrum Analysis." *Fiber Optic Test and Measurement*. Editor Dennis Derickson, New Jersey, Printice Hall, 1998. pp. 87-130.

[10] Robert M. Kimball, "Optical Performance Models for FDDI Links." *Fiber Networking and Telecommunications*. SPIE VOL. 1179, 1989, pp. 252-265.

BIOGRAPHY



J. David Schell

6801 River Place Blvd.
Austin, TX 78726

David Schell is an Advanced Development Engineer for 3M where he is involved with the ongoing development and integration of next-generation fiber optic network solutions for the LAN environment. He is currently working on advanced transceiver designs utilizing VF-45. His work also includes fiber network electronics that comprise switches, NICs, hubs, and media converters. David is also responsible for the ongoing system evaluation and modeling of 3M's Volition™ Fiber Optic Network Solution. Schell is an active committee member of IEEE 802.3. Prior to joining 3M in 1998, Schell was with United Technologies Optical Systems where he was involved in the development of laser beam control systems. With a BSEE from the University of Texas, David has more than 10 years of design engineering work in the area of fiber optics and laser technology.

THE OTDR TECHNIQUE AS A PROMISING APPROACH FOR DISTRIBUTED MEASUREMENTS IN OPTICAL FIBRES

F. Ravet, B. Heens, O. Lair, Y. Defosse, J.-C. Froidure and M. Blondel,

MULTITEL TELECOM - Faculté Polytechnique de Mons, Mons, Belgium.

ABSTRACT

In this paper, we start with a theoretical introduction reminding the basics of the method, the link between the Mode Field Diameter (MFD) and the determination of cut-off wavelength (λ_{co}) and Chromatic Dispersion (CD). Marcuse and Anderson approaches for CD determination are theoretically and experimentally evaluated and compared. We use how a multi-wavelength but standard OTDR (three wavelengths) and a calibrated fibre artefact can be used to derive MFD and then CD. Measurements are performed at 1.31, 1.55 and 1.63 μm on links composed of standard single-mode fibres (matched- and depressed-cladding fibres). All these results are achieved through an investigation on measurement uncertainty sources and their impact. This study shows how OTDR noise and linearity as well as an accurate knowledge of the reference fibres influence the accuracy of such a technique.

MODE FIELD DIAMETER DETERMINATION FROM OTDR WAVEFORMS

At low power level the dominant scattering mechanism is the Rayleigh scattering. This process is induced by small refractive index variations caused by doping, impurities and microscopic geometrical defects. A fraction of scattered light is transmitted in the backward direction. That amount of backscattered power depends on fibre parameters such as the Rayleigh coefficient, the refractive index and the fundamental mode spot-size¹ (the MFD is twice the spot-size). In many practical cases, the only parameter fluctuating along the fibre length is the spot-size. In such a case, the spot-size, and then the MFD, expresses² as

$$w(\lambda, z) = w(\lambda, z_0) 10^{-\frac{I_n(\lambda, z)}{20}} \quad (1)$$

where $I_n(\lambda, z)$ is the normalised imperfection term and $w(\lambda, z_0)$ the reference spot-size figure. Knowing the MFD at $z=z_0$, the MFD may be calculated at any point of the fibre link and then the MFD mapping at a given wavelength is easily represented. $I_n(\lambda, z)$ is derived from bidirectional OTDR measurements by calculating the average waveform^{3,4}. It contains all the information related to the fibre parameters fluctuations except the attenuation.

When mixing in a same link various fibre types, relation 1 is not applicable anymore as Rayleigh coefficient and refractive index vary along the length. We must then introduce in relation 1 a correction factor^{9,10} which takes into account the fibre characteristics variation along the link. A practical example of various fibre type mixing exists when considering dispersion compensated and dispersion managed links. Reference 10 and 11 present results on links composed of standard single-mode fibres and dispersion shifted fibres.

The wavelength dependence of MFD is the key behaviour in determining λ_{co} as well as for D_w and then Chromatic Dispersion. A common approach is to consider a derivation of the famous Marcuse⁵ relationship or Anderson⁶ approximation for the spot-size, and then MFD⁷. These relations express the spot-size as a function of wavelength with the core radius and the cut-off wavelength considered as parameters. It is well known that these relationships are accurate within a few percent in the neighbourhood of fibre cut-off wavelength.

CHROMATIC DISPERSION FROM MFD MEASUREMENTS

Let us first remind that CD is mainly the sum of Material Dispersion (D_M) and Waveguide Dispersion (D_W). Profile Dispersion contribution is not considered here as it is usually negligible.

The *MFD* drives the Waveguide Dispersion term as follows⁸

$$D_w = \frac{\lambda}{2\pi^2 cn} \frac{d}{d\lambda} \left(\frac{\lambda}{w^2} \right) \quad (2)$$

This relation emphasise the importance of the *MFD* wavelength dependence. A wavelength dependent relation may be obtained considering a generalisation of Marcuse or Anderson relationships. Marcuse^{9,10} equation has the following behaviour

$$w = g_0 + g_1 \lambda^2 + g_2 \lambda^6 \quad (3),$$

and Anderson equation,

$$w = g_0 + g_1 \lambda^r \quad (4).$$

These relations integrate the core radius and cut-off wavelength influence in the parameters g_0 , g_1 , g_2 and r . These coefficients may be determined thanks to *MFD* measurements at three wavelengths at least. Instead of the Marcuse polynomial, a second order law can be fitted on the three *MFD* values. We do not observe significant discrepancies between both approaches which is not true when comparing the results coming from Anderson and Marcuse approximations as illustrated in Figure 1. D_M is calculated from doping concentration by Sellmeier's relations. It is then assumed that it does not vary over the fibre or link length. Figure 1 and 2 illustrate the use of both models for CD determination respectively at 1310 nm and 1550 nm. In this example, we used a three wavelengths OTDR (1.31, 1.55 and 1.63 μm). Anderson distribution experiences seems to be less affected by fluctuations.

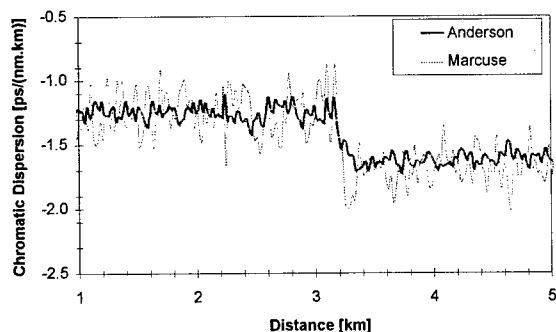


Figure 1. Chromatic Dispersion distribution at 1310 nm derived from three wavelengths OTDR measurements on a link composed of three fibres (mixing of matched cladding, depressed cladding and fibre manufacturers).

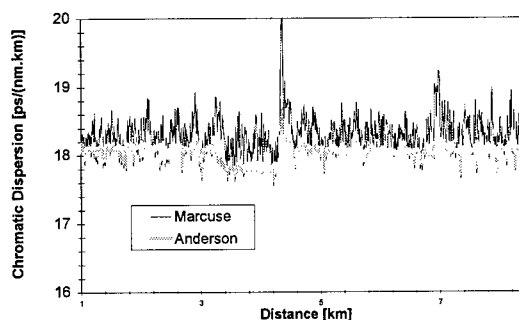


Figure 2. Chromatic Dispersion distribution at 1550 nm derived from three wavelengths OTDR measurements on a link composed of five fibres (mixing of matched cladding, depressed cladding and fibre manufacturers).

MEASUREMENT ACCURACY

Theoretical approach

When considering relation 2, it appears that D_w determination is sensitive to wavelength accuracy, Mode Field Diameter fluctuation and Mode Field Diameter wavelength dependence. This is expressed in the following equation

$$\delta D_w = \left| \frac{\partial D_w}{\partial \lambda} \right| \delta \lambda + \left| \frac{\partial D_w}{\partial w} \right| \delta w + \left| \frac{\partial D_w}{\partial \left(\frac{\partial w}{\partial \lambda} \right)} \right| \delta \left(\frac{\partial w}{\partial \lambda} \right) \quad (5)$$

The first term expresses the absolute error induced by the *MFD* wavelength accuracy. This term indirectly takes into account the approximation that has been chosen for the spot-size wavelength dependence (relations 3 or 4). This term is negligible when compared to the second and third ones. The second term depends on the *MFD* accuracy determination. It takes into account errors induced by OTDR waveform noise and the uncertainty on the reference spot-size figure $w(z_0)$. This appears more clearly when examining the following relation

$$\delta w = \frac{w(z)}{w(z_0)} \delta w(z_0) + w(z) \frac{\ln 10}{10} \delta S(z) \quad (6)$$

$\delta w(z_0)$ is the reference spot-size accuracy and $\delta S(z)$ is the OTDR waveform noise. Figure 3 presents the relative impact of both contributions to total spot-size fluctuations. The main impact of $\delta w(z_0)$ lies in *MFD* shift while the waveform noise induces random oscillations of the *MFD*

distribution. When reference MFD is known with an accuracy of $0.1\ \mu\text{m}$ and OTDR waveform experiences $0.02\ \text{dB}$ fluctuations, local MFD can be determined with an accuracy better than $0.15\ \mu\text{m}$. These results mean practically that using a high dynamic range and high linearity OTDR will improve the OTDR waveform flatness and then MFD fluctuations. The absolute accuracy implies an accurate measurement of the reference MFD. The main limitation here comes from the standardised measurement techniques for the characterisation of reference MFD. For instance, it is possible to achieve an absolute accuracy of about $0.05\ \mu\text{m}$ with a technique such as the Far Field Scanning. It is then reasonable to achieve an absolute accuracy of about $0.1\ \mu\text{m}$ for the MFD.

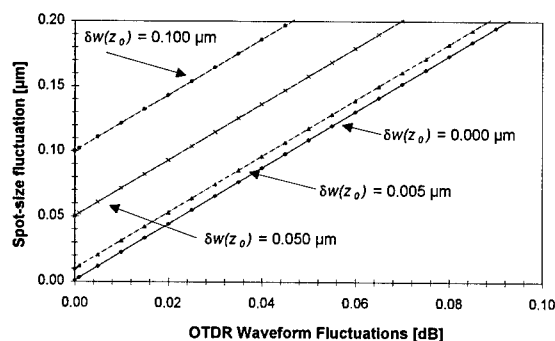


Figure 3. Calculated Mode Field Diameter dependence on OTDR waveform noise and reference MFD accuracy (evaluated at $1310\ \text{nm}$ for a reference fibre with an $\text{MFD}=9.18\ \mu\text{m}$ at $1310\ \text{nm}$).

The last term of relation 5 expresses directly the Waveguide Dispersion sensitivity to the spot-size wavelength dependence and then to the chosen model, which are in our case Marcuse¹⁰ or Anderson approximations. Figure 4 illustrates the impact of using one model in place of the other. Figure 4 is then the result of analytical and numerical computations carried out with relations 2, 3, 4 and 5. Anderson model is less sensitive to MFD fluctuations as it has been previously observed in Figure 1 and 2. An error of about $0.1\ \mu\text{m}$ in MFD determination means a deviation in Waveguide Dispersion of $1\ \text{ps}/(\text{nm.km})$ with the Anderson approach. The same error induces a deviation over $3\ \text{ps}/(\text{nm.km})$ using Marcuse approximation. These remarks can also be generalised to Chromatic Dispersion if we assume that Material Dispersion is constant all over the link length.

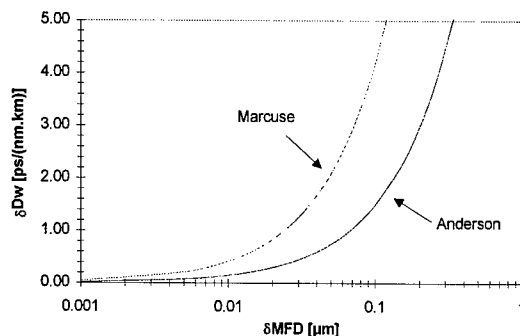


Figure 4. Impact of MFD accuracy on Waveguide Dispersion determination (MFD values used in the modelling are $9.18\ \mu\text{m}$ at $1310\ \text{nm}$, $10.47\ \mu\text{m}$ at $1550\ \text{nm}$ and $10.87\ \mu\text{m}$ at $1618\ \text{nm}$).

Experimental approach

The present section deals experimentally with the impact of OTDR waveform fluctuations on MFD determination and then Chromatic Dispersion. Main sources of these fluctuations are the waveform noise and linearity. Roughly, the first one can be improved by increasing the averaging time and using broader pulsewidth. The second one depends essentially on the photodiode linearity and the end user does not have access to that last parameter. These are the reasons why we only proceeded to a systematic study of pulsewidth and averaging time influence. The link for the test was composed of three fibres. We calculated the Chromatic Dispersion RMS trunk by trunk for each experimental condition (pulsewidth and averaging time). These results are summarised for the central fibre in Figure 5 and 6. They show the positive influence of the pulsewidth and the averaging time increase in deriving CD. Once again, Anderson model appears as a more stable approximation compared to the Marcuse one as RMS is lower in any cases. Using pulses broader than $100\ \text{ns}$ does not improve significantly the results. In many cases, it could degrade the measurement stability as the deadzone becomes larger. As a last comment, we observe on Figure 6 that increasing the averaging time over 10 minutes does not improve the results significantly. This is mainly due to the fact that residual fluctuations are caused by OTDR linearity. Asymptotic RMS CD value is about $0.1\ \text{ps}/(\text{nm.km})$. From Figures 3 and 4, we can then estimate OTDR fluctuation level which is lower than $0.01\ \text{dB}$ and corresponds to a typical OTDR linearity level ($0.05\ \text{dB/dB}$).

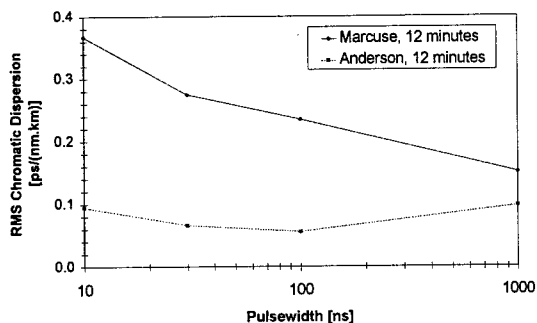


Figure 5. Comparison of Chromatic Dispersion RMS at 1310 nm as a function of the used OTDR pulsewidth. An averaging time of 12 minutes was applied here.

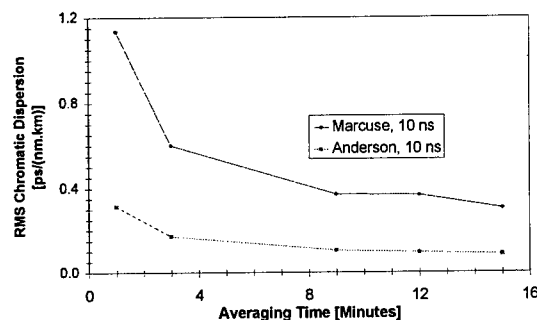


Figure 6. Comparison of Chromatic Dispersion RMS at 1310 nm as a function of the averaging time. A pulsewidth of 10 ns was used here.

Let us emphasise here the fact that these experimental results only show the waveform fluctuation influence on the MFD determination and then Chromatic Dispersion. They do not take into account Material Dispersion uncertainty and reference MFD accuracy. Comparing the observed behaviour to the computed uncertainties, we can say that a good relative accuracy can be achieved. This means that low noise OTDR is accurate relatively to itself while Material Dispersion and reference MFD accuracy will only shift the derived values. This has been discussed in a previous work¹¹ and is reminded hereafter.

Comparison with the Differential Phase Shift Technique

We also characterised some of the tested fibres by the Differential Phase Shift (DPS) technique. The comparison of these results with the ones we got from OTDR measurements are reported in Table 1. Values reported in the OTDR column are mean values derived from Marcuse approximation.

Table 1: Measurement results comparison

Fibres	CD @ 1310 nm [ps/(nm.km)]		CD @ 1550 nm [ps/(nm.km)]	
	OTDR	DPS	OTDR	DPS
MC 1	-0.25	-0.28	18.13	16.15
MC 2	-0.37	-0.35	17.95	16.68
DC	-0.45	-0.40	17.64	16.04

The results we achieved from both Chromatic Dispersion measurements present differences ranging from 4% to 13%. The DPS technique has an accuracy of 3%. We are then a little bit far from what we must expect for reliable and accurate measurements. We identify two main sources of errors. The first one can be attributed to the lack of informations we have on the core doping concentration and then on Material Dispersion. For a given Waveguide Dispersion, Material Dispersion shifts the Chromatic Dispersion to lower or higher wavelengths. As well as for MFD with the correction factor, such an information must improve significantly the results. The other one is induced by the mathematical processing. Fitting a two or three terms polynomial on a set of three experimental results is mathematically enough to determine the polynomial coefficients. From a scientific point of view, this is not sufficient and an improved accuracy can be reached if more than three wavelengths are available to fit the curve. All these remarks are currently investigated in a quantitative way.

Finally, the MFD of the reference fibre must also be considered as a key parameter for accurate measurements. This MFD value determines further MFD calculations. As already discussed in the section dealing with the numerical modelling of errors, a poor accuracy in the reference fibre MFD will degrade significantly the figures we can achieve with the OTDR technique.

CONCLUSIONS

In many practical cases, we can assert that the OTDR technique can be considered as a promising approach for the characterisation of Chromatic Dispersion. The main requirements to

achieve such an assertion are:

- the tested links are composed of similar fibres (or presenting very small differences) and Material Dispersion is constant all over the link length,
- the OTDR used has at least three wavelengths, good dynamic range and linearity,
- the reference fibre Mode Field Diameter must be known with a high accuracy.

Finally, the MFD of the reference fibre must also be considered as a key parameter for accurate measurements. This MFD value determines further MFD calculations. As already discussed in the section dealing with the numerical modelling of errors, a poor accuracy in the reference fibre MFD will degrade significantly the figures we can achieve with the OTDR technique.

REFERENCE

1. E. Brinkmeyer, Analysis of the backscattering method for single-mode optical fibers, *J. Opt.Soc. Am.*, Vol. 70, No. 8 August 1980, pp. 1010-1012.
2. M.S. O'Sullivan et al, Interpretation of SM fiber OTDR signatures, SPIE Proceedings Vol. 661 Optical Testing and Metrology (1986), pp. 171-176.
3. P. Di Vita et al, Backscattering measurements in optical fibres: separation of power decay from imperfection contribution, *Electronics Letters*, Vol.15, No.15 19th July 1979, pp. 467-469.
4. P. Di Vita et al, The backscattering technique: its field of applicability in fibre diagnostics and attenuation measurements, *Optical and Quantum Electronics*, 11 (1989), pp. 17-22.
5. D. Marcuse, Loss Analysis of Single-Mode Fiber Splices, *The Bell Systems Technical Journal*, Vol.56, No5, May-June 1977, pp. 703-718.
6. W. T. Anderson, Consistency of Measurement Methods for the Mode Field Radius in a Single-Mode Fiber, *Journal of Lightwave Technology*, Vol. 2, No. 2, April 1984, pp. 191-197.
7. EIA/TIA TSB62-6, Characterization of Mode Field Diameter and Cutoff Wavelength of

Single-Mode Optical Fiber by OTDR, August 1995.

8. C. Pask, Physical Interpretation of Peterman's strange spot size for single-mode fibers, *Electronics Letters*, Vol.20, No.3 2nd February 1984, pp. 144-145.
9. M. Ohashi et al, A nondestructive Technique for Measuring Chromatic Dispersion along a Single-Mode Fibre Bidirectional OTDR Measurement at Four Wavelengths, *Optical Fibre Measurement Conference*, Liège, September 1995, p.VII.2.
10. K. Nakajima et al, Chromatic Dispersion Distribution Measurement Along a Single-Mode Optical Fibre, *Journal of Lightwave Technology*, Vol.15, No. 7 July 1997, pp. 1095-1101.
11. F. Ravet et al, Extending the Capabilities of OTDRs for Single-mode Fibre Full Characterisation, Proceedings of the EuroCable conference, Delft, June 1999, pp. 110-117.

Acknowledgements. F. Ravet, B. Heens, Y. Defosse, J.-C. Froidure are working in the frame of an R&D contract commonly supported by *Ministère de la Région Wallonne* and the *European Commission* within the context of *OBJECTIF 1* funds. The technical support from Yves Choquet, David Biagi and Christophe Dumont, and Marc Wuilpart is greatly appreciated.

Cost reduction of miniature optical connector with glass-ceramic ferrule

Jun Hirose, Junji Takeshita, Fumihiko Shimizu, Yoichi Nakamura, Hirokazu Takeuchi*

Nishi Nippon Electric Wire & Cable Co., Ltd. Kasugaura, Oita, Japan

*Nippon Electric Glass Co., Ltd. Notogawa, Shiga, Japan

ABSTRACT

We have developed the optimum polishing conditions for 1.25mm ϕ glass-ceramic ferrule (GCF). The adoption of GCF leads to cost reduction of 50% when compared to conventional zirconia ferrule (ZrF). The polishing time of GCF is 200 seconds, a reduction from 400 seconds needed for ZrF. The polishing process in this study could use inexpensive polishing materials, such as alumina film, due to the lower Vickers hardness of GCF. In addition, the production cost of GCF is reduced by 50% because of the drawing process, which needs no final polishing on the inside and outside of the ferrule [1]. The total cost of the ferrule and the polishing process was halved. Furthermore, the optical connectors using GCFs achieved the same return loss with less than half the contact pressure of conventional optical connectors using ZrF's [2].

INTRODUCTION

Optical communication is reaching the public at large through projects such as FTTH (Fiber To The Home).

Cost and size reduction of optical connectors are requirements to construct such high-density intra-office optical systems. One of the most expensive parts of an optical connector is the ferrule, including the endface-polishing process.

Recently, many optical connectors are used not only in telecom field but also in datacom field. Optical connectors for these applications are required to make reliable contact easy. GCF is

suitable for that requirement due to its lower Young's modulus, lower than ZrF's.

In this paper, we first describe the features of the material, the manufacturing process of GCF, and the optimum polishing conditions for GCF, which has reduced the costs by 50%. Finally we present the various optical and reliability characteristics of miniature optical connectors using 1.25mm ϕ GCF.

Material of Glass-Ceramic

Glass-ceramic (GC) is material made up of crystals distributed throughout amorphous glass. Because of this structure, GC has many advantages such as a high bending-strength, a low thermal expansion coefficient and good environmental durability, which make GC suitable for use as an optical connector ferrule.

A rough sketch of the crystalline structure of the cerammed preform, a $\text{Li}_2\text{O}-\text{Al}_2\text{O}_3-\text{SiO}_2$ system with β -spodumene s.s., is shown in Fig.1.

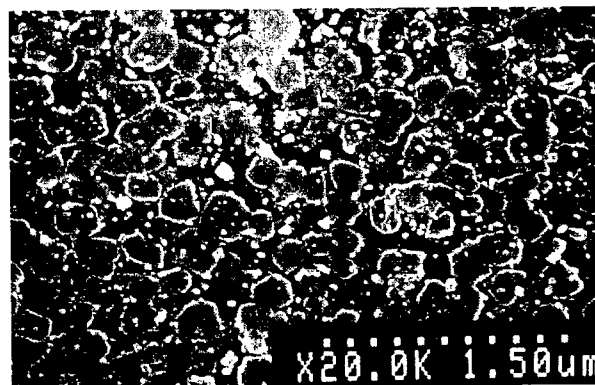


Fig.1 Crystalline structure of the cerammed preform

Table.1 shows a comparison of the properties of GC and other materials used for optical connector ferrules. The bending strength of the GC is approach to that of alumina [3]. The thermal expansion coefficient of GC is also much lower than other materials used for ferrules, therefore the stress caused by the differences between the thermal expansion rates of the ferrule and the fiber can be reduced. Furthermore, the Young's modulus of GC is lower than that of zirconia. As a result physical contact is facilitated and polishing process is made more efficient.

Table.1 Material properties

	GC	Alumina	Zirconia
Bending strength (Mpa)	500	580	1350
Thermal expansion coeff. (ppm/°C)	3.0	6.8	8.3
Young's modulus (Gpa)	80	380	190
Vicker's hardness	680	1800	1200

Fabrication of GCF

To apply GC to optical connector applications, a glass-ceramic preform with a hole in its center is drawn and cut continuously to form ferrules. Fig.2 shows the drawing process for a cerammed preform, GCF, which is inexpensive when mass produced.

No final polishing on the inside and outside is needed for GCF in contrast to the conventional injection formed ferrules [4].

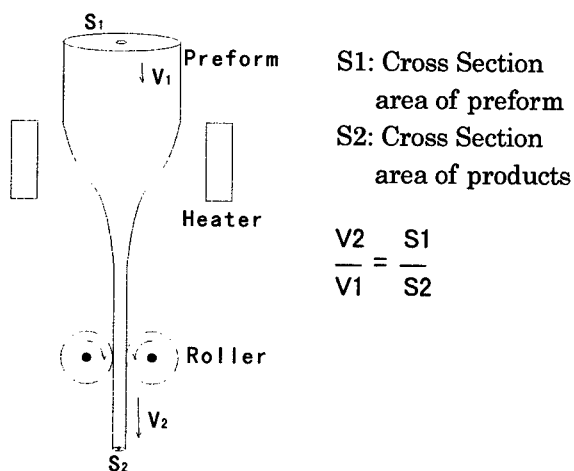


Fig.2 Drawing process of the cerammed preform

Bending Strength of GCF

We evaluated the bending strength of fabricated 1.25mm ϕ GCF, by measuring the breaking stress force applied at a position 1.5mm from the end of the ferrule. The results of ten tests were measured and the average value was 37.4N (3.8kgf), minimum 34.8N (3.6kgf). The result shows GCF has sufficient bending strength in the actual fabrication process and usage.

Optical Connection Characteristics of GCF

1) Measurement of return loss

To confirm the advantages of the GCF, we measured the return loss, which shows the physical contact performance of the optical connector, versus the contact pressure force using a test-bed, as shown in Fig.3.

The evaluated ferrules were polished to have an optional radius of curvature R and fiber undercut U, using a special polishing method.

The results of the measured return losses, comparing GCF and ZrF, are shown in Fig.3.

When the domain of R is small, 15mm, the return loss of both GCF and ZrF rose immediately when the contact pressure was increased.

However when the domain of R is large, 30mm and 60mm, the ZrF requires strong contact pressure, GCF needs only light contact pressure, less than 3.92N (400gf) for good optical connections. The reason for these results is the difference between Young's modulus of GCF and ZrF.

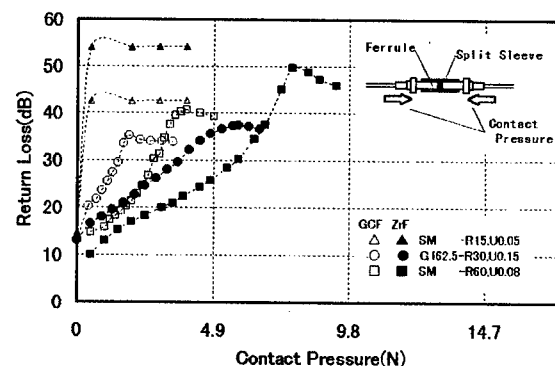


Fig.3 Measured return losses comparing GCF and ZrF

2) Calculation

We investigated the above results by calculating the Hertz Formula shown below. The Hertz Formula is used when there is an assumption that the contacted endface of the ferrule is sphere and the effect of the small hole present in the ferrule is neglected.

$$F = \frac{4EA^3}{3(1-P^2)R} + \frac{4ea^3}{3(1-p^2)R}$$

Where,

F :Contact pressure

E :Young's modulus of the ferrule

e : Young's modulus of the fiber

A :Radius of contact surface of ferrule

a : Radius of contact surface of fiber

P : Poisson ratio of the ferrule

p : Poisson ratio of the fiber

R: Radius of curvature of the ferrule and the fiber

The calculated relationship between the contact pressure and the return loss is shown in Fig.4.

When U is constant, the rising points are in proportion to the Young's modulus of each ferrule. When the radius of curvature increases, the pressure becomes larger due to the increase of the contact surface area.

Slope is in inverse proportion to the core diameters of SM and GI fibers. This calculated result is almost the same as the above experimental result.

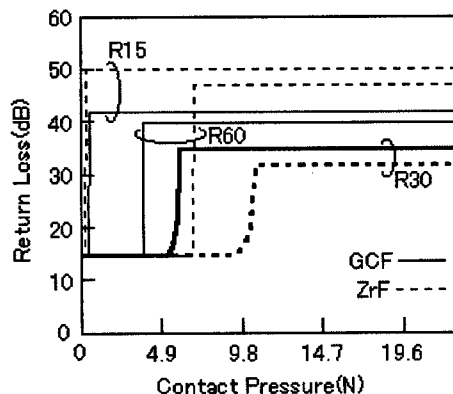


Fig.4 Calculated relationship the contact pressure and the return loss

3) Results

The optical connectors with GCF's achieve the same return loss with less than half the contact pressure required by conventional connectors using ZrFs. This means it is possible to make good physical contact with lower pressure, by using GCFs, even with the optical connectors using large R ferrules. The above result also means there is a possibility to reduce the polishing time, if the large R is acceptable [5]. Moreover, it is possible to increase tolerance of apex offset of GCF than ZrF.

Cost Comparison with Polishing Condition

GCF is expected to reduce the polishing process time and eliminate the need for diamond film as a polishing material, because the hardness of GCF is lower than ZrF. We have achieved optical properties and endface shapes as good as ZrF.

Our investigation of the optimum polishing condition for the endfaces of 1.25mm ϕ GCF has resulted in a cost reduction equivalent to half the cost of ZrF. The polishing conditions, which we used, are shown in Fig.5.

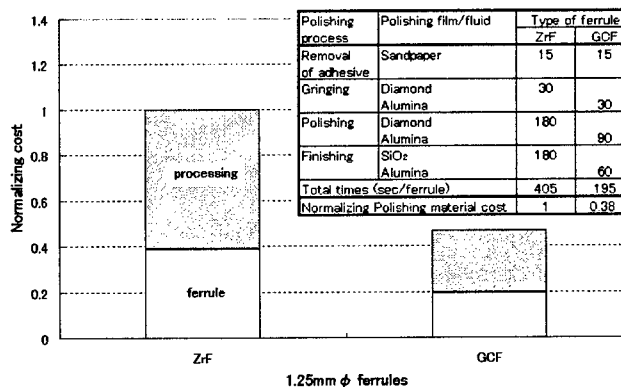


Fig.5 Cost comparison of the ferrule and the polishing process

In this process study, we used inexpensive polishing materials such as alumina film. We did not use diamond film or SiO₂ solution. The change of polishing material resulted in a cost reduction in polishing materials, 50% lower than the polishing cost of ZrF.

For example, the polishing time of GCF is reduced to an less than half that of ZrF, 195 seconds for GCF, 405 seconds for ZrF. Furthermore, the production cost of GCF is reduced by 50% because of the drawing process, which does not need final polishing, either inside or outside the ferrule. Fig.5 shows the cost comparison of the ferrule and the polishing process. The results show the overall cost of the ferrule is halved.

Performance and Reliability

We measured various aspects of the optical performance of MU (Miniature Unit coupling) connectors using GCF connected SM fiber.

First, we measured the insertion loss at a wavelength of $1.3\mu\text{m}$, which is the fundamentally performance of an optical connector. A histogram of insertion losses is shown in Fig.6. The average insertion loss of 0.14dB is equal to that of conventional ZrFs.

Second, the return losses of the connectors were also measured at a wavelength of $1.3\mu\text{m}$. The results of the histogram are shown in Fig.7.

Each return loss was better than 40dB, which indicates good optical connection called Advanced physical contact.

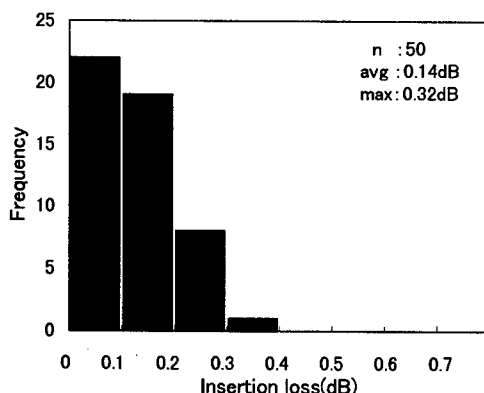


Fig.6 Insertion loss histogram

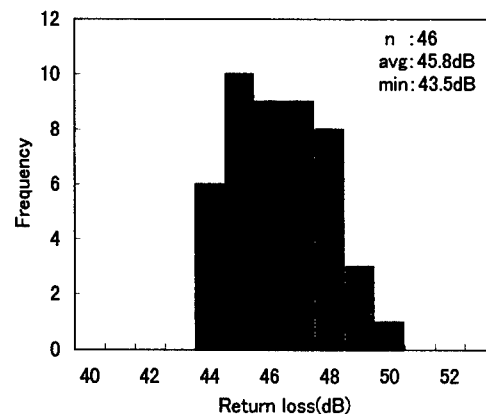


Fig.7 Return loss histogram

Third, we evaluated the reliability of the optical connectors by measuring the insertion loss changes after each of 500 connections. The change in the insertion loss is below 0.2dB, and there was no damage to the endfaces of the GCFs.

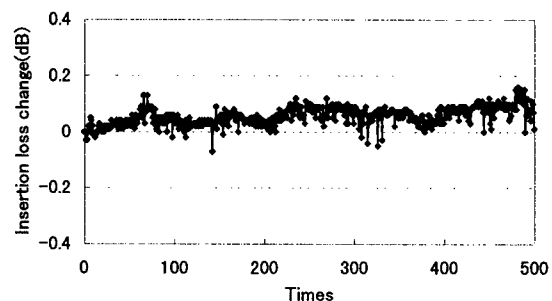


Fig.8 Insertion loss changes of the connectors by 500times reconnections

Finally, we evaluated the temperature change reliability and the temperature & humidity cycling reliability, which show the life expectancy of the ferrule. The insertion loss fluctuations of the connector were measured in two sets of environmental conditions, a temperature change test (-10°C to $+55^{\circ}\text{C}$, 2hours/cycle, 100cycles), and a temperature & humidity cycling test (-10°C to $+65^{\circ}\text{C}$, 93%RH, 24hours/cycle, 10cycles).

The results are shown in Fig.9 and 10, respectively. The insertion loss changes during both of those tests were within 0.1dB. The connector using GCF showed satisfactory performance.

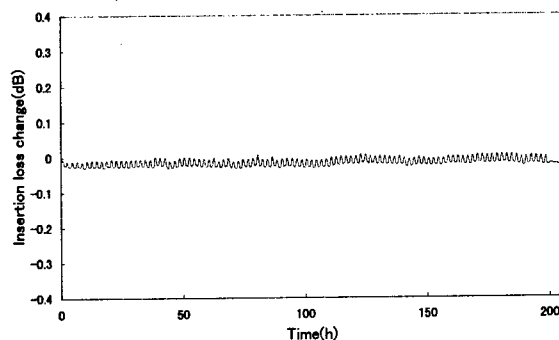


Fig.9 Temperature change test

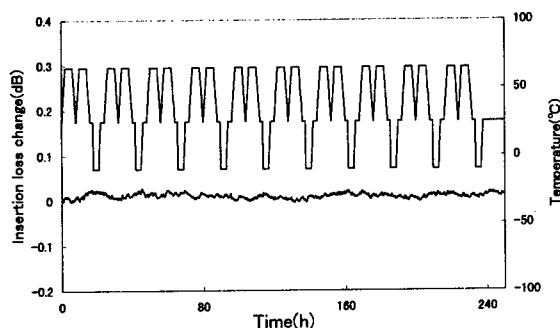


Fig.10 Temperature & humidity cycling test

CONCLUSION

We have investigated the miniature optical connector with a new 1.25mm ϕ GCF. The optical connectors have excellent physical contact performance with only half the contact pressure of ZrF's.

Furthermore, the GCF achieved overall cost reduction of the connector, when compared to conventional 1.25m ϕ ZrF.

Therefore, GCF is useful for achieving cost and size reductions for high density optical connector applications not only in the telecom field but also in the datacom field.

REFERENCES

- [1] Y. Takeuchi et. al., "High-Strength Glass-Ceramic Ferrule for SC-Type Single-Mode Optical Fiber Connector", IEEE PHOTONICS TECHNOLOGY LETTERS. VOL.9, NO.11, p.1502 NOVEMBER 1997
- [2] J. Hirose et. al., "Connecting properties of Glass-Ceramic ferrule for optical connector", Proceeding of IEICE March 1998, C-3-25 (in Japanese)
- [3] A.Sakamoto et.al., "Development of Glass-Ceramic Ferrule for Optical Connector", Proceeding of IEICE September 1997, C-3-53 (in Japanese)
- [4] A.Sakamoto et. al., Proc. 18th Int.Cong.Glass C6 (1998) p.62.
- [5] J. Takeshita et. al., "A study of endshape of Glass-Ceramic ferrule", Proceeding of IEICE March 1998, C-3-26 (in Japanese)



Jun Hirose was born in 1968. He graduated in mechanical engineering from Oita National College of Technology in 1988. He is joined Nishi Nippon Electric Wire & Cable Co., Ltd. in 1988. He has been engaged in development of optical connectors and their accessories. He is a member of the IEICE of Japan.

FIBER PERFORMANCE IN FERRULE-LESS INTERCONNECTS

Todd P. Berger*, James W. Laumer**, Christopher B. Walker Jr.**,
and James C. Novack**

*3M, Telecom Systems Division, Austin, TX.

**3M, Fiber Optics and Electronics Materials Technology Center, St. Paul, MN.

ABSTRACT

The next generation cabling systems for high-speed local area networks for data transmission will be based on optical fiber. One of the enabling technologies is the ferrule-less interconnect. The performance of this type of connector is enhanced when loss due to the gap between fiber end faces is minimized via bowing one of the fibers so that it creates an end face force.

A new high reliability optical fiber is discussed which consists of a glass core with a glass cladding diameter of 100 μ m, and a permanent polymer coating diameter of 125 μ m. The permanent polymer coat is not removed during stripping.

This paper examines the polymer coating which is a tough polymeric barrier, separating the stripper from the glass of the cladding. The protected, stripped fiber, coupled with the reduced application stress caused by the reduction in the glass diameter, proves to be a reliable mechanical fiber design.

INTRODUCTION

The evolution of small form factor connectors for glass optical fiber has brought a number of technological innovations to the market. However, to be successful for fiber-to-the-desk applications, the connector must be simple, low cost, easy to use and meet industry standard performance requirements. Among the new designs, which are half the size of traditional SC connectors, one design is fundamentally unique. It eliminates the need for ferrules and accompanying precision components.

To apply an end face force for low loss, a 45 degree bow in the fiber is designed into the connector. The effect of this added stress on the fiber was studied.

Several fiber designs are suitable for use with this interconnect. This testing examines the use of a fiber with a 100 μ m diameter clad and a permanent polymer coat with a 125 μ m outer diameter. This coating was designed to withstand abrasion. To evaluate the fiber strength a standard 125 μ m clad glass fiber is used for comparison

FIBER PROPERTIES

Fiber Tension Stress

A fiber's tensile strength, bending stress, and fatigue, can be used to model the failure rate of an interconnect design. To maintain the end face compressive force required for the fiber to remain in V-grooves and provide low attenuation and reflection, the bend stress in the fiber must remain above a minimum value. This stress is also important to maintain the fiber's position through impact, twist and flex testing.

The amount of stress required to break the fiber in tension is measured using EIA/TIA-455-28B (FOTP 28). The inherent strength and the strength distribution of the test fiber can be derived from the resulting Weibull plot. Inherent strength refers to the intrinsic flaw distribution in the fiber which is the product of raw materials and processes used to produce the fiber. Break strengths less than the inherent strength are due to larger extrinsic flaws in the glass which may have many sources including fiber

processing, proof testing, post processing (cabling), cable pulling and/or connectorization where the protective coatings are mechanically removed.

During testing, the inherent strength of both standard and permanent polymer coated fiber types was found to be nearly identical before stripping. However, after stripping, the strength distribution of the standard fiber showed the typical tail due to extrinsic defects caused by stripping. The fiber with the permanent polymer coat showed a small reduction in the mean tensile strength after stripping, and only small corresponding defects were created. The retention of the fiber's inherent tension strength is due to the protection provided by the permanent polymer coating.

Fiber Stress in Bending

An adaptation of FOTP 28 is a two-point bend test in which fiber is bent until breaking¹, rather than pulled until breaking. This additional test data shows that fiber with a permanent polymer coating as well as unstripped standard fiber remain identical in mechanical performance in the interconnect. However, when the buffer coat on standard fiber is removed, defects due to stripping have an obvious effect on performance in the interconnect. (See Figures 1 and 2.)

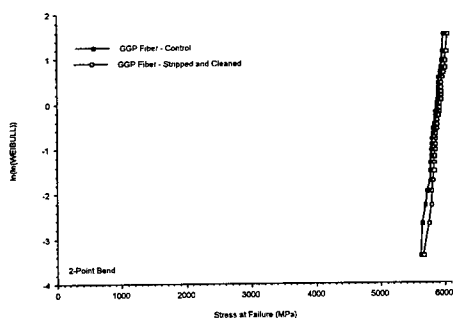


Figure 1 Weibull plots of the fiber with a permanent polymer coating 2-point bend.

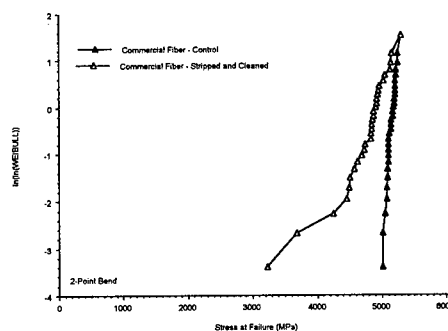


Figure 2 Weibull plots of the commercial fiber in 2-point bend.

The tests indicate that it is preferable, although not imperative, to use a buffered fiber or a permanent coated fiber rather than stripped bare glass.

Fiber stress in bending is directly proportional to Young's modulus and the fiber diameter, and inversely proportional to the bend diameter. Since bend stress is related to the fiber diameter, this must be a consideration during the design of the connector. The use of a permanent polymer coated fiber in the patch cord is an important method of reducing the fiber's bend stress. This fiber has standard core diameters, 62.5 μ m and 50 μ m, and 8.3 μ m but a smaller cladding diameter, 100 μ m vs 125 μ m, which reduces the bend stress at any given bend diameter. (See Figure 3.)

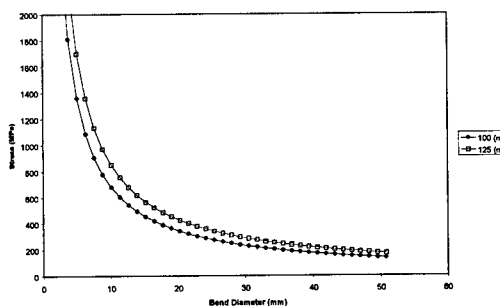


Figure 3 Stress as a function of Bend Diameter

Strength after Stripping

Typically, defects are created in the cladding of standard fiber during stripping, but the permanent polymer coat protects

the glass cladding in this fiber when stripping the buffer. The defects are created in this layer. The permanent polymer coat is resistant to damage and minimizes the stripping force. A standard fiber may require 4.5 N of force to strip the buffer coat, while the fiber with a permanent protective coating will typically only require 3.5 N.

MATERIAL PROPERTIES

Protection of the Glass

The specific chemical information regarding this material can be found in the literature². The protection of the glass cladding from stripping damage is a three-step process. First the diameter of the cladding is less than the standard 125 μm (100 μm). Second the difference in diameter is made of a layer of polymer. This layer of polymer reduces the required strip force by acting like a release liner. Finally, the material properties of this polymer layer are such that the material is tough and resistant to damage.

Physical Properties

The physical properties of interest for this polymer are the hardness, creep, and modulus. The harder the material the more protection it will give the glass provided that it is not exceptionally brittle. The hardness of the material is greater than 65, typically it averages around 70 shore D.

Creep is an important property for this polymer. As a material creeps, its dimensions may change such as its thickness. Similarly, its modulus may change with time and temperature under some applied stress. The majority of an applied load is applied to the glass and not to the permanent polymer coat. The stresses in the permanent polymer coat are much lower than the stresses in the glass.

Creep was measured on a 12.7 mm wide and 76.2 mm long specimen cut from a 10 mil thick film. A 25.4 mm gage length was defined on each sample. The stress (weights) was applied and the samples were hung in the appropriate environment. The

length of the gage was measured periodically and recorded. The percent change is reported after a range of aging conditions. The temperatures chosen for aging were 23, 40, and 60°C. The stress ranged from 1.5×10^4 to 1.5×10^5 Pa. All samples have been aged for at least 120 hours. The measured percent of change for all samples and aging conditions is less than the error in the measurement and are assumed to be zero. Data is being periodically recorded and will continue to be done so for the next few months.

The modulus of the polymer plays a major role in its ability to protect the glass from the stripper. A high modulus material is required for dimensional stability, low set, and good cohesive strength.

The modulus of a polymer is measured using Dynamic Mechanical Analysis. The measurement was performed with a TA Instruments Model 2980 Dynamic Mechanical Analyzer with the following parameters Clamp = Film Tension, Mode = multi-frequency tension, Strain Amplitude = 20 μm , Geometry = rectangular, Frequency = 1 Hertz, Static Force: 0.04 N, Length = 15 mm.

The results shown in Table 1 indicates a low visco-elastic component to the modulus.

Table 1
Dynamic Mechanical Analysis

	Aging Conditions (5 days)		
	25°C	85°C	85°C/85% RH
Modulus (MPa)	733	733	700
tan δ	0.064	0.064	0.072

Swelling

The permanent polymer coating along the fiber can be exposed to a range of cleaning solvents. Therefore, the material should swell very little when exposed to these solvent for short periods of time under ambient conditions. If the polymer swells

extensively, the modulus will decrease and physical dimensions may change.

The polymer material was immersed in the following solvents to determine their effect on the material: a mixture of 6% Texpure and deionized water from Texwipe (Texpure), Isopropyl alcohol (alcohol), and a blend of Methyl nonafluoroisobutylether and Methyl nonafluorobutylether (HFE). Swelling was measured on 25.4 mm square samples of film. The initial weight was recorded and the samples were immersed in the solvent. Periodically the samples were removed and weighed. The percent change was then calculated. (see figure 4).

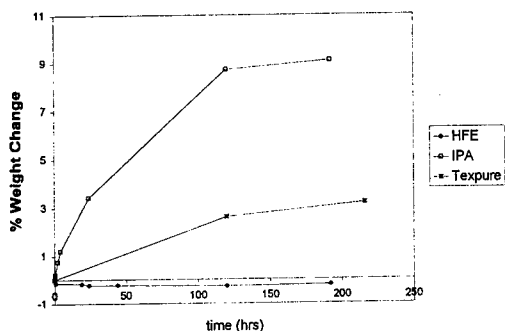


Figure 4 Weight Change as a Function of Time for HFE, IPA, and Texpure

The polymer swells the most in alcohol. Here the percent weight change is approximately 1% after two hours of total immersion at room temperature. The Texpure results in less percent weight change than the alcohol and takes about 5 days of total immersion to change about 2.6%. Either solvent is acceptable for use with polymer coated fiber. In application the polymer cannot be immersed into a solvent on all sides because it is coated onto fiber. Therefore, only one surface will be exposed. Further, typical cleaning procedures take a few minutes. Finally, it is expected that as the polymer is allowed to rest (dry), the solvent would evaporate out of the polymer thus reducing the percent change.

Immersing the polymer in HFE showed a slight decrease in weight initially, and then it stabilized without additional change. This modest initial decrease in weight if not attributable to experimental error may be due

to extraction. Here the solvent will extract one or more components of the material. It is well known that unreacted photoinitiator or initiator by products are often extractable. This solvent is also acceptable for cleaning the permanent polymer coating.

Water is of concern to any fiber optic component. The polymer was immersed in water and aged at two temperatures. The higher temperature is expected to be an accelerated condition (see figure 5).

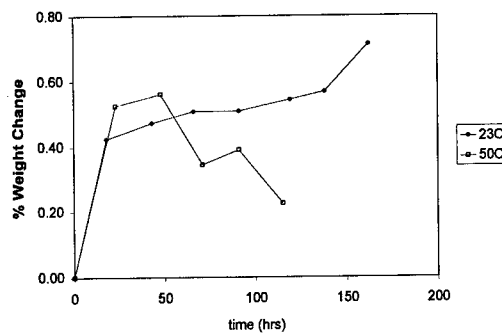


Figure 5 Weight Change of the Polymer as a Function of Time at 23 and 50°C.

As can be seen from the graph, the percent weight change is very small, and, even after 5 days it does not approach 1%.

CONCLUSION

The performance of the fiber is critical when used with optical fiber connectors. The fiber may be under constant stress after it has been stripped. Therefore, the damage to the glass during stripping must be minimized. One way to do this is by replacing part of the glass cladding with a hard, tough, permanent polymer coating.

This polymer has been shown to have excellent mechanical properties. The hardness of the material protects the glass from the stripper blade, and the material is also resistant to damage because of its high modulus.

The polymer may be exposed to a range of environments. It has been shown that the polymer does not creep extensively with

time or temperature. The polymer must be suitable for use with common cleaning solvents. The polymer does not swell extensively during exposure to these solvents under normal practices. Similarly it swells very little when exposed to water.

ACKNOWLEDGEMENTS

The authors would like to thank David Chang (3M Telecom Systems Division) for setting up the creep study.

REFERENCES

1. James C. Novack, Fredrick Bacon, Bryon J. Cronk, James W. Laumer, Julie M. Moser, and Bruce A. Rabine "Optical Fiber Design for Improved Mechanical Properties" Proceedings of the 44th International Wire and Cable Symposium, 1995.
2. Christopher B. Walker Jr., James C. Novack, and Todd P. Berger "Permanent Protective Coatings for Optical Fibers" American Chemical Society Polymer Preprints, Vol. 40, #2, 1271 to 1272, 1999.

Authors



Todd P. Berger is a Product Development Specialist for 3M Telecom Systems Division in Austin, Texas. He is currently responsible for the design and analysis of fiber strength in optical fiber connectors. His work also includes research in optical properties and materials for fiber optic components and cable accessories. He is also responsible for the ongoing support and analysis of the performance benefits of the VF-45 interface.

Prior to this position, Berger worked in 3M Electrical Products Division where he developed materials for high voltage splicing for the electrical industry. Berger holds both a bachelor's and master's of science degrees in physics and a doctorate in polymer sciences from the University of Akron.

James W. Laumer received a Bachelor of Science Degree in Chemical Engineering from Michigan Technological University. Jim joined 3M Company in 1977 and is currently a Research Specialist in the 3M Fiber Optics and Electronic Materials Technology Center. His research and development interests include fiber draw and coating process development, and plastic optical fiber product and process development.

Christopher B. Walker, Jr. received his BA in Chemistry from Carleton College in 1984, followed by a Ph.D. in Organic Chemistry from the University of Colorado at Boulder in 1989. After a postdoctoral year at the University of Illinois at Urbana-Champaign, Chris joined 3M in 1991 and has worked primarily in the area of UV curable materials. In 1997 Chris joined the Fiber Optics and Electronic Materials Technology Center and has developed new coatings for 3M optical fibers, including the Volition™ GGP fiber.

James C. Novack received a Bachelors of Science Degree in Chemistry from the University of Minnesota and a Masters of Materials Science from the University of Virginia. Jim joined 3M Company in 1977 and is currently a Research Specialist in the 3M Fiber Optics and Electronic Materials Technology Center. Jim's research and development interests include materials development for specialty optical fibers, fiber reliability, fiber optic Bragg gratings and index matching materials.

Performance of Plug and Jack

Hui-Fen Lin, Chi-Hsiang Hsieh, Shiow-Hwa Chou, Yih-Horng Hwang, Jin-Chung Lin,
His-Pai Hsu, Yih-chyuan Lin, Yuan-Kuang Tu

OSP, Telecommunication Laboratories, Chunghwa Telecom, Taiwan, R.O.C.

ABSTRACT

Reliability tests have been used to evaluate the performance of plug-jack assemblies in this study. Four reliability tests, Group A, Group B, vibration and stress relaxation, were examined. Both contact resistance and insulation resistance were used to qualify the reliability of connecting hardware after the specimens experienced these tests. The results ensure that the assemblies of modular plug and modular jack from different manufacturers are incompatible enough to drop the performance of plug and jack. Durability test and vibration test are too mild to qualify the performance of plug and jack. This study suggests that only reliability testing is not sufficient to characterize the performance of plug and jack, but is still useful to ensure the compatibility of plug and jack.

INTRODUCTION

Connecting hardware is usually used to connect two cables or cable elements for high-frequency, high-bandwidth applications. Modular plugs and jacks are famous as one kind of the connecting hardware for cabling system and they are widely used for broadband network in Taiwan. Mechanical and transmission performance requirements for connecting hardware have been specified in several international standards, TIA/EIA-568-A [1], ISO 11801 [2], and EN 50173 [3]. Reliability, as one of mechanical performance requirements for connecting hardware, is to assure its reliable operation over the usable life of the cabling

system.

Due to operational, environmental stress, such as insertion and withdrawal operations, and severe environmental conditions, contact resistance between elements of connecting hardware might be changed, which can negatively influence the transmission characteristics of the cabling system. Therefore, the reliability of connection hardware is very important to be used to characterize the performance of cabling system.

There are four tests to evaluate the reliability of connecting hardware, including Group A, Group B, vibration and stress relaxation tests [1-3]. Contact resistance measurement is mainly used to qualify the reliability of connecting hardware after the specimens experienced these four tests. In addition to contact resistance, insulation resistance is also required to examine the specimens after Group A test.

Some manufacturers, supplying both modular plugs and jacks, strongly suggest that both plugs and jacks are chosen from the same manufacturer to preserve high performance of plug-jack combination. However, the components from different suppliers can sometimes reduce the cost. Therefore, the compatibility of plug-jack combination from different suppliers is also an important issue in the cabling system.

The assemblies of modular plug and jack from the same suppliers and different suppliers are chosen to evaluate the performance of plug and jack in this study. Contact resistance measurements are used to find out

the compatibility and the reliability of these plug-jack combinations.

EXPERIMENTAL

Modular plugs were supplied from three manufacturers, identified as P, A and R, whereas modular jacks were from four manufacturers, identified as P, V, R and L. All manufacturers ensured that all elements meet category 5 requirements. There were four plug-jack combinations, referred as P-P, A-V, R-R and A-L, chosen for the reliability tests.

Test procedures for these four reliability tests, i.e. Group A, Group B, vibration and stress relaxation, were based upon the description in international standards [1-3]. Group A and Group B tests needed to be emphasized. For Group A test, the specimens have experienced thermal shock and humidity/temperature cycling, and then contact resistance and insulation resistance were measured. For Group B test, besides thermal shock and humidity/temperature cycling, the specimens also have experienced insertion and withdrawal cycles.

Contact resistance measurement was based on IEC 512-2 Millivolt Level Method [4], and 100 test points were required. In this study, the connector (modular plug or modular jack) was terminated with 4-pairs UTP cat-5 cable, and the other end of UTP cable was welded to test board. Two pieces of UTP cable were used to connect between plug-jack combination and test board to complete a test circuit. Each UTP cable was 15 cm in length. The test board was used to eliminate the abnormal stress on the contacts under test and avoid the movement of test cables.

The contact resistance automatic measuring system is a combination system including an HP 6181 DC current source, an HP 34401 multi-meter, a Keithley 2000 multi-meter and a Keithley 7001 switch system. By

connecting the test circuit to the contact resistance automatic measuring system, bulk resistance of plug-jack combination could be found out. By comparing initial bulk resistance with bulk resistance after reliability testing, the value of contact resistance change could be obtained.

Insulation resistance was measured in accordance with IEC 512-2, Test 3a, Method C, test voltage 500Vdc and 100 test points were required. In this study, General Radio 1863 Megaohmmeter was used to measure insulation resistance. Similar to the test circuit used to measure contact resistance, the connector (modular plug or modular jack) was terminated with 4-pairs UTP cat-5 cable, but the other end of UTP cable was directly connected with the Megaohmmeter.

RESULTS AND DISCUSSION

Initial values of bulk resistance

Because the connection point is more than 1.3 mm away from the voltage probe to test circuit, the raw data directly obtained from the measuring system is bulk resistance, not contact resistance. Bulk resistance measured includes contact resistance and the resistance contributed from the other components. However, to study the reliability of plug-jack combination, the values of contact resistance change during the tests are more important than the absolute values of contact resistance.

Figure 1 showed the distribution of the initial values of bulk resistance for various assemblies by Weibull distribution, characterizing the entire population of the bulk resistance for 100 connection points. The data shown in this figure clearly indicate that the value of bulk resistance for P-P is the lowest and ones for A-L is the highest. The median for the data is 46.93, 55.62, 63.56, and 76.35 mohm for the assemblies of P-P, A-V, R-R, and A-L, respectively. Based upon the values of initial bulk resistance, it was difficult to draw

conclusions. However, the distribution of bulk resistance values for P-P and R-R combinations is much narrower than that for A-V and A-L. The result suggests that the combination can provide more consistent performance if modular plugs and jacks are supplied from the same manufacturer, such as the combinations P-P and R-R.

Changes in contact resistance

After the specimens are subjected to these four reliability tests, the change in contact resistance is used to evaluate the performance of plug-jack combination. According to the requirements by international standards, the change in contact resistance of every connection point shall not be more than 5 mohm.

For Group A test, contact resistance should be measured five times for all specimens: after 50 thermal shock cycles and 100 thermal shock cycles and then after endured humidity/temperature cycle for 7, 14 and 21 cycles.

Among 100 test points subjected to Group A test, the number of contact resistance change over 5 mohm is listed in Table 1 for four assemblies of plug and jack. The data clearly indicate that the reliability performance of the combinations P-P and R-R under Group A test is much better than that of the combinations A-V and A-L. As the manufacturer's suggestion, the result implies that if modular plug and jack are supplied from the same manufacturers, then the combination provides good reliability.

For Group B test, contact resistance should be measured six times for all specimens: (1) after 100 insertion/ withdrawal cycles, as durability test; (2) after 50 thermal shock cycles and then 33 insertion/ withdrawal cycles; (3) after last 50 thermal shock cycles; (4) after 7 humidity/ temperature cycles and then 33 insertion/ withdrawal cycles; (5) after 7 more humidity/ temperature cycles; and finally (6) after last 7 more humidity/ temperature cycles and then 34

insertion/ withdrawal cycles.

Comparing with Group A test, in addition to thermal shock and humidity/ temperature tests, durability test or insertion/ withdrawal cycles was required. The results for Group B test are shown in Table 2. Similar to the results for Group A test, the reliability performance of the combinations P-P and R-R under Group B test is much better than that of the combinations A-V and A-L.

Based upon test procedures, Group B test was a more harsh test conditions than Group A test. But the results of both tests were similar. Therefore, durability test is not sensitive enough to evaluate the performance of plug-jack combinations. Furthermore, the data shown in Table 1 and 2 suggest that humidity/temperature test is a more sensitive test to evaluate the performance of plug-jack combinations.

For vibration test, three linear axes, X-axis, Y-axis and Z-axis need to be measured. Although contact resistance measurements for vibration test are completed in this study, within experimental error, no significant variations among plug and jack assemblies were observed. It suggests that the performance of the assemblies is hard to draw any conclusion only by vibration test.

For stress relaxation test, contact resistance should be measured three times for all specimens, after they endured stress relaxation test for 168, 336 and 500 hours. Among 100 test points, the number of contact resistance changed by more than 5 mohm is listed in Table 3. The performance of A-V assemblies is significantly worse than that of P-P, R-R, and A-L assemblies. The conclusion is that plug-A is completely incompatible with jack-V.

Except vibration test, a summary of the other reliability tests results for these four plug-jack combinations is listed in Table 4. The contact resistance results clearly ensure that the performance of P-P and R-R assemblies

is much better than that of A-V and A-L. Furthermore, as the manufacturers have stated, modular plug and modular jack supplied from the same manufacturer provides good performance, meaning that the compatibility of the assembly could be better if modular plug and modular jack were from the same manufacturer.

Insulation resistance

Insulation resistance measurement is required only for Group A test. According to the requirements by international standards, [1-3] insulation resistance should be measured before the test, and after enduring humidity/temperature cycle for 7, 14 and 21 cycles. Furthermore, insulation resistance between any two conductors should be at least 0.1 Gohm.

The insulation resistance for all assemblies is listed in Table 5. All data were stated as the average and the standard deviation of 100 tests. All insulation resistance values were above 0.1 Gohm. Although the insulation resistance of A-L assembly has slightly smaller values than that of the others, this measurement is not sensitive enough to evaluate the performance of plug and jack.

CONCLUSION

Reliability tests are useful to qualify the compatibility of plug and jack assembly, but is not completely enough to characterize the performance of plug and

jack assembly. Among these four reliability tests, durability test or insertion/withdrawal cycles is not sufficient to distinguish the performance of plug and jack. Furthermore, vibration test is also too mild. Based upon the results of reliability tests, P-P and R-R combinations always show much better performance than A-V and A-L. It strongly suggests that plug and jack from the same manufacturer are well compatible to each other. The compatibility of plug and jack is an important factor to influence the performance of assemblies of plug and jack, but not the only factor to characterize the performance of assembly of plug and jack. Further study of transmission properties to qualify the performance of plug and jack is required.

REFERENCE

1. TIA/EIA-568-A, Commercial building telecommunications cabling standard, 1995.
2. ISO/IEC 11801, Generic cabling for customer premises, 1995.
3. EN 50173, Generic cabling systems, 1996.
4. IEC 512-2, Electromechanical components for electronic equipment; basic testing procedures and measuring method, 1985.
5. IEC 603-7, Connectors for frequencies below 3 MHz for use with printed boards, 1996.

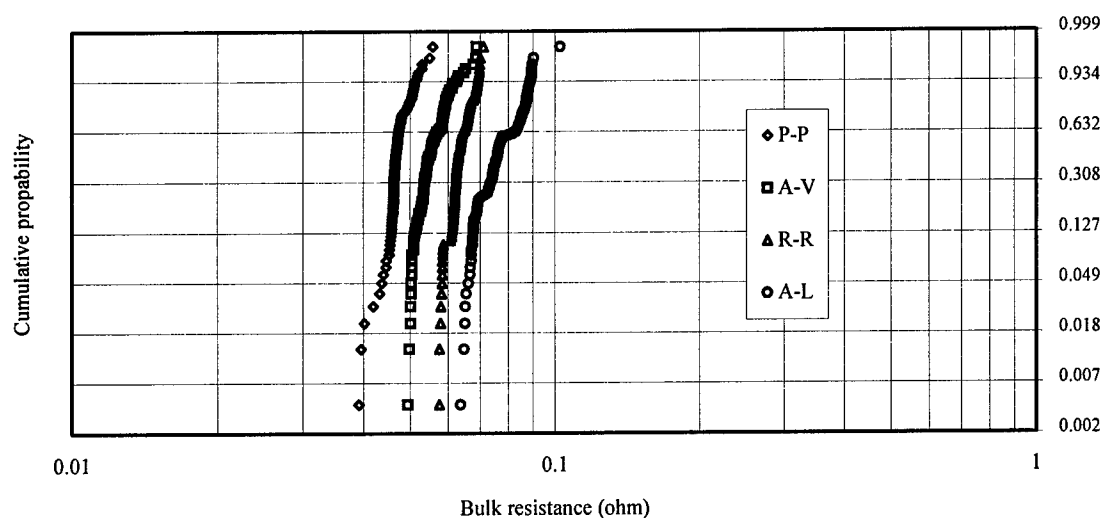


Fig 1: Initial values of bulk resistance

Table 1: The number of contact resistance change more than 5 mohm in 100 test points during Group A test.

items	Thermal shock		Humidity/ temperature cycle		
	50 cycles	100 cycles	7 days	14 days	21 days
P-P	0	2	0	0	0
A-V	1	13	16	13	22
R-R	0	1	0	1	0
A-L	0	2	25	24	20

Table 2: The number of contact resistance change more than 5 mohm in 100 test points during Group B test.

items	Durability	Thermal shock		Humidity/ temperature cycle		
	100 times	50 cycles and 33 insertions	100 cycles	7 days and 33 insertions	14 days	21 days and 34 insertions
P-P	0	0	0	2	0	0
A-V	1	3	16	20	23	30
R-R	2	1	5	1	1	1
A-L	0	1	3	21	23	10

Table 3: The number of contact resistance change more than 5 mohm in 100 test points during stress relaxation test.

Aging time	168 hr	336 hr	500 hr
P-P	0	0	1
A-V	31	20	31
R-R	1	0	2
A-L	2	0	0

Table 4: The number of contact resistance in 100 test points change by more than 5 mohm after 3 reliability tests.

Plug & jack	Group A	Group B	Stress relaxation
P-P	0	0	1
A-V	22	30	31
R-R	0	1	2
A-L	20	10	0

Table 5: Average insulation resistance during group A test. (unit: Gohm)

Plug & jack	Initial value	Humidity/ temperature cycle		
		7 days	14 days	21 days
P-P	14.0 ± 2.7	14.1 ± 2.0	14.5 ± 2.6	12.9 ± 2.4
A-V	11.5 ± 2.3	11.8 ± 2.3	13.0 ± 2.9	13.7 ± 2.6
R-R	14.0 ± 3.0	14.8 ± 2.4	15.6 ± 2.7	15.0 ± 2.3
A-L	9.1 ± 2.6	10.3 ± 2.1	11.4 ± 2.0	11.9 ± 3.0

DEVELOPMENT OF AN ULTRA HIGH FIBER COUNT RIBBON ADSS CABLE DESIGN

James W. Thornton, Nathan S. Hatch, & Richard G. Gravely, III

Fitel Lucent Technologies
10 Lucent Drive
Carrollton, GA 30117

ABSTRACT

A 432-fiber loose tube aerial cable has been designed for ultra-high fiber count applications. This cable was designed with fiber reliability, fiber attenuation, and hardware compatibility in mind. The cable design was tested for mechanical and environmental performance, and also for standard aerial tests such as galloping, aeolian vibration, and elevated temperature. The cable design has proven successful, and 100 miles (161 km) of the cable has been deployed in the Northeast United States.

INTRODUCTION

Opportunities abound in today's telecommunications market. There are ever changing needs for new products as new opportunities are created. As the demand for high bandwidth increases so too does the demand for increasingly high fiber count cables. The ultra high fiber count PowerGuide ADSS has been developed to compliment existing high fiber count constructions. The ADSS construction is important to those in the industry that can take advantage of existing pole structures where Rights of Way (ROW) access can be obtained. This paper discusses the application, design, and performance of a ribbon loose tube ADSS PowerGuide cable.

CABLE APPLICATION

The demand for ultra high fiber count optical cables is increasing at a rapid pace. There are multiple opportunities that require ultra high fiber count cables such as highly populated areas and dark fiber leasing. Dark fiber leasing is a high revenue opportunity where companies develop and install an embedded base of high density, high bandwidth, fiber optic cables. The bandwidth (i.e. fiber) in these cables is leased to different users such as telecommunication

service providers, Internet providers, governments and businesses.

There are three most commonly used deployment techniques for fiber optic cables. Cables can be installed in duct, directly buried or positioned aerially. Many factors are considered when determining the most efficient and cost effective approach to cable deployment. One primary consideration is Rights of Way (ROW). Companies that can secure economical ROW access can observe tremendous cost savings associated with cable installation. The 432-fiber ribbon loose tube PowerGuide product is designed for companies that can take advantage of installing cables on pole structures. Not only can installation costs be saved, aerial cables are immune to the number one cause of cable failure; Dig Ups. Millions of dollars are lost every year to outages caused by cable Dig Ups.

When considering high fiber counts in excess of 288, fibers in a ribbon format should be considered. The ribbon format allows mass fusion splicing where 12 fibers can be spliced together in a single operation. Ribbons are individually marked with specific identification so that each unit can be easily distinguished. This allows buffer tubes to contain multiple ribbons with no compromise in unit identification for splicing purposes. Optical shelves that transition optical fiber from a cable format to an individual fiber format come in standard fiber counts of 24, 48, 72 and 144. The 432-fiber ribbon ADSS cable was designed so that each buffer tube contains 72 fibers for ease of cable-to-shelf transition. The 432-fiber construction is achieved by using 6 ROL stranded buffer tubes, each containing six 12-fiber ribbons. This compartmentalized approach provides the user added security when dropping fibers from the backbone to a business facility or the like. When accessing the appropriate ribbon, for any given customer, the remaining 5 buffer tubes (360 fibers) can be routed through the closure with transition tubing. Once the transition tubing is applied to the buffer tubes, the ribbons can be moved aside so that the buffer tube of interest

can be opened and appropriate ribbons manipulated for splicing/drop purposes.

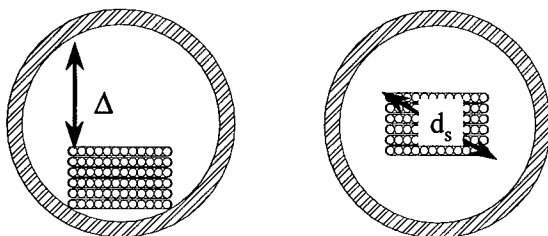
To address most aerial applications where ultra high fiber count cables are to be deployed, the ribbon PowerGuide product is designed to sustain quality performance in pole to pole span lengths of up to 600 feet under the NESC most severe loading conditions; Heavy Loading. This means a robust design for years of high quality service under some of the most demanding in-service conditions. The product is designed to be installed with a cable sag that is 1.5% of the pole to pole span. Sag values in extreme loading conditions depend on the span, installation tensions, and the conditions present during worst case loading.

CABLE DESIGN

Critical Parameters

During the early phases of the development, the design team identified various critical parameters for the design and solutions to those parameters.

Fiber Attenuation. The cable design must not exhibit any increase in fiber attenuation when subjected to tensile forces in the operating region of the cable. Since this design is self-supporting, the cable will be subjected to tensile forces as high as the maximum rated cable load (MRCL) and as low as the installation conditions over its entire life. In order to guarantee no increase in fiber attenuation and no fiber strength degradation over the cable's lifetime, the overall cable strain must be limited to ensure the maximum fiber strain will not exceed 30% of the fiber proof stress level.



$$\text{Clearance } (\Delta) = (id^2 - w^2)^{1/2} - nT \quad (1.1)$$

$$\text{Packing Density} = d_s/id \quad (1.2)$$

To ensure that the ribbon fibers will not exhibit any attenuation increase during temperature extremes, the clearance¹ and packing density of

the buffer tubes were chosen based on desired cable size and environmental performance.

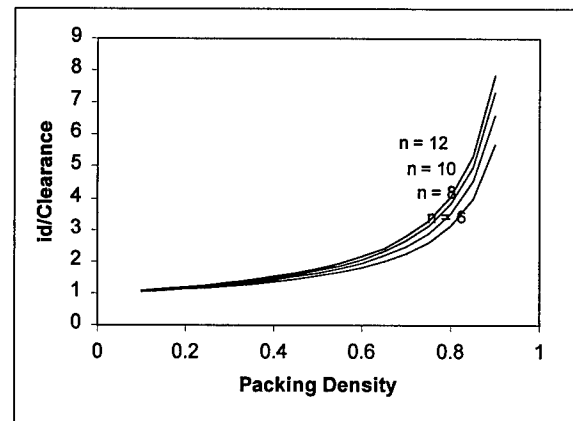


Figure 1: Clearance & Tube ID as Related to Packing Density

Figure 1 illustrates that effect of increasing ribbon stack size on the ratio of tube id and clearance. The curves suggest that larger ribbon stacks will perform in temperature extremes better than smaller stacks even if the same packing density is chosen for both. In practice, the excess ribbon/fiber length must be accounted for as well as the clearance and packing density to ensure acceptable optical performance at extreme temperatures.

Fiber Strength Reliability. The cable design must not subject the optical fibers to undue stresses that would result in the fiber strength reliability to degrade over the life of the cable. Most fiber manufacturers are in agreement that short and long term fiber stresses should be kept less than 30% of the fiber proof stress level, which will result in nearly a zero fiber failure probability for 40 years.

Hardware Compatibility. The cable design must be compatible with standard aerial self-supporting hardware at the rated loading conditions. Aerial self-supporting cables are subjected to crush forces from the cable hardware over its entire life. In order to guarantee that the cable design would be compatible, the buffer tubes are manufactured with engineered thermoplastics which exhibit good crush performance. The buffer tube gaps were chosen to be tight to provide better coupling. DryBlock™ technology was utilized for water-blocking the cable core, which also provides better coupling of the core elements.

Finally, the cable design consists of inner and outer polyethylene sheaths, which further provide good crush resistance.

Accessibility. The cable design must be craft-friendly and easy to access. Since the cable design shall contain a large number of optical fibers for craft technicians to handle, it was decided that ribbon technology would be preferable over loose fiber. Twelve fiber ribbons have been used by the industry for many years with the mass fusion splice technology, which has been shown to reduce splice costs and time. In addition, the color-coded buffer tubes, ribbon print legends, and color-coded optical fibers are significantly advantageous in identifying and managing the fiber at splice points. The loose tube core is stranded with reverse oscillating lay (ROL) and the distance between reversal points was limited to a maximum of five feet to aid with midspan accessibility. The cable core utilizes DryBlock™ technology to prevent the flow of water longitudinal down the cable. By using DryBlock™ technology and eliminating the use of viscous flooding compounds, field technicians can significantly reduce time and costs associated with cleaning the buffer tubes.²

Design Construction

This new cable design consists of 6 buffer tubes each containing six-12 fiber ribbons which gives an overall capacity for each buffer tube of 72 fibers. The buffer tubes are ROL stranded about a central strength member to provide midspan access to the buffer tubes and ribbons. The cable design is manufactured with a DryBlock™ core to ensure craft friendly accessibility. The cable's yarn strength elements separate the inner and outer jackets. High denier aramid yarn strands are applied in such a way as to be torque balanced. Strength of cable is designed to ensure that the cable can support expected loading conditions. The cable outer jacket can be manufactured with either a MDPE outer jacket or special anti-tracking jacket to withstand high electrical space potentials.

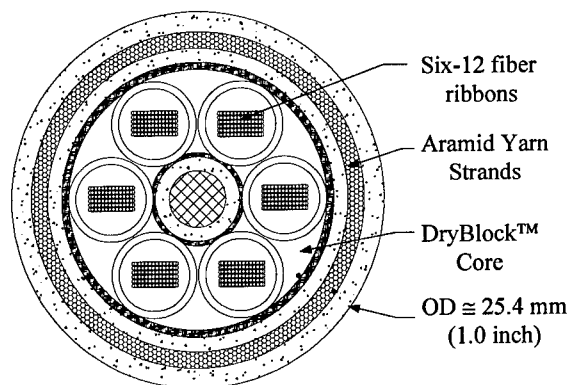


Figure 2: Cable Cross-section

CABLE PERFORMANCE

Initial qualification testing was conducted on a 432 fiber DryBlock™ Ribbon ADSS cable design to ensure excellent cable reliability through worst case environmental and mechanical conditions. The trial cable was manufactured with matched-clad fiber ribbons. The following tests were conducted:

Standard Qualification Testing

- Mechanical Testing per GR-20 Issue 1
- Environmental Testing per GR-20 Issue 1

Extensive Tensile Testing

- Tensile Cycling (8 cycles up to MRCL) per TR-1121 Issue 1

Outside Aerial Testing

- Galloping Vibration per IEEE P1222 Draft
- Aeolian Vibration IEEE P1222 Draft
- Tensile at Elevated Temperature (up to MRCL at 140°C)
- Extreme Tensile (150% of MRCL)

Standard Qualification Testing

Standard mechanical and environmental testing was performed per Telcordia (formerly Bellcore) GR-20-Issue 1, *Generic Requirements for Optical Fiber and Optical Fiber Cable*. The specifications for the tests performed are similar to TR-NWT-1121 Issue 1, *Generic Requirements for Self-Supporting Cable*.

Mechanical Testing. The 432-fiber ribbon design was tested to ensure acceptable mechanical resistance during installation and operating conditions. All tests were conducted in accordance with EIA/TIA test procedures. The following table summarizes the mechanical testing performance and test specifications.

Table 1: Mechanical Testing Summary

TEST PERFORMED	TEST PROCEDURE	PERFORMANCE
High Temperature Bend	TIA/EIA-455-37A	4 hours @ +60°C, mandrel dia. = 14 X Cable OD (300 mm) Max Δ change = 0.02 dB No visual damage observed
Low Temperature Bend	TIA/EIA-455-37A	4 hours @ -30°C, mandrel dia. = 14 X Cable OD (300 mm) Max Δ change = 0.02 dB No visual damage observed
Impact Resistance	EIA/TIA-455-25A	10 kg mass, 25 impacts @ 30 cycles/min. Max Δ change = 0.01 dB No visual damage observed
Compressive Strength	EIA-455-41A	220 N/cm, 10 min duration max Δ change = 0.02 dB No visual damage observed
Tensile Load and Bend Test	EIA-455-33A	2,660 N Tensile Load, 1 hour duration, 462 mm Universal Sheave Diameter Max Δ change = 0.03 dB No visual damage observed
Cable Twisting	TIA/EIA-455-85A	10 cycles of: 180° CW twist, 360 CCW twist, 180° CW twist Length = 1.7 meters Max Δ change = 0.00 dB No visual damage observed
Cable Cyclic Flexing	TIA/EIA-455-104A	25 x 180° flex cycles, sheave dia. = 18 X Cable OD (400mm) Max Δ change = 0.01 dB No visual damage observed

All test results were in accordance with the specifications listed in GR-20 Issue 1.

Environmental Testing. The same cable was also tested environmentally to ensure acceptable performance during the service life of the cable. All environmental tests were also conducted in accordance with EIA/TIA test procedures. The following table summarizes the environmental testing performance and test specifications.

Table 2: Environmental Testing Summary

TEST PERFORMED	TEST PROCEDURE	PERFORMANCE
Temperature Cycling	EIA/TIA-455-3A	Attenuation Coefficient Change @ 1550 nm (dB/km) Temp (°C) -40 +70 MAX Δ 0.04 0.02 AVG Δ 0.02 0.01
Cable Aging	EIA/TIA-455-3A Bellcore GR-20- Core, Issue 1	Attenuation Coefficient Change @ 1550 nm (dB/km) Temp (°C) -40 +70 MAX Δ 0.09 0.02 AVG Δ 0.03 0.01
Cable Freezing	EIA/TIA-455-98A	@ -2°C/24 Hrs, Max Δ change = 0.01 dB No visual damage observed
Water Penetration (unaged)	EIA/TIA-455-82B	Pressure head = 1 meter, Length = 1 meter 24 hour: max penetration = 27 cm
Water Penetration (aged)	EIA/TIA-455-82B Bellcore GR-20- Core, Issue 1	Pressure head = 1 meter, Length = 1 meter 1 hour: max penetration = 5 cm

All test results were in accordance with the specifications listed in GR-20 Issue 1.

Extensive Tensile Testing

Tensile Cycling. Tensile testing was performed repeatedly per TR-NWT-001121 Issue 1. The Ribbon ADSS was secured with dead-ends, and cycled eight times to the maximum rated cable load (MRCL) for one hour to simulate worst case installation conditions. Cable and fiber strains were monitored during each test. Figure 3 graphs the average actual cable and fiber strain characteristics for the tensile cycling testing along with the theoretical cable strain. The theoretical and average cable strain slopes differed by less than 1%. The average tensile window for the cable was 0.15%. Maximum attenuation during the MRCL tensile load condition was 0.02 dB/km.

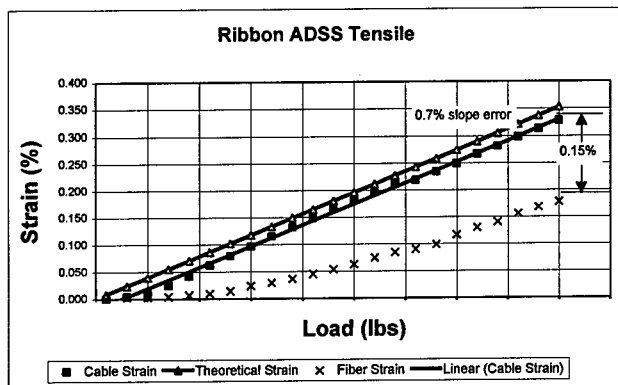


Figure 3: Tensile Test Results

Aerial Cable Tests

Galloping Test. The galloping test was conducted in accordance with Institute of Electrical and Electronics Engineers (IEEE) P1222 (draft) to determine the performance of the cable under sinusoidal wave conditions. Specifically, the ribbon ADSS cable was shaken at its fundamental frequency, or the frequency (f) required to excite the span in a single loop. A loop (l) is defined as one-half of the wavelength (λ).³ The velocity (V_t) of the cable can be calculated by the following equation:

$$V_t = \lambda f = 2 fl = \sqrt{\frac{Hg}{m}} \quad (1.3)$$

Where: H = tension in kg
 $g = 9.8 \text{ m/s}^2$
 m = mass per unit length (kg/m)

The number (n) of standing loops in a span is found by dividing the span length (S) by the loop length (l). The frequency of the cable vibration can then be found the equation:

$$f = \frac{nV_t}{2S} \quad (1.4)$$

If the number standing loops (n) is set to 1, the fundamental frequency is calculated. For the ribbon ADSS cable, a frequency of 2.9 Hz was used, with an 8-inch peak-to-peak amplitude. The cable was tensioned to at least 50% of its maximum rated installation tension throughout the 20-hour test. A diagram of the test is shown in Figure 4.

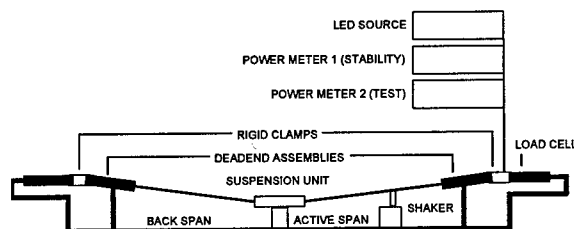


Figure 4: Galloping Test Set-up

The galloping test was performed for 210,000 cycles, more than twice the cycles required by IEEE 1222 Draft. The maximum attenuation change was negligible ($< 0.01 \text{ dB}$ at 1550 nm) and no damage was caused by the dead-end hardware.

Aeolian Vibration. The Aeolian Vibration test was also performed on the 432-fiber ADSS cable in accordance with IEEE P1222 Draft. A very similar setup to the galloping test, as shown in Figure 4, was used. This test simulates higher frequency, lower amplitude sinusoidal waves. In the test set-up, the static sag angle to horizontal was one degree. A frequency of 33.9 Hz, equivalent to a 16.1 km/hr wind, was used with an amplitude of 12.5 mm. The cable was tensioned to 100% of its maximum rated installation load and shaken for 38 days, or 110 million cycles. Fibers were concatenated and monitored for attenuation once an hour for the duration of the test. The maximum attenuation change during and after the test was negligible ($< 0.01 \text{ dB}$ at 1550 nm) and no physical damage was recorded during the 110 million-cycle test.

Elevated Temperature Test. The ribbon ADSS qualification cable was also tested under elevated temperatures to ensure excellent dead-end performance under extreme conditions. The cable was secured on both ends with dead-ends, and a solar simulator box, see Figure 5, was placed over one of the dead-ends and heated to 60°C (140°F).

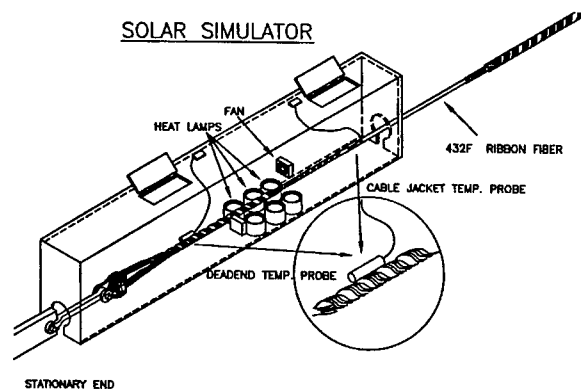


Figure 5: Elevated Temperature Setup

A load equal to 100% of the cable's maximum rated installation load was applied to the cable. The tensile load and elevated temperature were maintained for a 24-hour period. During and after the test, attenuation and dead-end movement were monitored and recorded. The maximum attenuation change during and after the test was negligible (< 0.01 dB at 1550 nm) and no of slippage of the dead-end was measured.

Extreme Tensile Test. After the elevated temperature test was complete, the solar simulator was removed and the cable tensile tested to 150% of its maximum rated cable load (MRCL) for 8 hours. During and after the test, attenuation and dead-end slippage were monitored. The maximum attenuation change in each fiber was ≤ 0.02 dB during and after the test. No slippage of the dead-end was measured during and after the test.

FIELD DEPLOYMENT

The first know application of a 432-fiber Loose Tube Ribbon ADSS cable involves a major Metropolitan network installed in the Northeastern United States. Approximately 100 miles of cable has been installed along Electrical Utility Rights of Way (ROW). This network was designed an implemented to secure revenue through the business of dark fiber leasing. Multiple end users will be paying to access the fibers in this network so that they can provide their customers with certain services.

Considerable amounts of bandwidth can be secured by employing optical systems that support DWDM technology. In DWDM signal

transmission, multiple wavelengths are multiplexed together within the same optical pulse. Each individual wavelength contains information that is de-multiplexed at the receiving location. Depending on the customer needs, the ultra high fiber count ribbon ADSS cable design can be treated with conventional Matched Clad singlemode and/or TrueWave™ Non Zero Dispersion fiber to support single wavelength operation and DWDM technology all within the same cable. Similar such cables have been installed in the Metropolitan network discussed earlier. Since this was the first known installation of this high count ADSS product, field testing of the fibers after installation was conducted. Technical Services personnel were dispatched to the installation locations where optical measurements on some of the fibers in these cables were made for evaluation. The Matched Clad fibers were tested at 1550nm with excellent performance. The TrueWave fibers were tested at 1625nm wavelength and also showed excellent results. Careful planning for this optical network allows this leasing company to support the bandwidth needs of today while protecting their investment with upgrade capabilities for the future.

CONCLUSION

Today's demand for high bandwidth creates the same demand on increased fiber count capabilities. The use of high fiber count ribbon constructions in a loose tube format has been applied to the aerial market. The ribbon loose tube ADSS PowerGuide construction provides the user with high fiber counts with a compartmentalized approach for ease of identification and handling. The ADSS PowerGuide has undergone extensive environmental, mechanical, and field testing to ensure a robust construction for years of quality service. Fiber optic cable customers now have multiple design options to choose from that best fit their application and their budget.

REFERENCES

- ¹ Gilbert/Commonwealth. *Transmission Line Reference Book - Wind-Induced Conductor Motion*. Electric Power Research Institute, 1979.
- ² Murata, H. *Handbook of Optical Fibers and Cables*. New York: Marcel Dekker, Inc., 1988.
- ³ Thornton, J. W., et al. "Materials, Development, and Field Trials of a Dry Core Cable." *National Fiber Optic Engineers Conference Proceedings*. 1996: 359-370.

ACKNOWLEDGEMENTS

We would like to thank Tommy King, Dulmison Inc., for his help in the extensive dead-end reliability testing.

SPEAKER BIOGRAPHY



Nathan S. Hatch

Nathan Hatch is a Project Engineer in the RD&E Department at Fitel Lucent Technologies. He received his BSMET degree from Southern Polytechnic University. Mr. Hatch's main responsibilities include product developments and supporting Lucent Technologies and Furukawa Electric Company's loose tube joint ventures.

DEVELOPMENT OF NEW AERIAL SELF-SUPPORTING CABLE WITH EXCESS FIBER RIBBON LENGTH IN SZ-SLOT

Daisuke Iwakura Ichiro Kobayashi Ryuji Takaoka
Hideyo Hiramatsu Yasuhiro Kamikura

THE FURUKAWA ELECTRIC CO.,LTD.
6, YAHATA-KAIGANDORI, ICHIHARA, CHIBA 290-8555 JAPAN

ABSTRACT

We developed a new aerial self-supporting cable with excess fiber ribbons of 0.2% relative to the cable length. We evaluated fiber ribbon movement caused by the excess fiber length in SZ-slot by several examinations. The results showed that fiber ribbons can move in the range of 5m from the end of the cable, and in the range farther than 5m from the end of the cable, they can not move in SZ-slot. The result of long-term field test, which is performed during 420days, were very good in terms of attenuation characteristics and fiber ribbon movement. These results suggest that the new self-supporting cable design with excess fiber ribbon length in SZ-slot is suitable for the aerial application.

1. BACKGROUND

In order to realize FTTH, economical construction of access network will be one of the most important targets in developing new cables. For example it may be demanded of cables to have good mid-span branching characteristics, and to have high fiber density. To meet these demands, stacked ribbon SZ-slotted rod cable was proposed for distribution cable. This cable type also has a superior prevention characteristics of fiber ribbons movement in slot. So this cable has been used for aerial distribution where the prevention of ribbon movement is a very important issue. It is generally known that aerial cables elongate by more than 0.2% under high temperature and strong winds. Thereby, one important point in cable design is to ensure that no strain is imparted to the fibers under such conditions. So the present aerial cable structure provides the

cable an excess length relative to the suspension member.⁽¹⁾⁽²⁾ (Fig. 1)

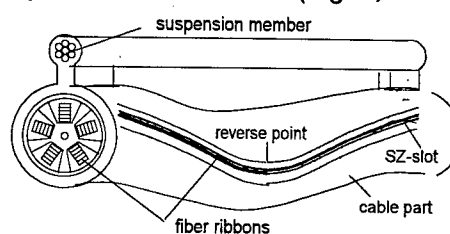


Fig.1 : Excess cable length model

In order to simplify the cable structure, we developed a new self-supporting optical fiber cable with excess ribbon length in SZ-slot⁽³⁾. (Fig. 2)

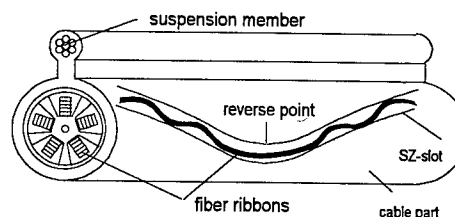


Fig.2 : Excess fiber length model

Listed below are the two effects of this new cable.

- (1) Both the sheath equipment and the manufacturing condition become simple.
- (2) Aesthetic impression of the cable after installation improves.

Subject of this development is to estimate ribbon movement in slot caused by the release of the buckling stress of the excess ribbon length. We examined the characteristics of ribbon movement in SZ-slot by several evaluations including long-term field test in

order to testify the feasibility of the cable for practical application.

2. CABLE DESIGN

2-1. Design of slot clearance

The slot is designed to give large clearance for the ribbon stack and ribbons are accommodated with buckling. The ribbon are bent to the thickness direction in a sine curve as shown in Figure.3.

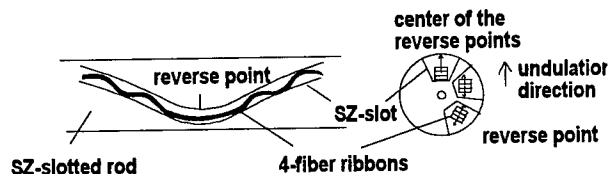


Fig.3 : Ribbon sine curve in SZ slot

The relationship between the radius of minimum sine curvature of the fiber and the increase of attenuation has been reported and the ribbon stack should be accommodated with suitable sine curve so that the loss increase and the stress stays within a tolerable limit⁽⁴⁾. We designed the slot dimension so that the inscribed circle of diameter D defined by equation (1) fits the slot. (Fig.4) Here $a(\beta)$ is the amplitude of the sine curve when excess fiber length is $\beta\%$.

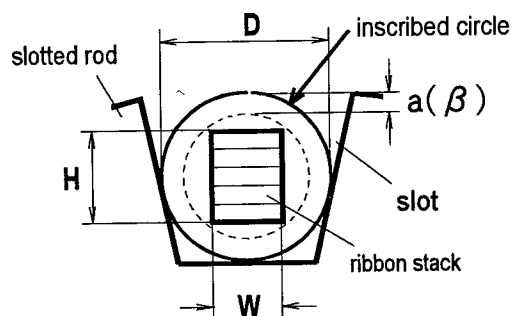


Fig.4 : Cross section of the slot and inscribed circle

$$D \geq (H^2 + W^2)^{1/2} + 2a(\beta) \quad (1)$$

H : the height of ribbon stack

W : the width of ribbon

In Figure 5, the relationship between excess fiber and cable diameter is shown for 100-fiber SZ cable. The cable diameter is determined by slot clearance. In the figure, three stress level caused by sine curve bending are shown.

In order to accommodate large fiber excess length, it is necessary to have large slot clearance and the cable diameter becomes large.

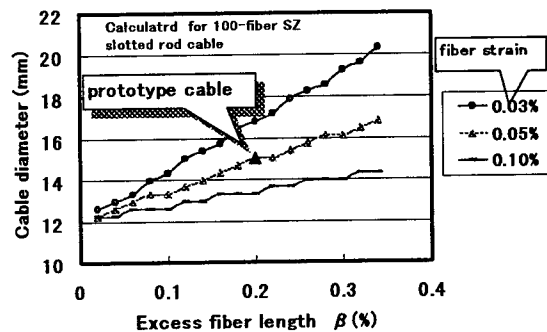


Fig.5 : Relationship between excess fiber length and cable diameter

We designed the cable with 0.05% fiber strain considering attenuation and long term reliability of the fiber.

2-2 . Design for the prevention of ribbon movement

In order to prevent ribbon movement , we should design the SZ-slot so that the pull out force of ribbons from the slot is sufficiently large. The pull out force of ribbons is mainly determined by the following parameters

- slot diameter
- slot clearance
- reverse pitch

As for the slot diameter and slot clearance we have already considered them in 2-1 from the view point of attenuation and fiber stress . So now we must determine the reverse pitch. Generally the shorter the reverse pitch becomes, the larger the pull out force becomes. In Figure6 the relationship between the reverse pitch and pull out force is shown.

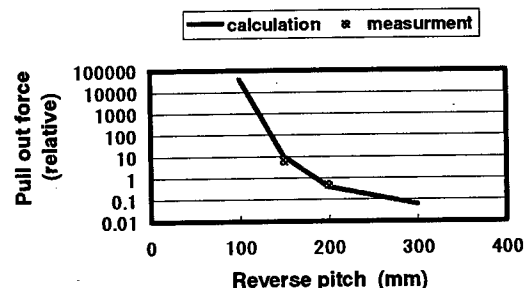


Fig.6 : Relationship between the reverse pitch and pull out force

we designed the reverse pitch so that the pull out force becomes larger than 20N/10m.

3. PROTOTYPE CABLE

3-1. Manufacture method

A tension was applied to the SZ slotted rod so that the rod was extended by more than 0.2% during the ribbon assembly process. The tension was then released to make the ribbon length longer than the slotted rod. (Fig.7)

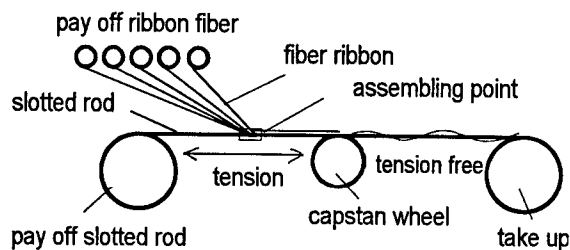


Fig.7 : Manufacture method during the ribbon assembly process

3-2. Prototype structure

A prototype cable was manufactured based on the design theory of section 2. The design details are shown in Table1. 5 of 4-fiber ribbon are stacked in each slot. The ribbon size is 0.3mm × 1.1mm. Excess ribbon length was designed to be 0.2%. Figure 8 shows the structure of the prototype cable. The tensile stress-strain characteristics of the cable is shown in Figure 9.

Table 1 : Design details of prototype

Slotted rod	the number of slots	5
	tensile strength member size	φ 2.6mm
Suspension member	diameter (mm)	12
	size	7 / φ 2.0mm
Cable	height (mm)	25
	width (mm)	15
Pull out force of fiber ribbon (N/10m)		25~30

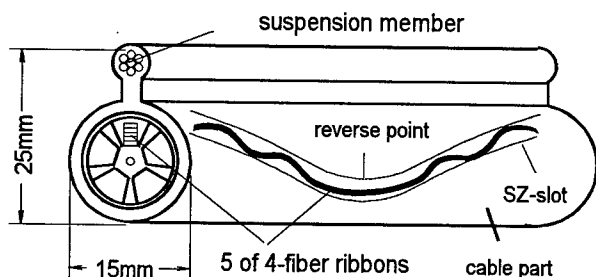


Fig. 8 : Prototype structure

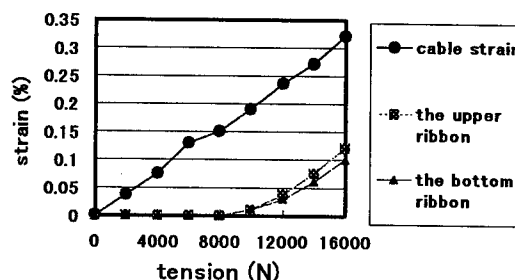


Fig.9 : Tensile stress-strain characteristics

Little fiber strain was observed when the cable strain is under 0.2% which is equivalent to the maximum cable elongation encountered under high temperatures and strong winds.

3-3. Characteristics

The attenuation, temperature, and mechanical characteristics of the prototype cable are shown in Table2. Good characteristics are obtained.

Table 2 : Characteristics of prototype cable

Item	Condition	Result
Attenuation	$\lambda = 1550\text{nm}$	0.20dB/km
Temperature	-30°C ~ 70°C	<0.05dB/km
Bending	R=100mm	<0.02dB
Lateral force	2000N/100mm	<0.02dB
Tensile	0.20%	<0.02dB
Squeezing	R:250mm	<0.02dB

4. EVALUATION OF RIBBON MOVEMENT

4-1. Ribbon movement factor

Ribbon movement in slot is caused by the following 4 factors.

- (1) Small amplitude oscillation by wind / machine (car etc.)
- (2) Dancing by strong wind
- (3) Tension cycle
- (4) Temperature change

We performed tests taking into consideration the above-mentioned factors.

As for items (1),(2),(3) we simulated by model experiments. For item(4) we performed long-term field test.

4-2. Small amplitude oscillation test

(1) **Condition and method.** Small amplitude oscillation of cable is caused by Karman-whirlpool generated on the cable surface when wind attacks the cable perpendicular to the surface. In this case the frequency is approx.40Hz according to the former report⁽⁵⁾. Therefore in our test, small oscillation of 40Hz (amplitude<1mm) was given to the cable and the ribbon movement was monitored. Figure 10 shows the make up of this test.

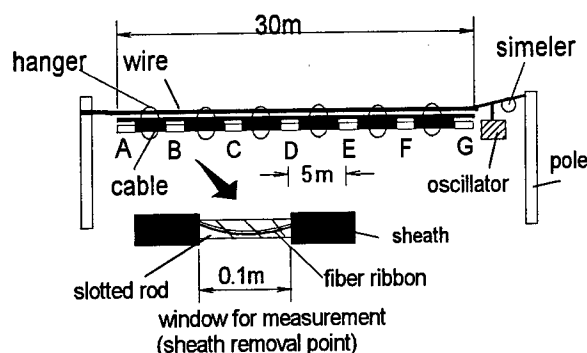


Fig.10 : Small amplitude oscillation test

The cable length is 30m. The cable jacket was removed at 5m interval and the windows A ~ G were made to observe the ribbon movement. Ribbons were kept in the slot. The test cable was suspended from a wire between 2 poles. So in this test, no tension is applied to the cable. Thus the cable was oscillated while maintaining the excess fiber length of 0.2%.

(2) **Result.** Table 3 shows the result of the test.

Table 3 : Length of ribbon movement in small amplitude oscillation test

Lapse of time (min.)	(mm.)						
	window						
	A	B	C	D	E	F	G
0	1	0	0	0	0	0	0
10	2	0	0	0	0	0	0
60	2	0	0	0	0	0	0
120	2	0	0	0	0	0	0
240	2	0	0	0	0	0	0
300	2	0	0	0	0	0	0

After 300 minutes of oscillation, the fiber movement of 2mm was observed only at point A. The movement was saturated after 10 minutes.

The result indicates that the ribbon farther than 5m from the cable end does not move.

4-3. Dancing test

(1) **Method and condition.** Dancing of the cable will occur as a function of the lifting force and the drag force when the wind hits the cable. Generally when dancing is likely to occur, the cable is twisted to suppress the dancing. In our test, the amplitude of oscillation was set up to be 300mm, and the frequency was 2Hz. The total of one million oscillation was given to the cable and the ribbon movement was observed. Figure 11 shows the test set-up.

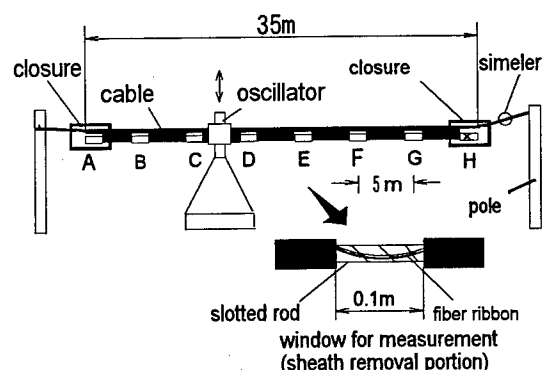


Fig.11 : Dancing test

The length of the test cable was 35m. Ribbons were kept in the slot. And at the end point H ribbons were fixed.

(2) **Result.** In the table 4 we will show the result.

Table 4 : Length of ribbon movement in dancing test

Oscillation (*10000 times)	(mm.)							
	window							
	A	B	C	D	E	F	G	H
0	1	0	0	0	0	0	0	-
1	1	0	0	0	0	0	0	-
5	1	0	0	0	0	0	0	-
10	1	0	0	0	0	0	0	-
50	1	0	0	0	0	0	0	-
100	1	0	0	0	0	0	0	-

After one million oscillation there was no ribbon movement. This result indicates that the ribbon does not move during dancing when oscillation amplitude is quite large.

4-4. Tension cycle test

(1) **Method and condition.** In this test we supposed a circumstance of strong wind at normal temperature. We added a stress of 0.1% to the test cable repeatedly. The stress was given for the duration of 10 minutes each time. Total number of cycle was 40 times. (Fig.12)

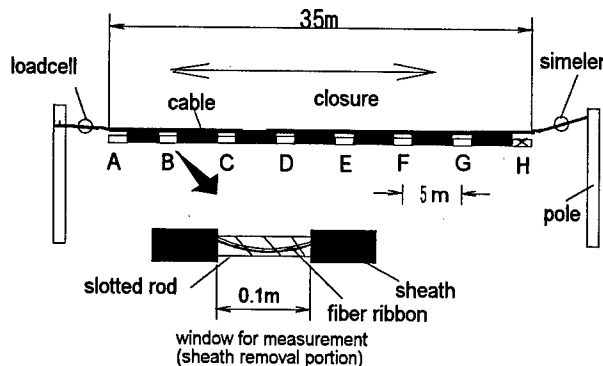


Fig.12 : Tension cycle test

The length of the test cable was 35m. Ribbons were kept in the slot. And at the end point H ribbons were fixed.

(2) **Result.** Table 5 shows the result of the ribbon movement during the test.

Table 5 : Length of ribbon movement in tension cycle test

tension cycle (times)	(mm.)							
	window							
	A	B	C	D	E	F	G	H
0	1	0	0	0	0	0	0	-
5	1	0	0	0	0	0	0	-
10	1	0	0	0	0	0	0	-
15	1	0	0	0	0	0	0	-
20	1	0	0	0	0	0	0	-
40	1	0	0	0	0	0	0	-

After 40 times , there was no ribbon movement. The result indicates that tension cycle does not cause the ribbon movement.

4-5. Long-term field test

(1) **Method and condition.** In order to examine the influence of temperature change, we performed long-term field test. In Figure 13 the test set-up is shown.

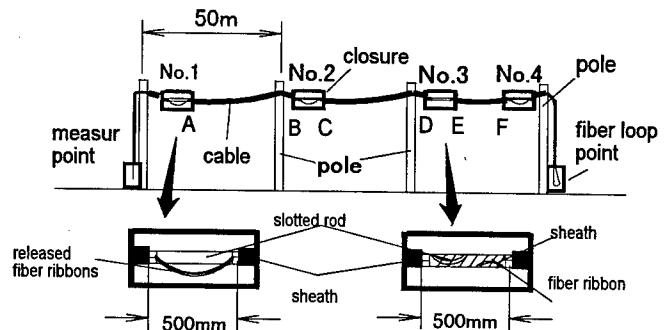


Fig.13 : Long-term field test

In this test, the cable is twisted every 10m. 4 closures were fixed at the side of each pole.

In the closure, the cable sheath was removed and the fiber movement was observed. At No.1, 2, 4 closures, ribbons were released from the slots. In No.3 ribbons were kept in the slots. The ribbon movement was measured at point A~F in the closures . All fibers were jointed at the cable end near No.4 closure in order to measure the attenuation change . In Figure 14 the change of temperature and wind velocity during the field test is shown. These data were made by the Meteorological Agency.

Temperature changed from -10°C to 25°C , and velocity from 3.7m/s to 7m/s in average. In the figure the ribbon movement measurement dates are indicated.

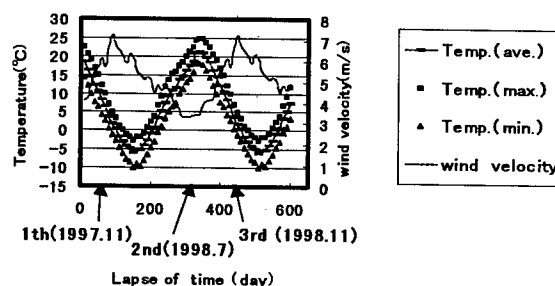


Fig.14 : The change of temperature and wind velocity during the test .

(2) **Result.** Table 6 shows the result of ribbon movement. Figure 15 shows the attenuation change.

Table 6 : Length of ribbon movement in long-term field test

Date	Lapse of time (day)	(mm.)					
		A	B	C	D	E	F
1th : Nov.1997	60	2	1	0	0	0	0.5
2nd : Jul. 1998	300	2	1	0	0	0	1
3rd : Nov.1998	420	2	1	0	0	0	1

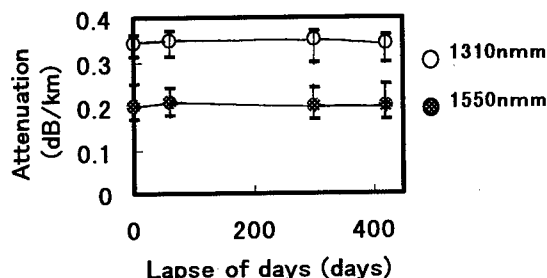


Fig .15 : The attenuation change

Only at the points A,B,F where ribbons are released from the slots, we observed the ribbons stick out by 1mm~2mm, and the value saturated after 300 days. At the points D and E where ribbons are kept in the slots we could not observe ribbon movement. These results show that the ribbons move only near the cable ends . This result coincides with the former test results of 4-2~4-4. As for the attenuation characteristic, there was no significant change during the test.

5. CONCLUSION

Table 7 summarizes the results of the tests we performed. The following results were obtained.

- In small oscillation test, ribbon movement of 1~2mm was observed only within 5m from the cable end.
- In dancing test, ribbon movement was not observed.
- In tension cycle test ,ribbon movement was not observed.
- In long-term field test, ribbon movement of 1~2mm was observed only near the cable end where ribbons are released from the slots .

In conclusion,

- (1) In the prototype cable , the ribbons can move in SZ-slot in the region within 5m from the cable end where ribbons are released from the slot.
- (2) The value of ribbon movement is saturated to 1or 2mm.
- (3) Small amplitude oscillation causes the ribbon movement more than dancing or tension cycle.

We designed new aerial self-supporting cable with excess fiber ribbon length in SZ - slot. The prototype cable had good characteristics for several tests which are attenuation, mechanical and ribbon movement. As a result, this new self-support cable is proved to be feasible for practical use. The relationship between the buckling stress caused by the excess ribbon length and the ribbon movement should be estimated theoretically in the future.

Table 7 : Summarize of results for ribbon movement tests

	Conditions	Length of the ribbon movement		Movement value
		Fiber movement place	Value (mm)	
Small amplitude oscillation	40Hz *300min	within 5m from cable end	2	saturated
Dancing	2Hz *one million times	not observed	0	—
Tension cycle	0.1% *10min *40times	not observed	0	—
Long-term field test	temp : -10°C~25°C wind velocity : 3.8~7.0m/s	near cable end with free ribbons	1~2	saturated

REFERENCES

(1)H.Iwata et.al."Design of Aerial Optical Fiber Cable System Suitable for Easy Branching" IWCS 1997

(2)I.Kobayashi, st.al. "Development of new aerial ditribution cables with 4-fiber ribbons" IWCS 1997

(3)D.Iwakura et.al "Development of stacked ribbon SZ-slotted rod cable" IWCS 1997

(4)S.Hatano et.al " A Study on Fiber Excess Length in a Cable Containing Optical Fiber Ribbons IEICE '86/11 Vol.J69-C No.11

(5)Okaya et.al " Cracking of Lead Cable Sheath and Characteristics of Lead Alloy" ELECTRICAL COMMUNICATION LABOLATORY TECHNICAL JOURNAL Vol.14 No.5

SPEAKER BIOGRAPHY



Daisuke Iwakura

The Furukawa Electric Co.,Ltd.
6,Yawata Kaigandori
Ichihara, Chiba
2908555, Japan

Daisuke Iwakura received his M.E.degree in Engineering from Electro - Communications University in 1993. He joined The Furukawa Electric Co.,Ltd. in 1993 and has been engaged in research and development of optical fiber cables. He is now a research engineer of Opto-Technology Laboratory. He is a member of the Institute of Electronics, information and communication Engineers of Japan

ALL-DIELECTRIC, SELF-SUPPORTING, TRACKING RESISTANT CABLE FOR USE ON LONG SPAN, HIGH VOLTAGE OVERHEAD POWER LINES

**Alexandre M. Simião, Janúncio A. Medeiros Neto, Cristina Kuniyoshi, João M. I. Furtado
and Leonardo Silvério.**

Furukawa Industrial S.A. Produtos Elétricos, Curitiba, Paraná, Brazil.

ABSTRACT

All dielectric self-supporting (ADSS) cable for use on overhead power lines has been developed as a result of the demand for optical fiber based communication systems in Brazil. However, some problems have been encountered. It is well known that when the ADSS cable is installed on high voltage lines the degradation of the cable sheath occurs due to high-induced voltages on its surface. In addition, when this cable is installed on long span, the aeolian vibration can reach severe level.

This paper describes the development of the new aerial cable for use on long span, overhead power lines. The structural design of this cable was investigated. Based on the results, this cable has been manufactured, and its performance was monitored in service environment conditions.

lightweight cable, which can be supported by the earth or phase conductors. Both approaches have proven to be practical and economical solutions, particularly during installation of new power lines or line maintenance. A potential disadvantage therefore is that for installation or maintenance of the optical cable the power line must be shut down.

The ADSS cable can be an alternative solution as it offers advantages to the operating company of more convenient installation at lower cost, especially in cases where support structures already exist. It is particularly attractive for electrical companies due to the possibility of expanding the capacity of existing optical communications.

These installation advantages are counterbalanced by other factors, which may affect the cable lifetime.

CABLE DESIGN

INTRODUCTION

Most of the optical fiber cables presently installed in Brazil are either directly buried or buried ducts. Although these practices are the most expensive, the customers have preferred these cables because aerial installations are exposed to harsher environments.

It is well known that the optical fibers can be installed on overhead lines using a variety of cables^{1,2}. These fibers may be packaged within the earth conductor or incorporated into a

The aerial cable designs must offer the optical fibers sufficient support to avoid the stresses caused by the weight of the cable and environmental loads. In order to avoid these problems, we projected the allowable free cable elongation to prevent any fiber strain under all loading conditions.

A loose tube dry core cable has been developed to reach a minimal cable diameter and weight. Therefore, the amount of strength members, which determine the maximum practical cable elongation, could be minimized.

An inner sheath was applied to protect the cable core and to give a solid base for the strength members, stranded around this inner jacket.

DRY CORE CABLE

In the last years, water-swellable materials have been largely used instead of flooding compounds to prevent the water ingress in the cable³. In this work, the cable was designed using dry waterblocking materials. Choosing these materials, we were able to decrease the cable weight and diameter as well as to improve coupling coefficients between cable components. Unfortunately, when this cable is exposed to a high humidity and temperature rates, some problems can occur, particularly, hydrolysis effects. However, it is important to choose a material with good performance against hydrolysis instability in order to increase the cable lifetime.

ELECTRICAL DAMAGE

It is well known that when ADSS cable is installed on overhead power lines, it suffers several damages due to the capacitive coupling between the cable, the ground and the phase conductors.

One of the most serious problems is the degradation of the cable jacket due to high-induced voltages on the surface of the cable. The voltage depends on a variety of factors, of which the system voltage is one of the most important⁴.

When the cable is initially installed, it does not retain water on its surface and therefore is free of damage. However, due to environmental effects like ultraviolet radiation of sunlight and polluted air, the properties of cable surface begin to deteriorate. The surface becomes more and more hydrophilic and the conductivity of the material surface increases significantly. Therefore, dry bands can be developed when the supply of water (rain) diminishes. This dry band interrupts the conductive surface and causes the original local potential gradient to change into a sharply increased potential step, which in turn can evoke arcing. Heating at the

arc roots can cause tracking damage, especially when the size and location of the dry band is stable⁵.

A field potential of at least 10 kV on the cable surface is another prerequisite for initiating dry band arcing, whereas the severity of tracking damage appears to increase strongly with the field potential^{6,7}. The following classes of remedies can be distinguished:

- choosing the most favorable suspension position for ADSS cable;
- applying tracking resistant sheath material.

In order to define the best position to install the ADSS cable, we developed software, which simulates the electrical field and the potential to which the cable can be exposed in service. The theoretical values were compared to experimental results. The values showed excellent agreement.

TRACKING RESISTANCE TESTS

To choose the best material to protect the cable against tracking damage several tests were carried out using different materials.

Tracking test in inclined plan

The first test was the tracking test in inclined plan in accordance with NBR 10296 METHOD 2, CRITERION A⁸. This test was considered efficient for the distinction of materials with great difference of resistance level to the tracking and erosion damages⁹. The setup of the experiment is shown in figure 1.

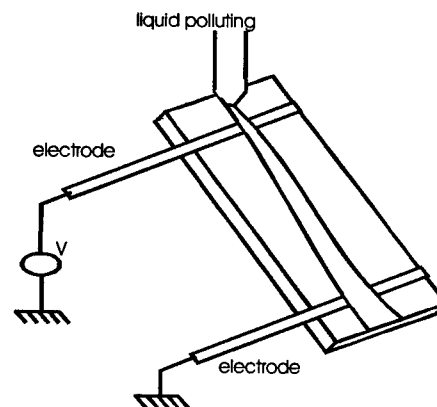


Figure 1 – Tracking resistance test in inclined plan.

In this test a variable voltage was applied over the plate made with a raw material to be analyzed. The sample test was wet with a polluted conductive liquid. The voltage was increased gradually until damages on the surface of the sample could be observed.

Dust and fog test

The dust and fog test was carried out for tracking resistance per ASTM D2132¹⁰. The test evaluates the performance of the raw materials against electrical discharge in the presence of pollutants¹¹. The setup of the experiment is shown in figure 2. In the test, a 1.5 kV was applied over a 140 mm section of the cable. During the test, the sample was sprayed with water. The test was interrupted until the damage, due to tracking or erosion in the surface of the sample, could be observed through visual inspection.

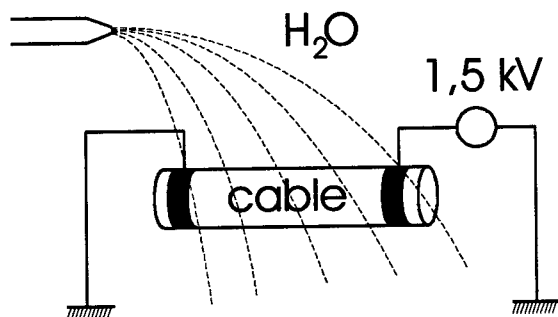


Figure 2 – Dust and fog test.

Electrical test

Another method for evaluating tracking resistant is the IEEE P1222 (draft)¹² standard. In such a test, the resistance of the cable sheath against erosion and tracking can be evaluated under combined electrical and mechanical stresses. The test setups are shown in figure 3 and figure 4. The cable was submitted to continuous salt fog while being energized with AC voltage. The cable was tensioned mechanically with its installed load. The test was made using a voltage of 25 kV.

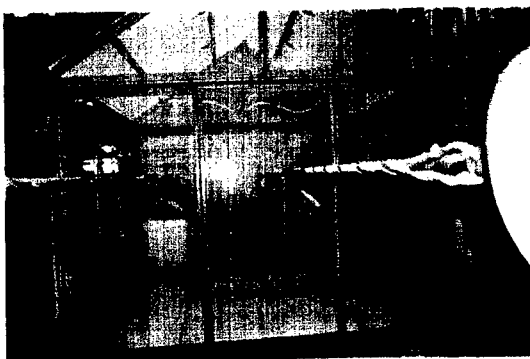


Figure 3 – Salt fog chamber and the samples.

The atomizing nozzles, which are located on the top of the chamber, were responsible for producing the salt fog. The test was conducted for 1000 hours. The testing was weekly suspended for brief observations to certify whether the jacket surface was not affected. At the end of 1000 hours, the cable was removed for a more detailed observation.

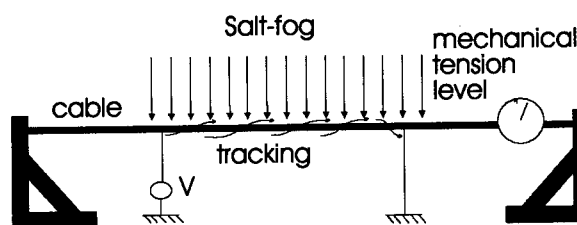


Figure 4 – Tracking resistance test per IEEE P1222 (draft).

MECHANICAL TESTS

From the mechanical point of view, the cable requires a high tensile strength, and the outer sheath must have good adhesion to the core to effectively couple the load to the cable. The cable must be designed to meet all requirements of the optical cable under all installation conditions such as, operating temperatures and environmental loading.

Aeolian vibration

The aeolian vibration occurs almost constantly on overhead power line cables of circular cross-section. Depending on the cable characteristics and environmental exposure the vibration can reach extremely severe levels¹³.

The damage resulting from aeolian vibration may be divided into two broad categories, fatigue and abrasion. Both types of damage are progressive and long-term in nature and can occur simultaneously.

The aeolian vibration test was carried out by BELLCORE TR-NWT-001121¹⁴. This test simulates the vibration effect induced by the laminar flow of the wind across the cable.

Galloping

Galloping of cables is an aerodynamic instability phenomenon¹³. It occurs less frequently than aeolian vibration, but deserves consideration because of its destructive effects. Galloping is typically associated with ice formation on a circular cable. The resulting cross-sectional shape can become a quasi-elliptical or an "air foil" profile. Under high-velocity wind, this profile causes lift forces promoting galloping. If the resultant of the lift and drag forces is in the general direction of the cable motion, oscillations can be sustained for hours, even in unsteady winds.

The galloping test was conducted by BELLCORE TR-NWT-001121¹⁴. This test allowed to analyze the damage due to oscillation on the cable, and dead-ends systems.

ENVIRONMENTAL TESTS

Some environmental tests were made to evaluate the performance of the cable against temperature variation and water penetration in the cable. The temperature cycling, cable freezing and the aging were made to simulate practical conditions.

Water penetration

We tested different configurations of dry core cables according to water penetration test in several conditions, such as:

- Pressure of 1 meter water column in 20 minutes;
- Water penetration in 1 hour;
- Water penetration in 24 hours;
- Water penetration after 14 days;
- Water penetration test after bending test;
- Pressure of 1 meter water column instantaneously;
- Water column of 2 meters;
- Water column of 3 meters;
- Water penetration test with water from manholes;
- Water penetration test after aging 7 days at 85°C;
- Water penetration test after aging 14 days at 85°C;
- Water penetration test after aging 21 days at 85°C;
- Water penetration test after cyclic bending test.

CABLE MATERIALS

The main test for materials used in dry core cables is the hydrolysis stability of the loose tube. The mechanical resistance of the optical fiber was also evaluated in order to check the protection of the tube material against high humidity and temperature rates. The loose tube material was also evaluated using different tests, such as tube kinking, tube compression resistance and material compatibility.

Hydrolysis instability

In order to define the best material to resist hydrolyses instability, some materials were aged during 45 days at 85°C in 85% relative humidity (RH). The maximum elongation at yield point after the aging was checked for each material.

Mechanical resistance of the optical fiber

We also evaluated the optical fiber resistance protected by the tube loose after aged. The tube loose was aged during 5 weeks at 85°C in 85% RH and immersed in water at 85°C. We measured the fiber strength in dynamic two-point bending test. After aging period, the fibers were carefully pulled out from the tubes and the filling compound was removed from individual fibers. We tested 30 samples. The plates velocity was 10 $\mu\text{m}/\text{sec}$ and the test environment was 23°C and 60% RH.

RESULTS AND DISCUSSION

Tracking tests results for two different materials are given in table 1. In respect to the electrical test in inclined plan, the material A failure at level of voltage below the specification limit, although for the dust and fog test both materials showed satisfactory performance. Based on the results obtained in the first test, we chose the material B to use as the sheath material for the prototype cable.

After choosing the sheath material and manufacturing the prototype cables, we evaluated the performance of the cable under electrical test. The results are given in table 1.

Table 1 – Results of electrical tests with the raw material and cable jacket.

Test	Material A	Material B	Limit
Tracking test in inclined plan (kV)	2,00	4,00	$\geq 2,25$
Dust and Fog Test (hours)	> 200	> 200	≥ 200
Electrical test	Variation of thickness (%)	5 %	< 50%

The electrical test results showed values below the specifications established limit. Electrical discharges happened constantly during the test as shown in figure 5. At the end of the test, we observed only a slight surface damage. The cable was also opened up to verify whether the aramid yarns had not been damaged. There were no failures or damage to the aramid yarns.

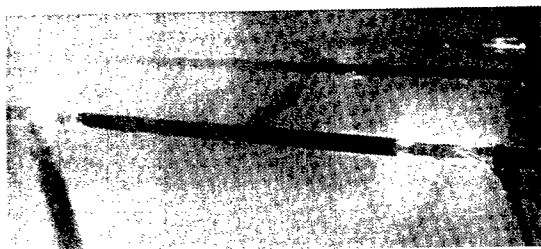


Figure 5 – Electrical discharges on the cable.

In table 2 lists the mechanical and environmental tests for the prototype cable. For the aeolian vibration test the cable was submitted to a 100 million vibration cycles and the maximum increase in attenuation was 0.02 dB. This result is 80 % below the limit value. For the galloping test the cable was submitted to a one hundred thousand galloping cycles and the maximum increase in attenuation was 0.06 dB. Again, the cable showed good performance.

Table 2 – Results of the mechanical and environmental tests.

Test	Reference	Conditions	Results
Tensile load	Bellcore TR-NWT-001121, IEEE P1222 (draft) and ABNT 03:086.01-020	Maximum installation load, < 0,10 dB and no fiber strain.	$\leq 0,02$ dB no cable jacket cracking or splitting; no fiber strain.
Galloping	Bellcore TR-NWT-001121	100.000 cycles < 0,10 dB	$\leq 0,02$ dB
Aeolian vibration	Bellcore TR-NWT-001121	100.000.000 cycles < 0,10 dB	$\leq 0,06$ dB
Twist	IEEE P1222 (draft)	50 cycles, +/- 180° < 0,10 dB	$\leq 0,02$ dB
Impact	Bellcore TR-NWT-001121	50 cycles, 6 kg wt < 0,10 dB	$\leq 0,05$ dB
Creep	IEEE P1222 (draft)	1000 h 75 % maximum installation load < 0,2 %	$\leq 0,15$ %
Water Penetration	Bellcore TR-NWT-001121 and IEEE P1222 (draft)	Conditions described in Environment Tests section	All conditions passed.
Crush	Bellcore TR-NWT-001121 and IEEE P1222 (draft)	220 N/cm 10 minutes < 0,10 dB	$\leq 0,08$ dB
Temperature cycling	Bellcore TR-NWT-001121 and IEEE P1222 (draft)	-40 °C a 70 °C 4 cycles and cable aging for 7 days < 0,10 dB	$\leq 0,04$ dB

*measurement wavelength : $\lambda = 1550$ nm.

Hydrolysis instability was checked to evaluate the performance of the loose tube material submitted to high temperature and humidity. The results of hydrolysis instability test are shown in the figure 6.

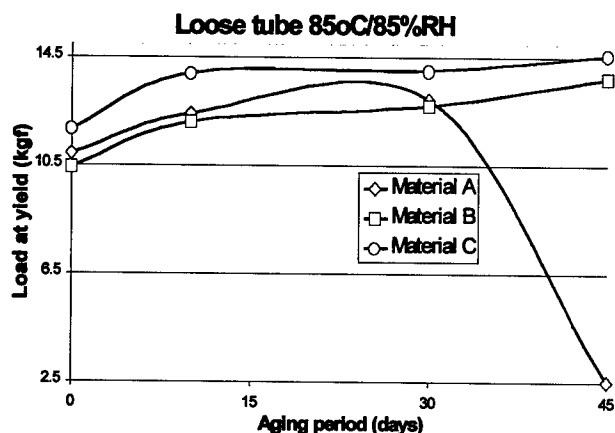


Figure 6 – Mechanical resistance of the loose tube after aging.

Material A had a sharply decreased after 30 days. Material B and C showed a good performance even after 45 days. Although the material B and C have almost the same behavior, we have used material C in the cable design, because material C showed better performance.

The two-point bending results are present in figure 7. All values have been normalized to the bending strength of the unaged samples.

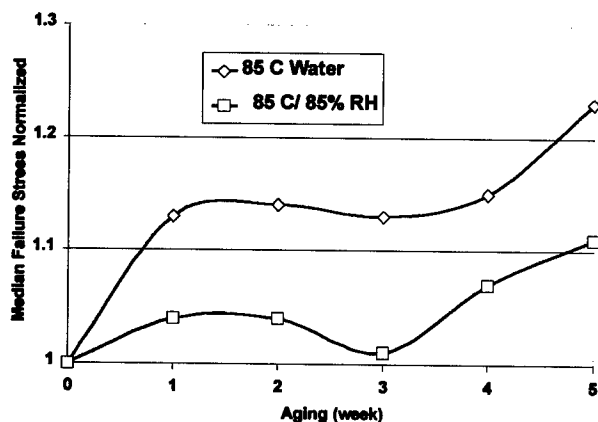


Figure 7 – Mechanical strength of optical fiber.

Two trends are noticeable. For the sample in water, the strength increased slowly with the aging time. For the other aging environments condition, the results showed that the strength remained essentially unchanged. Such gradual increases in strength are typically evidence of blunting of the strength-limiting surface crack overtime due to the action of the aging environment.

These results suggest that the strength of the aging fibers does not suffer degradation due to severe loose tube aging.

FIELD INSTALLATION AND MONITORING

The ADSS cables were installed in two different sites in order to check the performance of the cables against tracking, environmental loads and mechanical damage.

São Paulo site

The ADSS cable has been installed for 5 years in overhead power lines up to 230 kV and 300 meters of span. The overhead line is located besides of a road in São Paulo, as shown in figure 8. The cable has been exposed to a high level of pollution and electrical field of around 20 kV/m. We are monitoring the surface of the cable and the optical attenuation. No damage has been observed to date.

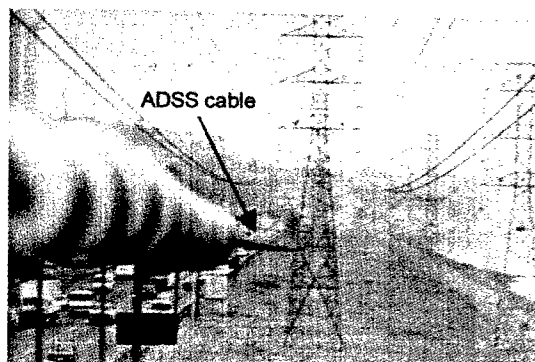


Figure 8 – ADSS cable installed in São Paulo site.

Cruz Machado site

The ADSS cable has been installed for 1 year on overhead power line up to 230 kV and 1137 meters of span, as given in the figure 9. The cable has exposed to a high wind speed and

electrical field (28 kV) because the cable was installed near the phase conductors.

The cable has been monitored in order to check the tracking damage, mechanical properties and optical attenuation. No damage has been observed to date.

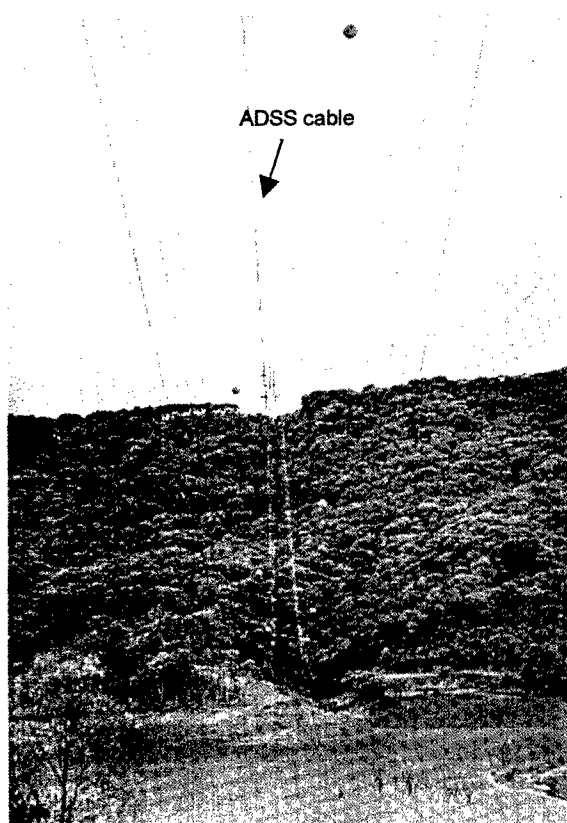


Figure 9 – ADSS cable installed in Cruz Machado site.

CONCLUSION

This paper described a new all-dielectric self-supporting fiber optical cable for use on overhead power lines. The advantage of this cable is that it withstands harsher environment. We investigated structural design of this cable and obtained optimum structures. Based on the test results, the cable was manufactured and its performance evaluated. We confirm that the characteristics are sufficient for practical application on long span, overhead power lines.

ACKNOWLEDGEMENTS

The authors would like to acknowledge the support of their colleagues in carrying out this work. Special thanks go out to Raquel Maia, Edio Engel, Jefferson Kishida, Fernando de Sa Brito, Federal University of Parana (UFPR), and Technological Institute of Central Laboratory of Research and Development (LACTEC).

REFERENCES

- [1] - J. R. Martin " Optical Fibres for Power Utilities"; CIGRE (1993) Australia, Paper 5.2;
- [2] G. Carlton, A. Bartlett, C. Carter, and A. Parkin. "UK Power Utilities Experience with Optical Telecommunications Cabling Systems". Power Eng. Journal Feb (1995) pp 7-14.
- [3] P. Gaillard, J. Mc Nutt, J. Holder, A. Bouvard, and O. Tatat. "Significant Improvement of Loose Tube Cable Spliceability Based on New Cable Dry Design". IWCS, 1996.
- [4] H. Lennartsson and B. Perrett. "Track Resistant Jacketing Material for Optical Cable", Private communications.
- [5] - S. M Rowland and I. V. Nichols. " Effects of dry-band arc current on aging of self-supporting dielectric cables in high fields"; IEE Proc. -Sci. Meas. Technol., 1996, pp. 10 – 14.
- [6] – O. Daneshvar, J. Hill and X. Mann " Development of All-Dielectric, Self-Supporting Cable for Use in High Voltage Environments"; Proc. 44 th IWCS, 1995, pp. 736 – 770.
- [7] - Carter C. N; Waldron M. A. " Mathematical model of dry-band arcing on self-supporting, all-dielectric, optical cable strung on overhead power lines"; IEE Proceedings-C, 1992, pp. 185 – 196.
- [8] - NBR 10296 "Material Isolante Eletrico – Avaliacao de Resistencia ao Trilhamento Eletrico e Erosao sob Severas Condições Ambientais", Maio/1988.
- [9] –W. Pinheiro, E. A. T Dirani, J. J. S. Oliveira, and E. G. B. E. Piazza. " Cabo coberto – avaliação frente ao trilhamento elétrico"; IV Seminário de Materiais no Setor Elétrico – COPEL/UFPR, 1994.
- [10] – ASTM " Standard Test Method for Dust-and-Fog Tracking and Erosion Resistance of Electrical Insulation Materials"; Standard D-

2132, 1989.

[11] –E. K. Duffy, S. Jovanovitch, and I. J. Marwick. "Discharge-Resistant Characteristics of the Polyethylenes for Wire and Cable"; IEEE Trans. On Power Apparatus and Systems, 1965, pp. 815 – 824.

[12] – "Standard for All Dielectric Self-Supporting Fiber Optic Cables (ADSS) for Use on Overhead Utility Lines" IEEE P1222 Draft, September 1995.

[13] –C. D. Sunkle, and J. R. Champa. " Testing of fittings and aerial fiber optic cables"; Conference Insulated Line and Cable Systems, 1991.

[14] – Bellcore, "Generic Requirements for Self-Supporting Optical Fiber Cable" TR-NWT-001121 Issue 1, October 1991.

SPEAKER BIOGRAPHY



Alexandre M. Simião - Furukawa Industrial S.A.
R. Hasdrubal Bellegard, 820 CIC 81450-140
Curitiba – Parana - Brazil

Alexandre M. Simião received a B.S. degree in Chemical Engineering in 1996 from Federal University of Parana (UFPR). He joined "Furukawa Industrial S.A." in 1997. He has worked with a variety of design and development projects in cables, materials and testing. Mr. Simião currently serves as a Product Development Engineer in the Cable Development Engineering Department.

THE DEVELOPMENT OF ALL DIELECTRICAL SELF-SUPPORTING FIBER OPTICAL CABLE (ADSS) FOR USE ON POWER LINES IN CHINA

Fu Binlan

Electric Power Research Institute of China, Beijing, P. R. China

ABSTRACT

On existing power lines, all dielectric self-supporting (ADSS) optical cable can be regarded as an attractive option and has been developed widely and rapidly in China. Since 1996 to early 1999, more than 4000-5000 km ADSS optical cables have already been installed on power lines. Among them, two fifth of ADSS optical cables are made in China. So far serious failure of installed ADSS optical cables had not appeared in service yet. However the discharges along the sheath of the cables during installation have occurred twice. In this paper, the development of ADSS optical cable is reviewed, including a description of the production, installation, operation, anti-electrical degradation, mechanical strength. Some suggestions on further development of ADSS optical cables are also presented.

INTRODUCTION

With the development of information expressway, the advent of optical fibers, having low loss, immunity from electrical interference and light weight, has made them an ideal transmission medium and they have been used widely. Optical cables to be installed on power lines can provide the best services at the lowest cost. There are 333,500 km 110 kV and above existing power lines in China, among them there are 118,000 km 220 kV, 7,000 km 330 kV and 17,000 km 500 kV lines. Optical cable installation on power line can meet not only the demand for interior needs of the power utility itself, but also for exterior needs of business circles. In early 1997, an application for optical cable installation on power lines had presented by Min-

istry of Power Industry joined with Ministry of Radio Film and Television and had been approved by the State Council. It brings about a great advancement in the application of ADSS optical cables in China.

For an overhead power line there are three different ways to lay optical cables on it. (a) The optical ground wire (OPGW) is generally the most reliable option. However on existing lines, the existing ground wires should be replaced with OPGW under power off state, and it is expensive; (b) Optical cables wrap around overhead ground wire. Some imported optical cables of this type were wrapped around operating overhead ground wires in China. But a few wrapped optical cables were broken off in service by guns or birds; (c) The all dielectric self-supporting optical cable (ADSS) is an attractive option on existing power lines, it separates from the power system and is facilitated installation under live line condition. So ADSS optical cables are often favored by power utilities in China. For newly building power lines the OPGW optical ground wire is still the favorite option.

At the beginning, ADSS optical cables were imported from the manufactories all over the world. In March 1996, Shengzhen SDG Optical Cable Co. LTD. in China has made the first ADSS optical cable. It has been put into operation at Daya Bay Nuclear Power Station, Guangdong Province. Fig. 1 shows the ADSS optical cable installed on 220 kV single circuit power line at Daya Bay Nuclear Power Station. In early 1998, more than 600 km ADSS optical cables made in China and about 1000 km imported cables were installed on power lines. In early 1999, about 4000-5000 km ADSS optical cables have already been installed on power lines. Among them two fifth of ADSS optical cables were

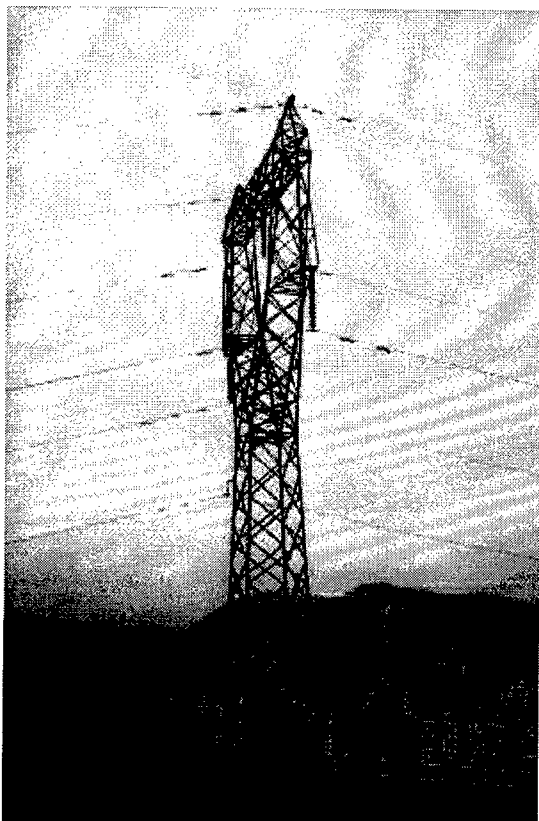


Fig.1 The ADSS optical cable installed on 220 kV single circuit power line at Daya Bay Nuclear Power Station

made in China, the rest was imported. It is estimated about 7000km ADSS optical cables will be installed in early 2000. The majority of ADSS cables on power lines are in the southeast provinces of China. In the most developed Guangdong Province, the first phase project of SDH optical fiber main network has been accomplished in zhujiang triangle area. Only in 1999, 1000km ADSS optical cables for the main network have been installed. Some of them are near the seaside.

Due to the fast development, it did not have enough time to consider some problems of ADSS optical cable operating in power networks in technique and management point of view. For example, ADSS optical cable installed on power lines will suffer from electrical degradation. And these optical cables need sufficient mechanical strength to withstand installation handing and operating under all severe weather conditions. The technical specification and the quality tests for ADSS optical cables in power system cannot keep up with the development. The first symposium on application technique of ADSS optical cables has been held in Guangzhou in April

1999. It was joint sponsored by The Chinese Society for Electrical Engineering (CSEE) Tele-Communication Committee and the CSEE Guangdong Branch Committee. Eight papers were presented at the meeting. The problems and experiences related to the application technique, installation and operating maintenance etc. have been discussed. This meeting promotes the further development of ADSS optical cable in China.

In this paper the development history of ADSS optical cables installed on power lines in China is briefly reviewed, including a description of the production, installation, operating, management etc. The problems of electrical degradation and mechanical strength of ADSS optical cable are described. The author also presents some suggestions on further development in ADSS optical cable.

DEVELOPMENT HISTRY

Production

Recently lots of ADSS optical cable manufactories have been constructed in China. Some of them are Chinese-foreign joint venture, for example, the main manufactories in China are the Alcatel Shanghai Optical Cable Co. LTD. the Jiangsu Zhanteng and Shenzhen SDG Optical Cable Co. LTD. Generally, the structures of ADSS optical cable are the layer stranded type and the central bundle-tube type. For producing ADSS optical cable all facilities and raw materials bought from the international market and produced in accordance with foreign producing technology, except for a small number of the optical fiber made in China. Each manufactory has its own ADSS optical cable standards. They were basically in accordance with the standard for ADSS optical cable for use on overhead utility lines (IEEE P1222 Draft) and with standards in the fields of telecommunication and power cable in China.

Installation and operation

For ADSS optical cables operating on the power lines, a quality competition of the products of different manufactories is naturally formed in China. Serious failures of installed ADSS optical cables had not occurred in service for 2-3 years, since the operating time was too short. In farthest to the north of China, Heilongjiang Prov-

ince, it is very cold. The cable suffers large temperature difference between day and night. In South China, the ADSS optical cables are hit by strong typhoons near seaside every year. For example the first ADSS optical cable (789m in span, 17.8mm in diameter) installed at Daya Bay Nuclear Power Station, has been hit by strong typhoon in 1996 - 1999. In July 1999, the trees, larger than 200mm in diameter along the two sides of the power line, uprooted by typhoon, however the operation of telecommunication of the Station was normal. The longest ADSS optical cable (made by SDG Optical Cable Co. LTD., China), 1060 m in span, on crossing tower of Yangtze River at Shishou City, Hubei Province has already been put in operation for 3 years.

In Guangdong Province, the sheath damage of a coil of ADSS optical cable supplied by factory had been found, very small air holes were found on the sheath surface and a piece of optical fiber was broken. In Fushan City, Guangdong Province, during the process of the optical cable clamp installation, the discharge along the optical cable surfaces to the ground though the pulley suspended on the tower has been discovered¹. It damaged the cable sheath, the sheath split about a 30mm long and 5mm width crack, the aramid was exposed and had some black traces by high temperature scorch. The sheath surface had already been melt out of shape. In Jiangmen City, during installation the induced voltage of the exposed aramid yarn was too high it caused discharge along the sheath, the optical cable was breakdown. It accounts for the occurrence that the personnel concerned did not understand the structure design of ADSS optical cable of this type to reduce electrical degradation. For this type of cable the aramid yarn should be grounded every section, but it was not suitably grounded during this installation process. After the event, some tests were conducted in China. It revealed that the discharge along the sheath of this type of ADSS optical cable is very easy. This type of cable is not applicable, especially for the area with rather high ground resistivity.

The traditional tension string technology is still conducted in the installation. In Heilongjiang Province the installation of ADSS optical cable can be safely conducted at -30C° ambient temperature. In the installation of ADSS optical cable some clamps made in China have already been used.

ELECTRICAL DEGRADATION

Optimum installation position

ADSS optical cables suspended on power lines can be failed due to sheath damage caused by electrical degradation. It results from dry-band arcing induced by electrical coupling with the power circuit². On the 220 kV and above transmission lines this problem is very important. Now the rated voltage of the power lines on which optical cable installed is 220 kV or 110 kV in China, where the designed induced voltage level on the ADSS cable is below or equal to 20 kV. To decrease electrical degradation, first of all the ADSS optical cable should be installed in an optimum position, in which it will suffer the lowest possible induced voltage. There are dozens of tower types on existing 110 kV and above power lines in China. Most of them are single circuit towers. The dimensions of each type of tower are not the same. The calculation of potential contour pattern on power line cross section at the tower is needed. Now the equal-potential pattern of the cross section of a power line at the tower has already been programmed and plotted by the Electric Power Research Institute of China. Fig. 2 shows an example of an equal potential pattern plot for 220kV double circuit power lines.

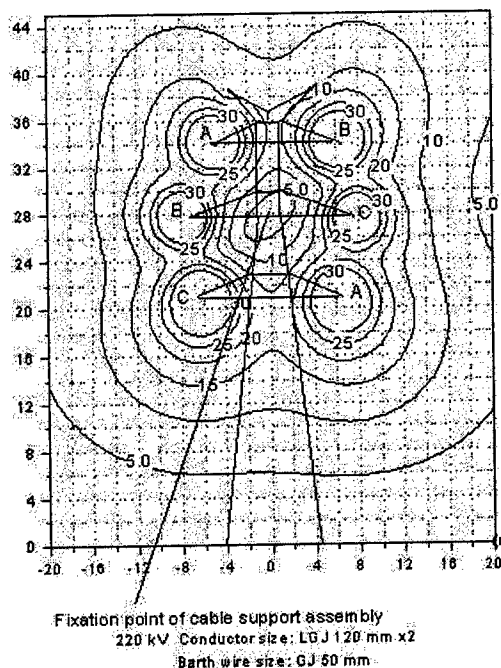


Fig. 2 Equal potential (kV) pattern plot
For 220kV double circuit power lines.

In April 1999 at the CSEE meeting, the design of suspension position of ADSS optical cable was discussed³. Due to the special characteristics of ADSS optical cable which have higher modulus of elasticity and lower thermo-expansion coefficient (mainly from effects of aramid). The sag of the cables is more sensitive to the mechanical load variation and it is slow in reacting to the temperature variation. However the variation of the sag of metal power line conductor is in opposite. So the relative position between the cable and conductors in the middle span is entirely different from their relative position near the towers. In the most unfavorable condition almost one-third optical cable can be located in the dangerous high electric field area. If it is in the annual average operating tension state, the relative position between cable and conductors in the middle span should be checked. But since most of the electrical degradation was found near at the tower (where the electrical field is the highest), such a check may be unimportant.

Add insulator

It is thought that anti-pollution insulators added between the clamps of ADSS optical cable and grounded towers could easily reduce the leakage currents along the sheath of the optical cable. An added insulators on 220 kV power line at Daya Bay Nuclear Power Station is also shown in Fig. 1. But when it is fog or light ring, the polluted surface resistivity of the insulator should be much greater than the polluted surface resistivity of ADSS optical cable ($10^6 - 10^7 \Omega/m$), otherwise the failure will still happen. However it is difficult to reach such a high resistivity. A company claimed in China that if insulators are added between the clamps and towers, then the anti-degradation sheath optical cable are no more needed, users can buy their general sheath optical cable. The author pointed out that the effect of the added insulators should be confirmed by long-term field operating. In fact, the ADSS optical cable is still grounded through the connecting boxes, which is fixed on the tower.

Quality test center

The quality test center should be built as soon as possible in China. It should conduct all tests

terms (electrical, optical and mechanical) basically according to the standard for ADSS optical cable for use on overhead utility lines (IEEE P1222 Draft). Especially, the salt fog test for resistance of the cable sheath to erosion and tracking under combined electrical and mechanical stresses is very important. The quality test center should be run by power utility. All ADSS optical cables intended to install on power lines should pass all of these test terms in the quality test center. It is suggested that all ADSS optical cables operated after 3 - 5 years should be checked to see whether the erosion or tracking on the sheath surface has been discovered or not.

MECHANICAL STRENGTH

The ADSS optical cable and the metal conductor of the power line have the same mechanical problems such as galloping, but the ADSS optical cable has its own characteristics. (a) The sag of the cable is more sensitive to the mechanical load variation, it has larger sag under the mechanical load. (b) Due to the lightweight of the cable, the swing angle of the ADSS optical cable might reach to 80° , the swing angle of the metal conductor only can reach to 43° . So the ADSS optical cable might approach to the conductors of the operating power line. (c) Due to the wind-induced vibration of the cable, the fatigue point can be reached, the damage of the optical cable has often been found. (d) In order to avoid the slide displacement or stretch of the cable sheath, the withstand tension strength of the clamp to the tower and of the optical cable should be properly coordinated.

If all test terms of ADSS optical cable according to IEEE P1222 Draft standard have been passed, generally, the mechanical strength of the cable can meet the demand of operation. Basically, the test terms have been put into effect in China. For long span optical cable, the wind-induced vibration of the cable should carry out a special design. For example, as above mentioned, on the longest span (1060 m) crossing Yangtze River, four dampers at each terminal of the ADSS optical cable have been equipped.

FURTHER DEVELOPMENT

Cable installation on 500kV power line

The 500 kV main power grids have already been connected in North, Central and South of China. In the future, the national interconnected power system will be fulfilled to realize power complement, regulation, loss reduction as well as power transmission from north China to south China. The rated voltage of the nationwide system will be 500 kV. Power utilities hope that ADSS optical cables can also be installed on the existing 500 kV power lines (including 330 kV power lines). For new 500 kV power lines some are double circuit lines where the optimum low induced voltage position can easily be found. However among 17,000 km 500 kV existing power lines, most of them are single circuit lines. The position where the induced voltage on the optical cable sheaths less than 20 kV can not easily be found. Some measures such as arc control devices reducing earth-leakage current and so on can be studied in the research projects to see if the ADSS optical cable can be installed on 500 kV power lines in China.

Management

The application of ADSS optical cable on power lines has just began in China. We should study the experience from abroad. Now the related technique rules and standards of ADSS optical cable for use on overhead lines are under compilation. The quality test center of ADSS optical cable is under construction. In the future all of the ADSS optical cables intended to install on power lines should get a license from the power utility.

CONCLUSION

In China, the application of ADSS optical cable on power lines has been developed widely and rapidly.

So far serious failures of installed ADSS optical cables have not been occurred in service in China, maybe the operating time was too short. It is very cold in farthest to the north of China. The installation of ADSS optical cable can be safely conducted at -30°C ambient temperature. In South of China the ADSS optical cables are hit by strong typhoons near seaside. However in

the install process, the discharges between optical cable to grounded objects have occurred twice.

Attentions have already been paid to the problems, including anti-electrical degradation of the cable sheath, the sufficient mechanical strength, the management etc., appeared during the operation. The problems have been solving with great efforts.

REFERENCE

- [1] The Trace report (4), "For Optical Fiber Main Network in Gaung Dong Province", Power Telecommunication, pp31, Feb. 1999
- [2] Fu Binlan, "The Technique Report Of ADSS Optical Cables On Power Lines", Technique Report of The Electric Power Research Institute of China, January 1998
- [3] Zhou Lionqi, "The Discussion of The Suspected Position In The Design Of ADSS Optical Cables", Power Telecommunication, pp33, Feb. 1999

BIOGRAPHIES



Fu Bin-Lan
Electric Power Research
Institute of China
Qing-he, Beijing
100085
P. R. China

Fu Bin-Lan graduated from the Department of Electrical Engineering of Tsinghua University in 1962.

After graduation she has been working in the field of high voltage engineering.

Her research areas are the corona characteristics and environmental effects stemming from HVDC transmission lines and on-line monitoring of substation apparatus.

Now she is engaged in the electrical degradation of the ADSS optical cable.

She is a senior engineer, professor of the Electric Power Research Institute of China.

ADSS Cable Design for No Voltage Limits

Kyung-Tae Park*, Jin-Han Kim

SAMSUNG Electronics Co., Ltd. Kumi-City, Republic of Korea

ABSTRACT

Optical transmission line construction with ADSS, All Dielectric Self Support cable using established pylon not only increases efficiency of national key establishments but also saves time and expenses.

ADSS cable is preferred to OPGW cable or wrapping cable because it can be installed and repaired without a voltage outage. This unique property of ADSS cable provides an independent operation of communication establishments from electric power transmission company.

Voltage outage is more difficult for higher voltage because higher voltage is much more electric power burden. Therefore, ADSS cable is preferable up to a higher voltage transmission line.

This advantage of ADSS cable would satisfy growing communication companies which want to establish optical back bone lines faster than a competitive or be independent from existing big telecommunication companies in short term by lease the right of way of pylon.

However accidents of ADSS cable have been reported due to dry-band arcing which leads to tracking, erosion and even melting of outer jacket at dead end point depending on surface current flows.¹

Up to now, so many countermeasures have been proposed but failed to prevent from dry band arcing assuredly.^{2,3}

In this paper, authors propose a theory of dry band arcing mechanism and examples of failures due to wrong installation. The solution introduced in this papers is easily acquired by calculating installation tension and positioning.

INTRODUCTION

Generally, ADSS cable manufacturers require an information of maximum voltage, maximum span and weather conditions to design optimal ADSS cable. With this information, ADSS cable is designed to meet a certain maximum allowable load to which ADSS cable can perform its responsibility without damaging the fibers or degrading optical performance up to a designed lifetime about 30 years. However with just this information cable manufacturers just can design maximum allowable tension, they can not design optimal ADSS cable, optimal installation tension and positioning to prevent dry band arcing. Because of preventing from dry band arcing some information added to the confined information to analyze movements of both ADSS cable and electric wire depending on wind velocity and temperature.

It is well known that the sag of electric wire made of metal can be shift more vertically according to temperature changes than ADSS cable due to its heavier mass and relatively high thermal coefficient. ADSS cable can be blow more to windward than electric wire due to its relatively light mass and low elastic constant. Therefore, ADSS cable is easily contacted with electric wire in storm.

ADSS cable is made of dielectric material, so it is immunity in contact with electric wire in dry weather condition. However in wet and rainy weather condition a layer of water film on ADSS cable surface provides a conduction path.

This paper discusses prevent the surface current flows with optimal ADSS cable design, control of ADSS installing tension and positioning.

DRY BAND ARCING MECHANISM

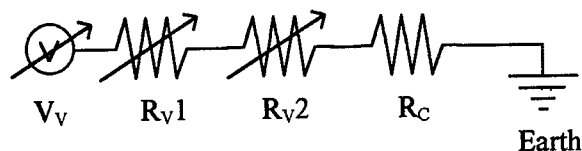


Fig. 1 Circuits of dry band arcing

Fig. 1 explains the tracing mechanism

- V_v , a voltage which exist on ADSS cable. This can be varied by the distance between ADSS cable and electric wire at mid span according to wind speed.
- R_{v1} , a air resistivity between ADSS cable and electric wire. This can be varied by the distance between ADSS cable and electric wire at mid span.
- R_{v2} , a surface resistivity on ADSS cable. It can be varied by surface contamination of ADSS cable by ionic substance or metallic dust. And R_{v2} is rapidly lowered when water coating is formed on ADSS cable surface.
- R_c is contact resistivity between ADSS cable and Armour Rod.

To explain roles of these parameters assuming a situation that the distance between ADSS cable and electric wire in mid span is closed by storm.

⇒ R_{v1} is rapidly lowered when arcing is initiated at mid span because dissociated ions and electron avalanche make a conduction path.

⇒ R_{v2} is lowered because DBA(dry band arcing) sticks ions on ADSS cable surface.

⇒ V_v is increased rapidly according to the distance being closed.

The current I is defined by as follows.

$$I = \frac{V_v}{(R_{v1} + R_{v2} + R_c)} \quad \text{-----(1)}$$

$$E(\text{energy}) = I^2 R_c t \quad \text{-----(2)}$$

The contact resistance R_c at Armor Rod is heated by electron avalanche and the quantity of current expressed in equation(1).

Temperature is increased at the contact area.

If the temperature is high enough to melting the jacketing material, ADSS cable is rapidly destroyed, otherwise thermal aging process is going on slowly.

During our laboratory test, DBA was initiated when ADSS cable was closed to electric wire about $0.5(\text{kV/mm})$ electric field at mid span in assumptive situation of a rainstorm weather condition.

INSTALLATION

ADSS cable is normally installed in an established electric power transmission facility. Therefore, ADSS cable should be designed regarding the already established electric power transmission systems.

However an insufficient information of electric power transmission system can lead to an insecure ADSS cable design.

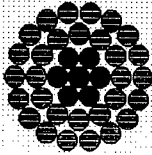
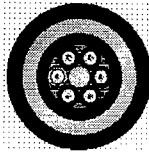
To prevent DBA, it is required to avoid approaching of ADSS cable to electric wire caused by wind using a appropriate installation tension and positioning of ADSS cable.

Installation Tension

Electric wire could be already sagged considering its geometry, weather conditions & span length. The installation tension of ADSS cable could be increased up to an allowance of maximum allowable tension of ADSS cable that is maximum installation tension of ADSS cable.

The characteristics of both electric wire and ADSS cable to be used in examples are listed in Table. 1.

Table.1 Characteristics of cable

Items	Electric wire	ADSS cable
Shape		
Outer diameter(mm)	21.0	15.0
Unit weight(kg/km)	974.0	178.0
Elastic modulus (kN/mm ²)	80.4	85.0
Coefficient of Thermal expansion (1/°C)	1.5E-5	6.7E-7
Supporting area(mm ²)	261.5	28.8
Installation tension(kN)	16.0	3.0, 6.0, 8.0

The outstanding differences between two cables are the unit weight, supporting area and coefficient of thermal expansion.

Sag & tension by span(30°C, No wind & ice)

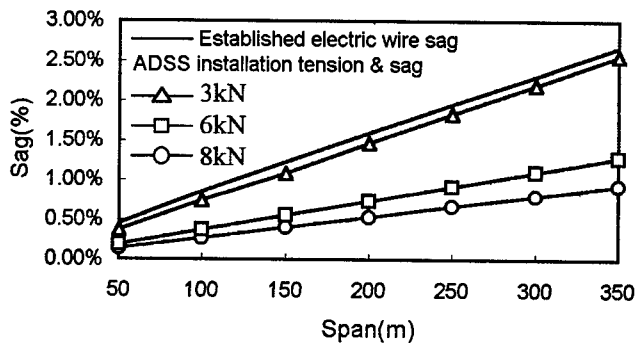


Fig.2 Sag distribution according to span

Fig. 2 shows sag distributions of electric wire and ADSS cable with different installation tensions. The ADSS sag increment lowered when installation tension is increased. The slop of ADSS installation tension of 3kN is the same as electric wire. And this ADSS cable can be installed up to the maximum installation tension of 8kN.

Wind effect

If ADSS cable has the same characteristics as electric wire, the best choice of ADSS installation tension would be 3kN. However due to the difference characteristics as shown in Table. 1, ADSS cable would be blown off further than electric wire.

Sag distribution at mid span

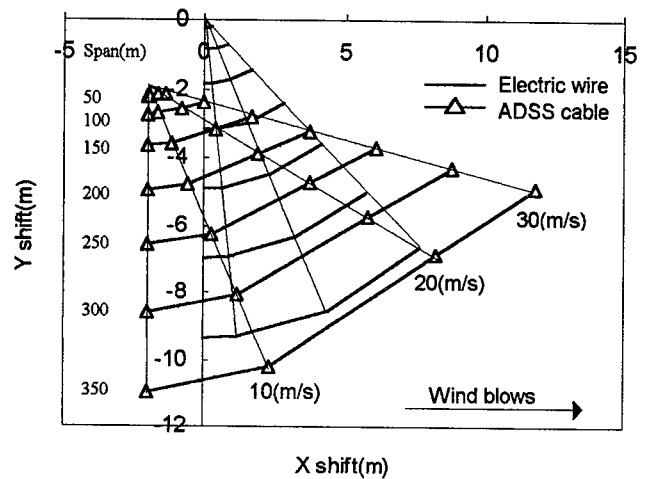


Fig. 3 Sag profiles of electric wire & ADSS cable(install tension 3kN) by wind

Fig.3 shows a sag profiles in mid span of established electric wire and ADSS cable installed with 3.0(kN) according to span 50m to 350m by 50m and wind velocity of 0m/s to 30m/s by 10m/s.

In Fig. 3 the ADSS cable installation coordinates is (-2, -2).

Any ADSS cable that has the same sag increment as electric wire will violate a ground clearance just as the Y-position difference of both cables if the dead-end installation position of ADSS cable is under the electric wire's.

Fig.4 shows a sag profiles of established electric wire and ADSS cable installed with 6.0(kN) in mid span according to span of 50m to 350m by 50m and wind velocity of 0m/s to 30m/s by 10m/s.

Sag distribution at mid span

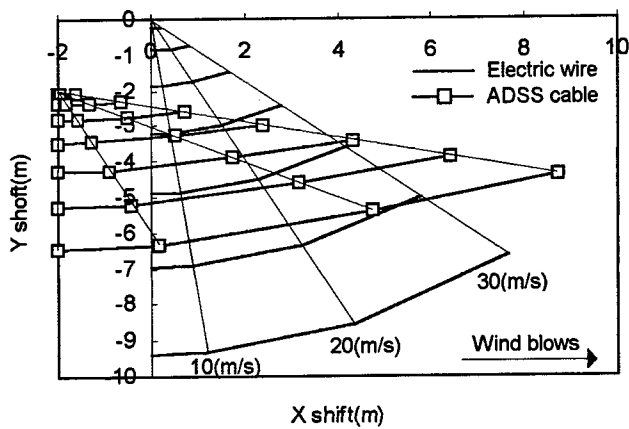


Fig. 4 Sag profiles of electric wire & ADSS cable(install tension 6kN) by wind

In this case, ADSS cable and electric wire in span around 250m are contacted in mid span when wind velocity reaches to 30 m/s. A span which is longer than 200m, ADSS cable is positioned above overhead ground wire that means ADSS cable is exposed lightening strike. When a span which is shorter than 200m, ADSS cable will violate ground clearance.

Fig.3,4,5 shows that increasing ADSS cable installation tension makes shorter the X-shift of ADSS cable by wind, this means that the contact risk is decreased, but a violation of ground clearance and a exposure of lightening strike are still problems.

All the situations are dependent on the tower structure and size. If the tower has a big margin of installation X-position the sag profile of ADSS cable will be shifted left position.

Sag distribution at mid span

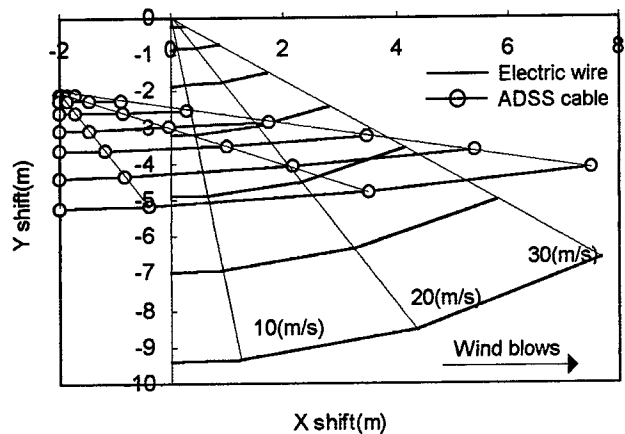


Fig. 5 Sag profiles of electric wire & ADSS cable(install tension 8kN) by wind

Positioning

To avoid violation of ground-clearance, exposure to lightening strike and contact risk, the Y installation position of ADSS cable should be changed according to span.

Sag distribution at mid span

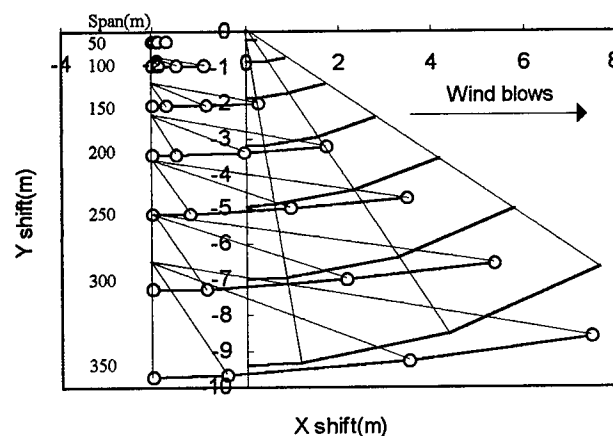


Fig. 6 Proper ADSS cable install Y-position

Table.2 ADSS install position according to span

Span	X,Y installation position of ADSS Cable
50m	-2.0, -0.2
100m	-2.0, -0.7
150m	-2.0, -1.5
200m	-2.0, -2.4
250m	-2.0, -3.5
300m	-2.0, -4.9
350m	-2.0, -6.3

If the tower is too compact to provide adequate X-installation position of ADSS cable then the ADSS cable installation tension should increase with more strengthening members to confine ADSS cable access to electric wire within electric field 0.5kV/mm .

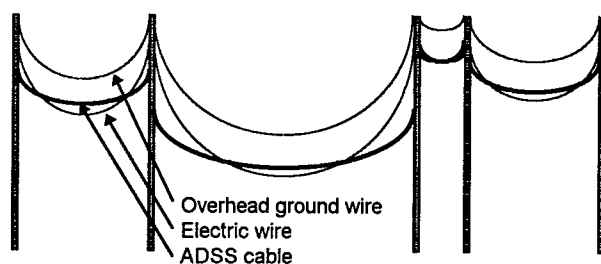


Fig. 7 A front view of two install positions

Fig. 7 shows the front view of sag. All supports have two installation points if the neighboring span length is not same.

Fig. 8,9,10 and 11 show sag distributions of ADSS cable and electric wire according to wind velocity 0, 20, 30m/s. with the span length of 350m. Fig. 8 shows the highest install position which is defined by a contact risk between ADSS cable and electric wire. Fig. 9 shows the lowest install position which is defined by ground clearance of electric wire at the highest temperature.

Therefore, the Y-installation position can be defined by analyzing Fig. 8 and 9 in case of the Y-install position being $-6.3 \pm 0.85\text{m}$.

Fig. 10 explains one Y-install position is raised up to -3.5m to connect a short span with one install point. Fig. 11 explains that one tower has a big margin of X-position, then the Y-install position is raised up to -1.7 .

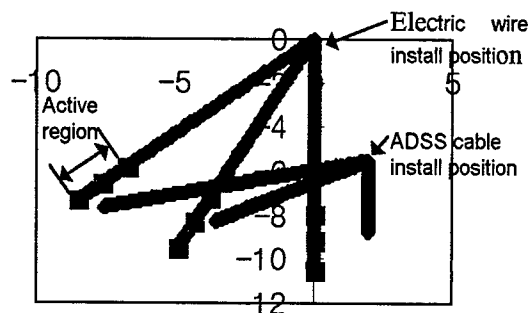


Fig. 8 Highest installation position

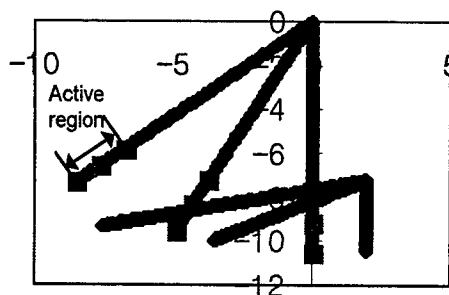


Fig. 9 Lowest installation position

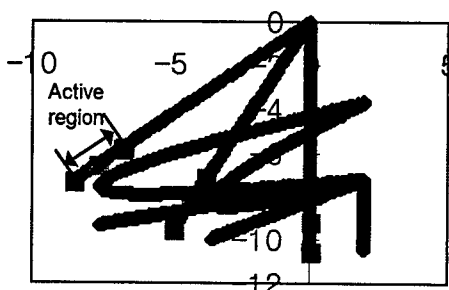


Fig. 10 Different Y installation position

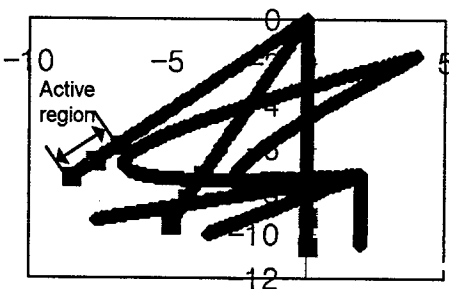


Fig. 11 Different X,Y installation position

Active region explains contraction and expansion of electric wire according to temperature.

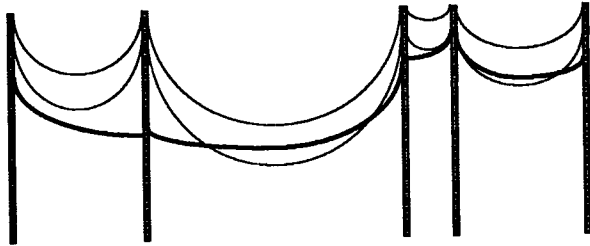


Fig. 12 A front view of one install position

Fig. 12 shows the newly introduced installation position method of ADSS cable regarding to neighboring span length. With this install method ADSS cable, there will be no contact of ADSS cable and electric wire.

DISCUSSION

Generally electric wires are getting thicker and heavier with higher voltage, and becoming a bundle type with two or four electric wires for super high voltage. Therefore, electric wire would not be blown far with higher voltage.

However, a large installation X-position window is provided for higher voltage because the pylon size increases with higher voltage. In addition, the closed distance between ADSS cable and electric wire under the electric field of at least 0.5 kV/mm is allowed at very high voltage.

Therefore, there is no reasons why the application of ADSS cable is limited under a confined voltage

CONCLUSION

In the step of ADSS cable design some information is required as shown in Table. 3 .

Table.3 Required information of optimal ADSS cable design

Items	Required information
Electric Wire	<ul style="list-style-type: none"> • Out diameter(mm) • Unit weight(kg/km) • Elastic constant(kg/mm²) • Thermal coefficient(1/°C) • Bundle number • Installation tension(kg) (final tension) • Max. allowable temperature(°C)
Weather condition	<ul style="list-style-type: none"> • Temperature range(°C) • Max. wind speed without sleet(m/s) • Max. wind speed with sleet(m/s) • Sleet thickness(mm) • Sleet density(g/mm³)
Others	<ul style="list-style-type: none"> • Max. span(m) • Compact towers drawing

With these information ADSS cable can be properly designed to make sure long term responsibility.

REFERENCE

1. Neil R. Haigh, Simon M. Rowland, Arif J. Taha, and Chris N. Carter, "A fully instrumented installation and trial of a novel ADSS cable for very high voltage overhead power lines", 45th Proc International Wire and Cable Symposium(1996) 60-66.
2. A.J. Peacock, J.C.G. Wheeter, "Development of aerial fiber optic cables for operation on 400kV power line", IEE Proc. Vol.139, no.6, (1992) 304-314
3. Ulrich H.P. Oestreich, Hani M. Nassar,

"Self-supporting dielectric fiber optic cables in high voltage lines", 37th Proc. International Wire and Cable Symposium(1988) 79-82.

AUTHORS

Kyung-Tae Park
Engineering and R&D
Group.
Optical Communication
Products Division.
Information &
Communication Business.
SAMSUNG Electronics
Co., Ltd.



Kyung-Tae Park was born in 1967. He received a bachelor's degree from Kwangwoon University Korea in 1992 and master's degree from Kwangwoon University in 1994. Now, he is a researcher of Engineering and R&D Group in Optical Communication Product Division.

Stress-Strain, Creep, and Temperature Dependency of ADSS (All Dielectric Self Supporting) Cable's Sag & Tension Calculation

Cristian Militaru

Alcoa Fujikura Ltd., Spartanburg, SC

Abstract

It has been common in the industry to calculate sag & tension charts for ADSS cables without taking into consideration the influence of creep, coefficient of thermal expansion (CTE), and the difference between the initial and final modulus. In some applications where the sag and tension performance of the cable is not critical, the presentation of data in this manner is appropriate. However, the great majority of applications require very exact determination of sag and tension, and the influence of the above factors is important. There is also confusion between the "final state" (after creep) and the "loading condition" (wind+ice), which are 2 different cases. Following thorough and repeated stress-strain and creep tests, this paper will show that ADSS cable has both an "initial state" and a "final state", each state having an "unloaded" (bare cable) and a "loaded" (ice and/or wind) case with resulting sag & tension charts as a function of creep and CTE. Additionally, the results of this work were compared and validated by common industry sag & tension software, including Sag10 and PLS-CADD.

Catenary Curve Analytic Method

Fig.1 presents an ADSS cable element under the extrinsic (wind and ice) stresses and intrinsic (cable weight) stresses, with a length, on the curve $y(x)$, given by the formula:

$$l = \int_{x_1}^{x_2} \sqrt{1 + y'(x)^2} \cdot dx \quad (1); \text{ yields: } \frac{dl}{dx} = \sqrt{1 + y'(x)^2} \quad (2)$$

Also, the equilibrium equations results in:

$$H_1 = H_2 = H \quad (3); \quad V_1 - V_2 = dV = w \cdot dl \quad (4)$$

considering rel. (2), the derivative of rel. (4) yields:

$$\frac{dV}{dx} = w \cdot \frac{dl}{dx} = w \cdot \sqrt{1 + y'(x)^2} \quad (5); \text{ also, the slope in any}$$

point of the catenary curve is defined as the first derivative of the function $y(x)$ of the curve:

$$V = H \cdot \tan \varphi = H \cdot \frac{dy}{dx} = H \cdot y' \quad (6); \text{ yields:}$$

$$\frac{dV}{dx} = H \cdot \frac{dy'}{dx} \quad (7); \text{ and: } \frac{dV}{dx} = H \cdot y'' \quad (8); \text{ using rel. (5)}$$

and (8), results: $H \cdot y'' = w \cdot \sqrt{1 + y'^2} \quad (9)$, and then:

$$\frac{y''}{\sqrt{1 + y'^2}} = \frac{w}{H} \quad (10); \text{ integrating rel. (10), results:}$$

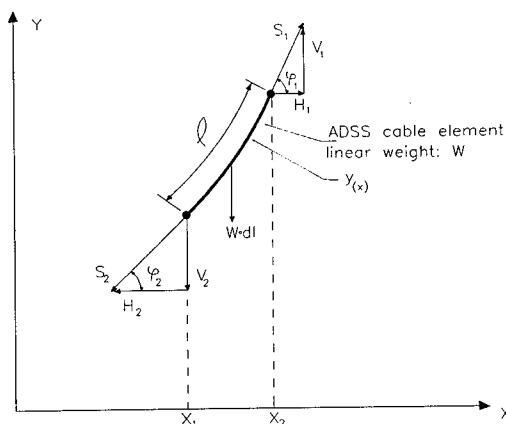


Fig.1 – Catenary Curve Analytic Method

$$\ln(y' + \sqrt{1 + y'^2}) = \frac{w}{H} \cdot x + k_1 \quad (11), \text{ followed by:}$$

$$y' + \sqrt{1 + y'^2} = e^{\left(\frac{w}{H} \cdot x + k_1\right)} \quad (12), \text{ which has as solution:}$$

$$y' = \sinh\left(\frac{w}{H} \cdot x + k_1\right) \quad (13); \text{ integrating rel.(13) results:}$$

$$y = \frac{H}{w} \cdot \cosh\left(\frac{w}{H} \cdot x + k_1\right) + k_2 \quad (14); \text{ for } x=0 \text{ results:}$$

$$y = \frac{H}{w} \quad (15) \text{ and: } y' = 0 \quad (16), \text{ so: } k_1 = k_2 = 0 \quad (17),$$

$$\text{resulting the catenary curve equation: } y = a \cdot \cosh \frac{x}{a} \quad (18)$$

$$\text{where the catenary constant is: } a = \frac{H}{w} \quad (19) \text{ and:}$$

$$y' = \sinh \frac{x}{a} \quad (20).$$

In Fig.2 the designations are:

S= span length

B=S/2= half span length (assuming level supports)

D= sag at mid-span

H= tension at the lowest point on the catenary (horizontal tension) - only for level span case, it is in the center of the span

T= tension in cable at structure (maximum tension)

P= average tension in cable

L/2=arc length of half-span

l= arc length from origin to point where coordinates are (x,y)

Loading Curve Type	Resultant weight: w_r [lbs/ft]	Cross Sectional area: A [in ²]	$S=1400$ [ft] Stress [psi] $\sigma = \frac{P}{A} = \left(\frac{P}{w}\right) \cdot \frac{w_r}{A}$
B	0.277	0.6447	$(9052) \cdot \frac{0.277}{0.6447} = 3889$
H	1.615	0.6447	$(9052) \cdot \frac{1.615}{0.6447} = 22676$

Tensions Limits:

- a) Maximum tension at 0° F under heavy loading not to exceed 51.35% RBS: $MWT=51.35\%RBS$ [lbs].

$$\sigma_{MWT} = \frac{MWT}{A} [psi]$$

Note: MWT (max. working tension) was selected **less than MRCL**, in order for this ADSS cable to cope with limit c) presented below.

- b) Initial tension (when installed) at 60°F w/o ice or wind ("bare" cable) not to exceed 35% RBS:

$$T_{EDS_i} = 35\%RBS \text{ [lbs]}; \quad \sigma_{EDS_i} = \frac{T_{EDS_i}}{A} [psi]$$

- c) Final tension at 60°F w/o ice or wind ("bare" cable) not to exceed 25% RBS:

$$T_{EDS_f} = 25\%RBS \text{ [lbs]};$$

$$\sigma_{EDS_f} = \frac{T_{EDS_f}}{A} [psi]$$

Catenary Table:

strain ϵ [%]	%sag D/S-100 [%]	Span S = 1400 [ft]					σ [psi]	
		D [ft]	T/w [ft]	H/w [ft]	P/w [ft]		B	H
0.025	0.9686	13.56	18088	18074	18081		7769	45294
0.030	1.0608	14.85	16520	16506	16513		7095	41366
0.040	1.2249	17.15	14308	14291	14300		6144	35822
0.050	1.3695	19.17	12800	12781	12791		5496	32042
0.075	1.6775	23.48	10459	10436	10448		4489	26173
0.100	1.9372	27.12	9065	9038	9052		3889	22676
0.150	2.3729	33.22	7413	7380	7397		3178	18530
0.200	2.7401	38.36	6430	6392	6412		2755	16063
0.250	3.0642	42.90	5761	5718	5740		2466	14379
0.300	3.3576	47.00	5267	5219	5243		2253	13134
0.350	3.6273	50.78	4883	4833	4858		2087	12169
0.400	3.8788	54.30	4575	4521	4548		1954	11393
0.450	4.1144	57.60	4320	4263	4292		1844	10752
0.500	4.3377	60.73	4105	4045	4075		1751	10208
0.550	4.5502	63.70	3920	3856	3888		1670	9740
0.600	4.7533	66.55	3759	3692	3725		1600	9331
0.650	4.9483	69.28	3618	3549	3584		1540	8978
0.700	5.1360	71.90	3492	3420	3456		1485	8657
0.750	5.3172	74.44	3378	3304	3341		1435	8369
0.800	5.4925	76.90	3276	3199	3238		1391	8111
0.850	5.6636	79.29	3182	3103	3142		1350	7871
0.900	5.8278	81.59	3098	3017	3058		1314	7660
0.950	5.9886	83.84	3020	2936	2978		1288	7460
1.000	6.1458	86.03	2948	2862	2905		1248	7277
1	2	3	4	5	6		7	8

Guide to Columns:

1 and 2 are the same for any span, any material.

3, 4, 5, 6 are the same, for the same span for any material: ACSR, AAC, EHS, ADSS, etc.

7 and 8 are different, from one material to another (ACSR, AAC, EHS, ADSS, etc.)

This catenary table is transformed in a Preliminary Sag-Tension Graph, in Fig.4. This graph has 2 "y" axes: left side: stress [psi], σ_B and σ_H ; B-bare cable; H-heavy load, and right side: sag: D [ft]. Also, it has 2 "x" axes, strain, ϵ [%] (arc elongation in percent of span) and temperature, θ [°F].

Stress-Strain Tests

Stress-strain tests on ADSS cable performed in the lab show (see Fig.3) that they fit a straight line, characterized by a polynomial function of 1st degree, whereas metallic cables (conductors, OPT-GW, etc.) are characterized by a polynomial function of the 4th degree (5 coefficients). From all the tests performed, results show, that differences exist between the initial modulus, E_i (slope of the "charge" curve) and the final modulus, E_f (slope of the "discharge" curve) and their values depend upon the ADSS cable design. There is also a permanent stretch, ϵ_p (also referred to as "set"), at the "discharge", which depends on the ADSS design.

Creep Tests

According to the ADSS cable draft standard, IEEE P-1222¹, the creep test must be performed at a constant tension equal to 50% MRCL for 1000 hours at room temperature of 60° F. In general, for ADSS cables, $MRCL=[\%MIN...\%MAX]RBS$ therefore the test is done at $T=[\%MIN/2...\%MAX/2]RBS=ct.$ (see Fig.3). Considering a "nominal" value of $MRCL=50\%RBS$, the "default" constant tension for the test would be: $T=25\%RBS$. The creep test on the cable design analyzed was performed at a constant tension: $T=50\%MRCL=28\%RBS$, because for this cable: $MRCL=56\%RBS$. The values were recorded after every hour (see Fig.5-"Creep Test, Polynomial Curve" and Fig.6-"Creep Test: Logarithmic Curve"). The strain after 1 hour, defined as "initial creep", was 42.69 $[\mu in/in]$. After 1000 hours (41.6 days) the strain was 314.10 $[\mu in/in]$. So the recorded creep during the test, defined as strain at 1000 [h] minus strain at 1 [h], is 271.41 $[\mu in/in]$. The extrapolated value after 87360 hours (10 years, 364 days/year) was 1142.69 $[\mu in/in]$. Therefore, the "10 years creep", which is defined as strain at 87360 [h] minus strain at 1 [h], was 1100 $[\mu in/in]=0.11$ [%]. Other creep tests performed on other ADSS cable designs showed "10 years creep" values in the same range. The curves on the stress-strain and tension-strain graphs are identical. The only difference is that on the ordinates (y) axis, when going from tension [lbs] to stress [psi], there is a division by the cross-sectional area of the cable, A [in²]. The values on the strain (x) axis remain the same. For the stress-strain graph (Fig.3) at a tension (stress) equal with the value for which the creep test was performed, $T=50\%MRCL$ ($\sigma=50\%MRCL/A$), a parallel to the x axis intersects the "initial modulus" curve in a point of abscise, $0.5 \epsilon MRCL$, and from that point, going horizontally, adding the "10 years creep" value of 0.11 [%], is obtained the point on the "10 years creep" curve corresponding to that tension for which the creep test was performed. Drawing a line from the origin through that point gives the slope (the modulus) for the "10 years creep", E_c . Always,

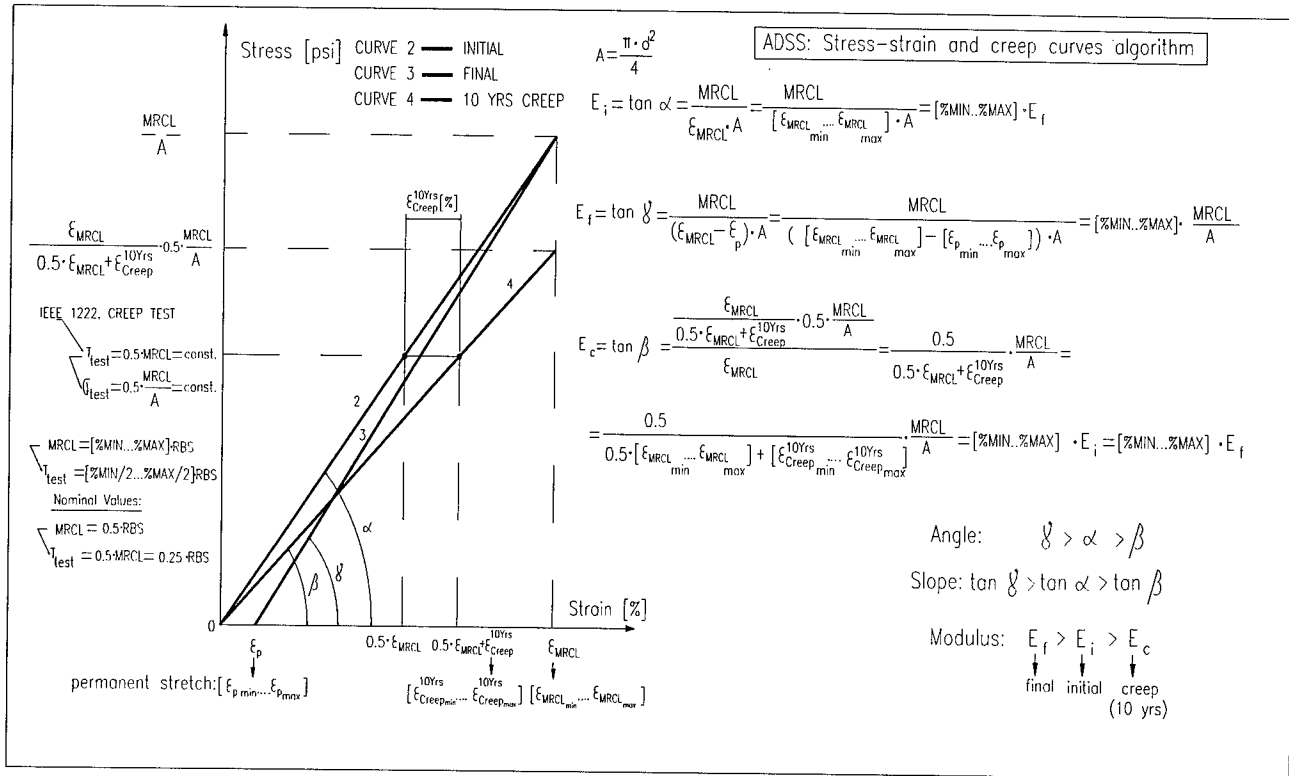


Fig. 3 – General Stress-Strain Chart for an ADSS cable

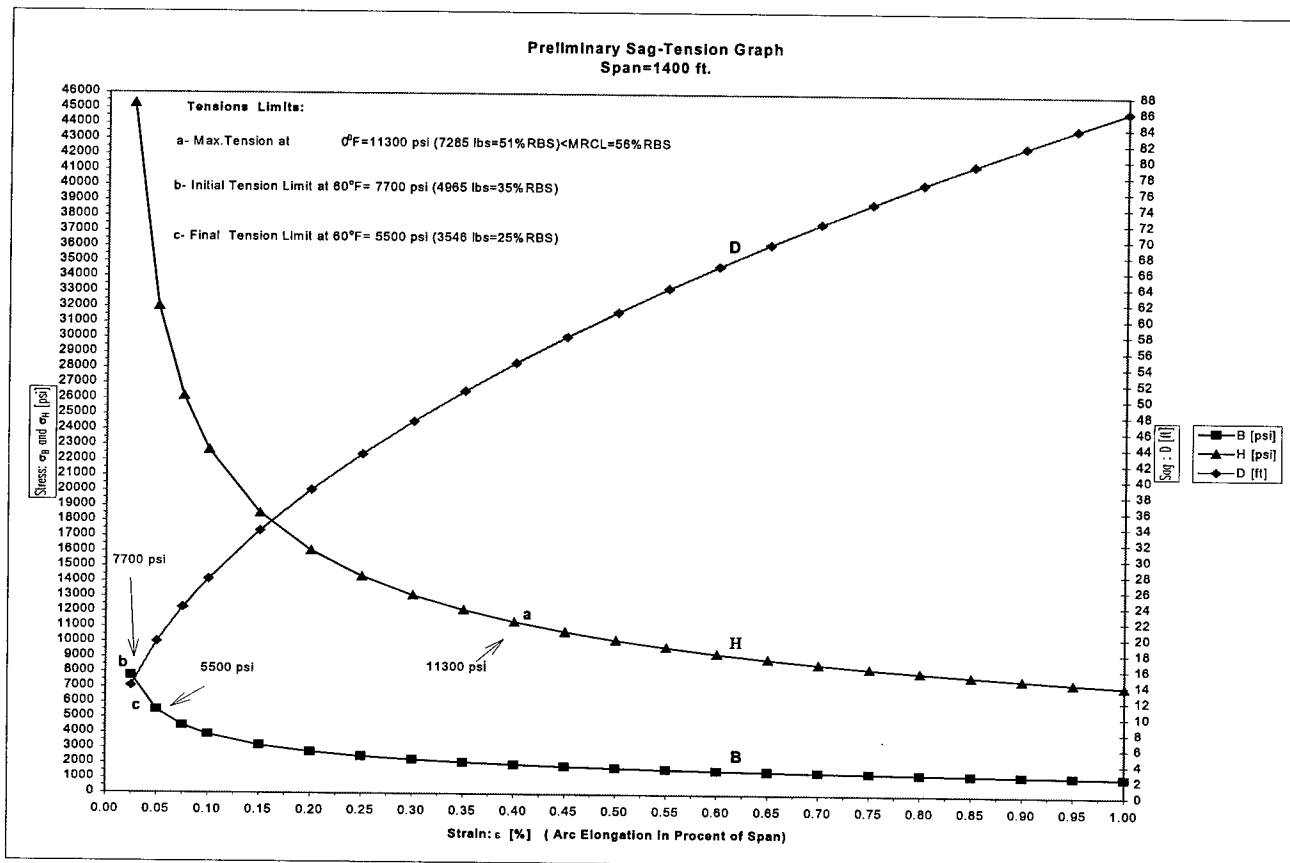


Fig. 4 – Preliminary Sag-Tension Graph for an ADSS cable

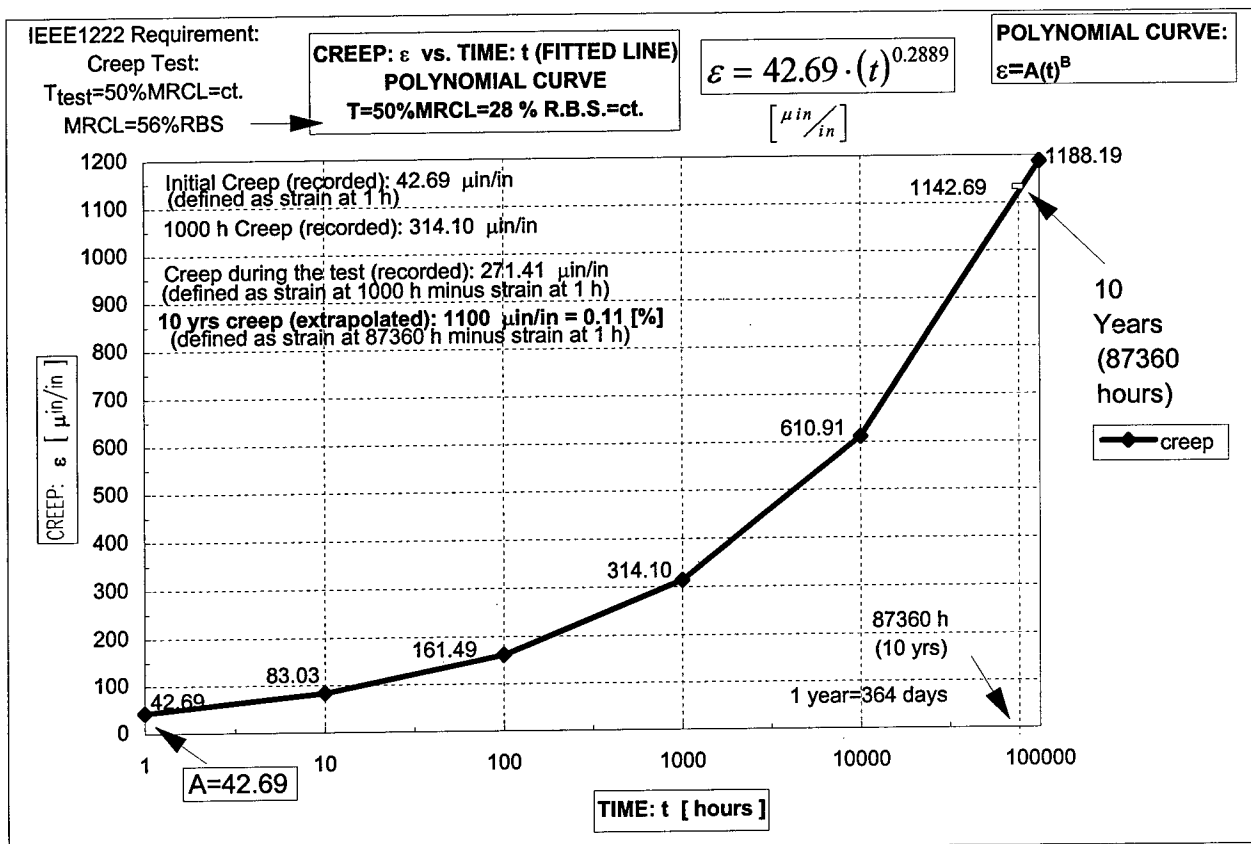


Fig. 5- Creep test for a particular ADSS cable : Polynomial Curve

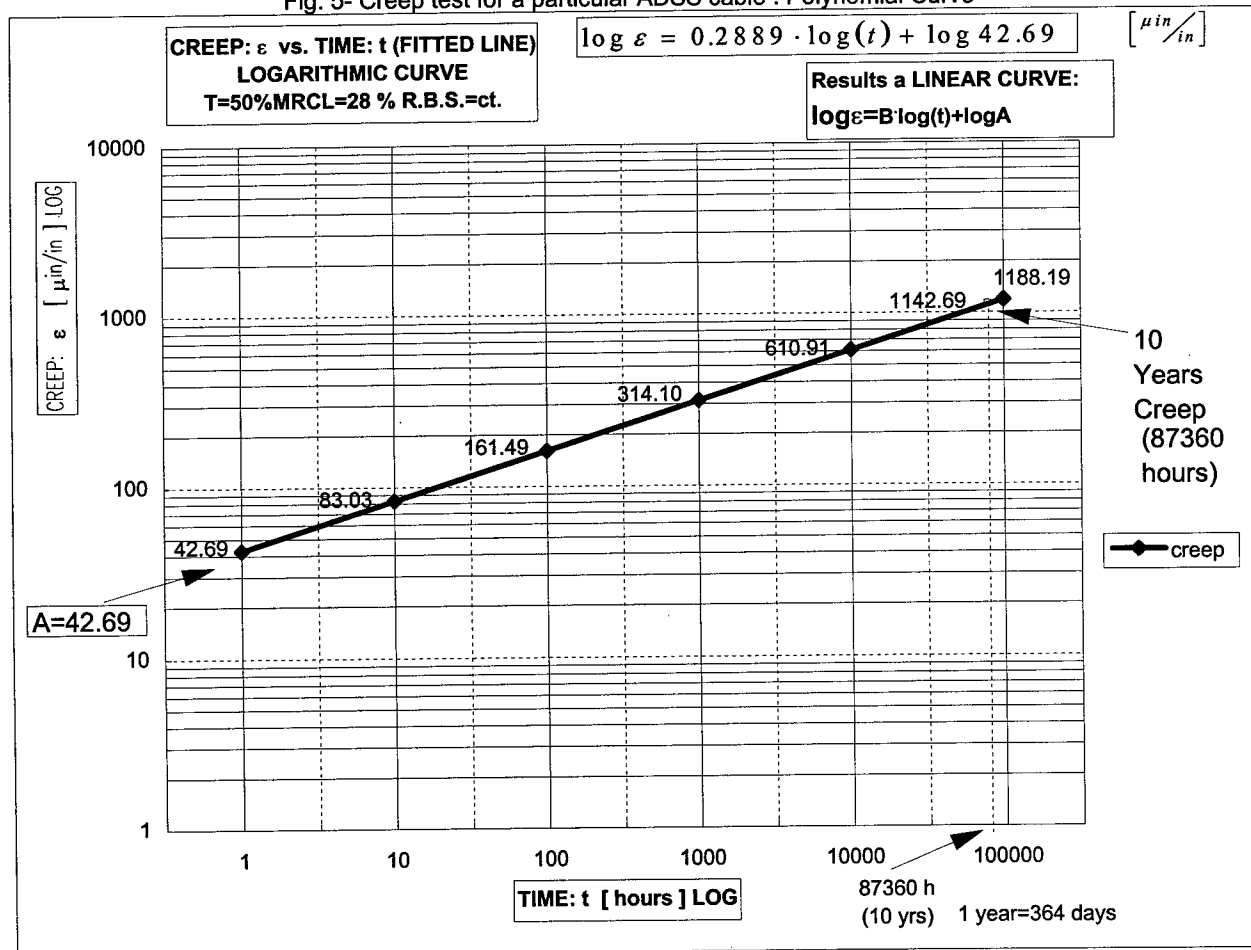


Fig. 6 - Creep test for a particular ADSS cable : Logarithmic Curve

for any ADSS design, the relation between the 3 moduli is $E_f > E_i > E_c$.

Coefficient of Thermal Expansion

The values for CTE (designated here as α) were determined by the individual material properties in a mixture

formula: $\alpha = \sum_{i=1}^n \alpha_i E_i A_i / \sum_{i=1}^n E_i A_i$ (39) where α_i , A_i , E_i are

the CTE, cross-sectional area and modulus of each one of the "i" elements in the ADSS construction respectively. For the great majority of ADSS cable designs, the influence of CTE is smaller than that of creep. Designs with a low number of aramid yarn ends (typically for short spans) will yield larger differences in sags due to temperature than designs with a high number of aramid yarn ends. This is due to the fact that the aramid yarn is the only element with a negative α , while the rest of the elements have a positive α . To appreciate the impact of the contribution of aramid yarn to the ADSS CTE, designs with low number of aramid yarn ends have a CTE typically in the range $2 \cdot 10^{-6}$ [1/°F] to $9 \cdot 10^{-6}$ [1/°F], which is relatively close to aluminum, CTE= $12.8 \cdot 10^{-6}$ [1/°F], and sometimes larger than steel, CTE= $6.4 \cdot 10^{-6}$ [1/°F]. The CTE for cables with higher numbers of aramid ends are often 100 to 1000 times smaller, $2 \cdot 10^{-8}$ [1/°F] to $8 \cdot 10^{-9}$ [1/°F], and so, for those designs, the influence of CTE on sag is negligible.

Sag-Tension Charts

The well known general equation of change of state:

$$\frac{w_2 \cdot S^2}{24 \cdot H_2^2} - \frac{w_1 \cdot S^2}{24 \cdot H_1^2} = \frac{H_2 - H_1}{A \cdot E} + \alpha \cdot (\theta_2 - \theta_1) \quad (40)$$

shows that the change in slack is only equal to the change in elastic elongation + change in thermal elongation, and does not include the change in plastic elongation (the creep). Therefore, the above relation is true only if the 2 states of the cable are in the same stage, initial or final. When viewing sag charts (Fig.11 & Fig.12), this equation will allow a user to go only vertically from one case to another case, but it will not allow him to go horizontally (same temperature, same loading conditions, from initial stage to final stage) due to the influence of creep. A simplistic way of solving this issue which is still used in some European countries is the following: the creep influence is considered to be equivalent with an "off-set temperature", " θ_{creep} ", given by the ratio (conductor 10 yrs. creep-initial elongation)/CTE. But this is not an exact method, because it only calculates an INITIAL sag&tension chart, with the FINAL sag&tension chart being identical with the initial chart, the only thing is that the initial chart, is moved to align it with the new corresponding temperature. Therefore, the final sag at temperature " θ " is equal with the initial sag at temperature " $\theta + \theta_{creep}$ ". The most accurate and exact solution is the graphic method. In this method, which was developed by Alcoa^{2, 3}, the stress-strain graph (Fig.3) of the ADSS cable is superimposed on the ADSS preliminary sag-tension graph (Fig.4), so their abscissas coincide and the whole system of curves from Fig.3 are translated to the left, parallel with the "x" axis, up until the initial curve, noted "2", in Fig. 3 (and also in

Fig.7) intersects the curve H on the index mark=11300 psi (tension limit a)] the imposed maximum tension at 0°F under heavy load. For purposes of this paper, a MWT of 51%RBS was imposed. This MWT, which is less than the cable's MRCL of 56%RBS, was used to be sure that neither tension limits b] or c] will be exceeded. Therefore, tension limit a] is the governing condition. The superimposed graphs then appear in Fig.7. The resultant initial sag at 0°F under heavy loading (54.10 ft.) is found vertically above point a] on curve D. The initial tension at 60°F, bare cable=6750 psi (4352 lbs) is found at the intersection of curve 2 with curve B, and the corresponding sag (15.59 ft) is on curve D. The final stress-strain curve 3a, which is the curve after loading to the maximum tension (MWT=51%RBS), at 0°F, is drawn from point a], which is the intersection point of curves 2 and H, parallel to curve 3, which is the final stress-strain curve after loading to MRCL=56%RBS, at 0°F. Now, the final tension at 0°F, after heavy loading =6440 psi (4151 lbs) is found where curve 3a intersects curve B. The corresponding sag (16.35 ft) is found vertically on curve D. The next operation is to determine whether the final sag after 10 years creep at 60°F will exceed the final sag after heavy loading at 0°F. Before moving the stress-strain graph from its present position, the location of 0°F on its temperature scale is marked on Fig.7 as reference point R. The temperature off-set to the right at 60°F (Fig.7) in %strain is equal to $\alpha \cdot 60^\circ F \cdot 100 = 0.01992$ [%] (41) where $\alpha = 3.32 \cdot 10^{-6}$ [1/°F] is the ADSS CTE. Therefore, the stress-strain graph is moved to the right with 0.01992 [%] (Fig.7) until 60°F on the temperature scale coincides with reference point R (Fig.8). The initial tension at 60°F=6530 psi (4210 lbs) is found at the intersection of curve 2 with curve B, and the corresponding sag (16.11ft) is found vertically on curve D (Fig.8). The final stress-strain curve 3 b, under heavy loading, after creep for 10 years at 60°F, is drawn from the intersection point of curves 4 and B, parallel to curve 3. The final tension at 60°F after creep for 10 years=5500 psi (3546 lbs) is located at the intersection of curve 3b (or curve 4) with curve B. The corresponding sag (19.13 ft) is found vertically on curve D (Fig.8). Since the final sag at 60°F after creep for 10 years=19.13 ft (Fig.8) exceeds the final sag at 0°F after heavy loading=16.35 ft (Fig.7), creep is the governing case. For this case, users of Sag10 will see the flag, "CREEP IS A FACTOR". SAG10 will print only the final chart after creep (not the final chart after heavy load). Users of PLS-CADD will see the same results in the chart called "FINAL AFTER CREEP" (see Fig.11 & Fig. 12). The final sag and tension at 0°F must now be corrected using the revised stress-strain curve. For this purpose, the temperature axis will have an off-set of 0.01992 [%] to the left (Fig.8) to provide the values at 0°F. Therefore, the stress-strain graph is moved to left (Fig.8), until 0°F on the temperature scale coincides with reference point R (Fig.9). The corrected final tension at 0°F, bare cable, (after creep for 10 years at 60°F)=5720 psi (3687 lbs) is found at the intersection between curves 3b and B. The corresponding final sag (18.40 ft.) is found vertically on curve D. The final tension at 0°F under heavy loading, (after 10 years creep at 60°F)=10900 psi (7027 lbs) is found at the intersection between curves 3b and H. It's corresponding resultant final sag (56.07 ft) it's on curve D (Fig.9). When

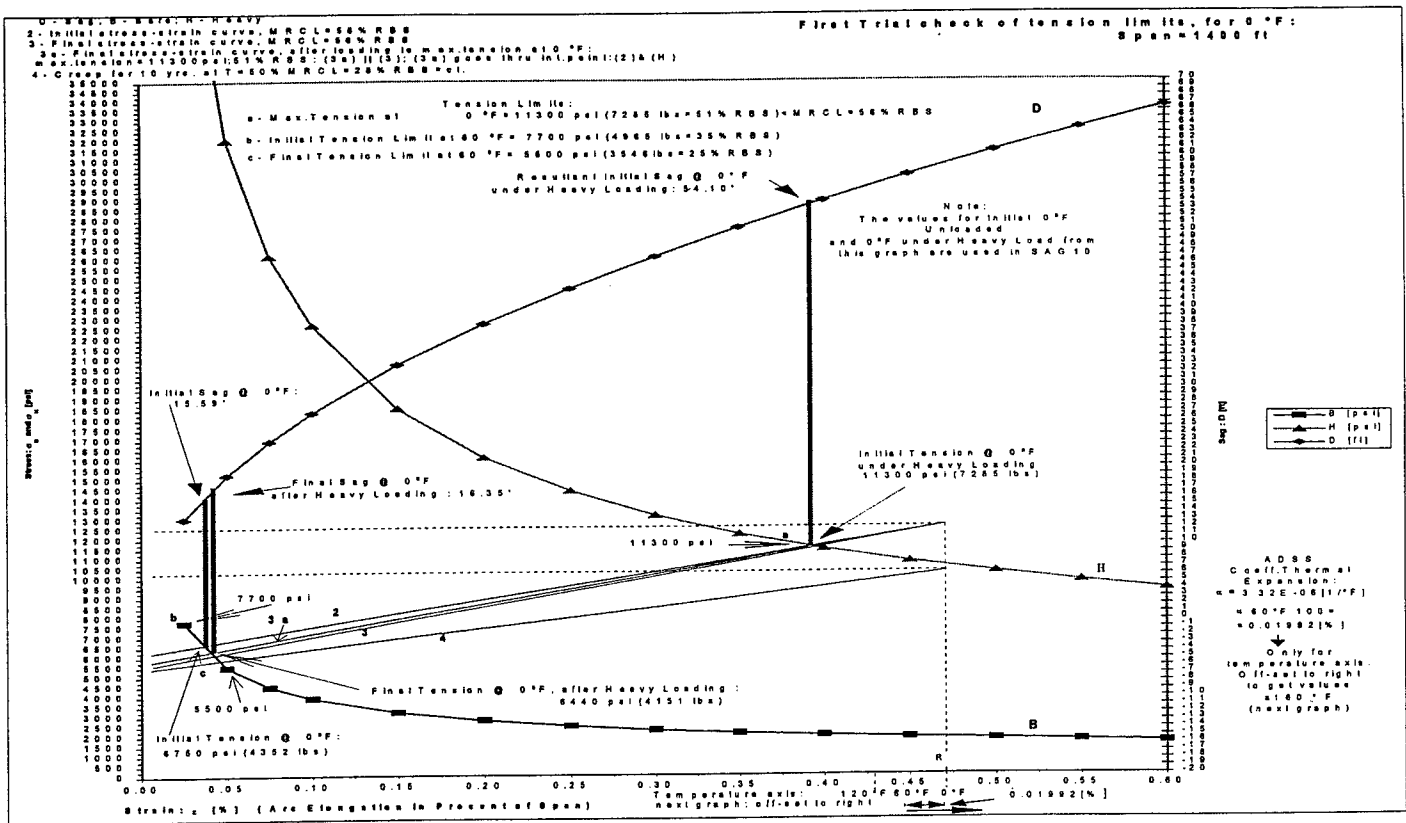


Fig. 7 - First Trial check of tension limits, for 0°F

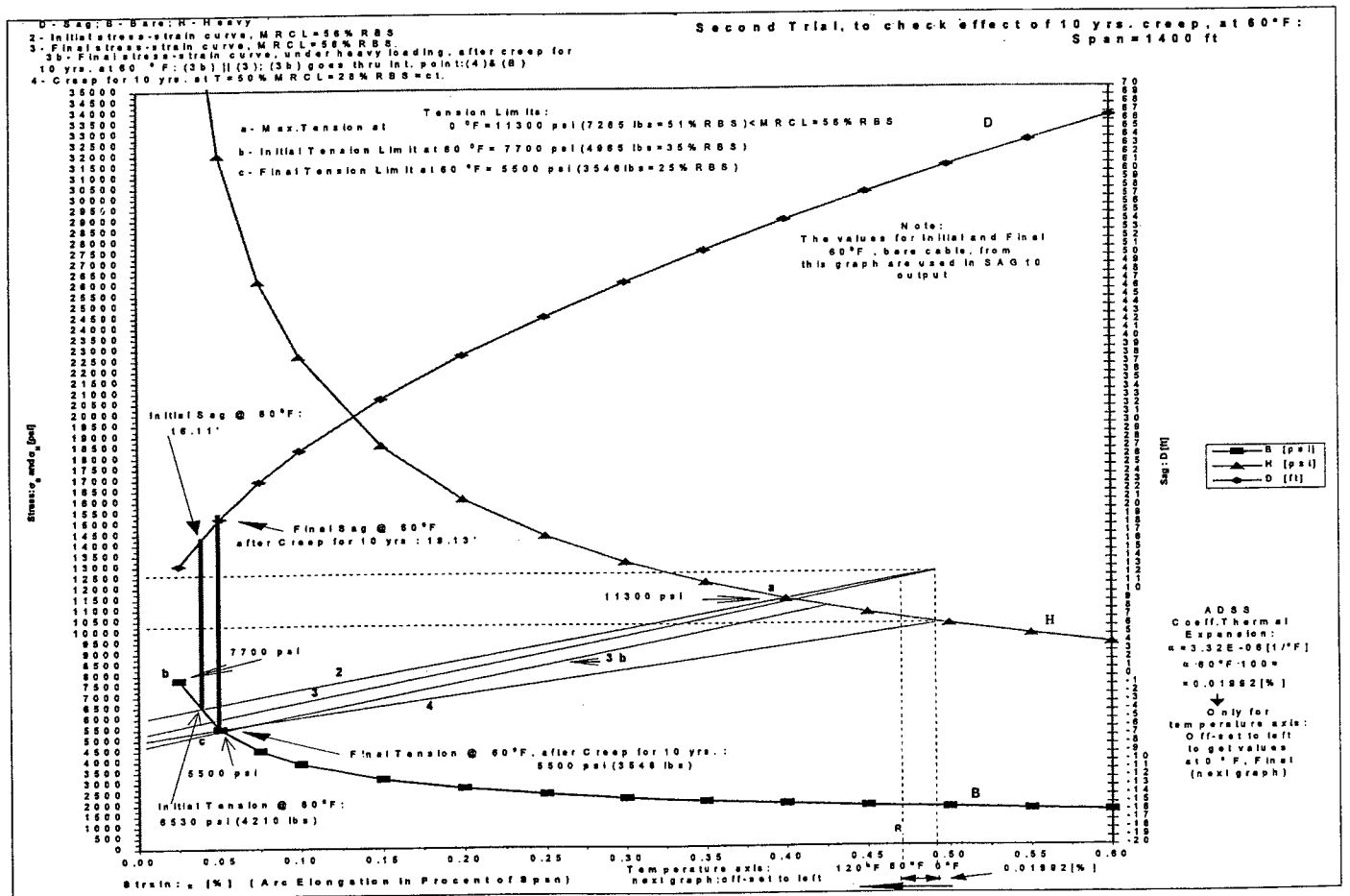


Fig. 8- Second Trial, to check effect of 10 years creep, at 60°F

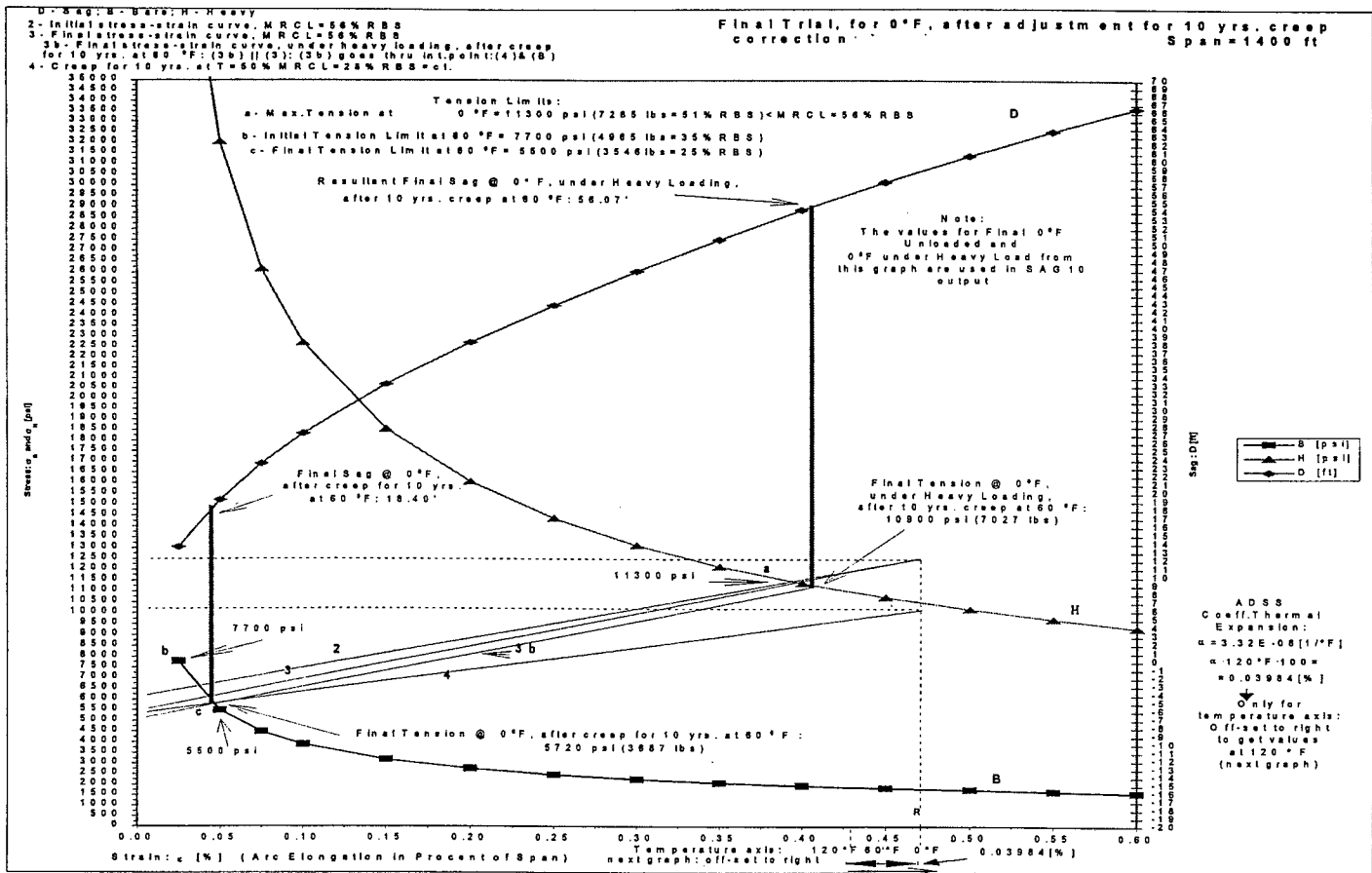


Fig. 9 – Final Trial, for 0°F, after adjustment for 10 years creep correction

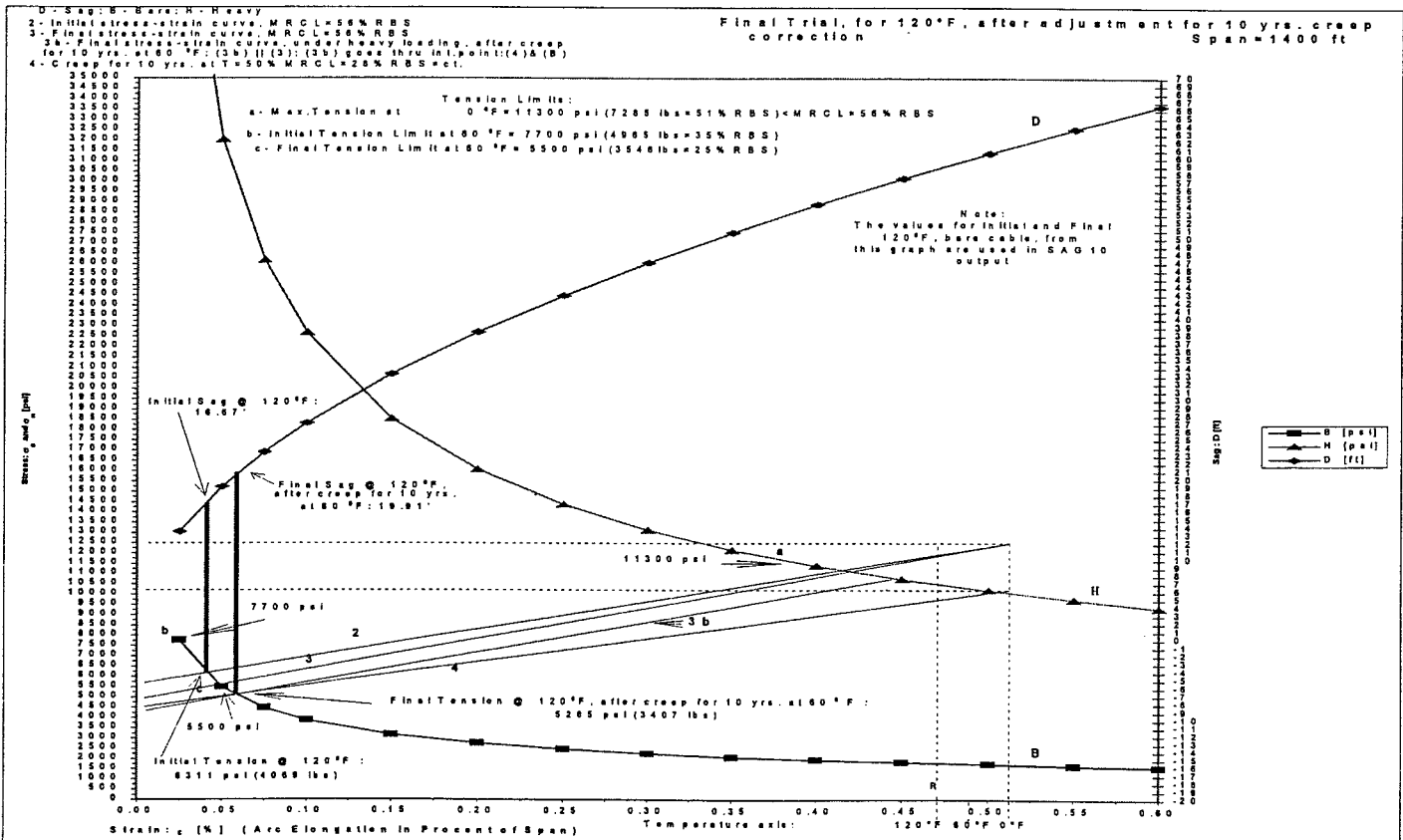


Fig. 10- Final Trial, for 120°F, after adjustment for 10 years creep correction

determining temperatures for calculation of sag and tension performance, the maximum temperature of the ADSS cable should be the maximum ambient temperature plus the heat absorbed by the cable. A reasonable assumption is 120°F (49°C). Electrical conductors can reach higher values, i.e. 167°F (75°C), or 212°F (100°C), due to the continuous current rating of the conductor, which does not exist for ADSS cables. Thus, for 120°F, the temperature off-set to the right (Fig.9) to get values at 120°F, in %strain is : $\alpha \cdot 120^\circ\text{F} \cdot 100 = 0.03984$ [%]. Therefore, the stress-strain graph is moved to the right with this value (Fig.9) until 120°F on the temperature scale coincide with reference point R (Fig.10). The initial tension at 120°F=6311 psi (4069 lbs) is found at the intersection of curve 2 with curve B, and corresponding sag (16.67 ft) is on curve D. The final tension at 120°F (after creep for 10 years at 60°F)=5285 psi (3407 lbs) is found at the intersection of curve 3b (or 4) and curve B, and corresponding sag (19.91 ft) is on curve D (Fig.10).

Conclusions

Using this ADSS cable characteristics as input data, the output in SAG10 is presented in Fig.11, while the output screen for PLS-CADD is presented in Fig.12. As can be noticed, the graphical method presented above produces very similar results in these two programs, as well as in other sag and tension programs on the market. As a note, for different ADSS designs and different span and loading conditions, there can be many situations when the **permanent elongation after heavy loading (due to the stretch of the cable, ϵ_p) is larger than the elongation after 10 years creep**. In these cases, for users of the SAG10 program, the flag "CREEP IS NOT A FACTOR" is shown, and the final sag printed is the sag after heavy load (no more after 10 years creep). Users of PLS-CADD will see the same result in the chart called "FINAL AFTER LOAD". The influence of creep on ADSS cable sags is different from one design to another. As an example, the difference between the final and initial sag can range from 0.5 ft up to 1.2 ft in a span range of 200-600 ft, and from 1.5 ft. up to 2.5 ft in a span range of 600-1400 ft, under NESC Heavy loading. For spans over 1800 ft the differences can be 3-3.5 ft. For spans under NESC Light or Medium loadings, the creep influence results in sag differences less than the numbers listed above. The influence of the coefficient of thermal expansion of the ADSS cables is smaller than that of creep: as an example, changes in sag due to temperatures ranging from -20°F to 120°F would yield 0.5 ft up to 1.75 ft for low aramid yarn counts applications, and becomes negligible (0.01 ft) for those designs with maximum numbers of aramid yarns.

References

1. IEEE 1222P- Standard for All Dielectric Self-Supporting Fiber Optic Cable (ADSS) for use on Overhead Utility Lines - Draft, April 1995
2. Aluminum Electrical Conductor Handbook, chapter 5- third edition, 1989
3. Alcoa Handbook, Section 8:"Graphic Method for Sag Tension Calculation for ASCR and Other Conductors"-1970

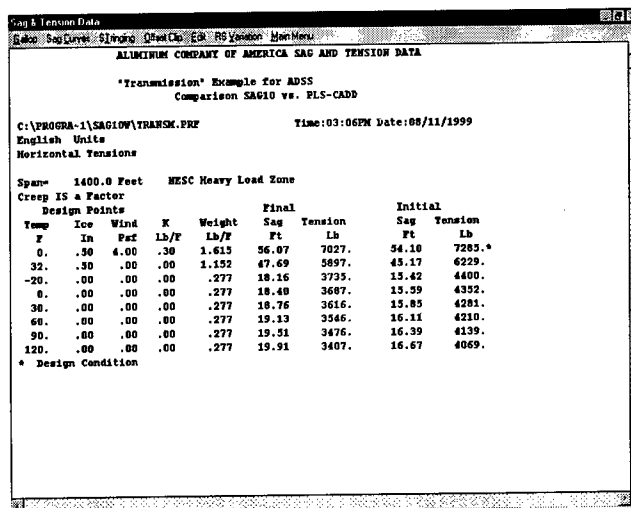


Fig. 11 – SAG10 Output for this ADSS design

PLS-CADD Version 4.60+ Thu Mar 25 13:06:33 1999
 Power Line Systems, Inc.
 Criticism notes:
 CONVERSION WITH SAG10
 Sag Tension Report
 Ordinator name 'c:\pls\pls_cadd\examples\cables\adss5'
 Section 1 from structure #1 to structure #2
 Ruling span (ft) 1400
 Weather case for creep '60'
 Weather case for final after load 'NESC HEAVY W/K'
 Sagging data: Category (ft) 15280.5 Condition I Temperature (deg F) 60
 + WEATHER CASE + + CABLE LOAD + + INITIAL COND. + + FINAL COND. + + FINAL COND. + +
 + + + + + + AFTER CREEP + + AFTER CREEP + + AFTER CREEP + +
 # DESCRIPTION H.R. VERT RES. MAX. HORIZ. % R.S. MAX. HORIZ. % R.S. MAX. HORIZ. % R.S. MAX. HORIZ. %
 LOAD LOAD LOAD TENS. TENS. UL C SAG TENS. TENS. UL C SAG TENS. TENS. UL C SAG TENS. TENS. UL C SAG
 + (lbs/ft) + (lbs) (lbs) (ft) (ft) (lbs) (lbs) (ft) (ft) (lbs) (lbs) (ft) (ft) (lbs) (lbs) (ft) (ft)

1 NESC HEAVY W/K	0.64	1.15	1.61	7372	7284	52	4511	54.42	7113	7022	50	4348	56.47	7372	7284	52	4511	54.42
2 0.5 ICE AT 32	0.00	1.15	1.15	6287	6235	44	5416	45.30	5953	5898	42	5123	47.90	6235	6182	44	5370	45.69
3 -20	0.00	0.28	0.28	4428	4423	31	15969	15.34	3759	3754	26	13553	18.08	4207	4202	30	15170	16.15
4 0	0.00	0.28	0.28	4380	4376	31	15798	15.51	3710	3705	26	13377	18.32	4155	4151	29	14984	16.35
5 30	0.00	0.28	0.28	4309	4304	30	15539	15.77	3639	3634	26	13120	18.68	4080	4075	29	14713	16.66
6 60	0.00	0.28	0.28	4237	4233	30	15281	16.04	3568	3563	25	12863	19.05	4005	4000	28	14441	16.97
7 90	0.00	0.28	0.28	4167	4162	29	15026	16.31	3499	3493	25	12611	19.43	3931	3926	28	14174	17.29
8 120	0.00	0.28	0.28	4096	4092	29	14772	16.59	3430	3425	24	12363	19.82	3857	3852	27	13908	17.62

Fig.12 – PLS-CADD Output for this ADSS design



Mr. Cristian Militaru received MS degree (1980-1985) and Ph.D. degree (1990-1995) in Electrical Power Engineering from Polytechnic University of Bucharest, Romania. He worked for 11 years as a Transmission Design & Consultant Engineer in the power utility industry in Europe, Middle East and SouthEast Asia. Since 1996 he has been employed with Alcoa Fujikura Ltd., USA, as a Development Engineer in the OPT-GW & ADSS cable and hardware department. Mailing Address: Alcoa Fujikura Ltd, P.O.Box 3127, Spartanburg, SC 29304-3127.

ADSS Cables Electrical Corrosion Tests

Cristian Militaru

Alcoa Fujikura Ltd., Spartanburg, SC

Abstract

This paper will present a different approach to the electrical corrosion test, that tries to replicate, in a laboratory, the "dry band arcing ("tracking") phenomenon noticed on ADSS cables in the field on extra high voltage (EHV) lines. This method is closer to real field conditions: **an indirect capacitive coupling** between the conductor and ADSS, versus the existing tests set-ups, including IEEE 1222, Annex A1, which recommend a **direct contact coupling**, or the tracking-wheel test. The paper presents also new measured values of linear resistance for ADSS cables with MDPE jackets, under "wet & polluted" case, different time intervals, and compares them to the figures used in literature for the last 10 years.

Methods of Calculation

1. Linear Charge Method (Image Method)

In this most commonly used method², the conductor is assumed to not be physically connected to ground, so the fact that the conductor is grounded or not at tower has a very small influence in the 2D space potential calculation at the ADSS framing location. However, the ADSS hardware is considered to be grounded, so the ADSS voltage at the towers is zero.

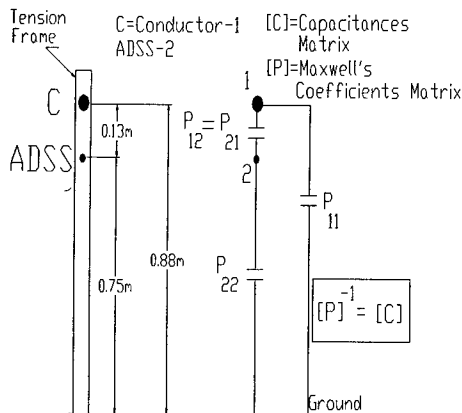


Fig.1- Linear Charge (Maxwell's Coefficients) Method

According to Fig.1 and Fig. 11, the test set-up has the following characteristics:

1. Dielectric constant (permittivity) of free space (air):
 $\epsilon = 8.8541 \cdot 10^{-12} [F/m]$

2. Coordinates:

Type	No.	x [m]	y [m]	Diameter :d [m]
Conductor	1	0.00	0.88	44.39E-03
ADSS	2	0.00	0.75	17.40E-03

Note: SRL rod diameter=3 mm.

3. Voltages: Suppose the secondary of the transformer from the HV section gives a phase-to ground voltage of 75 kV.

Phase-to-phase voltage: V_{ABS} ;

Phase-to-ground voltage: $V_{ABS}/\sqrt{3}$

Conductor: $V_{ABS1} = 130 [kV]$; Phase: $\phi_1 = 0[deg]$

ADSS: $V_{ABS2} = 0[kV]$

Components: Conductor:

$$V_{Re1} = V_{ABS1} \cdot \cos \phi_1 \cdot \frac{1}{\sqrt{3}} = 75[kV] \quad (1)$$

$$V_{Im1} = V_{ABS1} \cdot \sin \phi_1 \cdot \frac{1}{\sqrt{3}} = 0[kV] \quad (2)$$

$$\text{ADSS: } V_{Re2} = V_{Im2} = 0[kV] \quad (3)$$

4. Maxwell's Coefficients: $[P]$ [m/F];

Note: Capacities Matrix: $[C]=[P]^{-1}$ [F/m]

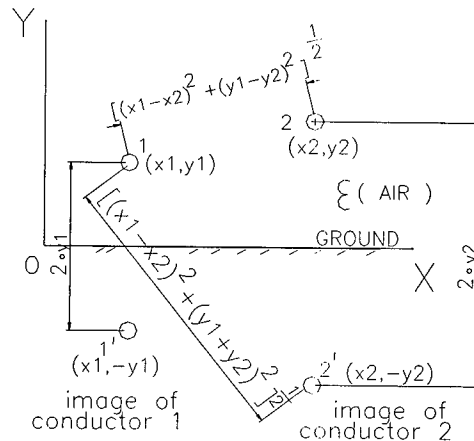


Fig. 2 - Image Method: General Case

According to Fig.2, which is for a general case, the derived relations:

$$P_{ii} = -\frac{1}{2 \cdot \pi \cdot \epsilon} \cdot \ln \left(\frac{d_i}{4 \cdot y_i} \right) [m / F] \quad (4)$$

$$P_{ij} = -\frac{1}{4 \cdot \pi \cdot \epsilon} \cdot \ln \left[\frac{(x_i - x_j)^2 + (y_i - y_j)^2}{(x_i - x_j)^2 + (y_i + y_j)^2} \right] [m / F] \quad (5)$$

when applied to this particular test set-up, give the results:

Conductor – ground: $P_{11}=7.861 \cdot 10^{10} [m/F]$;
 Conductor - ADSS: $P_{12}=P_{21}=4.545 \cdot 10^{10} [m/F]$;
 ADSS-ground: $P_{22}=12.41 \cdot 10^{10} [m/F]$.

Note: The space potential $V(x_2, y_2)$ at ADSS location (x_2, y_2) has the same value, independent of whether an ADSS cable is installed there or not, as will be proven below by rel. (8) and rel. (9). Therefore, the matrix for space potential calculation is reduced to $P=[P_{11}]$. Due to the derivative relation of its radial component, for electric field strength calculation, the matrix is:

$$P = \begin{bmatrix} P_{11} & P_{12} \\ P_{21} & P_{22} \end{bmatrix}$$

5. Maxwell's Equations:

$[V]$ = conductor line-to-ground voltages [volts]; VECTOR
 $[Q]$ = **linear charge densities** [C/m]; VECTOR; attention: **not charge [C]**.

$[P]$ = Maxwell's coefficients [m/F]; MATRIX

$[P]^{-1}=[C]$ =**linear capacities** [F/m]; MATRIX

$$[P] \cdot [Q] = [V] \quad (6); \text{ yields: } [Q] = [P]^{-1} \cdot [V] \quad (7)$$

Generally, both linear charge and voltage vectors have a real and imaginary component, but for this particular case, because the imaginary component of the voltage, for both conductor and ADSS, are 0, the imaginary components for charges are 0. So, for this particular case, after calculations not presented here, the space potential at $x_2=0; y_2=0.75$ [m] where the ADSS is located is given by:

$$V_{Re(x_2, y_2)} = \sum_{i=1}^{n=2} -\frac{Q_{Rei}}{4 \cdot \pi \cdot \epsilon} \cdot \ln \left[\frac{(x_i - x_2)^2 + (y_i - y_2)^2}{(x_i - x_2)^2 + (y_i + y_2)^2} \right] \quad (8)$$

$$= 43630 [V] = 43.63 [kV]$$

Note: due to the fact that the space potential is calculated at the ADSS location (x_2, y_2) , the second term due to ADSS contribution to the superposition method is zero, because when the subscript "i" becomes "2", we have:

$$(x_2 - x_2)^2 + (y_2 - y_2)^2 = 0 \quad (9)$$

$$\text{So: } V_{SP(2D)} = \sqrt{V_{Re(0.75)}^2 + V_{Im(0.75)}^2} = 43.63 [kV] \quad (10)$$

For the same input data, other programs used in the industry give the same result for the 2D unperturbed space potential $VSP(2D)$. This $VSP(2D)$ is independent of span length, and is a straight line in a voltage vs. span graph, as shown in Fig.5. Now, generally, the electric field strength being given by: $E_{(v)} = -\frac{dV}{dl}$ (11)

it can be splinted into 2 components (each, generally, having a real and an imaginary component):

HORIZONTAL (X) COMPONENT (also known as the axial or longitudinal component):

The **horizontal component of E is not a function of the ADSS charge**, because when subscript "i" becomes "2" in its derivative relation, not presented here, **both the first and second terms are zero**.

VERTICAL (Y) COMPONENT (also known as the radial or transverse component):

The **radial component of E is a function of the ADSS charge**, because when subscript "i" becomes "2" in its derivative relation, not presented here, the **second term is not zero**, so it is a function of the diameter of the ADSS. For a real field example with "n" conductors, 2 groundwires, and an ADSS cable, the calculus is more complex. The Maxwell's coefficients matrix for space potential calculation will have "n+2" rows and columns, while for the electric field strength will have "n+3", because the charge created on the

ADSS has to be taken into consideration. Field experience has shown that tracking may have not only a longitudinal "tree" shape, but also a circular, "ring" shape, which may not be located close to the hardware, but far in the span. Both shapes occurred in the cable samples during the tests.

2. Thevenin's Equivalent:

This method, shown in Fig. 4, yields, for the same input data as the previous method, a conductor-ADSS capacitance of:

$$C_1 = \frac{4 \cdot \pi \cdot \epsilon}{\ln \left[\frac{(x_1 - x_2)^2 + (y_1 + y_2)^2}{(x_1 - x_2)^2 + (y_1 - y_2)^2} \right]} = 21.999 [pF / m] \quad (12)$$

and an ADSS-ground capacitance of:

$$C_2 = \frac{2 \cdot \pi \cdot \epsilon}{\ln \left(\frac{4 \cdot y_2}{d_2} \right)} = 10.803 [pF / m] \quad (13)$$

Under "wet & polluted" conditions, the measured linear resistance of the ADSS MDPE jacket was $R = 9.9 \cdot 10^6 \approx 10^7 [\Omega / m]$, for which corresponds a characteristic impedance of:

$$z_0 = \sqrt{\frac{R}{\omega \cdot (C_1 + C_2)}} = 28.437 [M \Omega] \quad (14)$$

$$\text{where: } \omega = 2 \cdot \pi \cdot f; f = 60 [Hz] \quad (15)$$

and an "active span" of:

$$\delta = \sqrt{\frac{2}{\omega \cdot R \cdot (C_1 + C_2)}} = 4.02 [m] \quad (16)$$

Direct vs. Indirect Coupling Methods

All electrical stress tests on ADSS cable to this point in time have been performed using a method that directly couples the voltage to the ADSS cable. This direct coupling method incorrectly models the environment where the ADSS is deployed due to 2 reasons (see Fig.3). First, it shows the ADSS longitudinal resistance, $R \cdot dx$, to be in **series** with a capacitance located after the source, $C_1 \cdot dx$, and second, **the earth leakage current on the ADSS, I_l , is the same with the current coming from source to ADSS through the capacitance C_1, I_{C1} .**

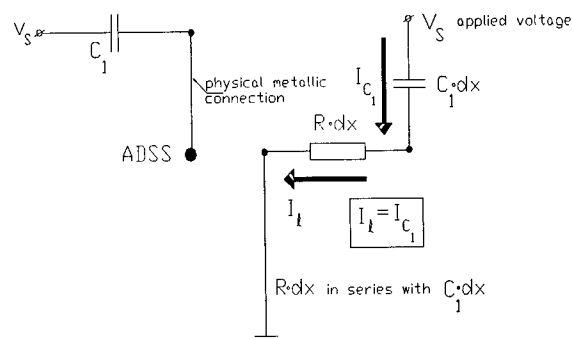


Fig. 3: Direct Coupling Method

In reality, in the field, there is an **indirect capacitive coupling** (see Fig.4). The ADSS resistance, $R \cdot dx$, is in

parallel with the ADSS-ground capacitance, $C_2 \cdot dx$ (both at the same potential differential, V-ground), and the earth leakage current through the ADSS cable resistance, I_l , is equal with the **difference** between the current that travels through the capacitance C_1 , I_{C1} , and the current that travels through the capacitance C_2 , I_{C2} . Therefore, an **equivalent impedance**, Z_{equiv} (Fig.4), results from the resistive impedance, $R \cdot dx$, in **parallel** with the capacitive impedance, $1/\omega C_2 \cdot dx$, that is in **series** with the capacitive impedance, $1/\omega C_1 \cdot dx$:

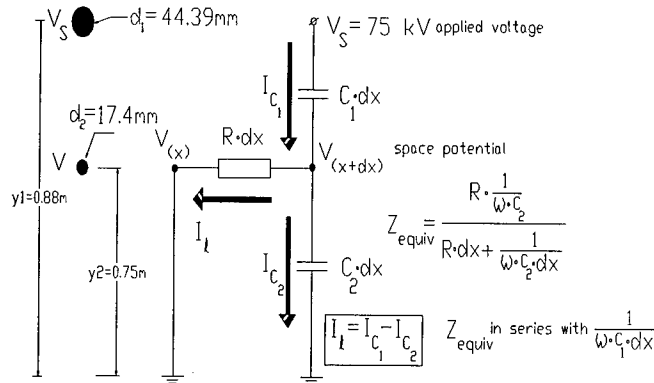


Fig. 4- Indirect Capacitive Coupling Method

$$I_l = I_{C1} - I_{C2} \quad (17)$$

this yields into the differential equation:

$$dI_l = j \cdot \omega \cdot C_1 \cdot dx (V_s - V) - j \cdot \omega \cdot C_2 \cdot dx V \quad (18)$$

and finally the system:

$$\begin{cases} dI_l = j \cdot \omega \cdot C_1 \cdot V_s \cdot dx - j \cdot \omega \cdot (C_1 + C_2) \cdot V \cdot dx \\ dV = -I_l \cdot R \cdot dx \end{cases} \quad (19)$$

When R tends to infinity, the first equation in rel. (19) becomes:

$$I_l = 0 \Rightarrow C_1 \cdot V_s = (C_1 + C_2) \cdot V_o \quad (20)$$

When R tends to zero, the first equation in rel. (19) becomes:

$$V = 0 \Rightarrow dI_l = j \cdot \omega \cdot C_1 \cdot dx \cdot V_s \quad (21)$$

Using the boundary conditions and hyperbolic functions attached to the complex numbers presented in a previous IEEE paper³, and the fact that the time constant, $R \cdot (C_1 + C_2) \cdot x^2/2$, at a distance equal with the "active span", $x = \delta$, is given by the inverse of the angular frequency, $1/\omega$, result rel.(16) and rel.(14). This method derives an earth-leakage current of:

$$I_l = V_s \cdot \omega \cdot C_1 \cdot \delta / \sqrt{2} = 1.769 [mA] \quad (22)$$

The previous IEEE paper³ is an important paper to the industry. However, in that paper, rel. (14) had an incorrect division by $\sqrt{2}$, resulting the characteristic impedance being 1.42 times smaller than the correct value, and in rel. (22), a division by $\sqrt{2}$ was forgotten, resulting in the earth-leakage current being 1.42 times bigger than the correct value. Rel. (22) shows that this current, at the tower, is independent of the span length.

3. Lossy Transmission Line Method:

A third method of modeling the electrical stress on the ADSS cable is the lossy transmission line method. This method was used to confirm the results obtained by using the Thevenin's Equivalent Method and as a cross check to the results seen in the laboratory tests. In this method⁴, if the longitudinal axis along the span length is " x ", the resulting induced voltage is given by:

$$V_{c(x)} = V_{SP(2D)} \cdot [1 - e^{-(1+j)x/\delta}] \quad (23)$$

Its magnitude will be:

$$|V_{c(x)}| = V_{SP(2D)} \cdot \sqrt{1 - 2 \cdot e^{-x/\delta} \cdot \cos(x/\delta) + e^{-2x/\delta}} \quad (24)$$

see also Fig.5 . The induced current is given by:

$$I_{c(x)} = \frac{V_{SP(2D)}}{Z_o} \cdot e^{-(1+j)x/\delta} \quad (25)$$

So it's magnitude is given by :

$$|I_{c(x)}| = \frac{V_{SP(2D)}}{Z_o} \cdot e^{-x/\delta} \quad (26)$$

See also Fig. 6. The induced axial field strength magnitude is given by:

$$|E_{c(x)}| = |I_{c(x)}| \cdot R \quad (27), \text{ or: } |E_{c(x)}| = \frac{V_{SP(2D)}}{Z_o} \cdot R \cdot e^{-x/\delta} \quad (28)$$

see also Fig. 7.

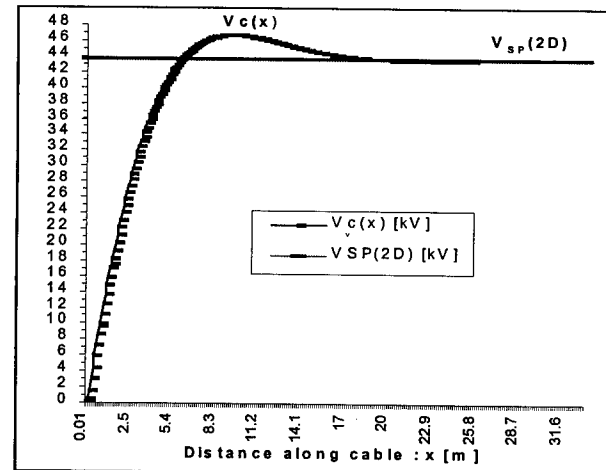


Fig. 5-Induced Voltage: $V_{c(x)}$ & Space Potential: $V_{SP(2D)}$

It's obvious from rel. (26) and rel. (28), that **at the tower, where $x=0$** , it will result:

$$|I_{c(0)}| = I_{c \max} = \frac{V_{SP(2D)}}{Z_o} \quad (29)$$

$$|E_{c(0)}| = E_{c \max} = \frac{V_{SP(2D)}}{Z_o} \cdot R \quad (30)$$

Rel. (29) and (30) demonstrate, that at the tower, where the induced current and the axial field strength have the maximum values, these values are not a function of span length, because they are a function only of: $V_{SP(2D)}$, Z_o , and R . These 3 variables are

independent of the span length, and because as long as the level of pollution is the same, R is constant.

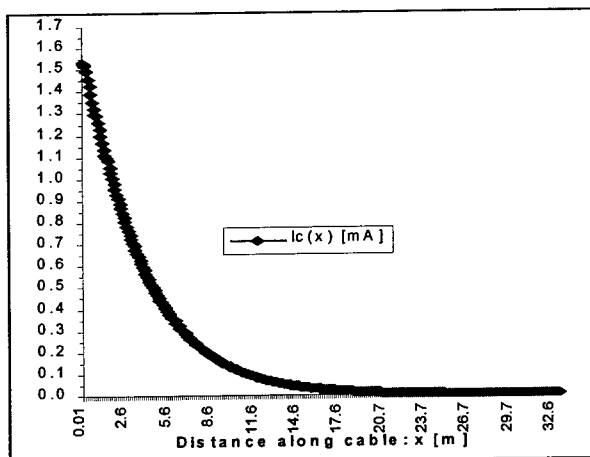


Fig.6 - Induced Current: $I_c(x)$

For the MDPE jacket ADSS sample, in the chamber, $V_{SP(2D)} = 43.63$ [kV], $Z_0 = 28.437$ [$M\Omega$], and because under the "wet & polluted" case the measured resistance was $R = 107$ [Ω/m], results, according to rel.(29) and (30), $I_{cmax} = 1.53$ [mA] and: $E_{cmax} = 15.3$ [kV/m] (see also Fig.6 and Fig.7). This electrical current result is similar to what was obtained with the Thevenin's Method. The maximum axial field strength cannot be measured inside the chamber during the test. The use of a field meter inside the chamber, close to the rods end, where the field strength is maximum, is impossible, due to the fact that the close proximity to the chamber wall will perturb the field, and give erroneous results. However, this theoretical value is quite reasonable, covering all possible field scenarios. During the tests performed in the lab, using the Indirect Capacitive Coupling Method (Fig.4), the output current meter (see Fig.14) showed values around 1.5-1.8 mA, very close to the values predicted by all theoretical methods.

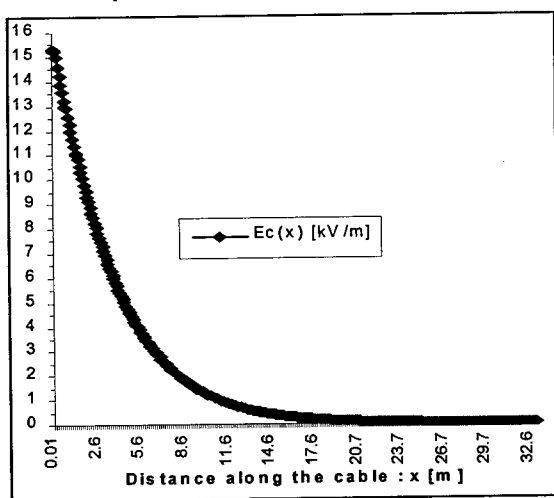


Fig. 7 - Axial Electric Field Strength: $E_c(x)$

As Fig.5 shows, the maximum of the induced voltage, $V_c(x)$, can be equal or slightly higher (7%) than the 2D space potential, $V_{SP(2D)}$, so the "worst case" is to

consider the value of the 2D space potential for the induced voltage. Ultimately, the driving forces for the dry band arcing phenomenon, see Fig.7 and Fig.6, are the **axial electric field strength** and the **induced current magnitude at the tower**. The 2D unperturbed space potential, $V_{SP(2D)}$, can be derived from them, by using rel.(29) and (30), and the induced voltage is a secondary characteristic for the phenomenon, and it can be replaced, for the "worst case", by the 2D unperturbed space potential.

Test Set-up

The tests were performed (see Fig.8) using a salt & fog chamber (salt solution, corresponding to a "heavy" pollution level), located over a tension frame, and a high voltage AC dielectric test set. The test duration is a maximum of 1000 hours, per IEEE P-1222, Annex A. As presented in Fig.11, the new proposed test set-up consists of a conductor strung horizontally (no sag) at a fixed height from ground, the ADSS cable sample, different designs (sizes) being located (no sag) under the conductor, in the same vertical plane, movable relative to the conductor. The ADSS cable preformed hardware is grounded at both ends, outside the chamber, to replicate field conditions (Fig.9).

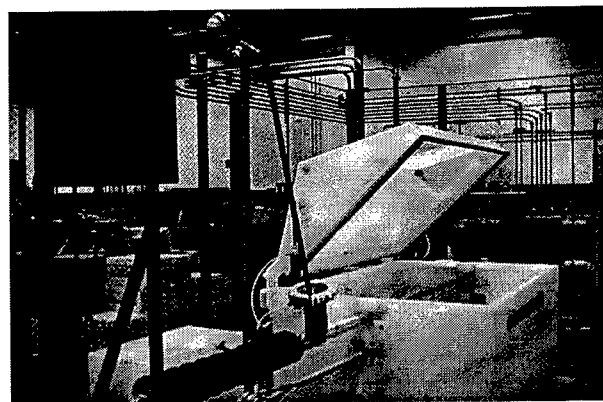


Fig.8- Longitudinal View of the AFL test set-up

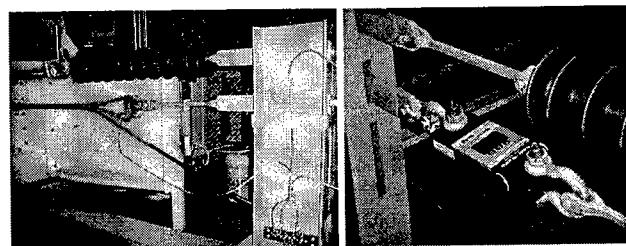


Fig.9-ADSS grounding

Fig10-Digital dynamometer

Test Procedure

To prove this method generates significant harmful dry band arcs, ADSS cable samples with MDPE jackets were chosen and located at a higher 2D space potential than their maximum allowable value when installed in the field, in order to provoke a track. A series of tests were performed on 3 samples of ADSS cable with MDPE jacket,

diameter 0.685 in (17.4 mm), under a tension of 1000 lbs (Fig.10), which corresponds to no sag in the span inside the chamber. The “y” coordinate was measured, for both the conductor and the ADSS cable, relative to the physical earth, not to the base of the chamber, or to the base of the tension frame. The reason is that the method used by AFL program to determine the 2 D unperturbed space potential is Image Method (Linear Charge Method), which is using the physical earth as a “mirror” line. The method calculates the coupling capacities (and their inverse values, which are the Maxwell’s Coefficients) between conductor-ground, ADSS-ground, conductor-ADSS, the linear charges induced, and ultimately the 2D space potential, based on the distances relative to physical ground. The flow rate at nozzles was set to 0.4 liters/hour for each m³ of chamber volume, according to the IEEE1222 requirement (see Fig.12). During the tests, 2 sensors continuously measured the temperature of 2 set points: SP (see Fig.13): one inside the chamber, in the exposed zone: at the “dry bulb”, and one outside the chamber: at the humidifying tower. The applied voltage on the conductor and the induced current on the ADSS cable were also measured continuously during the tests (see Fig.14).

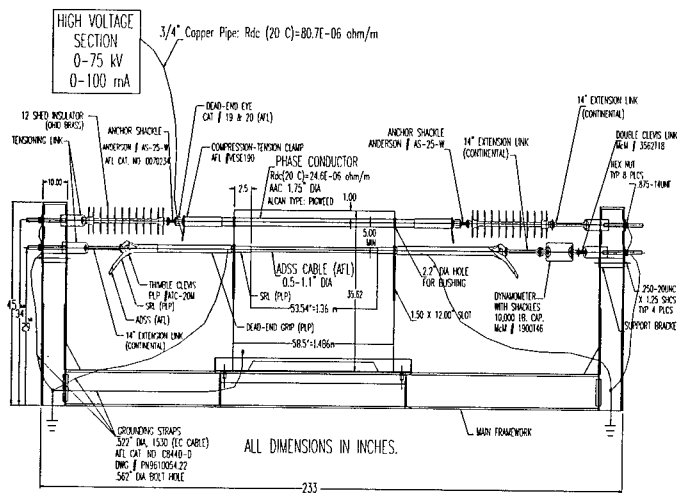


Fig.11- The Scheme of AFL ADSS Corrosion Test Set-up

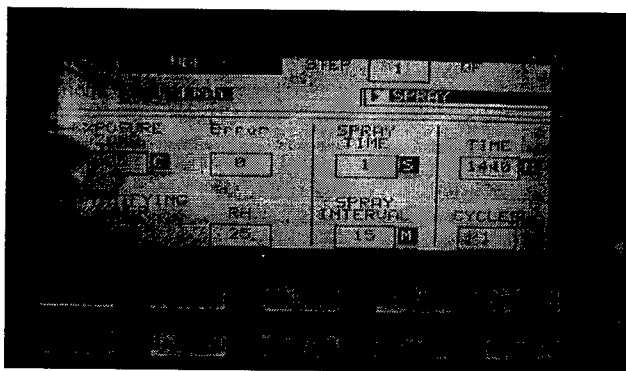


Fig.12- Corrosion Chamber Parameters Selection Screen

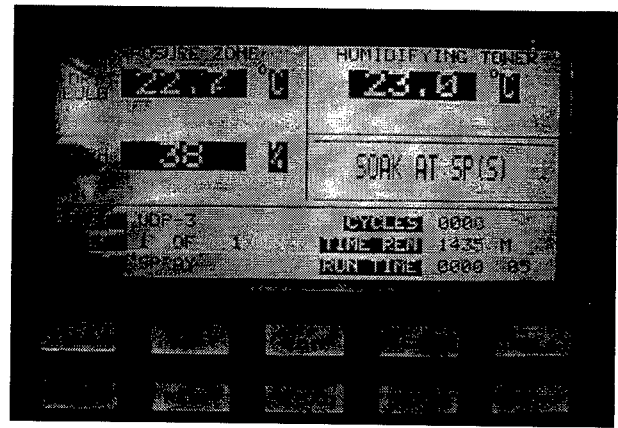


Fig.13- Corrosion Chamber Touch Screen Interface (PLC)

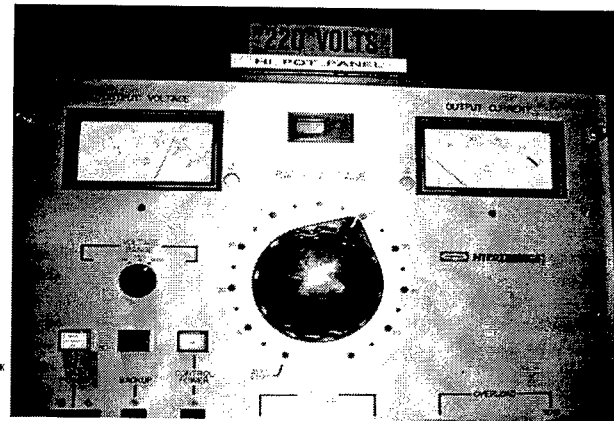


Fig.14 - AC Dielectric Test Front Panel Voltmeter and Currentmeter

ADSS Linear Resistance Measurements

During the electrical stress tests performed in the lab, there was no physical connection, no direct contact coupling, between the conductor and the ADSS cable. Separate from these tests, the longitudinal linear resistance of the ADSS cable with MDPE jacket was measured. For this, obviously, a physical metallic connection between the conductor and ADSS was necessary. A wire braid with 2 hose clamps was attached between the conductor and the ADSS cable, in the middle of the span. The cable length, from rod end to rod end, was 1.36 m. Since the ADSS hardware was grounded, the resulting sample length over which the resistance was measured was $L=0.68$ m. A current, I [mA], at the output current meter was measured, corresponding to an applied voltage, V [kV], over the sample length, L [m]. The linear resistance, R , is given by the formula:

$$R = \frac{V [kV]}{I [mA] \cdot L [m]} \quad [M \Omega / m] \quad (31)$$

The measurements were taken every 6 hours, for 1.5 days (36 hours), to see if the resistance was influenced by time, while the ADSS was sprayed with a constant flow rate at the nozzles, corresponding to the same salt solution in the chamber. The results, presented in Table 1 and Fig.15, show that the resistance decreases in time, but reaches

an asymptotic minimum value of $R = 9.9 \cdot 10^6 \approx 10^7 [\Omega/m]$ after about 36 hours.

The "classical" values for "wet & polluted" cases presented in literature are between 10^7 - $10^5 [\Omega/m]$. Future measurements will be performed on different MDPE jackets and TRC jackets, with different thicknesses, to see if this range of values still applies to all materials.

Case: "wet & polluted"				
Time t [h]	Applied Voltage V [kV]	Measured Current I [mA]	ADSS Length L [m]	ADSS Resistance R [M Ω /m]
4	71	8	0.68	13
12	72	9	0.68	11
18	73	10	0.68	10
24	74	11	0.68	9.9
30	74	11	0.68	9.9
36	74	11	0.68	9.9

Table 1

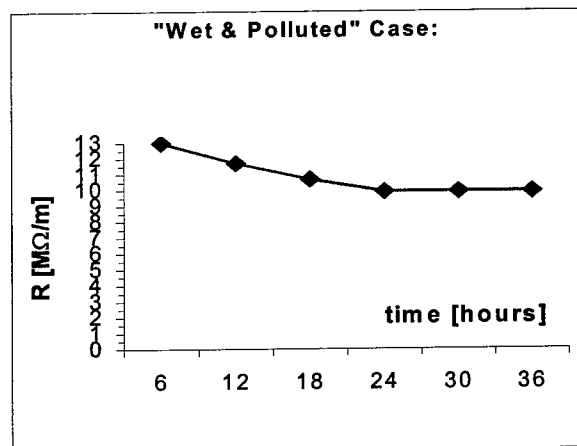


Fig.15- ADSS Longitudinal Linear Resistance

Tests Conclusions

For the chosen type of samples, AFL selected an applied voltage on the conductor of 55 kV, rms, phase to ground, resulting in a 2D-space potential at the ADSS location of 31.88 kV (see Fig. 20). This 2D space potential at ADSS location has to be high enough to produce dry band arcs, and resulting tracks on the MDPE jacket. For this applied voltage of 55 kV, the rest of input data being the same, the Thevenin's Equivalent earth-leakage current is $I_l = 1.29$ mA and the Lossy Transmission Line method shows a maximum induced current at tower of $I_{c(0)} = I_{cmax} = 1.12$ mA, and a maximum axial field strength of: $E_{c(0)} = E_{cmax} = 11.18$ kV/m. **The current measured by the output meter was 1.1-1.3 mA, again in the range predicted by the theoretical methods.** It was clear that the current generated was from dry band arcs as opposed to from extraneous sources for two reasons. First, the conductor was insulated at both ends from the metallic frame, through 2 polymer insulators, and the only way the current could flow was as follows: from secondary of the transformer, through the copper pipe connection, into the conductor, from the conductor through the air, due to the

coupling capacity, to the ADSS cable, then to the ADSS metallic hardware, and finally to ground through a grounding strap. The only high resistance in the circuit that matters is that of the ADSS cable (10 M Ω /m), the rest of resistances are much smaller ($\mu\Omega$ /m), and definitely are negligible. Second, when the ADSS cable was removed with the conductor still in place, the output from the current meter was zero.

The first sample showed signs of significant tracking after about 100 hours, the second one after about 95 hours, and the third one after 126 hours. Pictures were taken before the voltage was applied over the entire span length, to be compared with the ones taken when a track occurred. The tracks on the first two samples were longitudinally along the cable, over a length of about 60 mm, and cut through the jacket completely, exposing the aramid yarns. (See Fig.16 and Fig.17).

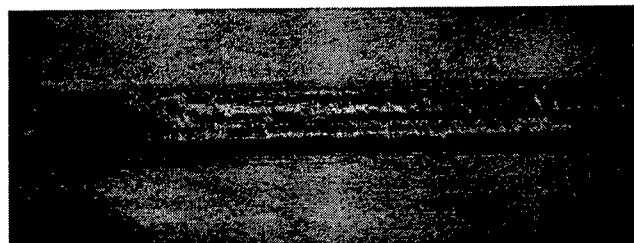


Fig.16- Sample 1 Track

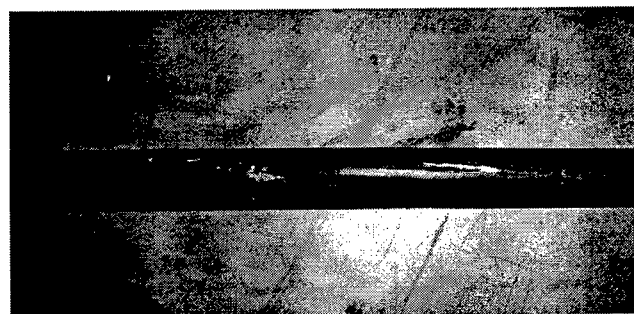


Fig.17- Sample 2 Track

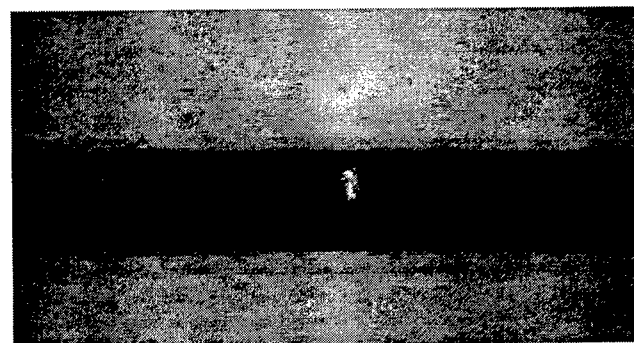


Fig.18- Sample 3 Track on the right side of the span

Pictures of the location of the tracks on the third sample are presented in Fig.18 and Fig.19. In Fig.18, tracks were seen at a distance of about 0.625 in (15.876 mm) from the tip of the rods of the SRL, located inside the chamber, on the right side of the cable. In contrast to the tracks seen in Fig. 16 and Fig. 17, the length of the tracks were

inspected by an optical system as shown in Fig. 1. From these factors and an assumed interaction mechanism between them, the loss is estimated.

This system works fine, if only the observed factors are responsible for the particular loss and their interaction is as expected. But especially under unfavorable conditions, where a risk of high losses is evident, the loss mechanism gets more complex. That can result in an underestimation of splice losses, offering the possibility of leaving undetected bad splices in the link.

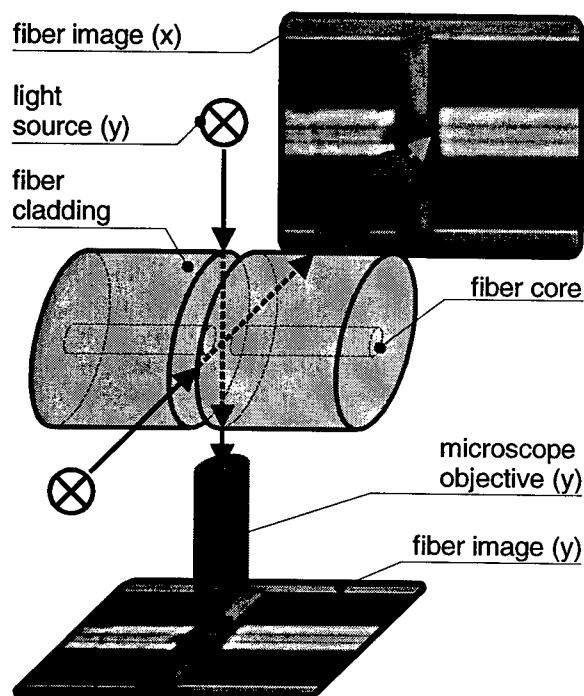


Fig. 1: Transverse optical fiber inspection

Measurement by Power-Through Technique

A way to measure the loss independently of its mechanism's complexity is the power-through technique. Light is coupled into the fiber just before the splice and coupled out afterwards. The attenuation of this light is measured¹. Therefore the real loss, which attenuates the transmitted signal when the line is active, is measured. This is also known as the LID system (local injection and detection).

The drawback of this technique is, that it is not applicable for special fibers which coatings are opaque. In this case local injection and detection of the light is not possible.

CONCEPT OF SPLICE SIMULATION

Our goal was to find a method that has the best of both worlds.

On one hand the new technique should be applicable to all fibers independently of the fiber coating type. This demand is fulfilled by a transverse optical inspection of the fiber core as shown in Fig. 1.

The fiber is illuminated via back light. An objective projects the picture onto a CCD camera, that allows computerized evaluation. To allow a three-dimensional analysis, the fiber is viewed from two axes. This principle is also known as profile alignment system (PAS). Fig. 2 shows a typical splicing machine that uses PAS.

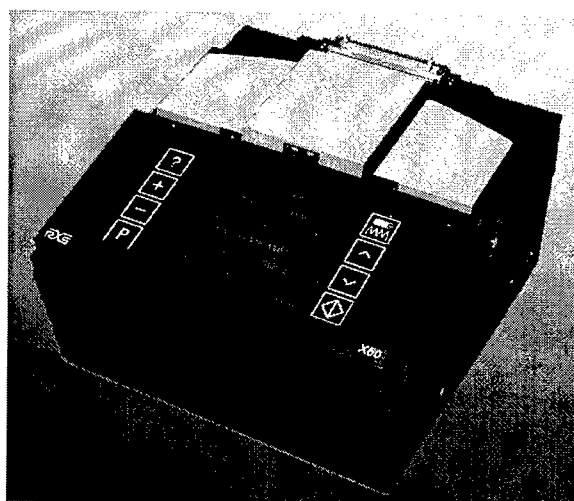


Fig. 2: Common PAS fusion splicer

On the other hand our new technique should take all loss mechanisms into account. This should be achieved without having to know the effect of each particular loss causing component. Further, the specific interaction between the loss components should also be considered automatically.

The idea is to create a virtual representation of the actual splice geometry. The representation includes all loss causing factors without having to know them in detail. The spreading of light through the splice is calculated by a numerical simulation. The exact splice loss is computed from the resulting intensity distribution. The system works similar to the LID system with the exception that it performs its job virtually. That solves all problems concerning the local coupling of light into and out of the fiber like opaque coating. Because of the virtual local injection and detection of light, the system is called VLID.

The application of this technique in reality requires the following steps to be performed.

1. The numerical model of the splice has to be built from the fiber pictures obtained by the transverse optical fiber inspection.
2. The specific light distribution caused by the splice has to be calculated.
3. The splice loss has to be computed from the calculated distribution.

Another highlight of this technique is that not only splices can be evaluated. Additionally particular aspects of any optical fiber distortion can be analyzed. An example of that kind of application will be shown in a later section.

BUILDING THE NUMERICAL MODEL

To keep the calculation time for the splice simulation step short, some worst case effects like inclusions or bubbles within the splicing area are excluded. These effects are easy to detect in the PAS fiber picture and cause a very high loss so that any high precision evaluation is of little interest.

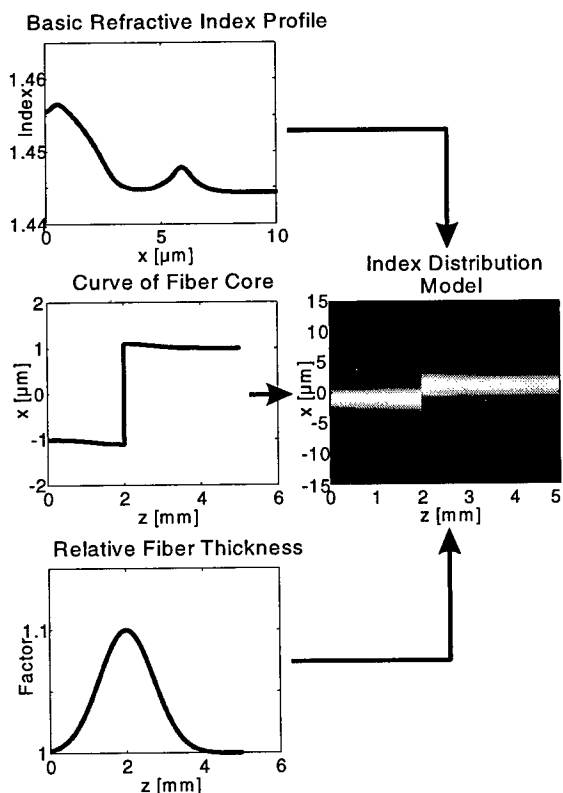


Fig. 3: Composition of Index Distribution

In normal splices the loss mechanism is exclusively caused by deformations of the fiber core. Therefore it is irrelevant to take the

cladding edge into account. The electromagnetic field has decreased to very small values at the outer boundary of the cladding. Further, the longitudinal width of the splicing area is relatively small (about 2 mm). This allows one to consider the fiber as a core surrounded by an infinitely extended cladding.

Regarding its loss, the splice is fully described by the three-dimensional distribution of its refractive index. Methods have been published to calculate the complete index distribution directly by a transverse observation of the fibers².

Because these methods require an expensive optical system, another approach is chosen. It is sufficient to obtain the fiber image by PAS. The final refractive index representation of the splice is composed of three components as illustrated in Fig. 3.

The index profile(s) of the spliced fibers are used as a starting point. Although it is not feasible to determine the complete profile from the PAS picture it is possible to recognize the different fiber families like standard, dispersion shifted (as used in Fig. 3) and so on. Within a family there is only little variation of the index profile, which does not influence the simulation significantly. That is why a typical index profile is chosen to represent the fiber family.

The next component is the curve of the fiber core. This curve is directly visible in the PAS picture and is used for an equivalent transverse shift of the basic index profile.

As the third component a compression or tension of the fiber leads to an enlargement or contraction of the core diameter. This is also directly detectable from the PAS picture. According to this information the width of the basic index profile is matched to represent a thickening or tapering in the splicing area.

After composing the numerical representation the next task is to perform the simulation of the splice by calculating the intensity distribution.

CALCULATING THE INTENSITY DISTRIBUTION

The calculation of the intensity distribution is the main part of the VLID method. It is performed by an algorithm known as the beam propagation method (BPM). Although there are full three-dimensional BPMs (3D-BPM) available³, this paper describes a two-dimensional implementation (2D-BPM), which uses less computing power and time. This makes it more convenient for research on particular aspects associated with splicing. Finally most splicing geometries can be split into one plane that

covers all the loss causing inhomogeneities, and a perpendicular plane that is nearly undisturbed. In this cases the 2D-BPM works as fine as the three-dimensional type.

The following sections describe the necessary steps.

Basic Assumptions

The fundamental formulas for the BPM are derived from Maxwell's Equations. Some restrictions are made to obtain a formula suitable for numerical computation.

Since losses of multi mode fiber splices are always very low due to the large light guiding area, this paper focuses on the evaluation of single mode fiber splices.

For an undistorted single mode fiber it is sufficient to examine the fundamental mode, the HE_{11} or LP_{01} mode. Generally this mode exists in two states of polarization. With an isotropic refraction index and a circular core both states are degenerated, which means that they have an identical phase coefficient⁴. So it is adequate to analyze one of the two polarization states, because telecommunication fibers fulfill the conditions for degeneration of both polarization states. In the following it is assumed that the direction of the electric field E_y is parallel to the y-axis, which is indicated by the subscript y. Single mode fibers have a weak guidance for the fundamental mode. That results in very small longitudinal field components compared to the transversal ones. The field is nearly transverse electromagnetic (TEM).

Reduction to a 2D-plane

This section describes how to reduce the problem from three down to two dimensions, which offers the advantages discussed above.

The given refractive index distribution can be divided into small slices along the z-direction as shown in Fig. 4. The index distribution within each slice can be considered constant in the z-direction. The electromagnetic field within this slice can be approximated by the field of a slice with an identical index distribution but an infinitely extent into z-direction. This approximation is very good, if the index variation along the z-axis is small, which is the case with splices. The special case of a core offset will be discussed in a later section.

Therefore the z-dependency of the field is considered sinusoidal with the propagation constant β . So the field is described by a two-dimensional Helmholtz equation

$$\frac{\partial^2}{\partial x^2} E_y + \frac{\partial^2}{\partial y^2} E_y + (k_0^2 n^2 - \beta^2) E_y = 0 \quad (1)$$

where k_0 is the wave number in free space, n is the refractive index.

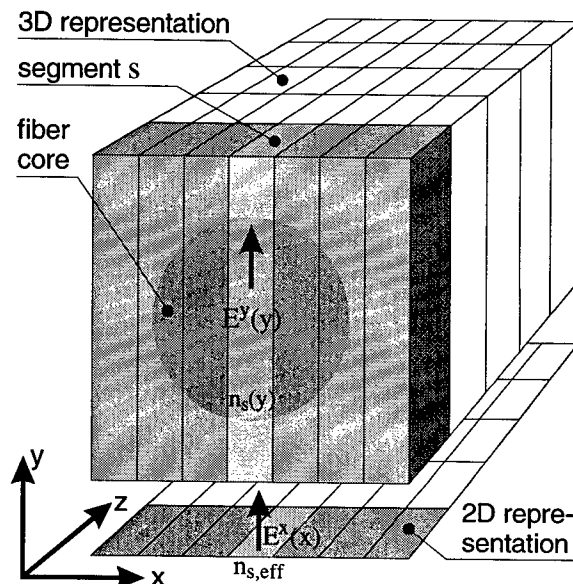


Fig. 4: Reduction from three down to two dimensions

Next the x-direction of each slice is split into segments. Again the size of each segment is so small, that the index distribution is nearly constant across x-direction. Now it is possible to separate the electric field strength E_y according to

$$E_y(x, y) = E_y^x(x) \cdot E_y^y(y) \quad (2)$$

into an x-dependent part E_y^x and a y-dependent part E_y^y . By inserting equation (2), equation (1) splits up into the two independent equations. The first one

$$\frac{\partial^2}{\partial y^2} E_y^y(y) + (k_0^2 n_s^2(y) - \beta_s^2) E_y^y(y) = 0 \quad (3)$$

describes the field in a segment s with its index n_s and the z-propagation constant β_s . The second one

$$\frac{\partial^2}{\partial x^2} E_y^x(x) + (k_0^2 n_{s,eff}^2 - \beta^2) E_y^x(x) = 0. \quad (4)$$

describes the field over all segments, but is only two-dimensional.

The information of the third dimension is contained in the effective index

$$n_{s,eff} = \frac{\beta_s}{k_0}. \quad (5)$$

of each segment s . The β_s is obtained by solving equation (3). After that only a two-dimensional problem described by equation (4) remains. Because of the use of an effective Index this method is known as Effective Index Method EIM⁵.

The next section shows how to obtain the effective indices by solving equation (3).

Calculation of the Effective Index

Instead of finding a solution to equation (3) it is equivalent to find a solution for

$$\frac{\partial^2}{\partial y^2} H_x^y(y) + (k_0^2 n_s^2(y) - \beta_s^2) H_x^y(y) = 0, \quad (6)$$

because electric field E_y^y and magnetic field H_x^y are convertible into each other.

The segment s for which the effective index should be calculated is again divided along the y -direction. The subsegments t of thickness d_t now have a constant refractive index in all spatial directions. A solution to equation (6) in such a subsegment t is given by

$$H_x^{y,t} = H_{x,0}^{y,t} e^{-jk_{y,t}y} e^{-jk_{z,t}z}. \quad (7)$$

The field strength of one subsegment's surface t is connected to the field strength of its opposite surface $t+1$ by

$$\begin{bmatrix} H_x^{t+1+} \\ H_x^{t+1-} \end{bmatrix} = \underbrace{\frac{1}{2n_t^2 k_{y,t+1}} \begin{bmatrix} m_{11} & m_{12} \\ m_{21} & m_{22} \end{bmatrix}}_{M_t} \begin{bmatrix} H_x^{t+} \\ H_x^{t-} \end{bmatrix} \quad (8)$$

with the transfer matrix M_t and its coefficients

$$\begin{aligned} m_{11} &= (n_t^2 k_{y,t+1} + n_{t+1}^2 k_{y,t}) e^{jk_{y,t+1}d_{t+1}} \\ m_{12} &= (n_t^2 k_{y,t+1} - n_{t+1}^2 k_{y,t}) e^{j(k_{y,t+1}d_{t+1} - k_{y,t}d_t)} \\ m_{21} &= (n_t^2 k_{y,t+1} - n_{t+1}^2 k_{y,t}) \\ m_{22} &= (n_t^2 k_{y,t+1} + n_{t+1}^2 k_{y,t}) e^{-jk_{y,t}d_t} \end{aligned} \quad (9)$$

All subsegments – especially the first $t=1$ and the last $t=m$ – are coupled via successive use of equation (8). That finally forms the equation

$$\begin{bmatrix} H_x^{m+} \\ H_x^{m-} \end{bmatrix} = M_m \cdot M_{m-1} \cdot \dots \cdot M_1 \cdot \begin{bmatrix} 1 \\ 0 \end{bmatrix} \quad (10)$$

with H_x^{1+} standardized to 1. Under the condition that an entering wave on the outer segments has to vanish, H_x^{m+} has to be zero like H_x^{1-} . The propagation constants $k_{y,t}$ in equation (10) are

now numerically varied to fulfill this. Then $n_{s,eff}$ is calculated by inserting

$$\beta_s = n_t^2 k_0^2 - k_{y,t}^2 \quad (11)$$

into equation (5).

Calculating the Propagation of the Field

The final step is now to calculate the propagation of the electromagnetic field into z -direction. This time we do not consider the field to be sinusoidal in z -direction and take the more general approach

$$\frac{\partial^2}{\partial x^2} E_y(x, z) + \frac{\partial^2}{\partial z^2} E_y(x, z) + k_0^2 n_{eff}^2 E_y(x, z) = 0 \quad (12)$$

to describe the field.

As mentioned earlier, the refractive index's dependency on the z -coordinate is very small. Therefore it is possible to divide the field into a fast oscillating term only depending on z and a slow one depending on x - and z -direction

$$E_y(x, z) = \tilde{E}_y(x, z) e^{-jn_0 k_0 z}. \quad (13)$$

n_0 is a reference refractive index and should be chosen as the fiber cladding index. For relatively small angles between z -axis and propagation direction, which is true for normal splices, equation (12) simplifies to

$$j2n_0 k_0 \frac{\partial}{\partial z} \tilde{E}_y = k_0^2 (n_{eff}^2 - n_0^2) \tilde{E}_y + \frac{\partial^2}{\partial x^2} \tilde{E}_y. \quad (14)$$

This equation is now discretized on a grid as shown in Fig. 5.

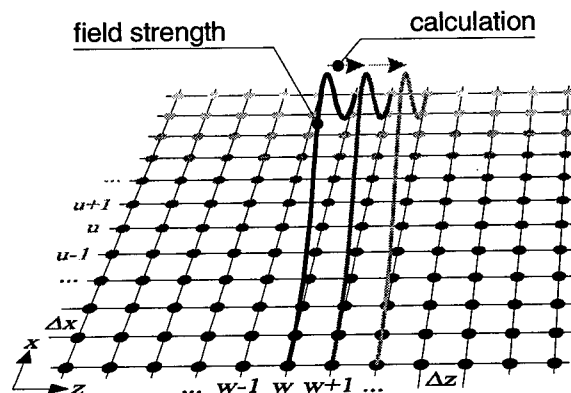


Fig. 5: Discretization grid for the BPM

On this grid the electromagnetic wave advances from left to right in positive z -direction.

The discretization leads to a linear system of equations

$$\tilde{E}_{u+1}^{w+1} + \alpha_u^+ \tilde{E}_u^{w+1} + \tilde{E}_{u-1}^{w+1} = -\tilde{E}_{u+1}^w - \alpha_u^- \tilde{E}_u^w - \tilde{E}_{u-1}^w \quad (15)$$

with the coefficients

$$\begin{aligned}\alpha_u^+ &= -2 - j4n_0k_0 \frac{\Delta x^2}{\Delta z} + k_0^2 \Delta x^2 \left((n_u^{w+1})^2 - n_0^2 \right) \\ \alpha_u^- &= -2 + j4n_0k_0 \frac{\Delta x^2}{\Delta z} + k_0^2 \Delta x^2 \left((n_u^w)^2 - n_0^2 \right)\end{aligned}\quad (16)$$

The indices w and u indicate the field strength or the index at position $w \cdot \Delta z$ or respectively at $u \cdot \Delta x$. This linear system of equations can be numerically solved on a computer. It allows to calculate the field strength \tilde{E}^{w+1} at grid column $w+1$ from the field strength \tilde{E}^w at the preceding column w .

This offers the possibility to compute the electric field distribution in consecutive steps. Only for the first step a start distribution is necessary. A method to obtain such a start distribution is explained in the next section.

In a previous section the case of a core offset was mentioned, where there is a refractive index step into z -direction. At first sight this violates the demand for slowly changing index into z -direction. The following explanation shows that that is not the case. If the BPM is stopped just before the offset, it delivers a resulting field distribution not interfered by the index discontinuity. That field is used to start a new BPM just behind the offset, also not influenced by the index step. This explanation only fails if there are consecutive discontinuities within a small distance. But this is not the case with splices, because only a single offset can occur at the transition from one fiber to the other.

Obtaining a Start Field Distribution

Although there are different ways of calculation, the easiest one is to use the fact that a single mode fiber is only capable to guide one single mode. So if an arbitrary starting field distribution travels through the fiber all unguided modes will be radiated out of the fiber.

This is computed by the use of the BPM mentioned in the previous section. After a sufficiently long distance only the guided fundamental mode remains in the fiber. This field distribution is ideal as a starting field distribution.

Calculating the Loss

The final thing to do is the calculation of the splice loss from the computed field strength distribution. The loss is the difference between the power that is sent into the fiber and the power that is still inside the fiber after the light has passed the splice. So the loss is calculated from the summed intensity of the first slice 1 divided by the summed intensity of the last slice n according to

$$L_{dB} = 10 \log_{10} \frac{\sum_u \tilde{E}_u^1 \cdot \tilde{E}_u^{1*}}{\sum_u \tilde{E}_u^n \cdot \tilde{E}_u^{n*}} \quad (17)$$

This calculation only delivers accurate results, if the complete power in the last slice is completely guided by the fiber. If there are still nonpropagating modes in it, the loss estimation will be too low. To prevent this the propagation distance must be long enough.

CALCULATION EXAMPLES

Fiber Splice with Simple Offset

First a splice with a simple offset of $1.63 \mu\text{m}$ is examined as shown in Fig. 6. The splice was made from eccentric fibers, which allow one to create a pure core offset without a cladding offset by an appropriate rotation of the fibers. Because of the aligned cladding and the use of a high precision fiber cleaver the asymmetrical glass flow is reduced to a minimum. So the only significant mechanism influencing the transmitted light is the core offset.

Fig. 6a shows the image of the offset obtained by a PAS. From this picture a numerical model was built and the intensity of the light travelling through the splice was computed by the BPM as described in the previous section. The simulation result is illustrated in Fig. 6b. The intensity along the z -axis is displayed. White indicates a high intensity, black shows no intensity. The offset is located 0.5 mm after propagation start.

The form of the path of the light after passing the splice is worth an explanation. First the offset shifts the path by $1.63 \mu\text{m}$ as expected. But in addition the light seems to follow a wavy line. To verify that this is not an artifact of the numerical algorithm, this phenomenon has to be proved in reality. A measurement inside the fiber itself is too complicated. Instead the fiber was cut approx. 1.3 mm behind the offset and the emerging electromagnetic field was examined. The field was scanned by another fiber at different x -offsets and different z -distances. The results are illustrated in Fig. 6c and Fig. 6d. To enhance visibility only the peak of the field distribution is shown and the natural decrease into z -direction is compensated.

If there is an offset inside the fiber, the emerging field shows the same wavy character (Fig. 6c) as simulated inside the fiber. If the scanned fiber contains no offset the field comes out straight (Fig. 6d).

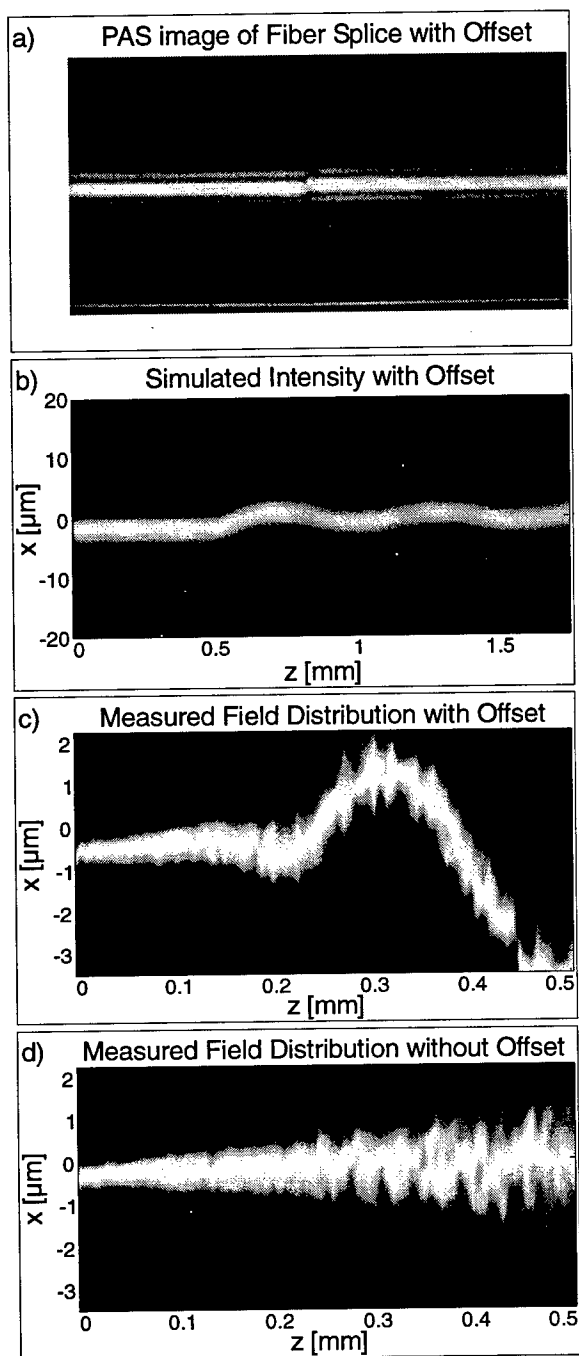


Fig. 6: Examination of Fiber Core Offset

The reason why the path of the light inside the fiber seems to be wavy is an interference of the fundamental and the second mode of the fiber. The second mode is stimulated by the offset and then propagates along with the fundamental mode. Due to the different propagation constants of the modes they show this wavy interference. In the second example the second mode is removed and it can be seen that the fundamental is travelling on a straight path.

The stimulation of the second mode by an offset is of interest for fiber joints lying within a small distance of a few centimeters. Our new technique offers a new approach to optimize such scenarios.

In normal fiber cables the cut off wavelength is smaller than for a single fiber. Therefore the second mode only propagates a few centimeters. This must be taken into account when calculating the splice loss from the simulation data as we see in the next example.

Real Splice

In this example a real existing splice is examined. The loss of the splice is 0.15 dB measured by an OTDR.

As described in the previous sections, the core geometry is evaluated by transversal optical inspection first. The core detail of the two PAS images are shown in Fig. 7a.

From these images the plane with the largest distortions of the core geometry was detected. The curve of the core in this plane is illustrated in Fig. 7b. From this the index distribution of the splice was composed and the splice was simulated numerically. The resulting field strength is presented in Fig. 7c. For a better visibility of the radiated field, the square root of the absolute value of the field strength is shown. The offset of the splice is located at a z-coordinate of 0.5 mm. The light enters the splice under an angle consistent with Fig. 7b. Behind the splice the light begins to radiate out of the fiber core and leaves the computation window. This vanishing of intensity causes the loss.

The guided light shows the same wavy path as in the first example. After 6 mm from the start of propagation the second mode is numerically removed and the guided fundamental mode remains.

The loss due to radiated intensity during the propagation is illustrated in Fig. 7d. Behind the splice it takes a small distance until the radiated intensity reaches the boundary of the computing window. From then the loss continuously rises until a maximum is reached after a propagated distance of about 7 mm. The dashed line shows the curve of the loss including the intensity guided by the second mode. The solid line shows the loss with the second mode removed. The loss value calculated by the new technique is 0.12 dB. If it is considered that there is no free parameter in this method for "empirical adjustment", the achieved accuracy of 0.03 dB is amazing.

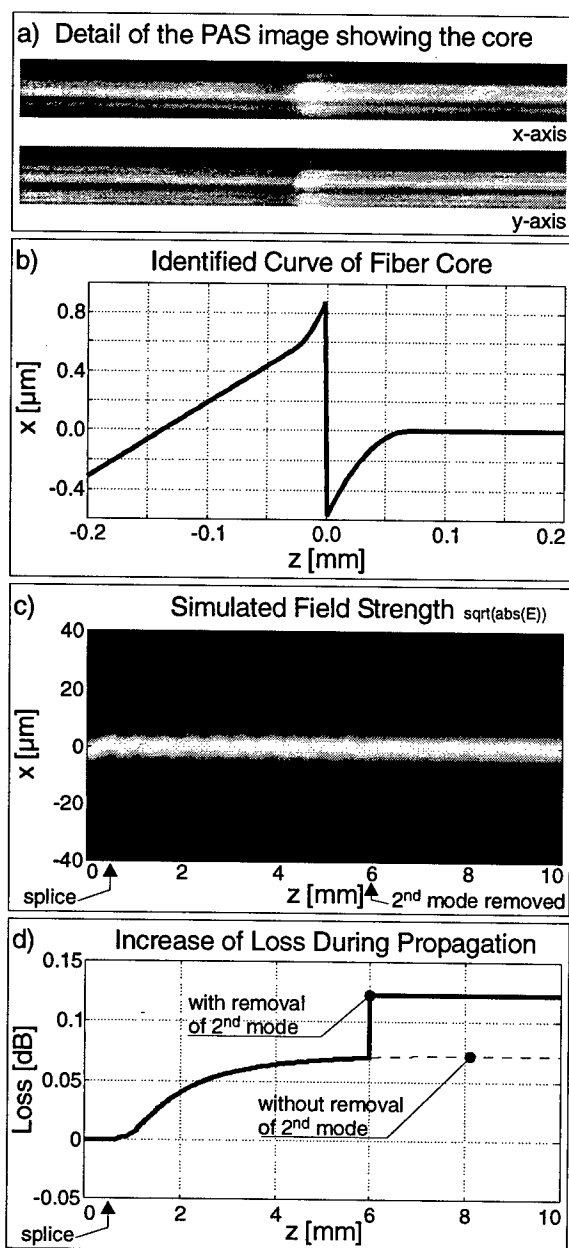


Fig. 7: Evaluation of a Real Splice

CONCLUSIONS

This paper has introduced a new technique for splice loss evaluation. The examples show, that the loss of real existing splices can be determined in an accurate way. The incorporation into commercially available splicing machines is a focus of our current research. An important point is that no additional or different hardware is needed to perform the new method. All common PAS fusion splicers will be able to benefit from this new technique by a simple software extension.

On the other hand this new method is a very useful instrument for analysis of specific loss mechanisms and their interaction. It is already in use for research on splice process enhancements. This will help future splicing machines not only to analyze splices more accurately, but also to improve splice losses.

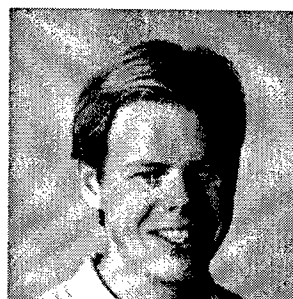
REFERENCES

- 1 "High Quality Fiber Optic Splices and Significantly Improved Splice Loss Measurement Accuracy", Bert Zamzow et al., Proceedings of the Forty-Seventh International Wire and Cable Symposium, pp. 854-863, 1998
- 2 "Principles of optical fiber measurements", D. Marcuse, Acad. Pr., 1981, ISBN 0-12-470980-X
- 3 "A Finite-Difference Vector Beam Propagation Method for Three-Dimensional Waveguide Structures", W.P. Huang et al., IEEE Photonics Technology Letters, Vol. 4, No. 2, pp. 148-151, February 1992
- 4 "Optische Nachrichtentechnik", H.-G. Unger, Hüthig, 1993, pp 144ff, ISBN 3-7785-2261-2
- 5 "All-optical switching in nonlinear integrated optic devices", G.J.M. Krijnen, Thesis Enschede, 1992, ISBN 90-9004929-0

BIOGRAPHY

**Bert
Zamzow**

Siemens AG, ICP CC E VT
Hofmannstr. 51
81359 Munich, Germany
bert.zamzow@mchk.siemens.de



Bert Zamzow graduated as an engineer of telecommunications. He received his degree as Diplom-Ingenieur from the Technische Universität Hamburg-Harburg. He joined the splicing machines

development department at Siemens in 1996. He is currently working on new splicing techniques and as a project manager on next generation fusion splicers. Further on he is responsible for managing the software development process for splicing machines.

FIBRE OPTIC SPLICE LOSS ASSESSMENT BY MEANS OF UNIDIRECTIONAL OTDR MEASUREMENT

Diego Suino (1), Francesco Montalti (2)

(1) CSELT, Torino, Italy (2) TELECOM ITALIA, Roma, Italy

ABSTRACT

The OTDR is widely used to measure the splice attenuation¹, but in order to have an accurate estimation of the splice losses it is necessary to perform the measurement from both sides of the optical line. The possibility to perform the measurement from one side only has been investigated.

Starting from statistical consideration a method to obtain an evaluation of the splices quality in an optical plant by means of unidirectional OTDR measurements has been developed.

This method was tested, with good results, by a Montecarlo simulation as well as processing a number of real data from the field.

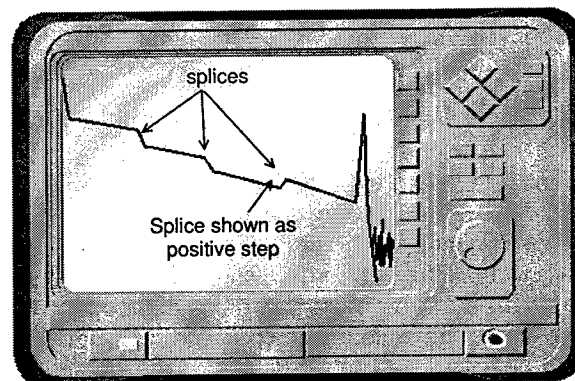
INTRODUCTION

In an optical fibre plant, the loss evaluation of the splice is performed by OTDR (Optical Time Domine Reflectometer) measurement. The principle of this method is well known: a light pulse is injected into the fibre under test and the backscattered power is collected at the receiver as a function of the time, and consequently of the space, giving an information about the attenuation distribution along the fibre.

In general, the trace shown on the instrument screen on the plane power vs. space, is a straight line with a constant slope dependent from the fibre attenuation coefficient. Points of discontinuity along the fibre, such as splices, connectors, sharp bending or other type of stresses, are shown as steps on this straight line. Usually, a down step (lower power level) accounts for a not reflecting discontinuity, as a fusion splice.

In the real situation, the level of the trace displayed on the instrument is related to the fibre

scattering coefficient, that changes lightly from a fibre to another. Consequently, the absolute level shown by the instrument could be not the same for two jointed fibres. Therefore, the value of the step between the trace of the two fibres, due only to the splice, will be altered. It is indeed frequent to see on the instrument screen splices shown as positive steps, (apparently as power gain), but of course this is not possible. This effect appears in a splice between two fibres of different scattering coefficients, when the difference in scattering levels between the second and the first fibre is greater than the splice loss. In fig.1 a typical OTDR trace of a line with fusion splices is shown.



splices between normal fibres.

Figure 1: Example of OTDR trace with splices

To overcome this problem it is necessary to perform the splice loss measurement from both the sides of the line and to average the two values. In this way the contribution due to the scattering coefficient differences of the two fibres are compensated.

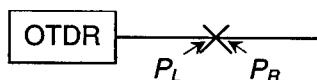
Therefore, the exact value of the splice attenuation is given by the average of the values acquired measuring the line in both directions. This operation requires a double measurement and so the cost of the plant characterisation

increases. Some methods were proposed to avoid the double measurement or to simplify the operations, as, for example, to joint in a loop the fibre of a line for performing the acquisition from only one side of the line, or to add a reflector at the end of the measured line so as to see the line as reflected in a mirror². However, each of these methods has some disadvantages, as for example the need of operating on the far end of the line.

In the present work, we propose a method based on statistical considerations to avoid the double measurement. This method has proved to be valid for splices between fibres of the same type and, at present, has been verified only on SM (G.652) fibres.

PRINCIPLES OF OTDR SPlice MEASUREMENT³

The optical power, acquired by the OTDR receiver, coming from a point on the line shortly before the splice, on the left side (P_L), and shortly after the splice, on the right side (P_R), can be written with the following formulas:



$$P_L = P_0 \cdot \alpha_{rL} \cdot S_L \cdot \frac{W}{2} \cdot e^{-2\alpha_L \cdot L_L} \quad (1)$$

$$P_R = P_0 \cdot \alpha_{rR} \cdot S_R \cdot \frac{W}{2} \cdot e^{-2\alpha_L \cdot L_L} \cdot T_{LR} \cdot T_{RL} \quad (2)$$

with:

$\alpha_{rL(R)}$ = Coefficient of the part of the fibre attenuation, on the left (right) of the splice, due to the Rayleigh scattering;

$\alpha_{L(R)}$ = Fibre attenuation coefficient on the left (right) of the splice;

$S_{L(R)} = \frac{3}{2} \cdot \left(\frac{\lambda}{2 \cdot \pi \cdot n \cdot w_{L(R)}} \right)^2$ is the portion of light backscattered into the fibre core;

λ = Light wavelength;

n = refractive index of the fibre core at the wavelength λ ;

$w_{L(R)}$ = Mode Field Radius (MFR) of the fibre on the left (right) of the splice;

W = Spatial length of the pulse;

$L_{L(R)}$ = Length of the fibre on the left (right) of the splice;

$T_{LR(RL)}$ = Splice transmission coefficient from left to right (from right to left);

Similarly, moving the OTDR instrument on the other side of the line, the formulas that describe the optical power acquired by the instrument from the point on the line shortly before the splice, on the left side (P'_L), and shortly after the splice, on the right side (P'_R), are:



$$P'_L = P_0 \cdot \alpha_{rL} \cdot S_L \cdot \frac{W}{2} \cdot e^{-2\alpha_R \cdot L_R} \cdot T_{LR} \cdot T_{RL}$$

$$P'_R = P_0 \cdot \alpha_{rR} \cdot S_R \cdot \frac{W}{2} \cdot e^{-2\alpha_R \cdot L_R} \quad (4)$$

when the instrument is on the left side of the splice (equations 1 and 2), we can write the splice loss, expressed in dB, shown by the OTDR, as:

$$\begin{aligned} A_{LR}^{OTDR} &= -\frac{1}{2} \cdot 10 \cdot \text{Log} \left(\frac{P_R}{P_L} \right) = \\ &= -5 \cdot \text{Log} \left(\frac{\alpha_{rR}}{\alpha_{rL}} \cdot \frac{S_R}{S_L} \cdot T_{LR} \cdot T_{RL} \right) = \\ &= -5 \cdot \text{Log} \left(\frac{\alpha_{rR}}{\alpha_{rL}} \right) - 5 \cdot \text{Log} \left(\frac{w_L}{w_R} \right)^2 + \\ &\quad - 5 \cdot \text{Log}(T_{LR}) - 5 \cdot \text{Log}(T_{RL}) \end{aligned} \quad (5)$$

In order to obtain this equation we have disregarded the possible differences between the refractive index of the two fibre, that are contained in the $S_{L(R)}$ factor. In the present commercial fibre, the differences on this parameter are in the range of 10^{-4} . A difference of this quantity affects the equation 5 with a few thousandths of dB.

The two last terms in the equation are simply the splice half attenuation from left towards right (A_{LR}) and from right towards left (A_{RL}). Therefore, we can write the 5 as:

$$A_{LR}^{OTDR} = -5 \cdot \text{Log} \left(\frac{\alpha r_R}{\alpha r_L} \right) - 10 \cdot \text{Log} \left(\frac{w_L}{w_R} \right) + \frac{A_{LR} + A_{RL}}{2} \quad (6)$$

Similarly the attenuation shown by the OTDR in the opposite direction is:

$$A_{RL}^{OTDR} = -5 \cdot \text{Log} \left(\frac{\alpha r_L}{\alpha r_R} \right) - 10 \cdot \text{Log} \left(\frac{w_R}{w_L} \right) + \frac{A_{LR} + A_{RL}}{2} \quad (7)$$

from this equation we can write:

$$\frac{A_{RL}^{OTDR} + A_{LR}^{OTDR}}{2} = \frac{A_{LR} + A_{RL}}{2} = A \quad (8)$$

where A is the real splice attenuation. Moreover, from the 6 and 7, we can obtain:

$$\begin{aligned} \frac{A_{RL}^{OTDR} - A_{LR}^{OTDR}}{2} &= \\ &= -5 \cdot \text{Log} \left(\frac{\alpha r_L}{\alpha r_R} \right) - 10 \cdot \text{Log} \left(\frac{w_R}{w_L} \right) \end{aligned} \quad (9)$$

In the last equation, the term containing the ratio between the attenuation coefficient due to the Rayleigh scattering, is negligible compared to the one containing the ratio of the MFR. This statement was verified comparing some real distribution of the half-difference of OTDR unidirectional measurements and the distribution of the last term of the equation 9. This distribution was obtained producing a number of MFR values with a Normal distribution, with mean value and standard deviation obtained from data measured by fibre producers on commercial product.

Fig. 2 shows the comparison of these two distributions. As the matching between the two distributions is very good, it is demonstrated that the contribution of the ratio of the Rayleigh attenuation coefficient is negligible in comparison with the contribution of the ratio of the MFR.

From this results the equation 9 can be rewritten as follows:

$$\frac{A_{RL}^{OTDR} - A_{LR}^{OTDR}}{2} = -10 \cdot \text{Log} \left(\frac{w_R}{w_L} \right) \quad (10)$$

So equations 6 and 7 become:

$$\begin{aligned} A_{LR(RL)}^{OTDR} &= -10 \cdot \text{Log} \left(\frac{w_{L(R)}}{w_{R(L)}} \right) + \frac{A_{LR} + A_{RL}}{2} = \\ &= -10 \cdot \text{Log} \left(\frac{w_{L(R)}}{w_{R(L)}} \right) + A \end{aligned} \quad (11)$$

This means that practically the error made in a unidirectional OTDR measurement of the splice attenuation is due to the differences between the MFR of the two fibres.

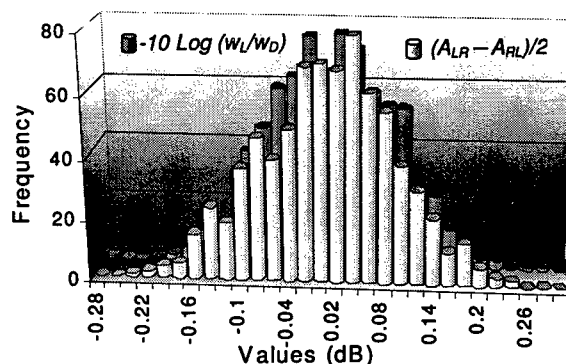


Figure 2: Comparison between the distributions of the OTDR unidirectional measurement half-differences and the MFR ratio.

This conclusion is important for this work because it allows to use for testing the proposed method a Montecarlo simulation based only on the MFR values, whose real values and distribution are known.

METHOD DESCRIPTION

The proposed method is based on the assumption that the fibres with different characteristics are arranged in the optical plant in a random way. Therefore, the effects of the fibre MFR differences on the splices can be considered equally distributed independently of the side of measurement of the line.

This hypothesis is confirmed by the experimental data. In fig 3, as an example, the histograms of the two unidirectional measurements, performed on a plant with 413 splices, are compared: the two distributions

appear to have the same shape and statistical parameters (mean value, μ , and standard deviation, σ)

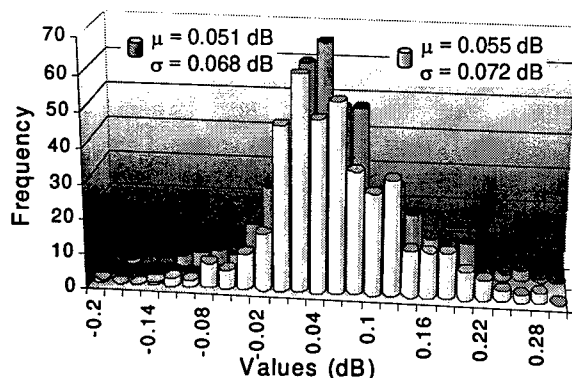


Figure 3: Distribution of OTDR unidirectional measurement on a plant with 413 splices

Unidirectional data processing

The symmetry between the measurements performed in the two directions involves, as a direct consequence, that the two unidirectional distributions have similar mean values. Consequently, as the exact splice attenuation value is given by the average of the unidirectional values (two-directional values), the mean value of the distribution of the real splice attenuation values will be similar to the mean values of the two unidirectional distribution.

Moreover, from a statistical point of view, we can suppose that, if the underestimated values of a unidirectional distribution are compensated, somehow, with the overestimated ones of the same distribution, we obtain a distribution comparable with the one of two-directional splice attenuation values. If this is true, from this distribution it will be possible to obtain an estimate of the standard deviation of the real values.

In order to verify this hypothesis several tests were performed, processing data coming from the characterisation measurement of single mode optical plants. The procedure described below was used.

In fig. 4, as an example, is shown the comparison between a distribution of two-directional splice attenuation values with one obtained processing a unidirectional distribution. The two distributions appear in good agreement.

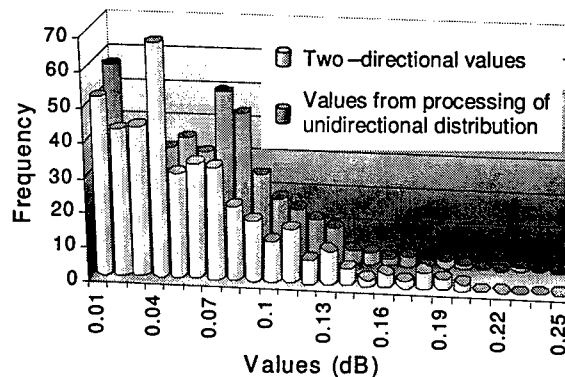


Figure 4: Comparison between the two-directional distribution and the unidirectional processed one

Proposed processing method

Starting from the above considerations, it is possible to develop a procedure based on unidirectional OTDR measurements to evaluate the splices of a single mode fibre plant.

Before defining the method it is important to define when it is applicable. As the method is based on statistical considerations and the information arising from its are of statistical type, it is of the outmost importance the statistical meaning of the tested sample. Therefore, it is better to limit the application of the method to plants with not less than 100 splices (however, from the test it appears that this procedure works well also with smaller number).

The splice attenuation must be measured by means of unidirectional OTDR measurement during the splicing of the fibres. As in the last generation single mode fibres the MFR difference can contribute to the measured value for a maximum of about 0.2 dB (see Fig. 2), when the splice loss values are 0.2 dB greater than the maximum value accepted for a splice, the splice has to be redone for a maximum of three times.

If the great attenuation value is due to bad splice execution procedure, it should reduce. On the contrary, if the loss measured remains high it should be due to the MFR difference between the fibre and so not real.

When the plant is finished, the mean value (μ) of the unidirectional values of all splices will be calculated. As discussed before, with good approximation this will be coincident with the mean value of the real attenuation value (that is

ones that would be obtained by the two-directional measurement).

In order to evaluate the standard deviation, it is necessary to process the data according the following procedure:

1. To count the number N of the negative values.
2. To extract from the measurements N data having the worse values (with N equal to the one obtained at the point 1).
3. To calculate the average between each negative value and one that will be randomly extracted from the ones identified at the previous item.
4. To substitute both negative and positive values, used at item 3, with their average (so this datum will be inserted twice).
5. To repeat the item 3 and 4 for all N negative values.

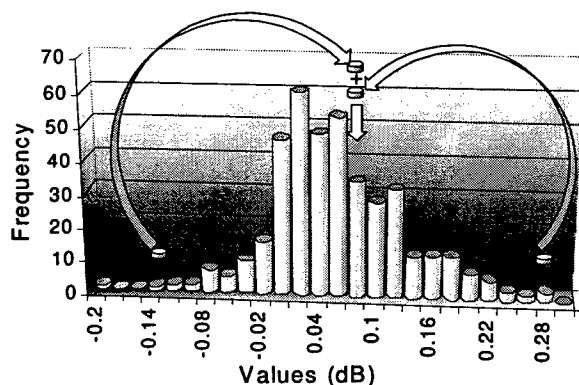


Figure 5: Graphical representation of the procedure used to obtain the distribution to estimate the standard deviation

In fig. 5 this procedure is graphically shown. The standard deviation (σ) of the distribution obtained with this procedure gives with good approximation an estimate of the one of the values that would be obtained by the two-directional measurement.

If both μ and σ are lower than the acceptance limit the plant splices will be considered in accordance with the requirements. Instead, if one of them or both are greater than the limit it will be necessary to perform the OTDR measurement also in the opposite direction. With the second series of data it will be possible to calculate the real splice loss values by means the two-directional estimate, and so to find and to do again the splice having high attenuation.

METHOD EVALUATION

The presented procedure was tested by comparing the mean values and the standard deviations of two-directional measured values distribution, relevant to 22 Telecom Italia optical plants (a sample of 4500 data), with the ones obtained from the relative unidirectional distributions by means this procedure.

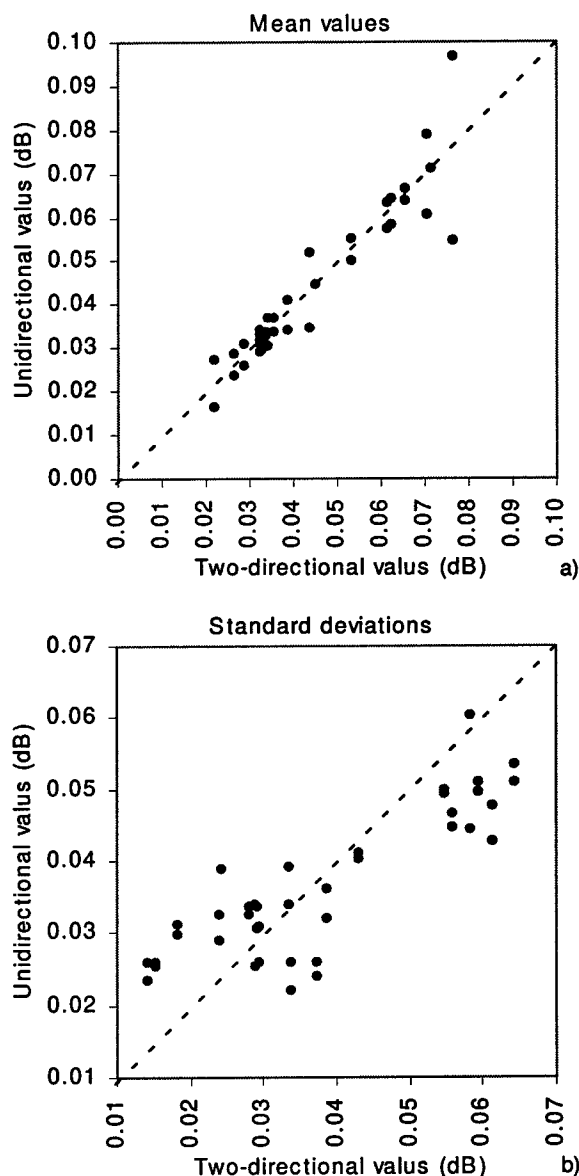


Figure 6: Mean values (a) and standard deviations (b) obtained by two-directional measurements compared with ones estimated from unidirectional data.

In Figure 6 the results of this comparison is shown. The sample was composed both of single fibre splices and multiple fibre splices (4

fibre ribbon). Each plant contains a number of splices in the range from 32 to 780. From this data it results that the differences between the statistical parameters (μ and σ) of the two-directional measurement and ones estimated from the unidirectional distributions are within 0.01 dB.

The proposed procedure was also tested by means a Montecarlo simulation. The scope was to evaluate what is the error rate analysing the splices of a plant using only unidirectional measurement in respect to using the two-directional data.

The simulator creates samples of data with a random number of elements from 80 to 800. Each element is a couple of values representing the two unidirectional measurements of a splice loss. These two values are written as:

$$A(dB) = -10 \cdot \text{Log} \left\{ \left(\frac{2 \cdot w_R^2 \cdot w_L^2}{w_R^2 + w_L^2} \right)^2 \cdot e^{-\frac{2 \cdot x^2}{w_L^2 + w_R^2}} \right\} + \pm 10 \cdot \text{Log} \left(\frac{w_R}{w_L} \right) \quad (12)$$

where x (randomly generated from a Normal distribution) is the lateral offset between the two fibres. The parameters of this normal distribution are chosen in a way to have the desired loss distribution. The values of the MFD (w) are generated from a normal distribution too, but in this case, the mean value and the standard deviation are taken from real data from fibre production.

The reliability of this random generator was tested comparing the splice loss distribution obtained by its with the real ones.

Two groups of samples were created: the first one with splice attenuation distributions like the ones for the real value measured in field (Telecom Italia plants both with single fibres and ribbon fibres). The second group was created with characteristics near to the acceptance limit according the Telecom Italia specification. In table 1 the typical μ and σ values for the two groups are given.

Table 1: μ and σ values typically measured in field data and ones representing the limit requirements in the Telecom Italia specification

	Typical values (dB)		Limit values (dB)	
	μ	σ	μ	σ
Single splice	0,03	0,02	0,06	0,04
Multiple splice	0,06	0,05	0,10	0,08

From the couple of values the two-directional values were calculated. Then the splices of the plant were valued on the base both of the two-directional and unidirectional values.

As a result in the case of distribution with characteristics similar to the real measurement the agreements between the judgements were of the 100%. In the case of distribution near the acceptance limits, the agreement was of 80%.

CONCLUSIONS

The necessity to perform the splice loss measurement of an optical plant acquiring the OTDR trace in two directions makes expensive and often not easy the plant characterisation procedure.

In this work the possibility of characterizing the splice by means of unidirectional OTDR measurement was investigated. The proposed method is based on a statistical approach valid for optical plant with single mode fibre and enough number of splices. The method uses as judgement elements the mean value and the standard deviation obtained from the unidirectional measurements

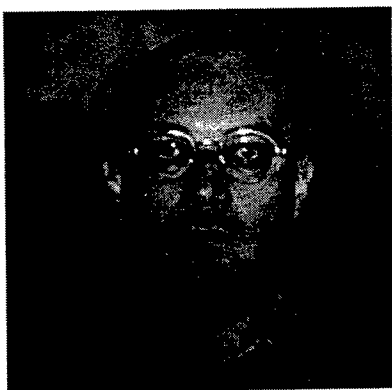
The method was tested with good results on a great number of data from the Telecom Italia plants both with single splices and multiple splices.

This method allows an estimate of the splice quality in an optical line using the data obtained from the OTDR measurements performed during the carrying out of them or however measuring the line from only one side.

REFERENCES

- [1] WG4 of SC86B IEC, "61300 — Part 3-4: Examination and measurements — Attenuation", August 1998
- [2] W. Stöcklein, "New OTDR Measurement Techniques" In Proceedings of EFOC91, pp. 139-142, 19-21 June 1991, London.
- [3] Calvin M. Miller et al., "Optical fiber splices and connectors", Optical Engineering Vol. 10, Marcel Dekker Inc., New York, 1986

AUTHORS



Diego Suino was born in Turin, Italy, in 1962. He received his doctorate in Physics from the University of Turin. In 1989 he joined CSELT where works in the Physical Carrier Qualification group engaging at the study and development of measurement techniques on optical fibre and passive optical components. His activity includes also passive component specification and characterisation. Moreover he is the Secretary of the Italian National SubCommittee 86B and his present responsibilities include IEC SC86B activities.

CLEAVABILITY OF TITANIA-CLAD OPTICAL FIBERS

Jesse C. Meyer

Corning Incorporated, Wilmington, North Carolina

ABSTRACT

A study designed to identify the material properties, mechanisms, and manufacturing process steps controlling the cleavability of titania-clad fiber is presented. In particular, a focus is placed upon the evaluation of hypotheses regarding titania thickness, titania concentration, and morphologies of cleaver-initiated flaws. While primarily empirical in nature, residual stress modeling is employed when appropriate, and optical/SEM imaging is called upon in an effort to tie experimental data to mechanistic theories. Data indicate that cleavability is a unique function of neither titania concentration nor thickness, but rather a consistent function of the combination of the two. As such, cleavability correlates weakly with maximum values of compressive residual stress, and controlling mechanisms appear to be more closely tied to routine flaw size decreases. The net result of the study is an improved understanding of the titania-clad fiber cleaving process.

INTRODUCTION

Optical fiber with a thin layer of titania (TiO_2) doped silica on the cladding surface shows superior fatigue and abrasion resistance compared to standard silica clad fiber.¹ Since the advent of this fiber with its intrinsic compressive residual stress in 1989, cleavability* has become a heightened topic of discussion and research. While questions regarding critical parameters, properties, and mechanisms have lingered, it has become fairly well recognized that titania-clad fiber can require different cleaving conditions than silica fiber.

* Within the context of this paper, cleavability is defined as a fiber's capacity to be fractured in such a manner as to produce a flat, mirrored fiber end.

Some cleaver manufacturers have even gone so far as to include multiple settings to accommodate customers who may need to cleave both standard silica and titania-clad fiber.

Internal studies performed over the past ten years have provided much insight into the levers controlling titania-clad cleavability, but have often revealed contradictions concerning the variable most critical to the process. As a result, the precise behavior underlying the controlled fracture of the fiber has not been completely quantified. Moreover, the design of cleavability studies hasn't always accounted for the *qualitative* events commonly of importance to a field user. Recent Corning experimentation has indicated that frequencies of qualitative imperfections can easily differentiate candidates when standard cleave angle results fail to do so.

Hence, the primary goal of this study is to better understand the material properties, mechanisms, and manufacturing steps which govern titania-clad fiber cleavability. Both cleave angle results *and* qualitative defect frequencies are emphasized, with particular attention paid to those areas projected to be of greatest importance to a field user. Efforts focus on the effects of the following three variables, deemed the most plausible (and certainly most quantifiable) of those potentially controlling titania-clad cleavability:

- 1) Titania Thickness
- 2) Titania Concentration
- 3) Morphologies of Cleaver-Induced Flaws

In the cases of titania thickness and concentration, large bodies of empirical data – including thousands of cleaves performed on multiple cleaver types – are examined to help resolve various hypotheses. Residual stress modeling is employed to shed stronger light on titania concentration results, while optical and

scanning-electron microscope images are used to tie experimental data to classical fracture theories regarding titania thickness and flaw morphology. An analysis of cleaver blade wear is also conducted in an attempt to identify possible sources of varying flaw morphologies.

The paper is arranged as follows. The initial section, *Overview of Testing Procedures*, describes the cleaving procedure, and the various types of cleaver tools employed in testing. The following section, *Measures of Cleavability*, establishes the various dimensions used to determine the cleavability of a test fiber. Subsequent sections entitled *Titania Thickness*, *Titania Concentration*, *Thickness/Concentration Combination*, and *Morphologies of Cleaver-Induced Flaws* detail the extent to which results correlate with each variable.

OVERVIEW OF TESTING PROCEDURES

Within the practical ranges of interest, titania-clad fibers of varying TiO_2 thickness, TiO_2 concentration, and manufacturing conditions were cleaved. In specific cases, standard silica fiber was also cleaved to generate comparative results in the absence of TiO_2 . Each titania-clad candidate was cleaved on a minimum of three different cleaver models. A test for a candidate consisted of ~ 2000 cleaves per cleaver type. Only single fiber cleaving was performed – ribbon cleaving was not undertaken.

All cleaver models used in testing fractured the fiber through the same basic routine:

- 1) Stripped fiber was aligned in v-grooves, clamped in place by elastomeric pads, and scored by a circular, metallic blade moving perpendicular to the fiber axis.
- 2) The fiber was then completely fractured by lowering an "anvil", which propagated the score through a small scale four-point bend test.

New cleaver blade positions were employed with the testing of each candidate. Moreover, after every 20 cleaves, the blade and surrounding components were cleaned with isopropyl alcohol and cotton swabs to minimize the effect of contamination on results. Fiber strippers were rinsed in isopropyl alcohol prior to each strip, as was bare fiber at each strip's conclusion.

Lastly, to ensure measurements taken on the optical interferometer (discussed in the following section) were not obstructed by residue, fully cleaved fibers were rinsed in isopropyl alcohol, and cleaved ends were touched to double-sided tape before a reading was taken. Critical components on the interferometer were also cleaned with every 20 cleaves (isopropyl alcohol and cotton swabs).

MEASURES OF CLEAVABILITY

Within the study, three measures were used to determine the cleavability of a given fiber:

- 1) *End angle measurements* of cleaved fiber ends
- 2) *Qualitative observations* of cleaved fiber ends
- 3) *Required blade height* for generation of "acceptable" cleaves

End angle measurements of cleaved fibers were gathered via an optical interferometer. When analyzed through its use (fiber is viewed in the "end-on" position), a cleaved surface displays a series of optical fringes which are directly proportional to its end angle. With knowledge of the diameter of the bare fiber, and the wavelength of light used by the interferometer, the number of optical fringes can easily be translated into fiber end angle (angle = # of fringes / 6 in current study). An ideal cleave generates a fiber end which is perfectly perpendicular to the axis of the fiber, and is assigned a 0° end angle. Non-ideal cleaves are assigned end angles greater than 0° , and are measured in reference to the 0° ideal (Fig. 1).

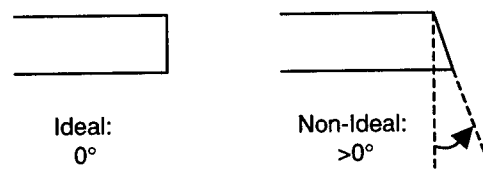


Figure 1: Ideal Vs. Non-Ideal Cleave End

Qualitative observations of cleaved fiber ends were also recorded through the optical interferometer. When a fractured surface is chipped or possesses rough areas (referred to as mist or hackle²), an optical interferometer will reveal abnormally dark regions across the

Table 1: Cleaver #1 End Angle Results

Candidate (N~2200 cleaves for each candidate)	< 1°	1-2°	> 2°
High TiO ₂ Thickness, Low TiO ₂ Concentration	55.5%	40.6%	3.9%
Med TiO ₂ Thickness, High TiO ₂ Concentration	59.6%	38.9%	1.4%
Low TiO ₂ Thickness, Med TiO ₂ Concentration	65.3%	31.8%	2.9%

cleave end. Whereas an ideal cleave will generate a mirrored surface, cleaves possessing chips, ridges, mist, or hackle will display regions less capable of reflection, and hence remain dark, or even black. In extreme cases, the entire face of the cleave end will remain black – these cleaves are referred to as “unreadable” in the study to follow. Moreover, cleave ends possessing ridges or high levels of residual stress will exhibit jagged or severely curved optical fringes. Each of these features can be a detriment in a subsequent splicing process, and were recorded throughout the study presented.

Finally, the *required blade height* for generation of “acceptable” cleaves – a field very closely tied to the qualitative observations discussed above – is also a strong measure of the cleavability of a fiber. In the current study, tests were most commonly started at the minimum blade height which would cleave standard silica fiber (note that this height was never the lowest setting for a cleaver, and it did not always cleave silica fiber “acceptably”). If necessary, blade heights were subsequently increased in increments of ~ 0.02 mm until an “acceptable” height was found. The criteria for an “acceptable” height was based upon the number of unreadable cleaves observed within a block of 100. This standard was chosen with the idea that unreadable cleaves are the ones most likely to be failed by a field user (either through high estimated splice losses, or unacceptably high end angles). Note that deteriorating qualitative results often mandated blade height increases in the latter portions of testing as well.

TITANIA THICKNESS

Results gathered through cleaver model #1 proved to correlate quite closely with the thickness of a given titania layer. As is shown in Table 1, cleave angle results clearly improved

Table 2: Cleaver #1 Qualitative Comment Frequencies/Blade Height Results

Candidate (N~2200 cleaves for each candidate)	Cleaves Requiring Qualitative Comments	Required Blade Height Increases
High TiO ₂ Thickness, Low TiO ₂ Concentration	13.51%	2
Med TiO ₂ Thickness, High TiO ₂ Concentration	18.34%	2
Low TiO ₂ Thickness, Med TiO ₂ Concentration	4.45%	1

with decreasing titania layer thickness. It is worthwhile to note that the candidate possessing the greatest TiO₂ thickness produced statistically significant[†] larger cleave angles than the other two candidates. Although Table 2 shows that qualitative defect frequencies exhibited a slightly weaker correlation to titania thickness, the results nonetheless indicate that thicker layer candidates will not achieve the performance of fibers with relatively small values of TiO₂ thickness. Correlations to titania concentration were not observed anywhere in the results of cleaver model #1.

Subsequent discussions regarding the data of cleaver model #1 focused upon the possible mechanisms which might cause TiO₂ thickness to be the critical variable to titania-clad cleavability. Thoughts centered upon the mode I stress intensity factor, K_I , which controls the “fast fracture” of the cleaving process (i.e., fracture takes place when K_I reaches a critical value, K_{IC}). Previous work has established that, for semielliptical surface cracks oriented perpendicular to the surface of a semi-infinite medium, K_I will most often vary in magnitude along the boundary of the flaw. More specifically, given a crack depth a , and a crack half-length surface trace of c , such a flaw would only possess a constant K_I along its boundary when $a/c = 0.8$. In cases where $a/c > 0.8$, K_I would be a maximum at the surface of the specimen, and when $a/c < 0.8$, K_I would be a maximum at the deepest point on the flaw.³ In either case, the point of maximum K_I specifies the origin of final failure (see Figure 2).

Given these ideas, the following hypothesis was proposed. If the origin of failure in the cleaving

[†] A 95% confidence level within independent t-Tests was used to establish statistical significance.

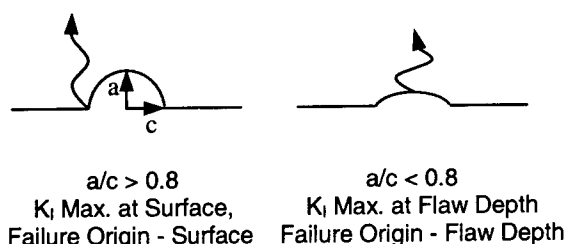


Figure 2: Semielliptical Crack Oriented Perpendicular to Surface of Semi-Infinite Medium - Location of Maximum K_I With Varying Flaw Aspect Ratio

of titania-clad fiber were in fact the surface of the fiber (a reasonable scenario if one considers that the TiO_2 layer's compressive residual stress might work to "pinch in" the surface trace of initial flaws), a failure crack would have to travel through the entirety of the titania layer before fracturing the fiber. Any such crack would have to overcome a compressive residual stress at its tip until it traveled completely through the titania doped region. If this were the case, it would be likely that the distance over which this compressive residual stress were "seen" by the crack (i.e., thickness of the titania layer) would be the critical variable to the process.

Hence, an attempt was made to verify the origin of fracture in the titania-clad fibers cleaved on model #1. Fully fractured surfaces were analyzed through a scanning-electron microscope, with the hope of identifying lines of crack arrest in areas where cleaver flaws meet the fiber surface. In the case at hand, lines of crack arrest are those denoting the end of subcritical crack growth slightly out of plane with the rest of the fracture surface. Evidence of lateral-type cracking in the vicinity of flaw/fiber surface intersections was also sought.

Figure 3 displays the region surrounding the initial flaw of a titania-clad fiber scored with cleaver model #1, and subsequently fractured. The fiber in the image has been slightly tilted in an attempt to accentuate the visibility of any "out of plane" behavior. As can be seen, there is evidence of subcritical damage just to the left of the flaw's maximum depth (lateral type-crack or "twist hackle" extending upward into fiber), but the regions where the flaw meets the fiber surface appear undisturbed. There is no evidence of cracks which might have "popped in" at the flaw/surface intersections during scoring, nor of subcritical crack growth which may have occurred prior to final failure.

The result displayed in Figure 3 is representative of the majority of images analyzed. While the process of analyzing precise crack propagation paths on glass fracture surfaces is certainly a science unto itself, it is clear that the initial scanning-electron images provide no evidence of failure initiation in areas where cleaver flaws meet the fiber surface. Moreover, judging that the cleaver scores appear to be much greater in width than depth (i.e., $a/c < 0.8$), one would expect that the origin of final failure would most commonly be the deepest point on the flaw, rather than the surface.

As cleaving results were acquired on additional cleaver models (discussed in the following section), it became clear that cleavability was *not* going to prove itself to be a unique function of titania thickness. Investigation of hypotheses regarding only titania thickness was therefore terminated, and ideas regarding titania concentration were addressed.

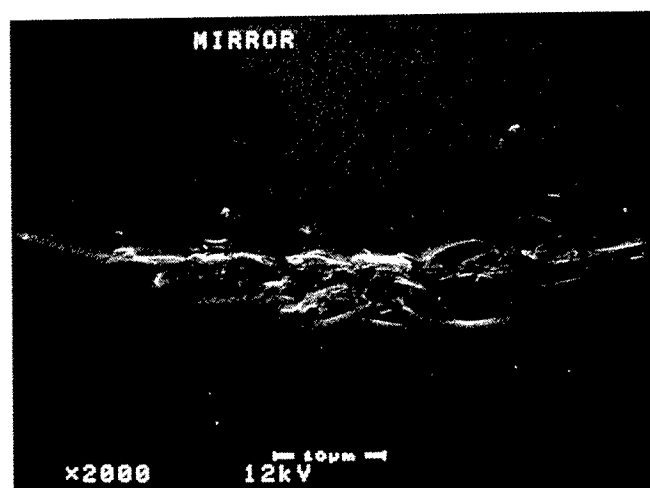


Figure 3: Titania-Clad Fracture Surface in Proximity to Flaw Imparted by Cleaver #1

TITANIA CONCENTRATION

As previously eluded to, results gained on subsequent cleaver models failed to show the same correlation to titania thickness as that seen on cleaver model #1. As one might expect, thoughts were therefore turned toward the possible significance of TiO_2 concentration to titania-clad cleavability. Rather than simply compiling the data and searching for a correlation, however; a slightly different approach was taken.

Knowing that the compressive residual stress within a titania layer is a *much* stronger function of titania concentration than thickness, results were tabulated as a function of each candidate's residual stress level. In doing so, not only were potential correlations with titania concentration uncovered, but the importance of compressive residual stress to the cleaving process was also observed.

To determine the level of compressive residual stress within each candidate, the results of a previously derived Corning model were used. Within the model, fiber equilibrium and strain compatibility are employed to develop the following relationship for the compressive residual stress within a titania layer.

$$\sigma_r = \frac{E'_s(\alpha_T - \alpha_s)\Delta T}{(E'_s/E'_T + A_T/A_s)} \quad (1)$$

Where, for the silica and titania doped layers:

α = Linear Coefficient of Thermal Expansion

E' = Effective Young's Modulus

A = Cross Sectional Area

ΔT = Temperature Drop in Fiber Cooling

Draw and quench stresses are accounted for in subsequent steps of the model's development, and were taken into consideration in the results to follow. It is worthwhile to note that, within the expression shown, the linear coefficient of thermal expansion for titania is *exclusively* a function of the titania concentration of a candidate. While the cross sectional areas are tied to the titania thickness, it is the TiO_2

concentration which ultimately dominates the overall relation.

Figure 4 displays the end angle results of cleaver models #1 and #2 as a function of the maximum (magnitude only) compressive residual stress within each candidate's titania layer. The results displayed for a value of zero compressive residual stress are those gained for standard silica fiber. Although the "within cleaver" mean end angle differences are certainly small, no particular correlation with compressive residual stress is observed.

In an effort to identify differences which might be more apparent to a field user, efforts were shifted to focus on *qualitative* results. Figure 5 displays the qualitative defect frequencies of cleaver models #1 and #3 as a function of compressive residual stress. As is shown, the results of cleaver model #3 did exhibit a trend with stress – namely, the cleaving process proved to be more difficult as stress levels increased (cleaver #3's blade height increases also showed the same trend). The results of cleaver model #1, however, did not show the same trend with stress. Given cleaver model #1's previous trends with titania thickness, this result was not unexpected.

While the qualitative comment frequencies of cleaver #3 did show a clear trend with compressive residual stress, the lingering results of cleaver #1 make it clear that expected trends may be sparsely observed, and any true correlations are likely more complicated than originally proposed.

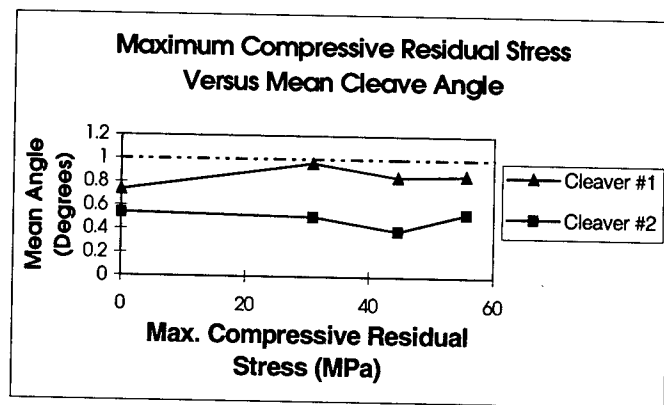


Figure 4: End Angle Results As a Function of Max Compressive Residual Stress (Each Data Point: N = Minimum of 1600 Cleaves)

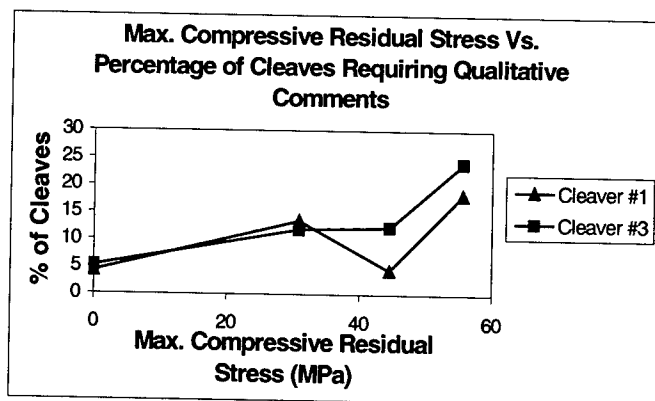


Figure 5: Qualitative Comment Frequency As a Function of Max Compressive Residual Stress (Each Data Point: N ~ 2200 Cleaves)

These findings do not, however, invalidate the thought that compressive residual stress is the primary source of mechanical benefit to titania-clad fiber. Cleaving flaws are much larger than any flaw that could pass the 100 kpsi (690 MPa) proof test level, and internal studies have revealed that cleaver scores can frequently penetrate the entirety of a given titania layer. Given that this is the case, it seems unreasonable to expect the compressive stresses of the titania layer to have a significant effect on crack tip opening displacements, or fast fracture in the cleaving process.

Nonetheless, consistent trends with titania concentration/compressive residual stress were not observed, and investigation of hypotheses regarding only titania concentration was terminated.

Manufacturing Process Impact on Titania Concentration and Cleavability

Testing was also performed on titania-clad candidates whose outermost layers of titania had been intentionally depleted of TiO_2 (to varying degrees) during manufacturing. The cleavability testing performed showed no notable differences between fibers, leading to the conclusion that manufacturing steps which might work to deplete *surface* (rather than average or bulk) TiO_2 concentration are not critical to cleavability.

General Note Regarding Cleavability Results

Within the data presented, there is evidence that the titania concentration and thickness ranges that are now considered practical (inside of which falls the formulation for Corning's SMF-28 with DuracladTM product) are capable of generating the cleavability results of standard silica fiber. In particular, the silica and titania-clad results displayed for cleaver #2 in Figure 4 were all generated at the same blade height, and no benefit (statistical or otherwise) was exhibited by standard silica.

THICKNESS/CONCENTRATION COMBINATION

Given the lack of a consistent trend with either variable, cleavability estimates for specific thicknesses and concentrations were still not feasible. In an effort to identify a reasonable

estimator, an attempt was made to correlate results with a *combination* of titania thickness and concentration. While a number of arrangements and weighting factors were considered, the product of the two variables provided the simplest, and most logical starting point.

The cleave angle results of experimentation did not prove to correlate particularly well with the product of concentration and thickness. However, as was noted in Figure 4, the differences between average candidate end angles for a given cleaver tended to be very small ($\sim 0.2^\circ$ at maximum). Moreover, with all fibers generating a mean angle less than the 1° reference typically cited by Bellcore^f, it is unlikely that a field user would have labeled any of the candidates as "difficult to cleave" based on end angle results alone.² Therefore, given the 20% differences previously observed in Figure 5, one would expect that *qualitative* comments (and associated blade height changes) would provide the key to candidate differentiation.

Figure 6 displays the product of titania concentration and thickness versus qualitative comment frequency for the data gained on cleavers #1 and #3. The data shown not only allows candidates to be easily differentiated – it also exhibits a very reasonable trend with the proposed measure of cleavability. A deterioration in cleavability is evident with

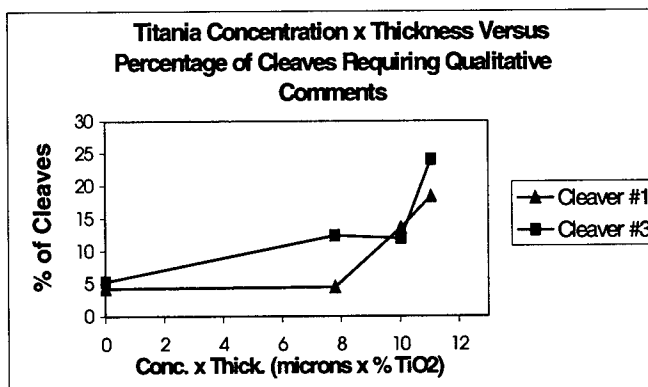


Figure 6: Qualitative Comment Frequency As a Function of Titania Concentration x Thickness (Each Data Point: N ~ 2200 Cleaves)

^f Candidates did not necessarily achieve Bellcore's "High Precision Perpendicular Cleaver" requirement of $90\% \leq 1^\circ$.

increasing values of concentration times thickness. Note that the "dip" seen in moving from a product of 8 to 10 on cleaver #3 is less than a 0.5% difference. Although not shown, the blade height increases for each cleaver exhibited the same trends.

Lastly, it is important to note that the qualitative frequencies gained on the two cleavers agreed to within 2% for two of the fiber candidates, and to within 6% for three. Figure 6, therefore, not only indicates that cleavability trends with the product of concentration and thickness, but also that the product is a useful *estimator* of cleavability.

MORPHOLOGIES OF CLEAVER-INDUCED FLAWS

While a reasonable estimator of titania-clad cleavability had been found, a mechanistic answer detailing why TiO_2 doped fiber has historically required different cleaving conditions than silica fiber had not. The results of the study made it clear that both thickness and concentration can work together to generate cleaving difficulties, but the underlying mechanism was, as of yet, undiscovered.

Given that the most obvious potential source – compressive residual stress – had proven to correlate inconsistently with cleavability, thoughts turned toward the morphology of the flaws imparted by the cleaver blade. Having observed that poor cleavability candidates also

tended to require relatively large blade height increases, it was proposed that both titania concentration *and* thickness might combine to yield smaller initial flaw depths/widths. Knowing the mode I stress intensity factor's dependence on such parameters, it was hypothesized that such changes would mandate larger values of applied stress to reach K_{IC} , and lend explanation to the mist, hackle, and even chipping (high stress cleaving events) frequently observed for poorly performing candidates.

The initial analysis focused on the amount of cleaver blade wear generated over the course of a test. Scanning-electron microscope images of cleaver blades were taken both before and after cleaving tests of standard silica and titania-clad fibers. In all cases, the blade wear induced by the titania-clad candidates was certainly no worse than that imparted by the standard silica fiber.

This result, however, did not preclude the idea that titania-clad fibers were more *sensitive* to blade wear, or simply reacted differently to new blade positions from the start. The hypothesis was tested by scoring both standard silica and TiO_2 doped fiber at new blade positions, and analyzing the residual flaws under scanning-electron and optical microscopes. Fibers were examined in their "before fractured" state to be certain that damage was not a function of final failure.

Representative images for both standard silica and titania-clad fibers are shown in Figures 7

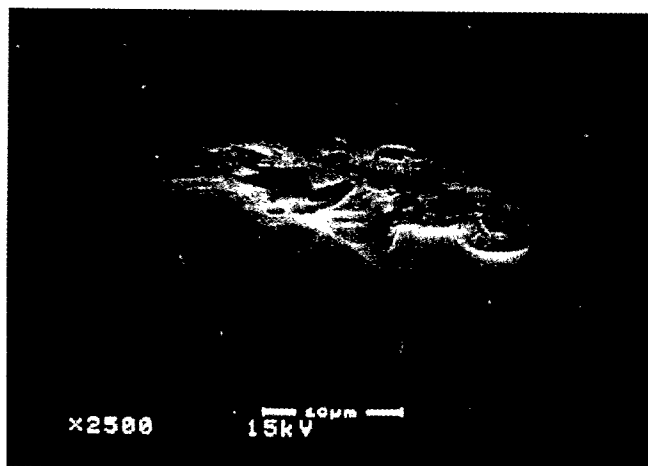


Figure 7: SEM Surface Image of Cleaver Score Imparted to Standard Silica Fiber

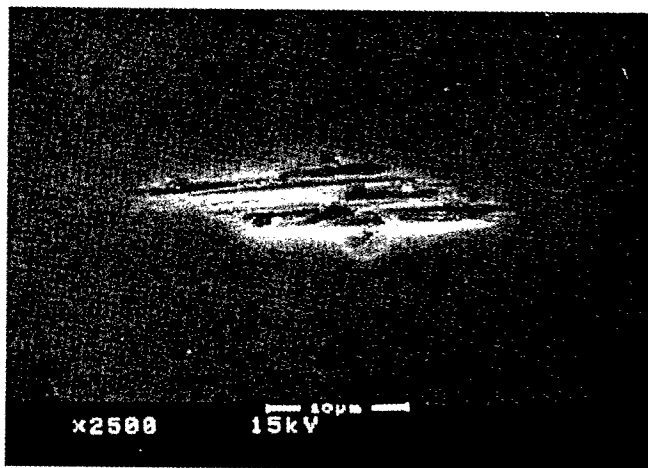


Figure 8: SEM Surface Image of Cleaver Score Imparted to Titania-Clad Fiber

and 8, respectively. As is shown, results indicate that the scores imparted to titania-clad fiber were more confined to the fiber surface, and exhibited less extensive pitting/chipping. While the standard silica scores consistently displayed notable lateral damage and relatively deep spalls, the titania-clad scores appeared to be better described as surface abrasions.

While follow-up analysis on the optical microscope could only reveal that all cleaver scores (standard silica and titania-clad) were 1-2 μm in maximum depth, the scanning-electron microscope images indicate that differences within this scale may exist, and that average depths are most certainly less for titania-clad cleaver scores.

Current plans to precisely quantify cleaver score differences involve the use of low viscosity epoxy resins to create detailed "positives" of each flaw. Analyses of such "positives" are again to be performed through the scanning-electron microscope.

CONCLUSION

The work performed in this study indicates that, within the practical ranges of interest, neither titania thickness nor concentration will consistently correlate with cleavability. Hence, the magnitude of compressive residual stress within a titania layer cannot uniquely predict a candidate's potential for ideal fracture, and should not be viewed as the sole source of optimal cleaving conditions which might be different than those of silica fiber. Instead, a consistent reduction to the damage imparted by a cleaver blade appears to be the origin of such a change.

The product of titania thickness and concentration is shown to provide a simple, and very reasonable estimator of titania-clad fiber cleavability. The net result of the study is an enhanced ability to identify and design titania-clad fibers which will be more "user-friendly" to field operators, while still maintaining the superior mechanical performance characteristic of TiO_2 doped fiber. The findings of this study were applied to the design of Corning's SMF-28 with DuracladTM product.

ACKNOWLEDGEMENTS

I'd like to thank Dr. G. Scott Glaesemann and Dr. D. J. Wissuchek for their valuable inputs with regard to the study presented.

REFERENCES

1. M. R. Backer, M. G. Blankenship, R. R. Cavender, B. De Jong, M. Elder, G. S. Glaesemann, P. C. Jones, U.S. Patent 5140665.
2. Bell Communications Research, "Generic Requirements for Optical Fiber Cleavers," Technical Reference TR-NWT-000264, Issue 2, December 1993.
3. G. S. Glaesemann, K. Jakus, and J. E. Ritter, Jr., "Strength Variability of Indented Soda-Lime Glass," *J. Am. Ceram. Soc.*, **70** [6] 441-444 1987.



Jesse C. Meyer
Corning Incorporated
310 North College Road
Wilmington, NC 28405

Jesse Meyer received his BS in Mechanical Engineering from Clarkson University in 1995, and his MS in Solid Mechanics from Harvard University in 1997. While at Clarkson, he was named an Alcoa Scholar, and winner of the Robert E. Rosati Award for Excellence in Mechanical Engineering. At Harvard, he was awarded the Courtlandt S. Gross Scholarship (Lockheed Martin Corporation), where his research focused on ultralight/cellular metal structures. Jesse is currently a Process Development Engineer at Corning's optical fiber plant in Wilmington, North Carolina.

DEVELOPMENT OF NEW OPTICAL FIBER FUSION SPLICER FOR FACTORY USE

Kohji Ohzawa, Shonosuke Yaguchi, Jun-ichi Suzuki,
Noriyuki Kawanishi, Shigeru Saito

Fujikura Ltd., Sakura, Chiba, Japan

ABSTRACT

Recently, the demand for optical fiber modules has increased, and various kinds of modules are being manufactured. These optical fiber modules consist of many kinds of specialty fibers. Specialty fiber is generally difficult to splice. Therefore, difficult requirements for splicing these fibers are increasing as new fiber types are introduced.

Standard fusion splicers have been developed for field-use in order to splice a few types of common telecommunications fiber. However, these splicers are unsuitable for splicing specialty fibers. Therefore, a new fusion splicer for specialty fiber splicing has been developed.

The new splicer is specifically designed for factory use for production of optical fiber modules. Various improvements have been applied to this splicer in order to splice specialty fibers with low loss and stable splicing performance regardless of operator skill. The splice loss estimation has also been improved. This splicer estimates the splice loss by taking various factors into consideration. Therefore the risk of unacceptable splices has been decreased.

INTRODUCTION

In the last few years, optical fiber amplifiers have been frequently used for the relay equipment of optical fiber telecommunication systems. The demand for fiber amplifiers has been greatly increasing recently. Optical fiber amplifiers consist of various specialty fibers including Erbium-doped fiber. Hence, production of the amplifiers requires splicing of

such specialty fibers. Other types of optical fiber modules utilize fibers with complicated refractive index profiles, such as WDM fiber and dispersion compensation fiber (DCF).

To meet the difficult splicing requirements of optical module production, a new fusion splicer has been developed. This new splicer has unique characteristics and has been specifically designed to splice specialty fibers in the factory.

FEATURES

This splicer has the following features:

- 1) Low splice loss for different types and combinations of specialty fibers
- 2) Stable splicing performance via improved arc discharge condition self-calibration and reduced dependency on operator skill
- 3) Accurate estimated splice loss in order to distinguish unacceptable splices

Methods to achieve these features (and the resulting performance) are detailed in the following sections.

IMPROVED SPLICE LOSS

Adequate Discharge Heating for Splicing Dissimilar Fiber Types

In the case of dissimilar fiber splicing, typically each fiber has a different mode-field diameter (MFD). In such cases, this MFD mismatch between the fibers may be a significant source of splice loss, and may be the dominant contributing factor. Assuming that the light ray

in the fiber is a gaussian shaped beam, the splice loss L (dB) in Figure 1(a) can be expressed by the following formula¹:

$$L = -10 \log \left(\frac{2 w_1 w_2}{w_1^2 + w_2^2} \right)^2 \quad (1)$$

where w_1 and w_2 are the MFDs of the two spliced fibers, and the loss L is the loss due to the MFD mismatch between the two fibers

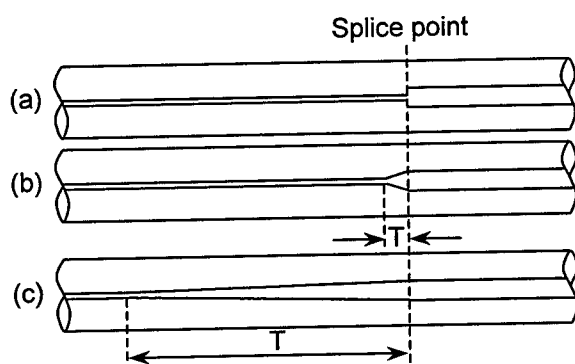


Figure 1. MFD Taper Length Change by Expansion of Discharge Heating Area

Generally, the MFD may be expanded by the heat of the fusion arc. This is especially true in the case of Fluorine-doped fiber. During the fusion arc, the MFD expands as the core dopants diffuse into the cladding. This enables decreasing the splice loss due to MFD mismatch by expanding the MFD as shown in Figure 1(b).

Furthermore, when the taper length T extends to infinity, the loss due to MFD mismatch can become lower according to the results of numerical analysis by the Beam Propagation Method.

Therefore, improved discharge heating to extend the taper length T as shown in Figure 1(c) has been developed. As a result, lower losses for splicing dissimilar specialty fiber combinations have been achieved with the new splicer.

Figure 2 shows the splice loss results for splicing SM fiber (with operating wavelength of 1310nm and MFD of approximately 10 μ m) to

Erbium-doped-fiber (with MFD of approximately 5 μ m) using the standard fusion splicer and the new splicer. The splice loss using the new splicer (with the expanded discharge heating area as in Figure 1(c)) is reduced compared with that of the standard splicer (in which the discharge heating is normal as in Figure 1(b)).

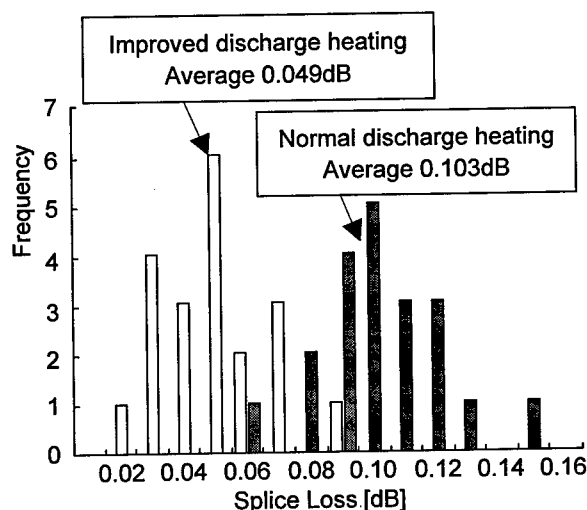


Figure 2. Splice Loss Change by Expansion of Discharge Heating Area

Prevention of Refractive Index Profile Distortion by Low Temperature Heating

For fiber in which the cladding near the core contains fluorine, especially DCF, it is easy for the refractive index profile near the core to become distorted and abnormal because of fluorine migration during heating. Therefore, the splice loss for these fiber types is easily increased due to heating during the fusion arc. In order to prevent high loss due to refractive index profile distortion, the heat applied during splicing must be very low. Therefore, the arc discharge current must be set as low as possible.

However, the discharge current value has a lower limit. If the current is below this threshold, the splicer cannot achieve or maintain a stable fusion arc discharge.

In order to achieve a reduced effective heat input during the fusion splice, an intermittent arc discharge has been adopted. In this case, the fusion arc is rapidly cycled on and off. This

method can be utilized in order to achieve a reduced fiber temperature during the fusion arc. This is illustrated in Figure 3 below. By this method, a splice loss decrease of 30% for splicing DCF to SM fiber may be achieved.

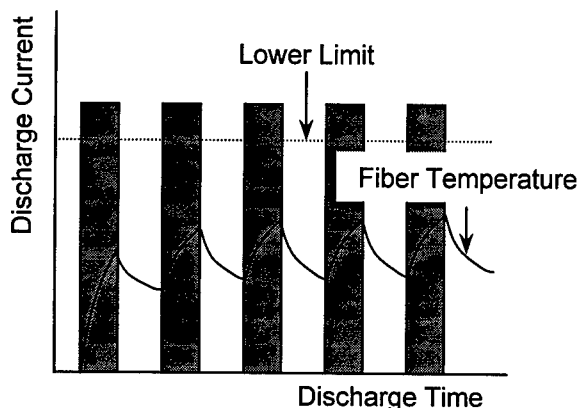


Figure 3. Low Temperature Heating by Intermitting Discharge

STABLE SPLICING PERFORMANCE

Discharge Power Compensation

The fusion splicer joins fibers by melting the fiber ends during discharge heating. Variation of the amount of heat applied to the spliced fibers easily changes the splice loss. The splice loss of specialty fibers is especially sensitive to variation of the amount of discharge heat input. Hence, it is important to maintain adequate arc discharge heat intensity. However, the intensity of the discharge heat is easily varied by the conditions of / or around the electrodes. Since this new splicer is intended for splicing specialty fibers, the splicer must recognize small variations of discharge heat intensity and must compensate automatically. In this splicer, a new discharge power compensation method has been adopted in order to achieve improved self-calibration.

During an arc discharge, any fiber axis offset that may be present will gradually decrease due to surface tension of the molten glass. This phenomenon is known as the "self-aligning effect". Figure 4 shows the decrease of fiber axis offset by self-aligning of the fiber due to surface tension.

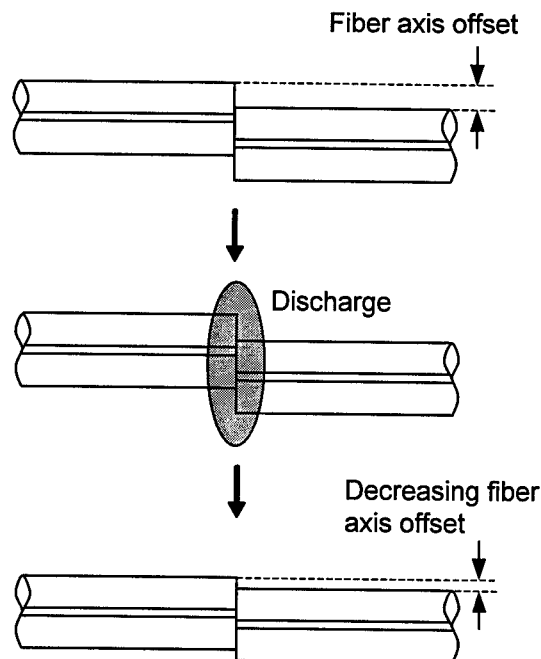


Figure 4. Decrease of Fiber Axis Offset by Self-Aligning Effect

The amount (and rate) of decrease of fiber axis offset is proportional to the intensity of the discharge heat. Therefore, the splicer can accurately recognize the heat intensity by measurement of the decrease of the axis offset. This measurement is accomplished by the splicer video observation system. This allows the splicer to self-calibrate the suitable heat intensity by applying a compensation factor to the arc discharge power. By using this compensation method, consistent heat intensity may be ensured which provides stable splice loss performance even with specialty fibers.

Fiber Holder System

If the fibers are not set into the splicer correctly and uniformly, the splice loss is not stable because of variability of the fiber endface overlap amount and variability of fiber clamping stress and position.

In the new splicer, a fiber holder system has been adopted as shown in Figure 5. This ensures that the fibers are set correctly and repeatably into the splicer.

The fiber holder system is also used in conjunction with a jacket stripper and cleaver in

order to ensure that the fiber preparation process is easy and repeatable regardless of operator skill.

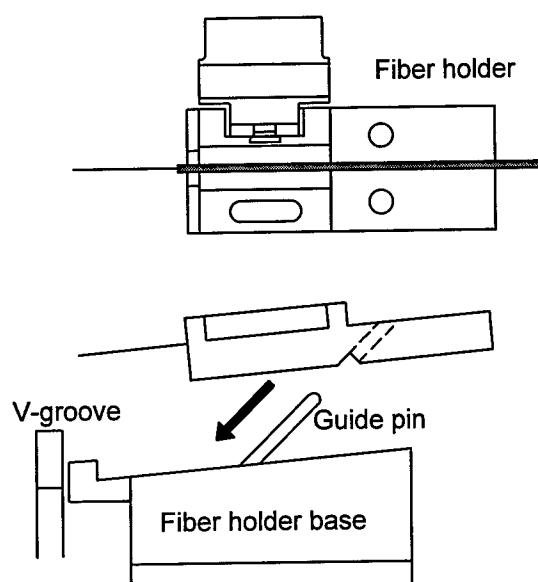


Figure 5. Fiber Holder System

ACCURATE ESTIMATED SPLICE LOSS

There are various splice loss factors as shown in Figure 6. Core axis offset is the most important factor when splicing standard telecommunications fibers. Hence, the standard splicer estimates the splice loss by observation of the core axis offset. The splicer also inspects for dust on the fiber, bubbles, and fiber diameter change at the splice point. If the splicer has judged that these factors affect the splice loss, the splicer warns the operator. The other splice loss factors in Figure 6 are not significant for normal SM fiber. Therefore, they are not considered in the standard splicer's loss estimation routine.

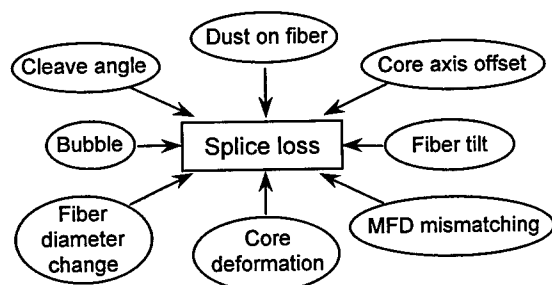


Figure 6. Splice Loss Factors

However, these factors require consideration in order to achieve accurate splice loss estimation of specialty fibers. These factors are important in splicing specialty fiber combinations in which one or more MFD is generally small, refractive index profiles may be more complicated, and other characteristics of the fibers may have an effect.

The new splicer estimates the splice loss not only by core axis offset, but also by fiber tilt angle, core deformation, and MFD mismatch at the splice point. Since the core deformation and the MFD mismatch are important factors for specialty fiber splicing, these factors have been studied in detail. The splice loss estimation improvements achieved through incorporation of these two factors are shown in the following sections.

Estimation by Core Deformation

Core deformation may be caused by small pre-splice fiber axis offset or by poor cleaved fiber ends. The most common shapes of the deformation can be classified as one of two patterns as shown in Figure 7. The type of deformation shown in Figure 7(a) is designated as "core curvature", and the type shown in Figure 7(b) is designated as "core step".

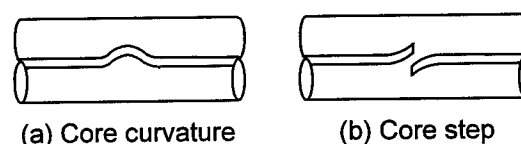


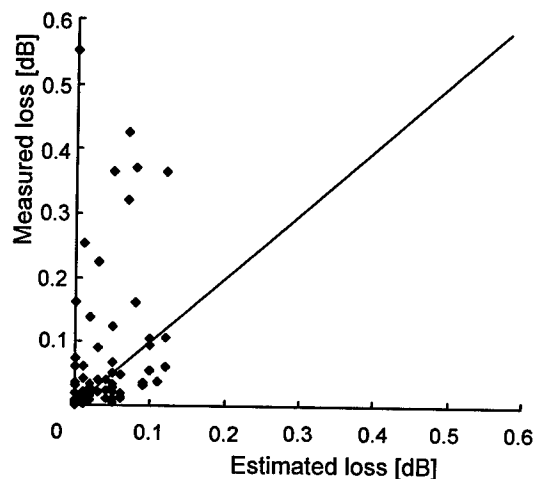
Figure 7. Core Deformation Shapes

Core curvature may readily occur due to poorly cleaved fiber ends. For example, a large cleave angle or a crack on the cleaved end may result in such a defect. Core step is generally caused by a small fiber axis offset before the splice.

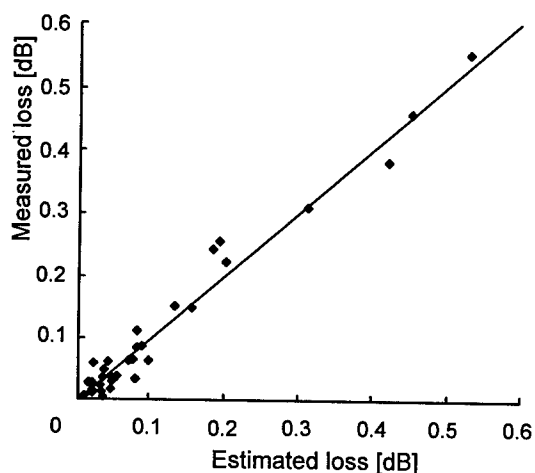
The splice loss due to core deformation is related to the type of the spliced fibers, the core deformation shape, and amount of the deformation. Hence, the splicer observes the splice point, discriminates between core curvature and core step, and estimates the splice loss due to the core deformation by measuring the amount of deformation.

Figure 8 shows the relationship between measured splice loss and estimated loss for a

SM fiber that has an operating wavelength of 980nm and a MFD of approximately $7\mu\text{m}$. The estimated loss values in Figure 8(a) do not include the loss due to core deformation. The estimated loss in Figure 8(b) is improved by including the calculation of loss due to core deformation. Including core deformation in the loss estimation routine results in a dramatic improvement, and accurate loss estimation is obtained by this method.



(a) Not including core deformation



(b) Including core deformation

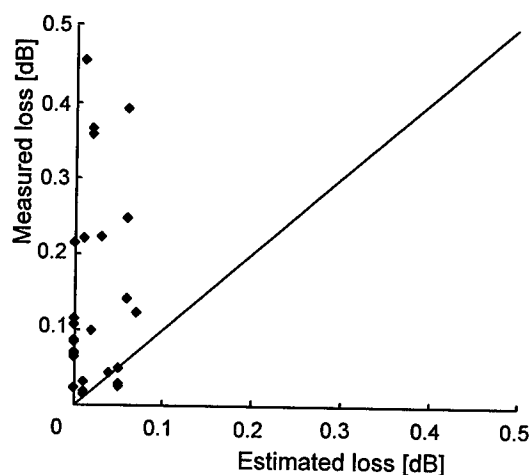
Figure 8. Improvement of Estimated Loss Accuracy by Core Deformation Observation

Estimation by MFD Mismatch

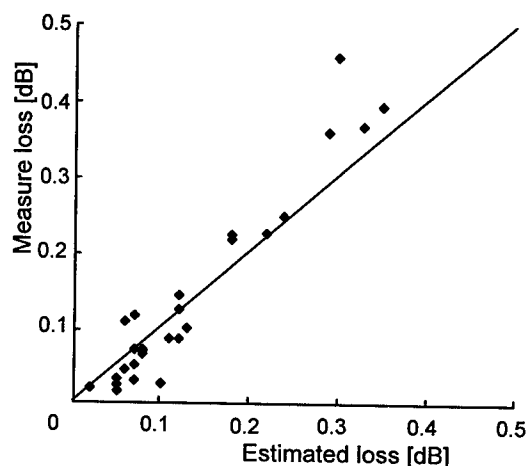
In the case of splicing two fibers that have different MFDs, the splice loss includes loss due to the MFD mismatch. This loss accounts for much of the total splice loss. Hence, it is necessary to take MFD mismatch into

consideration in order to obtain accurate loss estimation. Therefore, the new splicer observes the splice point and measures the amount of MFD mismatch. This allows calculation of the loss due to MFD mismatch.

Figure 9 shows the relationship between measured splice loss and estimated loss for a SM fiber (with MFD of approximately $10\mu\text{m}$) spliced to an Erbium-doped fiber (with MFD of approximately $5\mu\text{m}$). The estimated loss values in Figure 9(a) do not include the loss due to MFD mismatch, but that in Figure 9(b) is improved by including the calculation of loss due to MFD mismatch. As in the case of core deformation, the loss estimation is greatly improved, and accurate estimated loss is achieved by including loss due to MFD mismatch in the loss estimation routine.



(a) Not including MFD mismatch



(b) Including MFD mismatch

Figure 9. Improvement of Estimated Loss Accuracy by MFD Mismatch Observation

CONCLUSION

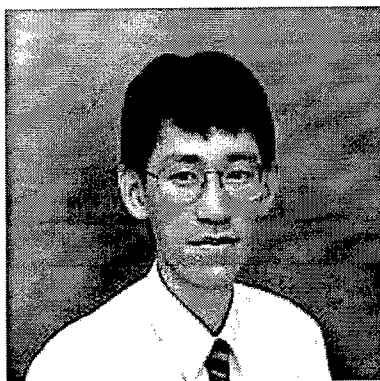
A new optical fiber fusion splicer has been introduced that has been designed for factory use in the production of optical fiber modules. This splicer has been improved to obtain low and stable splice loss for specialty fiber splicing. The splice loss estimation has also been improved to enable detection of poor quality splices.

In the future, many new types of specialty fibers will be introduced. Further improvements to the splicer may be developed and introduced to meet emerging fiber splicing requirements.

REFERENCE

1. D. Marcuse, "Loss Analysis of Single-mode Fiber Splices," B.S.T.J., Vol. 56, No.5, May-June 1977, pp. 703-718

AUTHOR



Kohji Ohzawa

Precision Instruments R&D Dept.
Fujikura Ltd.
1440, Mutsuzaki, Sakura, Chiba, 285-8550,
Japan

Kohji Ohzawa was born in 1967. He graduated with an electronics degree from Kyushu University in 1990.

He joined Fujikura Ltd. in 1990 and has been engaged in the research and development of optical fiber fusion splicers.

He is a member of the IEICE of Japan.

RECOVERY ANALYSIS OF DAMAGED OPGW CABLES DUE TO LIGHTNING STRIKES

Bernardo J. G. de Aragão ⁽¹⁾, Carlos Pitombo ⁽¹⁾, Paulo J. P. Curado ⁽¹⁾, Alexandre Bagarolli ⁽¹⁾, Sérgio Millo ⁽¹⁾, Américo M. D. Luz ⁽²⁾, Fábio R.B. Benayon ⁽²⁾, Luiz M. Lauria ⁽²⁾

(1) Fundação CPqD, Campinas, Brazil

(2) Embratel, Rio de Janeiro, Brazil

ABSTRACT

In this work repairing of an OPGW cable damaged by lightning strikes is discussed. It is shown that an emergency repair with a preformed product restores the performance of the cable. Assessment of the repair work included extensive analysis of both cables and stranded wires. The analysis consisted of two parts:

- a) Evaluation of the change in mechanical and optical properties of the cable with increasing number of broken stranded wires;
- b) Metallographic investigation of the stranded wires of a damaged cable to characterize the damages suffered by the wires due to lightning strikes.

The assessment was done with two samples of the cable investigated: the damaged cable and another undamaged one, taken as reference.

was carried out with and without the preformed product of Figure 1 to investigate the efficiency of the product in restoring the cable's integrity without the need for substitution of the whole span. At the same time, metallographic analysis of the stranded wires revealed some of the microstructural processes that may contribute to cable degradation during lightning.

The damage inflicted by lightning strikes to the cable consisted of the rupture of the stranded wire due to localized fusion (Figure 2). The tested cable design included 40 optical fiber in a channeled rod, enclosed in a metallic tube and 11 stranded wires. The stranded wires were aluminum clad steel wires of 2.50 mm diameter. In another study it will be shown that the repair work analyzed in this work has restored the cable electrical properties.

INTRODUCTION

With the increasing use of OPGW cables in Brazil, concern has arisen in regard to the integrity of these cables due to lightning strikes. Special attention has been given when some damage has been inflicted to a cable. Doubts arise about the extension of the damage to the cable or one of its components (e. g., optical fibers, stranded wires), the repair of the cable with preformed products and the impact of both (damage extension and repair) on the mechanical and optical performance of the cable. Frequently an emergency repair of the cable is carried out to quickly restore communication. Later evaluation of the cable may imply in its substitution.

This work deals with the repair of the damaged armor of OPGW cables due to lightning strikes. It describes an evaluation carried out of the optical and mechanical performance of an OPGW cable that had been damaged by lightning strikes in the field. Evaluation

EXPERIMENTAL METHODS

The following approach was adopted in this work:

- a) The performance of the damaged cable was compared with the performance of an unused portion of the same cable (referred as reference cable from now), tested under the same conditions as the damaged one;
- b) The performance analysis of the damaged cable consisted in the evaluation of the optical and mechanical performance of the cable and in the determination of the chemical, physical and mechanical properties of the metallic components of the cable (stranded wires, tube, channeled rod).

As work went on, it turned out that most of the above mentioned properties of the metallic components were within specifications and will not be analyzed here. However, complementary metallographic analysis was carried out to investigate the damages inflicted to the stranded wires by lightning strikes.

Optical and mechanical performance of the cable was investigated by means of the stress-strain and vibration tests according to IEC 60794-4-1. Figures 3 and 4 show the setup and the block diagram of both tests. As can be seen in the pictures, strain and optical attenuation of the fibers were measured simultaneously during the tests. The performance of 14 fibers were continuously monitored during the tests.

To investigate the effect of increasing damage on the mechanical and optical performance and also to find the limit of integrity of the cable, stress-strain testing was done with increasing number of intentionally broken stranded wires up to the limit when fracture of optical fibers initiated. Moreover, to verify the possibility of repair of the damaged cable, testing was done with and without the preformed product of Figure 1.

Vibration test followed stress-strain test and was done to compare the mechanical and optical performance of the cable before and after multiple stranded wire rupture. Before each test, cable specimen with wire rupture were preloaded to 16,3 kN (25% of estimated breaking load) for 3 minutes, following load relief. The reason for this was to simulate the load relief operation applied by craft persons to a damaged cable before attaching the preformed product on it. For reason explained below, testing was done only with the reference cable. Vibration frequency was calculated by the equation

$$f = \frac{830}{d}, \text{ where } d = 11.5 \text{ mm}$$

Hence, vibration frequency was 72 Hz.

To carry out the metallographic analysis of the stranded wires, wire samples were cut which were mounted for metallographic specimen preparation. After polishing and grinding, the wire cross-sections were analyzed with optical and scanning electron microscopes.

RESULTS

Stress-strain test

Figure 5 shows how fiber strain changed with increasing number of broken stranded wire, with and without preformed product, for both cables (field damaged cable and reference cable). As one would expect, for both cables, as the number of broken wires increased, so did fiber strain. On the other hand, the

preformed product diminished fiber strain after each wire breakage. However, the following differences were observed between the cables:

- a) For the damaged cable, the use of the preformed product reduced strain to less than 0.2%. This is the maximum allowable short term fiber strain in installed cables. For the reference cable, however, from the third wire breakage upwards, fiber strain reduction never reduced below 0.2%;
- b) During testing of the reference cable with six broken wires, an additional number of wires broke before the load of 19,6 kN (30% of estimated breaking load of the cable) was reached. One optical fiber broke as well. This point marked the limit of cable integrity and hence cable recovery;
- c) Strain of the reference cable was always higher than strain of the damaged cable, with and without preformed product.

Figure 6 shows attenuation change with increasing number of broken stranded wires, in the same way as Figure 5. As can be seen, for the reference cable, attenuation was not remarkably affected up to the rupture of five stranded wires. However, with six broken wire, at the limit of cable integrity, fiber attenuation of the reference cable increased due to the rupture of the additional stranded wires. For the damaged cable, the sixth broken wire did not affect attenuation.

Vibration test

Vibration tests were carried out based on the results obtained by the stress-strain test. Due to time constraints, it was decided to test only the reference cable as verified previously, i.e., with 4 and 5 broken stranded wires, and with the preformed product. The specimen tested with 4 broken wires was first tested without any broken wire for reference. The testing sequence was as follows: First, testing a specimen with 5 broken wires and 23 million cycles; Second, testing of another specimen with no wire breakage and 20 million cycles; Third, testing the same specimen of the second test, this time with four broken wires and additional 80 million cycles, making up a total of 100 million cycles for this specimen. Figure 7 shows the change of fiber strain with time. For practical purposes, the most important result was that for all cases investigated, fiber strain remained fairly stable, around 0.2%. No trend towards higher strain values with time was observed.

Figure 8 shows the change of fiber attenuation with time. Likewise strain, attenuation remained fairly

stable during cycling. Except for a few fibers, attenuation values remained low for all of the cases investigated. As one would expect, as some of the stranded wires broke, dispersion of the attenuation values increased.

Metallography

Figure 2 shows the rupture of stranded wires by lightning strikes. Rupture occurred due to local melting of the wires. However, fusion did not always extend throughout the whole cross-section of the wire, becoming sometimes restricted to a small portion of the surface ("fusion spot"). Figure 9 shows the aspect of such a fusion spot. The aluminum clad has melted down, leaving the steel core exposed to atmospheric corrosion. Small yellow corrosion spots were visible in the fusion spots. In Figure 10 a metallographic cross-section across the fusion spot shows how the microstructure at the wire surface changes abruptly from the continuous aluminum clad to the fusion zone. Typical fusion microstructure can be seen in this zone (Figure 11), with alloying between iron and aluminum, as shown by EDS microanalysis of the fusion zone (Figure 12). Moreover, metallography also showed that near the fusion damage the thickness of the aluminum clad was not uniform all over the cross-section of the stranded wires (Figure 13). At the points of minimum thickness, its value was less than 125 μ m, the minimum required by international standards for stranded wires with 2.50 mm diameter.

DISCUSSION

In the previous chapter the optical and mechanical performance of the cables was investigated by simulating gradually increasing armor damage. The discussion which follows now will focus on three goals:

- a) Assessment of the actual mechanical and optical performance of the cable after its armor was damaged;
- b) Determination of cable integrity and cable recovery, i.e., the maximum allowable number of broken stranded wires below which recovery of optical and mechanical performance of the cable is feasible and above which recovery becomes unfeasible due to permanent optical fiber rupture;
- c) Material properties relevant to the long-term mechanical performance of the cable armor.

It followed from the stress-strain test that – for the reference cable – the limit of cable integrity and recovery was when the armor damage summed up five

broken stranded wires. With five and less broken wires, it was possible to reduce optical fiber strain with the aid of the preformed product. Moreover, up to five broken wires, fiber attenuation was not markedly affected by the damage, even without the use of the preformed product. However, with the breakage of the sixth stranded wire, a limit condition seemed to have been reached beyond which recovery turned out to be unfeasible: additional stranded wires broke in uncontrollable ways. The load carrying capacity of the armor reduced drastically. As a result, optical fiber attenuation increased. Fiber strain showed a different behavior. It increased continuously with increasing number of wire breakage. The use of the preformed product reduced strain. However, starting with the third wire breakage, the reduction was not sufficient to lower fiber strain to less than 0.2% , the maximum allowable short term fiber strain in installed cables. At the limit condition of 6 intentionally broken stranded wire, fiber strain went up to as high as 0.6% and one case of optical fiber breakage was reported.

Compared to the reference cable, the damaged cable kept its optical and mechanical performance up to six broken stranded wires. Optical attenuation was not affected at all by the gradually increasing armor damage. Strain increased with increasing damage, however, at a slower pace than the reference cable. In any case, fiber strain was brought down to less than 0.2% with the preformed product. No fiber breakage was reported at any test.

The reasons for the better performance of the damaged cable than that of the reference cable are not clear. A possible cause could be differences between the load histories of both cables not accounted for in this work. These differences could also explain the occurrence of the fiber breakage in the reference cable. For some unknown reason, the fibers of the reference cable may have been stressed in the past, which promoted crack growth until it reached critical crack size during the stress-strain test. Besides loading history, the fiber breakage could be also due to fiber production or fiber handling. An attempt was made to locate the fiber rupture point in the cable for break source analysis, unfortunately, without success.

In regard to the vibration test, testing showed that the preformed product did not interfere with cable behavior during vibration. Both fiber strain and attenuation remained stable and within acceptable limits during testing.

Based on the optical and mechanical performance testing carried out on the cables, it was concluded that

the repair of the cable tested, after being damaged by lightning strike, is feasible with a preformed product of the type of Figure 1. The recovery of its optical and mechanical performance is possible provided that armor damage sums up no more than 5 broken stranded wire. Although the damaged cable investigated showed that recovery could be extended to the case of six broken wires, a safe criteria would be to restrict it to the case of five wires, based on the results of the reference cable. The cable repair should be checked with fiber strain and attenuation measurements. In regard to strain, its value with the preformed product should be below 0.2%, the maximum allowable short term fiber strain in installed cable. While restoration of the optical and mechanical performance was achieved, repairing with preformed product should be envisaged primarily as an emergency. Further analysis should investigate the need for substitution of the damaged cable.

Finally, the metallographic analysis has shown that material behavior during lightning strikes is an important factor to consider. The type of stranded wire of the cable investigated was aluminum clad steel wire. It has turned out that heating due to lightning strikes of this type of wire had provoked degradation of the aluminum coating by formation of fusion spots. At these spots, localized fusion of the aluminum clad had affected corrosion resistance of the wires by exposing the steel core to the atmosphere. While it has not been proven here, the fact that the thickness of the aluminum clad near the fusion damage was lower than required suggests that further investigation is needed to verify if there is a relation between clad thickness and localized fusion. Heating also promoted alloying between iron and aluminum, which could change locally and thus impair further the thermal properties of the aluminum clad. Therefore, it is recommended that a periodical check-up for fusion spots at the wire surface should be included during maintenance of OPGW cables with aluminum clad steel stranded wires.

CONCLUSION

1. Repair of the damaged armor of the OPGW cable investigated is feasible up to five broken stranded wire, with the use of a stranded product. Both the mechanical and optical performance of the original, undamaged cable can be restored.
2. Repair of a damaged cable shall include fiber attenuation and fiber strain measurements. Fiber breakage shall be investigated with break source analysis. Fiber strain after repair shall be below 0.2%.

3. Repair is feasible at least for emergency purpose. Further analysis should investigate the need for substitution of the damaged cable.
4. Periodic checking of the stranded wires' surface is recommended to look for fusion spots. These spots are a potential threat to armor and cable integrity. They affect long term thermal and corrosion resistance of the stranded wires.

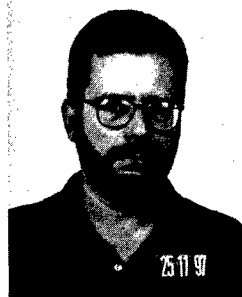
REFERENCES

1. Technical report PD.33.ER.CCO.0017A/RT-01-AA. CPqD/EMBRATEL (1999).
2. Technical report PD.12.AT.ENS.0527A/RT-01-AA. CPqD/EMBRATEL (1999)
3. ABNT NBR 14074:1998. Brazilian standard for composite overhead ground wire with optical fiber (OPGW).
4. ABNT NBR 13982:1997. Brazilian standard for test method for eolian vibration of composite overhead ground wire with optical fibers (OPGW).
5. ABNT NBR 13985:1997. Brazilian standard for test method for stress-strain test of composite overhead ground wire with optical fibers (OPGW).
6. ABNT NBR 10711:1989. Brazilian standard for hard-drawn aluminum clad steel wires with circular section for electrical purposes.
7. IEC 1232:1993. Aluminium-clad steel wires for electrical purposes.
8. IEC 60794-4-1:1999-01. Optical fibre cables – Part 4-1: Aerial optical cables for high voltages power lines.
9. Yokoya, M. et al. Development of Lightning-resistant Overhead Ground Wire. **IEEE Transactions on Power Delivery**, v. 9, n. 3, pp.1517-1523, (1994).

ACKNOWLEDGEMENTS

The authors are deeply indebted to the technical staff at CPqD and EMBRATEL who gave their valuable support at all stages of this work. Moreover, the authors express their gratitude towards the board of directors of CPqD and EMBRATEL for their encouragement to present this work at IWCS.

AUTHOR



Bernardo J. G. de Aragão has been a researcher at CPqD since 1983. He earned a B.S. degree in Metallurgical Engineering at the Federal University of Rio de Janeiro in 1982 and a M.Sc. degree in Materials Science and Engineering in 1993 at the University of Florida. His field of activity includes mechanical reliability studies of optical fibers and cables.

AUTHOR'S ADDRESS

Fundação CPqD
Rod. SP 340 Campinas – Mogi Mirim, km 118
C. P. 6070
Campinas – SP
CEP 13083-970
BRAZIL
E-mail: grbernardo@cpqd.com.br

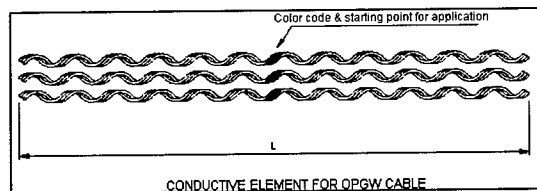


Figure 1: Preformed product



Figure 2: Rupture of stranded wire due to fusion

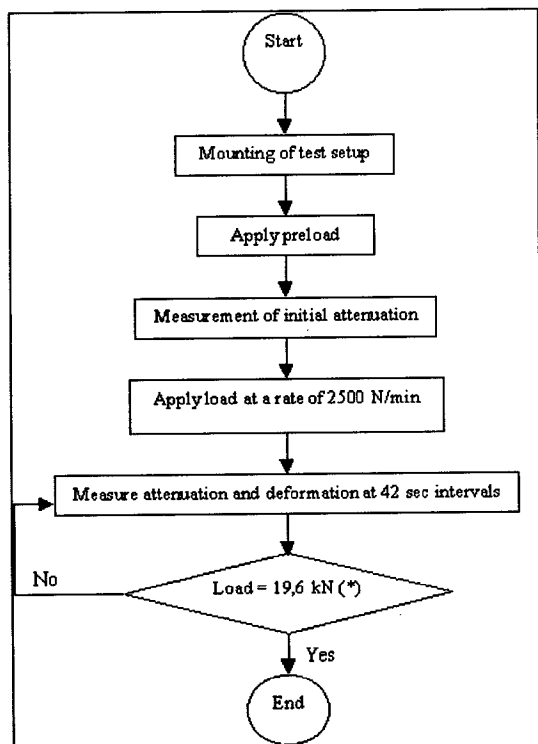
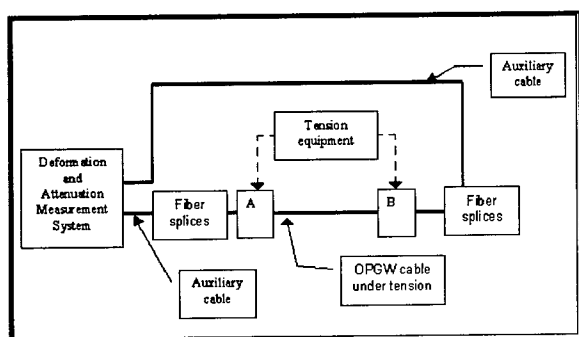


Figure 3. Stress-strain test. Above: Test setup; Below: Block diagram, (*) = 30% of estimated breaking load

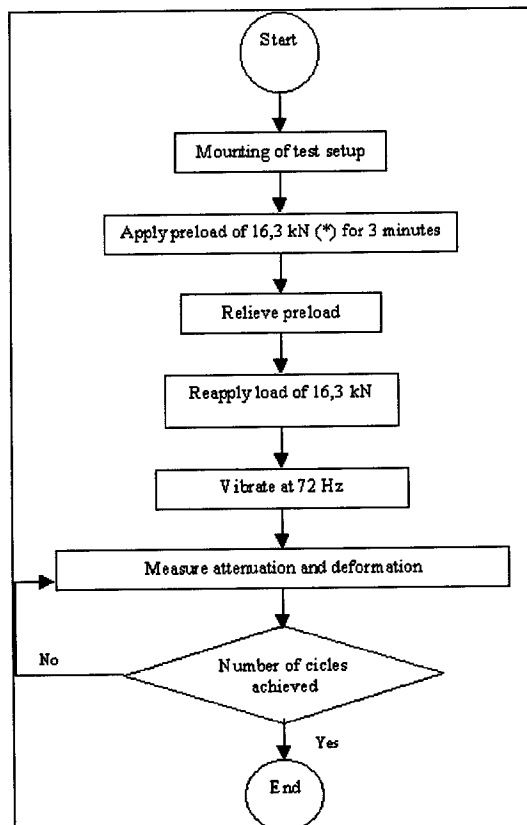
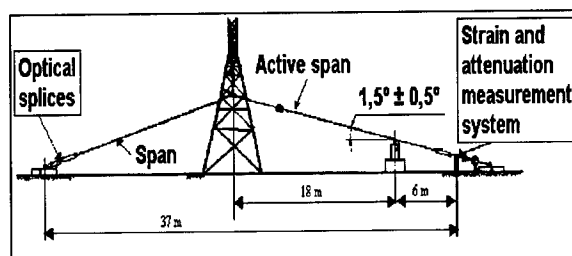


Figure 4. Vibration test. Above: Test setup; Below: Block diagram, (*) = 25% of estimated breaking load

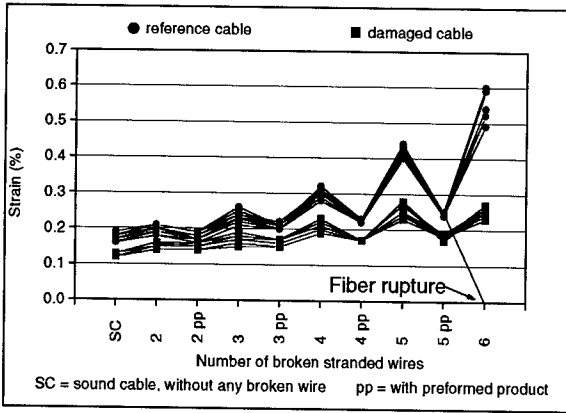


Figure 5: Fiber strain vs. number of broken stranded wires

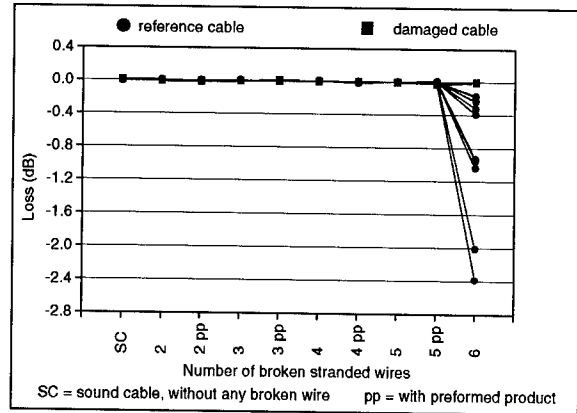


Figure 6: Fiber attenuation vs. number of broken stranded wires

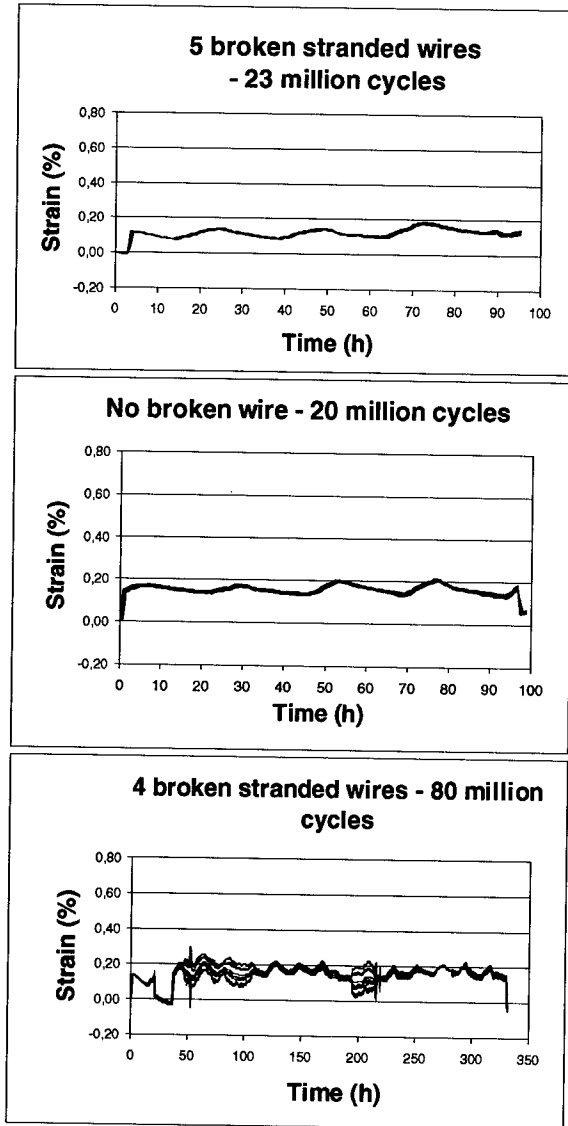


Figure 7: Strain during vibration test

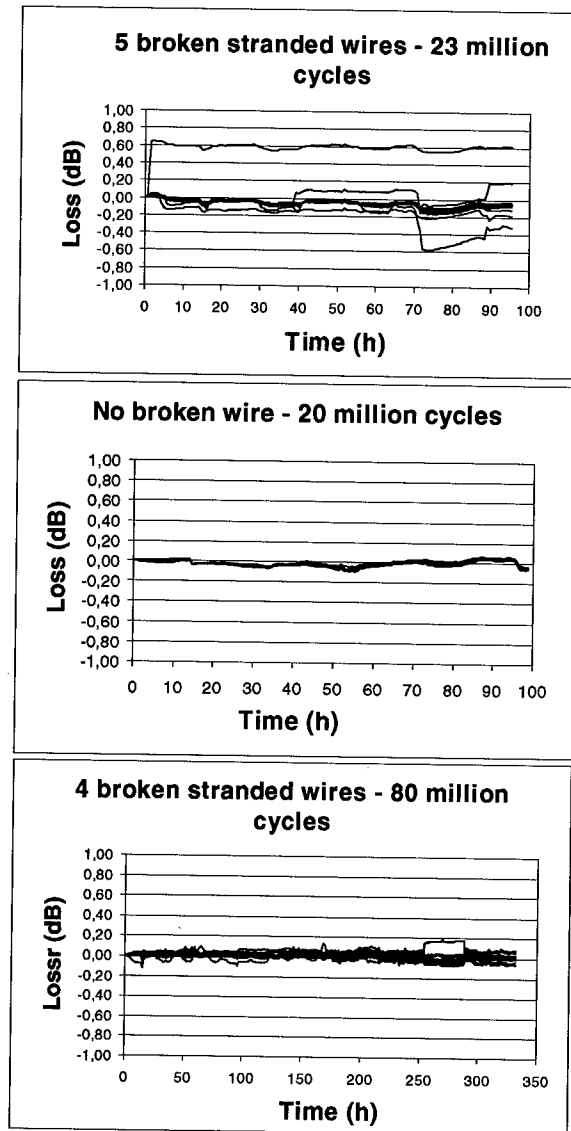


Figure 8: Attenuation during vibration test



Figure 9: Fusion spot



Figure 10: Metallographic cross-section across fusion spot. E = steel core, L = Fusion spot, Al = aluminum clad (Magnification 50X)

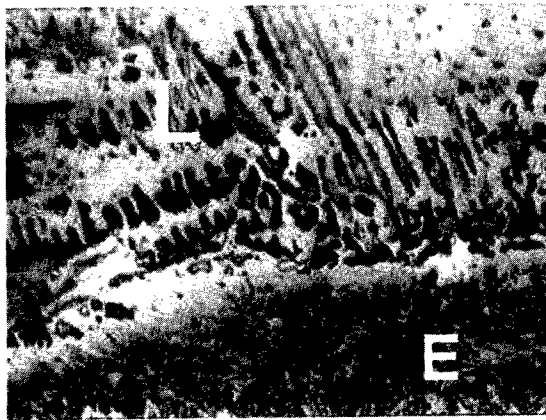


Figure 11. Typical fusion microstructure in fusion spot, somewhere at the steel core/aluminum clad interface (see Fig.10); L = iron-aluminum alloy, E = steel core (Magnification 1000X)

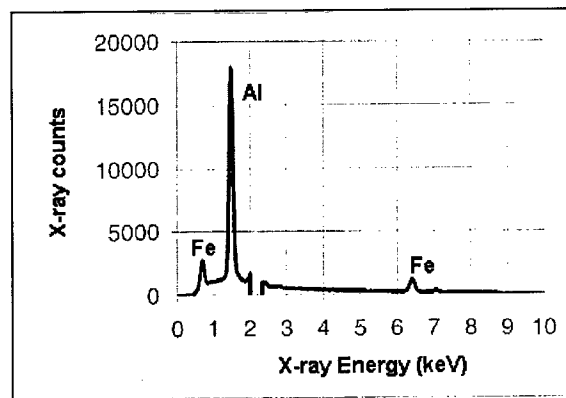


Figure 12: EDS spectra of iron-aluminum alloy of Fig. 11.

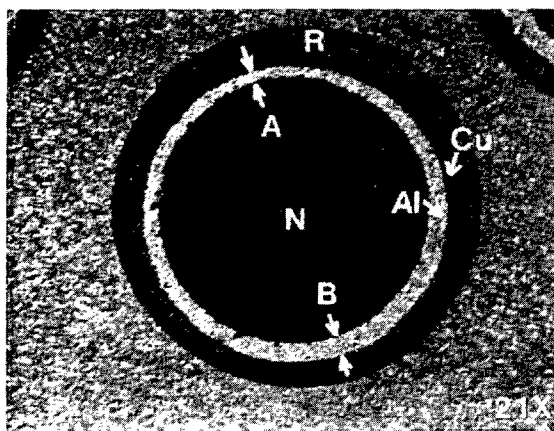


Figure 13: Metallographic cross-section of the aluminum clad steel wire; N = steel core, Al = aluminum, R = mounting resin, A, B = minimum and maximum thickness, respectively.

BOTDR ANALYSIS OF CABLE TENSILE TESTING

Richard Wagman, Jeffery Englebert, Allen Gregory and Keith Lail

Siecor, Hickory, North Carolina

ABSTRACT

A BOTDR measures fiber strain at locations along the length of an optical fiber using Brillouin scattering. The BOTDR was used to analyze a fiber optic cable tensile test, and show the characteristics of the fiber strain during a tensile test. Additionally, the BOTDR was able to locate fiber strain phenomena to within one meter.

Three different types of cable were tensile tested: single tube cable, stranded loose tube cable and an aerial slotted-core cable. A typical tensile test apparatus was used, and fiber strain was measured with a BOTDR and with typical equipment that measures average fiber strain.

Analysis of the BOTDR data showed that there can be incomplete coupling of the fibers to the cable at discrete locations. It showed that average fiber strain can be used to determine the cable strain where fiber strain begins. The analysis also showed that caution must be used when tensile testing non-round cables with grooved sheaves.

INTRODUCTION

A Brillouin Optical Time Domain Reflectometer (BOTDR) measures fiber strain at specific locations along the length of an optical fiber. This is different than typical fiber strain measurements where only the average of the fiber strain is measured^{1,2}. The BOTDR uses the phenomenon of Brillouin scattering to measure fiber strain. Brillouin scattering occurs at high levels of optical power where light traveling down a fiber at one wavelength is scattered at multiple wavelengths (or frequencies). The frequencies of the Brillouin scattering depend on a number of factors including fiber strain. The BOTDR makes use of this relationship to measure fiber strain along the length of an optical fiber.

The BOTDR used for this study has a strain measurement accuracy of 0.01% and a spatial resolution of five meters. Spatial resolution

means that the measured fiber strain at a point along the length of a fiber is calculated from data taken over a five meter length. To make a BOTDR measurement with the 0.01% accuracy, it takes between 6 to 15 minutes to measure one fiber, while typical fiber strain measurements take only seconds. It also takes longer to analyze the data from the BOTDR because of the larger amount of data. For example, in this study, measurements were made at 0.5 meter intervals along the length of the fiber so there were approximately 300 strain values for one BOTDR measurement of one fiber at one condition.

Despite the time consuming nature of the measurements, the BOTDR's unique capabilities have proven useful. It found the location of high fiber strain areas in a submarine cable³, monitored the fiber strain in a new type of aerial cable to determine its performance when deployed aerially⁴, and determined the maximum as well as average fiber strain in a cable tensile test⁵.

In this study, the BOTDR was used to analyze the tensile testing of a cable, to develop a new tensile testing method and to investigate how accurately the BOTDR can locate fiber strain phenomena. First, the tensile test and the cables tested for this study are described. Next, the results and analysis for each cable are presented. Finally, the results from all of the cables are used to study the resolution of the BOTDR.

TENSILE TEST

The tensile test is used to verify a fiber optic cable's ability to withstand tensile and bending forces. This laboratory test is a static test (the cable does not move during the test) that simulates some of the conditions seen during fiber optic cable installation (where cables are typically pulled into position). Both IEC 794-1¹ and EIA-455⁶ describe the type of tensile test performed in this study.

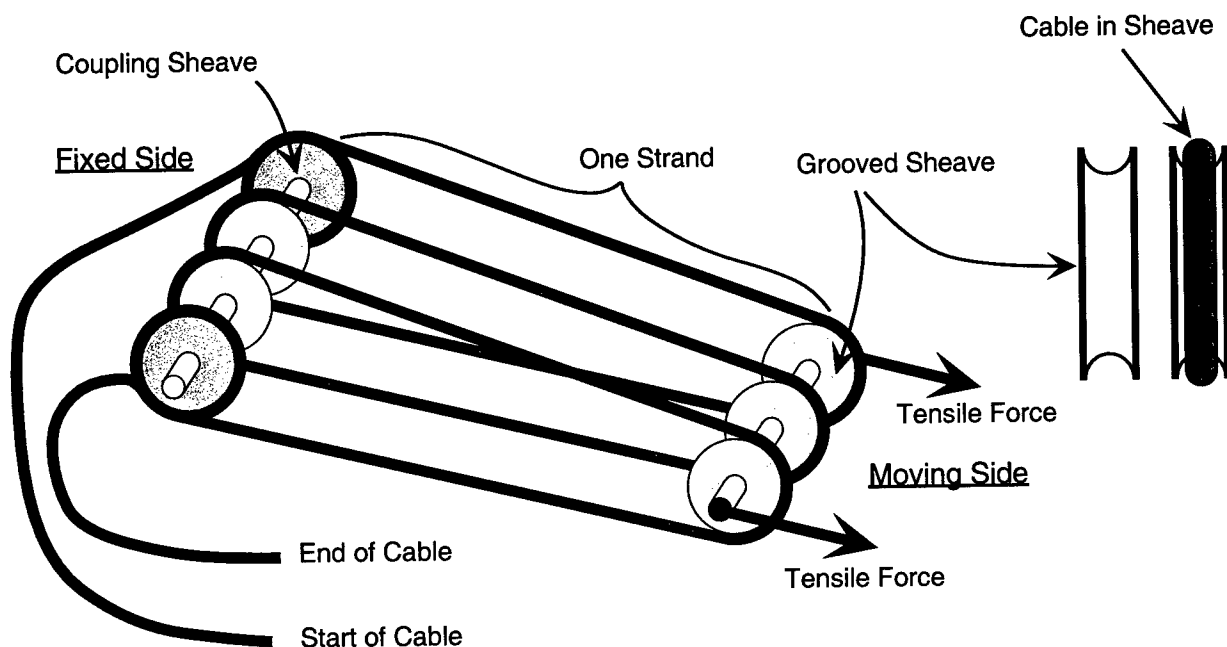


Figure 1. Schematic of the Tensile Test Apparatus

A schematic of the apparatus used to perform the tensile test is shown in Figure 1. At the start of the cable length, the cable is wrapped a number of times around one of the coupling sheaves, which holds the cable. The cable is then wrapped back and forth from the fixed side sheaves to the moving side sheaves to achieve the desired number of strands (number of lengths between the sides). Finally, the cable is wrapped a number of times around the other coupling sheave. This arrangement is similar to a pulley. To apply a tensile load to the cable, the sheaves on the moving side are pulled away from the fixed side. Typically, the fixed and moving sheaves are 15 to 25 meters apart, the sheave diameter is 560 mm, and the sheaves are grooved to keep the cable in place during the test.

For this study, cable stress, cable strain and fiber strain were measured. Cable stress was measured with a load cell, cable strain was measured with a 100 mm precision extensometer, and fiber strain was measured with both the BOTDR and a phase differential measurement system². The phase differential measurement system (because it can measure fiber strain quickly) was used with optical switches to measure many fibers during the tensile test. The phase differential system is based upon the principle that fiber strain is proportional to the amount of time required for light to travel down an optical fiber (time of flight). By comparing the time of flight in a

stressed cable to its time of flight before it was stressed, one can determine if the stress caused an increase in fiber strain.

The test apparatus and measurement system described here is very adaptable. It can be used to tensile test many different types of cables.

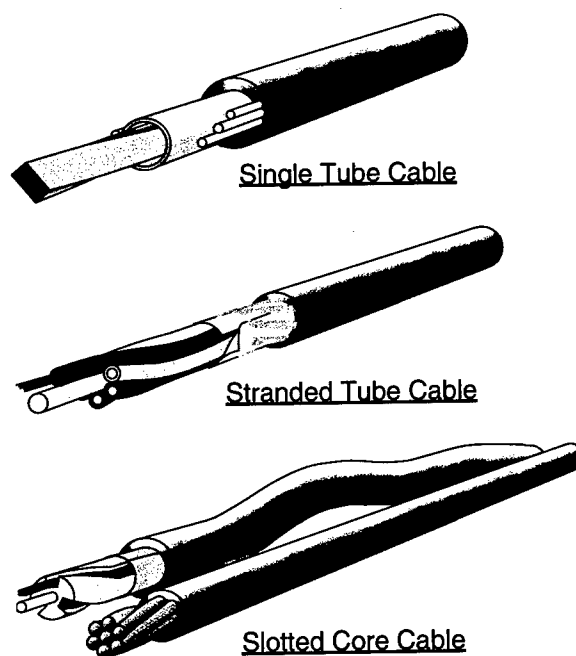


Figure 2. Cables Tested

CABLES TESTED

Three different types of cable were selected to investigate tensile testing with the BOTDR; a single tube cable, a stranded loose tube cable and a slotted core cable. These cable designs, shown in Figure 2, were selected for testing because of their differences. Although the specific cables tested were developmental cables, their behavior was representative of their corresponding cable types.

Single Tube Cable

The single tube cable was a 216-fiber ribbon cable. The ribbon stack was composed of 18 12-fiber ribbons twisted together. The tensile reinforcement for the cable was supplied by 6 fiberglass tensile elements embedded in the cable jacket. This cable design is sometimes called a "preferential bend" design. The fiberglass tensile elements are not stranded around the tube, and they are only on two sides of the cable. This tensile element configuration gives the cable a preferred bending direction.

Stranded Tube Cable

The stranded tube cable was a 72-fiber cable. The cable was constructed by stranding 6 buffer tubes with 12 fibers each around a fiberglass central element, applying a waterblocking tape,

wrapping tensile reinforcement yarns over the buffer tubes, and applying a polyethylene jacket.

Slotted Core Cable

The slotted core ribbon cable was a 24-fiber aerial self-supporting cable⁴. A 6.0 mm stranded steel messenger was used for the aerial support of the cable. The slotted core portion of the cable contained three slots with two 4-fiber ribbons per slot. The jacket of the slotted core cable was connected to the messenger jacket by plastic webs about every 500 mm. This occasional connection allows the slotted core cable to be about 0.2% longer than the messenger.

SINGLE TUBE CABLE TESTING

The developmental single tube cable was tensile tested using 6 strands (a strand is shown in Figure 1) that were each 22 meters long. The cable was taken to relatively high cable strains to investigate the behavior of the fiber strain. Fiber strain was measured on 3 fibers in the second ribbon from the top of the ribbon stack. The number of fibers measured was limited by the time required to make the BOTDR measurements. It took about 20 minutes to measure the 3 fibers with the BOTDR at each level of cable strain.

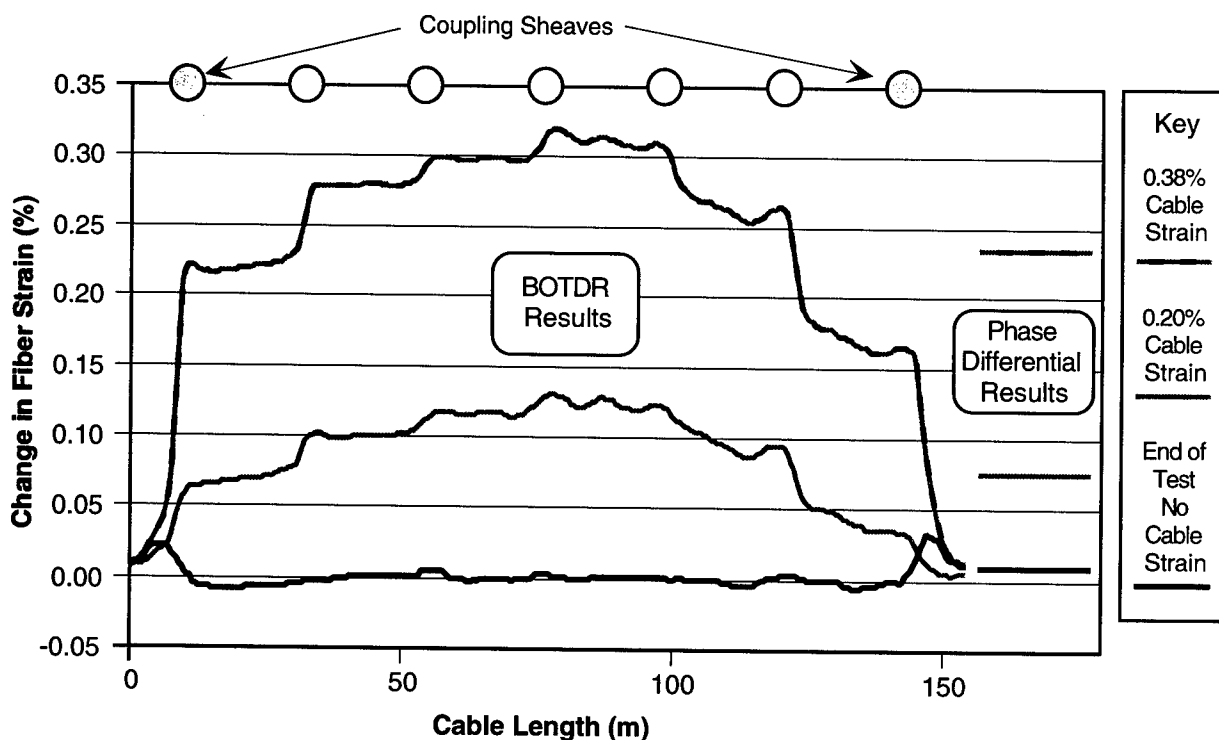


Figure 3. Single Tube Induced Fiber Strain Versus Length

A summary of the fiber strain results for one fiber is shown in Figure 3. All three fibers had similar values of fiber strain. The BOTDR results are plotted as change in fiber strain from the initial measurement (no tensile load) versus cable length. The positions of the sheaves (the sheaves of the tensile test apparatus shown in Figure 1) along the length of the cable are indicated at the top of the graph. The horizontal lines on the right hand side of the graph are the fiber strain results from the phase differential system

The peak values of the BOTDR fiber strain occur in the middle of the length under test. If the strain lines are followed from the middle towards the coupling sheaves, one can see that each successive strand has a decrease in strain. This tiered response indicates that ribbon movement occurs when the cable is subjected to a static load. At the coupling sheaves small amounts of ribbon length "leak" (move) into the length under test thereby decreasing the fiber strain. One indication of this leakage is the peaks in fiber strain at the coupling sheaves at the end of the test where there is no cable strain. To get the tiered response there must be ribbon leakage also occurring at the other sheaves. Obviously, the 560 mm diameter sheaves used in this static test do not completely couple the ribbon stack to

the cable. However, these sheaves were small enough to cause small increases in fiber strain. At 0.38% cable strain, there are small strain peaks at each of the sheaves.

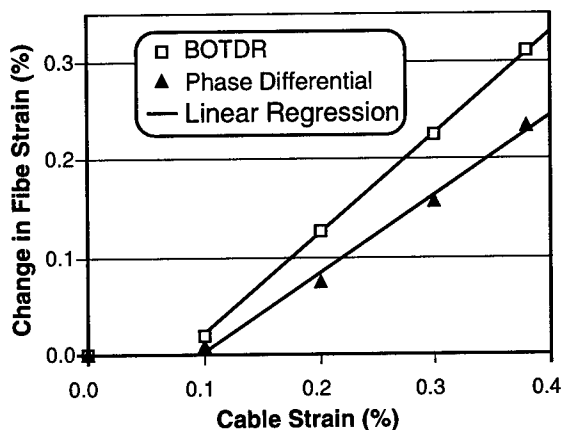


Figure 4. Single Tube Induced Fiber Strain Versus Cable Strain for Two Different Measurement Techniques

Although the phase differential results did not measure the maximum fiber strain, these results were within 0.01% of the average fiber strain measured by the BOTDR for all of the tested fibers. Additionally, the phase differential results can be used to determine where fiber strain

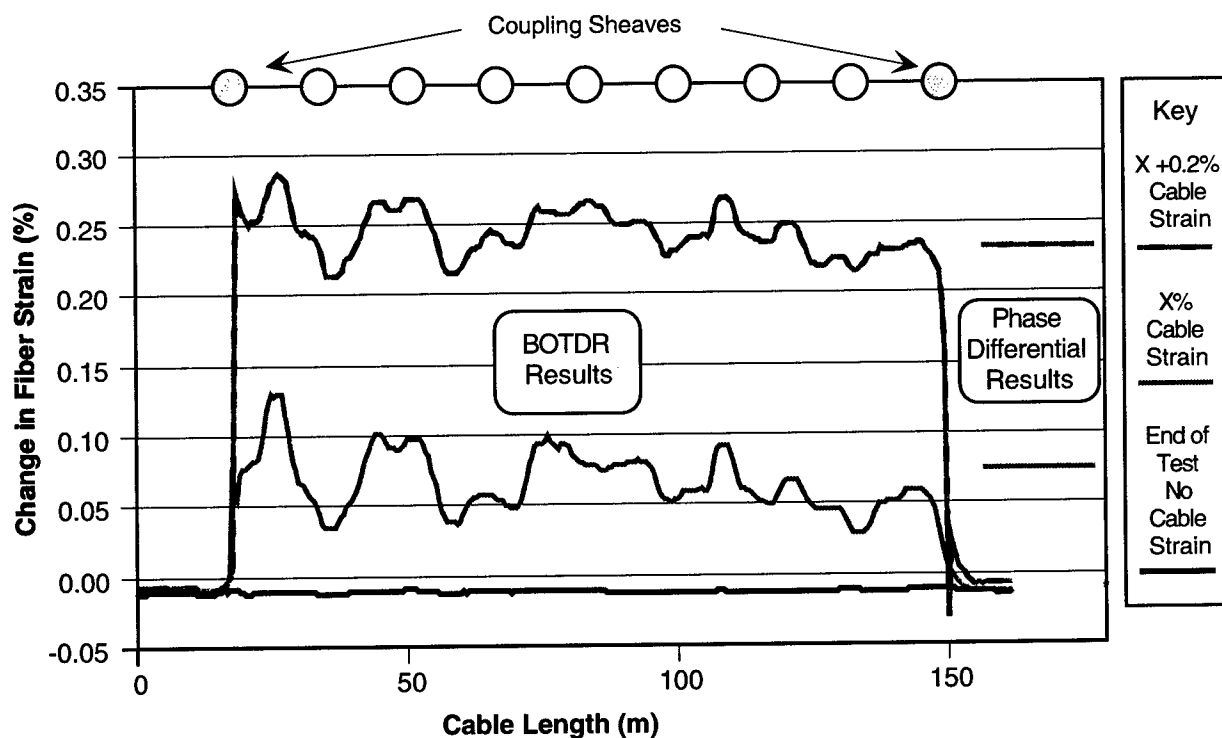


Figure 5. Stranded Tube Induced Fiber Strain Versus Length

began to occur in this cable. Figure 4 shows the graph of change in fiber strain versus cable strain for the same fiber graphed in Figure 3. The BOTDR results in Figure 4 come from a point in the middle of the cable length (87 meters). The lines in Figure 4 are the "best fit" lines from linear regression of both the BOTDR and phase differential results between 0.1% and 0.4% cable strain. These lines predict a cable strain where fiber strain begins. The predictions for the BOTDR and phase differential system are within 0.02% of each other.

For the single tube cable, the BOTDR was able to show the partial coupling of the ribbons to the cable at the coupling sheaves. It also showed that the phase differential measurements accurately predicted (to within 0.02%) the cable strain where fiber strain begins.

STRANDED TUBE CABLE TESTING

The developmental stranded loose tube cable was tensile tested using 8 strands that were each 15.6 meters long. The cable was also taken to relatively high cable strains to investigate the behavior of the fiber strain. Stranded loose tube cables are normally designed to see little if any fiber strain under normal installation and operating conditions.

BOTDR fiber strain was measured on one fiber in each of the six buffer tubes. The phase differential system was used to measure another fiber in each buffer tube.

A summary of the fiber strain results for one fiber is shown in Figure 5. This graph has the same format as the one in Figure 3. Only one fiber is shown because all of the fibers had similar trends.

There are two notable differences between this data and the data for the single tube cable. With the stranded tube cable (1) there are not increases in fiber strain at every sheave, and (2) there is good coupling of the fibers to the cable at the coupling sheaves. In contrast to the single tube cable, the BOTDR fiber strain drops off more rapidly at the coupling sheaves, and the BOTDR fiber strains are within $\pm 0.05\%$ of the fiber strain measured by the phase differential system.

For the stranded tube cable in Figure 5 there are a large number of peaks and valleys in the BOTDR fiber strain. These localized differences decreased at higher cable strains. This indicates movement of the optical fiber to equalize the fiber strains, but much less movement than seen with the single tube cable.

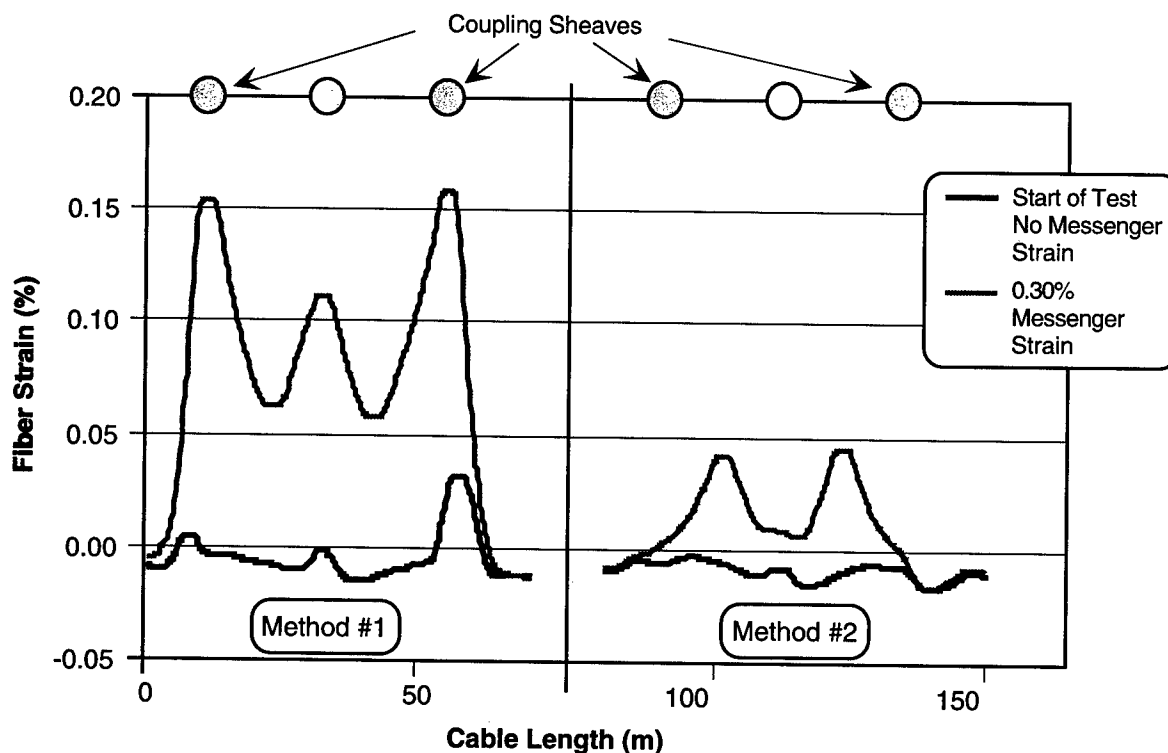


Figure 6. Slotted Core Induced Fiber Strain Versus Cable Length for Two Different Test Methods

The probable reason for the difference is the stranding. Just as bending around the coupling sheaves tends to couple the fibers to cable, the stranding of the tubes will tend to cause the same type of coupling. In the middle of the length under test, stranding minimizes fiber movement, while at the coupling sheaves, the extra bending from stranding combines with the bending from the sheave to achieve good coupling between the fibers and the cable.

For the stranded tube cable, the BOTDR was able to show the complete coupling of the fibers at the coupling sheaves. It also shows that the stranding of the buffer tubes inhibits the movement of the optical fibers along the length of the cable.

SLOTTED CORE CABLE TESTING

The developmental slotted core cable was tensile tested using 2 strands that were each 22 meters long. The intent of the testing was to identify the level of messenger strain where fiber strain begins to increase. In-process measurements indicated that the optical portion of the cable was between 0.20% to 0.25% longer than the messenger. For this testing BOTDR fiber strain was measured on one fiber in the cable, and the phase differential system measured all of the fibers in the cable.

Two tests were performed on the slotted core cable. A summary of the BOTDR fiber strain results is shown in Figure 6. This graph has the same format as in Figures 3 and 5 except the Y-axis is the measured fiber strain instead of change in fiber strain. Measured fiber strain is shown in this case because there was character in the fiber strain at the start of the test. In the

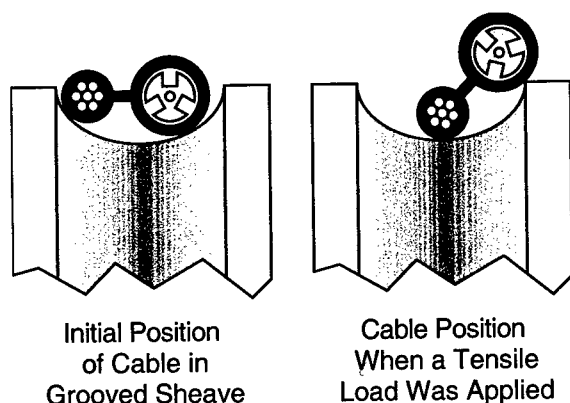


Figure 7. Cable Rotation in Grooved Sheave

first test (Method #1), there were high fiber strains at all of the sheaves. These strains are explained by observations made during the tensile test. As shown in Figure 7, the cable rotated in the grooved sheaves as the tensile load was applied. The messenger (the main strength component of the cable) was pulled into the middle of groove, and the optical portion of the cable was pushed out to a larger radius. This larger radius means that the optical portion had a longer path length around the sheaves.

To eliminate the problem with the grooved sheaves, the optical portion of the cable was separated from the messenger, and only the messenger was wrapped around the sheaves. The test results for this setup are shown in Figure 6 as Method #2. Because the optical portion of the cable was not wrapped around the coupling sheaves, only the stranding of the slots served to couple the ribbons to the cable. There was only complete coupling in the middle 5 meters of each strand. In Figure 6 these middle 5 meters appear as plateaus in the BOTDR fiber strain.

The average of the phase differential results for Method #2 and the maximum strain measured by the BOTDR are shown in Figure 8. In this graph the change in fiber strain is relative to the initial measurement. Both the BOTDR and the phase differential measurements show that fiber strain begins between 0.20 and 0.25% as predicted by in-process measurements. Just like the single tube cable, these phase differential results can be used to accurately estimate the cable strain where fiber strain begins.

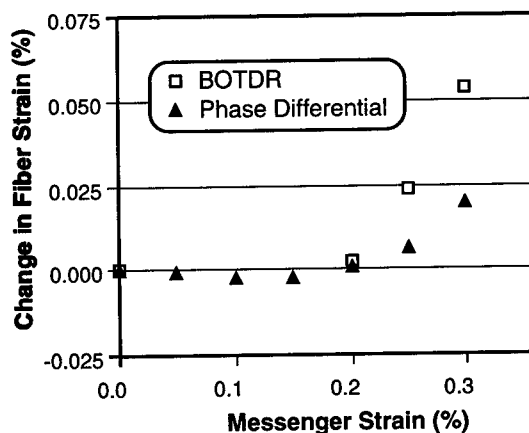


Figure 8. Slotted Core Induced Fiber Strain Versus Cable Strain for Two Different Measurement Techniques

For the slotted core cable, the BOTDR helped to identify a problem with the tensile test method, and it was able to verify that a different method adequately measured the cable parameter of interest. It also showed that the phase differential measurements accurately predicted the cable strain where fiber strain begins.

RESOLUTION OF THE BOTDR

As stated early, the BOTDR for this testing had a spatial resolution of 5 meters. Even with a 5 meter resolution, there are many cases of the BOTDR data identifying strain locations to within 1 meter of their actual location.

- For the single tube data (Figure 3), the BOTDR identified small increases in strain within 1 meter of the actual location of every sheave on the tensile test apparatus.
- For the stranded loose tube data (Figure 5), the strain changed from 0.0% to nearly 0.3% within 0.5 meters. This rapid change is shown on the left hand side of the BOTDR data in Figure 5.
- For the slotted core data (Figure 6) in Method 1, the highest strains occur at the sheaves. For Method #2, the highest strains occur in the middle of each strand.

The surprisingly good resolution of the BOTDR may be explained by considering the accuracy of the strain measurements. The 5 meter spatial resolution is given along with a fiber strain accuracy of 0.01%. This implies that while the location of a peak in strain may be determined with an accuracy of less than 5 meters, the value of the fiber strain at that point may not necessarily be accurate to within 0.01% fiber strain.

CONCLUSION

In this study, the BOTDR has proven useful in developing a more detailed understanding of the fiber optic cable tensile test. Because the tensile test is only a simulation of installation conditions, the results of this study are not directly applicable to actual cable installations. However, a number of points can be made about the tensile testing of cables.

- The phase differential method of measuring fiber strain does not measure the maximum fiber strain; however, this method can be used to determine the cable strain where fiber strain begins.

- Cable bending at the coupling sheaves is not always adequate to completely couple the optical fibers to the cable.
- Caution must be used when tensile testing cables that are not round if the sheaves of the tensile test apparatus are grooved.

This study shows the BOTDR has both advantages and disadvantages. For example, the BOTDR was able to locate strain phenomena in a cable to within 1 meter, while the number of fibers tested with the BOTDR was limited because of the length of time required to make a BOTDR measurement. These properties make the BOTDR an extremely useful analytical tool, but an inappropriate tool for routine testing.

ACKNOWLEDGEMENTS

This paper would not have been possible without the assistance of many people; however, the authors would like to especially recognize the guidance of the late Dr. Christopher Eoll.

REFERENCES

1. IEC 794-1, "International Standard Optical Fibre Cables – Generic Specification," Fourth Edition 1996-10, International Electrotechnical Commission.
2. EIA-455-38-95, "FOTP-38 Measurement of Fiber Strain in Cables Under Tensile Load" 1995, Electronic Industries Association.
3. C. Sandwith, W. McCormick, J. Thorton, D. Wise, R. Odom, "Fiber-Strain Measurement Using Brillouin Optical-Fiber Time-Domain Analysis," Proceedings of the 45th International Wire and Cable Symposium, pp. 415-427, 1996.
4. H. Iwata, M. Okada, S. Tomita, N. Kashima, T. Hoshijima, M. Kama, K. Nishizawa, "Design of Aerial Optical Fiber Cable System Suitable for Easy Branching," Proceedings of the 46th International Wire and Cable Symposium, pp. 4-11, 1997.
5. H. Iwata, M. Okada, J. Sogame, H. Akimoto, S. Tomita, Y. Dei, "Development of 2000-Fiber Cable with SZ-Stranded U-Grooves and Slotted Rod," Proceedings of the 47th International Wire and Cable Symposium, pp. 34-40, 1998.
6. EIA-455-33A, "FOTP-33 Fiber Optic Tensile Cable Loading and Bending Test," 1988, Electronic Industries Association.



Richard S. Wagman
Siecor - RD
P.O. Box 489
Hickory, NC 28603-0489

Richard Wagman was born in Dallastown, PA, in 1956. He received his B.S. degree in the Engineering Science honors program at Pennsylvania State University in 1978 and his B.S. in Electrical Engineering from Johns Hopkins University in 1984. He joined Siecor in 1985, where he has worked with cable, materials and test design. He is currently employed in the Research, Development and Engineering Department as a Subject Matter Expert in Cable Design.

A NEW MONITORING TECHNIQUE FOR PASSIVE OPTICAL NETWORKS

M. Bottanelli, E. Cottino, M. Maglio

Sirti. S. p. A. – R & D Dept. - Cassina de' Pecchi (MI) – Italy

ABSTRACT

The application of a particular technique for the optical monitoring of ribbon cable based PONs is reported. The advantages of this technique in terms of network protection and cost reduction are underlined.

This paper deals with a new monitoring technique for point-to-multipoint Passive Optical Networks. The advantages of this technique in terms of network protection and cost reduction are underlined.

INTRODUCTION

Nowadays, a number of administrations and operating companies have installed or are planning to install maintenance systems in order to monitor the quality of their optical fiber networks.

The last generation of high performance optical monitoring systems is based on powerful multitasking workstations, high dynamic range/resolution 1600-1650 nm OTDR and multichannel optical switches.

The fruitful utilization of optical monitoring system in core networks has been already demonstrated in the past firstly by means of field trials and afterwards on operating networks.

Nowadays, at international stage, a deep discussion about the application of monitoring techniques in the access network is in progress, particularly concerning Passive Optical Networks (PONs).

Although the application of monitoring techniques to PONs is generally considered useful, it is also generally considered premature and expensive. However, the simultaneous analysis of both the construction and the monitoring aspect can drive to the definition of cost-effective network solutions, especially for particular situations.

REFERENCE ACCESS NETWORK ARCHITECTURE

It is universally accepted that point-to-multipoint PON architecture constitutes a highly severe test bench for OTDR-based optical monitoring systems, due to the superimposition of back-reflections from the different arms of the splitting stages.

A limited number of solutions have been proposed to overcome this problem¹, the most of them being unpractical according to technical or economic considerations.

However the importance of the problem can be reduced and solved by considering a well-defined PON architecture instead of a generic one.

In the Italian country, for instance, due to a set of considerations, it seems to be reasonable a 16 typical number of ONUs for one single OLT; moreover, network design optimization and flexibility requirements suggest the adoption of two splitting stages along the network, the first directly placed in the central office and the second in the field; finally, traditional Italian distribution network is based on a ring topology and on 4 optical fibers ribbon cables. Figure 1/a sketches the described reference access network architecture.

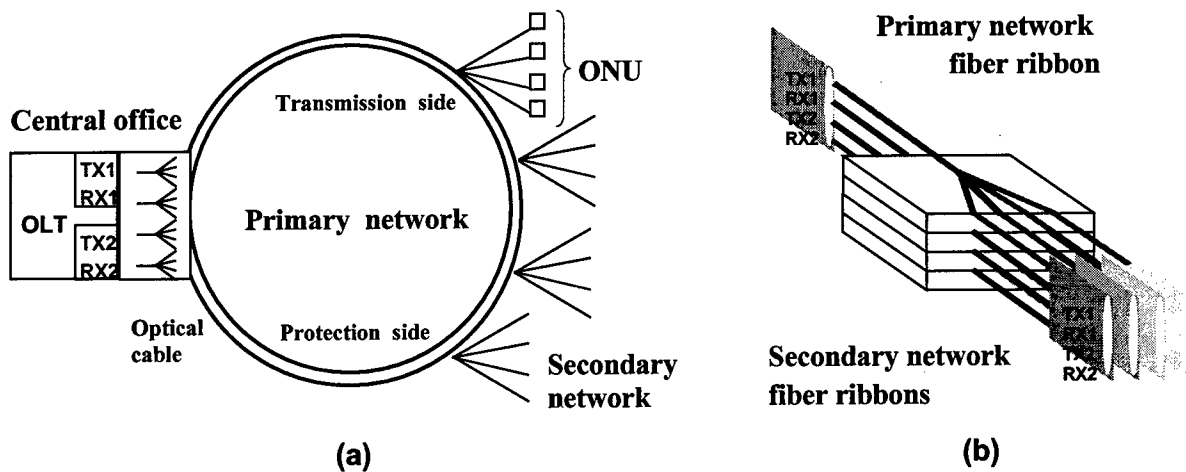


Figure 1 – Reference access network architecture (a) and integrated optical component for the second splitting stage (b)

It is worth to notice that the practical construction of such a network requires the availability of an integrated solution for the second splitting stage to simplify fiber junction operations in the field. Figure 1/b reports the scheme of a possible integrated optical component for this goal.

Moving from these considerations, a new optical monitoring technique has been developed and applied to the considered reference access network architecture.

A NEW INTEGRATED MONITORING TECHNIQUE FOR PASSIVE OPTICAL NETWORKS

Figure 2 illustrates our solution for the figure 1/a PON architecture (for the sake of simplicity, the first splitting stage is not illustrated and only 2 of the total 8 fiber per OLT are reported in the primary ring section of the network).

The solution is based on the two new integrated optical elements, which are sketched in figure 3: a splitting (SE) and a looping (LE) element. By means of these two elements, the point-to-multipoint PON architecture is reduced to a point-to-point one at the 1625 nm optical monitoring wavelength.

So, for instance, following the dotted line in figure 2, by means of an optical switch the monitoring system injects the 1625 nm OTDR signal into the TX2 fiber, just immediately beyond the first splitting stage in the central office. The 1625 nm signal passes then through the SE3-LE3-SE2-LE1 elements and through the 1-3 and 2-4 optical fibers of the secondary network arms 3 and 1. The OTDR trace can then be easily fully analyzed without any superposition, according to a properly configured PON network database. Monitoring performances of the same kind can be achieved injecting the 1625 signal into other fibers of the primary portion of the access network.

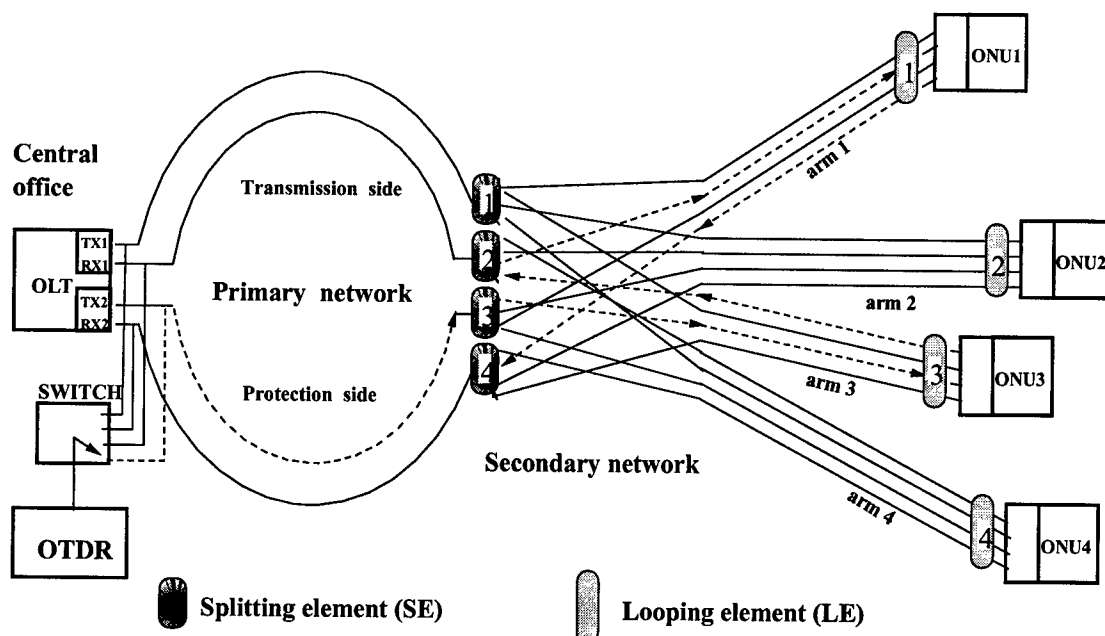


Figure 2 – Application of the new monitoring technique in the case of a 1x16 – 4 fibers ribbon based PON

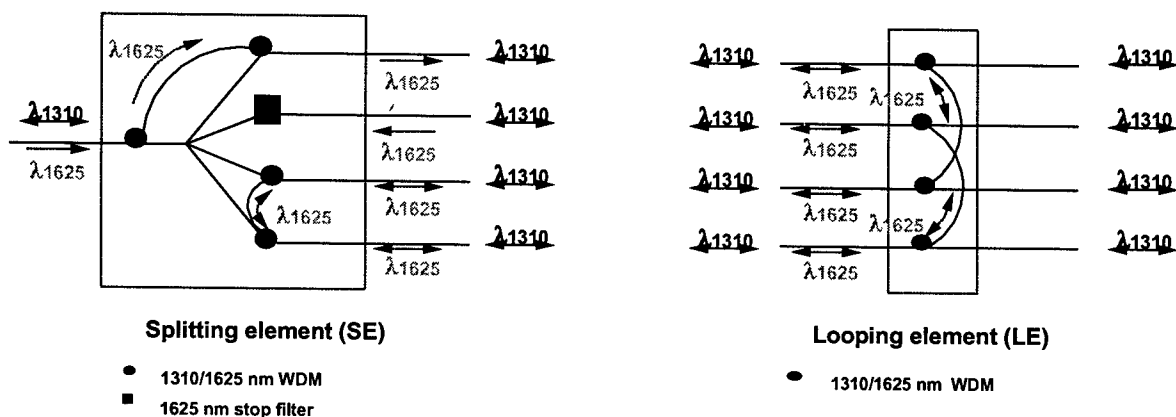


Figure 3 – Splitting and looping elements for the new monitoring technique

A quite similar solution (the so-called “Chained branches” technique) has been already proposed in the past, but it is generally considered

unpractical and expensive¹. However, the application to a particular reference access network architecture, the optimization of the

optical monitoring path with respect to the network protection mechanisms and the design of ad-hoc integrated optical components are peculiar features of the new proposed technique. These features make the new solution particularly attractive in terms of network protection and cost reduction.

Figure 4 reports a more detailed description of the new solution, with respect to the secondary portion of the access network only, emphasizing the different paths for the monitoring signal on the

different PON arms. The 1625 nm optical signal, travelling for instance into the TX1 fiber, monitors in sequence two fibers respectively of arm 1 and the arm 4: the remaining other 2 fibers of the two arms are monitored injecting the 1625 signal into the TX2 or the RX2 fiber, i.e. from the other side of the primary optical ring. By means of this ad-hoc protection scheme, in the case of fiber degradation or fault, in the primary or in the secondary portion of the network, it is always possible to monitor at least two optical fibers of every PON arm.

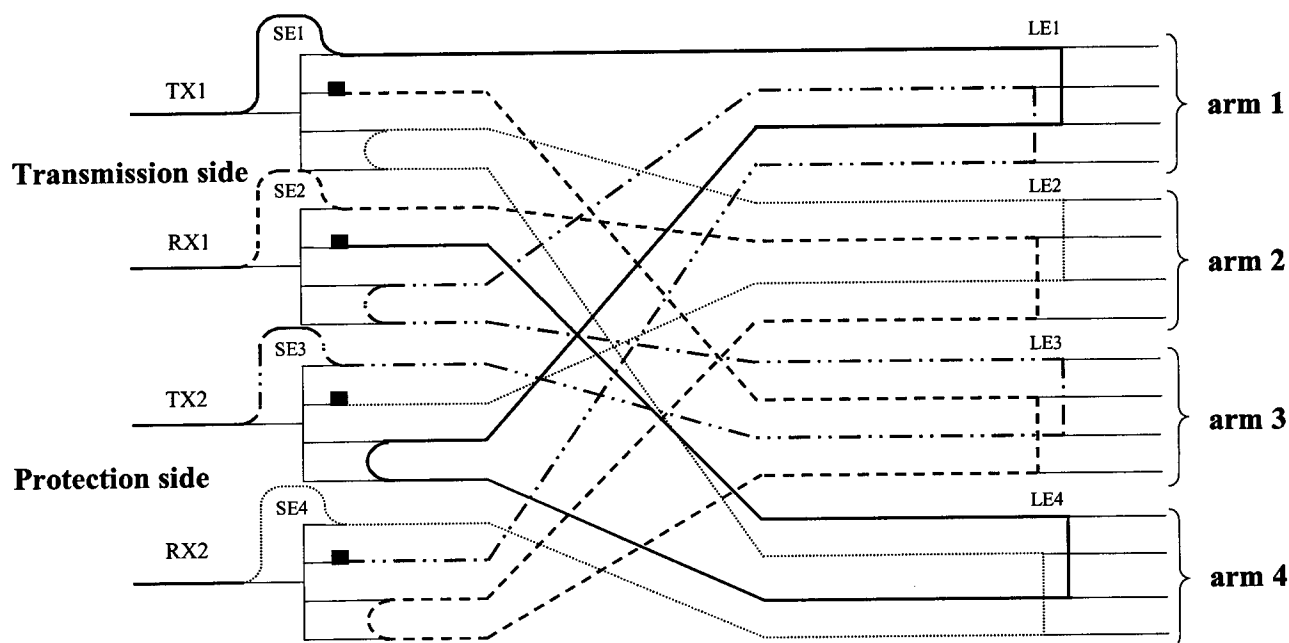


Figure 4 – Detailed scheme of the monitoring signal optical paths

The scheme of figure 4 has been simulated by means of a laboratory test-bed, using ITU-T G.652 type fiber and fusion splitters and WDMs, with a 4 km long primary network and a secondary network having two 0.6 km long arms and 2 km long other two arms. Figure 5 reports the OTDR trace, which has been obtained with reference to the situation of figure 2 (monitoring signal injected into TX2 fiber). In order to verify

the sensitivity of the system, a punctual stress has been simulated on the arm 1 fiber ribbon. Moreover, a SDH 155 Mbit/s 1310 nm signal has been transmitted along the test-bed network by means of a HP37717 source/analyzer: no influence of the monitoring signal on the SDH signal has been detected in terms of BER performances.

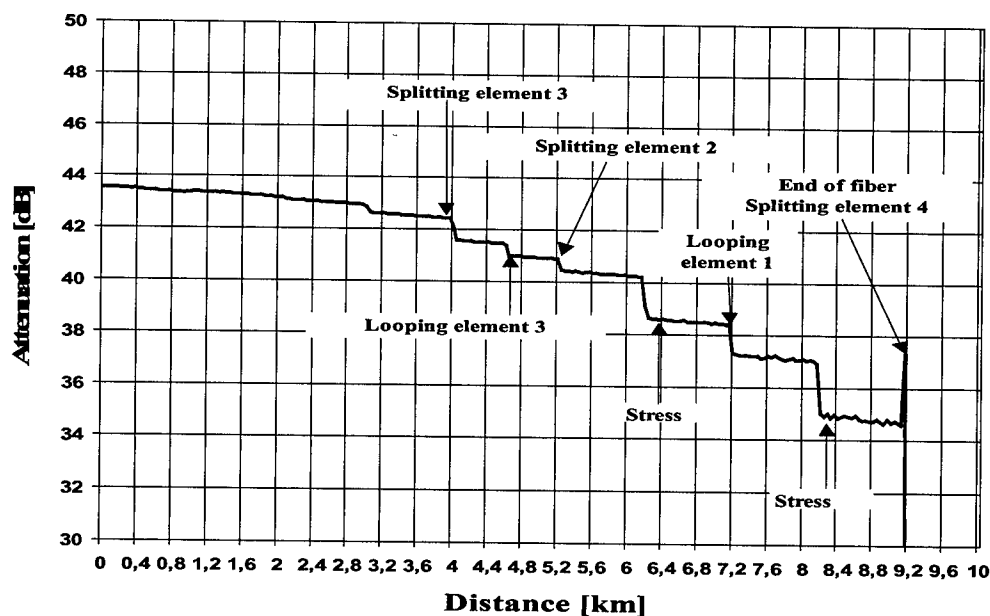


Figure 5 – OTDR trace for a test-bed simulation on the figure 4 scheme (the monitoring signal was injected into TX2 fiber)

INSTALLATION ASPECTS AND COST REDUCTION

Figure 2, 3 and 4 schemes can be simplified for practical applications according to the following considerations.

The most important problem is to avoid errors and speed-up the fiber junction operation in the field on the splitting and looping elements. This can be solved by means of factory pre-assembled splitting and looping modules with already ribbonized input and output fibers. With reference to figure 1/b, for instance, that can be achieved by using the proposed monitoring splitting elements (see figure 3), instead of the simple optical splitters, in the integrated optical component for the second splitting stage. The implementation of the looping modules is, of course, even simpler.

Splitting and looping elements can be obtained by assembling discrete fusion splitters and WDMs, or can be directly designed and implemented by

using planar silicon technology: in both the cases, splitting and looping modules have always the same configuration, with important advantages in terms of cost reductions.

Finally, note that adaptation to other different PON topologies and cable structures can be easily achieved (simplified SE and LE elements can be designed for single fiber cable networks, for instance).

Figure 6 reports a cost comparison (in terms of materials only) among the literature proposed main PON monitoring techniques (see reference¹ for details) and our new solution, whose cost has been supposed to be 100.

With respect to the considered reference access network architecture, our solution is the cheapest one.

Moreover, considering the 1:16 PON whole construction, the incidence of our new monitoring solution on the total costs can be limited at less than 3 %.

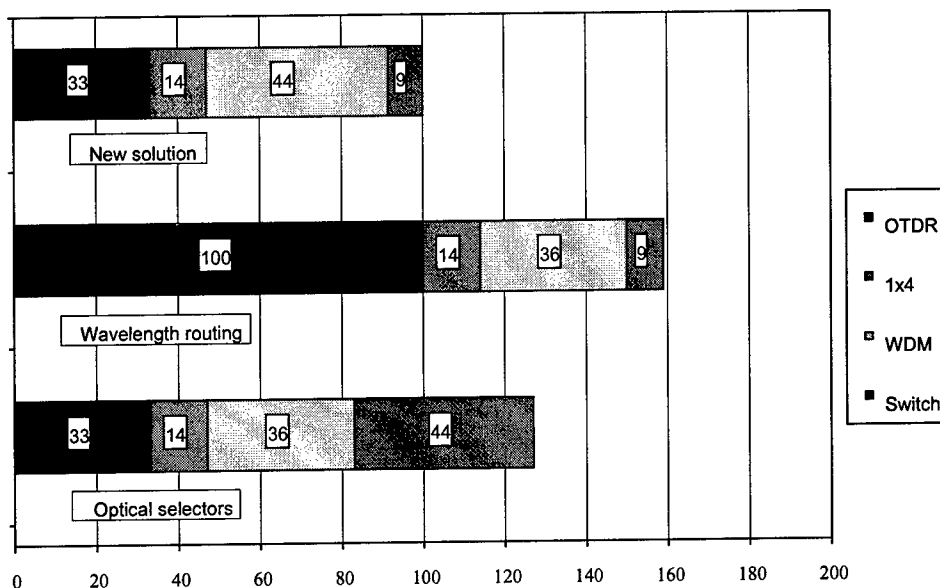


Figure 6 – Cost comparison among PON monitoring techniques

CONCLUSIONS

A new monitoring technique for point-to-multipoint Passive Optical Networks has been described.

The advantages of this technique in terms of network protection and cost reduction can be summarized as in the following:

- No trace superposition in the 1625 nm OTDR monitoring signal;
- Full protection against optical fibers network degradation or faults;
- Easy adaptation to different PON topologies and cable structures;
- Cost reduction with respect to traditional solutions, by means of the direct integration of monitoring function in the network design and construction.

REFERENCES

- [1] F. Caviglia, V. C. Di Biase
Optical Maintenance in PONs.
 Proceedings of ECOC '98, Madrid, September 20-24, 1998 - vol. 1, pp. 621-625.



Mauro Bottanelli

Cables and Optical
 Tech.-R&D Dept.
 SIRT I S.p.A.
 Via E. Fermi, 2 - 20060
 Cassina de' Pecchi (MI)
 ITALY

Mauro Bottanelli was born in 1963. He received the Dr. Ing. degree in Nuclear Engineering from the Polytechnic of Milan. After a two years activity in the field of industrial automation, he joined SIRT I in 1990 as research engineer in the field of optical fiber and optical component characterization, and of broadband access network design. He is a member of the ITU-T SG 6 National Working Group.

LOW SPEED CARBON DEPOSITION PROCESS FOR HERMETIC OPTICAL FIBERS

Eric A. Lindholm, Jie Li, Adam S. Hokansson, Jaroslaw Abramczyk
Spectran Specialty Optics Company, Avon, CT

Sara E. Arthur, David R. Tallant
Sandia National Laboratories, Albuquerque, NM

ABSTRACT

For optical fibers used in adverse environments, a carbon coating is frequently deposited on the fiber surface to prevent water and hydrogen ingress that lead respectively to strength degradation through fatigue and hydrogen-induced attenuation. The deposition of a hermetic carbon coating onto an optical fiber during the draw process holds a particular challenge when thermally-cured specialty coatings are subsequently applied because of the slower drawing rate. In this paper, we report on our efforts to improve the low-speed carbon deposition process by altering the composition and concentration of hydrocarbon precursor gases. The resulting carbon layers have been analyzed for electrical resistance, Raman spectra, coating thickness, and surface roughness, then compared to strength data and dynamic fatigue behavior.

INTRODUCTION

In applications that demand optical fibers with high resistance to static fatigue and hydrogen-induced loss, hermetic coatings are often used. Although organic polymeric coatings are usually applied to glass fibers to provide initial protection, these coatings cannot adequately prevent the diffusion of water or hydroxyl ions that lead to mechanical degradation. This is especially true in applications where the fiber is subjected to high temperatures and high pressures as in a geophysical or geothermal environment. For these applications, the primary function of the hermetic coating is to block water from reaching the silica glass surface to prevent the growth of microcracks and insure long-term

reliability. Research into hermetic coatings are split into two areas: metallic coatings and inorganic coatings.

Metallic coatings were first investigated to improve the static fatigue resistance of optical fibers (Pinnow, et al., 1979). Although methods for coating optical fibers with metal include sputtering, vapor deposition and dip coating, the only technique known to produce hermetic metal coatings is known as "freezing", i.e. drawing the fiber through a metal melt.¹ Some of the metals tested have been aluminum, tin, zinc, indium, silver and gold; as such, fibers coated with metallic coatings tend to be very expensive. In addition, the freeze-coat technique is reportedly difficult to control and not well understood.² The relatively thick coatings ($\approx 20\mu\text{m}$)³ can lead to unacceptable microbending losses and long lengths of pinhole-free fiber have proven elusive.⁴

Inorganic coatings are applied to the glass fiber during the draw process by means of chemical vapor deposition. For carbon coatings specifically, a hydrocarbon precursor gas is introduced to the fiber at an elevated temperature ($\approx 800\text{--}1000^\circ\text{C}$) and thermal decomposition (a.k.a. "cracking") of the gas leads to the deposition of carbon on the surface of the glass. The applied carbon layer is typically thin ($<100\text{ nm}$), opaque, electrically conductive, highly adherent to the glass surface via chemical bonding, and amorphous to X-ray diffraction.⁵ Ultimately, the reactor design, the precursor gas, and the reaction temperature, will have a strong influence on the deposition rate and the characteristics of the carbon layer.⁶

It is well-established that the retained heat of the fiber drives the pyrolysis of the hydrocarbon to produce the bonded carbon layer. Thus, carbon deposition is largely dictated by the position of the reactor and the draw speed, which determines the fiber temperature at the reactor. Huff, et. al., further maintain that a higher fiber temperature increases the number of broken Si-O bonds on the surface of the glass which augments the Si-C chemical bonding at the glass/carbon interface.⁷ Two corollaries that follow are that the fiber reactivity and thus the carbon deposition will be enhanced with 1.) higher draw speeds or 2.) application of the carbon coating as close to the neckdown area as possible. Moving the reactor closer to the pulling furnace has the added advantage of minimizing exposure to atmospheric water that may attach to the glass surface before the carbon layer is applied. High draw speeds (>5m/sec) are typical when drawing standard telecommunication fibers with UV-curable coatings. The retained heat of the fiber will be sufficient to crack the hydrocarbon in a reactor below the pulling furnace; indeed, on most high-speed towers, cooling tubes are employed to reduce the fiber temperature before the liquid coating is applied. However, the carbon deposition process takes on a special challenge when fiber is made at relatively low draw rates. This may be necessary when working with thermally-cured coatings that require a longer time to solidify on the fiber. Another limiting factor may be the in-line addition of plastic buffers (e.g. Tefzel) applied with extrusion equipment.

Because the amorphous carbon layer is conductive, the applied carbon thickness can be estimated through electrical resistance measurements. The formula⁸ relating the resistance to thickness is:

$$R = \frac{\rho}{\pi \bullet D \bullet T}$$

where: R = Electrical resistance (kΩ/cm)
 ρ = Carbon layer resistance (Ω•cm)
 D = Fiber diameter (μm)
 T = Carbon layer thickness (Å)

As the electrical resistance of the carbon layer decreases, either the applied carbon resistance is decreasing or the layer thickness is increasing; either of these characteristics is desirable for the

purposes of improving the static fatigue performance and hydrogen-loss prevention of the fiber. Nakamura, et. al., analyzed carbon through electron spin resonance and found that lower permeability of hydrogen correlates to an increased particle size which is further related to the extent of graphite-like carbon in the deposited layer.⁹ Similarly, Sikora, et. al., stated that the electrical resistance is a function of crystalline size, orientation and perfection. The larger the crystalline size, the smaller the energy gap between the valence and conduction bands, thus a lower resistivity.¹⁰

Table 1: Electrical resistance of carbon

	Carbon layer resistance
Amorphous carbon	$60 \times 10^{-4} \Omega \bullet \text{cm}$
Graphite crystal	$0.39 \times 10^{-4} \Omega \bullet \text{cm}$
Calculated ¹¹ resistance of 300Å thick carbon layer on 125μm fiber at 15 kΩ/cm	$17.6 \times 10^{-4} \Omega \bullet \text{cm}$

Assuming a constant resistivity, a lower electrical resistance would indicate a thicker applied layer. The accepted model for the applied carbon is that of disordered platelets (sometimes called "ribbons"), or small graphitic crystals, attaching to the glass surface and forming a continuous carbon structure. However, because of the random orientation of the platelets, microvoids can form as pathways for water or hydrogen permeation necessitating a minimum carbon layer thickness. That is, the carbon layer thickness required to insure hermeticity depends on the carbon structure. Generally speaking, it is preferable to have a high graphite content with the corresponding large crystal size with the platelets aligned to the surface of the fiber. Because the alignment of the platelets indicates the continuity of the carbon layer, the issue of carbon layer roughness has been explored. For example, Aikawa, et. al., analyzed carbon-coated fibers with similar carbon thicknesses, but with increasing roughness as measured by AFM. The samples with a smoother surface exhibited lower hydrogen-induced loss; the authors concluded that a smaller boundary area reduces the pathways for hydrogen diffusion.¹² In another study, roughness measured on STM was further related to resultant fiber strength.¹³

The strength penalty associated with carbon-coated fibers as compared to untreated fibers is well documented. The reasons for the strength reduction with carbon are related in part to the deposition method used and in part with the carbon layer itself. The thermal decomposition of the hydrocarbon gas generates soot particles as a side-product which can reduce fiber strength and interfere with the chemical bonding on the glass surface. If the reactor is hot enough, spontaneous reaction of the hydrocarbon may occur leading to soot in the reactive gas and deposited to the inside of the reactor. Therefore it is necessary to control the reactor design and deposition process to minimize soot generation and interaction with the bare fiber. The carbon layer itself is as brittle as the glass and, because it is deposited at an elevated temperature and has a different coefficient of thermal expansion than glass, will apply a residual tensile stress to the fiber upon cooling. In addition, because the carbon layer has a lower failure strain than pristine silica, the carbon layer will fail before the fiber. Several studies have indicated that a thicker carbon layer will produce a lower fiber strength but an improved resistance to fatigue and hydrogen ingress.¹⁴ For applications where a fiber will be cabled and operated below the fiber proof test level, a thicker carbon layer may be preferable to ensure a minimum thickness is present to exclude diffusion pathways caused by microvoids. Glaesemann has concluded that a carbon-coated fiber with a high fatigue constant (>150) can operate at up to 80% of the proof test level as opposed to silica fiber (with an "n" value around 20) that should not operate with a long-term stress above 20-30% the proof test level.¹⁵ In addition, for fibers used in harsh environments where static fatigue may be accelerated through water or OH⁻ permeation, DiMarcello, et. al., have concluded that an optical fiber should have a tensile strength of 500 kpsi or greater and a minimum fatigue factor of 150.¹⁶

Based upon this body of information, we here present our efforts to extend and improve the hermetic carbon deposition process within the confines of the low-speed draw process.

DATA AND DISCUSSION

Carbon deposition process

Fiber samples were drawn to a 125 μ m glass diameter and coated with a carbon layer then a thermally-cured polyimide coating to a size of 130 μ m. The electrical resistance of the carbon layer was measured with an ohm-meter after the draw speed had stabilized and before the polyimide coating was applied. By controlling the final draw speed, the pyrolysis temperature of the precursor hydrocarbon gases at the reactor was held close to a standard for each test. Two hydrocarbon precursor gases were used and two mixtures of gases in different concentrations: hydrocarbon "B" (Spectran's current standard or "base" hydrocarbon), hydrocarbon "A" (designated as "additive"), an 8:1 mixture of B:A by volume, and a 2:1 mixture of B:A by volume. To isolate the test fiber, short lengths were drawn to avoid deposition fluctuations caused by draw speed changes. The electrical resistance of the fiber was rechecked after drawing by stripping off the polyimide coating and measuring at varying points and lengths along the fiber.

To determine the effect of the different gas treatments on the applied carbon layer, samples were tested with Raman spectroscopy at Sandia National Laboratories. The samples were excited at a 514nm wavelength and the relative intensities of the Raman shift were measured. Pyrolytic graphite shows strong characteristic peaks at $\approx 1360\text{ cm}^{-1}$ and $\approx 1580\text{ cm}^{-1}$ which are referred to as the "D" and "G" peaks, respectively denoting the graphite disorder induced mode and the graphite E_{2g} modes in the carbon structure.¹⁷ Because the Raman shift is expressed as a relative intensity, the ratio of the "D" to the "G" peaks is often used to compare carbon phase structures. As Figure 1 indicates, the symmetries between the Raman curves and a comparison of the G/D ratios suggest the carbon structures of the different samples are very similar.

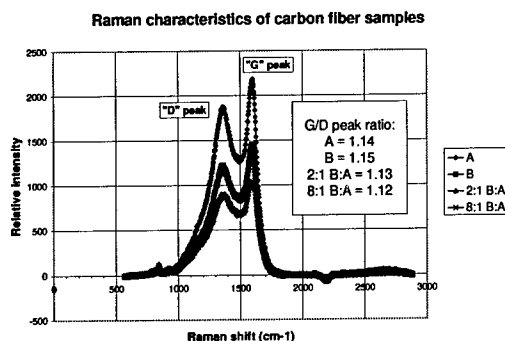


Figure 1

Since the pyrolytic carbon composition is similar from sample to sample, we can infer that the carbon layer resistance is near-equal when used in the layer thickness equation. Based on previous Spectran research¹⁸, we use the 16 kΩ-cm resistance / 300 Å carbon thickness as a basis for comparison to test fibers. Thus, using the equation above, the carbon layer thicknesses were calculated:

Table 2: Estimated carbon layer thickness

	Average Resistance	Estimated thickness
Hydro-carbon "B"	16.0 kΩ/cm	300 Å
Hydro-carbon "A"	45.5 kΩ/cm	105 Å
8:1 B:A mix	11.4 kΩ/cm	424 Å
2:1 B:A mix	5.9 kΩ/cm	812 Å

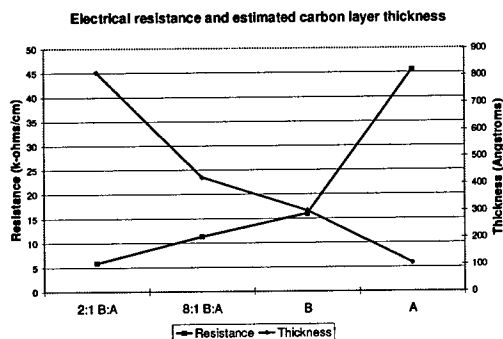


Figure 2

The addition of hydrocarbon "A" to the standard "B" has a marked effect on the carbon deposition process. This may be explained in part due to the fact that "A" is exothermic upon decomposition. It is proposed that the exothermic decomposition of hydrocarbon "A"

enhances the cracking of the "base" hydrocarbon "B". Thus, an 12.5% addition of "A" leads to a 41% carbon layer thickness increase for an 8:1 mixture as measured by electrical resistance. The 2:1 mixture (50% addition of "A") yields a thickness increase of 270%. The addition of the exothermic hydrocarbon is critical for the low-speed draw process since the reaction zone is usually much smaller than for a high speed process. By mixing the hydrocarbon gases, the reaction zone for decomposition is extended and a thicker carbon layer can be deposited.

It should be noted that when hydrocarbon "A" is used by itself in a low-speed draw run, the deposition process appears to be hindered by the inordinate amount of soot generated. During test runs, soot emerging from the reactor had to be directed from the fiber and there were difficulties tuning in the deposition process. The soot generated using this particular hydrocarbon precursor alone would clearly impart a detrimental effect on the fiber strength. The resulting carbon layer was calculated at only 105 Å and appeared much lighter in appearance than the standard fiber.

Fiber strength

Fiber strength was determined by performing two-point bend tests; 40 samples of each fiber were tested at a 4%/minute strain rate. A fiber sample without carbon was also tested to determine the strength penalty associated with the low-speed carbon deposition process.

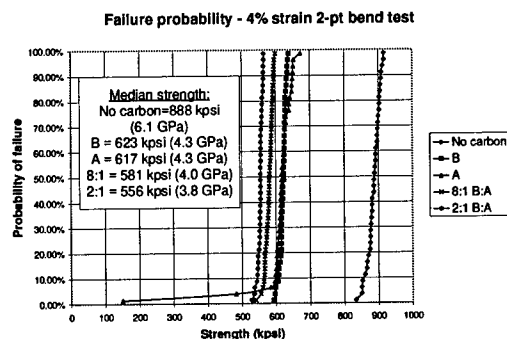


Figure 3

Although the data indicates a tight distribution, the strength penalty associated with carbon is >250 kpsi (1.7 GPa). Tensile strength tests (4%/min strain) comparing the standard carbon

fiber ("B") with a polyimide coating to polyimide fiber without carbon indicates a median strength drop of ≈ 170 kpsi (1.2 GPa); a similar shift is apparent in the dynamic fatigue test data shown below (figure 5). In addition, although hydrocarbon "A" exhibits a high intrinsic strength associated with the bonding of the carbon to the glass fiber surface, the soot generated during the deposition process likely caused the two low-strength measurements that dramatically altered the calculated Weibull slope (figure 4).

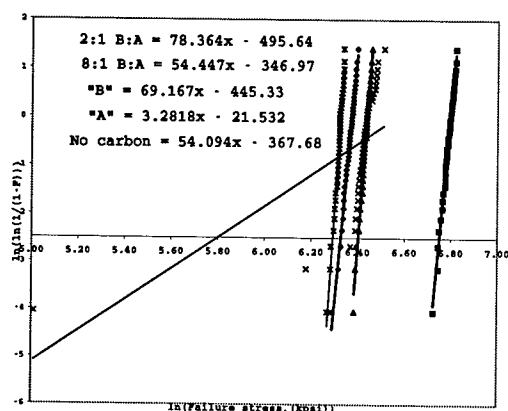


Figure 4: Weibull distribution

Dynamic fatigue

To gauge the effect of carbon on the dynamic fatigue characteristics of the fiber, fibers were strained at different rates to determine dynamic strength and fatigue parameters as dictated under FOTP-28. In this test, 125 μ m/155 μ m glass/polyimide fiber samples were strained at 25%/min, 2.5%/min, 0.25%/min and 0.025%/min; the resulting break stresses were used to calculate the stress corrosion factor (n). The samples tested were two non-carbon and two carbon-coated fibers, the latter using the standard "base" hydrocarbon.

Table 3: Fatigue parameters for test fibers

	n_d
Carbon "B"/polyimide sample #1	206
Carbon "B"/polyimide sample #2	205
No carbon/polyimide sample #1	22
No carbon/polyimide sample #2	21

Considering that the samples were produced from different runs, there is good agreement both

in terms of median strengths and calculated fatigue parameters suggesting a stable process.

Dynamic fatigue plot: carbon vs. non-carbon fiber (FOTP-28)

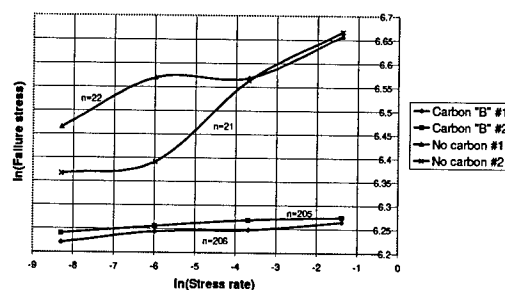


Figure 5

Samples of the test carbon fibers were strained at 25%, 2.5%, and .25%/min using two-point bend testing. Twenty samples were broken at each strain rate along with a non-carbon fiber sample. As with the standard FOTP procedure, the dynamic fatigue parameter was calculated based on the slope of the failure strength/strain rate slope. The stress corrosion factor *as calculated* were as follows:

Table 4: Fatigue parameters from 2-pt. bend test

	n_d (2-point)
Carbon "B"	>300
Carbon "A"	25
Carbon 8:1 B:A	>300
Carbon 2:1 B:A	>300
No carbon	17

Dynamic fatigue plot using two-point bend data

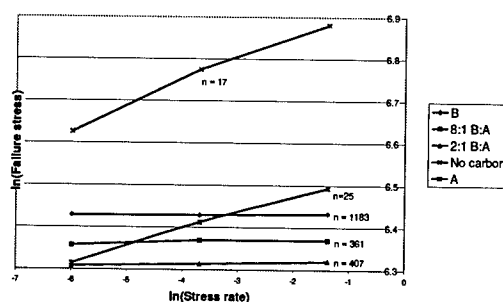


Figure 6

As with the fiber strength data, it is evident that the non-carbon fiber has a higher overall strength. However, the dynamic fatigue factor is an order of magnitude lower than the carbon-coated samples which show little degradation in strength at lower strain rates. The exception for hydrocarbon "A" is also consistent with the

strength data. Since the "A" carbon is very thin, it provides minimum protection from fatigue. Thus, the slope for the "A" carbon fiber is similar to the fiber with no carbon coating.

Carbon layer effect on strength

The carbon fiber samples were analyzed by atomic force microscopy (AFM) at Sandia National Laboratories. The mean roughness was calculated from measurements in a discrete area of $4\mu\text{m}^2$ or below to minimize variability caused by the curvature of the fiber and isolate the coating from extraneous contamination on the carbon surface. The mean roughness are noted here along with the estimated carbon layer thickness:

Table 5: Carbon roughness and thickness data

	Roughness	Thickness
Carbon "B"	16.6 Å	300 Å
Carbon "A"	15.8 Å	105 Å
Carbon "8:1"	38.7 Å	424 Å
Carbon "2:1"	24.6 Å	812 Å

As the data suggests, the roughness of the carbon surface does not appear to be directly related to the thickness of the applied layer. However, while a heterogeneous mixture of hydrocarbon gases may lead to an overall thicker applied layer, it may be postulated that a rougher morphology is based on the different reactions of the precursor hydrocarbons. That is, carbon platelets of a varied size are evolving at different temperatures both as a result of the mixed hydrocarbons and of the extended reaction zone.

The effect of carbon layer roughness and thickness on fiber strength may be seen here in Figures 7 and 8:

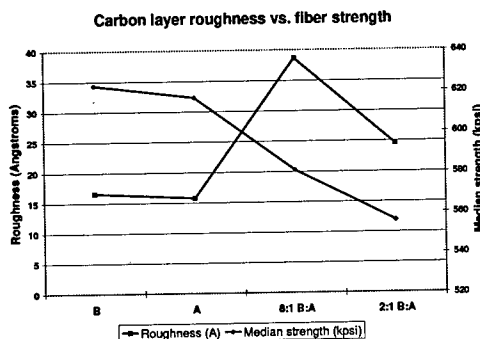


Figure 7

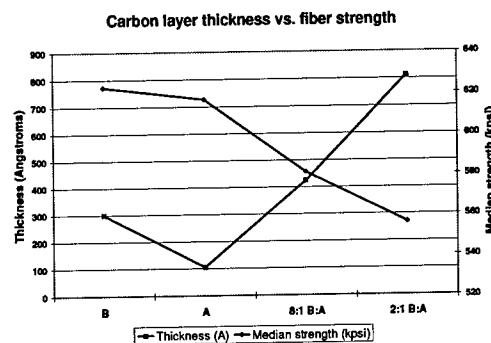


Figure 8

While there is some correlation with fiber strength versus carbon roughness, a stronger correlation of coating thickness is apparent. As noted, this may be attributed to the presence of pre-reacted carbon soot impacting the fiber during the deposition process. The "A" hydrocarbon alone was very sooty and the increasing concentration ratio may indicate the addition of the exothermic gas will lead to lower strength because of soot. The symmetry of the thickness trend to the median strength makes a strong case for thickness as the determinant of overall fiber strength. As noted, the thicker layer may be more susceptible to cracking due to the added residual stress on the carbon layer. In addition, if the deposited platelets are of varying sizes and phases, the alignment and bonding of the disparate platelets may lead to a weaker carbon layer due to additional microvoids in the structure.

CONCLUSIONS

In our efforts to improve and extend the low-speed carbon deposition process, we have shown the pyrolysis of a precursor hydrocarbon gas can be augmented with the addition of a hydrocarbon gas that is exothermic upon decomposition. The gas mixture produces a carbon layer with an increased surface roughness, but a deposited layer that is significantly thicker than when using a single precursor gas. The thicker carbon layer results in a fiber strength penalty, but has no appreciable effect on the stress corrosion factor when calculated using two-point bend testing. Based on the thickness data (as measured by electrical resistance), the strength and dynamic fatigue data of the test fibers, it is theorized the carbon layers deposited using the gas mixture will provide better protection from water and hydrogen ingress than the current base

standard. Work to show the effect of the new carbon layer on water and hydrogen ingress is in progress.

ACKNOWLEDGMENTS

The authors would like to thank Brian E. Slyman for support in generating fiber samples, Vessela Krasteva for performing dynamic fatigue tests and Jim Krumhansl of Sandia National Laboratories for arranging testing. Sandia is a multiprogram laboratory operated by Sandia Corporation, a Lockheed Martin Company, for the United States Department of Energy under Contract DE-AC04-94AL85000.



Eric A. Lindholm received his B.S. degree in Ceramic Engineering and his B.A. degree in English from Rutgers University in 1991. While at Rutgers, he worked in the Fiber Optics Materials Research Program under Dr. George Sigel. After college, he spent five years at Spectran Communication Fiber Technologies as a Fiber Draw Engineer before moving to Spectran Specialty Optics Company in 1996. As Senior Product Development Engineer at SSOC, he has focused much of his efforts on the development of optical fiber for adverse environment applications.

REFERENCES

- ¹ Kurkjian, C.R., Simpkins, P.G., Inniss, D., "Strength, Degredation, and Coating of Silica Lightguides", *Journal of the American Ceramic Society*, May 1993.
- ² Biswas, D.R., Kurkjian, C.R., Yuce, H.H., "Hermetic Coatings for Optical Glass Fibers", *International Wire and Cable Symposium*, 1995.
- ³ Ibid.
- ⁴ "Optical Fiber Telecommunications II" Miller & Kaminow, eds, p. 153, 1988.
- ⁵ Dimarcello, F.V., et. al. "High speed manufacturing process for hermetic carbon coated optical fibers", *Optical Fiber Communications Conference*, 1990.
- ⁶ Ibid.
- ⁷ Huff, R.G., Dimarcello, F.V., Hart, Jr. A.C., Walker, K.L., "Deposition of Hermetic Coatings on Silica Fibers" *Materials Research Society Symposium*, 1990.
- ⁸ Tuzzolo, M.R., Allegretto, A.E., Urruti, E.H., "Hermetic Product Performance: Ensuring the Uniformity of the Carbon Layer", *International Wire & Cable Symposium*, 1993.
- ⁹ Nakamura, et. al., "Structures and Characteristics of Carbon Films on Optical Fibers", *International Wire & Cable Symposium*, 1994.
- ¹⁰ Sikora, et. al., "Examination of the Strength Characteristics, Hydrogen Permeation, and Electrical Resistivity of the Carbon Coating of a Number of 'Hermetic' Optical Fibers", *International Wire & Cable Symposium*, 1991.
- ¹¹ Cusanello, V.A., Jacobson, N.J., Supczak, M.J., Stupak, P.R., "A Hermetic Carbon/Polyimide Coating Combination for Adverse Environments", *International Wire & Cable Symposium*, 1995.
- ¹² Aikawa, et. al., "Characteristics of Carbon-Coated Optical Fibers and Structural Analysis of the Carbon Film", *International Wire & Cable Symposium*, 1993.

¹³ Yoshizawa, N., Katsuyama, Y., "High-strength Carbon-coated Fiber", Electronics Letters Vol. 25, 1989.

¹⁴ Moore, K., Dwivedi, A., Sikora, E., "Review of Characteristics and Applications of Commercially Available Carbon-Coated Hermetic Fiber", International Wire & Cable Symposium, 1995.

¹⁵ Glaesemann, G.S., Gulati, S.T., "Design Methodology for the Mechanical Reliability of Optical Fiber", Optical Engineering 30(6), 709-715, 1991.

¹⁶ DiMarcello, et. al., U.S. Patent #5,000,541, 1991.

¹⁷ Dennison, J.R., Holtz, M., Swain, G., "Raman Spectroscopy of Carbon Materials", Spectroscopy 11(8), Oct. 1996.

¹⁸ Cusanello, V.A., Jacobson, N.J., Supczak, M.J., Stupak, P.R., "A Hermetic Carbon/Polyimide Coating Combination for Adverse Environments", International Wire & Cable Symposium, 1995.

CURE BEHAVIOR OF OPTICAL FIBER PRIMARY COATING ON DRAWING TOWER

Junji Yoshizawa, Yuji Naito, Hideaki Takase, Zen Komiya, Takashi Ukachi

JSR Corporation, Tsukuba Research Laboratories
25 Miyukigaoka, Tsukuba, Ibaraki, 305-0841, Japan

ABSTRACT

Relationships between cure behavior of optical fiber coatings and drawing conditions, especially UV lamp power for curing, were studied.

Gel fraction of secondary coatings became higher when the UV lamp power was increased. On the other hand the UV lamp power for primary coatings had an optimal point where the primary coatings gave maximum gel fraction.

In order to investigate the difference in the cure behavior of the primary and secondary coatings, several model coatings with various glass transition temperature (T_g) were prepared.

The coatings having T_g above room temperature cure better at higher intensity of UV irradiation or higher cure temperature. In contrast, the coatings having T_g below room temperature gave opposite tendency.

INTRODUCTION

UV-curable polyurethane acrylates have been favorably used for protective coatings of optical fiber, since the polyurethane acrylates provide wide variety of mechanical properties in addition to good chemical and weathering resistances.

Recent high demand for optical fiber requires coatings to be cured at high drawing speed. Accordingly it would be the most important to know the cure behavior of the polyurethane acrylates on a drawing tower. We reported previously that an increase of the UV lamp power improved the cure degree of the secondary coating at high drawing speed.¹ However, we found that the cure behavior of the primary coating was not that simple. By using the drawing tower, we carried out detailed experiments to investigate the difference of the cure behavior between the secondary and the primary coatings.

EXPERIMENTS

Materials

The primary coating, J-1, and the secondary coating, J-2, based on urethane acrylate were employed for this study. Table 1 are shown Young's modulus and glass transition temperature of cured films of J-1 and J-2.

Table 1. Characteristics of coatings, J-1 and J-2.

Cured film ¹⁾	J-1	J-2
Young's modulus (MPa)	1.0	1000
T_g (°C)	-10	90

1) Cured at 1J/cm² under air. Film thickness is 200 μ m.

For model experiments, urethane acrylate based model coatings with oligomers having various molecular weights were prepared (Table 2). The content of oligomer for each coating was kept constant. Decrease in the molecular weight of oligomer resulted in higher modulus with higher T_g (H-1 ~ H-3). In addition to these experiments H-4 and H-5 were prepared by employing much low molecular weight oligomer and monomer with high T_g , so these coatings were high modulus and high T_g . Conventional primary coatings correspond to H-1 and H-2, whereas the secondary coatings to H-4 and H-5.

Drawing Experiments

Drawing experiments were carried out using the 18-meter high drawing tower equipped with a furnace and one UV lamp for the primary coating and one or two UV lamp(s) for secondary coating (see Figure 1). A quartz glass rod was molten at 2000 °C and was drawn to give a fiber of 125 μ m of diameter. The primary coating was applied on the glass with 30 μ m of thickness and was cured with

Table 2. Formulation and Physical Properties of Model Coatings.

Formulation	H-1	H-2	H-3	H-4	H-5
Oligomer¹⁾					
A(Mw = 6000)	45	---	---	---	---
B(Mw = 3000)	---	45	---	---	---
C(Mw = 2000)	---	---	45	---	---
D(Mw = 1000)	---	---	---	45	---
E(Mw = 650)	---	---	---	---	45
Monomer					
A	5	5	5	5	5
B(T _g = -70°C)	47	47	23.5	---	---
C(T _g = 75°)	---	---	23.5	47	47
Photoinitiator					
	3	3	3	3	3
Young's modulus (MPa) ²⁾	1.4	2.6	9.6	490	690
T _g (°C) ²⁾	-33	-25	14	66	72

1) Number average molecular weight calculated from the stoichiometry of the raw materials for the oligomer preparation.

2) Cured at 1 J/cm² under air. Film thickness is 200 μm.

the UV lamp. The secondary coating was applied after the primary coating was cured. A doubly coated fiber with 250 μm of diameter was obtained after the secondary coating was cured with one or two UV lamp(s). A fiber coated with only the secondary coating was made in a similar manner to measure the gel fraction for the secondary coating.

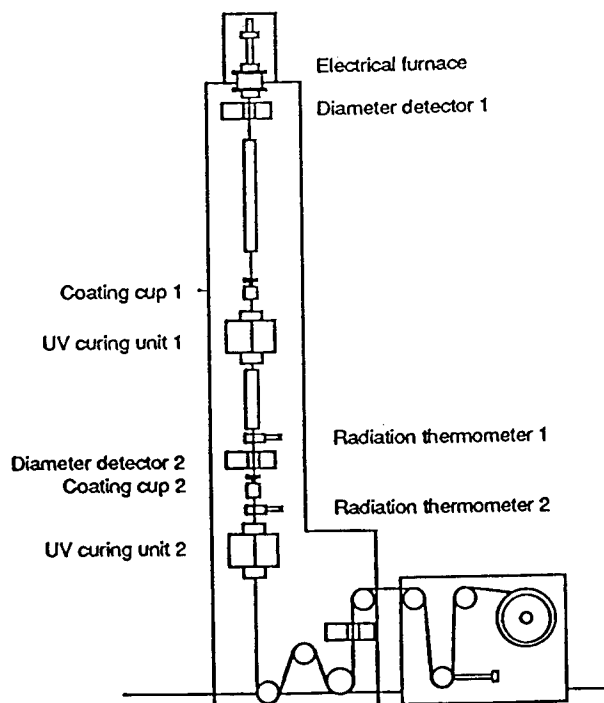


Figure 1. Schematic drawing of experimental Draw tower.

Film experiments

A liquid coating was drawn on a glass plate with 200 μm thickness using an applicator bar. The coating was cured by using a UV conveyor. The resultant film was peeled off from the glass plate and used for the following experiments.

Measurement of Gel fraction (Cured film)

Cured film was extracted in refluxing methylethylketone (MEK) for 12 hours and the resultant sample was dried under vacuum. Gel fraction was calculated from the amount of unextractables in the sample.

Measurement of Gel fraction (Cured fiber)

The gel fraction of the primary coating on the fiber cannot be measured directly since the primary coating cannot be separated from the secondary coating. The gel fraction of the primary coating was calculated from the total gel fraction and the gel fraction of the secondary coating. Estimation of the gel fraction of primary coating was done by subtraction of the gel fraction obtained from the singly coated fiber from that obtained from the doubly coated one by using following formula. The volume fraction of each layer was determined by observing of the cross section of the doubly coated glass fiber. Calculation was done by using following formula.

$$G_p = \frac{\text{Total} - G_s \times f_s}{f_p} \quad (1)$$

G_p : Gel fraction of primary coating
 G_s : Gel fraction of secondary coating
 f_p : Volume fraction of secondary layer
 f_s : Volume fraction of primary layer

RESULTS

Effect of UV intensity on curing behavior

Figure 2 shows changes in the gel fraction of secondary coating, J-2, using one UV lamp at various input power. The gel fraction became higher when the total input power was increased. As we previously reported¹, the secondary coating cures the better with the higher input power of UV lamp.

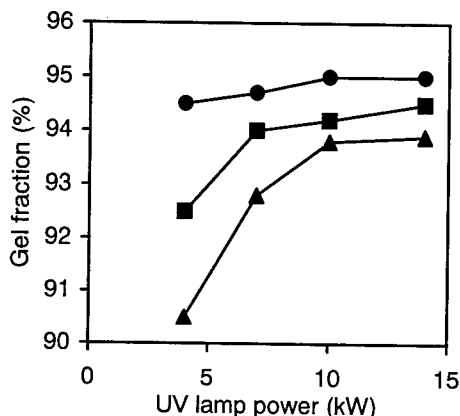


Figure 2. Gel fraction of secondary coating, J-2, by changing input power of UV lamp at three different drawing speeds. ●:200 m/min ■:400 m/min ▲: 550m/min.

Contrary to the secondary coating, the primary coating, J-1, behaved quite differently. Using the drawing tower equipped with one UV lamp for each coating, the effect of the UV lamp power for the primary coating was evaluated. The UV lamp power for the primary coating was varied with keeping the power for the secondary coating constant. In Figure 3, the gel fraction of the primary coating is plotted as a function of the UV lamp power for the primary coating. When the UV lamp power was increased from 1.8 kW to 7 kW, the gel fraction of the primary coating decreased. The interest was focused on the gel fraction when the UV lamp for the primary coating was turned off, which corresponded to the wet-on-wet process. The gel fraction at 0 kW was lower than that at 7 kW of UV lamp power. This result suggested that the UV lamp power for the primary coating have an optimal point between 0 kW and 1.8 kW. The optimal point did not seem to vary by an increase of the drawing speed, although the increase in drawing speed resulted in lowering the gel fraction. If there is an optimal energy dose, the input power of UV lamp giving

maximum gel fraction would move to high values as the increase in the drawing speed. However it is not the case.

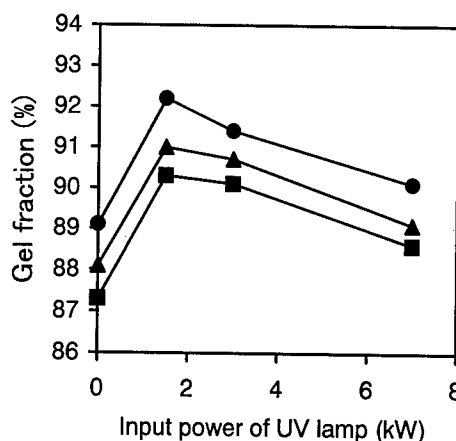


Figure 3. Gel fraction of a primary coating by changing input power of UV lamp at three different drawing speed. ● :200 m/min ▲ :400 m/min ■ :600m/min.

Effect of cure temperature of primary coating on drawing

If the UV energy dose or intensity is not the sole parameter to determine the gel fraction of primary coating, the other factor would be temperature. Temperature during curing is affected by not only the infra-red irradiation from the UV lamp but also heat evolution by polymerization reaction of the primary coating itself.^{2,3}

In order to see the effect of the cure temperature during curing, the temperature of the primary coating was changed with keeping the draw speed and the UV lamp power constant. In Figure 4, the gel fraction of the primary coating was plotted as a function of the temperature of the primary coating. The primary coating gives a tendency to show the lower gel fraction at the higher temperature. This behavior is also in good contrast to the relationship between the gel fraction of the secondary coating and the curing temperature as reported by H. Takase et al.⁴. Relatively small increase in the gel fraction of the secondary coating was found when the coating was cured at elevated temperature. This result implies that the behavior shown in Figure 3 could be a result of curing temperature. At the same drawing speed, the increase in the input power of the UV lamp also increases the infra-red irradiation from the lamp. It is considered that the behavior in Figure 3 is explained by the following

manner. Since the increase in the input power of the UV lamp cures the coating in short period of time, accumulation of the polymerization heat becomes faster. The curing condition, therefore, becomes more adiabatic and as the result, increase in curing temperature gives lower gel fraction. As discussed above, the drawing experiments do not tell us the contribution of UV light intensity and temperature separately, we decided to carry out the film experiments done on UV conveyor by employing model coatings.

Another interesting result was seen in regard to the change of the cure behavior of primary coating by changing the intensity of the UV irradiation. Figure 4 also indicates the effect of the number of UV lamps for the secondary coating on the primary coating. The increase of the number of the UV lamp for the secondary coating resulted in increase of the gel fraction of the primary coating. It seems that this tendency is in opposite to the behavior shown in Figure 3.

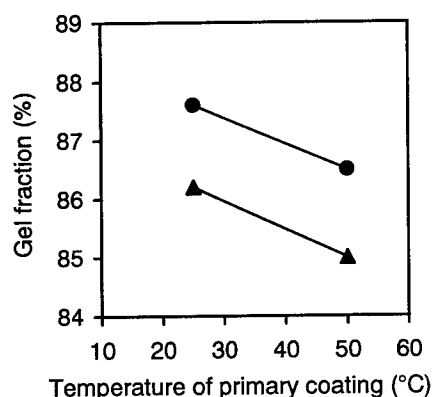


Figure 4. Temperature dependence of the gel fraction of a primary coating.

The primary coating was cured with one UV lamp. The secondary coating was cured with two or three UV lamps. Drawing speed was 550 m/min. ●:Three UV lamps for secondary coating ▲:Two UV lamps for secondary coating.

Effect of UV light intensity

Why does the curing behavior of primary coating on the drawing differ from that of secondary coating? The essential difference in the primary and secondary coatings is T_g . The primary coating has T_g lower than room temperature, so that it exhibits soft, rubber like properties. In order to investigate the effects of T_g on the cure behavior, the model

coatings listed in Table 2 were prepared.

These coatings were cured at various intensity of the UV light at constant conveyor speed, which corresponds to the increase in UV lamp power at constant drawing speed. Since the coatings were applied on a glass plate and the intensity of UV lamp for conveyor is far smaller than that for fiber drawing, the effect of temperature would be negligible comparing to the fiber drawing condition. The results are shown in Table 3 and Figure 5.

Table 3. Gel fraction (%) of the model coatings by changing the intensity of the UV irradiation.

	H-1	H-2	H-3	H-4	H-5
50 mW/cm	86.9	89.0	92.2	95.0	97.5
265 mW/cm	84.8	88.1	92.2	96.5	98.0
645 mW/cm	80.3	86.6	92.3	97.1	98.0

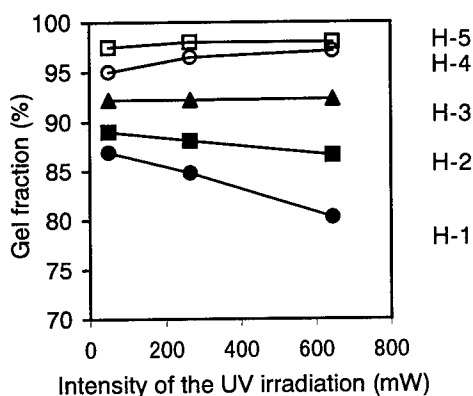


Figure 5. Gel fraction of the model coatings by changing the intensity of the UV irradiation.

The coatings with T_g s lower than room temperature (i.e. curing temperature), H-1 and H-2, exhibited a tendency to give lower gel fraction at higher intensity of UV irradiation. On contrary, the coatings with T_g s higher than room temperature, H-4 and H-5 gave slightly higher gel fractions at higher UV intensity. It is interesting to note that the coating with T_g close to room temperature (H-3) showed constant gel fractions regardless of the UV intensity. This behavior is in good accordance with what was observed in the drawing experiments as mentioned above.

Effect of temperature during curing

In order to investigate the effect of the curing temperature, the coatings H-1 ~ H-5 were cured by changing the cure temperature with keeping the intensity of the UV irradiation and conveyer speed constant. The results are listed in Table 4 and Figure 6. The coatings with T_g s higher than room temperature, H-4 and H-5, exhibited a tendency to show higher gel fraction at higher cure temperature. On the other hand, the coatings with T_g s lower than room temperature, H-1, H-2, gave a tendency to show the lower gel fraction at the higher curing temperature. The coating with T_g close to room temperature (H-3) gave slightly decreasing gel fraction as the increase of the curing temperature. This behavior agreed with the results of drawing experiments. Namely, the primary coating which has a T_g lower than room temperature gives low gel fraction by curing at high temperature, whereas the secondary coating with a T_g higher than room temperature cure better at higher temperature.

Table 4. Gel fraction (%) of the model coatings by changing curing temperature.

	H-1	H-2	H-3	H-4	H-5
25 °C	82.7	87.4	95.0	96.5	97.9
60 °C	77.4	85.0	93.9	97.7	98.7
90 °C	73.6	81.4	93.8	97.9	98.9

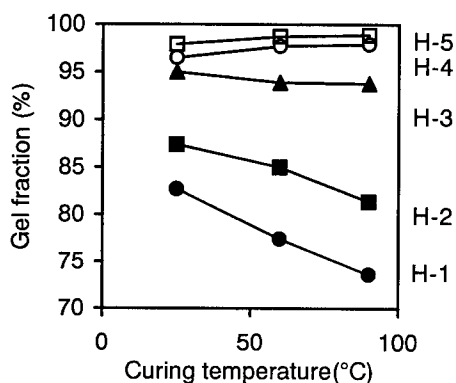
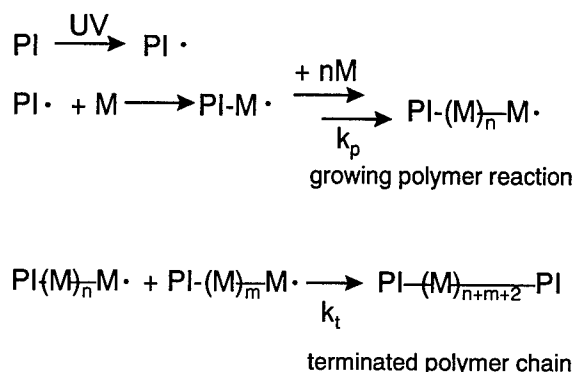


Figure 6. Gel fraction of the model coatings by changing curing temperature.

DISCUSSION

The model experiments described above demonstrated that the difference in the cure behavior between the primary and the secondary coatings is due to the difference in

T_g of the coatings. This clear difference is considered to be originated from the contribution of the polymerization reaction and termination reaction. Photo induced radical polymerization takes place according to the Scheme 1 as shown below. The radical polymerization accelerates at high temperature but termination reaction is also activated by temperature. Mainly, the termination reaction occurs by coupling of growing radical terminals (see Scheme 1)



PI : photo initiator
M : acyclic monomer
 K_p : polymerization rate
 K_t : termination rate

Scheme 1. Photo induced radical polymerization.

When a coating contains a crosslinkable multi-functional compound, for example urethane acrylate oligomer, the reaction medium turns into gel on the course of the reaction. Gelation restricts diffusion of the growing polymer radical. Nevertheless, relatively small acrylic monomer (M in Scheme 1) is less affected by gelation. Consequently, the termination reaction is suppressed and the polymerization reaction predominates. This effect is well-known as "gel effect"⁵. Both of the primary coating, J-1, and the secondary coating, J-2, contain difunctional urethane acrylate oligomer so that the gel effect is expected to work on the both coatings. However, gelled reaction medium of J-1 and J-2 are different because of the difference in T_g . Gelled reaction media for J-1 has T_g lower than room temperature, the restriction of the diffusion is less for J-1 comparing to J-2. If this is the case, when J-1 is cured at high temperature, it should produce more terminated polymer

chain (see Scheme I).

To examine this assumption, the primary coating J-1 was cured at 23°C and 100 °C at the same UV dose and intensity. The cured films were extracted with MEK and the extracted materials were analyzed by Gel Permeation Chromatography (GPC). As shown in Figure 7, the sample cured at high temperature gave broad peaks indicating the production of a large amount of terminated polymer chain.

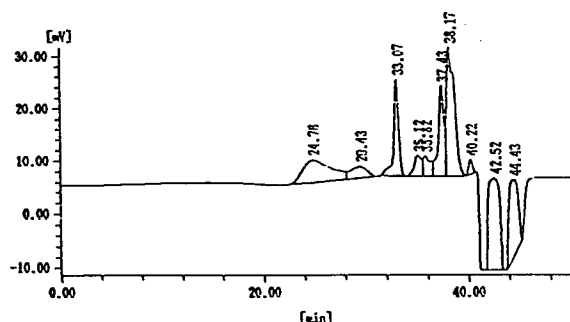


Figure 7-1. GPC chart for extracts obtained from the primary coating, J-1, cured at 23 °C.

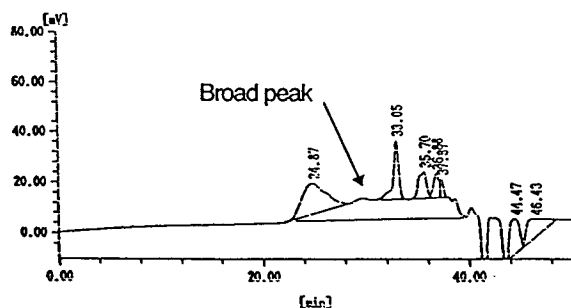


Figure 7-2. GPC chart for extracts obtained from the primary coating, J-1, cured at 100 °C.

The effect of UV light intensity can be understood in a similar manner. If the UV light intensity is high, photo initiator produces a large number of initiating radicals. High concentration of radicals accelerate the termination reaction since it is a bimolecular reaction. To examine this speculation, the primary coating, J-1, was cured at the same UV intensity with various UV dose by changing the conveyor speed. The results are listed in Table 5. Without changing the UV intensity

(i.e. keeping the concentration of the initiating radicals constant), the increase in UV dose resulted in high gel fraction. It was confirmed that if the initiating radical concentration is kept constant, increase in UV dose gives higher gel fraction or better cure degree. This result also accounts for the effect of the UV lamp for secondary coating on the primary coating. As shown in Figure 4, increase in the number of UV lamps for secondary coating enhanced the cure of the primary coating. This observation points out that the best method to obtain high cure degree of the primary coating is to irradiate it with high UV energy dose with low intensity. In an ideal situation, the primary coating should be cured as many UV lamps as possible with low UV light intensity. Additionally, it should be emphasized that the UV lamps for secondary coating are also effective to cure primary coating.

Table 5. Gel fraction of J-1 cured at the same UV intensity with various UV dose.

UV dose (mJ/cm ²) ¹⁾	Gel fraction(%)
500	91.7
10	87.0

1) UV intensity was 250 mW/cm², cured under nitrogen. Film thickness was 200 microns.

CONCLUSION

The cure behavior of the primary coating and the secondary coating was compared by using optical fiber drawing tower. The primary coating cured quite differently from the secondary coating. Namely, the secondary coating cured better as the increase of the UV lamp power, the primary coating had optimum UV lamp power at which it cures best. The temperature effect was not the same for the primary and the secondary coating either. High temperature during curing for the primary gave low degree of cure. All these observations were reproduced by film experiments done on UV conveyor. The essential cause of the difference is T_g of the cured film. Since the primary coating has T_g lower than room temperature, contribution of the termination reaction becomes larger as the increase of the reaction temperature or the intensity of the UV lamp. The experiments done on UV conveyor suggests that the primary coating should be cured with UV light with low intensity and high UV dose. This condition requires many UV lamps with

weak input power for primary coating. Fortunately, the drawing experiments indicated that the UV lamps for secondary coating effectively enhanced the cure of the primary coating.

REFERENCES

- ¹ S. Morita, Y. Naito, Z. Komiya, T. Naganuma, A. Fujimori, and T. Ukachi, Proceedings 44th IWCS, 513 (1995).
- ² T. Ukachi, A. Aoyama, Y. Naito, and K. Igarashi, Proceedings 41st IWCS, 261 (1992).
- ³ N. Saito, Y. Hashiguchi, Y. Takasugi, and T. Ukachi, Proceedings of RadTech Asia'93, 221 (1993).
- ⁴ H. Takase, Y. Hashiguchi, Y. Takasugi, N. Saito, and T. Ukachi, Proceedings 43rd IWCS, 72 (1994).
- ⁵ Polymer Science, A Materials Science Handbook, Ed., A. D. Jenkins, (North-Holland Publishing Co., 1972).



Junji Yoshizawa

Tsukuba Research
Laboratories,
JSR Co., Ltd.
25 Miyukigaoka,
Tsukuba, 305
Japan

Junji Yoshizawa received his M. E. degree in Organic Chemistry from Tsukuba University and joined JSR Co., Ltd. in 1995. He has been engaged in research and development of radiation curable materials for optical fiber coatings.

ADVANCES IN DESIGN AND DEVELOPMENT OF OPTICAL FIBERS FOR HARSH ENVIRONMENTS

Jie Li, Eric Lindholm, Jana Horska, and Jaroslaw Abramczyk

SpecTran Specialty Optics, Avon, CT

ABSTRACT

Optical fiber for harsh environments presents unique design challenges, particularly in coatings required to maintain the properties of the fiber. In a typical harsh environment application, the optical fibers are exposed to water, hydrogen or other harmful chemicals at elevated temperatures, e.g. $> 200^{\circ}\text{C}$. The fibers are commonly coated with a thin layer of carbon and further coated with thermosetting polyimide materials that can withstand significantly higher temperature than the common UV cured acrylate coatings. In this paper, we describe our recent efforts in understanding the impact of the environment on the fiber performance and report the advances in improving fiber and coating design to minimize the impact. Along with the discussion of the familiar fiber failure mechanisms, we also show the existence of a unique failure mechanism, i. e. the degradation of coating properties that leads to optical transmission loss.

BACKGROUND

Optical Fiber for Harsh Environments

Optical fibers have been proven advantageous over traditional copper based data communication media in many aspects such as high transmission capacity, immunity to electromagnetic interference, and size. More recently, optical fibers have also been successfully used in distributed sensing both as sensor and signal transmission link^{1,2}. Applications in harsh environments, where water, hydrogen, and other harmful chemicals are commonly present often under high pressures and temperatures, or where the fibers are under high stress, have prompted the development of optical fibers with specialty designs. Typical applications include monitoring of oil wells, undersea data communications, geophysical exploration, power cable

temperature monitoring, fire and leak detection, and geothermal well sensing. To meet these particular challenges, optical fibers with specialty coatings have been developed. A typical optical fiber of this kind consists of a silica glass lightguide, a thin carbon coating, and a polyimide coating. The carbon layer functions as a barrier to water and hydrogen diffusion, improving the fiber's resistance to fatigue and hydrogen induced optical loss. The polyimide coating provides additional protection for the carbon-coated fiber against mechanical damage, especially at elevated temperatures.

Failure Mechanisms

For successful application in harsh environments, it is imperative for an optical fiber to retain its characteristics, primarily mechanical strength and waveguide properties. An optical fiber can experience delayed fracture due to interaction with water and suffer reduced transmission as a result of macro-bend, micro-bend, and hydrogen diffusion. The effects of these deleterious processes on fiber are intensified under harsh conditions. There exist other failure mechanisms unique to the harsh conditions, such as degradation of the coatings caused by water or corrosive chemicals. Understanding of the failure mechanisms is therefore critical to optimize fiber design for the applications.

It is well known that the presence of surface flaws or cracks, induced mechanically or chemically, reduces the strength of silica optical fibers³. These flaws act as local stress concentrators under strain, resulting in a much lower tensile strength than the theoretical value of silica glass. Furthermore, the reaction of these flaws with moisture causes delayed fracture of the fiber or fatigue. Water molecules break the strained chemical bonds at the crack tip, forming two hydroxyl groups for each Si-O bond and leading to the crack growth³. This

impairs the long-term reliability of the fiber. To minimize the impact of water, coatings that are impervious to water molecules, e. g. carbon coatings were developed. Carbon coatings lower fiber tensile strength, but significantly increase the stress corrosion factor, the n parameter, which is a measure of the fiber's resistance to fatigue. The significant increase in n parameter allows the carbon-coated fiber to be reliably used under higher stress than that acceptable for non-carbon coated fiber.

Hydrogen-induced optical transmission loss is another common failure mechanism of optical fibers when used in hydrogen or water containing environments, such as undersea optical cables⁴. Mobile hydrogen molecules, generated as a product of the corrosion process of metal components, or released from polymer materials or water, diffuse into the core of the optical fiber, inducing optical loss. The optical loss is characterized by its wavelength dependence. Molecular hydrogen in GeO_2 -doped silica optical fibers shows several absorption bands in the spectral range from 1.08 μm to 2.42 μm , with the well known bands in the range from 1.08 μm to 1.24 μm ⁵. Another important characteristic of these absorption bands is their reversibility. They disappear when the hydrogen molecules are allowed to leave the fiber core⁵. The OH groups as a product of the reaction between molecular hydrogen and the glass matrix exhibit several absorption bands including one at near 1.38 μm . Different from the reversibility of the bands related to molecular hydrogen, the OH related bands are stable because the hydrogen in OH is strongly bonded to the glass matrix.

In addition to the hydrogen, water diffused into the fiber under high pressure has been observed to induce a fiber dimension change and a change in fiber index of refraction⁶. This change may be related to the water-induced structural relaxation of highly quenched glass matrix of the optical fiber. Carbon coating on the fiber surface has shown to be effective in preventing the fiber property change⁶.

Microbend loss is referred to the optical transmission loss in optical fibers caused by an external perturbation of the guiding condition of the fibers. Typical perturbation includes the variation in coating thickness, and residual stresses due to coefficient of thermal expansion (CTE) mismatch between the coating and the

glass. The loss exhibits much less wavelength dependence than macrobend loss, which is the loss observed when a fiber is bent to a radius of several centimeters. For standard telecommunication fibers, the microbend loss of the fiber is overcome by selecting a low modulus primary coating and a high modulus outer secondary coating. The harder outer coating provides high mechanical protection while the softer primary coatings serves as a cushion to absorb the external perturbation.

Design Considerations

It becomes clear from the preceding discussion of failure mechanisms that the success of the application of optical fibers in harsh environments relies, to a great extent, on the coatings and their survivability and reliability. Due to its suited properties and relative ease of processing, carbon is perhaps the most common material used for coating as barriers to water and hydrogen diffusion. Polymeric coatings are required to provide additional protection for the carbon-coated fiber against mechanical damage. Thermosetting polyimide coating is usually selected for its wider working temperature range than that of the common UV cured acrylate coating. However, in general the properties of polymeric materials are more sensitive to temperature and the environment, as compared to the inorganic silica glass and carbon. Therefore, the stability of the polymeric materials under harsh conditions dictates the reliability of the fibers, since the degradation of the properties of the polymeric coatings can lead to the degradation of the mechanical and optical properties of the fiber. Furthermore, waveguide designs may also need to be optimized to minimize the impact of the degradation of the polymeric coatings. Other characteristics of the coatings may be of particular importance in some applications, such as chemical durability, water resistance, and surface texture of the coatings. In the present work, we will provide experimental results on the degradation of polyimide coatings and its impact on the fiber performance and discuss the degradation as an important failure mechanism, particularly for the fibers used in harsh environments.

EXPERIMENTAL

Samples

Optical fibers used in the experiments were graded index multimode optical fibers coated with carbon and polyimide coatings,

manufactured at SpecTran. Table 1. Lists the type of the fibers used in the accelerated tests, their geometry, optical properties, type of polyimide coatings, and the type of water treatment.

More specifically, Fiber 1 was a standard fiber and Fiber 2 was a similar fiber, but with a type B polyimide coating. Fiber 3 was a same fiber as the Fiber 1, but was treated only in low-pressure water. Fiber 4 was essentially a Fiber 1 with a larger core size and a larger NA (Numerical Aperture). Type B polyimide has a higher elastic modulus and higher water resistance than Type A polyimide.

Mechanical Test

Fiber samples were tested for tensile strength according to the standard procedures described in FOTP 28, or TIA/EIA-455-28C. Briefly, the samples were tested using a gage length of 0.5 m at a strain rate of 4%/min. The stress corrosion factors were measured and derived using the procedure in the same TIA/EIA standard. A 0.5 m gage length, and strain rates of 25%, 2.5%, 0.25%, and 0.025% were used.

Thermal Test

Samples were tested for thermal stability of optical transmission according to the procedures described in FOTP 3, or TIA-455-3A. Specifically, in thermal soaking test, samples were heated and held at 300 °C in air for 50 hours while the transmission of the fiber was continuously monitored at 850 nm. In the thermal cycling test, the temperature varies between -65 °C and 175 °C while the fiber transmission was also continuously monitored.

Accelerated Test

This test is to examine the impact of harsh environments on fiber optical transmission, particularly under high temperatures in the presence of water in a laboratory environment. The fiber samples were soaked in water at ambient temperature and at high pressure (>100 atm.) for 2 hours and then at ambient pressure for more than 20 hours. The reference sample, Fiber 3, was soaked only at ambient pressure for the same period of time. The samples were removed from water and subsequently heated in nitrogen in a loose coil to temperatures ranging from 200 °C to 300 °C. The optical transmission of the samples was continuously monitored at 1.064 μm using an OTDR.

RESULTS AND DISCUSSION

Tensile Strength and Stress Corrosion Factor

Table 2 summarizes the tensile strength and stress corrosion factor for our standard carbon/polyimide coated fibers (New) and polyimide coated fibers (Non-Carbon). The properties of our fibers (Old) made before recent improvement of the carbon deposition process are also listed. The carbon/polyimide coated fiber showed a lower median strength than that of the polyimide coated fiber, as expected. However, the tensile strength was at least 10% greater than that previously reported⁷. More importantly, the average value for the stress corrosion factor, n , obtained from dynamic fatigue data is >200 while the value of n for polyimide coated fibers is about 20. The previously reported value for n of carbon/polyimide coated fiber was > 100. This improved strength along with the n parameter is an indication of better carbon coating quality and higher deposition efficiency of our modified process. For more detailed discussion, see the reference⁸.

Fig.1 compares the tensile strength of a typical carbon/polyimide coated fiber, same as the Fiber 1, and a typical polyimide coated fiber.

Surface Morphology

Scanning Electron Microscopy (SEM) was used to examine the effects of temperature and environment on the physical integrity of the polyimide coatings. Fig. 2 and Fig. 3 are the SEM micrographs of two fibers before and after the high-pressure water soaking and heat treatment in air at 300 °C for 2 days. The fiber samples shown in Fig. 2 are the same as the Fiber 1 and the fibers in Fig. 3 are the same type of fibers with an extra cured polyimide coating. Notice the fiber diameter is 155 μm .

After the treatment, the standard coating, Fig. 2 (b), has shown signs of surface degradation while the extra cured coating, Fig. 3 (b), remained unchanged. From the comparison above, the polyimide coating with the extra cure seems to have higher resistance to water and high temperature than the standard coating.

Thermal Cycling Date

The purpose of the test is to examine the thermal stability of the polyimide coating and its effect on the optical transmission of the fiber. In

the thermal soaking test, a standard polyimide coated, graded index multimode optical fiber showed an induced loss decrease of 0.6 dB/km at 300 °C, but no significant permanent induced optical loss when cooled down to room temperature, indicating reasonable thermal stability of the polyimide coating.

Fig. 4 shows a typical optical loss change in the same type of fiber as a function of temperature in a typical thermal cycling test. The initial drop in loss from 0.4 dB/km to 0 dB/km and the lack of response in loss to the temperature change in the first 10 hours are perhaps due to some experimental error and thus should be ignored. The induced loss decreases as the temperature increases. This is mainly caused by the reduction in compressive residual stress on glass fiber surface. There were also small peaks when temperature was held at the high temperature located between the large peaks in the loss curve. These peaks may be related to the stress change due to property changes of the polyimide coating. After the test, a permanent induced-loss of less than 0.4 dB/km was observed. To summarize, the variations in temperature have more severe impact on the coating and fiber than the high temperature soaking.

Loss-Temperature-Time Curves

Figs. 5 and 6 show the optical loss change of Fibers 1, 2, 3, and 4 during the accelerated tests. See Table 1 for the description of the fiber samples and the related water treatment.

From the curves, at least three significant observations can be made.

1. In all 4 samples, loss gradually increased under constant temperature and it became more severe when temperature was higher. Fiber 1 showed an enormous increase at 275 °C.
2. Loss in Fiber 2 with Type B polyimide coating decreased at each step increase in temperature. In Fibers 1, 3, and 4, the loss decrease was not significant until the temperature reaches 275 °C. It was much more prominent for Fiber 1 when temperature is increased from 275 °C to 300 °C.
3. Loss in Fibers 2, 3, and 4 remained relatively low while loss in Fiber 1 became unacceptable.

Loss Increases

As shown by the curve for Fiber 1 in Fig.5, the increase in optical loss became drastically higher when the fiber was heated to and held at 275 °C, reaching 70 dB/km from less than 10 dB/km in about 24 hours. Optical loss in Fiber 2 which has a more moisture resistant coating, however, stayed below 10 dB/km under 275 °C during the same period and started to increase when the temperature increased to 300 °C. The curve for Fiber 3 shown in Fig. 6 was from a same fiber, but was soaked in water only at the ambient pressure. The curve showed no increase in loss even at 300 °C, as does the untreated standard fiber of same type heated in air in the thermal soaking test. This indicates that soaking in water at low pressure has no significant effect on the coating properties. In contrast, the comparison of this curve with Fiber 1 shows clearly the effect of high-pressure water treatment. Since the fiber samples were treated in water and heated at elevated temperatures, the hydrogen or water diffusion directly into the core of the fibers will be naturally considered as a possible cause of the loss increase. To determine the nature of the induced transmission loss, which was observed also in several similar fibers, attenuation spectra of the samples were taken after the test. The spectra showed a broad, featureless background attenuation increase over a wide spectral range, with no distinguishable bands associated with hydrogen or OH groups, suggesting that the loss increase is not caused by direct diffusion of hydrogen or water molecules into the core of the waveguide. Therefore, we may eliminate the diffusion of hydrogen induced loss as a loss mechanism in this case. A more probable cause of the loss increase is microbend-related loss. As is well known, microbend loss can be induced by residual stresses developed due to the significant CTE mismatch between the glass and the polyimide. The CTE for silica glass, $\alpha = 0.5 \times 10^{-6}/^{\circ}\text{C}$ while that of typical polyimide fully cured will be at least $3 \times 10^{-6}/^{\circ}\text{C}$. As a result, tension and compression are likely to develop in the coating and on the glass fiber surface respectively when the fiber is cooled down to room temperature from the temperature at which the polyimide is solidified during fiber draw. However, one would expect no change in optical transmission at a constant temperature if the coating properties remain unchanged. Thus, the loss increase with time at given temperature may only be explained to be caused by the slow

build-up of residual stress as a consequence of the degradation of coating properties. Water-induced post curing of the polyimide coating is a most probable type of degradation at elevated temperature. Conceivably, the polyimide coating applied in-line during the fiber draw may be less cured and undergo more post curing during the subsequent heating, since the initial curing process is limited in time by the draw speed. Post curing of polyimide continues to convert the polyamic acid into a fully aromatic, insoluble polyimide and drive off the residual solvent. Consequently, post curing of the polyimide reduces the dimension of the polyimide coating and causes the elastic modulus to approach a larger value corresponding to the fully cured polyimide. At same time, the CTE decrease with increased cross-linking as post curing proceeds. Significant amount of residual stress can result from these changes in coating properties, thus leading to an increase in microbend loss.

Loss Decreases

Transmission loss decreases were observed for all 4 fibers when the temperature was abruptly increased. This is consistent with the loss behavior observed in Fig. 4. A large dip in transmission loss was observed for the Fiber 1 when the temperature was quickly increased from 275 °C to 300 °C. This observation was confirmed by similar dips observed in several similar fibers. This may be explained by the microbend loss related to the residual stress in the fibers. As expected, there is a partial release of the residual stress in the coating induced by the dimension increase of the coating, $\Delta L/L$, according to its CTE, α , and the temperature difference, ΔT , $\Delta L/L = \alpha \Delta T$, upon the increase in temperature. A decrease in elastic modulus as temperature increases may also contribute to the partial stress release. The dips with slightly larger amplitude observed in Fiber 2 at each step increase in temperature may be explained by the fact that only the Fiber 2 has a polyimide coating, derived from a polyimide, Type B, having an elastic modulus much higher than that of the coating Type A. Fibers with high elastic modulus coatings are more sensitive to microbend.

Microbend Loss

Thus far we have eliminated the possibility of hydrogen/water diffusion as a cause for the induced losses. We have also postulated that the loss increases with time are caused by

microbend due to residual stress build-up generated by the continuous dimensional reduction of the polyimide coating resulted from the water-induced post curing at high temperatures. To verify that microbend is the cause of the loss, Fiber 4, which is a high NA, carbon/polyimide coated fiber, was tested and its loss-temperature-time curve is presented as Fiber 4 in Fig. 6. It is clearly noticed that Fiber 4, which underwent the same treatment as for Fiber 1, showed no significant loss increase at temperatures up to 300 °C. This improvement is not surprising if microbend is indeed the major contributing cause of the loss. An empirical expression for microbend loss in a multimode optical fiber is given by⁹:

$$M_L \propto \left(\frac{a^4}{b^6 \Delta^3} \right) \left(\frac{E}{E_F} \right)^{3/2}$$

where M_L is the microbend loss for multimode fiber, a , core radius, b , fiber diameter, E_F , elastic modulus of the fiber, E , elastic modulus of the surrounding medium, Δ , index difference between core and cladding. According to this expression, to minimize the microbend loss, one can either increase the fiber diameter and fiber NA, or reduce core size or choose a softer primary coating. If Fiber 1 is replaced by Fiber 4, the model predicts a reduction in microbend loss greater than 60%, assuming that this model is also applicable for graded index fibers. Although the reduction shown by the comparison is much greater for some unknown causes, this comparison has strongly suggested that the loss and the loss increase are indeed microbend related. This model also indicates that the softer polyimide coating can reduce microbend loss. However, the stability of the physical dimension and of the elastic modulus of the coating becomes more critical when the coating is continuously being cured.

Role of Water

From the aforementioned comparison, the large loss increase in Fiber 1 is clearly correlated with the water present in the polyimide coatings. In the absence of water, the standard can retain their optical transmission at temperatures > 300 °C in air. Fiber 1 probably contains the largest amount of water while Fiber 2 contains less because the new polyimide coating is much more moisture resistant. This observation confirms the association of the loss with the presence of water. Fiber 3 contains perhaps the

least amount of water, since it was treated only in low-pressure water. Water in the polyimide may act as plasticizer at low temperature, lowering the elastic modulus of the coating. However, at higher temperature, water triggers some accelerated process, causing the loss to increase drastically with time.

It can be hypothesized that water present in the polyimide coating of an optical fiber enhances the post curing of the coating at high temperature, resulting in a coating dimensional change, creating higher compressive residual stress that leads to optical loss increase in the optical fiber. Water molecules may diffuse into the polyimide coating under high pressure and become bonded to the unreacted acid groups of the polyimide via weak bonding such as hydrogen bond. The presence of a significant amount of water in the polyimide may impede the reaction of post curing and also soften the material at low temperature. During subsequent heating, however, when the temperature is sufficiently high, the bonded water molecules are dissociated from the acid groups, evaporated, and probably driven out of the coating through the pores, making the acid groups available for the reaction of post curing. The residual solvent molecules that are released during curing dissolve in the water and are driven out of the system with water. This may also contribute to the acceleration of the curing process.

Minimizing the Impact

As has been shown, the thermal stability of polyimide coating properties in the presence of water is key to ensure successful applications. The need to prevent water from entering the polyimide coating becomes obvious. One can either avoid high-pressure water, or select more water-resistant coatings in case high-pressure water is expected. Polyimide coatings that allow a lesser amount of post curing may also increase the property stability. Polyimide primary coatings with lower elastic modulus and good thermal stability are also preferred to cushion the perturbations. As predicted by the microbend model and proven by the Fiber 4 result, fibers with higher NA, are much less sensitive to the perturbation. High Ge concentration in the core of the fiber required by higher NA can in some cases be beneficial, such as Distributed Temperature Sensing, which uses Raman back scattering for interrogation.

SUMMARY

We have reported recent advances in our efforts to improve design and performance of the fibers for harsh environment applications, specifically in fiber mechanical strength, coating durability, and the stability of optical transmission. We have successfully identified the degradation of the polyimide coatings as a primary cause of the optical transmission deterioration of the fibers at elevated temperatures in the presence of water. The degradation is suggested to be caused by the water-induced post curing of the polyimide coatings. Residual compressive stress is being developed in the fiber as the polyimide coating cures, inducing optical transmission loss in the fiber, or microbend loss. Improvements on fiber design and performance based on the model of microbend loss have proven the nature of the loss mechanism. Several recommendations as to minimize the impact of the coating property change have been made based on the experiment results. To prevent water from entering the polyimide coatings, avoid the exposure of the fibers to water at high pressure, and select polyimide coatings with high water resistance. High NA provides the fibers low susceptibility to microbend loss, and then allows more flexibility in coating selection. Work towards the more definitive verification of the loss failure mechanism is still in progress.

ACKNOWLEDGEMENT

The authors and the development team at SpecTran would like to thank Will Hawthorne of Sensor Highway of UK for providing the test results and helpful discussion, and James Krumhansl of Sandia National Labs for the SEM micrographs.

REFERENCE

1. R. Miller, J. Davies, G. Brown, "Fiber optics, advanced technologies complete ERD producer/injector", Oil and Gas Journal, July 1999, pp. 47-52.
2. C. Smithpeter, R. Norman, J. Krumhansl, D. Benoit, S. Thompson, "Evaluation of a distributed fiber-optic temperature sensor for logging wellbore temperature at the Beowawe and Dixie Valley geothermal fields", Proceedings, 24th Workshop on Geothermal Reservoir Engineering, Stanford University, Stanford California, Jan. 25-27, 1999.

3. C. R. Kurkjian, P. G. Simpkins, and D. Inness, "Strength, degradation, coating of silica lightguides", J. Am. Ceram. Soc., 76 [5] 1993, pp1106-1112.
4. P. J. Lemaire, "Reliability of optical fibers exposed to hydrogen: prediction of long-term loss increases", Optical Engineering, 30, 6, 1991, pp. 780-789.
5. J. Stone, "Interaction of hydrogen and deuterium with silica optical fibers: a review", J. Lightwave Technology, vol. LT-5, no. 5, May 1987, pp. 712-733.
6. J. R. Clowes, J. McInnes, M. N. Zervas, and D. N. Payne, "Effects of high temperature and pressure on silica optical fiber sensors", IEEE Photonics Technology Letters, vol. 10, no. 3, March 1998, p403.
7. V. A. Cusanello, N. J. Jacobson, M. J. Supczak, and P. R. Stupak, "A hermetic carbon/polyimide coating combination for adverse environments, IWCS proceeding 1995, pp 335-342.
8. E. A. Lindholm, J. Li, A. S. Hokansson, J. Abramczyk, "Low speed carbon deposition process for hermetic optical fibers", IWCS proceeding, 1999.
9. A. W. Snyder, I. White, and D. S. Mitchell, "Radiation from bent optical waveguides", Electronics Letters, vol. 11, 1975, p. 332

Table. 1 Fiber sample properties and treatment

Fiber	1	2	3	4
Core Size, μm	50	50	50	62.5
Clad Size, μm	125	125	125	125
Fiber Size, μm	155	155	155	155
NA	0.2	0.2	0.2	0.275
Carbon	Yes	Yes	Yes	Yes
Polyimide Type	A	B	A	A
Water Soaking Pressure, atm	> 100	> 100	1	> 100

Table 2. Fiber mechanical properties

Fiber	Median Fracture Stress, Gpa	Stress Corrosion Factor, n
Old	3.5	> 100
New	4	> 200
Non-Carbon	> 5	> 20

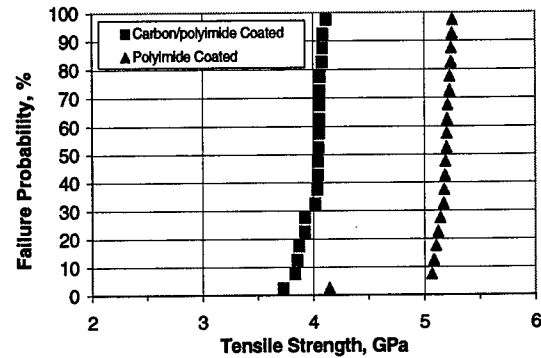
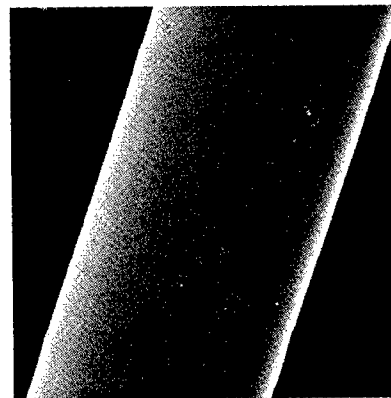
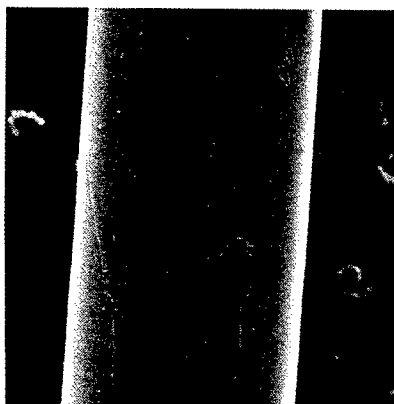


Fig. 1 Strength comparison of the carbon/polyimide coated fiber and the polyimide coated fiber.

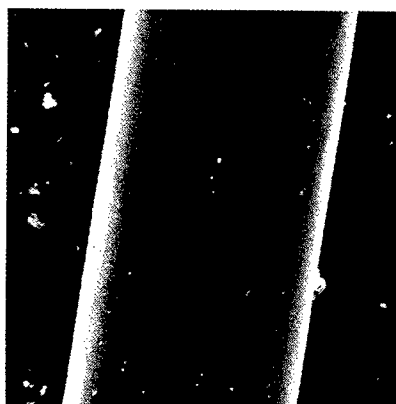


(b)

Fig. 2 SEM micrographs of the surface of the polyimide coating on the standard carbon/polyimide coated optical fibers before (a) and after (b) the high pressure water soaking and heating in air at 300 °C for 2 days.



(a)



(b)

Fig.3 SEM micrographs of the surface of the polyimide coating with the additional curing on carbon/ polyimide coated optical fibers before (a) and after (b) the high pressure water soaking and heating in air at 300 °C for 2 days.

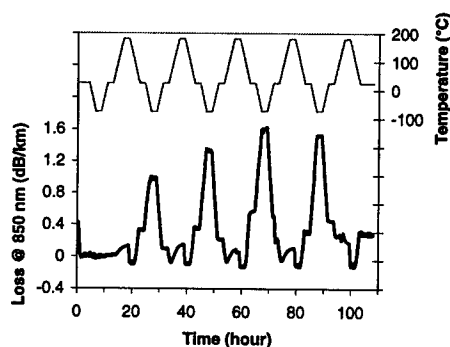


Fig.4 Induced optical loss of a standard polyimide coated, graded index, multimode optical fiber, the bottom curve, as a function of temperature change, top curve.

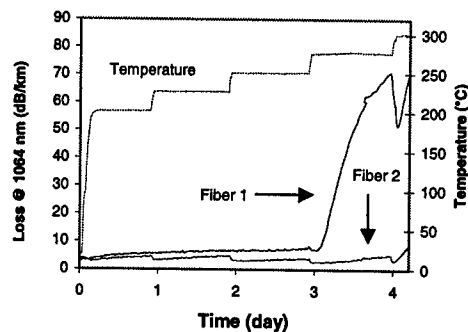


Fig. 5 Loss-temperature-time curves for Fibers 1 & 2.

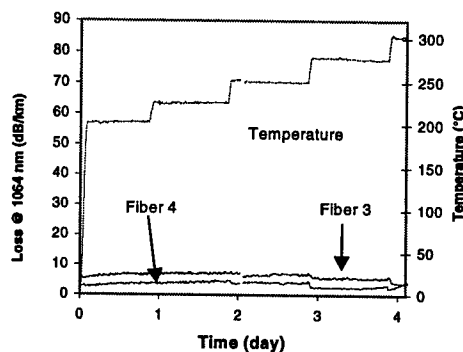


Fig. 6 Loss-temperature-time curves for Fibers 3 & 4.



Jie Li is a scientist at SpecTran Specialty Optics Company. He received a B. S. in Materials Science from Changchun Institute of Optics and Fine Mechanics, China, a M.S. in Materials Science and Engineering from Case Western Reserve University, and a Ph.D degree in Ceramic Science and Engineering from Rutgers University. He has been working in specialty preform/fiber design, development, and production since he joined SpecTran in 1996.

55 Darling Drive, Avon, CT 06001-1260 USA

COLORED MATRIX

Scott Coons, Nancy Moore, Tyson Norlin, Anthony Toussaint

DSM Desotech Inc., 1122 St. Charles Street, Elgin, IL 60120

ABSTRACT

Optical fiber ribbons are currently coded by colors. Ribbon identification markings are printed on the surface of the ribbon. This approach is cumbersome, involving the off-line printing of solvent-based ink onto the ribbon, and does not allow for the quick and easy identification of the ribbon.

Colored matrix materials have been used to color code ribbons. However only a limited number of colors are available. These colors also suffer from the fact of being translucent. In many instances this poses difficulty in distinguishing ribbons that contain fibers that have been coded with ink. It would be desirable to have ribbons that are coded with opaque colored matrix materials, whereby a set of twelve colors are available. The curing of pigmented materials poses numerous hurdles, especially curing thick materials necessary to form ribbons.

This paper describes the development of color coded matrix materials used in an online ribboning process. The color-coding was achieved using pigmented matrix materials. The ribbon properties and performance was greatly affected by the presence of pigment in the matrix. The effect of pigmentation is described in terms of their effect on ribbon properties and performance.

Colored matrix significantly expands the number of identifiable ribbons in a cable. For example, a cable consisting of 78 24-fiber ribbons yields over 1800 individually identifiable fibers. In the coming years, colored matrix could allow cable manufacturers to greatly increase the fiber counts in their cables to meet the increased demand for data transfer.

INTRODUCTION

With the increasing use of ribbonized optical fiber in cables, the challenge has moved to developing ribbons with an increasing number of fibers¹. Ribbonized fibers afford greater processability than single fibers in loose tubes due to the number that can be spliced at a time².

Colored inks were developed to code optical fibers, in a similar manner colored matrix materials have been used in part to code ribbons. However, these are translucent, and are only available in a limited number of colors.

The performance of ribbons is ever increasing^{1,3}. These performance requirements must still be maintained with colored matrix. To fully cure films, UV light besides being absorbed by photoinitiators in the top of the film must reach the bottom of the film. The presence of pigments further complicates this. Pigments reduce the light that can be absorbed by the photoinitiator and thus impact the film thickness that can be applied. This in turn impacts the performance of the matrix.

Inks are applied as thin layers of 6 microns or less. Penetration of light into the film is therefore not a major issue. The impact of pigment is overcome by adding high levels of photoinitiator. This approach cannot be used in thicker layers, since high levels of photoinitiator can also prevent penetration of the light. High absorption in the upper layer of the film causes a decrease in the amount of light reaching the bottom of the film⁴. The presence of pigment has its greatest effect at the bottom of the film. The impact of inadequate cure at the bottom layer of the matrix has a profound impact on the ribbon performance⁵.

EXPERIMENTAL

Materials

Clear, red and green pigmented matrix materials with varying levels of dispersed pigment were used in this study. The matrix materials were formulated with high and low T_g 's, relative to the temperature of the heat stripper. These are shown in Table I.

Mechanical properties of coatings

The coating samples used for characterization were prepared by curing a 75 μ m film on polyester at 1.0 J/cm², using a Fusion D-lamp under N₂.

Tensile measurements were performed on an Instron Model 4201 using a 20lb load cell. Films were preconditioned overnight at 23°C and 50% relative humidity. The test samples had gauge dimensions of 50 mm x 12.5 mm. The test samples were pulled at a rate of 25 mm/min. The reported values were averages of 5 measurements. The secant modulus was evaluated at 2.5% elongation.

T_g and E' were measured with a Rheometric Scientific, Inc. RSA-II Solids Analyzer, at a frequency of 1 rad/s. Measurements were made at intervals of 2°C. The T_g was determined from the peak of the $\tan \delta$ vs. temperature. The sample size was 25mm x 6.3mm. Samples were measured in triplicate.

Analysis of Cure

The degree of surface cure of the films and ribbon samples was measured using FTIR-ATR. A Nicolet Fourier Transform Infrared (FTIR) Spectrophotometer equipped with a diamond crystal was used. The degree of cure at the surface (to a depth of 1-3 μ m) of the matrix was measured. The percent reacted acrylate unsaturation (%RAU) was measured using a reference peak at either 810 cm⁻¹ or 1407 cm⁻¹.

Ribbon Preparation

Four-fiber ribbons were prepared using fibers that had been color-coded with red, blue, white and green DSM Desotech Cablelite® LTS ink. The approximate thickness for each of the colors was 6 μ m. All fibers were color-coded at 1000 m/min using two 10" lamps from Fusion UV Systems (D bulbs) on a Nextrom OFC 52 coloring machine. The fibers were made into four-fiber ribbons using a Nextrom OFC 21 fiber finishing line equipped with one 6" Fusion UV 500 watt/in lamp followed by one 10" Fusion UV 600 watt/in lamp. As in the color-coding process, both bulbs were Fusion D bulbs. The production speed ranged from 260-500 m/min and the lamp power ranged from 100% / 25%-100% / 100%(6" lamp / 10" lamp).

Stripability

Heat stripping tests were performed using a Sumitomo JR4A stripping tool at 85 and 120°C. The temperature in the heat-stripping tool was calibrated in the closed position using a thermocouple. Ribbon was placed in the tool, with between 25-30mm protruding from the end. The tool was closed for 5 seconds, after which it was pulled apart to strip the matrix leaving the fibers. The stripped ribbons were given a rating of 1-5, where 1 denotes a thoroughly clean strip with no residue left on the fibers, and 5 being incomplete strip, residue on fibers cannot be removed with alcohol wipes^{6,7}.

Peelability

Peelability was rated on a subjective scale of 1 to 5, where:

1. Denotes complete removal of matrix in a single peel.
2. Indicates complete removal with a single break or shred.
3. Signifies matrix removal is complete but breaks multiple times during peel.
4. Denotes a ribbon where the matrix does not peel and can only be chipped or flaked off.
5. Indicates a ribbon where the matrix can not be removed from the colored fibers or peel removes ink from the fiber.

All peel ratings reported here are averages of 5 or more test samples.

Midspace Fiber Access

Midspace fiber access was performed using a Siecor Peelable Ribbon Midspace Access Kit, TKT-060. A ~35cm length of single-sided cloth tape was applied to a rigid surface. Small drops of cyanoacrylate adhesive were placed at ~4cm intervals along the center 30cm of the tape. A 40cm sample of the ribbon was then aligned with the row of adhesive and lowered into place. Slight pressure was applied to the top surface of the ribbon with a wooden tongue depressor to ensure that the ribbon made adequate contact with the adhesive. The adhesive was then allowed to cure for ~10 minutes, and ribbon peel was initiated by lifting one end until the matrix began to peel. Peel was rated on a scale of one to five.

RESULTS AND DISCUSSION

Effect of Pigment

As expected, increasing the level of pigment in the matrix negatively impacts ribbon strippability and through-cure while not affecting cure at or near the outer surface of the matrix. Table II shows that when clear matrix C1 is colored with pigment, the inside %RAU of the films decreases from 95 with the clear matrix, to 89% with the highest level of pigment, R4. Sample R2 has 25% less pigment than R3, while R4 has 25% more pigment than R3. These cure results are not surprising since, the pigment absorbs UV light and inhibits the cure. However, reduced cure improves the peelability of the ribbon in part because fewer bonds form between unreacted sites in the ink and the matrix. In general heat strip was very good. With samples C1, R2 and R3, the matrix, ink and coating composite was removed as a single piece. There were slight traces of residue on the fiber, which was easily removed with one alcohol wipe. With R4 the matrix slightly crumbled leaving coating residue on the fiber. This was removed with a few alcohol wipes. The ease of mid-span fiber access of a ribbon also appears affected by cure. Matrix materials exhibiting a high degree of cure by %RAU on the inside surface showed decreased performance in this test. It should be noted that undercuring the matrix reduces its physical properties and can lead to ribbon failure for performance criteria such as strippability and twist.

Effect of T_g

The glass transition temperature (T_g) of a matrix can be very important to performance criteria such as ribbon strippability, especially when the matrix undergoes a phase transition during the stripping process⁸. Such a transition will occur when the temperature in the stripper is sufficiently high that the matrix exceeds its T_g during residence time in the stripper. Coatings were formulated with a low and high T_g relative to the temperature of the heat stripper. Low T_g materials were below 75°C, whereas high T_g materials were above 95°C. The performance of the red matrix with a high and low T_g is shown in Table III. The ribbon strip of the low T_g material R1 was poorer than that of R4. With R4, the matrix, ink and coating composite partially crumbled when stripped, leaving residue on the fibers. The residue was removed with multiple alcohol wipes. With R1, the composite completely crumbled, multiple alcohol wipes did not remove the residue. When the matrix exceeds its T_g during the stripping process, the ribbon loses its strippability and the matrix crumbles completely.

Effect of Modulus

The effect of modulus of the matrix on ribbon performance is shown in Table IV. With the clear matrix materials, which had the same elongation, increasing the modulus improved peelability. With the pigmented matrix materials R3 and R5 that have the same level of pigment, the modulus was increased which caused a decrease in elongation. This did not affect ribbon strip or peelability.

The ease of mid-span fiber access of a ribbon appears to be a function of both the modulus of the matrix material and the degree of cure of the ribbons. The matrix with the highest modulus, C2, exhibited the worst mid-span access rating, with the matrix being removed only where the adhesive secured it to the cloth tape. Also, matrices exhibiting a high degree of cure by %RAU on the inside surface showed decreased performance in this test.

Ribbon Run Conditions

Table V shows variations in ribboning conditions. The line speed was increased from

260 m/min to 500m/min. As seen, on increasing the speed the cure decreases. As expected the %RAU on the inside of the ribbon is affected more than the %RAU on the outer surface. This also caused a slight decrease in ribbon performance.

CONCLUSIONS

This report demonstrates the feasibility of colored matrix materials. The presence of pigment affects the cure, which ultimately influence the matrix performance. Many factors affect ribbon performance. The adhesion between ink and matrix, as well as properties of the primary and secondary fiber coatings are of major importance. By tailoring the formulation it is possible to optimize the matrix for the particular properties. These results are therefore applicable to this particular system. Variations in the primary and secondary fiber coating, as well as the ink will greatly impact the final ribbon performance.

ACKNOWLEDGEMENTS

The authors would like to thank the tireless efforts of Glenn Evans, Terry Ernst, and our Physical and Analytical Team.

REFERENCES

1. Konstadinidis, K., Sollenberger, N. W., Siddiqui, S., Jackson, K. W., Turnispeed, J. M., Au T. W., DeFabritis, R. P., Taylor, C. R., *Proceedings of the 46th International Wire and Cable Symposium*, p274 (1997)
2. Murate, A., Mitsuhashi, A., Oohashi, K., *Proceedings of the 46th International Wire and Cable Symposium*, p281 (1997)
3. Jackson, K. W., Parker, T. L., Petisce, J. R., Sollenberger, N. W., Taylor, C. R., *Proceedings of the 42nd International Wire and Cable Symposium*, p28 (1993)
4. Oldring, P. K. T. (Ed), *Chemistry and Technology of UV and EB Formulation for Coating Inks and Paints* (1991)
5. Kim, P.K., Sollenberger, N. W., Jackson, K. W., *Proceedings of the 44th International Wire and Cable Symposium*, p635 (1995)

6. Lochkovic, G. A., Moorjanina, S. K., Patel, N. I., Speights, R. J., Stephens, B. L., *Proceedings of the 46th International Wire and Cable Symposium*, p260 (1997)

7. Keesee, J. R., Lochkovic, G. A., Smith, D., Toler, J. R., *Proceedings of the 43rd International Wire and Cable Symposium*, p430 (1994)

8. Petisce, J. R., *Radtech'94 North America Conference Proceedings*, p282 (1994)

SPEAKER BIOGRAPHY



Dr. Scott Coons received his Ph.D. in Chemical Engineering from Michigan State University in 1996. Soon after graduation, Scott joined DSM Desotech as a Research Engineer where he is responsible for application and process development program.

Dr. Scott Coons
1122 St. Charles St.
Elgin, IL 60120

Table I.
Matrix material

Ribbon Sample	Color	Pigment level	T _g	Tensile (MPa)	Elongation (%)	Modulus (MPa)	E' (MPa)
C1	Clear	none	high	34	8	1010	48
C2	Clear	none	high	42	8	1180	45
R1	Red	high	low	27	19	713	30
R2	Red	low	high	34	7	940	50
R3	Red	med	high	32	8	940	49
R4	Red	high	high	36	11	970	49
R5	Red	med	high	41	8	1140	45
G1	Green	high	high	34	7	940	49

Table II.
Impact of Pigment Level on Ribbon Performance

Ribbon Sample	Pigment Level	%RAU of Ribbons		Ribbon Strip (85°C)	Midspan fiber access	Ribbon Peel
		Inside surface	Outside surface			
C1	Clear	95	98	2	3	2.3
R2	Low	94	98	2	5	2.0
R3	Medium	92	98	2	4	1.9
R4	High	89	98	3	3	1.6

Table III
Effect of T_g on Ribbon Performance

Ribbon sample	T _g	Ribbon %RAU inside surface	Ribbon Strip (85°C)	Midspan fiber access	Ribbon Peel
R1	Low	89	5	3	1.4
R4	High	89	3	3	1.6

Table IV
Effect of Modulus

Ribbon Sample	Secant Modulus (MPa)	%RAU of inside surface	Ribbon Strip (85°C)	Ribbon Peel
C1	1010	95	2	2.3
C2	1180	95	2	1.4
R3	940	92	2	1.9
R5	1140	94	2	1.6

Table V.
Process conditions

Ribbon Sample	Run conditions	%RAU of ribbon		Heat Strip	Midspan fiber	Ribbon Peel
		Inside	Outside			
R1	260/100/100	89	92	5	3	1.6
R1	500/100/100	84	91	5	4	1.7

SIMULATION OF FLOW IN DIE AND APPLICATOR FOR OPTICAL FIBER MANUFACTURE

Kunal Rattan

and

Yogesh Jaluria

**Department of Mechanical and Aerospace Engineering
Rutgers, the State University of New Jersey
New Brunswick, NJ**

ABSTRACT

A detailed analytical and numerical study is carried out on the flow field generated in a coating die and applicator during the coating process in the manufacture of optical fibers. Fairly generic configurations are considered and a wide range of fiber drawing speeds, ranging up to 15 m/s, is simulated. Different boundary conditions at the entrance of the moving fiber are considered. Different coating materials are simulated, along with a wide range of operating conditions and geometric designs. A finite volume numerical model is employed to obtain results on the flow. Though different temperatures are considered for the coating material, the flow is considered to be isothermal. The focus is on the flow pattern and the velocity field. The characteristics of the re-circulating flow that arises in many cases are investigated in detail. The results are obtained in terms of streamlines, velocity distributions and flow rates.

INTRODUCTION

The worldwide need for large quantities of high quality and low cost optical fiber for telecommunications requires high production rates with competitive fiber draw speeds, expected in excess of 20 m/s. This imposes strong demands on the available coating technology, which is a critical step in the manufacturing process. Despite the recognition of the crucial importance of coating in optical fiber manufacture, there is lack of fundamental

understanding of the flow and transport during this process.

The basic coating process involves drawing the fiber through a reservoir of coating fluid and then through a die that is used to control the thickness and concentricity of the coating layer. Coating thickness may also be controlled by metering the flow rate, while a flexible exit die may be used for centering the fiber. Viscous shear due to the moving fiber results in a circulatory fluid motion within the applicator. Centering forces within the tapered die contribute to the positioning of the fiber at the center.

The physical and theological properties of the coating material and their temperature dependence are of primary importance, not only for the flow within the applicator but also with respect to the curing process that follows. The influence of different coating materials on the fiber performance and on the fabrication process has been discussed in detail ^{1,2}. Defects like voids, lumps and uncoated sections can be controlled by optimizing coating liquid viscosity and die geometry to minimize bubble inclusion ¹.

When the fiber passes through the applicator the liquid close to it is set in motion because of the liquid viscosity. For higher velocities the effect at the die exit is largely due to inertia, neglecting the capillary suction effect, since the film that emerges with the fiber is the film that the fiber has entrained in the volume, i.e., the viscous

boundary layer³. Hence the film thickness is close to the viscous boundary layer thickness. Commercially available computational software, for modeling the flow within the applicator to compute the centering forces as function of the die taper angle, has been employed⁴. Liquid metal coatings, including the effect of fully developed flow region within the die on the lower meniscus, have been analyzed in detail⁵.

The flow field in the fiber coating applicator is complicated because of the geometry, coating material properties, moving fiber, and the presence of free surface near the top of the applicator and the free surface after die. A substantial amount of work has been done by several researchers on moving fibers and wires in channels and other enclosed regions⁶.

The main interest in the fiber coating process lies in the uniformity, concentricity, thickness and quality of the coating, particularly at high draw speeds. The present study is a numerical investigation of the fiber coating process that would not only lead to a better understanding to the fiber coating process, but will also yield quantitative information that will be useful in the design and optimization of the coating system and of the process. Fiber draw speeds varying from 1m/s to 15m/s are considered. Different applicator and die dimensions are numerically simulated to give the flow field in both the applicator and the die. When linked to the coating process, the characteristics of the final coating can be determined. Various fluids are simulated to understand the effect of fluid properties on the coating. Inflow of coating material from a side opening is employed to replenish the material taken up by the fiber. The effect of the meniscus at the applicator entrance is found to be negligible in terms of the flow distribution in the applicator and the die. Though different temperatures are considered for the coating fluid, the flow is treated as isothermal.

NUMERICAL METHOD

To solve for the velocity field in the applicator and the die, a finite volume numerical method is used. The governing equations for the steady state, viscous, non-Newtonian incompressible flow are solved for a transformed coordinate system (ξ - η). The governing equations in an axi-symmetric cylindrical coordinate system are

1. Continuity equation:

$$\frac{1}{r} \frac{\partial(\rho r u)}{\partial r} + \frac{\partial(\rho v)}{\partial z} = 0$$

2. u momentum equation:

$$\begin{aligned} \frac{1}{r} \frac{\partial(\rho r u^2)}{\partial r} + \frac{\partial(\rho v u)}{\partial z} = & -\frac{\partial p}{\partial r} + \frac{1}{r} \frac{\partial}{\partial r} \left(\mu r \frac{\partial u}{\partial r} \right) + \frac{\partial}{\partial z} \left(\mu \frac{\partial v}{\partial z} \right) \\ & + \frac{1}{r} \frac{\partial}{\partial r} \left(\mu r \frac{\partial u}{\partial r} \right) + \frac{\partial}{\partial z} \left(\mu \frac{\partial v}{\partial z} \right) - 2 \frac{\mu u}{r^2} + \rho g_r \end{aligned}$$

3. v momentum equation:

$$\begin{aligned} \frac{1}{r} \frac{\partial(\rho r u v)}{\partial r} + \frac{\partial(\rho v^2)}{\partial z} = & -\frac{\partial p}{\partial z} + \frac{1}{r} \frac{\partial}{\partial r} \left(\mu r \frac{\partial u}{\partial r} \right) + \frac{\partial}{\partial z} \left(\mu \frac{\partial v}{\partial z} \right) \\ & + \frac{1}{r} \frac{\partial}{\partial r} \left(\mu r \frac{\partial u}{\partial r} \right) + \frac{\partial}{\partial z} \left(\mu \frac{\partial v}{\partial z} \right) + \rho g_z \end{aligned}$$

The Landau¹⁴ transformation is applied to the equations to transform non-cylindrical, but axisymmetrical, domains to cylindrical. This is done to handle different die and applicator shapes. The new coordinates are defined as

$$\begin{aligned} \xi &= \frac{(r - R_{fiber})}{(R(z) - R_{fiber})} \\ \eta &= \frac{z}{L} \end{aligned}$$

The resulting transformed equations¹⁰ are solved for the resultant flow field using a numerical method based upon the SIMPLER algorithm¹⁵

The fiber considered is of radius 125 μm . The exit of the die is kept at 200 μm . The inlet to the die varies from 200 to 300 μm . The profile of the die is a parabolic curve. This was taken in favor of the conical die, which was also tried, because of greater versatility of the former. The diameter of the applicator was taken as 1cm and the length of the applicator and the die assembly was 1.7 cm, with a die length of 2mm. These dimensions were chosen to be of the same order of magnitude as an experimental setup, which is to be used eventually for model validation. Due to the large difference in the length scales for the die and the applicator, the

computational domain was divided into two parts. The die domain extended into the applicator domain and the boundary conditions at the shared boundaries for one was determined from the other. No-slip boundary conditions were applied at the walls and at the moving fiber. Fully developed flow was assumed at the die exit and the mass flow at the exit was calculated and introduced at the top corner of the applicator. An iterative scheme was used to converge to steady flow conditions

Both free and solid boundary conditions are tried at the top surface of the applicator. The fluid taken by the fiber during coating is replenished by a small opening with fluid inflow near the top of the applicator. This maintains the overall mass balance for the system. The inflow conditions are simulated quite satisfactorily and are found to influence the flow very insignificantly. Besides acrylates, several very viscous coating materials are considered to evaluate the effectiveness in providing a high quality coating at high draw speeds. Several interesting results are obtained that may be used to design the die and the applicator.

RESULTS AND DISCUSSION

A fairly generic open cup applicator design with a curved profile die at the bottom were chosen for simulation. The coating fluid was initially chosen to be glycerine, as used in the experiments carried out for the fiber coating process. The draw speed is a very important parameter. Fiber speeds of 1, 5 and 15m/s were chosen to represent the range of draw speeds commonly employed in practice. Stream function plots obtained for various fiber velocities are shown in Fig (1) for the applicator configuration with a free surface at the top.

Recirculatory flow regions were found to arise over most of the computational domain. As the draw speed was increased from 1 m/s to 5m/s and then to 15m/s, stronger recirculatory flows were obtained, along with a downward shift in the recirculation zone, away from the open boundary. At a fiber speed of 15 m/s, an onset of asymmetry was also observed. Higher speeds in excess of 15 m/s would require a pressurized applicator in view of the limit for air entrainment in open cup applicators.

For higher velocities the exit velocity at the die was seen to vary sharply as the fiber pulls the

fluid along with it due to viscous forces. At larger velocities the viscous boundary layer, is thin and limits the entrainment, resulting in a decrease in the film thickness. The viscous boundary layer regime arises in most industrial coating processes³.

Inflow of the coating material is achieved from a side opening but does not affect the overall flow distribution, as velocities are quite small. High shear flow, as seen for higher velocities is not desirable in the applicator since it may reduce the wetting of the coating material.

The boundary condition at the top surface may also strong influence the flow in the applicator. Results of two different cases, i.e., free surface and solid boundary, are given in Fig1 (a) and Fig (2). The streamlines show a stronger circulation as the flow comes near the fiber for the solid boundary condition. A free surface allows much stronger flows to develop, whereas a solid boundary curbs the flow even if only a portion of the boundary is a wall. Strong flows are found to give rise to oscillations that can adversely effect the quality of the fiber coating.

Fig (3) shows the horizontal velocity profiles for three different vertical locations in the applicator. The three locations chosen were near the top of the applicator, at the middle and at the bottom of the applicator before the die entrance. The u velocity shows a change in sign from the top to bottom of the applicator. In the middle region the horizontal velocity is negligible as expected for recirculating flows. The inlet mass flow rate accounts for the deviation in the horizontal velocity curve for the top section ($z = 0.0168$ m). The inlet mass flow near the top of the applicator, is equal to the mass of the fluid taken by the fiber, and results in a small value of the horizontal velocity.

There is a steep increase in the fluid velocity as one approaches the fiber near the solid boundary. The velocity profile for the free surface is smoother near the top of the applicator. The much faster decrease in the u velocity for the solid boundary accounts for the recirculating zones near the fiber.

Fig (4) shows the calculated v velocity profile for the two boundary conditions. The vertical velocity rapidly decreases as we go along the radius. The point along the radius where the v velocity starts increasing rapidly is the point

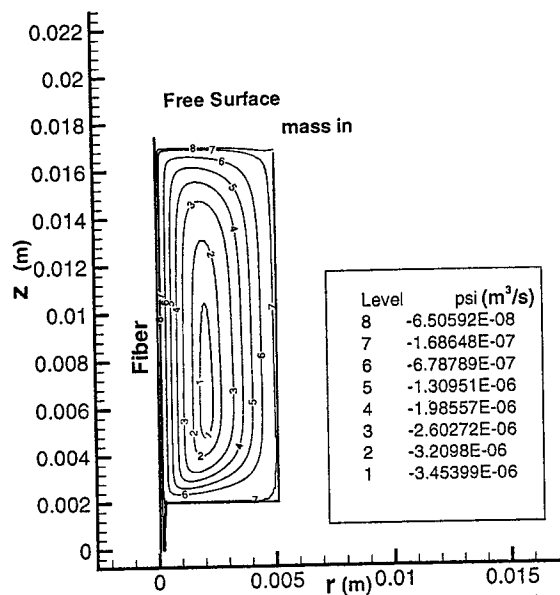


Fig 1(a) Stream function distributions for a fiber speed of 15m/s.

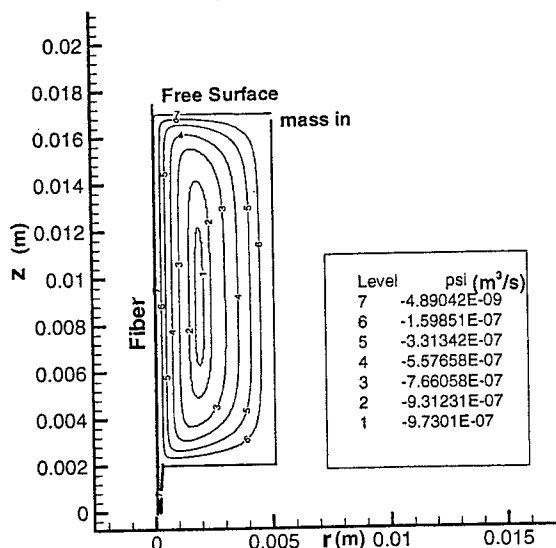


Fig 1(b) Stream function distributions for a fiber speed of 5m/s

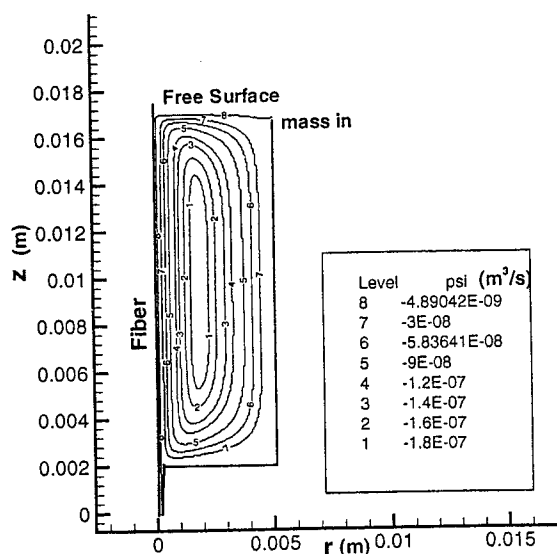


Fig 1(c) Stream function distribution for a fiber speed of 1m/s.

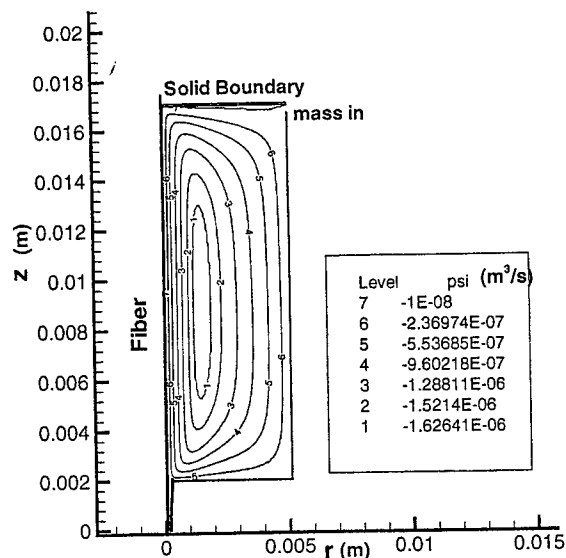


Fig 2) Stream function distribution for a fiber speed of 15m/s. (Solid Boundary at applicator top)

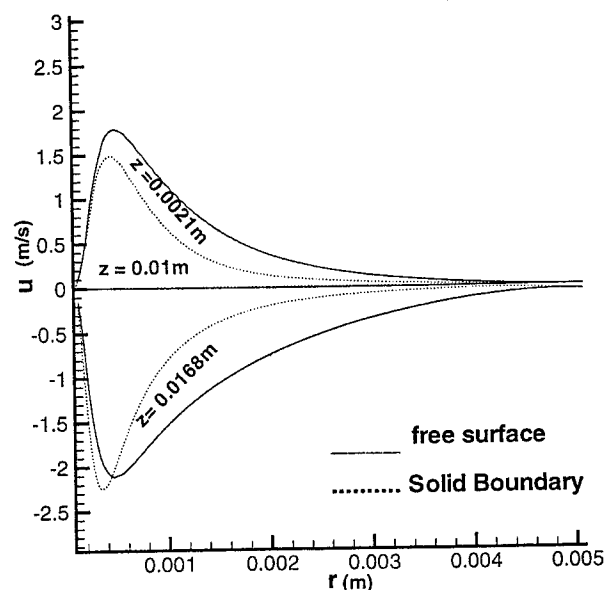


Fig 3) Horizontal velocity Profile at different vertical locations in the applicator (Fiber speed = 15 m/s)

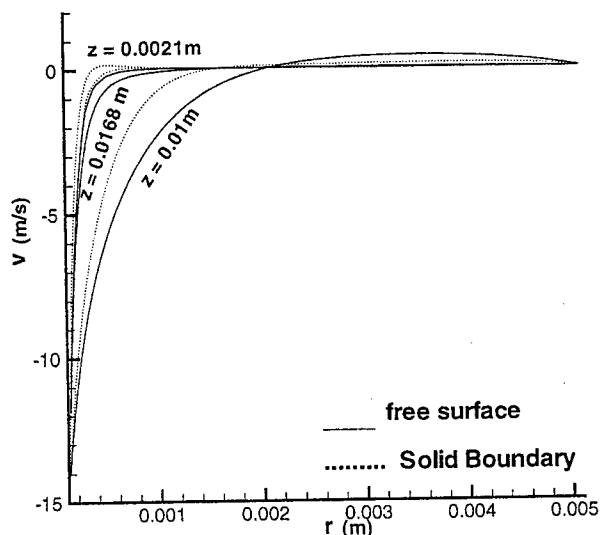


Fig 4) Vertical velocity for different vertical locations of the applicator (Fiber Speed = 15m/s)

where the u velocity starts decreasing in Fig (3). For the middle section the v velocity has a small positive value as expected in such a recirculating flow.

Fig (5) shows the vector plot for different inlet diameters of 200, 250, 300 μm for the same die exit which is kept constant at 200 μm . The vector plot clearly shows the development of the flow field as we go along the length of the die. For higher curvatures, the flow field becomes flatter as the die inlet is increased. The horizontal velocity is almost negligible in the die. The vertical velocity increases from the entrance to the exit for any radius because of the convergent die. A downstream meniscus at the die exit results primarily from a force balance between viscous and inertia forces, the surface tension being a relatively small effect³.

The transformations used for the die were also used to model the meniscus at the top of the applicator, using experimentally measured profiles. The effect of the meniscus on the flow field was found to be negligible.

A comparison between the results for a parabolic curve die and a conical die, for a fiber speed of 5 m/s, is shown in Fig 5(c) and Fig (6). There is a marked difference in the exit velocity profile for the two cases. The flow develops much faster for the curved die but remains constant at the later part of the die, whereas for the conical shaped die the flow develops gradually. As we move along the length of the convergent die the velocity profile tends to be flatter, being more for the conical die. The taper of the die is restricted between 2° - 8° as the self-centering force is maximized for the coating in this range¹⁶.

Different die exit diameters were also considered for constant die inlet diameter and applicator dimensions. Vertical velocity profiles for the different exit diameters are compared in Fig (7) for one particular value of die radius. The increase in the vertical velocity as one goes along the length of the die is due to the convergent profile of the die. The final coat is known to be strongly dependent on the exit diameter of the die.

The vertical velocity profiles for three different horizontal locations of the applicator are compared in Fig (8). The velocity increases sharply as we go along the length of the

applicator at a horizontal location of 200 μm i.e. very close to the fiber. The fluid enters the die with a decreased velocity because of the circulation near the die entrance. The velocity is significantly smaller at farther locations in the applicator.

Different materials were tried with a wide range of viscosities. The velocity profile at the exit for all these fluids is the same for the same die dimensions. It is known that the coating thickness is largely independent of the viscosity for an open cup applicator¹⁵. The exit velocity profiles for the different materials confirmed this trend.

The mass balance is obtained by replenishing the lost fluid, taken up by the fiber from the small inlet provided at the top. The mass flow rate obtained for different materials with different density and viscosities is shown in Fig (9). It is found to be in direct proportion to the density of the fluids, hence proving the small effect of the viscosity of the material.

Fig (10) shows the stream function plot for a smaller applicator. The streamlines show the presence of a strong recirculation zone for this dimension also. This shows that the applicator size does not have any major effect on the flow distribution in the die.

CONCLUSIONS

In this paper a quantitative evaluation of the flow in different applicator and die designs is carried out. Consideration of high speed coating applicator designs, or the optimization of the existing equipment, can only be accomplished if the influence of applicator geometry and operating conditions, coating material properties, and draw parameters such as fiber speed and diameter can be related to the properties of the final coating. The use of high draw speeds requires consideration of alternate pressurized applicator designs where pressure induced motion of the coating material is used to reduce the shear at the fiber surface. The effect of geometry, fiber speed, flow configuration, coating die dimensions and coating material is attempted. This analytical/numerical model of the coating process, gives the relationships between the parameters of the coating process and the characteristics of the coating material.

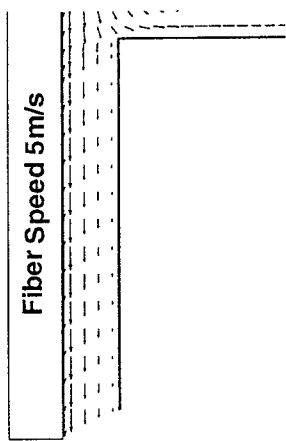


Fig 5(a) Die Inlet 200 μm

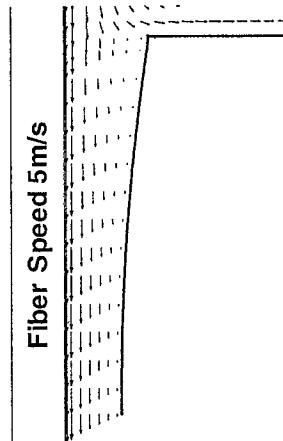


Fig 5(b) Die Inlet 250 μm

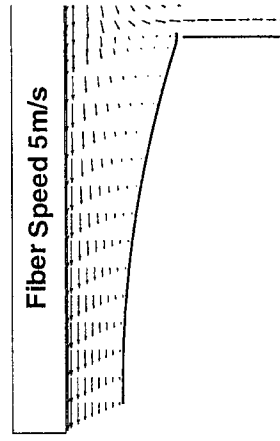


Fig 5(c) Die Inlet 300 μm

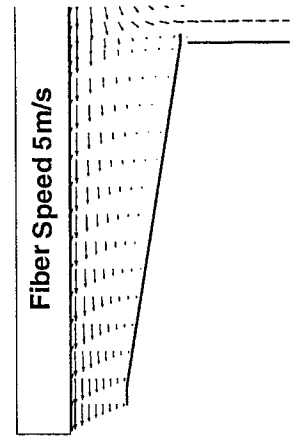


Fig (6) Die Inlet 300 μm
(Tapered Die)

Fig (5) Vector Plots for different die inlets

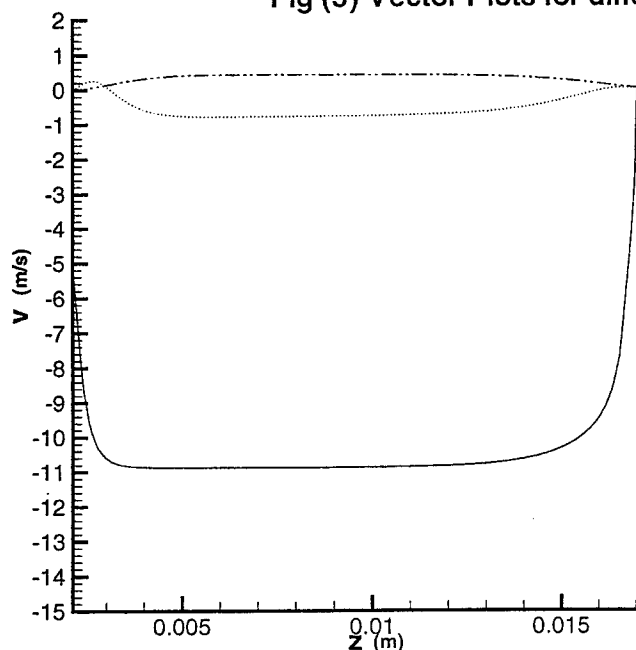


Fig (7) Vertical velocity at different horizontal locations of the applicator (Fiber speed 15 m/s)

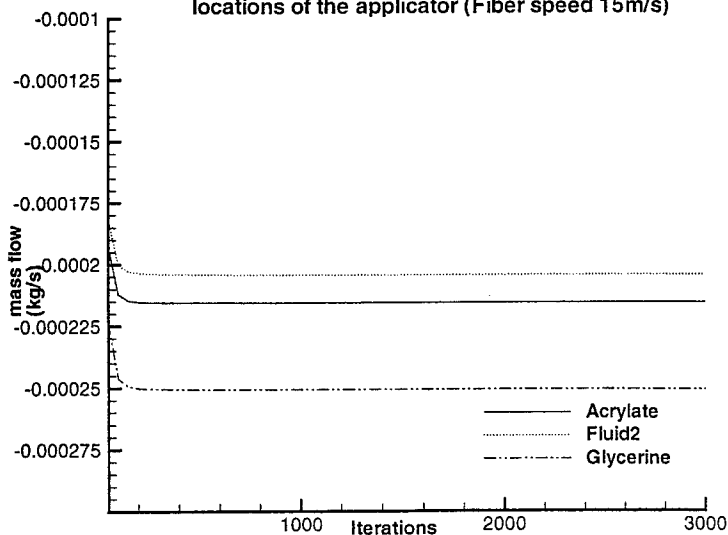


Fig (9) Mass Flow rate at die exit

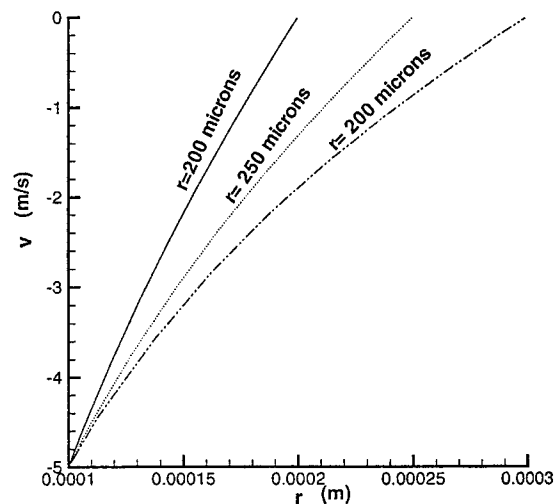


Fig (8) Velocity Profile at exit for different exit radius

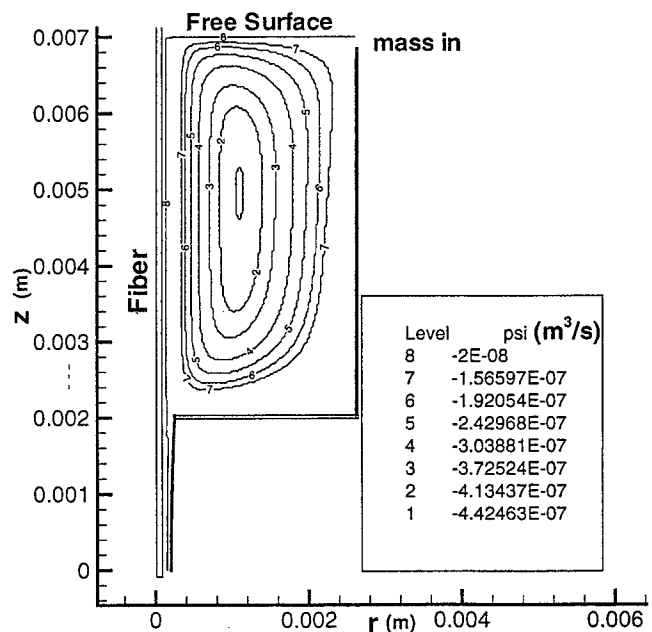


Fig (10) Stream Function distribution for different applicator dimensions

NOMENCLATURE

u	Horizontal velocity (m/s)
v	Vertical velocity (m/s)
R_{fiber}	Fiber Radius (m)
L	Die Length (m)
$R(z)$	Die radius profile (m)
p	Pressure (Pascal)
ψ	Stream Function (m^3/s)

Greek Symbols

μ	Viscosity (Poise)
η	Transformed vertical coordinate
ξ	Transformed horizontal coordinate
ρ	Density (kg/m^3)

Table 1. Properties of Coating Materials Considered

Fluid	Density, Kg/m^3	Viscosity(Poise)
Fluid 1	1250	10
Acrylate	1077	70
Fluid 2	1016	2
Fluid 3	1100	35

ACKNOWLEDGMENTS

This work was supported by the National Science Foundation through Grant CTS-9610102 supported this work, and by the Fiber Optic Material Research Program at Rutgers University. Discussions with Professor C.E. Polymeropoulos and Dr. W.K.S. Chiu are gratefully acknowledged.

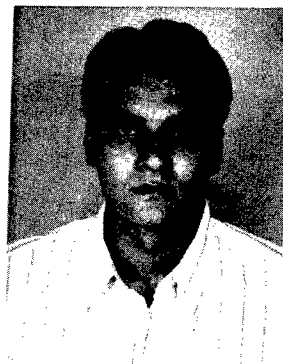
REFERENCES

1. Blyler, L. L., Di Marcello, F.V. (1980) "Fiber Drawing, Coating and Jacketing", Proc. IEEE, vol. 68, 1194-1198.
2. Chida, K., Sagaguchi, S., Wagatsuma, M., and Kimura, T. (1982) "High Speed Coating of Optical Fibers with Thermally Curable Silicon Resin Using a Pressurized Die", Electr. Lett., vol. 18, 713-715.
3. Quere, D., (1999) "Fluid Coating on a Fiber", Annu. Rev. Fluid Mech., vol. 31 347-384.
4. Abbot, J.S., and Francis, D.C., (1989) "Analysis of the Optical Fiber Coating Process Using FIDAP: Flow, Heat Transfer, and 3-D calculation of Centering Forces," Proc. 3rd FIDAP Users Conf.
5. Simpkins, P.G. (1994) "Thermal Response of Optical Fibers to Metalization Processing", Mat. Sci. and Engineering, vol. B-23, L5-L7.
6. Jaluria, Y., (1992) "Transport from Continuously Moving Materials Undergoing Thermal Processing", Ann. Rev. Heat Transfer, vol. 4, 187-245.
7. Paek, U.C., and Schroeder, C.M., (1979), "Coating of Optical Fibers with a Conical Shape Applicator", Fiber and Integrated Optics, vol. 2, 287-298.
8. Wagatsuma, M., Kimura, T., and Yamakawa, S., (1986) "Slip Mechanism in Optical Fiber Coating with Open Cup Applicators", J. of Lightwave Tech., vol. LT-4, No 9, 1414-1419.
9. Ruschak, K.J., (1985) "Coating Flows", Ann. Rev. Fluid Mech., vol. 17, 65-89.
10. Rodi, W., Majumdar, S., and Schonung, B. (1989), "Finite Volume Methods for Two-Dimensional Incompressible Flows with Complex Boundaries." Computer Methods in Applied Mechanics and Engineering, vol. 75, 369-392.
11. Karki, K.C., and Patankar, S.V., (1988) "Calculation Procedure for Viscous Incompressible Flows in Complex Geometries." Num. Heat Transfer, vol. 14, 295-307.
12. Peric, M., (1990) "Analysis of Pressure Velocity Coupling on Nonorthogonal Grids.", Num. Heat Transfer, Part B, vol. 17, 63-82.
13. Shyy, W., Tong, S.S., and Correa, S.M., "Numerical Recirculating Flow Calculation Using a Body-Fitted Coordinate System.", Num. Heat Transfer, vol. 8, 99-113.
14. Landau, H.G., (1950) "Heat conduction in a melting solid", Quart. Appl. Math., vol. 8, 81-94.
15. Patankar, S.V., (1980) "Numerical Heat Transfer and Fluid Flow", Hemisphere, Washington, D.C.
16. Paek, U.C., (1986) "High Speed High Strength Fiber Drawing", Journal of Lightwave Technology., vol. LT-4 No 8, 1048-1059.
17. Matsuda et al. (1992), United States Patent, No. 5,127,361.

Kunal Rattan was born in Chandigarh, India in 1977. He did his B.S. in Mechanical Engineering from Indian Institute of Technology, Kharagpur in 1998. He is currently doing his M. S./Ph. D. in Rutgers, the State University of New Jersey, in Thermal Sciences under Prof. Y. Jaluria.

Address :

Department of Mechanical and
Aerospace Engineering,
Rutgers, The State University of New Jersey,
98 Brett Road,
Piscataway, NJ 08854-8058



METAL-FREE HEAT-RESISTANT OPTICAL FIBER FOR FIBER OPTICS SENSING SYSTEMS IN OIL WELLS

Makoto Shimizu, Yuji Kubo, Tomoyuki Hattori, Katsuyuki Tsuneishi,
Robert Rubino*, Douglas Norton*

Sumitomo Electric Industries, Ltd.
Yokohama, Japan
*CIDRA Corporation
Wallingford, Connecticut

ABSTRACT

A metal-free, heat-resistant optical fiber for fiber optic sensing systems used in oil wells has been developed by applying a heat-resistant material as a new primary coating layer, in consideration of mechanical reliability of the optical fiber. This optical fiber has superior stability and optical and mechanical reliability when exposed to a downhole environment of hydrogen and temperatures of up to 250 °C.

INTRODUCTION

The technology needed to develop high temperature oil and gas fields has progressed quickly in the 1990s. However some projects had been confronted with the limitations of existing technology. The reservoirs, situated at around five thousand meters below the seabed, consist of oil, sand and water; hence, for efficiently gathering the oil portion, all key parameters such as the constitution, the pressure and the flow rate need to be precisely imaged and monitored along the length of the borehole.

The current technology of single point electronic sensors or wire-line logging does not meet the reliability requirements of these new

advanced oil wells. In this harsh environment, the average electronic sensor has a limited life span, and can exhibit inaccuracy due to electromagnetic interference. Currently, 3D seismic surveying is a standard approach used in the exploration of current reserves, but in many cases the high cost makes it prohibitive for many fields. The special application of the fiber optics sensors is a major breakthrough in the oil and gas fields. Figure 1 shows the concept of the fiber optics sensing system. The new technology of 4D seismic surveying via fiber optic sensors (3D seismic surveying with the added dimension of time) has inherent

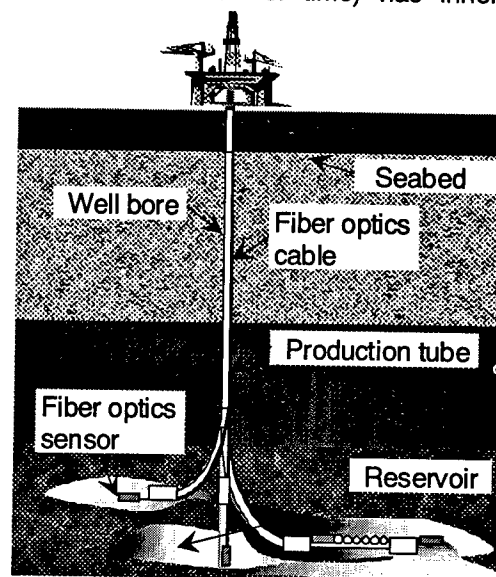


Figure 1 Fiber optics sensing system concept

advantages over the conventional electronic sensing technologies.

An optical fiber with metal coating had been considered as one of the optimal designs. Since this optical fiber can be damaged under the influence of the harsh environment such as electromagnetic interference and corrosive fluids, this optical fiber is not suitable for the oil and gas fields. The optical fiber used in such sensing systems must be durable when exposed to high temperature and partial pressures of hydrogen. A metal-free, heat-resistant optical fiber for fiber optic sensing systems capable of withstanding these harsh conditions is extremely desirable.

This paper describes further expanding the range of a conventional metal-free, heat-resistant optical fiber into the oil and gas fields, and the development of the new metal-free, heat-resistant optical fiber for higher heat environment.

FIBER DESIGN

We have investigated the following two metal-free, heat-resistant optical fibers.

- 1) **Conventional**; Optical fiber with silicone coating and tetra-fluoro-ethylene per-fluoro-alkyl-vinyl-ether copolymer (PFA) coating
- 2) **New**; Optical fiber with polyimide coating, silicone coating and PFA coating

These optical fibers realize a superior characteristic against hydrogen by adopting a pure silica core single-mode fiber, whose core area contains no additive at all.

Conventional

The conventional heat-resistant optical fiber with 400 μm diameter of silicone primary coating and 700 μm of PFA secondary coating has been reported¹ (Figure 2). This optical fiber was mainly developed for composite fiber-optic

overhead ground wire (OPGW). Because the optical fiber in OPGW is exposed high temperature in short period at lightning or short circuit trouble, required heat resistance performance for the oil and gas fields is different from that for OPGW.

To confirm the applicability of the conventional heat-resistant optical fiber to the oil and gas fields, we have conducted tensile strength tests after heat aging. As shown in Figure 3, tensile strength was not changed up to 200 $^{\circ}\text{C}$ heat aging, while deterioration of tensile strength was observed at heat aging with 250 $^{\circ}\text{C}$. Hence, it is found that this optical fiber is suitable for long-term use below 200 $^{\circ}\text{C}$.

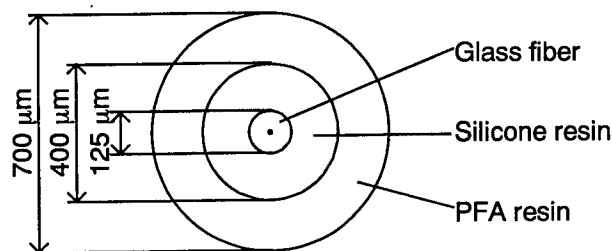


Figure 2 Cross sectional-view of conventional heat-resistant optical fiber

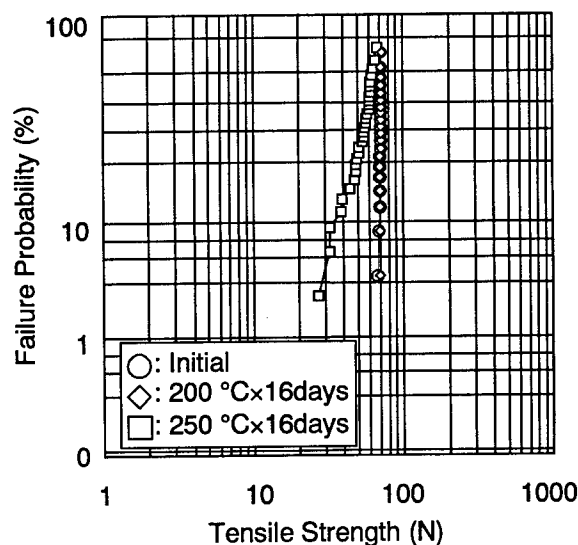


Figure 3 Weibull plots of the tensile strength for conventional heat-resistant optical fiber (Gauge length: 300 mm, Pull speed: 100 %/ min)

New

Temperatures of up to 250 °C can be found in several deep reservoirs. The higher heat-resistant optical fiber is required to secure the fiber optic sensing systems that can withstand harsh conditions.

Material. We estimated that the deterioration of the conventional heat-resistant optical fiber after 250 °C heat aging was caused by the decomposition of the primary coating layer. To develop the new primary coating material for the higher heat-resistant optical fiber, we have evaluated the weight loss measurements during heat aging. The result is shown in Figure 4. Polyimide material can be durable at temperatures of up to 400 °C; however, silicone material reduces the weight at temperatures of around 200 °C. This result proves that silicone material can not protect the vitreous silica at an atmosphere exceeds 200 °C.

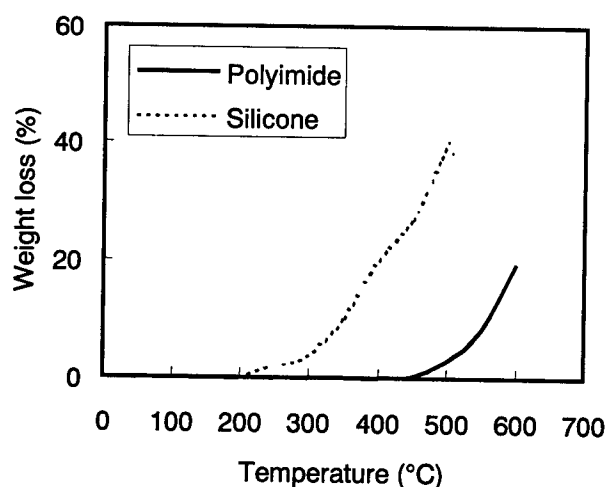


Figure 4 Weight loss results during heat aging

Tensile strength. The tensile strength of the conventional heat-resistant optical fiber should drop as water molecules pass through the decomposed primary coating layer and directly attack the vitreous silica as the following chemical reactions^{2,3}.

- 1) adsorption of water to Si-O bond of a bare glass fiber surface

- 2) concerted reaction involving simultaneous proton and electron transfer
- 3) formation of surface hydroxyl groups

Design. In order to protect the vitreous silica, polyimide material was coated on the bare glass fiber up to 140 μm in diameter as a primary coating (Figure 5). We applied silicone material and PFA material to the developed design as coating layers resembling the conventional design for the purpose to maintain superior mechanical characteristics. Figure 6 shows the result of the tensile strength of the developed optical fiber at a temperature of 250 °C.

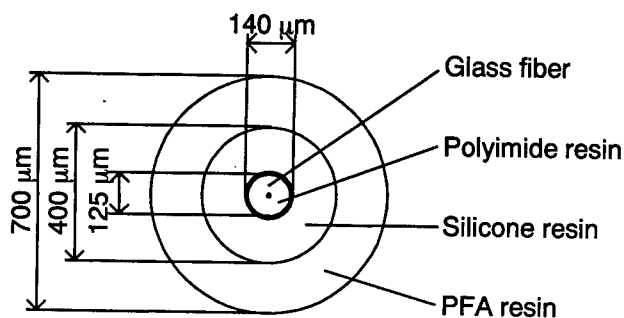


Figure 5 Cross sectional-view of developed heat-resistant optical fiber

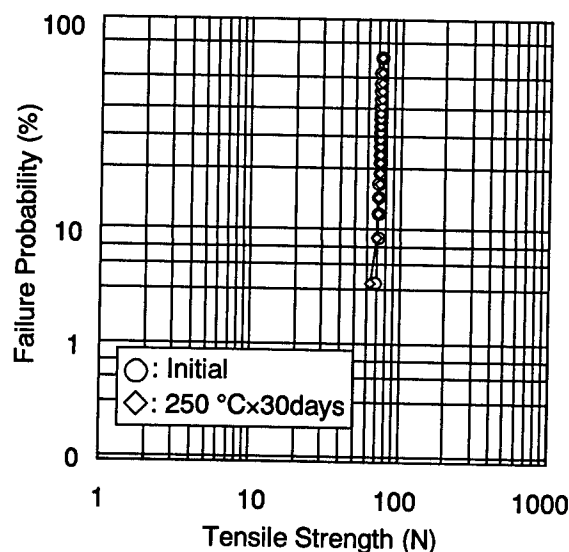


Figure 6 Weibull plots of the tensile strength for developed heat-resistant optical fiber (Gauge length: 300 mm, Pull speed: 100 %/min)

This result indicates that there is no significant deterioration after 250 °C heat aging. Hence, it is found that this optical fiber is suitable for long-term use up to 250 °C.

LABORATORY ANALYSIS

To ensure the robustness and integrity of the developed heat-resistant optical fiber, environmental and mechanical tests were evaluated against IEC 60793 and IEC 60794 standards.

Heat aging

The heat-resistant optical fibers were subjected to a 250 °C heat aging to confirm the durability in deep reservoirs. Figure 7 shows the result of attenuation measurements for a wavelength of 1550 nm during and after 250 °C heat aging. This result shows that no significant attenuation increase has occurred on the developed heat-resistant optical fiber compared with the conventional one.

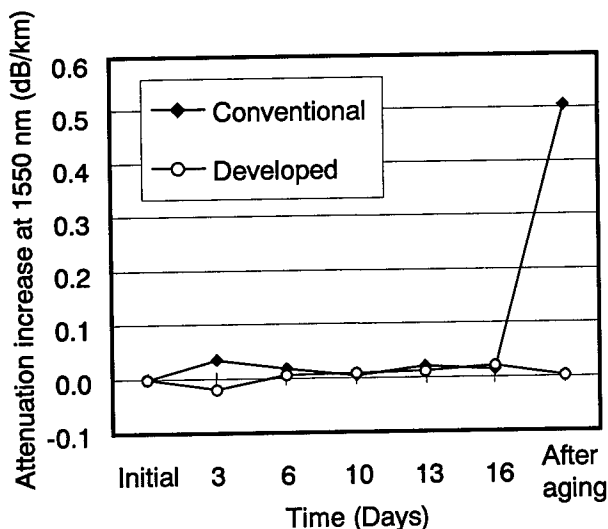


Figure 7 Attenuation Increase during and after 250 °C heat aging

By visual inspection, in the conventional heat-resistant optical fiber, we have confirmed the primary coating crumbles after heat aging.

Temperature cycling

The environment inside oil wells is believed to be comparatively high temperature. In order to evaluate the stability of the developed optical fiber against low temperatures at storage, we have conducted attenuation measurements for a wavelength of 1550 nm in the range of -60 °C to +85 °C. The result is shown in Figure 8. The optical fiber exhibited good characteristics with an attenuation increase of 0.03 dB/km or less even at a low temperature of -60 °C and no residual attenuation increase after the test.

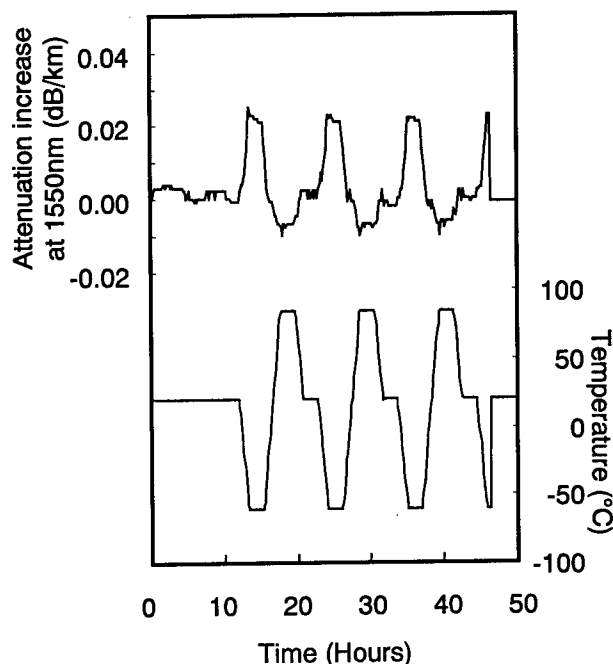


Figure 8 Attenuation Increase during temperature cycling

Shrinkage of coating layers at the low temperature may cause the attenuation increase to the optical fiber.

Mechanical tests

Mechanical tests were conducted to confirm the effect of 250 °C heat aging over 16 days on the developed optical fiber. It was found that the optical fiber met all the applicable conditions as shown in Table 1.

**Table 1 Summary of the key mechanical test results after 250 °C heat aging
for developed heat-resistant optical fiber**

Item	Conditions	Results	Test Procedure
Tensile strength for short lengths of optical fibers	Tensile strength ≥ 49 N (Median value) Gauge length: 300 mm Pull speed: 100 %/min. Number of samples: 20	Tensile strength ≥ 71 N	IEC 60793-1-B2A
Dynamic fatigue, axial tension	$N_d \geq 20$	$N_d \geq 25.3$	IEC 60793-1-B7A
Macrobending sensitivity	Attenuation increase at 1550 nm ≤ 0.20 dB Mandrel diameter: 60 mm Number of turns: 100	Attenuation increase at 1550 nm ≤ 0.00 dB	IEC 60793-1-C11
Crush	Attenuation increase at 1550 nm ≤ 0.20 dB Load: 300 N/ 100 mm	Attenuation increase at 1550 nm ≤ 0.09 dB	IEC 60794-1-E3
Repeated bending	No fiber breakage Bending radius: 150 mm Load: 5 N Number of cycles: 250 Duration of cycles: 2 sec.	No fiber breakage	IEC 60794-1-E6
Torsion	Attenuation increase at 1550 nm ≤ 0.10 dB Sample length: 500 mm Load: 5 N Number of cycles: 5 with $\pm 360^\circ$ and 1 with $\pm 1080^\circ$	Attenuation increase at 1550 nm ≤ 0.00 dB	IEC 60794-1-E7

FIELD APPLICATION

In addition to the need for long term mechanical reliability, optical fiber used for oil well sensing must be protected from other aspects of the harsh environment such as corrosive fluids. These fluids include sulfuric acid, drilling mud, brine, and gasses such as hydrogen, hydrogen sulfide and methane.

A common method of providing protection from these chemicals is the use of steel armoring or tubing as well as other polymeric and metallic jacketing materials. In the event that these materials were breached, the fiber must be resistant to the harmful effects of these corrosive fluids. The buffer layers of silicone and PFA provide a resistance to many acidic and caustic liquids including water, below their decomposition temperature. Also, these thicker

coatings provide a mechanical protection not provided by the polyimide primary coating, which is essential for the manufacturing processes of the downhole cable and for general handling and terminations.

Aside from the ruggedness and chemical resistance afforded by the developed coating systems, the glass composition is important to the viability of optical fiber in a well. The negative effects of hydrogen on the transmissive properties of optical fiber over a broad spectrum of useable wavelengths has been well documented^{4,5}. The exact concentrations and quantities of hydrogen gas present in many wells has been debated, but it is known that hydrogen is a by-product of corrosive reactions that commonly occur with steel alloys used for production piping in a well.

Finally, inasmuch as the fiber design is tolerant of the presence of downhole hydrogen and its buffer impervious to the ingress of corrosives deleterious to the mechanical strength of the fiber, cable engineering is extremely important for long-term downhole reliability. To this end, the downhole optical transmission cable has been designed to isolate the fiber from exposure to long-term stress that might otherwise promote stress corrosion aging of the fiber that could lead to premature mechanical failure. Additionally, cable materials were selected with special attention paid towards corrosion resistance, hydrogen generation and hydrogen permeability in an overall strategy to minimize long-term optical loss and thereby maximize system availability.

As a result of this environmentally robust fiber and cable design, downhole Bragg grating-based fiber optic sensor systems, installed in operating oil wells since March 1999, have shown no evidence of increased optical loss signaling the ingress of hydrogen or other mechanisms that may lead to the premature failure of the fiber.

CONCLUSION

We have described the development of the metal-free heat-resistant optical fiber for fiber optic sensing systems used in oil wells.

The ability of this optical fiber to withstand the harsh conditions was tested during significant aging in the laboratory as well as in the fields. As a result of the battery of tests, it can be concluded that this optical fiber has superior stability and reliability in the oil and gas fields.

ACKNOWLEDGEMENTS

The authors wish to thank Mr. Paul Sanders from CiDRA Corporation and Mr. Yasunori Saito from Sumitomo Electric Industries, Ltd. for their helpful information and advice.

REFERENCES

1. S. Okuyama, Y. Kameo, Y. Toda, Y. Kitayama, M. Yuto, "High heat-resistant optical fiber coated with thermal-cured

type silicone and fluorine polymer", International Wire & Cable Symposium Proceedings, 1986, p.183-188

2. Hakan H. Yuce, "Aging behavior of optical fibers", International Wire & Cable Symposium Proceedings, 1992, p.605-611
3. Terry A. Michalska, Stephen W. Freiman, "A molecular mechanism for stress corrosion in vitreous silica", Journal of the American Ceramic Society Vol. 66, 1983, p.284-288
4. S. R. Nagel, "Reliability issues in optical fibers," in Reliability Considerations in Fiber Optic Applications, D. K. Paul, Ed., Proc. SPIE 717, 8-19 (1986).
5. P. J. Lemaire, "Reliability of optical fibers exposed to hydrogen: prediction of long-term loss increases," Optical Eng., Vol. 30, No. 6., June 1991.

SPEAKER BIOGRAPHY



Makoto Shimizu

Makoto Shimizu joined Sumitomo Electric Industries, Ltd. in 1994 as a fiber optics engineer. He holds a B.S. degree in Applied Chemistry and a M.S. degree in Material Science from Keio University. He is active in the International Electro-technical Commission (IEC) with the standardization of optical fibers and cables.

A STUDY ON UV-TRANSPARENT UV-CURABLE RESIN FOR FIBER BRAGG GRATINGS WRITTEN THROUGH A FIBER COATING

Terunobu Iio, Kumiyo Hosotani, Hirokazu Kuzushita, Takeshi Genji, Kazuo Imamura

Mitsubishi Cable Industries, Ltd., Hyogo, JAPAN

ABSTRACT

Fabrication of fiber grating without removing the coating prevents degradation of fiber strength and simplifies the manufacturing process. As a coating material suitable for irradiating through the coating with good productivity, we studied on an aliphatic urethane acrylate UV(Ultraviolet) curable resin with improved transparency. We evaluated the transparency, mechanical characteristics, long term reliability of the resin and the properties of the coating before and after UV laser irradiation, and confirmed the new resin to have the good characteristics and reliability adequate as the coating for fiber gratings.

INTRODUCTION

In recent years, fiber gratings and its applications have been widely studied in the field of optical communications and fiber sensor systems. The technology is ready to be tried in practical uses. Fiber Bragg gratings create a periodic refractive index modulation lengthwise to the fiber using the photo induced refractive index change of the core. Therefore the fiber grating functions as a reflective filter for a particular wavelength in the same cycle as the refractive index modulation.

Fiber Bragg gratings are usually fabricated by irradiating UV laser on the fiber. The coatings are removed mechanically and chemically before the irradiation, because the coatings absorb the UV rays. This process weakens the fiber at the gratings¹⁾.

A method which directly irradiates UV laser on the coating can increase the productivity. The fabricated fibers would have long-term reliability as it would not require re-coating and makes packaging simple. For such a method, UV transparent resins were used to coat on a high

sensitive fiber to obtain satisfactory transmission characteristics and mechanical strength^{2),3),4),5)}.

We improved the transparency of UV curable resin which was normally used for a fiber coating and fabricated the fiber Bragg gratings through the coating using this resin. The fiber gratings showed promising peak reflectivity and mechanical strength⁶⁾.

In this paper, we report on the properties and the long-term reliability of the new UV curable resin and the coating after fabricating fiber Bragg gratings.

EXPERIMENTAL

I. Coating materials

UV curable resins generally used for communication optical fibers absorb the UV rays necessary for fabrication of the gratings. Conventionally, coating removal was necessary when fabricating fiber gratings.

We therefore developed an aliphatic urethane acrylate UV curable resin which eliminated all additives and had a decreased photo initiator concentration to increase the transparency in the UV region so that the optical incident energy would not dampen. The concept of this new resin is shown in Fig.1.

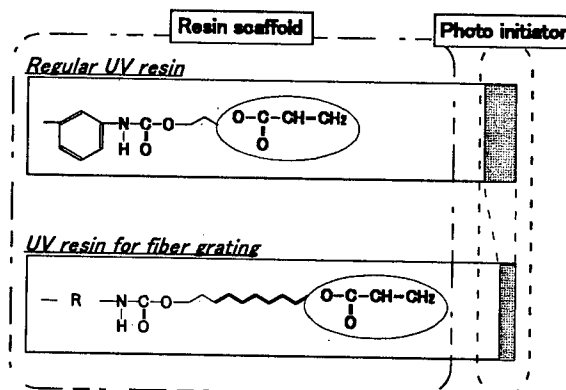


Fig.1. Fabrication of resins for gratings

II. Characteristics of the new material

The resin film was cured for evaluating the following characteristics.

[How test films are made]

A spinner was used to coat a glass plate with resin to an arbitrary film thickness. To prevent oxygen from curing the resin surface, the films were put under nitrogen atmosphere. Metal halide lamps were used to irradiate the coated glass with UV light to make the cured film.

① Absorption characteristics in the UV region

The UV absorption spectrum of the resin was measured. The film thickness was $10\mu\text{m}$, UV dose was $1000\text{mJ}/\text{cm}^2$. The absorbance is expressed in the equation below (Fig.2.) in accordance with the Lambert-Beer law. The spectroscopy used was a prism-diffraction grid double monochromator. The measurement results are shown in Fig.3. A significant improvement in the transparency can be observed in the UV region.

$$\text{Absorbance} = -\log(I/I_0)$$

I_0 : power of incidence

I : power of transmitted light

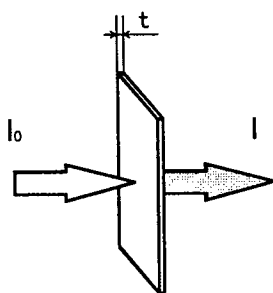


Fig.2. Principle of the absorption

I_0 : power of incidence

I : power of transmitted light

t : thickness of the film

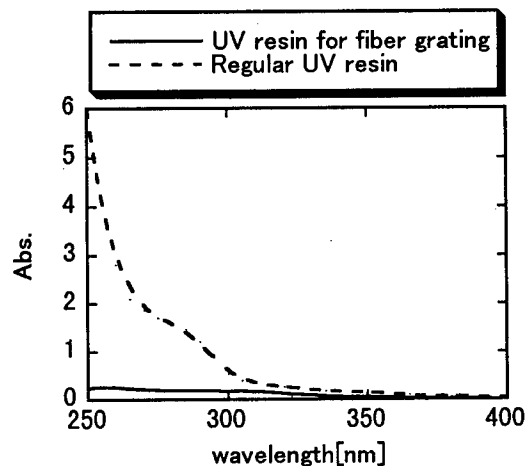


Fig.3. Absorption spectrum of the resin

② Basic characteristics

Table.1 shows the evaluations of basic characteristics required in a fiber coating material. The test film had a film thickness of $200\mu\text{m}$, UV dose of $1000\text{mJ}/\text{cm}^2$. Results indicate that they are suitable for coating material.

Table1. Characteristics of the new resin

Young's modulus [MPa]	-40°C	1895
	23°C	445
	60°C	24
Elongation[%]		50
Strength[MPa]		35

③ Curability

Fig.4. shows the curing speed of the resin. The UV dose was changed (from 50 to $1000\text{mJ}/\text{cm}^2$) for curing and the relative value of Young's modulus was compared. The obtained values were used to determine the fiber drawing conditions.

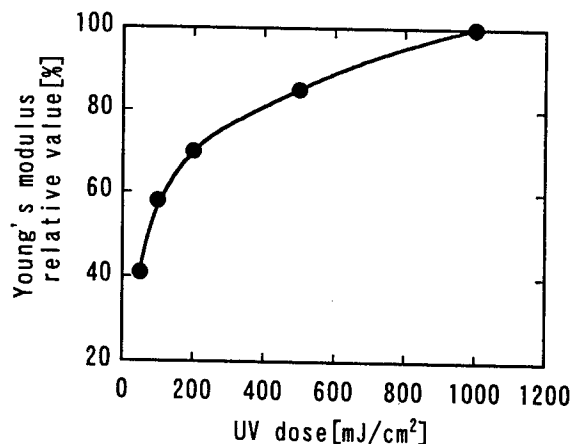


Fig. 4. Curing speed of UV resin for fiber gratings

④Long-term reliability

Though we have already indicated that the resin has sufficient basic characteristics to be used as a fiber coating, in the long term, its reliability is uncertain as additives such as antioxidants have eliminated to improve the transparency in the UV region. Therefore the resin was tested for heat aging and moisture heat aging.

[Testing conditions]

The film samples were placed in a fixed frame and put under an accelerated degradation test in the atmosphere shown below.

- heat aging ... 60, 80, 100°C-dry
- moisture and heat aging ... 80°C-95%RH

[Evaluation items]

a tensile tester measured:

- Young's modulus(2.5% elongation load)
- Tensile elongation

[Results and considerations]

Fig.5. and 6. show the results. In 80°C-dry, 80°C-95%RH atmosphere, the resin properties are stable with little change. As for the long term reliability, though there were concerns of effects from the decrease of photo initiator concentration and the absence of antioxidants, the resin is sufficiently adequate as fiber coatings.

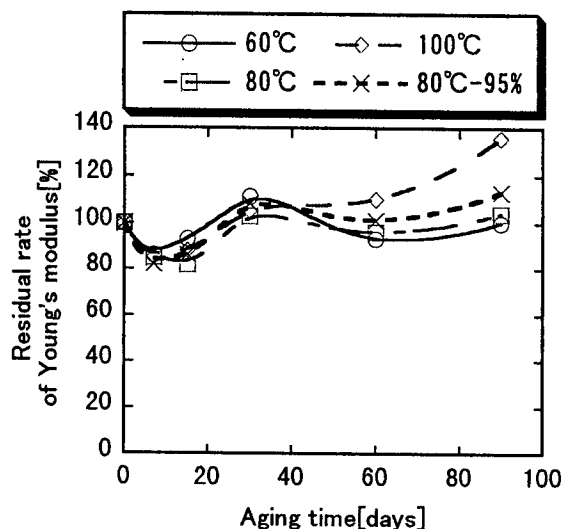


Fig.5. Changes in Young's modulus with time

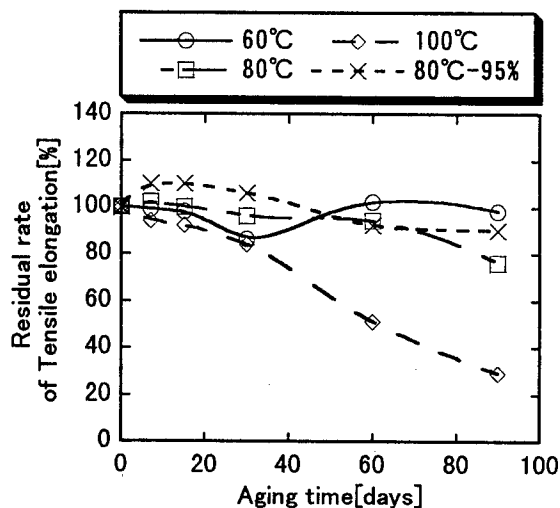


Fig.6. Changes in elongation with time

III. Fabrication of fiber gratings⁶⁾

① Coating the fiber

Coating the new resin on the fiber was done by a fiber drawing tower used for regular communication fibers. We confirmed the coating uniformly and no tacks. When the Young's modulus of the coating on the fiber was measured, we confirmed it to be completely cured.

② Grating through the coating and transmission characteristics

Short periodic fiber gratings were fabricated by the phase mask method using 266nm, the fourth harmonic of the Nd-YAG laser, as the UV source. 24mm gratings were made by direct exposure on the coating. A maximum reflectivity of more than 99% was obtained at 1.5kJ/cm² dose.

IV. Characteristic change caused by the UV laser

① Measurements of Young's modulus

It is assumed that UV laser rays on the coating could change the material characteristics of the exposed areas. To acknowledge the degree of change in the material, the change in Young's modulus of the coating exposed with UV laser was investigated. Fig.7. shows the change of relative values of Young's modulus measured at the UV exposed front side and its back side as the irradiation energy concentration changed.

Even when more than 3.0kJ/cm², twice the energy necessary for grating was irradiated, the change in Young's modulus for both the irradiated front and back side remained within 20%. We considered this a satisfactory initial characteristic for a coating material. However when the irradiation energy concentration became extremely strong (7.5kJ/cm²), differences between the front and backside of Young's modulus were observed. It is assumed that degradation occurred in the irradiated front. It is necessary to adjust the most optimum dose when fabricating gratings.

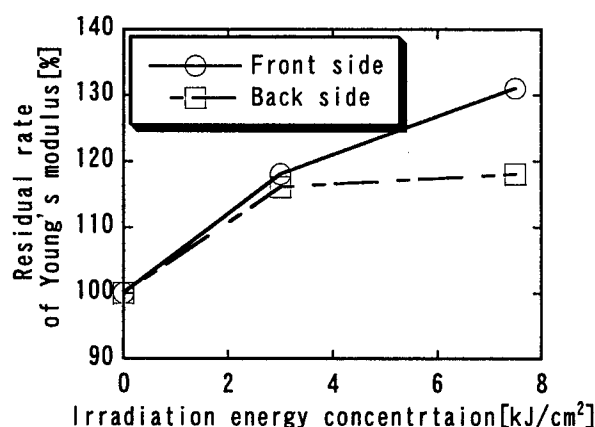


Fig. 7. Change in Young's modulus of the coating material

② Measurements of the infrared absorption spectrum

To investigate the degradation mechanism of the resin, the IR(infrared) absorption spectrum of portions of unexposed area, a front area irradiated with 7.5kJ/cm² and its back side were investigated. The measurements were made by the ATR-microscope method shown in Fig.8. The results are shown in Table 2. From the increase of the peak area of the carbonyl group seen at 1760cm⁻¹, it became clear that photooxidation degradation was proceeding after laser irradiation. Compared to the back side, the peak area changes on the irradiated front side is larger. The assumed reason is that the irradiated front side is exposed to higher energy concentration than the back side.

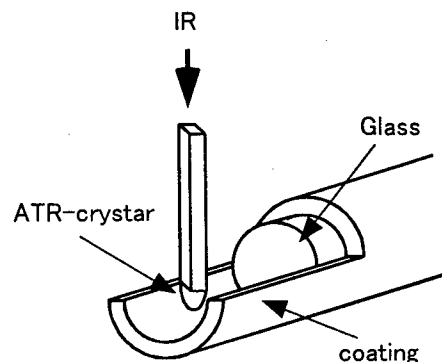


Fig.8. Scheme of ATR-microscope method for the IR measurement of the coating

Table2. Measurements of the IR absorption spectrum*1)

		Relative value of peak area*2)
Before irradiation		1
After irradiation	front	1.10
	back	1.01

*1)Change of the peak area
of the carbonyl group at 1760cm^{-1}

*2)The area before irradiation is
represented by a relative value 1.

③Reliability of the coating exposed to UV laser

From the IR absorption spectrum, we found that excess exposure to UV laser generates photooxidation on the irradiated coating. To examine the reliability of actual fiber gratings, Young's modulus and the change in the IR absorption spectrum was evaluated. We took three samples; portions of unexposed fiber, a front area irradiated with $1.5\text{kJ}/\text{cm}^2$ and its back side.

[Testing conditions]

The samples were place in a fixed frame and put under an accelerated degradation test in the atmosphere shown below.

- heat aging ... 80°C -dry
- moisture and heat aging ... 80°C -95%RH

Results are shown in Table 3. With or without gratings Young's modulus only changed a little in 30 days. The IR absorption spectrum also did not change. Therefore we found that there was little effect to coatings from the UV laser quantity used for the actual fabrication.

From the above results, we conclude that the new aliphatic urethane acrylate UV curable resin is a suitable coating material for fiber gratings.

CONCLUSION

As a coating material suitable for direct irradiation on the coating and with superior productivity, an aliphatic urethane acrylate UV curable resin with improved transparency :

- 1) can be coated on to fibers with a regular fiber drawing tower and has a good properties as a coating material;
- 2) has significantly improved transparency in the UV region, allowing direct writing through the coating for grating fabrication;
- 3) has sufficient reliability though antioxidants are not added.
- 4) has sufficient reliability with adequate UV laser dose, but excess irradiation during grating fabrication generates oxidation degradation.

REFERENCES

1. R. Feced, M. P. Roe-Edwards, S. E. Kanellopoulos, N. H. Taylop and V. A. Handerk : "Mechanical strength degradation of UV exposed optical fibres", Electron. Lett., 1997, 33 pp.157-159.
2. L. Dong, J. L. Cruz, L.Reekie, M. G. Xu and D. N. Payne : "Enhanced photosensitivity in Tin-codoped germanosilicate optical fibers", IEEE Photonics Technol. Lett., 1995, 7, pp.1048-1050
3. R. P. Espindora, R. M. Atkins, D. A. Simoff, K. T. Nelson and M. A. Paczkowski : "Fibre Bragg gratings written through a fibre coating", OFC '97 Tech. Dig., 1997, Postdeadline Paper PD-4
4. D. A. Simoff, M. A. Paczkowski, R. Ragan, D. Inniss, T. A. Strasser, J. M. Borick, J. R. PEedrauani, R. P. Espindola, R. M. Atkins, K. T. Nelson, J. Aspell and V. J.Kuck : "Coatings having enhanced UV transparency for the fabrication of optical fiber gratings", IWCS '97, 1997,pp.86-93

Table.3 Change in modulus aging for 30days

Sample	Initial	After aging at 80°C	After aging at $80^\circ\text{C}/95\%RH$
Coating before fabrication the gratings	100	105	97
Coating after fabrication the gratings(front side)	100	98	90

5. K. Imamura, T. Nakai, K. Moriura, Y. Sudo and Y. Imada : "Mechanical strength characteristics of tin-codoped germanosilicate fiber Bragg gratings by written through UV-transparent coating", Electron. Lett., 1998, 34, pp.1016-1017

6. T. Nakai, K. Imamura, Y. Sudo and Y. Imada : "Characteristics of tin-codoped germanosilicate fiber Bragg gratings written through an UV-transparent coating", IWCS '98, 1998, pp.938-943



Hirokazu Kuzushita
Mitsubishi Cable Industries, Ltd.
8,Nishinocho,Higashimukaijima,Amagasaki,Hyogo,
660-0856 Japan

H.Kuzushita received B.E. and M.E. degree in Industrial Chemistry from Kyoto University in 1977 and 1979 respectively. Then He immediately joined Mitsubishi Cable Industries, Ltd. And He has been engaging in the research and development of plastic materials for communication cables. He is now senior research engineer of Central Research Laboratory.

Panel Discussion Abstract—Session 19

IMPROVEMENTS IN MAINTAINABILITY AND PROCESS CONTROL IN DATA/TELECOM DRAWING MACHINERY

SEAN KILGALLEN, M.Eng.

Henrich, Inc. Huntersville, North Carolina

ABSTRACT

Data and telecom cables are constantly being expected to transmit more data and at faster speeds than ever before. This means that cable quality standards are becoming more critical and hence the quality of the copper wire within the cable must improve.

We believe that the quality of the wire used should be controlled from the rod. Wire quality cannot be improved by a drawing machine so it is critical to feed the inline drawing machine with the best possible wire from the rod breakdown machine. Henrich have been pioneering the use of individual drive rod breakdown machines for non-ferrous drawing for the last six years. By using a rod breakdown machine with adjustable elongation and controllable minimized slip, you can control the physical properties and surface quality of the wire to the optimum.

Henrich's new inline data cable drawing machines also uses individual drives for each cone pair.

The use of individual motors for each drawing shaft has the added effect of improving maintainability as they make the drawing machine very simple mechanically. There is no large noisy gearbox to maintain etc.

Improvements in annealing technology has also led to modular manufacture of assemblies which are easy to maintain and the Henrich use of Beta non contact preheaters removes another maintenance headache from the machine.

The Henrich philosophy on maintenance is to design out maintenance where possible and if it is not possible, to make the maintenance items as accessible and quick and easy to check and change as possible.

BIOGRAPHY

Sean Kilgallen is currently Sales Manager for North America based at the Henrich Inc. facility in Huntersville, North Carolina. He joined Henrich in 1995 and moved to the USA from England in March 1996 to develop the sales and service division of Henrich in the USA.

Panel Discussion Abstract—Session 19

DEVELOPMENT ON INCREASING PRODUCTIVITY FOR LAN COPPER PAIR

Philippe P. LETOUT
POURTIER Pere & Fils - France

The increasing demand in copper LAN cable has led to the research of new stranding method in order to increase the productivity. At the same time the need is to reach higher cable performance. A new method has been elaborated taking into account these 2 main requirements.

Existing process have reached their physical limits, and it clearly appeared that, using these conventional methods, productivity could not be increased anymore without attempting to product quality. Therefore POURTIER has led an extensive analysis, and a new process approach has been conducted.

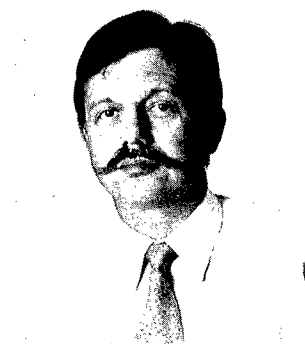
Test have shown that, with the new method, productivity is significantly improved. For example LAN pair can be produced at speed upto 7500 twists per minute using a triple torsion process.

At the same time, it gives the possibility to compensate – on line – the default of concentricity on insulated copper wire. The paper will present in detail the new principle which has been used for this improvement, and the limits versus quality of insulated wire.

The process may apply to :

- ✓ A complete new line for twinning of LAN copper pair.
- ✓ The up-grading of existing line, using conventional bunchers, by addition of new components on this line.

The results of the research shows that the method which has been developed (and patented) give good results for LAN cable cat 5, cat 5+, cat 6 and cat 7, with possible application on further development in copper LAN cable production, and other types of data cable using copper conductors



Philippe P. LETOUT
Sales Manager
At POURTIER P&F
Chelles - FRANCE

Philippe P. LETOUT is currently the sales manager at POURTIER Père & Fils – France. He joined POURTIER in 1987. He worked before for the Alstom Group after graduating from « Ecole Nationale Supérieure des Arts et Métiers » (ENSAM – Lille and Paris) as diplomed mechanical engineer). He started the operation for POURTIER in Asia by opening the Hong-Kong office in 1993, where he lived from 1993 to 1996. He has authored recently several papers about LAN cable, OPGW and special machinery concept from POURTIER.

Panel Discussion Abstract—Session 19

A BROAD AND FLEXIBLE APPROACH OF CABLE MANUFACTURING: TIGHT BUFFER, LOOSE TUBE AND RIBBON CABLES

François Legros
Swisscab, Switzerland

Philippe Letout
Pourtier Père et Fils, France

ABSTRACT

Primary Conclusion

The trend in cable manufacturing is to provide broad range, highly flexible, quality control orientated processing equipment. An extensive analysis of these requirements has been led by Pourtier and Swisscab, and a new approach has been conducted. The major result is a turnkey plant, globally supervised in the aim of best quality insurance in designing cables and product flow efficiency. The equipments are designed in order to take into account new cable designs, and to provide an optimized flexibility in product management. The global solution includes tight buffer, ribbons, loose tubes and ribbonized slotted core designs.

Background. Why Work Was Undertaken

Due to convergence of optical cable markets (WAN, MAN and LAN), and stringer requirements in cost management, the fundamental needs of cable manufacturers are more and more orientated towards higher flexibility, shorter times of return on investments. Since the offer has for long been designed for Telco mass production, it appeared recently that it has become inadequate.

Significant Finding of the Work

- Combined functions in a single line: the case is illustrated (i) in the stranding machine in which both loose tubes stranding and ribbons introduction in slots may be performed, and (ii) in the extrusion line where tight buffer, unitubes, loose tubes and elementary indoor cables can be manufactured.
- Global supervision of process: All lines are connected in a network, thus allowing to guarantee traceability of all raw materials, test results according to specifications. Moreover, software tools permit to optimize cable design in a view of better performance/cost ratio.
- The combination of these findings enhances significantly flexibility in cable design, and manufacturing process.

Panel Discussion Abstract—Session 19

ACSR CABLE PROCESS WITH DOUBLE TWIST STRANDING MACHINES

JOAN REITG

C.M. Caballé, S.A., Barcelona, Spain

1. OBJECTIVE

The objective of this document is to show the experience that Construcciones Mecánicas Caballé S.A. has to improve the productivity of the ACSR cabling process with double twist stranding machines.

2. PRODUCT

ACSR cables (Aluminium Conductors Steel Reinforced) are conductors made of one steel wire and six aluminium wires or one plus six steel wires and twelve aluminium wires stranded in a second step. (See the attached drawing).

3. BACKGROUND

Traditionally, ACSR cables have been stranded in the following machines:

- Tubular stranding machines
- Rigid stranding machines
- Planetary stranding machines

Making the 1+6 steel core in a tubular stranding machine in case of a nineteen-wire cable.

4. LINE DESCRIPTION

The necessary installation for stranding ACSR cables is as follows:

- Core backtwist pay-off:
It is used to feed the steel core with backtwist so that once the cable is stranded, it doesn't maintain any torsional stress. If the steel core maintains some stresses inside the cable, the so called "snake effect" occurs giving the cable a wavy shape. Besides, it can be dangerous when cutting the cable.

The backtwist percentage can be changed in order to get the best results for every material.

- Stem-packs pay-offs:

They are used to feed the twelve aluminium wires that are stranded over the steel core. Each one must have an adjustable brake to control the tension, and a wire-break sensor. It is advisable to have double pay-offs with automatic change since this allows changing stem-packs without stopping the line and thereby reduces the percentage of wasted time.

We recommend installing nineteen pay-offs instead of twelve so the line is more flexible, being able to process other types of conductors.

- Equalizer:

It is used to equalize and adjust all the aluminium wires tension before being stranded.

- Pretwister:

This machine is useful for giving the cable a percentage of torsion before entering in the strander. This makes the stranding easier. The percentage is adaptable depending on the material being processed.

- Double Twist Strander:

Finally the aluminium wires are stranded on the steel core. It is done in a double twist machine in order to get faster speeds and higher productivity. It is very important to take care of the cable passage through the machine because with ACSR cables, we have an aluminium external part very easily stripped and grooved and an internal steel core very stiff. Therefore, this strander is specially designed for this purpose.

5. ADVANTAGES

Manufacturing ACSR cables in Double Twist Stranding Machines offers the following advantages:

- Important increase of productivity:
A double twist stranding machine, provides approximately double the productivity of a tubular stranding machine, five times that of a rigid stranding machine and more than ten times that of a planetary stranding machine.
- Raise of the ratio Working time / Stop time:
Double Twist Stranding Machines have the great advantage of working with external feeding of aluminium wires. It minimizes the changing time and decreases the number of stops because of using high-capacity stem-packs. The efficiency can also be improved by using double stem-pack-feeders with automatic change. On the contrary, the Tubular, Rigid and Planetary stranding machines work with internal feeding with bobbins, so the changes are longer and more difficult and their capacity is lower so there are more stops. That is, they have long stop periods in comparison with working periods.
- Lower cost:
The cost of a Double Twist Stranding Line is lower than any other solution. (See the attached graphic).

6. RESULTS

The results obtained in some installations justify the investment in a Double Twist Machine. Some examples are as follows:

- Seven-wire ACSR cable (one steel wire and six aluminium wires)
Wires diameter: 3.37 mm.
Production speed: 1100 twists per minute.
- Nineteen-wire ACSR cable (1+6 steel wires and 12 aluminium wires)
Wires diameter: 2.12 mm.
Production speed: 1000 twists per minute.

7. CONCLUSIONS

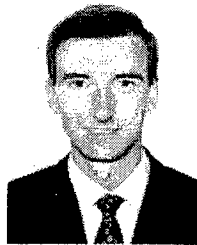
The conclusion of this abstract is that processing ACSR cables in a Double Twist Stranding Machine is much more productive than in any other type of stranding machine because the working speeds are higher and both loading times and installation cost are lower.

This line is also very flexible being able to work with other conductors at high efficiency.

It is also important to clarify that to work with ACSR nineteen wire cables, the core of seven steel wires must be made in a 7-bobbin tubular stranding machine. So the benefit of a Double Twist stranding machine is with respect to a 12-bobbin tubular stranding machine.

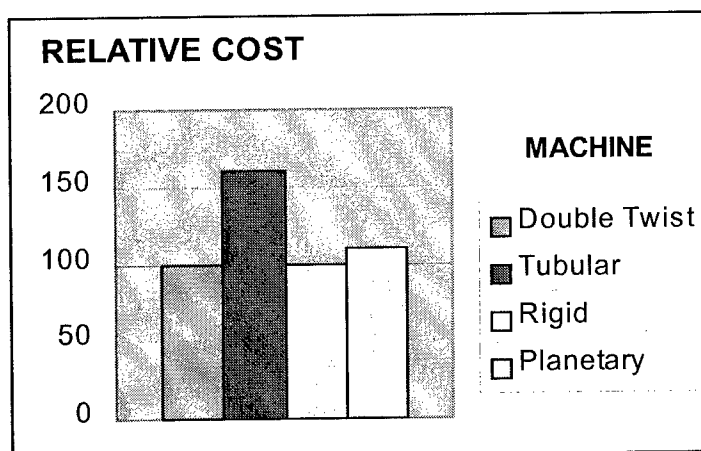
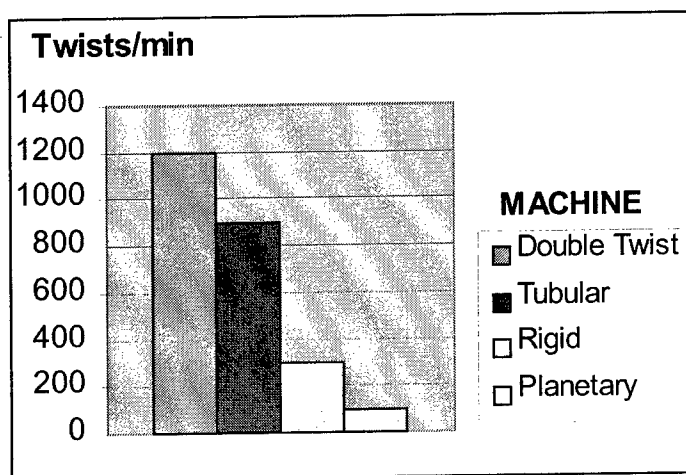
The results of this project are based on many years of experience in manufacturing machines for steel and aluminium in order to get a line that can work with cables of both materials.

At the same time, the shape and location of the different parts of the machine are also very important in order to get good results. For instance, deviation angles, guide and pulley shapes, backtwist percentages and so on are also very important.



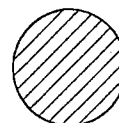
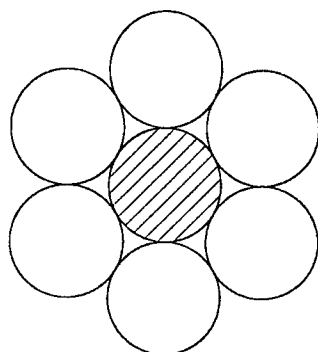
Joan Reigt
Systems Engineer

C.M. Caballé S.A.
Progreso, 293-299
08918 Badalona
Barcelona (Spain)
Tel: 34-93-460-14-13
Fax: 34-93-399-00-08

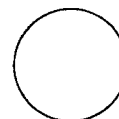


ACSR CABLES

ACSR 1+6

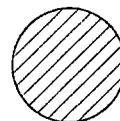
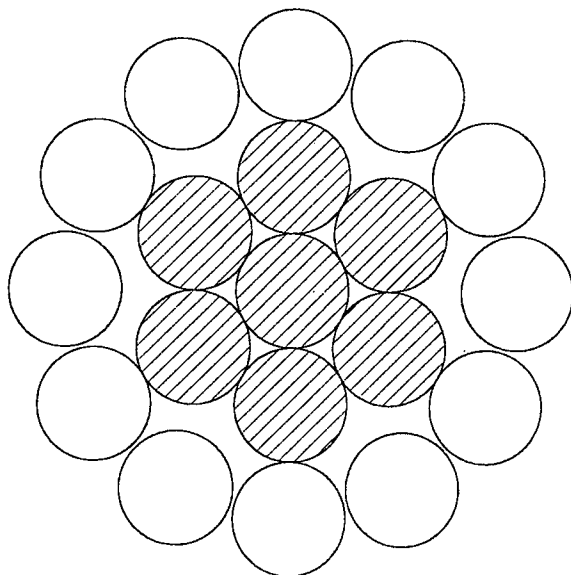


Steel



Aluminium

ACSR 1+6+12



Steel



Aluminium

Panel Discussion Abstract—Session 19

LAYOUT / METHODOLOGY FOR THE PRODUCTION OF CATEGORY 7 CABLES

Brett W. Hamner and Walter Thompson

Nextrom Ltd.
Concord, Ontario, Canada

ABSTRACT

Since the introduction of Lucent's (AT&T) Systimax® 1061 cable system in 1991, we have seen copper cable's performance escalate from the then 20 MHz sweep range to the present 600 (622) MHz. Accordingly, several administrative bodies have been working to keep cable standards in line with cable manufacturers' performance claims.

These bodies include UL, ETL, EIA/TIA, Anixter, EN 50173, ISO 11801.

In the early stages of these cables, manufacturers were able to meet the cable performance requirements, with little or no capital investment.

With the advent of the Anixter levels program in North America and Cenelec SC46XC in Europe, the evolution and manufacture of cable manufacturing equipment has been as dramatic as that of the cables themselves. The introduction of Lucent's Gigaspeed® Cable in 1997 has also been a driving force in equipment optimization.

Total process balance is the goal. This includes diameter, rotational, tension and speed control. This begins with tandem insulation and ends with packaging equipment. Optimization of the machinery's mechanical rotating parts, integration and control aspects of the various OEM gauging systems available and the tremendous advancements in AC drive systems with feed loops through PLC's. Advancements using Profibus technology has allow significantly simplified cabling systems and faster more accurate digital feed back from the gauging instruments.

Today it is imperative that the equipment manufacturers have a strong cable design background to better serve cable manufacturers with the right equipment. The benefits of being a turnkey equipment supplier, includes making the cable and testing in house.

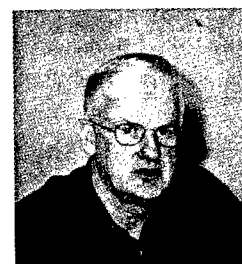
Brett Hamner
Sales Manager
Telecom
North America
Nextrom Ltd.



Mr. Hamner graduated in 1982 with an associate of science degree in Mechanical Engineering Technology from Vermont Technical College. He joined Nextrom Ltd. in Atlanta, GA as a Project Manager in 1995. In 1996 he moved into his current position of Sales Manager and now works out of the Concord Ontario office.

Prior to joining Nextrom, Mr. Hamner spent 13 years in various engineering disciplines of the wire and cable industry with Belden Wire & Cable, Harbour Industries and General Cable.

Walter Thompson
PF Group Twinning
Technical & Sales
Support Manager
Nextrom Ltd.



Mr. Thompson has an extension certificate from Brown University in Rhode Island in Mechanical Engineering. Walter Thompson has been employed by Nextrom (Ceeco) for 23 years and has held positions of Application Engineering Manager to Quality Assurance Manager to VP Wire Drawing Operations.

Mr. Thompson is also named on over 10 patents of various applications for wire and cable machinery.

Prior to joining Nextrom Ltd. Mr. Thompson was employed at General Cable Central Telecommunication offices in New Jersey and held the position of Equipment Design Engineering manager.

Panel Discussion Abstract—Session 19

INTELLIGENT ROBOT REEL HANDLING, STORAGE AND MANAGEMENT FOR FIBER OPTIC CABLE PRODUCERS

Dr. Otmar Volgger, ROBOTECH, Logistic Systems GmbH, Dornbirn, Austria
Frederick J. Hardy Cable Consultants Corporation, Larchmont NY

ABSTRACT

The globalization of sales and procurement markets and the increasing importance of "information" and its in-house utilization require that you take strategic decisions regarding the future orientation of your company on the one hand, but also offer the opportunity to set the course for the introduction of efficient internal material flow and information systems on the other hand. The magic formula you need is *LOGISTICS*. Today, *logistics* is perhaps the only field in which you still can achieve real cost advantages. *Logistics* is becoming more and more a decisive factor for your company. Material management is therefore the key for a competitive future. Based on product data and process data today's information technologies allow us to optimally control production and transport with a view to efficiency and quality. This, of course, requires suitable software tools. Investments in information and communication technology result in improved quality and faster availability of information.

A STATE-OF-THE-ART REEL MANAGEMENT SYSTEM AS AN INFORMATION AND COMMUNICATION TOOL

The key to successful use of automation is the *Material Management System*. In addition to the optimum factory layout reflecting material flow in the production process, we have to bear in mind the data flow accompanying the physical production process.

After all:

LOGISTICS = MATERIAL FLOW + DATA FLOW.

Based on product data and process data, today's information technologies allow us to optimally control production and transport with a view to efficiency and quality, to manage the material storage and handling efficiently as well as determine demand for

supplies in line with production formulas. This, however, requires suitable software tools.

The following provides a concise presentation of such a software tool, called *ROBO-SIS*. That has been specifically developed as a planning and coordination tool for the wire and cable industry.

ROBO-SIS REEL MANAGEMENT AND CLIENT/SERVER PLATFORMS.

Control structure.

The *ROBO-SIS* control concept is hierarchically structured in line with today's technical standards. The machine-level equipment (reel robot and material handling facilities) is controlled by a PLC of industrial standard. At the higher level of system computers *ROBO-SIS* uses a PC-based hardware platform with a client-server architecture that is flexible, modular and easily expandable.

Decentralized computer systems with a high performance allow for maximum modularization both in the field of hardware and software to meet complex requirements. Accordingly, all data is stored in databases on a server. The data is accessed from the workstations (clients) using the *ROBO-SIS* application software. Any number of workstations can be added to the system as the need for them arises and users can be granted different privileges.

MATERIAL MANAGEMENT SYSTEM:

- Store management (inventory, incoming and outgoing stocks), implementation of stock-keeping strategies (FIFO) as well as plans for store optimization;
- Control and monitoring of the entire material flow according to the organizational flow chart;
- Coordination of reel robots and material handling;

- Data transfer to all interfaces;
- Displaying and logging of machine slates to provide information for system maintenance.

The essential advantage of a material management system mainly is the fact that it allows for a continuous overview of material movement and inventory. The ROBO-SIS software is structured according to object-oriented aspects and the operator is supported in his work in an optimal way by a graphical user interface.

The important material data are directly transferred to the system computer via an on-line data interface by means of bar codes or by data input at simple operator terminals.

In the production of telecommunication cables, for example, the following data may be processed:

for product identification:

- core type, color, marking, core length, job number, machine number, working cycle, conductor diameter, lay length, operator code.

for quality determination:

- capacitance (maximum, minimum, and average) copper elongation, resistance, eccentricity.

For the stranding process the stranding formulas required can be easily established and edited on special screens of the system computer in a man-machine dialogue.

The first basic step is layout planning which includes conceptual work. In the process, the specifications and decisions are translated into a concrete layout. Since, as a rule, we are dealing with individual, customized solutions, close cooperation between the client and the planner is essential in this project stage. Here one can rely on the specialized expertise of the planner.

Dr. Otmar Volgger, President, ROBO-TECH

Dr. Volgger completed his studies at the University of Innsbruck, Austria in 1977 and formed the company ROBO-TECH Logiksysteme GmbH in Dornbirn, Austria in 1988. He has lectured extensively on material flow and information systems. Over the last 10 years he has developed and realized a considerable number of integrated material flow and information systems with well-known cable producers worldwide.

Frederick J. Hardy entered the cable industry in Germany in 1977. He joined Cable Consultants Corporation, Larchmont NY and Charlotte NC as VP & Director of Technical Services in 1993. After completing his mechanical engineering studies in London, UK his activities have been in the areas of technical service and marketing in Europe, Asia and the USA.



BALLISTIC RESISTANT ARMORED FIBER OPTICAL CABLE FOR AERIAL APPLICATIONS

Kenneth E. Bow and Marc D. Luker

The Dow Chemical Company, Midland, Michigan

Dr. Marc A. Adams

Jet Propulsion Laboratory, Pasadena, California

ABSTRACT

This paper describes the work to develop a coated steel armored fiber optical cable with ballistic protection for aerial applications. Ballistic intrusion into the fibers is a global problem. Statistical analysis of shotgun hit patterns were used to define the nature of the ballistic threat. This work indicated that for the larger pellet sizes from a shotgun, it is necessary to use a combination of coated steel and aramid fibers. There appears to be synergism between the two materials. The synergism results from the ability of the steel to reduce the energy of the pellet and the ability of the aramid to trap the pellet. The combination of coated steel and aramid allows for more economical ballistic resistant sheaths.

BACKGROUND

A number of Wire and Cable Symposium papers have dealt with ballistic protection. One of the first papers on the topic of anti-ballistic protection discussed the use of aramid yarn woven into a fabric.¹ A second paper described the use of woven aramid with a weight of 450 g/m². Two layers of the aramid were wrapped longitudinally over a layer of aramid yarns, which were acting as the tensile members. A third paper discussed an impact method to allow screening of materials for ballistic protection characteristics.³ A fourth paper discussed the possibility of replacing some of the aramid tape with a layer of modified polyamide.⁴ A subsequent paper on the use of modified polyamide 12 plus woven aramid attempted to quantify the performance of this combination of materials in shotgun tests of cable.⁵

In summary most work with woven aramid was carried out with the lighter gauge shotgun pellets, such as # 5, 6 and 7. The distance was varied from 15 to 40 m and a 12 gauge shotgun was used. Overall, the solution chosen for a given threat may not cover the full range of threats. Several authors pointed out that the longitudinal aramid strength member could be affected by the pellet. No attempts were made to assess the impact of pellet damage on mechanical performance of the cable. Several authors also pointed out that the woven aramids may stop the pellet but there is still penetration damage. One of the papers attempted to correlate penetration damage, which could cause attenuation of the light signals, with optical performance of the cable and found significant attenuation increases were possible.⁶

THE NATURE OF THE BALLISTIC THREAT

In most cases a cable buyer will specify a shotgun test which specifies a distance to the cable, a pellet size and a shotgun type in an attempt to quantify the performance of the cable that is desired to meet a perceived ballistic threat. Quite often the threat is based on assumption – i.e., what type of shotgun and pellet size would a typical hunter use for game hunting? It is often assumed that the hunter is looking for game and this would set the distance to the target, for example. In reality, there are two types of situations – the one is when the cable is in the line of fire. The other is vandalism where the cable is the target. It is obviously much more difficult to quantify the threat posed by the intentional shooter but it is reasonable to assume that they could be frustrated hunters.

Table 1
Immediate Causes of Aerial Cable Failure

Cause	% of Total
Vehicle	34
Power Line	24
Fire	7
Firearm	7
Falling Tree	7
Other	21
Total	100

Table 1 lists the causes of aerial cable failure in the USA. This information was gathered by the Network Reliability Council (NRC) which was charted by the US Federal Communications Commission (FCC).⁷ These data indicate that 7% of failures were due to firearms. Those data also indicate that aerial cable can be damaged by a wide variety of external factors. It is also important to recognize that aerial cable is frequently damaged by a series of events, for example, bad weather can cause a tree or branch to fall and damage the cable.

The characteristics for cartridges, including shot size, weight, material, wad, case and design are covered in reference 3. (An interesting table in that reference shows the difference in codes between the various countries). There are also firearm variables such as bore size (measured by gauge), choke and barrel length.

Another key variable is the performance level of the cartridge. The performance level is a combination of velocity, pellet size and total weight of the shot.

The decision to pick a certain type of shotgun, pellet size and performance level depends on the type of small game that is being hunted. The # 4 through # 8 pellet sizes are commonly used for small game.

Threat to Cable

The performance of fiber optic, aerial cable can be degraded by the impact of pellets from a shotgun blast through several damage mechanisms. Three categories of damage mechanisms, which occur during different but overlapping time periods, are: (1) the transmission of stress waves to the optical fibers, (2) impact of pellets or cable debris on the optical fibers and (3) local deformation of the

cable from the spatially and temporally distributed impulse of the pellet impacts on the cable.

The transmission of stress waves toward the optical core of the cable begins upon the initial impact of each pellet. These waves move through the various components of the cable and are dispersed and attenuated in a manner which is dependent on the materials and configuration of the cable elements. The velocity of the stress waves is much greater than the pellet penetration velocities into the cable; hence, these waves can damage the optical core before any pellet impact occurs on the core or even if no pellet or debris "penetrates" to the core. The stress waves from spatio-temporal proximate hits can interact causing higher stress levels and more damage than if only one pellet had hit the cable in a particular area.

The impact of pellets and/or cable debris on the optical core occurs when sufficient time has lapsed for the pellet/debris to penetrate to the core. Since shotgun pellets travel in a stream, all impacts do not occur at the same time. Stress wave transmission from later pellet impacts on the cable and the impact of pellet/debris on the core may be occurring simultaneously during some period in the event.

Later in the impact event, a length or segments of the cable respond to the spatially and temporally distributed impacts of the pellet. This response probably takes the form of local bending as segments of the cable are accelerated by various portions of the distributed impulses but are dynamically "fixed" at their ends by adjacent stationary cable segments which were not impacted by pellets. Whether this later time response can cause damage to the optical core depends on the magnitude of the local impulses on the segments and on the design of the cable.

Shotgun Hit Patterns

The amount of damage produced in a cable and the loss of optical transmission resulting from any of these damage mechanisms is dependent on the nature of the pellet hit pattern on the cable. The most significant source of variation in the results of replicated shotgun tests of cable armor is, most likely, the variation in pellet hit patterns between tests. The stochastic behavior of pellet hit patterns must be understood in order to interpret the results of limited cable testing or

to develop a "standard" ballistic test for armored cable.

A experimental and theoretical study has been initiated to characterize the stochastic behavior of the pellet hit patterns produced by a 12 gauge, full choke shotgun. Ballistic tests were performed at 10, 20 and 30 m using three shot sizes: American # 4, # 6 and # 7.5 as shown in Table 2. Five or six tests were performed for each condition of shot size. A 12 gauge shot gun with a 28 inch barrel was used to shoot "Federal Hi-Power Shot Shells" (2 3/4 inch, 70 mm long) made by Federal Cartridge Co. The manufacturer's specifications are listed in Table 2.⁸

Table 2
Specification of 12 Gauge
Shotgun Shells Used in Study

Shotgun Shell Destination	American Shot Size	Average Pellet Count	Pellet Diameter		Pellet Weight (g)
			mm	inch	
H127-4	4	169	3.1	0.120	0.167
H127-6	6	281	2.8	0.110	0.128
H127-7.5	7.5	437	2.3	0.090	0.083

Only the results and analysis of two of the series of tests, # 4 shot and # 7.5 shot at 20 m, will be discussed. Table 3 gives the ballistic range of data for the targets shot in these two series.

Table 3
Range Parameters of Test Series
for 20 m Target Distance

Target #	Temp (°F)	Wind 8 o'clock (mph)	Shot size	Pellet Velocity* (m/s)
1	68	0-3	4	372
2	68	0-3	4	374
3	73	0-3	4	381
4	73	0-3	4	370
5	73	0-3	4	373
6	73	0-3	4	373
13	74	3-5	7.5	371
14	74	3-5	7.5	362
15	74	3-5	7.5	362
16	75	3-5	7.5	362
17	75	3-5	7.5	367

*At 4.4 m

The targets were CelotexTM board aligned to be perpendicular to the axis of the gun barrel. Velocity measurements were made with Oehler velocity screens spaced 4.10 and 4.70 m from the gun muzzle. The shot targets were photographed with a 2000X2000 pixel, monochromatic CCD camera and the digital images were analyzed using image analysis software which automatically measured the geometric properties of the patterns. The basic statistics calculated from the observed patterns are given in Tables 4 and 5.

Table 4
Basic Pellet Hit Statistics for the Six Tests with # 4 Shot at 20 m Range

Target	1	2	3	4	5	6
Average X Hit Position (in)	14.02	13.11	11.89	12.53	11.82	11.89
Average Y Hit Position (in)	11.27	9.95	9.64	12.22	11.79	14.16
Standard Deviation of X Hit Position (in)	4.18	3.74	3.28	3.62	3.51	3.59
Standard Deviation of Y Hit Position (in)	3.65	3.61	3.53	3.84	3.52	3.62
Standard Deviation of R Hit Position (in)	5.54	5.20	4.82	5.27	4.97	5.10
Pellets on Target	172	172	165	175	178	171
Uniform Pellet Areal Density (pellets/in ²)	0.423	0.4813	0.5371	0.4757	0.5439	0.4968

Table 5
Basic Pellet Hit Statistics for the Five Tests with # 7.5 Shot at 20 m Range

Target	1	2	3	4	5
Average X Hit Position (in)	11.61	9.70	13.06	11.35	12.18
Average Y Hit Position (in)	11.71	12.24	12.85	12.01	11.71
Standard Deviation of X Hit Position (in)	4.07	3.95	3.99	4.42	3.88
Standard Deviation of Y Hit Position (in)	3.89	3.81	3.92	4.44	3.89
Standard Deviation of R Hit Position (in)	5.63	5.49	5.59	6.27	5.49
Pellets on Target	414	403	413	409	418
Uniform Pellet Areal Density (pellets/in ²)	0.9887	1.0124	0.9989	0.7877	1.047

The Gaussian probability distribution function is a good descriptor of the X and Y variations in pellet hit position. The average radial dispersion of the # 7.5 shot size was about 10% greater than the # 4 shot size.

The "uniform pellet areal density" shown in Tables 4 and 5 can be used as a basis for understanding the degree of clustering in the hit pattern. This areal density is calculated by determining the number of pellets in a circle of two radial standard deviations and dividing the number of pellets by the circular area. If the pellets were uniformly distributed over the area, they would possess this areal density.

The number of high pellet areal density clusters for the 3-hit and 4-hit clusters sizes is much larger for the # 7.5 shot than for the # 4 shot. Although the individual # 7.5 pellets are smaller than the # 4 pellets, the clustering behavior of the # 7.5 pellets may cause this shot size to be as hazardous as the # 4 shot under some conditions.

TESTING MATERIALS AND CABLE FOR BALLISTIC RESISTANCE

Test Program

The first phase of the test program was to screen the individual materials to obtain some data on their performance. The second phase of the test program was to look at combinations of aramid and coated steel to design a cable sheath that was resistant to a specific threat. The third phase of the program was to make and test cables having sheath designs that corresponding to the material combinations that provided ballistic protection in Phase 2.

Test Development

All workers in the field have experienced the same problem in designing cable for shotgun resistance. There needs to be a simple test that allows the material or cable to be screened for ballistic resistance. Several attempts have been made at simulation of pellet impact in the laboratory. But the proof of performance is found only with actual shooting of the sample. Faced with the issue of making and screening of many cables, the screening materials option was chosen because the time and effort in making cables was prohibitive. The method described in reference 4 was chosen for the screening process. This is basically a test in which a 12 gauge shotgun with a 26 in (66 cm) barrel and

full choke was used to shoot at various plaques. These plaques consisted of layers of various materials. They were assembled in the laboratory to represent the various layers in a cable. The last layer or reference plane was a layer of polystyrene 1.0 mm (40 mils) thick. (Designation DPS 628W). Since polystyrene is a brittle plastic, it will easily crack when subjected to the penetration impact of a pellet. By using a reference plaque, it was possible to see whether the pellet could possibly impose stress on the fiber core.

For all tests performed in Phase 1 and 2, the inner and outer jackets consisted of 1.9 mm(75 mils) of LLDPE. Although HDPE would be a better choice for ballistic protection (based on reference 2), it was felt the overall results would be more representative of an ideal aerial cable because LLDPE would offer more flexibility.

Ballistic Index

To rate the various combinations of materials in the plaque test a ballistic index was used. The ballistic index is defined as the percentage of pellets entering the plaque that were prevented from breaching the final layer of the composite. Therefore, if a particular combination of materials stops all the shotgun pellets from breaching the final layer, it will have a ballistic index of 100 (i.e., 100% stopped). If a sheath design allows all the pellets to breach the final layer, it will have a ballistic index of 0 (i.e., 0% stopped).

Armoring Materials

The materials chosen for armoring are shown in Table 6. The new material on this list is a 0.25 mm (10 mil) coated steel. This material was developed in response to the need for ballistic protection. It has a base steel of the same composition and tensile properties as the 0.15 mm (6 mil) which has been the standard of the industry. The coatings use the same copolymer. Adhesive properties and requirements are the same as the 0.15 mm (6 mil) product.

The woven aramid anti-ballistic tape is a standard product for protection of cables. It has a weight of 400 g/m² and is packaged as a 30 mm wide tape. This tape is normally spirally wrapped with an overlap to give a double layer on cable. Or 2 tapes can be applied longitudinally with an overlap to give a double layer.

Table 6
Materials for Ballistic Resistant Cables

Abbreviation	Definition	Specific Material Used
6 Steel	6 mil coated steel	S262
10 Steel	10 mil coated steel	S2102
Aramid	woven aramid fiber	30 mm wide Anti-Ballistic Tape (Weft 840 Dtex, Warp 840 Dtex, plain weave 1/1) 11.9 g/m

Phase 1 Tests

The first series of tests were designed to screen the materials for their ballistic resistance. The results are shown in Table 7. These tests were conducted with a # 4 shot at a distance of 20 m. From this phase of the testing it was learned that 2 layers of aramid won't stop a # 4 pellet but combinations of coated steel and aramid improved the ballistic protection.

Table 7
Screening of Materials for Ballistic Protection

Construction					
Outer Jacket	Steel Armor*	Woven Aramid	Inner Jacket	Inner Armor	Ballistic Index, %
LLDPE	-	1 layer	LLDPE	-	3.3
LLDPE	10 Steel	-	LLDPE	6 Steel	11.2
LLDPE	6 Steel	1 layer	LLDPE	-	15.3
LLDPE	10 Steel	1 layer	LLDPE	-	30.7
LLDPE	-	2 layer	LLDPE	-	47.6
LLDPE	10 Steel	-	LLDPE	10 Steel	58.9

* 6 = 6 mil (0.25 mm) coated steel code S262

* 10 = 10 mil (0.25 mm) coated steel code S2102

The second phase of tests looked at combinations of coated steel and woven aramid under the same set of test conditions (# 4 shot at 20 m). The data indicated that a combination of 2 layers of coated steel and one layer of aramid or a combination of one layer of steel and two layers of aramid will stop the # 4 pellet.

Cable Tests

Three sheath constructions which looked promising in phase 2 tests were manufactured

into cable of a loose buffer tube design. For the cables a high density polyethylene jacket was used. The thickness of the outer jacket was 2.5 mils (98 mils) and the inner jacket was 1.0 mm (39 mils). As shown in Table 8, all three cables passed the ballistic test using # 4 shot at 20 meters. The choice of a specific design can be made on economics and an assessment of the perceived threat. Limited testing indicated that higher levels of ballistic protection were possible. The third sheath design in Table 8 could stop a # 2 pellet for example. Overall the cable results confirmed the results obtained using the plaque test.

Table 8
Ballistic Resistance of Cable with Combinations of Coated Steel Armor and Aramid

Construction					
Outer Jacket	Steel Armor*	Aramid	Inner Jacket	Inner Armor*	Aramid
HDPE	10 Steel	-	HDPE	6 Steel	X
HDPE	10 Steel	X	HDPE	-	X
HDPE	10 Steel	X	HDPE	6 Steel	X

* 6 = 6 mil (0.25 mm) coated steel code S262

* 10 = 10 mil (0.25 mm) coated steel code S2102

DISCUSSION

There are other benefits of using armored cable for aerial applications besides the ballistic protection. One of the most important benefits is rodent protection. The squirrel has one of the highest biting pressures (in the range of 21,000 psi [145 Mpa])⁹ of the common rodents that attack aerial cable. However, the biting action of squirrels is more idiosyncratic than other rodents such as gophers and rats. A typical squirrel spends about 5% of the time gnawing (that represents about 45,000 bites/week). A solution to squirrel attack was to use cable with corrugated steel armor as a rodent (and woodpecker) barrier.¹⁰ After the cable was installed, it successfully reduced cable troubles due to sheath damage from squirrels and woodpeckers. But additional benefits were discovered. The armored cable reduced troubles caused by shotgun pellets, tree abrasion and other sources of mechanical damage.

The use of a bonded sheath provides the cable with a moisture barrier. The bonding of the

coated steel to the cable jacket and the sealing of the overlap integrates the steel into the sheath as both a radial and longitudinal barrier to moisture. The metallic moisture barrier inherent in the bonded sheath prevents accumulation of moisture due to day to night and seasonal temperature variations.¹¹ This property of the bonded sheath has been verified experimentally.¹²

Another problem with aerial cable is jacket shrinkage. The same temperature variations affecting the moisture resistance also can cause shrinkage of the jacket. Jacket shrinkage can cause problems at aerial termination points and splices. Most often the problem manifests itself in pull-out of the cable sheath at the closures. By locking the coated steel to the jacket with the adhesive coating on the steel, the ability of the jacket to shrink is controlled so that shrinkage is basically eliminated.

The most common concerns about use of armored aerial cable is lightning or contact with power conductors. However, it is misleading to believe that cables with metallic armors or strength members are more susceptible to lightning in the aerial environment. Tests and field experience have shown that dielectric cable does not have an advantage over self-supporting or lashed armored fiber optical cable in aerial plant.¹³ In these tests the metal strand or lashing wire carried most of the current associated with lightning, power transients and induction. Often armored aerial cables are protected by the shield wire of the power system (assuming they are hung on the same poles as the power conductors). The lower position on the poles also makes the armored fiber optical cables less vulnerable to lightning. The strand to which the cables are lashed or self-supported is normally well grounded. Good installation practice recommends a ground every two kilometers.¹⁴

A review of the literature and the work reported herein has indicated a need for the development of an industry standard for testing of ballistic or shotgun resistance. Although there was good correlation between the material screening test and the cable test, the proof of ballistic performance lies in the use of cables for testing. The test method for cable needs to have greater predictability to reflect the nature of the threat and the statistical probability of damage.

In addition to the shotgun pattern characterization studies described above, probabilistic models can be constructed which will enable the prediction of the probability of cable hits by particular pellet hit patterns in a burst. If ballistic testing has shown that an armor can defeat pellet hit patterns up to a certain level, the probability of survival of the cable in the field can be estimated using a model which gives the probability of occurrence of cable hit patterns more hazardous than those which can be defeated. This approach to the design of cable tests is being pursued.

CONCLUSIONS

A new and effective way to provide ballistic protection to aerial cables is to combine a coated steel armor with aramid. This combination of materials provides a synergy not present in either one separately.

The coated steel materials include a new plastic coated steel with a thickness of 0.25 mm (10 mils) and the standard 0.15 mm (6 mil) plus an aramid designated for ballistic protection of cables. The combination of jacket/0.25 mm coated steel/jacket/0.15 mm coated steel/aramid was effective against the larger # 4 pellet with a 3.3 mm diameter and a 0.200 g weight. The combination jacket/0.25 mm coated steel/aramid/jacket/0.15 mm coated steel/aramid was effective against a # 2 pellet with 3.6 mm diameter and a weight of 0.278 g.

The use of armored cable in aerial applications brings the additional benefits of rodent resistance, moisture barrier, control of jacket shrinkage plus the ballistic resistance. Field experience has shown that armored aerial cable is more robust with greater resistance to damage caused by tree abrasion and other sources of mechanical damage. Tests and field experience has shown that self-support and lashed fiber optical cables are equal in performance to all-dielectric cables in a lightning environment. The strand carries almost all the current if there is induced current due to lightning.

A standardized test for ballistic resistance needs to be developed. These tests need to consider the threat and take into account the parameters of the firearm, the cartridge and the statistical behavior of the pellets in causing cable damage.

REFERENCES

1. S.J.B. Bensink, W.W.J. Dekker, "Aramid Tapes as Anti Ballistic Protection of Aerial Optical Fibre Cables," International Wire & Cable Symposium Proceedings 1990, pp 632-367.
2. Camara, S., Cortines, C.G., "Evaluation of Antiballistic Sheathings for Aerial Fiber Cables," International Wire & Cable Symposium Proceedings 1991, pp 540-544.
3. Lang, I.D., Davies, M.V., Poole N.J., Cockrill K.J., "Evaluation of Impact Testing for Simulated Shotgun Damage of Optical Fibre Cable," International Wire & Cable Symposium Proceedings, 1995, pp 540-545.
4. Hochuli, M., "Ballistic Protection of Aerial Cables: A New Economical Solution with a Special Impact Modified Polyamide," International Wire & Cable Symposium Proceedings, 1996, pp 817-820.
5. Eichhorn, V., "Protection of Fibreoptic Transmission Media in Telecommunication and Data Transfer Cables by Thermoplastic Polymers, *Wire Industry*, May 1999, pp 298-305.
6. Ibid, Reference 3.
7. "Network Reliability: A Report to the Nation," Presented by the Federal Communication's Commission's Network Reliability Council, June 1993.
8. Trade Literature, "Upland Ammunition," Federal Cartridge Company, Anoka, MN, 55303, 1995.
9. N.J. Colgelia, G.K. LaVoie, and T. F. Glahn, "Rodent Biting Pressure and Chewing Action and Their Effects on Wire and Cable Sheath," Proceedings of the 25th International Wire and Cable Symposium, 1976.
10. P.J. Reale, Jr., and L.M. Borowicz, Jr., "Reinforced Self-Supporting Cable: A New Alternative in Protected Aerial Plant Facilities," Proceedings of the 28th International Wire & Cable Symposium, 1979, pp 34.
11. T. Maeda, s. Minematsu, K. Yata, T. Shintani, and A. Asia, "Laminate Sheath Cables: A Study of Moisture Barrier Factor and Mechanical Characteristics," *Dainichi - Nippon Cable Journal*, 39, July 1968.
12. R.C. Mildner, W.F. Ropp, and J.H. Snow, "The Evolution of Sheath Constructions for Communications Cable," 15th International Wire and Cable Symposium, 1966.
13. P.D. Patel and T. Coffman, "Aerial Plant Fiber Performs Well in Lightning," *Outside Plant*, July 1993, pp. 36-37.
14. J. Chamberlain, D. Vokey "Grounding Practices for Fiber Optical Cable," *Outside Plant*, July 1993, pp 36-37.

BIOGRAPHY



Kenneth E. Bow
The Dow Chemical Company
200 Larkin Center
1605 Joseph Drive
Midland, MI 48674

Kenneth E. Bow received a B.S. degree in electrical engineering from Michigan State University, East Lansing, MI, in 1962. Following graduation, he joined The Dow Chemical Company, Midland, MI, where he has been involved in the research and development of materials for the wire and cable industry for more than 30 years. He is currently the Chief Scientist for the development of polymer and coated metal products for wire and cable applications. His primary responsibilities are for the global development of applications and cable technology associated with cables using plastic-coated metallic shielding and armoring tapes. Ken is a senior member of the IEEE and the SPE. (E-mail: kebow@dow.com)

DEVELOPMENT OF THE BRANCH TYPE OF PREMISES OPTICAL CABLE TO REDUCE CONSTRUCTION COST

Osamu Koyasu*1 Yukihiro Hamada*2 Kazunaga Kobayashi*1 Matsuhiro Miyamoto*1

*1 FUJIKURA Ltd. Chiba, Japan

*2 Nishi Nippon electric wire & cable Co., Ltd. Ooita, Japan

ABSTRACT

We developed a new premises optical cable that is most suitable for use in constructing an optical telecommunication network within a building. Telecommunication networks using optical cable are finding increasing applications, and the demand for the optical cable for use in buildings is growing. The slotted-rod type premises optical cable used so far requires much time and cost not only for its installation but also for the connection work after installation. The new premises optical cable consists of optical units with 4-fiber ribbons stranded around the tension member and fastened with a wired wrapping tape, so the optical units are easily separable from the cable. Moreover, different types of connectors can be attached to the end of each unit, so the connection work can be done easily in a short time. Therefore, use of this cable makes it possible to reduce greatly the cost of cable installation in the construction of an optical telecommunication network within a building.

1. INTRODUCTION

In the case of construction a telecommunication network within a building, the conventional slotted-rod type premises optical cable needs to be branched at each floor after being laid in the shaft room, so it takes a long time and a high cost to install this type of cable. Particularly in the case of existing buildings, it is important to reduce the duration of construction work, noise and the communication stop time with consideration to the tenants.

At present, the trend toward higher speed and greater capacity of telecommunication is growing with a fairly high rate, increasing the demand for optical cable still more. From this point of view, it becomes more and more necessary to develop a premises optical cable that contributes to reducing the installation cost, irrespective of whether the building is a newly-built one or an existing one.

The premises optical cable of the new design described in this paper was developed with the aim of reducing the duration and cost of construction work and attaining characteristics equal to or better than those of the conventional premises cable.

2. CABLE DESIGN

In order to enable reduction in network construction cost, it is necessary to provide a cable designed to be easy to handle and connect. Installation and connection of this cable can be done in a short time, so it is possible to reduce the construction cost.

As shown in fig.1, the cable is designed so that each unit is cut to a length suitable for the floor to which to branch it and has connectors suitable for the system equipment attached to its end.

Concerning the outside diameter of the cable, the area to be occupied by the cable needs to be minimized because there is a limit to the capacity of the shaft room in which the cable is to be laid. It is necessary to prevent the fibers being strained by the elongation of the cable by its own weight because the cable is suspended. Moreover, it is necessary to reinforce the connectorized section at the end of each unit to protect the fibers and connectors against bending and squeezing by installation.

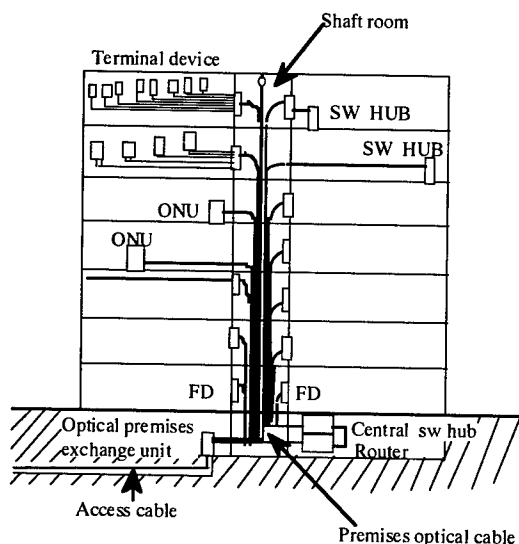


Fig. 1 The way of laying

2-1 Structure of Optical Unit

It is important that the optical unit be easy to separate from the cable proper and have some mechanical strength. As shown in fig.2, the unit has two 4-fiber ribbons coated together with UV resin and surrounded buffer layer, with two thin steel wires arranged on both sides of these parts. The result of thermal contraction in the presence or absence of 1m long optical unit are given in Table 1, from which the effect of the steel wires is apparent. In addition, the unit is sheathed with halogen-free polyethylene to provide flame resistance and prevent the discharge of toxic gases.

We manufacture some kinds of units as an experiment except for the figure -2, too. They are the units that an bare fibers, an Ny coated fibers and the optical code were bundled. These units had the good characteristic, too.

Table-1 Result of thermal contraction of the optical units(mm)

Structural		After 1day	After 2days	After 3days
With steel wire	n1	0	-0.4	-1.1
	n2	0	0	-0.7
	n3	-0.4	-0.5	-0.9
Without steel wire	n1	-5.5	-8.9	-20.1
	n2	-8.0	-11.0	-20.5
	n3	-7.5	-11.0	-20.8

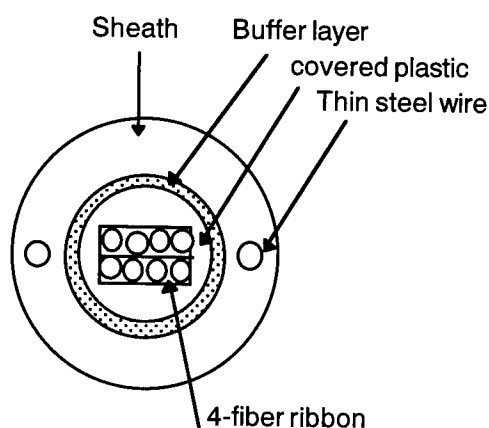


Fig.2 Section of the optical unit

2-2 Construction of Cable

We manufactured the cable as an experiment by using the ribbon fiber from some unit structure in consideration of the easiness of the connection. Fig. 3 shows a 16-unit type cable and Fig. 4 a 10-unit type cable. A plastic tape containing steel wire is wrapped around the stranded optical units to fasten them. This makes it easy to separate the units from the cable.

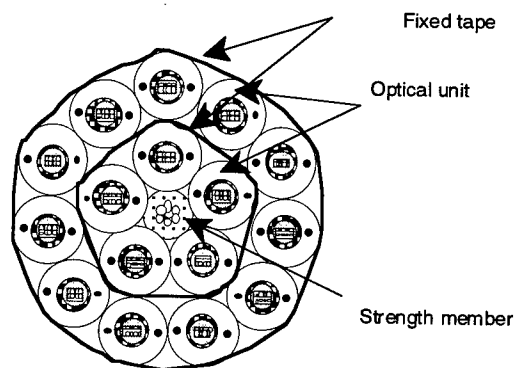


Fig.3 Structure of 16 unit cable

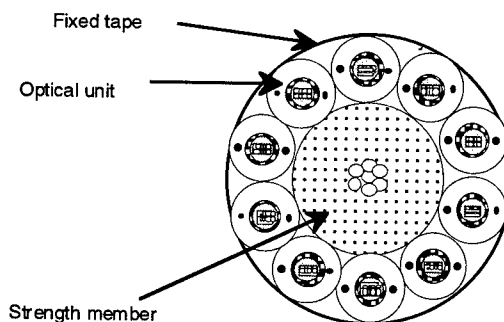


Fig.4 Structure of 10 unit cable

The size of the tension member depends on the elongation of the cable by its own weight and the strain applied to the fiber by this elongation. The reason is because the service life of the fiber is affected by the strain applied to it. The probability of failure by the strain applied to the fiber is calculated equation(1). *3

$$\lambda = \alpha \gamma N_p \frac{(\bar{\epsilon}_{ts})^{\beta}}{\epsilon_p t_p} \quad (1)$$

where

λ : probability of failure

ϵ : equivalent load strain applied to fiber

t_s : fiber life

ϵ_p : screening strain

t_p : screening time

n : fatigue factor at screening test *1

n_p : fatigue factor in the use environment *1

α : parameter expressing the crack distribution in the longitudinal direction *1

γ : parameter expressing strength

N_p : Probability of failure at screening test

β : $(n_p - 2)/(n - 2)$

Fig. 5 shows the relations between the fiber strain and probability of failure calculated by equation(1). The required probability of failure in 20 years is 0.0047 per fiber per km. The strain that satisfies this requirement is taken as 0.364% or less from the figure. Fig. 6 shows the relation between the cable weight and fiber strain with the size of the tension member as a parameter. In case the cable weight is 70 kg or less, the outside diameter of the tension member must be made equal to 1.4 mm or more in order to reduce the fiber strain to 0.364% or less. The cable requires flexibility because it has to be laid in a limited space. Therefore, we selected stranded steel wire for the tension member. Cable data are given in Table-2.

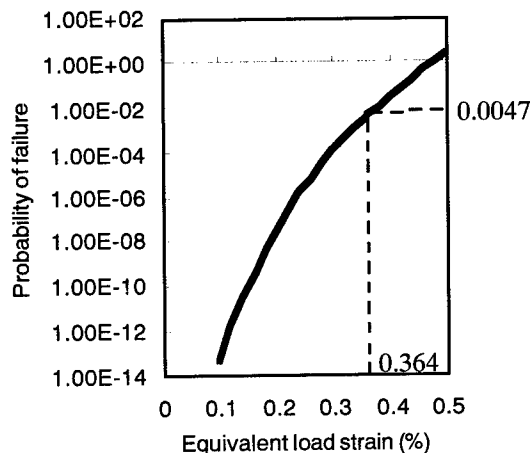


Fig. 5 Probability of failure of the optical fiber

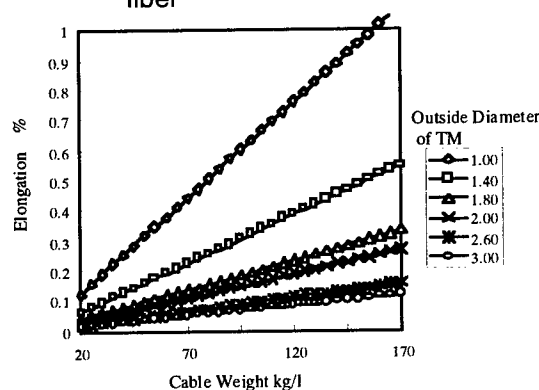


Fig. 6 Weight and elongation of the cable

Table-2 Cable Data

Item	16-Unit cable	10-Unit cable
Tape(W/T)	1.1/0.32mm	1.1/0.32mm
Opt.unit dia.	5.2mm	5.2mm
TM O.D.	7/0.8	7/0.6
TM coat dia.	3.2mm	11.6mm
Cable dia.	22.0mm	19.5mm
Weight	400g/m	360g/m

2-3 Branching structure*2

There are two important factors for this cable. First, the cable is designed to be easily separable. Second, the cable is laid with connectors attached to it. Therefore, the units stranded around the tension member are fastened with a tape sheathed with wire. This tape is flexible, so the optical units can be separated easily. In addition, a flexible, hardly crushable pipe is used to protect the branching part. Fig. 7 shows the reinforced branching part. At the

time of delivery, the reinforced part is fastened to the cable proper with an adhesive tape. After the cable is suspended, the branching part can be pulled out to the point of connection by removing the tape and pipe. Fig. 8 shows the leading end of the cable and Fig. 9 the terminating part of the cable.

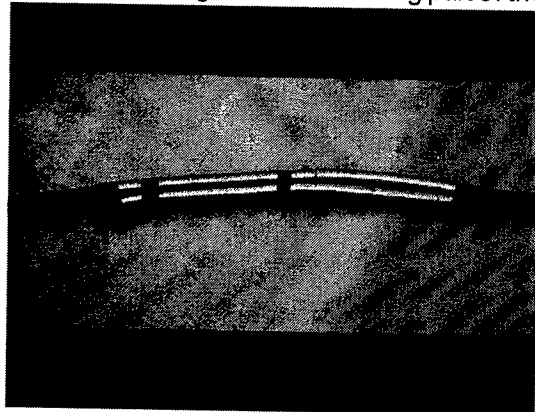


Fig. 7 Reinforced part in the middle section of the cable

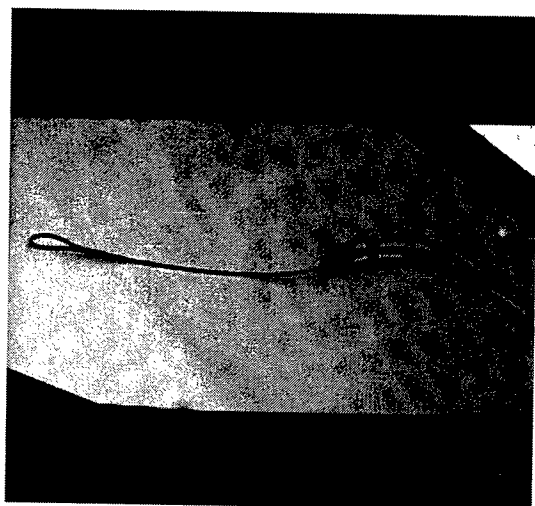


Fig. 8 Leading end of the cable

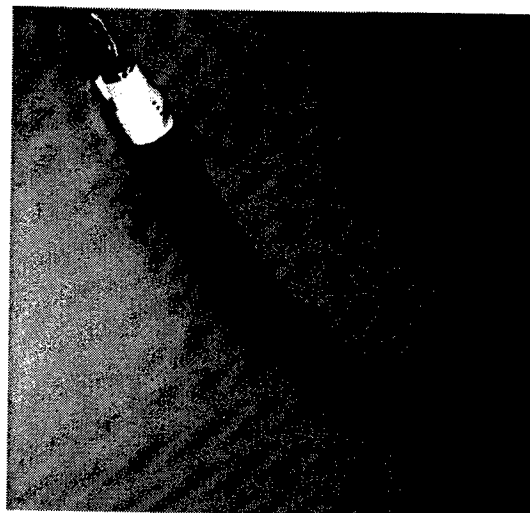


Fig. 9 Terminating part of the cable

3. CABLE CHARACTERISTIC

3-1 Temperature Characteristic

Fig. 10 shows the loss change in the 16-unit cable, measured at the wavelength of 1550 nm in the temperature range of -10-60°C. The fibers of all units in the inner layer and of some units in two sections of the outer layer were measured for loss change with LEDs and optical power meters by repeating two cycles. The loss change was ± 0.02 dB/km or less, so a good result was obtained.

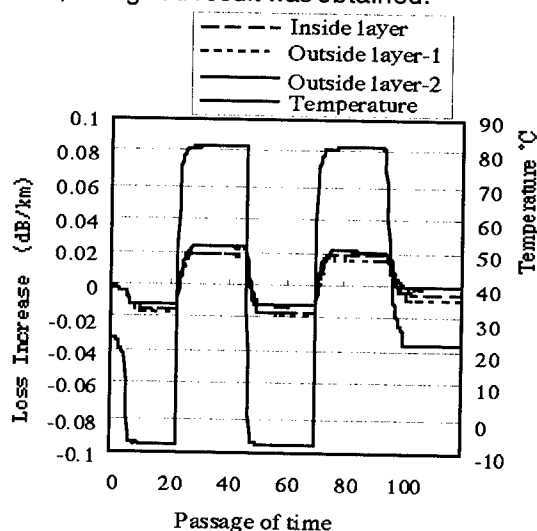


Fig. 10 Temperature characteristic of the 16-unit type

3-2 Mechanical Characteristic

3-2-1 Tensile test

A tension was applied to a 50m length of cable to measure loss change, cable elongation and fiber strain. The cable showed no loss increase when a

tension of as great as 200kN was applied. Fig. 11 shows the relation between cable elongation, fiber strain and tension.

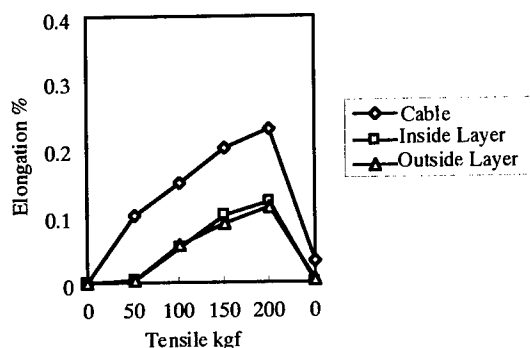


Fig.11 Tensile Test results (strain)

3-2-2 Lateral Pressure Test

A lateral pressure was applied to the cable with a 50mm wide flat plate. Measured for loss change were the fibers of all units in the inner layer and of units 7 and 8 and 15 and 16 in the outer layer. The flat plate was brought into contact with units 7 and 8 in the outer layer. Fig. 12 shows the loss change. The lateral pressure at which the loss increase was 200 kN/50mm or more, so a good result was obtained.

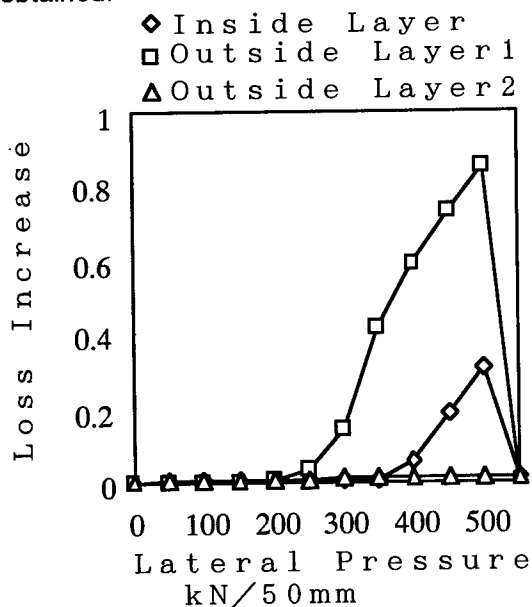


Fig.12 Lateral pressure test results

3-2-3 Other mechanical characteristics

The test results of other mechanical characteristics are given in Table 3. In these characteristic tests, good results were obtained in the respective conditions.

Table-3 Test results of others mechanical characteristics of 16 unit cable

TEST ITEM	TEST CONDITION	RESULT
IMPACT	20mm ϕ 1kg load Drop height 1m	No loss increase
BENDING	300mm diameter, ± 180 deg. 10 times	No loss increase
TORSION	± 360 deg. 5turns	No loss increase
SQUEEZING	600mm roller 100kg tension 3times	No loss increase

3-2-4 Mechanical characteristics of the optical unit

The test results of the mechanical characteristics of the individual optical units are given in Table 4. In the impact, lateral pressure, bending and repeated bending tests, good results were obtained.

Table -4 Test result of the optical unit

TEST ITEM	TEST CONDITION	RESULT
IMPACT	20mm ϕ 1kg load Drop height 1m	No loss increase
BENDING	300mm diameter, ± 180 deg. 10 times	No loss increase
LATERAL PRESSURE	100kN/50mm	No loss increase
REPEAT BENDING	300mmdiameter ± 90 deg. 10000 times	No loss increase

3-2-5 Combustion characteristic

In the IEC332-2 test, the burning length was 30cm and the flame height during combustion 70cm. With the stop of the fuel gas supply, the fire was extinguished within two minutes. Fig. 13 shows the burning part of the sample.



Fig. 13 Burning part of the sample

3-3 Mechanical characteristics after preparation for branching

The mechanical characteristics of the cable prepared for branching and reinforced were measured at the wavelength of 1550 nm.

3-3-1 Squeezing test

As the cable was to be laid through piping, it was tested for squeezing within piping. A pipe 60 mm in inside diameter was arranged as shown in Fig. 14, the cable prepared for branching was laid through it, and the appearance of the cable and the inside state of reinforced part were observed. The appearance showed no abnormality, and the fiber ribbons and connectorized section in the reinforced part showed no such abnormalities as break of fiber.

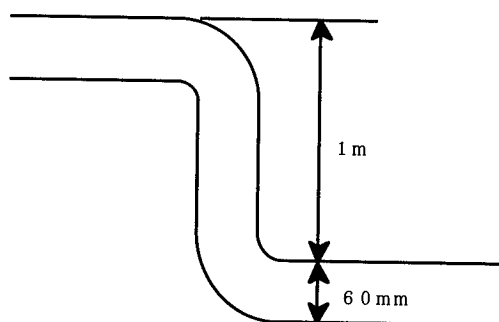


Fig. 14 Pipe for squeezing test within piping

3-3-2 Other mechanical characteristics

Lateral pressure, impact, bending tests were performed to check for loss increase at 1550 nm and for abnormalities in appearance. The results are given in Table 5.

Table-5 Test results of mechanical characteristics after preparation for branching

TEST ITEM	TEST CONDITION	RESULT
IMPACT	20mm ϕ 1kg load Drop height 1m	No loss increase
BENDING	300mm diameter, ± 180 deg. 10 times	No loss increase
LATERAL PRESSURE	100kN/50mm	No loss increase

4. RESULT and DISCUSSION

The cable was tested for temperature characteristic at -10 to 60°C . This temperature range was considered sufficient for the inside temperatures of buildings. The test conditions for mechanical characteristics were determined on the assumption that the following might occur at the time of cable installation: drop of tools or fixtures, smashing of cable by treading on it, bending of cable, and tensioning of cable when caught on something. Tests were made under such conditions, and good results were obtained. In mechanical characteristics, the present premises optical cable was confirmed to be equal to or better than the conventional slotted-rod type. Hence, the cable can be said to be suitable for use in constructing an optical communication network within premises.

In the preparation for branching, it was confirmed from the results of the repeated bending test that owing to the flexibility of the fastening tape the optical units are easy to pull out without causing any trouble at the time of installation. In mechanical characteristics, the reinforced part of the cable after prepared for branching were confirmed from the results of the squeezing test within piping to be sufficiently capable of withstanding the installation conditions. This means that the cable can be handled equally with the conventional cable. In addition, the cable weight is light, on the order of 20 kg, in the case of installing a 16-unit type cable in a 16-storied building, so any special method or machinery would not be required for installation of the cable. Therefore, there are no factors leading to higher cost of installation..

Of the cost factors, the most important is the connection work. In case of the slotted-rod type optical cable, mid-span branching operation has to be performed. The present cable is already prepared before shipping so as to have a structure

conforming to the building in which to install it. Therefore, it is possible to complete the connection work only by leading the connectors into the junction box after removing the fastening tape from the reinforced part and detaching the protective pipe. Because the connection work can be accomplished only with insertion of connectors without need for any operation which requires such technical skill as fiber splicing, the construction cost could be much reduced.

The characteristics of the individual optical units are good, so it can be used for wiring. That is, each unit separated from the cable can be used in that state for wiring the equipment.

5. CONCLUSION

We developed a premises optical cable of a new design and evaluated the characteristics and ease of handling of the cable as follows. As a result, it was confirmed that its use is beneficial to reducing the cost in the construction of a premises optical communication network.

- As the cable is easy to branch and has connectors attached to it, the installation and connection works can be completed in a short time, contributing to lower construction cost.
- The cable is equal to or better than the conventional premises slotted-rod type cable in transmission and mechanical characteristics.
- The flame resistance of the cable satisfies the requirements of IEC-322-2.
- The individual optical units have characteristics that enable them to withstand the service conditions when used for wiring within premises.

By investigating the cable characteristics, we could obtain good results as described above.

6. ACKNOWLEDGMENT

We would like to thank many people who helped us in trial this new cable.

And, we are also grateful to Mr. Wakui, Managing Director, and Mr. Kato, General Manager, Telecommunication Div., FUJIKURA Ltd. for appropriate guidance and kind consideration.

7. REFERENCE

- 1) KAWASE, et al.(1990):Optical Subscriber Loops by Non pressurized Optical Fiber Cable, The Transactions of IEICE J73-B-I,10

- 2) SIMIZU, KOYASU,et al.(1999):

Characteristics of Optical Fibers and UTPs Composite Cable, Proceedings of The 1999 IEICE General Conference

- 3) MITUNAGA,et al.(1983): Life-Time Design of Optical Cable Strength, The Transactions of IEICE J66-B,8

Osamu Koyasu

Research & Development Dept.
Telecommunication Cable Division
Fujikura Ltd.

1440, Mutuzaki, Sakura, Chiba, 285-8550, Japan



Osamu Koyasu was born 1953. He joined Fujikura Ltd. from Kisarazu Technical college in 1973 and has been engaged in research and development of telecommunication cable. He is now engineer in the telecommunication cable section and member of the IEICE of Japan.

MANAGING TEMPERATURE-INDUCED LOSS OF 50/125 μ m DUPLEX OPTICAL CABLES

Todd P. Berger
3M Telecom Systems Division
Austin, Texas

ABSTRACT

With the demand for higher bandwidth, and recent advances in low-cost paired-fiber connector technology, the development of duplex fiber cabling for the fiber-to-the-desk market is expected to grow substantially over the next 10 years. Several manufacturers of cables have responded to the premises market demand by incorporating 50 μ m fiber into their designs. Network designers are increasingly using this fiber for its cost and transmission speed advantages which are often ten to twenty percent cheaper with a bandwidth two-to-three times greater than that of 62.5 μ m fiber.

Over-coming the effects of temperature cycling has been found to be the most challenging element in duplex cable design. This paper examines the cable mechanics during the temperature cycling process supported through analytical observations, and their effects on optical properties. Suggested design parameters are offered to overcome the effects described resulting in an acceptable low loss cable performance.

INTRODUCTION

The use of duplexed cable, which is comprised of two-250 μ m fibers combined in a single loose tube "subunit" for fiber-to-the-desk applications has been noted for the ease of handling and management, improved fiber identification and labor savings it provides in the cable installation and termination process. By enabling tandem strippability and termination in as little as two minutes, duplex cable has proven cost advantages where large numbers of field terminations must be completed. In many instances, the cost of the cable itself is even lower than comparable simplex constructions due to the compact nature of the duplex design.

The benefits of the duplex construction, particularly those employing 50 μ m fibers, do come with the expense of additional design and manufacturing considerations. The engineering challenges associated with overcoming fiber-fiber stresses should not be overlooked, particularly in regards to the optical loss that can accompany compression, impact, and temperature cycling of poorly designed duplex cables. These losses become exacerbated for microbend-sensitive fibers and effective cable designs for 62.5 μ m fibers may be recipes for failure in 50 μ m systems.

Balancing the mechanical and environmental properties of the duplexed cables is a challenge within itself. Good compression resistance requires the fiber immobility and energy dissipation of a tight inner diameter cable sheath around the fibers and aramid, conversely, good impact resistance requires a loose inner diameter to absorb the shock energy and prevent stresses from reaching the fibers. In both of these cases, increased wall thickness is beneficial but restricted by the UL-specified tolerances. These same considerations must be taken into account for good temperature cycling results.

During temperature cycling, dimensional changes (axial and radial) in the subunit and cable sheath of traditional 50 μ m duplex cable contributes to low temperature loss. The natural low temperature response of the duplexed fiber to the axial instabilities of the subunit is a helical formation that produces potential loss from macrobending and microbending at the helical crossover points. The compressive forces generated from the radial instabilities of the cable sheath increase the stress at these microbending sites and generate a cumulative effect on overall cabled fiber

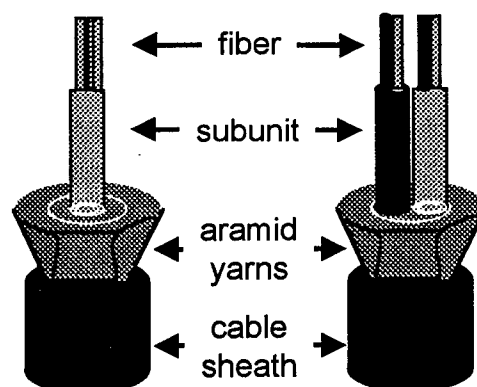
loss. Additionally, the change in Young's modulus, glass transition (measured via dynamic mechanical analysis and differential scanning calorimetry) and coefficient of thermal expansion as they relate to chemical and dimensional properties of the cable materials must be included in the construction design.

By governing the effects of microbending produced in low temperature environments, lower loss on the duplex cable will result. Three primary cable design adaptations can be used to minimize loss. First, it is critical to ensure subunit and cable jacket materials are chemically similar. Dimensional and geometric enhancements to the duplex cable and subunit have also been found to improve low temperature performance. For example, physically restricting subunit mobility within the cable sheath through tighter inner diameters can eliminate the source of microbending by minimizing the subunit dimensional change. Finally, shifting the glass transition towards lower temperature regimes maximizes the operating temperature range of the duplex fiber cable. The design of a 50 μ m duplex fiber cable for fiber-to-the-desk applications requires careful material selection and control of cable dimensions for effective cable performance.

Transmission failures from excessive loss have been an ongoing problem in low temperature environments. Most of the published reports have focussed on OSP cables that utilize singlemode glass fiber and have offered design improvements in the cable or fiber to overcome the high loss¹. The most prevalent cable design improvement has been found through frictional coupling of the cable sheath to the elements within the cable via central or circumferential strength members [Sugawara]. Other reports have suggested that low temperature losses can be minimized through altering the tight jacketing chemistry and thickness [Yabuta]². Yabuta et al contributes the high loss to a buckling formation of the fiber within the tight jacket and suggests maintaining a smaller inner diameter is preferred for controlling excess loss. They also offer material changes of the buffer coat as a means of minimizing loss.

Many investigations have concluded that the primary and secondary buffer coatings around the fiber are the controlling factors in minimizing loss. Shiuie also acknowledges loss can be minimized by controlling the Young's modulus, CTE, and Poisson's ratio of the primary and secondary buffer coats³. Shiuie states that the lateral pressure is proportional to the temperature drop and is a function of buffer material properties and coating thickness. Several researchers have taken these property changes to the chemical level. Kimura et al explains the chemical shifting of the T_g to minimize loss⁴.

The duplexed cable constructions considered in this investigation (see figure 1) offer additional challenges in that two 50/250 μ m multimode fibers are housed within a single subunit. The fibers can suffer external stresses from outside the subunit, as well as from fiber-fiber frictional stresses. The subunit is surrounded with aramid strength fibers and jacketed in a PVC or polyolefin sheath.



Horizontal Cable (2 and 4-fiber)

Figure 1 Diagram of a 2 & 4-fiber duplexed horizontal cable.

Looking beyond the fiber buffer properties, many design changes can be incorporated into the cable construction. The cable jacket has been found to shrink axially and radially while the fiber remains stable at low temperatures. In many constructions, the radial force component can have negligible impact on loss while the axial forces act as the key contributor to loss. Sugawara et al

have determined experimentally that microbending occurs at temperatures less than -10°C due to the axial contraction of the cable⁵. They have also derived expressions for the loss, showing a dependence of loss increase is cubic proportional to the expansion coefficient. Their solution is the incorporation of a steel tension member to moderate axial mobility. They opted to avoid dimensional and material changes in the cable jacket due to compromised cable bend and crush strength.

The extreme microbend sensitivity of $50\mu\text{m}$ fibers must be considered in the design of the cable. The objectives of this investigation are to isolate the optical loss mechanism(s) of cables exposed cyclically to low temperatures and to identify construction enhancements to improve performance. The axial and radial instabilities of the cable sheath and subunit and the fiber responses to these stresses are used to assess macrobending and microbending loss effects.

BENDING LOSSES

Macrobends are considered to be axial bends of relatively large radius ($>1\text{mm}$). The bend in the fiber causes higher-order modes to exceed the critical angle (light is no longer reflected back into the fiber core). Macrobending losses typically increase at higher wavelengths.

Microbends are formed through small displacements or cracks ($<10\text{mm}$) of the fiber in directions that are transverse to its axis that result in a cumulative transmission loss. The cracks are created when fiber comes into contact with rough surfaces such as from a spool, plastic jacket or aramid yarns. Microbend sensitivity is inversely proportional to numerical aperture and fiber core OD. That makes $50\mu\text{m}$ fibers more sensitive than $62.5\mu\text{m}$ fibers.

Temperature Cycling Studies

The temperature cycling test used in this study combines the TIA FOTP-455-3A requirement of two complete cycles with the temperature limits (-10 to 60°C) required in the ISO specification. The maximum allowable change in loss throughout the cycling is 0.60dB/km . Temperature cycling

studies have consistently shown unacceptably high values, particularly at low temperature (see figure 2).

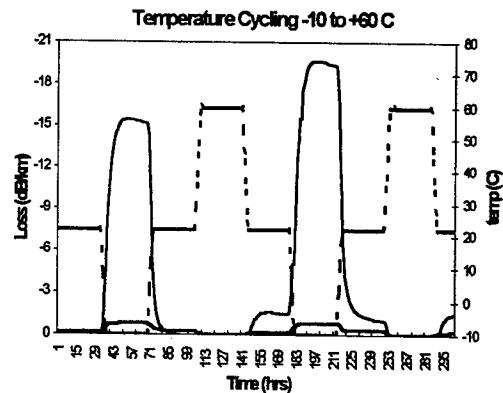


Figure 2 Temperature cycling from -10 to 60°C for two different cables.

In figure 2 the dashed curve represents the temperature and is shown on the right y axis. The attenuation values are shown on the left axis and are represented by the two solid curves. The higher of the two curves (lighter line) shows how the low temperature failures manifest themselves. However, when the correct materials and dimensions are chosen the loss is reduced and the cable meets the 0.60dB/km specification. This is shown by the lower (heavier) curve. The attenuation stays low for both cycles to low temperatures.

Response to Low Temperatures

The materials in the cable respond to low temperatures by shrinking. Each material will shrink to a different extent. The polymeric material of the subunit sheath will shrink to a greater extent than the glass fiber. The extra length in the fiber must go some-where, particularly if the cable and fiber are fixed at both ends.

The fiber will re-arrange itself within the subunit into a helical structure (see figure 3). This helical structure contains crossover points along the length of the cable. These crossover points create macrobend and microbend attenuation in the fiber's transmission properties.

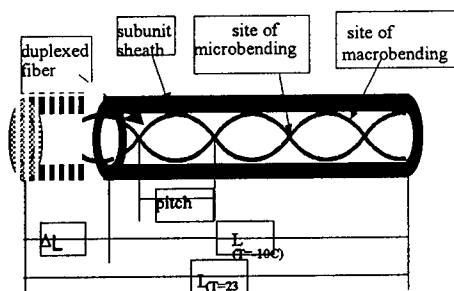


Figure 3 Diagram of the low temperature coiling effect.

Understanding this structure mathematically can lead to interesting and useful observations on the performance of the cable. As an example the number of crossover points per unit length of cable can be calculated. Minimizing this number will reduce the attenuation in the cable.

Material Influences on Microbending

The materials used to produce the cable will under go changes at low temperatures. In addition to the shrinkage of the materials, the modulus will increase as the temperature decreases. In addition to these changes, many polymeric materials under go a physical transition at low temperatures (see figure 4). This transition, called the glass transition (T_g), is indicated by a large increase in modulus. The higher the modulus the stiffer the material, the higher the microbend attenuation.

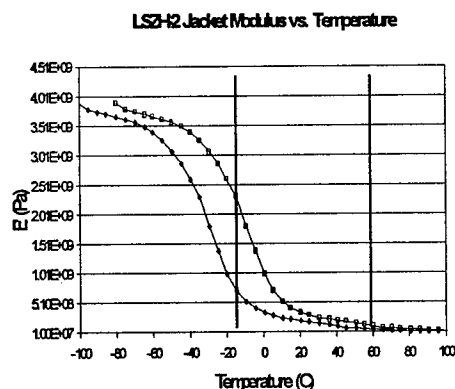


Figure 4 Modulus as a Function of Temperature for Sample A (□) and Sample B (◆). Showing one good and one poor cable with attenuation at -10°C .

The increase in modulus as the temperature decreases is shown for two materials in figure 4. At some temperature below 0°C , a sharp rise in the modulus is observed. The two materials are shown to demonstrate the difference a material can make. Sample A has a slightly higher glass transition temperature. When comparing the modulus of sample A and sample B at -15 to -20°C , for example, a large difference is found which results in higher microbend attenuation for Sample A at this temperature. This is true even though the materials have approximately the same modulus at room temperature.

CONCLUSION

This paper has described some of the considerations which must be taken into account when designing duplex $50\mu\text{m}$ fiber, for fiber-the-desk applications. Cable performance depends on the helical pattern which the fiber arranges itself into within the subunit jacket, therefore, the subunit dimensions must be carefully controlled in the design and manufacture process.

The materials of choice for this cable must be matched to operate together at low temperatures. The CTE, Modulus, and T_g must be such that there are no major changes in the temperature range from -10 to 60°C . Therefore, it is most advantage to have subunit jackets constructed of material in which the glass transition is less than -10°C .

REFERENCES

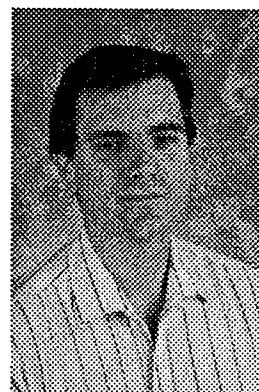
- 1 P. B. Gramado, O. S. Gebizlioglu, M. J. Zammit, and G. D. Kiss, "Low Temperature Transmission Loss in Loose Tube Fiber Optic Cables", SPIE Proceedings Int'l Society for Optical Engineering, 2290, 1994.
- 2 T. Yabuta, N. Yoshiawa, and K. Ishihara, "Excess Loss of Singlemode Jacketed Optical Fiber at Low Temperature", Applied Optics, Vol. 22, No. 15, 2356 to 2362, 1983..
- 3 S. Shiue, "Thermal Induced Microbending Losses in Double-coated Optical Fibers at Low Temperature",

Material Chemistry and Physics, 38, 186-190, 1994.

4. T. Kimura and S. Yamakawa, "Effects of Chemical Structure on Low-Temperature Modulus for UV-Curable Polybutadiene Acrylates as an Optical Fiber Coating Material", Journal of Polymer Chemistry: Part A: Polymer Chemistry, Vol. 24, 1161- 1171, 1986..

5. Y. Sugawara, T. Kobayashi, and M. Tanaka, "Attenuation Increase Mechanism of Jacketed and Cabled Fibers at Low Temperature".

Authors



Todd P. Berger is a Product Development Specialist for 3M Telecom Systems Division in Austin, Texas. He is currently responsible for the design and analysis of fiber strength in optical fiber connectors. His work also includes research in optical properties and materials for fiber optic components and cable accessories. He is also responsible for the ongoing support and analysis of the performance benefits of the VF-45 interface. Prior to this position, Berger worked in 3M Electrical Products Division where he developed materials for high voltage splicing for the electrical industry.

DUPLEX CABLE DESIGN FOR ENHANCED INDOOR AND SECURITY SYSTEM

Ho-Soon Lee*, Joong-Jin Hwang, Jin-Han Kim

SAMSUNG Electronics Co., Ltd. Gumi-City, Republic of Korea

ABSTRACT

Today, loose tube cables and ribbon cables are mainly used to construct trunk or backbone network. And intrabuilding cables - simplex, duplex, zip-cord, and distribution cables for indoor, etc - are widely used to meet the needs for FTTH(fiber-to-the-home) and FTTD(fiber-to-the-desk) due to their easiness of installation and special characteristics in operation. Nowadays the needs for intrabuilding cables are increasing rapidly.

Currently, the applications of intrabuilding cables are expanding to a variety of purposes(e.g, fiber optic security system). Therefore, the requirements for intrabuilding cables are becoming more complex.

The result of specially designed duplex cable and its application - especially for fiber optic security system - are discussed in this paper as follows ;

- mechanical characteristics
- environmental characteristics
- relationship between bending radius, attenuation change and applied load
- other required tests

As a result of these tests, the reliability of this cable type and some explanation for fiber optic security system are discussed. The information for security system using optical fiber cable is mentioned in the discussion section in detail.

INTRODUCTION

Generally, optical fiber cables with loose tubes and ribbon fibers are used to construct trunk or backbone for a national telecommunication

network. They can carry large quantity of optical fibers with small diameter due to their structure and low cost. Their mechanical and environmental characteristics match to use for telecommunication system. These advantages make them more frequently used in telecommunication industry and improve their properties for better operating condition. However, increasing demands for faster telecommunication system from many users have been requiring special optical fiber cable to be used for wide variety of applications - basically FTTH, FTTD, and other special application ; for an example, fiber optic security system. Therefore, many researchers have developed intrabuilding cables to meet those requirements.

In these intrabuilding cables, the distributing method and safety aspects are ensured with the use of tight buffered fibers and aramid yarns. This paper introduces more advanced and modified duplex cable design and different manufacturing process.

For intrabuilding cable applications, the suitable cable type should be selected by the condition of telecommunication system. Duplex cable is suitable to be widely used for indoor application and fiber optic security system. Traditionally, most of cable manufacturer uses s/z stranding or planetary manufacturing process to achieve safe optical and mechanical properties by giving enough fiber excess length and reducing the effect of bending radius. The manufacturing process of these traditional cable types are slow and difficult to adjust tension of each tight buffered fiber and to control the stranding pitch of them. Because of the stranding process, typical manufacturing process of duplex cable is slow and complicated. Therefore, these

disadvantages require more improved stranding method of tight buffered fiber and aramid yarn for easy, effective and economic manufacturing.

We approached the stranding method of tight buffered fiber to manufacture duplex cable by adapting basic theory - parallel-laid tight buffered fiber in duplex cable - and tried to sustain good optical and mechanical characteristics comparing with typical one.

The mechanical and environmental tests were conducted and results are described in this paper. These results can give clear and useful data to customers about modified product.

CABLE DESIGN

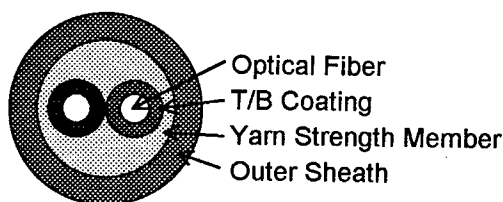


Fig. 1. Cross Section of Duplex Cable



Fig. 2. Typical Duplex Cable Design



Fig. 3. Modified Duplex Cable Design.

Fig. 1 shows the cross section of common duplex cable type and the consisting components tested are as follows ;

- optical fiber type : single mode fiber
- tight buffer : Polyvinyl Chloride
- yarn strength member : Twaron™ product
aramid yarn
- outer jacket : Thermoplastic Polyurethane
- outer diameter : Nom 5.0 (mm)
- weight : Nom. 20 (kg/km)

Fig. 2 shows the structure of typical duplex cable. It is comprised of tight buffered fiber and yarn strength member which is stranded - it would be s/z or helical stranding - to the cable length direction. It is expected to have some advantages of tensile strength and bending during operation due to excess fiber length and stranding pitch.

In Fig. 3 shows the modified duplex cable design. The tight buffered fibers and yarn strength members are laid parallel to the cable length. Basically, the disadvantages expected are as follows

- tensile strength :
its tensile strength could be lower than typical one because it does not have enough excess fiber length. In addition, those kinds of structure would cause strain increase and attenuation change to cable and fiber immediately.
- bending :
it may cause bending stress to tight buffered fiber due to lack of excess fiber length and crossovers. One - inside or outside - may show good optical characteristics but another is bad because one of two could be under severe stress inside the cable than the other.
- bending under load :
after installation, some portion of cable may be under bending and unexpected load can be applied. In this case, optical fiber cable should withstand such condition and should not cause large attenuation change during and after the load is applied

EXPERIMENT

To show the characteristics of the modified duplex cable, mechanical and environment tests were carried out and the results are as follows.

- Mechanical tests : compression resistance, repeated bending, minimum bending radius, bending under load and some other properties were tested. In normal operation of the duplex cable, bending under load occurs frequently and this is the theory applied for this type of cable. Therefore this bending under load test was deeply examined.

- Environmental tests : temperature range of optical fiber cable is between +85°C and -40°C, temperature cycling test is essential and checked 2 times for 4 samples.

Mechanical Characteristics

1. Compression Resistance

Basically, the crossovers in duplex cable are the weakest point against compressive force. And thick jacket and large number of aramid yarn can lead to satisfactory results but they require higher cost.

Therefore, we tried to cover this disadvantage by applying tight buffered fiber and yarn strength member being straight to cable length. The result show that this cable design satisfies mechanical requirements of cable users.

Some of the crossovers show that higher attenuation change than those of others. However, the higher values are slight and can be ignored.

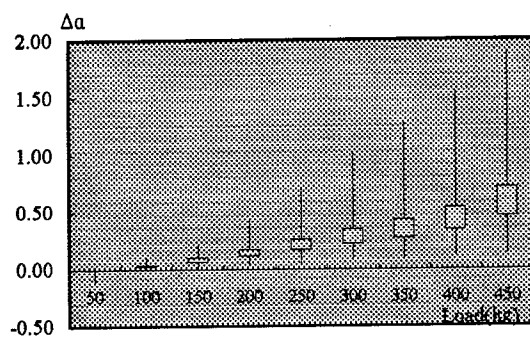


Fig. 4 Attenuation Change Vs Load

In Fig 4, the test was conducted 15 times by using 50mm length plate and load was applied up to 450kg. Up to 450kg load, average attenuation change was below 0.5dB, and there were no attenuation changes after test.

2. Repeated Bending

The characteristic of bending in duplex cable is the another weakest points.

When applying external forces to the modified

cable, outer positioned tight buffered fiber was severely damaged at first. However as number of cycles was increasing, attenuation change was not large enough to identify. It is because that tight buffered fibers were trying to restore their original position, so each tight buffered fiber was at their stabilized position.

As shown in Fig. 5, tight buffered fiber #1 is outside of cable core, so bending stress was severer than tight buffered fiber #2 which was inside of cable core. If this shape was maintained, the attenuation change would increase, but it would return to original position being most stable. Fig. 6 shows the result of repeated bending tests and the theory mentioned above is clear and proved.

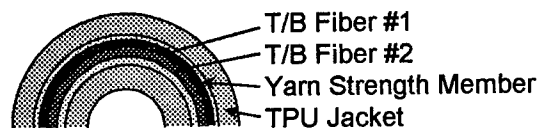


Fig. 5. Schematic Drawing of Cable when Bending Forces are applied.

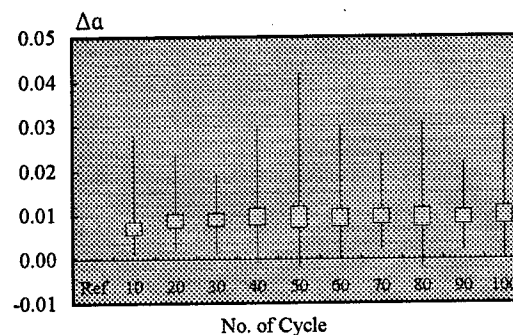


Fig. 6. Attenuation Change Vs Bending

- 100 cycles for bending tests were repeated to increase the reliability and accuracy of results.
- All of them show attenuation change below 0.1dB, and there were no attenuation changes after test.

3. Attenuation Change & Load & Bending Radius

Duplex cables are commonly installed inside of

buildings. After installation, they may be under bending within total cable length and sometimes unexpected load can be applied. In this case, such kind of external forces could cause optical failure or damage on the cables.

The results in this section shows that how small bending radius and how much load modified duplex cable -SEC designed - can endure without optical failure.

And when modified duplex cable is used for fiber optic security system, the basic concept of the system is to detect attenuation change occurred by the relationship between applied load and bending radius over duplex cable. It is tried to clarify the relationship between bending radius, attenuation change and applied load.

At first, both ends of duplex were fixed by mandrel to give bending effects to them. And, load from 0kg to 35kg applied to the cable center not giving any extra bending effects except cable under bending load.

Secondly, diameter of mandrel was changed from 20mm to 100mm step by step to figure out the effect of bending diameter.

- Bending(mandrel) dia. : 10mm ~ 100mm
- Applied load : 0kg ~ 35kg
- Interval between mandrel : 1m
- Diameter of mandrel & loads : manually changed

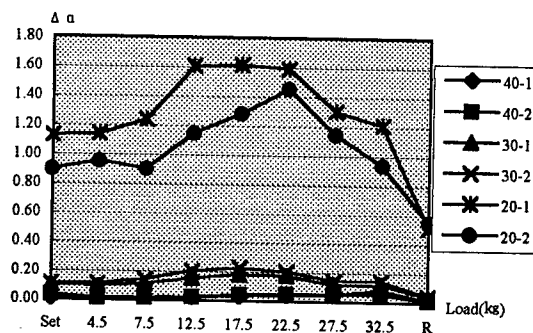


Fig. 7-1. Load, Diameter of Mandrel and Attenuation Change

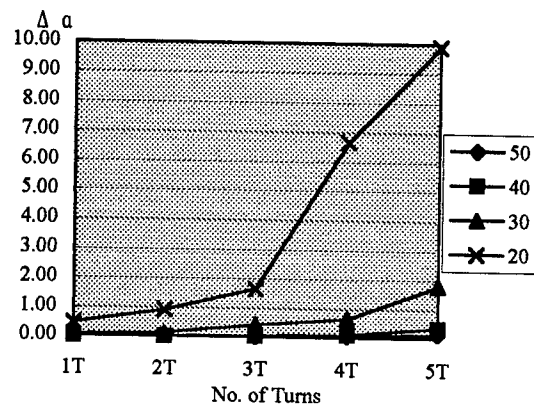


Fig. 7-2. Bending Diameter & Attenuation Change without Load

Dia. Vs Load	Dia. 40		Dia. 30		Dia. 20	
	#1	#2	#1	#2	#1	#2
Installation	0.01	0.04	0.10	0.11	1.13	0.90
4.5 kg	0.02	0.01	0.09	0.11	1.14	0.96
7.5 kg	0.02	0.02	0.11	0.14	1.24	0.91
12.5 kg	0.02	0.02	0.15	0.20	1.61	1.15
17.5 kg	0.03	0.04	0.18	0.23	1.62	1.29
22.5 kg	0.04	0.05	0.17	0.20	1.59	1.46
27.5 kg	0.05	0.05	0.02	0.14	1.30	1.14
32.5 kg	0.07	0.05	0.12	0.14	1.21	0.94
Removal	0.01	0.01	0.04	0.04	0.52	0.59

Table 1. Attenuation Change(dB) according to Mandrel Diameter and Load

turn/dia	50	40	30	20
1 turn	0.00	0.00	0.05	0.47
2 turn	0.00	0.01	0.11	0.91
3 turn	0.01	0.04	0.43	1.65
4 turn	0.05	0.10	0.65	6.66
5 turn	0.15	0.35	1.79	9.89

Table 2. Attenuation Change according to Mandrel Diameter.

In Fig 7-1, 7-2 and table 1, 2, show the attenuation changes according to the change of load and diameter of mandrel.

Fig 7-1, 7-2 and table 1, 2 shows that attenuation changes are most significant at 20mm and 30mm diameter of mandrel and at certain load ; from 12.5kg to 22.5kg. As diameter of mandrel increases, the attenuation changes are too small to identify any change especially over 50mm.

4. Mechanical Test Results

All the test results of mechanical characteristics are listed in table 3.

Items	Spec.	Criteria	Result
Crush	EIA-455-41	0.20dB	≤ 0.2dB
Tensile	EIA-45533A	0.20dB	≤ 0.2dB
Impact	EIA-455-25A	0.20dB	≤ 0.1dB
Flexing	EIA-455-104	0.20dB	≤ 0.1dB

Table 3. Mechanical Testing Results

All of the tests are conducted according to Bellcore Specificaion TR-NWT-000409, "Generic Requirements for Intrabuilding Optical Fiber Cable", and the results meet criteria.

Environmental Characteristics

1. Temperature Cycling Test

It was thought that tight buffered fiber and outer sheath can be expanded or shrunk as the temperature increases and decreases. Though, excess length of tight buffered fiber is almost zero, that can be easily affected much larger than traditional cable type. So, we tested modified duplex cable which is wound on a small diameter spool and conditioned in weather chamber for test. 2 spools were arranged for accurate test result.

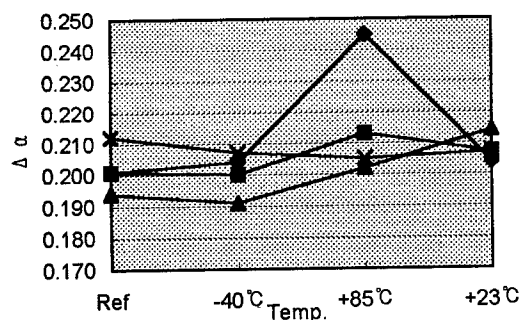


Fig. 8. Attenuation Change Vs Temp.

As shown in Fig. 8, the maximum attenuation change during all temperature cycles was 0.044dB/km and the other fibers showed almost 0dB/km.

This test was carried out two times and the

results were similar with the former one.

2. Jacket Shrinkage Test

Items	Spec.	Criteria	Result
Jacket Shrinkage	EIA-455-86	Max. 5%	Max. 1%

Table 4. Mechanical testing

As shown in Table 4, result was almost 0 and met specification.

Discussion

Regarding the results shown above, the following point can be specified ;

1. Duplex cable with parallel-laid tight buffered fibers and aramid yarns shows good mechanical and environmental results comparing with traditional one.
2. Bending characteristics of modified design show good results and range of attenuation change according to applied load.
3. The effects of outside factors – mechanical or environmental - during operation can be analyzed. 1) Compression does not affect severe damage to modified duplex cable unless over 50kg load was applied at 1cm width point. 2) Bending being occurred by outside load can increase attenuation loss up to certain level. The limited level are listed in table 5, and these results can be used for fiber optcial security system. As shown in table 5, when the diameter of bending point was over 40mm, it was hard to detect slight attenuation change in security systems - if possible, the security system requires more complicated and sensitive structure and may result often fault signal. The minimum diameter of bending applied to duplex cable should be below 30mm as shown in table 5.

Dia.	Load	Attenuation change
20mm	over 10kg	from 1.0dB
30mm	over 10kg	from 0.20dB

Table 5. Attenuation change comparision

Table 5 shows proper installation guide for normal fiber optical security system when using the modified duplex cable. It may vary according to cable structure and design. And the test results of Fig 7-2 and table 2 show that duplex cable is not required to be bent during installation. One can install it by giving different bending radius with a clamping tool. It means that the quantity of attenuation change during installation can be reduced by giving large bending radius. In addition, designing small diameter mandrel would result in increase of the attenuation change when certain load is applied.

Conclusion

Duplex cable can be produced faster and more efficiently than traditional duplex cable by inserting tight buffered fiber and aramid yarn being parallel to the total cable length without stranding process.

From the results of bending under load, the expected failure can be lead out. Duplex cable with modified design may fail when high load and bending is applied spontaneously and the criteria is mentioned in discussion section.

Finally, for fiber optic security system, test results of bending radius Vs load can guide process for more accurate and effective installation of system. By varying bending radius of optical fiber cable, user can control the range of detection and alarming. And this paper showed how much the bending radius of optical fiber cable is suitable for security system.

References

1. Bellcore Technical Reference TR-NWT-000409, "Generic Requirements for Intrabuilding Optical Fiber Cable", Issue 2, September 1990.
2. Daniel J. Rutterman "Delivering fiber-to-the-desk : a new low-cost solution" IWCS 1998.
3. W.S. Liu, K. Kathiresan, and J.B. Fluevog "A four-fiber tactical cable" IWCS 1990.

Ho-Soon Lee
Keram@samsung.co.kr
SAMSUNG Electronics
Co., Ltd.
#94-1, Imsoo-Dong
Gumi-City, Kyug-Buk,
Korea.



Ho-soon Lee was born in 1970. He received a bachelor's degree from Kyungpook National University in 1996 and is now working on research and developing of optical fiber cable in Engineering and R&D Group.

DEVELOPMENT AND APPLICATION OF A COMPOSITE FIBER/COPPER CABLE WITH REMOTE POWERING CAPABILITIES

John Heery, Mike Gimblet, James Register

**Siecor
Hickory, NC**

ABSTRACT

A composite cable was developed for a fiber-to-the-curb (FTTC) application that provides communications via optical fibers and remote powering to system electronics using copper twisted pairs. Both an outdoor version and a UL-1666 riser rated indoor/outdoor version are presented. Key items in the development included (1) removal of tensile yarns to reduce the cable diameter while still meeting tensile requirements, (2) compatibility of the flame rated cable's polyvinyl chloride (PVC) jacket with lubricating oil used in the armoring process and (3) optimizing the jacket to armor adhesion to meet mechanical performance requirements and pass water penetration tests.

A cable design utilizing the armor and twisted pairs as strength members was determined to be sufficient to meet the tensile requirements of the cable without adversely affecting the performance of the optical fibers or twisted pairs. In developing the riser rated version, no significant compatibility effects were seen between lubricating oil, used as a cooling medium in the corrugation process, and the PVC jacket. By optimizing the processing conditions for tooling and corrugation height, sufficient adhesion of the PVC jacket to the armor was achieved and was verified by the mechanical test performance of the cable.

INTRODUCTION

As optical fiber is deployed deep into the outside plant, the convenience to offer electricity to power remote electronics presents a logistical problem. While fiber can replace metallic conductors for voice, video and data transmission, it cannot carry electric power. This presents a problem powering electronics, such as network interface units (NIUs), as they are not always placed adjacent to electrical sources. To power NIUs, service providers would be required to transform and filter separate power conductors to each unit, increasing costs and installation requirements.

The demand for higher bandwidth forces a change in the approach to wiring solutions for the home and office and the outside plant telecommunications network. Broadband solutions are desired to carry the increasing bandwidth of voice, video, and data. To that end, local exchange carriers are looking for an alternate solution to the standard twisted pair that has carried voice and telephone power to the home.

APPLICATIONS

Optical fiber is the natural successor to copper in a broadband network. Its ability to support higher transmission and immunity from electromagnetic interference make it a

logical choice; however, fiber's inability to carry electricity can make the powering of electronics a costly, logistical problem. A solution of combining broadband signal and electrical power capabilities is required to bring down the cost of upgrading the existing infrastructure and providing a useful fiber-to-the-curb (FTTC) solution.

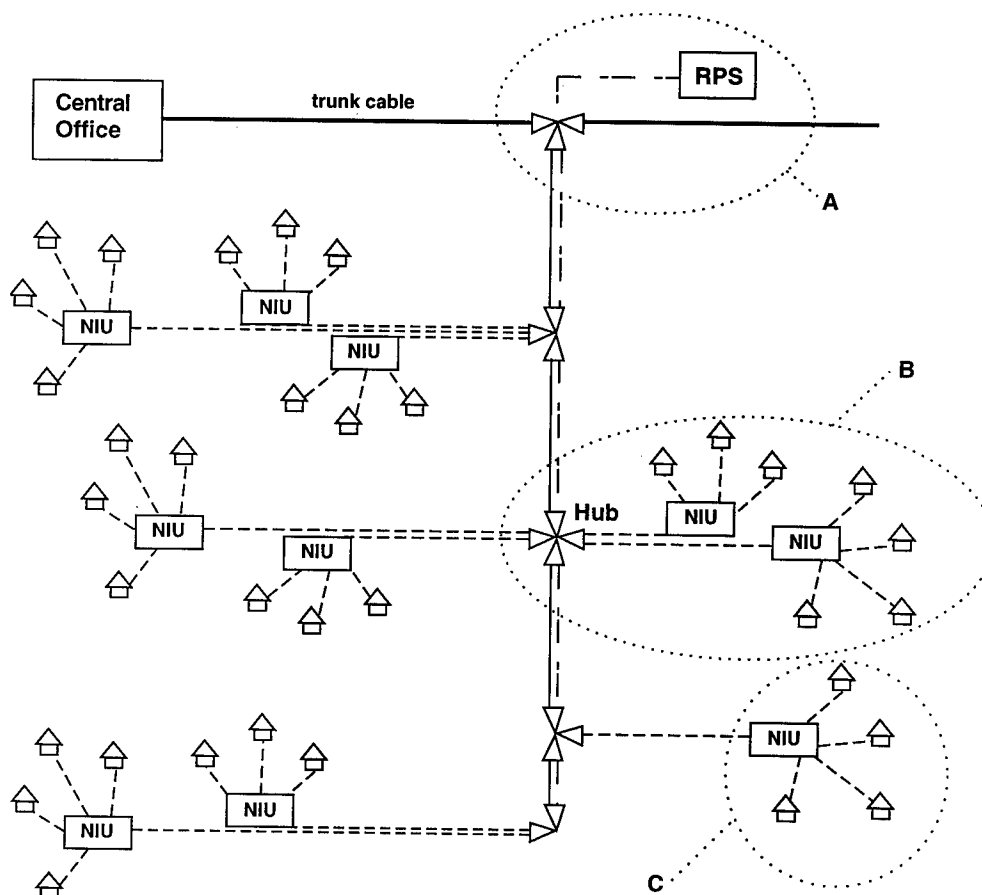
One solution to this problem is a composite cable containing optical fibers for telecommunications transmission and copper pairs for powering remote electronics.^{1, 2} This allows the powering of electronics to be handled by the service provider from the central office or distribution center. Power conductors can be included in the optical cable, eliminating the need for separate cabling and transformation of electrical power at the NIU.

Siecor worked with several customers to devise a network configuration that would

allow a more efficient FTTC architecture¹. As part of this network design, a new cable type was needed that would provide ease of handling and reduced installation cost. This cable type, known as DualCom™, utilizes a composite optical fiber and twisted copper pair design to provide both the broadband signal and the necessary electrical power.

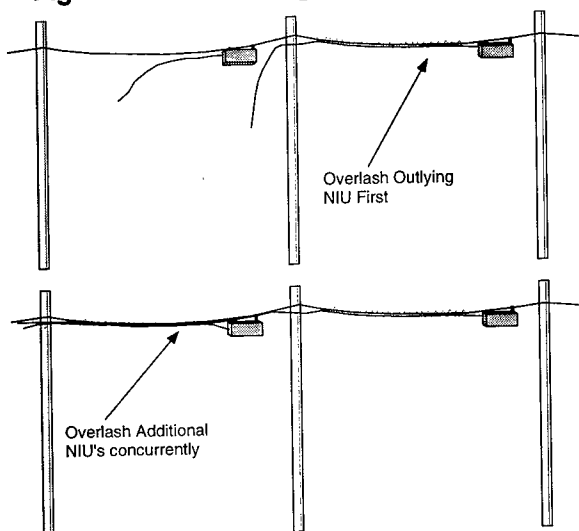
At select points along the optical fiber trunk line leading from the central office, optical cables are spliced to connect multiple hubs to the trunk line. Each hub handles two cables: an optical cable containing the data stream, and a copper cable containing electrical power for the network electronics (See Figure 1, Section A). Multiple NIUs are then connected to a hub using DualCom cables (See Figure 1, Section B). The electronics in the NIU are powered by a remote power station (RPS). Several homes are then connected to a single network interface unit (See Figure 1, Section C).

Figure 1: FTTC System Configuration



To eliminate costly splice points at each NIU, a star configuration was used to connect the homes to the hubs. The optical fiber and copper conductors that would be required in separate cables were combined into a composite cable with a single concentric sheath. By eliminating the installation of multiple cables, the overall process efficiency is improved. A DualCom cable connects each NIU to a hub. This led to the hub acting as the center of the star network. By starting with the furthest NIU and working back towards the hub, cables could be installed simultaneously using a combined overlapping installation (See Figure 2).

Figure 2: Overlashing of DualCom Cable

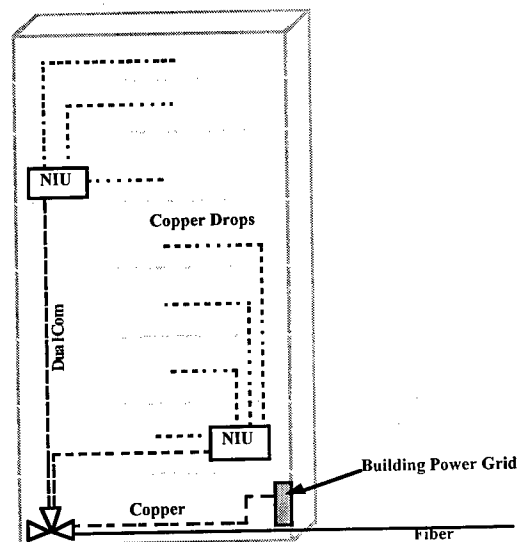


Connections between the NIU and the home would be accomplished using a twisted pair, co-axial, or combination solution. This would allow use of conventional equipment in the home already available on the market. Several homes may be connected to a single NIU in a star configuration.

In a more urban environment, individual dwellings and offices are not necessarily the typical configuration. In this case, the homes of Figure 1 might be replaced by the various floors of an office building or high-rise multiple family dwelling. NIUs would then connect the units of a single floor or multiple floors with the hub possibly being located in

the basement of the building (See Figure 3). In such a case, the star configuration still provides an efficient network solution; however, the addition of fire codes now places an additional requirement on the cable. Power can either be tapped from the building's power grid or supplied externally using a remote power supply.

Figure 3: Configuration of DualCom Cable within a Building



Customer Requirements:

To be effective as a FTTC solution, the cable must meet a number of customer requirements:

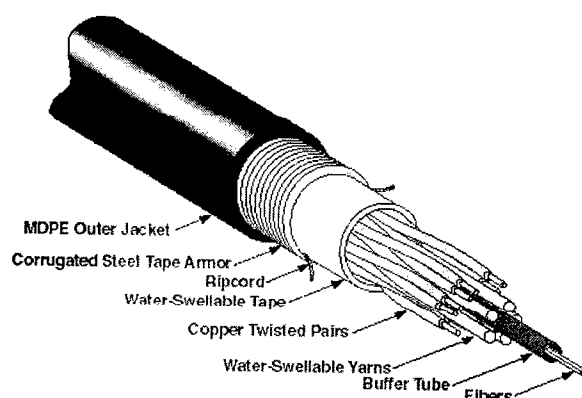
1. Contain high data rate fibers such as dispersion unshifted single-mode optical fibers,
2. Be available in low fiber counts (2-6) to meet the demands of a small number of end users while still being cost effective,
3. Have a sheath capable of withstanding the elements and meet applicable local building codes if being used indoors,
4. Provide waterblocking protection in the event of a breach of the sheath,
5. Provide the necessary electrical component to transmit power down the length of the cable,

6. Be a small concentric design with a minimized outer diameter for ease of handling and installation.
7. Utilize conventional materials, access tools and techniques.

OUTDOOR CABLE DESIGN

The DualCom cable is a central tube design, manufactured by surrounding a thermoplastic buffer tube containing optical fibers with copper twisted pairs and water absorbing yarns. Water absorbing tape and armor is formed around the core with a medium density polyethylene (MDPE) jacket extruded over the armor. Figure 4 illustrates the cable design.

Figure 4: DualCom Cable



Two crucial customer requirements for the cable design were to keep the outer diameter and cost to a minimum while maintaining reliability. To achieve these goals, the cable was designed without traditional optical fiber cable tensile elements. This was possible due the installation techniques and the customer's requirement of a 1350 N tensile rating. The DualCom cable design achieves tensile strength from the copper twisted pair and the armor tape.

The copper conductors will be under strain during tensile loading. It is important the

cable be designed so that the copper conductors will not elongate. Elongation would reduce copper conductor diameter and increase resistance of the copper conductors. This would lead to performance losses of the system.

Typical resistance changes during tensile testing are presented in Table 1.

Table 1: Results from Resistance Testing During Tensile Loading

Load (N)	Percent Resistance Increase (%)
0	0.000
450	0.000
900	0.001
1350	0.002
After 1 hour at 1350 N	0.004
0	0.002

The resistance changes in Table 1 are negligible. To give meaning to the insignificance of these resistance changes, the maximum resistance change of 0.004% is equivalent to the resistance change that occurs from a temperature change of 1°C. This is calculated by solving for the temperature delta, $(t_2 - t_1)$, in Equation 1, below.³

$$R_{t2} = R_{t1} [1 + \alpha_{t1} (t_2 - t_1)] \quad (1)$$

Where;

R_{t2} = Resistance at final temperature in °C

R_{t1} = Resistance at initial temperature in °C

α = Temperature coefficient of resistance of the material for the initial temperature t_1 . For copper having a conductivity of 100% of the International Annealed Copper Standard, $\alpha_{20^\circ\text{C}} = 0.00393$

t_2 = Final temperature in °C

t_1 = Initial temperature in °C

The initial resistance, R_{t1} , for the experimental results in Table 1 was 9.13 ohms. Additionally, fiber strain was not adversely effected.

Based on conceivable uses of the composite design, a family of cables was developed. The family includes the choice of 1 to 12 single-mode or multimode fibers with 4, 5, or 6 twisted pairs either 19 AWG or 22 AWG.

The outdoor cable performance met or exceeded industry specifications as shown in Table 2.

Table 2: Test Results Summary for Outdoor Design

GR-20 Issue 1	Test	Requirement	Pass/Fail
6.5.3	Cold/Hot Cable Bend	20x OD @ -30°C and 60°C	Pass
6.5.4	Impact Resistance	25 impacts	Pass
6.5.5	Compressive Strength	300 N/cm	Pass
6.5.6	Tensile Strength of Cable	1350 N	Pass
6.5.7	Cable Twisting	10 cycles \pm 180°	Pass
6.5.8	Cable Cyclic Flexing	25 cycles, sheave 20x diameter	Pass
6.6.3	Temperature Cycling	-40°C to 70°C Avg. Delta < 0.05 dB with no fiber > 0.15 dB	Pass
6.6.4	Cable Aging	85°C for 168 hours followed by two cycles -40°C to 70°C	Pass
6.6.7	Water Penetration	1 m static head on 1 m length	Pass

Delta Attenuation Requirements @ 1550 nm (except where noted): 90% of fibers \leq 0.05 dB, 10% of fibers \leq 0.15 dB

INDOOR/OUTDOOR CABLE DESIGN

The outdoor DualCom cable required modifications to be used in an indoor environment. To achieve a UL-1666 riser rating, a PVC jacket was introduced; however, PVC bonds poorly to laminate armors that are typically used in the industry. In the absence of good adhesion, a corrugated armor may split during bending due to the lack of support afforded by the jacket material.⁴ Continuity of the armor is essential since it is a ground path for potential shorts in the power conductors. To maintain proper adhesion between the jacket and armor, a change to the laminate was needed.

The UL-1666 test was used to screen jacket compounds. For the UL riser flame test, 5-position and 6-position twisted pair cables were tested with various jacket wall thicknesses. A PVC material with a 1.2 mm

jacket wall was found to be sufficient to meet UL-1666 requirements.

Compatibility

Compatibility of the PVC jacket material with the lubricating oil used in the armoring process was considered a potential issue. Lubricating oil is used during the armoring process to provide cooling, reduce machinery wear and minimize any degradation to the armor coating.

Initial testing examined PVC dumbbells soaked in the lubricating oil from the armoring process. Exposure to the oil resulted in a significant increase in stress and reduction in percent strain after 1 week at 80°C (See Figure 5 and 6). The material became increasingly brittle due to the leaching of plasticizers, a potential problem for mechanical performance requirements, such as impact and cable flexing.

Figure 5: Normalized Stress of PVC Dumbbells Exposed to Oil

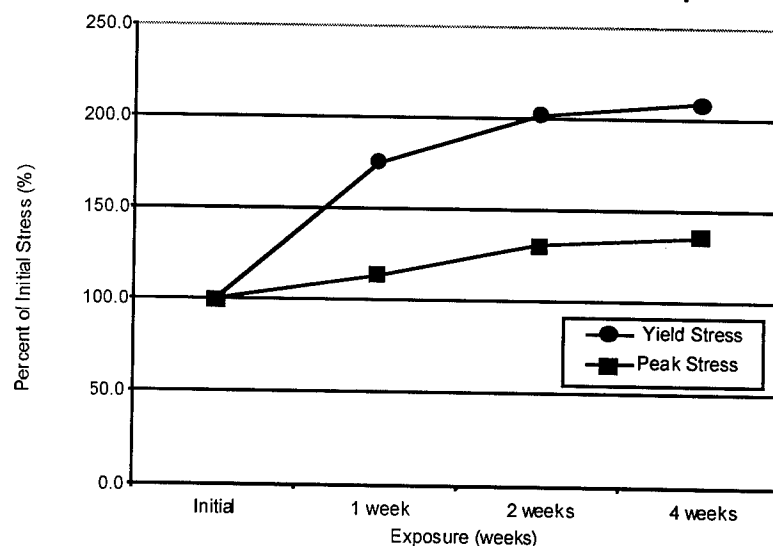
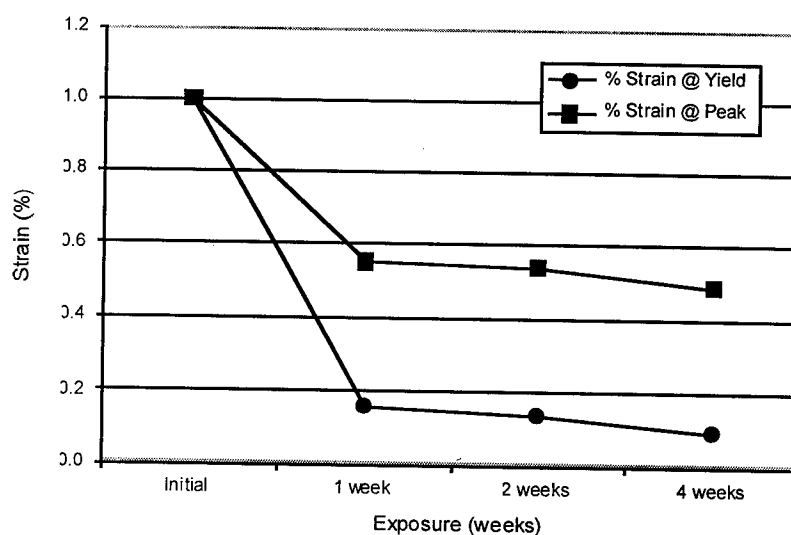


Figure 6: Normalized Strain of PVC Dumbbells Exposed to Oil



However, soaking samples of material was not a good test to simulate potential problems induced by a "thin film" of oil. Any increase in brittleness would probably be minor due to the limited amount of oil available to interact with and leach plasticizers from the PVC. To provide a better real world scenario, cables were manufactured with various potential lubricants. A 5-position, 19 AWG cable construction was tested with no lubrication as a control and with standard lubricating oil. After performing aging tests for one, two and four weeks at 80°C, flex, impact, and adhesion tests were evaluated against initials

to determine if any detrimental effects had taken place.

After performing flex and impact testing, the cables were dissected, and both the inner and outer jacket walls were inspected for damage. All observations of the jacket inner and outer surface after flex testing revealed no issues with stress cracking or other observable damage. Impact testing resulted in minor stress whitening in some samples at the impact point after the two-week aging period; however, the discoloration was not deemed a functional problem since the

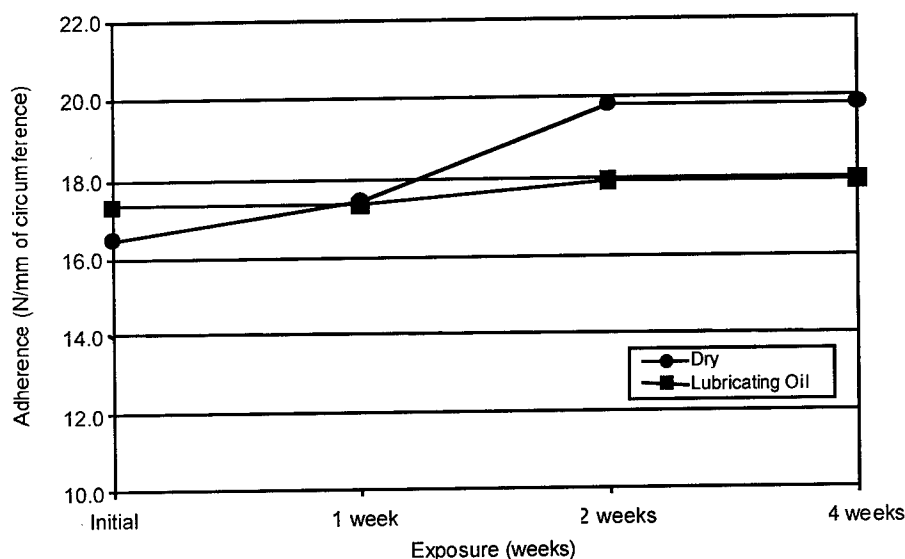
equivalent stress whitening was also observed in the control. Therefore, it was concluded that the thin layer of oil present during the manufacturing process did not create any compatibility problems.

Adhesion

Adhesion testing of the PVC jacket to the armor was performed according to ASTM D4565 as referenced in BellCore™ GR-20-CORE Issue 2 and ICEA S-87-640-1992. The specifications require a minimum of 14.0

N/mm of cable circumference to initiate slippage of a 12-inch section of jacket. If the jacket tears prior to slippage, the test constitutes a pass as long as the tensile strength of the jacket is met. The ASTM D4565 adhesion requirement was exceeded in all tests for all aged conditions. Results are shown in Figure 7 below.

Figure 7: Adhesion Testing for Various Corrugator Lubricants



Armor Crack Investigation

Flex and twist testing revealed an additional issue with armor cracking. The cracking was observed at the base of the armor corrugations and propagated radially around the armor tape. The onset of buckling was observed through the jacket typically after 12-15 cycles of the flex test apparatus.

Observations for both pressure extruded and tubing extruded samples, using PVC, noted that the compound did not adhere well to the armor and exhibited no bonding in the trough of the corrugations. Notwithstanding, the samples still met the ASTM D4565 requirement as noted previously. As an additional data point, a water penetration test performed on a one-meter sample of cable

readily failed. The water migrated down the armor seam and radially around the corrugation troughs. Therefore, the ASTM adhesion test may not be a very good indicator for armor adhesion characteristics required in an outside plant environment.

Processing parameters were also considered important and included the armor corrugation depth and the percentage of fill of the PVC compound into the corrugations.⁴ It is important that the corrugation depth and fill be optimized for a given cable design and compound formulation. An increase in corrugation depth, for a constant fill depth, tends to reduce the number of bends to failure for a given number of corrugations per inch. However, increasing corrugation depth

will also limit the depth of fill for the compound. As fill is decreased, an increased number of bends to failure will be seen. These two conflicting variables coupled with the specified compound need to be optimized to determine peak performance.

To correct the armor cracking, a two step approach was taken. First, the armor manufacturer reformulated the laminate using the selected PVC to optimize adhesion. Second, the new armor formulation was optimized using various processing conditions.

To compare the adhesion of the jacket to the laminate, a cabled jacket peel test from RUS bulletin 1753F-601 was performed for both the old and reformulated laminates. Peel strength testing showed an increase from the original to the reformulated laminate of 61.5%.

Variations in corrugation height and tooling were evaluated to optimize the adhesion of the jacket to the armor. It was desired that the corrugation height not be increased more than required due to the effect of increasing material usage and cable diameter and reducing the effective modulus of the

jacketed armor.⁴ Corrugation height was adjusted over a range of 0.10 mm and evaluated for its effect on armor cracking during flex testing. Both pressure and tubing tooling were also evaluated for the different corrugation height conditions. It was also noted that at decreased corrugation heights, orientation in the flex testing apparatus was important. When the armor seam is in-line with the flexing mandrel, the armor would not crack. When the armor seam was offset by 90 degrees, the armor cracked during flex testing. The effect of orientation was not observed at the increased corrugation heights. In addition to the corrugation height and tooling type, die heat and water trough configurations were also evaluated but showed only minor influence over the armor cracking. It was determined that an increased corrugation height coupled with a pressure extrusion setup resulted in eliminating the previously observed armor cracking.

Final Specifications

The riser rated version, being designed as an indoor/outdoor rated cable, was characterized to the specifications of GR-20-CORE Issue 2. A summary of testing for the indoor/outdoor version is shown in Table 3.

Table 3: Testing Results Summary at 1550 nm for Indoor/Outdoor Design

GR-20 Issue 2	Test	Requirement	Pass/Fail
6.5.3	Cold/Hot Cable Bend	20x OD @-30°C and 60°C	Pass
6.5.4	Impact Resistance	25 impacts	Pass
6.5.5	Compressive Strength	300 N/cm	Pass
6.5.6	Tensile Strength of Cable	1350 N	Pass
6.5.7	Cable Twisting	10 cycles \pm 180°	Pass
6.5.8	Cable Cyclic Flexing	25 cycles, sheave 20x diameter	Pass
6.6.3	Temperature Cycling	-40°C to 70°C Avg. Delta < 0.05 dB with no fiber > 0.15 dB	Pass
6.6.4	Cable Aging	85°C for 168 hours followed by two cycles -40°C to 70°C	Pass
6.6.7	Water Penetration	1 m static head on 1 m length	Pass

Delta Attenuation Requirements @ 1550 nm (except where noted): 90% of fibers \leq 0.05 dB, 10% of fibers \leq 0.15 dB

CONCLUSION

The DualCom cable is a composite optical fiber and copper cable that is designed to provide bandwidth via the optical fibers and low voltage powering to remote electronics using copper twisted pair. The cable was uniquely designed to eliminate tensile strands such as aramid or fiberglass typically used in optical fiber cables. An indoor/outdoor version was also developed and the armor to jacket adhesion, compatibility and mechanical performance were evaluated and optimized.



REFERENCES

1. K. Stause, M. Richards, C. Siebold, M. Ott, R. Tucker, "An Improved Network Deployment Strategy For FTTC," *National Fiber Optic Engineers Conference*, pp. 237-245, 1998.
2. W. Beasley, S. Stokes, G. Karl, "Delivering Fiber To The Node - A New Composite Service Cable," *National Fiber Optic Engineers Conference*, pp. 221-231, 1997.
3. Fink, Beaty: *Standard Handbook for Electrical Engineers*, 1978, eleventh edition, pp 2-4, 2-5, 4-37.
4. William F. Busch, Kenneth E. Bow, Daniel G. Pikula, "Effect of Sheath Processing Parameters on Cable Performance," *Proc. International Wire & Cable Symposium*, Nov. 1989, pp. 427-433.

James A. Register
Siecor
PO Box 489 RD
Hickory, NC 28603

Jim Register is currently a Senior Product Development Engineer for Siecor. He graduated from North Carolina State University in 1992 with a B.S. degree in Mechanical Engineering. He has previously worked for Siecor as a Field Engineer, Applications Engineer and as a Field Engineering Supervisor prior to joining Siecor RD&E.

Ribbon Slotted Core Cable with Non-zero Dispersion Shifted Optical Fiber for WDM Metropolitan Network

Makoto Katayama, Masaaki Kaino, Yuji Kubo, Masaharu Saeki

**Sumitomo Electric Industries, Ltd.
Yokohama, Japan**

SUMMARY

A ribbon slotted core cable with newly developed non-zero dispersion shifted fiber (NZ-DSF) produced by expanding conventional DSF manufacturing technology and using an advanced VAD method, has been developed for implementing large capacity fiber optic networks operated in metropolitan areas. The newly developed NZ-DSF has a small chromatic dispersion slope with a large effective core area while maintaining superior bending performance.

INTRODUCTION

To realize an information-oriented society and implement multi-national business operations, the construction of ultra high capacity fiber optic communication networks is essential. One approach to meeting this requirement is to integrate three multiplexing technologies - time division multiplexing (TDM), space division multiplexing (SDM), and wavelength division multiplexing (WDM) - to maximize the total system performance as economically as possible.

A fiber ribbon that has an outstanding advantage in space saving with mass-fusion technology provides an ideal solution to the production of high-fiber-count optical cables. It provides great economical benefit in implementing FTTH or FTTO systems since the labor cost that assumes a large part of

construction budget tends to increase year by year.

In addition, ribbon slotted core cable that provides superior mechanical resistance and high fiber packing density enables us to adopt ideal SDM technology for the construction of metropolitan WDM networks.

In Japan, major NCCs started operating the WDM system using the existing SMF cable networks. However, considering the advantage of an extended capacity that the WDM system provides, it is expected that the NZ-DSF will come to be more widely used for the construction of new cable networks.

Recently, we conducted a number of performance tests on the ribbon slotted core cable that comprises the newly developed NZ-DSF. This paper describes the design and characteristics of the NZ-DSF we developed and the characteristics of the ribbon slotted core cable we produced with the NZ-DSF.

NON-ZERO DISPERSION SHIFTED FIBER

Fiber Design:

When WDM signals are transmitted in optical fiber with high optical power, certain nonlinear effects may adversely affect the system performance. In order to suppress the nonlinear effects, high-bit-rate WDM systems require the below-mentioned properties:

- 1) Large effective core area
- 2) Zero dispersion wavelength shifted from

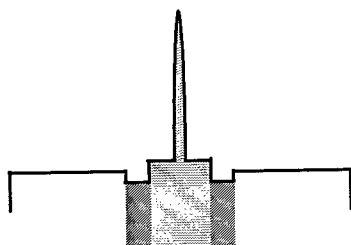


Figure 1 Refractive Index Profile of Designed NZ-DSF

transmission wavelength

3) Small chromatic dispersion slope

In addition, low polarization mode dispersion is required for the long-haul optical amplifier system, and for better productivity of high fiber count cable, excellent splicing performance is required.

Based on the requirements mentioned above, the NZ-DSF was designed and developed by expanding conventional DSF manufacturing technology and using the advanced VAD method. The profile of the NZ-DSF with dual shape core and depressed cladding is shown in Figure 1.

Increasing the number of signal channels for the WDM system is very important for metropolitan WDM networks. Therefore, the NZ-DSF is designed to make the dispersion slope small while keeping the effective core area large.

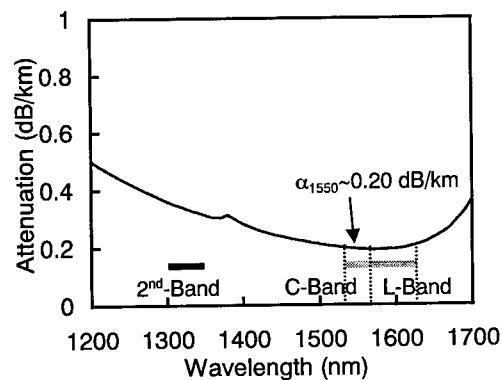


Figure 2 Spectral attenuation of NZ-DSF

Optical Parameters:

Major technical characteristics of the NZ-DSF are summarized in Table 1. The large effective core area (large MFD) is expected to suppress all nonlinear effects, and the small chromatic dispersion slope, 0.07 ps/nm²/km is expected to suppress cumulate dispersion.

The spectral attenuation of the NZ-DSF is shown in Figure 2. The figure shows that the attenuation level at 1550 nm is 0.20 dB/km and OH absorption at 1380 nm is very low, the outcome of the production by using the advanced VAD technology. Therefore, the NZ-DSF is applicable to not only C-band and L-band but also 2nd-Band including 1310 nm.

Environmental Characteristics:

Typical bending characteristics of the NZ-DSF are shown in Figure 3 compared with

Table 1 Major technical characteristics of NZ-DSF

Mode field diameter at 1550 nm	9.1 ± 0.6 μm
Core / Cladding concentricity error	≤ 0.5 μm
Cladding diameter	125 ± 1 μm
Primary coating material	UV curable acrylate
Diameter	245 ± 10 μm
Fiber curl radius curvature	≥ 4 m
Attenuation (at 1550 nm)	≤ 0.22 dB/km
Chromatic dispersion in 1530-1565 nm	1.0 – 6.0 ps/nm/km
Zero dispersion slope	Nom.0.07 ps/nm ² /km
Polarization mode dispersion	≤ 0.2 ps/√km
Cable cutoff wavelength	≤ 1260 nm

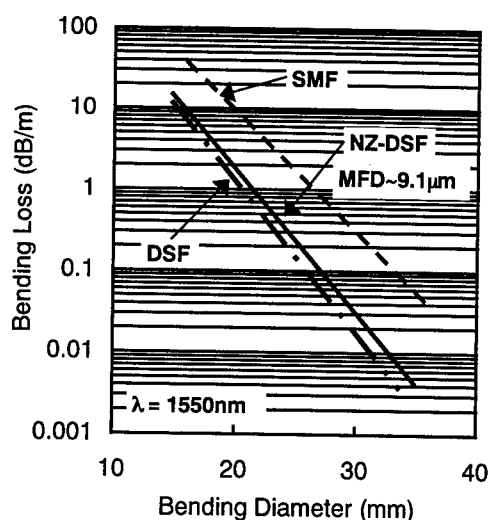


Figure 3 Bending Characteristic of NZ-DSF

those of SMF and conventional DSF. As shown in the figure, the bending performance of the NZ-DSF is superior to that of SMF and is almost as good as that of conventional DSF even with the effective core area approximately 30 % larger than that of the DSF.

Temperature dependence of the NZ-DSF in the range of -60°C to $+80^{\circ}\text{C}$ was also evaluated. Attenuation change at 1550 nm is less than 0.02 dB/km. It is equivalent to that of SMF or conventional DSF.

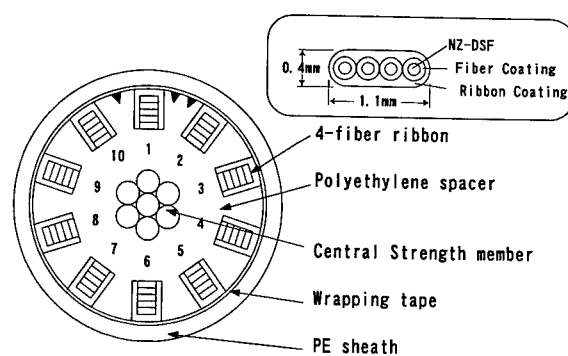
Through these evaluation results, It was learned that NZ-DSF has good environmental performance and can be applicable to the ribbon slotted core cable, for the verification of which, we produced the cable with fibers up to 200 count and ran a number of evaluation tests on it.

NZ-DSF RIBBON SLOTTED CORE CABLE

Ribbon and Cable design

As already mentioned, the fiber ribbon and the ribbon slotted core cable provide great economical benefit and are considered fit for metropolitan WDM networks.

Figure 4 shows the cross sections of both NZ-DSF 4-fiber ribbon and ribbon slotted core cable.



Cable Dimension

Fiber count	Max. 200
Fiber ribbon	4-fiber ribbon
Cable Diameter	19mm
Cable Weight	240kg/km

Figure 4 Cross section of cable

Characteristics of Ribbon

Temperature characteristics:

Figure 5 shows the temperature dependence of the attenuation of the 4-fiber ribbon in the range of -30°C to $+70^{\circ}\text{C}$. The attenuation was measured at 1550nm in wavelength. The change of the attenuation was 0.02dB/km or less.

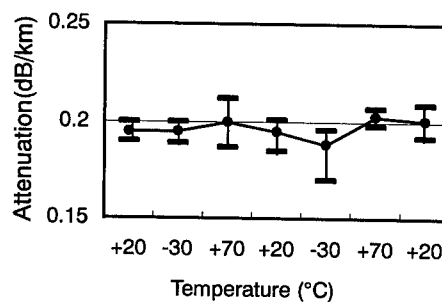


Figure 5 Temperature Characteristics of NZ-DSF 4-fiber ribbon

Lateral pressure characteristics:

The attenuation remained unchanged though the lateral pressure up to 1500N/100mm was applied to the 4-fiber ribbon.

Characteristics of Cable

Attenuation characteristics in manufacturing process:

Figure 6 shows the attenuation change of the test cable at each manufacturing process.

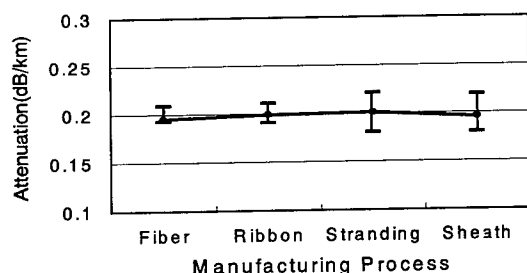


Figure 6 Attenuation changes in Cable manufacturing process

The change was less than 0.02dB/km at 1550nm. It was verified that this cable has stable attenuation characteristics in each manufacturing process.

Temperature characteristics:

Figure 7 shows temperature characteristics of the cable in the range of -30°C to $+70^{\circ}\text{C}$. The change of the attenuation was 0.01dB/km

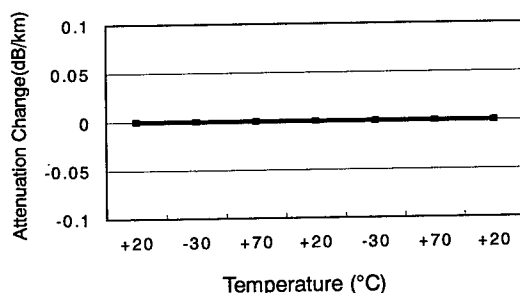


Figure 7 Temperature Characteristics

Table 2 Mechanical characteristics

Test	Conditions	Result (Attenuation change)
Bending	380mm ϕ , 180° 	Less than 0.01dB
Tensile	3900N 	Less than 0.01dB
Torsion	$\pm 90^{\circ} \times 3$ times 	Less than 0.01dB
Lateral pressure	980N/50mm 	Less than 0.01dB

or less.

Mechanical characteristics:

Table 2 shows the mechanical testing methods and the results.

From a number of test results mentioned above, it was learned that ribbon slotted core NZ-DSF optical cable has performance equal to that of the conventional ribbon slotted core SMF cable.

SPLICE LOSS OF 4-FIBER RIBBON

In actual construction works, mass-fusion splicing is normally employed to shorten splicing time. To evaluate the fusion splicing characteristics of the NZ-DSF 4-fiber ribbon, we tried to splice the same type of fibers or different types of fibers, and ran a number of tests on them as described below. In splicing NZ-DSF and NZ-DSF fibers (Figure 10), and NZ-DSF and SMF fibers (Figure 11), we used Sumitomo's Type-63 mass-fusion splicer and the splicing conditions adopted for splicing DSF 4-fiber ribbons were applied.

Figure 8 shows the splicing results of conventional SMF and SMF fibers, and Figure 9 shows those of conventional DSF and DSF fibers. As noted from them, both of the average splicing losses were 0.04~0.06dB.

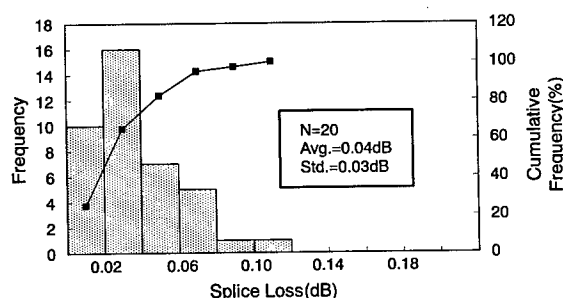


Figure 8 Splice Loss distribution (SMF and SMF)

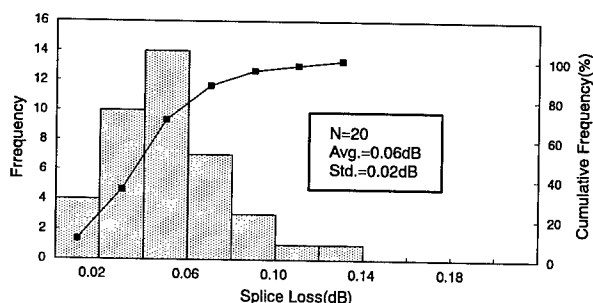


Figure 9 Splice Loss distribution
(DSF and DSF)

Figure 10 shows the splicing loss for NZ-DSF and NZ-DSF fibers. The average splicing loss was 0.06dB and was as good as those for the above-mentioned fiber combination.

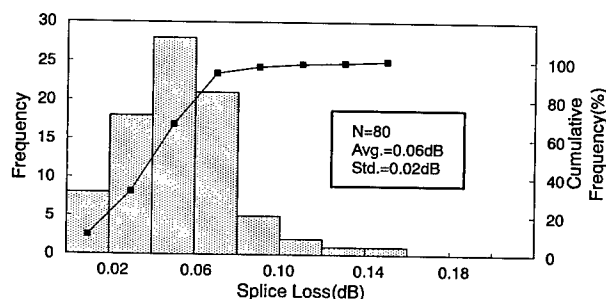


Figure 10 Splice Loss distribution
(NZ-DSF and NZ-DSF)

The splicing results of NZ-DSF and SMF fibers, the combination common with networks in city areas, are shown in Figure 11. The average splice loss was 0.08dB. The increase of the loss, we consider, was due to the types of fibers having been different and splicing conditions not optimum, which however, would matter little from practical point of view.

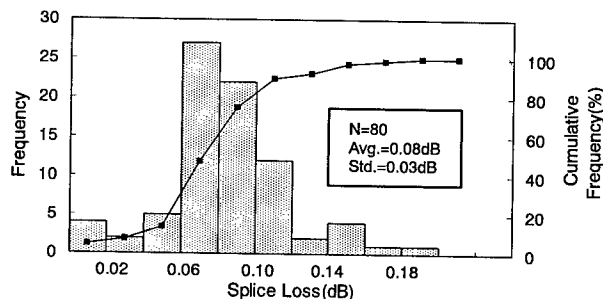


Figure 11 Splice Loss distribution
(NZ-DSF and SMF)

Through these tests, it was learned that the mass-fusion splicing can be employed for splicing the NZ-DSF, too.

CONCLUSION

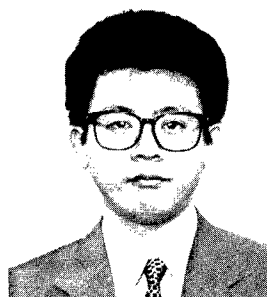
In an effort to meet the needs of the times, we designed and developed new NZ-DSF suitable for WDM having a small dispersion slope ($0.07\text{ps/nm}^2/\text{km}$) with a large effective core area. With the NZ-DSF, we also produced ribbon slotted core cable and ran a number of tests on it. The results proved satisfactory. In other words, the cable with the NZ-DSF expected to provide great economical benefit is fully fit for practical use in implementing FTTH or FTTO networks.

Heading toward information-oriented society, we expect that the ribbon slotted core cable with the NZ-DSF up to 1,000 count will come to be adopted more extensively in the near future.

ACKNOWLEDGEMENTS

The authors wish to acknowledge Yasunori Saito and Yasuo Sakata for their useful discussion and comments.

SPEAKER BIOGRAPHY



Makoto Katayama

Sumitomo Electric
Industries, Ltd.
1, Taya-cho,
Sakae-ku,
Yokohama, Japan

Makoto Katayama received his M. E. degree in electronic engineering from Tottori University in 1993. He joined Sumitomo Electric Ind., Ltd. in 1993 and has been engaged in design and development of fiber optic cables.

Optical Talk Set Based on Fiber Ring Interferometer

Yasushi Nakamura*1, Shinichi Niimi*1, Katsuyuki Arai*1, Yoshiharu Unami*2

Fujikura Ltd. Chiba, Japan

*1 Optical System Research and Development Department

*2 System Component Engineering Department

ABSTRACT

We have developed an optical talk set using a new external modulation method to single mode fiber. The fiber ring interferometer is adopted to convert the vibration given on the fiber to the electrical current signal. The fiber ring interferometer configuration well detects phase-modulated signal from a local unit 20km away from the base station.

1. Introduction

Recently, optical talk sets are becoming indispensable instruments during installation and maintenance of optical cables. Conventional optical talk sets require the access of fiber ends for optical signal launching and detection, therefore, fiber cutting and splicing operations are unavoidable. An optical talk set free from such complicated and loss-inflicting operations is strongly desired as an ideal instrument.

Today, local light injection and detection ⁽¹⁾ are known to be useful methods to realize such kind

of talk sets that operate without fiber ends. Furthermore, two external modulation methods for optical talk sets have been already reported, one is the external loss modulation ^(2,3), another is the polarized wave external modulation ⁽⁴⁾. In this paper, we describe an optical talk set using a new external modulation, and report its principle and the system performance of a prototype.

2. System Configuration

Figure1 shows an example of system configuration. This system is composed of one master unit at a network center and local units at field access points. Optical fibers to be applied are single-mode 4 or 8 fiber ribbons. The master unit has two optical ports that are connected with two optical fiber ribbons in a loop configuration. The local units can be installed at any point along the fiber ribbon. In case of more than two local units, multi-point simultaneous communication is established except for the communication between local units.

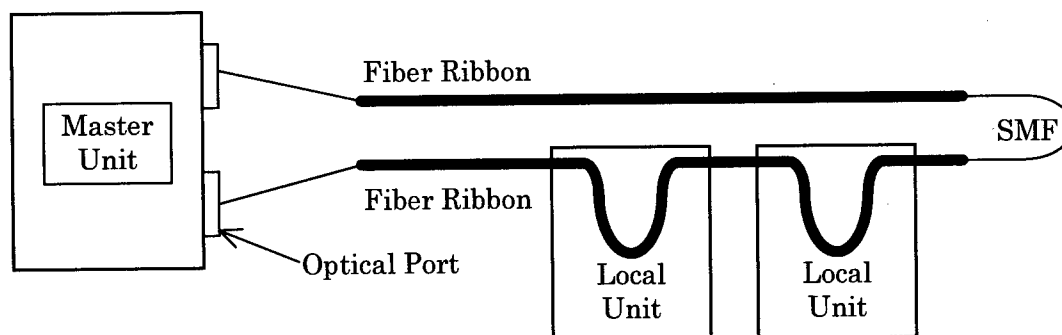


Fig.1 an Example of System Configuration

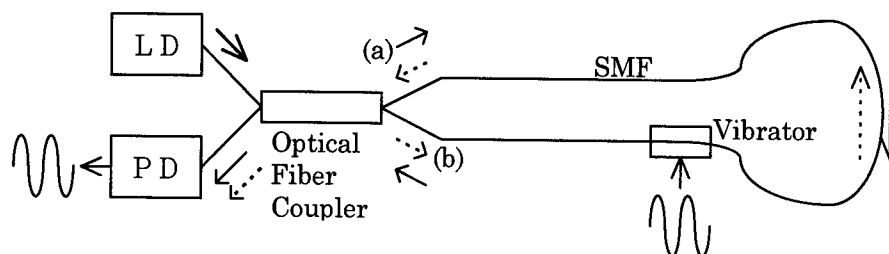


Fig.2 Configuration of Ring Interferometer

3. Principle

3.1 Principle of Fiber Ring Interferometer

Figure 2 shows the configuration of a fiber ring interferometer. The detection scheme is based on the delayed self-homodyne. This interferometer consists of a LD (Laser Diode), a PD (Photo Diode), a 3dB-fiber coupler, an optical fiber ring and a vibrator which for phase shift modulation. The light from LD propagates both (a) clockwise and (b) counter-clockwise through the 3dB coupler with the identical power. These two lights are coupled again at the 3dB coupler, and detected by PD. The photocurrent reflects on the result of interference between these two lights.

In Fig. 3, $\phi(t)$ is a phase shift applied by the vibrator at the vibration point to the electric field of a light propagated through the loop. The light (a) is emitted by the LD at a certain time point and is propagated through the loop. The vibrator at the vibration point shifts the phase of an electric field of the light (a) at time t_1 . The light (b) is emitted by the LD simultaneously with the light (a) and is oppositely propagated through the loop. The length of an optical path to the vibration point for the light (b) is longer than that for the light (a). And therefore, the light (b) arrives the vibration point temporally behind the light (a) and the vibrator at time t_2 shifts the phase of the electric field of the light (b). As a result, a phase shift $\phi(t_1)$ in the electric field of the light (a) differs from a phase shift $\phi(t_2)$ in the electric field of the light (b) due to the difference between t_1 and t_2 . The difference between t_1 and t_2 is dependent on the position of the vibration point in the loop and corresponds to the difference between the phase shifts $\phi(t_1)$ and $\phi(t_2)$.

The phases of the electric fields of the lights (a) and (b) are shifted at the vibration point, and the lights (a) and (b) are coupled together by the 3dB coupler. Figure 4 shows the waveforms of the phases of the electric fields of the lights (a) and (b) arrived at the PD. At the vibration point, the light (a) receives the phase shift $\phi(t_a)$ and the light (b) the phase shift $\phi(t_b)$. An angular frequency of light is ω_0 , and the amplitudes of the electric fields of the light (a) and (b) entering the loop from the 3dB coupler are A and B, respectively. The lengths of clockwise and counterclockwise optical paths of the lights (a) and (b) along the loop are equal to each other. The influence of polarization is ignored for the sake of simplicity of calculations.

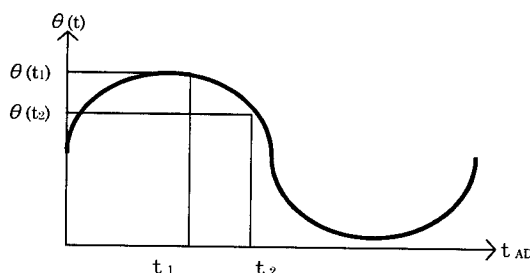


Fig.3 Configuration of Additional Phase Shift Waveform at the Vibration Point

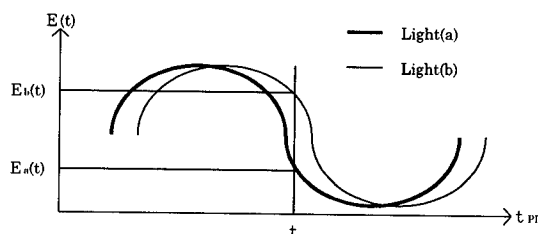


Fig.4 Configuration of the Electric Field Amplitude Waveform of The light (a) and (b) at The PD

The electric field of the light (a) phase-shifted by the vibrator and arrived at a receiving face of the PD is expressed as follows:

$$E_a(t) = A \cos(\omega_0 t + \phi(t_a)) \quad (1)$$

In the 3dB coupler, the phases of coupled lights at a cross-port are $\pi/2$ behind those of emitted lights at a through port. Since the light (b) is passed through the cross port of the 3dB coupler twice, the electric field of the light (b) is expressed as follows:

$$E_b(t) = B \cos(\omega_0 t + \phi(t_b) - \pi) \quad (2)$$

The PD receives the overlapping of the electric fields of the expression (1) and (2), and an optical current of the received lights is proportional to the power of the lights. Therefore, an output current I of the PD is expressed as follows:

$$\begin{aligned} I \propto P &= (E_a(t) + E_b(t))^2 \\ &= (A \cos(\omega_0 t + \phi(t_a)) + E_b(t) \\ &\quad + B \cos(\omega_0 t + \phi(t_b) - \pi))^2 \end{aligned} \quad (3)$$

This expression is developed and rearranged, and a term related to an optical angular velocity that the PD is unable to detect is ignored. Then, the output current I is expressed as follows:

$$\begin{aligned} I \propto A^2/2 + B^2/2 \\ + AB \cos(\phi(t_a) - \phi(t_b) - \pi) \end{aligned} \quad (4)$$

This expression shows that a signal reproduced from the optical current involves a change of $|\phi(t_a) - \phi(t_b) - \pi|$ that corresponds to a phase shift $\phi(t)$ at the vibration point, i.e., a change in the amplitude of the vibration at the vibration point. If the vibration point is at the midpoint of the loop, $\phi(t_a) = \phi(t_b)$ to make the difference zero. In this case, the expression (4) provides a constant to cause no change in the output of the PD. If the level of the signal reproduced from $|\phi(t_a) - \phi(t_b) - \pi|$ is smaller than a noise level, it is impossible to detect the signal. To secure the level of the reproduced signal so that the signal is detectable, $|\phi(t_a) - \phi(t_b) - \pi|$ must sufficiently be large. For this purpose, an optical delay unit is installed at the midpoint of the loop as shown in Fig. 11. The delay unit is made of a drum of an optical fiber whose length is dependent on the properties of the apparatus. The delay unit secures a sufficient

time difference of " $t_a - t_b$ " so that the reproduced signal based on the output of the PD is surely detectable.

3.2 Principle of Signal Transmission.

The basic configuration of a master unit and a local unit are shown in Fig.5 and Fig.6 respectively. The master unit consists of a LD, a PD and a 3dB optical fiber coupler. The local unit consists of a vibrator, which gives vibration on the optical fiber and a PD with a fiber-bending device for local detection. A voice signal of master unit is converted to optical signal by LD and detected by PD in the local unit with local detection technique.

On the other hand, the voice signal transmission from the local unit to the master unit is achieved by the principle described above. The vibrator in the local unit makes phase shift modulation to the both lights from two optical ports of the master unit. PD in the master unit detects the voice signal as a result of the interference between the two lights.

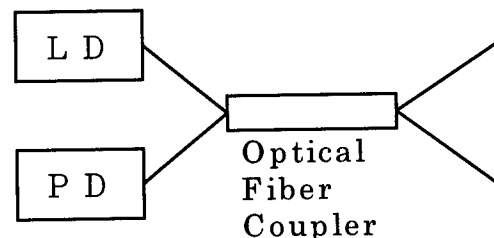


Fig.5 Basic Configuration of Master Unit

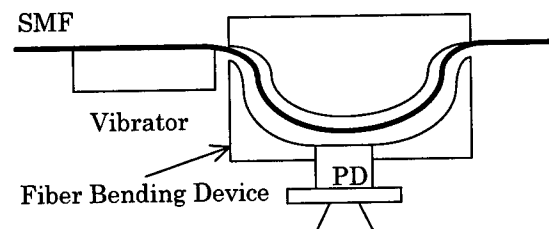


Fig.6 Basic Configuration of Local Unit

4. Design of Talk Set

4.1 Master Unit

Figure 7 shows the block diagram of the master unit. The light emitting device is a highly coherent DFB (Distribution Feed Back) laser diode to emphasize an effect of interference. We adopt 1.55 μm wavelength for lowest optical fiber transmission loss and efficient local detection. An optical isolator inserted between LD and optical fiber coupler avoids an influence the back reflected light to LD. The transmitter circuit consists of a LD driver, a FM (Frequency Modulation) modulator, and a microphone. The receiver circuit consists of a pre-amplifier, an ALC (Auto Level Control) circuit, a voice range LPF (Low Pass Filter) and an earphone. The reason why we use FM in the master unit is to distinguish between the signal from the master unit and those from the local units, because PD also detects the signal from master unit in the master unit at the same time. We adopt a pulse FM to simplify the LD driver circuit. These pulses are also used in ALC circuit in the local unit. To remove the influence of light polarization change, polarization diversity technique is useful. The outside view of the master unit is shown in Fig. 8.

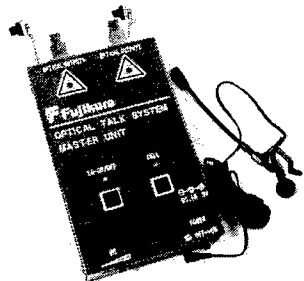


Fig. 8 Outside View of Master Unit

4.2 Local Unit

Figure 9 shows the block diagram of the local unit. An audio speaker is used as a vibrator. A vibration of the speaker diaphragm is directly given on the optical fiber. A large diameter PD and a fiber-bending device realize local detection function, the bending diameter is large enough not to damage the optical fiber. The transmitter circuit consists of only a microphone and a vibrator driver. The receiver circuit consists of a pre-amplifier, an ALC circuit, a FM demodulator and an earphone. The outside view of the local unit is shown in Fig. 10.

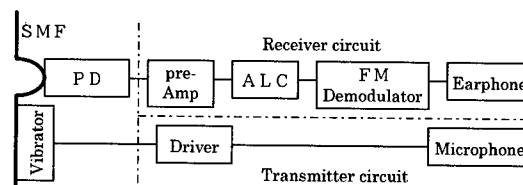


Fig. 9 Block Diagram of Local Unit

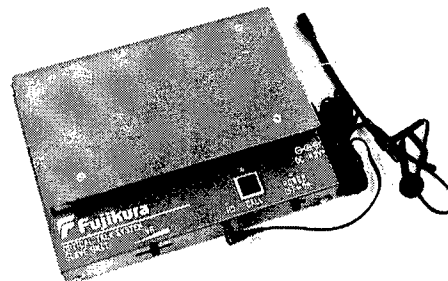


Fig. 10 Outside View of Local Unit

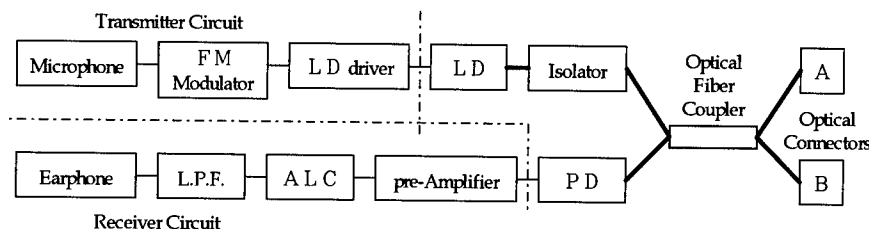


Fig. 7 Block Diagram of Master Unit

4.3 Optical Delay Line

An optical delay line shown in Fig 11 is used to give a certain amount of time difference between two lights in case of necessity.

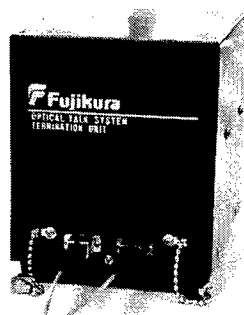


Fig.11 Outside view of Optical Delay Line

5. Performance

5.1 Experimental Configuration

Figure 12 shows the experimental configuration. Two optical connectors of a master unit are connected by two 20km long 4-fiber ribbons and a 2km long optical delay line. All optical fibers are the standard single mode fibers. A local unit is installed at the point ① and the point ②. We evaluate a received signal waveform at the master unit and S/N (Signal to Noise ratio) at both the master and local unit.

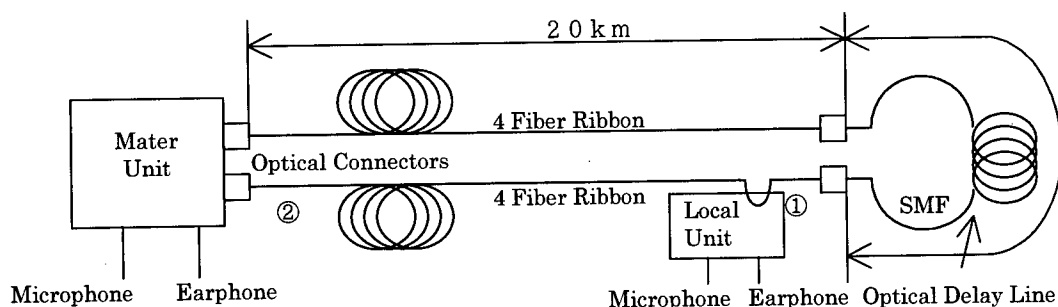
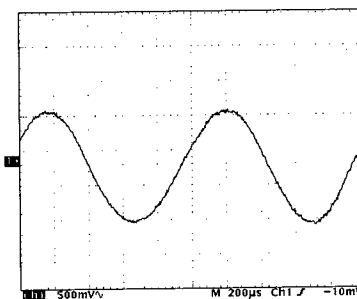


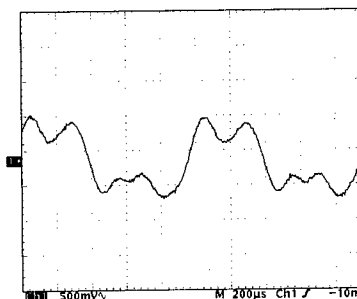
Fig. 12 Experimental Configuration

5.2 Waveform detected at Mater Unit

Figure 13 shows the received wave forms at the phase shifted at the point ① and ②. The time difference between two lights is the smallest at point ① and the largest at the point ②. We can observe the phase shift of more than $\pi/2$ in the wave form at the point ②. This indicates that the local unit can give enough phase shift difference to the two lights through the coating of the 4-fiber ribbon.



Wave form at point ①



Wave form at point ②

Fig.13 Configuration of Wave Forms

5.3 S/N Performance

Figure 14 shows the measurement results of received signal S/N both at the master unit and the local unit.

At the signal frequency of 1kHz, The S/N is 35.2dB at the local unit and 29.9dB at the master unit. This shows that the prototype system has the enough capability to practical use of a voice communication system.

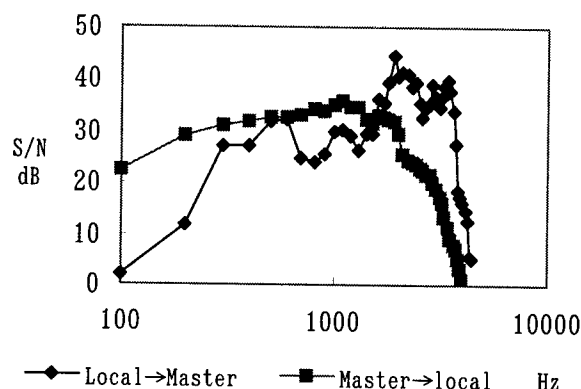


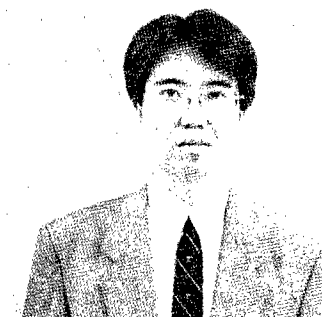
Fig.14 Characteristic of S/N

6. Conclusion

We have designed an optical talk set with a new external modulation method and found the fiber ring interferometer is useful for such a kind of communication system. This time, experimental results are optical received waveform and S/N. We are going to continue to another experiment. Finally, we are grateful to all the parties concerned for their helpful suggestions and encouragement.

7. Reference

- (1) M.Shimizu et al, :Identification Method for Optical Fiber Transmission Operation Lines with Local-Light Injection and Detection, 39th, IWCS, 1990
- (2) Y.Unami et al, :Wide Dynamic Range Optical Talk System Using External Loss Modulation, 41st, IWCS, 1992
- (3) Y.Azuma et al, :Non-destructive Optical Fiber Amplitude Modulator for Optical Talk System over 80km, 41st, IWCS, 1992
- (4) A.Fujisaki et al, :Optical Talk Set and Optical Cable Identifier using Polarized-Wave-External-Modulation Method, 39th, IWCS, 1990
- (5) T.Takashima et al, :Development of Optical Talk Set with Fiber Ring Interferometer, National Convention of IECE of Japan, B-10-95, Spring 1999



Yasushi Nakamura
Fujikura Ltd.
Mutsuzaki, Sakura-shi
Chiba-ken, 285-8850
Japan

Yasushi Nakamura was born in 1961. He joined Fujikura Ltd. after his graduation from Tokyo Electric University with B.E. degree in 1983 and has been engaged in research and development of optical systems. He is now an engineer of optical equipment group.

STRAIN DISTRIBUTION MEASUREMENT IN BENT OPTICAL CABLES USING A FIBER RIBBON WITH MULTI-POINTED FIBER BRAGG GRATINGS

Takeshi Genji, Kazuo Imamura, Tadahiko Nakai, Yoshiyuki Imada
MITSUBISHI CABLE INDUSTRIES,LTD., Itami, Hyogo, Japan

ABSTRACT

Strain distribution along an optical fiber inside a cable were optically measured by placing Fiber Bragg Gratings (FBG) of different reflecting wavelengths on the fiber. As a method for controlling the reflecting wavelength of each grating, different tension was applied to the fiber during UV exposure. We controlled the Bragg wavelength for 17nm (approx. 1.4% tension) with a single mask. Gratings were fabricated at regular intervals on a fiber for a slot type optical-fiber cable. The strain distribution induced by bending the cable was observed. Distribution measurements in a spatial resolution of 50mm, strain measurement accuracy of 0.002% was possible. We confirmed a strain distribution responding in accordance to the structure of the slot type cable. The fiber has the mechanical strength of normal fibers as the FBGs are made by UV exposed over the coating. The fibers can be used in the cabling process and also in traction and laying.

INTRODUCTION

The generally used method to measure the strain on optical fibers inside cables is observation of scattering light which involves the B-OTDR (Brillouin Optical Time Domain Reflectmeter). The measurement accuracy is approximately 0.015% and has a spatial resolution of more than 10 meters. However, with this method the strain distribution of fibers caused by the figure of its containment, such as fibers stranded in a 500mm pitch cannot be measured nor its maximum value be evaluated. If FBGs are made on optical fibers of cables, strain distribution along the fiber can be observed optically from the reflected light by spatial resolution of the grating spacing.

In this paper we introduce a sensor fiber having multiple high-strength FBGs fabricated by UV

exposure from over the coating. By observing the reflected light from a sensor fiber placed in a cable, strain distribution was measured. The sensor fiber with multi wavelength FBGs is obtained by controlling the reflecting wavelength using the fiber elasticity. Usually many phase masks for each wavelength are necessary to make FBGs with varied reflecting wavelengths. However, by applying tension to the fiber during UV exposure through a phase mask, various wavelengths can be produced with a single mask by controlling the tension.

FABRICATION OF THE SENSOR FIBER

The reflecting wavelength of the FBG changes linearly according to the amount of strain applied to the fiber. By placing FBGs with different reflecting wavelengths on a single fiber, we can observe on real-time operation, the amount of strain and its direction applied on the fiber by the spatial resolution of the FBG intervals. In order to have as many sensor points as possible, the grating intervals must be short and as many gratings as possible must be placed in the measuring wavelength region. Therefore it is necessary to make the wavelength of the FBG short and accurate. To fabricate a continuous line of FBG without flaw and have sufficient mechanical strength, it is necessary to increase the mechanical reliability of each FBGs from the fabrication process.

The Fiber

The parameters of the fibers we used for our experiment is shown in Table 1. The core of the fibers were codoped with germanium and tin to enhance the photosensitivity under UV exposure. We used an UV-transparent coating which had a larger transparency rate of UV light (for fabricating FG) (266nm) than regularly used coatings. FBGs were fabricated by exposure

above the coating, without removing the coating.^{1,2,3,4,5} The test fibers were put under pressure of approximately 20MPa of hydrogen loading for two weeks before the fabrication.

Table 1: Parameters of tin-codoped germanosilicate fibers

Relative index difference Δ , %	0.97
Sn concentration, ppm	15000
Al concentration, ppm	900
Mode field diameter, μm	5.55
Cutoff wavelength, μm	1.27
Cladding diameter, μm	125
Coating diameter, μm	200

Fabrication of the gratings

The light source for fabricating the gratings was coherent UV light at wavelength 266nm which is the fourth harmonic of Nd-YAG laser. The grating fabrication system is shown in Figure 1. FBGs were fabricated by exposing the fiber under a sweep light through a phase mask with the grating portion strained. UV exposure is made without removing the coating. With this method a very strong FBG is made as there is no damage on the fibers caused by coating removal. We used an SLD light source and a spectrum analyzer, connected to the fiber via 3dB coupler. The reflected wavelength during fabrication was observed. The reflecting wavelength was controlled by the amount of tension applied to FBGs during UV exposure. Figure 2 shows the tension control and exposure system. The fiber is fixed to the drums at either end, then tension is applied by winding a drum rotated by a stepping motor. At this shape, the FBG is fabricated by exposure of UV light sweeping over the phase mask. The tension can be controlled by changing the rotation angle of the drum. On a single fiber, we changed the tension to have FBGs of 20 different levels of reflecting wavelength at 50mm intervals which was made continuously with a single mask (without changing the mask).

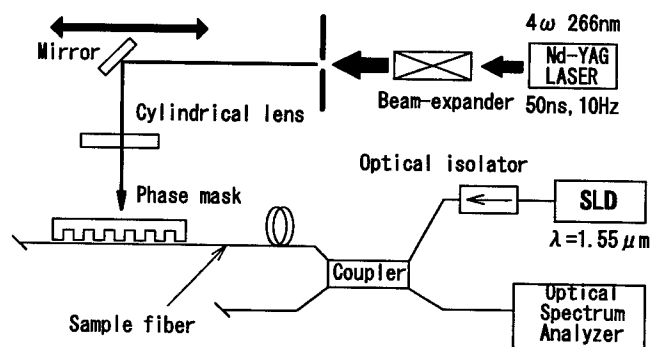


Fig.1 Structure of fiber grating fabrication system

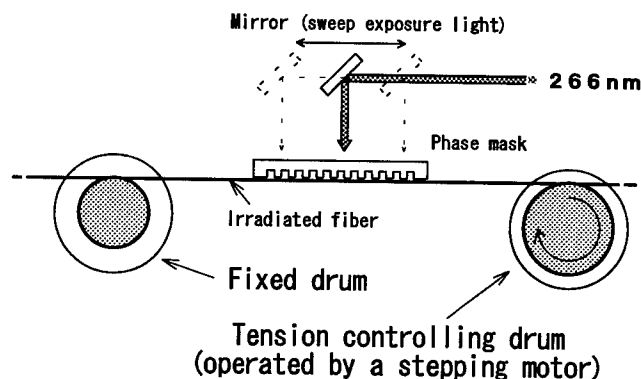


Fig.2 Tension control and exposure system

Control of reflecting wavelength by applying tension during UV exposure

Figure 3 shows the reflected spectrum of the strain sensing fiber. 20 FBGs were placed on a single fiber with about 0.82nm intervals of wavelengths.

Figure 4 shows the reflection wavelength of each FBGs during fabrication and after release. We can see that, the reflecting wavelength shortening at tension release can be linearly controlled by the elongation of the fiber during UV exposure. We can also see that the reflection wavelength is shortened due to decrease of the refractive index from the tension applied to the fiber core. A maximum of approximately 1.4% of fiber elongation shortened the wavelength approximately 17nm. It would be impossible to apply such a large tension on fibers made in the usual method which involves stripping of the coating. Figure 5 shows the change in wavelength at

tension release via the reflected wavelength during fabrication (applying tension) which is index of the tension on fibers. A better linearity can be seen, compared to the wavelength shortening characteristic against the elongation obtained from the rotation amount. If the tension is controlled accurately, a highly accurate wavelength control is possible.

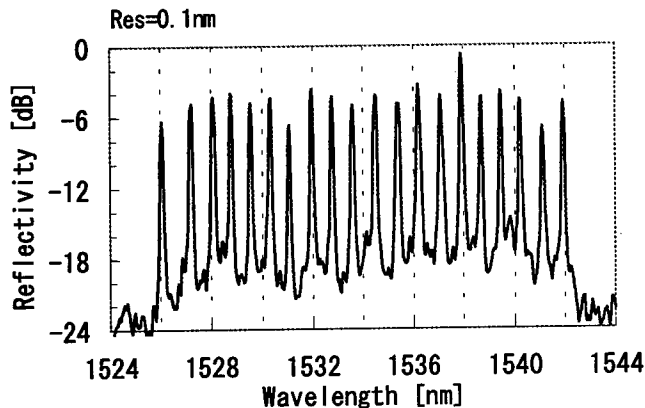


Fig.3 Reflection spectrum of strain sensing fiber.

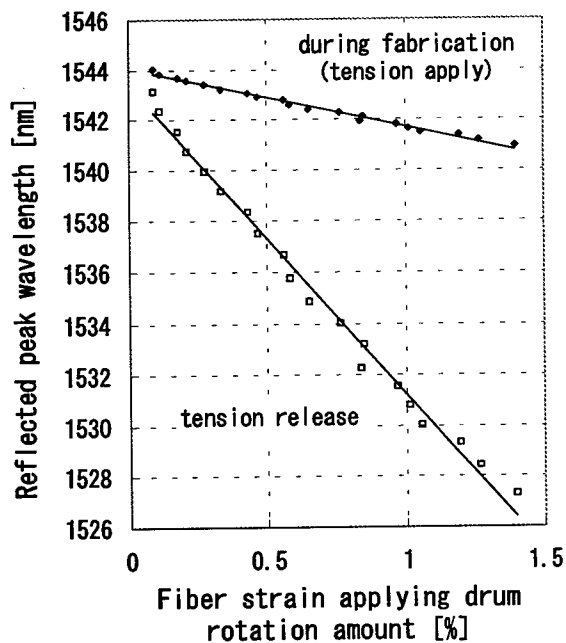


Fig.4 Drum rotation amount vs. FBG reflection wavelength

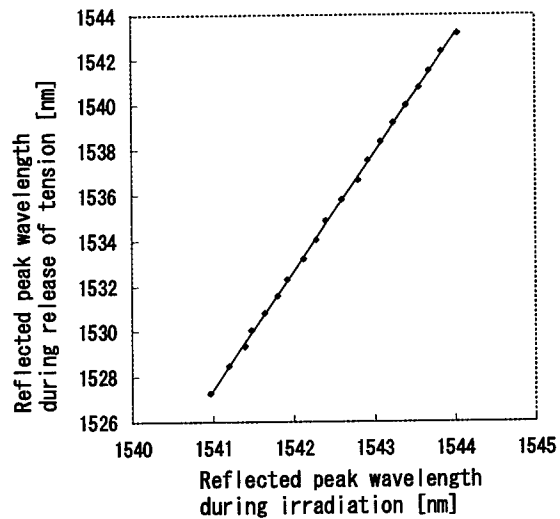


Fig.5 Wavelength during fabrication vs. wavelength during release

MEASUREMENTS OF STRAIN DISTRIBUTION INSIDE THE CABLE

Mounting the sensor fiber

The sensing fibers were placed together with normal communication fibers and made into a four-core ribbon. The fiber ribbon was placed into an optical cable having an outer diameter of 13mm and a slot pitch of 500mm with other fiber ribbons (Figure 6). Normal communication fibers were used for the three remaining cores besides the sensing fiber and the four tapes placed in the lower layer of the slot. The slot carried five tapes including the fiber sensor tape.

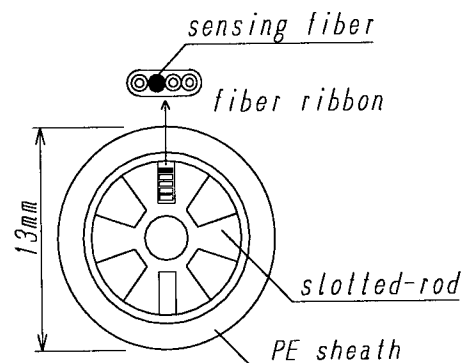


Fig.6 Sensor fiber in cables

Strain distribution measurement in bent cables

We bent the cable mounted with a sensor fiber ribbon, and strain distribution in the inner fiber caused by cable bending were measured. As shown in Figure 7, the sensor fiber is connected to the reflected wavelength measuring system. Then the reflected wavelength of straightened cables and bent at a radius of R were measured. The difference of the reflected peak wavelength from their respective FBGs was calculated.

Figure 8 shows the results of the measurements for Z-grooved slot-type cable. From previous experimental results, the tension applied to the FBG and the reflected wavelength variation is obtained as factor $1.34[\text{nm/N}]$ ($11.83[\text{nm}/\%]$) and used to mark the right side tension axial. Repetition of tensile and compression direction strain in the slot pitch generated a strain deviation caused by the cable shape was observed. The strain sensing accuracy for both directions were approximately 0.002%.

Figure 9 shows the results of the measurements for SZ-grooved slot-type cable. The experiment cable has an outer diameter 14mm, SZ-pitch of 320mm and reversing angle of 270° . For bending the cable, three different groove locations were considered that groove locus is outside of cable bent, inside of cable bent, and side of cable bent. We could confirm the difference of strain distributions in bending direction.

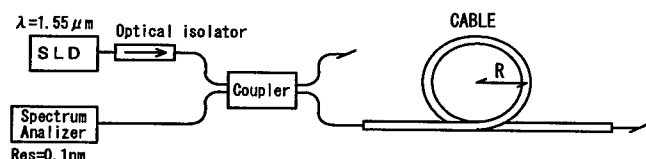


Fig.7 Inner cable stress measurement by reflected light observation

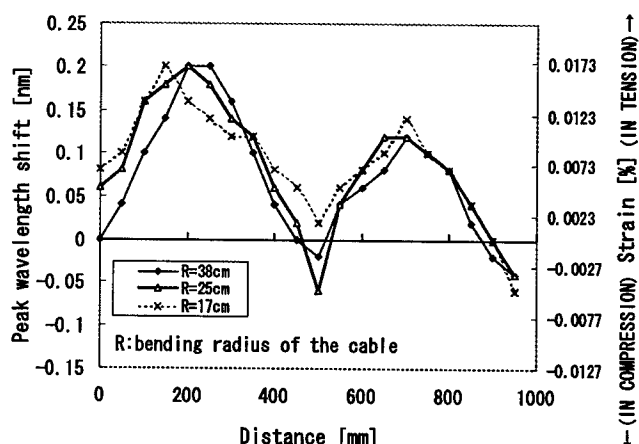


Fig.8 Strain distributions along the fiber in a bent optical cable. (Z-groove type)

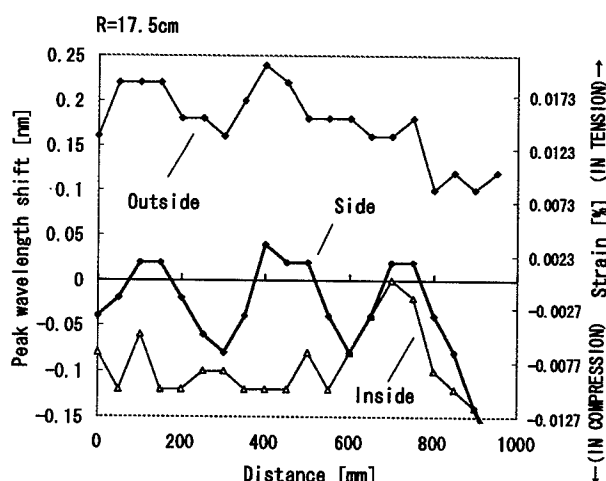


Fig.9 Strain distributions along the fiber in a bent optical cable. (SZ-groove type)

CONCLUSION

A strain sensing fiber made by 20 wavelengths of FBG was fabricated to measure the strain distribution inside optical cables. By controlling the tension, a multi point strain sensing fiber with 20 FBGs of 0.82nm of different reflecting wavelengths was fabricated by using only a single mask.

The fabricated fiber was placed in a slot type optical cable to measure inner cable strain

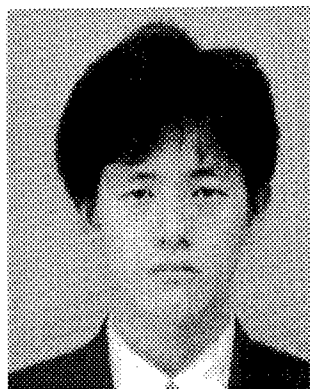
distribution. Strain deviation induced by cable bending was observed in stranded type cables in accordance with the shape of the cable. We succeeded in measuring strain at a spatial resolution of 50mm by a simple observation of the reflected optical spectrum.

The strain sensing fiber has the same mechanical strength as normal communication fibers. It can be used in the cabling process, cable traction and laying. The method can be also applied to normal communication fibers without having to install a special fiber for sensing. If the sensor wavelength is adjusted to avoid general communication wavelengths, by irradiating the communication fiber from over the coating, strain can be monitored during ordinary communication.

REFERENCES

1. L.DONG,et al., "Enhanced photosensitivity in Tin-codoped germanosilicate optical fibers", IEEE photonics Technol.Lett., 1995, vol.7, pp.1048-1050.
2. R.P.ESPINDORA,et al., "Fiber Bragg gratings written through a fiber coating", OFC'97 Tech.Dig., 1997, Postdeadline paper PD-4.
3. D.A.SIMOFF,et al., "Coatings having enhanced UV transparency", IWCS'97, Track1, Session2-7, 1997, pp.86-93
4. K.IMAMURA,et al., "Mechanical strength characteristics of tin-codoped germanosilicate fiber Bragg gratings by writing through UV-transparent coating", Electron.Lett., 1998, vol.34, pp.1016-1017.
5. T.NAKAI,et al., "Characteristics of tin-codoped germanosilicate fiber Bragg gratings written through an UV-transparent coating", IWCS'98, Track2, Session20-5, 1998, pp.938-943.

SPEAKER BIOGRAPHY



Takeshi Genji
Mitsubishi Cable Industries, Ltd.
4-3, Ikejiri, Itami, Hyogo, 664-0027, Japan

Mr.Genji, research engineer of Electronics & Communication Research Lab., is engaged in design and development of optical communication components. He received his M.S. degree in Electrical Engineering from Kyoto Institute of Technology in 1994. He is a member of the Japan Society of Applied Physics.

INVESTIGATION OF 1625 NM LOSS PERFORMANCE OF FIBREOPTIC CABLES INTENDED FOR USE AT 1550 NM

Svend Hopland

Telenor Nett AS, Oslo, NORWAY

INTRODUCTION

During the last 10-12 years, nearly all of the installed fibre optic cables have been specified and intended for use at 1550 nm. At this wavelength, the cable properties have been extensively measured and well documented in type tests as well as in field investigations.

Recently, the WDM-technology has put forward the need for a significant extension of the 1550 nm wavelength window. One is presently discussing the use of wavelengths of up to 1625 nm for signal transmission. An important issue is therefore to investigate the possibility of using these wavelengths in the existing cable network.

It is well known that induced losses in cabled fibres due to phenomena such as macro- and microbending, as well as molecular hydrogen, increase with increasing wavelength. Induced losses may be caused by environmental factors such as temperature, crush and tension on the cable, or hydrogen evolution in the cable. In addition, the bending of fibres in splice boxes could result in extra losses.

Since the current cable specifications are valid for 1550 nm transmission, we can not rely on satisfactory transmission at 1625 nm.

In this work we have performed extensive field measurements on different cable types such as duct-, aerial-, and underwater cables, installed during the last 10-12 years. We have measured fibre attenuation at 1550 nm and 1625 nm, and present comprehensive loss data at these wavelengths. The results are evaluated and discussed.

In addition we have performed laboratory cable tests such as temperature-, tension-, and crush tests on cable samples representative for our installed cables. All attenuation increases are measured at 1550 nm and 1625 nm. The results are evaluated and discussed.

HISTORY

Cable types and fibre types

Since 1986, our fibre cable core consists of fibres in stranded loose tubes or fibres in a slotted core construction.

The basic fibre cable core elements are surrounded by different kinds of protection and tension members to form the different cable types such as duct-, directly buried, aerial- and underwater cables.

The fibre type has been standard G652-fibre throughout the entire period.

Installed cables

Before 1988, Telenor installed small amounts of fibre cables specified for use in the 1310 nm window. We have tested and field measured these cables. The transmission properties at 1625 nm and 1550 nm are questionable, which have been shown in the measurement results.

In the period 1986-1991, Telenor installed underwater cables with no hydrogen barrier along the coastline as well as in the lakes. These cables included single or double layers of armour wires. We have in earlier work¹ shown that the hydrogen-induced losses in these cables have stabilised after several years at a level of maximum 0.03-0.04 dB/km at 1550 nm for the

double armoured cables. This work presents the hydrogen-induced losses at 1625 nm.

Since 1992, hydrogen barriers, which have proven to be 100 % effective, were included in all our underwater cables.

Our directly buried cables include thin armour, which normally should not give any measurable additional loss due to hydrogen. These cables are also investigated.

Since 1988 and up to 1998, Telenor has basically installed cables from two manufacturers. The cables are specified for 1550 nm use. Moreover, there have been no significant changes in the cable constructions during the 1990's.

In 1999, Telenor is installing cables from other cable manufactures.

MEASUREMENTS

Equipment and method

In the field measurements, as well as during cable testing, we have used a dual wavelength OTDR operating at 1550 nm and 1625 nm.

The individual lengths of our land cables are typically 1500-4000 m and underwater cables are usually longer than 5000 m. In the field, we have generally selected cable lengths greater than 1500 m in order to obtain high measurement accuracy.

For the same reason, the optical measurements of distributed loss increases during cable testing have been performed on fibre loops with total length of more than 500 m.

All splice losses are calculated from two-way OTDR-measurements.

FIELD MEASUREMENTS

Fibre attenuation in cables on drum

In order to establish a level for comparison with installed cables, we measured several cable lengths on drum. The cables and the fibres were

manufactured in 1999. The fibres were produced by the OCVD-method, similar to more than 95 % of the fibres in our cable network. The results are shown in Figure 1.

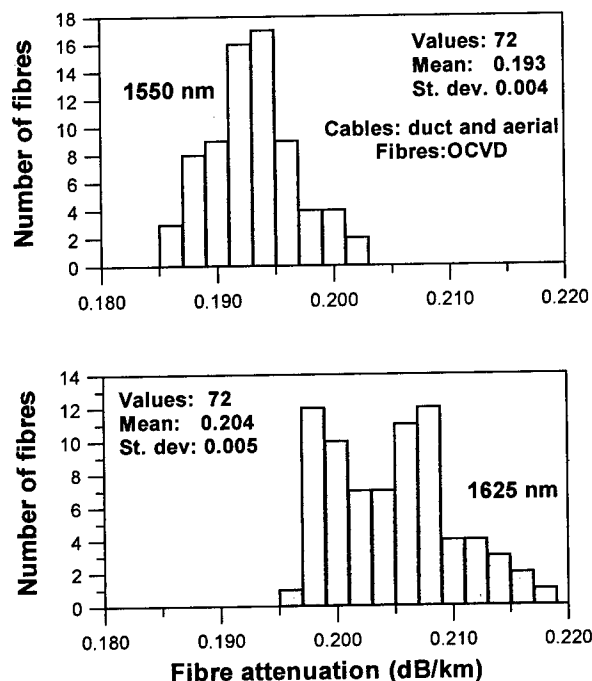


Figure 1: Attenuation distributions in cables at 1550 nm and 1625 nm, measured on drum.

We note that the average attenuation value at 1625 nm is 0.011 dB/km greater than at 1550 nm. This is due to the intrinsic fibre loss, which increases with increasing wavelength above 1550 nm.

Fibre attenuation and splice loss in new installations

In order to establish a reference level for comparison with older installed cables, we measured fibre and splice loss distributions for recently installed cables. The cables were manufactured and installed in 1999, and spliced together by a team from Telenor Installation Department.

The results are shown in Figure 2 for the attenuation distributions, and in Figure 3 for the splice loss distributions.

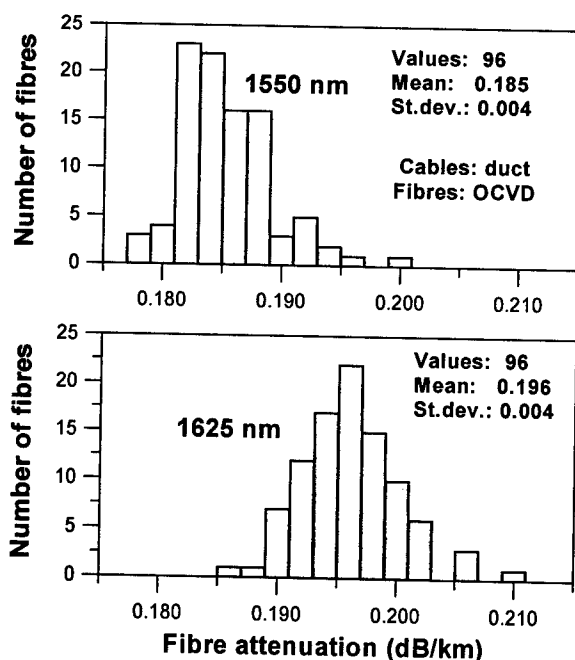


Figure 2: Attenuation distributions at 1550 nm and 1625 nm for duct cables installed 1999.

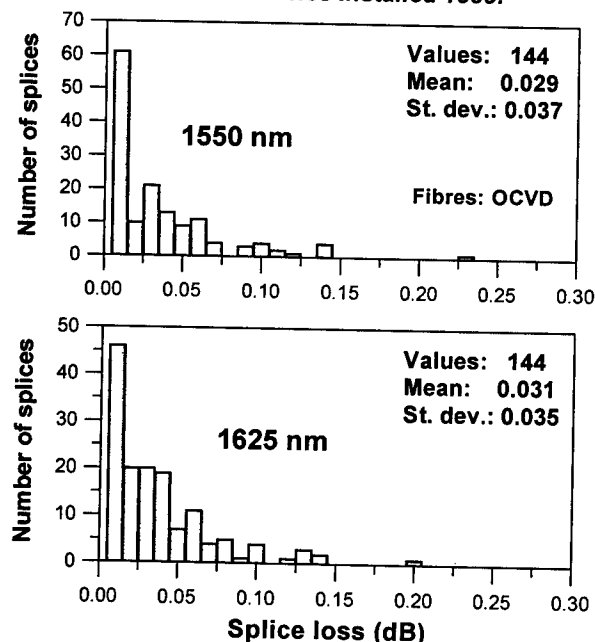


Figure 3: Splice loss distributions at 1550 nm and 1625 nm for cables installed 1999.

We note here that the average values of the attenuation has decreased with 0.008 dB/km at 1550 nm and 1625 nm, compared with the measurements made on drum. The fibres experience obviously some small extra bending

loss when the cable is wound on drums with bending diameter of 1.0 -1.5 meters.

The increase in attenuation at 1625 nm is still 0.011 dB/km compared with 1550 nm, which is equal to the drum measurements.

The splice loss distributions are almost equal at 1550 nm and 1625 nm, and exhibit very low average values of approximately 0.03 dB at both wavelengths. This indicates that the current fibres, splicing machines and splice box fibre arrangements will generally not cause splice loss increases at 1625 nm.

Splice loss in old installations

We have also measured splice losses in older cable network. In Figure 4 and Figure 5 are shown splice loss distributions in cable network installed in 1996 and 1987, respectively.

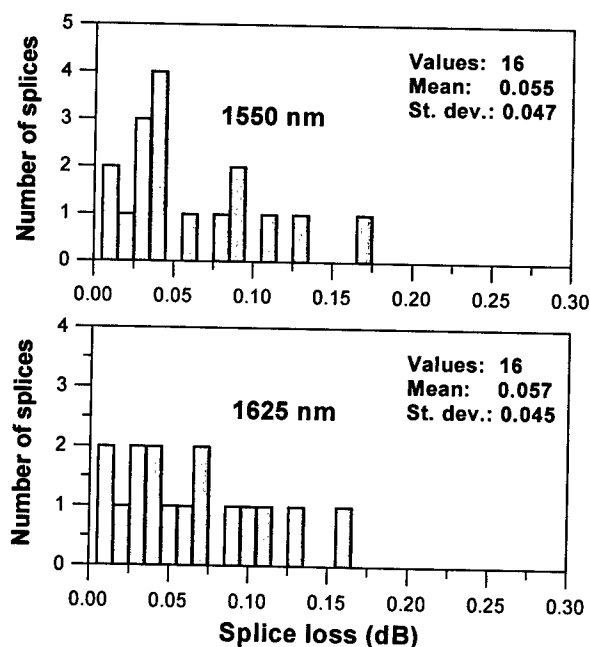


Figure 4: Splice loss distributions at 1550 nm and 1625 nm for 1996- installation

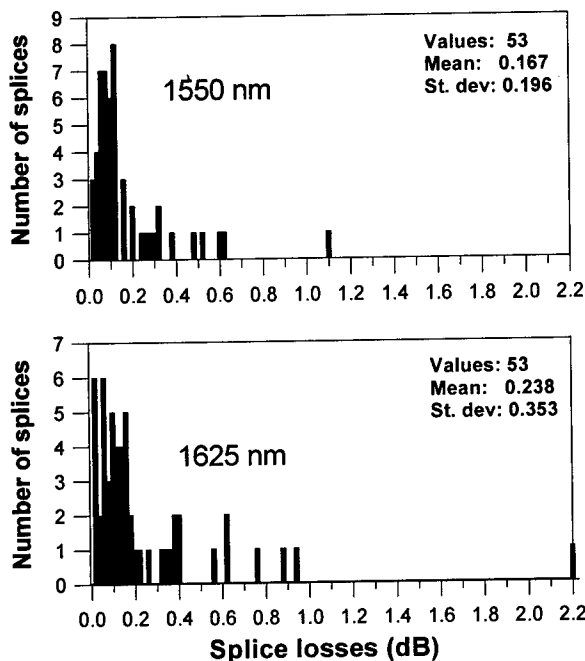


Figure 5: Splice loss distributions at 1550 nm and 1625 nm for 1987-installation

It is clearly shown that the average splice loss at both wavelengths increases with increasing age of the installation. We believe that this is due to the development of better fibres, splicing equipment and splice boxes during the last 10-12 years.

However, the differences in splice loss distributions at 1625 nm and 1550 nm, are marginal, except for the 1987-installation. In this case, the splice loss distributions could probably be improved by resplicing fibres and changing splice boxes.

The results show that splice losses at 1625 nm are nearly equal to splice losses at 1550 nm, even in the oldest installations.

Fibre attenuation in old installations

Non-armoured cables

Our non-armoured cables are duct and aerial cables, which constitute a major part of our network.

We have measured a significant number of individual cable lengths of each cable type in different parts of the network installed in the

period 1988-90, with a corresponding high number of individual fibres.

In Figure 6 are shown the average attenuation values at 1550 nm and 1625 nm, including the measurements from the recently installed cables:

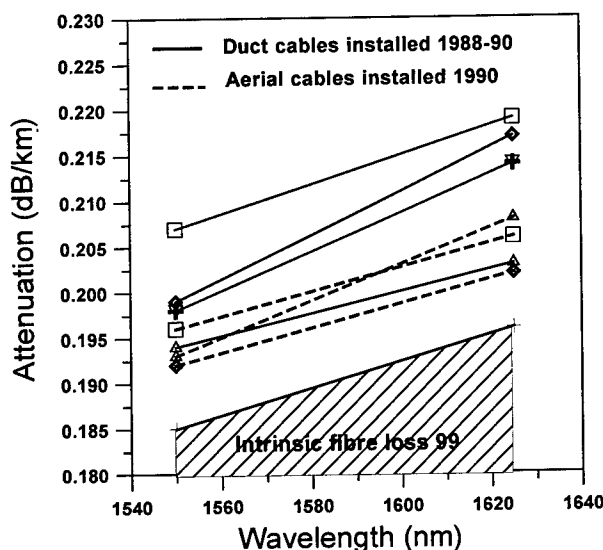


Figure 6: Mean attenuation at 1550 nm and 1625 nm in duct and aerial cables installed 1988-90

We observe that all loss values at both wavelengths are somewhat higher than the values measured in the recently installed cables. In addition, we note that the duct cable loss values are on average a little higher than the aerial cable loss values at both wavelengths.

Armoured cables

Our armoured cables are underwater cables comprising basically three types of armour, which are light single armour, normal single armour and double armour, in lakes and in the sea environment, respectively. Up to 1991 our underwater cables included no hydrogen barrier.

In Figure 7 are shown the measured mean values at 1550 nm and 1625 nm for a number of cables in each armour category. The cables were installed in the period 1987-1990. The measurements from the recently installed cables are also included.

We have earlier shown¹ that the added losses in our armoured cables are caused by hydrogen. We can deduce from Figure 7 that the hydrogen

induced losses at 1625 nm are in the range 0.03 - 0.11 dB/km, depending on the type of armour.

These values imply that the hydrogen-induced losses at 1625 nm are 2-3 times greater than the hydrogen induced losses at 1550 nm¹.

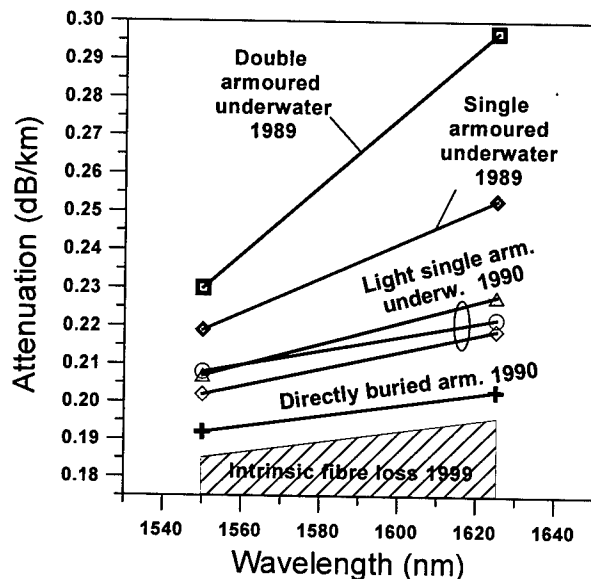


Figure 7: Mean attenuation at 1550 nm and 1625 nm in armoured cables installed 1987-90.

Attenuation values of 0.22-0.30 dB/km in armoured cables at 1625 nm will generally not influence greatly the loss budget, since the amount of underwater cable in a typical link from the relevant time period is less than 50 %.

Our directly buried cables have included a thin layer of armour, which is normally covered by a filling compound. It is evident from Figure 7 that the hydrogen level is insignificant

However, a small amount of directly buried cables with dry armour were installed before 1990. In this case, humidity has direct access to the armour wires, and a strong hydrogen reaction occurs, which may cause attenuation increases even with thin armour.

In Figure 8 is shown the measured attenuation in a few directly buried cables with dry armour installed 1990.

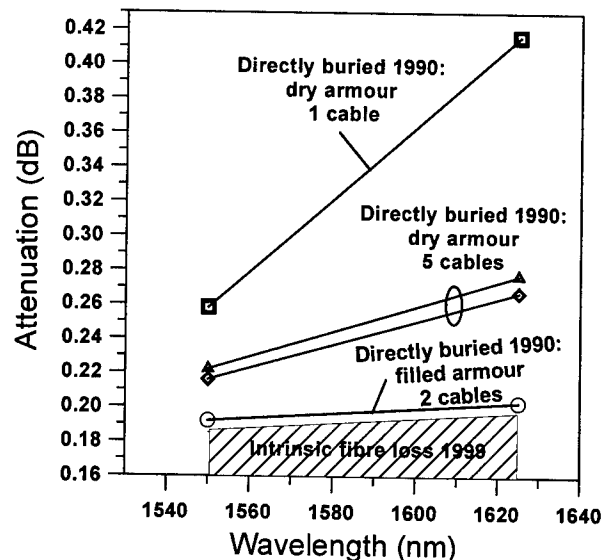


Figure 8: Mean attenuation at 1550 nm and 1625 nm in dry armour buried cables installed 1990

We observe that the measured hydrogen levels in these cables are similar to underwater cables, and in one case even higher.

CABLE TESTS

Investigating the attenuation level in installed cables does not give the full overview of possible loss increases in the cables. In order to reveal the extreme behaviour of our cables at 1625 nm, we performed temperature test, tension test and crush test on a selection of cable samples.

We selected the following samples:

- Duct cable A: specified for 1310 nm
- Duct cable B: loose tube specified for 1550 nm
- Duct cable C: slotted core specified for 1550 nm

Cables B and C are representative for the majority of our installed duct cables during the 1990's.

Tension test

The cables were tested well above the limit for fibre elongation in order to investigate the attenuation increases at 1550 nm and 1625 nm.

In Figure 9 and Figure 10 are shown the results for cable B and cable C.

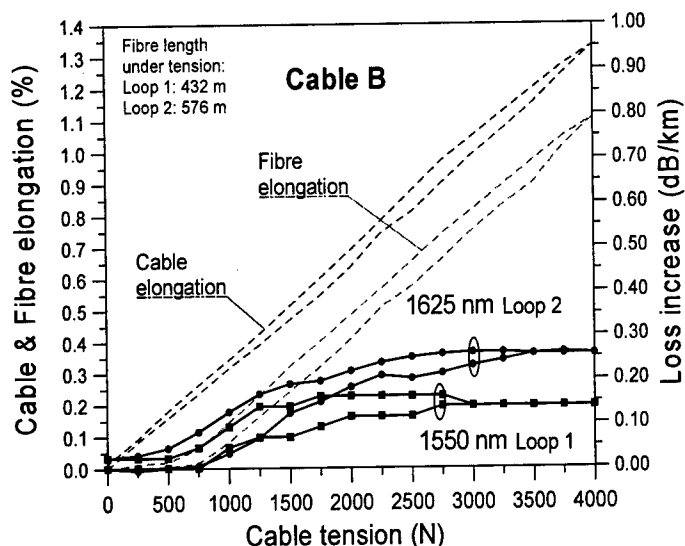


Figure 9: Tension test on loose tube duct cable B.

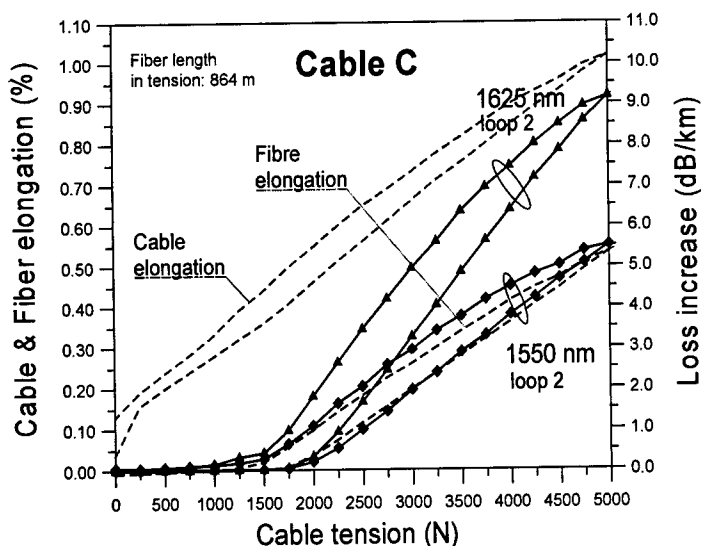


Figure 10: Tension test on slotted core duct cable.

Several features are evident from the results of the tension test. For both cables, the attenuation increase at 1625 nm is approximately 1.5-2.0 times the attenuation increase at 1550 nm, when the fibre is in tension. This is in accordance with

expected microbend induced loss when the fibres reach the inner wall of the slotted core or tube. Secondly, the attenuation increases at some fibre elongation level are much higher for Cable C than for Cable B. This is due to the different surface structures of the slotted core material and the tube material, resulting in different microbend loss characteristics.

If the test criteria states no fibre elongation at maximum tension, as in our case, then 1625-nm operation is ensured. If some attenuation at 1550 nm is allowed at maximum tension, then approximately double attenuation should be expected at 1625 nm.

Mandrel-plate crush test

The mandrel-plate crush test is very difficult for the cable to resist completely, and the attenuation increase, if any, may differ greatly from one crush to another.

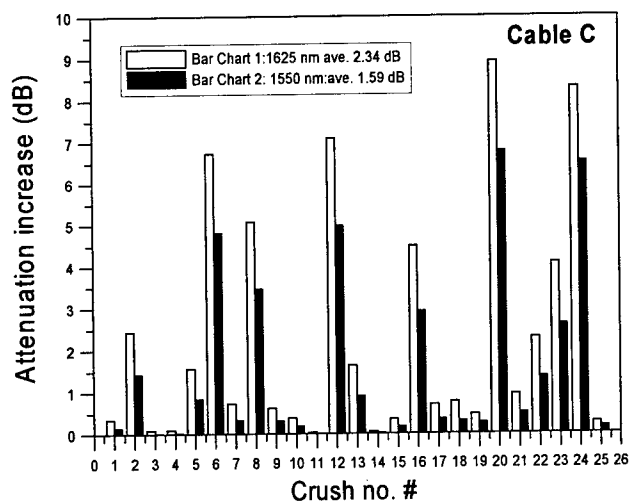


Figure 11: Mandrel-plate crush test on slotted core duct cable C.

The test results are of statistical nature, to which acceptance criteria are related. Usually, the magnitude of the loss increase is not included in the test criteria.

In Figure 11 and Figure 12 are shown the results for Cable C and Cable A.

We note that the attenuation increases at 1625 nm are on average 1.5-2.0 times greater than at 1550 nm, for slotted core cable C as well as for loose tube cable A.

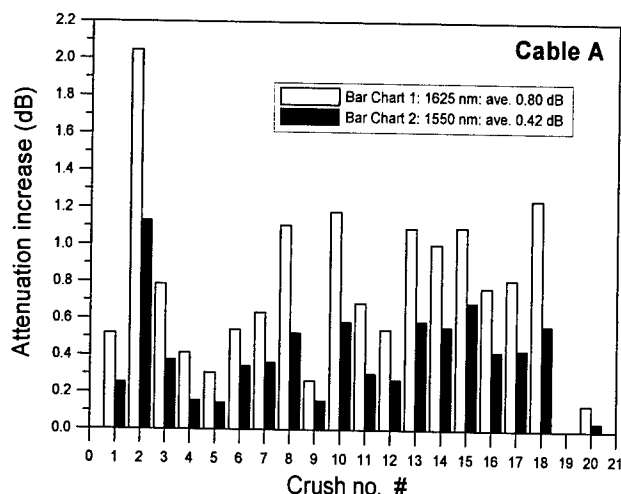


Figure 12: Mandrel-plate crush test on loose tube duct cable A.

However, it is not clear from these results if acceptance criteria with distinguish between the two wavelengths, and further study is required.

Temperature test

The temperature test is the most important test for our areas, where winter temperatures often can reach -40° Celsius. Hence, our acceptance criteria for temperature induced loss at 1550 nm is 0.1 dB/km at -40° Celsius.

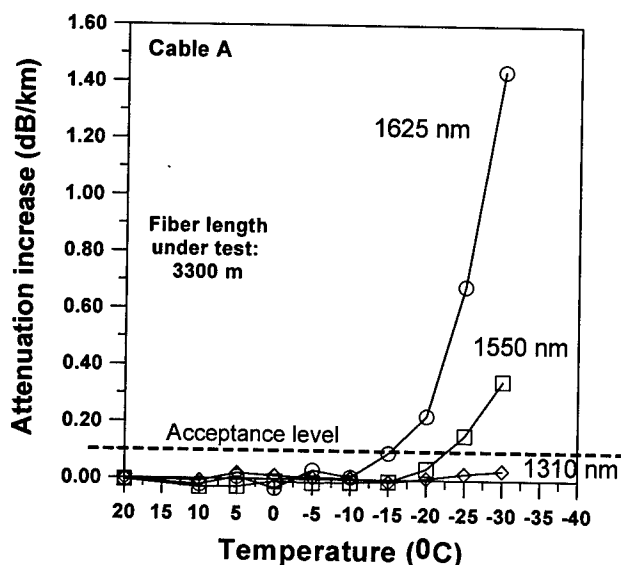


Figure 13: Temperature induced loss increases at 1310nm, 1550 nm and 1625 nm in cable A.

In Figure 13 are shown the temperature dependent attenuation increases for cable A at 1310 nm, 1550 nm and 1625 nm.

Cable A is specified only for 1310 nm transmission, and it is evident that it will work well down to below -30° Celsius at this wavelength. However, at this temperature, the attenuation increases at 1625 nm and 1550 nm, are far above the acceptance level. In fact, cable A will not work at 1625 nm at temperatures lower than approximately -15° Celsius.

We observe from Figure 13 that the temperature induced loss increase at 1625 nm is approximately 5 times the loss increase at 1550 nm, independent on temperature. We may assume that this ratio is characteristic for our fibre in tube/slotted core cable constructions.

In Figure 14 and Figure 15 are shown the temperature dependent loss increases at 1550 nm and 1625 nm for cable B and cable C, respectively.

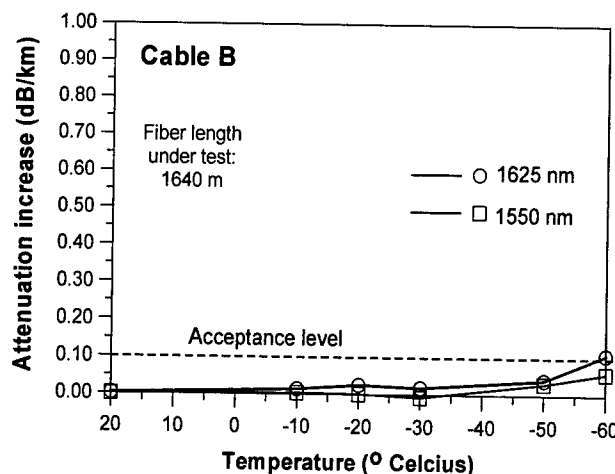


Figure 14: Temperature induced loss increases at 1550 nm and 1625 nm in cable B.

Here, the results are more encouraging. For cable B and cable C the temperature induced losses at 1625 nm are less than 0.1 dB/km even down to -50° Celsius and -60° Celsius for cable C and cable B, respectively.

These results show that our cable constructions have safe built in margins for 1550 nm operation, which in addition also are sufficient for 1625 nm operation.

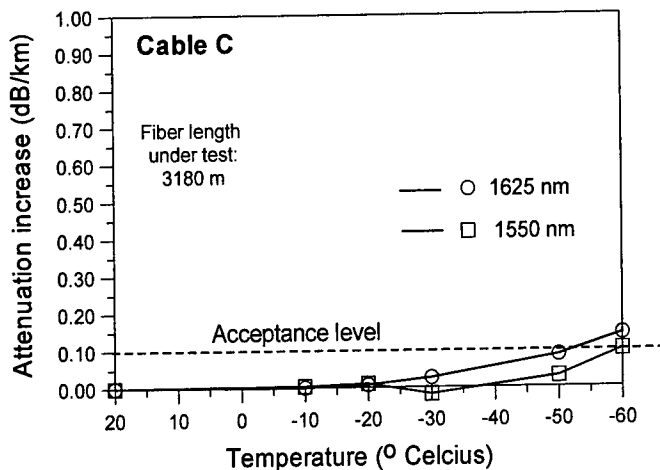


Figure 15: Temperature induced loss increases at 1550 nm and 1625 nm in cable C.

However, one can not rely on margins to ensure 1625 nm operation. Therefore, other or new cable constructions have to be tested separately in order to reveal the low temperature 1625 nm loss performance.

CONCLUSIONS

We have investigated the loss behaviour of our fibreoptic cables at 1625 nm wavelength. Extensive attenuation measurements have been performed on installed cables of different age. In addition, we have performed selected cable tests to reveal the 1625 nm loss performance of the cables at environmental extremes.

We have found that new fibres generally have 0.011 dB/km higher loss at 1625 nm than at 1550 nm, which can be attributed to the intrinsic fibre attenuation.

Measurements on new installations have shown that average attenuation values of 0.185 dB/km and 0.196 dB/km can be expected at 1550 nm and 1625 nm, respectively. In new installations, the average splice losses at both wavelengths were found to be well below 0.05 dB. Although the magnitude of the average splice losses are increasing in older installations, we have shown that splice losses at 1625 nm are nearly equal to splice losses at 1550 nm, even in the oldest installations.

Furthermore, we have found that the losses at 1625 nm and 1550 nm in duct and aerial cables in older installations are slightly higher than in new installations.

In armoured underwater cables without hydrogen barrier, in which the fibres are subjected to hydrogen ingress from the armour wires, we have measured the fibre attenuation at 1625 nm to be in the range 0.22-0.30 dB/km depending on different types of armour. This implies that the hydrogen-induced losses are approximately 0.03-0.11 dB/km, which is a factor of 2.5-3.0 times greater than the corresponding hydrogen induced losses at 1550 nm.

Considering the limited amount of this cable type being present in a typical link, such attenuation values should not have a great influence on the link loss budgets at 1625 nm

Tension tests have shown that the induced losses at 1625 nm when the fibre is tensioned are approximately a factor of 1.5-2.0 greater than at 1550 nm. This is however insignificant when the acceptance criteria requires no fibre elongation at maximum tension.

The mandrel-plate crush test have shown that attenuation increases at 1625 nm are 1.5-2.0 times greater than at 1550 nm, which will influence the test results statistics. However, further study is needed to clarify how acceptance criteria will distinguish between the two wavelengths.

Temperature test performed on cables specified only for 1310 nm operation, have shown that the temperature induced losses are approximately 5 times greater at 1625 nm than at 1550 nm. This cable type is not useable for 1625 nm operation at low temperatures.

However, temperature tests on our cables specified for 1550 nm operation, have shown that our acceptance criteria is fulfilled with good margins at 1625 nm as well as 1550 nm.

However, this is not valid for other cables specified for 1550 nm operation, since the built in margins to temperature induced loss at 1625 nm, are generally not known.

ACKNOWLEDGEMENT

The author greatly appreciate the hard work of Idar Gangø, Telenor Nett, who has performed the major part of the field measurements and cable tests with great skills. Also thanks to Knut Langeland, Telenor Nett, for his assistance during measurements.

REFERENCES

1. S. Hopland: "Long term behaviour of hydrogen induced loss in installed fibreoptic submarine and underwater cables": Proceedings IWCS 1997.



Svend Hopland

Telenor Nett AS ,
P. Box 6701 , St. Olavs Plass
0130 Oslo, NORWAY.

Office: Lysaker Torg 15,
Lysaker

Svend Hopland graduated from the Norwegian Institute of Technology in 1985 with a PhD. on optical fibres. In 1986 he joined Telenor and is presently a senior engineer on fibreoptic cables.

LOSS BEHAVIOUR OF OPTICAL FIBRE CABLE NETWORK FOR FUTURE WDM SYSTEMS

Eino Jauhiainen and Risto Pulliainen

Sonera Ltd., Helsinki, Finland

ABSTRACT

Most of the today's high capacity optical transmission systems operate at wavelengths around 1550 nm. System development suggestions have been made concerning the implementation of new wavelengths above the existing wavelength region. This paper will present the measurement results of Sonera's existing optical fibre cable network in view of the future optical systems.

INTRODUCTION

ITU-T SG15 standardises interfaces for optical transmission systems. Existing standards^{1,2} for SDH-systems (Synchronous Digital Hierarchy) and systems based on WDM (Wavelength Division Multiplexing) specify operating wavelengths within the conventional 1550 nm window. As more capacity is needed, further enhancements to extend the operating wavelengths up to 1625 nm are proposed.

Sonera Ltd (former Telecom Finland) has had optical fibre cables in successful operation since 1979. The total amount of optical cables in use is about 30 000 km. Sonera's long-distance network covers the whole Finland (Fig.1).

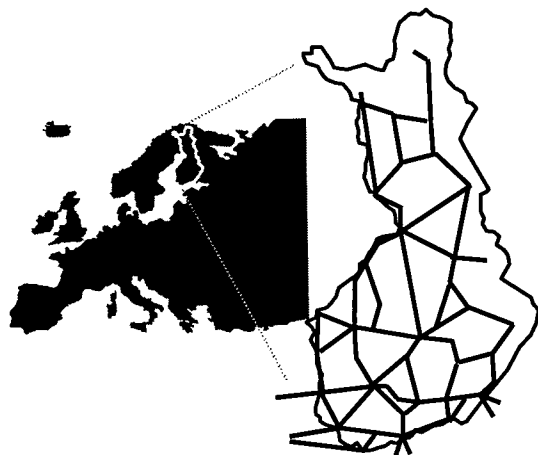


Fig. 1: Sonera's long-haul network

The network is based on SDH technology. Recently, systems also using WDM are taken into use.

Finland has been one of the "early adapters" of new technologies, like mobile phones and internet services. Thus, there is a huge demand for network capacity. Therefore, Sonera has studied the performance of the existing network for use of future optical transmission systems. This study was carried out in order to evaluate the ability of the existing single-mode optical fibre cable network to carry traffic at wavelengths longer than 1600 nm.

First single-mode optical fibre cables had performance requirements only at the 1310 nm region, and consideration was needed to evaluate their capability to carry traffic at 1550 nm. Today's attenuation performance is based on 1550 nm measurements. When operation is shifted towards longer wavelengths the performance of installed cables cannot be assured based on measurements only at 1550 nm, as long as further information on the spectral loss behaviour of fibres is not available (Fig.2).

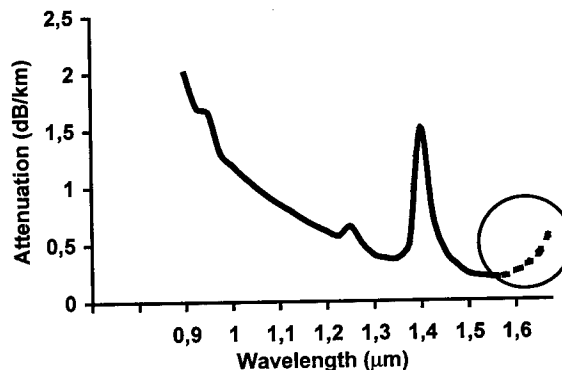


Fig. 2: Spectral attenuation of fibre

The present ITU-T G.652³ contains a spectral attenuation model for wavelengths up to 1600 nm. This model is for uncabled fibre attenuation. To be able to use the same model, additional information is needed to cover cabling effects and environmental effects.

Macrobending or microbending may increase the attenuation at longer wavelengths. The additional loss based on macrobending may be due to fibre curvature inside the cable, or fibre bending in joint closures. Microbending can arise particularly at low temperatures due to shrinking of the fibre coating and other cable elements.

CABLE ROUTES UNDER INVESTIGATION

The routes were selected to contain different cable types of different ages. The fibre type in the cables is single-mode fibre in accordance with ITU-T G.652. Cables contain 6 to 96 fibres.

Cables are specified to operate in the temperature range of -45 - +60 °C. The performance of the cables in that particular temperature range has been measured during the type approval procedure of the cable design, and also periodically at the factory before cable delivery. The acceptance criterion in the whole temperature range is today 0.10 dB/km for the maximum change in attenuation when measured at 1550 nm. In the early 1990's and in the 1980's the acceptance criterion at the extreme temperatures was 0.30 dB/km for the maximum change in attenuation.

The typical distance between splices is 2 km. Splicing is done by an automatic fusion splicer with active alignment. The minimum diameter for fibre loops in the joint closures is 60 mm, typically size of the loops is ≥ 80 mm. Fibre characteristics related to bending sensitivity are listed in Table 1.

Table 1: Fibre characteristics

Characteristic	Value
Mode field diameter	8.5 - 10 μm
Cut-off wavelength, λ_c	1180 - 1330 nm
Cut-off wavelength, λ_{cc}	< 1270 nm

Cables are terminated within the distribution frame either by SC-connectors or by FC/PC-connectors. Connectors are located in a temperature-controlled environment.

The directly buried cables are installed by ploughing along the roads or railroads. Aerial cables are installed on pole lines with a nominal span of 50 m.

The cables were installed during 1989 - 1998.

MEASUREMENT SET-UP

The measurement set-up contains a white light source (halogen lamp) together with a monochromator, filters and an optical power meter (Fig 3.). To increase accuracy, a stabilised power source is used for the halogen lamp.

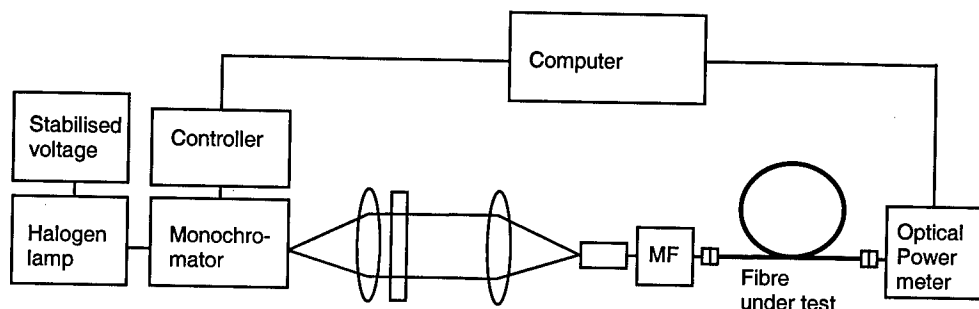


Fig 3: Measurement set-up

The wavelength range of the equipment is 0.8 – 1.76 μm . In field measurements, the control channel for the controller is provided either by a modem connection or, alternatively manually by using two separate computers. The measurement bandwidth is set by the monochromator. The value of 16 nm was selected in order to achieve the dynamic range required for measuring the cable routes up to approximately 60 km.

MEASUREMENTS

The measurements were carried out by the alternative test method for attenuation as presented in ITU-T G.650. This method is insertion loss method, which is non-destructive and therefore suitable for the field use. The light source is coupled to a short single-mode reference fibre having the same nominal characteristics as the fibre under test. The reference fibre is equipped with the mode filter. The fibre is selected not to allow propagation of cladding modes. The connector losses at both ends are included in the attenuation results.

The total amount of measured cable routes was 877 km. Of all the routes, at least two fibres were measured. The length of continuous repeater sections was between 15 and 63 km (typically 30 - 40 km). The total number of measured sections is 21. These measured sections form four different routes (399 km, 265 km, 162 km and 51 km). Individual cable delivery lengths were not measured.

Measurements were carried out partly during wintertime in order to include the thermal effects.

The measured routes contain 769 km of cable installed in the ground and 108 km of aerial cables. The cable core constructions are single loose tube (665 km), stranded loose tube (130 km) and slotted core (82 km).

All cables were also measured by OTDR at the 1546 nm or 1552 nm wavelength.

RESULTS

The attenuation coefficients at 1550 nm varied between 0.20 dB/km and 0.28 dB/km (Fig. 4). There is a clear correlation between the age of the route and basic attenuation at 1550 nm. This is obvious as the first single-mode optical fibre cables had attenuation requirements only at 1310 nm.

The section with the highest attenuation at 1550 nm has also a much higher attenuation coefficient at the lower end of the 1550 nm wavelength window, whereas the older cables had higher "water peak" than fibres today.

Low temperature results

Four directly buried cable repeater sections (tot. 140 km) were measured during the wintertime. The results are shown in Fig. 5.

The results were compared to other measurements of the same cable types, and no temperature-related difference could be noted. Low temperature behaviour of the existing cables is satisfactory at longer wavelengths as well.

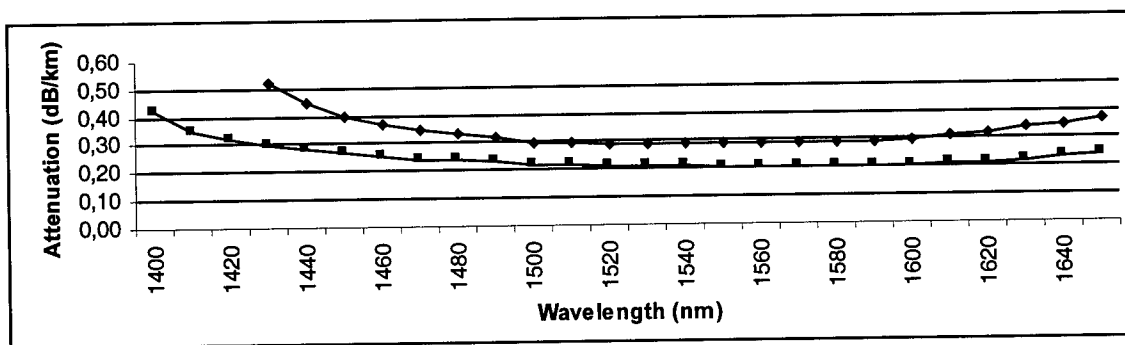


Fig. 4: Attenuation coefficient according to 1550 nm results

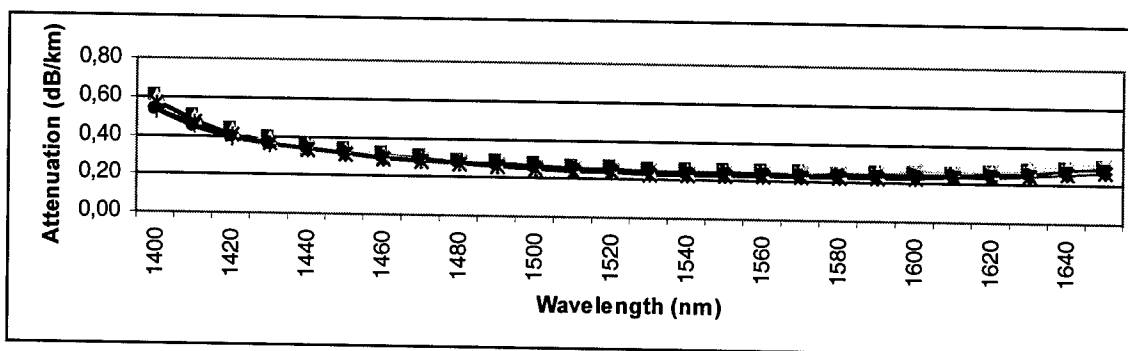


Fig. 5: Directly buried cables in frozen ground

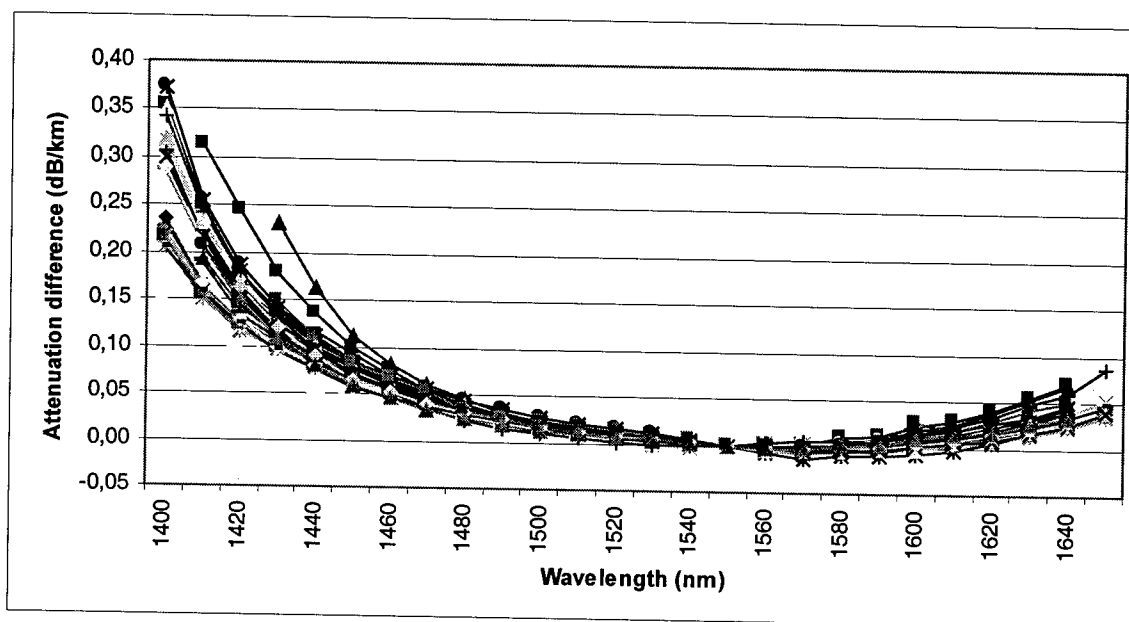


Fig 6: Spectral attenuation curves of the repeater sections

Spectral attenuation:

The results of the measured repeater sections are shown in Fig. 6. The attenuation coefficient at 1620 nm was compared to the value at 1550 nm. The difference from 1550 nm to 1620 nm is between 0.01 dB/km and 0.04 dB/km.

There is no clear relation between spectral behaviour and the age of the cable. The oldest cables did not always show the biggest difference between 1550 nm and 1620 nm values.

Distribution of attenuation differences is shown in Fig. 7.

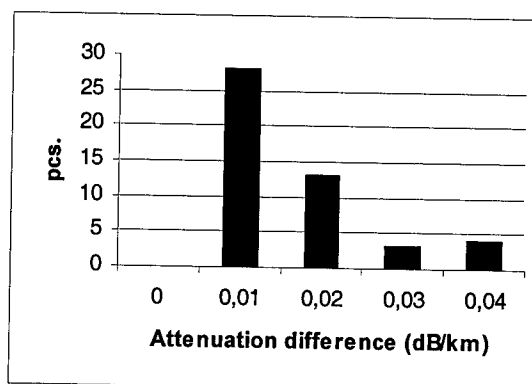


Fig. 7: Distribution of attenuation differences

Since the wavelength region from 1620 nm to 1650 nm may be used for monitoring purposes, the attenuation values at 1650 nm are also analysed. The difference compared to values at 1550 nm was 0.04 dB/km to 0.11 dB/km.

Route results:

The results of three different routes (A, B and C) are shown in Fig. 8.

The cables of route C were installed during 1992-1997. Routes A and B contain also cable sections installed in the late 1980's. They represent cable routes of older type containing different cable types from different manufacturers. The attenuation coefficient at 1620 nm is 0.02 dB/km higher than at 1550 nm. The difference between 1550 nm and 1650 nm is on the order of 0.04 dB/km – 0.06 dB/km. The details are shown in Table 2.

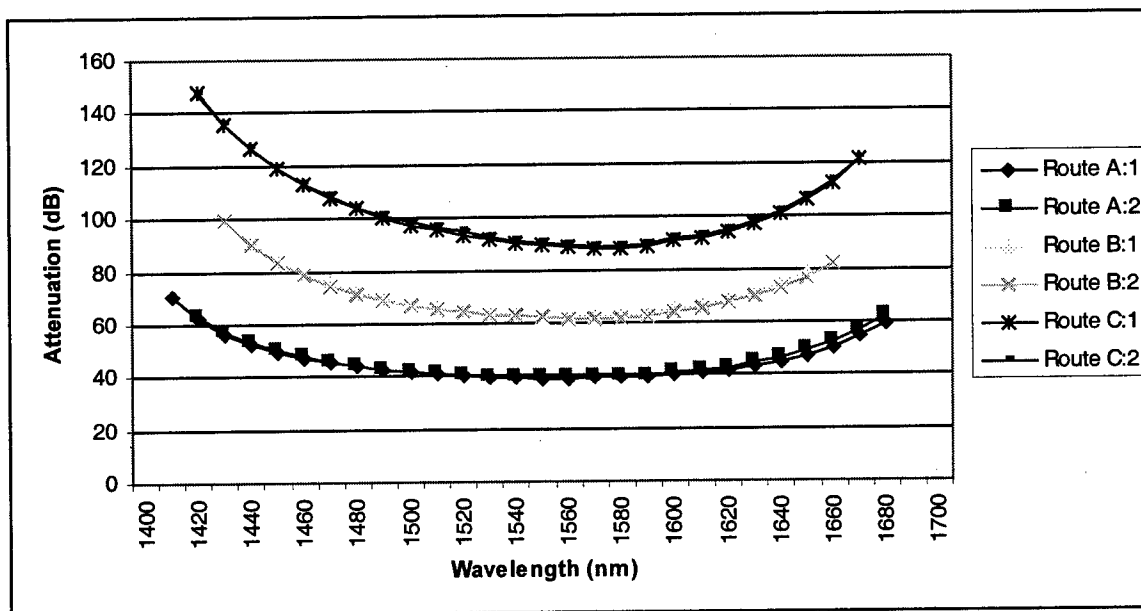


Fig 8: Route attenuation

Table 2: Route measurement results

	A		B		C		D
Length (km)	162		265		400		51
Number of spans	4		5		11		1
Number of measured fibres	2		2		2		8
Att. at 1550 nm (dB/km)	0.239	0.243	0.235	0.234	0.225	0.226	0.212 – 0.236
Att. at 1620 nm (dB/km)	0.258	0.264	0.258	0.254	0.236	0.237	0.230 – 0.257
Att. at 1650 nm (dB/km)	0.292	0.305	0.297	0.291	0.266	0.267	0.263 – 0.301

CONCLUSION

Route D, consisting of only one repeater span, is used as a reference. It was installed in 1996 and it represents a new optical fibre cable installation.

In the final installation the overall attenuation could be lower if the various connectors are replaced by fusion splices, since the existing repeater sections are rather short compared to the possible amplifier spacing.

The spectral attenuation of 877 km of optical fibre cable routes was measured. The aim of the study was to examine the capability of the existing network to carry traffic at the wavelength above 1600 nm.

The measured attenuation difference from 1550 nm to 1620 nm was between 0.01 dB/km and 0.04 dB/km over the repeater span length. At

1650 nm, the similar difference was from 0.04 dB/km to 0.11 dB/km. Over the long routes, consisting of several individual repeater spans, the attenuation differences at 1620 nm and 1650 nm compared to 1550 nm were 0.02 dB/km and 0.06 dB/km, respectively.

The measurements display an excellent performance for today's transmission systems, including WDM. The existing cables and installations are qualified for the use of wavelengths up to 1580 nm. It is shown that performance of the network is satisfactory also above this wavelength. Therefore, it is possible to enhance network capacity for future needs by adding new optical channels at longer wavelengths.

However, when operation is shifted towards longer wavelengths, it is necessary to accept an attenuation curve that is not "flat". Over long spans (i.e. hundreds of kilometres of route), the measured difference in attenuation is 0.02 dB/km. Thus the difference in the attenuation coefficient value is rather small but when calculating a span of 600 km (one of the target distances in ITU-T) 0.02 dB/km becomes 12 dB, which system needs to meet.

ACKNOWLEDGMENTS

The authors would like to express their thanks to Mr. M. Pikkarainen for helpful information and advice and to Mr. G. Melander for the measurement work.

REFERENCES

1. ITU-T G.957: Optical interfaces for equipments and systems relating to the Synchronous Digital Hierarchy
2. ITU-T G.692: Optical interfaces for multichannel systems with optical amplifiers
3. ITU-T G.652: Characteristics of a single-mode optical fibre cable

SPEAKER BIOGRAPHY



Eino Jauhiainen
Sonera Ltd
PO Box 800
00051 Helsinki
FINLAND

Tel: +358-20401

Fax: +358-2040-2646

Email: eino.jauhiainen@sonera.fi

Eino Jauhiainen received his M.Sc. degree in Electrical Engineering from University of Oulu in 1988. He joined Sonera (then Telecom Finland) in 1988, to work on optical fibres and optical fibre cables. He is a member of various international standardisation organisations. Presently he works as Development Manager in Network unit of Sonera.

MATERIALS RELIABILITY OF FLOODED AND DRY-CORE ADSS CABLE

Swati Neogi, Brian G. Risch, and Matt Soltis

OFCCC, Alcatel, P.O. Box 39, Claremont, NC 28610-0039

ABSTRACT

Reliability of All Dielectric Self-supporting (ADSS) aerial optical cables has been investigated. The scope of the study includes the effects of aging on mechanical performance of the both dry-core and flooded cable designs with a filled thermoplastic, track resistant outer jacket. Environmental stress crack resistance of the outer cable jacket material and hydrolytic stability of the PBT buffer tubes in flooded and drycore cables was studied. Additionally, the effects of electrical testing on the filled thermoplastic track resistant jacket material of both dry-core and flooded ADSS cable has also been investigated. A comparative study has been performed to demonstrate the superiority of the performance of the filled thermoplastic track resistant jacket material over HDPE outer jacket material.

INTRODUCTION

All Dielectric self-supporting (ADSS) fiber optic cable offers a rapid and economical solution for utility and telecommunication companies to deploy optical fiber cables along existing electric and telephone utility pole rights of way assets. ADSS cables offer an alternative solution over other aerial application cables such as lashed or Figure-8 cables. All dielectric solutions are preferred and sometimes mandatory for installation in or

near electric power lines on utility structures where cables containing metallic elements are not advised.

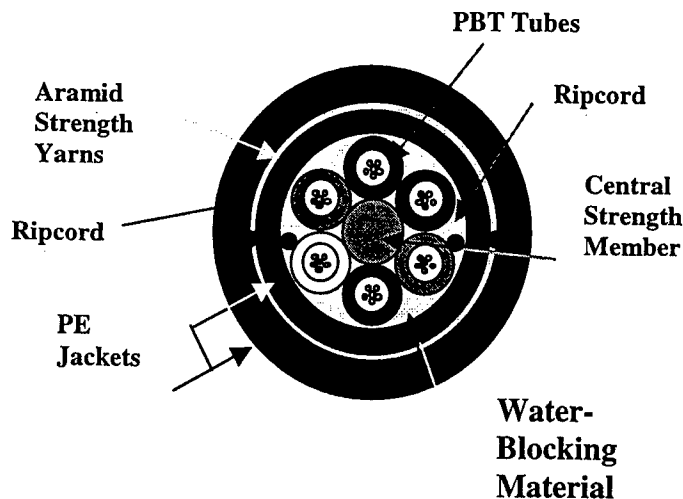
Lashing of optical cables to existing steel messenger wires may be useful for applications where additional cables may be added at a later date, using the same messenger. One drawback is that multi-cable lashing can be complex and make maintenance time-consuming. Figure 8 cables are often used in difficult terrain for easy and rapid installation as an alternative to lashing. With the messenger wire incorporated in the cable, Figure 8 cables may require special installation procedures.

ADSS cable may also be installed over long distances on H pole structures, steel poles, and towers used for high voltage systems. Optical Groundwire (OPGW) cable may be preferred for extremely long span requirements. OPGW cables embed optical fibers within steel tubes and aluminum groundwires for transmission along power grids. In general, ADSS cable is less expensive, more accessible, and easier to install than OPGW cable for many applications. Installation of OPGW also requires that electric power be turned off during installation¹; although highly specialized helicopter installation crews have performed, live installation in special cases. OPGW cable is also typically limited to 96 fibers or less so that higher fiber counts require ADSS or other cable alternatives.

ADSS cables are designed and optimized for specific system requirements to ensure long-term reliability. A cross section of a typical ADSS cable design has been shown in Figure 1. Buffer tubes are helically stranded around a central strength member forming an inner core. In Flooded ADSS cable the interstices between buffer tubes is filled with a dielectric gel whereas in dry design watertightness is ensured by superabsorbent coated binders. Hydrolytically stabilized polybutylene terephthalate (PBT) has been selected as the buffer tube material over polypropylene to

provide improved crush and creep resistance especially at hardware fixture points. For the additional protection of the optical fiber, the inner core is jacketed by MDPE polymeric sheath. To minimize the cable weight, thereby minimizing forces on the pole structures, while also providing maximum stress protection to the optical fibers within the cable, aramid yarns have been used as strength elements between the inner and outer jacket of the cable. A sufficient amount of aramid yarns have been added to ensure Maximum Rated Cable

Figure 1. Schematic Representation of the Cross Section of Typical ADSS Cable.



Load (MRCL). The MRCL of the cable is large enough to support the compounding stress effects of large span distances and various environmental conditions such as wind and ice loading.

Selection of the proper cable jacket material is very important to guarantee the long-term reliability of the cable. This selection depends upon the phase to phase voltage of the power utility system, the environment, and the position of the ADSS cable within the electrical field. In very low field voltage environments, a typical High Density polyethylene (HDPE) material is used. However, in higher field voltage special track resistant jacket material is required to prevent the dry band arcing caused by proximity to high voltage lines. Cross linked or filled thermoplastic materials

have shown the best resistance to electrical activity. Previous research has shown² that filled thermoplastic jacket materials containing approximately 2.5% carbon black provide a superior combination of electrical and mechanical properties for protection of the cables. A thermoplastic track resistant jacket with acceptable carbon black content provides a three pronged solution to dry band arcing. First, the addition of carbon black ensures the ADSS will be resistant to UV aging, thus preventing collection of salt/pollution on cable sheath lowering and subsequent the cable resistance. Second, thermoplastic jacket materials minimize carbon surface tracking better than cross linked materials. This assures a high electrical stability of the cable jacket. Finally, the tough filled thermoplastic track resistant jacket is resistant to heat or

ablation (vaporization of material resulting in pitting) damage if arcing does occur^{3,6}. A filled thermoplastic also provides similar abrasion resistance to HDPE jacket material.

Some cable manufacturers consider a Mid Span Space Potential of 12 kV as the standard threshold for specifying special jacket materials for ADSS cable^{4,5}. But a previous study² concluded that this threshold voltage provides inadequate protection against premature failure of the cable. Other factors also need to be considered such as climate, pollution level, wet/dry cycles etc. In this study² it has been recommended the protection of the cable with track resistant materials at mid span space potentials of >4 kV. Table 1 is the list of the jacket materials of ADSS cables in different electrical field voltages used by Alcatel and other ADSS cable manufacturers.

Table1. List of jacket materials used in ADSS cables by Alcatel and other manufacturers depending on electrical field voltage.

Electric field voltage	Jacket material	
	Alcatel	Other Manufacturer
≤4 kV	HDPE	HDPE
≥4 kV, ≤12 kV	Antitracking thermoplastic	HDPE
≥12 kV	Antitracking thermoplastic	Antitracking material

EXPERIMENTS

Experiments were carefully designed to study the reliability of the drycore and flooded ADSS cables with filled thermoplastic antitracking jackets. Also a comparative study was performed to evaluate the superiority of the antitracking cable outer jacket to the HDPE cable outer jacket. A list of cables studied is as follows.

1. Dry ADSS cable with antitracking cable outer jacket
2. Flooded ADSS cable with antitracking cable outer jacket
3. Flooded ADSS cable with HDPE cable outer jacket

The three cables were of a similar construction in which six PBT tubes containing optical fibers were stracnded around a central strength member. In the flooded cables the interstices between the tubes were filled with dielectric gel. In dry designs there was no dielectric gel between tubes. Instead of the gel, superabsorbent water blocking materials were used. The whole arrangement was surrounded by an inner MDPE sheath. Between the inner sheath and outer sheath Aramid strength yarns were applied. The outer sheath was made either with a filled thermoplastic track resistant material or HDPE. Details of the construction of these three cables are presented in Table 2.

The antitrack material used is a specially formulated filled thermoplastic. The track resistance of the material is about 2.75 kV measured according to the method ASTM D-2303. Performance of cable made with the specially formulated material in salt fog test and UV test has been studied and reported previously².

Table2. Materials of construction of different cables tested for the reliability study.

No	Description	Buffer Tube Material	Waterblocking material	Cable outer sheathing material
1.	Dry antitrack ADSS	PBT	No dielectric gel in interstices of buffer tubes in the inner core	Special Track resistant material
2.	Flooded antitrack ADSS	PBT	Flooded core	Special Track resistant material
3.	Flooded ADSS	PBT	Flooded core	HDPE material

The reliability study included the investigation of the following:

1. Effects of aging on mechanical performance of the antitracking outer jacket materials for dry and flooded ADSS cable
2. Comparison of the Environmental Stress Crack Resistance (ESCR) of Antitrack material and HDPE.
3. Effect of aging on hydrolytic stability of buffer tubes in dry cable design.
4. Effect of dry band arcing on the cable outer jacket material of both dry and flooded design after subjecting cables in electrical field voltage.

Effect of aging on mechanical performance of the outer cable jacket:

Cables were aged in a humidity oven at a constant temperature of 85°C and at 85% relative humidity for 60 days. The mechanical properties such as the tensile strength and the elongation of the outer cable jacket after aging were measured according to the method FOTP 89 and compared with that of the unaged outer cable jacket. An Instron model 4202 was used for tensile measurement.

Comparison of ESCR of different outer cable jacket material

Environmental Stress Crack Resistance of both HDPE and antitrack cable jacket materials were measured following ASTM D1693. Cables were aged before the testing at a temperature at 85 °C and at 85 % relative humidity for 60 days.

Hydrolytic Stability of Buffer tubes

Hydrolytic stability of the buffer tubes was determined in a dry ADSS cable and compared with that of a flooded ADSS cable. Both dry and flooded ADSS cables were aged in a humidity oven at 85 °C temperature and 85% relative humidity. During the testing moisture penetrated the cable and reached the buffer tube in radial direction. Ends of the cables were sealed to prevent the ingress of moisture through the end in the axial direction.

Moisture content of buffer tubes was measured after 30 days and 60 days of aging. Mechanical properties such as tensile strength and elongation of buffer tubes were also investigated to determine the degradation of the buffer tubes. For the measurement of moisture in the tubes, a Carl Fischer Moisture Analyzer, made by Mitsubishi, model Ca-06 was used.

Buffer tube Mechanical properties were measured using a Monsanto, model 2000 Tensometer according to FOTP 89.

Effect of dry band arcing

Effects of dry band arcing on the performance of both dry and flooded ADSS cables with filled thermoplastic antitracking jackets were studied by subjecting the cables to electrical field voltage after aging. A flooded cable with an HDPE outer sheath was also subjected to the same test to compare the performance the HDPE outer jacket material to the antitrack outer jacket material. The design of electrical experiments and details of the test method are described below.

Performance of cables in electrical fields against dry band arcing is highly dependent on the cable aging. On a newly installed dry cable, the surface sheath resistance is obviously quite high ($>10^9$ Ohm/m) so the induced currents are insignificant. Additionally, the cable surface is highly hydrophobic so moisture and contaminants are not prone to build up and thereby reduce surface resistivity. However, as a cable ages from thermal oxidation and exposure to the ultraviolet rays of sun, contaminants such as salt and/or pollutants and moisture adsorb on the cable sheath. The surface impurities can significantly reduce the electrical resistance to current flow on the surface of the cable.

Due to the inherent hydrophobic nature of polyethylene, the newly extruded ADSS jacket is not prone to collection of moisture, pollution, etc. on the cable jacket surface. As the cable surface begins degradation, the cable sheath material may be wetted from rainfall. Additionally resistance may be lowered from salt or

pollution. With a wetted and/or polluted cable surface, dry bands of high resistance surrounded by wetted sections of much lower resistance may develop. As these bands develop, the possibility of arcing across the dry band exists which can damage an unprotected sheath by heat and ablation (vaporizing of jacket material causing pitting). The surface of a new cable and that of an old unprotected cable with heavy contaminants have been illustrated in Figure 2 and Figure 3.

Figure 2. New cable: water beading, near zero current, no arcing

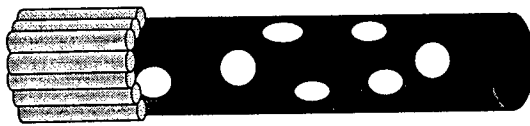
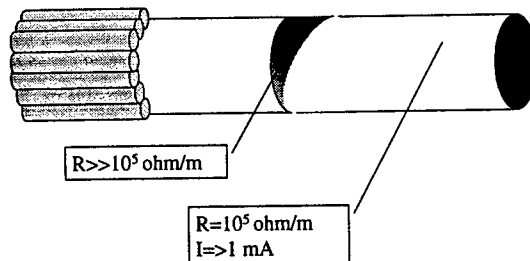


Figure 3. Worst case: old, unprotected cable with heavy contaminants.



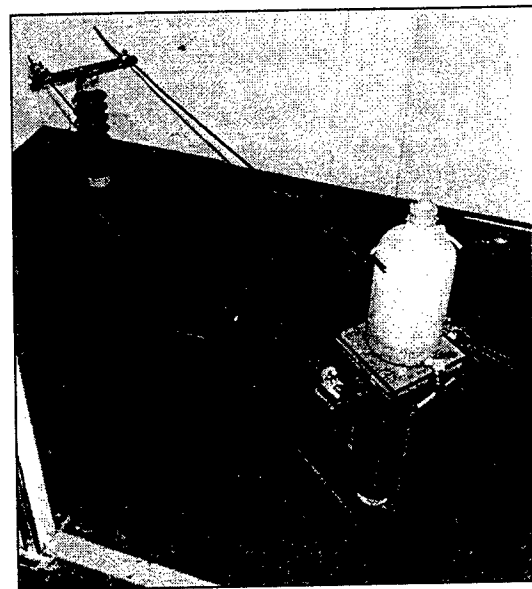
To simulate the worst case scenario for dry band arcing. ADSS cables have been aged before the cables were subjected to the electrical field voltage. All the cables were aged at 85 °C temperature and at 85 % relative humidity for 60 days before electrical testing.

The electrical test was also designed to reproduce the most severe service conditions by attempting to initiate a failure from moisture ingress along the inside of the ADSS cables. Tap water was introduced to the cable during electrical testing to simulate a puncture of the outer cable sheath. The humidity level was selected to recreate conditions that would be representative of service experience and to achieve the wetting of the cable surface and

the deposition of some conductive pollution as a result of the temperature cycle.

A test rig used for electrical testing has two porcelain insulators bolted to either end of a 3m length steel channel. Approximately 3.5m of each cable was cut, degreased, and one end sealed using Raychem adhesive-lined heat shrink tubing. Each sample was then installed on the test rig with stress relieving electrodes attached to the h.v and earthy ends of the cable. A nominal tension was applied to each cable by physically pulling on them until the sag was less than 50 mm. The cable clamps were then tightened to prevent the cables from slipping. Water was introduced to the open (H.V.) end of each cable through nylon tubing, which was attached to the cable with heat shrink tubing. The cable ends were coated with silicone grease to help prevent any cavities in those regions. A picture of the test arrangement is shown in Figure 4.

Figure 4. Typical test arrangement for electrical testing.



The tests were performed within a climatic chamber where the temperature and humidity could be controlled. The cables were subjected to a temperature cycle, which was selected to represent the diurnal temperature variation experienced in the service. The cycle went from 10 °C to 40 °C within a 30 min ramping period and a 40°C residence time of 30 mins. The temperature

was again ramped down to 10 °C within 30 mins ramping time and a 10°C residence time of 30 mins. giving an overall cycle time of 2 hours. The test duration was 200 hours. During the testing period the cable experienced the temperature variation equivalent to the diurnal temperature variation of 100 days. The humidity in the chamber was maintained between 84 and 100% RH.

A voltage of 30 kV was applied to the cable at the start of the first cycle and it was only interrupted during inspections, which were performed approximately every other day.

The following properties were investigated to determine the effect of dry band arcing.

1. Surface examination
2. Mechanical performance evaluation
3. Environmental stress crack resistance of the outer cable jacket

The cable outer jacket surfaces were examined visually as well as by scanning electron microscope (SEM). The Scanning Electron Microscope used for this study is made by Philips, model XL30 with a secondary electron detector. Samples were coated with gold to a thickness of approximately 100 nm and an electron acceleration voltage of 12 kV was used.

Mechanical properties of the outer jacket material and inner buffer tubes were

measured after electrical testing and compared with that before electrical testing to determine the effect of dry band arcing on the mechanical performance of the cable. Mechanical properties of outer jacket material were measured using the tensile measuring equipment, made by Instron, model 4202. A Monsanto, model 2000 Tensometer was used to measure the mechanical properties of buffer tubes. Method FOTP 89 was used to measure all the mechanical properties.

Environmental stress crack resistance of the antitrack and HDPE outer jacket material after electrical testing has been measured and compared with that before electrical testing to determine the effect of dry band arcing on the environmental stress crack resistance. Method ASTM D1693 was used for the measurement of ESCR.

RESULTS AND DISCUSSION

Effect of aging on mechanical performance of the outer cable jacket

Mechanical properties of outer cable jacket of aged and unaged flooded and dry ADSS cables are listed in the Table 3. Jacket materials in both cable designs are filled thermoplastic antitracking material. Cables have been aged at 85° C and at 85% relative humidity.

Table 3. List of values of tensile stress and elongation before and after aging.

Cable Design	Outer Jacket Material	Tensile stress, Mpa		Elongation, %	
		Before aging	After aging	Before aging	After aging
ADSS dry	Antitrack filled Thermoplastic	16.46	17.9	597	687
ADSS flooded	Antitrack filled Thermoplastic	16.46	17.3	597	601

Effects of aging on the mechanical performance of the outer cable jacket in both dry and flooded design is shown in Figure 5 and Figure 6. No significant difference was

seen in the mechanical or aging performance of the outer jacket material between dry and flooded cable designs. This is expected since the outer jacket

material is same in both designs and the presence of dielectric gel between the interstices between buffer tubes should not affect the mechanical performance of the outer jacket. Elongation of the material was slightly improved after aging.

Figure 5. Effect of aging on tensile strength of cable outer jacket in both dry and flooded design.

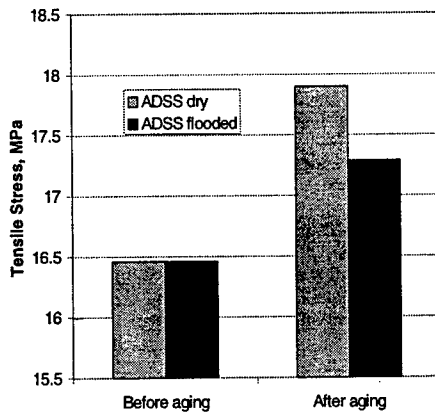
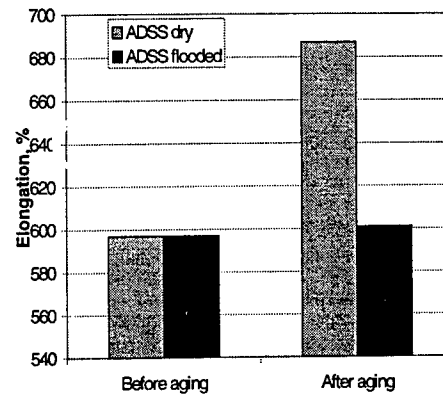


Figure 6. Effect of aging on elongation of cable outer jacket in both dry and flooded design.



Comparison of ESCR of different outer cable jacket material

Environmental stress crack resistance of the cable outer jacket material, HDPE and antitrack filled thermoplastic, is more than 1000 hrs even after aging for 60 days.

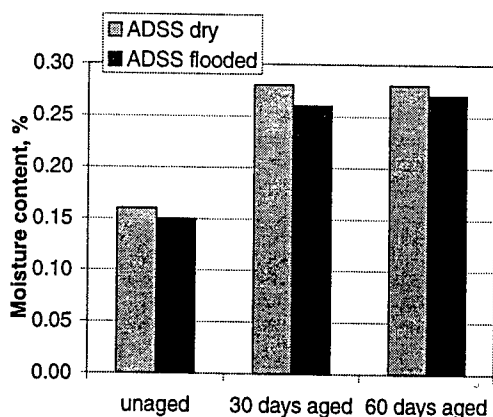
Hydrolytic stability of buffer tubes

Moisture content of PBT tubes of both ADSS dry and flooded design after aging is given in Table 5. It is evident from Figure 7 that the moisture content of PBT tubes in the dry design is not substantially different than the flooded design. Also the moisture penetrates the core within 30 days and remains almost unchanged after 60 days of aging.

Table 5. Moisture contents of the buffer tube after aging in different cable design.

Cable design	Moisture Content, %		
	unaged	30 days aged	60 days aged
ADSS dry	0.16	0.28	0.28
ADSS flooded	0.15	0.26	0.27

Figure 7. Variation of moisture contents of buffer tubes in dry and flooded cable design with different aging time.

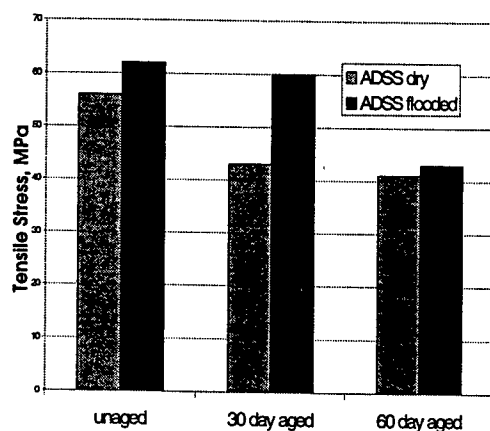


Tensile stress and elongation of the buffer tubes after aging are listed in Table 6.

Table 6. Tensile stress and elongation of buffer tubes after different aging times.

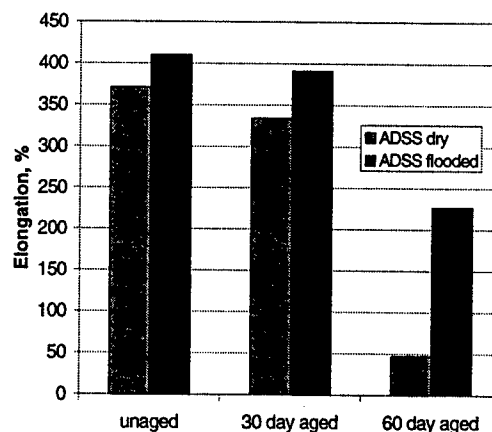
Cable Design	Tensile stress, Mpa			Elongation, %		
	unaged	30 day aged	60 day aged	unaged	30 day aged	60 day aged
ADSS dry	56	43	41	371	334	47
ADSS flooded	62	60	43	410	391	227

Figure 8. Effect of aging on tensile stress of PBT buffer tubes in both dry and flooded cable design.



Effects of aging on mechanical behavior of PBT tubes in both dry and flooded design is shown in Figure 8 and Figure 9. It is evident that the performance of the PBT tubes in ADSS flooded design is better than that of PBT tubes in dry design after aging. This data indicates that although the flooding gel does not totally prevent radial moisture ingress through the sheath, it does provide an added moisture barrier to deter tube hydrolysis. Though the performance of PBT tubes in dry cable designs is not as good as the flooded design. More than 10 % elongation is still retained after 60 days of aging at 85°C and at 85% relative humidity. This result is quite good relative to earlier studies on stabilized and non-stabilized PBT buffer tubes and should be sufficient to guarantee many years of service under normal operational conditions^{7,8}.

Figure 9. Effect of aging on elongation of PBT buffer tubes in both dry and flooded cable design



Effect of dry band arcing

Visual inspection of the cables after 200 hrs of dry band arc testing reveals that both dry and flooded ADSS cables with an outer sheath made of filled thermoplastic antitrack material have survived the test without either tracking or puncture. Some dry band activity was suggested by a dull and slightly rough cable surface in certain areas. The ADSS cable (flooded) with HDPE outer cable jacket suffered from severe damage and a punctures at the earth end, and the cable sheath had also been partially melted along a line that extended from the earth electrode. Pictures of the dry and flooded ADSS cables with antitrack outer cable material and the ADSS cable with HDPE material (flooded) are shown in Figure 10, 11 and 12 respectively.

Figure 10. Pictures of ADSS dry cable with antitrack material showing minimal effect.

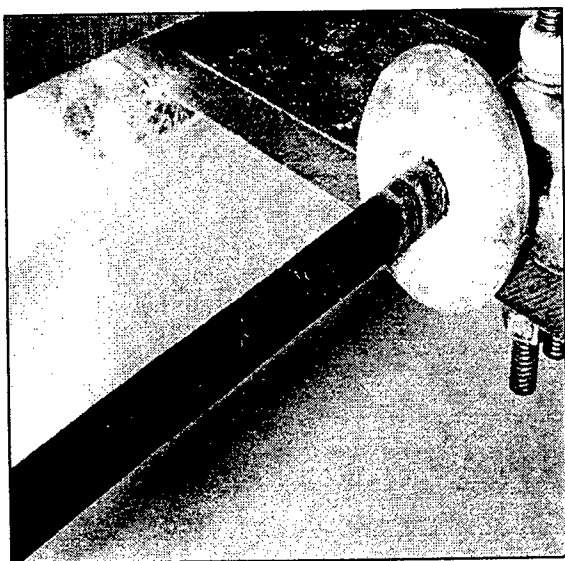


Figure 11. Pictures of ADSS flooded cable with antitrack material showing no puncture of the jacket material.

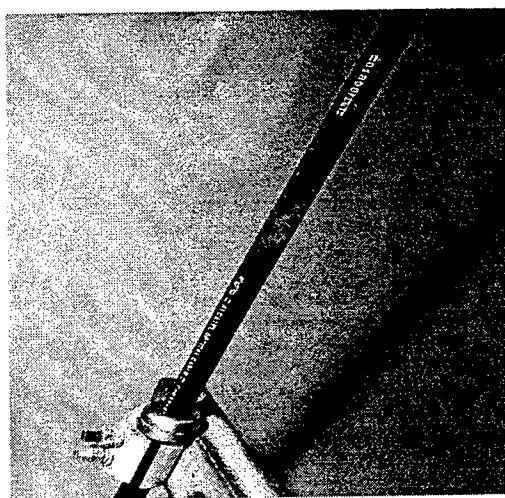
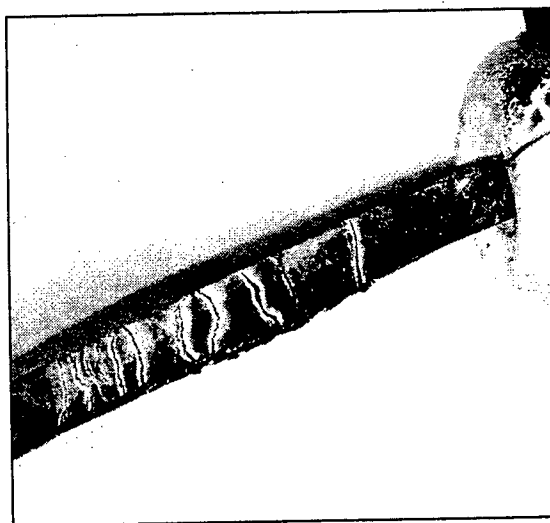


Figure 12. Picture of Flooded ADSS cable with HDPE outer cable jacket showing the punctures and partially melted sheath.



Examination of the outer jacket surfaces from all these cables with SEM also reveals the microscopic damage of the surfaces. SEM pictures of antitrack material at the end of dry band arc testing is given in Figure 13 whereas Figure 14 represents the SEM scan of the ADSS cable with HDPE outer jacket at the end of the test. Figure 14 clearly shows the more severe surface

damage and pitting for HDPE compared to the antitrack material.

Figure 13. Surface of the antitrack outer jacket material after testing under SEM.

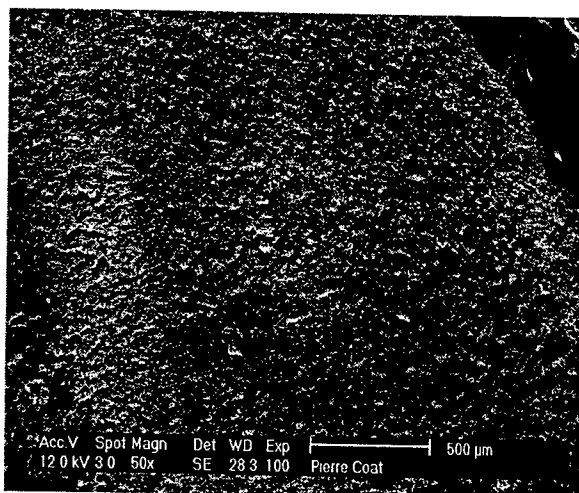
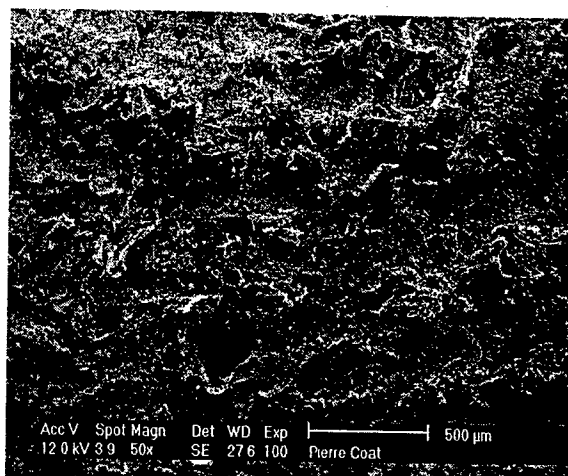


Figure 14. Surface of the HDPE outer jacket material after testing under SEM



Values of tensile stress and elongation of the antitrack outer jacket material in both dry and flooded cable designs are listed in Table 7. Figure 15 and 16 compare the tensile stress and elongation of the antitrack jacket materials in dry and flooded cable design before and after dry band arc testing. From these two figures it is evident that the electrical activity had virtually no effect on mechanical properties of antitrack jacketing material.

Table 7. List of values for tensile stress and elongation of outer jacket material after dry band testing

Outer material	jacket	Cable design	Tensile stress,Mpa		Elongation, %	
			before band test	dry after band test	before band test	dry after band test
Antitrack		dry	17.9	17.3	687	697
Antitrack		Flooded	17.29	17.25	601	628

Figure 15. Effect of dry band arc testing on tensile strength of outer cable material of dry and flooded ADSS cable design.

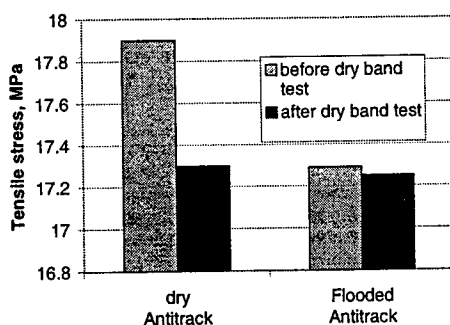
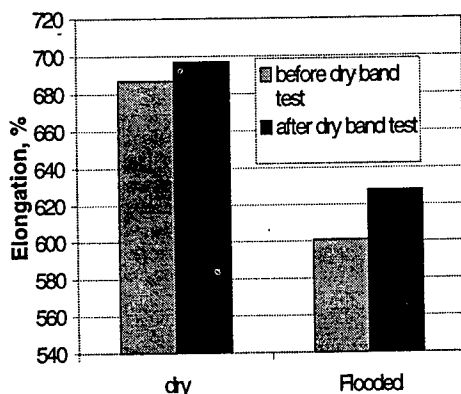


Figure 16. Effect of dry band arc testing on elongation of outer cable material of dry and flooded ADSS cable design.



After dry band arc testing the environmental stress crack resistance of both HDPE and antitrack material exceeds the 1000 hrs as required by industrial standards for unaged materials.

ACKNOWLEDGEMENTS

We would like to thank Danny Ammons for his assistance on mechanical testing, Pierre Coat for SEM analysis, and Jeff Auton for performing ESCR test. We would like to thank specially to Bill Dewitt and Alstom UK Ltd. For their contribution on the Dry Band testing.

REFERENCES

1. Yoshida et al, "winding of Optical Fiber Cable onto Existing Ground Wire", 35th International Wire and Cable Symposium, 1986
2. Keller, D.A, D.J. Benzel, J.P. Bonicel, C. Bastide, F. Davidson, "Continued Investigation of ADSS Designs and Reliability Considerations with respect to Field Voltage Tracking and Cable Installation Practices", International Wire and Cable Symposium, 1997.
3. Vaughan, A.S., S.G. Swingler, M. Lanfear, H. Weingandt and H. White, "Laser Ablation and Thermal Decomposition studies of Fiber Optic Cable Sheathing Materials", IEEE proceedings, October 1992.
4. 5. Carter, C., et al. "Mathematical Model of Dry Band Arcing on Self Supporting All Dielectric Optical Cables on Overhead Power lines", IEE Proceedings-C, Vol. 139, No 3, May 1992.
5. Rowland S., et al. "Electrical Aging and Testing of Dielectric Self Supporting Cables for Overhead Power lines", IEE Proceedings-A, Vol. 140, No 5, September 1993.
6. Vaughn A.S., Robbie D A., Hosier I.L., Sutton S.J., "Simulations of Surface Discharge Damage on Self Supporting Fiber Optic Cables", Plastics in Telecomm. Proceedings, 6E, September 1998.
7. Risch B.G., Auton J., and Tata O., "Advanced Impact Polypropylene buffering material for superior long term hydrolytic and thermooxidative stability", International Wire and Cable, 1998.
8. Gebizlioglu O., and Plitz I., "Monitoring Accelerated Aging of Polyester Buffer Tubes in Fiber Optic Cable", International Wire and Cable Symposium, 1993.

Speaker:



Swati Neogi
Alcatel OFCCC
2512 Penny Rd.
P.O. Box 39
Claremont, NC 28610

Swati Neogi is the Material Scientist at Alcatel Telecommunications Optical Fiber Cable Competence Center. She received Ph.D in Chemical Engineering from Ohio University. During her Ph.D she worked on modeling of simultaneous mass transfer and reaction of Disc ring reactor used in the manufacturing process of polyethylene terephthalate. Before joining Alcatel, she worked in comissioning a PET plant.

Co-Authors

Brian G. Risch is the Materials Technology Manager at Alcatel Telecommunications Optical Fiber Cable Competence Center. He holds a B.A. degree in Physics from Carleton College and a Ph.D. in Materials Science and Engineering from Virginia Polytechnic Institute and State University. His Ph.D. research was in the area of polymer crystallization and structure property relationships in polymers. Directly after he finished his Ph.D. he worked for ORD laboratories in the area of optical polymers developing new polyurethane and polythiourethanes for high performance ophthalmic lens applications. Since 1996 Brian has worked for Alcatel's Optical Fiber Cable Competence Center (OFCCC) in the area of thermoplastic cable materials. His specialization has been in the area of and crystallization behavior and materials reliability for thermoplastic cable materials.

Matt Soltis is a Design Engineer and Project Manager of aerial development at Alcatel Telecommunications Optical Fiber Cable Competence Center. He accepted his BS in Aerospace Engineering from the US Naval Academy. Before joining Alcatel, he was an Officer and Aviator in the US Marine Corps.

DESIGN OF POLYETHYLENE CABLE JACKET COMPOUNDS OF SUPERIOR JACKETING PERFORMANCE

Tong Chen and James R. Leech
Union Carbide Corporation
Somerset, New Jersey

ABSTRACT

This work demonstrates that the important jacket performance parameters (e.g., processability, shrinkage, stress crack resistance, modulus, etc.) of a polyethylene jacketing compound are dictated by the polymeric molecular architecture, molecular weight (MW) and molecular weight distribution (MWD), short-chain branching characteristics and certain morphological elements. A given structural attribute may be very valuable for certain jacket performance considerations but, at the same time, less valuable or perhaps even undesirable for others. Our ability to control and regulate, independently, the polymer MW, MWD and branching (density) and the ability to introduce other important structural entities allow for optimized combinations of the desirable polyethylene structural attributes to ensure delivery of the target jacket performance.

New advanced HDPE and MDPE jacketing compounds have been developed using the UNIPOL™ Process polyethylene resins to offer substantial enhancements over some traditional jacketing grades in such performance as extrudability, post-extrusion shrinkage and jacket environment stress crack resistance.

(UNIPOL™ Process is a trade mark of Union Carbide Corporation.)

INTRODUCTION

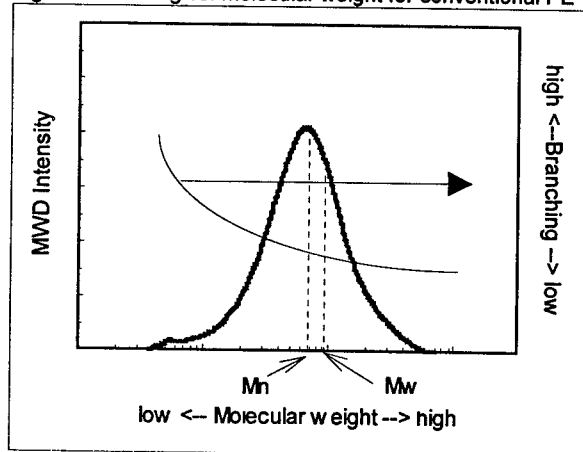
Polyethylene materials have been used to jacket a broad range of communications cables since 1940s. Today's jacketing grades, comprising polyethylene resins such as LDPE, LLDPE, MDPE and HDPE, offer unique combinations of excellent properties and performance characteristics for cabling designs and

applications. Evolution in telecommunications and cabling technologies continue to call for jacketing products with still improved material performance to meet the emerging telecommunications cable manufacturing and end-use needs. Continuous advancements in polyethylene manufacturing technologies, including catalysis and reaction process among others, have made it possible to engineer new jacketing compounds that can deliver the performance required for these cabling applications.

In particular, growth of the fiberoptic communications cable industry led to the development by Union Carbide of a MDPE polyethylene jacketing compound that provides excellent signal attenuation performance during temperature cycling to suit specific cable designs and applications. Now, polyethylene compounds offering improved extrusion and low cable shrinkage characteristics may be valuable for the newer smaller-diameter and higher fiber-count designs and applications. In addition, high jacket robustness as characterized by superior stress crack resistance is also critical to assuring long cable service life. Traditional jackets such as high-molecular-weight HDPE, while still the appropriate jacketing for many applications, may no longer provide the best cabling performance combination for newer designs and applications from either a cable manufacturer's or end-user's standpoint. In response to this emerging market demand for new jacketing products for fiberoptic cables, we have taken a systematic approach in designing several new polyethylene jacketing compounds using the underlying relationships between polyethylene material fundamentals and jacketing performance. This has been enabled by the versatility of UNIPOL Process technology. Molecular weight, its distribution and chain branching are the key structural parameters that largely determine performance of polyethylene

jackets. For conventional linear PE, the frequency of branching that results from the amount of comonomer used normally decreases with increasing MW, as shown in Figure 1. The breadth of molecular weight distribution, often related to the PE jacketing processability, is measured by the ratio of weight-average MW to number-average MW, or M_w/M_n , the polydispersity index.

Fig. 1: Branching vs. molecular weight for conventional PE



For PE with similar MWD, MW is always inversely related to compound melt index. Likewise, branching frequency is also inversely proportional to compound crystallinity, the latter being commonly inferred by PE density. For a given family of PE materials, there exist quantitative relationships between MW and MI, and between branching and density. Therefore, one often uses MI and density values to estimate jacket compound performance. However, these relationships may not be the same when dissimilar PE are compared that have different MWD or branches.

EXPERIMENTAL

Wire extrusion experiments were conducted on a 2.5" Davis-Standard line using a sleeve die with 4:1 drawdown and 14 AWG Cu. Line speed was set at 260 feet/min. Pressure readings at breaker plate were used to rank jacket processability.

Shrinkage tests were performed on 30-cm long wire samples aged overnight at ambient temperature followed by aging at 100°C for 24 hours on a bed of talc. Changes in plastic wire

length relative to conductor length were taken as the shrinkage measure.

ESCR tests were conducted per ASTM D-1693 using 10% Igepal solution at 50°C, with F_0 as the time for zero cracks. Flexural modulus was determined per ASTM D-790. Tensile properties were measured according to ASTM D-638. Abrasion tests were done using a UCC internal method similar to the standard Taber test.

Dynamic modulus tests were done on Rheometrics RSA-II in temperature sweep mode using a frequency of 6.28 rad/s.

DSC melting results were obtained with TA Instruments DSC 2010.

RESULTS AND DISCUSSION

Table 1 lists some of the compounds used in this work, listed in the order of increasing compound densities.

Table 1. List of jacketing compounds

Compound	Density (2) g/cm ³	Melt Index g/10 min
PE-1 (1)	0.932	0.6
PE-2	0.939	1.2
PE-3 (1)	0.941	0.7
PE-4 (1)	0.945	0.7
PE-5	0.952	2.5
PE-6	0.952	2.3
PE-7 (1)	0.954	0.7
PE-8 (1)	0.958	0.15

(1). UCC commercial grades

(2). Compound densities with 2.5% carbon black

1. Polymer molecular weight (or MI) effect

Molecular weight distribution being constant, higher MW or lower MI polyethylene compounds give rise to increased melt viscosity, thus becoming more difficult to process. Higher-MW PE materials are characterized by slower stress relaxation following reshaping of chain molecules by melt extrusion. The level of built-in stress in a finished cable jacket may be quantitatively related to the degree of shrinkage.

Figure 2 shows wire extrusion pressure and post-extrusion shrinkage values as a function of

MI for both MDPE and HDPE compounds. MWD is kept relatively constant to the extent that all consist of broad MWD PE resins. For MDPE jackets (Fig. 2a), significant reductions in both extrusion pressure and shrinkage were achieved when the jacket MI was changed from 0.7 to 1.2. The similar trends of improvement in processability and shrinkage were also observed for HDPE jackets (Fig. 2b). Here, higher MI compounds (PE-5 and PE-7) offer reductions of 30% or more in extrusion pressure and 40% or more in shrinkage, as compared to traditional HMW-HDPE jacket (PE-8).

Fig. 2a: MI effect on extrusion and shrinkage
MDPE: Density = 0.939-0.942 g/cm³

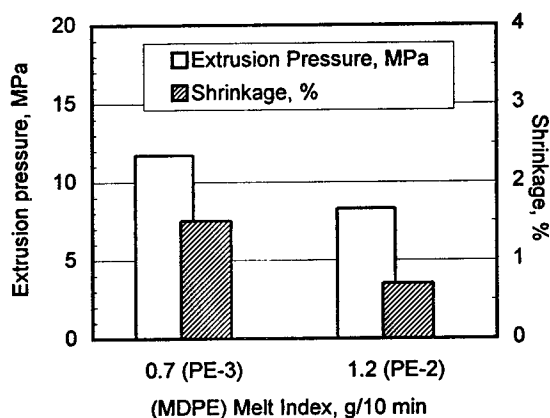
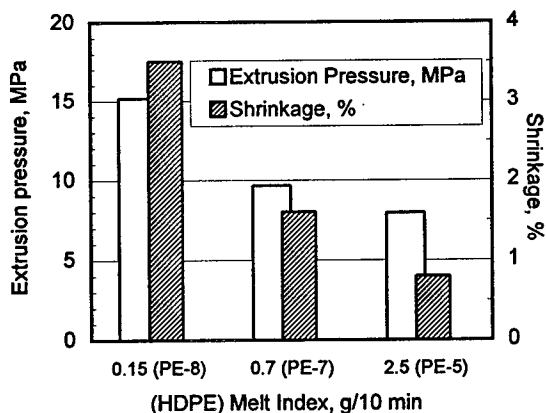


Fig. 2b: MI effect on extrusion and shrinkage
HDPE: Density = 0.952-0.958 g/cm³



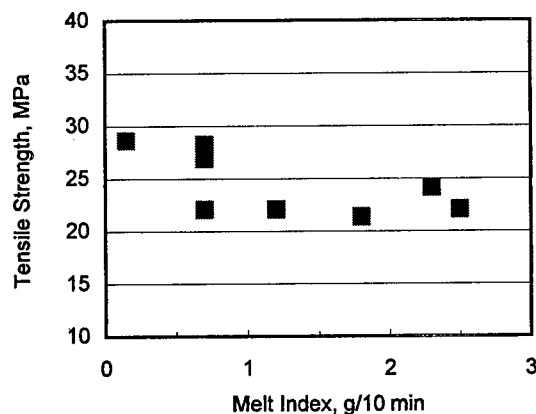
Of particular interest are the characteristics of the 2.5 MI HDPE compound (PE-5), i.e., less than one-fourth in shrinkage and only about 50% in extrusion pressure compared the HWM-HDPE. The compounds with such low shrinkage performance as well as excellent processability

are valuable to the emerging fiberoptic cable designs and applications, allowing for significantly higher jacketing speeds (cabling outputs) than achievable with the HMW-HDPE jackets.

Note that while lower MW or higher MI can provide better jacket processing and shrinkage performance, it may on the other hand affect certain jacket mechanical properties such as tensile strength. It is known that mechanical properties normally increase with increasing molecular weight. It is also true that these mechanical properties display only finite changes within certain intermediate MW ranges. Reduced mechanical properties may be compensated for largely by adjusting the molecular weight distribution.

Figure 3 shows tensile strength at break as a function of MI for several MDPE and HDPE jackets that also have differing MWD. Only limited variations in tensile strength were seen for these compounds with MI between 0.7 and 2.5. This demonstrates that one can control the material strength by properly balancing MW vs. MWD for a given product. In other words, lowering jacket MW in the range considered significantly favors extrusion and jacket shrinkage performance, with only limited, if any, tradeoff in tensile properties. PE-2 and PE-5 are two such examples of balancing mechanical properties vs. extrusion and shrinkage performance.

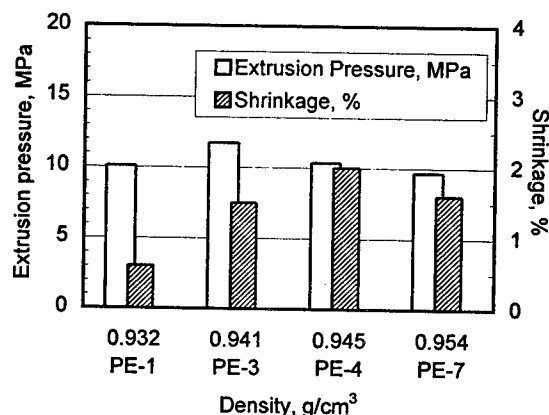
Fig. 3: MW (or MI) effect on tensile property
Density: 0.939-0.958 g/cm³



2. Polymer crystallinity (or density) effect

As previously discussed, the crystallinity of a polyethylene jacket is another key structural parameter that controls many solid-state properties of importance to overall cable performance. Jackets with higher crystallinities, often characterized by higher compound densities, tend to have larger proportions of yet-to-crystallize crystallizable polymer chains when the extruded cable jacketing becomes solidified by fast cooling. Cables can be subject to test or service environments where the temperature variations are significant. The process by which these crystallizable chains undergo staged crystallization or recrystallization when cables are subject to changing temperatures usually results in morphological changes which in turn affect the dimensional integrity of the cables usually in a form of shrinkage.

Fig. 4: Density effect on shrinkage (MI: 0.6~0.7 g/10 min)



As such, jacket shrinkage is usually higher for higher-density jackets when other material parameters and jacketing conditions are held constant. Figure 4 illustrates such behavior for four jackets including one LLDPE (PE-1), two MDPE (PE-3 and PE-4) and one HDPE (PE-7), all with similar MI. The fact that PE-7 has lower shrinkage but at a higher density than PE-4 is attributed to the different branching vs. MW distribution to be discussed later.

In practice, allowing the extruded jacket to crystallize in a fast but uniform way during jacketing extrusion, for example, by using gradient cooling conditions adjusted to suit exit melt temperature, can also help reduce post-extrusion shrinkage.

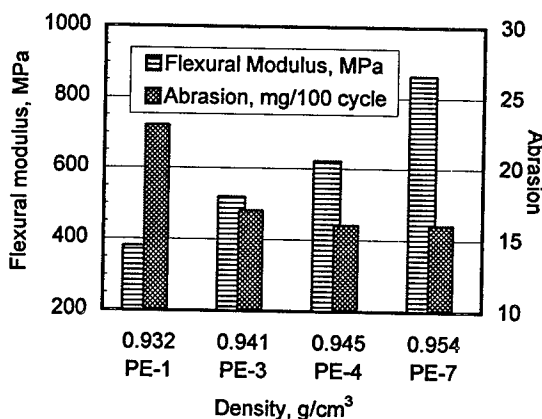
Most commercial polyethylene compounds used for jacketing fiberoptic cables are linear polymers

containing some short-chain branches. Short-chain branching normally has very little effect on the rheological behavior of a jacket compound during its melt processing. Figure 4 shows minimal variations in extrusion pressure for the four compounds with similar MI but differing densities or short-chain branching.

Moduli of a jacket material, often proportional to stiffness, are related to both crystallinity and averaged crystallite sizes. Jackets with lower crystallinity or density will have lower material stiffness and moduli. On the other hand, abrasion resistance of a jacket increases with increasing crystallinity particularly at the low to medium density range. Further finite increases in density only improve the abrasion performance marginally as the increased density mainly manifests itself in a form of thickened lamella layers, which have a limited effect on the bulk material abrasion characteristics.

Figure 5 shows increasing flexural modulus and abrasion resistance (expressed in weight loss per 100 cycles, thus the lower value the better abrasion resistance) with increasing densities for the same four jacket compounds of similar MI. As shown, the dependence of flexural modulus on density is significant going from LDPE to MDPE to HDPE. Again, the fact that PE-7, though with a higher density, has the abrasion resistance similar to PE-4 is related to unique branching vs. MW distribution in PE-7.

Fig. 5. Density effect on mechanical properties (MI: 0.6~0.7 g/10 min)



Clearly, the material moduli and shrinkage characteristics are affected by the jacket density in opposite ways. This presents challenges in

selecting an appropriate jacket meeting the application performance requirements on both modulus and shrinkage.

Another important performance parameter for cable jacketing is its environmental stress crack resistance, or ESCR. Closely related to the material toughness, ESCR also depends on the jacket compound density along with other factors. Compounds with lower densities contain more inter-crystallite tie molecules that play a key role in imparting excellent toughness.

Table 2. Density effect on ESCR

Compound	Density g/cm ³	ESCR, Fo, hours
PE-1	0.932	>2000
PE-3	0.941	>2000
PE-4	0.945	>1000
PE-7	0.954	>400

Table 2 lists the ESCR results for several jacket compounds including LLDPE, MDPE and HDPE, all with very similar MI. As density increases, the number of tie molecules per unit material volume quickly diminishes, decreasing the ESCR performance. This density effect by way of the tie molecules provides a means to enhance the ESCR performance of HDPE jackets as illustrated below. This effect is more significant for the HDPE jackets than MDPE or LLDPE based jackets.

3. Polymer morphological effect

In addition to those fundamental structural parameters including molecular weight and branching, several morphological elements of a jacket compound also have important effects on the overall jacket performance. For a given set of jacket compounds with the same nominal MI and density values, there can be significant performance differences among the compounds depending on the prevailing difference in the polymer morphology. Understanding how given jacket properties are related to a specific morphological element enables one to enhance the jacket performance by incorporating the specific structural element.

3A. Tie molecules

Table 3 shows property comparisons of two HDPE jackets of nearly identical MI and density values and very similar MWD, therefore with comparable extrusion and shrinkage characteristics. By incorporating more tie molecules into HDPE-B as compared to HDPE-A, a significant enhancement in ESCR performance is achieved, i.e., Fo>500 hours for HDPE-B vs. Fo<300 hours for HDPE-A. While the difference in the amount of tie molecules between HDPE-A and HDPE-B did not alter the overall crystallinity and crystallite sizes (DSC data), this difference is enough to cause significant morphological changes critical to the toughness characteristics of the HDPE materials.

On the other hand, the morphological change as a result of the incorporation of more tie molecules into this HDPE jacket invariably leads to a modulus reduction of about 10%.

Table 3. Effect of tie molecules

Property	Unit	HDPE-A	HDPE-B
Tie molecules		less	more
Density	g/cm ³	0.955	0.955
Melting point	°C	129.2	128.8
Heat of fusion	J/g	205	193
ESCR, Fo	Hours	<300	>500
Flexural modulus	MPa	950	850
Abrasion	mg/100 cycle	15	15

3B. Higher-order structures

For semicrystalline polymers such as polyethylene, the second-order structural details, including average lamella layer thickness, average spherulite size and size distribution, bear important influences on key solid-state properties.

Table 4 compares three MDPE compounds, made from different base resins, but with similar final MI, density values and MWD. These three compounds are characterized by different second-order structural details, notably the apparent lamella thickness and spherulite size distribution characteristics as indicated in the table.

The three MDPE display qualitatively comparable modulus vs. toughness (ESCR)

characteristics as expected from their similar DSC endothermic behaviors, i.e., the first-order phase transitions. However, the higher-order morphological differences present among these three MDPE have led to the better combination of modulus vs. shrinkage balance for MDPE-B relative to PE-3.

Both MDPE-A and MDPE-B also show notable processability improvements (i.e., lower extrusion pressures) over PE-3 because of the differences in the base resin structures. This demonstrates that adjusting the higher-order structural details, while keeping compound MI and density unchanged, can help maximize the overall jacket performance. To this end, MDPE-B has been designed to improve the jacketing processability and modulus-shrinkage balance over PE-3 while retaining its other excellent properties.

Table 4. Property comparison of MDPE compounds of differing second-order structural elements

Property	Unit	PE-3	MDPE-A	MDPE-B
Ave. lamella thickness		smaller	inter-mediate	larger
Spherulite size distribution		broad	broad	narrow
MI	g/10 min	0.7	0.8	0.8
Density	g/cm ³	0.941	0.942	0.942
Melting point	°C	124.3	124.2	125.1
Heat of fusion	J/g	159	155	155
Yield strength	MPa	14.5	15.2	15.2
Flexural modulus	MPa	520	550	620
ESCR, Fo	Hours	> 2000	> 2000	> 2000
LTB	°C	< -75	< -75	< -75
Tan δ (E''/E') @ -48°C		0.045	0.038	0.035
Extrusion pressure	MPa	11.4	9.4	9.2
Shrinkage	%	1.5	1.4	1.0

The fundamental structure parameters being comparable, the higher-order morphological characteristics of a polymer can also affect its viscoelastic behavior. Figure 6 shows elastic modulus (E') and loss modulus (E'') as a function of temperature for the three MDPE listed in Table 4. While the three compounds have very similar elastic modulus-temperature relationships, they display noticeable differences in loss modulus (thus $\tan \delta$) particularly at very

low temperatures (PE-3 vs. MDPE-B). Slightly higher E' and lower E'' for MDPE-B vs. PE-3 at very low temperatures can make the former a better jacketing material particularly when cold-impact performance is an important concern.

Fig. 6a: Viscoelastic behavior: elastic modulus

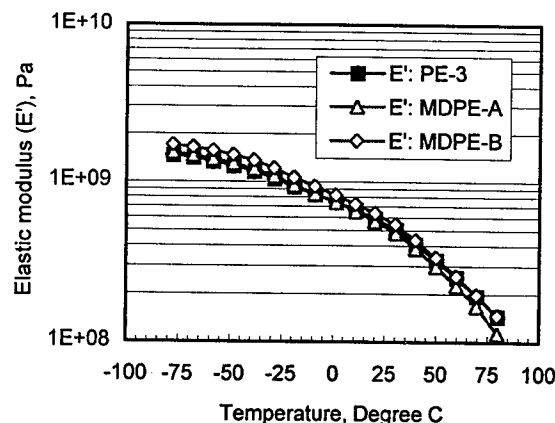
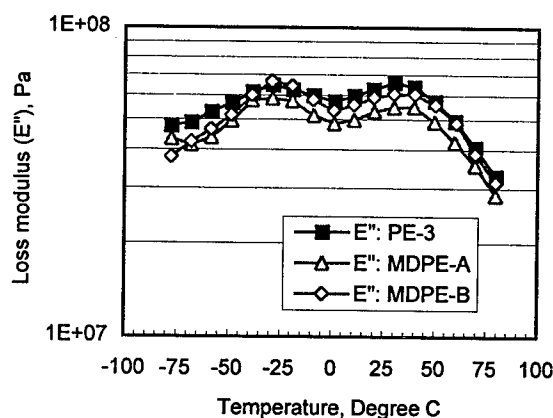


Fig. 6b: Viscoelastic behavior: loss modulus



4. Effect of polymer bivariant distributions of molecular weight and chain branching

While both molecular weight (or MI) and chain branching (or density) characteristics of a polyethylene resin control the overall jacket performance as discussed earlier, how the branches are positioned relative to any given macromolecular chain of the certain length or MW also affects the jacket's performance. In other words, selectively placing a specified amount of chain branches at the specific locale along those polymer chains with a specified length – the so-called bivariant distribution of MW vs. branching – has been found to be an

effective means to further optimize the product performance.

Union Carbide's Unipol Process for producing polyolefin resins is widely known for its capability of making a wide range of polymers with varying molecular structure characteristics. Using this process, we are able to achieve the polymer compositions with such bivariate distributions to provide the desired jacket properties and performance.

Table 5. Effect of bivariate MW vs. branching distribution

Property	Unit	PE-5	PE-6	Ref-HDPE (1)
MWD		broad	broader	-
Branching distribution across MW		flat profile	flatter profile	-
MI	g/10 min	2.5	2.3	1.7
Density	g/cm ³	0.952	0.952	0.954
ESCR, Fo	Hours	> 4000	> 4000	> 1000
Tensile strength	MPa	22	23	20
Elongation	%	800	900	800
Flexural modulus	MPa	760	830	850
Abrasion	mg/100 cycle	18	17	18 (2)

(1) Ref HDPE is a non-UCC sourced broad-MWD jacket; supplier's literature data are shown unless otherwise noted.

(2) measured value

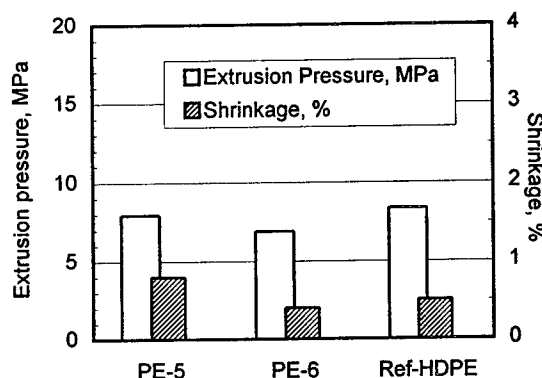
Two HDPE compounds (PE-5 and PE-6) have been developed using the specially designed Unipol process polymers. In comparison to those traditional polyethylene that usually show less branching at higher molecular weights as displayed by Fig. 1, PE-5 and PE-6 have distinct bivariate distribution characteristics (i.e., less dependency of branching on MW). Table 5 shows a property comparison of these two compounds. Figure 7 further shows the jacket processability and shrinkage comparisons.

As shown, between PE-5 and PE-6, they both have comparable physical properties and processability with superior stress crack resistance. The fact that PE-6 has slightly higher modulus but lower shrinkage relative to PE-5 is related to the difference between the two compounds in their bivariate distribution characteristics. This illustrates that through properly designing the bivariate distribution of branching vs. MWD for a jacket polymer

structure, one can also achieve notable enhancements in jacketing performance.

It is also interesting to note that PE-6 behaves very competitively relative to Ref-HDPE in jacket properties and performance as measured.

Fig. 7: Bivariate distribution effect - HDPE compounds



5. Optimization of Jacket modulus and shrinkage balance

It was mentioned earlier that modulus of a given jacket usually scales with post-extrusion shrinkage. Increased compound densities can lead to increased jacket shrinkage as well as higher modulus. While one may apply the "higher-order structure" effect as discussed earlier to achieve better balanced modulus vs. shrinkage performance, the ability to control compound modulus independently of the jacket shrinkage characteristics is of high value to the fiberoptic cable industry and end users.

Next generation jacketing compounds now offer such control. In these compounds, the polymer chains that are less susceptible to contributing to shrinkage are integrated with the chains that serve as the structural origin of moderate to high modulus. These compounds also takes into account the need to meet jacket extrudability and cold-impact requirements.

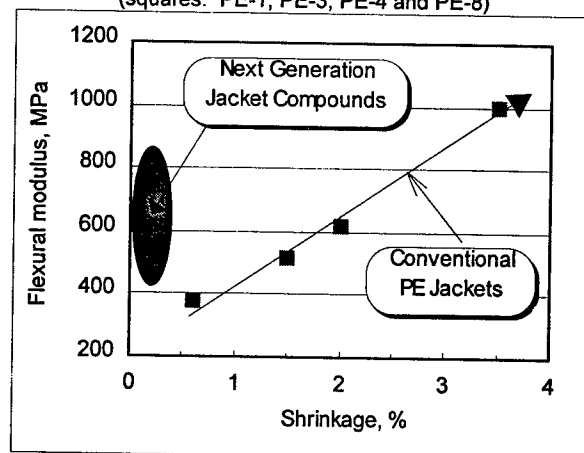
Table 6 compares two next generation jacket compounds with a commercial MDPE for flexural modulus in relation to wire extrusion and shrinkage characteristics. The performance advantages, i.e., lower shrinkage, easier processability and higher modulus, are clearly demonstrated.

Table 6. Next generation (NG) jacket compounds vs. MDPE

Property	Unit	PE-3	NG-A	NG-B
MI	g/10 min	0.7	0.7	0.9
Flexural modulus	MPa	520	600	670
Extrusion pressure	MPa	10	7	5.5
Shrinkage	%	1.5	<0.3	<0.3

The performance difference between the next generation jacketing compounds and traditional compounds is further illustrated in Figure 8, with the squares representing conventional compounds. The next generation compounds clearly overcome the undesirable modulus vs. shrinkage interrelationship inherent of today's polyethylene-based jackets. This will allow cable manufacturers to choose a jacket compound with the required modulus without tradeoffs in cable shrinkage.

Fig. 8: Modulus vs. shrinkage - next generation jacketing compounds vs. conventional PE compounds (squares: PE-1, PE-3, PE-4 and PE-8)



CONCLUSIONS

Polyethylene jacket performance is mainly affected by the polymer MW and crystallinity. Lower MW (or higher MI) and lower crystallinity (or lower densities) favor lower post-extrusion shrinkage; lower MW compounds too have better jacketing processability. The jacket toughness performance such as ESCR or cold impact may be enhanced by means of instituting tie molecules or other higher-order structural elements into the polymer. The overall performance of the jacketing compounds can be further enhanced by selecting appropriate

bivariant distribution of molecular weight vs. chain branching of the base resin polymer. Independent control of the material modulus while maintaining low jacket shrinkage can be achieved in the next generation jacketing compounds.

Using the understandings on polyethylene structure-property-performance relationships, we have developed several new jacketing compounds (both HDPE and MDPE grades) that offer cable manufacturers and end-users the enhanced performance characteristics of easy-processing, low-shrink and superior toughness.

ACKNOWLEDGEMENTS

The authors wish to thank Robert Mazet, Kris Knudson and Joe Adams for their able laboratory assistance, and Joe Smilek, Roger Brengel and Gene Westbrook for providing pilot plant support. We also thank Union Carbide for permission to publish the results.

Tong Chen received his BS and M.Eng. degrees in chemical engineering from Tianjin University and his Dr. of Science from MIT also in chemical engineering, all with a polymer major. He has been with Union Carbide since 1991 working first in the Polymer Materials Science Skill Center and presently in Wire and Cable as a research engineer. His current research effort focuses on new polymer material development for fiber optical cable applications.

Jim Leech is Technology Manager for Union Carbide's Telecommunications business. He has had over 25 years in polymer research and development, the last 23 at Union Carbide. He holds an M.S. in Chemistry (University of Pittsburgh) and an M.B.A. in Chemical Marketing (Fairleigh Dickinson University). He has been involved in PE product development since the late 1970s for applications ranging from injection molding to pressure pipe and wire and cable. He has served on the IWCS Board of Directors since 1995, as Chairman in 1997 and this year as Treasurer.

THE IMPACT OF CARBON BLACK MORPHOLOGY AND DISPERSION ON THE WEATHERABILITY OF POLYETHYLENE

Christine Van Bellingen¹, John V. Accorsi²

Cabot Corporation

¹Pepinster, Belgium ²Billerica, Massachusetts, USA

ABSTRACT

Carbon black is one of the most widely used and most effective ultraviolet (UV) light stabilizers for plastics applications. Several important segments of the plastics industry rely on carbon black for UV stabilization of weather-resistant products, including telecommunications and power cable jacketing, plastic pipes, geosynthetic membranes and agricultural films. Recent research at Cabot Corporation confirms that the quality of the dispersion of the carbon black in a plastic medium (i.e. polyethylene) is an important component of both the UV-resistance and mechanical properties of the finished plastic article. There is a significant body of research into the linkage between carbon black morphology, including particle size, and UV performance. There is also anecdotal evidence demonstrating the linkage between dispersion quality and overall weatherability. In this study, Cabot will demonstrate that incremental improvements of carbon black dispersion can positively influence the expected life of plastic articles. With industry standard carbon blacks as a reference point, Cabot documents the morphological considerations of UV energy absorption and presents laboratory data demonstrating the link between dispersion and weatherability as well as between morphology and weatherability.

INTRODUCTION

Carbon black (CB) is more than a colorant. In addition to its tinting power, electrical or filler action, it provides plastics with a long-term and low cost UV protection, stabilising polyolefins and other polymers against sunlight [1-4]. The UV protection property of CB is dependent on its morphology, loading and surface chemistry. However if the CB is poorly dispersed or diluted, its full benefit will not be realized.

These effects will be highlighted by comparative weathering results and UV absorption data obtained for low density polyethylene films.

1) Basic Information on Carbon Black

• Production

CB results from incomplete combustion or thermal cracking of a hydrocarbon raw material (figure 1). Nowadays almost all carbon black is manufactured by the *oil furnace process*: a highly aromatic feedstock is partially burned by atomization into a hot flame made of natural gas and preheated air, the reactor temperature reaching more than 1500°C. At the process end, *powder* ("fluffy") or *pelletized* carbon black is collected. The oil furnace process permits efficient control of end product physical and chemical properties.

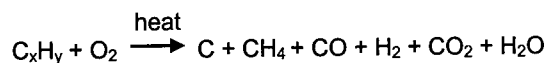


Figure 1: partial oxidation of aromatic hydrocarbons.

• Form

Carbon black is a particulate form of industrial carbon which exhibits a "*quasi-graphitic*" microstructure (figure 2). The manufacturing process leaves various forms of oxygenated groups on carbon black layer planes: mainly phenolic, quinolic and carboxyl chemisorbed complexes [5]. During the nucleation process (figure 3), three to four layers form *crystallites*, which combine to form *primary particles* which continue to grow into *aggregates*. *Agglomerates* are a dense collection of aggregates formed due to the small distances between them and the strong van der Waals forces present. CB dispersion into a polymer matrix will require the breaking of these links. An *aggregate* is *indivisible* and represents the carbon black "*base unit*", although a carbon black is often characterized by its *primary particle size*, as we will do further on.

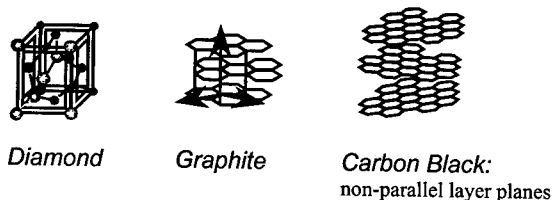


Figure 2: carbon black "quasi-graphitic" microstructure compared to the two regular crystalline forms of carbon (diamond and graphite).

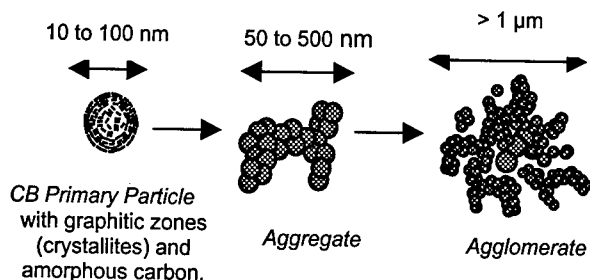


Figure 3: CB primary particles fuse together in the reactor and form aggregates and agglomerates.

2) Some Carbon Black Fundamental Characteristics (figure 4)

- **Particle size (nm):**
arithmetic mean of diameters of a sufficient number of primary particles of a carbon black grade. Diameters are determined by TEM (Transmission Electron Microscopy) measurements using ASTM D-3849.
- **Surface area (m²/g):**
specific surface area is determined by nitrogen adsorption capacity using the BET (Brunauer-Emmet-Teller) procedure. Small particles will confer a large surface area per unit weight.
- **Structure or DBP oil absorption (ml/100 g):**
the amount of DBP (di-butyl-phthalate) adsorbed on 100g of carbon black at a fixed torque value, according to ASTM D-2414. Structure or the DBP adsorbed is function of the aggregates void volumes and describes the degree to which the CB particles have fused together to form aggregates: a low structure black (low DBP) is made of few primary particles compactly fused together while a high structure black (high DBP) is made of many primary particles with considerable branching and chaining.

3) Polyethylene Degradation

Finished materials designed for external applications may degrade in use, with time. They are said to "weather" when their structure changes due to *light, heat, moisture* and *oxygen* contact. Materials like plastics absorb sunlight radiations and undergo photo-chemical reactions.

Oxidation occurs leading to an alteration of their colour, texture or composition resulting in impact loss, embrittlement, chalking or surface cracking. Out of the whole solar emission spectrum (range defined by CIE [6]), only the smallest part, the 290-400 nm UV region, is responsible for most of the polymer damage [7]. Photo-oxidation of polyethylene proceeds by a free radical chain mechanism in presence of oxygen: the ultraviolet light absorbed by the polyethylene provides sufficient energy to break key molecular bonds and generate free radicals that propagate to give *hydroperoxides*, compounds containing *hydroxyl, carbonyl and vinyl groups*, which also absorb UV radiation and undergo further degradative processes (i.e. Norrish type I and II reactions of the carbonyl group). As a result, succession of chain scissions and chain recombinations (cross-linking), including more fragile units, induces drastic physical degradations [1].

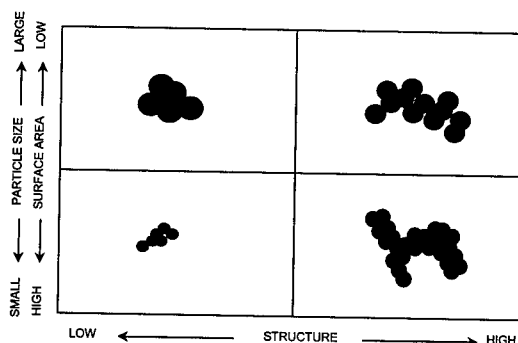


Figure 4: visualisation of carbon black particle size / surface area and structure.

EXPERIMENT

Polyethylene protection from UV degradation can be achieved by adding appropriate additives like antioxidants, typical UV stabilisers (i.e. HALS) or carbon black. Parallel to its colorant function, carbon black is known to act as a UV absorber and antioxidant [8, 9]: it offers the best UV protection for many materials, by absorbing / screening out damaging wavelengths, and by inhibiting photo-oxidation via its surface chemical properties. The following experimental data highlight morphology, dispersion and dilution influence on carbon black UV stabiliser role.

1) Influence of carbon black morphology, emphasis on particle size [experiment 1]

Several black pigmented LLDPE (linear low density polyethylene) films were submitted to an accelerated weathering test.

Material lifetimes versus particle sizes and loadings are shown. CB morphology influence on weathering performance is discussed.

• Sample preparation

Cast films of 75 μm thickness were made from LLDPE Mi0.5 with 1.5, 2.5 and 3.5% CB of particle size ranging from 15 to 60 nm. Masterbatches were first produced at 35% loading on a 30 mm twin-screw extruder, then diluted to the above % in a second extrusion step. CB main characteristics are detailed in Table 1. The films were exposed in a QUV accelerated weathering machine at 60°C using UVA-340 nm (*) fluorescent lamps (ASTM G53-95) with no condensation cycle and irradiance level of 1.25 W/m²@340 nm. (*) Sunlight simulation in the region of 295 to 400 nm with max. at 340 nm.

• Weathering results

Tensile properties were measured on an Instron 4204 per ASTM D882-9. Failure time was determined when % elongation at break reached 50% of the original value. Material lifetime is expressed as a function of CB particle size, at the same CB loading (figure 5) and for various CB loadings (figure 7). Clear LLDPE film was also tested (figure 6).

Table 1. CB characteristics. [Experiment 1]

particle size ASTM D-3849 (nm)	surface area BET / N ₂ ads. (m ² /g)	structure DBP abs. ASTM D-2414 (ml/100g)
63	30	72
50	41	125
24	78	72
23	79	102
18	120	114
15	252	68

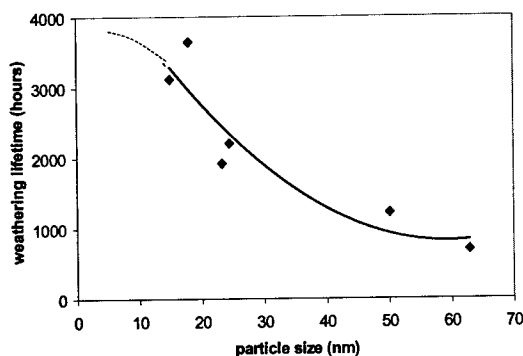


Figure 5. Influence of CB particle size - at same loading - on UV stability. (75 μm LLDPE films, 2.5% CB). [Experiment 1]

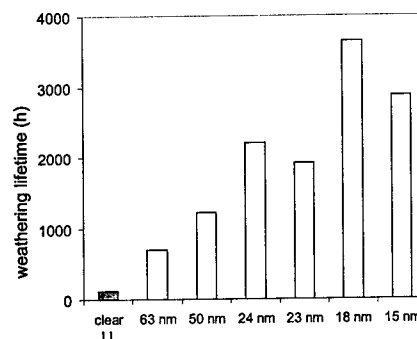


Figure 6. Weathering lifetime of clear LLDPE versus black LLDPE (75 μm , 2.5% CB). [Experiment 1].

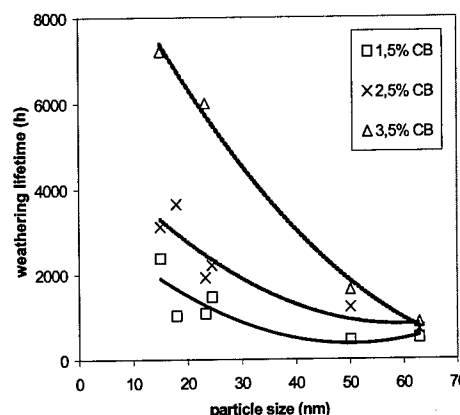


Figure 7. Influence of CB particle size - at different loadings - on UV stability. (75 μm LLDPE films, 1.5, 2.5% and 3.5% CB). [Experiment 1].

• Results discussion

Virgin LLDPE exhibits very poor weathering stability. CB addition strongly improves weathering performance (figures 5 and 6): LLDPE lifetimes are 6 to 30 times higher when 2.5% CB is added. Maximum performance was achieved with CB with particle size <20 nm and high structure.

The UV stability effectiveness of a carbon black increases with decreasing particle size (as already reported in [10]) with some comments:

- close particle size blacks (e.g. 23 and 24 nm) may be differentiated by their structure. Lower structure tends to provide slightly better UV protection [11] provided the CB's are equally well dispersed.
- very small particle size blacks (e.g. 15 nm) see their protection benefit tempered by the difficulty to disperse them completely.

The higher the CB loading, the better the UV protection. (figure 7)

- CB loading may be limited by physical properties of the compound or other considerations.

In a paper to be published by J.R. Wilson [11], a theoretical model is proposed which shows the 2-dimensional projected surface area of the CB aggregate is directly correlated with its ability to absorb light. Hence, *both particle size and structure* (to a lesser extent) are important parameters affecting UV protection. However both of these parameters also affect dispersion characteristics, so in practice the actual performance of the carbon black in the compound is dependent on a number of factors.

2) Influence of Carbon Black Dispersion

Choosing small particle size blacks is a must to reach good weathering performances. However, to get that total benefit, care must be taken to disperse them correctly in the polymer matrix. Dispersion quality impacts on final carbon black agglomerate size in the polymer:

- an optimal dispersion is one that evenly distributes carbon black throughout a polymer down to the smallest carbon black units, the aggregates,
- a poorer dispersion results in larger agglomerates (figure 3).

In the presence of agglomerates, UV light is more likely to be rather scattered than absorbed, and polymer UV degradation may start as CB screening protective effect is reduced. *Accelerated weathering tests* [experiments 2 and 3], *transmitted light measurements* [experiment 2] and COA (375 nm UV absorption coefficient) [experiment 4] have been carried out on well and deliberately badly (or less well) dispersed carbon blacks in low density polyethylene films. All other parameters were kept constant.

a) Effect of dispersion on weathering [Experiment 2]

• Film preparation

- Three different CB, of various particle sizes, were analysed: 60, 25 and 20 nm.
- 30 to 40% CB masterbatches were prepared on a Banbury BR 1.5 mixer: the different CB were incorporated into LDPE Mi7 with a slight and constant amount of lubricant (0.1% lubricant per 10% CB).
- 2.5% CB compounds were obtained by diluting the above masterbatches in LDPE Mi4 and extrusion in a Betol BK32 machine (L/D=30; single screw extruder with additional CTM mixing unit).
- 55 µm cast films were made on a semi-industrial Collin extruder (L/D=27; compression ratio 3:1; 210°C).

The deliberately under-dispersed (UD) samples

were obtained by reducing the Banbury mixing time and shear. **Table 2** summarises CB dispersion quality and films involved.

• Dispersion quality assessment

Via *Screen 100 mesh* (#) and *film* tests:

- The *screen 100 mesh* test consists of extruding 40 g of MB, slightly diluted in LDPE Mi2, through a Betol extruder ended with a 100 mesh screen. The number of particles trapped in the screen is then counted. Results are in "particle number".
- The *film* test consists of making a 50 µm blown LDPE Mi0.3 film containing 1% of CB. The film is then sufficiently translucent for analysis by transmission on a light cabinet. Spots are detected by touch and visually counted. Results are in "speks per gram".

• Accelerated weathering test

- Films were placed in an *ATLAS xenon arc machine* and exposed to the standard accelerated weathering norm for films ISO 4892-2, with conditions: ATLAS Ci65A machine, 6500 W xenon lamp, borosilicate-s / borosilicate-s filters (*), irradiance = 0.35 W/m²@340 nm, cycles = 102 minutes light followed by 18 minutes light + specimen spray, light cycle temperature = 65°C (BST), light cycle relative humidity = 65%. (*) Simulation of total solar emission spectrum, starting from 290 nm.
- Five rectangular 10 mm wide strips were submitted after exposure to a traction test using an Instron 4466 machine complying with ISO 527-3 norm. The percentage of elongation at break (% E at B) in function of weathering exposure time was recorded to trace material degradation.

• Results and discussion

- *Impact of dispersion on initial properties.*

Initial physical properties of a material are dependent from the sample preparation or sample "history" (resin type, loading, processing conditions, thickness...). Care was taken to work comparatively, to only link CB type and dispersion degree to weathering performance, all other parameters were similar.

Unaged materials' initial elongation at break (figures 8 & 9) appears to be directly dependent on dispersion quality or "global dispersion ranking" (table 2): the better the CB dispersion quality, the better the initial physical properties; the poorer the dispersion or the higher the UD gap within same CB particle size, the higher that physical property difference (table 2, figure 10).

Table 2. Dispersion results and ranking (UD= under-dispersed). Description of films involved in **experiment 2**.

CB Type	Screen Test 100#	Film Test	Global Dispersion Ranking	Dispersion Comparison by CB Type	Films Submitted To Weathering - identification -
<i>particle size</i>	<i>particle number</i>	<i>speks per gram</i>	<i>from best (1) to worst (6) - arbitrary scale -</i>	<i>UD gap compared to reference</i>	<i>LDPE 55µm 2.5% CB</i>
60nm	4	0.7	1	Reference = R	60nm
60nm "UD"	9	0.8	3	(3-1) → = R +2	60nm "UD"
25nm	6	7.2	4	Reference = R'	25nm
25nm "UD"	10	11	5	(5-4) → = R' +1	25nm little "UD"
20nm	5	0.5	2	Reference = R"	20nm
20nm "UD"	10	>20	6	(6-2) → = R" +4	20nm very "UD"

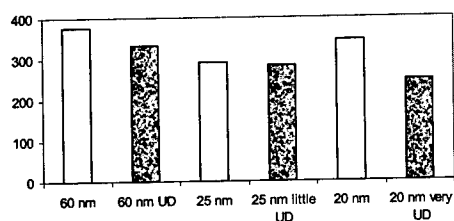


Figure 8. Initial % E at B of 55 µm LDPE films (2.5% CB). [Experiment 2].

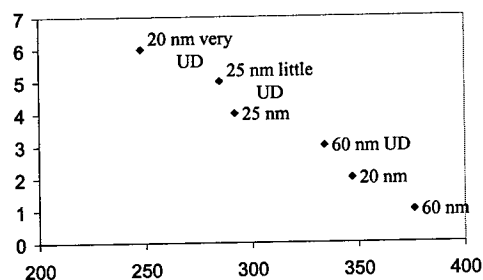


Figure 9. Dispersion quality ranking (1 = best dispersion, 6 = worst dispersion) in function of initial % E at B of films. [Experiment 2].

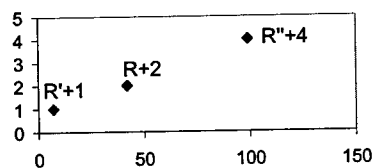


Figure 10. UD gap (within same CB particle size) in function of initial % E at B difference. [Experiment 2]

- Impact of dispersion on properties retention.

(figure 11) To make things objectively comparable, the initial mean % elongation at break has been indicated and a bold dotted line

has been drawn at half that value: the test end limit is set at 175% E at B (in accordance with CEN for agricultural films recommendation + safety margin). Weathering lifetimes: see figure 13. Magnification of weathered films: see figure 12. UD gap versus lifetime loss: see figure 14. Shorter weathering lifetimes are obtained with under-dispersed samples except for "25 nm" where UD gap is the smallest. The highest UD gap induces the highest lifetime difference.

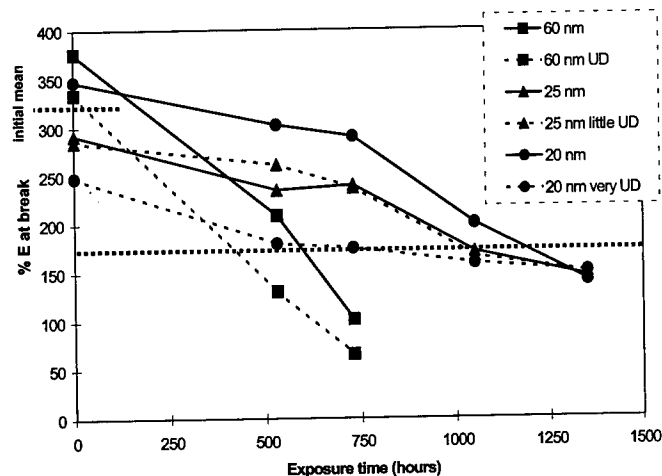


Figure 11. Dispersion influence on weathering stability - 55 µm LDPE films, 2.5% CB: Atlas xenon arc (ISO 4892-2 / ISO 527-3), % E at B in function of exposure time. [Experiment 2].

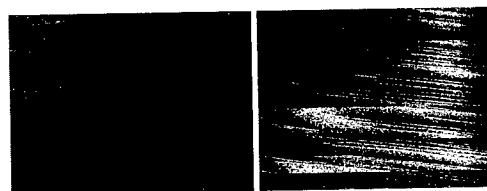


Figure 12. Magnification (15x) of weathered films - 800 hours ageing: left= 60 nm: right= 60 nm UD. [Experiment 2].

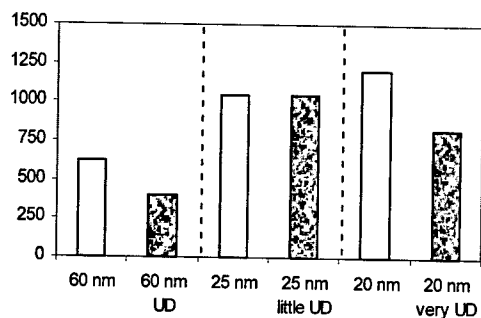


Figure 13. Film weathering lifetimes (hours) [Experiment 2].

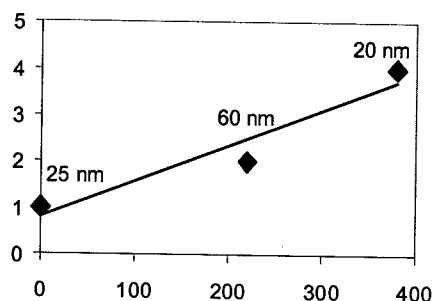


Figure 14. UD gap in function of lifetime loss (hours). [Experiment 2].

- Transmitted light study

Films have been placed between a powerful 100,000 lux light source and a luxmeter with detection in the visible range. The number of lux transmitted through the film is expressed in figures 15a, b. Light transmission effectiveness is correlated to weathering performances (figures 16a, b). These figures, as well as figure 11, spot the 2 different groups: the 60 nm and the 25, 20 nm. First group transmits more light, second group is more effective to trap it. Additionally, *the UD films transmit more light or absorb less, inducing worse UV stability, except the "25 nm" where UD gap is very low.* Initial visible light

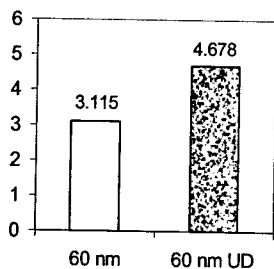


Figure 15a. Transmitted light (Lux). [Experiment 2].

transmission data are linked with UV stability data.

• Results Discussion

Weathering and opacity results are in line: the lower the transmission (higher the opacity), the better the UV stability. Both are function of CB type and %, film thickness, and on a microscopic scale, seem a function of dispersion. Poor dispersion induces lower opacity and poorer weathering performances. From what we may deduce dispersion and UV stability are directly dependent, with however a major impact of dispersion on initial physical properties.

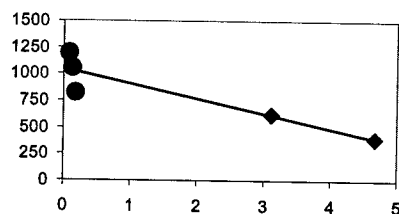


Figure 16a. Lifetime (hours) in function of transmitted light (Lux). [Experiment 2].

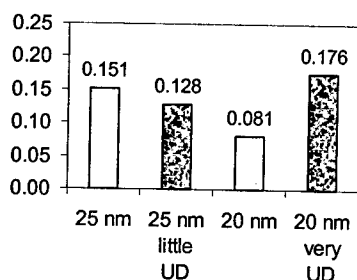


Figure 15b. Transmitted light (Lux). [Experiment 2].

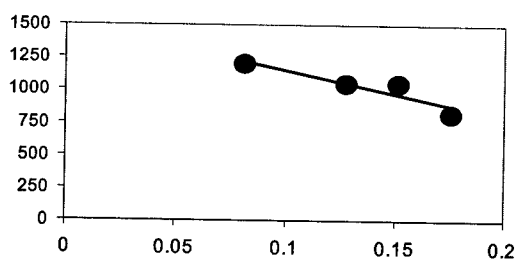


Figure 16b. Lifetime (hours) in function of transmitted light (Lux). (= Zoom of a 16a region). [Experiment 2].

b) Effect of dispersion on weathering
[Experiment 3]

• **Weathering results and discussion**

Table 3. Experiment 3 results. * bad dispersion

CB Particle size nm	Failure Time days to reach 50% retention
None	5
60	21
19	43
15	99
15	39*

Above film samples (1.5% CB) were prepared and tested as in **experiment 1**. The 15 nm CB sample which exhibited shorter than expected failure time was examined for dispersion quality. Thin sections (100 nm) were prepared using an RTE ultra-cryomicrotome then viewed at 50,000X magnification by Transmission Electron Microscope. Numerous agglomerates of CB were detected, as illustrated in **Figure 17**. The other film samples, examined in a similar manner, showed no such defects. *These results also clearly show the impact of bad dispersion on weathering performance of the LLDPE.*

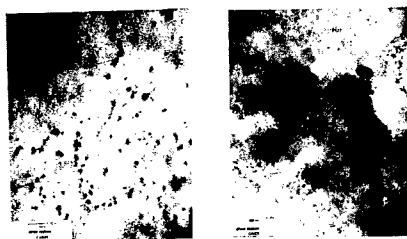


Figure 17. TEM images: *left*= 15 nm CB sample "good dispersion"; *right*= 15 nm CB sample "bad dispersion".

c) Effect of dispersion on COA
[Experiment 4]

• **Sample preparation**

Three CB with different primary particle sizes were compounded into LLDPE Mi20 resin on a laboratory size Kobelco internal batch mixer at three different loadings (**table 4**). Masterbatches (except 2.5%) were then letdown (i.e. diluted) in LLDPE Mi0.7 using the Kobelco mixer to 2.5% CB loading.

Table 4. Experiment 4 samples

CB particle size nm	CB masterbatch loading %
19	35, 20, 2.5
25	40, 20, 2.5
60	50, 20, 2.5

• **Coefficient Of Absorption**

COA was measured per ASTM D-3349*. This test measures the amount of light transmitted through a black pigmented film (typically less than 5% CB). Conversely, the amount of light *not* transmitted is absorbed, forming the basis for the calculation of the COA parameter (Beer's Law).

COA test procedure*:

1. Thin films are pressed to approximately 0.01mm.
2. Samples are exposed to UV light at 375 nm wavelength using a Beckman Model B spectrophotometer.
3. COA is calculated based on the absorbance value and sample thickness.
4. COA units are (1000 absorbance unit / meter).
5. ASTM D-3349 Least Significant Difference (within lab): $S_r = 24$.

• **Dispersion evaluation**

Dispersion was evaluated using image analysis. Six small pieces of each sample were pressed on a glass slide at 215°C for 5 minutes. The pressings were examined at 100X magnification. Agglomerates were sized and counted using Kontron Image Analysis software. Results are shown in **figures 18 and 19**.

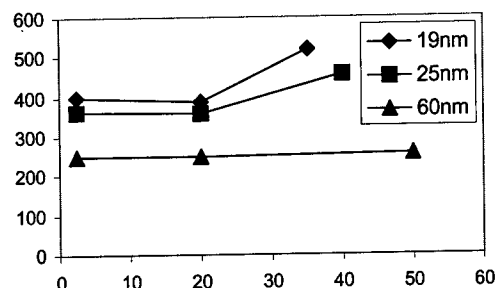


Figure 18. COA versus initial masterbatch loading (% CB) - for different CB particle sizes, at 2.5% CB in final letdowns. [Experiment 4]

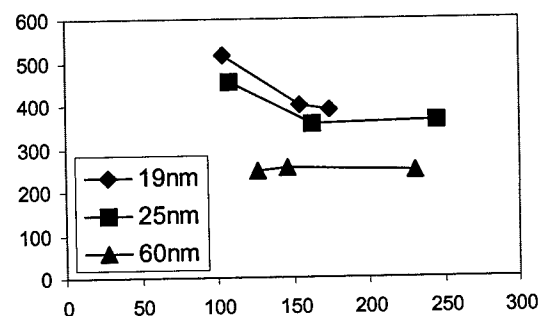


Figure 19. COA versus total agglomerates (# of pips), for different CB particle sizes at 2.5%. [Experiment 4]

Results discussion

COA shows a significant improvement at higher masterbatch loadings for the 19 nm and 25 nm CBs, presumably from better dispersion resulting from increased shear stress at higher masterbatch viscosity. The COA for the more easily dispersible 60 nm CB was flat over the range of loading studied. For the 19 nm and 25 nm CB the COA was highest for samples which had the fewest total agglomerates, an indicator of dispersion quality.

3) Influence of Carbon Black Dilution

• Experimental results

In experiment 2 dispersion study, films were made via the masterbatch and compound route: the cast film Collin extrusion line used did not mix and homogenize material sufficiently well to work directly with masterbatches. Without that last compounding step, films would have been very poorly diluted and full of fragile, less concentrated zones. We included however in the same study an additional film (19 nm CB) based on direct dilution. Figure 20 shows comparative weathering evolution for "good" and "poor" dilution quality.

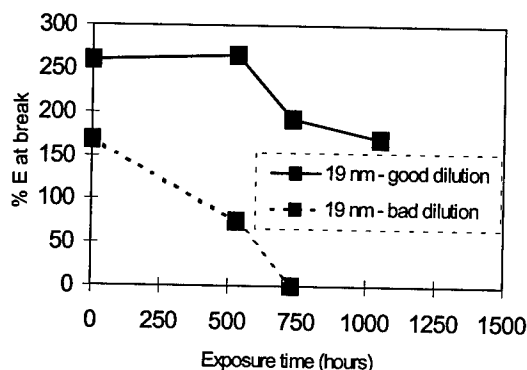


Figure 20. dilution influence on weathering stability - 55 µm LDPE films, 2.5% CB: Atlas xenon arc (ISO 4892-2 / ISO 527-3); % E at B in function of exposure time. [Experiment 2+].

• Discussion

A bad dilution can adversely affect polymer performance and weathering stability. The way to incorporate CB in a polymer matrix must be in total harmony with the equipment design and requirements or vice versa.

CONCLUSION

Black polymer UV resistance prediction is always a combination of several parameters, especially CB morphology, loading and dispersion quality. This study has demonstrated the very positive influence of small particle size CBs on

polyethylene weatherability as well as the importance of good dispersion and dilution quality to maintain that benefit. Although dispersion quality is mainly affecting the initial physical properties of the films, retention of those properties with ageing time has been shown: physical property drop appears to be directly dependent on the dispersion degree. These results were consolidated with light transmission data which show an increased transmission with poorly dispersed samples.

ACKNOWLEDGEMENTS

The authors wish to thank Baudouin Valange (Manager, Product Support and Development Plastics, CABOT, Belgium) and Tom MacMullin (Manager, Cable & Pipe, CABOT, Billerica) for their confidence and encouragements, as well as the many colleagues and other people who contributed and boosted the project at all levels.

REFERENCES

1. Wypych G., *Handbook of Material Weathering*, 2nd Edition, ChemTec Publishing, Canada 1995, 328-337, 505.
2. Christie R. M., *Pigments, Structures and Synthetic Procedures*, Oil & Colour Chemists Association, Scotland (1993), 9.
3. Davis A., Sims D., *Weathering of Polymers*, Applied Science Publishers, London (1983).
4. Bigger S. W., Delatycki O., *J. Mat. Sc.*, **24** (1989), 1946-1952.
5. Rivin D., Surface Properties of Carbon, *Rub. Chem. Tech.*, **44** (2) (04/1971), 307-343.
6. International Commission on Illumination, CIE 20 (1972) and 85 (1989).
7. Kockott D., Conditions techniques pour que les résultats du vieillissement accéléré soient exploitables dans la pratique, Atlas Publication (01/1993).
8. Mwila J., Miraftab M., Horrocks A. R., Effect of Carbon Black on the Oxidation of Polyolefins - an overview, *Pol. Deg. Stab.*, **44** (1994), 351-356.
9. Kovacs E., Wolkober Z., The Effect of the Chemical and Physical Properties of Carbon Black on the Thermal and Photooxidation of Polyethylene, *J. Pol. Sc., Symposium No 57* (1976), 171-180.
10. J. B. Howard and H. M. Gilroy, Natural and Artificial Weathering of Polyethylene, *Pol. Eng. Sc.*, **9** (4) (07/1969), 286-294.
11. Mingguang Liu, Internal Report, Bolton Institute, UK (1995).
12. Wilson, J.R., Cabot Internal Report, Billerica Technical Center (07/97).



Mrs Christine Van Bellinghen
CABOT Product Support and Development,
Plastics
rue Prévôchamps 78
B - 4860 Pepinster
Belgium.

Christine Van Bellinghen graduated as Industrial Engineer in Chemistry from the 'Institut des Industries de Fermentations – Institut Meurice Chimie', Brussels, in 1991. She worked for 'EXXON Chemical Belgium' on plasticizers development, then for 'MONSANTO Technical Center' in the ABS Department, where she was in charge of polymer colour / stability testing. She joined CABOT mid 1996, where she became 'Project Leader, Weathering Center' as part of the 'Films and UV Skill Center'. Her current work focusses on assessment of weathering stability of polymers.

DEVELOPMENT of a NEW UNI-MODAL FIBRE OPTIC MDPE JACKETING COMPOUND

Eric Brunner and Lars Westling

NOVA-BOREALIS Compounds LLC, Port Murray, NJ

ABSTRACT

A new medium density polyethylene (MDPE) in black compound form was needed to replace an existing commercial grade that was proving deficient to more recent Fibre Optic Cable jacketing designs.

By careful selection of the polyethylene (PE) manufacturing process, balancing resin parameters, and retention of key learnings from the existing grade, a successful compound was formulated which met and even surpassed the latest jacketing requirements.

The new material is known as MD-X for the purposes of this paper.

INTRODUCTION

A MDPE black compound (hereafter known as MD-1) as made by a Solution Process developed in Canada ⁽¹⁾ was introduced in the 1960's for copper cable telecommunication and low voltage power applications. It became the standard in the industry at that time due to being the only true synthesised linear MDPE. Its consistent properties proved superior to the Low Density Polyethylene (LDPE) and High Density Polyethylene (HDPE) melt blends available from other polyethylene suppliers at that time. With a base density of 0.935 g/cc, MD-1 placed in the middle of the American Society for Testing Materials (ASTM) density designation for MDPE grades (refer to the table following as referenced from the ASTM Standard D 1248) and offered an excellent balance of HDPE-like strength and temperature resistance while exhibiting low temperature flexibility and toughness properties typical of LDPE and the Linear Low Density Polyethylene (LLDPE) grades when they became available in the late 1970's.

Density Designations:

Type	Designation	Density Range
I	LD or LLD	0.910 to 0.925 [g/cc]
II	MD	0.926 to 0.940
III	HD	> 0.941

Moreover as Fibre Optic Cables were developed with some of their unique requirements such as concern about shrink-back, MD-1 was found to perform very satisfactorily. Shrink-back, which is more sensitive with increasing resin density, was not an issue with this material due to its very linear molecular chain configuration and minimal side chain branching which created very low melt stress retention of the polymer when exiting the die.

Reference: Graph 1 Shrink-back

However, with recent changes in fibre optic cable configurations and designs, MD-1 was found not to consistently meet new cable and compound tests which put more emphasis on the flexibility and toughness resistance of the material. A "twist test" which had been instituted to confirm the internal integrity of cable shielding and/or the jacketing compounds' resistance to shielding cut-through was being better met by competitive MDPE materials.

Clearly, a new MDPE compound was required for fibre optic cable jacketing use while the existing MD-1 would continue for copper cable and low voltage power applications where it functioned very well.

Within the Joint Venture organisation, one was then faced with the luxury of deciding which linear PE process to use in devising a new grade. Two uni-modal systems were available from the Domestic partner (ie the above mentioned Solution Process as well

as a Gas-Phase System) and from the European parent, one could choose between Gas-Phase Systems and a new and very interesting Bi-Modal Process ⁽²⁾.

In designing a resin, one must look at all the properties and decide how to match and balance these properties so as to best meet the requirements of the customers specification for the particular fibre optic cable jacket. Properties such as:

- Density
- Melt Index (MI)
- Molecular Weight Distribution
- Additive Levels
- Carbon Black
- Purity

The customer's requirements to consider are:

- Processing
- Shrink back
- Toughness
 - Abrasion
 - Cut-Through
- Die Lip Build-up (DLBU)
- Tensiles
- Heat Aged Tensiles
- Antioxidants
 - Levels
 - Types
 - Dispersion
- Carbon Black
 - Type
 - Level
 - Dispersion

The decision was made to use the domestic Gas Phase Process because it already was producing a "family" of Wire and Cable (W&C) grades and their known characteristics would greatly aid in the design of necessary resin parameters to yield the best balance of properties for MD-X.

DEVELOPMENT WORK

The first criteria to decide was density as it would have the greatest effect upon toughness which was the main deficiency of MD-1. Since MDPE is defined as having a resin density (in the case of black compounds, the base resin density is still the value to decide) of 0.926 to 0.940 g/cc (as per the ASTM Table shown on the

previous page), the set point would have to be selected at the lower end of this range to minimise stiffness (as measured by Flexural Modulus). Lowering the Modulus would result in improved flexibility and resiliency relative to the 0.935 g/cc density of MD-1.

Reference: Graph 2: Stiffness
Graph 3: Toughness

Moreover, shrink-back for a Gas-Phase grade was perceived to be more sensitive to density than the Solution Process.

Reference: Graph 4. Shrink-back

In terms of processing viscosity, the measurable property Melt Index (or Melt Flow Rate measured at 190°C and 2.16 kg as per ASTM D1238) is generally required to be < 1.0 dg/min to ensure achievement of the resin properties specified in various specifications.

As an aside, Bi-Modal resins will tend to have MI values above 1.0 which in no way infers that they cannot meet physical properties of Uni-Modal < 1.0 MI grades.

By the correct selection of resin manufacturing systems, one can ensure that choosing a flow rate (MI) in the upper quartile of the < 1.0 requirement for uni-modal grades, will allow processing ease while still achieving the final jacketing product properties.

Gas-Phase Processes do not lend themselves to any great variety of Molecular Weight Distribution (MWD), which when "narrowed" further increases toughness. However, within the "family" of Wire and Cable resins being made on the particular system used, it was expected that candidate MD-X would benefit from the inherent MWD available to further enhance its resiliency.

The additive levels of antioxidants, anti-die drool, and carbon black as well as the very important aspects of type, and dispersion uniformity of these additives, were done as based upon the many years of experience making MD-1 so no deficiencies were expected.

Purity and consistency were also to be controlled to the manufacturing standards of

the current family of W&C grades being made in the Gas Phase plant.

RESULTS

Numerous versions of candidate MD-X were made and tested. The basic parameters for the base resin were selected as:

Density: 0.927 g/cc
Melt Index: 0.75 dg/min

Plaque tensiles easily met requirements. Heat aged tensiles (100°C exposure for either 48 hours or 7 days and then tested to ensure exceeding 85% retention of the normal plaque tensiles) were also satisfactory. Data indicates that lowering the density improves meeting the retention standard.

Reference: Graph 5 Heat Ageing

The resin was compounded black using the same facilities as used for MD-1. Production-sized batches were then tested to ensure that all resin properties complied with known industry specifications and confirmed to be better than MD-1 for fibre optic applications. MD-X was then extruded in a customer's facility side-by-side with MD-1 to make equivalent fibre optic cables of a variety of types and sizes that would be the most sensitive and demanding to compound characteristics.

Processing ease and consistency were similar to the high standards of MD-1 as was expected. DLBU was also not an issue.

Tests were then conducted on the jackets of these finished cables with specific emphasis on toughness-type tests such as torsional twisting to study how well the jacket material would resist penetration and cut-through by the internal corrugated steel core along its spiral seam. While MD-1 would exhibit some undesirable failures (ie internal penetration of the steel seam through the jacketing thickness) as it had done previously in multi-twist orientations, MD-X would not allow any internal piercing. In fact, the degree of twisting had to be increased significantly beyond the customer's specification before any failures would occur.

CONCLUSIONS

By careful selection of an uni-modal polyethylene manufacturing process, choosing correct resin parameters and making use of past MDPE experience and systems, a successful MDPE Jacketing compound for Fibre Optic Jacketing has been created.

ACKNOWLEDGEMENTS

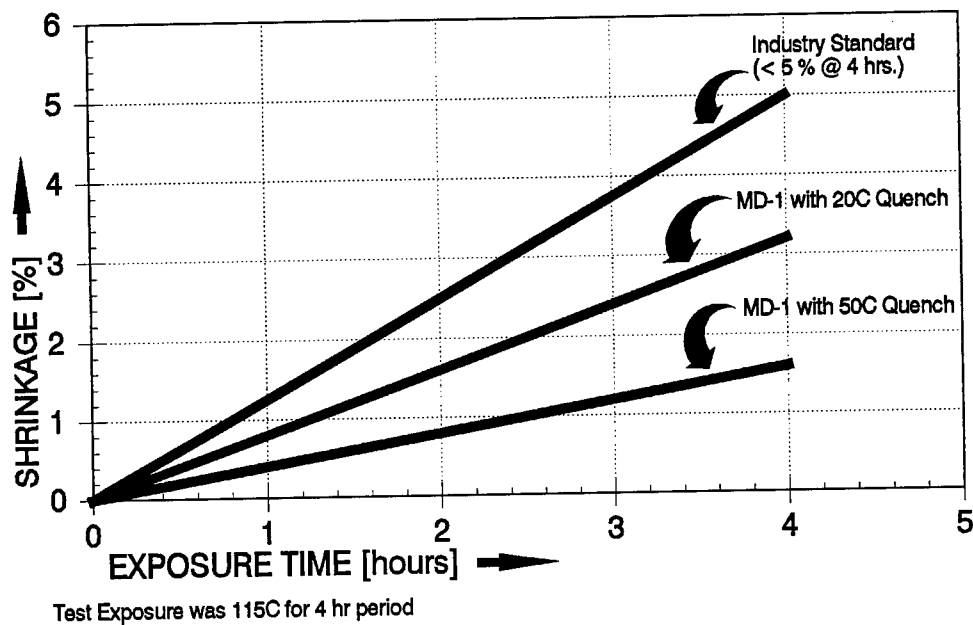
The authors would like express their appreciation for assistance to members of the NOVA Chemicals Moore and St. Clair River Works PE Plants in Sarnia, Ontario, the NOVA Chemicals Technical Service Centre in Calgary, Alberta, the Borealis Skills Centre in Stenungsund, Sweden and the NOVA-BOREALIS Port Murray, NJ Technical Centre.

REFERENCES

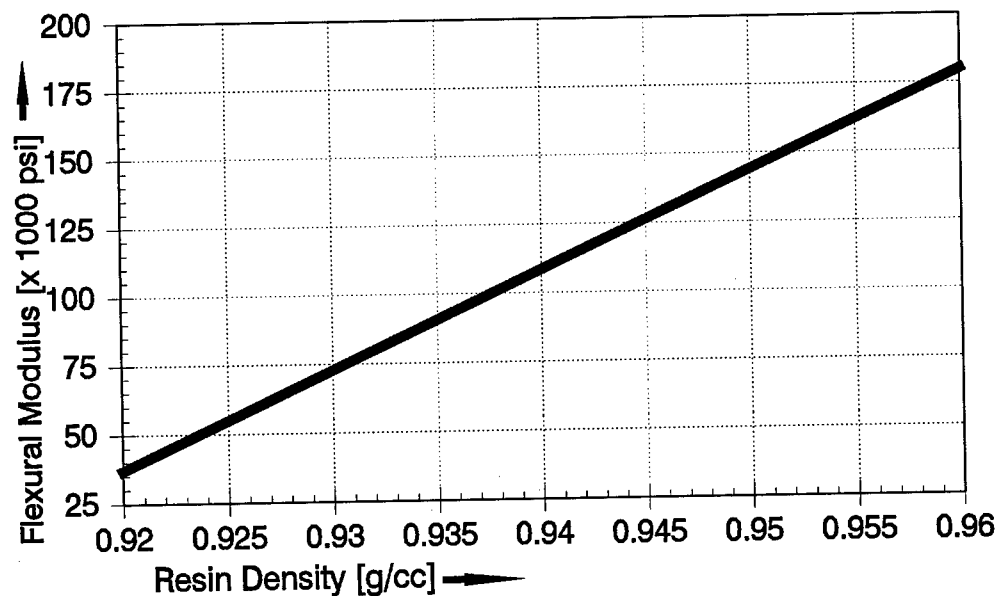
1. Houston, AJ, Monro, HAB, O'Brien, ET, DuPont Canada, "Intermediate and Low Density Low-Pressure Polyethylenes-Their Properties and Applications in the Wire and Cable Industry", IWCS Proceedings 1963
2. Rogestedt, Laila and Martinsson, Hans-Bertil, Borealis AB, "A New Generation Polyethylene Resin for Cable Jacketing Applications", IWCS Proceedings 1997

GRAPH 1: Cable Shrink-Back Data:

For grade MD-1 at two water quench temperatures

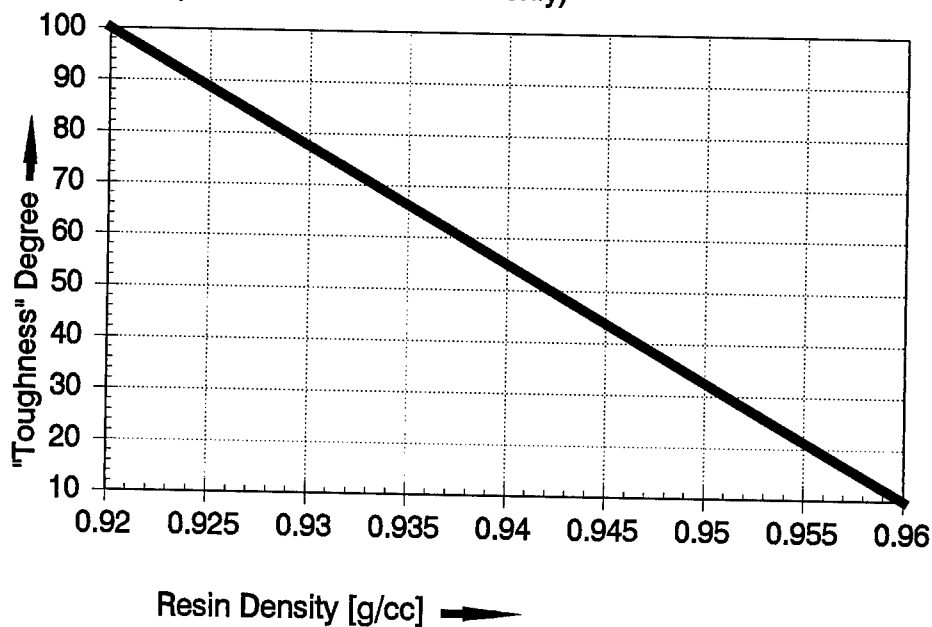


GRAPH 2: Stiffness Relationship vs. Resin Density (Flexural Modulus as per ASTM Procedure D 790 Method 1)

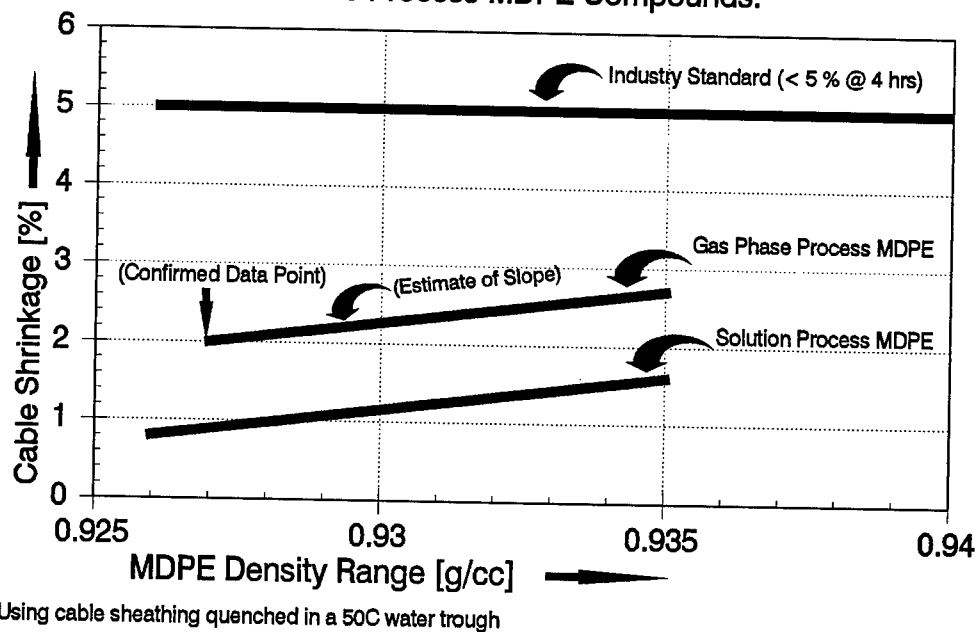


Please note that data is for resins in natural form, not compounded black

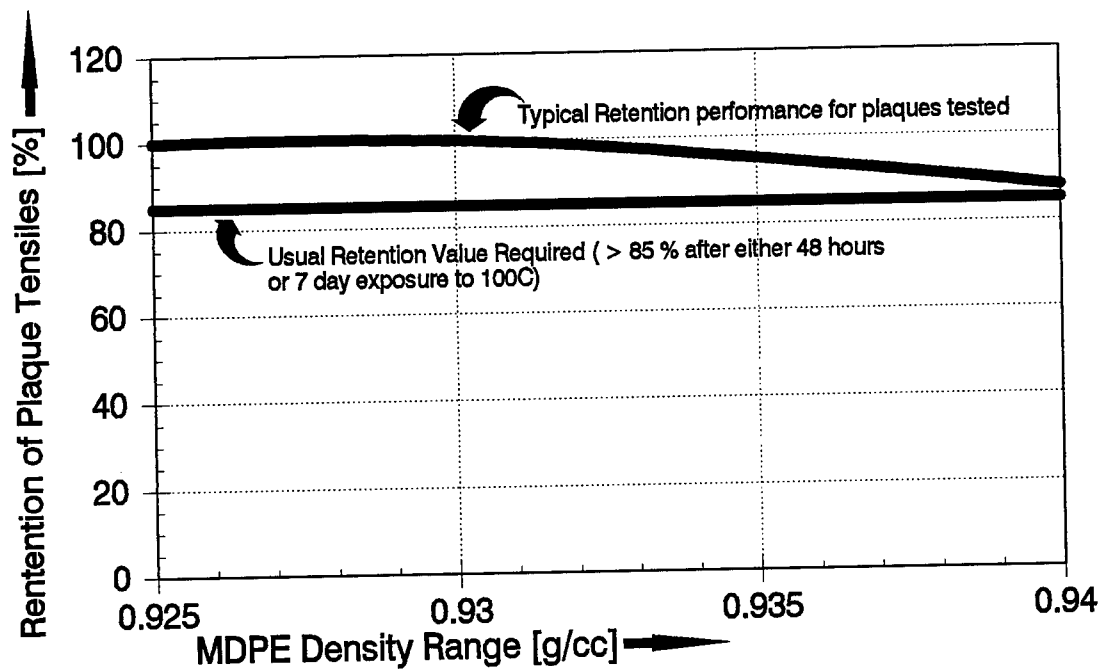
GRAPH 3: "Toughness" Relationship with Density
(use as a trend indicator only)



GRAPH 4: Shrink-Back Tendencies for Resin Types
Showing differences between Solution and Gas Phase Process MDPE Compounds.



GRAPH 5: Heat Aged PlaqueTensile Retention
Showing sensitivity to resin density increase.



SPEAKER BIOGRAPHY



ERIC BRUNNER

NOVA-BOREALIS Compounds LLC,
176 Thomas Road,
Port Murray, NJ 07865

Eric Brunner has been associated with Wire & Cable plastic materials for many years, beginning with DuPont Canada's Linear Polyethylene Division and continuing through its acquisition by NOVA Chemicals of Calgary, Alberta. He has a Bachelors Degree in Applied Science (Mechanical Engineering) from the University of British Columbia at Vancouver, Canada and currently is a Senior Products Engineer with the NOVA-BOREALIS Joint Venture specialising in Telecom applications involving SCLAIR®, NOVAPOL®, Borealis, BORSTAR® and NOVA-BOREALIS resins and compounds.

CO-AUTHOR BIOGRAPHY

Lars Westling is the Technical Centre Manager for NOVA-BOREALIS Compounds LLC. He received his Masters of Science Degree in Chemical Engineering from Chalmers University in Gothenburg, Sweden in 1979 and after graduation, was initially involved in the Explosives Industry, which resulted in one patent. Subsequently he began working in the R & D organisations of Borealis / Neste / Unifos in which he specialised in Moulding, Film and Wire & Cable applications. He left Europe 5 years ago for what is now the NOVA-BOREALIS Joint Venture organisation in the US.

THERMOPLASTIC POLYURETHANE MATERIALS FOR CABLE JACKETING

Jeffrey L. DeGross

BASF Corporation, Wyandotte, Michigan

ABSTRACT

Polyurethane offers many advantages as a cable jacketing material, including excellent abrasion resistance, very good mechanical properties, and outstanding resistance to fuels, oils and many chemicals. These properties are especially useful in very adverse environments such as those experienced by cables used in ocean floor oil exploration, vehicle anti-lock braking systems, surface mining applications, robotics control cable sheathing, and power cables used at construction sites.

In addition, these thermoplastic polyurethanes or TPUs as they are commonly referred to, exhibit excellent cold temperature properties for applications in Alaska or Scandinavian countries. The high elasticity of TPU products is also maintained over a broad temperature range and makes it a very practical product for cable applications in a variety of temperature environments.

TPU characteristics are similar to cross-linked elastomers, though polyurethanes are thermoplastic and are thus processed by conventional extrusion means.

By employing self-extinguishing additives, several types of flame-resistant TPUs are now common in the market. The additives employed are typically high molecular weight halogen-containing polymers found in many thermoplastics. Lately however, due to environmental pressures, especially in Europe, some new non-halogen flame resistant grades are appearing on the market.

The general properties of TPU are discussed. In addition, there is a discussion of the features and benefits of the different types of flame-resistant TPU products, including the new non-halogenated materials and what these materials can offer today's cable market.

INTRODUCTION

TPU materials are preferred in wire and cable applications where protection of the primary insulation from environmental exposure, low temperatures, rough handling, and physical abuse is the norm. For example, TPU is utilized in applications such as mining cables, automotive electrical cables, cabling for train systems, oceanographic exploration and research, seismic bundles for detection or disposal of mines, towed array cables for noise generating decoys, and oil exploration. All these applications benefit from the features of TPU materials. These are: high tensile and tear properties, low temperature flexibility down to -50°C, superior abrasion and puncture resistance as well as resistance to microbial attack, fungus, and ozone.

Other applications in the computer industry, e.g. robotics control cables, coaxial TV cables, and mag-lev train power cables, all take advantage of TPU's cut resistance and flexibility. Applications such as power cables for hand held power tools, medical lead wires, and marine telephone cables utilize TPU due to the high replacement costs of these cables. TPU extends the useful life of the finished product, thus reducing and even eliminating the need for replacement.

One of the newer applications for TPU, which takes advantage of all the benefits TPU has to offer, is the wheel speed sensor cable for the ABS brake systems on cars and trucks. Additionally, some fiber optic cable jacketing utilize TPU because it helps maintain signal strength by protecting the filaments from the external environment.

The important properties of TPU for wire and cable applications are discussed. Additionally, the properties of flame retardant TPU grades, including those of some newer developments, are shown.

CHEMISTRY OF TPU

Thermoplastic polyurethanes are produced via poly-addition reaction of di-isocyanates with polydiols and short chain diol "chain extenders" such as 1,4-butane diol. The reaction of an isocyanate with one of the hydroxyl groups of either of the described diols yields the urethane link as depicted in Fig. 1.

Typically, TPU manufacturers produce grades utilizing polyether and polyester polydiols, and thus the generic term polyester TPU or polyether TPU. Additionally, by varying the ratio of di-isocyanate to diol, polymers of similar chemistry but of differing hardness and therefore stiffness are obtained. Since the di-isocyanate, which is typically diphenyl methane di-isocyanate or MDI as it is also known, can react with either the polydiol or the short diol chain extender, the TPU molecule is "segmented". Figure 2 is a schematic representation of TPU depicting that it is made up of such soft and hard segments. The soft segment of the TPU molecule is the long chain polyester or polyether diol reaction product with MDI while the hard segment is the reaction product of MDI with the short chain diol chain extender. Typically, there are "islands" of repeating hard segments interspersed throughout the TPU polymer molecule resulting in a crystalline phase. Again, the higher the ratio of hard segment to soft segments, the harder the TPU grade.

Because the di-isocyanates and diols are linear in structure, a linear polymer results without interchain cross-linking and so, TPUs are indeed thermoplastic and can be processed via typical injection molding or extrusion. At processing temperatures, the urethane link reversibly disassociates and as such, care must be taken to remove moisture from the material. Pre-drying the material prior to processing is sufficient to prevent the hydroxyl group of a water molecule from reacting with the now "free NCO" thereby acting as a chain terminator, thus reducing molecular weight and mechanical properties.

TPU PROPERTIES

Commercial TPU products are available within a hardness range of around 75A on the shore A scale for softer grades and 80 shore D for the harder grades. In addition, by using plasticizers,

grades of TPU are available down to around 60A. Figure 3 shows how TPU compares in hardness with the typical elastomers and thermoplastic materials in a general sense, and shows the overlap of the various hardness scales. For example, individual materials within the family of commercial elastomers, including rubber, have hardnesses within a range of about 20A on the low or soft end of the hardness spectrum, and about 75D on the hard end. Thermoplastics exist within a range starting at around 55D and up. TPU is of course, considered one of the elastomers and as can be seen from this graphic depiction, exists on the higher end of the hardness range for the elastomer materials. As such, TPUs have relatively high tensile properties and very good load bearing capability compared to the softer elastomers. TPUs, however, maintain many of the attributes of the softer elastomers, especially low temperature flexibility. This combination of high mechanical properties and excellent low temperature flexibility makes TPU very useful for cable applications in very cold climates.

Fig. 4 is a similar depiction with more detail and includes familiar elastomer and thermoplastic materials for comparison.

A. Abrasion Resistance

TPUs are noted for outstanding abrasion resistance compared to other elastomers and thermoplastics. Table 1 is a comparison of the typical abrasion resistance of TPU and some other common materials. Along with cold temperature flexibility and grease, oil, and chemical resistance, it is this outstanding feature of TPU that makes it attractive for wire and cable applications. TPU is utilized as jacket material in robotics and other high-speed machinery as well as in the construction industry because of its excellent wear resistance as implied by the abrasion values shown here.

B. Mechanical Properties

Table 2 shows typical mechanical properties of wire and cable grade, standard TPUs (non-flame retardant). For comparison purposes, properties for both polyester and polyether TPU are shown. Due to higher elasticity and ease of processing, TPU cables are typically produced from TPU grades having hardness around 85 shore A. Specific gravity of ester TPUs are slightly higher than ether grades, but still considerably less than PVC. Also noteworthy is the fairly high ultimate tensile strength of TPU, around 40

N/mm². This property, combined with excellent flexibility as evidenced by the ultimate elongation value of around 550%, are indicative of the good combination of high mechanical properties and flexibility offered by these materials. Abrasion values shown here differ from the previous slide as they are measured via the 'DIN' method. TPUs also have very high tear strengths, as well as cut resistance, with esters slightly better than ethers. Esters also have better compression set properties at elevated temperatures. Compression set of TPU is, of course, less than what would be expected of cross-linked elastomers like rubber.

Table 3 is a comparison of TPU mechanical properties vs. two materials commonly used for wire and cable, PVC and rubber. As shown by this data, TPU exhibits superior properties compared to these materials in areas of interest to the wire and cable industry. TPUs have better tensile and tear properties and, of course, much better abrasion resistance compared with these materials.

C. Fluid Resistance

TPU has very good resistance to greases and oils, fuels, and some solvents as well. Table 4 is a comparison of TPU vs. PVC and Rubber exposed to common fluids and test fuels. TPU jacketed cables can, as seen by this chart, be in contact with mineral and hydraulic oils, and fuels. On the other hand, TPU cannot be used in highly acidic environments or in the presence of strong solvents.

D. Thermal Properties

Obviously important to the wire industry is the ability of the jacket or insulating material to withstand elevated or very cold temperatures. The insulating material can either soften prematurely at high temperature, or become too brittle and unable to withstand repeated flexing outdoors in cold weather. Based on the following information, TPU materials have found acceptance within a wide temperature range of -50°C to +90°C.

When considering the high temperature end of the stated range, TPU of course is a thermoplastic material and behaves as such at elevated temperatures. Above the plasticizing temperature, TPU flows within a typically narrow range¹. TPU cables, therefore, must not come into contact with anything hot (ca. 160-170 °C).

In the 80 – 90°C range however, TPU does not noticeably flow and is therefore useful as a jacket material with continuous exposure at or below this temperature. Wire grade TPUs can withstand intermittent exposure up to 140°C. Fig. 5 is an Arrhenius plot developed to indicate the lifetime of TPU materials when exposed to elevated temperatures utilizing defined failure or end criteria of 50% of original ultimate tensile strength. Using this criterion, and targeting 20,000 hrs. lifetime, the maximum long-term temperature exposure for the polyether TPU is around 90°C.

The low temperature flexibility of TPU materials down to temperatures as low as -50°C, allows its utilization as a jacket material for such applications as surface mining cables. As a comparison, even the weather-resistant, chlorinated synthetic rubber compounds are rated to just -25°C.² To illustrate this, the torsional modulus of wire grade TPU vs. temperature is shown in fig. 6. Both ester and ether TPUs show flexibility at very low temperatures. Additionally, Table 5 showing impact resistance, is another demonstration of the cold temperature properties for TPU products. As shown in Table 5, TPU products do not break when impact tested (unnotched) down to a temperature of -60°C. When tested via the notched impact test, ester TPU exhibited no break down to -40°C, while the polyether type exhibits no break down to -50°C.³ The superior low temperature flexibility is yet another advantage of polyether TPUs for wire and cable applications compared with ester based TPU.

When considering the choice of ether-based TPU vs. ester for wire and cable applications, another big advantage for ether TPU is the superior hydrolysis resistance. Fig. 7 is another Arrhenius plot, this time comparing the hydrolysis resistance of ester and ether TPU totally immersed in water. Again, using the end criteria as time necessary to reach 50% of original tensile strength, polyether TPU would last 20,000 hours at 72 °C. On the other hand, hydrolytically stabilized Polyester TPU would reach the end criterion at just 54 °C.

E. Environmental Exposure

Polyether TPUs are very resistant to microbial attack and fungus while polyester TPUs are not, another advantage of polyether grades for typical wire and cable applications.

All TPUs are extremely resistant to ozone, showing no cracks when exposed to the ASTM D1149 test procedure for ozone exposure. Exposure to UV light, on the other hand, is a different situation as TPU will discolor (yellow) after exposure to UV for extended periods. The use of color concentrates improves this greatly, the darker the color the more effective the UV resistance. For the most extreme exposure applications, TPU suppliers offer UV stabilized grades to the wire and cable industry and such grades are widely used. QUV and Xenon Weatherometer data are typically available from TPU producers for their stabilized grades for those interested in details. Because there are several types of stabilizer mechanisms available, making general statements in regards to UV resistance for TPU grades is difficult. Consult your supplier of TPU material for specific information.

F. Electrical Properties of TPU

Table 6 shows the typical electrical properties of TPU materials used in wire and cable applications. Also included is the data for a fire retardant grade. The properties of fire retardant TPU will be discussed later in detail. With respect to electrical insulation, the dielectric loss and surface resistance are important characteristics. The surface resistance of TPU is not as high as PVC or rubber materials, however, values are still in the range of 10^{10} - 10^{12} ohm. TPUs are relatively lossy compared to most materials used in wire and cable applications but this does not preclude the use of TPU as insulation for low or medium voltage cables (<1kV)⁴. The distinct property advantages of TPU typically outweigh the negligible dielectric loss.

FLAME RETARDANT TPU MATERIALS

By employing self-extinguishing additives, several types of flame-resistant TPUs are now common in the market. The additives employed are typically high molecular weight halogen-containing polymers found in many thermoplastics. Lately however, due to environmental pressures, especially in Europe, some new non-halogen flame resistant grades are appearing on the market.

TPU is considered an engineering material having very high mechanical and other properties as shown. When TPU materials are

required to meet flame-retardant standards such as UL94 (or UL VW-1 for TPU jacketed cables), the material and the cable need to be able to comply with these conditions without a very large decrease in the properties that make TPU the material of choice to start with.

A. Halogenated Flame Retardant TPU

Halogen-containing flame retardant (FR) TPU grades have been on the market for several years. As mentioned, new development in the area of halogenated flame retardant TPU has been slowed by the environmental pressures in European markets. As such, most of the new development is with non-halogenated FR TPU. This is not the case in North America, however, where use of halogen-containing FR TPU continues. In fact, BASF is presently developing, and plans to market by the start of the next year, new formulations for halogen containing, flame retardant polyether-based TPU which have an excellent combination of flame resistance and mechanical properties. At the time of this writing, only preliminary data for these new formulations are available for comparison and this is shown in Tables 7 and 8.

Table 7 shows the basic mechanical properties of three new FR formulations, two 85A and one 95A hardness. These are compared with a standard 85A TPU and a competitive, halogen-containing FR TPU product being marketed presently. Again, the objective is to develop grades that maintain very TPU-like properties and the results shown in Table 7 appear to be promising, with only small variations from standard product observed. The commercially available competitive product is shown as a benchmark. The difference in properties for this grade compared with a standard TPU is, however, indicative of what can be expected with present technology.

Table 8 continues the same comparison, this time including tear, abrasion, and combustion data as given by the UL-94 flame rating and the limited oxygen index (LOI) values. The significant decrease in the abrasion resistance for flame retardant grades of TPU is noteworthy, especially for the competitive product. It is the objective of our recent development to minimize this decrease and, as shown in Table 8, the preliminary results are again very positive. Abrasion loss is higher for the new formulations compared with standard TPU, but an improvement compared with the competitive

product is seen. Additionally, all these products, despite the difference from standard TPU, still have very good abrasion resistance properties compared with other materials.

The UL94 flame rating is the result of a flame test where the value V0 or V2 is an index indicative of certain burning time and flaming drip criteria. V0 is the index indicating the highest level of flame resistance per the UL94 test. UL 94 HB is a similar test, but the specimens are mounted in a horizontal versus vertical position. Therefore, a 'V' rating is more difficult to obtain than the 'HB' rating. The limited oxygen index indicates how much of an oxygen-enriched atmosphere is necessary for a flame-retardant material to sustain a flame for a particular distance or time period.

One of the two new 85A formulations is rated UL-94 V0 as is the competitive product. This is significantly improved over the standard TPU material which has only a UL-94 HB rating. This test is particularly sensitive to the thickness of the test strip. In fact, UL flame ratings are given at a particular thickness and typically, the thinner the gage of the test strip, the more difficult it is to obtain a 'V0' rating. The sample thickness for all materials shown in Table 8 was just .020" (0.5mm).

The two formulations for the new 85A FR TPU products differ in the amount of flame retardant additives and therefore flame rating. This is evidenced not only by the difference in UL 94 rating, but also by the difference in the LOI; 25% for the first formulation and 30% for the second. This would have an impact on the design of a cable intended to pass UL VW-1 and so it is important to have both the UL-94 rating and the oxygen index value when designing a cable requiring flame retardant properties.

Future work is intended to compare the new halogenated FR grades with other standard TPU physical properties, especially with regard to elevated temperature aging, cold flexibility, and fuel and oil resistance.

B. Non-Halogenated Flame Retardant TPU

There is a great deal of development ongoing in the area of non-halogenated flame-retardant TPU materials. As stated previously, European environmental pressure has increased the interest in such materials. The key is finding a balance between cost, properties retention, and

flame resistance. BASF has introduced a non-halogenated TPU grade to the worldwide market that meets the German VDE standards for mechanical properties and has a UL-94 V2 rating at .030" thickness. In addition to this material, which is a nominal 85A, polyether based material, several other new formulations are being developed for markets here in North America with the objective to produce a grade having a V0 rating at .030". Along with this 'FHF' grade, (for flame retardant, halogen free), some TPU suppliers, including BASF, also offer plasticized grades of TPU that have the unique combination of being halogen free and translucent. The 'FHF' types (as well as the halogenated) employ inorganic additives that make the material entirely opaque. Conversely, these plasticized grades do not contain inorganic flame retardant additives and maintain a measure of clarity like natural TPU.

Tables 9 and 10 shows a comparison of the mechanical properties for these commercially available non-halogenated TPUs. The mechanical properties are compared again with standard 85A TPU and here, there is more of a properties difference than shown before with the halogenated FR materials. Additionally, a V0 flame rating at thin gages is not available and is the emphasis for future work in this area. Obviously the objective is to gain a V0 rating without too much of a decrease in TPU properties, however, the advantage of introducing no halogens to the environment is an important consideration to many customers. The abrasion loss for these products is still superior to most any material and there is an advantage in terms of smoke generation.

Table 11 shows the smoke density for flame retardant TPUs as measured via ASTM E662. Shown here for comparison is a halogenated grade, a non-halogenated 'FHF' grade, and a non-halogenated plasticized grade compared with chlorosulfonated PE, a material widely used in mining cables and other constructions. Note that in both the flaming and non-flaming mode, the 'FHF' non-halogen type of flame retardant TPU shows less smoke generation via this test. All the TPUs had lower smoke generation than CPE in the non-flaming mode.

CONCLUSION

The distinguishing advantages offered to the cable industry by TPU compared to other

insulating and sheathing materials are a combination of properties such as excellent abrasion resistance, very good mechanical properties and cold flex, good resistance to fuels and oils as well as a selection of flame retardant grades.

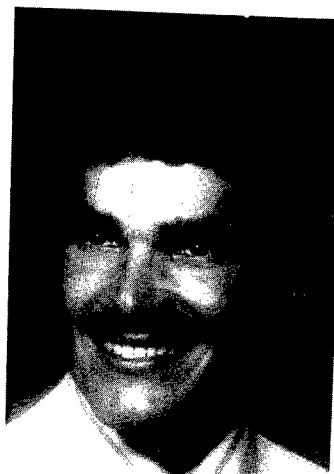
These properties make TPU ideal for use in mining applications, construction, high-speed machinery and robotics, shipyards, geophysical exploration, etc. Of course, these are applications in which the finished cable is exposed to rather severe and abrasive handling conditions. The high tensile, tear, and cut resistance enables a TPU jacketed cable to be pulled across rough ground, sharp edges, and adjacent cable with metal mesh protectors without a great deal of damage. The low temperature properties of TPU are another advantage over other cable materials, particularly considering climates in Alaska and Scandinavia where operating temperatures can reach -50°F or lower. The cables must be able to function (flex) and be flexible enough to install. Applications in environments with exposure to fuels, oils, and greases are also where TPU has a distinct advantage. TPU products yield small to moderate volume swell and weight changes.

Halogen-containing flame-retardant grades of TPU offer very good properties compared to that of standard TPU. New grades with improved properties are being developed. Recent new developments in non-halogenated flame retardant grades of TPU have the advantage of lower smoke and acid gas generation compared with halogenated materials.

REFERENCES

1. Richter, S. Polymers in Mining, International Conference, Plastics and Rubber Institute, 1989
2. Richter, S. Polymers in Mining, International Conference, Plastics and Rubber Institute, 1989
3. Bertels, A., Thermoplastic Polyurethanes, Elastogran Div. BASF AG
4. Bertels, A., Thermoplastic Polyurethanes, Elastogran Div. BASF AG

BIOGRAPHY

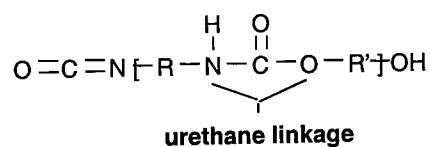
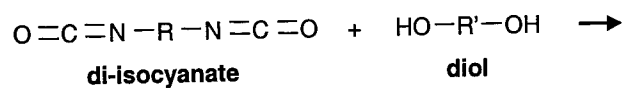


Jeff DeGross
BASF Corporation
Technical Service Representative
Polyurethane Elastomers (TPU)
1609 Biddle Ave
Wyandotte, MI 48192
Tel: (734) 324-6157
Fax: (734) 324-6639

Jeff DeGross is a Senior Technical Service Representative for the BASF Corporation Polyurethanes Division Elastomers Group. He has been in this capacity for the past three years. Jeff has nearly twenty years experience as a development engineer in the plastics industry, primarily on the converting side. Before his recent experience in the plastic resin industry with BASF, he was a Project Manager for Johnson Controls Plastics Machinery Division for 5 years. His other experience is with plastics packaging converters Sonoco Products Company in Hartsville, SC and Owens-Illinois in Toledo, Ohio. Jeff graduated from the University of Toledo with a Bachelor's degree in Chemistry in 1980.

Fig. 1

Basic TPU Chemistry



TPU Chemistry

Structure of thermoplastic Polyurethane

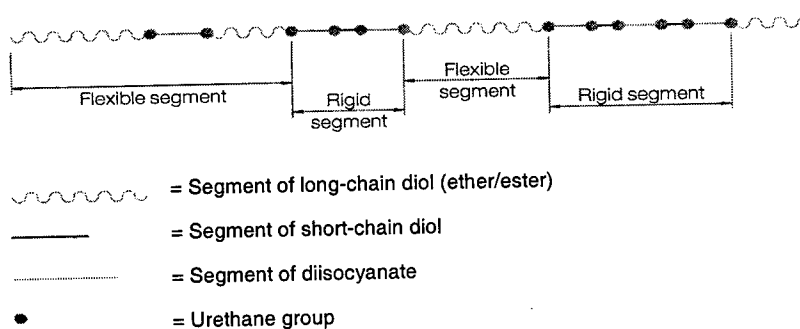


Fig. 2

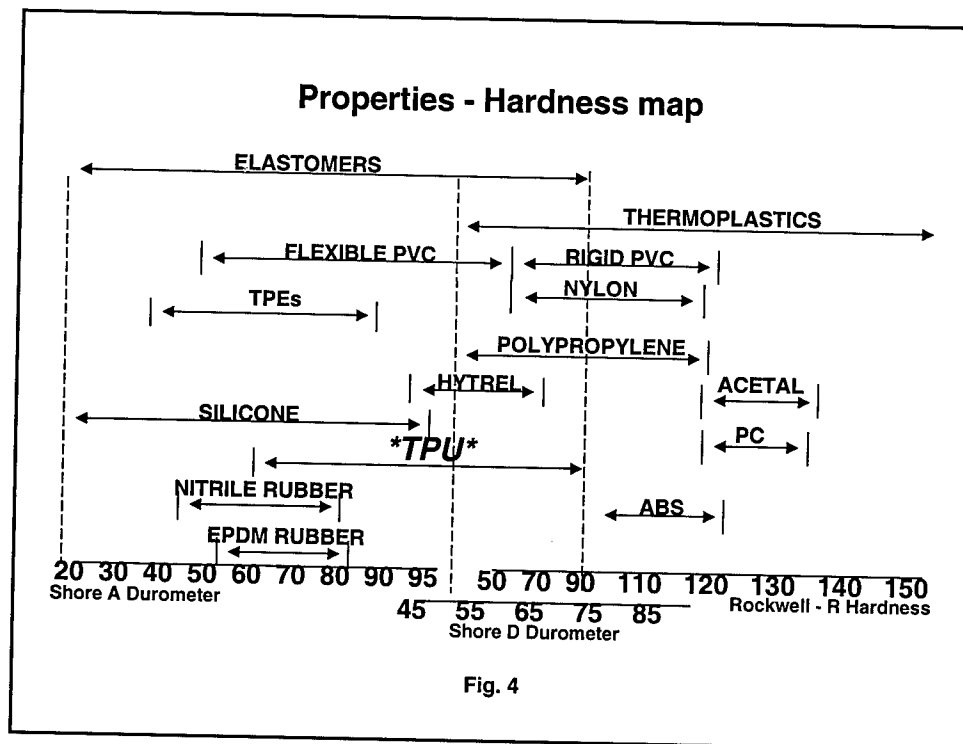
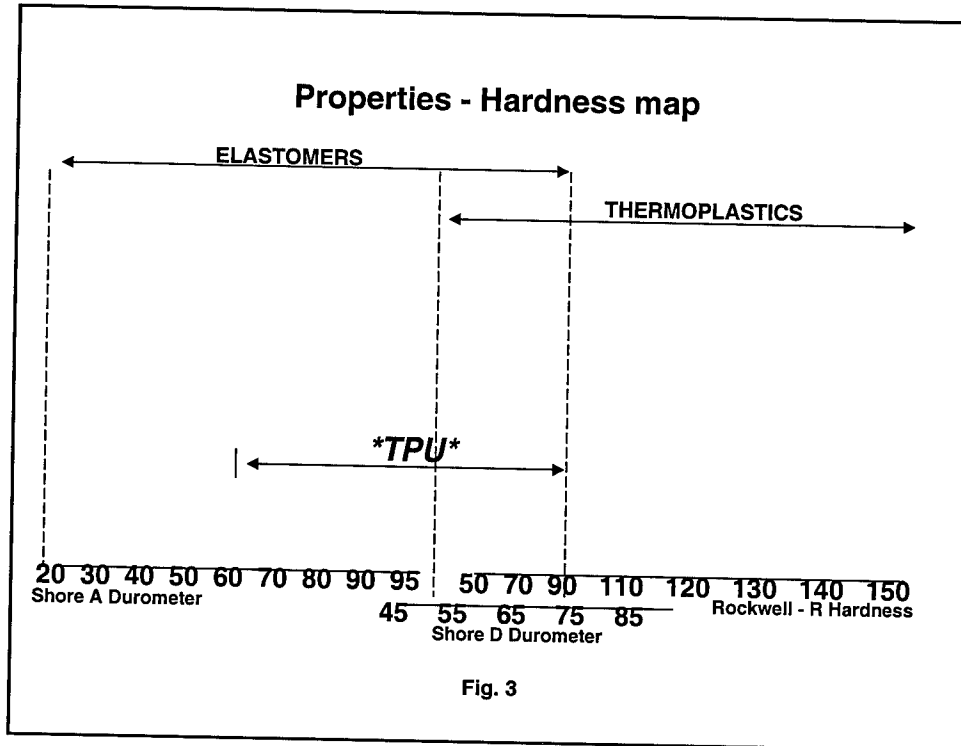


Table 1
Abrasion Resistance

<u>Material</u>	<u>Weight Loss, mg</u>
TPU	0.4-3.2
Ionomer	12
Nylon 6/10	16
Nylon 11	24
HDPE	29
PTFE (Teflon)	42
Nitrile Rubber	44
Nylon 6/6	58
LDPE	70
Natural Rubber Tread Formulation	146
Styrene-Butadiene Rubber Tread Formulation	181
Plasticized PVC	187
Butyl Rubber	205
ABS	275
Neoprene	280
Polystyrene	324

Taber Abrasion, CS17 Wheel, 1000g Weight, 5000 Revolutions
Ref: Handbook of Thermoplastic Elastomers, Litton Educational Publishing, 1979

Table 2
TPU Mechanical Properties

PROPERTY	UNIT	METHOD	ETHER TPU	ESTER TPU
HARDNESS	SHORE 'A'	D2240	87	87
DENSITY	g/cm ³	D792	1.12	1.19
TENSILE STRENGTH	MPa	D412	40	40
ELONGATION	%	D412	550	550
E-MODULUS	MPa	D412	20	21
100% MODULUS	MPa	D412	5	5.5
300% MODULUS	MPa	D412	9	9.5
ABRASION RES.	mm ³	DIN 53516	30	30
TEAR STRENGTH	N/mm	D624	70	75
COMPRESSION SET @ ROOM TEMPERATURE	%	D395 (B)	25%	25%
COMPRESSION SET @ 70C	%	D395 (B)	45%	35%

Table 3
Mechanical Properties Comparison

PROPERTY	UNIT	TPU	PVC INSULATION SHEATH		RUBBER INSULATION SHEATH	
TENSILE STRENGTH	N/mm ²	40	16	14	8.5	9.5
ELONGATION	%	550	260	330	420	350
20% MODULUS	N/mm ²	2.5	3.4	3.2	1.5	1.6
HARDNESS	SHORE 'A'	87	90	84	70	68
TEAR STRENGTH	N/mm	70	18	13	10	6
ABRASION LOSS (DIN 53516)	mm ³	35	180	160	280	340

Table 4
Fluid Resistance

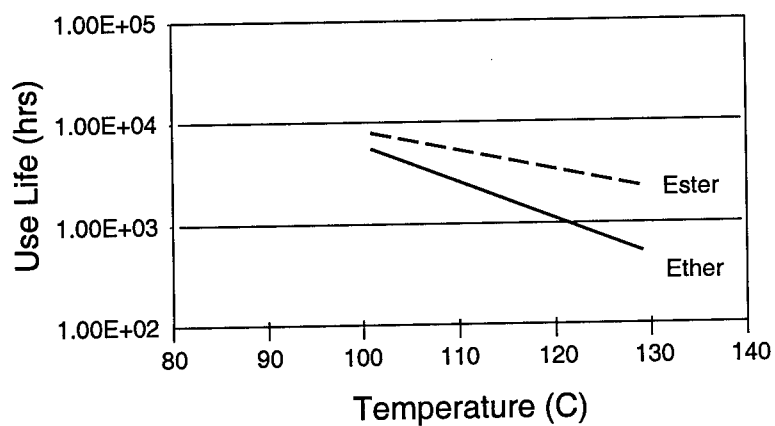
MEDIUM	°C	TPU	PVC INSULATION SHEATH		RUBBER INSULATION SHEATH	
MINERAL OIL	20	++	+	+	-	-
FUELS	20	++	+	+	-	-
BRAKE FLUID	20	+	0	0	++	+
KETONES	20	+	+	+	+	+
ALCOHOLS	20	+	+	+	++	+
HYDRAULIC OIL	80	++	0	0	-	-

++ resistant, minor mass variation
 + limited resistance, considerable mass variation
 0 not resistant under most conditions, possibly ok for short immersion time
 - not resistant, strong attack within short time

SOURCE: Richter, S. Polymers in Mining, International conference, 1989

Fig. 5

Dry Heat Aging - 85A Ether vs. 85A Ester TPU



*End criterion = 20 MPa Tensile

Fig. 6

Torsional Modulus of TPU

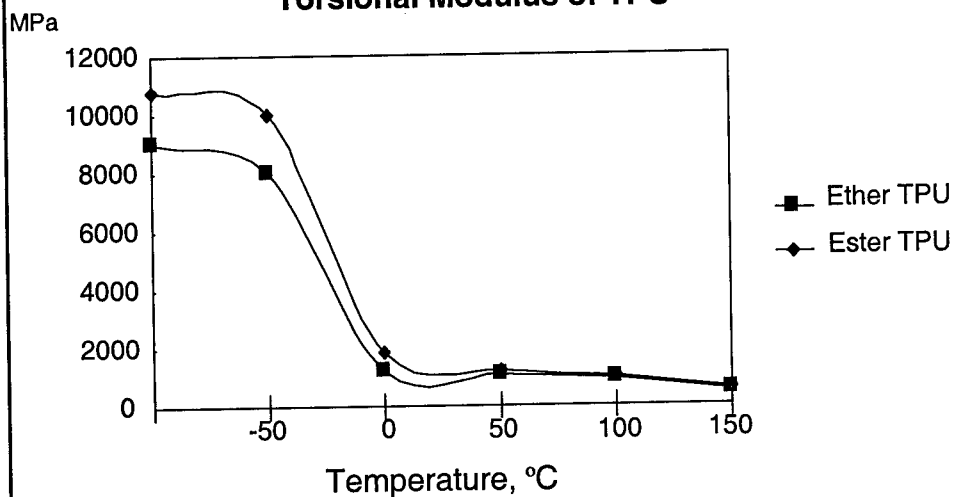
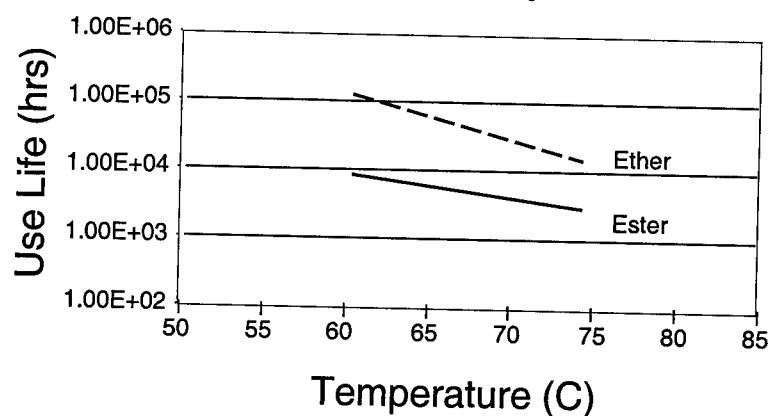


Table 5
Cold Temperature Impact

Sample	Temp. °C	Impact Strength Ether TPU - 87A KJ/m2	Impact Strength Ester TPU - 87A KJ/m2
Notched	-40	No Break	No Break
Notched	-50	No Break	53
Notched	-60	35	10
Un-notched	-60	No Break	No Break

*via DIN 53453

Fig. 7
Hydrolytic Stability



*End criterion = 20 MPa Tensile

Table 6

Electrical & Burn Properties of TPU

Properties	Unit	Standard	Polyether-based TPU				
			75A	80A	85A	90A	85AFHF*
Dielectric Strength	kV/mm	DIN 53481/VDE 0 303 p. 2	40	40	40	40	40
Surface Resistance	ohm	DIN 53482/VDE 0 303 p. 3	10 ¹¹	10 ¹¹	10 ¹¹	10 ¹²	10 ¹¹
Volume Resistivity	ohm-cm	DIN 53482/VDE 0 303 p. 3	10 ¹¹	10 ¹¹	10 ¹¹	10 ¹²	10 ¹¹
Dielectric Constant - 50Hz	-	DIN 53483/VDE 0 303 p. 4	8.0	8.0	7.5	7.0	8.0
1 KHz	-	-	7.6	7.6	7.2	6.6	-
1 MHz	-	-	6.5	6.5	6.1	5.5	-
Combustion Behavior (thickness 1/16")	-	UL94	V2	HB	HB	HB	V0

*FHF = Halogen-free FR grade TPU

Table 7

Halogenated FR TPU -Properties

Properties	85A-F (1)	85A-F (2)	95A-F	Comp. "F"-type	Std. 85A TPU
Type	Hal	Hal	Hal	Hal	None
Hardness	87	87	95	87	86
Tensile Str, psi	5263	6116	6567	4224	7350
300% Modulus, psi	2926	3067	5803	1766	2900
100% Modulus, psi	1444	1272	2858	928	1232
Elongation, %	505	505	340	558	555
E Modulus, psi	3193	3293	10608	2942	3057

(1), (2) - denotes different formulations

Table 8
Halogenated FR TPU -Properties

Properties	85A-F (1)	85A-F (2)	95A-F	Comp. "F"-type	Std. 85A TPU
Split Tear, pi	272	NA	523	382	380
Graves Tear, pi	329	NA	715	410	488
Taber Abrasion (mg loss, H18 wheel)	82	NA	79	165	34
UL-94 RATING, .020"	V2	V0	V2	V0	HB
Oxygen Index (LOI)	25%	30%	24%	29%	23%

Table 9
**Properties of
Non-Halogen FR TPUs**

Properties	85A-FHF	85A-W	Std. 85A TPU
FR Type	Non-Hal	Plast.	None
Hardness	89	84	86
Tensile Strength, psi	4500	6037	7350
300% Modulus, psi	1682	1158	2900
100% Modulus, psi	549	921	1232
Elongation, %	505	1575	555
E Modulus, psi	3357	1078	3057

Table 10
Properties of
Non-Halogen FR TPUs

Properties	85A-FHF	85A-W	Std. 85A TPU
Split Tear, pi	298	216	380
Graves Tear, pi	256	461	488
Taber Abrasion (mg loss, H18 wheel)	64	67	34
UL-94 RATING, .030"	V2	V2	HB
UL YELLOW CARD	Y	Y	
Oxygen Index (LOI)	25%	NA	23%

Table 11
Smoke Density of FR TPU

Properties		85A-F	85A-FHF	75A-W	CPE*
Type		Hal	Non-Hal	Plast.	Hal
SMOKE DENSITY (ASTM E662, NBS)					
Flaming Mode:	90 sec Ds	541	55	299	265
	4 Min Ds	729	243	563	570
	Dm	693	229	565	635
Non Flaming Mode:	90 sec Ds	2	6	4	45
	4 Min Ds	140	56	68	450
	Dm	399	266	253	630

*chlorosulfonated PE

STP-CABLE FOR TYRE PRESSURE CONTROL SYSTEM OPERATING AT 433/315 MHZ

Daljit S. Parmar, Günter Behlau, Helmut Wichmann

Kroschu Kabelweke, Kromberg & Schubert GmbH u. Co
46414 Rhede
Germany

ABSTRACT

A new STP-Cable for tyre pressure control system has been developed in an effort to continuously increase the safety and comfort in an automobile. Aim of this development work was to gather and evaluate important information during driving, e.g. tyre pressure and tyre temperature.

Evaluation of this information with the help of the control system informs the vehicle driver in advance whether the vehicle is operating with the correct tyre pressure. A sensor integrated in the wheel-rim-bed, determines the actual tyre pressure and the tyre temperature at certain intervals. These data is transferred to a receiver antenna with the help of a transmitter which is also integrated in the wheel body. The Transfer frequency used, as per the national specification is either 433 MHz or 315 MHz. A special STP-Cable, designed to suit the control system, carries the data to the control equipment for evaluation. Any deviation from the set values would alarm the driver in time (Fig. 1).

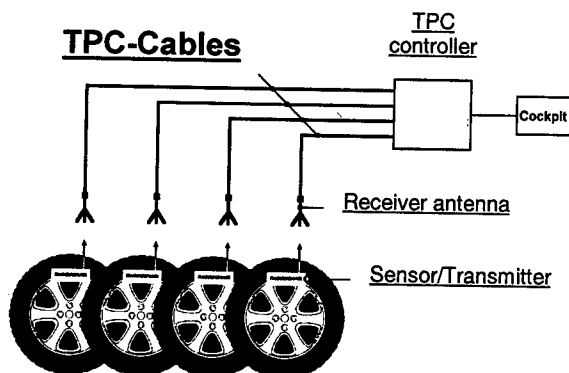


Figure 1: Principle Sketch of the Tyre Pressure Control (TPC) System

REQUIREMENTS ON THE CABLE

A twisted pair cable is developed to transfer information from the antenna to control equipment. This cable should be able to transfer low signals with possible low loss throughout the cable length. Depending upon the vehicle type and installation, about 10 meter length of the cable is required. The characteristic impedance (Z_0) has to be compatible to the electronic. To minimize or if possible to avoid any external influence (EMC) a suitable screen design is important.

The requirements of the automobile manufacturers and assemblers have also to be taken into consideration while developing the cable to guarantee the functioning of the system during the operation conditions.

Design Requirements

Electrical Requirements:

- Conductor resistance max. 60 mOhm/m
- Attenuation max. 6 dB/10m at 433 MHz
- Characteristic impedance (70 ± 7) Ohm between (295 - 453) MHz
- A suitable screen

Thermal Requirements:

- maximum operating temperature +105°C for 3000 hours operating time
- flexibility at low temperature as low as -40°C

Chemical Requirements:

- Resistant against Oils and detergents
- Resistant against Fuel
- Flame resistance

Mechanical Requirements:

- Tensile strength min. 200 N
- low bend radius
- high abrasion resistance

Processing Requirements:

- Standard conductor size and crimpability of the cores
- simplicity in assembly
- small outer diameter of the cable

MATERIALS OF CONSTRUCTION

In a data transmission cable where the low attenuation constant (α) is important, an insulation material with low dielectric constant (ϵ_r) has to be selected to achieve low capacitance (CB). Also important is the loss angle ($\tan \delta$) of the material which influences the attenuation change. So the dielectric properties of the insulation materials are of utmost importance.

PVC, the mostly used insulation material in the automotive industry can not be considered due to its unsuitable dielectric characteristics. While selecting the insulation material, the experience in the telecommunication cable teaches the use of Polyethylene (PE) due to its superior dielectric characteristics and processability on all the extruder lines. The only disadvantage of Polyethylene is its relative lower operating temperature which limits its application in the automotive industry. Another material from the Polyolefine group which has adequately good dielectric and processing properties is Polypropylene (PP). In addition, PP as compared to PE can be set to much higher operating temperatures. The normal PP-homopolymer has a disadvantage at low temperatures and it is very sensitive against bare copper since it causes ageing problem at higher temperatures.

A suitable PP Compound (chemically foam able) was formulated to withstand copper contact and it operates both at low and high temperatures. Table 1 shows typical electrical characteristics of PP in comparison to PE and a standard PVC insulation compound. An insulation with the special formation cellular PP Compounds permits smaller insulation wall thickness to achieve same dielectric characteristics. The designed PP Compound in chemically foam able using the standard extrusion equipment and foam-skin technology. A skin layer using solid PP Materials gives the core a very robust structure for the further processing of the element.

In selecting a jacket material, special care was taken to guarantee against thermal, mechanical

and chemical influence. A special PVC Compound to suit the automobile environment was selected which is economically and fulfils the requirements.

CABLE DESIGN

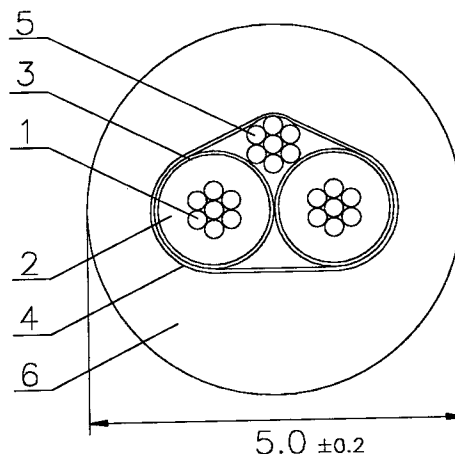


Figure 2: STP-Cable for Tyre Pressure Control (TPC) System

1. Stranded Copper conductor (bare) 0.35 mm²
2. Insulation: Cellular PP Compound
3. Skin layer: PP Compound
Core diameter max. 1.4 mm
4. Screen: composite metal foil
5. Drain wire Tinned Copper strand (0.35 mm²)
6. Sheath (special PVC Compound)
Outer diameter (nominal) 5.0 mm

CABLE PRODUCTION

After careful selection of materials of construction, a precise and clean manufacture of cable is necessary. To guarantee the necessary transfer characteristics and the symmetry of the cable, following requirements are of utmost importance:

- the centricity of the conductor within the insulation
- the homogeneity of the foam structure of the insulation
- diameter control
- homogeneity of both the cores

Due to very stringent requirements of the electrical transmission properties, the manufacturing process conditions have to be

observed with great care. Automatic colour-changing equipment has proved to be very successful in producing cores without significant difference in capacitance unsymmetry. Taping equipment during the stranding of the cores with drain wire should be precise enough to avoid any unsymmetry in the cable core.

TEST RESULTS

The test results are described in the Table 2. All the tests were done according to the design requirements, DIN 72551 and DIN ISO 6722. The Transfer impedance and Attenuation measurements are shown in Fig. 3 and Fig. 4 respectively. Capacitance of a section of 10 meters of cable at operating temperatures from -40°C up to $+105^{\circ}\text{C}$ is plotted in the Figure 5 where as the Figure 6 shows the attenuation characteristics. The results of bending flexibility according to the DIN VDE 0472 Part 603 (Test

type J) are presented in the Figure 7. The attenuation behaviour after bending is as per the Figure 8. The measurements of attenuation after Immersion in Oil (Figure 9), Fuel (Figure 10) and after the tensile strength test (Figure 11) show that the Cable is robust and would withstand the operating conditions of the vehicle.

CONCLUSION

The development results reveal a high frequency cable which fulfils the stringent requirements of transmission electronic in respect of Attenuation and transfer impedance and as per the requirements of the automobile industry. The cable has been found suitable for application in the temperature range of -40°C - $+105^{\circ}\text{C}$ for 3000 hours operation time. The cable is flame resistant and also fulfils the requirements in Oil and Fuel environment.

	Polypropylene (PP)	Polyethylene (PE)	Polyvinylchloride (PVC)
dielectric constant (ϵ_r)			
1 MHz	2.3 – 2.5	2.1 – 2.3	3.4 – 3.9
loss angle ($\tan \delta$)			
1 MHz	0.0004 – 0.0005	0.0001 – 0.0003	0.015 – 0.03
volume resistivity (Ohm*cm)	10^{17}	10^{17}	10^{14}
maximum operating temperature (3000h)	$+110^{\circ}\text{C}$	$+80^{\circ}\text{C}$	$+105^{\circ}\text{C}$

Table 1: Typical electrical characteristics of insulation compounds

Test	Requirement	Result
Conductor resistance (DC, $+20^{\circ}\text{C}$)	60 mOhm/m	52 mOhm/m
Resistance to abrasion (Core)	≥ 200	> 300
Electric strength (1 Min.)	$\geq 1.2 \text{ kV}$	$> 1.2 \text{ kV}$
Pressure test at $+80^{\circ}\text{C}$ (Wall thickness)	$> 0.12 \text{ mm}$	0.22 mm
Volume resistivity ($+70^{\circ}\text{C}$)	$> 10^{10} \text{ Ohm x cm}$	$1.4 \times 10^{12} \text{ Ohm x cm}$
Long time operating temperature (3000 hours)	$+105^{\circ}\text{C}$	$+105^{\circ}\text{C}$
Flexibility at low temperature	-40°C	-40°C
Shrinkage by heat ($+150^{\circ}\text{C}$ / 15 Min.)	$\leq 4 \%$	1 %
Resistance to flame propagation	$\leq 30 \text{ sec.}$	2 sec.
Resistance to abrasion (Sheath)	-	> 5000
Resistance to oil (Alteration of diameter)	$\leq 4 \%$	1.3 %
Resistance to fuel (Alteration of diameter)	$\leq 6 \%$	5.6 %
Mechanical tensile strength	$\geq 200 \text{ N}$	$\geq 200 \text{ N}$
Capacitance	-	62.9 pF/m
Attenuation at 433 MHz	max. 6 dB/10m	passed
Characteristic impedance at (295 - 453) Mhz	(70 \pm 7) Ohm	passed

Table 2: Test results according to DIN 72551 and DIN ISO 6722

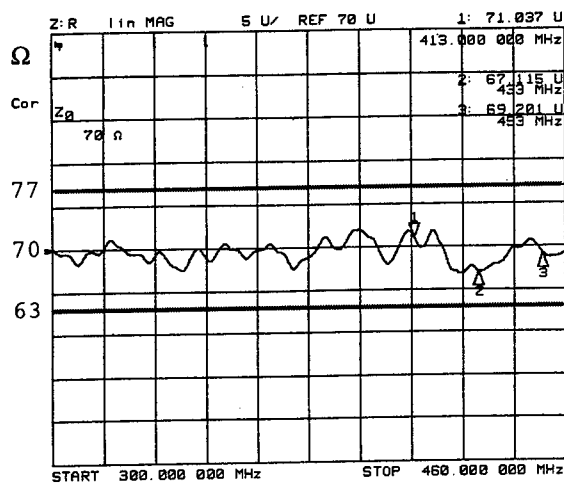


Figure 3: Characteristic impedance for 100 meter

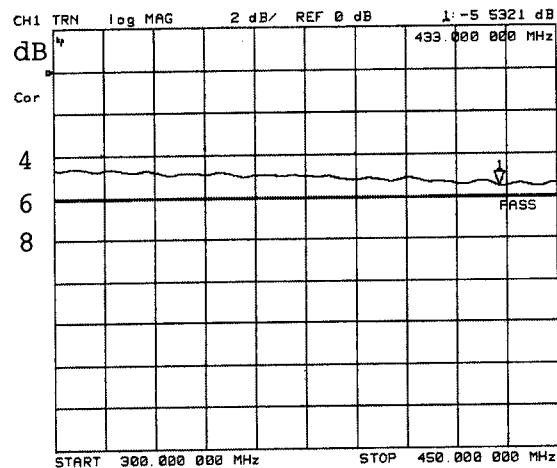


Figure 4: Attenuation for 10 meter

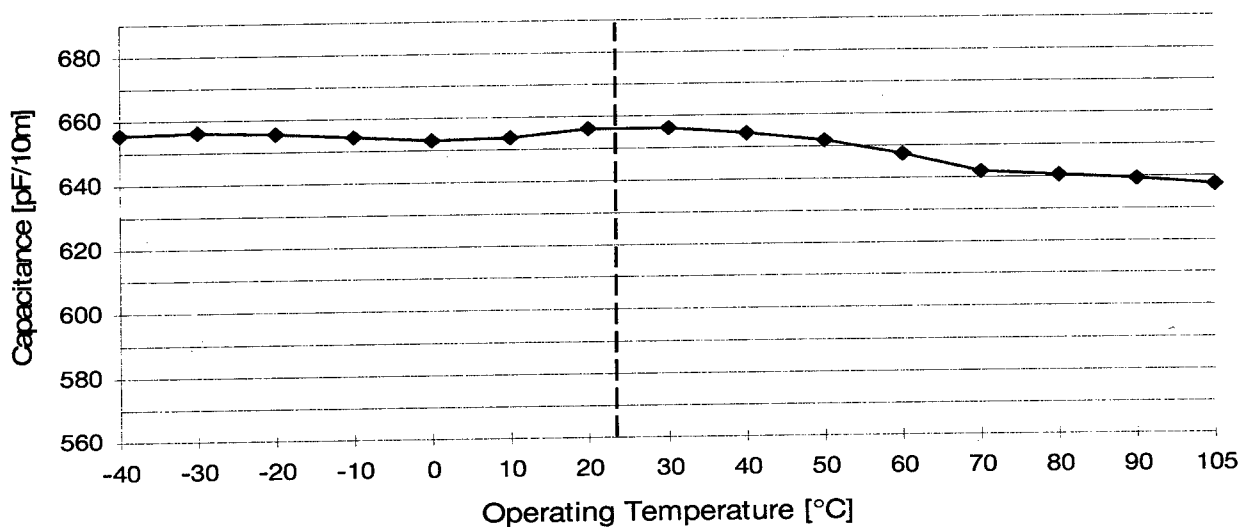


Figure 5: Capacitance for 10 meter

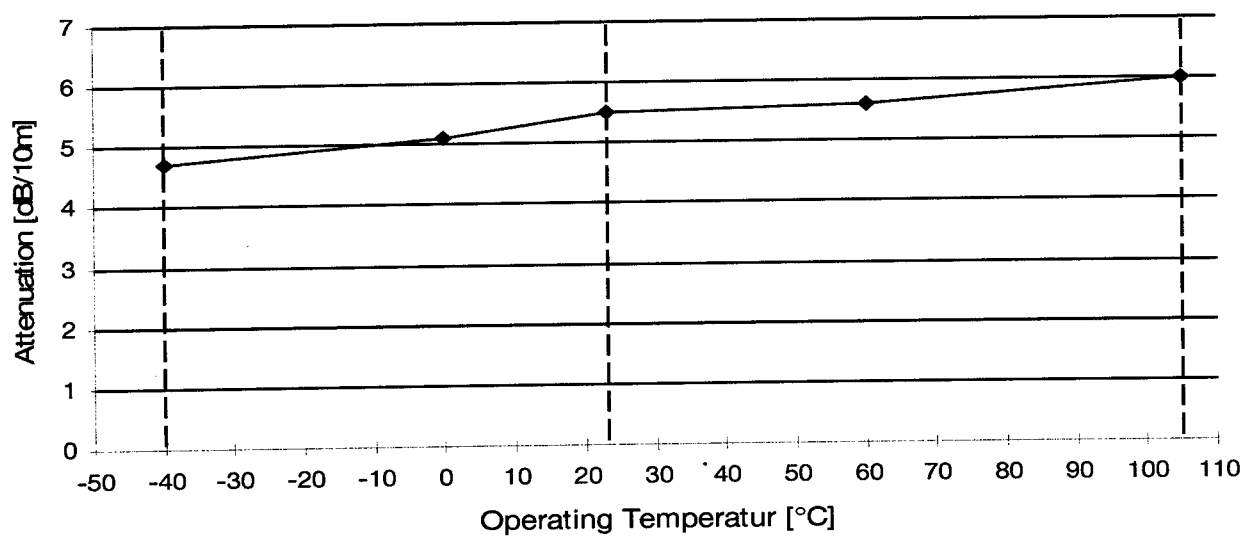


Figure 6: Attenuation for 10 meter

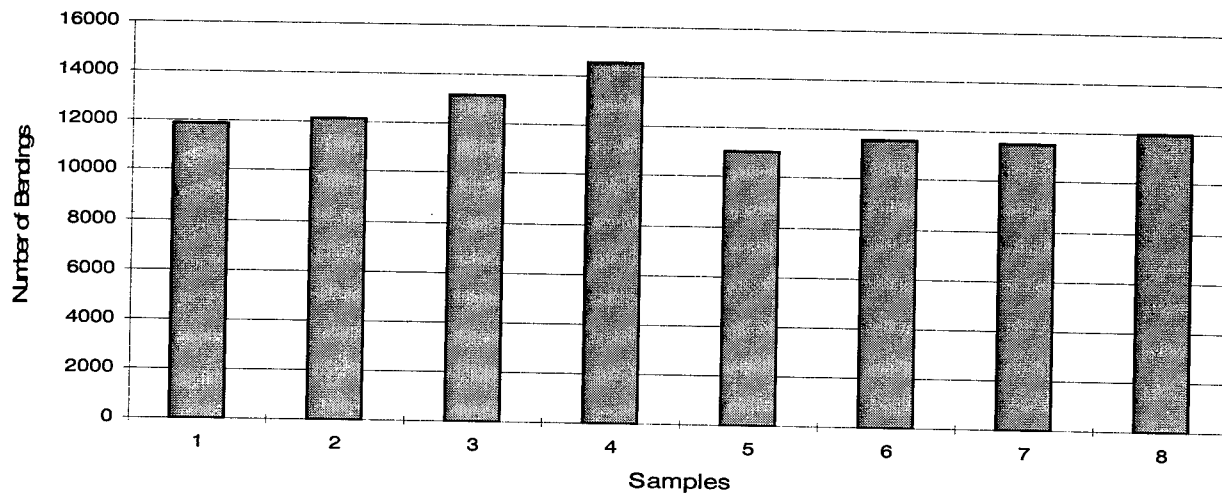


Figure 7: Test according DIN VDE 0472 Part 603 (Test type J); Bend Diameter 50 mm; Load 500 g

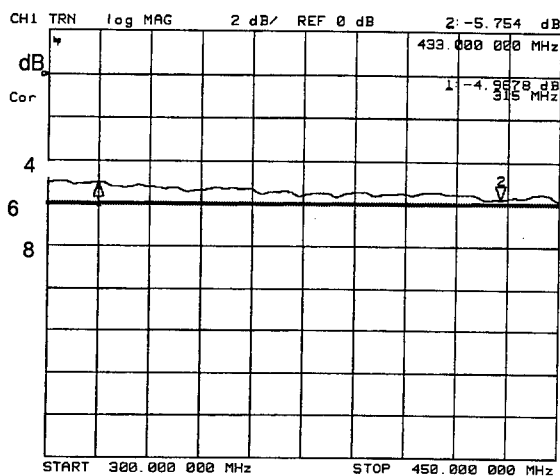


Figure 8: Attenuation for 10 meter
after Bending Test
10 Bends, Bend Diameter 50 mm

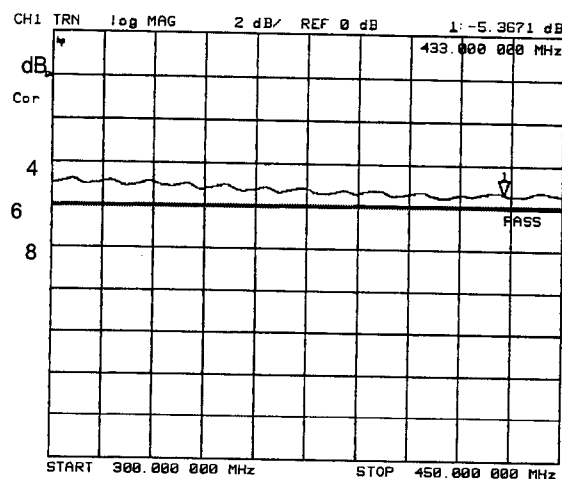


Figure 9: Attenuation for 10 meter
after Oil Immersion Test
Immersion Length 200 mm

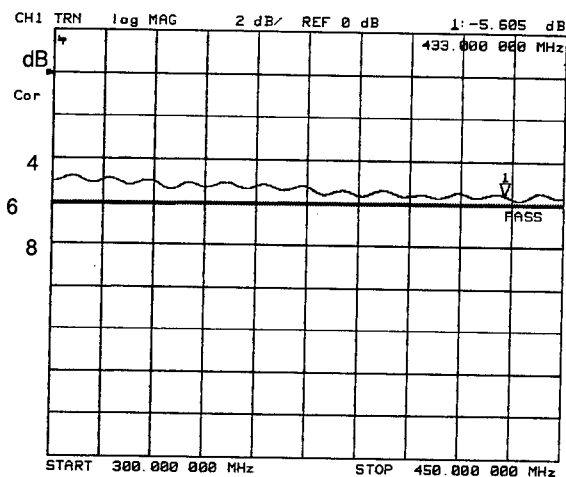


Figure 10: Attenuation for 10 meter
after Fuel Immersion Test
Immersion Length 200 mm

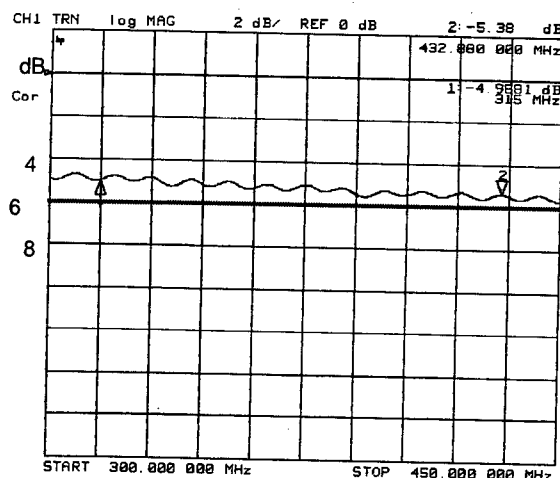


Figure 11: Attenuation for 10 meter
after Tensile Strength Test
Test Length 200 mm

ACKNOWLEDGEMENTS

The authors wish their sincere appreciation to Mr. Centurion, Mr. Friedrich and Mr. Hüls for constructive assistance in testing the cable.



Daljit S. Parmar is head of Engineering and Marketing of the Kroschu Kabelwerke. He received his B.Tech. in Chemical Engineering from the University of Madras, India in 1968 and M.Sc. in Process Engineering from the University of Bradford, UK in 1970. He holds a Ph.D. in Engineering

Management from Kennedy-Western University, California State Education. He has specialized in the field of Cable Technology and has more than 20 years of experience in the process development and production of a wide variety of wire and cable. Since 1986, he is member of the senior executive staff of the Kromberg & Schubert GmbH u. Co group.

OUTDOOR COVERAGE BY RADIATING CABLES

Erhard Mahlandt

RFS kabelmetal, Radio Frequency Systems GmbH, D-30179 Hannover, Germany

ABSTRACT

Various different types of radiating cables have been measured in free space at distances of up to 30 m. Radiating mode cables as well as coupling mode cables have been measured at the frequencies of 150, 450, 900 and 1800 MHz. The measurements were performed using dipoles and $\lambda/4$ antennas, at various distances from the cables, both parallel and perpendicular to the cable's axis.

The results show that some new theoretical approaches are necessary to correctly model the behaviour of our radiating cables, when evaluating the effect of cable-antenna distance. Another result of our investigations is that the effect of distance is similar for coupling mode and radiating mode cables.

INTRODUCTION

In the telecommunication world of today there is a growing need for high percentage geographical RF coverage, especially for cellular/mobile radio. It is therefore important to include or add areas where coverage has hitherto been poor or non-existent.

Very often it is not possible to achieve sufficient coverage inside confined areas like buildings and tunnels from outside base station sites because of the shielding effect of the building structure. Traditionally radiating cables have been used very successfully to overcome this problem. Compared with antennas they can cover a relatively long distance without any additional expensive active component.

But also outside of confined areas, radiating cables can be used to advantage under certain circumstances, for example in mountainous areas where antenna beams cannot follow undulations in the landscape.

Inside confined areas the characteristics of

radiating cables are largely influenced by the local conditions like cross-section, material, screening losses etc. These influences are not present in free space but other conditions are dominant. In particular the distance between mobile and cables can be much larger than in most confined areas.

There are theoretical approaches that describe the radiation characteristics as a function of distance in which they distinguish between the coupling mode and the radiating mode. Our investigation addresses theory and practice.

CABLE TYPES

Coaxial radiating cables generate leakages of the inner signal by apertures in the outer conductor. All apertures produce spherical waves with higher order modes as well as cylindrical waves which are propagated along the cable axis. The field strength of spherical

waves decreases by $\frac{1}{r^2}$ while cylindrical waves

decrease by $\frac{1}{r}$.

The resulting field is the superposition of all various fields. If no mode is dominant the field contribution is called *coupling mode*.

If the apertures in the outer conductor are arranged periodically, the superposition of spherical waves is coherent at frequencies with half wavelengths that are shorter than the apertures distance. In this case a transverse wave is generated and the field contribution is called *radiating mode*. The propagation direction of the transverse wave depends on the phase velocity inside the cable and the relation of wavelength to the aperture distance.

At multiples of the first resonant frequency higher modes are produced which lead to unwanted interferences. Different techniques

with special slot arrangements and shapes are known to suppress higher modes [1], [2]. Below the first mode the cables operate in the coupling mode.

For the described investigation one cable operating in coupling mode only and two cables operating in radiating mode with different higher mode suppression were used.

The coupling mode can be generated by a long slot along the entire cable or by slots arranged in a short period. Another method is to use groups of slots which are widely separated. For this investigation a cable with slot groups was used. It is called type A.

One of the radiating mode cables - type B - has slots which are arranged in the direction of the circumference. The slot pattern has a period of about 1 m so that the cable operates in radiating mode starting at $f \approx 125$ MHz with perfect suppression of higher modes up to 1 GHz. The mode suppression is also effective in the 1800 MHz band. In free space the optimum dipole polarization is in the horizontal plane.

The second radiating mode cable - type C - has sloped slots with the main expansion in direction of the cable axis. This pattern produces a field which is mainly vertically polarized. The period of the slot pattern is 0.5 m so that the first radiating mode appears at $f \approx 270$ MHz. Due to the slot arrangement higher modes are suppressed up to 1 GHz.

CARRYING OUT OF THE MEASUREMENTS

The performance of the investigated cable types is well known under the standard installation in free space according to the IEC 61196-4 [3]. On a test range that is in conformity to the standard the cables are measured at a height above ground of 2 m and an antenna distance of 2 m using a halfwave dipole.

In this case all three cables were installed together underneath an external messenger wire between three poles with a space of about 0.2 m between the cables and a length of 100 m. The height above ground was between 3 and 3.5 m due to sag. This arrangement was chosen as it could be a practical solution if a cable is installed on telegraph-poles.

The cables were measured with a dipole installed on a trolley held by a special pole that affects the measurements only marginally and with a vertically polarized quarter wave antenna installed on the roof of a car to reflect realistic operation condition.

Under ideal conditions the test should be carried out along the middle part of a very long cable in order to eliminate end effects. But the available area limited the cable length to 100 m.

Measurements

System loss measurements were performed parallel to the cable at distances of 2, 4, 6, 8, 10, 15, 20 and 30 m at the frequencies of 150, 450 900 and 1800 MHz with tuned halfwave dipoles as well in vertical as in horizontal polarization. Additional measurements were made perpendicular to the cable axis in the middle of the test range to get more information about the cables' behaviour. The same test series was performed with car-mounted vertically polarized quarterwave antenna to get information about the influence of a car.

The measurements were performed with a fast test receiver that is able to measure about 400 points per second so that following the recommendation of the IEC 61196-4 [3] about 20 points per half wavelength could be measured at a reasonable time. The measurements were triggered by a distance sensor to obtain the best accuracy and to be independent of speed.

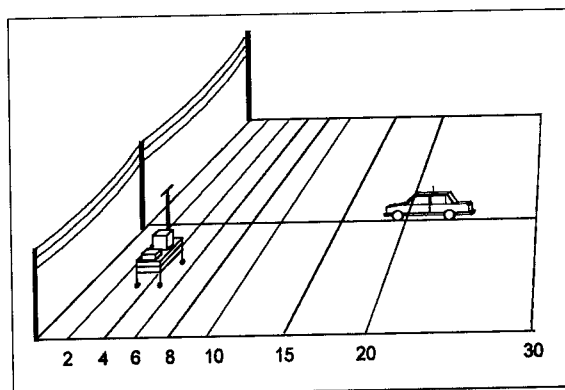


Figure 1: Test range.

Analysis Of Results

The task of the investigation was to find a mathematical rule of the distance depending coupling loss.

The coupling loss of a radiating cable is defined as the difference of the level inside the cable and

the received level at the antenna at a certain location perpendicular to the cable axis.

$$a_{cc}(z) = -(L_{in} - a(z) - L_m) \quad (1)$$

$a_{cc}(z)$: coupling loss at location z

L_{in} : input level of radiating cable

$a(z)$: longitudinal loss up to location z

L_m : measured level

This is correct for radiating cables operating in coupling mode or if the antenna is close to the cable. For cables operating in radiating mode the angle of the main lobe has to be considered in form of an offset because the radiated field is shifted according to the angle of the main lobe parallel to the cable.

The lobe angle α is calculated by (2):

$$\alpha = \arccos(\sqrt{\epsilon_r} - \frac{\lambda}{d}) \quad (2)$$

α : lobe angle

ϵ_r : permittivity of dielectric

λ : wavelength

d : aperture distance, period of slot pattern

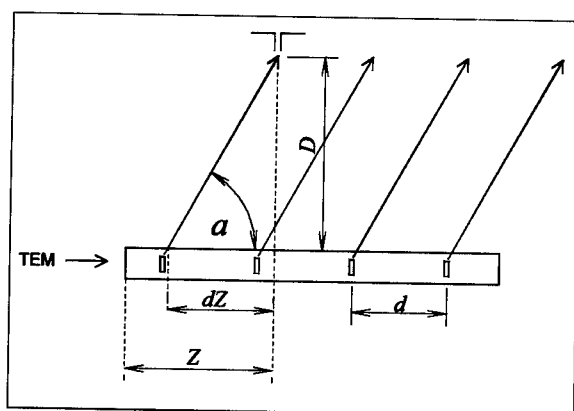


Figure 2: Field shift of radiating mode cables.

The effect can be proved by figure 3 which shows the system loss trace of a radiating mode cable with a field shift of about 25 m at an antenna distance of 20 m.

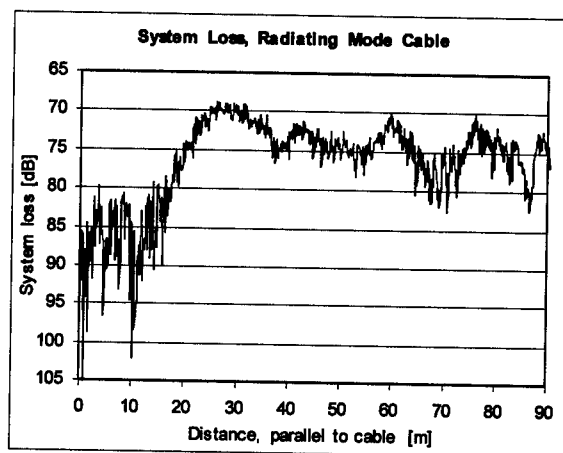


Figure 3: System loss trace of radiating mode cable.

In order to calculate the coupling loss correctly the attenuation of the piece of cable dZ (figure 2) has to be added.

$$dZ = \frac{D}{\tan(\alpha)} \quad (3)$$

dZ : cable length to be corrected

D : antenna distance

α : lobe angle

The coupling loss of radiating mode cables then follows

$$a_{cr}(z) = -(L_{in} - a(z) + a(dZ) - L_m) \quad (4)$$

$a(dZ)$: longitudinal loss of cable length to be corrected

The coupling loss traces parallel to the cable are characterized by the statistical evaluation of the 50 % and 95 % reception probability figures a_{cs} . The traces of the measured statistical coupling loss figures versus antenna distance are described quite well by a logarithmic trend curve with two coefficients (5).

$$a_{cs}(D) = A \cdot \ln(D) + B \quad (5)$$

a_{cs} : statistical coupling loss figure

When doubling the antenna distance the increase of coupling loss yields

$$\Delta a_{cs} = a_{cs}(2D) - a_{cs}(D) = A \cdot \ln(2) \quad (6)$$

Δa_{cs} : increase of coupling loss

Test results of coupling mode cable type A

According to [4], [5] an increase of coupling loss of 6 dB for distance doubling could be expected for the coupling mode cable type A. But the measured figures are only in the range of 2.2 dB to 4.4 dB depending on frequency, antenna type and antenna polarization.

Figure 4 shows the measured coupling loss obtained at 1800 MHz with the vertical car antenna moving perpendicular to the cable axis normalized by the level inside the middle of the cable. In this diagram the 50% figures of the coupling loss measured parallel to the cable by car are included as well as their logarithmic trend curve.

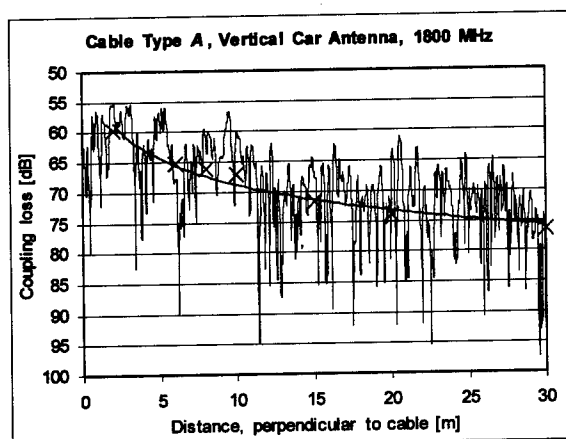


Figure 4: Cable type A, measured at 1800 MHz with a car, moving parallel and perpendicular to the cable.

Figure 5 shows the 50% figures of coupling loss measured parallel to the cable with the halfwave dipole in vertical polarization. At the most

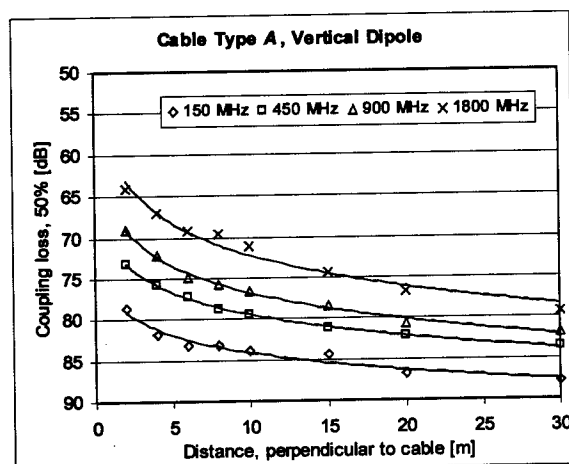


Figure 5: Cable type A, coupling loss 50% figures measured with vertical dipole.

frequencies the trend curve fits the measured figures very well. The deviation of individual points is only in the range of ± 1 dB. This is within the typical repeatability of coupling loss measurements.

Table 1 shows a comparison of all measurements parallel to the cable axis. It can be noticed that the coupling loss increase is most stable if measured with the car antenna. In this case the increase is in the range of 3.6 dB to 4.4 dB. But in no case the predicted increase of 6 dB when doubling the distance occurs.

f [MHz]	Coupling Loss Increase Δa_{cs} [dB]		
	$\lambda/2$ dipole horizontal	$\lambda/2$ dipole vertical	$\lambda/4$ antenna vertical
150	4.3	2.2	3.7
450	2.6	2.7	3.6
900	3.7	3.3	4.0
1800	3.4	3.9	4.4

Table 1: Cable type A, increase of coupling loss 50 % figure.

The 95 % reception probability figures were always 10 dB to 12 dB higher than the 50 % figures.

Test results of radiating mode cable type B

The cable type B operates in radiating mode at all measured frequencies. If there is a difference in increase of coupling loss compared to a coupling mode cable it should be recognizable at this cable.

The measurements at 1800 MHz could not be considered at distances larger than 10 m because of the limited test area and the field shift at this frequency. Due to period of the slot pattern the angle of the main beam is very flat towards the termination ($\alpha \approx 10^\circ$, (2)).

At 150 MHz and 450 MHz the statistical coupling loss figures are well described by a logarithmic curve (figure 6). At 900 MHz the values are not very consistent. The measured coupling loss at 20 m for example was 5 dB lower than at 15 m.

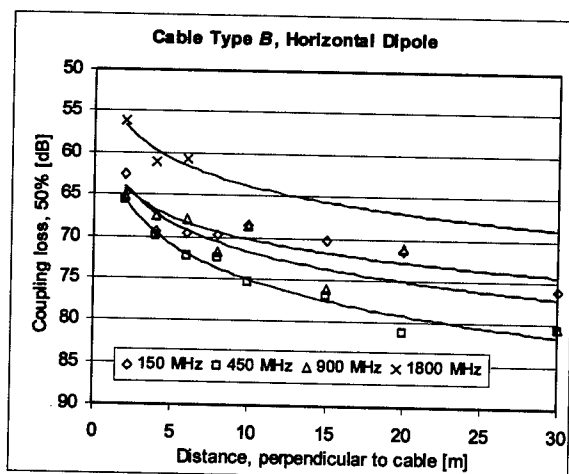


Figure 6: Cable type B, coupling loss 50% figures measured with horizontal dipole.

Measured with the car antenna the results are more consistent. In this case the increase in coupling loss is in the range of 2.3 dB to 4.1 dB. That means the behaviour is very comparable to the coupling mode cable A.

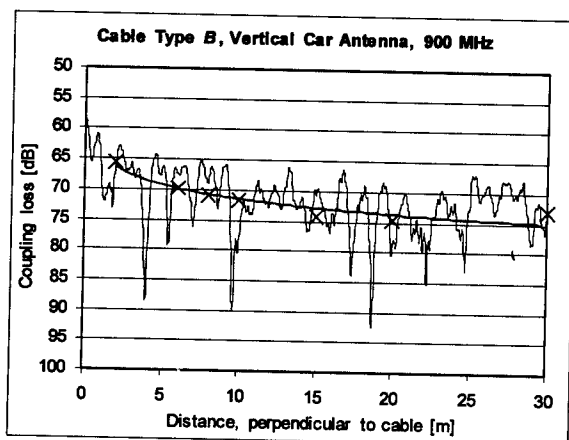


Figure 7: Cable type B, measured at 900 MHz with a car, moving parallel and perpendicular to the cable.

f [MHz]	Coupling Loss Increase Δa_{cs} [dB]		
	$\lambda/2$ dipole horizontal	$\lambda/2$ dipole vertical	$\lambda/4$ antenna vertical
150	2.6	2.3	3.7
450	4.1	3.5	3.4
900	3.4 ¹⁾	2.4 ¹⁾	2.8
1800	2.6 ^{1) 2)}	2.6 ²⁾	3.3 ²⁾

Table 2: Cable type B, increase of coupling loss 50 % figure.

¹⁾ Trend curve does not fit measured points satisfactorily.

²⁾ Only 4 points measured.

Test results of radiating mode cable type C

The results of this cable are very interesting, as both modes appear within the measured frequency band. At 150 MHz it operates in coupling mode and at all other frequencies in radiating mode. Figure 8 and 9 show the test result at 150 MHz and 450 MHz perpendicular to the cable with the included 50 % figures of the coupling loss measured parallel to the cable. The comparison of both traces shows that in principle there is no significant difference in the way the coupling loss increases versus antenna distance.

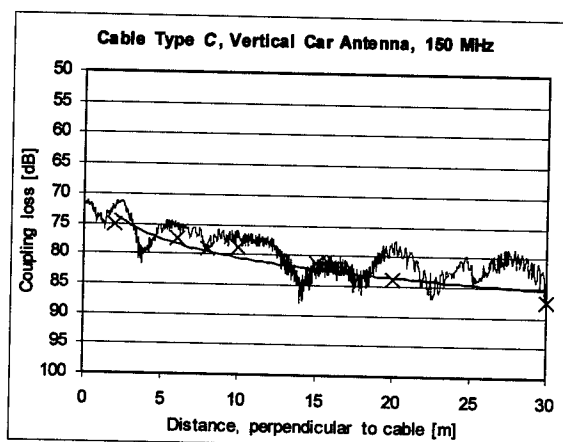


Figure 8: Cable type C, measured at 150 MHz with a car, moving parallel and perpendicular to the cable.

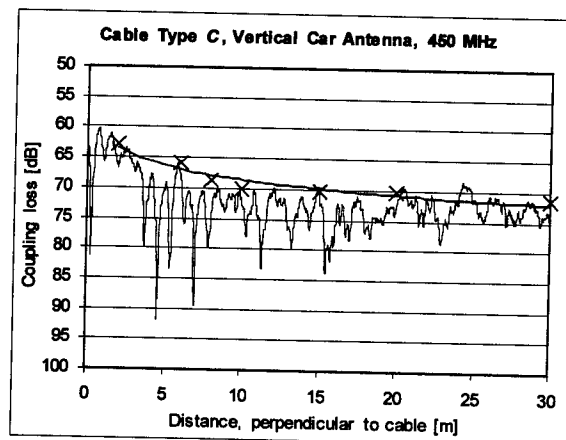


Figure 9: Cable type C, measured at 450 MHz with a car, moving parallel and perpendicular to the cable.

In figure 10 all measurements with vertical dipole can be compared. The typical curves at all frequencies are nearly parallel independent of frequency and mode.

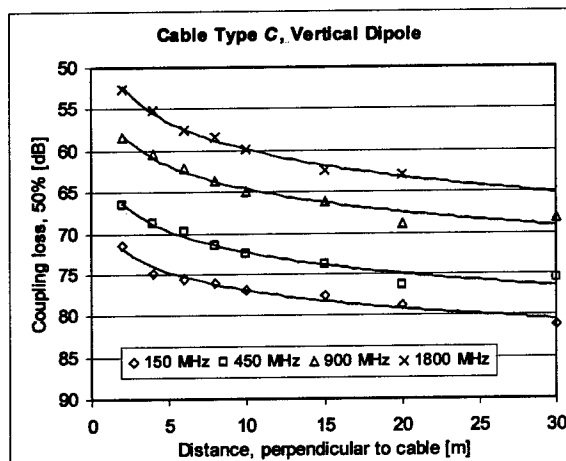


Figure 10: Cable type C, coupling loss 50% figures measured with vertical dipole

Although the cable operates in coupling mode at 150 MHz the coupling loss increase is less than at 450 MHz, where the cable operates in radiating mode. Measured with the car antenna the coupling loss increase at 150 MHz is higher than at 450 MHz but even less than at 900 MHz (see table 3). With horizontally polarized dipole the trend curve does not fit the measured points very well.

If the cable is measured under standard conditions (2 m distance) the 95 % reception probability value is about 4 dB to 5 dB higher than the 50 % value at 450 MHz and 900 MHz. This low signal variation along the cable can also be noticed at larger distances. For example at 15 m a difference of the 95 % to the 50 % value of 6 dB at 450 MHz and 8 dB at 900 MHz was found with the car antenna. Even at 30 m the difference at 450 MHz was just 4 dB.

f [MHz]	Coupling Loss Increase Δa_{cs} [dB]		
	$\lambda/2$ dipole horizontal	vertical	$\lambda/4$ antenna vertical
150	4.1	2.2	3.1
450	4.0 ¹⁾	2.6	2.3
900	2.9 ¹⁾	2.9	4.4
1800	3.4	3.3	4.2

Table 3: Cable type C, increase of coupling loss 50 % figures.

¹⁾ Trend curve does not fit measured points satisfactorily.

Comparison of measurements

At 150 MHz two cables operating in coupling mode (types A and C) can be compared with a cable in radiating mode (type B). The results with

the car antenna (table 4) are identical for the cable types A and B (3.7 dB). Type C which is in coupling mode has the lowest but very similar increase of 3.1 dB.

The coupling mode cable A does not have a higher coupling loss increase than the other cables. This is true for the more practical measurement with a car antenna and the measurement with a dipole on a trolley.

f [MHz]	type A		type B		type C	
	Δa_{cs}	mode	Δa_{cs}	mode	Δa_{cs}	mode
150	3.7	c	3.7	r	3.1	c
450	3.6	c	3.4	r	2.3	r
900	4.0	c	2.8	r	4.4	r
1800	4.4	c	3.3	r	4.2	r

Table 4: Coupling loss increase in [dB], measured with vertical car antenna.

c: coupling mode

r: radiating mode

f [MHz]	type A		type B		type C	
	Δa_{cs}	mode	Δa_{cs}	mode	Δa_{cs}	mode
150	2.2	c	2.3	r	2.2	c
450	2.7	c	3.5	r	2.6	r
900	3.3	c	2.4 ¹⁾	r	2.9	r
1800	3.9	c	2.6	r	3.3	r

Table 5: Coupling loss increase in [dB], measured with vertical dipole.

¹⁾ Trend curve does not fit measured points satisfactorily.

CONCLUSION

Three different types of radiating cable were measured at antenna distances of up to 30 m.

All cables show comparable increases of coupling loss versus distance independent of operation in either coupling or radiating mode.

Measurements using a car with an antenna yielded consistent results whilst measurements with a dipole showed higher variation.

The hypothesis that the coupling loss of coupling mode cables increase by 6 dB when doubling the distance evidently does not apply. It was found rather that in all cases an increase of 3 to 4 dB is realistic.

The measurements have enabled coverage evaluations and predictions to be performed on radiating cables in large open spaces to a more accurate and reliable degree than has hitherto been possible.

ACKNOWLEDGEMENTS

The author would like to thank Mr. Davies, Dr. Nagel and Mr. Fischer for their valuable discussions and Mr. Frähmke for his commitment to the measurements.

REFERENCES

- [1] U. Petri: Die Berechnung von geschlitzten Koaxialkabeln für den UKW-Funk, Ph.D.thesis, TH Aachen, 1977
- [2] A. Levisse: Leaky Or Radiating? Radiation Mechanisms Of Radiating Cables And Leaky Feeders – Channel Tunnel Applications, International Wire&Cable Symposium Proceedings, 1992
- [3] IEC 61196-4(1995-7) Radio Frequency Cables - Part 4: Sectional Specification For Radiating Cables
- [4] P. Delogne: Leaky Feeders and Subsurface Radio Comminucations, IEE Electromagnetic Waves Series 14, Peter Pelegrinus Ltd., 1982
- [5] Cree, D. J., and Giles, L. J. (1975): Practical Performance of Radiating Cables, Radio & Electron. Eng.

AUTHOR



Erhard Mahlandt

RFS kabelmetal
Radio Frequency
Systems GmbH

Kabelkamp 20
30179 Hannover
Germany

Erhard Mahlandt was born in 1963. He received his Dipl.-Ing (FH) degree in 1990 and joined RFS kabelmetal in the same year. He is responsible for the development and measurement techniques of radiating cables and foam dielectric cables.

MODELLING THE TRANSFER IMPEDANCE OF SHIELDED CABLES

Tomas Nälsén
Stefan Andersson

Habia Cable AB, Söderfors, Sweden

ABSTRACT

Several authors have during the last 20-30 years investigated the problem of measuring and predicting the transfer impedance of braided cables. A lot of progress has been made during these years but there is still no generally useful mathematical model that describes the behaviour of the shield well enough for manufacturing purposes.

This project's main goals were:

1. Investigating the different mathematical models available today and evaluating them.
2. Use and evaluate two different computer modelling techniques, one neural network program and one program for linear regression.

INTRODUCTION

The problem of predicting and measuring the transfer impedance is of great interest today for cable manufacturers since customers are raising their demands on the manufacturers. During the investigation of mathematical models it was found that Thomas Kley's¹ model was one of the most useful for pre-design of single-braids.

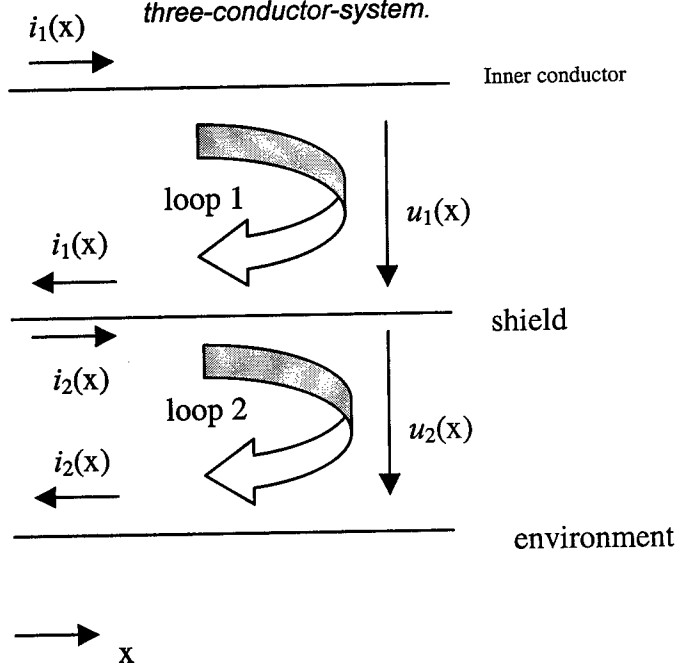
For the computer modelling techniques, neural network and linear regression, two commercially available programs were used.

For verification of the mathematical model and evaluation of the computer programs data from 50 single-screened cables was used.

SINGLE-SCREENED CABLES

There has been a lot of work done on explaining the different factors influencing the

FIG. 1 The two loops in the three-conductor-system.



electromagnetic coupling to and from shielded cables. In his dissertation¹ Thomas Kley uses a model that is independent of the shield geometry (Fig.1)

With this model you can describe the transfer impedance using the following equation:

$$Z_t = \frac{du_1/dx}{i_2} \Big|_{i_1} = [\Omega / \text{m}]$$

The three basic phenomena that describe the coupling are:

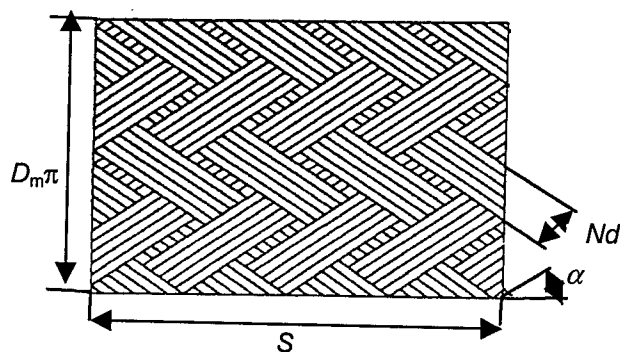
- Diffusion of E and H fields through the shield material.
- Penetration of the fields through the small apertures of the braided shields.
- An induction phenomena due to overlapping of the individual carriers of the shield.

When discussing woven braided shields you talk mostly of these six parameters:

- C – the number of carriers in the shield.
- N – the number of filaments of each carrier.
- d – the diameter of the filaments.
- d_0 – the diameter under the braid.
- α – the weave angle.
- K – the optical coverage of the braid.

Here the 6th parameter, the optical coverage, is determined by the five other parameters.

FIG. 2 Weave layout of a normal woven braid. N is one filament, i.e. one conductor in the braid.



Kley's model for the transfer impedance looks as follows:

$$Z_t = Z_R + j\omega L_T + (1 + j)\omega L_S$$

where:

- Z_R is the transfer impedance of the equivalent solid tube with holes.
- L_T is the penetration inductance.
- L_S is the skin inductance.

The equivalent solid tube with holes is a tube as thick as the braid and with as many elliptical holes, equally distributed around the tube, needed to get the same optical coverage as the braid has.

Each of these three terms in the expression of the transfer impedance is proportional to ω in some way:

$$Z_R \propto \frac{\sqrt{\omega}}{\sinh \sqrt{\omega}} \quad \omega L_T \propto \omega \quad \omega L_S \propto \sqrt{\omega}$$

ARTIFICIAL INTELLIGENCE

One of the techniques used in this project for analysing and predicting data is a neural network.

Artificial neural networks were first invented to behave as the biological ones, particularly as the human brain, in order to get a better understanding of how the human brain works. Today this is not always the intended use.

Almost all neural networks have some kind of training rule according to which the weights of the connections are adjusted due to the data in the training set. This means that neural networks learn from examples and get some capability for generalisation beyond the training data.

TEST OF THOMAS KLEY'S MODEL

In order to test and verify Kley's model and see how it behaves when changing the parameters a math-program was used.

Thomas Kley's model is based upon both theory and measurements. Kley fit the model to the test data after having first assumed a proportionality factor (from the physics) for each part of the model.

Robustness

Since the Kley model is based primarily upon measurements it is of great interest to see how stable the model is when the measurement-based constants are varied. In order to test this all the parameters in the model were changed $\pm 10\%$ and the output results were compared with the original model.

When comparing the output results from the changed models with the original model it was found to be no extreme changes, just the expected $\pm 10\%$ change in output. The model is therefore considered to be fairly stable for variations in the measurement-based constants.

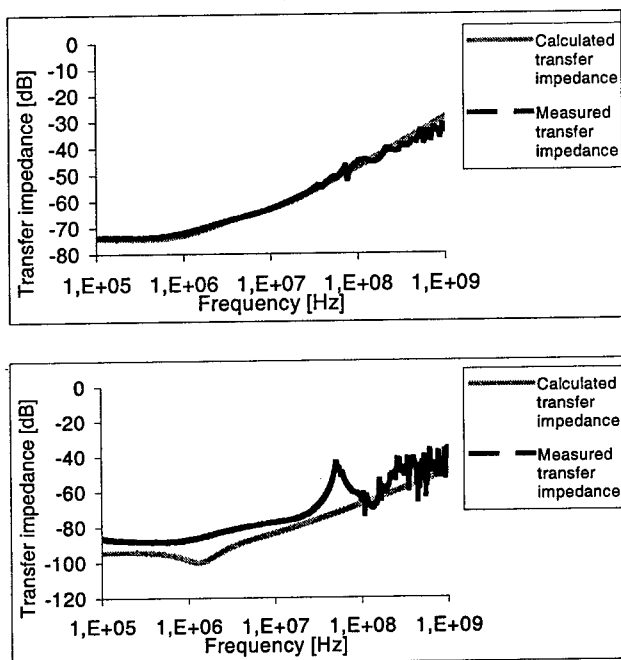
Verification of the model

When verifying the model Excel was used for plotting both the measured values and the dB-values (reference 100 Ω/m), both were plotted for both the model and the actual measured values.

The plots were then classified as 'OK' or 'not OK' depending on the difference between the measured values and the model values. For being classified as OK, a difference of up to 3 dB was allowed.

With the above definition half of the samples were classified as being OK. The other half that was not OK lies in the range of 5-10 dB off of the measured curve, most of them however with a similar curve profile.

FIG. 3 Comparison between calculated and measured values for the transfer impedance. Best fit at the top and worst fit below.



This verification and evaluation procedure lead to a new test series that is right now under manufacturing for deeper investigation in this field of transfer impedance.

COMPARISON ARTIFICIAL INTELLIGENCE – LINEAR REGRESSION

The comparison of the programs that uses the neural network technique and the linear regression is made through comparing the predictions from the programs.

The training of the neural network is rather simple, the problem is to find the proper settings for the training parameters in order to get the most out of the program. Unfortunately the manual to the program does not give many hints on how to set-up the program so it is just trial and error to see what the parameters do. However a number of different settings were found to give about the same result so it was found to be not that important how the set-up was done.

The linear regression program is much easier to use since it only has one model to fit the data against.

Predictions with neural network/linear regression

After the training of the neural network and the development of a model with linear regression, both methods have been used for predictions.

The neural network is clearly better than the linear regression when it comes to predictions of data that lies in the range of the training data. When trying to predict with data that lies outside the range of the training data, both methods fail. It is therefore obvious that in order to get a really useful neural network/linear model to predict with, it is necessary to have a wide range in the input parameters of the training data set.

The neural network gives generally better prediction than the linear regression and definitely better prediction than the Kley model. The neural network managed to predict 80% of the samples reasonably well while the linear regression program only managed to predict 40% reasonably well.

As can be seen (from fig 4 to fig 6) the neural network is always a little bit better than the linear regression and also most often better than the Kley model.

FIG. 4 The best fit with linear regression.
LR = linear regression, NN = neural network

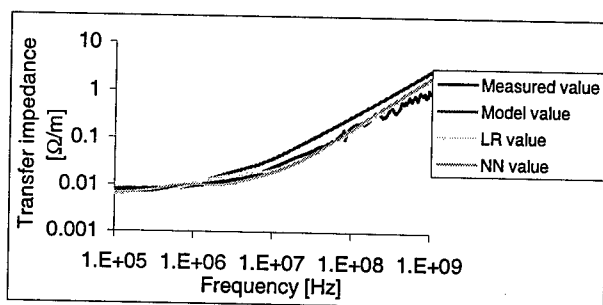


FIG. 5 The worst fit with the neural network.

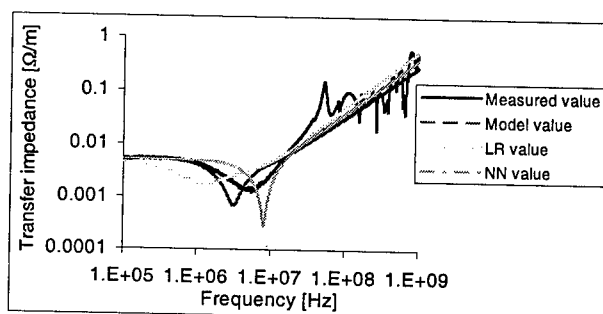
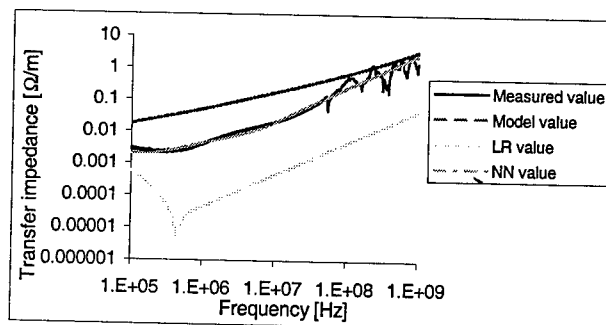


FIG. 6 The worst fit with the linear regression
and the best fit with the neural network.



For most of the sample the neural network fit follows the measured curve as it does in figure 4.

One advantage with Kley's model is that you can use it as a rough estimation of the transfer impedance over the whole possible range of input parameter variation.

Neural networks have the limitation that they get more accurate the smaller the variations in the training data set are. For best results with predictions with the help of neural network technology there should be several networks

trained, each of them covering a little piece of the input parameter range.

CONCLUSION

The problem to find a model for single-braided shields that is accurate enough for pre-manufacturing design seems to remain. So far the only models presented have been models for single-braided shields – when good shielding is needed, two braids on top of each other or foils and braid etc have to be used.

The verification of the model showed that Kley's model is so far not accurate enough.

The comparison between the neural network technology and the linear regression showed clearly that in this case a neural network is more accurate. Only when rough estimates of the transfer impedance is wanted should linear regression be used. It is also possible to use a functioning neural network in conjunction with a program that presents a user-friendlier interface.

The new test series that is under manufacturing right now will hopefully give more information and a better trained neural network.

REFERENCES

1. Kley, T. – *Optimierte Kabelschirme Theorie und Messung*, Abhandlung zur Erlangung des Titels Doktor der Technischen Wissenschaften (Diss. ETH Nr 9354), Zürich, 1991
2. IEC 96-1, Amendment 2 – Radio Frequency cables, part 1 – *General requirements and measuring methods*, 1993
3. Cheng, K.D. – *Field and Wave Electromagnetics*, Addison-Wesley Publishing Company, ISBN 0-201-52820-7, USA, 1989
4. Rachidi, F, Tesche, F.M, Ianoz, M.V. – *Electromagnetic coupling to cables with shield interruptions*, EMC 1997 12th International Zürich Symposium and Technical Exhibition on Electromagnetic Compatibility. Swiss Federal Inst. Technol, Zürich, Switzerland, 1997.
5. Tesche, F.M, Ianoz, M.V, Karlsson, T. – *EMC analysis methods and computational*

models, John Wiley & Sons Inc, New York,
ISBN 0-471-15573-X, 1996

6. Vance, E.F. – *Shielding effectiveness of Braided-Wire Shields*, IEEE transactions on Electromagnetic compatibility, vol. EMC-17, No. 2, 1975

BIOGRAPHIES

T. Nälsén
Habia Cable AB
Tierpsvägen 8
815 75 Söderfors



tomas.nalsen@habia.se

Tomas Nälsén is working in the R&D department at Habia Cable AB. He achieved his MSc in Electrical Engineering in 1999 and is since then employed at Habia.

Stefan Andersson is working in the R&D department at Habia Cable AB. He achieved his MSc in Electrical Engineering in 1975 and started working as a teacher. Since 1982 he is employed at Habia.

DEVELOPMENT OF THE BRAIDLESS COAXIAL DROP CABLE

Dean J. Yamasaki

Siecor; Hickory, North Carolina

ABSTRACT

The design of coaxial cables for drop applications has remained virtually unchanged since the mid-1970's. These legacy cable designs are susceptible to degradation from several mechanisms. Historically, the service life of field-deployed coaxial drop cable has been reduced by a combination of moisture ingress into the cable interstices and environmentally induced dynamic forces acting upon the cable. The use of wire braid in coaxial drop cable construction, while contributing to overall mechanical strength, also plays a significant role in advancing the adverse effects related to moisture attack and cyclic flexure of the cable.

This paper discusses a braidless coaxial drop cable design that incorporates several technical innovations. The material selection of components and arrangement of these components in the cable construction enhances the mechanical strength and electrical performance of this cable. Additionally, the bonded construction of this cable significantly reduces the potential for moisture ingress. This braidless coaxial cable design meets or exceeds industry accepted mechanical and electrical performance standards and maintains compatibility with existing, commercially-available F-connectors.

INTRODUCTION

One or more layers of aluminum wire mesh braid are included in the construction of most coaxial drop cables used in today's telecommunication systems. Coaxial drop cables are heavily used in Hybrid Fiber Coax (HFC) system designs utilized by Community Antenna Television (CATV) service providers. The origin of the utilization of a braided outer conductor in this type of cable can be traced to surplus military

cables obtained by upstart CATV companies a few years after the end of the Second World War.¹ Originally, coaxial cable designs with metal braid were used in all transmission applications – trunk, distribution and drop. As system performance requirements increased and technology advanced, the braided cable designs for trunk and distribution applications were phased out and replaced with higher performance braidless designs. The absence of braid improved both reliability and longevity of this portion of the cable plant. The development work for these trunk and distribution cable products was driven by the concept that improving performance would ultimately lower the overall operating cost of the system. These same design principles, used successfully in trunk and distribution cables, were then carried forward to the drop cable portion of the system. This initial push toward a braidless drop cable occurred more than 25 years ago.

Early attempts to achieve a complementary drop cable design without metal braid involved cold forming a solid aluminum tube around the cable core in place of the braid. This cable was very stiff and required special connectors for termination. When this design was field deployed, especially in free-swinging, unsupported aerial applications, the solid metal cracked when exposed to repeated flexure. This shield cracking, combined with the fact that this cable was incompatible with existing connectors, doomed this design. Follow-on drop cable designs without metal braid incorporated aluminum tapes similar in size and thickness to those used in braided cable designs. Early versions of aluminum tapes were susceptible to radial cracking (commonly referred to as "Tiger Striping") when exposed to repeated flexure. The radial cracks degraded cable performance to an unacceptable level and the absence of braid was perceived to worsen the condition. These issues were significant enough to halt

further development work for many years. This situation led to a widespread belief that a cost-effective braidless drop cable, with acceptable mechanical and electrical performance, was not achievable. System operators resigned themselves to use the braided drop product and live with the known limitations of the design.

Modern engineering and manufacturing processes have addressed braidless drop design issues experienced in the past. The use of laminated aluminum tapes and a bonded cable construction overcomes the shield integrity endurance issues experienced by past designs. An innovative design concept has resulted in a braidless coaxial drop cable with performance and long-term reliability comparable to even the most capable wire mesh braid drop cable designs. A reliable braidless coaxial drop cable product, to complement the braidless trunk and distribution cables, is now available for field use.

WIRE MESH BRAID – BENEFITS AND LIABILITIES

Wire mesh braid provides both mechanical and electrical benefits to the coaxial drop cable. Mechanically, the wire mesh braid provides strength under both applied flexure and tensile forces. The interwoven construction of the braid assumes imparted loads and provides support to other components such as the aluminum shielding tape. Most of the individual components of braided coaxial cables are free to move relative to one another until frictional coupling unifies their movement. In this manner, the braid will grab and hold the jacket and aluminum tape when mechanical loading is applied. Electrically, the aluminum braid provides low frequency signal shielding.

Unfortunately, the wire mesh braid also applies a compressive force on the portion of the cable it encircles as it assumes loading. The mechanics creating the compressive force are identical to the operation of a wire mesh pulling grip used in cable installation. Unlike cable installation, the compressive effects within the coaxial cable are long term and are cumulative. Because the braid coverage is nonuniform, there is an uneven force distribution as the mesh constricts around the cable core. Repeated compressive cycling can typically alter the foil's surface appearance from smooth and uniform to dimpled and uneven. This unevenness adds variability to the spacing between the inner and outer conductors

of the coaxial drop cable and could potentially impact impedance performance. This same compressive cycling can also create separation points at the foil tape overlap region that can create a pathway for signal egress and ingress.

Wire mesh braid contributes to the shielding performance of the drop cable primarily at frequencies generally below 200 MHz. The specific frequency where the shielding impact of braid diminishes is dependent of the system operating parameters. For example, in 75 ohm impedance CATV systems, the mesh braid is most effective below 50 MHz. The surface coverage achieved by wire mesh braid alone is never 100 percent and the gaps between braid wires are ineffective for shielding at higher frequencies. Many HFC systems today operate over a frequency band of 50 to 750 MHz, and higher frequencies are actively being considered. The wire mesh braid is effective at shielding approximately 20 percent of the utilized bandwidth.

Furthermore, the uneven surface of the wire mesh braid layer(s) within braided cable designs is conducive to water migration into the cable. The non-uniform braid coverage forms multiple pathways for moisture to migrate into the interior regions of the cable. Although gel flooded versions of braided cable designs are available, braided coaxial drop cables that incorporate more than one layer of braid are typically not fully flooded. Manufacturing process limitations typically allow only the outermost layer of braid wire to be covered with flooding compound.

Each of these issues has been addressed by the braidless coaxial drop cable design discussed in this paper. Consideration of impacting issues, design concepts, and performance verification testing will now be covered.

FAILURE MECHANISMS

In CATV systems, coaxial drop cable is responsible for up to 70 percent of subscriber service calls.² Many field-related issues associated with the system's coaxial drop cable plant are related to electrical performance degradation from the formation of corrosion within the cable structure or shield degradation due to damage to the shielding material. Wire mesh braid can be a catalyst, a cause, or both in supporting the mechanisms that lead to these types of problems.

Oxidation of the cable's metallic components permanently alters the electrical properties of the metal and consequently its transmission performance. Severe corrosion of the cable's conductive elements can ultimately lead to failure of the cable. Water migration into the cable is usually the precursor to corrosion formation. The presence of dissolved ionic chemical constituents, such as seawater salts, will exacerbate the conditions. The most likely entrance points for moisture are at the ends of the cable or at a point along the cable where the jacket integrity has been compromised. The magnitude of the problems caused by the corrosion is entirely dependent upon the moisture penetration distance into the interior of the cable. Greater moisture penetration distances equates to more severe degradation.

Shielding degradation can also significantly impact transmission quality and reliability. Inadequate shielding allows signals to leak out of the cable as well as allowing "over-the-air" signals to leak into the cable causing interference. Relative motion between the wire mesh braid and foil tape is one of the most likely internal mechanisms promoting shielding degradation and can be caused by a number of conditions. Environmental temperature variation combined with the differing coefficient of expansion of cable materials results in movement due to expansion and contraction. Wind induced movement will occur as the cable swings in aerial drop applications. Ice accumulation during winter months adds weight to the installation conditions and induces tensile forces on the cable. The uneven surface of the braid can mar the surface of the foil and potentially puncture the foil resulting in degraded shielding performance. The severity of the degradation is dependent upon the degree of damage imparted to the foil.

DESIGN CONCEPTS

With the primary failure mechanisms in mind, design work was conducted to develop a new coaxial drop cable which would improve long-term reliability. The two primary concepts for the new coaxial drop cable design were:

1. Eliminate the use of wire mesh braid.
2. Mechanically bond the constituent layers of the cable together to increase strength and reduce the potential for water migration.

Elimination of the wire mesh braid was a significant objective; nevertheless, other related objectives were targeted to optimize the functionality of the product. These other objectives included:

- Achieve the desired level of shielding performance utilizing only laminated foil tapes formed around the cable core.
- Select and arrange cable components to reduce moisture penetration potential of the cable. Specific considerations to bonding components together were made.
- Use field-proven materials wherever possible.
- Ensure compatibility with existing "F"-connector constructions and develop a simple method to install these connectors.
- Compensate for mechanical strength reduction caused by removing wire mesh braid from the cable design

The primary obstacle for previous braidless designs was induced cracking of the outer conductor (solid tube or tape) created by cyclic flexure after installation. Both input material properties (aluminum tapes) and added mechanical strength via cable construction technology (bonded construction) were used to improve the performance in this area.

Aluminum Tapes

The construction of aluminum tapes has matured and incorporated new technology since the radial cracking failures were experienced in early designs. Aluminum tape integrity is an important feature for all types of drop cables, not just braidless designs. In order to increase the overall reliability, these tapes have evolved from a single uniform thickness of metal to a laminated construction made up of several layers of different materials. The laminated tapes are sized and constructed to provide the same functional performance as their all-metallic predecessors. The laminated shielding tapes currently in use consist of a tear-resistant layer of plastic sandwiched between two individual layers of aluminum. This laminated construction increases the overall strength and is resistant to radial crack formation.

Mechanical Strength

Removing the metal braid from the cable design also removes the inherent mechanical strength

associated with the braid. Previous braidless designs did not adequately compensate for the reduction in strength; therefore, fatigue cracking of the outer conductive element resulted. The mechanical bond between the constituent cable layers builds additional strength back into the cable that compensates for the reduction in strength from braid removal. Applied mechanical forces are mitigated by the entire cable structure acting as a single unit. The bonded construction prevents any single component from accepting the entire applied load and thus reduces the potential for damage from induced stress.

BRAIDLESS CABLE DESCRIPTION

The braidless coaxial drop cable that resulted from the research and development process achieved the major concepts and objectives established during the design phase. Wire mesh braid has been eliminated and the bonded construction of the cable significantly improves this cable's performance when subjected to industry accepted water penetration testing. This cable design (see Figure 1) has been manufactured and tested using industry established test practices and conditions.

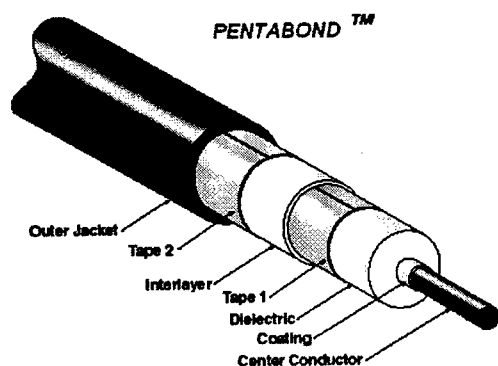


Figure 1. Braidless Coaxial Drop Cable

The input materials for this braidless cable design have been used for many years and are well known to the cabling industry.

- Center conductor – copper clad steel
- Dielectric – foamed polyethylene (PE) including the coating which bonds dielectric to center conductor
- Shielding tapes – aluminum laminated with tear-resistant plastic
- Interlayer – polymer elastomeric material
- Jacket – PE or polyvinylchloride (PVC) options are available

All materials used in the cable have established long-term performance records under actual deployment conditions. Each material has been used in either CATV or utility cable applications for many years.

All materials are applied, formed or extruded into a smooth, concentric unit and each layer is uniformly bonded to each adjacent layer.

Standard, commercially available "F" fittings are compatible with this braidless coaxial drop cable design and can be installed using a simple installation procedure.

The mechanical strength and shielding performance are comparable, and in some cases superior, to those of all braided coaxial drop cable designs.

TEST AND EVALUATION

Environmental Performance

Environmental forces significantly contribute to performance failure of braided coaxial drop cables in the field. The following laboratory tests were conducted to evaluate the braidless coaxial cables performance in a variety of adverse environmental conditions. The following tests were conducted:

- Heat Aging
- Temperature/Humidity Cycling
- Temperature Cycling
- Salt Fog Exposure
- Water Penetration

The test methods and conditions were based upon established procedures within the cabling industry. In some cases no standard test method was available to evaluate the coaxial drop cables under the targeted conditions. In these instances, test procedures and conditions were based upon industry accepted optical fiber

braidless coaxial cable design. Heat aging, temperature/humidity cycling and temperature cycling were based upon testing requirements specified by the United States Department of Agriculture (USDA) Rural Utilities Service (RUS) in 7 CFR 1755.900 (formerly PE-90).³ The RUS evaluates the functionality and appropriateness of outside plant optical cable designs based on this document.

Salt fog exposure was evaluated using the Society of Cable Telecommunications Engineers (SCTE) Test Procedure IPS-TP-017, "Moisture Inhibitor Corrosion Resistance."⁴

Water penetration testing was evaluated using Electronic Industries Association/Telecommunications Industry Association (EIA/TIA) Fiber Optic Test Procedure (FOTP) – 82, "Fluid Penetration Test for Fluid-Blocked Fiber Optic Cable" (ANSI/EIA/TIA-455-82B-1991).⁵

Heat Aging

In this test the attenuation and capacitance performance of the cable sample is measured before and after conditioning. The sample is conditioned by exposing it to a temperature of $65 \pm 2^\circ\text{C}$ for 14 days. Before conditioning and after conditioning measurements are then compared. A change of less than five percent is designated as the acceptance criteria (See Tables 1 and 2).

Frequency (MHz)	Initial (dB)	After Aging (dB)	% Change
5	3.27	3.33	1.8
50	8.53	8.65	1.4
100	11.78	11.86	0.7
500	26.18	26.55	1.4
1000	37.20	38.00	2.1

Table 1. Heat Aging Attenuation

Frequency (KHz)	Initial (nF)	After Aging (nF)	% Change
1	10.27	10.29	0.2

Table 2. Heat Aging Capacitance

Temperature/Humidity Cycling

In this test, the attenuation and capacitance performance of the cable sample is measured before and after conditioning. The sample is conditioned by exposing it to 100 temperature cyclings with the relative humidity in the test chamber maintained at 90 ± 2 percent. One complete temperature cycle consists of beginning at a stabilized chamber and test sample temperature of $52 \pm 2^\circ\text{C}$. The temperature is then increased to $57 \pm 2^\circ\text{C}$ and the chamber is allowed to stabilize. When the temperature of the test sample is stabilized at this level, the temperature is lowered back to $52 \pm 2^\circ\text{C}$. Before conditioning and after conditioning measurements are then compared. A change of less than five percent is designated as the acceptance criteria (See Tables 3 and 4).

Frequency (MHz)	Initial (dB)	After Aging (dB)	% Change
5	3.27	3.40	4.0
50	8.53	8.72	2.2
100	11.78	11.86	0.7
500	26.18	25.94	0.9
1000	37.20	36.70	1.3

Table 3. Temperature/Humidity Attenuation

Frequency (KHz)	Initial (nF)	After Aging (nF)	% Change
1	10.27	10.30	0.3

Table 4. Temperature/Humidity Capacitance

Temperature Cycling

In this test, the attenuation and capacitance performance of the cable sample is measured before and after conditioning. The sample is conditioned by exposing it to 10 temperature cycles between -40°C and $+60^\circ\text{C}$. The test sample must be held at each temperature extreme for a minimum of 1.5 hours during each cycle of temperature. The air within the temperature chamber must be circulated throughout the duration of the cycling. Before conditioning and after conditioning measurements are then compared. A change of less than five percent is designated as the acceptance criteria (See Tables 5 and 6).

Frequency (MHz)	Initial (dB)	After Aging (dB)	% Change
5	3.27	3.29	0.6
50	8.53	8.61	0.9
100	11.78	11.89	0.9
500	26.18	26.48	1.1
1000	37.20	37.60	1.1

Table 5. Temperature Cycling Attenuation

Frequency (KHz)	Initial (nF)	After Aging (nF)	% Change
1	10.27	10.28	0.1

Table 6. Temperature Cycling Capacitance

Salt Fog Exposure

This test evaluates the corrosion resistance of the coaxial drop cable. Each sample is prepared for this test by cutting three rectangular slots through the cable jacket (6.35 mm by 25.4 mm) to expose the metallic components of the cable. The test method involves subjecting the prepared sample to a predetermined simulated corrosive environment (temperature range of 33.3 °C to 36.1 °C; 5 % salt solution; fog concentration 100 % humidity) for 144 hours. An additional 25.4 mm of jacket is removed from both sides of the original slots. The newly uncovered areas of the test samples are then inspected for visible signs of corrosion. The results are passing if no corrosion is visible to the unaided eye. Visible corrosion is designated a test failure.

Testing was conducted on braided and braidless designs for comparison purposes. The results of this testing are summarized in Table 7.

Corrosion Inhibition Test Results SCTE Test Procedure IPS-TP-017	
Braidless (PVC jacket)	PASS
Braidless (PE jacket)	PASS
Tape/Braid (no flooding)	FAIL
Tape/Braid (PVC jacket; flooded)	PASS
Tape/Braid (PE jacket; flooded)	PASS
Quadshield (no flooding)	FAIL
Trishield (flooded)	FAIL

Table 7. Salt Fog Test Results

Water Penetration

One of the major adversaries of the deployed coaxial drop cable is water. Moisture intrusion into the interstices of the drop cable leads to

corrosion and degraded performance. Typical pathways into the cable have historically been through the connectorized end of the cable or via a breach in the jacket. Sealed connectors have been introduced to minimize the potential for water penetration via the cable end; however, additional measures can be taken to reduce the system impact should moisture find its way into the cable core.

Historically, wholesale replacement of the drop cable was the common corrective action when evidence of moisture penetration was discovered. The formation of corrosion on the interior surfaces of the connector was typically the observed evidence of moisture penetration. Unfortunately, the only definitive conclusion that could be drawn was that an access point to the interior of the cable had been exposed to moisture. However, it was unclear what penetration distance had been achieved and there was no good method available to determine the portion of the cable that was susceptible to degradation by corrosion. The conservative action, taken to minimize the probability of repeated site visits, was to replace the entire length of drop cable at the site.

Flooding compounds have been utilized to address the water migration issue in both aerial and buried drop applications. Tape and braid designs are reasonably protected in this manner; however, multiple layer tape cables (quad-shield and tri-shield) can be more susceptible to water migration because the flooding compound is typically applied to the outermost layer only. While this is adequate to address a breach in the outer jacket, this configuration does not provide the same level of protection should an open cable end (similar to a connectorized end) be exposed to moisture.

The braidless design significantly reduces the potential for water migration. Its bonded construction prevents moisture flow because there are no penetration pathways. Water penetration testing using test samples one meter in length demonstrates the difference in performance. The procedure used was adapted from an existing document used for optical fiber cable. This test is conducted by applying a one meter pressure head of water on the open end of the test sample. Any test fluid escaping from the opposite end is collected and measured. The test pressure is applied for one hour. Results are tabulated in Table 8.

Cable Type	Average Leak Rate (ml/hr)	Standard Deviation
Tape and Braid (no flooding)	154.00	4.62
Tape and Braid (with flooding)	1.55	4.62
Tri-shield (with flooding)	149.00	6.63
Braidless	0.05	0.05

Table 8. Water Penetration Test Results

Mechanical Performance

Mechanical forces can degrade the performance of the coaxial drop cable by altering its electrical properties. Two significant performance parameters are impedance which defines the signal reflection properties of the cable and transfer impedance which defines the shielding effectiveness of the cable. Performance comparisons were conducted to evaluate the performance of the new braidless design relative to existing braided cable designs. The following comparisons were conducted:

- Impedance performance in conjunction with applied compressive loading.
- Transfer impedance performance after applied cyclic flexure.

Performance Under Compression

Compression testing was conducted to compare relative performance between a braidless cable and a quad shield braided cable. A quad shield braided cable was used because this design provided the most metal mass around the cable core and should provide the greatest degree of protection. The comparative compression testing was conducted as follows. The cable under test is placed between two flat plates with rounded edges (See Figure 2).

A time domain reflectometer is attached to the sample to conduct continuous impedance measurements. A compressive force is applied at a rate of 10 N/minute until a 0.5 ohm impedance change occurs, the applied force is momentarily held, and the load is recorded. The application of force is then resumed until the impedance change attains 3.0 ohms. The applied force is momentarily held and the load is

recorded. The applied load is then released and the recovery in impedance is measured. The results of this comparison demonstrate that the bonded construction of the braidless coaxial cable can assume a greater loading level than braided cables. In addition, the bonded construction does not impede performance recovery after a transient load is removed. The braidless coaxial cable demonstrated the same degree of recovery as the braided coaxial cable even when loaded to a higher level (See Table 9). The results of this test indicate that the mechanical strength of the braidless coaxial cable is at least equivalent, if not superior, to the quad shield braided cable.⁷

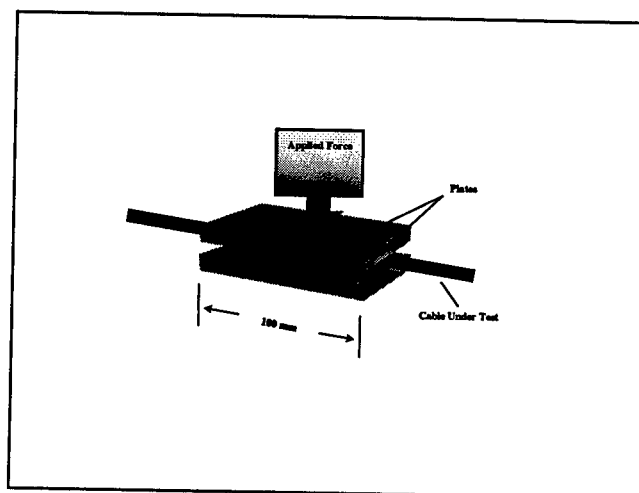


Figure 2: Compression Test Set-up

Cable Type	Loading to achieve 0.5 ohm Δ	Loading to achieve 3.0 ohm Δ	Recovery after Load Release
Braidless	202 lb	336 lb	67%
Quad-shield	88 lb	197 lb	63%

Table 9: Results of Compressive Loading Testing

Shielding Performance After Cyclic Flexure

Transfer impedance establishes the shielding effectiveness of the device or component being evaluated. Transfer impedance of a coaxial cable is measured using a triaxial test fixture and using the method described in The Society of Cable Telecommunications Engineers (SCTE) Document IPS-TP-011, "Test Method for

Transfer Impedance.”⁶ Lower values of transfer impedance are indicative of better shielding performance. For this comparison, the test samples were conditioned prior to measurement by flexing each sample over a series of mandrels. This conditioning was intended to simulate anticipated flexure in a field installed condition. A comparison of shielding performance reliability after mechanical aging has been generated by plotting the results of various simulated aging tests of different designs (See Figure 3). The braidless cable demonstrates shielding performance exceeding that of standard tape and braid cables and comparable to that of larger, heavier and more expensive tri-shield and quad-shield cables.

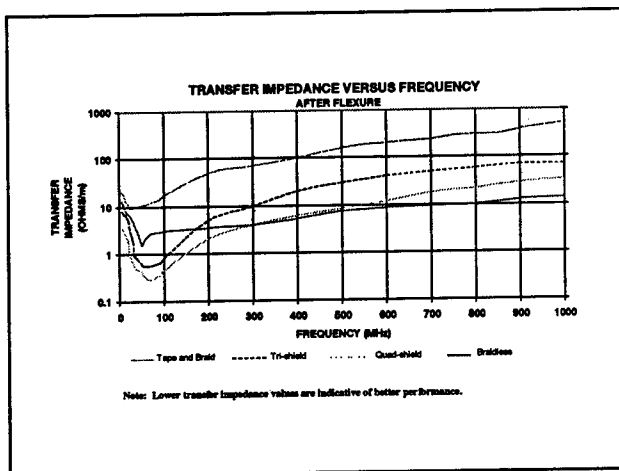


Figure 3. Transfer Impedance

CONCLUSION

The braidless coaxial drop cable design discussed in this paper provides the first real technological advances for this type of coaxial cable application in 20 years. This braidless cable design is compatible with existing, commercially available tools and connectors. The mechanical and environmental performance results demonstrate that this new cable design equals or exceeds the performance of existing braided drop cable products.

Acknowledgments

The author would like to recognize Tim Dugan for his efforts and support of this paper.

References

1. C. Kuhl, "A Retrospective: 50 Years of Technology," A Special Supplement to CED Magazine, June 1998
2. R. Hranac, "Bulletproof Your Drop," Communications Technology, April 1999
3. United States Department of Agriculture, Rural Electrification Administration, 7 CFR Part 1755 RIN 0572-AA57, "Specification for Filled Fiber Optic Cables," Federal Register, Vol. 59 No. 127, July 5, 1994
4. IPS-TP-017, "Test Method for Moisture Inhibitor Corrosion Resistance," Society of Cable Telecommunication Engineers, February 1994
5. ANSI/EIA/TIA-455-82B-1991, "Fluid Penetration Test for Fluid-Blocked Fiber Optic Cable," Electronic Industries Association/Telecommunications Industry Association
6. IPS-TP-011, "Test Method for Transfer Impedance (Preliminary)," Society of Cable Telecommunication Engineers, May 1993
7. D. Yamasaki, "Improving Reliability Of HFC Broadband Networks Using Braidless Coaxial Drop Cable," National Fiber Optic Engineers Conference 1999 Proceedings, September 1999



Biography

Dean Yamasaki is a Senior Applications Engineer with Siecor responsible for providing technical support for optical fiber cable, coaxial drop cable and deployment requirements. He is a graduate of the United States Naval Academy; Annapolis, Maryland. He served as a Nuclear Engineer in the US Navy prior to joining Siecor. He has published several papers on cable applications in telecommunications and is a member of the Society of Cable Telecommunication Engineers (SCTE).

Bending Fatigue Failure Analysis & Testing of a Radar Frequency Co-Axial Cable
Sean Kery, Senior Engineer
Antenna Group
Northrop Grumman Corp. ESSS

Abstract:

The work described in this paper is the result of a field service cable failure encountered on an aircraft based radar antenna. The cable feeds RF energy to an after market feature, added to the original antenna. The cable undergoes cyclic bending where it passes the azimuth and elevation gimbal axis. The principal functions of the antenna were fed past the gimbal axis through a slip ring assembly and are not subject to this failure mode.

This paper, in three sections describes the analysis of the field failures, a discussion of mitigation strategies, and testing to qualify the improvements. The first section describes the investigation of the failure mode or modes. The second section describes the development of strategies to extend the life of the cable. The third section describes a test program to qualify the suggested improvements and to attain a quantitative estimate of the field life with improvements.

Problem Geometry:

A top view of a stylized azimuth gimbal is shown in figure one. The gimbal cap is approximately 3.25 inches, (8.25 cm) in diameter. The cables under consideration vary from .195 to .25 inches, (5 to 6.3 mm) in diameter depending upon brand and construction detail discussed later. A second cable consisting of numerous small single conductors inside a woven fiber jacket runs in parallel with the co-axial cable and contributes to the path of bending. The gimbal cap to Coaxial cable diameter ratio is 3.5 to .195 or approximately 18:1, far less that a more optimal 40:1. Ref. 1 The loop geometry is constrained by the antenna geometry. There appears to be as much as 30 degrees, (+/-15) of torsional rotation about the cables longitudinal axis that completely reverses on each cycle. This is spread out over about 16 inches, (41 cm) of cable length. The exact amount was difficult to measure accurately because the amount of the rotational motion attributable to axial torsion versus bending along the motion path varies somewhat from cycle to cycle and from antenna to antenna.

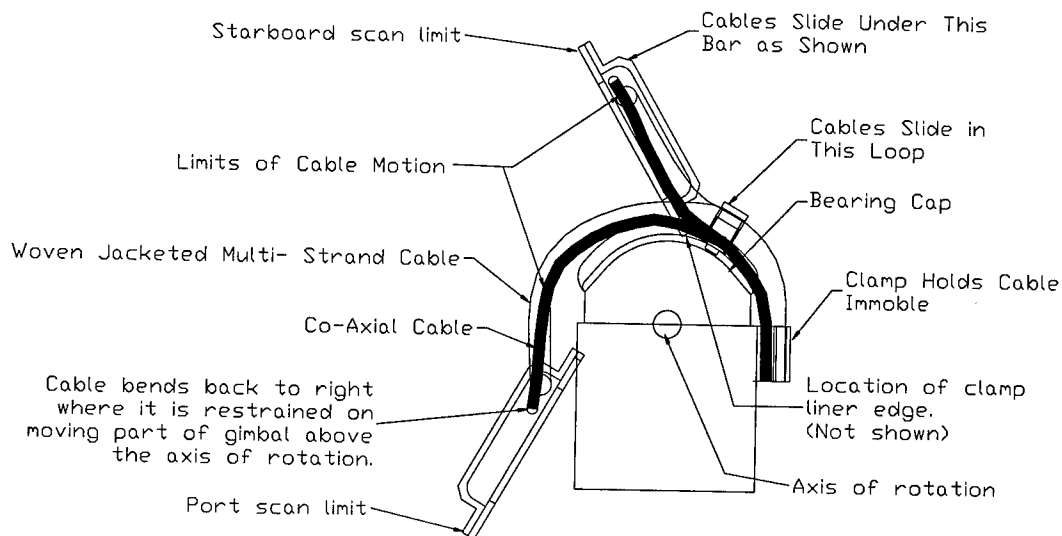


Figure 1. Cable Flexural Geometry.

Analysis of field samples:

A total of 7 complete cables at various life stages were acquired for evaluation of the field problem. All of the observed failures occurred at exactly the same point along the cable length associated with a Nylon clamp liner on the azimuth gimbal. No field reports associated any failures with the elevation gimbal axis so that axis was not studied further. It was fairly obvious that all of the failures, manifested as jacket cracks, occurred at exactly the point where the cable touched a 135 degree edge, (top of a 45 degree chamfer) on a nylon clamp liner. This clamp liner is located just after the last place that the cable is held rigidly.

Assessment of the failure path through the cable was complicated by the field practice of taping up the jacket and continuing to use the cable until it completely failed. This practice effectively eliminates any information about the intermediate stages of the failure.

To improve the cable design, it is necessary to understand the bending behavior of the cable in its entirety and the path of failure propagation through the cable structure. The analysis of the samples is described below:

The analysis began by dissecting and measuring an undamaged section of cable that had not been subjected to cyclic bending to establish a construction and design baseline. The cable consists of a tube extruded fluoropolymer jacket over a braid shield, a layer of Teflon tape, then a served, silver plated copper foil tape shield. Next comes the primary insulation composed of served layers of Teflon tape. The conductor core is a 1 by 19 contrahelical construction of silver plated copper.

Original Cable Construction:

Outside diameter: 0.195 inches, (4.95mm).

Braid OD is .175 inches, (4.44mm). The braid in the original cable consists of 16 carriers of 9 strands at a 45 degree lay angle. The braid material is given in the part spec as silver plated copper.

The foil shield is composed of a silver plated copper foil wound with about a 50% overlap. In the undisturbed condition the helix of this foil is very uniform. The edges of the foil used by this manufacturer give a sharp almost file like texture to this layer of the cable.

The primary insulation consists of various layers of Teflon tape.

The conductor core is a 1 by 19 contrahelical construction, (12 around 6 around 1) with a standard left hand lay outer and a right hand lay inner layer. All wires are the same diameter. What is unusual, compared to a wire rope construction, are the low lay angles used. Ref 1. The inner layer lay angle is 7.6 degrees and the outer layer lay angle is 10 degrees. In wire rope construction, it is more typical for the outer layer to have a smaller lay angle than the inner and for the lay angles in general to be between 16 and 24 degrees. The higher lay angles spread any bending out over a longer length of metal, which would reduce stress and prolong the fatigue life.

The use of higher lay angles would also allow the design to approach torque balance which becomes important when cyclic torsion or cyclic axial stresses are encountered.

Table 1. Summary of damage to cables inspected.

Description Number	Hours in service*	Visible Damage	Damage visible on X-Ray
1	42	Crack in outer jacket. No other damage	none
2	152 **	No visible damage	No visible damage
3	Unknown	Jacket and outer shield damaged	N/A
4	358	Field Service wrapped the contact area with tape	No visible damage
5	142	Field Service wrapped the contact area with tape	No visible damage
6	530	Both Shields severed	N/A
7	352	Taped by field service	Visible damage.

*Actual flight hours. ** Note: this antenna was brought in for service for an unrelated problem with the cable in good working order.

The seven samples ranged from samples 2,4 and 5, which had no apparent damage to cable 3, which had severe damage to the jacket, both shields and the core.

Sample 1 was removed from service after only 42 flight hours when a crack was noticed in the cable jacket. A careful visual, X-ray and dissection inspection revealed no other damage. A careful examination of all 7 cables suggested that the jacket is failing first. This then causes a marked reduction in bending stiffness at the crack, which focuses the fatigue stresses in a narrow band on the metallic components.

Part 1 Field Data Analysis, Conclusions:

1. The damage on all cables showing damage, occurred where the cable jacket came in contact with the nylon clamp bed edge. A simple score and snap test suggests that the jacket is notch sensitive. The failure initiation mode appears to be jacket cracking.

2. There was a point of ambiguity on the cable installation drawing that allowed for any of 3 different routings with respect to a multi conductor woven jacketed cable that runs in parallel with this co-axial cable. Only 1 of the 3 routing paths provided the co-axial cable with adequate freedom of movement. The cable that failed after only 42 hours was installed in an unfavorable routing such that the adjacent cable restricted its movement at critical points in the gimbal swing. This caused the bending to take place over a shorter length of the cable than normal.

3. One possibility considered was a possible low temperature ductility loss of the plastic jacket material. Subsequent material property research suggested that this was not a likely scenario.

Part 2. Mitigation strategy:

Four different parallel efforts were pursued to increase the fatigue life of this cable towards the goal of 1000 flight hours.

1. The first and simplest fix was to redesign the clamp bed part to eliminate the offending edge. This was accomplished by simply extending the plastic smoothly out past the point where the cable could possibly make contact. The new part even uses the same fasteners as its predecessor facilitating field replacement.

2. The cable routing issue was solved by rewording the installation instructions and by adding additional markings to one of the plastic clamps which makes the preferred installation routing clear.

3. The original vendor and nine additional candidate vendors were contacted and asked for advice and for samples of cables that they thought might perform better in this application. The original vendor and three others responded with candidate cables. The other six companies did not return bids based upon the mechanical and electrical specification document that was sent to them.

4. A test fixture was developed that would exactly represent the cable routing and flexing geometry to allow testing of mitigation methods and alternative cables.

Test Fixture Description:

The test fixture uses a geared down off the shelf electric motor to turn a bell crank at twice the rotational rate encountered in the field. This allowed the test to be accelerated by a factor of 2 while keeping the speed slow enough that the cables would not whip around in an uncharacteristic manner. The bell crank moves a common shaft on which are mounted 6 test bays that have exactly the same geometry as the actual antenna with respect to where it makes contact with the cable. All of the various plastic clamps liners and saddles were made from the production parts drawings. See Figure 2 below.

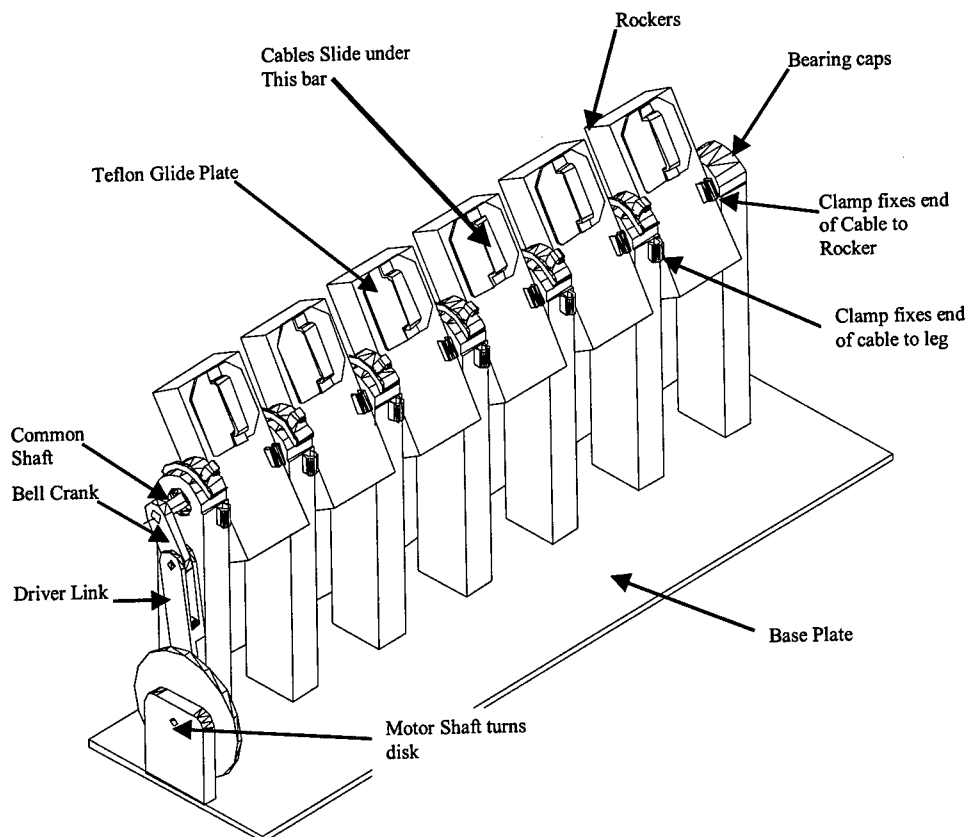


Figure 2. Test fixture design.

The cycle count was recorded on a commercial off the shelf, 6 digit mechanical counter.

The test was conducted in an environmental chamber that allowed temperature to be cycled over the range encountered in service of +100 to -30 degrees C. The high temperature was reduced to +50 degrees C because the problem was thought to be aggravated by low temperatures and the test fixture motor was not designed to operate at higher temperatures. The temperature was cycled a total of 24 times over the life of the test.

All three conductors were tested for DC continuity once per day both with the test fixture stopped and running. It was not feasible to terminate the short test lengths for an RF frequency test because the end terminations effects would swamp any signal caused by cable degradations.

Phase One Test Description:

A short sample of each of the four vendors candidate cables was dissected and the details of the construction documented. One candidate was disqualified at this time when it

was found to have a large diameter core wire with one layer of small wires wrapped around it. This construction was thought to be less than ideal for surviving high cycle fatigue.

Three samples of the original cable were loaded onto the first 2 bays of the test machine. Bay one used the sharp edge clamp as on the production antenna's. Bay's two through six used the improved smooth clamp liner.

Bay four was occupied by a variation on the original cable in which additional Teflon tape layers were added and the outer jacket was made considerably thicker. The thicker jacket resulted in a noticeably stiffer cable.

Bay five was occupied by another vendor's cable with the following design differences. The outer jacket was clear over a Mylar tape. The shield braid was made of stainless steel instead of silver plated copper. The central conductor was a 1 by 19 but in unilay instead of contrahelical construction. This cable was also stiffer than the original cable.

Bay 6 was occupied by the third vendor's cable with some marked design differences. Primary among these is the total absence of an extruded jacket. The jacket is

composed of a fiber braid over layers of Teflon tape. The braid shield is similar to the braid of the original cable but uses 8 wires per carrier instead of 9. The foil tape braid has much smoother texture than the original cable suggesting that the edges of the foil received some rounding treatment before the serving operation. The conductor core is a 1 by 19 contrahelical with lay angles of about 15 degrees on both inner and outer layers. These lay angles are an improvement on the original cable and should offer improved cable life.

Phase One Test Results:

Sample 4 with the thick stiff jacket showed damage to the jacket after only 96000 cycles. Sample 5 showed discoloration of the Mylar suggesting that the stainless braid is abrading the Mylar tape.

By 120,000 cycles sample 4 had a crack running all the way around the jacket and all of the bending was concentrating in that area.

At 357,000 cycles samples 1, 2 & 3 showed discoloration of the jacket on the top tension side of the bend. Cable 4 has all of the metallic conductors broken and was removed from test. Cable 5 has a stainless braid wire sticking through the outer jacket suggesting that the braid is starting to fail in metal fatigue. By 500,000 cycles the core and the foil shield were showing intermittent DC continuity indicating that cable sample 5 was no longer a viable candidate.

At 553,000 cycles sample 1, the original cable bending over the original sharp clamp has a jacket crack about 3/8", (1cm) away from the clamp edge. The position of the adjacent braided cable is acting like a soft sheave and forcing the bending in the coaxial cable to be spread out over a considerable distance which was not noticed before. All of the original cables have the braid and foil shields shorted at this time and all have significant discoloration of the jacket in the area that bends the most.

At 662,000 cycles, sample 1 now had 2 cracks in the jacket, the second appearing as expected where the cable makes contact with the clamp liner.

As samples fail they are removed for the test fixture and new cable put up in their

place with the counter reading at start labeled on them.

At 993,000 cycles, sample 1 has intermittent continuity on all conductors and is removed from test. Sample 3 has a jacket crack at about 7/8", (2cm) from the first clamp.

This left one of the original cables in bay two intact and the fiber jacketed cable in bay six intact.

At 1,792,000 cycles, the core conductivity on the longest lasting original cable went intermittent signifying complete core failure.

The fiber jacketed cable in bay six was removed from test with no apparent damage at 2,056,000 cycles.

Analysis of Failed Specimens:

All cables from the first phase of testing were visually and X-Ray inspected and then dissected to learn as much as possible about the failure modes and propagation path.

General Conclusions, Phase One Testing:

1. All failures occurring before 1 million cycles were initiated by cracking of the extruded jacket.
2. The new cable routing and smooth clamp bed appear to extend the fatigue life of these cables. Failures will no longer be associated with a single point on the cable.
3. The two stiffest cables failed the first suggesting that the greater jacket thickness used to increase the cable stiffness hurts more than it helps.
4. The discoloration of the jacket on the original brand of cable is due to broken wires in the braid shield. Dissection of specimens shows that there is a directional bias in which braid wires fail first which is consistent with torsional fatigue acting on top of bending fatigue.
5. The new cable in bay six with the fiber outer jacket did not have a single broken braid wire in 2+ million cycles of bending. Two sources of this marked performance difference are surmised. First, the slight difference of 8 wires per carrier instead of 9 allows the wires to not bend as sharply as they pass over and under adjacent wires in the braid, which reduces bending stress and encourages slippage. The plastic jacket on the original cable gets slightly flattened as the tube extrusion is

bent which crimps down and further limits the sliding motion of the braid wires in that cable.

Phase Two Testing:

Only one sample of the longest lasting cable was tested on the first phase. It was now necessary to increase the number of samples of that cable and repeat the test to gain confidence in the result and make sure that the sample of one did not represent a statistical outlier. A total length sufficient to make 4 new samples of the fiber jacketed cable was available. These were loaded onto the test fixture and it was restarted with the counter set to zero's.

All samples performed adequately and were removed from test without visible damage or change in DC electrical properties at 1,156,000 cycles. All 4 samples were then dissected to determine what if any damage had occurred in that time.

Other Testing:

Two additional fiber jacketed cables were procured with terminations per the original specification and were subjected to a full suite of electrical and RF tests as per the spec. These were tested on an HP8510 Spectrum Analyzer calibrated for the frequencies of interest. Fit tests and range beam pattern tests on an actual antenna scanning in normal operational modes were also conducted.

Phase Two Results:

1. All 4 cables survived with no signs of cosmetic damage and no loss of DC continuity.
2. The two terminated samples passed all electrical tests including insertion loss and VSWR tests. All tests were within normal ranges observed and specified for the original cable.

Comparison Results, Selected Samples: Table 2.

Cable Type	Cycles tested	Braid Damage?	Foil Shield damage?	Core Wires Broken?	Jacket Crack?
Original 1	793k	severe	broken	all 19	2 places
Original 2	1,791k	severe	broken x1	all 19	no
Original 3	993k	severe	broken	all 19	yes
Original 4a	1,122k	severe	broken x3	4 inner	yes
Original 5a	1,067k	severe	none	8 outer, all inner	yes
Fiber Jacket 6	2,055k	none	some slip	6 outer	N/A
Fiber Jacket 2b	1,156k	none	none	none	N/A
Fiber Jacket 3b	1,156k	none	some slip	6 inner	N/A
Fiber Jacket 4b	1,156k	none	4 cracks	6 outer, all inner	N/A
Fiber Jacket 5b	1,156k	none	none	none	N/A

Conclusions Based Upon all Test Results and Observations:

1. Core Construction:

In an average of 1,411 thousand cycles, the original cable suffered 80% breakage in the core wires. The fiber jacketed cable had only 26.3% breakage in 1,336 thousand cycles. The small increase in lay angle appears to have a meaningful effect on the fatigue life without

having a meaningful effect on the RF properties. The torque ratio of the original cable was 4.33:1 whereas the fiber jacketed cable had a torque ratio of 3.43:1. The higher torque ratio may have contributed to the more rapid fatigue failure of the original cable.

All of the manufacturers that submitted samples expressed great reluctance to change any aspect of the core construction for fear of losing RF performance. There was no

measurable difference in RF performance measured for core lay angles, or core construction varying by manufacturer for the cables tested. This result suggests that further increase in lay angles and or an attempt to more closely approach torque balance in the core is unlikely to profoundly effect RF performance.

2. Braid Construction / Damage:

The early and severe braid degradation of the original cable in contrast to no visible braid damage on the fiber jacketed cable is remarkable. The braid damage in the original cable which led to jacket discoloration may happen before and contribute to the jacket cracking. The braid damage is though to be due to reduced wire mobility causing stress concentrations in the individual wires. The loss of mobility is caused by too high a percentage fill and by the squeeze of the extruded jacket as it distorts out of round in bending.

The fiber jacketed cable does not have an extruded jacket and therefore the distortion out of round on bending is not significant. The slight difference in percentage fill allows the individual wires to move slip with less friction as the cable flexes significantly reducing the stress.

3. Jacket Damage / Cracking:

Any thermoplastic jacketing material that can be extruded and that will work within this cables temperature range will have a fatigue life that is at least one order of magnitude less than the copper conductors. Ref. 2 The fiber jacket over Teflon tape, if it is possible to define a fatigue life, is orders of magnitude greater than that of the copper conductors. Clearly switching to the fiber jacketed cable removes the jacket as the primary failure initiation mechanism.

4. Foil Tape Shield Distortion and Breakage:

All of the cable samples analyzed suggest that the foil tape is the last metallic component to fail or it's tied for last place with the cable core. In all of the samples showing damage to the foil shield, there was significant slip distortion of the tape lay angle associated with and occurring prior to metallic fracture. In several cases the dislocation occurred in the same location as the fractures in the cable core wires. This brings up the question of which causes which.

There is further ambiguity in that the test samples were not terminated in the same way as the actual cables used in the field and some of the slip distortions observed may have been artifacts of insufficiently restraining the construction at the ends of the short test samples. Slipping and cracking of the foil shield is associated with the longest lasting cables. Attempts to improve this part of the cable design would only be worthwhile if all other cable components were improved first such that this became the dominant failure initiation mode.

It is worth noting that when damage did occur to the foil shield it always took place on the inside, (compression side) of the bend. Most frequently the crack was limited to the overlapping half of the foil width. In several cases the crack goes straight across half way and then splits 90 degrees to follow the overlap in both directions. This results in a T or Y shaped crack.

5. Teflon Tape Layers:

On the original cables, there is a single filled Teflon tape layer that separates the two shield layers. This was insufficient to prevent the two shield layers from shorting to one another any time from new cable delivery to a few tens of thousands of cycles. This was most likely aggravated by the extruded jacket going out of round on bending and crushing the braid shield onto the sharp upper edges of the foil shield.

This shorting was not observed on the fiber jacketed cable. The foil tape shield was smoother to start with, the braid did not fracture into little scraps of wire that could easily perforate the soft tape. There was no significant crushing force introduced by a tubular jacket deforming in bending.

General Comments:

The fiber jacketed cable has been added to the source control drawing for this part as the cable of choice and the original cable has been demoted from sole source to second choice alternate.

The test fixture and setup accurately models the actual use geometry but it is not possible to model the acceleration and acceleration for duration events encountered on an actual aircraft as it maneuvers. A shaker table can reproduce the acceleration but not the acceleration for duration.

Many other mitigation methods including increasing the number of channels on the slip ring were suggested and discussed. The methods chosen are a cost effective, field installable upgrade that will most likely at least double the cable life over the original cable. While some of the results would suggest an even larger increase in life, the small test sample population does not provide a valid basis for a more exact conclusion.

Acknowledgements:

The author would like to acknowledge the advice, assistance and encouragement of many people but most especially my teachers in cable science over the years, Dr. Walter Paul, Henri Berteaux, Bob Walden, John Cobb, Doug Bentley, Phil Gibson, Carl Hikes and Earl Diamond. The assistance of the various vendor contacts in supplying samples to test and information is gratefully acknowledged. I can't name names here but you know who you are. Thanks also to M. Brence, K. Devlin, S. Stem, J. Gifford, D. Yelverton, J. Steidl, B. Pearson and the rest of the many people at Northrop Grumman who made this possible.

References:

1. "Handbook of Oceanographic Winch, Wire and Cable Technology" A.H.Driscoll, Editor, Published by the Author under a grant from the US Navy Office of Naval Research and the National Science Foundation, 1982.
2. "Handbook of Tribology and Fatigue Curves for Plastics" published by the Plastic Design Library

Biographical Information:



Sean Kery began studying tow and mooring cables in 1985, while employed at the Woods Hole Oceanographic Institution. Mr Kery also worked with tow cables at Northrop Grumman's Oceanic Systems Division in Annapolis, MD. He is currently employed by the Radar Antenna Group at Northrop Grumman's Baltimore, MD facility where this work took place. Mr Kery has a BS in Mechanical Engineering from the University of Rhode Island and is pursuing a master of science in Systems Engineering at Johns Hopkins University. Sean Kery is the author or co-author of 22 other technical publications. He resides in Southern Maryland with his wife and 4 children.

AUTHOR INDEX

Name	Page	Name	Page
ABE, I.....	148	DEFABRITIS, R. P.....	66
ABIRU, T.....	312	DEFOSSE, Y.	550
ABRAHAM, A.....	520	DEGROSS, J. L.	831
ABRAMCZYK, J.....	672, 687	DOLE, C.	233
ACCORSI, J. V.	815	DUPIRE, P.....	464
ADAMS, M. A.....	730	EBERT, T.....	421
ANDERSON, M.	621	EMETERIO, M. G. S.....	106
ANDERSSON, S.....	859	ENGEL, R.	61
ANDREASSEN, J. S.	285, 305	ENGLEBERT, J.	658
ARAI, K.	769	FENTON, D. K.	275
ARAI, O.....	148	FINNIMORE, A. L.	221
ARIKAWA, T.	324	FROIDURE, J.-C.	550
ARTHUR, S. A.....	672	FUJIWARA, K.	346
ATKINSON, D. L.	221	FULOP, D. A.....	471
BAGAROLLI, A.	650	FURTADO, J. M. I.....	446, 585
BARBER, M.	199	FURUKAWA, H.....	346
BEHLAU, G.....	846	GAILLARD, P.....	106
BELLINGEN, C. V.....	815	GAMBRELL, D.....	428
BENAYON, F. R. B.	650	GANDHI, P.	421
BENZEL, D.	416	GAO, Z.....	61
BENZEL, D. J.	157	GEBIZLIOGLU, O. S.....	213
BERGER, T. P.	560, 744	GENJI, T.	714, 775
BINLAN, F.....	593	GERDES, R. J.	427
BISSELL, S. T.....	72	GHIRARDINI, S.	184
BLEICH, L. L.....	421	GIACAGLIA, M. V.	471
BLONDEL, M.	550	GIMBLET, M.	755
BONANNI, P.	184	GODDARD, T. G.	377
BONICEL, J. P.....	106, 416	GRAVELY, III, R. G.	571
BOOKWALTER, T. A.	488	GREGOR, P. E.	170
BÖR, J.	255, 268	GREGORY, A.	658
BOTTANELLI, M.	666	GREGORY, A. C.	525
BOW, K. E.	730	GRIFFIOEN, W.	152
BOWMER, T. N.	213	GROGAN, G. E.....	525
BREEN, D. C.	221	GRÜNER-NIELSEN, L.....	483
BRINGUIER, A. G.....	492	HAAG, H. G.	176
BRUNNER, E.....	824	HAMADA, Y.	737
CAIN, J.	511	HAMNER, B. W.	727
CAMILO, G.	409	HARDWICK, N. E.	118
CHANDRAIAH, V.....	66	HARDY, F. J.	728
CHANG, T.-C.....	501	HATANO, S.	332
CHAPIN, J. T.	421	HATCH, N. S.	571
CHARLES, Y.	464	HATTORI, T.....	708
CHARUK, B.	409	HAYANO, T.	312
CHEN, H.-J.	501	HAYASHI, Y.....	346
CHEN, T.	807	HEENS, B.	550
CHENG, M.	516	HEERY, J.	755
CHOU, S.-H.	476, 565	HEINO, E.-L.	205
CHU, T. C.	292	HEINO, M. T.	385
CLERICO, G.	184	HILLBERG, J.	205
COONS, S.	695	HIRAMATSU, H.	31, 51, 578
COTTINO, E.	184, 666	HIROOKA, A.	20
CURADO, P. J. P.....	650	HIROSE, J.	555
DA MOTA, J. R.	471	HOGARI, K.	20
DALLAS, G.	199	HOKANSSON, A. S.	672
DAMMERT, R. C.	205	HOPLAND, S.	780
DE ARAGÃO, B. J. G.	650	HORE, L.	79

Name	Page	Name	Page
HORSKA, J.	687	KORALEK, A. S.	221
HOSNER, J.	416	KOSILEK, J. H.	248
HOSOTANI, K.	714	KOYASU, O.	737
HSIAO, C.-M.	501	KUBO, Y.	708, 764
HSIEH, C.-H.	476, 565	KUHN, L.	170
HSING, K.	79	KUNIYOSHI, C.	585
HSU, H.-P.	476, 501, 565	KUROSAWA, Y.	148
HUANG, Y.	506	KUWAKI, N.	101
HULIN, J.-P.	157	KUZUSHITA, H.	714
HWANG, J.-J.	749	KWON, O.-J.	393
HWANG, Y.-H.	476, 565	LAIL, K.	658
IIO, T.	714	LAIR, O.	550
IMADA, Y.	775	LAUMER, J. W.	560
IMAMURA, K.	714, 775	LAURIA, L. M.	650
IMAZU, N.	324	LAZARINI, R.	93
ISACSSON, M.	297	LEE, B.-G.	141
ITO, Y.	359	LEE, H.-S.	749
IWAKURA, D.	578	LEECH, J. R.	807
IWASHITA, K.	340	LEGROS, F.	722
IWATA, H.	20	LESTEN, K.	255
JACKSON, K. W.	66, 118	LETOUT, P.	722
JALURIA, Y.	700	LETOUT, P. P.	721
JAUHIAINEN, E.	789	LEW, K.-J.	393
JEON, Y.-H.	393	LI, J.	672, 687
JIE, X.	340	LIBERT, J.	464
JOLY, B.	157	LIESE, W.	176
JONES, R. K.	488	LII, J.-C.	501
JÖRGENSEN, J.	297	LIN, H.-F.	476, 565
KAINO, M.	764	LIN, J.-C.	476, 565
KAMATA, Y.	25	LIN, Y.-C.	476, 501, 565
KAMBE, H.	25	LINDHOLM, E.	687
KAMIKURA, Y.	31, 51, 578	LINDHOLM, E. A.	672
KANBAYASHI, S.	101	LOGAN, E. R.	12
KANDA, R.	317	LUKER, M. D.	730
KANEKO, K.	364	LUZ, A. M. D.	650
KAPRON, F. P.	55	LY, H.	66
KATAYAMA, M.	764	MACK, H.	401
KATSUKI, S.	352	MAEYASIKI, H.	352
KATSURASHIMA, W.	165	MAGLIO, M.	666
KAWANISHI, N.	644	MAHLANDT, E.	852
KELLER, D. A.	409	MANCARELLA, F.	184
KERUMA, H.	459	MARTINSSON, H.-B.	205
KERY, S.	872	MATAI, R.	506, 511
KILGALLEN, S.	720	MATSUOKA, R.	25
KIM, J.-H.	598, 749	MATTHIJSSE, P.	87
KIM, S.-H.	393	MCGUINNESS, H. A.	221
KIM, Y.-S.	141	MCKENNA, D. F.	452
KIMURA, N.	459	MENDES, E. C.	471
KINARD, M. D.	118	MERRETT, R.	429
KINCAID, J.	233	MEYER, J. C.	636
KISH, P.	431	MIKAMI, M.	25
KITAMURA, Y.	165	MILITARU, C.	605, 614
KLUG, R.	438	MILLO, S.	650
KNOP, W.	621	MILLS, G. A.	529
KNUDSEN, S. N.	483	MITSUHASHI, K.	312
KOBAYASHI, I.	31, 51, 578	MIURA, M.	5
KOBAYASHI, K.	364, 737	MIYAMOTO, M.	112, 127, 312, 737
KOMIYA, Z.	680	MIZUGUCHI, H.	5
KONDA, E.	31	MOHR, S.	248
KONSTADINIDIS, K.	66	MONTALTI, F.	629

Name	Page	Name	Page
MOORE, N.	695	RAVET, F.	550
MOORJANI, S.K.	72	REGISTER, J.	755
MORGANTI, U.	184	REITG, J.	723
MORIKAWA, G.	165	RICHAUME, F.	157
MORIKAWA, R.	317	RISCH, B.	409
MORIMOTO, M.	51	RISCH, B. G.	199, 795
MOYERS, K. W.	213	RIVARD, D.	157
MU, Z.	511	ROGESTEDT, L.	205
MUKASA, K.	51	ROSKO, J.	409
MUNDAY, S.	409	ROUSE, D.	409
MURAKAMI, Y.	332	RUBINO, R.	708
NAGASAWA, S.	332	RUEGENBERG, G.	621
NAGATOMI, O.	317	RYBINSKI, V.	240, 436
NAITO, Y.	680	SAEKI, M.	764
NAKAI, H.	148	SAITO, S.	644
NAKAI, T.	775	SAKABE, I.	165
NAKAMURA, Y.	555, 769	SANTANA, M. R.	118
NAKANO, M.	5	SASAKURA, K.	364
NÄLSÉN, T.	859	SATO, K.	20
NARAOKA, S.	359	SATO, T.	148
NASSAR, H. M.	12	SATO, Y.	127
NATUME, S. S.	446	SCERBO, E. E.	79
NAUR, M.	471	SHELL, J. D.	543
NEMOTO, K.	459	SCOCCO, M. A.	471
NEOGI, S.	795	SHARIFF, M.	430
NETO, J. A. M.	585	SHEN, S. X.	533
NICOLARDOT, M.	369	SHIMIZU, F.	555
NIIMI, S.	769	SHIMIZU, M.	708
NIU, G.	516	SHIMOJI, N.	340
NOMURA, Y.	346	SHIMOMICHI, T.	312
NORLIN, T.	695	SIDDIQUI, S.	66
NORRIS, R. H.	134	SILVÉRIO, L.	446, 585
NORTON, D.	708	SIMÃO, A. M.	446, 585
NOTHOFFER, K.	106, 176, 416	SJÖLIN, K.	297
NOVACK, J. C.	560	SLAVIN, L. M.	79
O'DONNELL, A. G.	221	SMALL, JR, R. D.	134
OBST, A.	260	SODHI, S. S.	525
OHSAKO, T.	459	SOLLENBERGER, N. W.	66
OHZAWA, K.	644	SOLTIS, M.	795
OISHI, H.	101	SON, M.	141
OKADA, N.	112, 127	SPEIGHTS, R. J.	529
OKUDA, M.	359	STAPEL, W.	176
OLENIK, J. J.	452	STAPPERS, V.	157
OMIZU, S.	359	STEINBERG, H.	44
OMURA, K.	148	STINGL, A.	61
OOHASHI, K.	312	SUDO, Y.	459
ORCEL, G.	369	SUGIZAKI, R.	51
OVERTON, B.	409	SUINO, D.	629
PARK, E.-D.	141	SUNKLE, D. S.	452
PARK, K.-T.	598	SUVANTO, M. T.	385
PARMAR, D. S.	846	SUZUKI, J.-I.	644
PASTUSZKA, S.	106	SUZUKI, K.	340
PFANDL, W.	61	SUZUKI, Y.	51
PHILLIPS, R. P.-G.	385	SZWEC, J. R.	66
PITOMBO, C.	650	TABATA, M.	352
POLYMEROPOULOS, C.	520	TAKAHASHI, K.	101
PRIEST, J. R.	492	TAKAHASHI, T.	352
PULLIAINEN, R.	789	TAKAOKA, R.	31, 578
PUNCH, JR., N. A.	72	TAKASE, H.	680
RATTAN, K.	700	TAKAYA, M.	332
RAVELA, J. T.	385	TAKESHITA, J.	555

Name	Page	Name	Page
TAKEUCHI, H.	555	WALKER, JR., C. B.	560
TAKIZAWA, K.	324	WANG, S.	506
TALLANT, D. R.	672	WASSERMAN, S. H.	190
TAMAKI, Y.	324	WATANABE, K.	101, 112, 127
TAYLOR, C. R.	66	WEI, W.	511
TERUI, K.	352	WEIMANN, P. A.	134
TESCHNER, W.	176	WEISS, A.	106, 170, 176, 416
THOMPSON, W.	727	WESSELS, R.	434
THORNTON, J. W.	571	WESTLING, L.	824
TOMITA, S.	20	WHITMAN, R. J.	37
TOUSSAINT, A.	695	WICHMANN, H.	846
TRAVIESO, R.	118	WILHELM, D.	260
TSUNEISHI, K.	708	WILLIAMS, K. E.	72
TU, Y.-K.	476, 501, 565	WOJNO, J. B.	488
UKACHI, T.	680	YAGUCHI, S.	644
UNAMI, Y.	769	YAMAGUCHI, J.	364
UTESCHILL, R.	438	YAMAMOTO, K.	317
VADEN, S.	240, 437	YAMANAKA, M.	112, 127
VAINIO, T.	205	YAMASAKI, D. J.	864
VAINIO, T. P.	385	YAMAZAKI, T.	340
VAN WINGERDEN, A.	152	YATABE, H.	25
VAN'T HUL, C.	152	YEAP, T. H.	275
VANDERLAAN, P.	233, 435	YODER, R.	409
VEYRAT, A.	157	YOSHIZAWA, J.	680
VINTERMYR, I.	285, 305	YOSHIZAWA, T.	364
VOGT, R.	305	YU, W.	506
VOLGGER, O.	728	ZAMZOW, B.	621
WAGMAN, R.	658	ZAMZOW, P. E.	44
WAGMAN, R. S.	12	ZHANG, M.	516
WAKAMATSU, H.	317	ZIEMANN, O.	44